2001

Proceedings of the 23rd Seismic Research Review:
Worldwide Monitoring of Nuclear Explosions

Vol. I

Proceedings of the
23rd Seismic Research Review:
Worldwide Monitoring of Nuclear Explosions

October 2--5, 2001

Jackson Hole, Wyoming

Volume I

Seismic Regional Characterization
Seismic Event Detection, Location, and Identification Methods
Seismic Source Characterization
Regional Wave Propagation

Approved for Public Release; further dissemination unlimited

To view these Proceedings online, visit

http://www.nemre.nn.doe.gov/review2001/ .

LA-UR-01-4454

Table of Contents - Volume I

Seismic Event Detection, Location, and Identification Methods, cont.

Seismic Event Detection, Location, and Identification Methods, cont.

Seismic Regional Characterization

DEVELOPMENT OF CALIBRATION DATASETS FOR SOUTHERN ASIA

Jessie L. Bonner, James M. Britton, and James F. Lewkowicz

Weston Geophysical Corporation

Sponsored by the National Nuclear Security Administration
Office of Nonproliferation Research and Engineering
Office of Defense Nuclear Nonproliferation

Contract No. DE-AC04-99AL66423

ABSTRACT

We have recently initiated the collection of waveform and event catalog datasets for seismic stations in southern Asia, spotlighting the Indian subcontinent, as high-quality regional data for this region continues to be lacking. In the initial phase of our database development, we have focused on the compilation of readily available regional waveform datasets from different sources. In subsequent phases, we will obtain local and regional network bulletins through on-going interactions with our Cambridge University and Indian colleagues. To date, we have collected broadband waveforms from over 1000 events with $m_b > 4.0$, as listed in the Prototype International Data Center (pIDC) Reviewed Event Bulletin (REB) between 01 January 1995 and 01 January 2000 as recorded on the GEOSCOPE station HYB. This station, currently operated by the National Geophysical Research Institute of India, has been in operation in south central India since 1989. We have also started assembling a waveform database for over 300 events recorded on the short-period Gauribidanur (GBA) array between 01 January 1995 and 27 July 1996. The data recorded at HYB and GBA, which are very high quality, supplemented with current studies in the region, will be used to develop improved velocity models as well as to highlight regional propagation effects that can be used for calibrating the stations in the region for future nuclear monitoring efforts. The final product will be an extensive, comprehensive waveform database that can be used to: 1) develop improved velocity models needed for enhanced location capability and 2) increase understanding of regional wave propagation, which is critically important for the development and validation of discriminants for this region of high monitoring interest.

KEY WORDS: seismic waveform data, ground-truth database, 3-D velocity model

OBJECTIVES

Introduction

The primary objective of this project is the development of a seismic research database (DB) for nuclear explosion monitoring in southern Asia. There are large regions of southern Asia, including the Indian subcontinent, for which current real-time seismic waveform data are unavailable for regional seismic characterization studies. However, during the past three decades, several open stations have operated within southern Asia for which data have been compiled at different locations for varying purposes. Thus, one of the tasks of our current research effort will be to determine the location of and gain access to historical databases for stations that have operated (or currently are operating) in southern Asia. The compilation of these data into a single DB with a consistent format will provide access to thousands of events with associated waveforms, preliminary analyses, and metadata. These data could be used to calibrate International Monitoring System (IMS) primary and auxiliary seismic stations in the region or other stations that may be needed to bridge gaps in station/data coverage. Upon completion of the seismic research DB, we will begin integration of the deliverables into the DOE Knowledge Base (KB) for future use and continued development.

The research DB will consist of primary data products, including raw waveform data, phase bulletins and event catalogs, ground-truth (GT) data, phase-pick information, and station data. The database is modeled after the

Lawrence Livermore National Laboratory (LLNL) research DB for the Middle East and North Africa as described by Ruppert *et al*. (1996). Our database will include the following categories of primary data:

- Waveform data for thousands of regional events of varying GT quality.
- Data analyses for determination of GT classification, including location and depth of the event, origin time, and source type.
- Metadata for the waveform data and analysis.
- Catalogs and phase bulletin data obtained from global and local organizations.
- Station information, including location, seismometer response files, and station noise data.

Ruppert *et al*. (1996) compiled additional data in the LLNL DB, which they designated derived data products, such as kriged correction surfaces, surface wave group velocity measurements, travel-time and velocity models, regional discriminants, and additional features that are all beyond the scope of our current DB development. We are currently in the initial phases of the development of this seismic research DB for southern Asia, and we will show the progress made in compiling the waveform data as well as in locating mining explosions as sources of calibration data.

RESEARCH ACCOMPLISHED

Data Retrieval

We have initiated the data retrieval phase of our project to develop a seismic research DB for southern Asia. Table 1 shows the stations for which we have started collecting historical data to populate the database, and during the remainder of the contract, we will continue to seek additional stations/sources of seismic waveform data. We have downloaded all events formed in the Reviewed Event Bulletin (REB) of the Prototype International Data Center (pIDC) between 1995 and 2000 within 25 degrees of the three-component (3-C) station in Hyderabad, India (HYB). HYB is part of the GEOSCOPE network operated by the Institut de Physique du Globe de Paris and has been in operation since 15 January 1989. It includes long-period and broadband sensors, and the data are teletransmitted from the station to the data center in France. The current telemetry status of data from HYB is lagging between 12 and 18 months of the present date. For our purposes, we query the GEOSCOPE data access page (http://geoscope.ipgp.jussieu.fr) for all available channels and components for HYB for events of interest. Figure 1 shows the location of over 1000 seismic events (blue circles) of HYB waveform data downloaded to our database. We only considered regional events with $m_b > 4.0$ for inclusion in the database. Examination of these data shows that, in some cases, only the longer period surface waves are available for analysis, whereas for other events, a full spectrum of body and surface waves is observed. In the upcoming months, we will supplement additional event data for time periods prior to the pIDC operation to complete our waveform database for HYB.

The second station we are currently downloading seismic data for is the Gauribidanur Seismic Array (GBA) in central India. This medium-aperture seismic array has twenty short-period seismometers arranged along two perpendicular arms (i.e. a cross array) with data sampled at 20 samples/sec for each sensor. The array was operated by the Atomic Weapons Research Establishment (AWRE) of the United Kingdom between 04 March 1979 and 27 July 1996, upon which station control and maintenance were transferred to local authorities. Since this transfer, GBA data are no longer readily available for study; however, a great deal of relevant data exist for the array prior to 1996. These data for GBA are available through AutoDRM at the AWRE, and we are in the process of downloading all regional REB events with m_b greater than 4.0 occurring during the last 1.5 years of open station operation. These events are shown in Figure 1 as the red plusses, and it should be noted that there is overlap with the data downloaded for HYB. We will continue to supplement the REB event data at GBA with additional historical events occurring prior to pIDC operation.

Table 1. Historical stations in southern Asia for which waveform data collection has been initiated for development of a seismic research database.

Station	Location	Type	Network	Latitude	Longitude	Operation Dates
HYB	Hyberabad, India	3C	GEOSCOPE	17.417	78.553	15 Jan 1989 - present
GBA	Gauribidanur, India	Array	AWE	13.6042	77.4361	04 Mar 1979- 27 July 1996
SHIO	Shillong, India	3C	USGS-GDSN	25.5666	91.8830	11 May 1978-15 Oct 1985

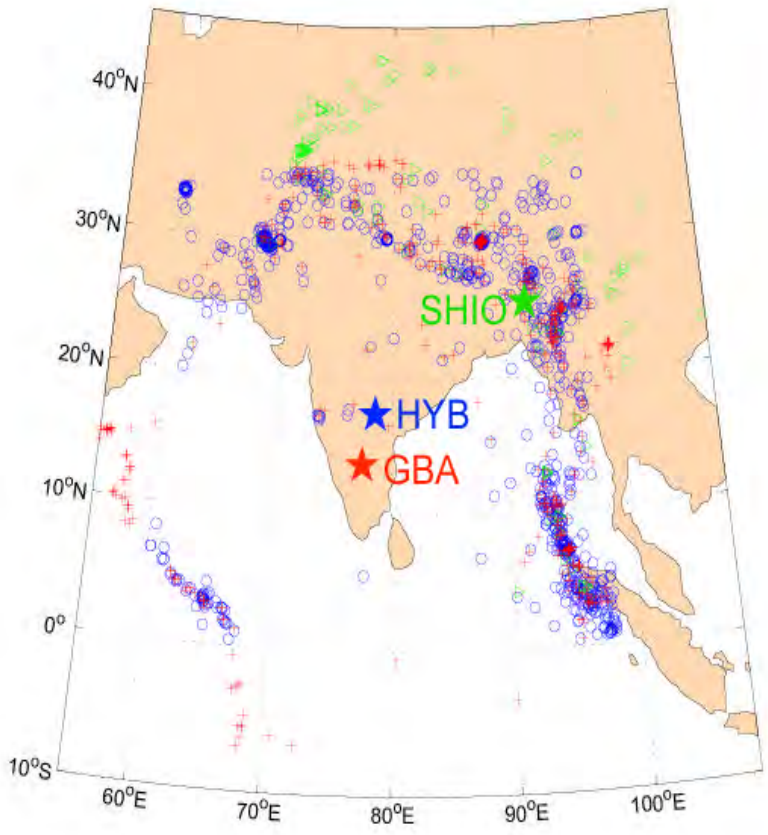

Figure 1. Locations of seismic events in southern Asia for which waveform data are being compiled in the research database. Red triangles show the GBA recorded events; blue circles designate HYB events, and green triangles show the location of SHIO recorded earthquakes.

The final station for which waveform data are being collected is Shillong, India (SHIO). This 3-C station was operated from 11 May 1978 to 15 October 1998 as part of the Global Digital Seismometer Network (GDSN). A limited dataset from SHIO has been compiled at the Incorporated Research Institutions in Seismology (IRIS) Data Management Center (DMC). We searched the United States Geological Survey's (USGS) Preliminary Determination of Epicenters (PDE) earthquake databases for all events within 25° of SHIO ($m_b > 5$) that occurred during periods of SHIO operation. We then used the AutoDRM capabilities at the IRIS DMC to download waveform data for these events (green triangles in Figure 1) for inclusion in the DB.

Database Structure

The data downloaded from each station are converted from their initial format (either SEED or GSE) into CSS3.0 as documented in Figure 2. We currently use MatSeis -1.5 (Harris and Young, 2001) to analyze each waveform. The waveforms are stored as .w files with header information compiled in the wfdisc files. Metadata compiled for each station include station operation dates, channel names and types, instrument specifications and responses, sampling responses, and locations. These metadata are usually in the form of CSS3.0 siteaux, siteremark, instrument, network, sensor, affiliation, site, and sitechan files. In addition to these CSS3.0 metadata files, we also are compiling the seed response files (SEED RESP).

We have access to various bulletins for southern Asia and have begun incorporating these data into the research DB. The pIDC REB bulletins and the USGS PDE catalogs and bulletins are also available through the database. The data are assigned a unique event identification number for relative ease in access.

Database Uses

Surface Wave Group Velocity Data. The database will ultimately provide scientists with the waveform and bulletin data necessary for seismic calibration of southern Asia. Weston Geophysical is currently using the database to aid in the development of velocity models for the region. For each event with measurable surface waves, we are determining group velocity dispersion curves through multiple filter analyses (Dziewonski *et al*., 1969) and phase match filtering (Herrin and Goforth, 1977) as coded by Herrmann (2001). An example of the results of this processing for regional events recorded at HYB is shown in Figure 3. We plan to use the surface wave dispersion curves for a tomographic velocity inversion in order to create a high-resolution 3-D shear wave velocity model of southern Asia.

Mining Explosions as Ground-Truth Data. Location calibration requires accurate travel-time tables that can often be empirically derived from GT data. GT events include earthquakes or explosions for which the uncertainties estimated for their locations are small. Mining explosions are an excellent source of GT data, especially when detailed information (such as blast location, source dimensions, and yield) can be obtained from the engineers responsible for the blasts. As part of the current study, we are actively pursuing sources of active calibration, and we are using the database to examine mining explosions in central India.

To identify mining explosion sources, we began parsing through the HYB data for January and February 1999. It became clear, based upon the number of detections during daytime versus nighttime hours, that over 95% of the routine seismicity recorded at HYB resulted from construction and mining practices (blasting that primarily occurs during daytime hours) at near-regional distances. We began compiling an event catalog for these data for events in which more than two phases could be associated with the same source. This excludes small events in which only the *Lg/Sg* phase is observed. For each catalogued event, we measured the *P*, *Lg/Sg*, and *Rg* arrival times, amplitudes, phase velocities, and polarization backazimuths. Three seismic signatures were repeatedly observed with well-dispersed fundamental mode Rayleigh waves (*Rg*), a phase that suggests the source is shallow (Kafka, 1990) and thus may possibly be a mining explosion. Since these events were repeated on a daily basis only during daytime hours, we assumed these events were the result of mining explosions. Figures 4, 5, and 6 show 3-C waveforms for these events as recorded at HYB as well as the results of the back azimuth calculation on the *Pg* phase. The relative amplitudes of *Rg* on the vertical and horizontal channels provide insight into the varying back azimuths for these three events.

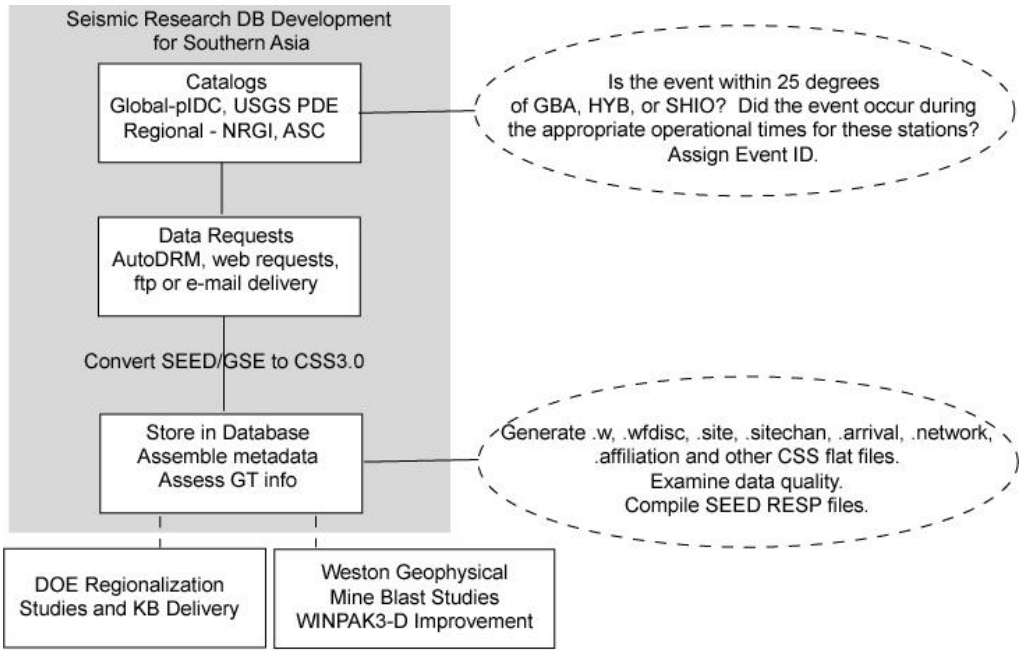

Figure 2. Schematic showing the process by which data are chosen for archiving, downloaded from various network data centers, and archived in the seismic research DB for southern Asia.

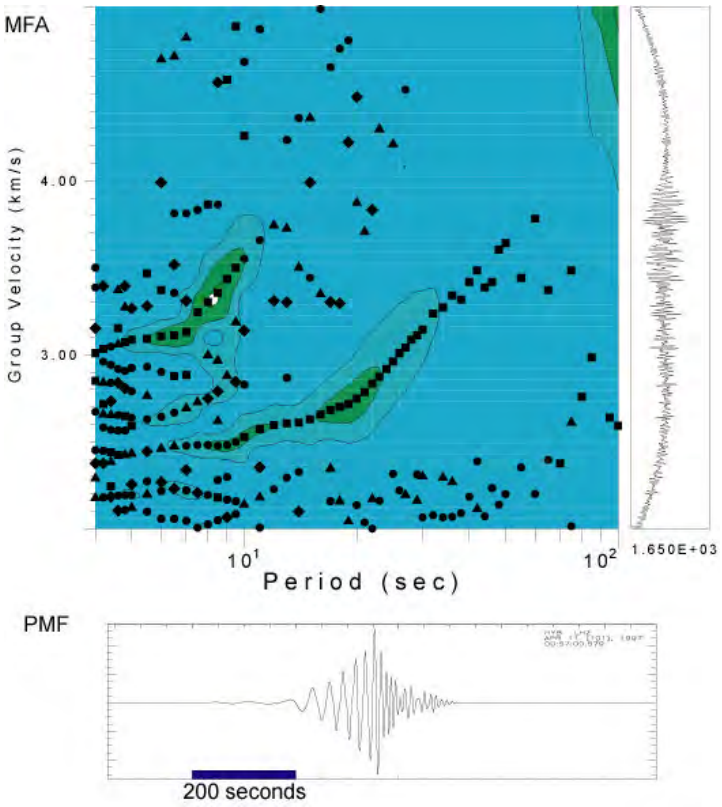

Figure 3. Weston Geophysical is using the seismic research DB to aid in velocity model studies currently ongoing in southern Asia. We are using multiple filter analyses (MFA; upper plot) and phase match filtering (PMF; lower plot) to extract surface wave dispersion curves for a future tomographic inversion.

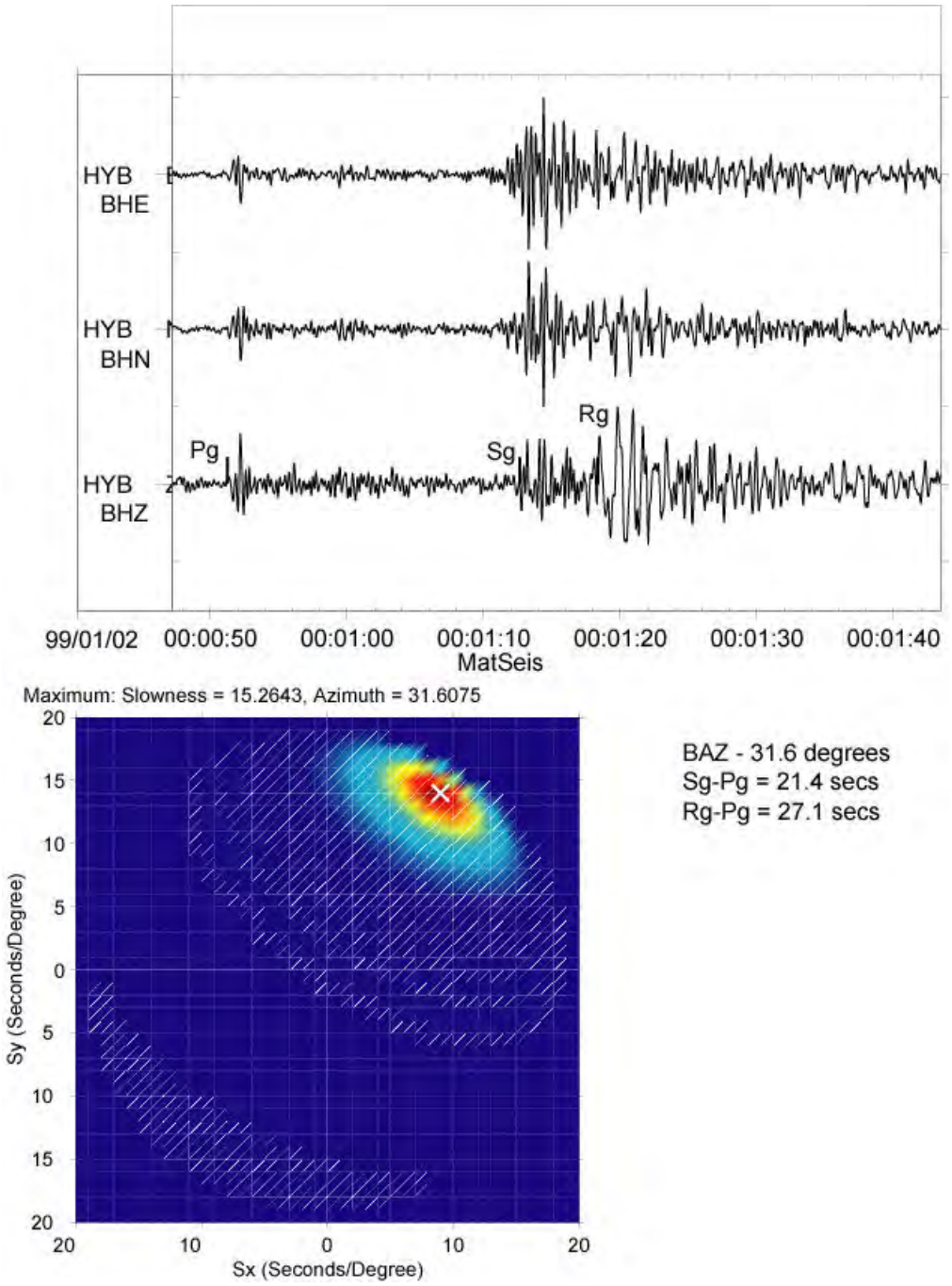

Figure 4. (Upper) Three-component waveforms recorded at HYB from an assumed mining explosion. (Lower) Results of polarization analysis for the Pg phase. Based upon the time separation of the Pg, Sg, and Rg phases and a backazimuth of 31.6 degrees, we locate the event near the Karimnagar coal-mining district.

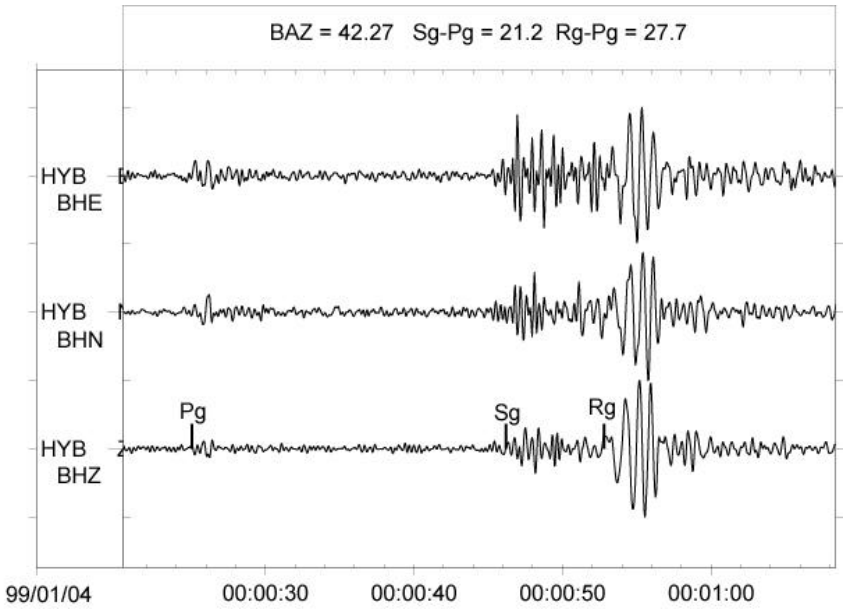

Figure 5. Three-component waveforms recorded at HYB from an assumed mining explosion. Based upon the time separation of the Pg, Sg, and Rg phases and a backazimuth of 42.3 degrees, we locate the event near the southern end of the Karimnagar coal-mining district.

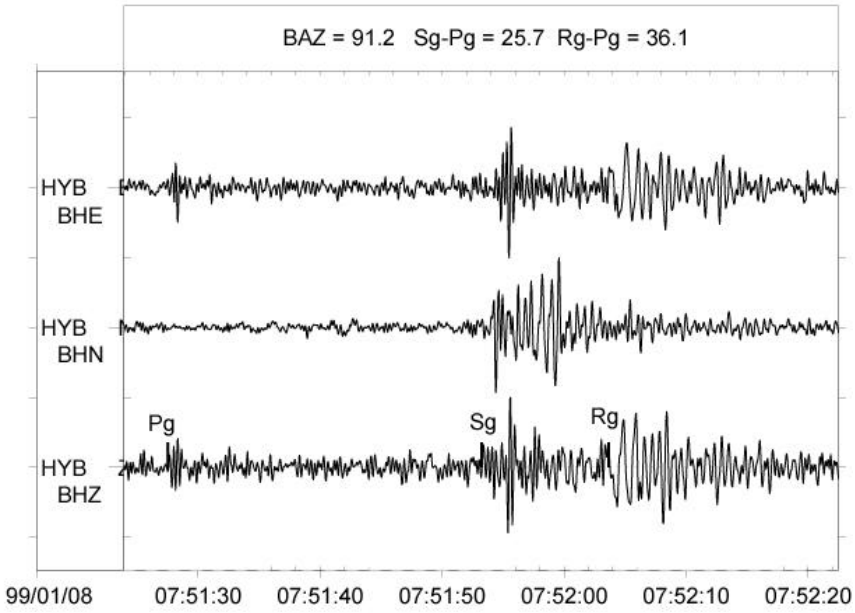

Figure 6. Three-component waveforms recorded at HYB from an assumed mining explosion. Based upon the time separation of the Pg, Sg, and Rg phases and a backazimuth of 91.2 degrees, we locate the event near the Khammam coal-mining district.

We incorporated the backazimuth together with travel-time curves obtained from previous studies (Rai *et al*., 2000) in the central Indian shield region to estimate the epicenter of the explosions. A search of the literature available on mining and mineral extraction in the Andhra Pradesh region (Infobase Pvt. Ltd, 2001) of India found the locations coincide with large coal-mining deposits on the Warangal Plateau (Figure 7). The separation of the locations into two distinct clusters is a result of blasting at mines in the Karimnagar and Khamman districts. We note that there is also a large coal-mining district in Warangal for which we did not observe explosions during our preliminary study. Using contacts with scientists working in the region, we hope to make contact with these mines to obtain detailed source information. These data will offer validation data for a 3-D model that we are currently developing for this region (Johnson and Vincent, 2001).

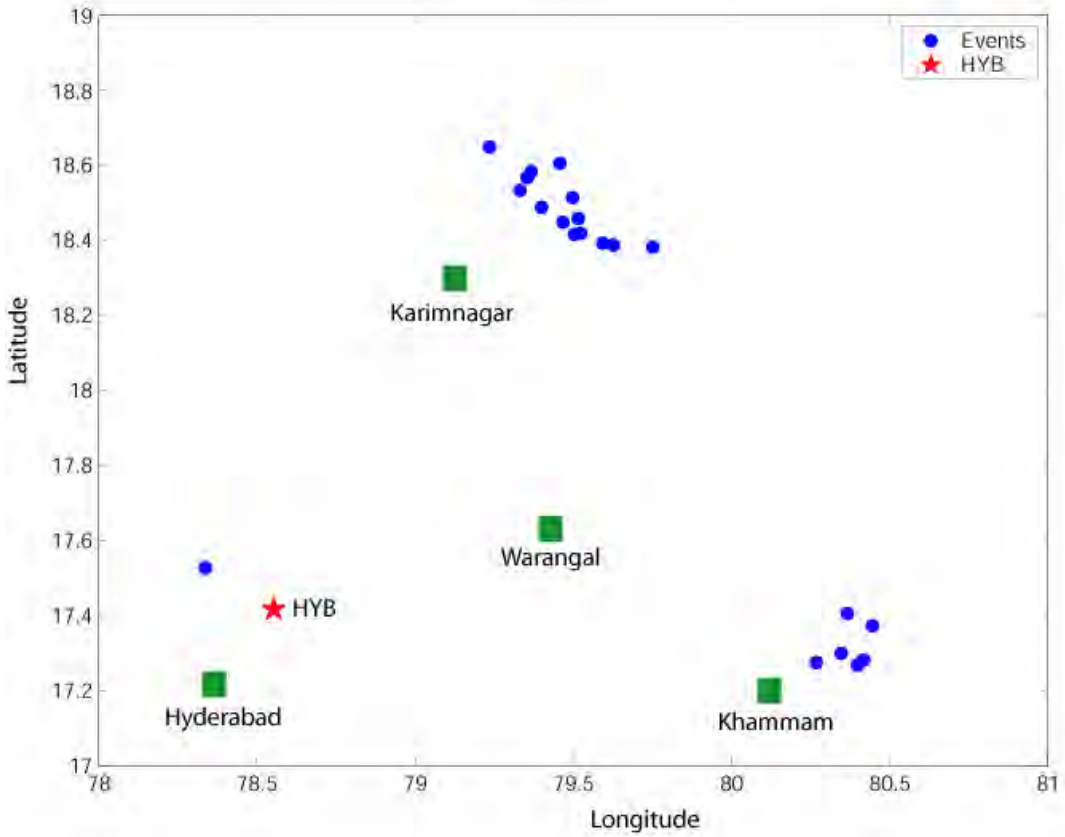

Figure 7. Locations (blue circles) derived from Sg-Pg travel-time tables and polarization backazimuths for mining explosions in southern India as recorded at HYB (red star). The locations correspond to coal mining districts north and east of the cities of Karimnagar and Khammam (green squares). There are also coal mines near Warangal; however, in our initial analysis of the data, we have not located any events near this district.

CONCLUSIONS AND RECOMMENDATIONS

The calibration of southern Asia for the purpose of nuclear explosion monitoring is complicated by minimal amounts of available data (both real-time and historical) within the region. Weston Geophysical is currently developing a seismic research database (DB) that will include as much historical seismic data from stations operating in Southern Asia as can be acquired. During the initial phase of this project, we have downloaded data from over 1200 events to the stations at HYB, GBA, and SHIO, and have included detailed station

metadata with the waveform files. During the remainder of this contract, we will continue to download and incorporate additional seismic data from these and other stations into the DB. The second phase of this project will include the collection of regional ground-truth data from mining explosions in southern Asia. Using contacts with scientists working in the region together with published mining literature for India, we have already identified several mines in the region as candidates for calibration and ground truth data. Ultimately, upon delivery to the KB, the DB will provide scientists with the waveform and bulletin data necessary for seismic calibration of southern Asia.

REFERENCES

Dziewonski, A., S. Bloch and M. Landisman (1969), A technique for the analysis of transient seismic signals, *Bull. Seism. Soc. Am.* **59**, 427-444.

Harris, J. M. and C. J. Young (1996), MatSeis: a seismic toolbox from Matlab, Proceedings for the 18th Annual Seismic Research Symposium, Phillips Laboratory.

Herrmann (2001), Computer Programs in Seismology. St. Louis University, St. Louis, Missouri.

Herrin, E. and T. Goforth (1977), Phase-matched filters: application to the study of Rayleigh waves, *Bull. Seism. Soc. Am.* **67**, 1259-1275.

Infobase Pvt. Ltd (2001), Mineral map of Andhra Pradesh. http://www.mapsofindia.com

Johnson, M. and C. Vincent (submitted, 2001), Development of a 3-D Velocity Model of the India-Pakistan Region for Improved Seismic Event Location, *Bull. Seism. Soc. Am.*

Kafka, A. (1990), *Rg* as depth discriminant for earthquakes and explosions: a case study in New England, *Bull. Seism. Soc. Am*, **80**, 373-394.

Rai, S.S., K. Suryaprakasa, D. Srinagesh, K. Priestley, and V. Gaur (2000), Crustal shear velocity structure of the south Indian shield, Abstracts with Programs for the Fall 2000 American Geophysical Union Meeting, San Francisco.

Ruppert, S.D., T. F. Hank, R. Leach, and J. L. O'Boyle (1996), LLNL Middle East and North Africa research database, Proceedings for the 18th Annual Seismic Research Symposium, Phillips Laboratory, 736-734.

3-D CRUSTAL STRUCTURE IN SOUTHWESTERN CHINA

W. W.Chan[1], C. Y. Wang[2], and W. D. Mooney[3]

Multimax, Inc.,[1] Institute of Geophysics, Beijing, China,[2] United States Geological Survey[3]

Sponsored by National Nuclear Security Administration
Office of Nonproliferation Research and Engineering
Office of Defense Nuclear Nonproliferation

Contract No. DE-FG02-99-ER-82837

ABSTRACT

Using P and S arrival data of 4,625 local and regional earthquakes recorded at 174 seismic stations and associated geophysical investigations, we present a 3-D crustal and upper mantle velocity structure of southwestern China (21 ^{o} - 34 ^{o} N, 97 ^{o} - 105^{o} E). Southwestern China lies in the transition zone between the uplifted Tibetan plateau to the west and the Yangtze continental platform to the east. In the upper crust, a positive anomaly velocity zone exists in the Sichuan basin, whereas a large-scale negative anomaly velocity zone exists in the western Sichuan plateau, which is consistent with the upper crustal structure under the Tibetan Plateau. The boundary between these two positive and negative anomaly zones is the Longmen Shan fault. The Tengchong volcanic region, as well as the strike-slip faults such as the Xianshuihe fault, the Anninghe fault, the northern segment of the Red River fault, and the southern segment of the Xiaojiang fault, are in areas with a negative anomaly zone in the upper crust.

In the mid-crustal depth, we found that there is a general consistency between the negative velocity anomaly and seismicity. The negative velocity anomalies at the depth of 50 km in the Tengchong volcanic area and the Panxi tectonic zone appear to be associated with the temperature and composition variations in the upper mantle. The Red River fault is the boundary between the positive and negative velocity anomalies at 50-km depth. The overall features of the crustal and the upper mantle structures in southwestern China are the low average velocity, the large crustal thickness variations, the existence of a high conductivity layer in the crust or/and upper mantle, and a high geothermal value. All these features are closely related to the collision between the Indian and the Asian plates.

KEY WORDS: crustal structure, southwestern China

OBJECTIVE

In this project, we provide a comprehensive database for all of China. Digital seismic waveform data from the newly operational China National Digital Seismic Network (CNSDN) will be analyzed along with the seismic bulletins prepared from this network. Tomographic inversion will be performed to obtain regional three-dimensional velocity models for calculation of travel-time correction surfaces.

RESEARCH ACCOMPLISHED

Southwestern China lies in the transition zone between the uplifted Tibetan plateau to the west and the Yangtze continental platform to the east. In this paper we present a 3-D crustal and upper mantle velocity structure of this region of China (21° - 34°N, 97° - 105°E), which is based on the P and S arrival data from 4625 local and regional earthquakes recorded at 174 seismic stations and earlier geophysical investigations. In the upper crust, a positive anomaly velocity zone exists in the Sichuan basin, whereas a large-scale negative anomaly velocity zone exists in the western Sichuan plateau. These results are consistent with the upper crustal structure under the Tibetan Plateau (Ni et al., 1995). The boundary between these two positive and negative anomaly zones is the Longmen Shan fault. The Tengchong volcanic area, as well as the strike-slip faults, such as the Xianshuihe fault, Anninghe fault, the northern segment of Red River fault, and the southern segment of Xiaojiang fault, are

in regions with a negative anomaly zone in the upper crust. For the middle crust, we found that there is a general consistency between the negative velocity anomaly and the seismicity. The negative velocity anomalies at the depth of 50 km in the Tengchong volcanic area and the Panxi tectonic zone appear to be associated with the temperature and composition variations in the upper mantle. The Red River fault is the boundary between the positive and negative velocity anomalies at 50-km depth. The overall features of the crustal and the upper mantle structures in southwestern China are the low average velocity, the large crustal thickness variations, the existence of a high-conductivity layer in the crust and/or upper mantle, and a high geothermal value. All these features are closely related to the collision between the Indian and the Asian plates.

A schematic map of tectonics in southwestern China is shown in Figure 1. The Sichuan-Yuanan region (SYR) is an active transition zone between the Yangtze platform to the east and the Tibetan plateau to the west. It is generally believed that this transition zone was formed 45 Ma when the Indian plate collided with the Eurasian plate. This continental collision created a large-scale tectonic deformation in the Sichuan-Yunnan region that is still ongoing. This is evidenced by the high level of seismicity in this region, which is the most active in China. The major tectonic units in southwestern China are as follows: 1. Bomi-Tengchong Fold System; 2. Zuogong-Genma Fold System; 3. Tibet-Yunnan Fold System; 4. Songpang-Ganzi Fold System; 5. Yangtze Platform; 6. South China Fold System.

Figure 2 shows major faults and seismicity of the Sichuan-Yunnan Region. There are seven major active seismic zones in the SYR: 1. the Longmen Shan seismic belt (i.e. Songpan-Pinwu seismic belt), 2. the Xianshuihe seismic belt, 3. the Anninghe seismic belt, 4. the Xiaojiang seismic belt, 5. the Red River seismic belt, 6. the Lancang-Gengma seismic belt, and 7. the Tengchong -Longling seismic belt. A majority of the suite of large seismic earthquakes (M>7) in the region is associated with these faults. Fan (1978) also indicated that most earthquakes in the region are associated with these fault lines, including the 1970 Tonghai earthquake (M=7.7), the 1973 Lu Fu earthquake (M=7.6), the 1974 Zhaotung earthquake (M=7.1), the 1976 Longning earthquake (M=7.4), the 1976 Songpan earthquake (M=7.2), the 1988 Nanchong-genma earthquake (M=7.6), the 1995 Mengnian earthquake (M=7.4), and the 1996 Lijiang earthquake (M=7.0).

Figure 3 shows the three-dimensional Moho surface map for the Sichuan-Yunnan region. The depths to Moho in the SYR are determined by seismic reflection profiles and Bouguer gravity data. The Moho depth increases from SW to NW in the region. In the southern and SW part of Yunnan, the Moho depth is around 38 km; it increases to about 56 km in NW Yunnan. The Moho depth in the Sichuan Plateau is about 60 km, whereas in the Sichuan Basin, it is around 35 to 40 km. We have adopted the tomographic inversion using a LSQR calculation by Zhao (1991) and Zhao et al. (1992). This method takes into considerations the complex structure of the crustal and upper mantle discontinuities.

This study utilized seismic data from 174 short-period seismic stations in the SYR; the station locations are shown in Figure 4. Not all stations are operating concurrently at all times. The stations in Yunnan are more evenly distributed, whereas those in W. Sichuan are sparsely distributed. Figure 5 shows the distribution of earthquake epicenters in the SYR used in this study, based on a total of 4625 earthquakes between 1982 and 1999. The event locations are adopted from the seismic catalogues from Sichuan and Yunnan. The travel-time readings for the P phases are accurate to 0.1 s while the S phases are accurate to 0.2 s. The majority of these earthquakes are located with location errors within 10 km. Data that are accurate to over 20 km are not included in this study. In order to achieve normal convergence in the tomographic inversion, we have allowed for the following constraints:

1. station azimuthal gaps are within 160 degrees;
2. the least number of P observations is 8 for each earthquake; and
3. the largest travel-time residual is 3.0 sec.

Additional considerations are also taken into account to maximize the coverage of the region. The total number of arrival phases used in this study is 112240 readings. Among them, 65170 are P phases and 47070 are S phases.

We used over 6000 earthquakes from the regional catalogs between the period 1982 and 1999 to compile the P and S travel-time curves for the SYR (Figure 6). At about 220 km, the P phases split into Pbar and Pn. Such a feature is not observable on the S phase data. Over 50% of the phase data are considered as Pn arrivals. Our

tomographic inversion uses a 3-D mesh grid model taking into consideration Moho and crustal discontinuities. The horizontal grids are divided into 0.5-degree spacings between 25 N and 34 W and 97 E and 105 E. The total number of grids is 2550 within the 3-D space. The resolution test uses the checkerboard method of Inoue et al. (1990). The test results on P phases, shown in Figure 7, indicate that the grids at different depths are quite resolvable. For example, the P wave grids at 10 km for most regions are quite resolvable except at the NW region (100.5 W, 28 N) where station-event coverage is sparse. At 30-km depth, the region of poor resolution is more confined than that at 10 km, but the overall resolution is not as good as that at the shallower depths. This reduction in resolution is mainly due to the lack of P phase data refracted from the Conrad discontinuity. Due to the abundance of high-quality Pn phase data, the resolution is quite good at about 50-km depth, comparable to that at the shallower depths.

Three-dimensional models derived from tomographic inversion of P and S wave data are shown in Figures 8 and 9, respectively. SYR has a highly heterogeneous structure with varying topography. The velocity models for as deep as 10 km are related to the surficial structural geology. The lateral heterogeneity in the SYR is characteristic of this region. The velocity in the Basin shows a negative velocity anomaly at the shallow depth of 1 km, whereas at the 10 km-layer, the velocity anomaly is positive. For the western Sichuan Plateau there is a broad region of negative velocity anomaly at 10-km depth. This agrees with the characteristics velocity structure of the adjacent Tibetan Plateau. The Longmen Shan fault is situated at the boundary between the negative and positive velocity anomalies. At the SW flank of this fault, there is an indication of a local positive velocity anomaly. For faults that are associated with strike-slip motion, the velocity model indicates a negative anomaly. These are represented by the Xiansuihe fault and Anning which are quite aseismic. The negative velocity anomaly at the Tengchun region is most likely related to heat flow activities. There is a distinct positive S-wave velocity anomaly at 10-km depth from the west flank of the Longmen Shan fault extending southward to the northern end of the Anning fault. At the 30-km depth (lower crust), most seismic belts in SYR, such as Xianshuihe and Xiaojiang, exhibit negative P-wave velocity anomaly. Similar observations are noted for the S-waves (Figure 9). The Red River fault lies in the transition between positive and negative anomalies. The region in the north shows positive velocity anomaly. The slow velocity in the north agrees with reflection profile studies of Hu et al (1986).

In the upper mantle, the inversion results at 50-km depth show broad negative velocity anomaly in the Panxi orogeny and the Tengchong geothermal region. Reflection profile results agree with our observations in the Panxi region (Xiong, 1986). Moreover, the velocity anomalies are greatly affected by the faults that extend to great depths. For example, the Longmen Shan fault separates the regions with positive and negative velocity anomalies and the Xianshuihe and the Xiaojiang faults are associated with negative velocity anomalies. Nonetheless, the degree of velocity anomalies is less than that in the Panxi region. Similar to the lower crust, the upper mantle P-wave velocity for the major seismic belts shows negative anomaly. As discussed in Figure 6, the S phase travel times do not show as clear a phase separation as the P phases for the mantle refractions, indicating that the shear velocity is less resolvable.

CONCLUSIONS AND RECOMMENDATIONS

Our study indicates strong lateral variations in crustal thickness in southwestern China. The crustal thickness for SYR shows a gradual increase from SE to NW. Near the Burma-China border in the south, the crustal thickness is 38.5 km. The Sichuan Basin has a crustal thickness of 40 km, whereas the crustal thickness of the Sichuan West Tibetan region reaches over 65 km. The crust of the adjacent the Longmen Shan belt differs by up to 13 km in thickness. The thick crust in SYR is definitely associated with the Indian plate collision.

The crust/upper mantle velocities in southwestern China are generally low. The average crustal velocity in SYR is 6.25 km/s. This relatively low average crustal velocity, accompanied by the negative velocity anomaly in the lower crustal and upper mantle layers, are characteristics of an active tectonic region (Mooney and Braile, 1987). The low velocity anomaly at 10-km depth in western Sichuan is similar to that observed for Tibetan Plateau (Ni et al., 1995). The average upper mantle velocity for the SYR is around 7.75 km/s, which is generally lower than the average global Pn velocity of 8.1 km/s. This low velocity is probably related to the heating process (Mooney and Braile, 1989). Possible intrusion of molten material into the lower crust may have caused the low-velocity anomalous zones and caused the Moho to be indistinct. At the same time, the low-

velocity anomaly at the top of the upper mantle has dissipated the reflective energy from the Moho, as observed by DSS profiling in the region (Kan et al., 1986).

REFERENCES

Fan, P. (1978), Outline of the Tectonic Evolution of Southwestern China, *Tectonophysics*, 45, 261-267.

Inoue, H., Y. Fukao, K. Tanabe, and Y. Ogata (1990), Whole Mantle P-Wave Travel Time Tomography, *Phys. Earth Planet. Inter*., 59,294-328.

Kan, R., H. Hu, R. Zeng, W. Mooney, and T. V. McEvilly (1986), Crustal Structure of Yunnan Province, People's Republic of China, from Seismic Refraction Profiles, *Science*, 234, 433-437.

Mooney, W. D. and L. W. Braile (1989), The Seismic Structure of the Continental Crust and Upper Mantle of the Continental Lithosphere, A Global Review, *Reviews of Geophysics*, 25, 723-742.

Zhao, D. (1991), A Tomographic Study of Seismic Velocity Structure in the Japan Islands, Ph.D. Thesis, Tohoku University.

Zhao, D., A Hasegawa, and S. Horiuchi !992), Tomographic Imaging of P and S Wave Velocity Structure Beneath Northeastern Japan, *J. Geophys. Res*., 97, 19909-19928.

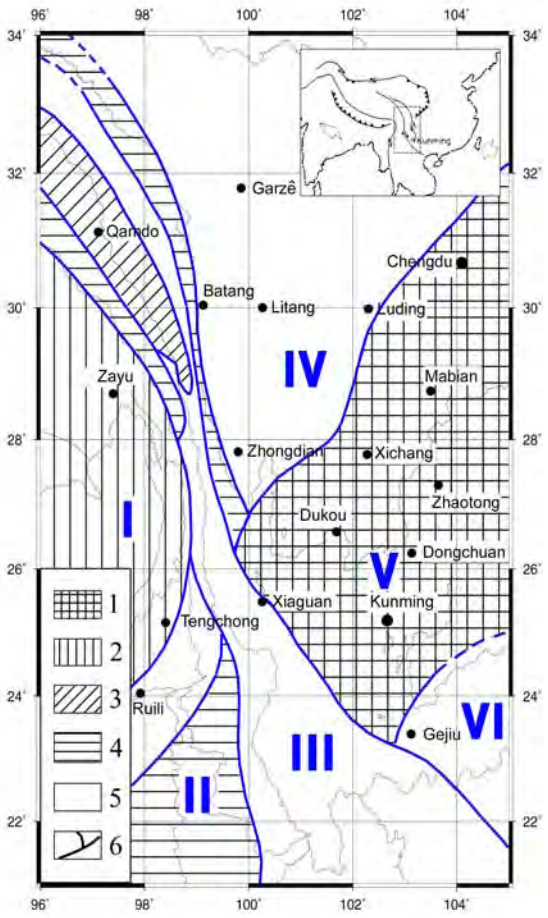

Figure 1. Schematic map of tectonics in southwestern China

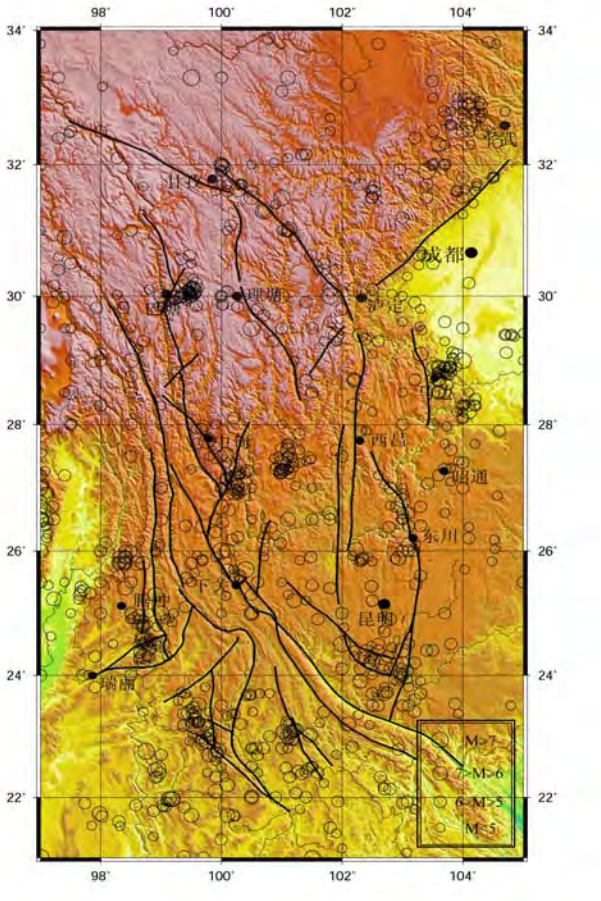

Figure 2. Major faults and the seismicity of Sichuan-Yunnan Region

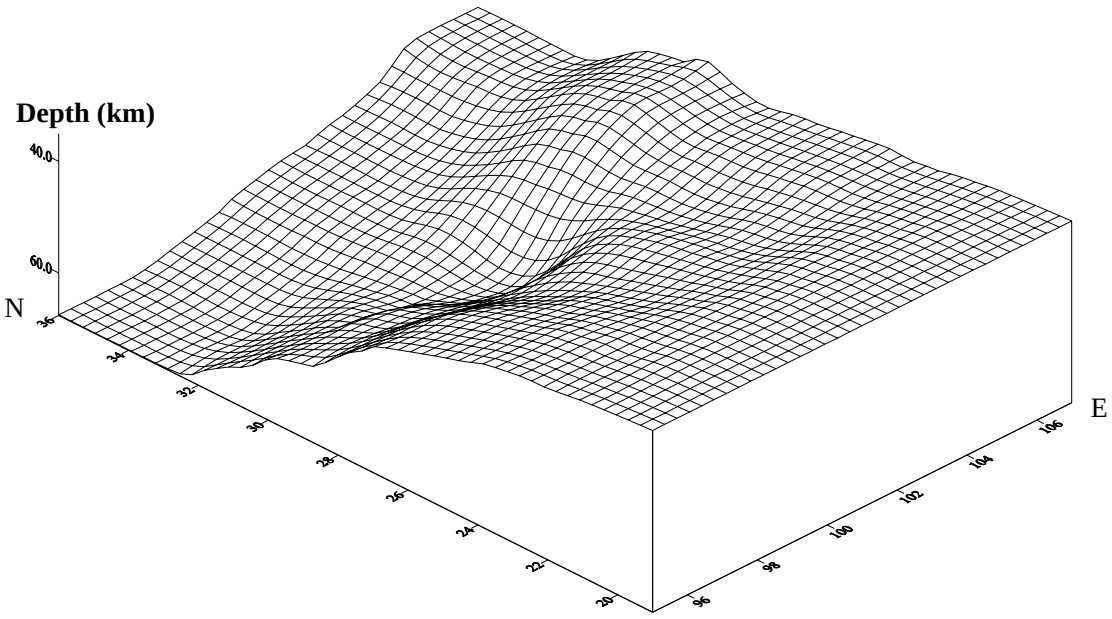

Figure 3. Sichuan-Yunnan Region 3-D Moho surface map

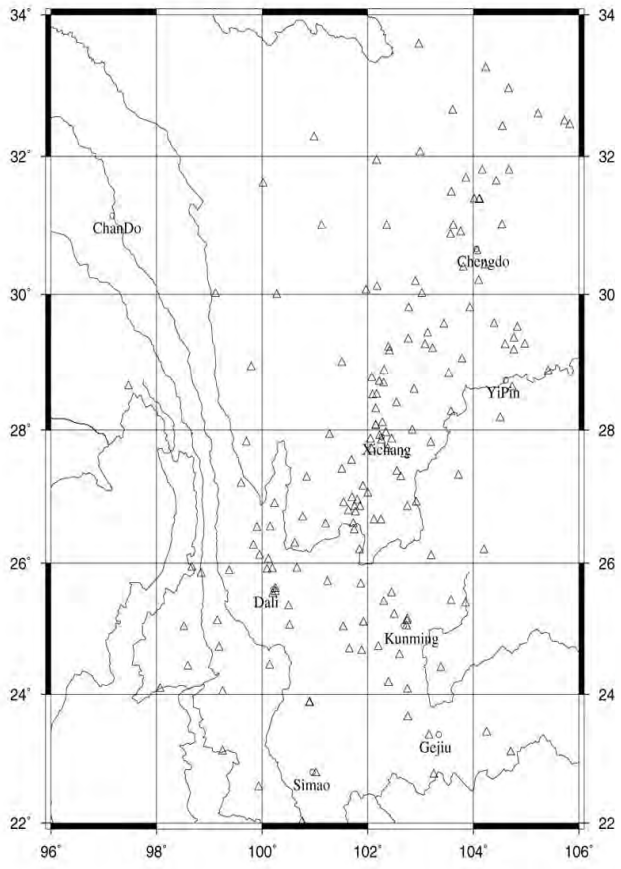

Figure 4. Station locations in SYR

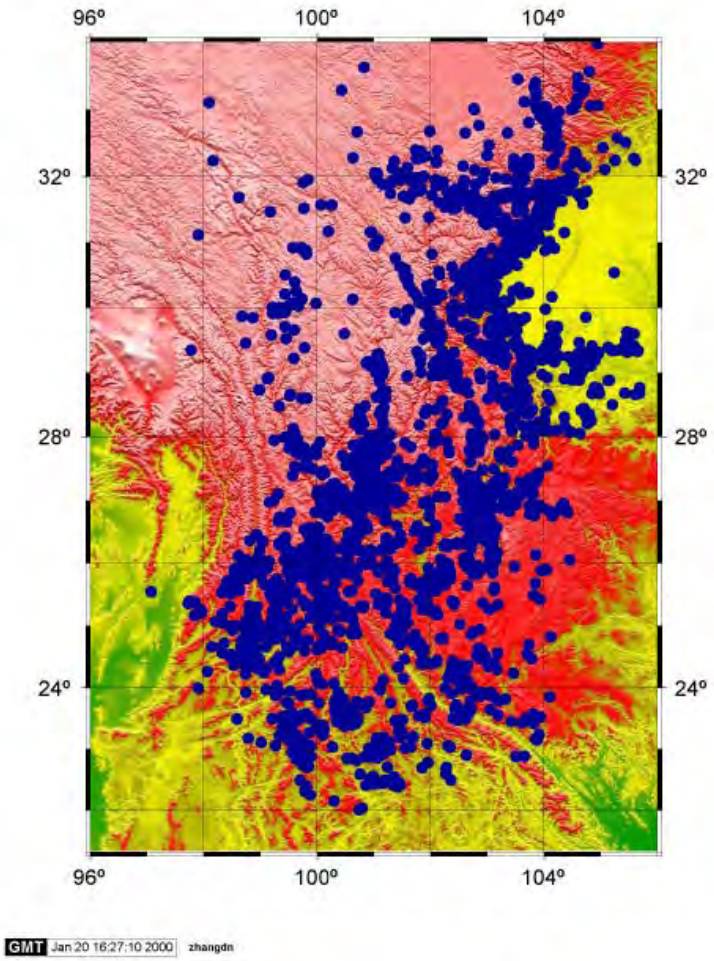

Figure 5. Earthquake distribution in the SYR

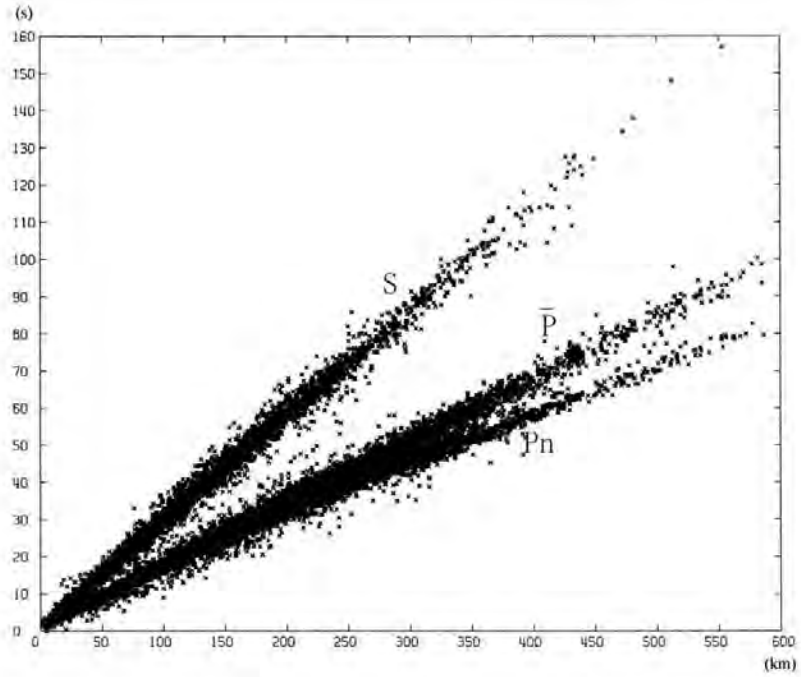

Figure 6. Travel-time curves for the SYR

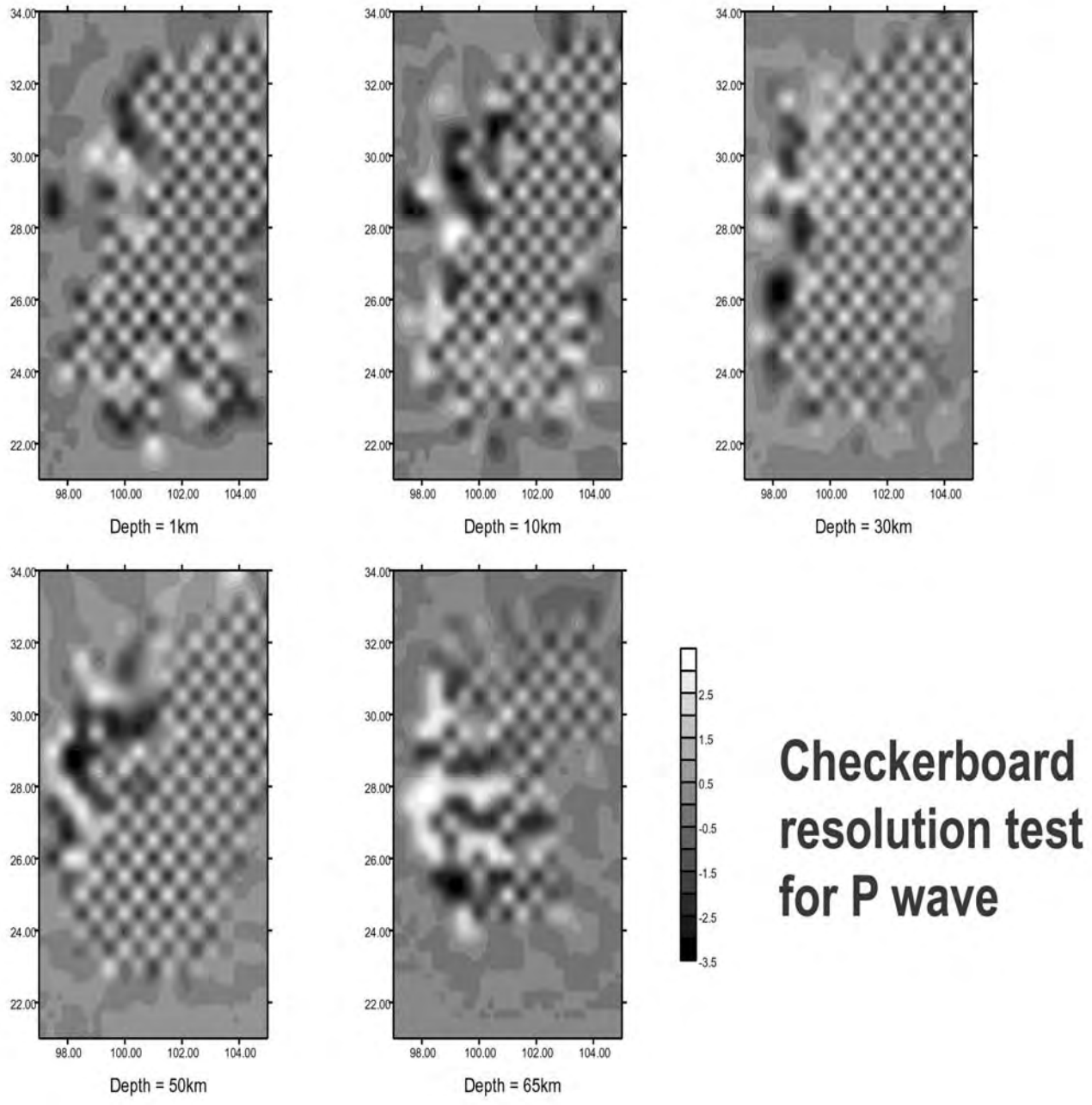

Figure 7. Checkerboard Resolution Test (CRT) on P phases

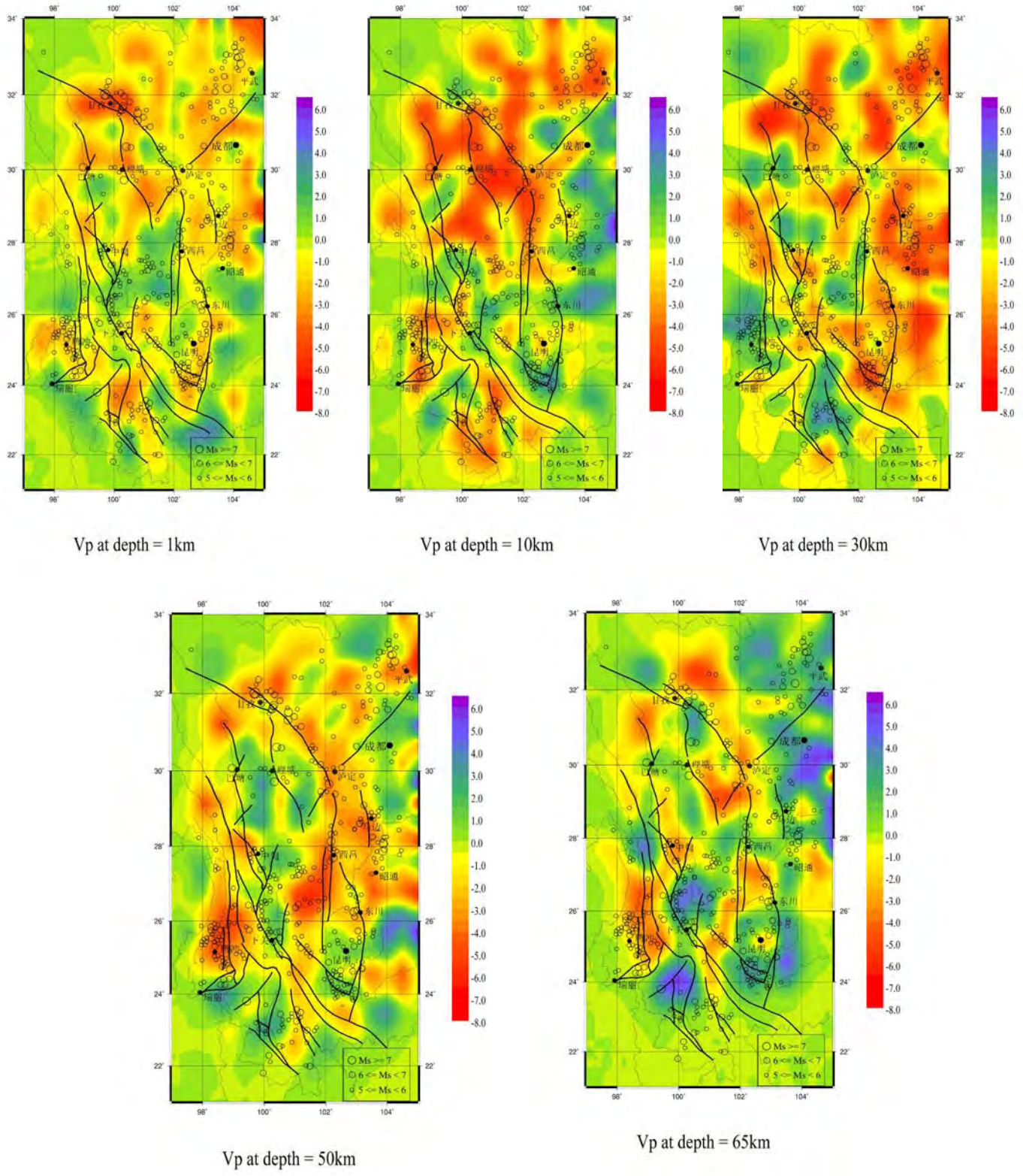

Figure 8. Tomographic inversion results for P waves

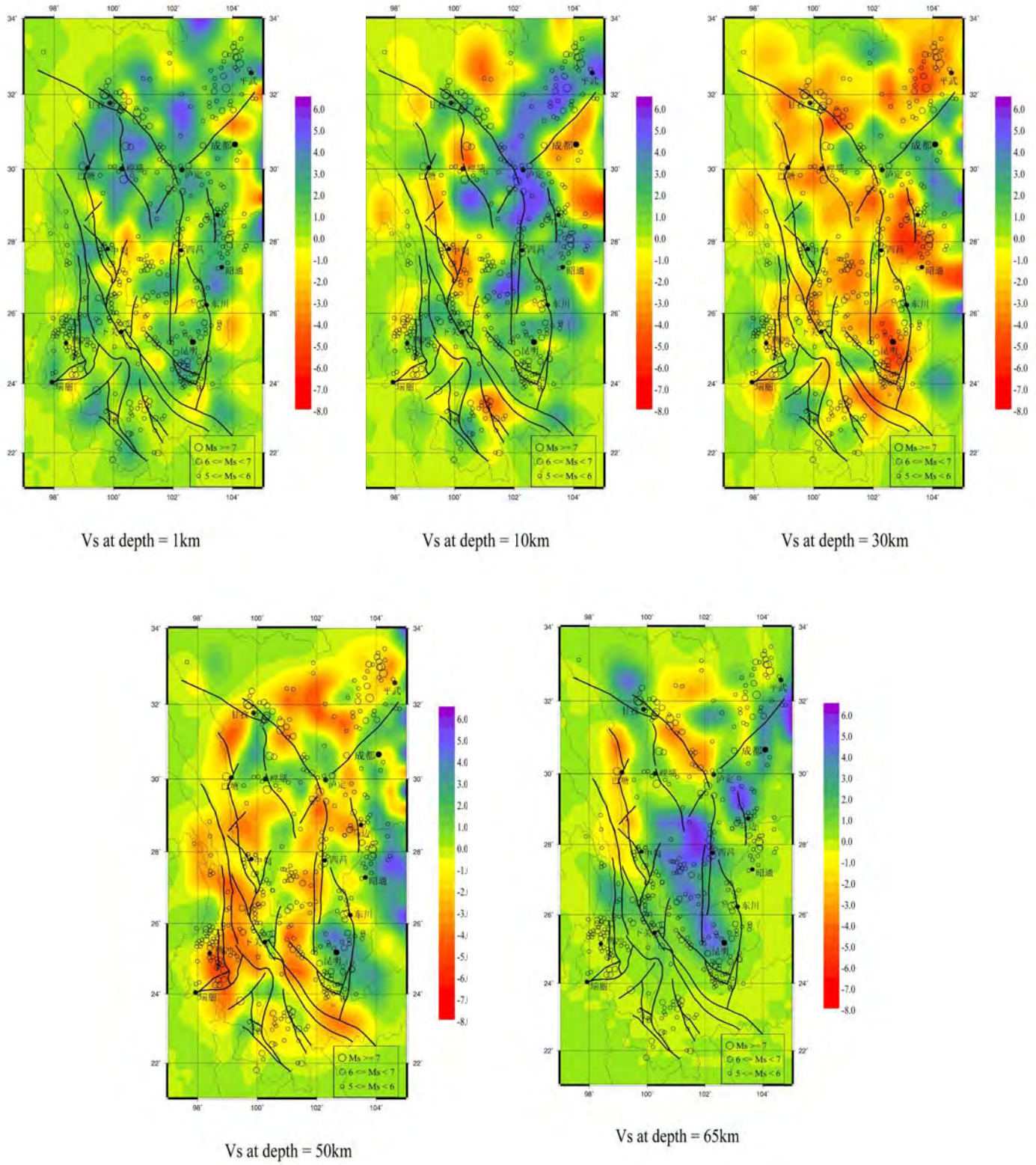

Figure 9. Tomographic inversion results for S waves

REGIONAL SEISMIC DATABASE FOR SOUTHWEST CHINA

Winston Chan, Wenjie Jiao, Robert Wagner, and Indra Gupta

Multimax Inc.

Sponsored by Defense Threat Reduction Agency

Contract No. DTRA01-00-C-0068

ABSTRACT

We have built a database of high-quality 3-component digital broadband and short-period recordings from 23 stations of a regional digital seismic network in southwestern China. There are frequent natural earthquakes and man-made seismic activities in the region, which provides an immense amount of data for regional seismic studies. The database contains mainly the regional digital broadband waveform data recorded at the newly implemented regional digital seismic network. Each seismic station in this network has digital broadband seismographs and short-period seismographs with 16-bit A/D converters, as well as data processing and transfer facilities. The bandwidth of the digital broadband seismograph is about 20 sec - 25 Hz. The major specifications of the instrument are: (1) sensitivity of $1\sim2x10^{-8}m.s^{-1}$/LSB; (2) dynamic range greater than 90dB, (resolution equal to or greater than 2^{-15} for 16 bit); (3) linearity greater than 10^{-3}; (4) time error less than 1 ms. The center of the regional digital seismic network has the function of seismic data collection, storage, processing and maintenance.

This study will report on the seismic characteristics of regional phases in the region. Multimax has obtained and examined the digital waveform data for over 900 seismic events recorded by the regional digital seismic network. We also performed detailed time- and frequency-domain analyses of local and regional signals detected from events for which some ground-truth information about the seismic sources may be known. Our preliminary analyses of the waveforms have shown that such data provide insights to the studies of the excitation and propagation of regional phases in the region. These studies include seismic event locations, Pg/Lg spectral ratio, coda attenuation, identification, and regional structure model from tomographic inversion.

KEY WORDS: regional seismic characteristics, regional digital seismic network, regional broadband waveform database, ground truth

OBJECTIVE

Introduction

The Lg/Pg ratio has been shown to improve in discriminant performance as the frequency content increases, with frequencies higher than 5 Hz, leading to good separation of explosion and earthquake populations in most regions where it has been tested (National Research Council, 1997). For example, in their study of discrimination between Nevada Test Site (NTS) explosions and earthquakes, Walter *et al*. (1995) noted improved performance at higher frequencies. Other examples are the regional discrimination study of explosions and earthquakes in the eastern United States and in southern Russia by Kim *et al*. (1993, 1997), who observed significantly improved discrimination capability of the amplitude ratio P/Lg in the 5- to 25-Hz band than in the lower frequency bands.

Several recent studies (e.g., Baumgardt and Schneider, 1997; Rodgers and Walter, 1997; Walter *et al.* 1997) have observed significant variability of regional phase ratios, such as Pn/Lg or Pg/Lg, which are generally powerful regional discriminants. Their characteristics vary significantly from one tectonic or geographic region to another and may also be strongly dependent on frequency (e.g. Baumgardt and Der, 1994). Southwestern China is known to have complex geology with large Q variations (e.g. Qin and Kan, 1986), so that several

combinations of distinct source and receiver regions will need to be calibrated. It is important to understand and quantify these differences in order to accomplish improved regional discrimination in a region of complex geology, such as southwestern China.

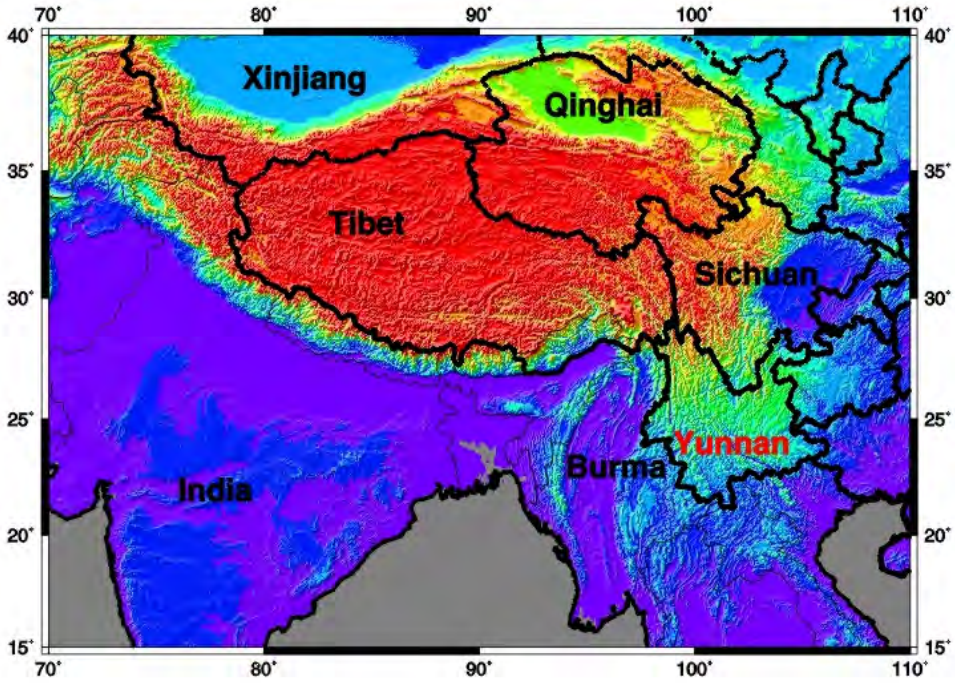

Figure 1. Yunnan and its surrounding area.

Yunnan Province is located at the south segment of the North-South Earthquake Zone in China, close to the Himalaya Orogenic Belt (Figure 1). Tectogenesis is strong in the region. Long and deep earthquake faults criss-cross and spread over almost the entire region, and strong earthquakes occur frequently. As one of the most seismogenically active regions in China, western Yunnan is an earthquake prediction experiment field operated by the China Seismological Bureau. There is a well-developed seismic network in the region and a large volume of seismic data has been collected. Considerable efforts have been made on the study of the geological and geophysical features in the region. Wang, et al. (1994) investigated the 3-D velocity structure under Kunming seismic network and found an uplift of Moho in central Yunnan. They also found that the Red River Fault cuts through the Moho discontinuity. Liu, et al. (1993) studied the 3-D crustal and upper mantle structure in Yunnan and the vicinity and found that there are strong correlations between the upper crustal structure and the topography in the region. Complex crustal velocity structures, including a low-velocity plume and low-velocity layers were also revealed in the study. Lin, et al. (1993) found significant lateral heterogeneity in the crustal structure in western Yunnan based on several DSS profiles. They concluded that the velocity in the crust increases from south to north. Regional seismic characteristics in such an area are of high interest for discrimination studies.

Technical Objectives

The challenge for nuclear explosion monitoring and treaty verification will be to maintain reliable discrimination of small seismic events in diverse regions of the world by using sparsely distributed recording stations. At regional distances, Lg is often the largest seismic phase from both explosion and earthquake sources and may sometimes therefore be the only reliably observed phase from small events. The ratio of S- to P-wave energy (or Lg/Pn and Lg/Pg for regional data) has so far been found to be the most promising regional discriminant for earthquakes and explosions. Use of broadband data, whenever available, will allow us to investigate how low- and high-frequency data may be combined to enhance regional discrimination. The spectral characteristics of regional phases are known to vary drastically from one region to another. It is

therefore important to investigate the variability of regional discriminants in a geologically complex region such as southwest China. Results of the proposed research will lead to more effective and reliable discrimination of small events in various geological settings.

The objectives of this project include: 1) Construction of a digital seismic waveform and ground truth database for southwest China; 2) Regional discrimination studies, including location, spectral ratio, coda, and structure tomography (combined with other projects); and 3) Product delivery. Currently the project is in the middle stage. In the next section, we will mainly discuss the construction of the waveform database and preliminary analyses of the spectral ratio. The tomography results are to be presented separately.

RESEARCH ACCOMPLISHED

The Waveform Database

We have constructed a database of digital waveforms recorded by both the regional digital broadband network and the portable seismic arrays.

Data Recorded at the Regional Digital Broadband Network

In their 1995 Five-Year-Modernization Plan, the Chinese government has proposed efforts to upgrade the Chinese Digital Seismic Network. Additionally, certain regional analog stations should be upgraded to digital recording format. The Chinese Digital Seismic Network consists of national digital seismic networks, regional digital seismic networks, portable digital seismic networks, regional seismic arrays and digital strong earthquake networks. A regional digital seismic network has 30 digital broadband seismic stations, including telemetric ones. The bandwidth of the digital broadband seismograph is about 20 sec - 20 Hz (Figure 2). Each seismic station has digital broadband seismographs and short-period seismographs with a 16-bit data sampling board, data processing and transfer facilities. The major specifications of the regional digital seismographs are: (1) sensitivity of $1\sim2\times10^{-8}$ m.s^{-1}/LSB; (2) dynamic range greater than 90dB; (3) resolution greater than 2^{-15}, 16 bit; (4) linearity greater than 10^{-3}; (5) time error less than 1 ms. The center of the regional digital seismic network has the function of seismic data collection, storage, processing and maintenance.

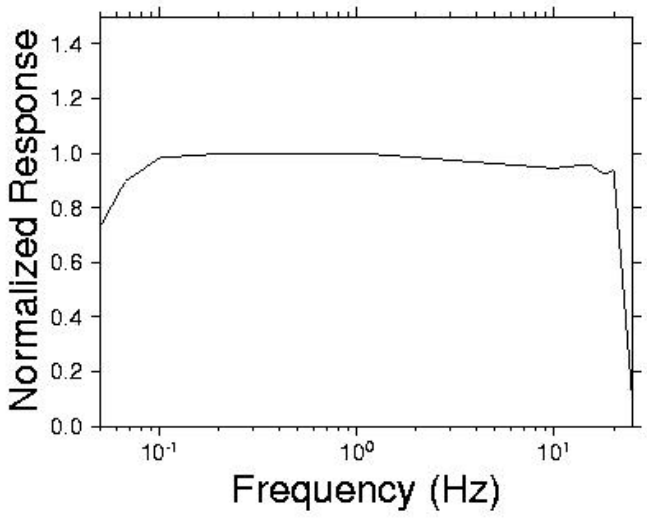

Figure 2. Instrument response of the digital broadband seismographs used in the regional digital seismic network in Yunnan, China.

Twenty-three digital broadband seismographs have been implemented in the Kunming regional digital seismic network in recent years (Figure 3). This is the first fully functional regional digital seismic network in China that provides high-quality continuous 3-componant digital broadband waveform data. The seismographs are

velocity recording with a 50-Hz sample rate, 16-bit sampling board. The network has been in operation since 1997 and a large volume of good quality digital seismic data have been collected. Multimax has obtained and examined the digital waveform data for over 900 seismic events recorded by the Yunnan regional digital seismic network. This is the first time that the high-quality regional digital broadband waveform data from China are available to U.S. seismologists. Figure 4 shows a comparison of the events recorded at this regional network with those reported by the International Seismic Centre, the International Data Centre, and the Institutes for Research in Seismology DMC for the same period. Clearly, the regional network has a much better coverage of the regional seismic events, which are very important for regional seismic studies.

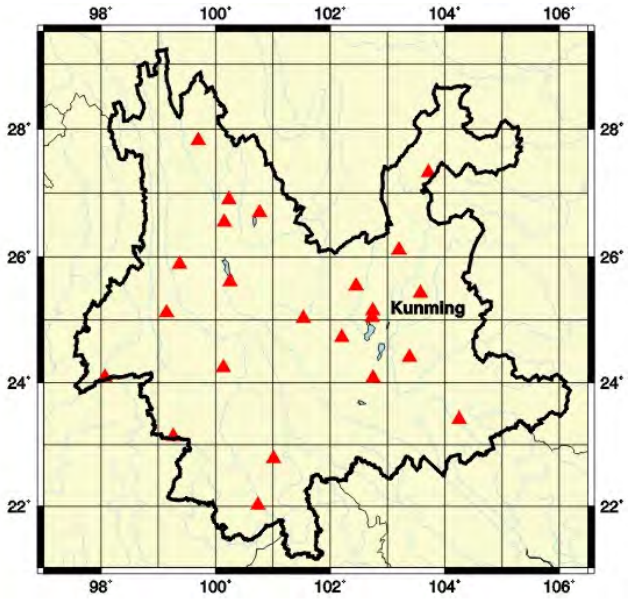

Figure 3. The digital broadband seismic network in Yunnan.

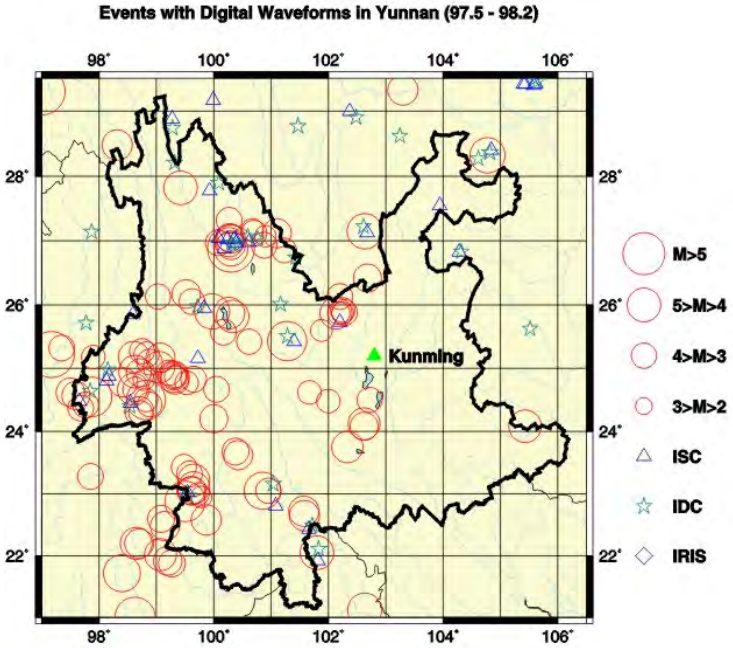

Figure 4. A comparison of the regional events recorded at the Yunnan digital network and those reported in several other global catalogs.

As an example, Figure 5 shows the vertical component of the waveforms recorded by the regional network for a M5.5 local earthquake. A typical 3-component waveform recording for a local event 110 km away is shown in Figure 6. We have established a data retrieval mechanism to access the digital broadband data from the regional digital seismic network through our Chinese collaborators. Over 30,000 waveforms with the same quality have been obtained in this project. There are an abundance of seismicity and mining activities in Yunnan, which provides a valuable data source for the study of regional seismic discriminants.

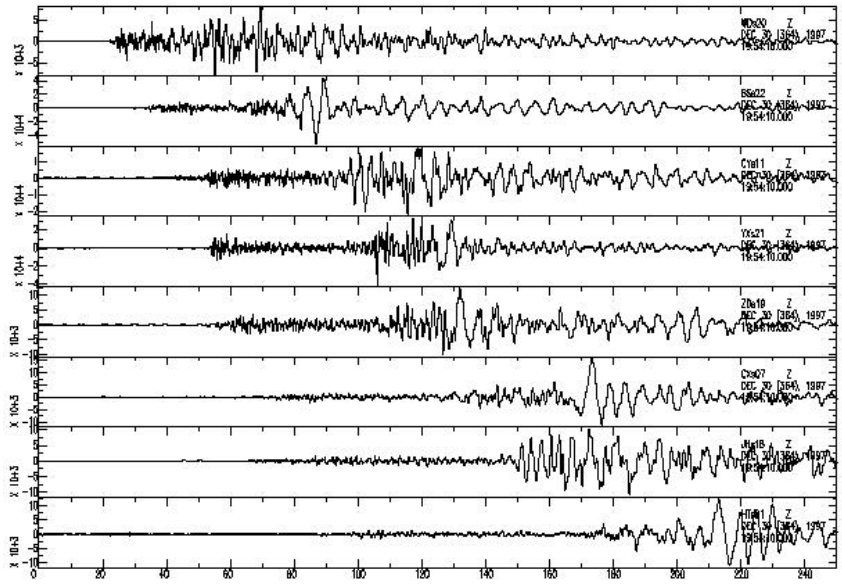

Figure 5. The vertical component of the waveforms of a M5.5 event recorded at the regional digital network.

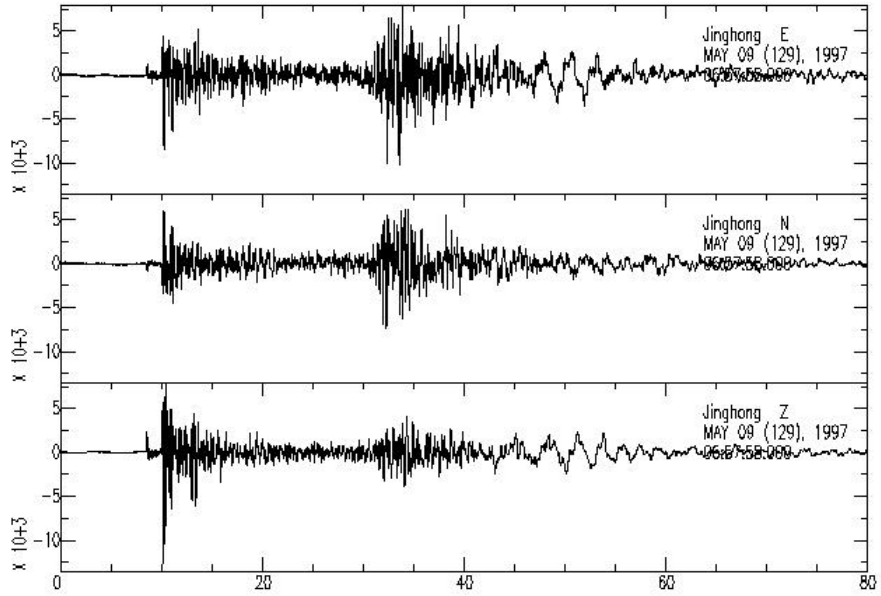

Figure 6. An example of 3-component waveforms of a local event (110 km away) recorded at one station of the regional digital network.

Data Recorded by Portable Broadband Arrays

We have also collected the waveform data recorded at two portable broadband seismic arrays for seven underwater or underground explosions and four local earthquakes. All explosions are controlled ones in southwest China, and are about 1,000 kg TNT. Figure 7 shows the waveform of one underwater explosion

recorded at the portable broadband array. These controlled explosion data are high-quality ground truth information. Figure 8 shows the waveform of a local earthquake recorded by a similar portable array in the same area of the explosions. Such data sets provide very good opportunities for discrimination studies.

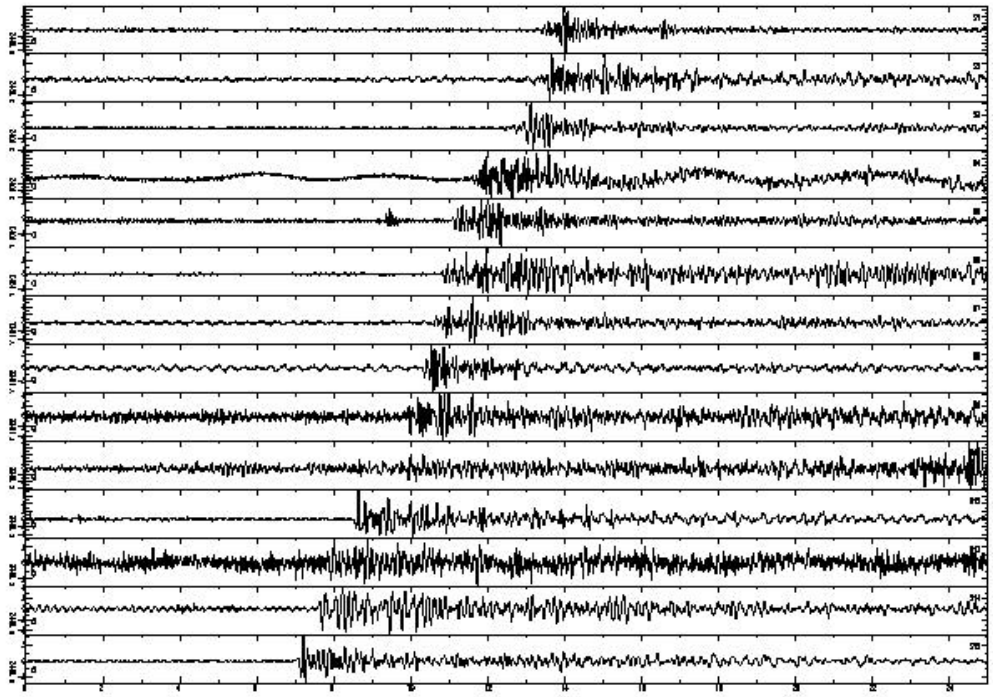

Figure 7. The vertical component of waveforms of an underwater explosion recorded by a portable broadband seismic array.

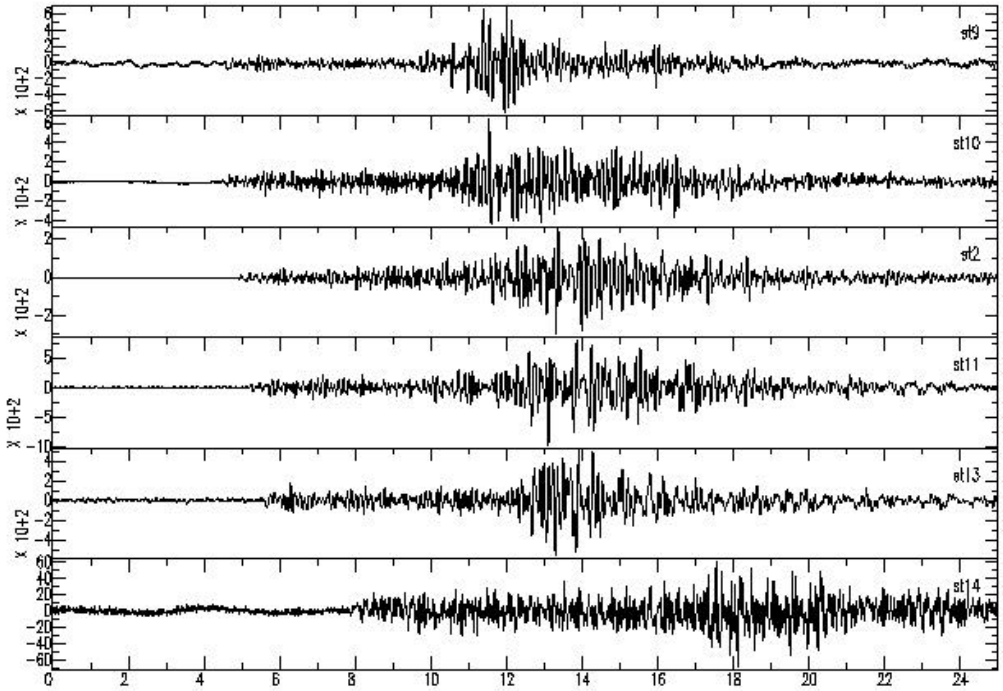

Figure 8. The vertical component of waveforms of an earthquake recorded by a portable broadband seismic array in the same area as the explosion shown in Figure 7.

Preliminary Analyses on the Data Set

Most of the waveform data have been reduced to absolute ground velocity in m/sec. The digital data so reduced are quality controlled, have their P and S-arrival times picked, and are filtered in narrow frequency bands. Then the spectral analysis is conducted in each frequency band. A table is finally created for further multivariate statistical analysis from each filtered waveform which contains event-station information, peak filtered motion, smoothed Fourier velocity spectra, duration, and signal envelope information. To give an example of the spectral analysis, the spectral ratio for a local earthquake and a local explosion are shown in Figure 9 and Figure 10 respectively. All the phase picks are also assembled together with other data obtained by Multimax Inc. into a comprehensive bulletin for the region.

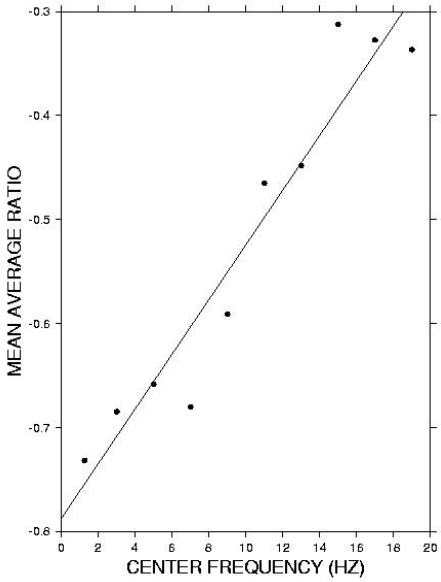

Figure 9. Spectral ratio of Pg/Lg for an earthquake.

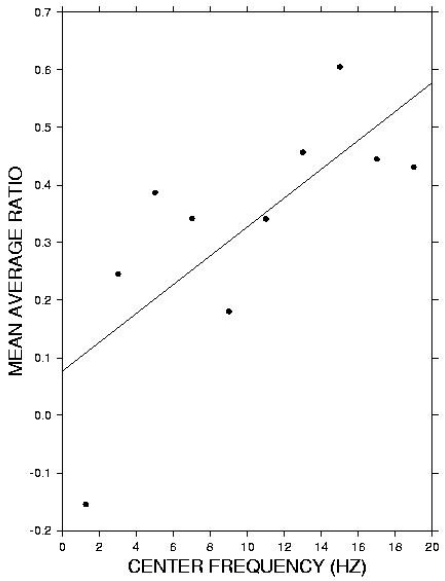

Figure 10. Spectral ratio of Pg/Lg for an underground explosion. Note the difference from the previous figure.

CONCLUSIONS AND RECOMMENDATIONS

In summary, we have accomplished the following tasks in the first stage of this project for studying the regional seismic characteristics in southwest China:

1. **Compiled a regional waveform database**. This is the first digital waveform database from China regional networks. Currently, over 30,000 waveforms reduced to the absolute ground velocity have been archived in the database.
2. **Assembled local bulletins with arrivals and phase picks**. Such bulletins have much better coverage than the national or global bulletins. They are very useful in re-location and tomography studies.
3. **Obtained ground-truth information for seven local explosions**. These data contribute tremendously to the regional discrimination studies.

Preliminary analyses show that these data are of high quality and have broad research applications. Further researches in the next stage will include

1. Evaluate various available parameters for their discrimination capability.
2. Magnitude and distance corrections (Yazd, 1993; Raoof *et al*., 1999; Malagnini, 1999).
3. Multivariate analyses (e.g. Gupta *et al*., 1984; Fan and Lay, 1998).

REFERENCES

Aki, K. (1980), Attenuation of shear waves in the lithosphere for frequencies from 0.05 to 25 Hz, *Phys. Earth Planet. Inter*., 21, 50-60.

Baumgardt, D. R. and Z. A. Der (1994), Investigation of the transportability of the P/S ratio discriminant to different tectonic regions, PL-TR-94-2299, Phillips Laboratory, Hanscom Air Force Base, Massachusetts.

Baumgardt, D. R. and C. M. Schneider (1997), Multivariate canonical correlation of P/S ratios and propagation path parameters for Iran, *Proc. 19th Annual Seismic Research Symposium on Monitoring a Comprehensive Test Ban Treaty* (Editors: M. J. Shore, R. S. Jih, A. Dainty, and J. Erwin), Defense Special Weapons Agency, Alexandria, 14-23.

Boore, D. M. (1983), Stochastic simulation of high-frequency ground motions based on seismological models of the radiated spectra, *Bull. Seism. Soc. Am.* 73, 1865-1894.

Cartwright, D.E. and M. S. Longuet-Higgins (1956), The statistical distribution of the maxima of a random function, *Proc. Roy. Soc. London* Ser. A237**,** 212-232.

Chen, P. S., F. T. Liu, Q. Li, and J. Z. Qin (1991), The lateral inhomogeneity in Yunnan province. China, *Science in China (Series B),* 34 (5), 630-640.

Cui, Z. Z., D. Y. Du, J. P. Chen, Z. Y. Zhang, and L. Y. Huang (1987), The Deep Structure and Tectonic Features of the Crust in Panxi Area, *Chinese J. Geophy*., 30(6): 566-580 (in Chinese).

Fan, G. and T. Lay (1998). Statistical analysis of irregular wave-guide influences on regional seismic discriminants in China, *Bull. Seism. Soc. Am.*, 88, 74-88.

Frankel, A., A. McGarr, J. Bicknell, J. Mori, L. Seeber, and E. Cranswick (1990), Attenuation of high-frequency shear waves in the crust: measurements from New York state, South Africa, and southern California, *J. Geophys. Res*., 95, 17,441-17,457.

Ge, B. R., and K. Y. Yang (1990), Mesozoic-Cenozoic Tectonic Features in Panzhihua-Xichang Area, *Chinese J. Geophy*., 33(1): 64-69 (in Chinese).

Herrmann, R. B., and C. J. Ammon (1997). Faulting parameters of earthquakes in the New Madrid, Missouri region, *Engineering Geology* 46**,** 299-311.

Hu, H. X., et al. (1986), Explosion Investigation of the Crustal Structure in Western Yunnan Province. *Chinese J. Geophy*., 29(2), 133-144 (in Chinese).

Hu, H. X., Z. Y. Lin, Y. J. Bian, C. Y. Wang and L. B. Zhu (1996), Study on the Characteristics of Crust-Mantle Transition Zone in Western Yunnan Province, *Acta Seismologica Sinica*, 18 (4): 444-450 (in Chinese).

Kim, W. Y., D. W. Simpson, and P. G. Richards (1993), Discrimination of earthquakes and explosions in the eastern United States using regional high-frequency data, *Geophys. Res. Lett*. 20, 1507-1510.

Kim, W. Y., V. Aharonian, A. L. Lerner-Lam, and P. G. Richards (1997), Discrimination of earthquakes and explosions in southern Russia using regional high-frequency three-component data from the IRIS/JSP Caucasus Network, *Bull. Seism. Soc. Am***.** 87, 569-588.

Lin, Z., et al. (1993), The Preliminary Interpretation of Deep Seismic Sounding in Western Yunnan, Acta Seismologica Sinica, 15 (4): 427-440 (in Chinese).

Liu, R. F., P. S. Chen, and Q. Li (1993), Three-Dimensional Velocity Images in Yunnan and Its Neibouring District, *Acta Seismologica Sinica*, 15 (1): 61-67 (in Chinese).

Liu, Z., R. B. Herrmann, J. Xie, and E. D. Cranswick (1991), Waveform characteristics and focal mechanisms of five aftershocks of the 1983 Goodnow, New York, earthquake by polarization analysis and waveform modeling, *Seism. Res. Letters*, 62, 123-133.

Malagnini, L. (1999), Ground Motion Scaling in Italy and Germany, *Ph. D. Dissertation*.

National Research Council (1997), Research Required to Support Comprehensive Test Ban Treaty Monitoring, National Academy Press, Washington, D.C.

Qin, J. Z., and R. J. Kan (1986), Q Values and Seismic Moments Estimates Using the Coda Waves of Near Earthquakes in the Kunming and Surrounding Regions, *Chinese J. Geophy*., 29(2): 145-155 (in Chinese).

Raoof, M., R. B. Herrmann, and L. Malagnini (1999), Attenuation and excitation of three-component ground motion in Southern California, *Bull. Seism. Soc. Am.* 89, (Aug. 99) preprint.

Rodgers, A. and W. Walter (1997), Regionalization and calibration of seismic discriminants, path effects, and signal-to-noise for station ABKT, *Proc. 19th Annual Seismic Research Symposium on Monitoring a Comprehensive Test Ban Treaty* (Editors: M. J. Shore, R. S. Jih, A. Dainty, and J. Erwin), Defense Special Weapons Agency, Alexandria, 143-151.

Sun, K. Z., J. W. Teng, D. M. Jin, and Y. Zheng (1987), Q-Value and Its Lateral Variations in Pan-xi Tectonic Belt, *Chinese J. Geophy*., 30(1): 101-104 (in Chinese).

Walter, W. R.,, K. M. Mayeda, and H. J. Patton (1995), Phase and spectral ratio discrimination between NTS earthquakes and explosions. Part1: empirical observations, *Bull. Seism. Soc. Am.* 85, 1050-1067.

Walter, W. R., D. B. Harris, and S. C. Myers (1997), Seismic discrimination between earthquakes and explosions in the Middle East and North Africa, *Proc. 19th Annual Seismic Research Symposium on Monitoring a Comprehensive Test Ban Treaty* (Editors: M. J. Shore, R. S. Jih, A. Dainty, and J. Erwin), Defense Special Weapons Agency, Alexandria, 459-468.

Wang, C. Y., X. L. Wang, and Q. Z. Yan (1994), Tree Dimensional Velocity Structure Beneath the Kunming Telemetered Seismic Network. Acta Seismologica Sinica, 1994, 16 (2): 167-175 (in Chinese).

Xiong, S. B., J. W. Teng, Z. X. Yin, M. H. Lai , and Y. P. Huang (1986), Explosion Seismological Study of the Structure of the Crust and Upper Mantle at Southern Part of the Panxi Tectonic, Belt, *Chinese J. Geophy*., 29(3), 235-244 (in Chinese).

Xiong, S. B., et al. (1993), The 2-D Structure and Its Tectonic Implications of the Crust in the Lijiang£-Panzhihua£-Zhehai Region, *Chinese J. Geophy*., 36(4), 434-444 (in Chinese).

Yazd, M. R. S. (1993), Ground motion studies in the Southern Great Basin of Nevada and California, *Ph. D. Dissertation*, Saint Louis University, 189p.

Zhu, P. D., Y. M. Li, L. M. Zhang, P. Y. Shu and S. H. Liang (1986), On the Study of the Seismic Telemetry Network in South Sichuan and North Yunnan Provinces, *Chinese J. Geophy*., 29(3), 245-254 (in Chinese).

CONSTRUCTION OF 3-D EARTH MODELS FOR STATION SPECIFIC PATH CORRECTIONS BY DYNAMIC RAY TRACING

Vernon F. Cormier

University of Connecticut

Sponsored by the Defense Threat Reduction Agency

Contract No. DTRA01-00-C-0029

ABSTRACT

Three-dimensional models of the crust and mantle structure beneath Area 1 International Monitoring System stations in Eurasia are constructed for use with either asymptotic ray or numerical methods of waveform modeling. The models combine crustal and upper models of varying resolution specified on latitude and longitude grids having variable spacing. Model parameters are interpolated using Delaunay triangulation in 3-D (tetrahedra). Unless accurate narrow-angle crustal reflections and reverberations are required, ray bookkeeping is simplified by making all first-order crustal discontinuities narrow transition zones. Station-specific path corrections (SSPC's) for travel times are obtained in these models by dynamic ray tracing (DRT). DRT provides information on wavefront that can be used to accurately interpolate travel times by a paraxial approximation in the vicinity of end points of rays. By this method travel times are computed in 3-D models at dense grids specified around each IMS station. Each grid point will contain travel time and quantities needed to interpolate travel times spatially at finer intervals. These interpolating quantities can also be useful to event relocation. The grid of values is given as a binary, direct access file. The wavefront curvature information provided for each path includes information needed for path integrated attenuation (t*), geometric spreading, and ray-synthetic seismograms.

KEY WORDS: SSPC's, calibration, travel times, dynamic ray tracing, three-dimensional earth models

OBJECTIVE

Travel-time tables will be generated for paths of regional seismic phases within and to area 1 IMS stations in Eurasia using three-dimensional models of crustal structure. The task assigned to the University of Connecticut is to develop algorithms for constructing three-dimensional models of the crust and upper mantle and to compute travel times and ray theoretical waveforms for regional seismic waves propagating in these models. The results of this work will provide accurate regional phase travel times for improvements in the IDC's location estimates based on data from IMS stations in Eastern Asia. The incorporation of three-dimensional structure will correct for the effects of off-azimuth paths on travel times, which are pervasive throughout this region.

RESEARCH ACCOMPLISHED

Method of computing travel times and SSPC's

Under work completed by the co-Principal Investigator under an AFOSR contract, a three-dimensional dynamic ray tracing program was written to enable prediction of Lg from SmS ray paths in three-dimensionally varying crustal models. Rays were traced by integrating kinematic and dynamic ray tracing equations (Cerveny and Hron, 1980; Cerveny, 1985). The dynamic ray tracing system gives information needed to compute wavefront curvature, which can be used to compute geometric spreading and quantities needed for summation of Gaussian beams, a technique of seismogram synthesis closely related to the Maslov-WKBJ method. These techniques have been applied by the co-PI to a wide variety of applications requiring two-point ray tracing (e.g., Cormier and Beroza, 1987) and ray theoretical synthesis of seismograms in three-dimensionally varying media (e.g., Cormier and Anderson, 1999; Cormier, 1986).

Three-dimensional dynamic ray tracing

Station-specific path corrections (SSPC's) will be obtained from travel times computed by dynamic ray tracing (DRT). DRT provides information on wavefront that can be used to accurately interpolate travel times by a paraxial approximation in the vicinity of end pints of rays. By this method travel times will be computed in 3-D models at dense grids specified around each IMS station. Each grid point will contain a travel time and quantities needed to interpolate travel times spatially at finer intervals. These interpolating quantities can also be useful to event relocation. The grid of values will be given as a binary, direct access file, and will be the first deliverable product of the work. The wavefront curvature information provided for each path will also provide information needed for path integrated attenuation (t*), geometric spreading, and ray-synthetic seismograms.

Travel times for arbitrary 3-D paths

The second stage in this effort will consist of a simple code that retrieves the ray end-point quantities from that file and calculates the travel time of a specified phase from a source by a paraxial approximation. An important advantage of the paraxial approximation is the avoidance of expensive two-point ray tracing, which must find the exact ray-path connecting source and receiver to high accuracy. This will enable rapid retrieval of travel times for any arbitrary path in a fully three-dimensional structure, including the effect of three-dimensional path deviation from a great circle. In the theory of dynamic ray tracing, the paraxial approximation calculates the travel time from position x_o to position x by

$$T(x, x_o) = T(x) + \underline{p} \cdot \Delta \underline{x} + \underline{\underline{H}}\ \Delta \underline{x}\ \ \underline{\underline{M}} \Delta \underline{x}^t\ \underline{\underline{H}}^t ,$$

where p is a vector slowness at the ray end point, M is a 3 x 3 matrix of second derivatives of the travel time field in ray-centered coordinates at the ray end point, x is the Cartesian vector difference between the station location within a grid box and the ray end point in the grid box, and H is a 3 x 3 matrix whose columns consist of the vectors of the ray-centered coordinate basis. The algorithm of the proposed code simply evaluates the

above equation using 25 quantities stored in grid boxes for each IMS station corresponding to paths from all other boxes not containing that station. It is simple to include among these quantities the path integrated attenuation (t*) for regional phases using measurements from models determined from the DSS data analyzed by the University of Wyoming group.

Ray paths need not precisely connect source and receiver. The paraxial equation above accurately corrects the travel time to the time that would be computed for the exact ray, provided that the source and receiver are not too distant from a frequency-dependent region of validity often termed the "paraxial vicinity." In tests of the algorithm for the models and ranges proposed here, use of the paraxial approximation at ray end points to extrapolate travel times within 25 km x 25 km boxes were found to produce travel times accurate to within 0.01 sec.

Previous work (Cormier and Anderson, 1999) modeled the Moho and the boundary between a sedimentary layer and hard-rock layer (basin topography) as surfaces interpolated by splines under tension. The Moho and basement surfaces were assumed to spatially continuous transition zones. With surfaces of discontinuities so modeled, all rays become either (1) turning rays and multiply surface reflected rays within the model or (2) rays that dive deeply, leaving the bottom of the model. This procedure eliminates the need for computing many reflection coefficients and complex descriptions of rays interacting with multiple first-order crustal discontinuities.

Starting three-dimensional models

Starting models for three-dimensional structure were assembled from published models for the crust and upper mantle of Eastern Asia (Fielding et al, 1992; Barazangi et al., 1996; Mooney et al, 1998; Ritzwoller and Levshin, 1998; Sambridge and Gudmundsson, 1998). Each of these models were constructed to satisfy different types of data and reported with differing degrees of resolution. Hence, there is no guarantee at the outset that a hybrid model incorporating features of all these models will be successful in reducing the travel time residuals from ground truth events calculated from laterally homogeneous reference models.

The Cornell model of Barazangi et al. (1998) reports the depth to the Moho and depth to a hard-rock basement in the crust at 0.1 x 0.1 deg resolution. Crust 5.1 by Mooney et al. (1998) incorporates many published local and regional refraction studies in a global 7 layered crust model reported at either a 1 x 1 deg resolution for crustal and basement thickness or a 5 x 5 deg resolution for the detailed 7 layered model. The University of Colorado Model (or CU model) of Ritzwoller and Levshin (1998) is obtained from surface wave group velocities and some Pn velocities. Except for the P velocity at the underside of the Moho constrained by Pn, the P/S velocity ratio is not well constrained. Although Sambridge and Gudmundsson's (1998) Regionalized Upper Mantle (RUM) model is based on a tectonic age regionalization (Jordan, 1981) at a spatially fine scale, it has been inverted from primarily teleseismic data. RUM, as it name implies, is a model of the upper mantle rather than of the crust.

Since previous work by Cormier and Anderson (1999) demonstrated the importance of fine scale moho (10 km and less) basement topography on the progagation of Pn and Lg, it was decided to incorporate into a hybrid model the high resolution model (0.1 deg x 0.1 deg) of basin thickness and Moho topography of the Cornell model. Since Crust 5.1 provides high detail in the vertical direction (up to 7 layers), it was used for structure above the Cornell high resolution Moho. (The high resolution basin structure of the Cornell model has yet to be included in test models.) The RUM model has been used for structure below the Cornell Moho.

Parameterization and interpolation of three-dimensional models

The varying types of data for crust and upper mantle structure, collected at widely different spatial scales, and the highly uneven distribution of ground truth events present a challenge to the parameterization a three-dimensional model for travel time computation. The chosen model parameterization should be flexible enough to be specified at high resolution where data is available and at lower resolution where it is not. Resolution should be high to describe features important to regional wave propagation, such as Moho and basin

topography, but can be lower near interfaces having smaller velocity contrasts and lower with increasing depth in the mantle, where heterogeneity power decreases. To allow a smooth transition from the regional times and waveforms to teleseismic times and waveforms, the parameterization should incorporate the near sphericity of earth and its major structural discontinuities. The parameterization should also be economical in the specification of the number of knots.

The proposed algorithm of kinematic and dynamic ray tracing requires known first and second spatial derivatives of a 3-D model, which can be met by the use of spline interpolation using polynomials of order 3 or higher. Since the investigator had previously applied splines to interpolate model parameters in 3-D, tests were performed to determine whether this type of interpolation could also be applied to the 3-D structure beneath IMS stations. The routine previously used with dynamic ray tracing employed splines under tension at equally spaced knots in Cartesian co-ordinates (Cormier, 1986). The FITGRID[1] code previously employed under tension code was not easily adaptable to our IMS model. Its restriction to equally spaced knots requires cumbersome and constant resampling to incorporate both earth sphericity and spatially variable resolution. In future experiments, the software described by Wessel and Bercovici (1998), which may allow for irregularly spaced 3-D data, will be tested for application to dynamic ray tracing.

The most recent release of the NCAR graphics package[2] has a set of routines named CSAGRID[3] that can interpolate by splines on an irregularly spaced Cartesian grid. Unfortunately, tests showed that without an available tensioning factor in the current version of CSAGRID, the splines very poorly tracked realistic seismic velocity variations within layers. This deficiency could be remedied only be expensive densification of knot points, ultimately making its use as cumbersome as spline routines having regularly spaced grids.

The next and preferred parameterization and interpolation scheme tested is the one used and advocated by Sambridge et al. (1995) in the construction of the RUM model. This scheme parameterizes 3-D earth models by knots connected by tetrahedra. A linear gradient in velocity is assumed for the interpolated quantity within each tetrahedral element, making it possible to analytically integrate within each tetrahedron both the kinematic and dynamic (geometric spreading and wavefront curvature) ray tracing equations. A public-domain software package named qhull (Barber et al, 1996), maintained by the Computational Geometry Center at the University of Minnesota[4] , is available for performing the Delaunay tetrahedral tesselation of a model volume given a set of knots and model values. The file containing model values at knots may be given with knots occuring at any arbitrary order or spacing. Qhull returns a list of index numbers of the 4 knots describing each tetrahedron. Routines for navigating though the tetrahedra are available from Sambridge [5].

Figure 1 shows an example of a hybrid 3-D model constructed from qhull tetrahedrall tesselation using the Cornell Moho, the Crust 5.1 crust, and the RUM mantle. The example is for a 200 x 200 x 200 km block whose surface is centered at Nilore, Packistan. Note the thickening of the Moho to the north of Nilore, an effect of the crustal root that has grown from Indian-Eurasian plate collision. Some spatial variability is also seen in the low-velocity zone given by RUM. The sampling of the low velocities in the upper most crust 2.5-4km/sec needs to be densified to remove some artifacts associated with too broad tetrhedron facets at the surface of the earth.

Ray tracing

Although the tetrahedral tesselation of the model allows analytic integration of the ray tracing equations, intitial tests of travel times have used a Runge-Kutta numerical integration to shoot rays. Figure 2. Shows an example of ray end points shot at uniform increments vertical and azimuthal take-off angles from NIL. Note some effects of three-dimensional structure are evident in the scatter of rays at longer distances. A strong shadow zone is seen around 10-15 degrees. In this distance range, the first arrival is a Pn phase just grazing the underside of the Moho.

CONCLUSIONS AND RECOMMENDATIONS

Additional hybrid 3-D models will will be constructed for testing SSPC's for IMS using the a tetrahedral tesselation described in this report. A denser sampling will be incorporated in the upper 2-3 km of the crust to better describe the known three-dimensional variations in soft sediment cover. To speed-up forward modeling of travel times and dynamic ray tracing quantities, an analytic integration (Menke and West, personal

communcations) for kinematic and, eventually dynamic ray tracing within tetrahedra, will be substituted for the numerical integration currently used. A test of the spline under tension parameterization of Wessel and Bercovici (1998) will also made to see if it offers any greater flexibility in model parameterization compared to the tetrahedral parameterization.

It will also be important to test the accuracy of travel time calculations, which may be affected by the choice of parameterization and the accuracy of paraxial approximations against other methods. A test will be performed with at least one model comparing the results of dynamic ray tracing and the results of the numerical eikonal solution method of Vidale (1988) being used by the MIT led consortium.

The model construction described in this report relies on hybrid models constructed from several global models of the crust and upper mantle. In work during the second year, University of Connecticut, in cooperation with the other members of our consortium, starting hybrid models will be refined to be consistent with ground truth travel times being assembled.

REFERENCES

Barazangi, M., Fielding, E., Isacks, B. & Seber, D., (1996), Geophysical And Geological Databases And Ctbt Monitoring: A Case Study Of The Middle East. In: E.S. Husebye And A.M. Dainty (Eds), Monitoring A Comprehensive Test Ban Treaty, Kluwer Academic Publishers, 197-224.

Barber, C.B., Dobkin, D.P., and Huhdanpaa, H.T., (1996), The Quickhull algorithm for convex hulls," *ACM Trans. on Mathematical Software*.

Cerveny, V., and Hron, F. (1980), The ray series method and dynamic ray tracing systems for three-dimensional inhomogeneous media, *Bull. Seismol. Soc. Am.*, 70, 47-77.

Cerveny, V. (1985), The application of ray tracing to the propagation of shear waves in complex media, In *Seismic Exploration*, (S.Treitel and K. Helbig,, eds) (Geophysical Press, London), 1-124.

Cormier, V.F., and G.C. Beroza, (1987). Calculation of strong ground motion due to an extended earthquake source in a laterally varying structure, *Bull. Seism. Soc. Am.*, 77, 1-13

Cormier, V.F., (1986). An application of the propagator matrix of dynamic ray tracing: The focusing and defocusing of body waves by three-dimensional velocity structure in the source region, *Geophys. J. R. Astr. Soc*., 87, 1159-1180.

Cormier, V.F., and T.S. Anderson, (1999), Efficiency of Lg propagation from SmS ray tracing in laterally varying crustal waveguides, Pure and Appl. Geophys., submitted (preprint download[6]).

Fielding, E., Isacks, B.L., and Baragangi. M. (1992), A Network Accessible Geological and Geophysical Database for Eurasia, *Proceedings of the 14th Annual PL/DARPA Seismic Research Symposium*, PL-TR-92-2210.

Jordan, T.H., (1981), Global tectonic regionalization for seismological data analysis, *Bull. Seism. Soc. Am*., 71, 1131-1141.

Mooney, W.D., Laske, G., and Masters, G. (1998), CRUST 5.1: A global crustal model at 5^ox5^o, *J. Geophys. Res.*, 103, 727-747.

Ritzwoller, M.H., and Levshin, A.L., (1998), Eurasian surface wave tomography: Group velocities, *J. Geophys. Res.*, 103, 4839 – 4878.

Sambridge, M, Braun, J., and McQueen, H., (1995), Geophysical parameterization and interpolation of irregular data using natural neighbours, *Geophys. J. Int.*, 122, 837-857.

Vidale, J., (1988), Finite-difference calculation of traveltimes: Bull., Seis. Soc. Am., 78, 2062-2076.

Wessel, P., and D. Bercovici, (1998). Gridding with splines in tension : A Green function approach, *Math. Geol.*, 30, 77-93.

Sambridge, M., and Gudmundsson, O, (1998), A regionalized upper mantle (RUM) seismic model., *J. of Geophys. Res.*, 103, 7121-7136.

Endnotes:

1. http://www.scd.ucar.edu/softlib/FITPACK.html

2. http://ngwww.ucar.edu/ng4.2/index.html

3. http://ngwww.ucar.edu/ngdoc/ng4.1/ngmath/csagrid/csahome.html

4. http://www.geom.umn.edu/locate/qhull

5. http://rses.anu.edu.au/seismology/projects/RUM/rum_download.html

6. http://coulomb.geol.uconn.edu/~cormier/pageophrays.pdf

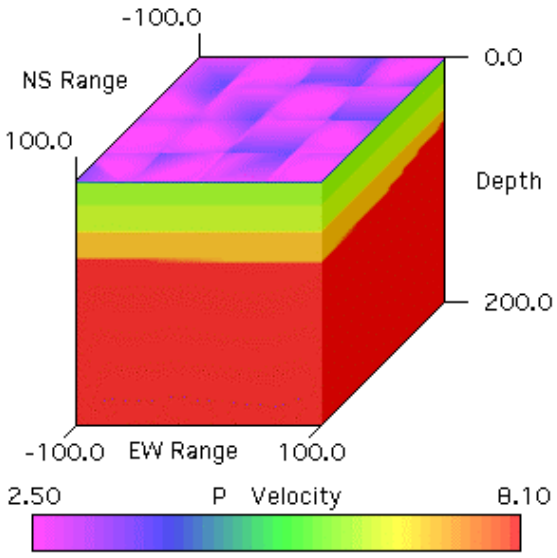

Figure 1. Three-dimensional crust and upper mantle structure beneath Nilore, Pakistan (IMS station NIL) assembled from the Cornell Eurasian Moho, Crust 5.1, and the RUM upper mantle. Note the tetrahedral parameterization in the uppermost 4 km needs to be densified to better describe shallow structure and eliminate artifacts.

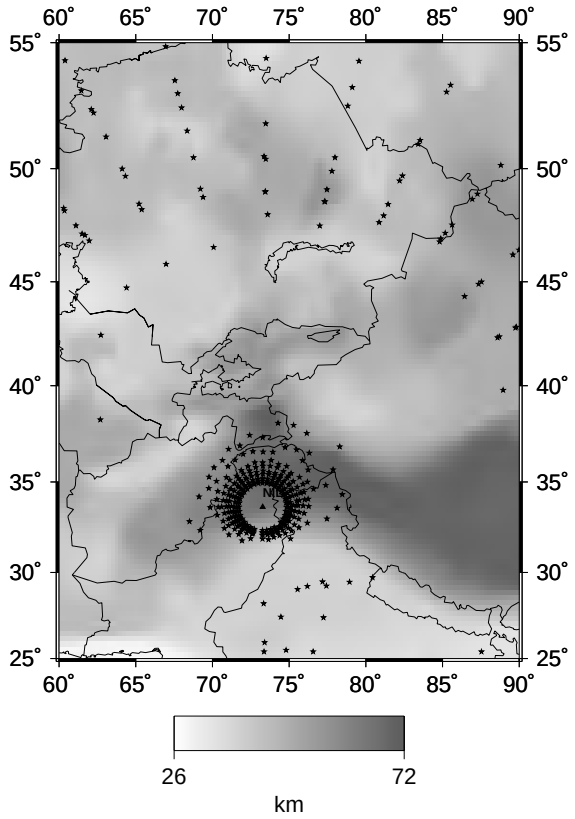

Figure 2. P Ray endpoints in the vicinity of NIL for rays shot at constant increments of vertical and azimuthal take-off angles. The Cornell Eurasian Moho topography is superposed. The hybrid 3-D model in which rays were shot was parameterized by tetrahedra of variable size and its size is 25° lat x 25° long x 700 km deep. Spacing of knots at tetrahedron vertices ranged from 10 to 50 km.

TOMOGRAPHY AND LOCATION PROBLEMS IN CHINA USING REGIONAL TRAVEL-TIME DATA

Thomas M. Hearn and James F. Ni

New Mexico State University, Physics Department

Sponsored by Defense Threat Reduction Agency

Contract No. DTRA01-99-C-0016

ABSTRACT

Phase data from the Annual Bulletin of Chinese Earthquakes (ABCE) are being collected and used for tomographic inversion and event location problems within China. So far, we have seven years of data in computer form and six more in catalog form. Current efforts focus on regional tomography of China, comparing locations between the ABCE and other earthquake catalogs, and developing station corrections for International Monitoring System (IMS) stations in and around China.

We used the Pn phase data from the ABCE catalog to image the uppermost mantle velocity and anisotropy structure beneath China. Raypaths cover most of central and eastern China; coverage in western China and Tibet is poor. The data quality is exceptional, with Pn phases routinely identified and picked for distances from 1.5 to 9 degrees. Over 25,000 arrivals have been used in the Pn tomography algorithm. The average uppermost mantle velocity beneath China is 8.0 km/s. The Tarim, Junggar, Tsidam, and Sichaun basins have the highest Pn velocities (over 8.2 km/s). These places are cratonic terrains that were accreted to southern Asia before the Indian-Asian collision. The high velocities imply higher density mantle that may have aided in the development of these basins. The eastern Tien Shan has normal Pn velocities of 8.0 to 8.1 km/s. Pn velocity beneath Tibet decreases from south to north as previous studies have also found. Late station delays in and around Tibet attest to its 70-km thick crust. Along the southeastern Tibet margin, low Pn velocities are found, suggesting that high temperatures and possible partial melt exist in the uppermost mantle there. A region of high anisotropy surrounds Tibet. Eastern China has lower Pn velocities and thinner crust as a result of Cenozoic extension of eastern China. A very low Pn velocity (<7.7 km/s) is found north of Hainan Island. This feature may be related to the opening of the South China Sea.

We made regional travel-time plots for the ten CDSN stations in China. Two of these stations, BJI and HLR, are now IMS stations. Thus, these travel-time curves can be used for event location. Average Pg, Pn, Sg, and Sn velocities beneath these Chinese stations are 6.1 km/s, 8.0 km/s, 3.5 km/s, and 4.5 km/s respectively.

KEY WORDS: China, tomography, Pn

OBJECTIVE

New Mexico State University seismologists, in conjunction with seismologists from the Institute of Geophysics of the China Seismological Bureau (IG/CSB), have collected seismic data to calibrate IMS stations in China and to document regional phase propagation characteristics in China. We are approaching these problems through regional tomography, characterization of regional wave propagation, station calibration, and an analysis of current location capabilities in China (Figure 1).

RESEARCH ACCOMPLISHED

Data collection

Our data set of the Annual Bulletin of Chinese Earthquakes (ABCE) consists of both paper catalogs and digital data sets provided by our colleagues from the China Seismological Bureau (CSB). Paper catalogs spanning 1983 to 1995; 1991 to 1995 were also given to us in digital form. The 1986 through 1990 catalogs were typed into the computer, and work on earlier catalogs is proceeding. The data quality from the ABCE is exceptional, with Pn phases routinely identified and picked for distances of up to 9 degrees (Figure 2). Pn arrivals form the linear first-arrival portion of the travel-time curve between distances of 200 to past 1500 km.

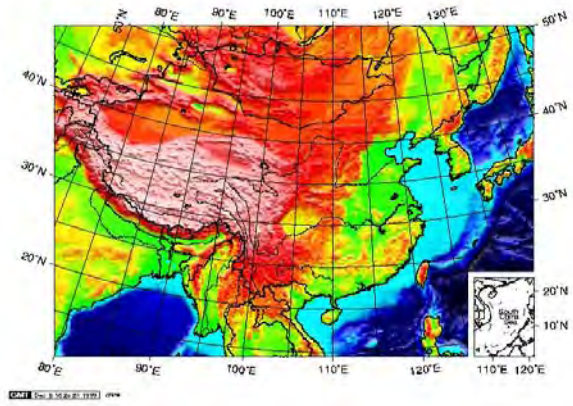

Figure 1. Shaded topography of China.

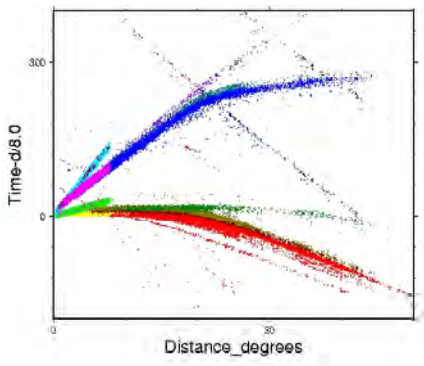

Figure 2. P-wave first arrival travel times from the Chinese bulletins (ABCE) for 1991 through 1995. Pg, Pn and a distant P branch are clearly visible. The ABCE routinely identifies arrivals as Pg, Pn, P, PP, pP, Sg, Sn, S, SS, sS, sP, PcP, S11, ScS, P11, ScP, PcS.

Station-Specific Travel Times

We have prepared travel-time curves for the CDSN stations in China (Figure 3). The two IMS stations in China, BJT and HIA, were not in existence when these data were collected; however, they replaced two nearby stations, BJI and HLR. We determined Pg, Pn, Sg, and Sn velocities for each of these stations via straight line fits. The ABCE identifies these phases to distances to 9 degrees.

Pn velocities vary from 7.9 to 8.1 km/s and Sn velocities are always 4.5 km/s. The lack of variation in Pn and Sn velocities is due to the large geographical averaging over a circle of 9 degrees radius (254 square-degrees). Pg velocities vary from 6.0 to 6.3km/s; Sg velocities vary fare 3.5-3.7 km/s. Higher Pg velocities are at Lhasa and Urumqi, both regions of thicker crust. A table of these velocities for different stations is shown below.

Table 1. Intercepts and apparent velocities for Pg, Pn, Sg, and Sn phases at CDSN stations

Station	Location	Pg	Pn	Sg	Sn
BJI	Baijiatuan	-1.1s, 6.14km/s	4.99s, 7.91km/s	-0.56s, 3.66km/s	10.26s, 4.52km/s
ENS	Enshi	0.8, 6.17	8.6, 8.13	0.5, 3.54	11.1, 4.52
HLR	Hailar	-0.2, 6.06	6.9, 8.06	-0.4, 3.52	10.1, 4.51
KMI	Kunming	0.1, 6.17	7.0, 7.94	0.7, 3.58	10.9 4.45
LSA	Lhasa	0.3, 6.28	8.4, 8.02	0.4, 3.55	13.5, 4.52
LZH	Lanzhou	-1.1, 6.07	8.0, 8.00	-1.6, 3.53	12.7, 4.55
MDJ	Mudanjiang	-0.6, 6.09	6.28, 8.01	-1.9, 3.52	9.9, 4.5
QIZ	Qiongzhong	too little data			
SSE	Shanghai	-0.6, 6.09	poor data	-1.4, 3.53	9.1, 4.47
WMQ	Urumqi	0.7, 6.29	8.5, 8.08	0.7, 3.57	13.3, 4.55

numbers refer to intercept - velocity pairs in seconds and km/s

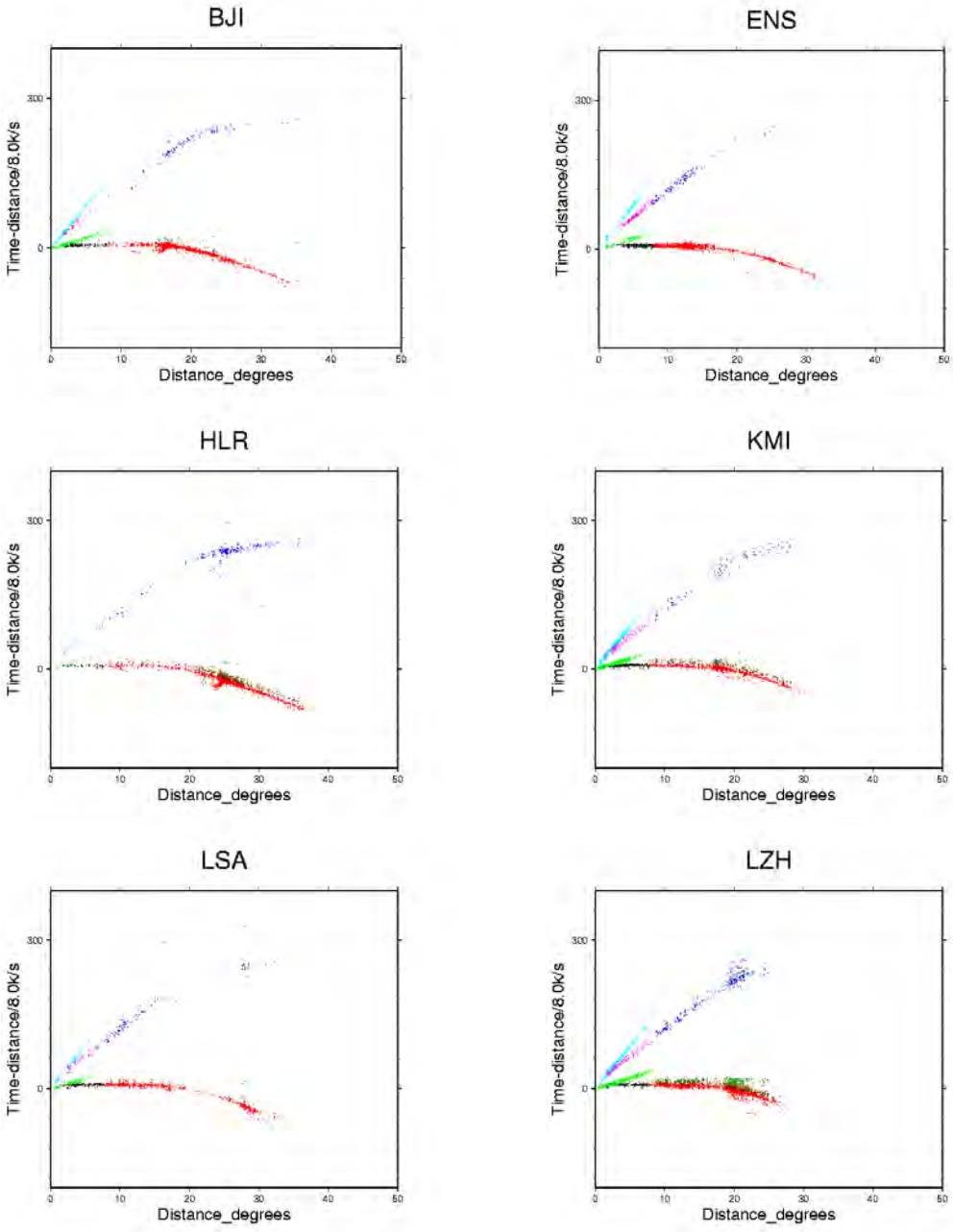
BJI
ENS
HLR
KMI
LSA
LZH
Time-distance/8.0k/s
Distance_degrees

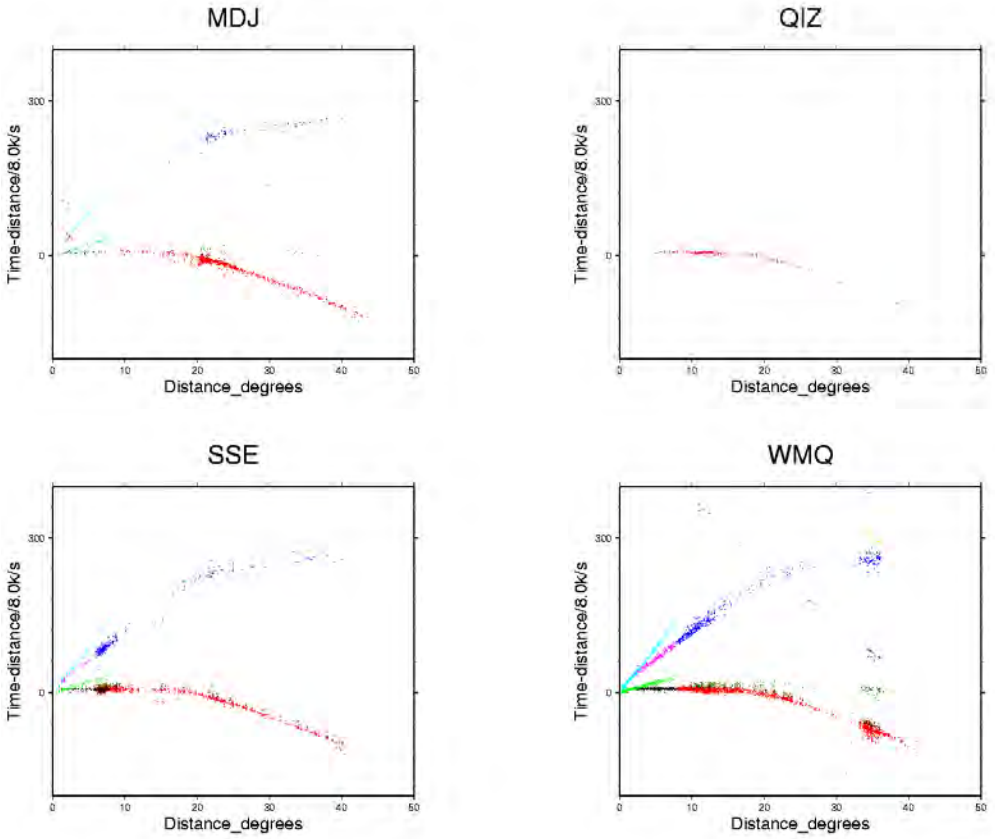

Figure 3. Reduced travel-time plots for CDSN stations. Stations BJI and HLR are next to IMS stations BJT and HIA.

Pn Tomography Beneath China

We have applied the Pn tomography algorithm of Hearn (1999) to Pn data from the ABCE to image the P-wave velocity and anisotropy at the surface of the mantle. Raypaths for these data cover most of central and eastern China; coverage in western China and Tibet is poorer, but we are now beginning to include data from other sources to remedy this. We used raypaths between 1.8 and 15 degrees distance and only stations and events with more than 9 arrivals at them. The final Pn data contains over 40,000 arrivals that span most of China (Figure 4).

The tomography algorithm has been modified to minimize the Akaike Information Criteria (AIC) as a norm (Akaike, 1973; McQuarrie and Tsai, 1998). From a practical viewpoint, the AIC is used to determine the damping constants in a damped least-squares inversion. We use it to determine the appropriate levels of the velocity and anisotropy variations in the seismic tomography. From a theoretical viewpoint, however, the AIC determines a solution that has optimal prediction capability. Thus, in seismic tomography, it will produce the best model for event location.

The inversion yields an average Pn velocity of 8.05 km/s for all of China. Figure 4 shows the regionally varying Pn velocities and anisotropy from the inversion. On Figure 5 the Pn velocity variations are superimposed upon shaded topography to demonstrate the correlation between them. The high Pn velocity regions are stable cratonic areas – Junggar Basin, Tarim Basin, Taidam Basin and Sichuan Basin. These cratonic areas were not greatly affected by tectonic and magmatic activity since their formation and hence there is lower temperature in the mantle lid and higher Pn velocity. These shield regions must also be regions of strong lithosphere. Their higher density mantle may have aided in the development of these basins. Pn velocity beneath Tibet decreases from south to north as has been found in previous Tibet studies (McNamara, 1997). This suggests that the subducted Indian plate ends somewhere beneath central Tibet. Eastern China has much lower Pn velocities. Along the southeastern Tibet margin, low Pn velocities are found suggesting that high temperatures and possible partial melt exists in the mantle there. Anisotropy is shown in Figure 4 by short line segments oriented along the fast anisotropy direction. Major regions of anisotropy are beneath the eastern Himalayan syntaxis, Sichuan Basin and Taiwan. Our resolution in the velocity and anisotropy is between two and three degrees. Because anisotropy can vary on shorter distance scales, much of it remains unresolved.

Both station and event delays represent the combined effect of crustal velocity and thickness (Figures 6 - 8). Event delays, however, are also susceptible to errors in origin time or depth in the event location. In most Pn tomography studies (e.g. Hearn, 1999), these errors create such scatter in the event delays that they are of little use. This is not the case for the ABCE data, and it indicates that events in China are exceptionally well located.

The station delays can be interpreted as a rough map of crustal thickness in China. For a constant velocity crust, 1 second of delay time represents approximately 10 km of crustal thickening. Late station and event delays in Tibet then imply that the crust there is 30 to 40 km thicker than the crust in eastern China. Events north of the Tarim Basin and in the Tien Shan also show late delays indicating crust that is 10 to 20 km thicker than eastern China. A thin crust is also apparent southeast of Tibet where extension is occurring.

Variation in Pn velocity within the Tibetan Plateau has been observed. Southern Tibet has a high Pn velocity and is probably underlain by the under-thrusting Indian continental lithosphere (Barazangi and Ni, 1983; Ni and Barazangi, 1984; Beghoul et al., 1993; Nelson et al., 1996; Huang et al., 2000). Our data in Tibet, with limited ray coverage, barely resolve the Pn velocity between northern and southern Tibet. In northern Tibet, the Pn velocity is about 7.9 km/s (also see McNamara et al., 1997). The relatively low velocity in northern Tibet has been interpreted as thermally weakened Asian mantle lid that is being squeezed between the advancing Indian lithosphere to the south and similarly rigid Tsaidam and Tarim lithosphere to the north and west (Huang et al., 2000). Unresolved is the issue of what ultimately caused the heating, and consequent weakening, of the upper mantle beneath northern Tibet. Convective removal of part of the mantle lid or prior subduction of water-rich mineral into the upper mantle leading to weakening and subsequent station heating (e.g. Yin and Harrison, 2000, Huang et al., 2000) are possibilities. In regions adjacent to the southeastern edge of the Tibetan plateau where coverage is good, we found low Pn velocity (<7.8 km/s) regions. These regions correspond to magmatic (extensive Quaternary basalt) and tectonic activity in the Panxi rift and Xiaojiang fault system. The tendency of NNE alignment of the Panxi rift suggests an orientation controlled by the simple shearing motion in the Asian lithosphere. Such an interpretation is consistent with the observation that the Panxi rift and Xiaojiang pull-apart lie in a trans-extensional tectonic environment produced by the sharing between India and Asia plate, which is currently taking place on a transform boundary along the right-lateral Sagaing fault (Guzmann-Spazelie and Ni, 1993).

Eastern China comprises the Archean North China block and South China block. These cratonic blocks collided first during the late Permian. After the collision, it experienced widespread tectono-thermal reactivation events during Late Mesozoic and Cenozoic, as indicated by emplacement of voluminous late Mesozoic granites and extensive Cenozoic volcanism (Yin and Nie, 1996). The events were associated with subduction of Pacific and Philippine plates. These tectono-thermal events also resulted in replacement of the old, cold, thick, and depleted lithospheric mantle by young, hot, thin, and fertile lithospheric mantle accompanied by lithospheric thinning. Widespread Cenozoic rifting and associated alkaline basalt in the North China block are well documented. GPS measurements indicate that the South China block is moving southeastward at ~10 mm/year while the North China block is moving eastward at ~ 5 mm/year (Chen et al., 2000; Michel et al., 2000; Holt et al., 2000). The faster motion of the South China block produces shearing on the North China block. The Pn velocity image shows that low-velocity structures are NNE-elongate and correspond to a pattern of young volcanism and regions of large extension. The Shanxi rift, a continental rift located on the eastern edge of the Ordos Plateau, is characterized with low Pn velocity that mimics the en-echelon pattern of the right stepping Shanxi grabens. Beneath the Tai Shan, where the Tan Lu fault crosses, a very pronounced Pn velocity zone was imaged. The high elevation of this mountain region must be partially supported by the buoyant mantle, a cause that was not known before this study. The Hannuoba alkaline basalt that occurs north of Beijing and extends into Inner Mongolia is underlain by low Pn velocity. The overall low Pn velocity pattern and correlation with magmatism clearly demonstrate that the lithospheric mantle beneath the North China block is hot and partially melted. This interpretation is also consistent with the observed inefficient Sn propagation in this region (Rapine and Ni, 2001).

The interior of the North China block consists of the elevated Ordos plateau and the Yin Chuan rift located east of the Ordos plateau. Pn velocities beneath these regions are normal and indicate that Yin Chuan rift is a structural rift in an early stage of rifting and the thick crust there mostly supports the Ordos plateau.

The eastern part of South China block was a magmatic arc during much of the Mesozoic to Cenozoic. Low Pn velocity regions correlated well with region of Cenozoic magmatism. The ray coverage near Taiwan is poor and thus imaged features are not interpretable. A very low velocity feature is found north of Hainan Island in the Guangdong province. The close proximity of this feature to the Red River fault and South China Sea suggest a possible relationship between the opening of the South China Sea and the low Pn velocity feature.

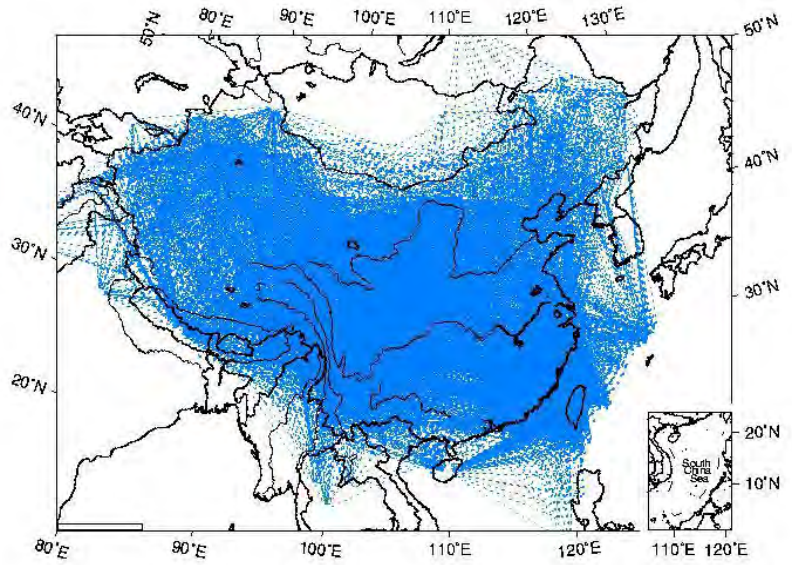

Figure 4. Pn raypaths used in the tomography. Distances were restricted to 1.8 to 15 degrees. About 25,000 raypaths are shown.

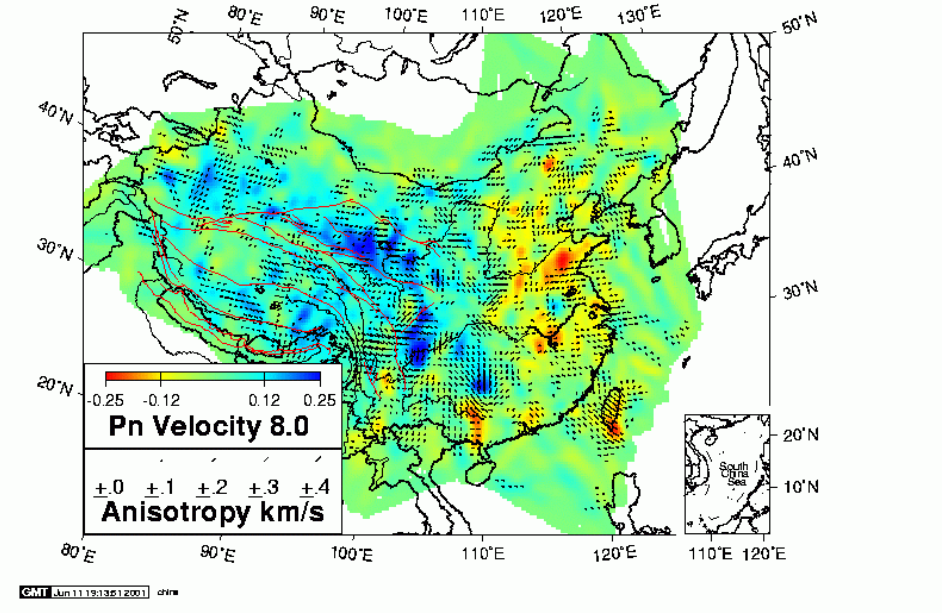

Figure 5. Pn velocity beneath China. Shades represent variations from a mean Pn velocity of 8.0 km/s. Line segments show the anisotropy with the line oriented in the fast direction. The Tarim, Tsidam, and western Sichaun basins have the highest Pn velocities. These places may be cratonic terrains that were accreted to southern Asia before the Indian-Asian collision. Eastern China has lower Pn velocities.

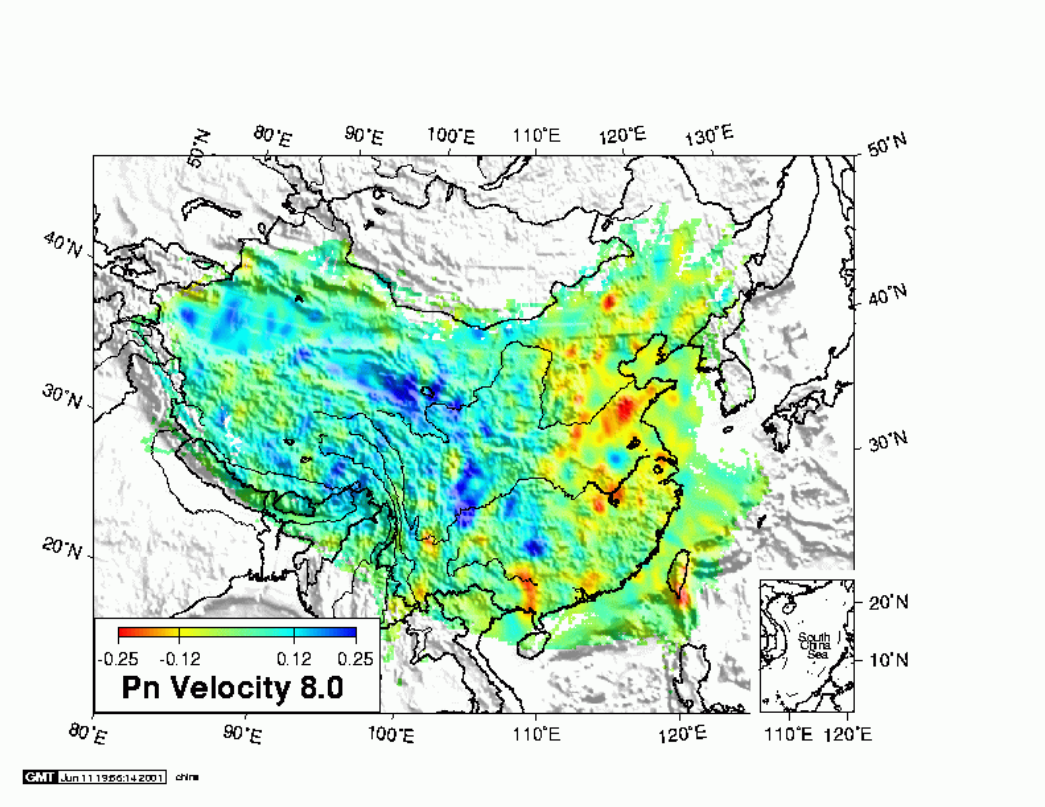

Figure 6. Pn velocity beneath China superimposed upon a shaded topographic relief map. Higher Pn velocities correspond to cratonic areas.

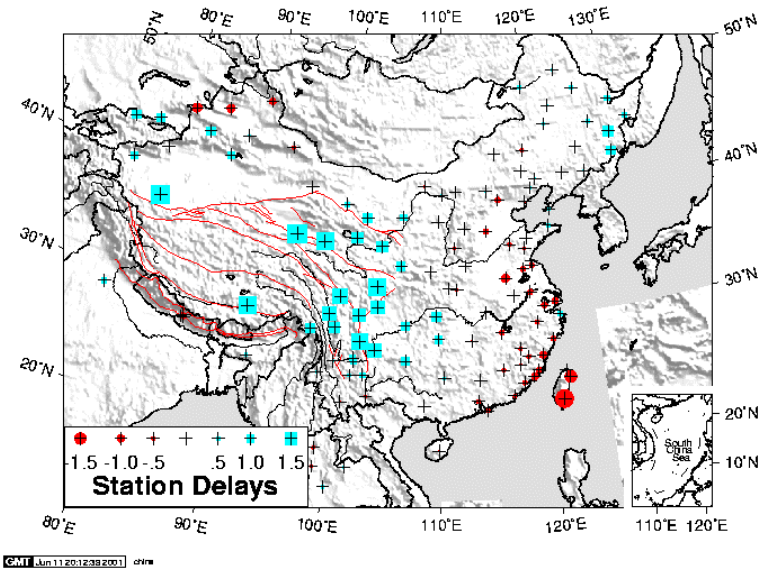

Figure 7. Station delays beneath China (zero-mean). These delays depend on both crustal thickness and crustal velocity. For a constant velocity crust, one second of delay corresponds to about 10 km of crustal thickening. Late arrivals in Lhasa, Tibet, and around the edges of the Tibetan Plateau result from the 70-km-thick crust. Early delays in the east and in Taiwan are the result of thinner crust.

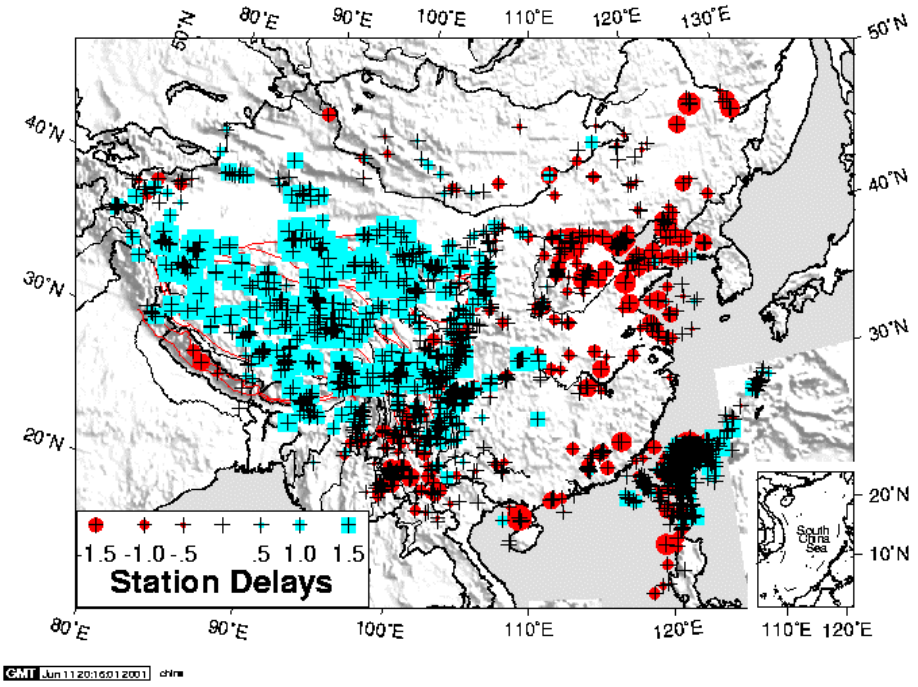

Figure 8. Event delays beneath China (zero-mean). Event delays also show the contrast between thick crust in the west and thin crust in the east.

CONCLUSIONS AND RECOMMENDATIONS

- The quality of the ABCE catalogs is excellent, with all seismic phases picked and identified on over 1030 stations. The consistency of the tomography event delays shows that the event locations are also of high quality and can be useful for CTBT station calibration purposes.
- Estimates of Pg, Pn, Sg, and Sn velocities as observed at 10 CDSN stations show little variation due to regional averaging. Pg velocities are typically 6.1 km/s; Pn velocities are 8.0 km/s; Sg velocities are 3.5 km/s; Sn velocities are 4.5 km/s.
- China shows a bimodal distribution of seismic velocity and crustal thickness. Western China, especially Tibet, has higher Pn velocities and thicker crust. High velocities generally represent older cratonic fragments, while lower velocities represent tectonically active regions. Variations in mantle velocity and crustal thickness beneath China will create bias in event locations unless corrected for.

REFERENCES

Akaike, H. (1992), Information theory and an extension of the maximum likelihood principle, in *Breakthroughs in Statistics, Vol. I, Foundations and Basic Theory*, S. Kotz and N.L. Johnson, eds, Springer-Verlag, New York, 610-624.

Annual Bulletin of Chinese Earthquakes (1982-1995), China Seismological Bureau.

Barazangi, M., and J. Ni, Velocities and propagation characteristics of Pn and Sn waves beneath the Himalayan Arc and Tibetan Plateau: Possible evidence for underthrusting of Indian continental lithosphere beneath Tibet, *Geology*, 10, 179-185, 1982.

Beghoul, N, M. Barazangi, B. Isacks (1993), Lithospheric structure of Tibet and Western North-America: Mechanisms of uplift and a comparative study, *J. Geophys. Res*, 98, 1997-2016.

Chen, W., B. Burchfiel, Y. Liu, R. King, L. Royden, W. tang, E. Wang, J. Zhao, and X. Zhang (2000), Global positioning system measurements from eastern Tibet and Their implications for India/Eurasia intercontinental deformation, *J. Geophys. Res.*, 105, 16215-16277.

Guzman-Speziale, M, and J. F. Ni (1993), The opening of the Andaman Sea: Where is the short-term displacement being taken up?, *Geophysical Research Letters*, 20, 2949 -2952.

Hearn, T. (1999), Uppermost mantle velocities and anisotropy beneath Europe, *J. Geophysical Research*, 104, 15,123-15,139.

Holt, W. (2000), Correlated crust and mantle strain fields in Tibet, *Geology*, 28, 67-70.

McNamara D.E., W. R. Walter, T. J. Owens, C. J. Ammon (1997), Upper mantle velocity structure beneath the Tibetan Plateau from Pn travel time tomography, J. Geophysical Research, 102, 493-505.

McQuarrie, A. and C-L Tsai (1998), *Regression and Time Series Model Selection*, World Scientific.

Michel, G., M. Becker, D. Anermann, C. Reigher, E. Reinhart and the GEOSSEA-Team (2001), New evidence for crustal motion in E and SE Asia from GPS measurements, *Earth Planet. Sci. Let*., 187, 239-244.

Nelson K.D., W. J.Zhao, L. D. Brown, J. Kuo, J. K. Che, X. W. Liu, S. L. Klemperer, Y. Makovsky, R. Meissner, J. Mechie, R. Kind, F. Wenzel, J. Ni, J. Nabelek, L. S. Chen, H. D. Tan, W. B. Wei, A. G. Jones, J. Booker, M. Unsworth, W. S. F. Kidd, M. Hauck, D. Alsdorf, A. Ross, M. Cogan, C. D. Wu, E. Sandvol, M. Edwards (1996), Partially molten middle crust beneath southern Tibet: Synthesis of project INDEPTH results *Science*, 274(#5293), 1684-1688.

Ni, J. and M. Barazangi (1983), Velocities and propagation characteristics of Pn, Pg, Sn, and Lg seismic waves beneath the Indian Shield, Himalayan Arc, Tibetan Plat eau, and surrounding regions: High uppermost mantle velocities and efficient Sn propagation beneath Tibet, *Geophys. J. R. Astr. Soc*. 72, 665-689.

Rapine, R. and J. Ni (2001), Propagation characteristics of Sn and Lg in northeastern China and Mongolia, *J. Geophys. Res.*, submitted.

Wei-Chuang H., J. F. Ni, F. Tilmann, D. Nelson, J. Guo, W. Zhao, J. Mechie, R. Kind, J. Saul, R. Rapine, and T. M. Hearn (2000), , Seismic polarization anisotropy beneath the central Tibetan Plateau, *Journal of Geophysical Research*, 105, 27979-27989.

Yin A, T. M. Harrison (2000), Geologic evolution of the Himalayan-Tibetan orogen, *Annual Review of Earth and Planetary Sciences*, 28, 211-280.

Yin, A. and S. A. Nei (1996), Phanerozoic palinspastic reconstruction of China and its neighboring regions, in *The Tectonic Evolution of Asia*, Cambridge University Press, 442-485.

APPLICATION OF JOINT RECEIVER-FUNCTION SURFACE-WAVE DISPERSION FOR LOCAL STRUCTURE IN EURASIA

Robert B. Herrmann, Charles. J. Ammon, and Jordi Julia
Saint Louis University

Sponsored by Defense Threat Reduction Agency

Contract No. DTRA01-00-C-0214

ABSTRACT

Subsurface geology generally has a broad wave number spectrum containing sharp, or high wave-number, changes in velocity near major geologic boundaries and smooth low wave-number variations in regions of relatively uniform geologic structure. Access to the full spectrum of earth structure requires that we exploit signals that span a wide frequency range and that are sensitive to the entire spectrum of heterogeneity. Our research is targeted at improving resolution of the full range of earth heterogeneity by combining seismic data sets traditionally analyzed separately. We will present the results of our efforts to combine teleseismic P-wave receiver functions and surface-wave dispersion measurements in a joint inversion for the variation in shear-wave velocity with depth in the lithosphere. Receiver functions are primarily sensitive to shear-wave velocity contrasts and vertical travel times, whereas surface-wave dispersion measurements are sensitive to vertical shear-wave velocity averages. Their combination bridges resolution gaps associated with each individual data set. The data are inverted using a joint, linearized inversion scheme which accounts for the relative influence of each set of observations, and allows a trade-off between fitting the observations, constructing a smooth model, and matching *a priori* constraints. Receiver functions are readily calculated using P-waveforms from distant earthquakes, and waves arriving from different directions can provide information on lateral variations in earth structure. Intermediate- to long-period dispersion values are available from global and regional tomographic studies and can be supplemented at the shortest periods using direct measurements from recordings from nearby events (when they are available). We will illustrate our work using applications to station TAM in North Africa and Eurasia (several portable stations in Tibet, station KIV, NIL, ABKT, BRVK, KURK, and WUS). Naturally, the inversion results depend on the quality of the data, and we are also investigating the changes in earth structure parameters that result from using dispersion values from different tomographic studies. To test the estimated earth models, we compare high-frequency regional-distance synthetic seismograms and regional earthquake waveforms.

KEY WORDS: earth models, shear-velocity, surface-wave dispersion, receiver functions

OBJECTIVES

Although epicentral location can be a clear discriminant in many cases, instances in which waveform measures such as accurate event depth or $M_S \backslash m_b$ ratios will be needed to help resolve ambiguity remaining after accurate event location. To study small seismic events, we must produce models that are useful for isolating and enhancing small-event seismic signals, which generally have small amplitudes and are noisy (Figure 1). The better we can enhance these marginal signals, the better we can estimate parameters such as event size, location, and depth. Our research is directed towards developing and applying methods for refining shear-velocity earth models to the point where they can contribute to mode isolation and enhancement, particularly at short periods where surface-wave tomography results can be extrapolated, but are limited by sparse data availability. Such models may also help with the most difficult event location parameter, depth. We have adopted the philosophy that advances in lithospheric structure modeling require the simultaneous fitting of complementary data to constrain the entire wave number spectrum of seismic velocity variations. In addition, *a priori* information on geologic structures, thermal environment, and tectonic history will likely be needed to construct the reliable estimates of subsurface geology. Our focus in this contract has been to test

and to exercise the joint inversion of receiver function and surface-wave dispersion (e.g. Julia et al., 2000) by comparing earth model estimates with those developed independently and by investigating the use of these models for seismogram modeling.

Combining Seismic Data in Composite Inversions

Subsurface geology generally has a broad wave-number spectrum, containing sharp, or high wave-number, changes in velocity near Earth s surface, at the sediment-basement transition, near the crust-mantle boundary (usually), and in the upper-mantle transition zone, and smooth low wave-number variations in regions of relatively uniform geologic structure. Access to the full spectrum of earth structure requires that we exploit signals that span a wide frequency range and that are sensitive to the entire spectrum of heterogeneity. For example, surface-waves, travel times, and direct-wave amplitudes are sensitive to smooth variations in earth structure; reflected and converted waves are sensitive to the velocity contrasts.

Joint inversions is an obvious approach to improve estimates of earth structure. Refraction seismologists have long used seismic wave travel times, amplitudes, and gravity variations to study the structure along one-dimensional surface profiles that illuminate the two-dimensional subsurface geology. To successfully combine data in an inversion, we must insure that all the data are sensitive to the same (or related) physical quantities and that they sample or average structure over comparable length scales. Recent advances in surface-wave tomography have provided an opportunity to combine localized surface-wave dispersion estimates with other data such as P- and S-wave receiver functions.

Surface-wave dispersion measurements are sensitive to broad averages, or long wave-number components of earth structure (e.g. Brune, 1969; Der et al., 1970; Braile and Keller, 1975, Ozalaybey, et al., 1997). They provide valuable information on the absolute seismic shear velocity but are relatively insensitive to sharp (high wave-number) velocity changes. Generally surface-wave inversions must be constrained using a particular layer parameterization (e.g. near-surface, upper-crust, lower crust, mantle lid, deep mantle), must resemble an *a prior* model, or must be substantially smoothed to stabilize earth-structure estimation Receiver functions are time series, computed from three-component body-wave seismograms, which show

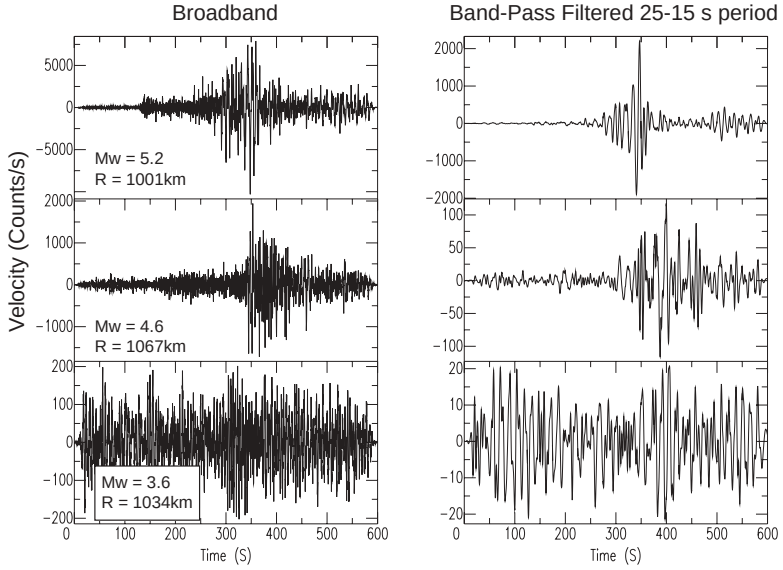

Figure 1. Illustration of the variation of signal frequency content for a source-receiver distance of about 1000 *km*. The signals on the left were generated by earthquakes in the Tien Shan region and recorded at station WMQ in central Asia. Those on the right are band-pass filtered version of the raw signals with a filter passing periods between 25 and 15 second (spanning the 20s Ms measurement range). The surface wave of the *Mw* 3.6 event is visible in the noisy trace at the bottom. Enhancing the signal to make an Ms measurement would require an appropriate short-period phase-match filter. *Mw* values are from moment-tensor inversion (Ghose et al., 1998).

the relative response of Earth structure near the receiver. Source effects are removed from the seismograms using a deconvolution that sacrifices P-wave information for isolation of near-receiver effects. Receiver function waveforms are a composite of P-to-S (or S-to-P) converted waves that reverberate within the structure beneath the seismometer (e.g. Langston, 1979; Ammon et al., 1990; Ozalaybey, et al., 1997). Modeling the amplitude and timing of those reverberating waves can supply valuable constraints on the underlying geology. In general, the receiver functions sample the structure over a range of 10 s of kilometers (roughly the one -to-two times the depth of the deepest interface) from the station in the direction of wave approach. Stations sited near geologic boundaries can produce different responses for different directions.

RESEARCH ACCOMPLISHED

Improved Receiver Function Estimation Procedure

When the data are high-quality and the receiver structure is not too complex, the choice of a deconvolution procedure used to estimate receiver functions does not make much difference. However, when the noise in the seismograms is substantial, or the receiver structure is complex, different deconvolution approaches have strengths and weaknesses. We compute receiver functions using the iterative time-domain deconvolution procedure described by Ligorria and Ammon (1999). We prefer the iterative approach, which is based on the Kikuchi and Kanamori (1982) source-time function estimation algorithm, for several reasons. First, in the iterative approach the receiver function is constructed by a sum of Gaussian pulses which produces a flat spectrum at the longest periods. The flat long-period spectrum can be viewed as *a priori* information that helps reduce side-lobes that may result of spectral or singular-value truncation stabilization procedures. The reduction of side-lobes eases the interpretation and helps stabilize low-frequency receiver functions. Second, the iterative approach constructs a causal receiver function, which is what we expect in all cases of reasonable earth structure. This is a subtle difference from spectral techniques [*e.g. Langston, 1979; Park, 2000*] which can always introduce a component to the receiver before the P-wave. The acausal component of the spectral signal may be small, but still important to the satisfaction of the convolutional model that defines a receiver function, *i.e.:*

$$R(t) = Z(t) * E_R(t) . \quad (1)$$

In equation (1), $R(t)$ and $Z(t)$ are the radial and vertical seismograms, and $E_R(t)$ is the radial receiver function (a similar equation holds for the transverse component). The point is that even when the receiver function estimation is unstable, spectral deconvolutions may satisfy (1) quite well. The iterative time-domain approach, which can be restricted to produce the best *causal* solution, may not always satisfy (1). Experienced modelers have always been able to identify failed receiver functions, but the misfit to (1), available from iterative deconvolutions, provides quantitative information that can be be used to quantify deconvolution reliability, and thus used when stacking signals, or in extreme cases, to discard obviously failed deconvolutions.

An Illustration of the Joint Inversion: Station ABKT, Alibek, Turkmenistan

At the Research Review, we will present results from several stations throughout North Africa and western Asia. Here we illustrate the joint inversion procedure using a single example from central Asia, station ABKT, Alibek, Turkmenistan (Figure 2). ABKT is located along a northwest-southeast striking boundary between the Iranian Plateau and the Russian Platform (Figure 2). Southwest of the station lies the Iranian Plateau, a region elevated as a result of continental collision and part of the high-elevation plateaus that stretch from southern Europe to eastern Asia. North and east of ABKT is the southern Russian Platform, or specifically, the KoPet-Dag foreland. ABKT is situated within the thrust belt formed by the overthrusting of the Iranian Plateau onto the Russian Platform. Recent motion is not pure reverse, most of the larger, recent nearby focal mechanisms suggest right-lateral movement along structures parallel to the boundary (or left-lateral motion perpendicular to the boundary) (Figure 2).

To estimate the structure in the vicinity of ABKT, we used Stevens *et al.s* (2001) Rayleigh-wave dispersion estimates and receiver functions sampling the structure to the east of the station, towards the southern Russian Platform. ABKT is well situated for receiver function analysis because of a large number of teleseismic

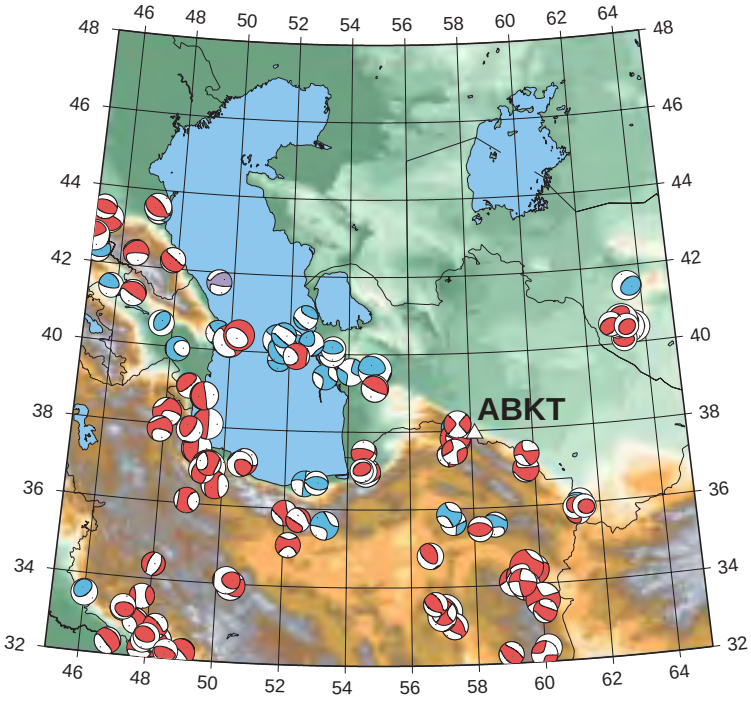

Figure 2. Location of station ABKTat Alibek, Turkmenistan (37.9304N, 58.1189E, 678 m), shown with topographic variations and focal mechanisms from the Harvard CMT catalog. Mechanisms are shaded by depth (red indicated depths from 0 to 32 *km*; blue depths from 33 to 70 *km*; and purple depths greater than 70 *km*).

events in the western Pacific subduction zones. The teleseismic P-waveforms are unevenly distributed with back azimuth (Figure 3), with a superb concentration to the east-northeast, but few signals arrive from the west-southwest. The number of events archived at the IRIS data management center decreases through the years 1995-1999. Although the data are sparse to the west, the sampling to the east will allow an analysis of variations in response to changes in incidence angle and eastern azimuths. The panel on the left shows few details in the receiver functions but clearly illustrates the available data distribution. The expanded view on the right of receiver functions sampling the structure from the northeast to southeast of ABKT illustrates strong coherence of many arrivals and some systematic changes. Arrivals approaching from the northeast contain two distinct arrivals at about 4.5 and 7.4 seconds, and a less coherent multiple arrives at about 13 seconds. The initial peak amplitude is shifted about 0.8 seconds late for northeast arriving waves and 0.2 seconds for southeast arriving waves. The shift is indicative of a large *Ps* conversion from the base of a sedimentary basin, which is expected to be more prominent at this site for waves coming in from the northeast.

We present results that correspond to the structure east of ABKT, computed using a subset of radial receiver functions using P-waves approaching from the east with relatively shallow incidence angles (ray parameters > 0.07 *s/km*) (Figure 4). For surface wave dispersion we use the Rayleigh wave dispersion curve from the model of Stevens *et al.* (2001), which is part measured and part extrapolated using *a priori* information. Dispersion values are very low at the short periods (Figure 4), indicative of a thick sequence of sediments. The deep mantle structure is constrained to merge with PREM to insure consistent results with global models. The inversion results are summarized in (Figure 4). The estimated shear-velocity model is fairly simple, with one unusual high-velocity layer near the crust-mantle boundary that was probably introduced to fit a trough in the receiver function. The fit to the dispersion is superb with the exception of the shortest periods. The model contains a 10- to 12-km sequence of low shear-velocity material that is likely the sediments of the KoPet-Dag foreland. Crustal thickness is about 42 km, although the transitional crust mantle boundary makes a precise thickness estimate difficult. The model agrees reasonably well with a structure near

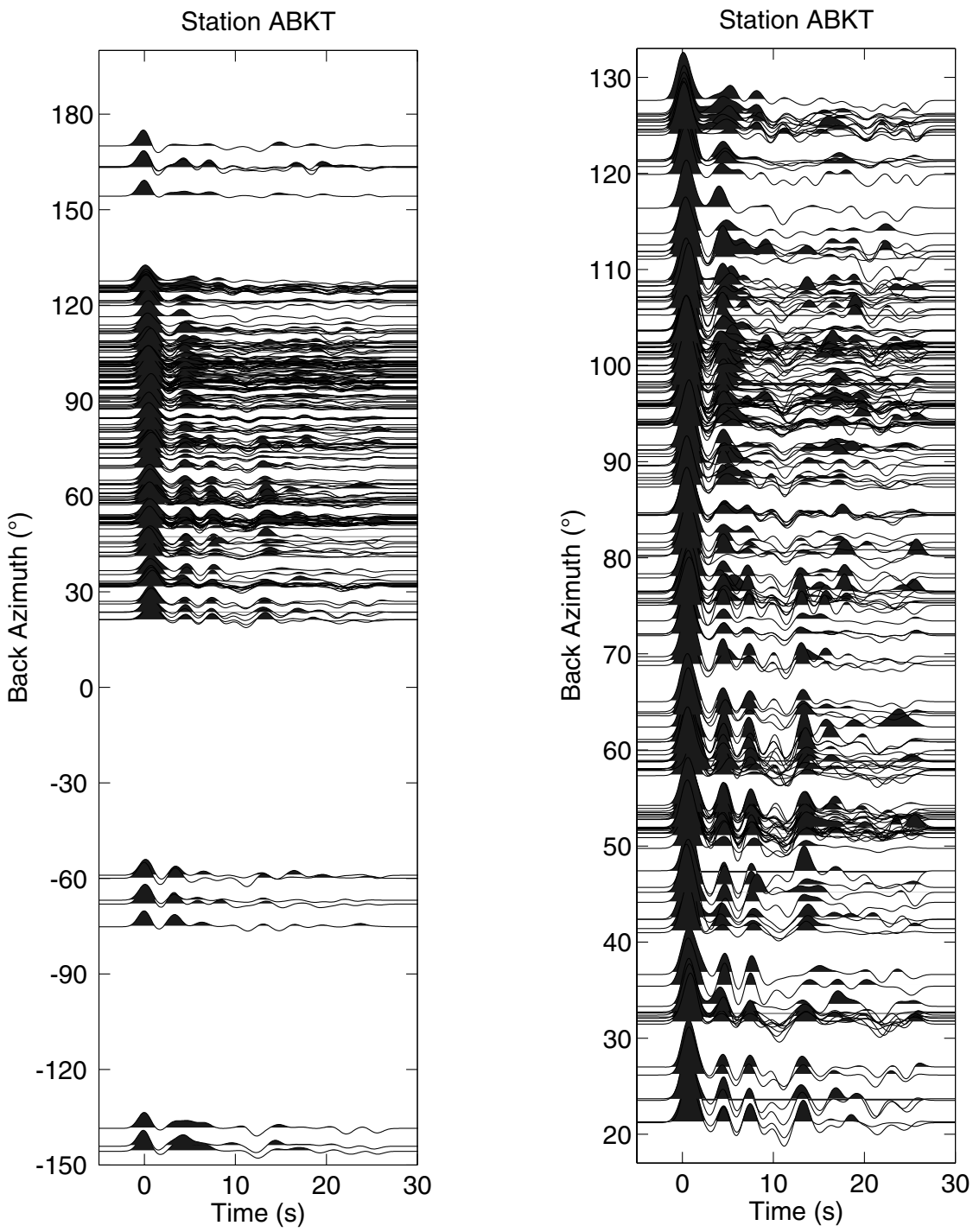

Figure 3. Receiver function estimates that meet a prediction misfit criteria of less than 10% of the power in the P-waveform. The full set of data are shown on the left, the panel on the right is an expanded version of the waveforms approaching the station with back azimuths between 20¡ and 130¡. Positive polarities are shaded. The data distribution is strongly biased tow the east-northeast, where ample data from the subduction zones provide a near continuous azimuthal distribution. Sparse data from the western azimuths makes imaging the Iranian Plateau structure more difficult (always a risk with stations near large geologic boundaries).

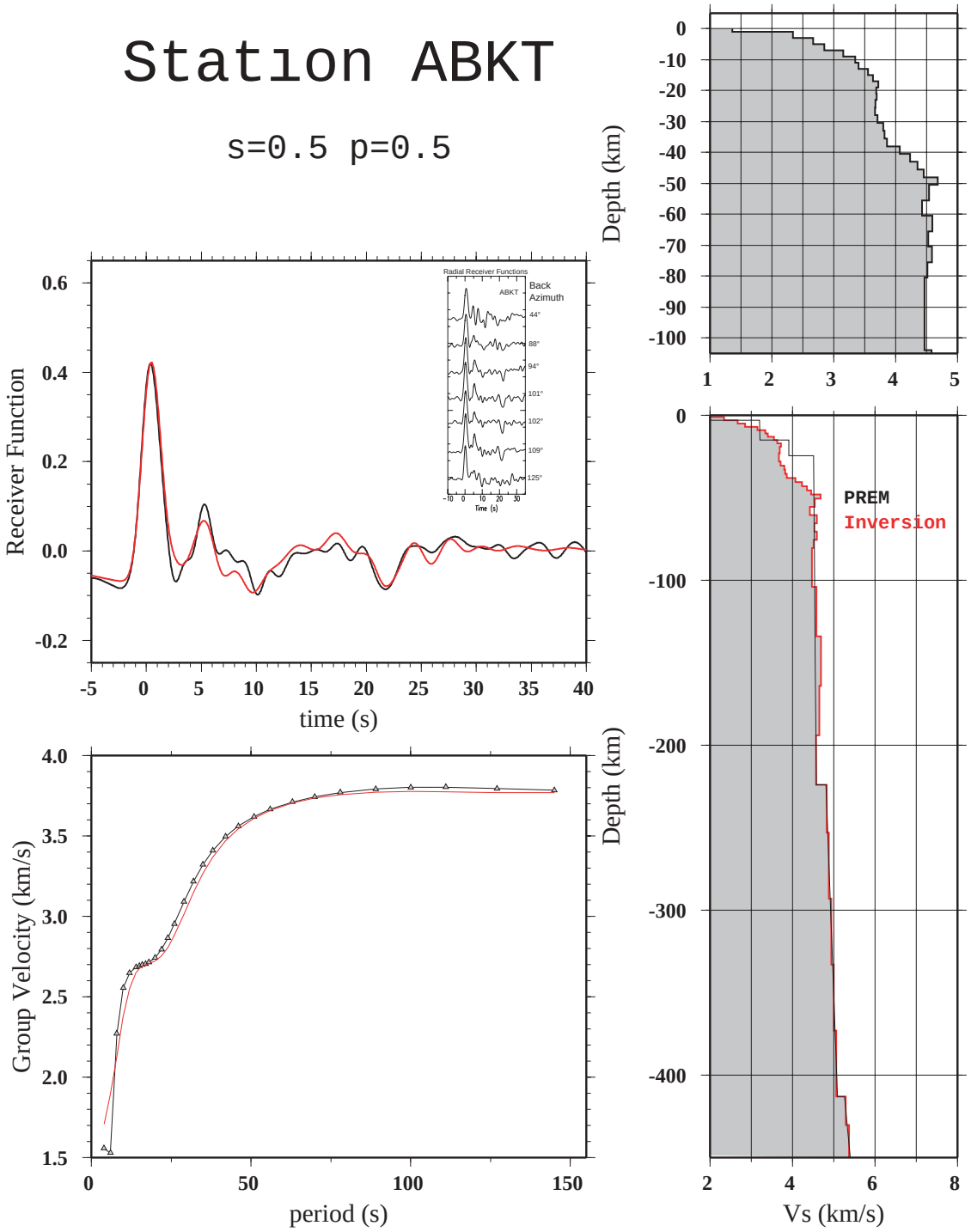

Figure 4. Inversion results for station ABKT using Stevens dispersion model and a receiver function appropriate for the region east-northeast of the station. Red lines identify predictions, black lines (and symbols) the observations. The subset of receiver functions used to compute the stack used in the inversion is shown in the inset of the upper left panel. The gray shaded models is the result of the inversion.

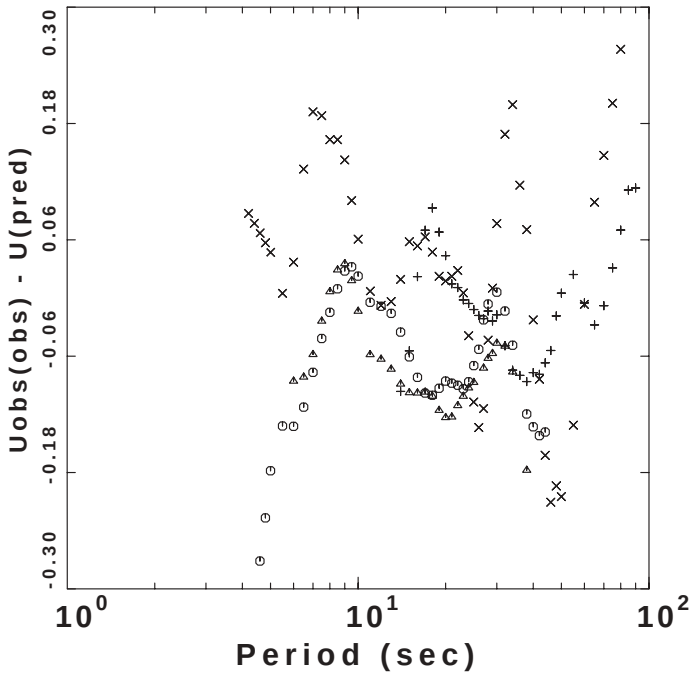

Figure 5. Difference between observed and predicted group velocity dispersion along 4 paths to the INCN station.

37.32¡N, 60.60¡E, listed in Christensen s article in the CRC Practical Handbook of Physical Properties of Rocks and Minerals (The original reference to work on Russian Platform in central Asia by Godin et al., 1961).

Dispersion Measurements

The surface-wave dispersion near the seismograph station is the least known quantity. One can use existing regionalizations (Stevens, Harvard, Colorado) or derive local dispersion. The Stevens technique provides Rayleigh-wave group velocity dispersion curves in the 4 - to 400-second-period range, uses a 1 x 1 degree global grid, is rooted in a global crustal model, and is constrained by observations in the 10 - to 100-second-period range. The Harvard regionalization provides phase velocity dispersion at longer periods.

We have tested the Stevens predictions in two different regions: northeast China platform near Korea and the central U. S. To study wave propagation near Korea, waveform data from the Inchon station were used. Figure 5 presents the difference between the observed Rayleigh-wave group velocity and that predicted between the epicenter and the Inchon station. The distances ranged from 450 to 1120 km. The Stevens predictions are good in the 10- to 100-second period range, but a similar comparison in the central U. S. shows that the Stevens predictions at shorter periods are not adequate over short paths because the shallow shear-wave velocities underlying his predictions are not correct and because shallow geology changes significantly over distances of 100 km.

We are working with researchers and students at Seoul National University to apply the joint-inversion method at 11 stations of the current KMA broadband network in the southern Korean peninsula. Previous work on receiver functions (Yoo, 2001) indicates the presence of a simple crust which can be modeled as a single layer over a half-space with a 32 km-thickness. We are acquiring waveform data from the KMA network to determine the receiver functions and also to estimate phase velocities. We are evaluating several phase velocity estimation techniques: interstation cross-correlation and p-tau stacking (McMechan and Yedlin, 1981). The p-tau stacking technique works surprisingly well. Figure 5 shows the locations of the KMA

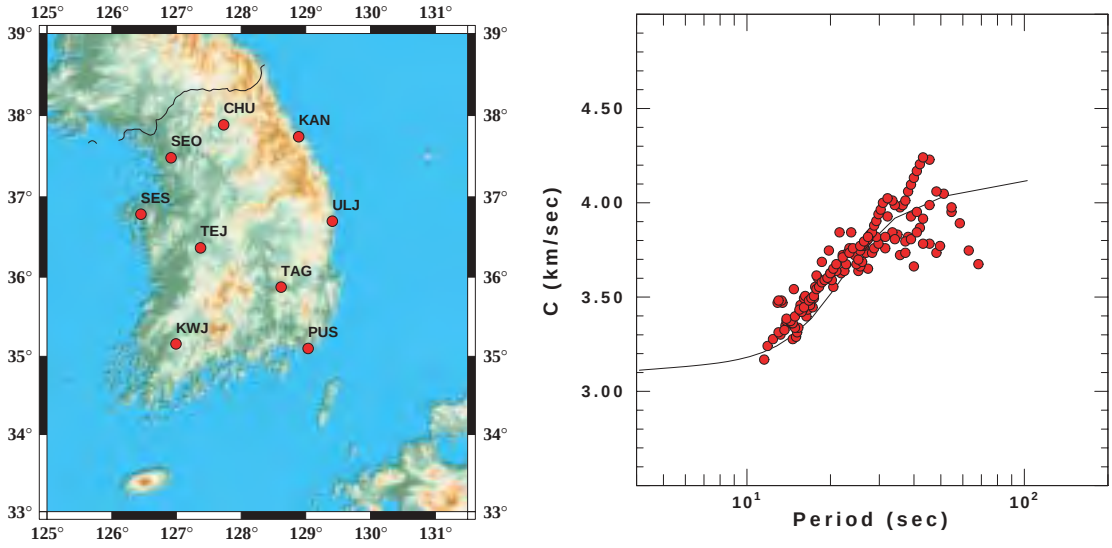

Figure 6. (Left) Location of 9 KMA stations used for phase velocity analysis. (Right) Comparison of theoretical fundamental mode Rayleigh-wave phase velocity dispersion for a simple velocity model for Korea and the p-tau processing results for three events at distances of 500, 2500 and 4000 km from Korea.

stations used a comparison of the derived phase velocity and a model prediction. The stability of the p-tau technique for both Love and Rayleigh waves is encouraging.

CONCLUSIONS AND RECOMMENDATIONS

The combination of receiver functions and surface waves produces robust earth models when the data are high quality. Our analysis generally shows that the models are consistent with other subsurface imaging results. To reliably constrain shear velocities in the upper crust, short-period 5- to 15-s surface waves are needed. Variations in earth structure estimates can be traced back to variations in surface-wave tomographic reconstructions. Additional tomographic work and direct comparisons of various models are needed to help better resolve uncertainties in the dispersion curves available for joint inversions. The Stevens group velocity prediction tool is very useful in regions for which no dispersion observations are available. It would be very useful if the Stevens tool could also predict Love-wave dispersion. Dispersion data for periods less than 10 sec must be acquired in order to properly constrain the upper crustal structure. The joint inversion technique succeeds in defining a local crustal structure for modeling intermediate- to long-period waveforms.

REFERENCES

Ammon, C.J., G.E. Randall, and G. Zandt (1990). On the non-uniqueness of receiver function inversions, J. Geophys. Res., 95, 15303-15318.

Braile, L., and G.R. Keller (1975). Fine structure of the crust inferred from linear inversion of Rayleigh-wave dispersion, Bull. Seism. Soc. A., 65, 71-83.

Brune, J.N. (1969). Surface waves and crustal structure, in The Earth's Crust and Upper Mantle, edited by P.J. Hart, pp. 230-242, American Geophysical Union, Washington, D.C.

Der, Z., R. Masse, and M. Landisman (1970). Effects of observational errors on the resolution of surface waves at intermediate distances, J. Geophys. Res., 75, 3399-3409.

Juli , J., C.J. Ammon, R.B. Herrmann, and A.M. Correig (2000). Joint inversion of receiver function and surface wave dispersion observations, Geophys. J. Int., 143, 1-19.

Kikuchi, M., and H. Kanamori (1982). Inversion of complex body waves, Bull. Seism. Soc. Am., 72, 491-506.

Langston, C.A. (1970). Structure under Mount Rainier, Washington, inferred from teleseismic body waves, J. Geophys. Res., 84, 4749-4762, 1979.

Ligorria, J.P., and C.J. Ammon (1999). Iterative deconvolution of teleseismic seismograms and receiver function estimation, Bull. Seism. Soc. Am., 89, 1395-1400.

McMechan, G. A. and M. J. Yedlin (1981). Analysis of dispersive waves by wave field transformation, Geophysics 46, 869-874.

Ozalaybey, S., M.K. Savage, A.F. Sheehan, J.N. Louie, and J.N. Brune (1997). Shear-wave velocity structure in the northern Basin and Range Province from the combined analysis of receiver functions and surface waves, Bulletin of the Seismological Society of America, 87 (1), 183-199.

Park, J., and V. Levin (2000). Receiver functions from multiple-taper spectral correlation estimates, Bulletin of the Seismological Society of America, 90 (6), 1507-1520.

Stevens, J. L. (2001). Global Rayleigh Wave Dispersion Atricle, Pure and Applied Geophys., in press.

Yoo, Hyun-Jae (2001). Crustal structure under the TJN station by receiver function methods, M. S. Thesis, Seoul National University, 56pp.

REGIONAL VARIATIONS IN THE SHEAR-WAVE Q STRUCTURE OF SOUTHERN ASIA

Alemayehu L. Jemberie and Brian J. Mitchell

Saint Louis University

Sponsored by Defense Threat Reduction Agency

Contract No. DTRA-01-00-C-0213

ABSTRACT

Models of shear-wave Q (Q_μ) have been obtained for a broad region of southern Asia that stretches across most of China and Mongolia. The models were derived using two methods. The first method inverts attenuation coefficients of the fundamental Rayleigh mode obtained using a standard two-station technique and the second method matches theoretical amplitude spectra for fundamental- and higher-mode Rayleigh waves computed for assumed velocity and Q models, and earthquakes with known source depths and focal mechanisms, to observed spectra. The latter method provides much better regional coverage than the first and allows us to map lateral variations of shear-wave Q at various levels in the crust and uppermost mantle.

For the single-station, multi-mode method, we assumed an Earth model consisting of three Q_μ layers, layer 1 being 10 km, layer 2 being 20 km, and layer 3 being 30 km thick. From data collected to date, Q_μ in layer 1 achieves lowest values (about 40) in portions of western China, including part of the Tibetan Plateau, and attains highest values in regions of southeastern China (as high as 220) and in westernmost China near the Tarim Basin. Layer 2 displays lowest Q_μ values in the southeastern Tibetan Plateau (as low as 60) and highest values in a small part of south-central China (180 or more), along the coastal region of eastern China (up to 140), and in a north-south trending band through central China (120-140). Although the resolution of crustal variations is poorer for layer 3 than for the shallower layers, some variations can be detected. The Q_μ map for that layer displays maxima under north-central China (200 or more), northwestern China (160 or more), and south-central China (about 120). A band of low Q_μ (40-60) separates the maximum in northwestern China from the maximum in north-central China. Our models indicate that Q_μ decreases with depth in eastern China and increases with depth in western China throughout the upper 30 km of the crust.

Q_μ at all depths is lower everywhere in southern Asia than it is in stable regions of the world, but not as low as in much of Iran and Turkey. Differences in the depth distribution of Q throughout this region, as well as those found earlier in the Middle East, suggest that discriminants will not be transportable unless they have been corrected for regional and depth variations in Q.

KEY WORDS: attenuation, Q, fundamental-mode surface waves, multi-mode surface waves

OBJECTIVE

The overall objective of this research is to map regional variations of surface-wave attenuation throughout the Tethysides belt of southern Asia (Sengör, 1987) in as much detail as possible and to determine models of seismic Q that explain those variations in attenuation. When our maps are completed we plan to determine how regional variations of Q_μ and its depth distribution will affect the propagation of regional phases. Some practical questions that we will address are the extent to which those Q_μ variations will affect magnitude determinations and the transportability of discriminants using regional phases.

RESEARCH ACCOMPLISHED

We have determined Rayleigh-wave attenuation coefficients (γ_R) corresponding to 51 paths in nine sub-regions of southern Asia using a standard two-station method and have inverted those values for Q_μ structure of the crust and uppermost mantle. We have also obtained three-layer models of Q_μ, between depths of 0 and 60 km,

for 25 different paths between single events and single stations using Rayleigh waves and a multi-mode method that matches observed to computed multi-mode amplitude spectra (Cheng and Mitchell, 1981; Cong and Mitchell, 1998). The two-station method, while it allows us to invert for multi-layered models, suffers from poor areal coverage and the data sometimes exhibit effects of focusing or defocusing. The single-station method, while providing simpler Q_μ models, provides better areal coverage and is less affected by focusing/defocusing. We have therefore used the single-station method to construct contour maps of Q_μ variation in three layers.

We will emphasize single-station results in this paper, but will compare models obtained from single-station observations with those obtained from the inversion of two-station attenuation coefficient data. Suffice it to say that we obtained attenuation coefficient values for the fundamental Rayleigh mode by measuring spectral amplitudes over periods between about 5 and 100 seconds, and correcting them for the effect of wave spreading. We then inverted those attenuation coefficient values to obtain models of Q_μ for nine regions of China.

Figure 1 shows the locations of the single-station paths used in this study. We attempted to restrict all paths to being completely continental, so as to avoid well-known adverse effects encountered when surface waves traverse continental margins. Figure 1 indicates that, with only one exception, we were able to do that. The path coverage is sufficiently great that we can develop maps of Q_μ variations at different depths. We decided to use three layers, the first being 10 km in thickness, the second being 20 km in thickness, and the third being 30 km in thickness. The total span of thickness (60 km) is similar to the largest crustal thickness known in the region (the Tibetan Plateau). The increasing layer thickness with depth reflects the fact that our ability to resolve detail decreases with increasing depth.

The single-station method entails the measurement of spectral amplitudes for the fundamental Rayleigh mode between periods of about 5 s and 80 s and of the superposition of higher Rayleigh modes at periods between about 3 and 10 s. Theoretical spectra are computed for an assumed velocity model, a known earthquake focal mechanism, and various crustal models of Q_μ. The Q_μ model is changed until the theoretical spectra the model produces, exhibits the same levels and shapes as the observed spectra. Examples, from a recording at station XAN, appear in Figure 2. Both examples use observed spectra for a recording at station XAN. The upper example compares those spectra with theoretical spectra obtained using the Q_μ model obtained from the inversion of fundamental-mode Rayleigh-wave attenuation data obtained using the two-station method in region 2 in southeastern China. The lower example compares the same observed spectra to theoretical spectra for a three-layer model. Figure 3 shows that the two models are very similar throughout the upper 60 km of the crust and mantle.

It is not possible to obtain such good agreement in all cases. Figure 4 shows a comparison of models obtained using the two-station and single-station methods in the northeastern-most portion of our study area (southeastern Siberia). The upper 20 km of the models exhibit excellent agreement but the model obtained using the two-station method (group 6) exhibits a zone of very high Q_μ at depths between about 20 and 45 km depths. We believe that the anomalously high values are due to focusing of Rayleigh-wave energy at longer periods for the more distant station in the two-station method. The focusing is likely due to lateral variations in velocity structure in the region.

Figures 5-7 present preliminary maps of Q_μ variation at three depths beneath southern Asia. Figure 5 indicates that for layer 1 (10 km thick) Q_μ is highest in southeastern China, where it reaches about 250, and could be higher further to the east if we had data coverage for that region. The high values in this regions, relative to surrounding regions, are consistent with the variations of Lg coda Q in Eurasia found by Mitchell et al. (1997). Q_μ decreases from east to west and reaches a minimum of about 40 in parts of western China, including part of the Tibetan Plateau. Further to the west Q_μ increases in a region that comprises the Tarim Basin and parts of southwestern China.

Figure 6 shows the variations of Q_μ in layer 2 (20 km thick). Those values are also highest in eastern China (as high as about 140) and are lowest in the eastern part of the Tibetan Plateau (about 60) and in the southern-most part of central China (about 80). Between the two regions of low Q_μ a band of relatively high values (with

maximum values of about 140) extends northward to Mongolia. North of the China-Mongolia border a region of low Q_μ (60-80) lies within the broader band of high values.

Figure 7 shows the variations of Q_μ in layer 3 (30 km thick). This layer contains a concentrated zone of high Q_μ values (as large as 200) in north-central China and another concentration of high values (up to 160) in northwestern China. The two regions of high Q_μ are separated by a north-south trending band of low Q_μ values (40-60). Eastward from the high values in central China, Q_μ decreases, first rapidly then gradually, to about 100 throughout eastern China.

In eastern China, Q_μ appears to decrease with depth through the upper 30 km of the crust (layers 1 and 2) while in western China it appears to increase with depth. A zone in which Q_μ stays relatively constant with depth separates the two regions.

Q_μ throughout our region of study was determined using Rayleigh-wave attenuation at periods between about 5 and 80 s. The values that we found are low (40-200) compared to those found at those periods in many stable regions of the world (about 300-1000) in earlier studies (see Mitchell, 1995). They are, however, not as low as those found in the upper 30 km of the crust in the Iran/Turkey Plateaus (50-70), a region of active plate collision (Cong and Mitchell, 1998).

CONCLUSIONS AND RECOMMENDATIONS

Our analysis of single-station multi-mode propagation in southern Asia indicates that Q_μ varies systematically in an east-west direction across China. The overall trend going from east to west is a relatively large decrease in Q_μ in the uppermost 10 km of the crust and a smaller decrease in the underlying 20 km of the crust. These trends lead to models in which Q_μ in the eastern part of China that decrease with depth and in the western part of China that increase with depth. These differences suggest that discriminants based upon amplitude ratios of phases that traverse the deep crust or upper mantle (such as Pn) to those that traverse the upper crust (such as Pg), or average the entire crust (such as Lg), will not be transportable unless the phases are corrected for different Q distributions.

It will be important to improve data coverage throughout this entire region so that regional variations of Q_μ and their distribution with depth can be mapped in greater detail. We should also determine the effect that variations in the depth distribution of Q_μ will have on various regional phases that might be used in proposed discrimination schemes.

ACKNOWLEDGEMENTS

We thank Dr. Lianli Cong for providing his programs for determining and plotting multi-mode spectra.

REFERENCES

Cheng, C., and B.J. Mitchell (1981), Crustal Q structure in the United States from multi-mode surface waves, *Bull. Seism. Soc. Am., 71*, 161-181.

Cong, L., and B. Mitchell (1998), Seismic velocity and Q structure of the Middle Eastern crust and upper mantle from surface-wave dispersion and attenuation, *Pure and Appl. Geophys., 153*, 503-538.

Mitchell, B.J. (1995), Anelastic structure and evolution of the continental crust and upper mantle from seismic surface wave attenuation, Rev. *Geophys., 33*, 441-462.

Mitchell, B.J., Y. Pan, J. Xie, and L. Cong (1997), Lg coda Q variation and the crustal evolution of Eurasia, *J. Geophys. Res., 102*, 22767-22779.

Sengör, A.M.C. (1987). Tectonics of the Tethysides: Orogenic collage development in a collisional setting, *Ann. Rev. Earth Planet. Sci., 15*, 213-244.

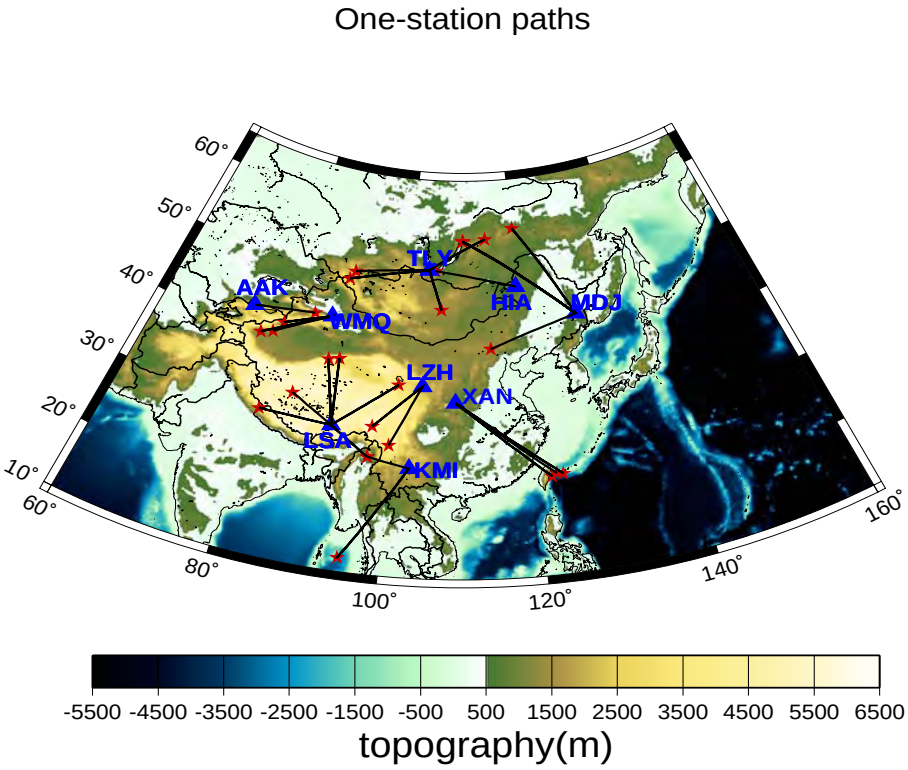

Figure 1. Map of single-station paths used in this study. Stars denote earthquake epicenters and triangles denote seismic stations.

Figure 2. Examples of observed and theoretical amplitude spectra. Open circles indicate amplitude spectra of fundamental-mode Rayleigh waves and closed circles indicate amplitude spectra of the composite of higher modes at periods between 2 and 8 seconds. The upper example compares observed spectra at station XAN with theoretical spectra for a model obtained from the inversion of fundamental-mode Rayleigh-wave attenuation coefficient data using the two-station method. The lower example compares the same observed spectra with theoretical spectra for a three-layered Q model in the same region.

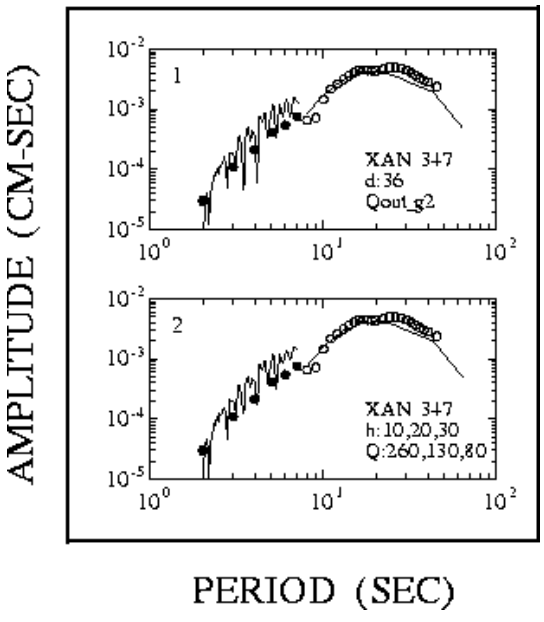

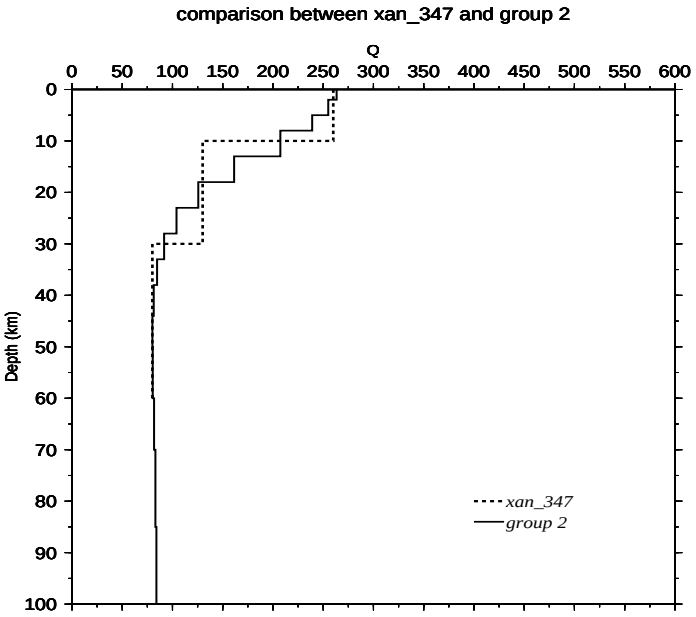

Figure 3. Shear-wave Q models obtained from the inversion of two-station attenuation coefficient data (solid line) and from trial-and-error matching of observed and theoretical multi-mode spectra (dashed line).

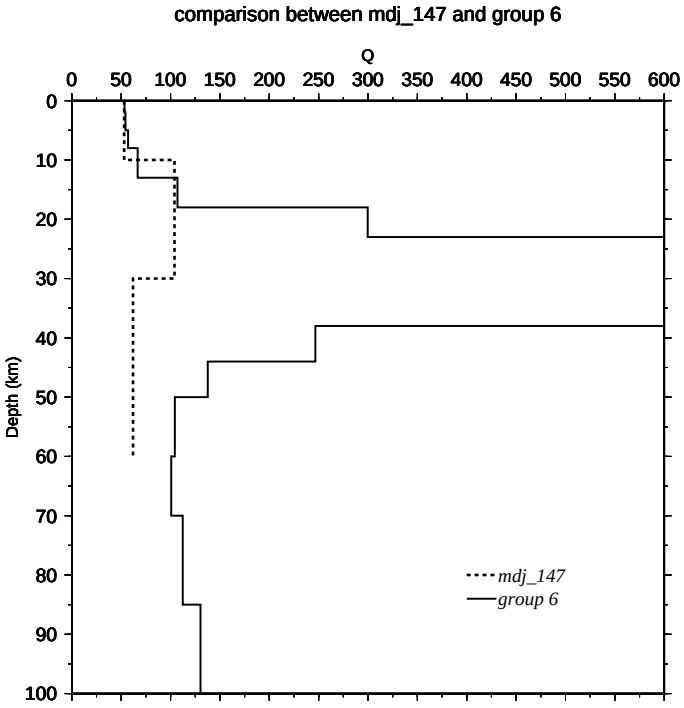

Figure 4. Comparison of models obtained using the two-station method (solid line) and the single-station method (dashed line) for the northeastern-most portion of our map (southeastern Siberia). The anomalous high-Q layer centered at about 30 km is likely due to contamination of the two-station attenuation coefficient data by focusing at the distant station.

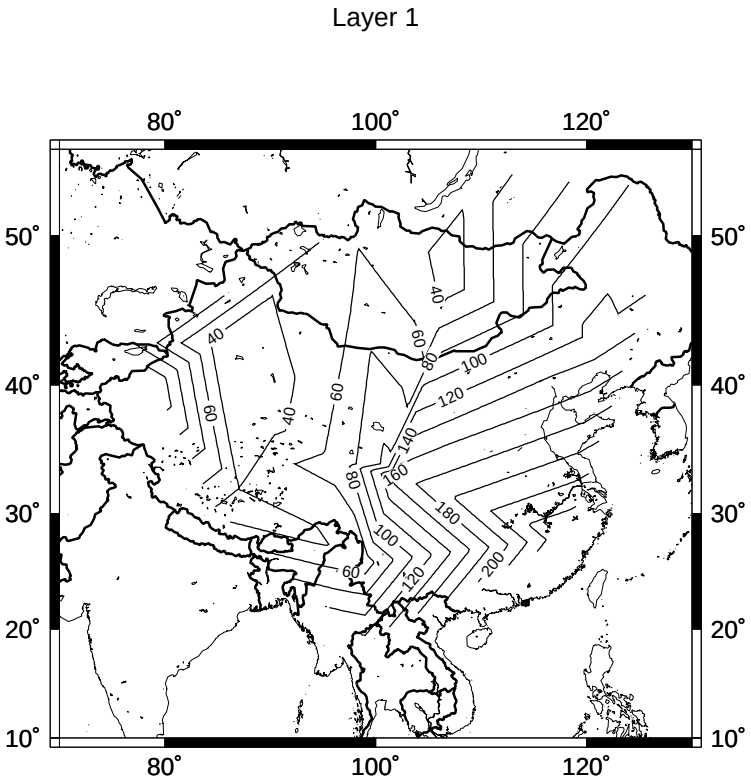

Figure 5. Contour map of shear-wave Q variation in the upper 10 km of the crust (layer 1) in the region of study. The contour interval for Q is 20.

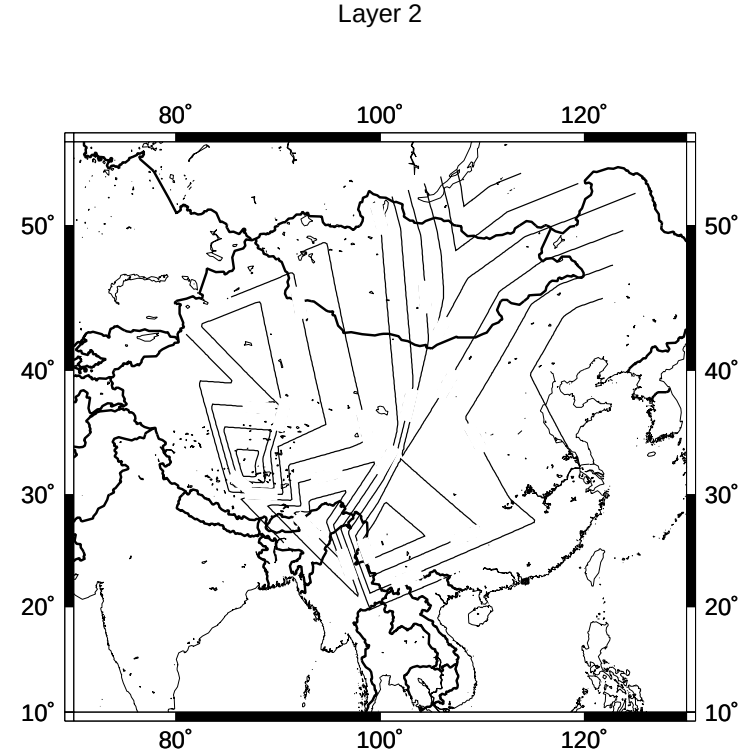

Figure 6. Contour map of shear-wave Q variation in the depth range 10-30 km in the crust (layer 2). The contour interval for Q is 20 km.

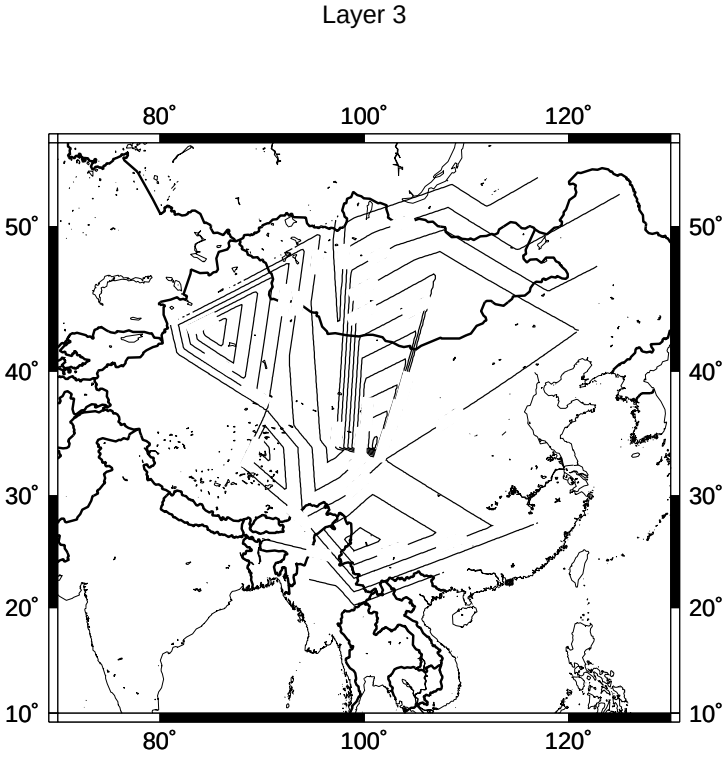

Figure 7. Contour map of shear-wave Q variation in the depth range 30-60 km (layer 3). The contour interval for Q is 20.

A BROADBAND SEISMIC EXPERIMENT IN YUNNAN, SOUTHWEST CHINA

Wenjie Jiao,[1] Winston Chan,[1] and Chunyong Wang[2]

Multimax Inc.,[1] Institute of Geophysics, China Seismological Bureau[2]

Sponsored by Defense Threat Reduction Agency

Contract No. DTRA01-00-C-0081

ABSTRACT

A broadband portable seismic network has been deployed in Yunnan, southwest China, to collect seismic data for advanced studies on regional crustal and mantle structures, earthquake prediction, and regional characteristics of wave propagation and seismic sources. The region in southwest China is situated in an evolving tectonic region transitioning between the uplifted Tibetan plateau to the west and the Yangtze continental platform to the east. The region displays varying crustal thickness from 35 km to over 60 km with seismic activity strongly associated with the locally mapped active faults.

The temporary seismic network, consisting of 25 portable broadband and narrow-band seismic stations, is deployed in the region of 98°E-105°E, 21°N-29°N. There are also 23 permanent digital broadband seismic stations recording in the region. Yunnan has the strongest intra-plate seismic activities in China. Moreover, there are several strong seismic zones in its surrounding areas, such as Tibet, Sichuan, Burma, and India. The strong seismicity in Yunnan and its surrounding areas provides the foundation for success of this deployment. Preliminary analyses have yielded an enhanced ground truth database, a 3-D structure model (together with some other analyses) for improving location, and characteristic spectral ratios for different events. Moreover, analysis of the recordings of some events of special interest, such as the January 26, 2001, M7.7 India earthquake and the February 14, 2001, M5.0 Yajiang, Sichuan, earthquake, has provided useful information on the source, path, and site effect, that are important for regional seismic studies.

KEY WORDS: Yunnan, Southwest China, broadband network, regional seismology, crustal structure

OBJECTIVE

The major purpose of this project is to collect fundamental ground truth data for advanced studies on regional crustal and mantle structures, earthquake prediction, and regional characteristics of wave propagation and seismic sources in Yunnan, China, through deploying a broadband portable seismic network in the area. The region in southwest China is situated in an evolving tectonic region transitioning between the uplifted Tibetan plateau to the west and the Yangtze continental platform to the east. The region displays varying crustal thickness from 35 km to over 60 km with seismic activity strongly associated with the mapped active faults. Figure 1 shows the topography of the Yunnan province. Yunnan has the strongest intra-plate seismic activities in China. There are several strong seismic zones in its surrounding areas, such as Tibet, Sichuan, Burma, and India. Moreover, there is an abundance of mining activities in this area. The strong seismicity and the intensive mining activities in Yunnan and its surrounding areas provide the foundation for success of this deployment.

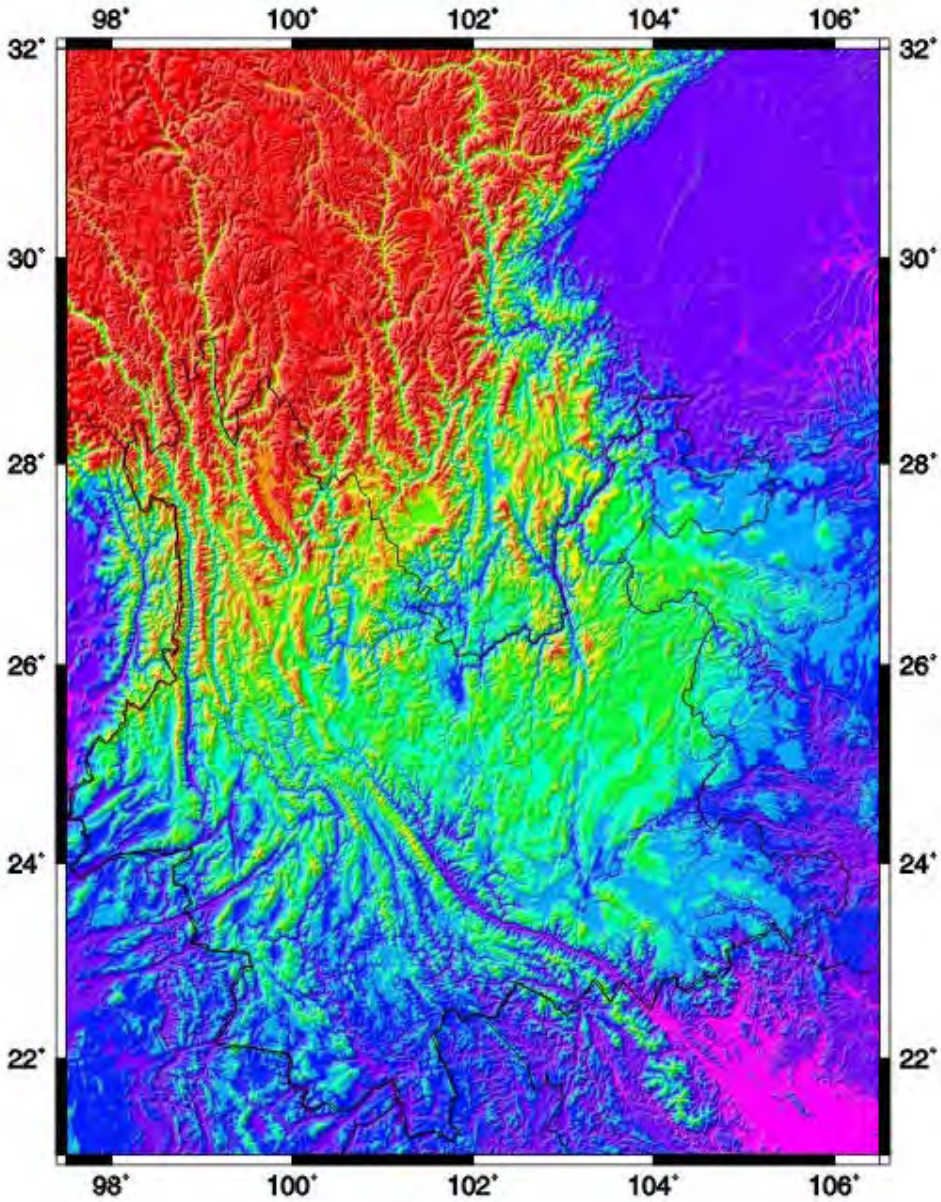

Figure 1. The topography in Yunnan, China. Large river valleys are often the places that the active faults cut through.

RESEARCH ACCOMPLISHED

More than 25 broadband portable stations have been deployed in Yunnan, China, jointly by Multimax Inc. and the Institute of Geophysics, China Seismological Bureau. The region covers 98°E-105°E, 21°N-29°N (Figure 2).

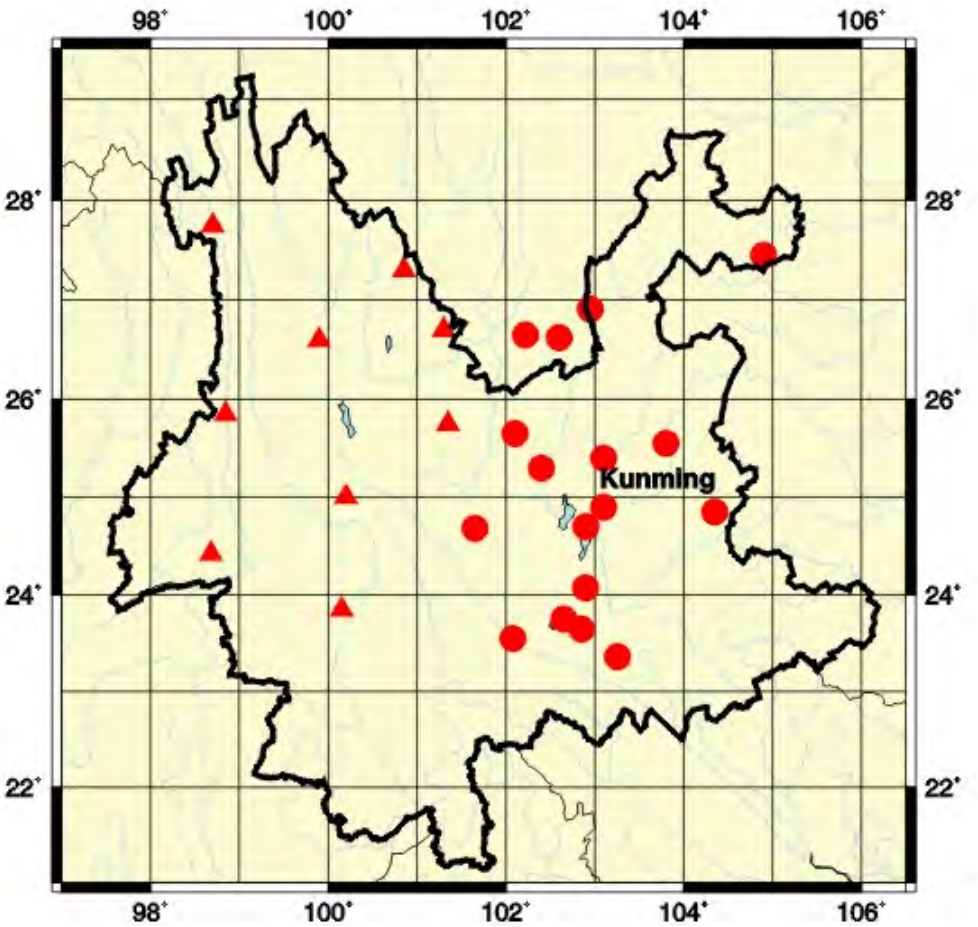

Figure 2. The stations of the portable broadband seismic network. Triangles are PASSCAL-type stations deployed by Multimax Inc. Circles are Chinese broadband instruments deployed by the Institute of Geophysics, CSB.

Most of the instruments are deployed alongside the existing short-period stations of the Yunnan Seismological Bureau (Figure 3a). The instruments are installed in vaults that are typically 30 meters deep extending horizontally into the hillside (Figure 3b). The local provincial bureaus provide the support in the security and maintenance of the instruments. Due to the remoteness of some of these stations, consistent power source remains a major issue that requires a high level of maintenance from our local collaborators. U.S. technicians return to the sites at regular intervals to perform data collection and maintenance of the instruments. The deployment and data collection will continue through June of 2002.

At the present stage of research, the data are being retrieved and transferred to Beijing and Washington from the field sites. The systematic analyses will be performed once a more complete data set becomes available. Several examples of different events recorded at various distances are shown in Figures 4 through 7 displaying the data quality.

Figure 3(a): Top – Broad-band instruments installed side by side to short-period Chinese SK-type instruments
Figure 3(b): Bottom – Entrance to vault housing the seismic instruments at one site in Yunnan, China

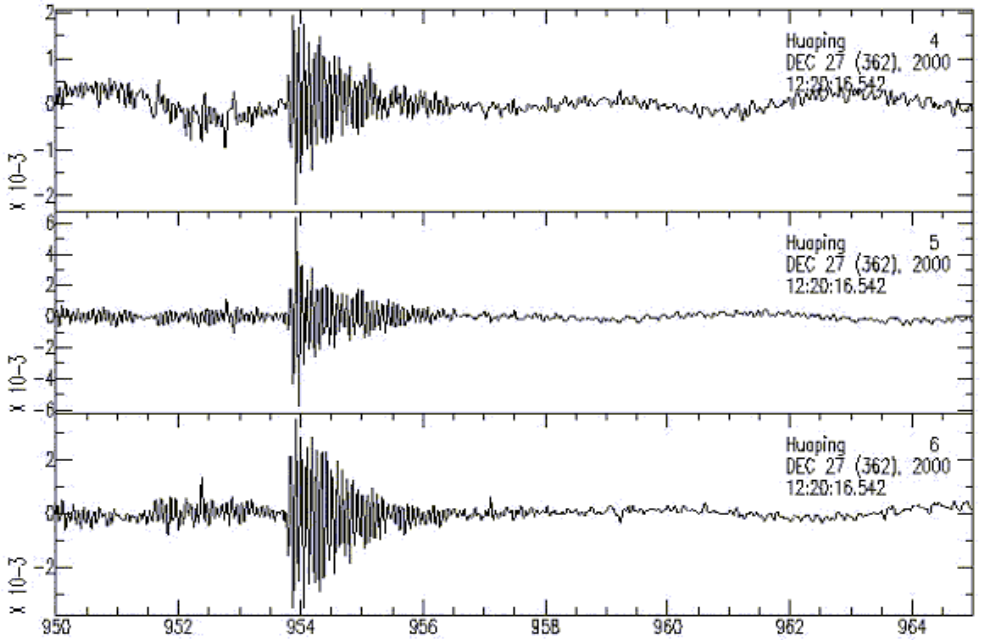

Figure 4. An example of local events. These events are in large amount. Some of them are explosions at local mines.

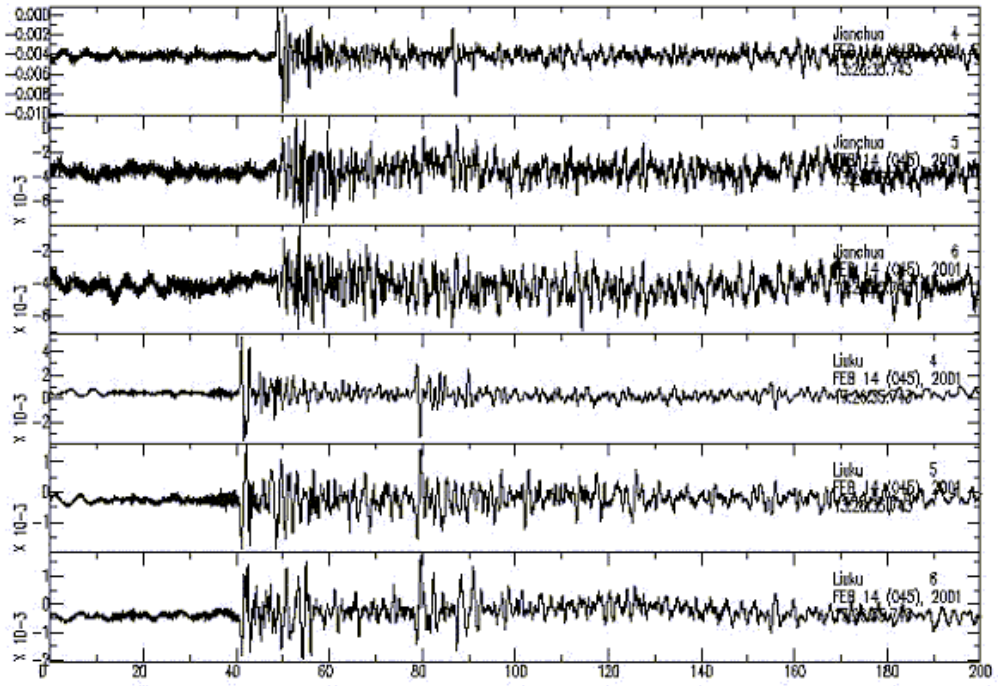

Figure 5. Example waveforms of a local (Δ~5°) M5.0 earthquake that occurred in Yajiang, Sichuan Province.

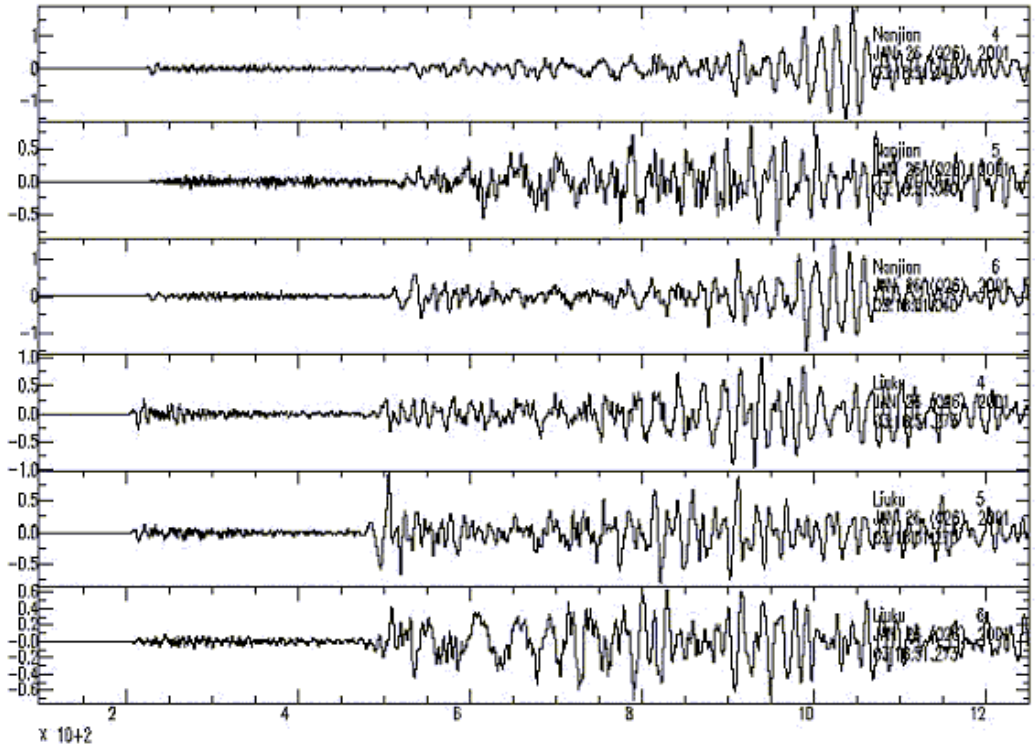

Figure 6. Example waveforms of a regional (Δ~26°) M7.7 large earthquake that occurred in India.

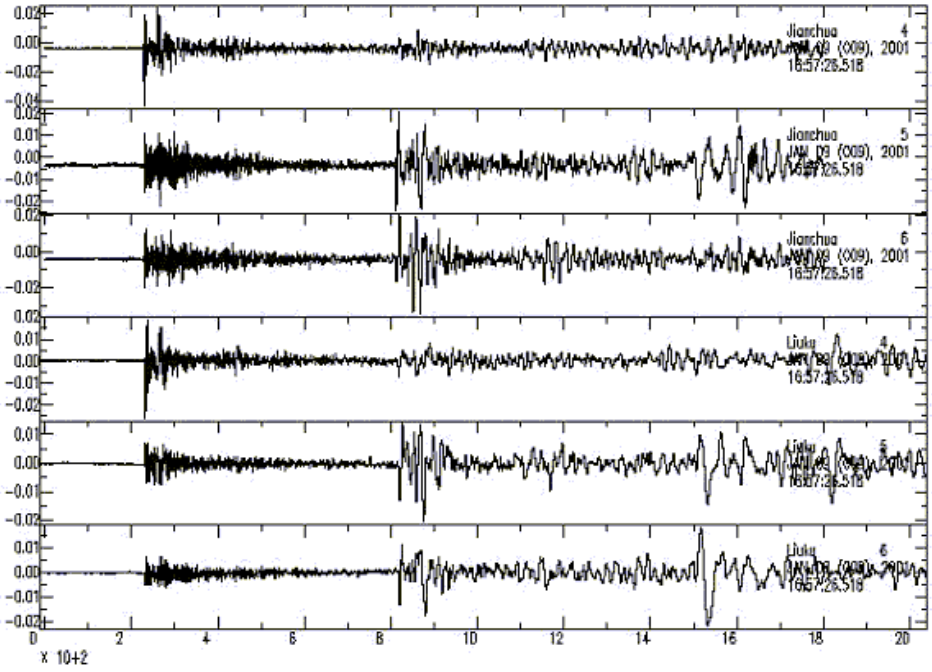

Figure 7. Example waveforms of a teleseismic (Δ~77°) M7.0 large earthquake that occurred in Vanuatu Islands.

CONCLUSIONS

High-quality waveform data with a full compliment of epicentral distances have been recorded by the portable broadband network. The complete dataset of this deployment will contribute tremendously to the ground truth information of Yunnan area. Such data are very important for studies in seismic source, earthquake prediction, and earthquake hazard reduction.

REFERENCES

Aki, K. (1980), Attenuation of shear waves in the lithosphere for frequencies from 0.05 to 25 Hz, *Phys. Earth Planet. Inter*., 21, 50-60.

Chen, P. S., F. T. Liu, Q. Li, and J. Z. Qin (1991), The lateral inhomogeneity in Yunnan province. China, *Science in China (Series B),* 34 (5), 630-640.

Cui, Z. Z., D. Y. Du, J. P. Chen, Z. Y. Zhang, and L. Y. Huang (1987), The Deep Structure and Tectonic Features of the Crust in Panxi Area, *Chinese J. Geophy*., 30(6): 566-580 (in Chinese).

Ge, B. R., and K. Y. Yang (1990), Mesozoic-Cenozoic Tectonic Features in Panzhihua-Xichang Area, *Chinese J. Geophy*., 33(1): 64-69 (in Chinese).

Herrmann, R. B., and C. J. Ammon (1997). Faulting parameters of earthquakes in the New Madrid, Missouri, region, *Engineering Geology* 46**,** 299-311.

Hu, H. X., et al. (1986), Explosion Investigation of the Crustal Structure in Western Yunnan Province. *Chinese J. Geophy*., 29(2), 133-144 (in Chinese).

Hu, H. X., Z. Y. Lin, Y. J. Bian, C. Y. Wang and L. B. Zhu (1996), Study on the Characteristics of Crust-Mantle Transition Zone in Western Yunnan Province, *Acta Seismologica Sinica,* 18 (4): 444-450 (in Chinese).

Lin, Z., et al. (1993), The Preliminary Interpretation of Deep Seismic Sounding in Western Yunnan, Acta Seismologica Sinica, 15 (4): 427-440 (in Chinese).

Liu, R. F., P. S. Chen, and Q. Li (1993), Three-Dimensional Velocity Images in Yunnan and Its Neibouring District, *Acta Seismologica Sinica*, 15 (1): 61-67 (in Chinese).

Liu, Z., R. B. Herrmann, J. Xie, and E. D. Cranswick (1991), Waveform characteristics and focal mechanisms of five aftershocks of the 1983 Goodnow, New York, earthquake by polarization analysis and waveform modeling, *Seism. Res. Letters*, 62, 123-133.

Malagnini, L. (1999), Ground Motion Scaling in Italy and Germany, *Ph. D. Dissertation*.

National Research Council (1997), Research Required to Support Comprehensive Test Ban Treaty Monitoring, National Academy Press, Washington, D.C.

Qin, J. Z., and R. J. Kan (1986), Q Values and Seismic Moments Estimates Using the Coda Waves of Near Earthquakes in the Kunming and Surrounding Regions, *Chinese J. Geophy*., 29(2): 145-155 (in Chinese).

Raoof, M., R. B. Herrmann, and L. Malagnini (1999), Attenuation and excitation of three-component ground motion in Southern California, *Bull. Seism. Soc. Am.* 89, (Aug. 99) preprint.

Rodgers, A. and W. Walter (1997), Regionalization and calibration of seismic discriminants, path effects, and signal-to-noise for station ABKT, *Proc. 19th Annual Seismic Research Symposium on Monitoring a*

Comprehensive Test Ban Treaty (Editors: M. J. Shore, R. S. Jih, A. Dainty, and J. Erwin), Defense Special Weapons Agency, Alexandria, 143-151.

Sun, K. Z., J. W. Teng, D. M. Jin, and Y. Zheng(1987), Q-Value and Its Lateral Variations in Pan-xi Tectonic Belt, *Chinese J. Geophy*., 30(1): 101-104 (in Chinese).

Wang, C. Y., X. L. Wang, and Q. Z. Yan (1994), Tree Dimensional Velocity Structure Beneath the Kunming Telemetered Seismic Network. Acta Seismologica Sinica, 1994, 16 (2): 167-175 (in Chinese).

Xiong, S. B., J. W. Teng, Z. X. Yin, M. H. Lai , and Y. P. Huang (1986), Explosion Seismological Study of the Structure of the Crust and Upper Mantle at Southern Part of the Panxi Tectonic, Belt, *Chinese J. Geophy*., 29(3), 235-244 (in Chinese).

Xiong, S. B., et al. (1993), The 2-D Structure and Its Tectonic Implications of the Crust in the Lijiang£-Panzhihua£-Zhehai Region, *Chinese J. Geophy*., 36(4), 434-444 (in Chinese).

Yazd, M. R. S. (1993), Ground motion studies in the Southern Great Basin of Nevada and California, *Ph. D. Dissertation*, Saint Louis University, 189p.

Zhu, P. D., Y. M. Li, L. M. Zhang, P. Y. Shu and S. H. Liang (1986), On the Study of the Seismic Telemetry Network in South Sichuan and North Yunnan Provinces, *Chinese J. Geophy*., 29(3), 245-254 (in Chinese).

RESULTS OF 1-D LOCATION CALIBRATION STUDIES RELATED TO THE TERRITORY OF NORTHERN EURASIA

Victor V. Kirichenko and Yury A. Kraev
Western Services Corporation
Under subcontract to
Science Applications International Corporation

Sponsored by The Defense Threat Reduction Agency

Contract No. DSWA01-98-C-0029

ABSTRACT

During the last three years, new regional travel-time tables for different geotectonic provinces of Northern Eurasia were developed in the framework of the Russian Seismoacoustic Research for Comprehensive Nuclear-Test-Ban Treaty (CTBT) Monitoring project. One of the main objectives of the project is to calibrate travel times for regional seismic waves travelling to the seismic stations of the Russian Academy of Sciences included in the International Monitoring System (IMS).

The territory of Northern Eurasia was initially subdivided into 13 provinces based on the results of the analysis of Pn travel times as well as taking into account recently published papers on seismic and tectonic regionalization of Northern Eurasia. We presented newly developed travel-time tables for different geotectonic provinces at the 21st and 22nd Seismic Research Symposiums. Upon completion the effort on collection and analysis of travel-time data for 13 studied provinces, we came to the conclusion that the territory of Northern Eurasia may be subdivided as follows: only three large geotectonic provinces for Pn and Sn phases (platform areas, paleozoic massifs and young platform as well as tectonically active regions); only two provinces for Pg phase and the only province for Lg phase. We present the recent regionalization of Northern Eurasia for our 1-D location calibration studies as well as newly constructed travel-time tables and their comparison with the IASPEI-91 tables. Also, source-specific station corrections (SSSCs) for the stations of the RAS included in the IMS are presented as well as their comparison with SSSCs developed by other research groups.

In the framework of our project performance we review recently published and historical data on peaceful nuclear explosions (PNE) in the former USSR. In the result we concluded that ISC location estimates for the number of PNEs are subjects of large (from about 20 km to 40 km and even more) errors. Details of our analyses are presented.

The newly constructed travel-time tables as well as their modeling errors were used for tests on re-location of the underground nuclear explosions in the former Soviet Union. A comparison between the mislocation estimates for the newly constructed travel-time tables, the IASPEI-91 travel-time tables and the ISC results is presented. We conclude that the newly developed 1-D regional travel-time tables are an effective tool to be used for seismic source location in Northern Eurasia.

KEY WORDS: seismic regional characterization, location calibration.

OBJECTIVE

This work presents the results of the three year effort on the development of regional travel-time tables for different geotectonic provinces of Northern Eurasia. The overall objective is to calibrate travel times for regional seismic waves travelling to the seismic stations of the Russian Academy of Sciences included in the IMS. The newly developed travel-time tables may be directly used to improve seismic event location as well as to test and to validate 3-D travel-time models currently being developed. This project is being performed by SAIC and its subcontractors: the Western Services Corporation, the Geophysical Survey (GS) of the Russian Academy of Sciences (RAS) and the Complex Seismological Expedition (CSE) of the United Institute of Physics of the Earth (UIPE) of the RAS.

RESEARCH ACCOMPLISHED

Calibration Events

At the final stage of the generalized travel-time tables development we used only underground nuclear explosions with precisely known origin times and locations. This set of explosions includes peaceful nuclear explosions conducted in the former USSR (Sultanov et al, 1999), underground nuclear explosions at the Semipalatinsk Test Site (Bocharov et al, 1989) as well as on Amchitka Island (Springer et al, 1971 and Springer et al, 1975).

Data on Travel Times

Data resources were formed on the basis of seismic observations conducted during the time framework of 1965 - 1990 by the GS of the RAS and the CSE of the UIPE of the RAS. Values of arrival times for major regional seismic phases (Pn/P, Pg, Sn/S and Lg) were measured, analyzed and collected. The total number of the GS's stations used for the purposes of seismic calibration is about 300. The total number of the CSE's stations used for the purposes of seismic calibration is about 200. Data of seismic observations of the RAS's institutions was added by the data of about 300 station in Northern Eurasia providing data to the International Seismological Center.

Regionalization

The regionalization of Northern Eurasia was carried out on the basis of recent neotectonics, geodynamics and seismicity studies (Seismicity and Seismic Zoning of Northern Eurasia, 1995; Grachev (2000)) as well as taking into account the results of our analysis of Pn/Sn travel times. Finally, the territory of the Northern Eurasia was subdivided into 13 provinces: Central-East-European territory, Timan and Pechora Plate, Scythian and Turanian Plates, Cenozoic folded regions, Ural folded region, West-Siberian platform, Kazakh massif, Altai and Sayan region, Siberian platform, Baikal rift zone, Amur and Maritime territory, North East territory, Chukot Peninsula and Kamchatka-Kuril-Sakhalin region. The polygon vertices for the specific provinces are presented in Table 1. The upper part of the Figure 1 presents the aforementioned regionalization of the territory of Northern Eurasia.

Results

The regional travel-time curves were constructed using linear regression of the experimental travel time data using one or two linear regressions for the residual standard deviation minimization. Modeling errors were calculated as standard deviations of the experimental data from the estimated lines in a 2-degree moving window with a 50 % overlap.

The basic equation and the parameters of the developed travel-time tables are presented in the Table 2. Upon completion the effort on construction and analysis of newly developed travel-time tables for 13 studied provinces, we concluded (based on the geological and tectonic features of the studied provinces as well as statistical tests) that the territory of Northern Eurasia may be subdivided as follows: only three large geotectonic provinces for Pn and Sn phases ((1)platform areas, (2) paleozoic massifs and young platform as well as (3) tectonically active regions); only two provinces for Pg phase and the only province for Lg phase (see the below part of the Figure 1). The polygon vertices for the generalized provinces of Northern Eurasia are presented in Table 3. The parameters of the generalized travel-time tables are presented in the Table 4 and appropriate modeling errors are presented in the Table 5.
The SSSCs for the stations of the Russian Academy of Sciences included to the IMS were calculated based on Bondar's approach (Xioping Yang et al, 1998). The Table 6 presents a comparison based on IASPEI-91 and SSSCs travel-time residuals for the IMS stations of the RAS. The improvement is obvious.

Tests on Relocation

We have located 44 historical PNEs in the former USSR with published ground truth origin times and locations (Sultanov et al, 1999) using the IASPEI-91 travel-time tables. Then, we relocated the aforementioned set of the explosions using the newly developed travel-time tables for the generalized provinces. To support our relocation tests the SSSCs were calculated for about 50 surrogate stations.

Relocation results for the aforementioned set of PNEs are presented in the Table 7 and may be summarized as follows:

- 84% of events moved closer to the GT epicenters with an average improvement of 8.4 km and a median improvement of 7.3 km;
- 82% of events moved closer to the GT epicenters by 20% or more with an average improvement of 8.3 km and median improvement of 7.2 km;
- 16% of events moved away from GT epicenters with an average deterioration of 6.3 km and a median deterioration of 5.4 km;
- 14% of events moved away to the GT epicenters by 20% or more with an average deterioration of 5.7 km and median deterioration of 4.9 km;
- average mislocations by using the IASPEI-91 tables and the SSSCs are 26.6 km and 8.6 km, respectively;
- median mislocations by using the IASPEI-91 tables and the SSSCs are 23.3 km and 7.3 km, respectively;
- 27% of GT epicenters are within the calculated 90% uncertainty ellipses by using the IASPEI-91 tables and 89% of GT epicenters are within the calculated 90% uncertainty ellipses by using the SSSCs;
- average uncertainty ellipse area is 861 km^2 for the IASPEI-91 tables and 547 km^2 for the SSSCs;
- median uncertainty ellipse area is 673 km^2 for the IASPEI-91 tables and 458 km^2 for the SSSCs;
- average and median decrease of 90% uncertainty ellipse size is 314 km^2 and 458 km^2, respectively;
- average bias in origin time estimation is 3.0 sec with an associated standard deviation of 1.6 sec for the IASPEI-91 tables and -0.2 sec with an associated standard deviation of 0.8 sec for the SSSCs.

CONCLUSIONS AND RECOMMENDATIONS

1. New regional travel-time tables for the different geotectonic provinces of the Northern Eurasia were developed and compared with the IASPEI-91 tables. The developed regional travel-time tables differ substantially from the IASPEI-91 travel-time tables. It was shown that the variety of geotectonic provinces may be presented for location calibration studies by the three extended provinces for Pn/Sn phases, by two provinces for Pg phase and the only province for Lg phase.
2. Validation testing for the set of 44 peaceful nuclear explosions conducted in the former USSR shows that estimates of event locations and time origins are significantly improved and location error ellipses are substantially reduced using the newly developed regional travel-time tables.
3. The developed regional travel-time tables are an effective tool to be used for seismic sources location at the territory of Northern Eurasia despite the fact of their one-dimensional origin.

ACKNOWLEDGEMENTS

The authors would like gratefully to thank Dr. Gerald Kent of SAIC for the overall program management, Dr. Oleg Starovoit of the GS RAS and Prof. Yury Kopnichev of the CSE of the UIPE of the RAS and their staff for providing data on travel times, computing support and fruitful discussions of research results.

REFERENCES

Bocharov, V.S., S.A. Zelentsov and V.N. Mikhailov, Characteristics of 92 Underground Nuclear Explosions at the Semipalatinsk Test Site, Atomnaya Energiya, 87, 3, 210-214 (in Russian).

Grachev A.F., Editor (2000), Neotectonics, Geodynamics and Seismicity of Northern Eurasia, Moscow, PROBEL Publishing House, United Institute of Physics of the Earth of the RAS, Fedynsky Center of Regional Geophysical and Geoecological Researches GEON of the Ministry of Natural Resources of Russia (in Russian).

Seismicity and Seismic Zoning of Northern Eurasia (1995), 2-3, Moscow, United Institute of Physics of the Earth of the RAS (in Russian).

Springer, D.L. and R.L. Kinnaman (1971), Seismic Source Summary for U.S. Underground Nuclear Explosions, 1961-1970, Bull. Seism. Soc. Am., 61, 1073-1098.

Springer, D.L. and R.L. Kinnaman (1975), Seismic Source Summary for U.S. Underground Nuclear Explosions, 1971-1973, Bull. Seism. Soc. Am., 65, 343-349.

Sultanov, D.D., J.R. Murphy, and Kh.D. Rubinstein (1999), A Seismic Source Summary for Soviet Peaceful Nuclear Explosions, Bull. Seism. Soc. Am., 89, 3, 640-647.

Xioping Yang, Keith McLaughlin, Robert North, SSSCs for Regional Phases at IMS Stations in North America and Fennoscandia, Technical Report CMR-98/46.

Table 1. Regionalization of Northern Eurasia

No.	Region Name	Polygon Vertices, Lat. (deg. N)-Long. (deg. E)
I	**Central-East-European territory**	70-48 67-48 67-49 66-49 66-50 65-50 65-51 64-52 63-52 63-53 62-53 62-54 61-54 61-56 60-57 57-57 57-56 46-56 46-49 47-49 47-47 48-46 49-46 49-40 47-40 47-27 48-27 08-26 49-26 49-25 50-25 50-10
II	**Timan-Pechora Plate**	69-48 69-62 68-62 68-64 67-64 67-63 66-63 66-59 65-59 65-58 63-58 63-57 60-57 60-56 61-56 61-54 62-54 62-53 63-53 63-52 64-52 64-51 65-51 65-50 66-50 66-49 67-49 67-48
III	**Ural folded region**	77-58 77-69 76-69 76-66 75-66 75-61 74-61 74-58 73-58 73-57 72-57 72-56 71-56 71-61 70-61 70-68 67-68 67-67 66-67 66-64 65-64 65-62 64-62 64-61 58-61 58-62 54-62 54-63 51-63 51-62 49-62 49-61 48-61 48-59 47-59 47-56 57-56 57-57 63-57 63-58 65-58 65-59 66-59 66-63 67-63 67-64 68-64 68-62 69-62 69-58 70-58 70-54 71-54 71-52 73-52 73-54 74-54 74-55 75-55 75-56 76-56 76-58
IV	**Scythian and Turanian Plates**	51-62 51-65 47-65 47-66 46-66 46-67 44-67 44-68 42-68 42-67 43-67 43-64 38-64 38-61 37-61 37-59 38-59 38-57 39-57 39-56 38-56 38-55 37-55 37-54 39-54 39-52 40-52 40-50 41-50 41-49 42-49 42-48 43-48 43-44 44-44 44-43 45-43 45-33 46-33 46-30 47-30 47-40 49-40 49-46 48-46 48-47 47-47 47-49 46-49 46-56 47-56 47-59 48-59 48-61 49-61 49-62
V	**Cenozoic folded regions (Carpathians, Crimea, Caucasus, Kopet-Dagh, Tien-Shan)**	50-20 50-25 49-25 49-26 48-26 48-27 47-27 47-30 46-30 46-33 45-33 45-43 44-43 44-44 43-44 43-48 42-48 42-49 41-49 41-50 40-50 40-52 39-52 39-54 37-54 37-55 38-55 38-56 39-56 39-57 38-57 38-59 37-59 37-61 38-61 38-64 43-64 43-67 42-67 42-68 44-68 44-67 45-67 45-69 44-69 44-70 43-70 43-75 44-75 44-77 45-77 45-79 46-79 46-81 49-81 49-84 48-84 48-86 47-86 47-87 46-87 46-90 45-90 45-100 40-100 40-76 34-76 34-40 41-40 41-20
VI	**Kazakh massif**	53-63 53-65 54-65 54-70 53-70 53-72 52-72 52-75 51-75 51-81 46-81 46-79 45-79 45-77 44-77 44-75 43-75 43-70 44-70 44-69 45-69 45-67 46-67 46-66 47-66 47-65 51-65 51-63
VII	**West-Siberian platform**	77-69 77-113 74-113 74-106 73-106 73-105 72-105 72-101 71-101 71-90 70-90 70-86 67-86 67-87 66-87 66-88 63-88 63-89 62-89 62-90 60-90 60-91 59-91 59-92 57-92 57-89 56-89 56-86 57-86 57-85 56-85 56-83 54-83 54-82 52-82 52-81 51-81 51-75 52-75 52-72 53-72 53-70 54-70 54-65 53-65 53-63 54-63 54-62 58-62 58-61 64-61 64-62 65-62 65-64 66-64 66-67 67-67 67-68 70-68 70-61 71-61 71-56 72-56 72-57 73-57 73-58 74-58 74-61 75-61 75-66 76-66 76-69
VIII	**Altai and Sayan region**	59-92 59-94 55-94 55-99 54-99 54-101 53-101 53-102 43-102 45-90 46-90 46-87 47-87 47-86 48-86 48-84 49-84 49-81 52-81 52-82 54-82 54-83 56-83 56-85 57-85 57-86 56-86 56-89 57-89 57-92
IX	**Baikal rift zone**	52-102 52-105 53-105 53-107 54-107 54-108 56-108 56-109 57-109 57-111 58-111 58-113 59-113 59-117 58-117 58-121 57-121 57-123 56-123 56-125 55-125 55-120 54-120 54-117 53-117 53-112 52-112 52-110 50-110 50-102
X	**Siberian platform**	74-106 74-127 69-127 69-125 68-125 68-124 67-124 67-125 65-125 64-127 64-130 63-130 63-136 59-136 59-134 58-134 58-133 57-133 57-131 56-131 56-128 55-128 55-125 56-123 57-123 57-121 58-121 58-117 59-117 59-113 58-111 57-111 57-109 56-109 56-108 54-108 54-107 53-105 52-105 52-102 53-102 53-101 54-101 54-99 55-99 55-94 59-94 59-91 60-91 60-90 62-90 62-89 63-89 63-88 66-88 66-87 67-87 67-86 70-86 70-90 71-90 71-101 72-101 72-105 73-105 73-106
XI	**North East territory and Chukot Peninsula**	73-127 73-170W 60-170W 60-160 59-160 59-140 55-140 55-128 59-160 59-140 55-140 55-128 56-128 56-131 57-131 57-133 58-133 58-134 59-134 59-136 63-136 63-130 64-130 64-127 65-127 65-125 67-125 67-124 68-124 68-125 69-125 69-127
XII	**Amur and Maritime territory**	55-120 55-140 44-140 44-120
XIII	**Kamchatka-Kuril-Sakhalin region**	59-160 60-160 60-164 50-164 50-157 48-157 48-154 46-154 46-150 43-150 43-140

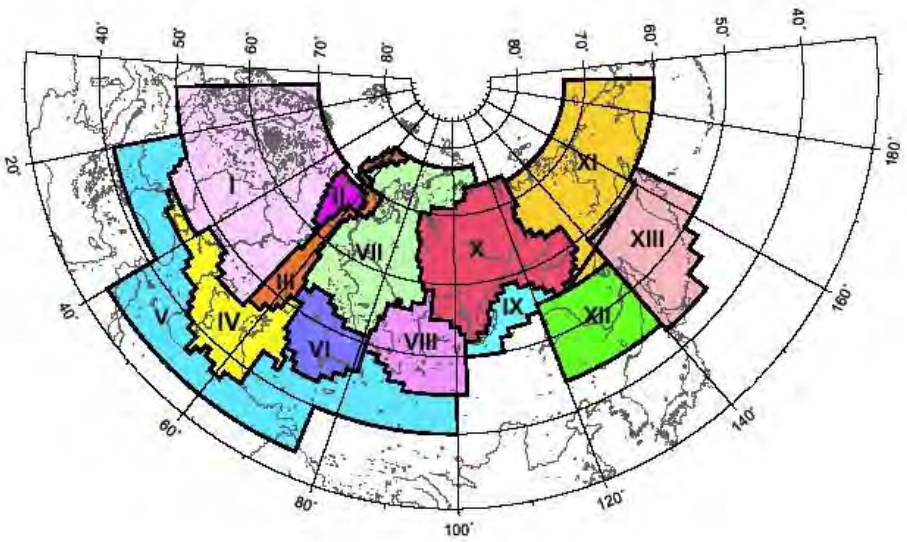

Pn, Sn

Lg

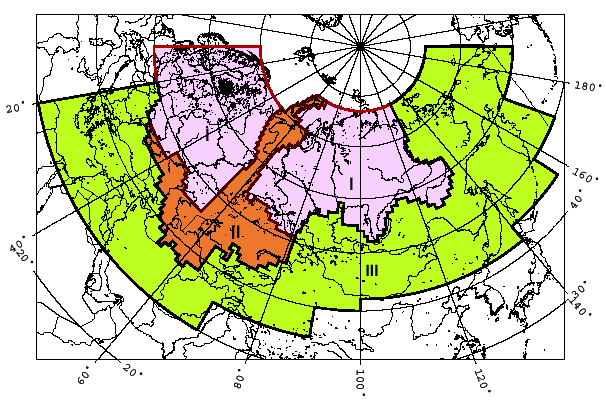

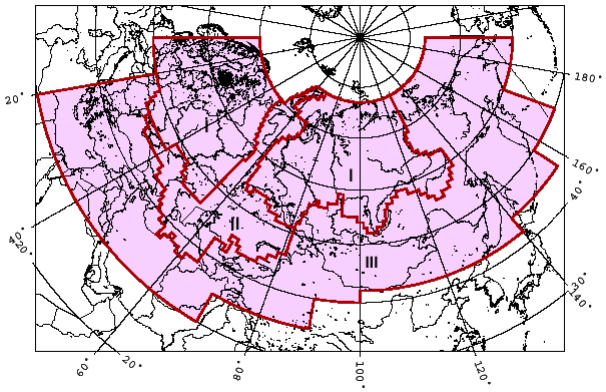

Pg

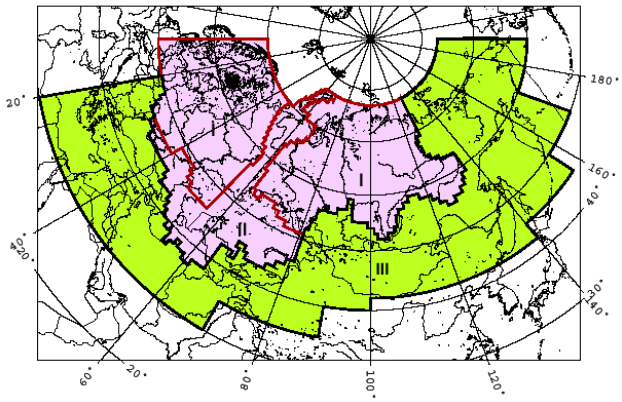

Figure 1. Regionalization of Northern Eurasia.

Table 2. Parameters of the Developed Travel-Time Curves (Depth = 0 km)
Basic Equation: $T-R/V_{red} = (A\pm\sigma_A) - (B \pm \sigma_B)\times R$

Phase	Range, km	V_{red}, km/sec	A	σ_A	B	σ_B	N	r	SD, sec
I. Central-East-European territory									
Pn	220-1100	8.0	7.78	0.36	0.0040	0.0004	43	0.83	0.7
	1101-2200	8.0	13.24	0.60	0.0089	0.0004	108	0.92	1.1
Sn	220-2200	4.62	14.86	1.88	0.0046	0.0018	50	0.34	3.1
Pg	220-1400	6.0	0.88	0.87	0.0066	0.0010	29	0.80	1.5
Lg	220-2200	3.5	2.86	2.42	0.0077	0.0021	167	0.13	5.0
II. Timan-Pechora Plate, IV. Scythian and Turanian Plates									
Pn	200-2000	8.0	8.26	0.69	0.0042	0.0011	29	0.58	0.9
Sn	350-1400	4.62	16.08	1.47	0.0031	0.0020	20	0.35	2.0
Pg	350-1000	6.0	-1.16	2.31	0.0044	0.0034	17	0.31	2.6
Lg	350-1500	3.5	3.20	2.23	0.0085	0.0030	23	0.52	3.4
III. Ural folded region									
Pn	300-2000	8.0	8.89	0.36	0.0047	0.0003	33	0.95	0.7
Sn	300-2000	4.62	12.54	1.90	-0.0006	0.0015	30	0.08	3.2
Pg	300-1200	6.0	1.13	2.80	0.0074	0.0030	14	0.57	2.8
Lg	300-2000	3.5	-2.80	3.16	0.0026	0.0025	20	0.24	4.8
V. Cenozoic folded regions									
Pn	200-990	8.0	8.20	0.41	0.0018	0.0006	91	0.32	1.2
	991-2000	8.0	10.88	0.88	0.0048	0.0006	51	0.75	1.1
Sn	200-2000	4.62	14.19	0.82	0.0001	0.0009	51	0.01	2.1
Pg	200-1100	6.0	0.77	1.04	0.0039	0.0014	29	0.49	1.4
Lg	220-2200	3.5	2.86	2.42	0.0077	0.0021	167	0.13	5.0
VI. Kazakh massif									
Pn	200-1800	8.0	9.42	0.22	0.0050	0.0002	64	0.94	0.7
Sn	200-1800	4.62	15.10	0.82	0.0029	0.0008	51	0.47	2.3
Pg	300-1200	6.0	1.13	2.80	0.0074	0.0030	14	0.57	2.8
Lg	300-2000	3.5	-2.80	3.16	0.0026	0.0025	20	0.24	4.8
VII. West-Siberian platform									
Pn	220-2200	8.0	8.22	0.22	0.0061	0.0002	70	0.90	1.3
Sn	220-2200	4.62	12.82	1.47	0.0021	0.0010	56	0.28	3.5
Pg	250-1200	6.0	1.26	2.17	0.0083	0.0022	22	0.64	2.4
Lg	220-2200	3.5	-2.96	2.77	0.0038	0.0018	44	0.30	6.3
VIII. Altai and Sayan region									
Pn	200-2200	8.0	8.71	0.24	0.0021	0.0002	113	0.66	1.0
Sn	220-2200	4.62	14.85	0.72	-0.0017	0.0006	47	0.35	2.0
Pg	200-1200	6.0	0.54	1.03	0.0038	0.0012	36	0.47	1.7
Lg	200-2200	3.5	-2.52	1.12	0.0011	0.0009	57	0.16	3.4
IX. Baikal rift zone, XII. Amur and Maritime territory									
Pn	200-2000	8.0	7.01	0.27	0.0011	0.0003	44	0.56	0.9
Sn	200-2000	4.62	12.26	0.90	-0.0032	0.0009	33	0.54	2.7
Pg	200-1200	6.0	-0.88	0.77	0.0030	0.0010	28	0.50	1.5
Lg	200-2200	3.5	-1.18	0.79	0.0016	0.0006	41	0.34	2.6
X. Siberian platform									
Pn	220-999	8.0	7.75	0.74	0.0043	0.0010	33	0.62	1.1
	1000-2200	8.0	10.89	0.69	0.0074	0.0004	80	0.90	1.3
Sn	200-2000	4.62	15.78	1.11	0.0057	0.0007	91	0.63	3.3
Pg	200-1100	6.0	-1.80	1.36	0.0035	0.0015	39	0.36	2.3
Lg	220-2200	3.5	-4.57	1.28	0.0002	0.0008	82	0.01	4.1
XI. North East territory and Chukot Peninsula									
Pn	220-1900	8.0	7.57	0.51	0.0020	0.0004	26	0.68	0.9
Sn	220-2000	4.62	11.17	1.73	-0.0033	0.0013	18	0.54	3.2
Pg	200-1200	6.0	-0.76	1.77	0.0020	0.0024	7	0.35	1.9
Lg	200-2200	3.5	-0.71	2.09	0.0018	0.0013	21	0.29	4.3
XIII. Kamchatka-Kuril-Sakhalin									
Pn	200-1800	8.0	6.99	0.51	0.0015	0.0004	43	0.47	1.0
Sn	220-2000	4.62	17.89	2.96	0.0010	0.0021	21	0.10	3.3

Note: **T - travel time, sec; R - epicentral distance, km; V_{red} - reduction velocity, km/sec; N - data set; r – correlation coefficient; SD - residual standard deviation, sec.**

Table 3. Generalized Regionalization of Northern Eurasia

No.	Region Name	Polygon Vertices, Lat. (deg. N) – Long. (deg. E)
I	Platform areas	70-10 70-48 67-48 67-49 66-49 66-50 65-50 65-51 64-51 64-52 63-52 63-53 62-53 62-54 61-54 61-56 60-56 60-57 57-57 57-56 46-56 46-49 47-49 47-47 48-47 48-46 49-46 49-40 47-40 47-27 48-27 48-26 49-26 49-25 50-25 50-10 77-69 77-127 69-127 69-125 68-125 68-124 67-124 67-125 65-125 65-127 64-127 64-130 63-130 63-136 59-136 59-134 58-134 56-123 57-123 57-121 58-121 58-117 59-117 59-113 58-113 58-111 57-111 57-109 56-109 56-108 54-108 54-107 53-107 53-105 52-105 52-102 53-102 53-101 54-101 54-99 55-99 55-94 59-94 59-92 57-92 57-89 56-89 56-86 57-86 57-85 56-85 56-83 54-83 54-82 52-82 52-81 51-81 51-75 52-75 52-72 53-72 53-70 54-70 54-65 53-65 53-63 54-63 54-62 58-62 58-61 64-61 64-62 65-62 65-64 66-64 66-67 67-67 67-68 70-68 70-61 71-61 71-56 72-56 72-57 73-57 73-58 74-58 74-61 75-61 75-66 76-66 76-69
II	Paleozoic massifs and young plates	77-58 77-69 76-69 76-66 75-66 75-61 74-61 74-58 73-58 73-57 72-57 72-56 71-56 71-61 70-61 70-68 67-68 67-67 66-67 66-64 65-64 65-62 64-62 64-61 58-61 58-62 54-62 54-63 53-63 53-65 54-65 54-70 53-70 53-72 52-72 52-75 51-75 51-81 46-81 46-79 45-79 45-77 44-77 44-75 43-75 43-70 44-70 44-69 45-69 45-67 44-67 44-68 42-68 42-67 43-67 43-64 38-64 38-61 37-61 37-59 38-59 38-57 39-57 39-56 38-56 38-55 37-55 37-54 39-54 39-52 40-52 40-50 41-50 41-49 42-49 42-48 43-48 43-44 44-44 44-43 45-43 45-33 46-33 46-30 47-30 47-40 49-40 49-46 48-46 48-47 47-47 47-49 46-49 46-56 57-56 57-57 60-57 60-56 61-56 61-54 62-54 62-53 63-53 63-52 64-52 64-51 65-51 65-50 66-50 66-49 67-49 67-48 70-48 70-51 72-51 72-52 73-52 73-54 74-54 74-55 75-55 75-56 76-56 76-58
III	Tectonic active regions	77-127 77-170W 60-170W 60-170 50-170 50-157 45-157 45-140 42-140 42-100 40-100 40-90 35-90 35-70 30-70 30-20 50-20 50-25 49-25 49-26 48-26 48-27 47-27 47-30 46-30 46-33 45-33 45-43 44-43 44-44 43-44 43-48 42-48 42-49 41-49 41-50 40-50 40-52 39-52 39-54 37-54 37-55 38-55 38-56 39-56 39-57 38-57 38-59 37-59 37-61 38-61 38-64 43-64 43-67 42-67 42-68 44-68 44-67 45-67 45-69 44-69 44-70 43-70 43-75 44-75 44-77 45-77 45-79 46-79 46-81 52-81 52-82 54-82 54-83 56-83 56-85 57-85 57-86 56-86 56-89 57-89 57-92 59-92 59-94 55-94 55-99 54-99 54-101 53-101 53-102 52-102 52-105 53-105 53-107 54-107 54-108 56-108 56-109 57-109 57-111 58-111 58-113 59-113 59-117 58-117 58-121 57-121 57-123 56-123 56-125 55-125 55-128 56-128 56-131 57-131 57-133 58-133 58-134 59-134 59-136 63-136 63-130 64-130 64-127 65-127 65-125 67-125 67-124 68-124 68-125 69-125 69-127

Table 4. Parameters of the Generalized Travel-Time Curves (Depth = 0 km)
Basic Equation: $T\text{-}R/V_{red} = (A \pm \sigma_A) - (B \pm \sigma_B) \times R$

Phase	Range, km	V_{red}, km/sec	A	σ_A	B	σ_B	N	r	SD, sec
I. Platform areas									
Pn	220-1190	8.0	8.18	0.36	0.0049	0.0004	103	0.75	1.0
	1191-2200	8.0	12.49	0.49	0.0085	0.0003	262	0.88	1.3
Sn	220-2200	4.62	14.54	0.73	0.0043	0.0005	246	0.50	3.6
Pg	220-1400	6.0	-0.44	0.73	0.0047	0.0010	109	0.42	2.1
Lg	200-2500	3.5	-1.69	0.59	0.0020	0.0005	462	0.20	5.3
II. Paleozoic massifs and young plates									
Pn	200-2200	8.0	8.95	0.17	0.0047	0.0002	153	0.93	0.9
Sn	350-1400	4.62	14.40	0.70	0.0016	0.0007	100	0.24	2.7
Pg	220-1400	6.0	-0.44	0.73	0.0047	0.0010	109	0.42	2.1
Lg	200-2500	3.5	-1.69	0.59	0.0020	0.0005	462	0.20	5.3
III. Tectonic active regions									
Pn	200-1800	8.0	8.54	0.17	0.0024	0.0002	342	0.62	1.2
Sn	200-2000	4.62	13.18	0.57	-0.0018	0.0005	165	0.25	3.0
Pg	200-1400	6.0	-0.44	0.52	0.0026	0.0007	98	0.37	1.6
Lg	200-2500	3.5	-1.69	0.59	0.0020	0.0005	462	0.20	5.3

Note: **T - travel time, sec; R - epicentral distance, km; V_{red} - reduction velocity, km/sec; N - data set; r - correlation coefficient; SD - residual standard deviation, sec.**

Table 5. Modeling Errors for the Generalized Geotectonic Provinces of Northern Eurasia

Dis-tance, deg.	I. Platform areas				II. Paleozoic massifs and young plates				III. Tectonic active regions			
	Modeling Error, sec				Modeling Error, sec				Modeling Error, sec			
	Pn	Pg	Sn	Lg	Pn	Pg	Sn	Lg	Pn	Pg	Sn	Lg
2	0.6	1.4	0.4	3.4	0.5	1.4	2.6	3.4	0.9	1.2	2.7	3.4
3	0.6	1.2	0.3	3.2	0.5	1.2	2.1	3.2	1.0	1.4	2.9	3.2
4	0.8	1.8	2.3	3.3	0.8	1.8	2.0	3.3	0.9	1.3	2.4	3.3
5	0.8	2.2	2.1	3.7	0.8	2.2	2.0	3.7	0.9	1.3	2.0	3.7
6	0.8	2.4	1.9	3.8	0.8	2.4	2.2	3.8	1.2	1.3	2.3	3.8
7	1.0	2.7	2.8	3.9	0.9	2.7	2.7	3.9	1.2	1.6	2.7	3.9
8	1.5	2.2	2.9	4.1	0.9	2.2	2.9	4.1	1.2	2.0	3.6	4.1
9	1.2	2.1	3.3	5.6	1.0	2.1	3.1	5.6	1.4	2.0	3.8	5.6
10	1.2	3.0	3.4	5.3	1.0	3.0	1.7	5.3	1.3	2.0	3.4	5.3
11	1.3	2.8	3.3	5.1	1.0	2.8	2.8	5.1	1.3	1.9	4.2	5.1
12	1.3		3.8	6.7	0.9		4.1	6.7	1.2		4.4	6.7
13	1.3		3.7	6.3	1.2		3.4	6.3	1.3		3.2	6.3
14	1.3		3.4	6.4	1.1		3.2	6.4	1.4		3.1	6.4
15	1.4		4.2	6.4	0.9		3.5	6.4	1.2		3.1	6.4
16	1.3		4.5	6.4	1.0		3.4	6.4	1.5		4.4	6.4
17	1.4		3.9	6.3	0.9		3.5	6.3	1.5		3.1	6.3
18	1.3		3.4	5.7	0.9		3.3	5.7	1.5		2.3	5.7
19	1.3		3.5	5.3				5.3				5.3
20	1.1			6.2				6.2				6.2

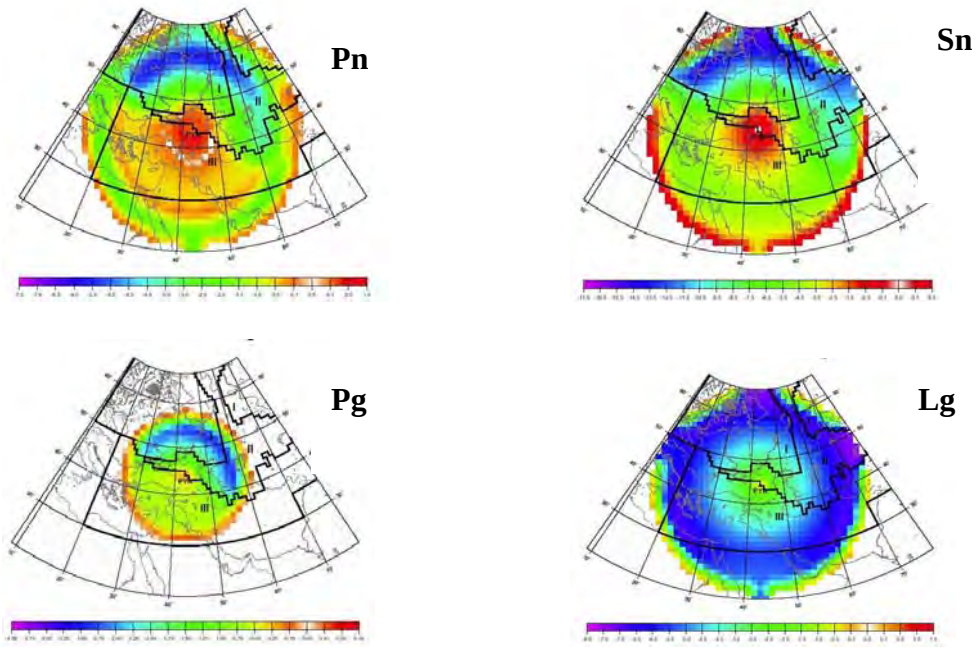

Figure 2. Examples of SSSCs for KIV0 developed using 1-D models.

Table 6. Travel-Time Residuals

IMS Station	Surrogate Station	Dist., km	Phase	N	IASPEI-91		1-D SSSCs	
					Mean, sec	SD, sec	Mean, sec	SD, sec
OBN	OBN	0.0	Pn	37	-3.1	1.6	0.7	1.1
			Sn	20	-11.7	4.0	-1.5	2.8
			Pg	13	-3.2	3.6	0.4	1.6
			Lg	17	-2.3	2.4	2.6	2.7
ARU	ARU	0.0	Pn	48	-3.3	1.7	0.2	1.2
			Sn	33	-7.2	4.8	0.6	4.2
			Pg	13	-3.4	2.3	-1.1	2.2
			Lg	24	-6.1	3.9	-2.0	5.7
KIV0	PYA	28.9	Pn	20	-2.6	1.4	-0.7	0.7
YAK	YAK	0.0	Pn	21	-3.6	2.5	0.0	1.5
			Sn	16	-12.4	5.7	-1.9	3.3
			Pg	6	-2.8	1.9	-0.3	1.9
			Lg	14	-2.8	4.2	2.2	4.1
TIXI	TIK	0.0	Pn	18	-4.0	1.3	0.3	1.3
			Sn	16	-10.8	4.3	-0.2	2.5
			Pg	4	-4.6	2.1	-2.2	2.0
			Lg	13	-2.5	3.4	2.4	3.6
TLY	IRK	75.9	Pn	22	-1.9	2.5	0.0	1.3
			Sn	15	-12.0	4.1	-3.2	3.0
			Pg	8	-1.7	1.2	1.1	1.0
			Lg	15	-3.2	3.9	2.4	3.1
MA2	MA1	0.0	Pn	10	-2.7	1.3	0.6	1.1

Table 7. Relocation Results for PNEs (GT0) Conducted in the Former USSR

No.	Date yy/mm/dd	Ndef (GAP)	IASPEI-91				SSSCs (1-D)			
			Mis-location, km	Ellipse area, km^2	To Res, s	GT within ellipse	Mis-location, km	Ellipse area, km^2	To Res, s	GT within ellipse
1.	69/09/02	18(120)	26.7	641	4.2	-	3.1	470	-0.6	+
2.	69/09/08	25(120)	33.3	397	3.5	-	7.9	360	-0.4	+
3.	69/09/69	14(106)	23.2	798	2.7	-	4.9	537	-0.1	+
4.	69/12/06	10(146)	59.6	798	0.2	-	4.4	572	1.4	+
5.	70/12/23	12(82)	9.1	648	1.9	+	13.8	435	-0.3	-
6.	71/07/02	18(129)	10.1	758	4.5	+	10.8	474	-0.4	+
7.	71/07/10	26(104)	10.3	625	4.2	+	15.8	407	-1.3	-
8.	71/09/19	20(143)	23.1	377	1.6	-	4.9	332	-0.6	+
9.	71/10/04	19(131)	12.2	430	3.5	-	5.8	335	-0.3	+
10.	72/08/20	17(103)	11.4	1156	3.4	+	9.5	500	-0.2	+
11.	72/09/21	14(132)	33.9	927	2.3	-	10.8	558	-0.8	+
12.	72/10/03	17(94)	30.1	781	2.9	-	10.5	461	1.2	+
13.	72/11/24_1	16(133)	16.1	650	-3.0	-	3.8	396	-0.9	+
14.	72/11/24_2	12(175)	4.4	1164	2.7	+	6.9	656	-1.2	+
15.	73/08/15	13(157)	21.4	1051	1.6	-	7.3	547	0.0	+
16.	73/08/28	12(153)	4.9	564	1.6	+	1.3	410	-0.5	+
17.	73/09/19	12(158)	26.7	1001	0.8	-	13.2	674	-1.3	+
18.	74/08/14	8(227)	45.4	3932	3.3	-	3.8	1952	1.4	+
19.	74/08/29	16(192)	35.7	1494	2.2	-	12.2	695	-0.2	+
20.	75/08/12	10(125)	41.7	1052	2.0	-	5.4	454	-0.8	+
21.	75/09/29	13(177)	48.8	713	2.9	-	12.6	1083	-0.4	+
22.	76/05/11	19(108)	17.2	426	4.3	-	5.4	345	-0.6	+
23.	77/07/26	13(210)	61.2	941	2.9	-	9.3	1196	-0.9	+
24.	77/08/10	12(218)	20.9	1571	-0.3	+	4.4	870	0.1	+
25.	77/08/20	18(120)	2.1	570	4.7	+	7.3	438	0.1	+
26.	77/09/10	16(156)	63.8	1198	2.5	-	19.4	576	-0.2	-
27.	77/09/30	12(206)	35.9	2597	2.6	-	6.6	1154	-1.9	+
28.	78/08/09	16(98)	17.2	679	2.5	-	7.3	379	0.4	+
29.	78/08/24	19(97)	30.5	451	4.9	-	14.0	379	0.5	-
30.	78/09/21	18(118)	56.2	419	4.3	-	10.6	363	0.0	+
31.	78/10/17_1	17(105)	23.4	667	3.3	-	5.8	348	-0.5	+
32.	78/10/17_2	17(119)	23.1	541	6.9	-	6.9	398	0.4	+
33.	79/08/12	16(94)	64.2	599	2.3	-	13.9	447	-0.1	+
34.	79/09/06	15(94)	2.9	594	4.9	+	3.8	435	0.2	+
35.	79/10/04	17(123)	10.3	580	3.7	+	6.2	463	0.3	+
36.	80/10/08	13(96)	23.1	939	4.5	-	7.0	481	1.1	+
37.	81/09/26_1	14(107)	27.4	895	3.1	-	10.5	473	-0.6	+
38.	83/07/10_1	16(132)	25.3	497	2.0	-	5.8	443	-1.2	+
39.	83/09/24_1	14(138)	20.0	983	3.7	-	10.1	544	1.1	+
40.	84/07/21_1	16(81)	9.8	609	3.7	+	6.9	393	0.1	+
41.	84/09/17	15(114)	51.3	935	2.7	-	14.6	472	-0.4	+
42.	85/07/18	17(104)	25.9	506	3.6	-	16.7	401	-1.3	-
43.	88/08/22	17(98)	27.7	355	4.3	-	7.6	418	0.4	+
44.	88/09/06	16(84)	5.4	379	4.7	+	8.5	327	0.5	+
Mean:			**26.6 km**	**861 km^2**	**3.0 sec**	**27%**	**8.6 km**	**547 km^2**	**-0.2 sec**	**89%**
SD:			**17.2 km**	**621 km^2**	**1.6 sec**		**4.0 km**	**298 km^2**	**0.8 sec**	

SEISMIC CALIBRATION AND DISCRIMINATION IN NORTHEAST RUSSIA

Kevin Mackey and Kazuya Fujita

Michigan State University

Sponsored by Defense Threat Reduction Agency

Contract No. DTRA01-98-C-0168

ABSTRACT

In an effort to obtain ground truth (GT) classifications in support of nuclear explosion monitoring for continental regions of northeastern Russia, we relocated and assigned GT classifications to 118 seismic events reported in the International Seismological Centre (ISC) supplemented with previously unavailable local data. Of the relocated events, 26 events are classified as GT10. From these events, consistent patterns of residuals, essentially source-specific station corrections (SSSC's), show upper mantle velocities are elevated under the Siberian platform and slower below the northern Sea of Okhotsk.

To further improve calibration capabilities in northeast Russia, we have been analyzing data from a small network of digital seismic stations deployed in the Magadan region. The stations are located close to areas of both tectonic seismicity and active mining, thus record signals from both. We have been undertaking routine phase time picking and hypocenter determination of both local and near regional seismic events and confirmed/suspected mine explosions.

Using waveforms of both tectonic events and mine blasts, we have begun the process of explosion discrimination using amplitude ratios of various Lg frequencies. Preliminary results indicate that the ratio Lg(4-8Hz)/Lg(0.75-1.5Hz) using peak amplitudes may not be sufficient to discriminate mining explosions from earthquakes in northeast Russia. Additional, more comprehensive research is underway.

We have undertaken efforts to acquire improved ground truth data for both earthquakes and explosions. In January 2001 two moderate earthquakes occurred approximately 100 km west of Magadan. We deployed two temporary stations to investigate the aftershock sequences of both events. About 15 events were locate-able although several more were recorded. To obtain ground truth data for explosions, we have deployed temporary stations and recorded quarry blasts near Magadan, and are currently undertaking an experiment to record explosions at a coal mine several hundred kilometers north of Magadan.

KEY WORDS: GT classification, ground truth, explosion discrimination, northeast Russia

OBJECTIVE

The objective of our research is to improve epicentral coordinates to better locate and identify ground truth seismic events in northeast Russia in support of Comprehensive Nuclear-Test-Ban Treaty (CTBT) monitoring A second aspect of our research to improve CTBT monitoring capability in northeast Russia is to deploy a network of digital stations for obtaining ground truth events and using waveform characteristics for event discrimination.

RESEARCH ACCOMPLISHED

GT Classified events

In effort to obtain ground truth (GT) classifications in support of Comprehensive Nuclear-Test-Ban Treaty monitoring for continental regions of northeastern Russia, we have relocated 118 seismic events reported in the International Seismological Centre (ISC) catalog which occurred from 1970 through 1997 (Figure 1). ISC solutions for this region utilize data from very few local or regional stations. In this study, we have supplemented ISC data with local and regional arrivals from Russian regional seismic networks. Local unpublished data from the bulletins of the Kamchatka, Magadan, Yakutsk, Amur, Sakhalin, and Irkutsk networks were used. For many of the events, selected original seismograms were inspected to obtain arrival times not otherwise recorded. Often this was for stations in one network for an event which occurred within the area covered by another network, since data are not normally exchanged between networks.

In the process of combining local network data with ISC arrivals, it was found that for stations up to 10^o distance, phases reported in ISC are sometimes misidentified. The most common misassociation is the secondary Pg or Sg phase identified as a Pn/P or Sn/S arrival. This misidentification of phases can result in poor hypocenter determinations by ISC, particularly for events with few receiving stations or poor azimuth distribution to stations. These errors arise due to the fact that arrival times and phases reported to the ISC for many of the Russian stations are the result of preliminary data analysis. The local data bulletins contain the final analysis of arrival times and phase associations. Also, in many cases, ISC reported times are rounded to the nearest second, while local bulletins report arrivals to a tenth of second. In both cases, local bulletin data take preference over that from ISC for relocations computed in this study.

Each event was relocated three times using combined local and teleseismic arrivals, only arrivals within 20^o, and only arrivals within 10^o. The specific location methodology uses locally calibrated crustal velocity travel time curves, which are discussed extensively in Mackey (1999), Mackey and Fujita (1999), and Mackey and Fujita (2000). To best evaluate which set of data produce the best locations, particular attention was paid to aftershock sequences, and how closely events cluster using the different data sets. Locations computed using only data either within 10^o or 20^o cluster best, although locations including local and teleseismic data are clearly improved over those from ISC alone. In general, for events with good azimuthal coverage of stations within 5^o the best locations are those computed with only the local ($<10^o$) and regional ($<20^o$) data, while events having poor azimuthal coverage of close-in stations are better located by including teleseismic data. Based on the general distribution and residuals of stations, a preferred location was selected for each event analyzed.

All relocated events are assigned GT levels, with 26 events meeting or exceeding the GT10 criteria (e.g., Yang and Romney, 1999; Figure 1). A few events which formally met these criteria were excluded from our GT10 classification due to high station residuals for some close in stations, or other odd station distribution problems which can result in poor epicenter control. It should also be noted that many of our relocated events miss the formal GT10 criteria, but we suspect that the location determined here is within 10 km of the true epicenter based on proximity to fault traces, etc. Most of the remaining relocated events meet GT25 criteria. Although no events formally qualify as GT5, several events are likely within that accuracy

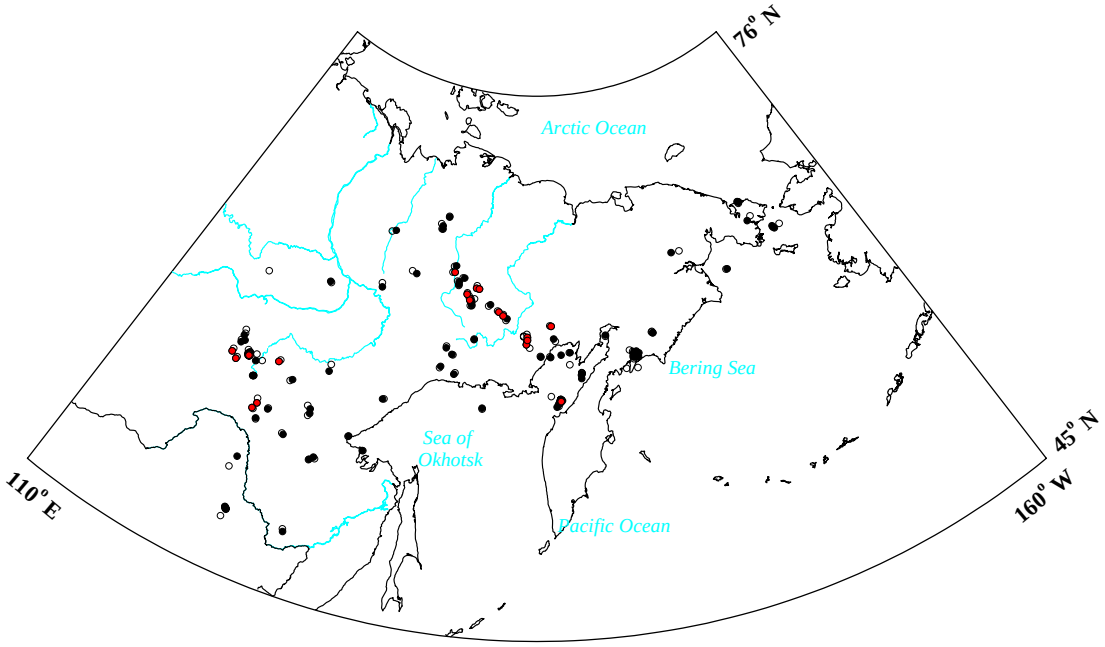

Figure 1. Comparison of ISC epicenters (open circles) and relocations (filled circles). Red filled (grey) circles represent relocations that meet or exceed GT10 criteria. Note that relocations cluster tighter and form better lineaments near the center of the figure.

Travel-time variations in northeast Russia

To further improve epicentral locations by determining station dependent path corrections, we investigated travel-time residuals relative to JB at nine regional stations from events in northeast Russia. The stations had epicentral distances from the events of about 1 - 20E.

The results for Tiksi (TIK, TIXI; Figure 2), based on all the events studied, are characteristic. High negative residuals, indicating fast velocities, are observed from events in south Yakutia. These rays pass through sub-Siberian shield mantle, which is expected to have higher velocities. Slightly negative residuals are obtained from the Chersky Range, indicating some higher velocity upper mantle exists in the region of the Kolyma-Omolon superterrane. Events from the eastern Sea of Okhotsk and Koryakia have somewhat positive residuals, and suggest that there may be slower mantle due either to lithospheric rifting (Penzhina and Parapol basins; Worrall et al., 1996) or to effects of the supra-subduction mantle wedge. Similarly, a few events with slightly positive residuals in northeast Amur District may be related with extension along the western Sea of Okhotsk (Shantar-Liziansky basin) also proposed by Worrall et al. (1996). One event in the Yana River valley gives a high positive residual which may be related to the present or recent extension of the Arctic Mid-Ocean ridge into the continent. The restricted number and distribution of GT10 events provides only information from southern Yakutia and the Chersky Range, but leave no doubt as to the faster velocities to Tiksi from those two regions. Travel paths under the Siberian platform to Norilsk yield consistently negative residuals of a magnitude similar to those at Tiksi.

Arrivals at Yuzhno Sakhalink confirm that ray paths through the sub-northern Sea of Okhotsk mantle yield high positive residuals (Figure 3). Events from the Amur region with origins in the Siberian platform west of the proposed rift again yield slightly positive residuals, suggesting that their respective higher and lower velocities tend to cancel out each other. All arrivals at Petropavlovsk are late, indicative of passage through the supra-subduction zone upper mantle. Similar to Yuzhno Sakhalinsk, as events occur farther into the higher velocity

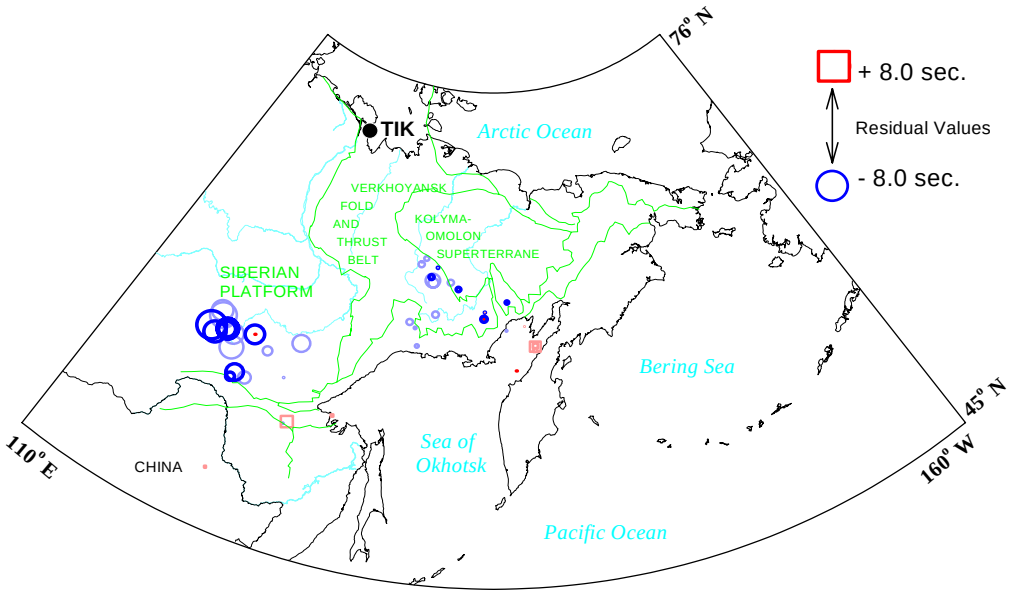

Figure 2. Residuals for arrivals received at Tiksi (TIK, TIXI). High negative residuals from the south of Tiksi indicate higher than average velocities under the Siberian platform. Velocities associated with the Verkhoyansk fold and thrust belt indicate only slightly elevated seismic velocities. Heavier shading indicates GT10 events.

Siberian platform relative to Petropavlovsk residuals become less negative.

Bilibino also yields slightly positive residuals from the northern Sea of Okhotsk and negative residuals for the Kolyma-Omolon superterrane and Koryakia, suggesting that upper mantle velocities in far northeast Russia are slightly fast. Peleduy, however**,** yields late arrivals from the Kolyma-Omolon superterrane**.** Arrivals from the northern Sea of Okhotsk are again late, and early arrivals are observed on Siberian platform crossing paths from the Verkhoyansk Range.

Residual patterns for Seymchan and Magadan are similar. The arrivals from Shelikhov Bay (northeast Sea of Okhotsk) and the Amur region are again all late, while a mix of residuals is observed from the Chersky seismic belt. From these stations, Chukotka paths are slightly slow. Finally, Yakutsk shows a wide mix of arrivals with generally early arrivals from the Aldan shield and the Verkhoyansk Range and very late arrivals from Shelikhov Bay and Chukotka.

Taken as a whole, it is clear that ray paths traversing the upper mantle under the Siberia platform are fast, while those originating from, or traversing, the supra-subduction zone or rift regions of the Sea of Okhotsk are very slow. There is an indication of low velocities under the northern Amur district, although this is less distinct. Velocities under Chukotka are less certain. The situation in the Chersky Range is also less clear, although ray paths traveling greater distances may be marginally faster than those to nearby stations. These observations will help in constraining upper mantle velocities and indicate that future development of Source Specific Station Corrections (SSSC's) may yield positive results.

Regional network deployment

We continue development of our digital station network in northeastern Russia to improve epicenter locations

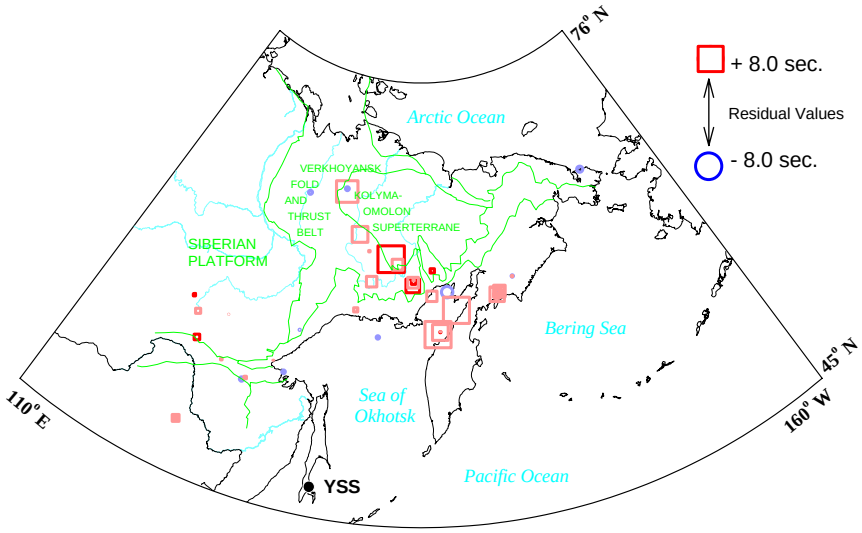

Figure 3. Residuals for arrivals received at Yuzhno Sakhalinsk (YSS). Heavier shading indicates GT10 events.

and begin a program to develop seismic discriminants for CTBT monitoring by digitally recording local explosions and earthquakes. To obtain better records for study, we began converting existing photo paper analog stations in the Magadan and Yakutsk networks to digital data acquisition. At present, we have seven stations deployed in northeast Russia, most in the Magadan region (Figure 3). Since the initial deployment, a couple of stations have had to be moved due to logistical reasons. We have also deployed a few stations in temporary locations for the purpose of recording small aftershock sequences (Talon and Tauisk) and known mine explosions (Tal'Yuryakh). Approximately 170 earthquakes have been located by the network since January 2000, although many more smaller events are locate-able with additional analysis. All stations are 3 component, with three stations recording broadband instruments (Seymchan - STS-1, Okhotsk - Guralp CMG-40T, and Omsukchan - CMG-40T). The remaining stations use short-period Russian seismometers (SKM-3 or SM3-KV). All seismometer outputs are digitized at 30 samples per second with 24-bit resolution and logged on a PC. In addition, we are supplementing our digital data with records from the IRIS station at Magadan, MA2, and other regional analog photo paper stations.

Explosion ground truth and discrimination

We have recorded mine blasts from many locations throughout our study region with yields ranging up to or exceeding 40 T. To obtain ground truth information on explosions, we have either visited or deployed a temporary station at mine sites to obtain information on blast size and location. Figure 5 depicts a seismogram of one of several 40 T blasts which occurred near Neksikan in April/May 2001, about 20 km southwest of the station in Susuman. On this seismogram, note the large amplitude Rg component, as well as a clear infrasonic arrival about 70 s after Pg. Lg arrivals from several of the Neksikan blasts were recorded at Magadan (MA2) and our farthest station, Okhotsk, over 400 km distant (Figure 6). Lg arrivals recorded at Magadan and Okhotsk are characterized by low frequency arrivals (0.7-1.5 Hz) with higher frequencies (4.0-8.0 Hz) being absent or completely obscured by background noise.

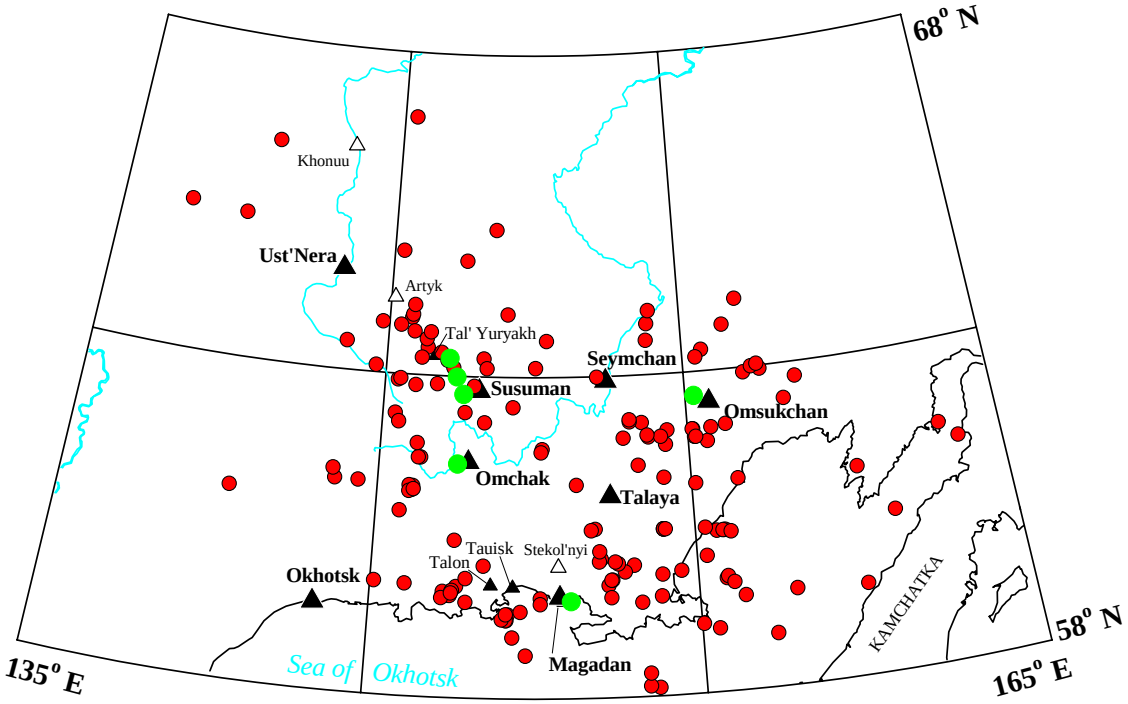

Figure 4. Digital seismic network deployed by Michigan State University in eastern Russia (permanent stations - large black triangles, temporary stations - small black triangles, and supporting analog stations - white triangles). Also shown are earthquakes located from January 2000 through May 2000 (small red circles) and explosion sources (large green circles).

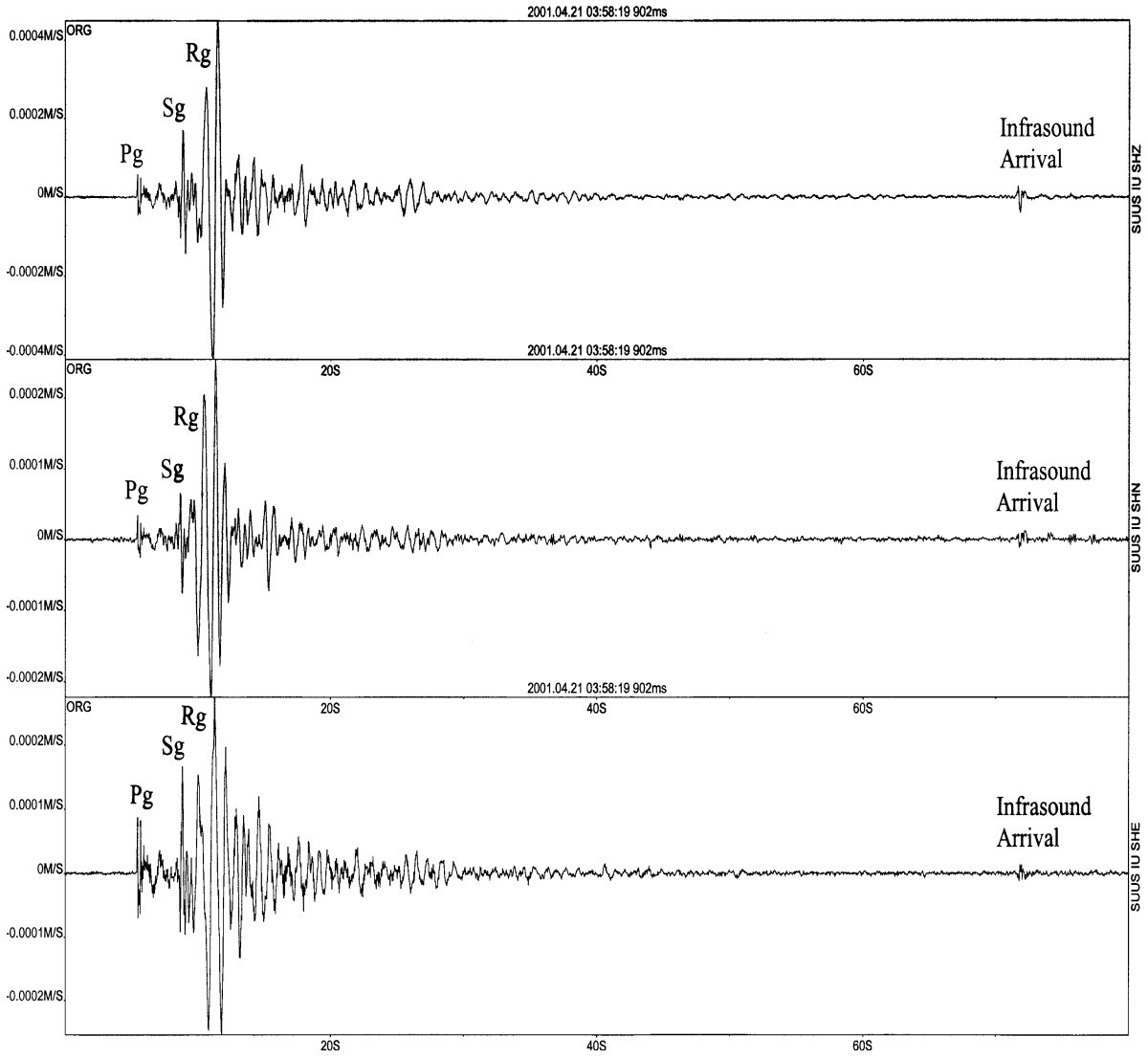

Figure 5. 3-component seismogram (top - Z, middle - N-S, bottom - E-W) of a 40,000-kg explosion recorded at Susuman. This blast occurred April 21, 200, in a placer gold mine near the town of Neksikan, about 21 km southwest of Susuman. Note the clearly developed Pg, Sg, and Rg arrivals, as well a clear infrasound arrival recorded on all seismometer components about 70 seconds after Pg.

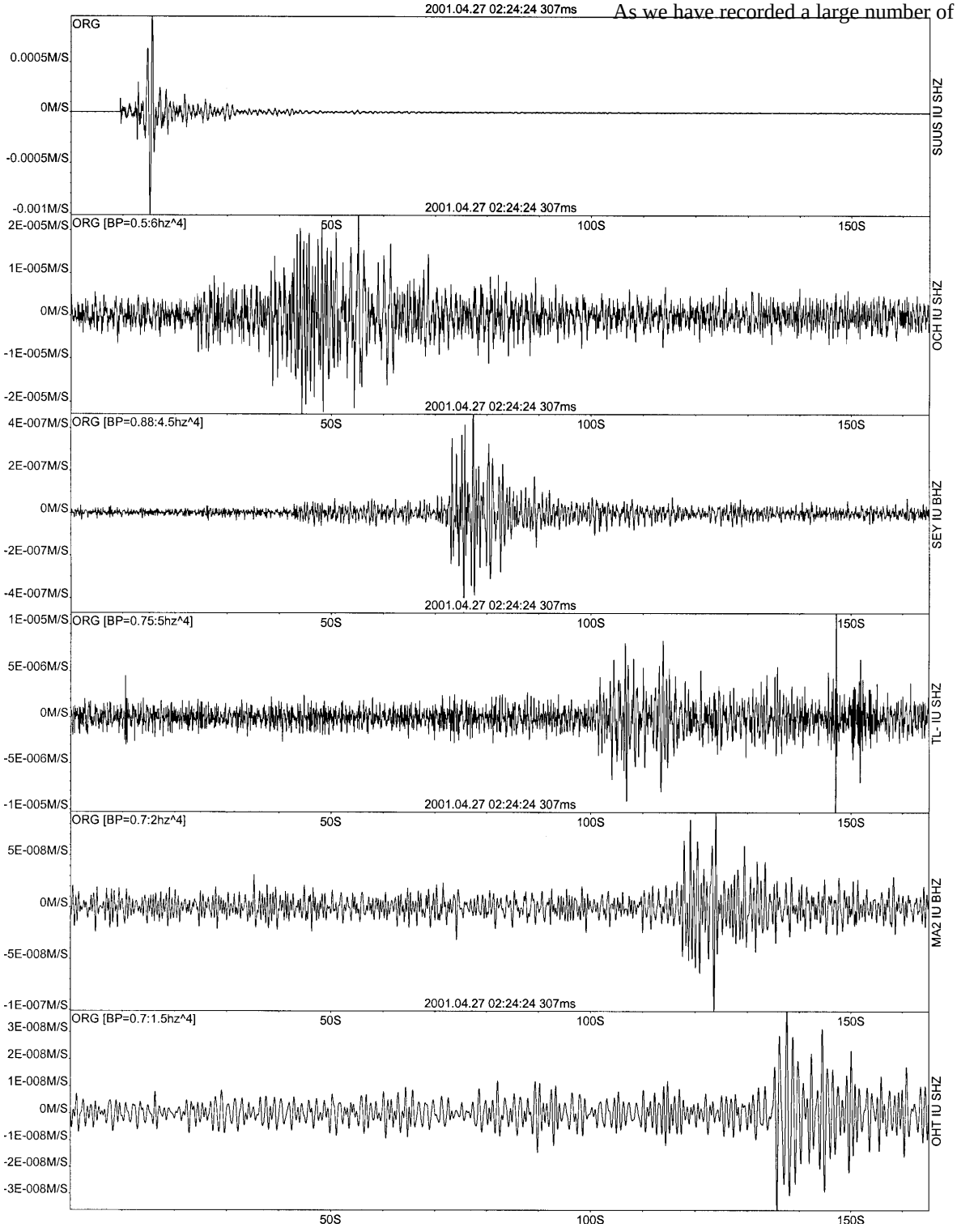

Figure 6. 40,00-kg blast of April 27, 2001, as recorded by several of our stations (top to bottom: Susuman (22 km), Omchak (111km), Seymchan (236), Talaya (297 km), Magadan (MA2; 381 km), and Okhotsk (441 km). Note the well developed low-frequency Lg arrival at Okhotsk. All records except Susuman are bandpass filtered.

As we have recorded a large number of

earthquakes and explosions at throughout the study region. We can attempt to discriminate between explosions and earthquakes using various Lg amplitude ratios. Preliminary results indicate that the ratio Lg(4-

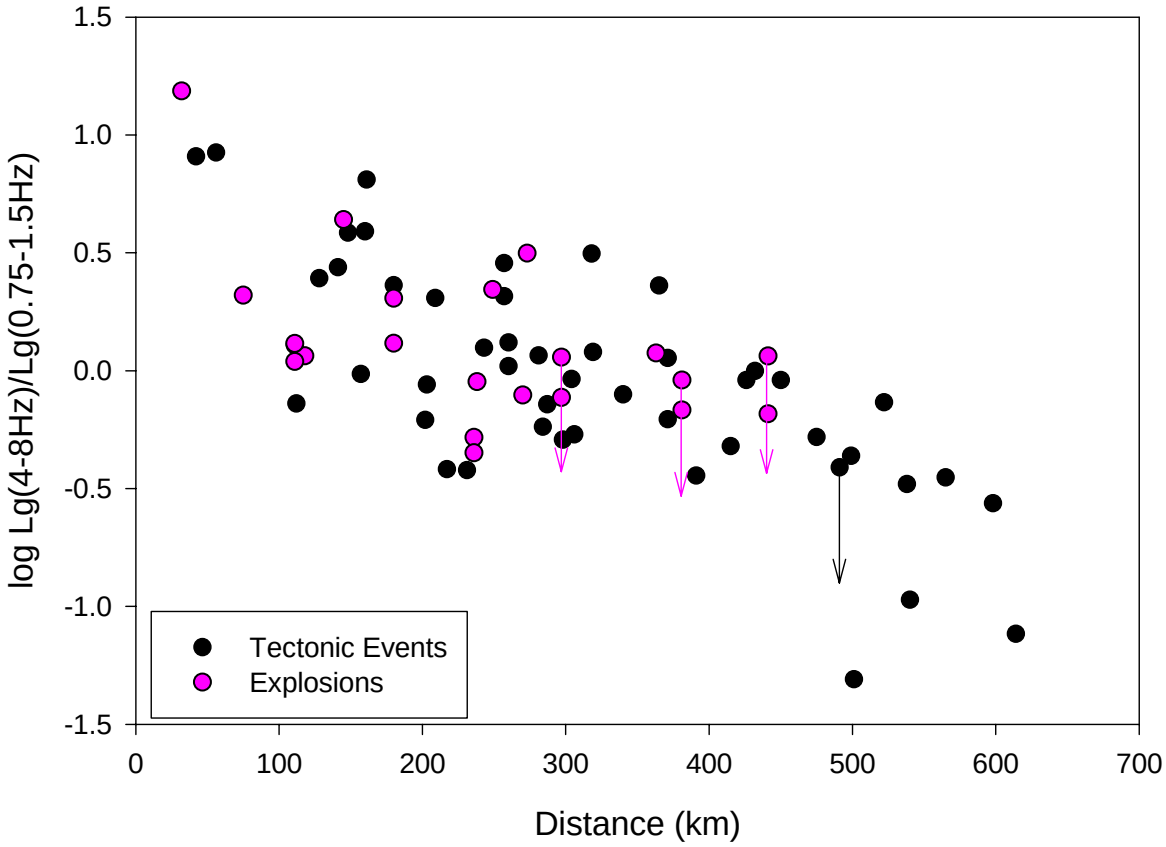

Figure 7. Composite plot of Lg spectral ratio vs. distance for tectonic events and explosions. Lg amplitudes used were maximum peak to peak. This plot contains data for all deployed stations (including MA2, but excluding Omsukchan, which was deployed July, 2001). There is no apparent difference in the plotting of earthquakes and explosions; thus, discrimination is not possible by using this method in this region at these distances. Points with arrows represent maximum possible ratio for arrivals with a clear low-frequency Lg arrival (see Okhotsk, Figure 6) but no apparent high-frequency arrival. In this case, the high-frequency Lg is substituted with the high-frequency background noise amplitude.

8Hz)/Lg(0.75-1.5Hz) using peak amplitudes is not be sufficient to discriminate mining explosions from earthquakes for local and near regional distances (<500km) in northeast Russia (Figure 7). In general, the overall relationship (slope and intercept) between earthquake Lg ratios vs. distance is nearly identical to that of HIA (Hartse, 2000). It should be noted that this represents only the most simple approach to an Lg discriminant for northeast Russia. Additional more comprehensive research is underway to look at the RMS amplitudes of the full Lg wave packet (Hartse, 2000) as opposed to peak amplitudes. Additional phase amplitude ratios (Pg/Lg, Pn/Lg, etc.) will also be investigated.

CONCLUSIONS AND RECOMMENDATIONS

Use of regional and local phase arrival data has greatly improved epicentral coordinates in northeast Russia and should also provide SSSCs when analyzed in detail. Combined with the identification and removal of

anthropogenic sources, this will greatly improve our monitoring capability as well as our understanding of the baseline natural seismicity of the region.

The deployment of digital recording systems has opened the possibility of explosion discrimination studies in northeast Russia. A large number of chemical explosions from known mines have been recorded by our network which contributes ground truth information to improve travel-time curve calibration and explosion discrimination. In contrast to northern China and south central Siberia (Hartse, 2000), preliminary results indicate that high frequency/low frequency Lg ratios are insufficient for discrimination purposes in northeastern Russia. Further analysis is underway. Continued study of waveform characteristics will be critical to the discrimination process and will further enhance our ability to discriminate natural earthquakes from explosions throughout the study area. To see if these results are characteristic only of the Magadan district or of northeast Russia as a whole, additional field deployments throughout the region are required.

ACKNOWLEDGMENTS

We thank Hans Hartse and Lee Steck for helpful discussions on waveform-based discrimination and development of SSSC's.

REFERENCES

Hartse, H. E. (2000), Regional Seismic Event Discrimination: in *22nd Annual DoD/DOE Seismic Research Symposium Proceedings, "Planning for Verification of and Compliance with the Comprehensive Nuclear-Test-Ban Treaty (CTBT),"* Volume II, p. 137-146.

Mackey, K.G., and Fujita, K. (1999), The northeast Russia seismicity database and explosion contamination of the Russian earthquake catalog: in *Proceedings of the 21st Seismic Research Symposium: Technologies for Monitoring The Comprehensive Nuclear-Test-Ban Treaty, 21-24 September, 1999, Las Vegas, Nevada*, v. 1, p. 151-161.

Mackey, K. G., and Fujita, K. (2000). Event relocation and seismic calibration in northeast Russia: in *22nd Annual DoD/DOE Seismic Research Symposium Proceedings, "Planning for Verification of and Compliance with the Comprehensive Nuclear-Test-Ban Treaty (CTBT),"* Volume II, p. 223-232.

Worrall, D. M., Kruglyak, V., Kunst, F., and Kuznetsov, V. (1996), Tertiary tectonics of the Sea of Okhotsk, Russia: Far-field effects of the India-Eurasia collision: *Tectonics*, v. 15, p. 813-826.

Yang, X, and Romney, C. (1999), PIDC ground truth event (GT) database: *CMR* technical report CMR-99/15, 25 pp.

A REVIEW OF NEW SEISMIC CONSTRAINTS OF CRUST AND MANTLE STRUCTURE FROM CHINA AND INDIA COUPLED WITH SEISMIC Q_S AND TEMPERATURE ESTIMATES FOR THE UPPER MANTLE

Walter. D. Mooney[1], Robert G. Coleman[2], P.R. Reddy[3], Irina Artemieva[1, 4], Magali Billien[5], Jean-Jacques Lévêque[5], and Shane T. Detweiler[1]

U. S. Geological Survey [1]; Stanford University [2]; National Geophysical Research Institute, Hyderabad, India[3]; Uppsala University, Sweden[4]; Institute of Earth Science, Strasbourg, France[5]

Sponsored by National Nuclear Security Administration
Office of Nonproliferation Research and Engineering
Office of Defense Nuclear Nonproliferation

Contract No. DE-A104-98AL79758

ABSTRACT

Reliable data regarding the seismic structure of China and India significantly improve the determination of seismic source parameters for the purposes of monitoring nuclear test explosions in those countries. To provide some of this information, we present seismic cross-sections for China and India and new maps of S-wave attenuation in Eurasia.

We present a new deep crustal section across northwest China and the northeastern Tibetan Plateau based on seismic refraction experiments and geologic mapping. The crustal velocity structure and Poisson's ratio (σ) for the 2,700-km-long transect, which provide a constraint on crustal composition, were determined from P- and S-wave data. The crustal thickness along the profile was determined, and the crust was found to have three layers with P-wave velocities (Vp) of 6.0-6.3 km/s, 6.3-6.6 km/s, and 6.9-7.0 km/s, respectively. We interpret the consistent three-layer stratification of the crust to indicate that the crust has undergone partial melting and differentiation after Paleozoic terrane accretion. P_n velocities are ~7.7 to 7.8 km/s.

We likewise present deep structural details of central India using reprocessed seismic data. A shallow mid-crust and a thick high-velocity lower crust are found to be characteristic features of the region. The study area exhibits high mantle heat flow and shallow lithospheric thickness compared with other cratons and mobile belts of the Indian shield. The geophysical anomalies of the region are thought to be in response to mantle plume and other tectonic activities during the Neoproterozoic-Phanerozoic period. Some of the magmatic and tectonic events of this region have been correlated to global tectonics and episodes of supercontinent formation during the Neoproterozoic.

Finally, we compare maps of the thermal structure of the continental lithosphere with the seismic attenuation of shear waves (Q_S) determined from surface wave amplitudes. The thermal structure is taken from a recent study (Artemieva and Mooney, 2001) that utilizes thermal parameters (radiogenic heat production and conductivity). Q_S values are taken from the study of Billien et al. (2001) that used the Trampert and Woodhouse (2001) data set. We find that maps of Q_S correlate more closely with lithospheric temperature than any other physical parameter, such as P- or S-wave velocities. We compare values of Q_S and temperature at depths of 50 km and 100 km in the continental lithosphere. The correlation coefficient between temperature and seismic parameters is low and ranges from 0.2 to 0.4.

KEY WORDS: crustal velocity structure, Poisson's ratio, collision, Qs, seismic attenuation, China, India

OBJECTIVE

Seismic refraction profiling is one method of collecting ground truth data that may be used to evaluate the performance of monitoring networks and data analysis systems. A vast amount of seismic refraction data has

been collected in India and China, with new data being added every year. For example, a 2,700-km-long seismic refraction survey was conducted across northwest China and the Tibetan Plateau (Figure 1) by the former Ministry of Geology and Mineral Resources (MGMR). Likewise, deep seismic studies in the cratons and mobile belts of India have provided valuable information on the structure and tectonic evolution of that region. Though there have been only a limited number of seismic reflection studies in both of these regions, there so far seems to be evidence that the geodynamic processes that occur there also occur on a global scale. The goal of this project, then, is to gain a better understanding of the deep crustal structure beneath different tectonic provinces in the area, which may be used in the monitoring of nuclear explosions in these and other regions.

As part of these efforts, we also include information about seismic attenuation (Qs). Qs is another parameter which can be measured and utilized effectively when attempting to calibrate instruments to monitor nuclear explosions at large distances. The rate of degradation of seismic signal is imperative to know, if one is to accurately locate where an event has occurred.

RESEARCH ACCOMPLISHED

China

Western China is a showcase of complex geological and geophysical features, including sedimentary basins, regimes of continental collisional tectonics, and the thickest crust found on earth. To be able to accurately monitor western China for nuclear explosions, we must first understand as much as possible about the crustal structure there. In this paper, we present results of a seismic refraction profile across western China (Wang et al., 2001). Seismic energy for this profile was provided by 12 chemical explosive shots fired in boreholes. The charge size ranged from 1500 to 4000 kg, sufficient to provide clear first arrivals to a maximum distance of 300 km. The distance between shotpoints ranged from 63 to 205 km, and the interval between portable seismographs was between 2 and 4 km. The profile was recorded along existing roads, and provided nearly straight profile segments.

During the experiments, both P- and S-wave data were acquired, even for data recorded by single-component geophones. The reflection from the Moho was especially strong, and this made it possible for us to derive the crustal composition using the crustal Poisson's ratio or Vp/Vs ratio which could be obtained from the crustal P- and S-wave velocity structures.

In the correlation of phases, reduction velocities of 6.0 km/s and 3.46 km/s were used for P- and S-waves, respectively. The time scales used for S-waves were multiplied by a factor of 0.58 in the S-wave record section so they would match the P-wave arrival times. Because digital filtering introduces a slight time shift, the unfiltered P-wave data were used for phase correlation and travel-time picking. In order to improve the signal-to-noise ratio for phase correlation, the S-wave data were filtered with a band pass of 0-6 Hz.

Based on the phase correlation, the first arrivals of the P_g phase were used to invert the upper crustal velocity structure using the finite-difference tomographic method of Hole (1992). The reflection phases were used to determine the one-dimensional crustal velocity structure using the X^2-T^2 method (Giese, Prodehl and Stein, 1976) and the Reflectivity method (Fuchs and Muller, 1971). With one-dimensional crustal velocity structures from each shotpoint, a crustal P-wave velocity structure was established using a 2-D dynamic ray-tracing program to model both kinetic and dynamic features of the observed seismic wave field (Cerveny, Molotkov, and Psencik, 1977; Cerveny and Psencik, 1984). The different phases on the record sections were all appropriately fitted for travel times and amplitudes. Figures 2 and 3 show our final velocity models. We have divided the seismic profile into two segments- the northern segment from the Altai Mountains to the Altyn Tagh fault (Figure 2), and the southern segment from the Altyn Tagh fault to the Longmen Shan (Figure 3). It is clear that the transect shows three-layer stratification with P-wave velocities of 6.0-6.3 km/s, 6.3-6.6 km/s, and 6.9-7.0 km/s. Upper mantle (Pn) velocities of 7.7-7.8 km/s were found.

The accuracy of the final model is dependent on a number of factors, including the shotpoint interval, receiver density, and thickness of sediments in the shallow crust. Model accuracy primarily depends on the correct identification of the various phases and the density of rays penetrating a particular volume of the model, however. Perturbation of the models has shown that, depending on the uniformity of structure and the density of

rays, the resolution of velocity and depth to interface may be accepted as better than 2% and 5%, respectively. By the relationship between the Poisson's ratio and the Vp/Vs ratio, the Poisson's ratio is determined to within an uncertainty of less than 2%.

India

Like China, the Indian subcontinent has a complex geological and geophysical history that must be better understood for the purposes of accurately monitoring nuclear explosions. To accomplish this, we have recently obtained P-wave data from the Indian subcontinent. Twenty DSS profiles have been conducted since 1972 totaling more than 6000 km. Long-range refraction and wide-angle reflection techniques with a dense detector spacing of 80-200 m and a shot point interval of 10-40 km were used to acquire these data. Measurements of crustal thickness fall into the range of 35-40 km (Figure 4), with the biggest exception being the Himalayas, which are known to have thicknesses of up to 80 km (Mahadevan, 1994). We show three velocity models that were developed as a result of these experiments in Figures 4a-c. The Moho depth is seen to be around 38 km, and we note several deep lenses of 7.3 km/s velocity across the subcontinent. Also, the transition depth from the lithospheric to the asthenospheric mantle fluctuates by about 50 km across the profile.

The velocity model of Kaila et al. (1990) for the SW Marwar Terrain (Figure 4c) shows a shallow midcrust with 6.6 km/s velocity and a lower crustal velocity of 7.3 km/s. The high-velocity lower crustal layer in this region is believed to be due to the underplating of the crust by mantle upwelling, crustal extension and continental rifting related to the Reunion hotspot. A thick, high-velocity lower crustal layer (7.0-7.5 km/s) is often observed between the lower crust and upper mantle in areas of continental rifts, where extension has been the last deformation process to occur (Mooney et al., 1983; Catchings and Mooney, 1988).

This extensional process is attributed to igneous accretion of the upper mantle material at the base of the crust (White and McKenzie, 1989; Furlong and Fountain, 1986) and is observed at several rift zones of the world. In this case, this plume activity coincides with the breaking up of the Rodinian supercontinent, of which the Indian continent was a part, during the Mid-Neoproterozoic (750 Ma). During periods of supercontinent break-up, rifting generally takes place at old suture zones, as these are relatively weak and therefore prone to rifting (Vink et al., 1984). The location of the rifting event (750 Ma) in the Marwar Terrain is in close proximity to the earlier Delhi Suture (1100 Ma), and strikes in the same direction (NE-SW) as the earlier Aravalli Delhi Fold Belts. It seems then that there is much to support the idea that the Indian shield has evolved through processes that are known to be active on a global scale.

S-Wave Seismic Attenutation (Qs) and Temperatures (T) in the Mantle

Attenuation is important for monitoring nuclear explosions because researchers need the ability to model how seismic waves travel through the crust in order to accurately locate events. Attenuation is determined by modeling the temperatures in the lithosphere. The thermal structure of the continental lithosphere has previously been estimated from heat flow data by numerous authors (e.g. Pollack and Chapman, 1977; Sclater et al., 1980), and borehole measurements have been used to constrain these data. Models of heat production and thermal conductivity are discussed in Artemieva and Mooney (2001), and it was found that the results are reliable for stable continental regions where the assumption of a steady-state thermal regime is valid. The Tibetan plateau, however, is less well constrained, and results there are based on petrologic and non-steady-state constraints.

In order to quantify the effects of seismic attenuation on the crust, we performed a two-step inversion. First, from phase and amplitude measurements, we estimated phase velocity and Qs for several periods. Then, we performed a depth-inversion to obtain a 3-D model of the shear wave attenuation factor. We took into account the focusing effects of wave amplitude, but did not specifically model variations due to scattering effects.

At 50-km depth, the crustal influence is too large for us to accurately model the shear-wave velocity of the lithosphere, shear-wave quality factor and temperature. At 100-km depth (Figure 5), however, the resolution of velocity and Q are at a maximum. In northern Eurasia, the velocity anomaly maps show positive values to depths where temperature is 130 degrees, where the Q map shows an alteration from high to low Q. In contrast, the southern Eurasian suture zone is evident only in the map of temperature. Resolution is lower at 150-km depth (Figure 6), with temperatures in non-cratonic regions reaching 1300 degrees. Northern Eurasia is clearly

seen on these maps to oscillate laterally (west to east) in both shear velocities and temperatures. Eastern Eurasia, by contrast, shows low velocity, low Qs, and high temperature.

CONCLUSIONS AND RECOMMENDATIONS

Crustal and Upper Mantle Structure of China and India

Our work to date has formed a firm basis for understanding the crust and upper mantle structure of China and India. However, gaps in our knowledge remain, and any new information regarding the seismic structure of China or India would significantly improve the determination of seismic source parameters for the purposes of monitoring nuclear explosions. As much of the data for both nations is now being made available to Western researchers, we should take advantage of this opportunity and analyze this wealth of new data for greater insight and understanding into the crustal structure of Asia. It is thus imperative that institutes in China, India and the United States be allowed to continue their cooperative exchange programs. Such a reasonable exchange of data will foster new research and collaborative efforts that may lead to long-term, stable relationships among our nations.

S-Wave Seismic Attenutation (Qs) and Temperatures (T) in the Mantle

There exists a good correlation between seismic attenuation and temperature. This is likely due to the fact that anelasticity is primarily due to thermal effects. In addition, high Q was found to correlate with cratonic regions. It is notable that the relation between temperature and seismic properties is not linear, and these are likely not the only variables we need to study in order to more fully understand how attenuation varies throughout the crust. Once we have improved our modeling of seismic Q, efforts to locate seismic events at large distances should vastly improve. When we know how seismic waves propagate through the crust, we can then pinpoint with more accuracy where those waves originated.

REFERRENCES

Artemieva, I. and W.D. Mooney (2001), Thermal state and evolution of Precambrian lithosphere: A global study, *J. Geophys. Res.*, 106, in press.

Billien, M., J.-J. Leveque, and J. Trampert (2000), Global maps of Rayleigh wave attenuation for periods between 40 and 150 seconds, *Geophys. Res. Lett.*, 27, 3619-3622.

Catchings, R.D. and W.D. Mooney (1988), Crustal structure of the Columbia Plateau: Evidence for continental rifting. *J. Geophys. Res.*, 93, 459-474.

Cerveny, V., I.A. Molotkov, and I. Psencik (1977), *Ray method in seismology.* Prague.: Univerzita Karlova, p. 57-158.

Cerveny, V. and I. Psencik, eds. (1984), SEIS83-numerical modeling of seismic wavefield in 2-D laterally varying layered structures by the ray method, in: E. R. Engdahl (editor), *Documentation of earthquake algorithms*. World data center (A) for solid earth geophysics, Boulder, Colo., Rep. SE-35, 36-40.

Fuchs, K. and G. Müller (1971), Computation of synthetic seismograms with the reflectivity method and comparison with observations, *Geophys. J. Roy. Astr. Soc.*, 23, 417-433.

Furlong, K.P. and D.M. Fountain (1986), Continental crustal underplating: Thermal considerations and seismic-petrologic consequences. *J. Geophys. Res*., 91, 8255-8294.

Giese, P. C. Prodehl, and A. Stein (1976), *Explosion Seismology in Central Europe.* Berlin Heidelberg, New York.: Springer-Verlag, p. 146-161.

Hole, J. (1992), Nonlinear high-resolution three-dimensional seismic travel time tomography. *J. Geophys. Res., 97*, 6553-6562.

Kaila, K.L., H.C. Tewari, V.G. Krishna, M.M. Dixit, D. Sarkar, and M.S. Reddy (1990), Deep seismic sounding studies in the North Cambay and Sanchor Basins, India. *Geophys. J. Int*., 103, 621-637.

Mahadevan, T.M. (1994), Deep Continental Structure of India: A Review, *Geol. Soc. India Memoir*, 28, Bangalore, 569 pp.

Mooney, W.D., M.C. Andrews, A. Ginzburg, D.A. Peters, and R.M. Hamilton (1983), Crustal structure of the Mississippi embayment and a comparison with other continental rift zones. *Tectonophysics*, 94, 327-348.

Mooney, W.D., G. Laske, and G. Masters (1998), CRUST 5.1: A global crustal model at 5º x 5º, *J. Geophys. Res.*, 103, 727-747.

Trampert, J., and J.H. Woodhouse (2001), Assessment of global phase velocity models, *Geophys. J. Int.*, 144, 165-174.

Vink, G.E., W.J. Morgan, and W.L. Zhao (1984), Preferential rifting of continents: A source of displaced Terranes. *J. Geophys. Res.*, 89, 10,072-10,076.

Wang, Y.X., W.D. Mooney, X.C. Yuan, and R.Coleman (2001), The crustal structure of northwest China-Geoscience transect from Altai to Altyn Tagh. *J. Geophys. Res., submitted*.

White, R. and D. McKenzie (1989), Magmatism at rift zones: The generation of volcanic continental margins and flood basalts. *J. Geophys. Res.*, 94, 7685-7729.

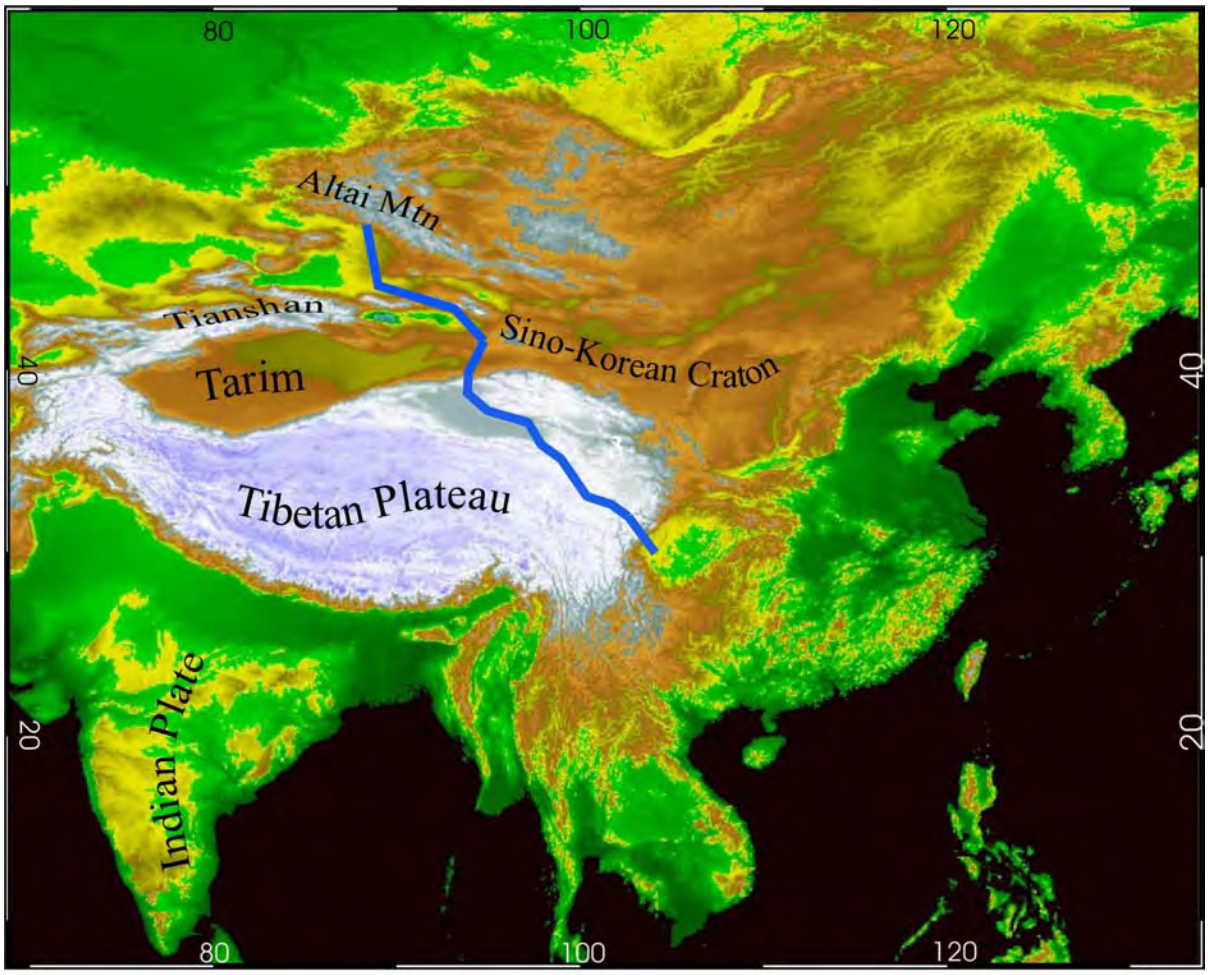

Figure 1.Topographic relief map of southeast Asia with seismic transect indicated by a heavy, dark line. The entire transect is composed of linear segments, and runs from the Altai mountains in the north to the Longmen mountains in the south, crossing the Tibetan plateau.

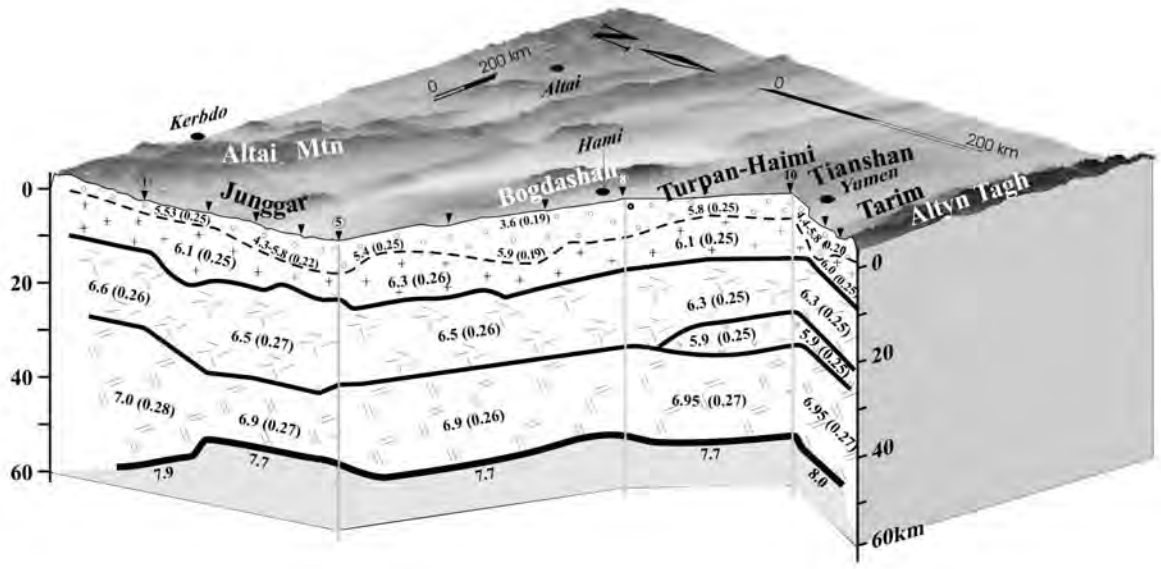

Figure 2. Crustal structure along the seismic transect from the Altai mountains to the Altyn Tagh fault. Dashed lines indicate the top of the crystalline basement. Three distinct layers are present along this transect which we identify as the upper, middle, and lower crust. Velocity values are given, as is Poisson's ratio (in parenthesis). The Moho is shown as a heavy, dark line.

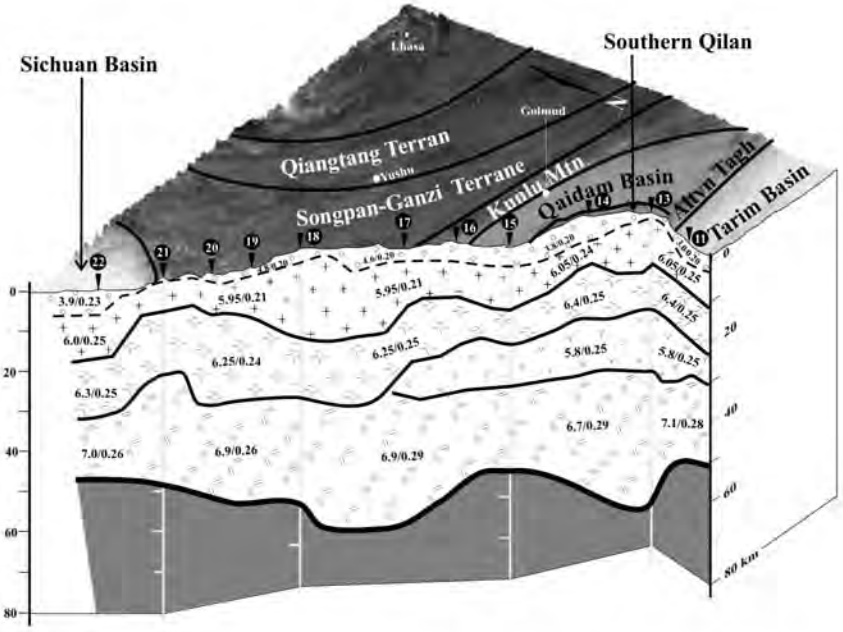

Figure 3. Crustal structure along the seismic transect from the Altyn Tagh fault to the Longmen mountains. Dashed lines indicate the top of the crystalline basement. Three distinct layers are present along this transect which we identify as the upper, middle, and lower crust. Velocity values are given, as is Poisson's ratio (in parenthesis). The Moho is shown as a heavy, dark line.

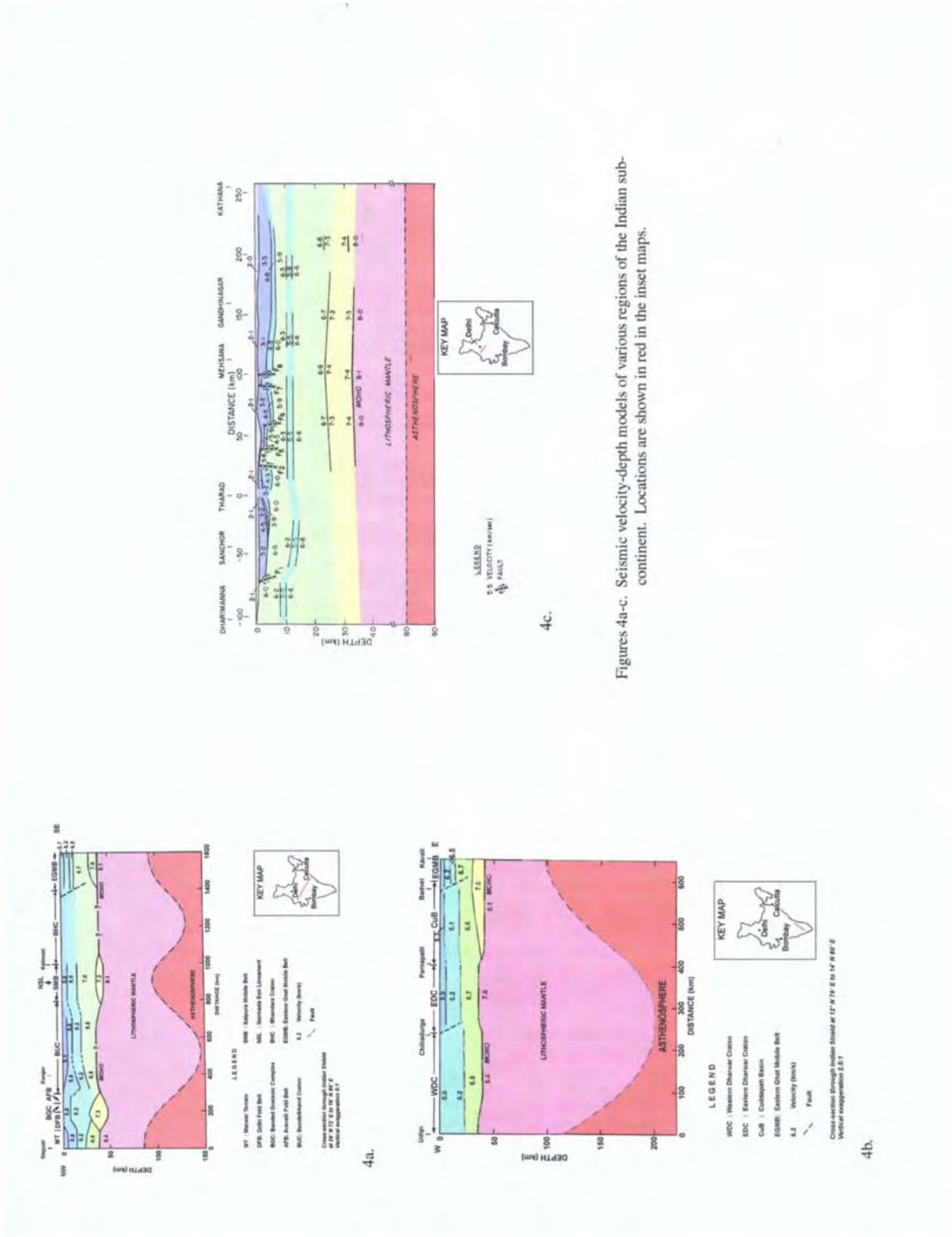

Figures 4a-c. Seismic velocity-depth models of various regions of the Indian sub-continent. Locations are shown in red in the inset maps.

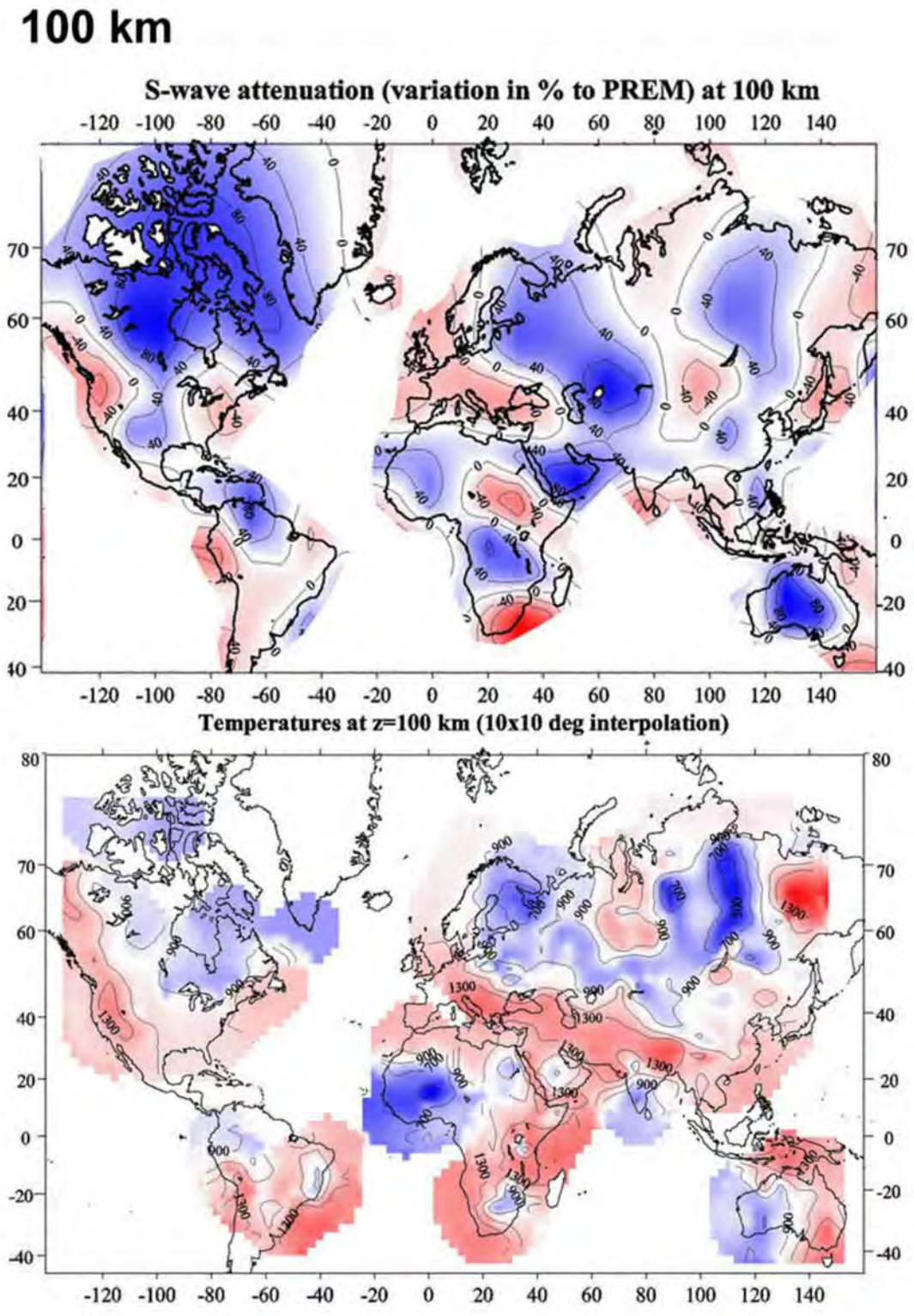

Figure 5. Seismic attenuation as a percentage of PREM at 100 km. Bottom figure shows temperatures at 100 km depth.

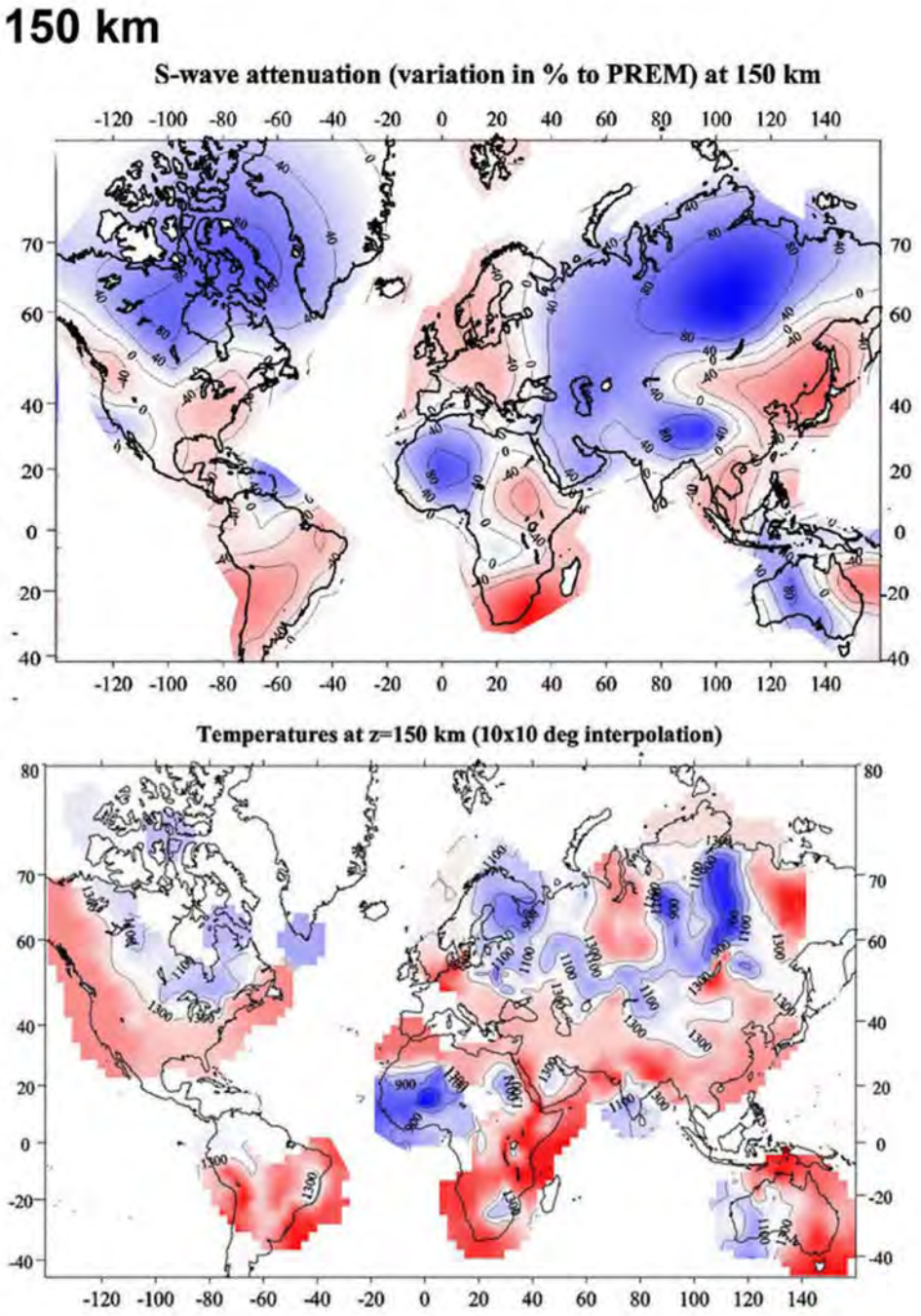

Figure 6. Seismic attenuation as a percentage of PREM at 150 km. Bottom figure shows temperatures at 150 km depth.

BROADBAND SEISMIC STUDIES IN SOUTHERN ASIA

Keith Priestley,[1] Vinod K. Gaur,[2] S. S. Rai,[2] Jessie L. Bonner,[3] and James F. Lewkowicz[3]

Cambridge University,[1]
Center for Mathematical Modeling and Computational Sciences, Bangalore, India[2]
Weston Geophysical Corporation[3]

Sponsored by Defense Threat Reduction Agency

Contract No. DTRA01-00-C-0028

ABSTRACT

We are continuing efforts to develop 3-D velocity models for southern Asia through the collection and analysis of broadband waveform data acquired on the Indian subcontinent. The geology of India is diverse, but can be divided into three main regions: the Himalayas, the Indo-Gangetic plain, and the Indian Shield. Our initial focus has been on the southern Indian shield, and we have also completed studies in the trans-Himalayas and the Shillong Plateau. The goal of our work is to determine the crust and upper mantle velocity and attenuation structure and to characterize regional seismic waveform propagation of the Indian subcontinent. Teleseismic receiver function data, S-to-P conversions, and short-period surface wave phase velocity data have been interpreted for seismograms recorded along a 700-km north-south profile of the southern Shield. These data show that the shield velocity structure is extremely uniform, simple, and consists of a surface wave velocity of approximately 3.45 km/sec and a moderate gradient of 0.20 km/sec/km with the Moho at 35±1 km depth. To the south of the shield in the granulite terrain, the crust is both thicker (44±1 km deep) and more complicated, with a mid-crustal discontinuity at approximately 25-km depth. We constrain the upper mantle structure with phase velocity measurements of long-period surface waves; these show that the seismic lithosphere is approximately 150 km thick and underlain by a weak low-velocity zone. We have also modeled the regional waveforms of a moderate earthquake that occurred near Koyna, India, in September 2000 and of the 26 January 2001 Bhuj main shock and its aftershocks to calibrate paths to the regional stations.

KEY WORDS: waveform modeling, velocity models, surface waves, receiver functions

OBJECTIVES

The objectives of our research effort are fourfold. The first is to increase the amount of high quality seismic data that are available by deploying additional seismic stations in the India/Pakistan region. The second is to use these data to refine the regional attenuation characteristics, the regional travel time corrections, and the crust and upper mantle structure of the region. The third is to use the analysis of these data to refine Weston's 3-D velocity model for India and Pakistan (WINPAK3D) and to validate the model. The fourth is to provide a cooperative forum for the exchange of information and ideas on the analysis of the data and modeling of the region.

This research is motivated by the fact that calibrated regional velocity models for the India/Pakistan region will be essential to improve upon the location capability of global networks. For example, Table 1 lists five earthquakes that occurred in the Koyna-Warna region along the western coast of India. Yet, even with some overlap in the datasets processed by the three institutions, the locations formed by the networks show significant scatter (Figure 1). In fact, of the 15 different locations for the five events, only four locations fall within or near the boundary of the seismicity cluster regions determined for the Koyna-Warna region by Mandal *et al*. (1998). This region is well known for the clustered seismic activity that started in 1962 after the impoundment of the Koyna reservoir. The events were recorded on global seismic networks and located by the Prototype International Data Center (pIDC), United States Geological Survey (USGS), and International Seismic Centre (ISC). In addition to the locations, we present the range of group velocity dispersion curves generated for HYB data (Figure 2) using the event source locations and origin times presented in Table 1. For reference, we have plotted the theoretical dispersion curve generated using our shear wave velocity model for the southern Indian

shield that is discussed later in this paper and presented in Figure 4. Because the path from these events to HYB (Δ - 525 km; azimuth - 90°) is essentially the same for all events in the region, and focal mechanisms for all three clusters are similar (Mandal, *et al*, 1998), differences in the dispersion curves must be related to location and/or origin time errors. The average dispersion curve generated by these data at shorter periods has approximately ± 0.2 seconds error and thus would incorporate considerable error if used to develop a shear wave velocity model for the region. For the model development described in the following sections of this paper, we have searched for and examined only well-located events in order to reduce such model error. The results are high-quality regional velocity models for southern Asia that have been incorporated into WINPAK3D and are being used to more accurately locate regional seismic events in southern Asia.

	pIDC				ISC				USGS			
EVID	OT	Lat	Long	Depth	OT	Lat	Long	Depth	OT	Lat	Long	Depth
19950312	08:22:54.9	17.19	73.58	15	08:22:55.4	17.38	73.91	17.7	08:22:54.69	17.64	73.77	10F
19950313	03:09:47.0	17.20	73.47	15	03:09:37.9	17.41	73.98	16.9	03:09:42.5	17.52	74.12	54
19960426	12:19:34.8	17.09	73.49	17.9	12:19:34.1	17.19	73.72	29.0	12:19:33.4	17.16	73.56	22
19980211	01:08:52.5	17.13	73.76	16	01:08:49.1	17.32	73.96	33F	01:08:49.3	17.16	73.79	33F
19980214	00:59:49.0	17.15	73.66	18	00:59:50.8	17.38	73.87	33F	00:59:51.6	17.25	73.52	33F

Table I. Source parameters from the pIDC, ISC, and USGS for five earthquakes near the Koyna-Warna region of western India.

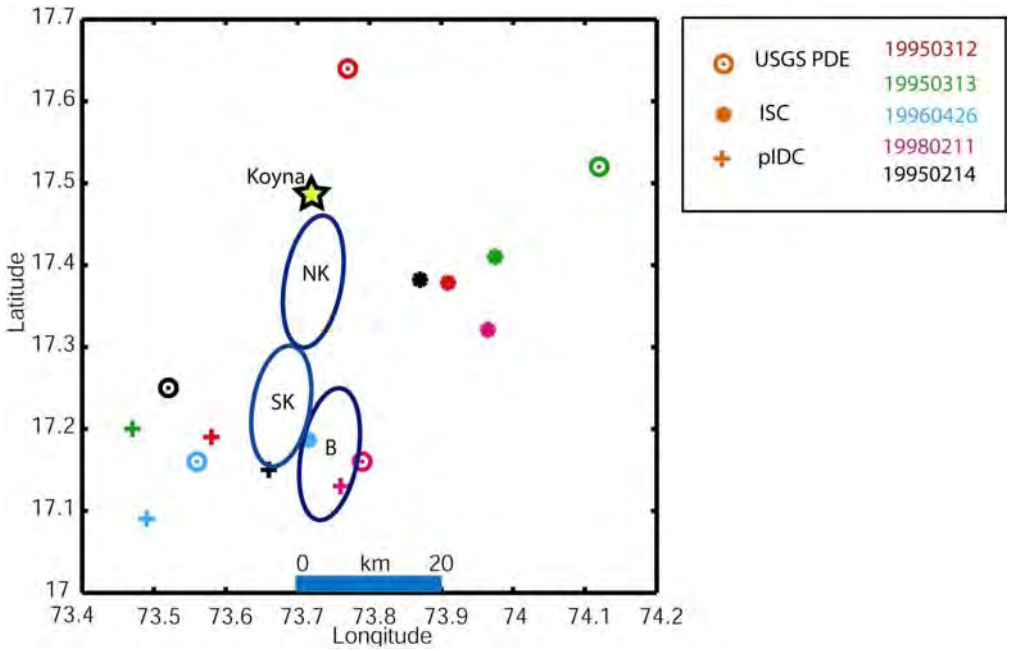

Figure 1. USGS, pIDC, and ISC network locations for the five earthquakes listed in Table 1. The three ellipsoids represent the distinct regions of the Koyna-Warna seismic zone where the majority of the seismicity occurs (Mandal et al., 1998) The abbreviations for each cluster include NK - Northern Koyna; SK - Southern Koyna; and B - Bhogiv.

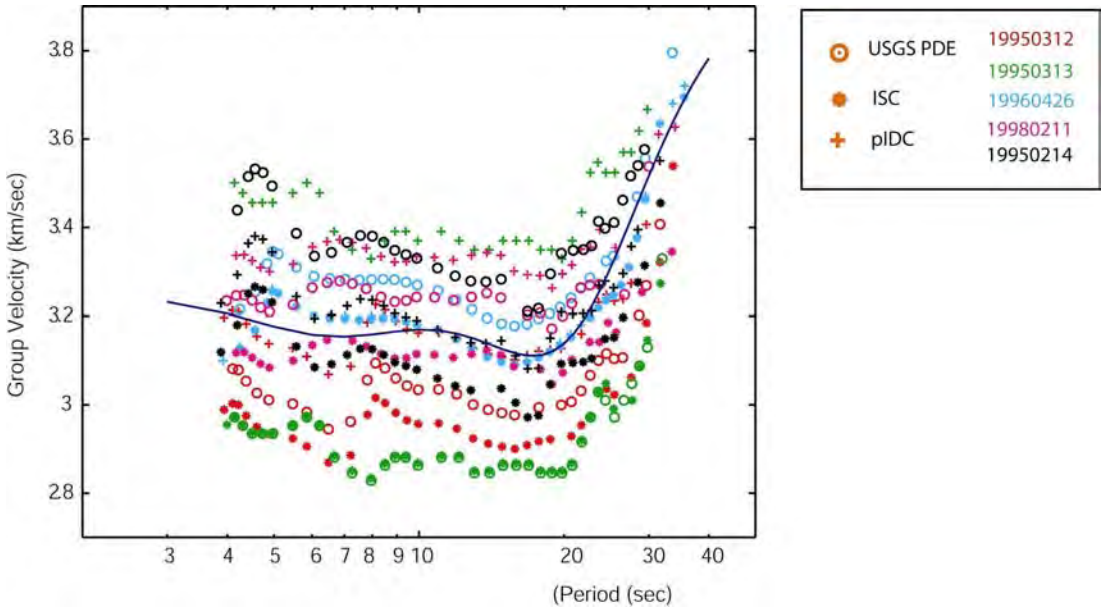

Figure 2. Group velocity dispersion for paths between the Koyna-Warna region and station HYB. The scatter in the dispersion curves is related to location and origin time errors and illustrates the need for using only high-quality event data to generate the calibrated regional velocity models. The blue line is the theoretical dispersion curve for the south Indian shield as determined by research discussed in the following section.

RESEARCH ACCOMPLISHED

Installation of Broadband Seismographs in India

In early February we received five broadband seismographs from Guralp Systems Limited, which we deployed in India in March/April of this year. Figure 3 shows the location of these stations and other stations we are currently operating in India in cooperation with the National Geophysical Research Institute at Hyderabad and the Indian Institute of Astrophysics at Bangalore.

Crustal structure beneath southern India

Short-period surface wave studies. Surface wave phase velocities for fundamental mode Rayleigh waves have been measured for a number of paths across the south Indian Shield (Figure 3). The analysis of surface wave dispersion data gives an average crustal model for the south Indian Shield that is used as a starting model in the receiver function inversions discussed below, and provides additional constraints in the joint receiver function - surface wave inversion.

We determined an average short period fundamental mode Rayleigh wave dispersion curve using various two-station pairs along the North-South (NS) profile using the transfer function method of Gomberg *et al.* (1988). This technique poses the problem of phase velocity determination as a linear filter estimation problem in which the seismogram at a more distant station from an event is the convolution of the seismogram at a close station with the Earth filter (the phase velocity curve) to be determined. Smoothness constraints are imposed based on an approximate knowledge of the group velocity. We used the dispersion results of Bhattacharya (1992) as an initial dispersion model. To ensure the starting dispersion curve was appropriate, we tested a number of initial dispersion models and smoothing criteria; the final dispersion curves (Figure 4a) are the ones where the results were stable in the sense that the resulting dispersion curve

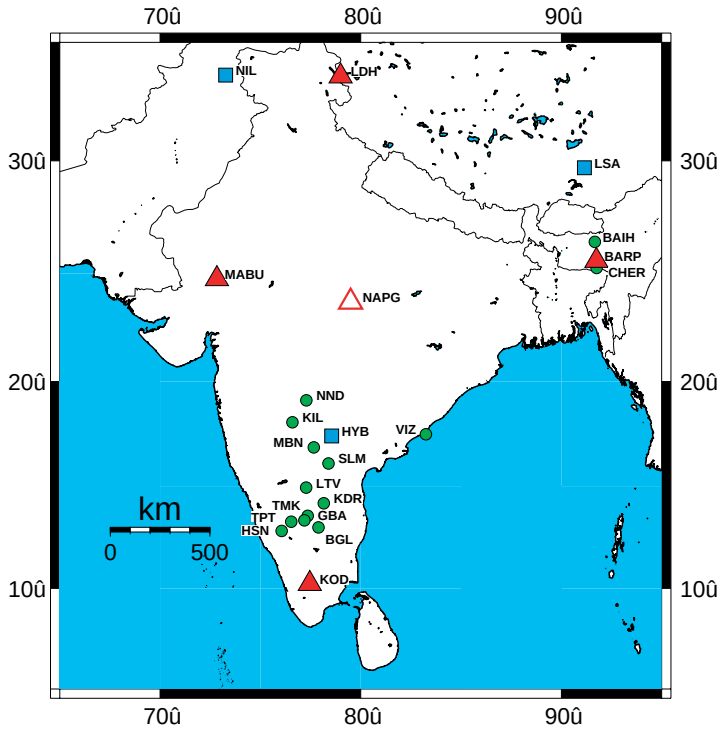

Figure 3. Map showing the stations locations: triangles - permanent stations of Indian Institute of Astrophysics/University of Cambridge; dots - temporary recording sites of National Geophysical Research Institute/University of Cambridge; squares - global digital seismic network stations.

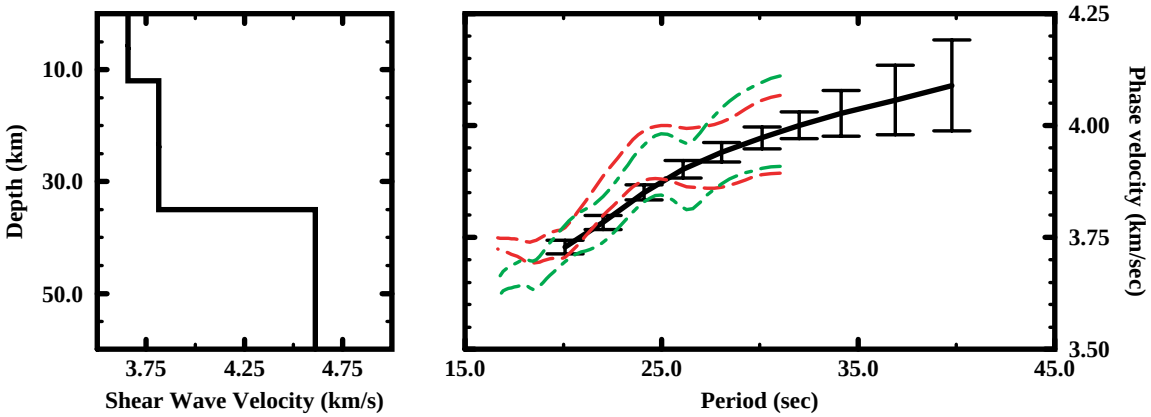

Figure 4. Right - Fundamental mode Rayleigh wave dispersion curves: solid line with error bars - average dispersion for the NS profile; dashed lines - dispersion bounds for the northern portion of NS profile; dot-dash lines - dispersion bounds for the southern portion of NS profile. Left - Crustal velocity model derived from inversion of the average dispersion curve.

was not strongly influenced by realistic changes in the initial dispersion model and smoothing criteria. The dispersion curves in Figure 4a were determined simultaneously from multiple station pairs, but we also determined dispersion curves for all individual two-station paths separately to verify that there were no large outliers amongst the various two-station combinations.

We invert the Rayleigh wave phase velocity data using the stochastic least-squares routine of Hermann (1994). This expresses the standard least-squares problem in terms of eigenvalues and eigenvectors and uses singular value decomposition to invert the matrix giving the solution vector, the variance-covariance matrix, and the resolution matrix. Since the dispersion data for the northern portion, southern portion, and whole profile were nearly identical, and since the crustal models from refraction data at the northern (Krishna *et al*., 1999) and southern (Krishna and Ramesh, 2000) ends of the profile are similar, we inverted only the average dispersion curve. The starting model for the inversion is from the average crustal model for the Indian Shield of Singh *et al*. (1999) and consisted of an upper crustal layer 13.8 km thick with Vs 3.55 km/s and a lower layer 24.9 km thick with Vs 3.85 km/s, over a 4.65 km/s half-space. The final inversion model and the fit of the dispersion curve for this model to the observed dispersion are shown in Figure 4. The average crustal structure beneath the profile consists of two layers (h_1 12 km, V_{s1} 3.65 km/s, h_2 23 km, V_{s2} 3.81 km/s) overlying a mantle with S_n velocity 4.61 km/s.

Receiver function analysis. Figures 5 and 6 illustrate the receiver function analysis we have performed using data from Bangalore (BGL). BGL is situated on the western edge of the eastern Dharwar craton close to its contact with the Closepet granitic intrusion (Figure 3). Figure 5 shows the BGL receiver function with respect to back azimuth. The eastern quadrant is well sampled, but there is only one event from the west. The small variation in the Ps converted phase (4.0±0.1) and the small amplitude of the tangential receiver function relative to the amplitude of the radial receiver function justify modeling the crust beneath BGL as 1-D.

Figure 6 (left) shows a receiver function stack for BGL consisting of 10 events with distance 76±7° and back azimuth 99±3° E. The receiver function has a large amplitude positive arrival at about 4 sec (PS) followed by a prominent positive arrival at about 14 seconds (PpP_mS) and a negative arrival at 16-18 seconds (PpS_mS + PSP_mS)). These phases are also apparent in many of the individual receiver functions making up the stack. Below the stack is the tangential receiver function. Amplitudes of the tangential arrivals are small compared to those of the radial arrivals.

The receiver function stack was inverted for 1-D crustal velocity models. To test the sensitivity of the inversion to the starting model, we used three different initial models: (1) the refraction model for the GBA region of Krishna and Ramesh (2000), (2) the average crustal model derived from the surface wave phase velocity dispersion (Figure 4), and (3) a model derived from the timing of the conversions and reverberations in the receiver functions and the average *P* wave velocity of the crust from Krishna and Ramesh (2000). Zandt *et al*. (1995) pointed out that the average crustal properties can be estimated directly from the arrival time differences of the pP, PS, PpP_mS and PpS_mS + PSP_mS phases in the receiver function. The PS - pP time difference is dependent on the average V_p/V_s ratio of the crust and the crustal thickness. The PS - PpP_mS time is the two-way *P* wave travel time and the {PpS_mS + PSP_mS} - pP time is the two-way *S* wave travel time through the crust for a ray with ray parameter *p*. The ratio of PS – pP to PS - PpP_mS is independent of crustal thickness but weakly dependent on V_p; the ratio of PS - PpP_mS to {PpS_mS + PSP_mS} is proportional to the V_p/V_s ratio and independent of crustal thickness.

We inverted the receiver functions using the linearized inversion of Ammon *et al.* (1990) both with and without the surface wave dispersion constraint and the final inversion results were nearly identical for the three starting models. We then simplified the model by grouping adjacent model layers with similar wave speeds to form a more coarsely parameterized starting model and reinverted the receiver function. We repeated this procedure until we found the velocity model with the minimum number of parameters that fit both the main features of the receiver function and the short period surface wave phase velocity. Finally, we tested the main features of the crustal model (e.g., thickness of the low velocity surface layer, thickness of the gradient at the base of the crust, Moho depth) using a forward-modeling model to estimate how well these model features were constrained by arrivals in the observed receiver function.

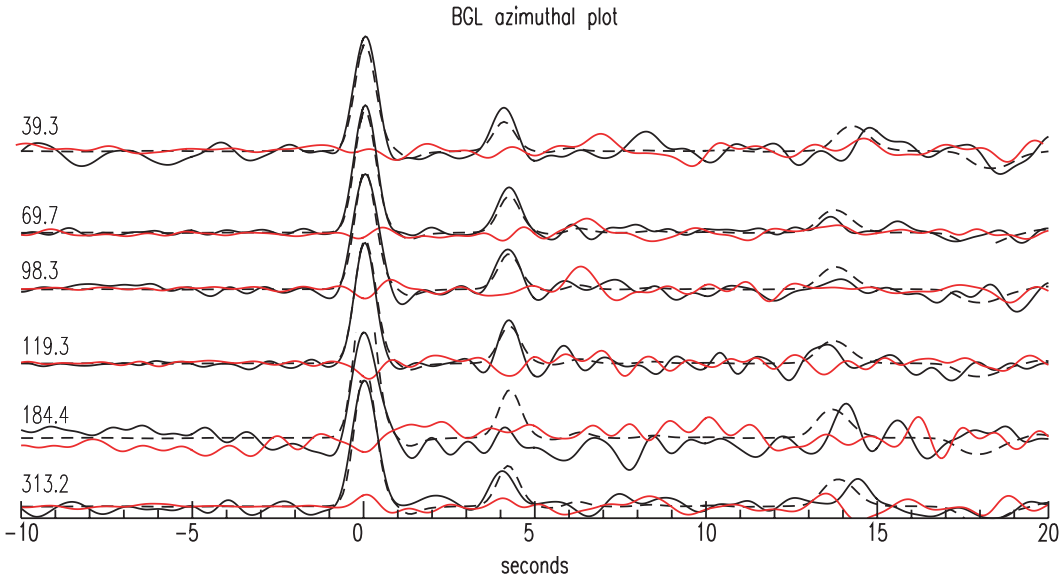

Figure 5. BGL receiver functions vs. azimuth: heavy solid line - radial receiver function; red solid line - tangential receiver function; dashed line - radial receiver function calculated for the final crustal velocity model shown in Figure 6.

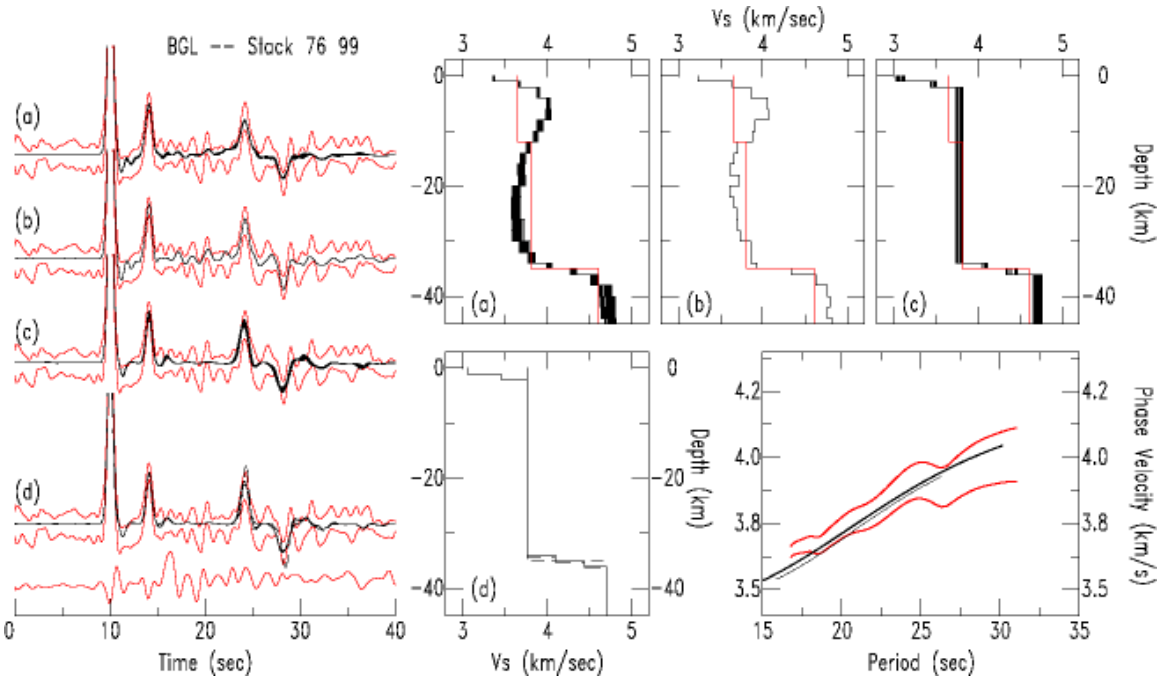

Figure 6. Receiver function analysis summary for BGL. Right: (a) initial inversion results; (b) results of joint receiver function/surface wave inversion; (c) final inversion models; (d) forward modeling test; (e) match between the observed phase velocity and the phase velocity calculated from the models shown in (b) and (c). Left: Match of the receiver function calculated for the four velocity models at right and the ±1 σ bounds for the BGL receiver function stack.

These steps are summarized in Figure 6 (right). The initial inversion model without the dispersion constraint shows a smooth velocity gradient from about V_s 3.1 km/s at the surface to about 3.75 km/s in the lower crust and a Moho discontinuity at 35±2 km depth (Figure 6a). The inversion with the surface wave dispersion constraint (Figure 6b) produces a model identical to those shown in Figure 6a. The final velocity model (Figure 6c) shows a thin (2-4 km) low velocity surface layer, an almost uniform velocity crust (3.5-3.6 km/s), and a Moho discontinuity at 35±1 km depth. The fits of the synthesized receiver functions for the various velocity models to the ±1σ bounds of the observed receiver function stack are shown in Figure 6 (left).

In the forward modeling test, the upper mantle *Pn* and *Sn* velocity were fixed at 8.2 km/s (Krishna and Ramesh, 2000) and 4.72 km/s (Huestis *et al*., 1973), respectively, but, in fact the receiver functions are relatively insensitive to these parameters. Neither the difference in the near surface layer, the mid-crustal discontinuity, nor the gradient at the base of the crust from the inversion of the different stacked receiver functions is significant, and we find that considering the noise in the data, one crustal velocity model fits all the receiver function stacks for BGL. Figure 5 compares the synthetic receiver function for the BGL crustal model which the observed receiver functions as a function of azimuth. This agreement indicates little lateral variation in the crustal velocity structure about BGL. If the small systematic variation in the PS - P time suggested by Figure 5 is real, this could result from a systematic variation of crustal velocity about BGL or a systematic variation in Moho depth. If the crustal velocity variation is spread through the whole 35 km thickness of the crust, it would correspond to a ±0.1 km/s variation in shear wave velocity. If the variation is due to a systematic azimuthal variation in the Moho depth, this corresponds to a ±1 km lateral variation in the Moho depth about BGL.

We have analyzed data from 14 broadband sites in southern India in this manner and the resulting Moho depths are shown in Figure 7. The Moho is at almost constant depth along the western edge of the eastern Dharwar craton. However, the two sites on the western Dharwar craton show the Moho there is about 5 km deeper, a result also noted in the Kavali - Uduppi refraction study (Kaila and Krishna, 1992). To the south of the shield in the granulite terrain (KOD, Fig. 1) the crust is 43 km thick. Thus, there are significant differences in Moho depth over southern India, but the results we have to date suggest they are well correlated with the surface geology.

Upper mantle structure beneath southern India. Figure 8 shows the fundamental mode Rayleigh waves dispersion measurement from seven two-station pairs using the combination of the stations NND/HYB in the north and GBA/KOD in the south. Inter-station path lengths for the two-station pairs vary from 600 to 800 km. The coherency plot shows that the dispersion is well constrained to ~180 sec period. Previous measurements of fundamental mode Rayleigh wave phase velocity have extended only to ~50 sec period (Hwang and Mitchell, 1987; Bhattacharya, 1992). This increased period range of our dispersion measurement is important in constraining the deep structure of the south Indian Shield. For comparison, the dispersion curve for the Canadian Shield (CANSD - Brune and Dorman, 1963) is also plotted in Figure 8. The crustal thickness of the south Indian Shield from the receiver function study discussed below is 36±1 km, and the crust of model CANSD is 35 km thick. The short period (<35 sec) and long period (>130 sec) portions of the two dispersion curves are similar, but between 40 and 125 sec period the phase velocities for the south Indian Shield are low compared to those of model CANSD. The preliminary inversion of the Indian phase velocity curves indicated the presence of a high velocity upper mantle lid with *S* wave velocity ranging from ~4.62 km/s at 40-60 km depth to ~4.72 km/s at 80-120 km depth and a low velocity of ~4.5 km/s at 150-220 km depth.

CONCLUSIONS AND RECOMMENDATIONS

During the past year, we have initiated a study to collect seismic data from southern Asia for the purpose of developing high quality velocity models to aid in regional seismic event location. We have installed five broadband sensors in southern Asia and are now collecting data. Using these data collected from the current deployment, along with other data sources from the region, we have completed surface wave and receiver function studies. Based upon surface wave phase velocity measurements, we have developed a shear wave velocity structure for the crust and upper mantle of the south Indian shield. The average crustal

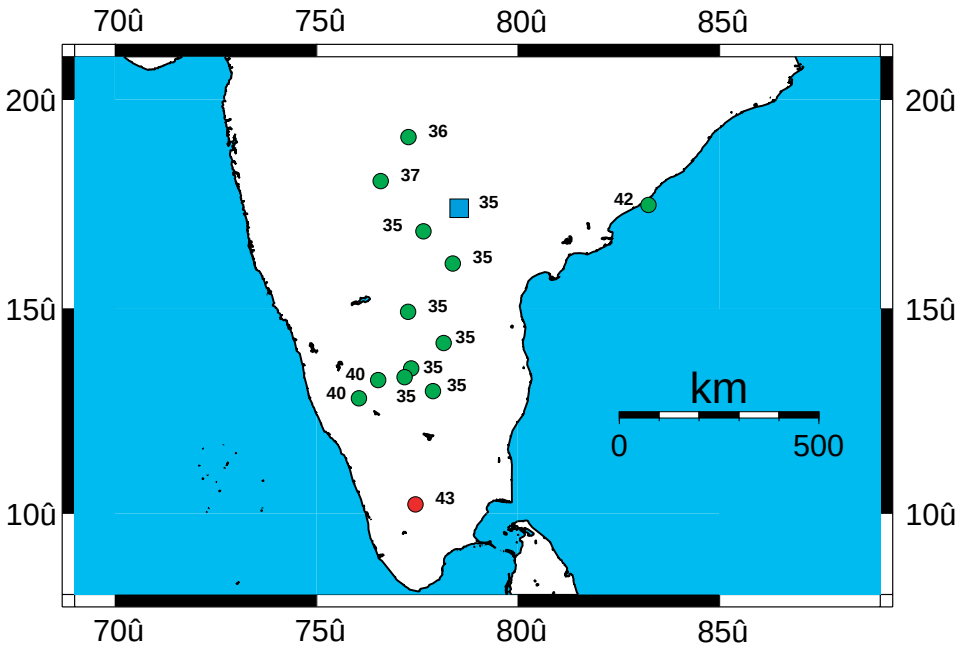

Figure 7. Moho depth from receiver function analysis.

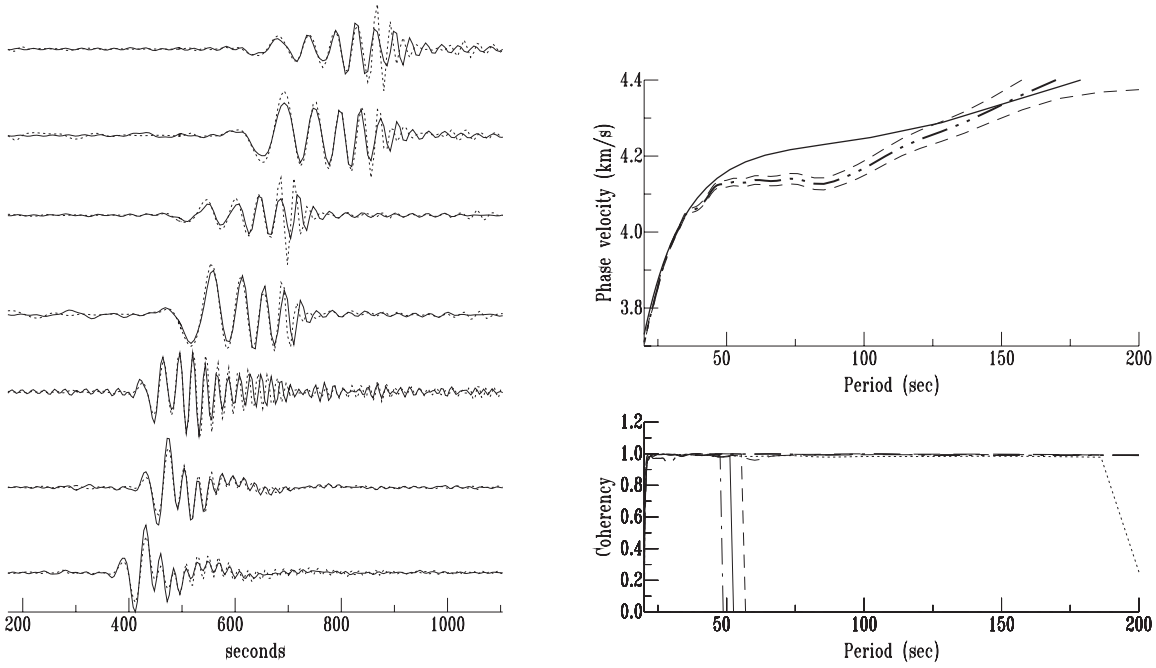

Figure 8. Long-period fundamental mode Rayleigh wave phase velocity dispersion. Left: Match of the far waveform (solid line) and near seismogram (dashed line) after being filtered by the determined transfer function. Right: Upper - dispersion curve for the south Indian Shield (dot-dash line) and ±1σ bounds (dash lines) and dispersion curve for model CANSD of Brune and Dorman (1963) (light solid line); Lower - coherency vs. period.

structure beneath the profile consists of two layers (h_1 12 km, V_{s1} 3.65 km/s, h_2 23 km, V_{s2} 3.81 km/s) overlying a mantle with S_n velocity 4.61 km/s. Inversions of the phase velocity curves indicate the presence of a high velocity upper mantle lid with *S* wave velocity ranging from ~4.62 km/s at 40-60 km depth to ~4.72 km/s at 80-120 km depth and a low velocity of ~4.5 km/s at 150-220 km depth. We have also analyzed receiver function data from 14 broadband sites in southern India and determine the velocity structure is similar to the surface wave results. The Moho is at almost constant depth along the western edge of the eastern Dharwar craton. However, the two sites on the western Dharwar craton show the Moho there is about 5 km deeper, a result also noted in the Deep Seismic Soundings from the region. To the south of the shield in the granulite terrain the crust is 43 km thick We have also modeled the regional waveforms of a moderate earthquake that occurred near Koyna, India, in September 2000 and of the 26 January 2001 Bhuj main shock and its aftershocks to calibrate paths to the regional stations. In the next stage of this project, we will continue the data collection and velocity model development, however our research focus will be shifted northward to central and eastern India, including the Shillong Plateau.

REFERENCES

Ammon, C.J., G.E. Randall and G. Zandt (1990), On the non-uniqueness of receiver function inversions. *J. geophys. Res.*, **95**, 15,303-15,318.

Bhattacharya, S.N. (1992), Crustal and upper mantle velocity structure of India from surface wave dispersion. In Gupta, H.K., S. Ramaseshan, (Eds.), Seismology in India - An Overview. *Curr. Sci.; Spec. Issue*, **62**, 94-100.

Brune, J.N., and J. Dorman (1963), Seismic waves and earth structure in the Canadian shield, *Bull. seism. Soc. Am.*, **53**, 167-210.

Du, Z.J., and G.R. Foulger (1999), The crustal structure of northwest fjords, Iceland, from receiver functions and surface waves, *Geophys. J Int.*, **139**, 419-432.

Gaur, V.K., and K.F. Priestley (1997), Shear wave velocity structure beneath the Archaean granites around Hyderabad, inferred from receiver function analysis, *Proc. Indian Acad. Sci. (Earth Planet. Sci.)*, **106**, 1-8.

Gomberg, J.S, K. Priestley, T.G. Masters, and J.N. Brune (1998), The Structure of the Crust and Upper Mantle of Northern Mexico, *Geophys. J. R. astr. Soc.*, **94**, 1-20.

Huestis, S., P. Molnar, and J. Oliver (1973), Regional *Sn* velocities and shear velocity in the upper mantle, *Bull. seism. Soc. Am.*, **63**, 469-475.

Johnson, M. B., S. Rieven, C. Vincent, D. Reiter, and W. Rodi (2000), Empirical analysis of a 3-D Pakistan regionalized velocity model for improved seismic event locations, Proceedings of the 22nd Annual DoD/DOE Seismic Researh Symposium, 43-52.

Hwang, H. G., and B. J. Mitchell (1987), Shear velocities, Q_β, and the frequency dependence of Q_β in stable and tectonically active regions from surface wave observations, *Geophys. J. R. astr. Soc.*, **90**, 575-613.

Kaila, K.L., and V.G. Krishna (1992), Deep seismic sounding studies in India and major discoveries. In Gupta, H.K., S. Ramaseshan, (Eds.), Seismology in India - An Overview. *Curr. Sci.; Spec. Issue*, **62**, 117-154.

Krishna, V.G., C.V.R.K. Rao, H.K. Gupta, D. Sarkar, and Baumbach (1999), Crustal seismic velocity structure in the epicentral region of the Latur earthquake (September 29, 1993), southern India: inferences from modeling of the aftershock seismograms, *Tectonophysics*, **304**, 241-255.

Krishna, V.G., and D.S. Ramesh (2000), Propagation of crustal waveguide trapped Pg and seismic velocity structure in the south Indian shield, *Bull. seism. Soc. Am.*, **90**.

Mandal, P., B. K. Rastogi, and C. S. P. Sarma (1998), Source parameters for Koyna earthquakes, India, *Bull. seism. Soc. Am.*, **88**, 833-842..

Singh, S.K., R.S. Dattatrayam, N.M. Shapiro, P. Mandal, J.F. Pacheco, and R.K. Midha (1999), Crustal and Upper Mantle structure of peninsular India and source parameters of the 21 May 1997, Jabalpur earthquake (Mw = 5,8): Results from the new regional broadband network, *Bull. seism. Soc. Am.*, **89**, 1631-1641.

CRUSTAL STRUCTURE FROM WAVEFORM INVERSTION OF SHEAR-COUPLED PL

Jay Pulliam, Mrinal K. Sen, Cliff Frohlich, and Steve Grand

The University of Texas at Austin

Sponsored by the Defense Threat Reduction Agency

Contract No. DTRA01-00-C-0060

ABSTRACT

One strategy for discriminating between explosions and natural events depends on accurate determinations of event locations, including focal depths. If a seismic event could be reliably determined to have a focal depth greater than a few kilometers, one could be confident that the event is not an explosion. But to determine focal depths accurately, one must first have a fairly accurate model of the crustal structure in the vicinity of the event. Unfortunately, sufficiently accurate models do not exist for many regions of interest to the nuclear explosion monitoring community. Our previous work focused on developing and evaluating strategies for locating events using a single three-component seismic station; velocity models were obtained via crustal receiver function modeling, and waveform correlation methods were used to determine focal depths for which synthetics fit the data best. However, for an event at a regional distance from a given station, the sampling provided by the teleseismic phases used for receiver functions is not ideal. These waves tend to approach the station at a steep angle, sampling just a narrow cone beneath the station.

Better sampling is provided by shear-coupled PL (SPL) phases, which sample the crust over 1000 km or more as they approach the station. This sampling provides a better lateral average of the crust and more closely resembles the sampling of phases emanating from seismic events at regional distances. Our current research centers on modeling SPL phases using a novel modeling algorithm that uses the reflectivity method to compute synthetic seismograms while holding deeper portions of the mantle fixed, in terms of pre-computed and stored reflectivity and transmission matrices. Layers of the crust and upper mantle are allowed to vary over broad ranges and the entire algorithm is powered by a variant of simulated annealing, a global optimization method. Using the results of all trials we are able to compute the posterior probability distribution for model parameters and thereby assess the strength of the constraints placed upon the model parameters by the data.

We report on progress in developing the modeling code and demonstrate, through synthetics computed for receiver function models produced for China, that the sampling provided by SPL is significantly different from that provided by receiver functions. Mismatches between synthetics and data for S-wave windows including the Sp converted phase, SsPmP, and SPL, indicate that each model, while it may represent structure in the immediate vicinity of a station, does not reflect structure over a broader area around the station. Given the sampling of the SPL phase, trial-and-error modeling is very difficult and time-consuming. These results confirm, however, that Sp, SsPmP and SPL phases carry additional, valuable information that can help constrain crustal and upper mantle velocity models.

KEY WORDS: discrimination, event location, crustal structure, wave propagation

OBJECTIVE

Introduction

"Receiver function" methods, which typically use the reverberations of P phases, contained in the P coda, to constrain a 1-D model beneath a seismographic station, have been quite successful in matching important characteristics of existing refraction models. Receiver function methods allow the crust beneath a given station to be estimated with much less effort and cost than are required for active-source experiments. However, because receiver function methods use rays that arrive at the station with steep

angles of incidence (e.g., Zhao and Frohlich, 1996), they sample only a narrow cone beneath the station. The result is a 1-D model that does not represent a broad regional average, i.e., the medium through which signals from a later event of unknown provenance and location would propagate. Furthermore, the predominantly vertically propagating reverberations that make up the P coda reflect steeply off the crust's internal layers. They therefore do not emulate the propagation of regional phases, which reflect at more oblique angles or are refracted by these layers. This is a problem for locating and/or determining focal depths of small, regional seismic events. In short, because of the data they use, the models produced by receiver function methods may be inadequate for the purposes of Comprehensive Nuclear-Test-Ban Treaty (CTBT) monitoring.

We are developing a new method for modeling the crust and upper mantle that retains the time and cost advantages of P-coda receiver function methods but which uses types of data that are more appropriate for CTBT purposes: Shear-coupled PL phases (SPL), Sp phases converted at the Moho, and SsPmP. SPL samples the crust and upper mantle in the vicinity of a station most broadly compared to Sp, SsPmP and P. Modeled simultaneously (where they exist), SPL, Sp, and SsPmP offer the potential for producing azimuthally dependent structural models.

What is shear-coupled PL? Frazer (1977) and Baag and Langston (1985) review previous work on SPL extensively; we will summarize aspects that are relevant for our proposed CTBT monitoring research.

The conventional S phase is the initial, relatively sharp and pulse-like arrival that signals the beginning of a wavetrain with generally longer periods and normal dispersion. The particle motion associated with the S phase is rectilinear, and all three components of motion are in phase. The dispersive wavetrain that follows S exhibits prograde elliptical particle motion that is confined to the vertical plane. Oliver (1961) named this wavetrain "shear-coupled PL" because it is analogous to the PL wavetrain, which appears between P and S arrivals at regional distances. Oliver (1961) presented a theory, based on the observed group and phase velocity of SPL that explained the phase as coupling between S and the fundamental leaking mode of Rayleigh waves in the crustal waveguide. According to this theory, shear energy radiated by an earthquake (or explosion) travels through the Earth as a body phase, whereupon it impinges upon the Moho. Afterward it travels through the crustal waveguide as trapped P-waves and leaky SV-waves. The only difference between a PL phase, which is observed at regional distances from a source, and SPL phases, which are observed at teleseismic distances, is that SPL is generated by a shear wave impinging upon the Moho at regional distances from the observing station. Chander et al. (1968), Frazer (1977), and Baag and Langston (1985) essentially validated Oliver's hypothesis by presenting computational methods for synthesizing SPL. However, Chander et al. (1968) present only approximate seismograms and do not include S waves. Frazer's method does not include the effects of anelastic attentuation, nor did he explore the effects of near-source structure on SPL generation and propagation.

While previous work has elucidated the origin and propagation characteristics of SPL (e.g., Oliver, 1961; Chander et al., 1968; Alsop and Chander, 1968; Poupinet and Wright, 1972; Frazer, 1977; Baag and Langston, 1985) attempts to use a portion of the S coda to model the crust explicitly are quite limited (e.g., Helmberger and Engen, 1974; Swenson et al., 1999). Modeling of Sp and SsPmP have received slightly more attention (e.g., Jordan and Frazer, 1975; Langston, 1996). This disparity is understandable; synthesizing SPL is computationally intensive (Frazer, 1977; Baag and Langston, 1985). Because of the difficulty in computing waveforms, the inverse problem of determining structure along the propagation path from observed SPL has not been adequately explored. Our objectives are (a) to evaluate the usefulness of shear-coupled PL, Sp, and SsPmP phases for modeling crustal and upper mantle structure using real and synthetic data, (b) develop a waveform inversion technique based on a novel implementation of the reflectivity method and global optimization algorithms, and (c) apply the inversion technique to model the crust and upper mantle beneath China. Figure 1 shows examples of synthetic seismograms computed for three models that differ in their upper mantles and crusts. One can clearly see the sensitivity in timing, pulse width, and relative amplitudes of S, Sp, SsPmP, and SPL phases. Successful modeling of data that contain these phases will provide strong constraints on regional P and S velocity models.

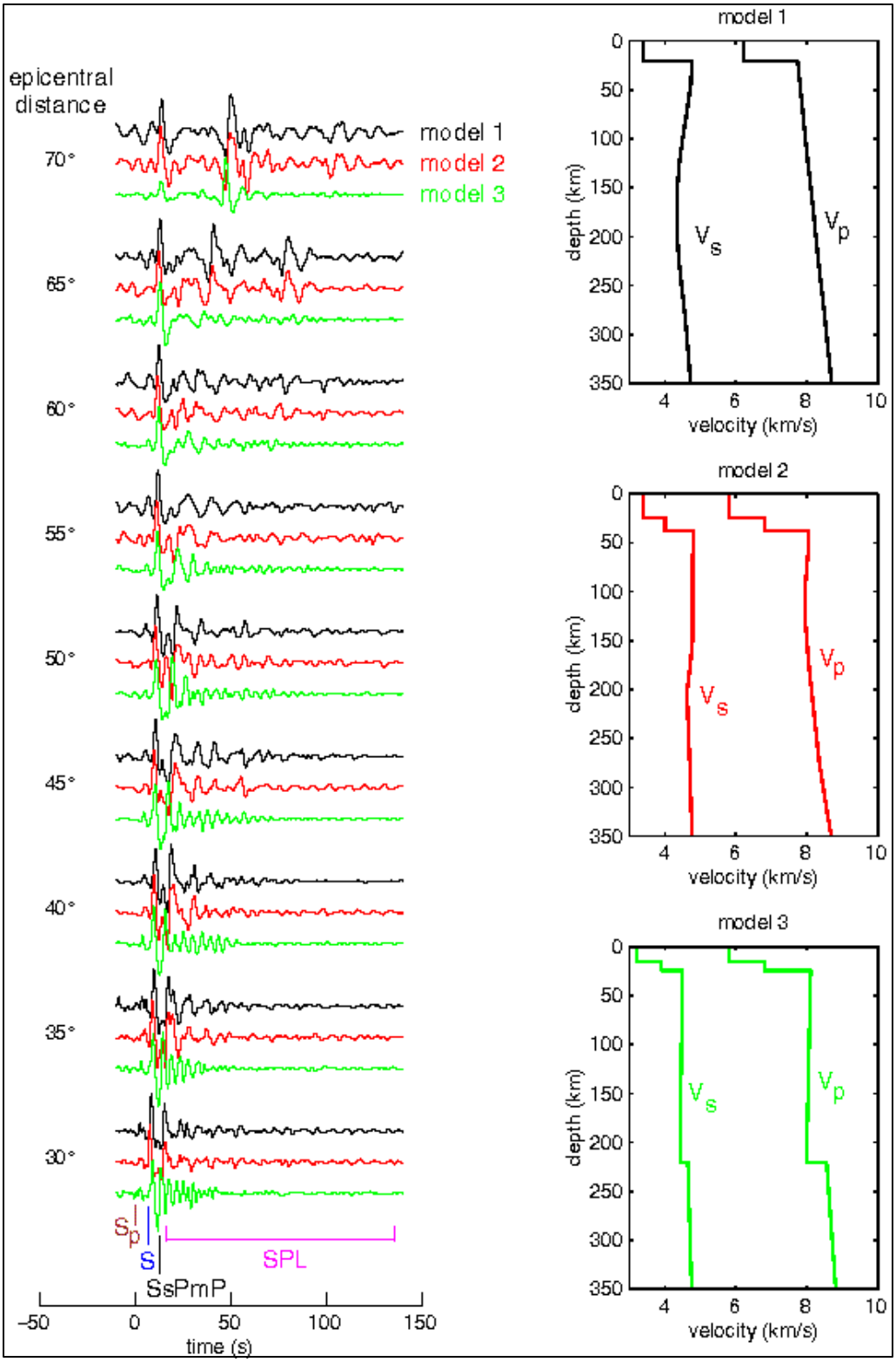

Figure 1. A comparison of vertical-component synthetic seismograms showing S, Sp, SsPmP, and SPL waves computed using the models shown at right. These seismograms were computed using our reflectivity code for frequencies between 0.001 and 1 Hz and a dip-slip dislocation source at 600 km depth.

RESEARCH ACCOMPLISHED

Development of the Modeling Technique

The reflectivity calculation involves computation of reflectivity matrices for a stack of layers as a function of ray parameter (or wavenumber) and frequency. The computation of reflectivity responses for different ray parameters and frequencies is completely independent of each other. We took advantage of this independence to develop a reflectivity code that can be run on parallel computer architectures. We parallelized our code over the ray parameters, i.e., to each node we assign a certain number of ray parameters to compute. The number of ray parameters to be computed can be determined based on the processor speed. If all the processors are of the same speed, they are assigned equal number of ray parameters. At the end, the master node assembles the partial responses and performs the inverse transformation to generate synthetic seismograms at the required azimuths and distances.

We used MPI for message passing and ran our code on a PC cluster consisting of 16 nodes; each node is a 660-MHz alpha processor with 8-MB cache and 1-GB of RAM. A Myrinet interconnect is used to communicate between nodes. Figure 2 shows timing statistics for the reflectivity code on our PC cluster.

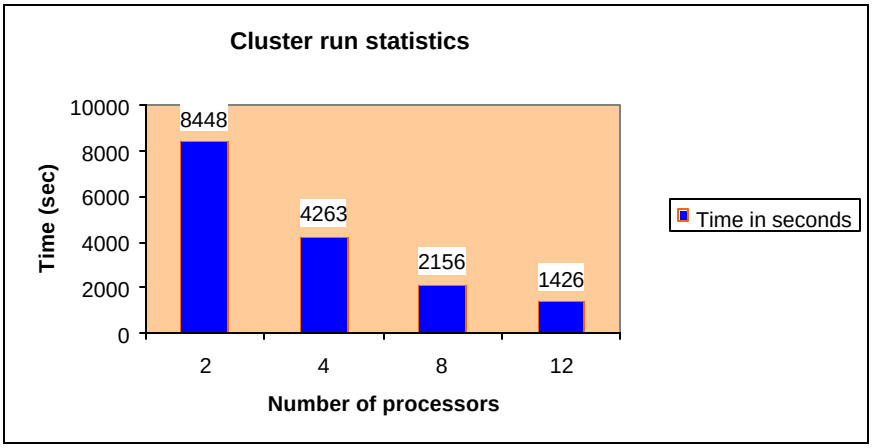

Figure 2. The statistics of an example run to compute complete seismograms for frequencies from 0 to 0.5 Hz (number of frequencies = 2000, no of layers=192, no of ray-parameters=6000) on the DEC Alpha cluster. Note the near linear speedup of the algorithm with the increase in the number of processors.

We plan to obtain further increases in computational speed by using additional processors (we have been unable to use all 16 processors due to minor hardware difficulties), tailoring the number of ray parameters more carefully to the structure being modeled, and by pre-computing and storing reflectivity matrices for parts of the mantle that will not vary in our modeling. The high frequencies needed to compute body waves accurately over the distances to which SPL is observed contribute to the difficulty in computing SPL. We propose to essentially remove these complications by storing pre-computed products for fixed parts of the Earth model.

The modeling process will be controlled by a global optimization algorithm called Very Fast Simulated Annealing (VFSA) (e.g., Sen and Stoffa, 1995). Simulated annealing (SA) is analogous to the natural process of crystal annealing when a liquid gradually cools to a solid state. The SA technique starts with an initial model $\mathbf{m}_0$, with associated error or energy $E(\mathbf{m}_0)$. It draws a new model $\mathbf{m}_{new}$ from a flat distribution of models within the predefined limits. The associated energy $E(\mathbf{m}_{new})$ is then computed and compared against $E(\mathbf{m}_0)$. If the energy of the new state is less than the energy of the initial state, the new model is

accepted and it replaces the initial model. However, if the energy of the new state is higher than the initial state, $\mathbf{m}_{new}$ is accepted with the probability of $\exp\left(\left(E(\mathbf{m}_{new}) - E(\mathbf{m}_0)\right)/T\right)$, where T is a control parameter called temperature. This rule of probabilistic acceptance (also called the Metropolis rule) allows SA to escape local minima. The process of model generation and acceptance is repeated a large number of times with the annealing temperature gradually decreasing according to a predefined cooling schedule. A variant of SA, called Very Fast Simulated Annealing (VFSA) speeds up the annealing process by drawing each new model from a temperature dependent Cauchy-like distribution centered on the current model. This change with respect to SA has two fundamental effects. First, it allows for larger sampling of the model space at the early stages of the inversion (when "temperature" is high), and much narrower sampling in the model space as the inversion converges and the temperature decreases. Second, each model parameter can have its own cooling schedule and model-space sampling scheme. VFSA therefore allows for individual control of each parameter and the incorporation of a priori information.

Uncertainty Estimation: PPD, Posterior Covariance and Correlation

In seismic waveform inversion, more than one model can often explain the observed data equally well and trade-off between different model parameters is also common. It is therefore important not only to find a single, best-fitting solution but also to find the uncertainty and level of uniqueness of that solution. A convenient way to address this issue is to cast the inverse problem in a Bayesian framework (e.g., Tarantola, 1982; Sen and Stoffa, 1995) in which the posterior probability density function (PPD) is the answer to the inverse problem. The PPD is proportional to the product of a likelihood function and the prior. It can be shown (e.g., Tarantola, 1982) that the PPD $\sigma(\mathbf{m}|\mathbf{d}_{obs})$ is given by

$$\sigma(\mathbf{m}|\mathbf{d}_{obs}) \propto \exp(-E(\mathbf{m})). \tag{6}$$

Since the PPD is a multi-dimensional function, one generally evaluates marginal PPD, mean, covariance and some higher order moments. All these quantities can be represented by the following multi-dimensional integral

$$I = \int d\mathbf{m}\ f(\mathbf{m})\sigma(\mathbf{m}|\mathbf{d}_{obs}). \tag{7}$$

Thus, we are now left with the problem of finding efficient methods of evaluating a multi-dimensional integral. Importance sampling based on a Gibbs sampler or a Metropolis rule (Sen and Stoffa, 1996) can be used effectively to evaluate these integrals and to estimate PPD, posterior mean, covariance and correlation matrices. The posterior covariance and correlation matrices clearly demonstrate the trade-off between different model parameters. Sen and Stoffa (1995) showed that multiple VFSA runs with different random starting models could be used to sample models from the most significant parts of the model space. These models, when used to evaluate equation (7) result in estimates that are fairly close to the values obtained by theoretically correct Gibbs sampling. Multiple VFSA, however, is computationally very efficient.

Application to Data

After exploring available data and relevant previous studies, we decided to focus first on China (Figure 3), for which several studies of crustal receiver functions have been made. The fairly thick crust beneath China produces good separation between Sp, S, and SsPmP phases, which makes China an ideal location for a first application of the modeling method. We selected eight deep events at epicentral distances ranging from 22° to 58°, rotated, filtered and windowed the data around the S arrival. Figure 4 shows data for a single station (BJT, although it is the former station BJI for the 1990 event), including the results of a polarization filter (radial component multiplied by the vertical component), which aids in identifying phases. Since radial and vertical motion are correlated for rectilinear motion, P-type energy shows up as positive values whereas SV-type energy is negative. The best examples of Sp, SV, SsPmP, and SPL are marked with arrows in Figure 4. These arrivals, which also appear clearly in our sample synthetics (e.g., Figure 1), are highly sensitive to the structure of the crust and upper mantle and offer strong modeling

constraints on that structure. However, due to the nature of their propagation, modeling these phases by trial-and-error would be extremely time-consuming and frustrating—if it is feasible at all.

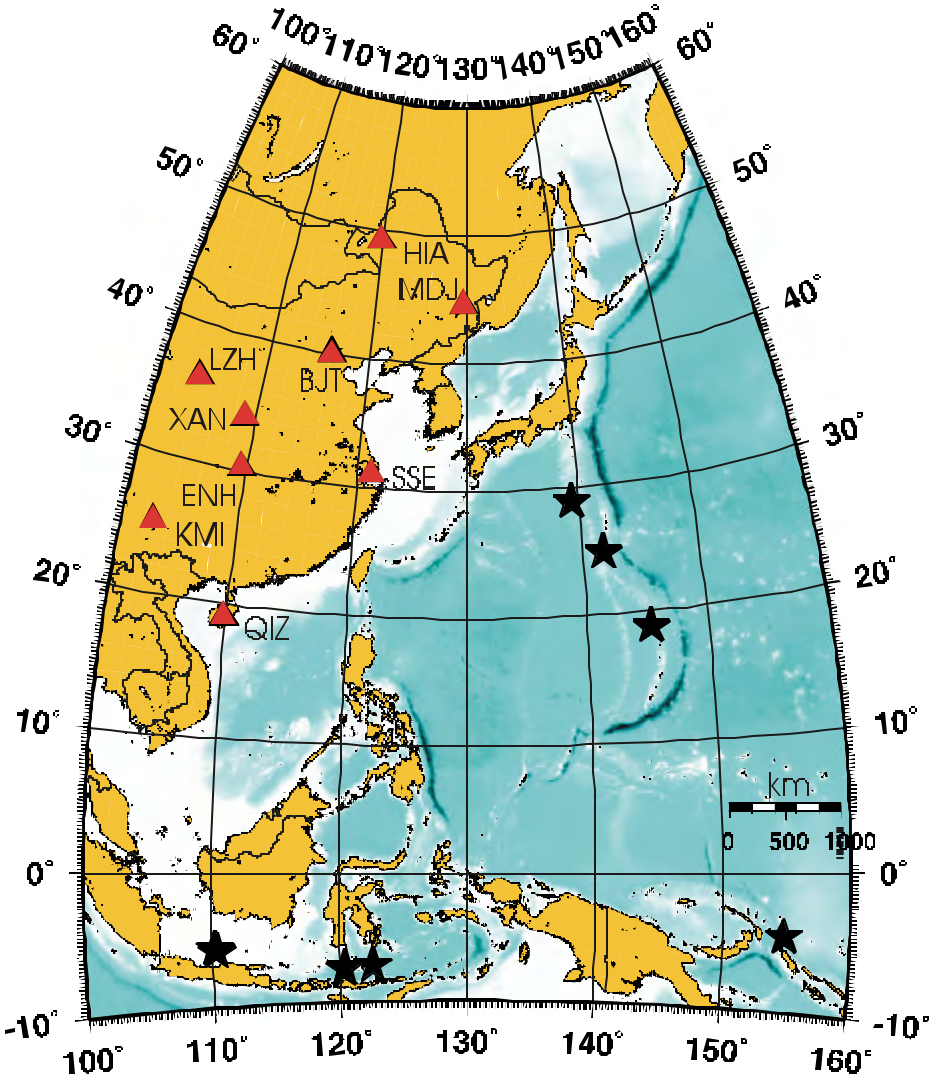

Figure 3. Map of China, including the earthquakes (stars) and stations (triangles) used in this study. See Epicentral distances range from 22° to 58°. See Table 1 for earthquake parameters.

Table 1. Events used in this study.

	Year	Month	Day	Hour	Min	Sec	Latitude (°)	Longitude (°)	Depth (km)	Mag
1	1990	5	24	20	9	23.2	-7.363	120.363	588.9	6.4
2	1994	9	28	16	39	51.7	-5.786	110.352	637.5	6.6
3	1994	11	15	20	18	11.3	-5.589	110.186	560.6	6.5
4	1995	8	23	7	6	2.8	18.856	145.218	594.9	7.1
5	1996	5	2	13	34	29.0	-4.548	154.833	500.0	6.6
6	1996	6	17	11	22	18.5	-7.137	122.589	587.3	7.9
7	1998	2	7	1	18	59.5	24.821	141.746	525.3	6.4
8	1998	8	20	6	40	55.8	28.932	139.329	440.5	7.1

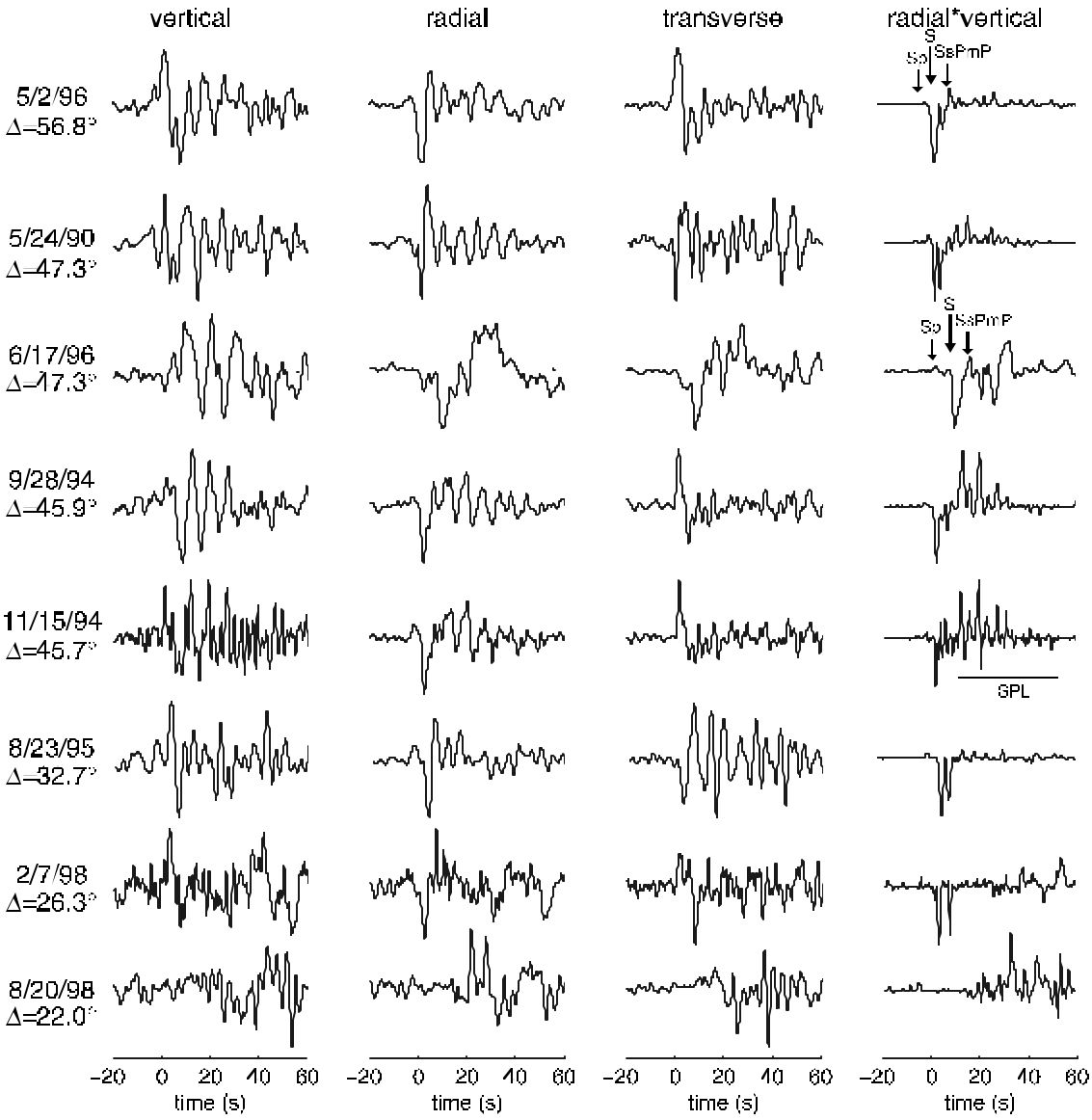

Figure 4. Vertical-, radial-, and transverse-component data from the events listed in Table 1 for the single station BJT (BJI for the 1990 event). These velocity records have been bandpass-filtered with a 5-pole Butterworth filter with corner frequencies at 0.01 and 0.5 Hz. At far right is the result of a simple polarization filter consisting of the vertical component multiplied by the radial component. Rectilinear P-type motion is indicated by positive values and rectilinear SV motion is indicated by negative values, which aids in the identification of phases.

We implemented a number of the crustal models obtained by Mangino et al. (1999) and computed synthetic seismograms via reflectivity for deep events at distances of 30°-60° to compare to the data. These P-velocity models were converted to S models by means of a simple proportionality (1.8). Synthetics were computed up to frequencies of 0.5 Hz and were convolved with the Harvard CMT solutions for each event. Our synthetics matched some aspects of the data—generally we obtained a good match to the SV wave but

failed to match the Sp, SsPmP, and SPL phases (Figure 5). Even this level of agreement is impressive. Receiver functions, as discussed above, model reverberating waves that sample the crust differently than do the shear wave converted phases. Second, the S model we used was converted simply from P models. Lastly, in order to compute synthetics over teleseismic distances, we took the liberty of inserting Mangino et al.'s models into PREM, essentially replacing the PREM crust. The structure of the uppermost mantle, including the thickness of the crust and the velocity contrast across the Moho, play crucial roles in the Sp/SV time separation, waveshapes and amplitude ratios. Modeling these aspects accurately will have to await the completion of our modeling scheme.

CONCLUSIONS AND RECOMMENDATIONS

Although we believe the method we are developing holds strong promise, we have several concerns to address. Among the issues that must be settled are the questions:

Is SPL responsible for the S coda?

An important assumption underlying this research is that at teleseismic distances, SPL waves are responsible for a significant proportion of the energy in the S coda. Our modeling approach would be invalid if the coda structure were controlled instead by fundamentally different processes, such as multipathing or scattering from lateral heterogeneity. However, we believe that the latter case is unlikely because of the considerable previous success of investigators such as Frazer (1977) and Baag and Langston (1985), who generated SPL waves to reproduce the essential features of signal that followed the S phase. Moreover, SPL generally contains considerable power in a relatively narrow frequency range, and even in the presence of scattered energy it is likely that usable signals will emerge with suitable filtering. Finally, multipathing may be responsible for coda structure at some stations. However, it is unlikely that this is true at the majority of stations; identifying the near-station geological conditions which imply that SPL does not control coda structure is an implicit goal of this project.

Do lateral variations in structure prohibit 1-D modeling via reflectivity?

We believe that the relatively long-period nature of SPL and its broad averaging properties offer an opportunity to obtain an accurate 1-D average of even laterally heterogeneous regions. The extent to which SPL's averaging holds for strong and/or short-wavelength lateral variations is unclear, but it is likely that large regions of the world will admit 1-D reflectivity modeling of SPL waves. Our method would provide an accurate (i.e., laterally-averaged) 1-D model of the propagation path, which is more practical for monitoring purposes than a 3-D model. Our contention, which we will evaluate in the course of this research, is that a 1-D model may be "good enough" to locate seismic sources in much of the Earth, provided it accurately reflects the crustal and upper mantle structure *between* the source and the station, not just *beneath* the station.

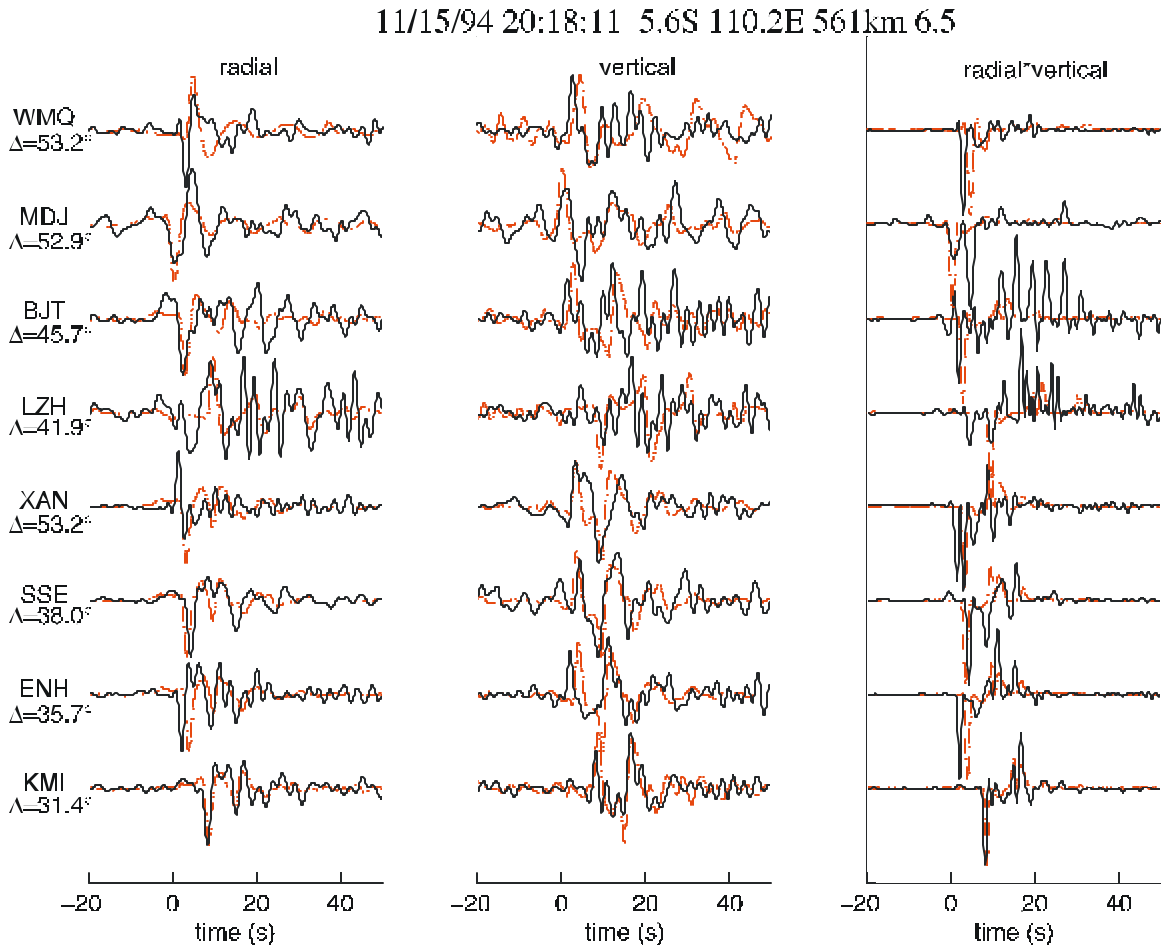

Figure 5. Comparison of data from the 11/15/94 Indonesian event (black lines) with synthetics (gray lines) generated using Mangino et al.'s (1999) crustal receiver functions inserted on top of a PREM mantle. Models were not provided for ENH, SSE, and XAN; here we show the best-fitting synthetics from among the models provided. Note that the SV arrival is well matched, in many cases, but the Sp, SsPmP, and SPL phases are generally poorly matched. The good SV match is impressive, particularly since the receiver functions consist of P velocity models—we obtain S velocities through a constant proportionality (1.8). The poor match of converted phases is not surprising, since these phases sample the crust more broadly than do the P phases used for receiver functions and therefore experience different structure. This comparison illustrates the potential usefulness of these phases for modeling regional structures in a manner most useful for monitoring purposes.

Can we avoid significant source-side contributions to SPL?

Baag and Langston (1985) elegantly demonstrate the large contribution to recorded SPL that arises from reverberations near the source for shallow earthquakes. We intend to model SPL propagation in the receiver region, which means we need to isolate receiver-side from source-side contributions. We can do this most effectively by restricting our applications to deep events. Consequently, we will have fewer events at our disposal and, ultimately, less complete coverage of the world than if we were to use both shallow and deep events. Applications to shallower events, in order obtain more complete worldwide coverage, can be explored later.

Do we have the computing power to invert SPL for velocity structure?

The process of inverting SPL to find crustal structure is highly nonlinear. Even though we will use state-of-the-art forward modeling and inverse methods, they will still require that we calculate SPL synthetics for hundreds or thousands of crustal models. Figure 2 demonstrates that we have the capacity to evaluate hundreds of models in a day's time and that computational speed increases nearly linearly with an increase in the number of processors. More and faster processors are easily obtainable, so computational constraints are not a problem.

The method we are developing will be especially useful for CTBT purposes because it will allow us to produce structural models in regions that (a) have little or no seismicity, (b) average over a broad region in the vicinity of the seismographic station, and (c) are especially well suited to modeling regional phases, due to the propagation characteristics of these converted phases. Models with these characteristics will be useful for locating small-magnitude events at regional distances with a sparse network of broadband stations, such as the International Monitoring System.

REFERENCES

Baag, C.-E. and C.A. Langston (1985), Shear-coupled PL, *Geophys. J. R. Astr. Soc.*, **80**, 363-385.

Chander, R., L E. Alsop, and J. Oliver (1968), On the synthesis of shear coupled PL waves, *Bull. Seism. Soc. Am.*, **58**, 1849-1877, 1968.

Crotwell, H.P., T.J. Owens, and J. Ritsema (1999), The TauP toolkit; flexible seismic travel-time and ray-path utilities, Seism. Res. Lett., **70**, 154-160.

Dziewonski, A. M. and D. L. Anderson (1981), Preliminary reference Earth model, *Phys. Earth. Planet. Int.*, **25**, p. 297-356.

Frazer, L.N. (1977), Synthesis of shear coupled PL. *Ph.D. thesis*, Princeton University, 54 pp.

Helmberger, D.V. and G.R. Engen (19740, Upper mantle shear structure, *J. Geophys. Res.*, **79**, 4017-4028.

Jordan, T.H. and L.N. Frazer (1975), Crustal and upper mantle structure from Sp phases, J. Geophys. Res., **80**, 1504-1518.

Langston, C.A. (1996), The SsPmP phase in regional wave propagation, *Bull. Seism. Soc. Am*., **86**, 133-143.

Mallick, S. and L.N. Frazer (1987), Practical aspects of reflectivity modeling, *Geophysics*, **52**, 1355-1364.

Oliver, J. (1961), On the long period character of shear waves, *Bull. Seism. Soc. Am.*, **51**, 1-12.

Poupinet, G. and C. Wright (1972), The generation and properties of shear-coupled PL waves, *Bull. Seism. Soc. Am.*, **62**, 1699-1710.

Sen, M. and P. L. Stoffa (1995), *Global Optimization Methods in Geophysical Inversion*, Elsevier Science Publishing Company, The Netherlands.

Swenson, J.L., S. L. Beck, G. Zandt (1999), Regional distance shear-coupled PL propagation within the northern Altiplano, Central Andes, *Geophys. J. Int.*, **139**, p. 743-753.

Tarantola, A. (1987), *Inverse Problem Theory: Methods for Data Fitting and Model Parameter Estimation*, 613 pp., Elsevier, Amsterdam.

Zhao, L.-S. and C. Frohlich (1996), Teleseismic body waveforms and receiver structures beneath seismic stations, *Geophys. J. Int.*, **124**, 525-540.

REGIONALIZED VELOCITY MODELS IN CENTRAL ASIA

Bradley B. Woods, Chandan K. Saikia, Hong Kie Thio, and Gene Ichinose

URS Group Inc.

Sponsored by Defense Threat Reduction Agency

Contract No. DTRA 01-98-C-0151

ABSTRACT

We have developed regional velocity models to improve the location of small seismic events near the central Asian test sites. Specifically we have used seismograms recorded by International Monitoring System (IMS) stations, along with ISC and Calibration Event Bulletin (CEB) travel-time information, to generate velocity profiles extending radially from the Lop Nor Test Site; the best coverage is for the path to the northwest through the Semipalantinsk Test Site to, at the far end, the station BRVK. Most available crustal models developed for central Asia have a P_n velocity of 8.0 km/s; whereas the velocity profiles developed put P_n in the range of 8.3-8.4 km/s. Predicted travel times of P-waves traveling to the northwest of Lop Nor using these various models all yield negative residuals on the order of 2-6 seconds, suggesting these models are slower than the actual regional velocity structure. Hence, we examined a model for the Siberian Craton, the path over which these waves travel. The modified Leith model (Langston, 1998) has a Moho velocity of 8.3 km/s, closer to the velocities we found. Applying this model results in smaller travel-time residuals (0.5 sec. < *t*) rather than the 2-4 sec. residuals using the IASPI model, suggesting this model is more appropriate for the region. Similarly, a more appropriate model has been developed for paths to the NE and SE of Lop Nor, with a moho velocity of *8.26* km/s.

KEY WORDS: travel-time calibration, regional velocity model, location

OBJECTIVE

We have developed techniques to better locate small (mb< 4.5) seismic events, particularly for regions surrounding known nuclear test sites. Reliably locating and identifying these snaller events is of paramount concern to CTBT monitoring. Events of this size are usually only observed regionally (Δ <°20) as was the case of the August 16, 1997 Kara Sea event (Israelson *et al.*, 1997). Consequently we are concentrating on improving location capabilities for stations within 20° of test sites in central Asia. To this end we have developed two regional velocity models for this area and compared them to the IASPI (Kennet and Engdahl, 1991) earth model. Where possible, velocity profiles were generated and analyzed to infer the P_n velocity of the regional crustal waveguide. Figure 1 is a map of the area of interest, denoting IMS and auxiliary stations, test sites and more recent (1988+) moderate-sized earthquakes in the region.

RESEARCH ACCOMPLISHED

After examining a number of existing crustal models for the region, both with respect to waveform modeling and travel time analysis, we found that these models, all of which had moho velocities of, or near, 8.0 km/s did not yield smaller travel-time residuals than the IASPI model. Travel time data used were from the ISC and the IMS's Calibration Bulletins; for some additional IMS station travels times were measured from records. Origin times and locations were taken from the the catalog of Engdahl *et al*. (1998) – afterwards referred to as the EHB catalog – when available. For the more recent Lop Nor explosions (1996) we used ISC locations, which were found to be compatible with the EHB solutions; the ISC origin times were modified by adding 1.7 seconds which, on average, is the difference between the EHB and ISC origin times for these nuclear explosions, reflecting the less accurate J-B model used in the ISC locations.

In order to arrive at a better crustal model we made a velocity profile to the N.W. of the Lop Nor test site

(LNTS) as this azimuth contains the four stations WMQ, MAK, KURK, and BRVK (the latter three of which are IMS stations), which provides the best source-station geometry for a velocity profile in the region. Figure 2 shows the constructed velocity profile; least-squares fitting yields a velocity of 8.40 ± 0.034 km/s. Table 1 provides the individual 2-station velocities, with "Profile Av." being the average of the separate individual 2-station path velocities; the bottom two entries are for paths respectively to the NE and SE of LNTS. The latter two paths only had available two stations per profile; hence they are considered less-robust velocity estimates; however, they also do suggest a difference in the moho velocity regimes.

The high P_n velocities found for the N.W. profile were found to be compatible to the modified Leith model for the Siberian Craton (Langston, 1995), which has a moho velocity of 8.35 km/s. The velocities for the NE and SE path are consistent with that found by Ni and Barrazangi for the Tien Shen (1983).

Given the P_n velocities we found, we decided to modify the IASPI model accordingly and redetermine travel times. For this we made two models, a further-modified Leith-Langston model (LL) for the NW path, and a more generalized central Asian model (modified IASPI) by incorporating a moho velocity of 8.26 km/s as well as a more appropriate crustal section into the IASPI model. Figure 3 compares these three models' *P*-wave velocities.

Table 2 compares the average travel-time residuals for the two modified models with the those from the IASPI model. The modified LL model yields smaller residuals for stations to the N.W., although residuals for stations at other azimuths tend to be as great or larger, suggesting that this model does better reflect the velocity structure to the N.W. of LNTS, into the Siberian Craton. The modified IASPI model does better, on average, than either the Siberian craton model or the IASPI model, suggesting that it, better reflects the average regional crustal waveguide and moho velocity than do either the IASPI or Siberian craton models.

CONCLUSIONS AND RECOMMENDATIONS

Our results suggest two regional models to be used for locating events centered about the LNTS. To the northwest of LNTS a crustal and upper-mantle structure reflecting the Siberian craton (moho velocity = 8.35), put atop the IASPI model, provides the best improvement in travel-time residuals; while for the other azimuths a regionalized crustal waveguide model with a moho velocity of 8.26 yields smaller residuals on average than either the IASPI or Siberian craton model. Thus it appears that the region can be modeled by two regional velocity models: the modified LL model for the N.W. azimuth, while the modified central-Asian IASPI model works for other azimuths. Similar analysis should be done for the path due west of LNTS, towards AAK. Results at the conference will include analysis of relocated earthquakes' travel times; these events are shown in Figure 1. These finalized regional models should then be tested on larger data sets to verify their improved locating ability for events in central Asia.

REFERENCES

Engdahl, R. E., R. van der Hilst, and R. Buland (1998), Global teleseismic earthquake relocation with improved travel times and procedures for Depth Determination, *Bull. Seism. Soc. Am., 88, 772-743.*

Israelsson, H., M. D. Fisk, X. Yang, and R. G. North (1997), The August 16, 1997 event in the Kara Sea, *CMR Technical Report*, CMR-97/38, Alexandria, VA.

Kennett, B. L. N. and E. R. Engdahl (1991). Travel times for global earthquake location and phase identification, *Geophys. J. Int.*, 105, pp. 429-465.

Langston, C. A. (1995), Anatomy of regional phases and source characterization of the Soviet Joint Verification Experiment, *Bull. Seism. Soc. Am.*, 1416-1431.

Ni, J. and M. Barazangi (1983), High-frequency seismic wave propagation beneath the Indian Shield, Himalayan Arc, Tibetan Plateau and surrounding regions: high uppermost mantle velocities and efficient S_n propagation beneath Tibet, *Geophys. J . R. astr. Soc.*, 72, 665-689.

Table 1. Apparent Pn Velocities

Path	Velocity	σ	Num.
KURK-BRVK	8.34 km/s	0.099	6
MAK-KURK	8.45 km/s	0.025	6
WMQ-MAK	8.43 km/s	0.071	4
Profile Av.	8.39 km/s	0.099	23
WMQ-TLY	8.29 km/s	0.065	3
GTA-LZH	8.26 km.s	0.033	8

Table 2. Travel-time Residuals

Sta	IASPI	Mod. LL	Mod. IASPI
WMQ	3.6 ± 0.72	0.3 ± 0.28	0.6 ± 0.42
MAKZ	-0.8 ± 0.44	1.0 ± 0.33	-0.1 ± 0.23
AAK	-2.6 ± 1.18	-0.3 ± 0.30	-2.0 ± 0.58
KURK	-2.4 ± 0.20	0.1 ± 0.15	-1.8 ± 0.19
LSA	2.9 ± 0.68	5.9 ± 0.70	3.9 ± 0.73
LZH	-0.7 ± 0.51	2.4 ± 0.58	0.3 ± 0.53
TLY	1.4 ± 0.13	4.5 ± 0.19	2.1 ± 0.16
ULN	-1.2 ± 0.09	2.8 ± 0.14	0.4 ± 0.10
NIL	-3.4 ± 0.47	0.3 ± 0.35	-2.2 ± 0.41
BRVK	-6.8 ± 0.16	-4.0 ± 0.12	-6.9 ± 0.18

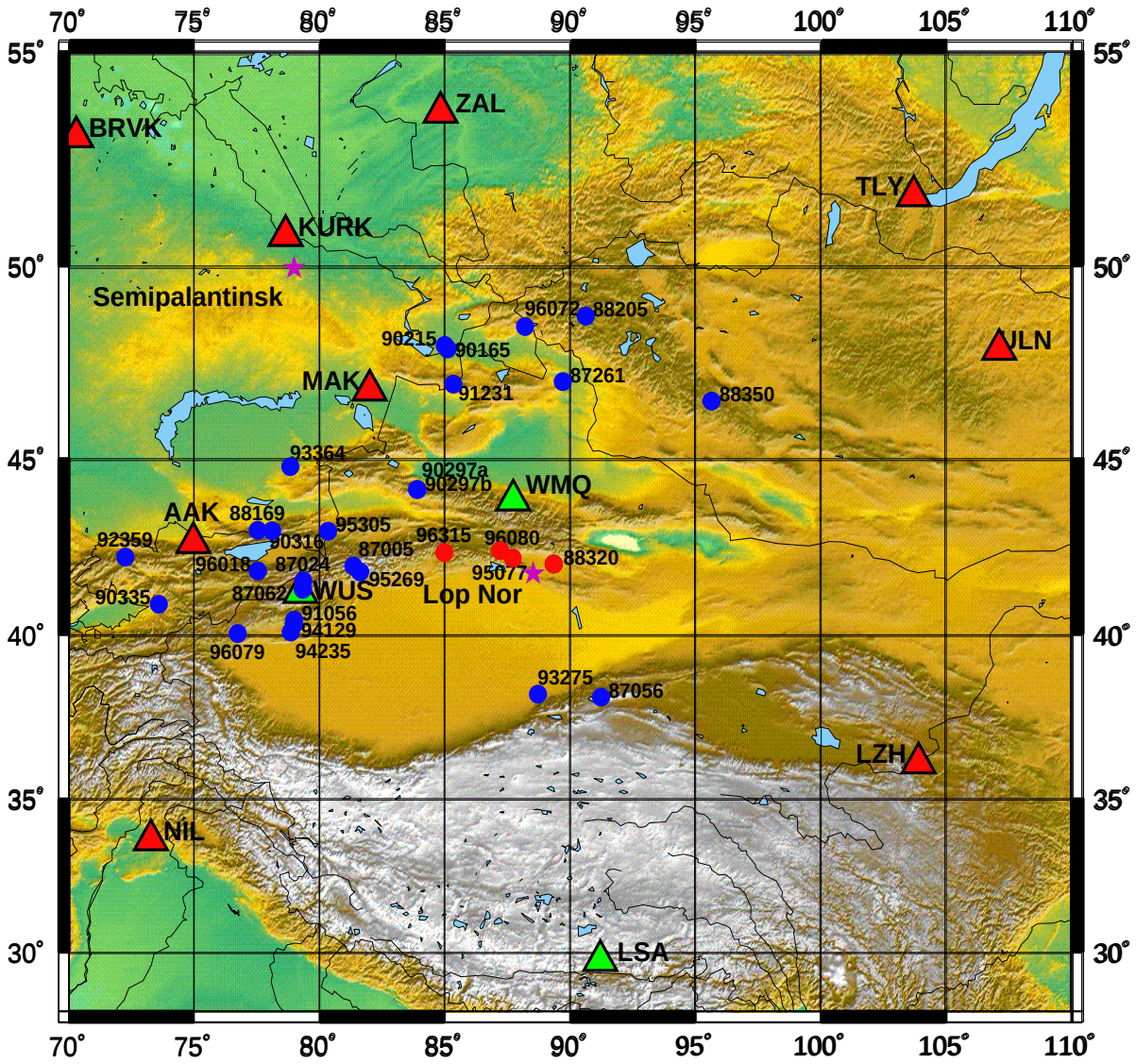

Figure 1. Map of study area showing IMS stations as well as the two auxiliary stations WMQ and LSA (all triangles); test sites are denote by stars, and moderate-sized recent earthquakes by small circles.

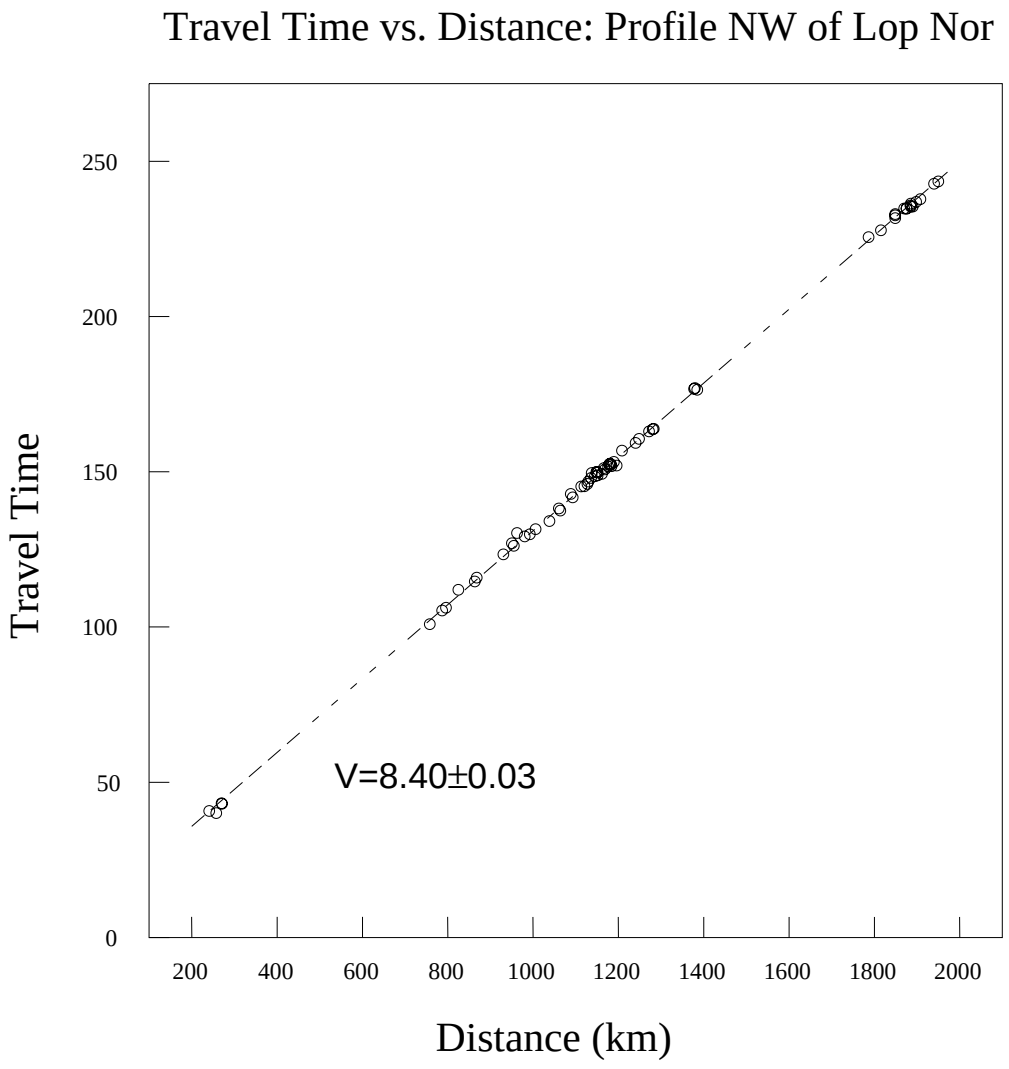

Figure 2. Velocity profile for the azimuth to the N.W. of Lop Nor. The dashed line represents the least-squared derived velocity of *8.403 ± 0.034* km/s.

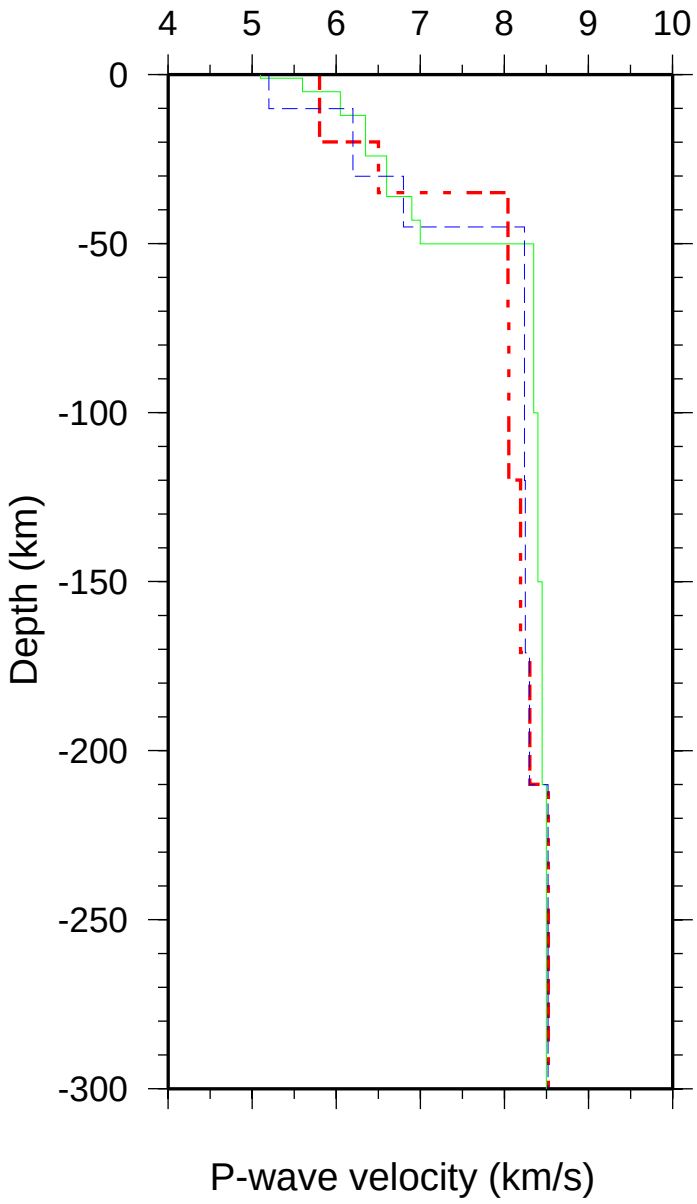

Figure 3. Comparison of velocity models: IASPI (long dash), modified Leith-Langston model (solid line), and the modified IASPI model (short dash).

(This Page Intentionally Blank)

Seismic Event Detection, Location, and Identification Methods

EVENT IDENTIFICATION, ERROR PROPAGATION AND CALIBRATION ASSESSMENT

Dale N. Anderson[1], Stacey A. Hartley[1], Charles A. Lo Presti[1],
Alan C. Rohay[1], Steven R. Taylor[2], Aaron A. Velasco[2] and Chris J. Young[3]

Pacific Northwest National Laboratories[1]
Los Alamos National Laboratories[2]
Sandia National Laboratories[3]

Sponsored by National Nuclear Security Administration
Office of Nonproliferation Research and Engineering
Office of Defense Nuclear Nonproliferation

Contract No. DE-AC06-76RLO-1830

ABSTRACT

One component of nuclear explosion monitoring (NEM) research and engineering (R&E) is directed at the development of mathematical techniques that take full advantage of all information in a seismic signal. Regularized Discrimination Analysis (RDA) is a multivariate seismic event identification method that can be applied to a number of highly correlated regional discriminants. The parametric formulation of RDA includes Linear Discrimination (LDA), Quadratic discrimination (QDA) and Euclidean distance-based nearest-neighbor discrimination. We present methods to optimally select RDA parameters.

Error propagation is another focus area in the NNSA NEM R&E program. The detection and timing of seismic arrivals play a critical role in the ability to locate seismic events, especially at low magnitude. Errors can occur with the determination of the timing of the arrivals, whether these errors are made by automated processing or by an analyst. One of the major obstacles encountered in properly estimating travel-time picking error is the lack of a clear and comprehensive discussion of all of the factors that influence phase picks. We have developed a multivariate statistical model, experimental design, and analysis strategy that can be used in this study. We have embedded a general form of the International Data Centre (IDC)/U.S. National Data Center (USNDC) phase pick measurement error model into our statistical model. We can use this statistical model to optimally calibrate a picking error model to regional data.

We also present work on the development of statistical methodologies for comparing effects of station-specific correction surfaces on predicted seismic event locations and event location uncertainty from network model Monte Carlo simulation runs. Research and development work includes the investigation of Latin Hypercube Sampling (LHS) to design Monte Carlo simulation runs, the development of appropriate statistical models to describe travel-time correction surface errors, and the proper simulation of errors in phase identification and association processes. Also under investigation are statistics-based methods for visualizing and assessing differences between event locations and location uncertainty from different correction surfaces in network model simulations.

KEY WORDS: seismic identification, phase pick errors, error propagation, seismic network model simulation, surface correction assessment, event location.

OBJECTIVE

The objectives of the PNNL statistics effort are to

- contribute to the development of optimal regional discrimination techniques that properly account for uncertainties in seismic signal processing, and
- develop efficient statistical metrics and visualization methods to measure or assess the improvement of location accuracy and precision as predicted using Monte Carlo network simulation that result from changes to velocity/travel-time calibration correction surfaces.

RESEARCH ACCOMPLISHED

Regional Discrimination

Ridge Discrimination techniques, first proposed by Smidt and McDonald (1976), were developed to address the problems associated with discrimination in high-dimension, co-linear settings. These methods are readily adaptable to linear, quadratic and outlier identification rules. Ridge Discrimination is a special case of Regularized Discrimination Analysis (RDA) developed by Friedman (1989). RDA includes LDA; QDA and Euclidean distance-based nearest-neighbor discrimination in its parameterization. These techniques can be used to transition from an outlier analysis approach for seismic identification to classical discrimination, as quality explosion calibration data are collected. Ridge Discrimination and RDA provide the statistical structure to model highly correlated seismic measurements. Omitting the correlation structure between seismic measurements in event identification can aggravate identification errors and give an erroneous impression of capability. With RDA, a large number of discriminants can be used and no *a priori* sub-selection of discriminants is necessary. We propose an information theory approach to the optimal selection of RDA parameters. These methods are based in the Kullback divergence index. Complete details of the proposed methods were submitted to the *Bulletin of the Seismological Society of America* for formal publication.

Explorations in Assessing Calibration Surfaces through Seismic Network Simulation

Background. For purposes of nuclear explosion monitoring, it is desirable to continuously improve calibration travel-time/velocity corrections in order to produce more accurate and precise predicted seismic event epicenters versus ground truth. Improvement may be expressed as reduction of the distance between the predicted epicenter and the true event epicenter, and also as reduction in the epicenter uncertainty taken as the area of the confidence ellipsoid area (CEA). Comparisons may be absolute, when ground truth is present and well understood, or comparisons may also be relative in the sense of comparing alternative correction surfaces.

Locating seismic events with depth depends on at least three receiving stations detecting at least four phases associated with the same event. Through iterative application of triangulation algorithms with an overall global velocity model and velocity or travel-time correction surfaces, the event can be positioned geographically and depth-wise within a small region (Sleep & Fujita, 1997). Seismic event locations are often expressed as a predicted epicenter surrounded by a 90% CEA. Methods for performing event location calculations are well documented (e.g., Bratt & Bache, 1988)

Network Simulation Models. One approach toward comparative assessment of correction surfaces is to use network simulation models such as NetSim (Sereno, Bratt, and Yee, 1990; Sereno, 1991) and its follow-on systems to generate simulated locations of synthetic events. Network simulation models are computer codes, which generate simulated phases at specific frequencies to express seismic events of specified magnitude and depth. They then model the propagation of these phases through the earth by applying specified velocity and travel-time correction surfaces, and model each receiving station's reception in the presence of local noise. This includes simulating the phase-picking process. Simulations may also account for station up-time reliability and local station signal-to-noise conditions. Once the simulated phases are detected and arrival times and perhaps bearings calculated, these systems solve for the predicted epicenter, depth, magnitude, and other parameters of interest. Since the input correction surfaces, noise models, and other factors are known only with uncertainty, it is current practice to generate random samples of inputs through Monte Carlo experiments to introduce uncertainty into various stages of the detection and location processes, perhaps through Latin HyperCube Sampling (McKay, Conover, and Beckman, 1979).

A very important principle in seismic network simulation is to consistently form realistic events in tune with sound geophysical science. From the viewpoint of event location, this implies that for any particular event, the simulation has the capability to select receiving stations in accordance with sound seismological practice. It needs to make reasonable decisions as to whether a particular simulated event is solvable in terms of parameters of interest. Consequently, it is useful to include criteria for deciding whether a particular data set represents events typically formed by standard practice. It is also critical that estimates of uncertainty for input variables be realistic.

Azimuthal Gap Patterns to Assess Potential for Obtaining Stable Event Locations. One way to determine whether an event is well located is to consider the distribution of azimuthal gaps around an event formed by the pattern of detecting stations. These are measures of the arcs between the bearings from the event-node to each station. A poorly located event, difficult to triangulate, may have a very large maximum azimuthal gap, greater than 250 or so degrees. A large maximum azimuthal gap indicates that all stations that detect the event have bearings in one quadrant around the event, thereby controlling location in only one direction. Another way to obtain a poorly located event is that all detecting stations have bearings in two opposite quadrants around the event such that the two largest azimuthal gaps be of the order of 150 degrees, so that location is still controlled in only one direction. For good location results, ideally the station bearings are distributed such that location is controlled from several directions, thereby allowing the most effective triangulation. Azimuthal gaps may be less useful when bearings as well as travel times are used to solve for the epicenter.

Assessing Changes in Event Location and Uncertainty from Two Simulation Runs. Two issues are *comparison metrics* and representative event *sampling* for performing assessments.

The goal for *comparison metrics* is to define measurements or counts which express change in detection accuracy and/or precision for events simulated at given grid nodes, individually and ensemble. Assessing accuracy pertains to measuring differences between estimated and input epicenters. Assessing precision pertains to measuring differences between confidence ellipsoid areas, and perhaps ellipsoidal shapes and orientations (strikes) as well.

With regard to *sampling*, it is desirable to simulate events and detections in regions and with station networks associated with the calibrations under consideration. Moreover, since discrete regions of the globe may behave seismically in unique ways, tectonic provinces, surface roughness, and other geological characteristics also need to be considered (Ryaboy, 2000; Zhang, Lay, Schwartz, & Walter, 1996). This results in a need for sampling from the set of events, locations, and event-station pairs so that the results have minimal sampling biases, which could lead to false conclusions about the calibration surfaces.

To this end, the following grouping (or stratification) of events on the event-node grid is suggested. In some cases, the event grid-nodes only form study groups; in other cases the combinations of event grid-nodes and receiving stations taken together form study groups.

- Events chosen from inside or outside the convex hull of the station network
- Events chosen by surface topography or land areas versus oceanic
- Event-location/station subsets grouped into geophysically homogeneous regions such as tectonic provinces with regard to propagation path
- Event-location/station subsets grouped into regions where calibrations are changed vis a vis calibrations remain unchanged (control versus experimental regions)

Although the prime focus of a calibration improvement study would be to assess differences, the study might be more valuable if a control region is also available. A control region is a region with no calibration changes over propagation paths to a subset of stations, such that changes in predicted epicenters are not expected from the two runs. If changes are detected in a control region, contrary to expectations, this requires special evaluation, because it may mean the simulations were not working as expected.

Numerical Stability in Computations to Solve for Location. The event location process depends on solving the triangulation equations, which estimate the epicenter. These equations (Bratt & Bache, 1988) are often solved by maximum likelihood for the set of travel times, which jointly minimize residuals. In addition, some formulations also allow for inclusion of bearings from station to postulated event. This process of associating travel times (P-wave picks in time) to an event also has inherent uncertainty (and the possibility of misassociating picks from different events is not presently modeled). If the equations are well posed, the solution converges rapidly to a minimum-error solution, and the eigenvalues for the resulting covariance matrix (expressed as major and minor confidence ellipsoid axes) are such that the ellipse is not far from round. For the poorly posed cases, the equations are numerically unstable, the eigenvalues are grossly unequal, and the major and minor axes are also quite unequal. To obtain reliable results, it is critical to identify the cases that will not

or did not converge to a reliable solution. This information can assist in understanding why the location process failed.

Three Approaches toward Comparing Results from Network Simulation Runs: ensemble, paired event-node, and paired events.

Ensemble analysis: The network simulation model is run N times (N large) and means, variances, and skewnesses are collected for key variables such as CEA and predicted epicenters at each event grid-node. Then, assessments of differences between two simulation runs are based on comparing distributions for the key variables expressed as means and variances at each event-node, without pairing.

Analysis on individual event grid-node pairs: The network simulation model is run N times at each event-node, same as above. The data at each event-node from the two calibrations are paired. The random number generator is not coordinated between the two runs so there is no control over calculation starting points. Assessment is performed based on the ensemble of mean differences between each event-node pair. The basic statistical test is the two-sample t-test at each event node to compare distributions of differences between pairs. Pairing event-nodes is a more powerful statistical test than comparing overall distributions in ensemble analysis.

Individual events at event-node pairs: The network simulation model is run N times, and data are collected for each individual event realization. Ideally, the random number generator is coordinated between the two runs so that results from each calibration for individual simulated events form pairs that can be directly compared, with all things equal except the experimental variables (calibrations). Assessment is performed based on the ensemble of individual event differences between the two calibration runs. The statistical test is the paired t-test at each event-node. Because the paired t-test is the most powerful statistical test in this situation, fewer simulation runs are needed to detect a given difference when individual simulated events are paired. One drawback with applying this approach is the nontrivial problem of coordinating the random number generator so that each simulated event has in effect the same starting point.

A Collection of Analysis Tools for Assessing Difference Between Two Runs. Two potential primary measures for assessing performance in locating simulated events are CEA and offset from CEA centroid to true location. The following lists of plots and tables is based on analysis and visualization of these two measures and related input parameters. It is not in any way complete.

Table 1. Displays showing differences or "movement" in primary measures for events. These may be expressed in terms of change in measured values or as percent change in measured values.

Item to Plot/Tabulate	**What It Shows/Interpretation**
Change in mean CEA	Improvement in location precision
Change in Relative Standard Deviation	Display variability in CEAs, a measure of stability
t-test statistics or alpha probabilities	Displays statistically significant changes
Percent of events below 1000 km2	Associated with external criterion for a "good" event
Major/Minor axis ratio	Expresses stability in detecting station configuration
Change in Offset	Shows whether predicted events from new calibrations are closer to true location
Percent of CEAs actually covering true event locations	Gross measure of accuracy

Table 2. Secondary Measures involving counts of events satisfying various criteria

Item to Plot	**What it Shows/Interpretation**
Proportion of well-located events to total events	Provides an idea of quality of station coverage
Proportion of events which have low (good) covariance matrix condition numbers	Provides an idea of quality of numerical processing, and ultimately station coverage. (This is expected to be high)
Coverage: proportion of events inside convex hull of stations	Provides an idea of quality of station coverage

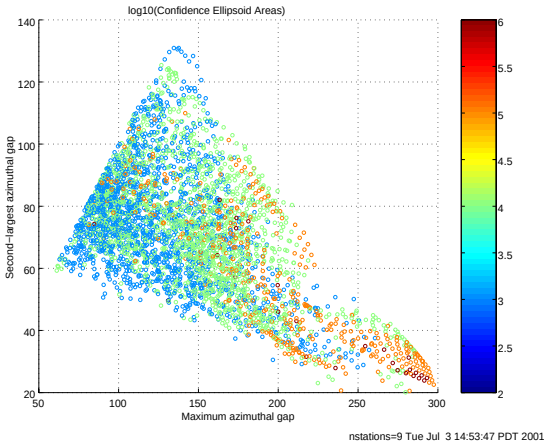

Figure 1: Plotting mean 90% confidence ellipsoid areas at each event-node against the largest and second-largest azimuthal gaps based on the nine closest stations for calibrations of CALIB1 and CALIB2. These are theoretical, not based on detections. Although large CEAs are found throughout, the largest CEAs are most likely found where the maximal azimuthal gap > 250°.

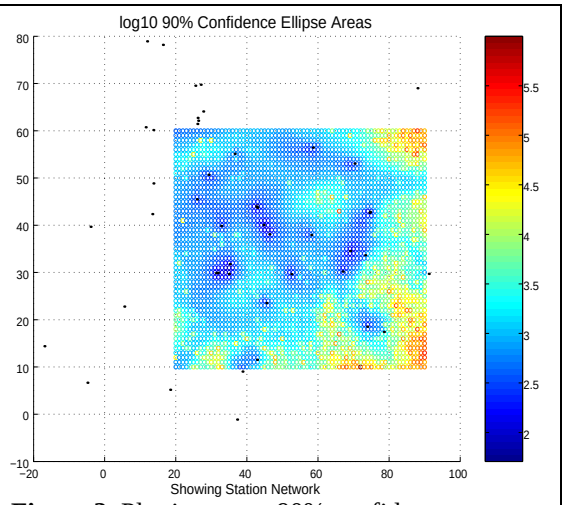

Figure 2: Plotting mean 90% confidence ellipsoid areas geographically at with the station network shown based on CALIB1 and CALIB2. The largest CEAs lie outside or on the edge of the station convex hull, where maximum azimuthal gap is expected to be largest. CEAs (shown in $\log_{10}$ scale) range from ~50 km^2 to over 250,000 km^2.

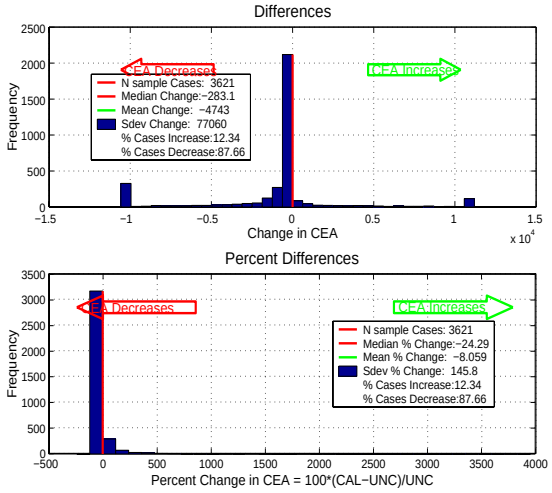

Figure 3: Summary histogram plots of differences between mean 90% CEAs from CALIB1, a baseline calibration and CALIB2, a new calibration. These plots allow assessment of "movement" of sets of CEAs. In this case, fully half the data set of mean CEA's decreased in size by at least 24.3% as a result of new calibrations.

		CALIB2	
	Threshold	*<1000* km^2	*>1000* km^2
CALIB1	*<1000* km^2	1019 *(28.14%)*	15 *(0.41%)*
	>1000 km^2	592 *(16.34%)*	1995 *(55.09%)*

Figure 4: Tabulating the "movement" of mean 90% CEAs across the 1000 km^2 threshold from estimates from two calibration surfaces. In this case, there were 592 instances in which the CEA for CALIB1 was initially > 1000 km^2 and with CALIB2 became small enough to cross the threshold. There were 15 instances in which CEAs initially smaller than the threshold were made larger as a result of CALIB2.

Materials and Methods for Generating Data. The CAT network simulation model was used to generate case study data for the plots shown in this report applying two calibrations here termed CALIB1 and CALIB2, with the goal of determining whether CALIB2 gives more precise results than CALIB1. The data shown are based on 4.25 mb event magnitude calibration runs. The confidence ellipsoid areas are means of N=1000 realizations per event-node. Also available were corresponding standard deviations of CEAs.

Discussion. Figure 1 illistrates how the two largest theoretical azimuthal gaps seem to be associated with larger mean 90% CEAs, at least for this case. Figure 2 plots the same set of CEAs geospatially; and illustrates how the larger CEAs lie outside the convex hull of stations, where station coverage is less optimal. These two plots together illustrate a way to demonstrate relative station coverage over a region of interest. Figure 3 presents an ensemble of event-pair differences between mean CEA estimates at each event-node from two calibrations applied in pre-test/post-test order. Both absolute differences and percent difference relative to CEAs from the pre-test calibrations are shown with summary statistics. In this case, almost 88% of the event-nodes show decreases in mean CEA. Regions with increases in CEA as a result of applying calibrations can be pinpointed by appropriate geospatial plots. Figure 4 analyses changes in mean 90% CEAs as a result of applying the two calibrations in pre-test/post-test order. Here the statistic of interest is the proportion of mean CEAs from the ensemble of event-nodes crossing (becoming larger or smaller than) 1,000-km^2 90% CEA threshold.

Any of these displays can be partitioned into subsets, either based on a priori stratification, or a posteriori observation, in order to explore fine-structure of response to calibrations. Examples are events in different geographic regions, or events detected by certain stations, or events-station pairs for which seismic travel paths cover certain regions of interest in order to explore fine-structure of response to calibrations.

In regions without good station coverage or well-known velocity structure, it is more difficult to obtain accurate regional event locations. Moreover, the standard CEA may lead to an impression of more accurate event location than actually is the case (Kadinsky-Cade et al., 1995). Much depends on the choice of appropriate phases for given regions, as well as reliability in detecting and picking phases. Seismic event location is complicated by the presence of uncertainty. Many of the inputs are simply not well known, and are subject to quasi-random processes, which means that sometimes events will be detected, sometimes not. Sometimes enough stations detect the event to allow triangulating an event location, sometimes not. The degree to which the signal is visible above noise may also be random, and the weaker the signal, the more uncertain will be the predicted location. To consider the impact of these uncertainties is one reason to perform network simulations with Monte Carlo techniques.

Uncertainty in Regional Phase Picks

The detection and timing of seismic arrivals play a critical role in the ability to locate seismic events, especially at low magnitude. Errors can occur with the determination of the timing of the arrivals, whether these errors are made by automated processing or by an analyst. One of the major obstacles encountered in properly estimating travel-time picking error is the lack of a clear and comprehensive discussion of all of the factors that influence phase picks. We have developed a multivariate statistical model, experimental design, and analysis strategy that can be used to study possible factors that need to be modeled to properly study phase arrival time picking errors. We have embedded a general form of the International Data Centre (IDC)/U.S. National Data Center (USNDC) phase-pick measurement error model into our statistical model. We can use this statistical model to optimally calibrate a picking error model to regional data.

CONCLUSIONS AND RECOMMENDATIONS

A sampling of statistical and visualization tools for comparing simulation results from two calibrations is briefly described. These tools can be based both on primary measures directly output by the simulation runs, or based on counts of categorized input or variables. To obtain reliable results, it is critical that computed results are obtained through numerically stable computations, that appropriate stratification has been applied, either regionally or by other variables of interest, to avoid sampling biases, and that realistic uncertainties are applied to inputs to Monte Carlo runs. The most powerful statistical tests are tests based on pairs of event grid-nodes and on pairs of individual event realization from the two calibrations, if all other factors are equal.

REFERENCES

Bratt, S. R., and T. C. Bache (1988). Locating Events with a Sparse Network of Regional Arrays. Bull. Seism. Soc. of Am., Vol. 78, No. 2, pp 780-798, April.

Claassen, J. P. (1994). The Monitoring Potential of the Open Worldwide Networks. SAND93-1931, Sandía National Laboratories, Albuquerque NM.

Kadinsky-Cade, K., R. O. Joh, A. Dainty, and J. Cipar (1995). Practical Issues in Location of Small Events: Poor Station Coverage and Poorly Known Velocity Structure. Proceedings of the 17th Annual Seismic Research Symposium on Monitoring a Comprehensive Test Ban Treaty, 12-15 September 1995, PL-TR-95-2108, Phillips Laboratory, Hanscom AFB, MA.

McKay, M. D., W. J. Conover, and R. J. Beckman (1979). A Comparison of Three Methods for Selecting Values of Input Variables in the Analysis of Output from a Computer Code. Technometrics, Vol 221, pp. 239-245.

Ryaboy, V. (2000), IMS Calibration in North America and Northwestern Eurasia Utilizing 3-D Crustal and Upper Mantle Velocity Models to Refine Location of Regional Seismic Events. 22nd Annual DoD/DOE Seismic Research Symposium, Volume II, pp 349-358.

Sereno, T. J. (1991). Simulation of the Detection and Location Capability of Regional Seismic Networks in the Soviet Union. Annual Technical Report SAIC-91/1061, Sci. Appl. Intl. Corp., San Diego, CA.

Sereno, T. J., Bratt, S. R., Yee, G. (1990). NETSIM: A Computer Program for Simulating Detection and Location Capability of Regional Seismic Networks. Annual Technical Report SAIC-90/1163, Sci. Appl. Intl. Corp., San Diego, CA.

Sleep, N. H. and K. Fujita (1997). Principles of Geophysics. Blackwell Science Publishing, Malden, Massachusetts.

Zhang, T-R., T. Lay, S. Schwartz, and W. R. Walter (1996), Variation of Regional Seismic Discriminants with Surface Topographic Roughness in the Western United States. Bull. Seism. Soc. of Am., Vol. 86, No. 3, pp 714-725, June.

MULTI-RESOLUTION GLOBAL MODELS FOR TELESEISMIC AND REGIONAL EVENT LOCATION

Michael Antolik, Göran Ekström, Adam M. Dziewonski, Lapo Boschi, Bogdan Kustowski, and Jianfeng Pan

Harvard University

Sponsored by Defense Threat Reduction Agency

Contract No.: DSWA01-97-1-0017

ABSTRACT

Reconciliation of structures shown in global models of Earth structure with those shown in detailed, high-resolution regional models has become one of the most important tasks in seismic tomography. Recent studies have shown that combination of regional seismic phases with teleseismic phases can greatly increase location accuracy; however, for this to be the case, the velocity structure has to be well resolved on a fine scale. The most efficient method to accomplish this task is development of multi-resolution models using local (but smooth) basis functions that increase in resolution from regions with sparse data coverage to regions of dense coverage. This paper reports on recent results from an ongoing project designed to bridge the gap between regional and global seismic tomography and achieve correspondingly incremental improvements in event location. We have previously developed a moderately high-resolution global model (equivalent to spherical harmonic degree 18) using local spline functions. This model improves locations using teleseismic phases over other more finely parameterized models (Antolik et al., 2001). Here we extend the same techniques to simultaneous development of more detailed regional models for inclusion within the global model. We describe progress in constructing a new regional model of the Africa/Mediterranean region which makes use of surface wave dispersion data, regional travel times and waveforms, and teleseismic phase arrivals. This model also incorporates shear wave anisotropy and agrees well with other published models for the region. Other regions for which we intend to develop combined regional/global models include the former Soviet Union and North America.

Tomographic models can also be vastly improved through the use of sources with calibrated travel-time data (i.e., reference events with accurately known locations). However, the current database of such events still suffers from sparse coverage (particularly in oceanic regions). A parallel element of the current project includes improvement of event locations on mid-ocean ridges by making use of focal mechanisms and accurate bathymetry. We have developed a database of some 1500 large events and are expanding to smaller events using the Joint Hypocentral Determination technique. We present the results along with experiments designed to test the accuracy of these locations.

KEY WORDS: Event location; seismic tomography; mantle heterogeneity

OBJECTIVE

The aim of this project is to ultimately improve the locations of earthquakes and other seismically recorded events in order to enhance the ability to monitor the Comprehensive Nuclear-Test-Ban-Treaty (CTBT). Our strategy is based on developing new, detailed 3-D models of the mantle, with an emphasis on P wave structure. This involves the construction of global high-resolution models with more detail in certain areas where particularly good data coverage is available. In our approach, 3-D velocity structure is represented in terms of a horizontally layered and laterally varying crust of variable thickness, overlying a mantle whose heterogeneous P- and S-velocity structure is parameterized radially and laterally in terms of cubic B-spline functions of variable density. The spline functions are split radially at the 670-km discontinuity in order to better resolve changes in heterogeneity patterns across this boundary (Gu et al., 2001). The shallow mantle is parameterized as an anisotropic medium in shear velocity. We have previously developed a new joint P and S velocity global velocity model of the mantle parameterized in spherical B-splines (Antolik et al., 2000). This model, with a nominal horizontal resolution equivalent to degree 18 in a spherical harmonic expansion, improves the average mislocation for explosions in Kennett and Engdhahl's (1991) database and the Prototype International Data Centre's Reference Event database by $>$20% over more finely-parameterized models (see Table 1). We are now moving to take advantage of better data coverage obtainable in certain regions of the globe by inverting for multi-resolution models with finer parameterization confined to certain regions. The first half of this paper describes an anisotropic model of shear wave velocity developed for the African/Mediterranean region developed using this technique. This and other similar models will be used to combine both regional and teleseismic travel times for the improvement of event locations.

Model	Explosions	Earthquakes
PREM	12.92	18.83
SP12	7.83	15.37
MK12	9.53	17.40
BDP98	9.80	17.13
VWE97	10.51	17.33
P362-17	6.27	13.75

Table 1: Average mislocation for 112 test events consisting of explosions and earthquakes using PREM (Dziewonski and Anderson, 1981) and five 3-D mantle models. P362-17 is our new global model of P wave velocity described in Antolik et al. (2000). Only teleseismic P wave arrivals were used to calculate the locations. Location errors for the explosions are significantly smaller than for the earthquakes, which may reflect greater errors in the earthquake reference locations. See Antolik et al. (2001) for description of the other 3-D models and the location method used.

A second, subsidiary objective concerns the development of additional techniques used in locating events teleseismically and regionally with sparse datasets, and with assessing the improvement in accuracy afforded by the new techniques and models. To address this, we are attempting to improve the quality of locations for events in remote regions where the number of reference events is currently small. We use a combination constrained inversion/JHD technique to reconsider the

locations of earthquakes on mid-ocean ridges and transform faults.

RESEARCH ACCOMPLISHED

As recent tests have shown that compilation of accurate travel times for regional ($\Delta < 20^{\circ}$) first-arriving phases can significantly improve location accuracy (Chen and Willemann, 2001), we have begun to make rapid progress in the development of regional velocity models of both P and S velocity, including consideration of anisotropy. The North African/Mediterranean region is one where the current data availability is such that velocities in the upper mantle can be resolved with higher precision than that obtainable globally. The Mediterranean Basin is a geophysically complex area, governed by the slow collision between Africa and Eurasia. The boundary between the two plates is not entirely well defined. Although there is clear geodetic and seismic evidence of northward subduction under the Aegean and Calabrian arcs, diffuse seismicity around the Adriatic Sea and Western Mediterranean requires a more complex description of plate interaction, which is the subject of current research. The densely populated Italian peninsula has a long history of destructive earthquakes, and a better understanding of the regional tectonics would have a significant role in the context of seismic hazard mitigation efforts. Tomographic studies are naturally a means to this end (e.g., de Jonge et al., 1994; Faccenna et al., 2001).

In recent years, seismic images of the Mediterranean Basin have been derived by researchers at University of Utrecht (Wortel and Spakman, 2000) and at I.N.G.V. in Italy (Piromallo and Morelli, 1997). Both groups have focused on explaining observations of body-wave (rather than surface-wave) travel times; the Italian group have emphasized regional data, while the Dutch group, with the recent work of Bijwaard (1999), have derived a high resolution regional model within the framework of a variable resolution model encompassing the whole globe.

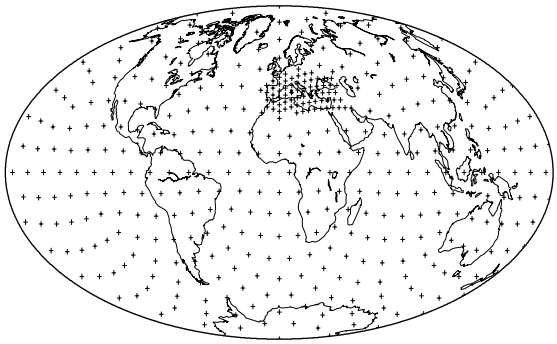

Figure 1: Locations of horizontal spline knots for parameterization of the multi-resolution global model of anisotropic shear velocity.

Free parameters of our least-squares inversions are lateral variations in horizontally and vertically-polarized shear velocities throughout the upper mantle, described as linear combinations of radial and horizontal cubic splines (Boschi, 2001). The basis functions are more densely distributed within the Mediterranean Basin, to achieve a higher nominal resolution. Figure 1 shows the horizontal locations of the spline knots. Globally, the resolution of the inversion approximates a degree 18 spherical harmonic expansion (as in the inversion for joint P and S velocity described above), but becomes more dense within the region of interest. The measured variations in phase delay for Rayleigh and Love waves between periods of 30 and 300 s are defined as

$$\delta\Phi_j(\omega) = \omega \sum_{i=1}^{2} \sum_{k=1}^{K} x_{ik} \int_0^{\Delta_j} \int_0^a K_i(r,\omega) f_k(r,\theta,\phi) dr ds, \quad (1)$$

where the index j represents the individual measurements, the f_k represent the horizontal and radial spline functions, the x_{ik} are the model parameters, and the index i refers to the specific quantities being sought in the inversion, in this case the horizontal and vertical shear velocities. The K_i functions are known as the "sensitivity kernels" (Anderson and Dziewonski, 1982) or partial derivatives. An original feature of this modeling is that the sensitivity kernels are treated as laterally varying, .i.e, the reference model used is not one-dimensional. Instead, we calculate the partial derivatives for model CRUST5.1 (Mooney et al., 1998) overlying a PREM upper mantle. The resulting model shows significant differences in absolute amplitude of the anomalies when compared to models constructed in the conventional manner with a 1-D reference model (Boschi and Ekström, 2001).

Figure 2 shows images at several depths of the global model of vertical shear velocity and the regional Mediterranean model, while Figure 3 shows a cross-section across the western Mediterranean comparing the v_{SV} model to other published velocity models. Among the global features shown in the new model is the high-velocity anomaly in vertical shear velocity in the top of of the upper mantle underneath the central Pacific first reported by Ekström and Dziewonski (1998). Our new Mediterranean model has many features in common with others published for the region. High-velocity anomalies associated with African subduction and the European shield can be readily seen in Figure 2, as well as low-velocity models associated with extension (e.g., Aegean Sea). The cross section shown in Figure 3 indicates that, by accounting for a crust of laterally varying properties in the reference model, we have successfully reproduced the strong slow anomaly (associated with tectonic extension) predicted by de Jonge et al. (1994); in the same region, where the crust is anomalously thin, Spakman et al. (1993) have mapped a fictitious fast anomaly. The thickness of the crust, whose lateral variations Spakman et al. (1993) do not consider, trades off with the imaged shallow upper mantle velocities.

We are currently refining our imaging techniques. While the model described above only accounts for measurements of surface-wave phase velocity, we expect to be able in the near future to derive a single model from the simultaneous inversion of surface-wave phase velocity, surface-wave group velocity (from a local data set assembled and made public by the Lawrence Livermore National Laboratory), body-wave travel times, and mantle waveforms, including joint consideration of P and S velocities. This step should improve the effective resolution of our image in the upper mantle, and provide a reasonable coverage of the lower mantle.

In addition to the construction of more detailed and accurate global velocity models, we have

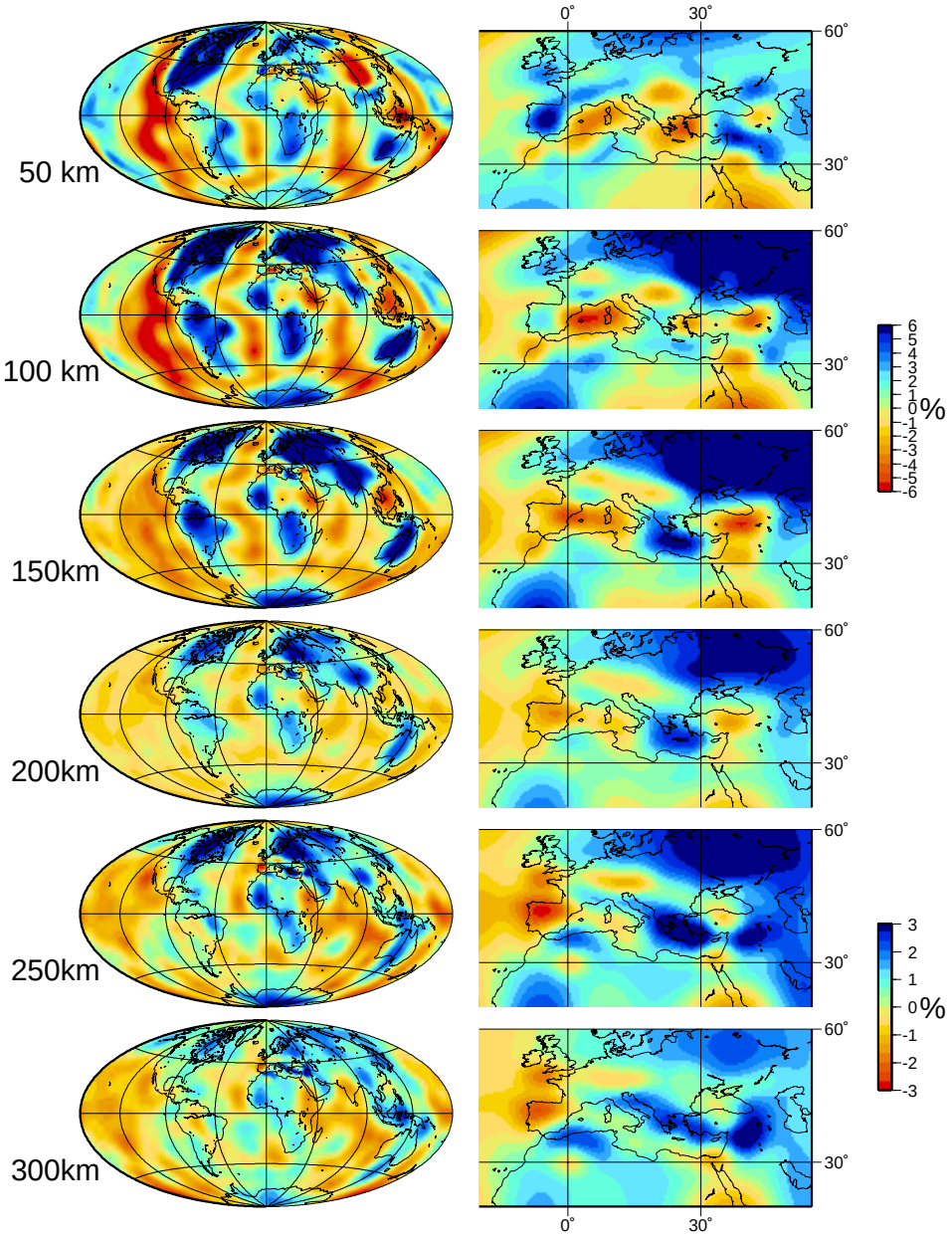

Figure 2: Global (left) and local (right) percent heterogeneity $\delta v_{SV}/v_{SV}$ at six depths in the upper mantle from the variable resolution model of anisotropic shear velocity.

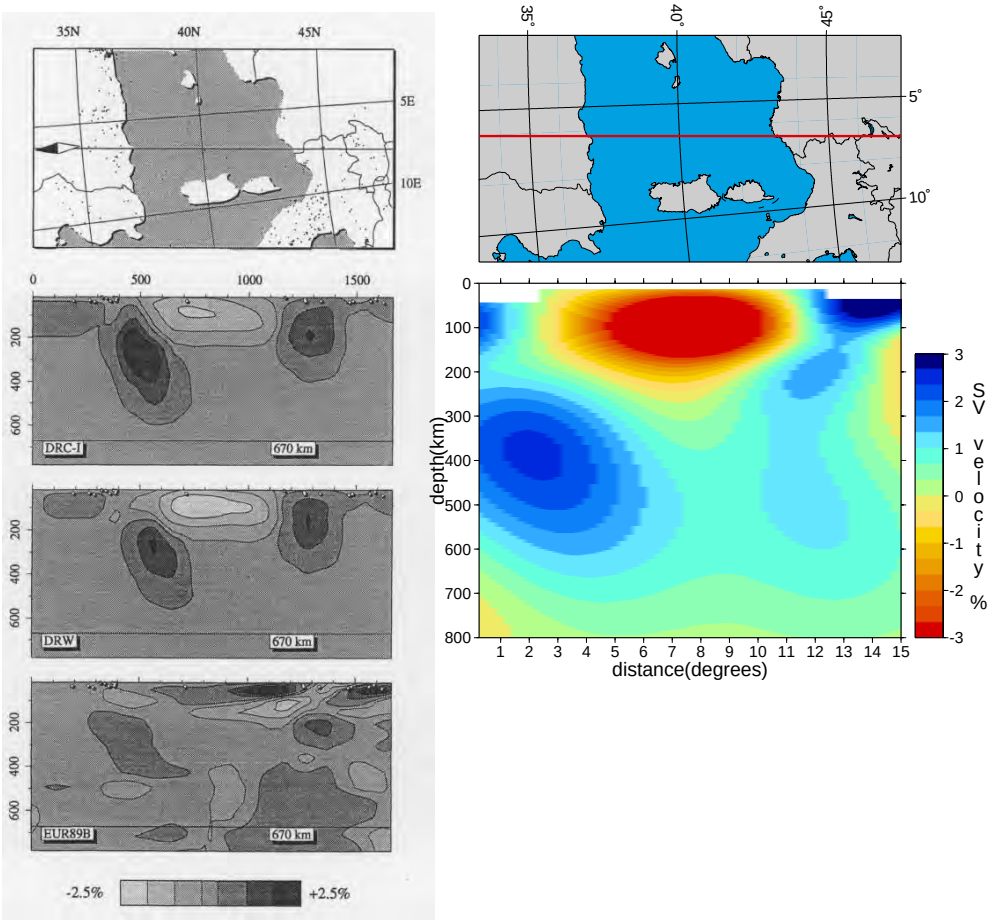

Figure 3: Comparison between four different images of the upper mantle, shown (in cross-section) in the region underlying the Western Mediterranean; the left panels are from de Jonge et al. (1994). DRC-I and DRW are theoretical P-velocity models, computed by de Jonge et al. (1994) on the basis of Dercourt et al.'s (1986) and Dewey et al.'s (1989) tectonic reconstructions, respectively. EUR89B is the tomographic P-model of Spakman et al. (1993), based on regional and teleseismic P-travel time measurements, and including a simplified 1-D reference crustal model. On the right is our own v_{SV} model derived from surface wave phase velocity observations.

focused our efforts on building a larger database of reference or "ground-truth" events to be used for model calibration. So far, the geographical distribution of events with locations known to an accuracy of 5 km or better is extremely limited. Many of these events are nuclear explosions and are concentrated in only a few source regions, making comprehensive testing of velocity models and calibration of new seismic stations very difficult. We have established a catalog of $\sim$1500 large ($M > 5.5$) earthquakes located along mid-ocean ridge and transform faults using a constrained inversion technique where the event is confined to the nearest appropriate plate boundary feature (ridge or transform fault) based on the CMT focal mechanism. The inversion problem is thus reduced to determination of a single distance. Figure 4 shows the global distribution of these large events. We refer to these events as "master events" in the discussion that follows.

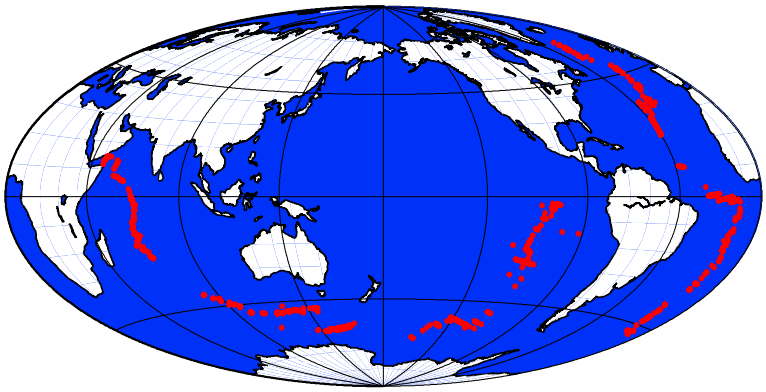

Figure 4: Global locations of relocated master events from the CMT catalog along mid-ocean ridges and transforms.

Improvement in the location of smaller events, for which a focal mechanism has not been determined, might be obtained using the Joint Hypocentral Determination (JHD) technique. To do this, we form clusters of events using those events in the ISC catalog within a circle of radius 100 km about a master events. The differences between our inversion and those of other JHD procedures (e.g., Pavlis and Booker, 1983; Jordan and Sverdrup, 1981) are that we solve for source parameter and station corrections simultaneously, and that the locations of the master events are held fixed during the inversion process. Stations for which there are fewer than 3 observations for a cluster are not included, and we use the LSQR algorithm (Paige and Saunders, 1982) to perform the inversion in order to take advantage of the sparsity of the inner product matrix. The depths of all the events are assumed shallow and are fixed at 10 km. Figure 5 shows the results of one JHD inversion along the Romanche Fracture Zone in the central Atlantic. After inversion the events are drawn toward the fracture zone represented by the low in the bathymetry.

Additionally, we combined the inversion for each master event together to solve for relocation vectors and station corrections for a regional cluster of earthquakes (i.e., JHD with multiple master events). Just as in the single-master-event inversion, each master event influences only those events within a radius of 100 km. In the combined matrices, we apply a smoothing weighting function to the phases of each master event

$$w_j = \sum_K e^{-10\times(\Delta_{jk})^2}, \tag{2}$$

where Δ_{jk} is the distance between the jth and kth master events in the region under study and the sum is over all of the K master events. The phase weights for the smaller non-master events in the inversion are fixed at unity, and all events for which fewer than 30 P phases exist are omitted. We again use an iterative, LSQR algorithm to solve the equations. This process has been applied to approximately 1100 total events within the central Atlantic between 30° S and 30° N.

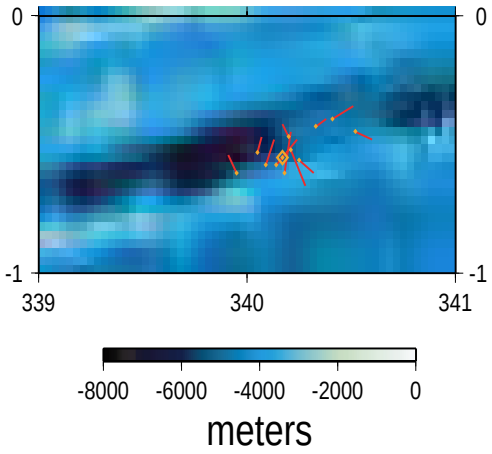

Figure 5: Results of JHD cluster analysis with a single master event (open diamond). Lines show relocation vectors of the smaller events in the cluster, with the new location given by the small diamonds. The vectors have been enlarged by a factor of two in length. The location of the master event was held fixed. Bathymetry is taken from Smith and Sandwell (1997).

Figure 6 shows the regional inversion locations for 148 events along the Romanche Fracture Zone (40 master events). The relocation vectors are shown in the bottom panel, and indicate that most of the epicenters become better aligned along the linear transform fault, except near the eastern edge where there is considerable complexity in the intersection of the transform fault and adjoining ridge. In this region the seismicity shows significant deviation from the great circle defining the plate boundary. The maximum movement obtained for the smaller events in the JHD process (∼50

km) is comparable to that observed for the original master events. We find that, after the JHD inversion, the majority of the smaller events show improvement in the residual RMS (w.r.t. the PREM model) over the initial ISC location (the ISC uses the Jeffreys-Bullen travel time tables). After 3 iterations, a reduction in the weighted RMS residual of ∼50% is achieved for the Romanche Fracture Zone events. The significant variance reduction achieved for the residuals suggests that the accuracy of the new locations is higher than the original catalog locations. The locations obtained in this step can be compared with those obtained using the single-master-event cluster analysis in order to assess their reliability.

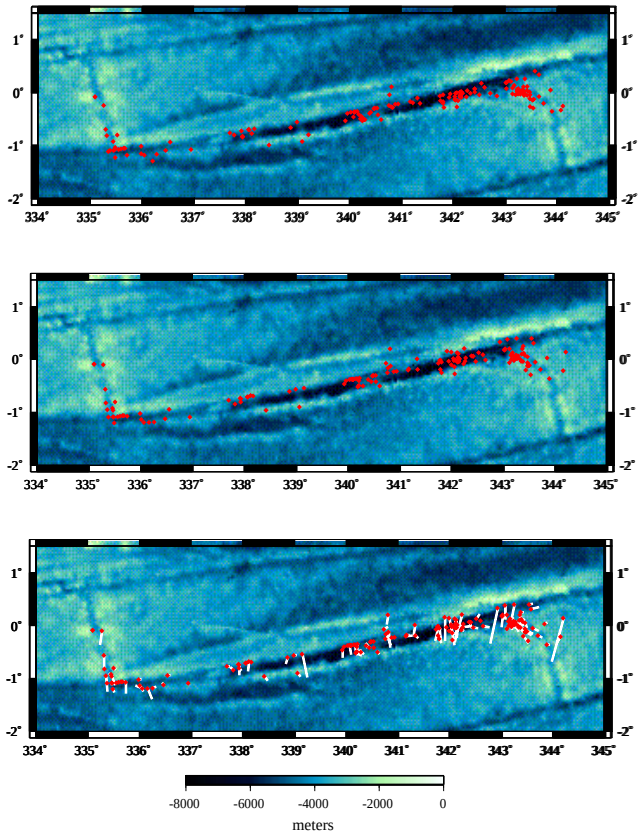

Figure 6: Regional, combined JHD inversion for 148 total events along the Romanche Fracture Zone. Top panel shows the initial ISC locations for the smaller events in the inversion, the middle panel the new locations, and the bottom panel shows the relocation vectors. The 40 master events included (which were fixed) are not shown.

CONCLUSIONS AND RECOMMENDATIONS

Although the current generation of global velocity models provides substantial improvement over 1-D velocity models for teleseismic earthquake location (Smith and Ekström, 1996; Antolik et al., 2001), there is still much room for improvement. The consistent accurate location of small events to within the area specified for on-site inspection under the CTBT (1000 km^2) will likely require the use of regional phases in addition to teleseismic travel times, and also possibly consideration of anisotropy or arrival angle data. To this end, we are developing new global models which combine a local parameterization with the advantages of smoothness over large distances. This will enable straightforward replacement of portions of the global model by a more detailed model covering a particular region. The smooth parameterization will allow simple computation of 3-D raypaths. Our detailed modeling of velocities in the Mediterranean shows the promise of simultaneous consideration of regional and teleseismic data in the tomographic inversion problem.

Testing of new global and regional velocity models, as well as calibration of newer IMS stations, will benefit from the compilation of reference events in remote regions. Our database of relocated events on mid-ocean plate boundaries will also enable construction of more accurate travel time and phase velocity datasets. Since published locations in these regions are known to contain large errors, this database may be of considerable use even if the relocated epicenters are accurate only to within 10 km.

REFERENCES

Anderson, D. L. and A. M. Dziewonski (1982), Upper Mantle Anisotropy: Evidence From Free Oscillations, Geophys. J. R. Astr. Soc., 69, 383-404.

Antolik, M., G. Ekström, and A. M. Dziewonski (2001), Global Event Location With Full and Sparse Datasets Using Three-Dimensional Models of Mantle P Wave Velocity, Pure Appl. Geophys., 158, 291-317.

Antolik, M., G. Ekström, A. M. Dziewonski, Y. J. Gu, J. Pan, and L. Boschi (2000), A new Joint P and S Velocity Model of the Mantle Parameterized in Cubic B-splines, in *Proceedings of the 22nd Annual D0D/DOE Seismic Research Symposium: Planning for Verification of and Compliance with the Comprehensive Nuclear-Test-Ban Treaty*, Vol. 2, 15-23.

Bijwaard, H. (1999), Seismic Travel-time Tomography for Detailed Global Mantle Structure, *Ph.D. thesis*, Utrecht University, Netherlands.

Boschi, L. (2001), Applications of Linear Inverse Theory in Modern Global Seismology, *Ph.D. thesis*, Harvard University, Cambridge, Mass.

Boschi, L. and G. Ekström (2001), New Images of the Earth's Upper Mantle From Measurements of Surface-Wave Phase Velocity Anomalies, J. Geophys. Res., submitted.

Chen, Q. and R. J. Willemann (2001), Global Test of Seismic Event Locations Using Three-dimensional Earth Models, Bull. Seism. Soc. Am., submitted.

Dercourt, J., L. P. Zonenshain, L.-E. Ricou, V. G. Kazmin, X. Le Pichon, A. L. Knipper, C. Grandjacquet, I. M. Sbortshikov, J. Geyssant, C. Lepvrier, D. H. Pechersky, J. Boulin, J.-C. Sibuet, L. A. Savostin, O. Sorokhtin, M. Westphal, M. L. Bazhenov, J. P. Lauer, and B.

Biju-Duval (1986), Geological Evolution of the Tethys Belt From the Atlantic to the Pamirs Since the Lias, Tectonophysics, 123, 241-315.

Dewey, J. F., M. L. Helman, E. Turco, D. H. W. Hutton, and S. D. Knott (1989), Kinematics of the western Mediterranean, in *Alpine Tectonics*, edited by M. P. Coward, D. Dietrich, and R. G. Park, Spec. Publ., Geol. Soc. London, 45, 265-283.

Dziewonski, A. M. and D. L. Anderson, Preliminary Reference Earth Model (PREM) (1981), Phys. Earth Planet. Inter., 25, 289-325.

Ekström, G. and A. M. Dziewonski, The Unique Anisotropy of the Pacific Upper Mantle (1998), Nature, 394, 168-172.

Faccenna,C., T. W. Becker, F. P. Lucente, L. Jolivet, and F. Rossetti (2001), History of Subduction and Back-arc Extension in the Central Mediterranean, Geophys. J. Int., 145, 809-820.

Gu, Y. J., A. M. Dziewonski, W. Su, and G. Ekström (2001), Models of Mantle Shear Velocity and Discontinuities in the Pattern of Lateral Heterogeneities, J. Geophys. Res., 106, 11,169-11,199.

de Jonge, M. R., M. J. R. Wortel, and W. Spakman (1994), Regional Scale Tectonic Evolution and the Seismic Velocity Structure of the Lithosphere and Upper Mantle: The Mediterranean Region, J. Geophys. Res., 99, 12,091-12,108.

Jordan, T. H. and K. A. Sverdrup (1981), Teleseismic Location Techniques and their Application to Earthquake Clusters in the South-central Pacific, Bull. Seism. Soc. Am., 71, 1105-1130.

Kennett, B. L. N. and E. R. Engdahl (1991), Traveltimes for Global Earthquake Location and Phase Identification, Geophys. J. Int., 105, 429-465.

Mooney, W. D., G. Laske, and G. Masters, CRUST5.1: A Global Crustal Model at $5^\circ \times 5^\circ$ (1998), J. Geophys. Res., 103, 727-747.

Paige, C. C. and M. A Saunders (1982), LSQR: An Algorithm for Sparse Linear Equations and Sparse Least Squares, ACM Trans. Math. Soft., Vol. 8 No. 1, 43-71.

Pavlis, G. L. and J. R. Booker (1983), Progressive Multiple Event Location (PMEL), Bull. Seism. Soc. Am., 73, 1753-1777.

Piromallo, C. and A. Morelli (1997), Imaging the Mediterranean Upper Mantle by P-wave Travel Time Tomography, Annali di Geofisica, 40, 963-979.

Smith, G. P. and G. Ekström (1996), Improving Teleseismic Event Locations Using a Three-dimensional Earth Model, Bull. Seism. Soc. Am., 86, 788-796.

Smith, W. H. F. and D. T. Sandwell (1997), Global Sea Floor Topography From Satellite Altimetry and Ship Depth Soundings, Science, 277, 1956-1962.

Spakman, W., S. van der Lee, and R. D. van der Hilst (1993), Travel–time Tomography of the European–Mediterranean Mantle Down to 1400 km, Phys. Earth Planet. Inter., 79, 3-74.

Wortel, M. J. R. and W. Spakman (2000), Subduction and Slab Detachment in the Mediterranean-Carpathian Region, Science, 290, 1910-1917.

3-D EARTH MODELS AT REGIONAL AND GLOBAL SCALES

Claudia M. Aprea, Christopher R. Bradley and Lee K. Steck

Los Alamos National Laboratory

Sponsored by National Nuclear Security Administration
Office of Nonproliferation Research and Engineering
Office of Defense Nuclear Nonproliferation

Contract No. W-7405-ENG-36

ABSTRACT

We are developing a simple and efficient MATLAB tool for creating improved 3-D lithospheric models for nuclear explosion monitoring. The goal of the model maker is to provide a means for producing 1-D, 2-D and 3-D gridded or layered velocity and attenuation models for travel-time and full waveform synthetic seismic estimates. In the implementation of this code, we include the capability to produce multiple models based on the same *a priori* information by allowing for multiple construction rules. *A priori* rock property information can take the form of surface discontinuities (such as the crust-mantle interface, topography, and basins) or any kind of 1-D, 2-D, or 3-D regional information. Because of the flexibility of the tool, models may be readily updated as new information becomes available. Our current model includes regions of North Africa, Europe, and Asia and is based on the previous Los Alamos National Laboratory model for China, the Maxwell (SAIC) global surface wave model and the Lawrence Livermore National Laboratory Middle East/North Africa/Former Soviet Union model. Models are validated by comparing model-based and empirically derived correction surfaces for important stations in Western China. Waveforms from these stations for events of special interest are also used to test the accuracy of the model using a full waveform finite difference algorithm. We also test the sensitivity of the model predictions to different types of *a priori* data (e.g. structural interfaces like the Moho and 1-D velocity models for geophysical provinces).

KEY WORDS: lithosphere model, Western China, finite difference, travel time, propagation effects, MATLAB

OBJECTIVE

Introduction

Many regions of particular importance for nuclear explosion monitoring are either aseismic or contain few ground truth events. As a result, calculation of correction surfaces or estimation of the propagation effects through these regions is hampered by the large uncertainties associated with sparse data. One solution for mitigating the effects of these uncertainties is to estimate accurate lithosphere models in poorly controlled regions from well known geologic models and rules.

To address this need, we have developed a geophysical model tool that can incorporate various types of geologic/geophysical information and create an estimate of the lithosphere based on various geologic rules.

The primary motivations for developing this modeling tool are to:
1. improve the location of events that fall outside regions where ground truth events exist, and
2. provide insight into the physical basis for propagation effects on discrimination in the regions of interest (e.g. the effects of attenuation, crustal thickness, scattering into anomalous phases).

The purpose of this paper is to present the basic properties of the model tool and to show the initial composite models generated to help in locating, identifying and characterizing events in Asia, parts of the

Former Soviet Union, North Africa, and the Middle East. Our goal is to provide an integrated, validated, and easily implemented set of products to assist the user in location of events where empirical corrections surfaces are poorly defined and give insight into the crustal propagation effects for near-regional, regional and near-teleseismic events. We present some of the work we have completed for Asia.

RESEARCH ACCOMPLISHED

The Modeling Tool: China-East Asia

The purpose of this MATLAB tool is to easily create and manipulate regional models, to aid the discrimination and location of earthquakes and explosions. Previous lithosphere models were created using Stratamodel, a computational toolbox for modeling heterogeneous structural models in 3-D. Certain limitations of Stratamodel have been overcome with our new tool.

The base of the building technique of this code is to include and weight appropriately the available geophysical information for interpolation/extrapolation of a 3-D model based on the fewest non data-based hypotheses. The *a priori* information can be of the type:

- **hard surfaces**: local topography, sedimentary basins, crust mantle interface, any other hard surface imposing a discontinuity (e.g. Conrad Discontinuity, bathymetry) of some sort or very high gradients normal to the surface (in very local models this could include faults and erosional surfaces);
- **any 1-D/2-D/3-D regional information** such as P-wave velocity Vp(x,y,z), density ρ(x,y,z), geophysical province boundary, etc.

The dimensions and grid samples of these input files are not required to be the same. Volumes, layers and point data are re-sampled to output a uniform model. Our 3-D model is a layered model (curved surfaces in 3-D space) constructed in between hard surfaces. Gradients can exist, either implied by the velocities above and below these interfaces or as absolute grids whose attributes reflect the spatially changing properties.

The model building process can be broken down into a number of steps. The simplified steps in building a model are:

- **Building the geometrical framework or skeleton of the model**. This is based on the number of hard surfaces and on the number of conformal (or non-conformal) layers between the hard surfaces. The number of layers in between hard surfaces is chosen by users to match their conception of the complexity of the crust. First, all hard surfaces are reduced to a common grid. Second, the vertical distance between two consecutive hard surfaces at each (longitude, latitude or kilometer or sub-kilometer) grid point is calculated and divided by the number of layers the user had chosen. These intersection points are used to build the layers.

- **Extrapolating/interpolating available information in a form of 1-D/2-D/3-D profiles**. First, all profiles (even 2-D/3-D), are reduced to a set of (longitude, latitude, z, attribute) or pseudo-1-D profiles. Second, the intersection of the data points (longitude, latitude, z, attribute) with the layers is computed and used to evaluate the modeled variable at each layer using an appropriate interpolation scheme (’nearest-neighbor’, ‘linear’, ’cubic’, ’spline’, etc.). Note that each region in between hard surfaces is interpolated independently. This preserves the discontinuity marked by each hard surface. Third, a 2-D interpolation is done at each layer (parallel to the layer’s surface) independently of one another. At this stage a 3-D model is already built but the data are still in a non-uniform vertical grid. Fourth (optional), a final extrapolated 3-D model can be obtained for a uniform 3-D grid to satisfy the requirements of any travel-time code, waveform code, etc.

The conformal layering is one of the geologic “rules” that can be enforced or relaxed to varying degree. Hard boundaries are interpreted as “geologic sequence” boundaries. If, for example, the sequence bounding surfaces are topography and basin depth, then the basins will be subdivided by layers that conform gradually from the topography to the bottom of the sedimentary basins. This is conceptually how

these layers were deposited in nature. Non-conformal boundaries (e.g. faults) can be created by introducing additional hard surfaces.

Case Study: Western China

Hard Surfaces

Below, we present one possible model for Western China. The model extends from 22 to 54 degrees North latitude and 65 to 130 degrees East longitude. The model was built from the three hard surfaces or gridded horizons. The gridded horizons we have chosen are the topography, basin and Moho surfaces accessible via the Cornell database (http://www.atlas.geo.cornell.edu/ima.html). Figure 1 shows the topography, basin and Moho relief from the IPE Cornell data set. Previous modeling studies of path effects through western China (e.g., Jones et. al, 1998; Bradley and Jones, 1998), have used these surfaces as a framework around which individual crustal models (e.g. Romanowitz, 1982; Kosarev et al., 1993; Curtis and Woodhouse, 1997; Jih, 1998; Mahdi and Pavlis, 1998, Mooney, 2000) have been used to improve upon the model.

These data surfaces divide the lithosphere into sequences that have undergone distinct geophysical processes in time, pressure and temperature, and logically should be treated differently by the model creation process. These surfaces are the reference for the lithospheric model. and subdivide the model into geophysically independent sequences. These sequences are the basin (and topography) structure, crustal structure, and Moho or lower lithosphere structure. The 1-D/2-D/3-D regional information controls layering within each of these sequences.

1-D/2-D/3-D regional information

In an oil reservoir there may typically be well data to enhance the information on the geostratigraphy. In a similar vein, there are many detailed studies of regions of interest in western China, some encompassing extensive regions (Jih, 1998; Li and Mooney, 1998; Mooney, 2000; Stevens and Adams, 1999). These individual studies provide 1-D and 2-D information about specific geophysical provinces. Figure 1 shows the geophysical provinces we have chosen for the initial model of western China. There are 33 distinct provinces, each of which has a 1-D structural model associated with it. The preliminary velocity models were derived from Jih, 1998, and Li and Mooney, 1998. Currently there are 15 1-D models for the 33 provinces so there is some redundancy, but we have allowed for expansion.

The 1-D structural models are treated like wells in the model tool. They provide the detailed information for the sub-layering within each sequence. This information is called the “attribute” model.

Once the stratigraphic framework is built to describe structure and stratigraphy and well models are in place for the correlation of individual provinces, the attribute model must be defined. The attribute model describes how the geophysical rock parameters are distributed throughout the model grid. This distribution can be based on simple mathematical relations or higher order geostatistical parameters.

Within each model cell, the search radius, the mathematical bias relative to the “well” data and the interpolation scheme determine the attributes associated with it. For our current model, we are calculating Vp, Vs, density, and the intrinsic attenuation coefficients for P-waves, Qp, and S-waves, Qs (Figure 1).

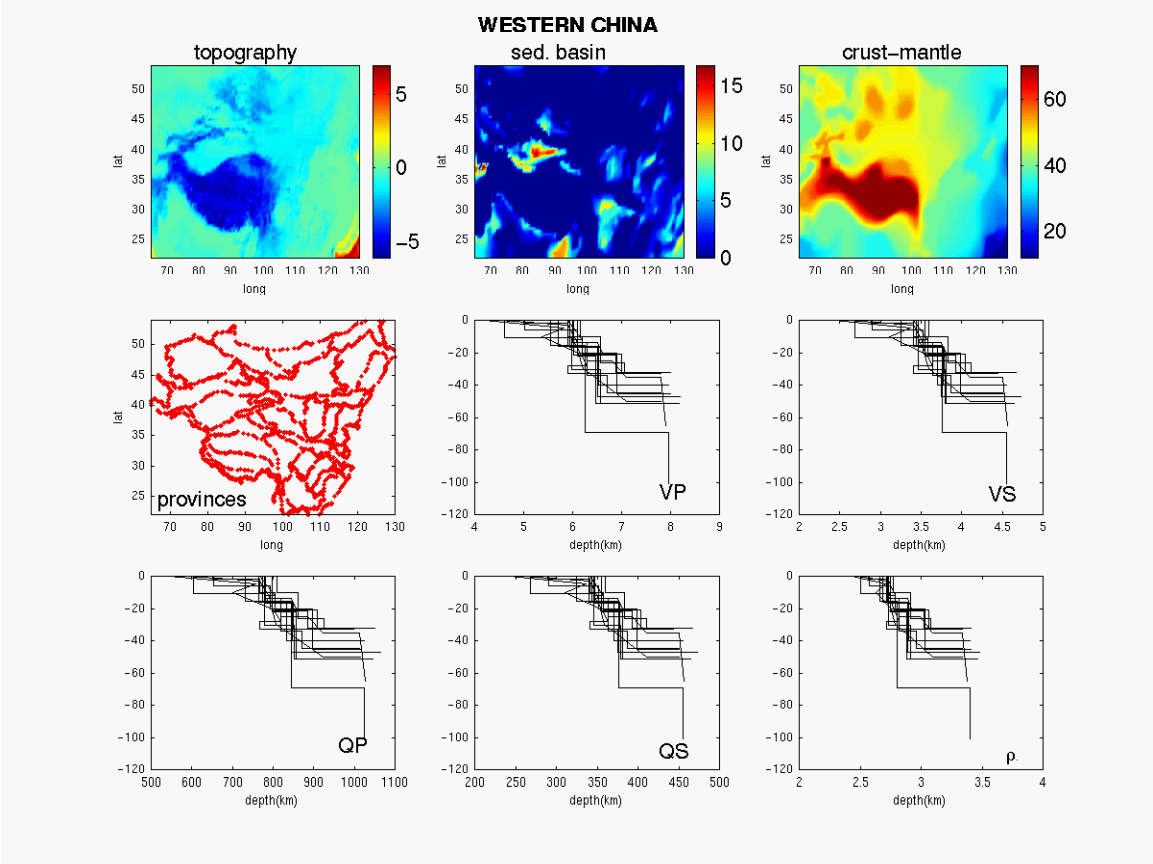

Figure 1. *A priori* information to build a model for Western China. Upper panels: hard surfaces, topography, sedimentary basin's depths, crust-mantle interface. The color bar indicates depth in km. Left middle panel: 1-D profiles are available for 33 provinces in Western China, this is a map showing these provinces. Rest of panels: 5 panels showing each the 33 superimposed 1-D profiles for P-wave velocity, S-wave velocity, Qp, Qs, and density

These are the basic building blocks for this model. Additional data sets that are used to improve on the model include Crust 5.1 (Mooney et al., 1998) and Moho and crustal P- and S-wave velocity/structure maps provided by Mooney, 2000.

An example of the model created from this data set is presented below. In Figure 2, we show the 3-D perspective of the provinces and the 1-D "wells" at their center. The calculation of the velocities within each province is enforced as a function of distance from the center of gravity of the province. In this example we have chosen 3 basin layers and 6 crustal layers. The velocities at layer 5 (a crustal layer) are plotted in the lower right panel (Figure 2-D). The province boundaries are strictly enforced in this example by forcing the 1-D velocity model to be unchanged over 80% of the province. This requirement can be relaxed if a smoother merging of province boundaries is desired.

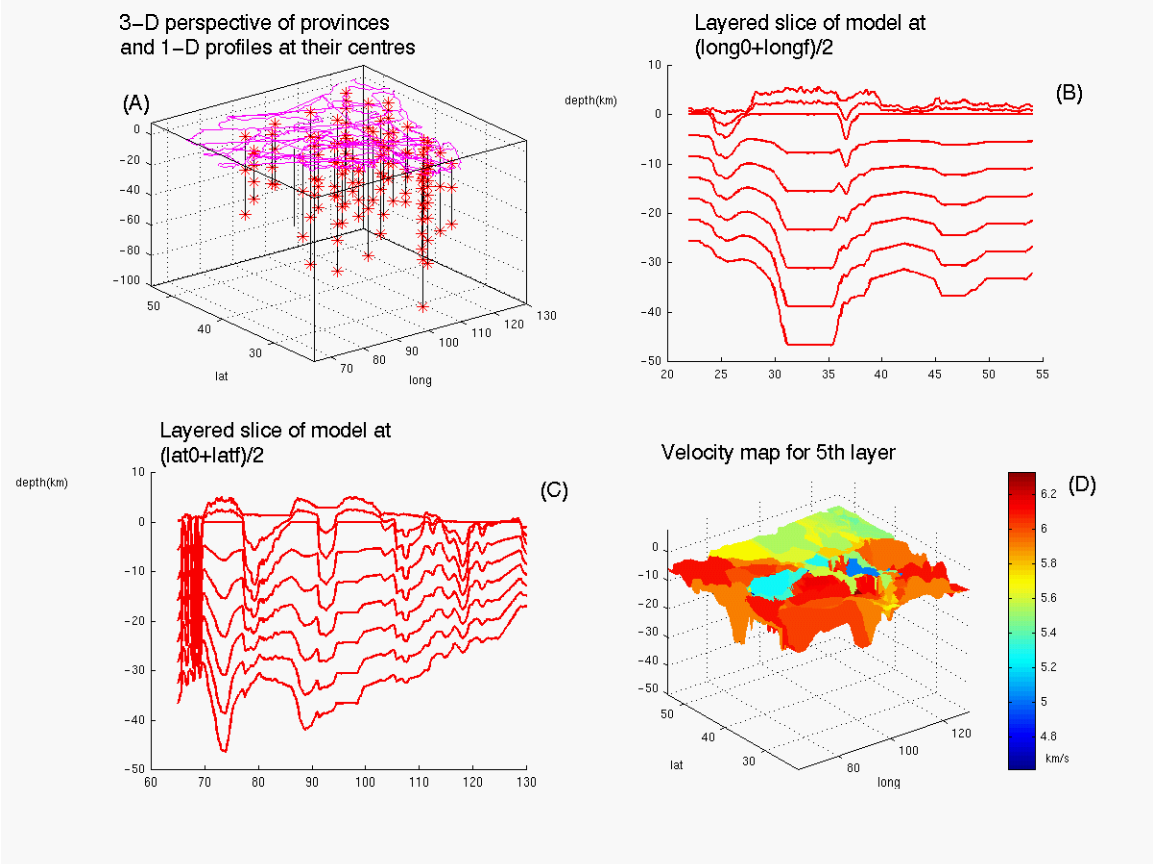

Figure 2. (A) a 3-D visualization of the 33 Chinese provinces (purple lines) and the vertical grid (red stars) for the 1-D profiles, located at the center of the provinces only for reference.(B) The 3-D model is composed by a number of layers, here a 2-D slice at the mid longitude showing a detail of the skeleton of the model; and (C) the same at the mid latitude of the model. (D) example of the fifth layer for a 3-D model of Vp.

Validation and Testing

The above model can be validated in two important ways. First, model-based correction surfaces for stations of importance to nuclear explosion monitoring can be created and compared to those empirically derived. An example of this is shown in Figure 3a for station LSA in Tibet. The models will also be validated by reserving a portion of the travel-time picks used to create the correction surfaces to test and estimate the accuracy of the model in a given geophysical province. The correction surface was generated by first calculating all the travel times to the free surface from a synthetic event at station LSA. This result was then subtracted from those times predicted by IASPI91. In general, the times are in good agreement up to approximately 1000 km. Improvements to the model can be made to increase the accuracy of the surface out to greater distance. Once we have reasonable assurance that the model is accurate, corrections surfaces for future stations can be used to help calibrate them. Calibration experiments can also be planned based in part on the geophysical model.

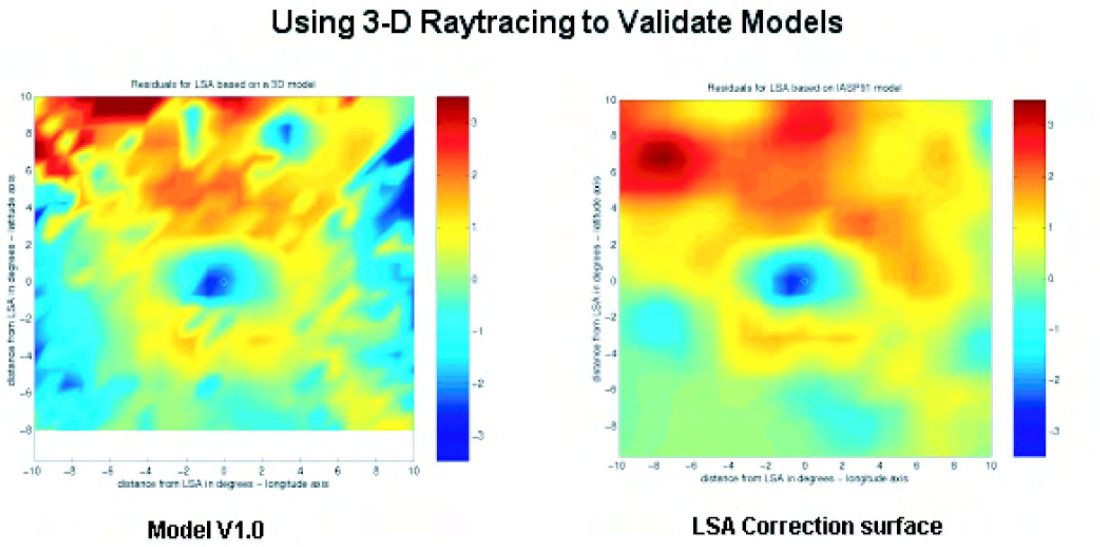

Figure 3a. A comparison of model-based and empirically derived correction surfaces for station LSA. Travel-time residuals for the model are calculated using a 3-D ray-tracing algorithm.

In addition to the travel-time calculations, full waveform finite-difference calculations are made along paths of limited range (<1500 km) with a limited bandwidth (0-1.0 Hz) and compared with ground truth data. Figure 3 shows the initial model from an event near Lop Nor to Station MAK. Figure 4 shows an example of several synthetics created with a 2-D finite-difference forward wave propagation code using several different source mechanisms.

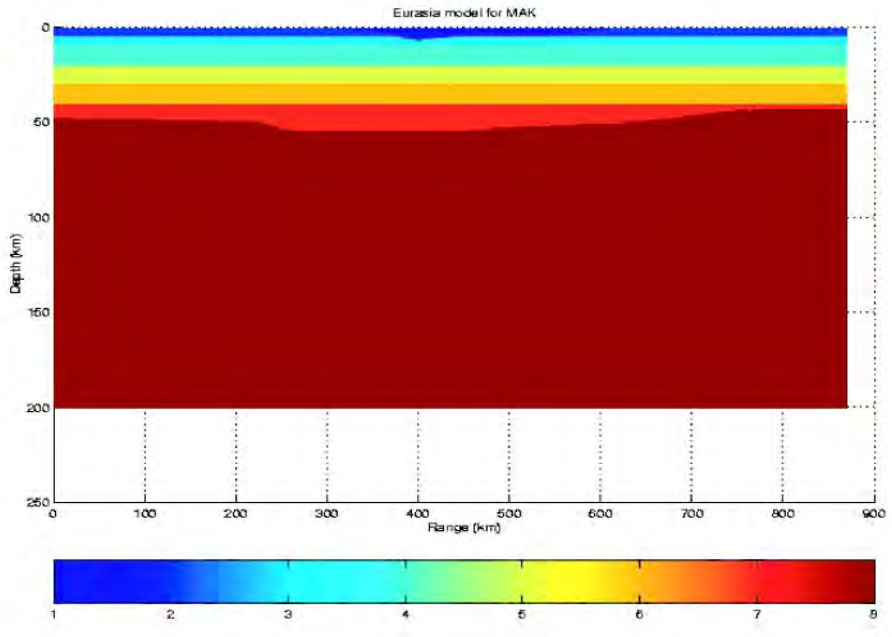

Figure 3b: Initial model of the path from the event to station MAKZ. Layercake stratigraphy is created by modifying the Kosarev model to match body wave travel times.

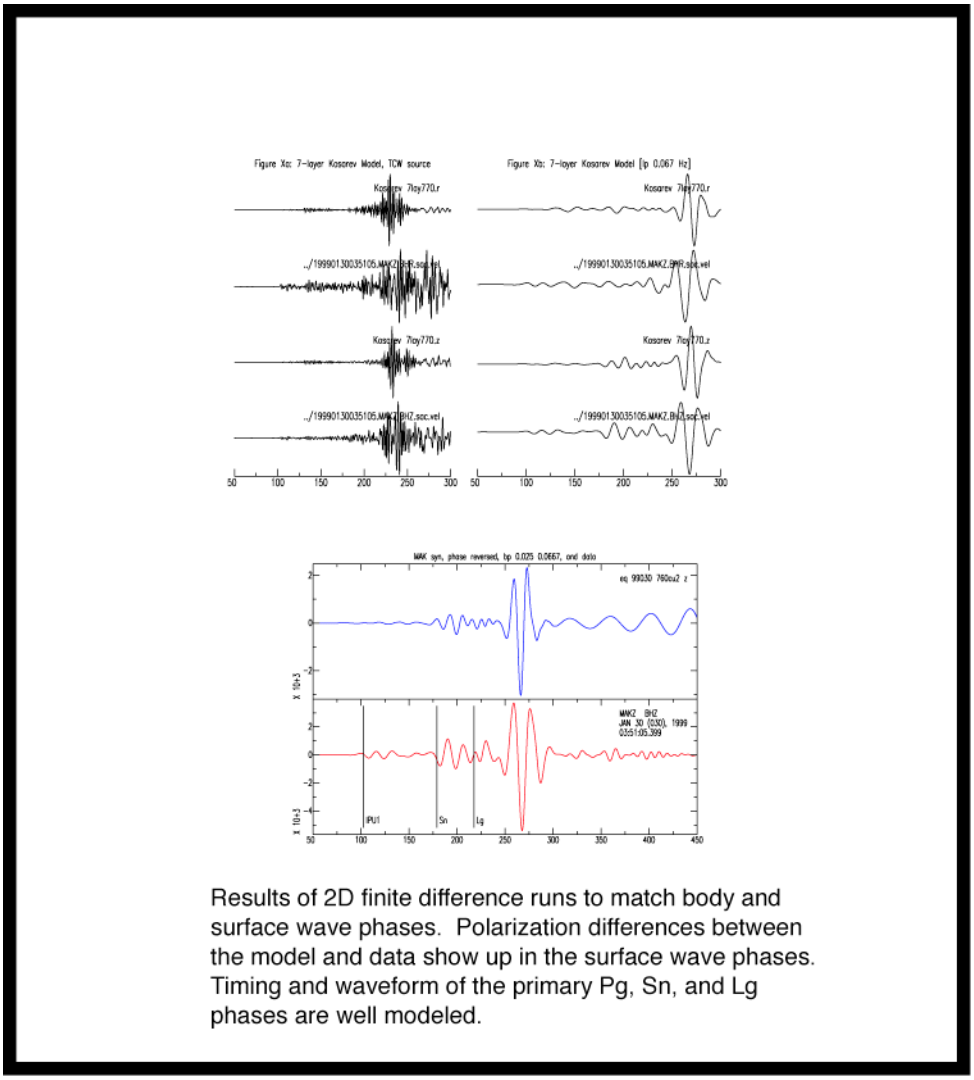

Results of 2D finite difference runs to match body and surface wave phases. Polarization differences between the model and data show up in the surface wave phases. Timing and waveform of the primary Pg, Sn, and Lg phases are well modeled.

Figure 4: Results of 2-D finite-difference synthetics for an event near Lop Nor to Station MAK. Low-frequency features are well modeled.

Full 3-D wave propagation including intrinsic attenuation has been used to validate specific paths of interest. Areas of particular interest for the validation are the overlap zone and near test sites. In Figure 5 we show the 3-D wavefield for the 26 January 2001 earthquake. This calculation was done using a 4 order staggered-grid finite-difference code. The code employs a new memory-efficient algorithm for calculation of the full 3-D anelastic wavefield (Day and Bradley, 2001). Memory-efficient schemes like this increase the practicality of 3-D full waveform simulation.

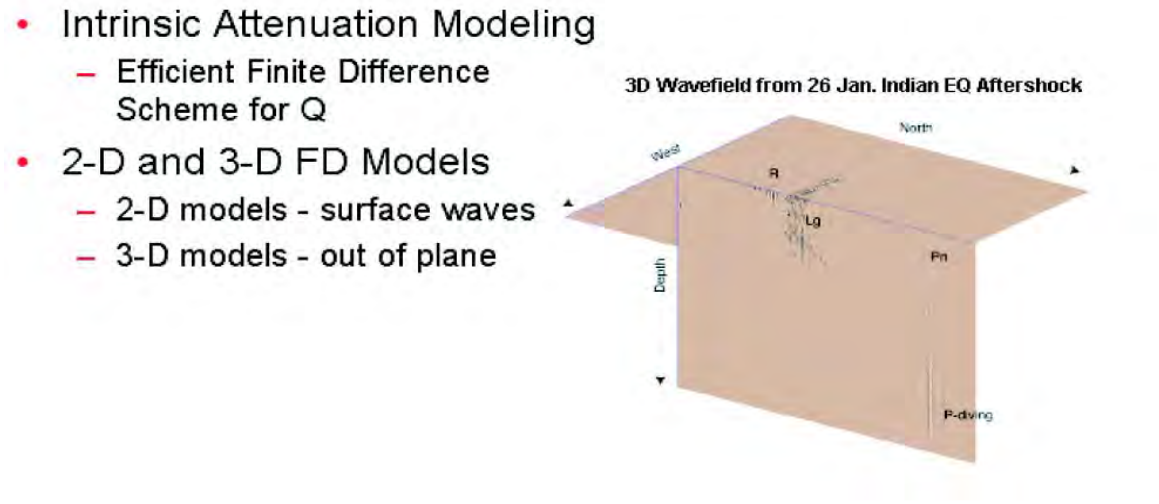

Figure 5. 3-D wavefield from simulating the 26 January 2001 Indian Earthquake. The distance to the station is approximately 20 degrees. Primary discrimination phases are indicated on the orthogonal planes.

CONCLUSIONS AND RECOMMENDATIONS

There is a need for improved models in regions of interest and particularly where there are few ground truth events. This model tool provides a method for updating and improving models. Intrinsic Q and topography will play a greater and greater role in amplitude and travel-time tomography. Having a versatile tool for incorporating the effects of these two attributes will benefit both location and discrimination efforts in nuclear explosion monitoring.

The initial models have performed well in generating model-based correction surfaces but are not yet accurate enough to model high-frequency (> 1-Hz) features in the waveform data. Both Q and topography play a role in these misfits as well as the uncertainty in the model. Models should be primarily validated using the travel-time correction surfaces. Though the discretization of the model is a user-defined function within the model tool, the accuracy of the model is a function of the input surfaces and 1-D models. Users may need to define a greater number of interfaces for their modeling efforts.

In the future, Q tomography and stochastic model extrapolation should be used to create models accurate enough to simulate the full 3-D analastic wavefield. For low-frequency simulations, 2-D models perform well; however, for higher frequency simulations, estimating the effects of the full 3-D lithosphere is necessary.

REFERENCES

Aprea, C., C. Bradley and L. Steck (2001), Calibration of 3-D Earth Models at Regional and Global Scales, LA-UR-01-XXXX.

Bradley, C. R. and L. E. Jones (1999), Full Waveform Modeling of the Effects of Q and Structure Over Subregional Paths in Western China, 21st Annual Research Symposium on Monitoring a CTBT.

Bradley, C. and E. Jones (1998), Modeling propagation effects from explosions in western China and India, Proceedings of the 20th Annual Seismic Research Symposium on Monitoring a CTBT, Santa Fe, NM.

Curtis, A. and J. H. Woodhouse (1997), Crust and upper mantle shear velocity structure beneath the Tibetan plateau and surrounding regions from interevent surface wave phase velocity inversions, *J. Geophys. Res.*, 102(B6), 11,789-11,813.

Day, S. and C. Bradley (2001), Memory-efficient simulation of anelastic wave propagation. Bull. Seis. Soc. Am., 91, 520-531.

Jih, R.-S. (1998), Location calibration efforts in China, in Proceedings for the 20th Annual Seismic Research Symposium, 12pp.

Jones, E., C. Bradley, F. App, R. Bos, and H. Patton, (1998), Modeling seismic propagation from large scale structural features in western China. LANL Memorandum, LA-UR-97-4186.

Kosarev, G.L., N.V. Petersen, L.P. Vinnik, and S.W. Roecker 1993), Receiver functions for the Tien Shan analog network: Contrasts in the evolution of structure across Talasso-Fergana fault, J. Geophys. Res., 98, 4437-4448.

Li, S. and W. D. Mooney (1998), Crustal structure of China from deep seismic sounding profiles, Tectonophysics, 288, 105-113.

Mahdi, H., and G. Pavlis (1998), Velocity variations in the crust and upper mantle beneath the Tien Shan inferred from Rayleigh wave dispersion: Implications for tectonic and dynamic processes. *J.. Geophys. Res., 103(B2*) , 2693-2703.

Mooney, W. D. (2000), Crustal and upper mantle structure of China and adjacent areas. Interim Report (9/28/99-9/29/00): Data compilation and results, DOE IA (ID): DE-A104-98AL79758.

Mooney, W. D., G. Laske, and T. G. Masters (1998), CRUST 5.1: A global crustal model at 5° X 5°: Journal of Geophysical Research, 103, 727-747.

Romanowitz, B. (1982), Constraints on the structure of the Tibet Plateau from pure path phase velocities of Love and Rayleigh waves. *J. Geophys. Res.*, 87(B8), 6865-6883.

Smith, W. H. F. and P. Wessell (1990), Gridding with continuous curvature splines under tension, Geophysics, 55, 293-305.

Steck, L. K., A. A. Velasco, A. H. Cogbill, and H. J. Patton (2000), Improving regional seismic event location in China, accepted at Pageoph, March.

Stevens, J. L. and D. A. Adams (1999), Improved methods for regionalized surface wave analysis, Annual report Submitted to DTRA, November.

INVESTIGATION OF THE PARTITIONING OF SOURCE AND RECEIVER-SITE FACTORS ON THE VARIANCE OF REGIONAL *P/S* AMPLITUDE RATIO DISCRIMINANTS

Douglas R. Baumgardt, Zoltan Der, and Angelina Freeman

ENSCO, Inc.

Sponsored by Defense Threat Reduction Agency

Contract No. DTRA01-00-C-0043

ABSTRACT

In this project, we are investigating problems associated with applying regional-phase amplitude ratios, such as *Pn/Sn* or *Pn/Lg* ratios, for discrimination of explosions and earthquakes for monitoring the CTBT. Using multiple array recordings of groups of events in the same source region, the factors that contribute bias or the scatter of *P/S* ratio measurements after correction for path effects are characterized. These factors include both receiver site effects and source mechanism effects on *P/S* ratios. The study of site effects will be focused on arrays where we have seen site variations in *P/S* ratios, including the Scandinavian regional arrays (NORES, FINES, ARCES, FINES), and other new arrays in the International Monitoring System (IMS). The variance in the *P/S* ratio around regional arrays and large aperture arrays reveals the extent to which site affects cause variations in *P/S* ratios around different arrays in different regions. The partitioning of the variance between source, path, and receiver effects is examined by analysis of variance (ANOVA). We have performed an initial study of a group of presumed underwater explosions in the Gulf of Bothnia recorded by regional arrays in Scandinavia. We find that *P/S* and *P/S* amplitude ratios vary by as much as a factor of 3 around the FINES and NORES arrays, with apertures of 3 km, as well as similar variations for the different sources. These variations appear to be driven by variations in *Pn* and *Pg* amplitudes, whereas *Lg* amplitudes appear to be more stable. For source mechanism effects, we have been concentrating on earthquakes in the Zagros thrust belt of Western Iran, where, in a previous study, azimuthal variations in *P/S* ratios have been observed. Regional *P/S* ratios have been measured on these events and ANOVA is being used to determine to what extent the azimuthal variance can be partitioned between source effects, including focal mechanism and depth of focus, and propagation path effects. The results of this study will quantify the factors, other than propagation-path effects, that may bias the use of *P/S* ratios for seismic discrimination and provide a priori estimates of site variance for discrimination techniques.

KEY WORDS: discrimination, amplitude ratios, regional arrays, site effects, analysis-of-variance, underwater explosions

OBJECTIVE

The International Monitoring System (IMS) for the Comprehensive Test Ban Treaty (CTBT) faces the serious challenge of being able to accurately and reliably identify seismic events in any region of the world. This requirement extends to a very low magnitude threshold, mb=2.5, which is in the range of the sizes of local and regional seismic activity, both natural and artificial. Much research has been performed in recent years on developing discrimination techniques that classify seismic events into broad categories of source types, such as nuclear explosion, earthquake, and mine blast.

The seismic waveform discriminant which has been commonly investigated is the regional *P(Pn, Pg)/S(Sn, Lg)* amplitude ratio. Seismic source physics suggests that earthquakes, being dislocation sources, should be intrinsic sources of shear waves whereas explosions, being pure compressional sources, should only generate *P* waves. Therefore, explosions should have higher *P/S* amplitude ratios than earthquakes. This has been generally

observed to be true, although the separation of explosions and earthquakes amplitude ratios is generally larger at high frequency (> 5 Hz) than at lower frequencies.

Observationally, nuclear explosions and earthquakes appear to be well separated by this discriminant (e.g., Baumgardt, 1993; Baumgardt and Der, 1994; Hartse et al., 1997). For example, Russian nuclear explosions observed at a Chinese station WMQ records no shear wave energy at frequencies above 6 Hz whereas Chinese earthquakes produce significant shear wave energy above 6 Hz. However, studies of mine blasts in Scandinavia and Germany (Baumgardt, 1993) indicate that many of the mine blasts seem to be intrinsic sources of shear waves, perhaps because they induce shear in fracturing and spallation in mines. Thus, low *P/S* ratios may be an indication of earthquakes, but many mine blasts may also have low values. However, we generally observe that most nuclear explosions will have high *P/S* ratios at high frequency compared to earthquakes, and mine blasts can also have high *P/S* ratios at high frequency.

Although *P/S* ratios appear to give promising discrimination between earthquakes and explosions, they have also been shown to have high degree of scatter which reduces the confidence of identification using such discrimination techniques as the outlier method (Fisk et al., 1996). Likely causes of this scatter includes the following:

1. Propagation path effects – These include differential attenuation of *P* and *S* and unmodeled propagation path effects, such as variations in elevation, crustal depth, and depth to basement (sediment thickness). Empirical studies of variations of *P/S* ratios with distance (e.g., Fisk et al, 1996) have resulted in distance corrections. Correlation studies for *P/S* amplitude ratios with crustal parameters (e.g., Zhang et al., 1994; Fan et al., 2001) have demonstrated that these correlations can reduce the variance of *P/S* ratios caused by unmodeled path effects.

2. Source effects – These may include ripple fire patterns in mine blasts, which can usually be identified by spectral techniques, magnitude differences (Xie and Patton, 1999; Ringdal et al., 2000), and possible differential radiation pattern effects on *P* and *S* amplitudes. The latter has usually been assumed to be small for high frequency regional waves. As mentioned above, mine blasts may also intrinsically excite shear waves to different degrees, depending on the local tectonic environment and the blasting practice, which can contribute high variance in *P/S* ratios. Finally, variations in depth of focus of earthquakes may also produce significant variations in *P/S* ratios.

3. Site effects – These include variations in *P* and *S* amplitudes caused by variations in the geology immediately below the site itself. These effects are usually local and not included in propagation-path corrections. Baumgardt and Der (1994) showed examples of site variance effects around the Iranian Long Period Array (ILPA) where both earthquake- and explosion-like *Pn/Lg* amplitude ratios were observed for sensors separated by several kilometers.

This paper addresses possible causes of scatter and bias in the use of regional *P/S* amplitude ratio discriminants that have not been much studied in previous research, although their importance has been noted. These effects may contribute to the residual variance in distributions of *P/S* ratios for earthquake populations even after the application of propagation-path corrections. These include of station site effects, perhaps due to variation in amplification of *P* and *S* waves by variable site geology, on the *P/S* ratios, as evidenced by the variation in *P/S* amplitude ratios around regional arrays. Also, earlier research (Baumgardt, 1996) has revealed that source radiation patterns from earthquakes in the Zagros mountains of western Iran, recorded at ILPA, may cause significant variation in *Pn*/*Lg* ratios. This study will follow up on that observation and investigate the effect in more detail to determine if the effect is due to source or propagation-path effects. Overall, this study will determine the likely maximum a priori variance that may be caused by these effects that may be useful in discrimination studies that must rely on single site measurements of regional *P/S* ratios.

RESEARCH ACCOMPLISHED

In this paper, we describe an initial study of site variances using regional arrays. Using multiple array recordings of groups of events in the same source region, the factors that contribute bias or the scatter of *P/S* ratio measurements are characterized. These factors include both receiver site effects and source effects on *P/S* ratios. The study of site effects will be focused on arrays where we have seen site variations in *P/S* ratios,

including the Scandinavian regional arrays (NORES, FINES, ARCES, FINES), and other new arrays in the International Monitoring System. The variance in the *P/S* ratio around regional arrays and large aperture arrays reveals the extent to which site affects cause variations in *P/S* ratios around different arrays in different regions.

Regional Array Recordings of Underwater Explosion Group in the Gulf of Bothnia

We have chosen as an initial study to analyze a group of events located in the Gulf of Bothnia that have been shown in a previous study (Baumgardt, 1999) to be several underwater explosions that occurred there in a single day on 18 May 1996. These events were discovered by searching the Reviewed Event Bulletin (REB) of the Prototype International Data Center (PIDC) for events located in offshore areas. The locations and the propagation paths to Scandinavian regional seismic arrays are shown in Figure 1. Baumgardt and Der (1998) previously discovered other events in the Gulf of Bothnia and showed that their spectral and cepstral characteristics were consistent with they're being underwater explosions. Baumgardt (1999) described a cepstral modeling and inversion approach for inferring the depth and yield of underwater explosions by inverting cepstra for underwater explosions. For the 18 May 1996 group of presumed underwater explosions, we found that the cepstra were very similar, and the resulting inversions gave very similar results. The yields ranged between 141 to 183 kg and depths from 69 to 72 m. These depths were consistent with the known bathymetric depths in the Gulf of Bothnia. There may have been some correlation between local magnitude and yield, since the cepstra for events with local magnitudes of 3.6 gave the higher yields of between 179 to 183 kg whereas the 3.4 to 3.5 events give yields between 141 and 165 g.

Figures 2 and 3 show a plots of the waveforms at the different array elements at FINES and NORES, respectively, from on of the 18 May 1996 events. The FINES array elements are between 304 and 306 km from the events, and *Pn* and *Pg* are difficult to separate there. NORES, on the other hand, at distances between 481 and 484, had clearly observable *Pn* and *Pg* phases. Both arrays recorded strong *Lg* waves from all the events. Figure 4 shows bandpass filtered waveforms recorded at the center elements of each array. These plots show that the range of frequencies for the highest signal-to-noise ratios is between 1.5 and 18 Hz for FINES and 1.5 and about 12 Hz for NORES. The peaking of the signal-to-noise ratios in the 2 to 4 Hz band at both arrays is due to the spectral modulations produced by the bubble pulse and surface reflections, discussed above.

Analysis of Site Variance of *P/S* and *P/S* Ratios

We measure the *P/S* and *P/S* ratios off of filtered waveform envelopes computed by calculating the RMS amplitudes in 1 second windows shifted down the traces. Figure 5 shows the array-stacked envelopes, called incoherent beams, with the phase picks shown. These same envelopes have been computed for each array element at NORES and FINES and the maximum phase amplitudes were measured in a 5 second window following the *Pn*, *Pg*, and *Lg* phase picks. *Pn*, *Pg*, and *Lg* amplitudes were determined in all the filter bands shown in Figures 4 and 5. *P/S* and *P/S* ratios were computed only when the signal-to-noise ratios exceeded 3. These measurements were made for 8 events in the Gulf of Bothnia.

Figure 7 shows examples of scatter plots of *P/S* ratios in the 3 to 6 Hz band at FINES and NORES array elements plotted versus the amplitudes of *Pn* and *Lg* for one of the events. These plots show that *P/S* amplitude ratios have a range of about .3 to .5 log units, or between a factor of 2 to 3. Moreover, the plots of *Pn/Lg* versus *Pn* amplitudes indicate higher correlation than those versus *Lg* amplitudes. This indicates that the *Pn* amplitude variations around both FINES and NORES control the *Pn/Lg* amplitude variations.

To explore this more rigorously, we apply a two-way analysis of variance (ANOVA2) test for the variation in the amplitudes of *Pn*, *Pg*, and *Lg* and the amplitude ratios of *Pn/Lg* and *Pg*/ *Lg* for the 7 Gulf of Bothnia events. In ANOVA2, we fit the following model to the amplitudes and amplitude ratios:

$$y_{ijk} = \mu + \alpha_{,j} + \beta_{i,} + \varepsilon_{ijk}$$

where y_{ijk} are the array element amplitudes or amplitude ratios, μ is the mean of all the data, $\alpha_{,j}$ is the source term, $\beta_{i,}$ is the site term, and ε_{ijk} is the error term. This model is fit to the logarithms of amplitudes and amplitude ratios where it is assumed that the amplitudes and ratios are log-normal and dependent on both the additive event and the site effects both of which are specified to have a zero sum. The errors are assumed to be normally distributed. ANOVA2 in essence tests the hypothesis that the data come from the same population

with a common mean (Johnson and Wichern, 1988). In this study, we focus on the variations in the site terms and ignore for the time being the significance tests on the commonality of the mean.

Figure 7 shows the configurations of the FINES and NORES arrays with color-coding for the different array elements, grouped by rings. Figure 8 shows the site terms for NORES in the 2-4 Hz, 3-6 Hz, and 4.9 to 9 Hz frequency bands obtained by this analysis for *Pn/Lg* amplitude ratios and *Pn* and *Lg* amplitudes. The histograms refer to the site term values for the different array elements in the rings color-coded as in Figure 7. These plots show that the greatest variability in *Pn/Lg* ratios occurs for the NORES sensors that have the greatest spatial separation or aperture, i.e, rings C and D. The *Pn* phase also has correspondingly large systematic variation that is largest for the sensors in the rings with the largest aperture. The *Lg* site terms are relatively small, except for the 4.5 to 9 Hz band, and essentially independent of the separation of the sensors. The same result resulted for the *Pg/Lg* amplitude ratios, and *Pg* and *Lg* amplitudes at NORES shown in Figure 9. Finally, Figure 10 shows the variation in site terms for the *Pn/Lg* ratios at FINES. These again show the same systematic variations. The source terms had similar variation, which is on the order of 0.3 to 0.5 in the log of the *Pn/Lg* and *Pg/Lg* amplitude ratios.

CONCLUSIONS AND RECOMMENDATIONS

This paper has described a method for analyzing site variance in regional *P/S* ratios and a preliminary application to data recorded by Scandinavian regional arrays for a group of underwater explosions in the same location. We have found that the amplitude ratios *Pn/Lg* and *Pg/Lg* varied by between a factor of 2 to 3 around the elements of both NORES and FINES regional arrays in all the frequency bands with signal-to-noise ratios in excess of 3. This variation, which occurs only over a spatial aperture of 3 km for both arrays, appears to be systematic, with the largest variations between sensors with the largest separation, which is up to 3 km, and correlates more strongly with *Pn* and *Pg* amplitudes than with *Lg* amplitudes. *Lg* appears to be more stable than *Pn*, and *Pg*, or less sensitive to site effects, except perhaps in the higher frequency bands, where stronger but more random variations in *Lg* site terms are observed.

In this project, we will apply this same analysis for other groups for events, including mine blasts and earthquake groups, and investigate if these same kinds of variations occur for other source types. Also, this same analysis will be applied to arrays in other regions, including more tectonically active regions than the Scandinavian shield region.

For source mechanism effects, we have been concentrating on earthquakes in the Zagros thrust belt of Western Iran, where, in a previous study (Baumgardt, 1996), azimuthal variations in *P/S* ratios have been observed. In that study, we speculated that variations may be explained by the predominantly thrust mechanism of the earthquakes in the Zagros, but only a limited number of waveforms were examined. For this study, an extensive database of waveforms of regional recordings of Zagros events of different magnitudes and depths has been collected. Regional *P/S* ratios have been measured on these events and ANOVA is being used to determine to what extent the azimuthal variance can be partitioned between source effects, including focal mechanism and depth of focus, and propagation path effects. The results of this study will quantify the factors, other than propagation-path effects, that may bias the use of *P/S* ratios for seismic discrimination.

REFERENCES

Baumgardt, D.R. (1993). Regional characterization of mine blasts, earthquakes, mine tremors, and nuclear explosions using the Intelligent Event Identification System, Final Report to ARPA, SAS-TR-94-12, ENSCO, Inc., Springfield, VA.

Baumgardt, D.R. and Z. Der (1995). Investigation of the transportability of the *P/S* ratio discriminant to different tectonic regions, Scientific Report No. 1, *PL-TR-94-2299*, 6 December 1994, ENSCO, Inc.

Baumgardt, D.R. (1996). Investigation of *Lg* blockage and the transportability of regional discriminants in the Middle East, *Scientific Report No. 1, Pl-TR-96-2294*, ENSCO, Inc., Springfield, VA.

Baumgardt, D.R. (1999). Characterization of underwater explosions by spectral/cepstral analysis, modeling, and inversion, Annual Report submitted to DTRA, November, 1999, ENSCO, Inc., Springfield, VA.

Baumgardt, D.R. and Z. Der (1995). Investigation of the transportability of the *P/S* ratio discriminant to different tectonic regions, Scientific Report No. 1, *PL-TR-94-2299*, 6 December 1994, ENSCO, Inc.

Baumgardt, D.R. and Z. Der (1998). Identification of presumed shallow underwater chemical explosions using land-based regional arrays, *Bull. Seism. Soc. Am.* , **88**, 581-595.

Fan, G-W., T. Lay, and S. Bottone (2001). Path corrections for source discriminants: a case study of two International Seismic Monitoring stations, submitted to *Pure and Applied Geophys.*

Fisk, M., H.L. Gray, and G.D. McCartor (1996). Regional event discrimination without transporting thresholds, *Bull. Seism. Soc. Am.*, 1545-1558.

Hartse, H.E., S.R. Taylor, W.S. Phillips, and G.E. Randall (1997). Regional event discrimination in central Asia with emphasis on western China, *Bull. Seism. Soc. Am.*, **87**, 551-568.

Johnson, A, .and D.W. Wichern (1988). *Applied Multivariate Statistical Analysis*, Prentice Hall, Englewood Cliffs, New Jersey.

Ringdal, F., E. Kremenetskaya and V. Asming (2000). Observed characteristics of regional seismic phases and implications for *P/S* discrimination in the European Arctic, submitted to *PAGEOPH Special Issue on CTBT Monitoring*.

Xie, J. and H. Patton (1999). Regional phase excitation and propagation in the Lop Nor region of Central Asia and implications for the physical basis of *P*/*Lg* discriminants, *J. Geophys. Res.*, **104**, 941-954.

Zhang, T., S.Y. Schwartz, and T. Lay (1994). Multivariate analysis of waveguide effects on short-period regional wave propagation in Eurasia and its application in seismic discrimination, *J. Geophys. Res.*, **99**, 21929-21945.

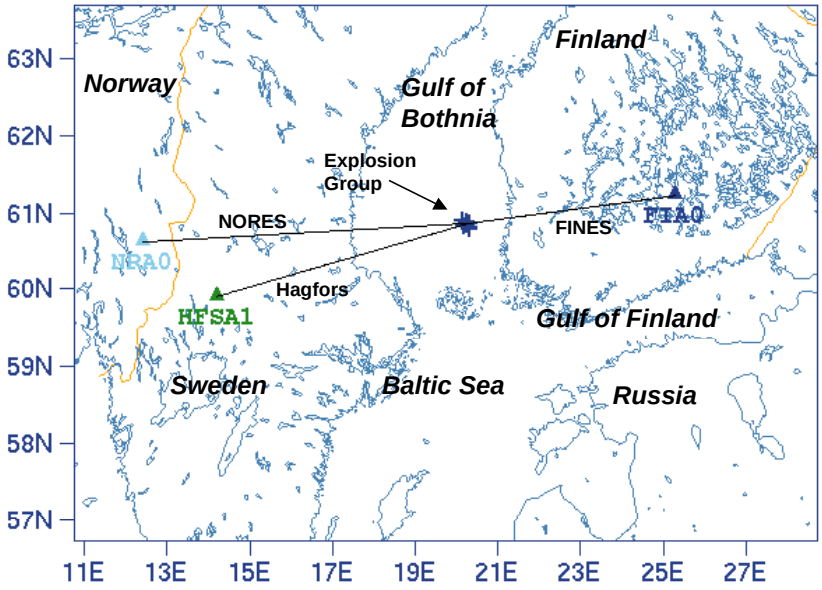

Figure 1. Map showing location of presumed underwater explosions recorded by the three seismic arrays in Scandinavia, NORES, FINES, and Hagfors.

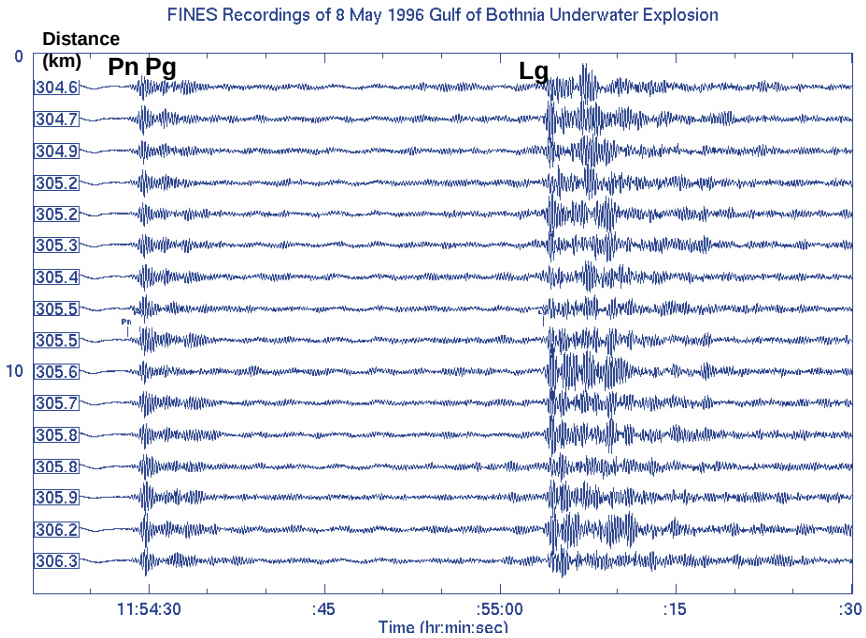

Figure 2: Waveforms recorded at FINES from one of the underwater explosions in the Gulf of Bothnia.

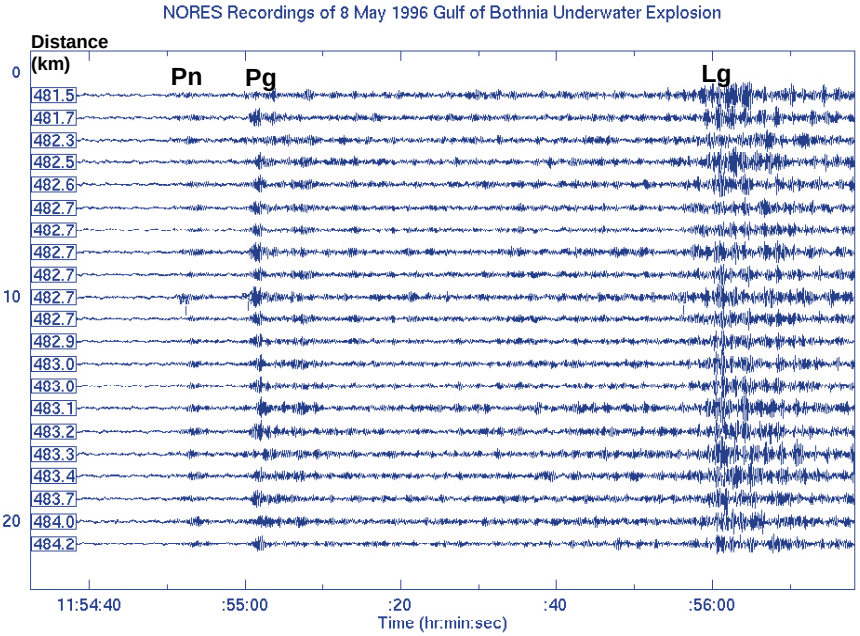

Figure 3: Waveforms recorded at NORES from one of the underwater explosions in the Gulf of Bothnia.

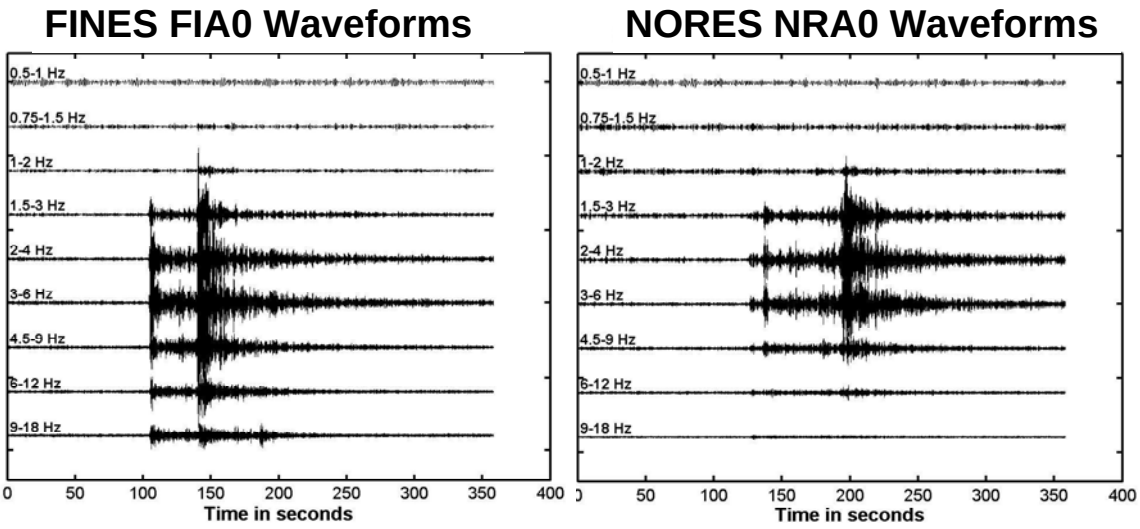

Figure 4: Bandpass filtered waveforms recorded at the center elements of the FINES arrays (left) and the NORES array (right) from one of the Gulf of Bothnia explosions.

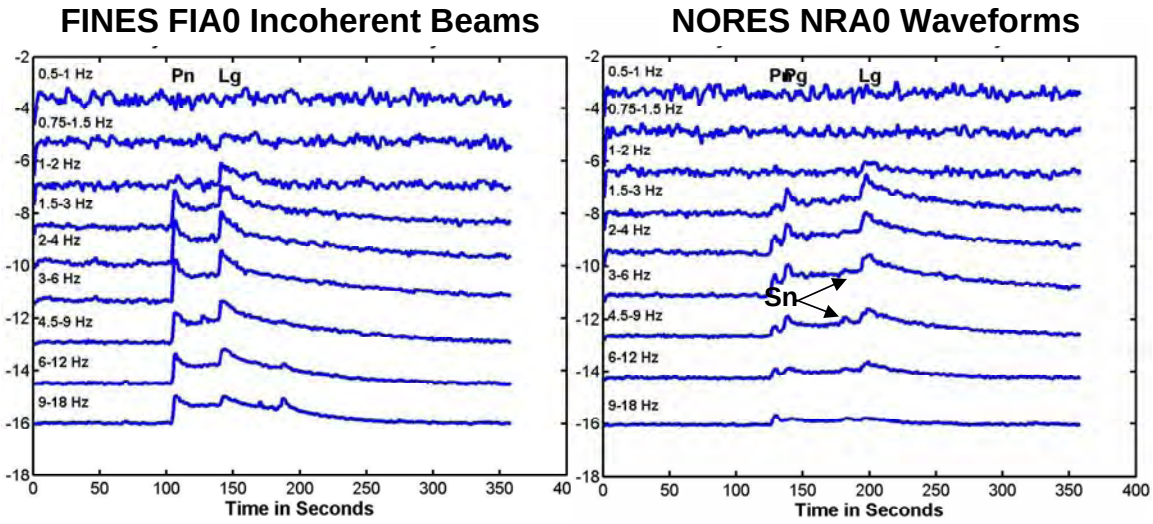

Figure 5: Log RMS incoherent beam plots of the filtered waveforms for FINES (left) and NORES (waveforms). Regional phases picked on waveforms are indicated at the top. Amplitudes of phases are measured off maximum values of RMS envelop plots of each channel and on incoherent beams.

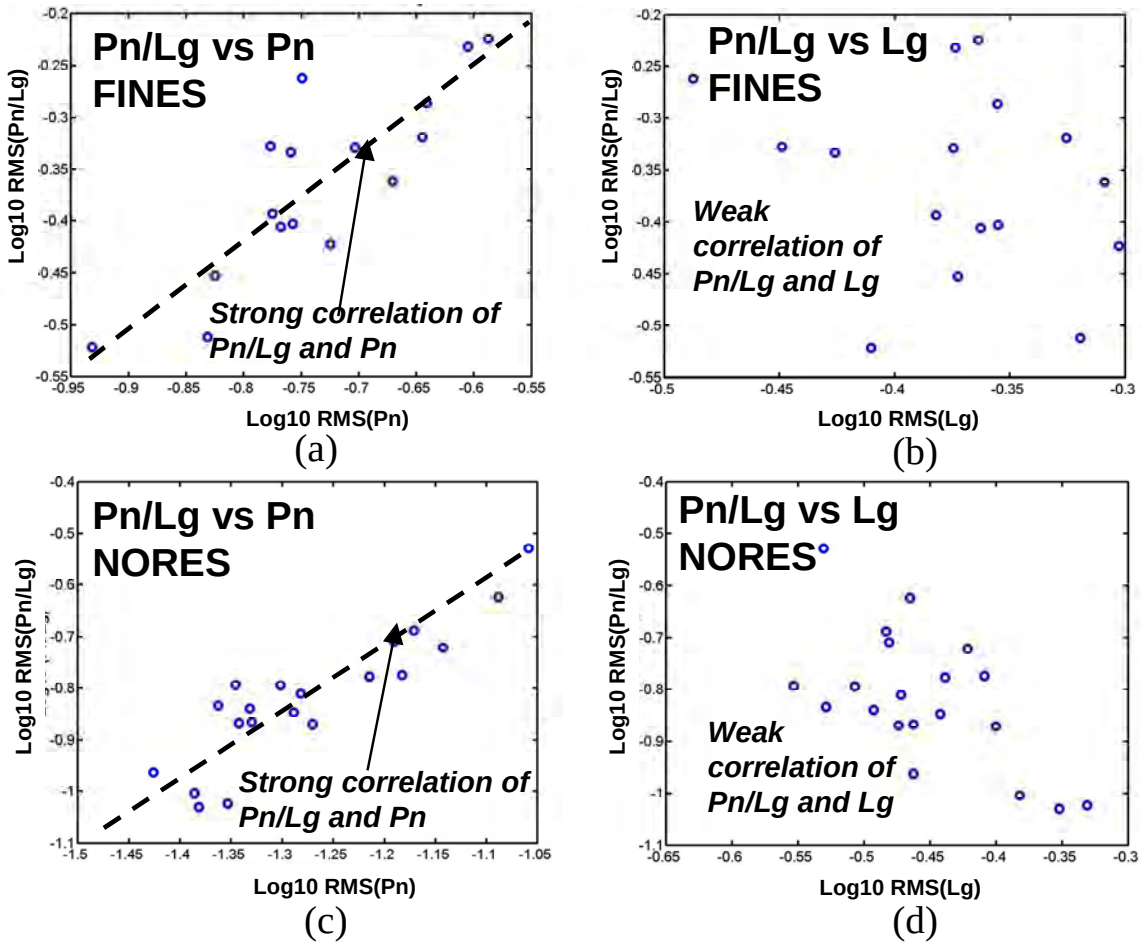

Figure 6: Scatter plots of the *Pn/Lg* ratios versus *Pn* and *Lg* amplitudes in the 3 to 6 Hz frequency band for the regional arrays for one of the Gulf of Bothnia underwater blasts. (a), (b) Scatter plots for FINES. (c), (d) Scatter plots for NORES.

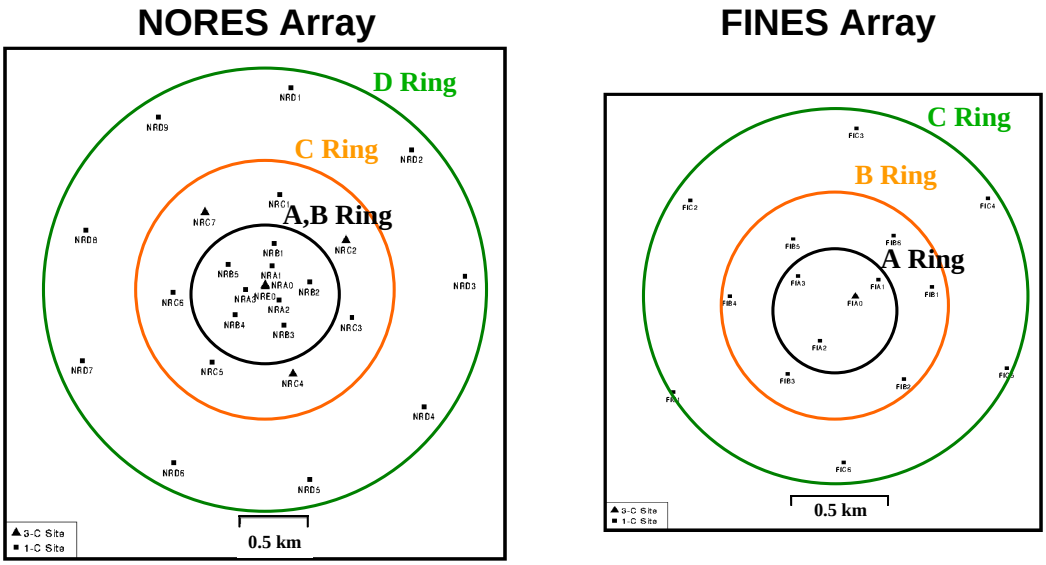

Figure 7: Site layouts for the NORES (left) and FINES array. Colors green, red, and black refer to large, medium, and small aperture rings, respectively, for the arrays.

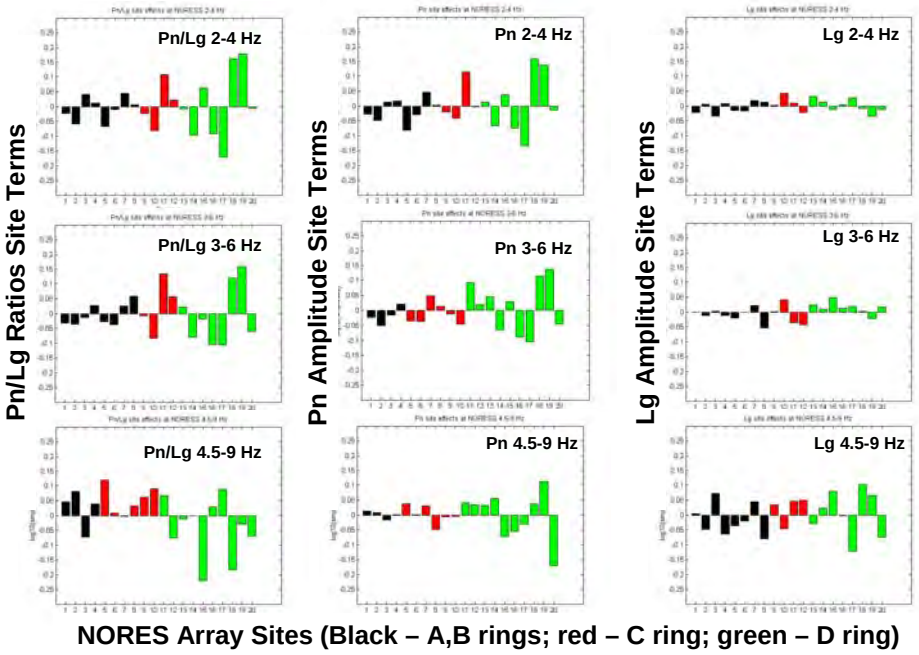

Figure 8: ANOVA2 path terms for *Pn/Lg* amplitude ratios, *Pn* and *Lg* amplitudes for NORES in three frequency bands.

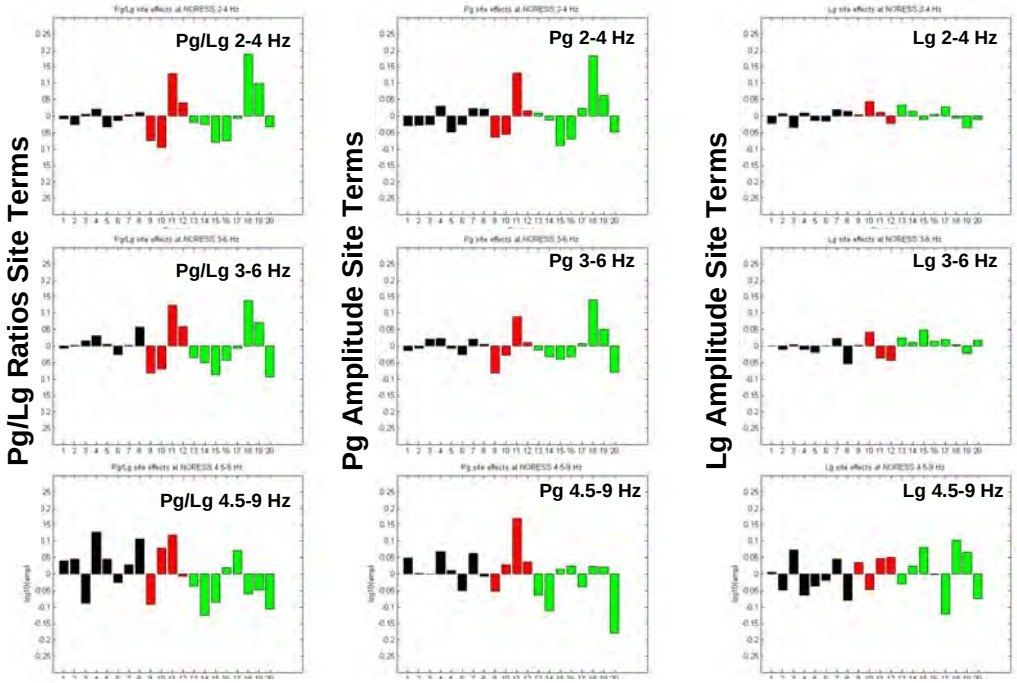

Figure 9: ANOVA2 path terms for *Pg/Lg* amplitude ratios, *Pg* and *Lg* amplitudes for NORES in three frequency bands.

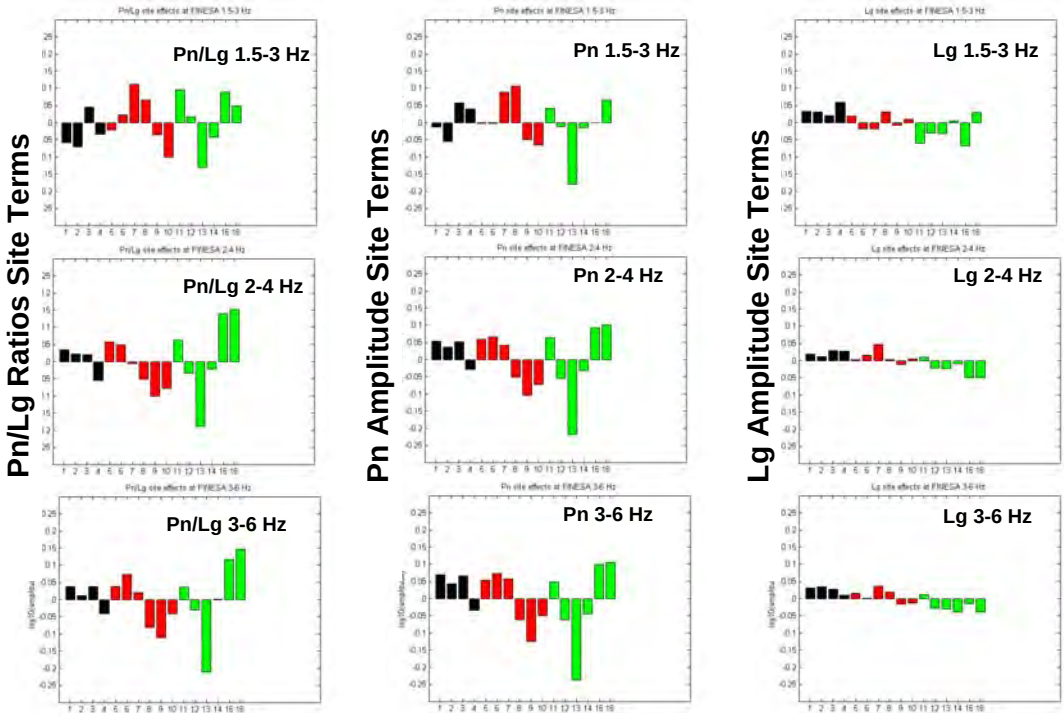

Figure 10: ANOVA2 path terms for *Pn/Lg* amplitude ratios, *Pn* and *Lg* amplitudes for FINES in three frequency bands

IDENTIFICATION OF ROCKBURSTS AND OTHER MINING EVENTS USING REGIONAL SIGNALS AT INTERNATIONAL MONITORING SYSTEM STATIONS

Theron J. Bennett and Margaret E. Marshall

Science Applications International Corporation

Sponsored by Defense Threat Reduction Agency

Contract No. DSWA01-98-C-0153

ABSTRACT

Rockbursts present some unique challenges for seismic event identification at low-magnitude monitoring thresholds. Teleseismic discriminants, including traditional determination of focal depth and M_S-versus-m_b, are not likely to work for these types of sources. Since many rockbursts are small, their identification depends heavily on observations from a few regional stations. This research program is designed to identify rockburst regions with respect to their significance to nuclear test monitoring, assess the capability of prototype International Data Centre (PIDC)/IDC screening procedures for application in rockburst regions worldwide, and determine ways to improve event identification for such mining regions.

During the time period from 1995 to 2000, more than 1100 events were reported in the Reviewed Event Bulletin (REB) within 50 km of 43 historical rockburst sites. Most of these had magnitudes in the range 3 to 4. No REB events were located in proximity to 61 other rockburst sites, although small events (below the REB threshold) may be occurring in those areas. Waveform data from regional International Monitoring System (IMS) stations for Reviewed Event Bulletin (REB) events in each rockburst area are being collected and analyzed. For many of these events, we have been able to establish better ground truth information using local and regional seismic bulletins or, in some cases, information reported from the mines or other agencies; and we have been seeking to establish ground truth information for events in more mining areas. This ground truth information is valuable for event location (as some of the small events are significantly mislocated) and in some cases for identifying event source mechanisms, which permits better understanding of signal variability.

We have been carefully analyzing the regional signal characteristics for REB events from several of the more active rockburst areas. We have found differences and variability in the regional signals between events as well as between source types. Although the evidence seems to indicate that on average L_g/P and S/P ratios are larger, particularly at high frequencies, for earthquakes and rockbursts than for underground nuclear tests, there appears to be considerable variability between events and some overlap. In particular, we have found regional signals from underground nuclear explosions which have L_g/P_g and L_g/P_n ratios at high frequencies (4-6 Hz and 6-8 Hz bands) larger than similar ratios for rockbursts and mineblasts and as large as those for some earthquakes, under similar propagation conditions. This could lead to identification mistakes or missed events if these events were screened out. This problem may be solved by more careful analyses as well as alternative identification methods. We are continuing to investigate alternative regional discriminant measures (including regional M_S/m_b, SP/LP, L_g spectral ratios, signal complexity, P-wave first motion) to supplement current event screening and source identification methods for mining events. Our improved ground truth data for rockbursts and other seismic sources in their vicinity have also revealed some potential questions related to identification of non-nuclear blasts. Proposed IDC regional screening procedures based on high-frequency P/L_g ratios screen out some known mineblasts. While this result may be reasonable in principle, it is indicative of a range in behavior from chemical blasts, which is related to source mechanism differences, and could be a cause for false alarms, missed events, or potential evasion. A broader range of regional discriminants may be useful for more precise identification of some of these chemical blasts.

KEY WORDS: rockburst, mining, seismic, regional, identification, discrimination, screening, IMS, IDC

OBJECTIVE

Rockbursts and other mining sources present unique problems for discriminating and screening seismic events. Shallow focal depths and anomalous source mechanisms from these mining events often produce seismic signals similar to those of underground nuclear explosion tests. Because of their small magnitudes, the strongest and most distinctive signals for these events tend to be those recorded at regional stations. The goal of this research project has been to analyze the results of PIDC/IDC screening procedures in mining areas with a known history of rockbursts and to develop better discrimination techniques using the signals observed at regional IMS stations for seismic source screening.

RESEARCH ACCOMPLISHED

Mining-induced seismic activity occurs in mining regions all over the world. During prior stages of this research program, we identified 104 historical rockburst areas worldwide (cf. Figure 1), although other mining areas may also be subject to such events. We collected parametric information and IMS station waveforms for 1108 events reported by the PIDC/IDC during a five year monitoring period (1995-2000) for 43 of these areas; activity in the other areas appears to be absent or below the PIDC/IDC detection threshold. We also analyzed the PIDC/IDC screening results for events from the vicinity (within 50 km) of each of the known rockburst areas. Screening procedures based on teleseismic discriminants (including M_S-versus-m_b and focal depth estimates) are generally found to be ineffective for these mining areas, mainly because the events have magnitudes below the screening threshold or because the data are insufficient to form the signal measurements needed to determine the screening parameters. However, we also found indications that LP excitation (and hence M_S) is often low for rockbursts, which makes them appear explosion-like with respect to M_S-versus-m_b; and their focal depths are in the same range as underground nuclear tests. Therefore, screening methods based on alternative measures, which discriminate other kinds of source differences, and in particular on regional discriminants are needed for these mining events. In addition to P/L_g ratios at high frequencies, which are currently proposed for use by the PIDC/IDC in event screening, other potential regional discriminants that may prove useful include regional P-wave complexity, P-wave first motions, L_g spectral ratios, and a regional version of M_S-versus-m_b.

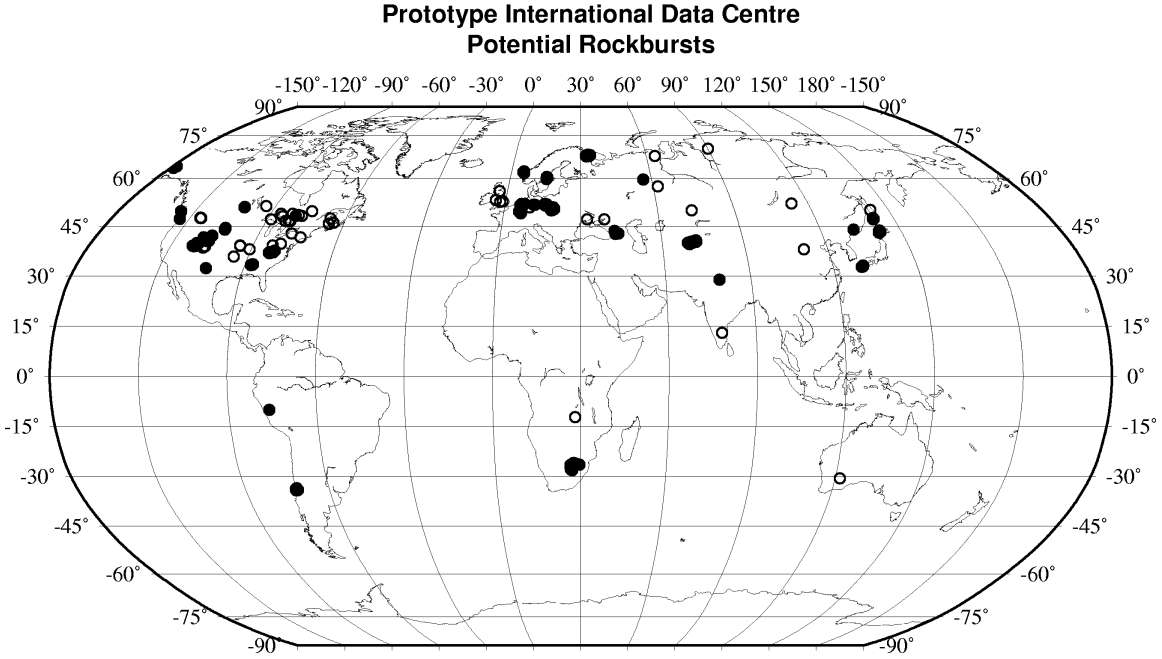

Figure 1. Locations of 1108 events in 1995 - Present PIDC REB database that are within 50 km of 104 historical rockburst sites. Solid circles indicate sites with at least one REB event, and open circles show sites with none.

We have been looking closely at the signals recorded at regional IMS stations from seismic events in rockburst areas to identify characteristics which can be used for source discrimination. These events include rockbursts and mine collapses, but also nearby mining explosions and earthquakes. For comparison, we have also selected several older underground nuclear explosion tests recorded at regional distances. Unfortunately, the latter observations are not available at regional IMS stations, because very few nuclear tests have occurred while the IMS network has been operational. However, many historical nuclear explosions have been recorded at high-quality digital stations [e.g. the Lawrence Livermore National Laboratory (LLNL) seismic network]; and these provide the best basis for comparison with signal characteristics at similar regional distances for IMS stations.

In our initial studies of signal characteristics, we looked at more general properties of events from several of the more active rockburst areas. These included coal and copper mining areas in Poland, several deep gold mining areas in South Africa, and coal mining areas in the Kola peninsula of Russia. More recently, we have focused on events with better ground truth including mining areas in the western U.S. and Europe. By looking at events with better ground truth and analyzing more carefully potential discriminant measures, we hope to develop better understanding of the variability between source types and the regional signals they produce. In some of these areas, different types of seismic sources (viz. mineblasts, rockbursts, and earthquakes) may occur in the same mining area. However, it is sometimes difficult to identify events with regional signals above background noise for rockbursts and other source types that have similar propagation paths to regional IMS stations. This is certainly the case for comparable nuclear test sources, as described above. One option is to attempt to correct regional signal amplitude measurements for propagation differences (cf. Bennett et al., 1997; Fisk et al., 2000), so as to isolate source effects; however, such corrections are expected to have strong regional dependence and may, therefore, lead to results which mix propagation effects with source differences, if the propagation corrections are inaccurate. In this study, we have tried to follow an alternative approach using more direct comparisons between regional signals from different sources at similar observation distances and, where possible, with propagation paths in the same or similar tectonic regions.

The region where this approach seems most appropriate is the western U.S. Within the western U.S. the most active rockburst areas (cf. Figure 2) are in the Wasatch Plateau-Book Cliffs region of southern Utah, where the events are generated in association with underground coal mining. Another area of rockbursts occurs in association with trona mining in southwestern Wyoming, where infrequent mine collapses have sometimes been quite large. Finally, there are some other scattered areas (viz. in northern Idaho, western Washington, and southern New Mexico) where small mining-induced events occur but are not usually detected at regional IMS stations. Most mines utilize chemical explosions to some degree in normal operations; however, such mineblasts are often small, and only a relatively small number of these events (usually strip-mine blasts) are large enough to be detected at IMS stations. Figure 2 shows several mineblasts in the western U.S. that were detected and located by the PIDC/IDC in southwestern and eastern Wyoming, southern Montana, northeastern Colorado, and Utah. Ground truth from United States Geological Survey (USGS) mining reports (cf. Dewey and Leeds, 2000) and regional seismic bulletins (e.g. University of Utah) can often provide more precise locations. The ground truth locations often show tighter clustering around the known mines; and, in some cases, indicate significant mislocation. Underground nuclear explosions in southern Nevada have in some cases been recorded at seismic stations common to the PIDC/IDC, and these events recorded at similar regional distances provide an excellent basis for comparison to other source types and regional discriminant analysis. Finally, there are numerous earthquakes in the region, including many with ground truth from regional seismic bulletins; and these too have available waveform data from regional IMS stations during this time period. In Figure 2 we show several earthquakes in proximity to the Utah rockburst area, and others are located adjacent to the Nevada Test Site which provide good regional signals for use in these discrimination analyses.

Direct comparisons of regional signal characteristics for identifying screening discriminants are somewhat more difficult for ground truth events from Europe. Although we still have rockbursts, chemical explosions, and earthquakes recorded at some regional European IMS stations at similar distances, the propagation paths are sometimes more complex, particularly at larger distances; and there are no nuclear explosion tests which can provide comparisons for this or similar tectonic regions. Figure 3 shows a comparison of event locations determined by the PIDC/IDC for selected rockbursts, earthquakes, and

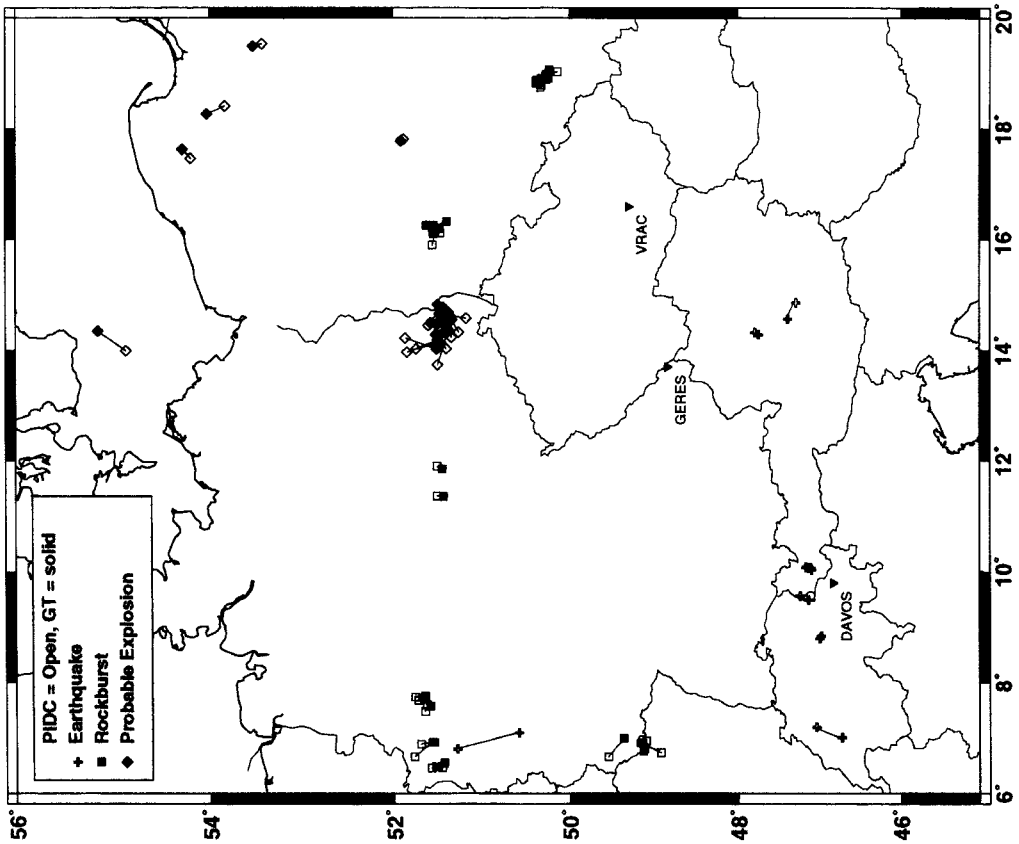

Figure 3. Comparison of PIDC and ground truth (GT) locations of selected rockbursts, explosions and earthquakes recorded at the IMS regional stations in Europe.

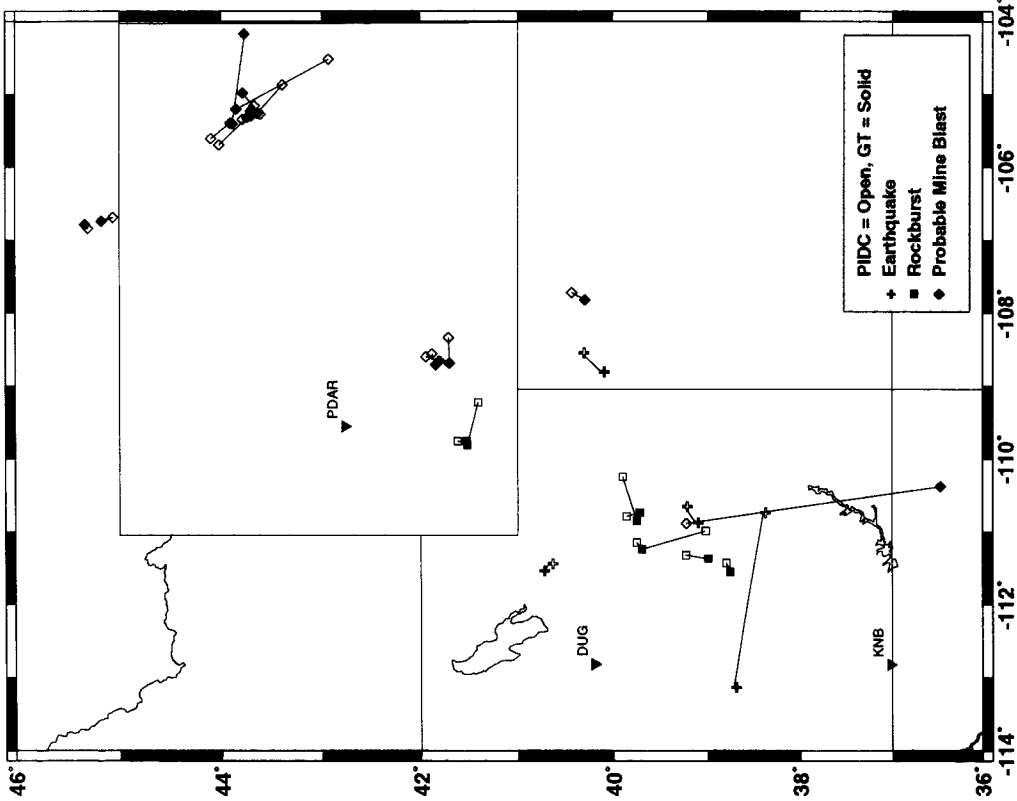

Figure 2. Comparison of PIDC and ground truth (GT) locations of selected rockbursts, explosions and earthquakes recorded at the IMS regional stations in the western U.S.

chemical explosions in Europe. The most active areas for rockbursts are shown by the two event clusters in Poland located in the copper mining area near Lubin (to the west) and in the Upper Silesia coal mines (to the east). There have also been infrequent, but large, mine collapses in eastern Germany near Völkerhausen and frequent, but small, rockbursts in the Ruhr valley coal mines of western Germany. Areas of mineblasts, including many reported in the PIDC/IDC REB, are known in eastern Germany; and several other chemical blasts with good ground truth are known in Poland. There are also several sources of known natural earthquakes scattered throughout Europe, with some of the larger events located in the Alps. Coverage by local seismic networks throughout Europe is good; and we have been using information compiled by the Federal Institute of Geosciences and Natural Resources in Hanover, Germany and by the Institute of Geophysics of the Polish Academy of Sciences to establish better ground truth for many of the REB events. In Figure 3 we show the location differences between the REB and local network ground truth; the differences are generally small with largest differences occurring for earthquakes. In general, the ground truth locations tend to show tighter clustering around known mines.

Over the past year, we have been looking more closely at the regional signals at IMS and similar high-quality stations from several of these events with better ground truth. As noted above, P/S or P/L_g amplitude ratios based on observations at regional stations have been identified as one of the most promising regional discriminant measures for use in event screening (cf. Taylor et al., 1988; Bennett et al., 1992; Fisk et al., 1999). As we have shown in prior reports (cf. Bennett et al., 1996, 1999, 2000), there also appear to be systematic differences in L_g/P ratios between rockbursts and underground nuclear tests; and the differences are often most apparent within limited frequency bands and most notably at higher frequencies. We have shown in prior studies that L_g/P_g ratios at IMS stations are, on average, larger in high-frequency bands for rockbursts and earthquakes than for underground nuclear explosions and mineblasts. However, we also found some evidence of scatter for individual events; and we have, therefore, been looking at alternative regional discriminants for problem events.

Figure 4 shows the regional signals at ELK from different source types in the western U.S., including a Utah rockburst, a Utah earthquake, the GORBEA nuclear test, and a southern Nevada earthquake, all recorded at similar distances (between about 400 and 435 km). We show the bandpass filtered signals for two passbands (viz. 2-4 Hz at the top and 6-8 Hz at the bottom). As noted in the preceding paragraph, GORBEA is one explosion which appeared to produce an anomalous result when analyzing the L_g/P_g ratio at high frequencies; and, in fact, we see in Figure 4 that the L_g/P_g ratios for GORBEA are greater than 1.0 (unlike the average behavior for NTS explosions for which the ratios are smaller than 1.0). In Figure 4 the biggest differences appear to be in the more energetic P_n signal for GORBEA, which is most notable in the higher frequency band. So, it seems likely that more careful analyses of the regional P_n may, in this case, be diagnostic; however, it is also noteworthy that P_n for some of the other source types has relatively low signal-to-noise, particularly in higher frequency bands. Therefore, L_g/P_n ratios may present a different kind of problem for application to event screening.

Considering the relative strength of P_n for the nuclear explosion in Figure 4 and prior studies suggesting P first motion (e.g. Pomeroy et al., 1982) or regional P-wave complexity (e.g. Blandford, 1993) as potential discriminants, we have looked more closely at the initial P signals recorded at regional IMS stations for some of these events. Blandford found that mining explosions in Scandinavia, when high-pass filtered (with low-frequency corners at 1 Hz and 2 Hz), produced impulsive initial P over a distance range from 200 to 720 km; while earthquakes from the same region and in the same distance range with the same processing produced emergent P arrivals. We have attempted to apply similar signal processing to the P_n signals from the same western U.S. events (i.e. Utah rockburst, two earthquakes, and GORBEA nuclear test) as those shown above in Figure 4. At the top of Figure 5, we show the initial P signals at station ELK after high-pass filtering with the low-frequency corner at 1 Hz; and at the bottom, alternative processing after high-pass filtering with the corner at 4 Hz. Several observations can be made from these records. First, the impulsive nature of the initial P is difficult to discern in these records; although the initial P for the GORBEA nuclear explosion has higher signal-to-noise than for the other source types, the regional P for GORBEA and the other events as well appears to show a gradual build up over the first several seconds after onset. Furthermore, while the P-wave first motion for GORBEA appears to be clearly compressional, first motions for all the other events are ambiguous. There are no unambiguous dilatational P first motions

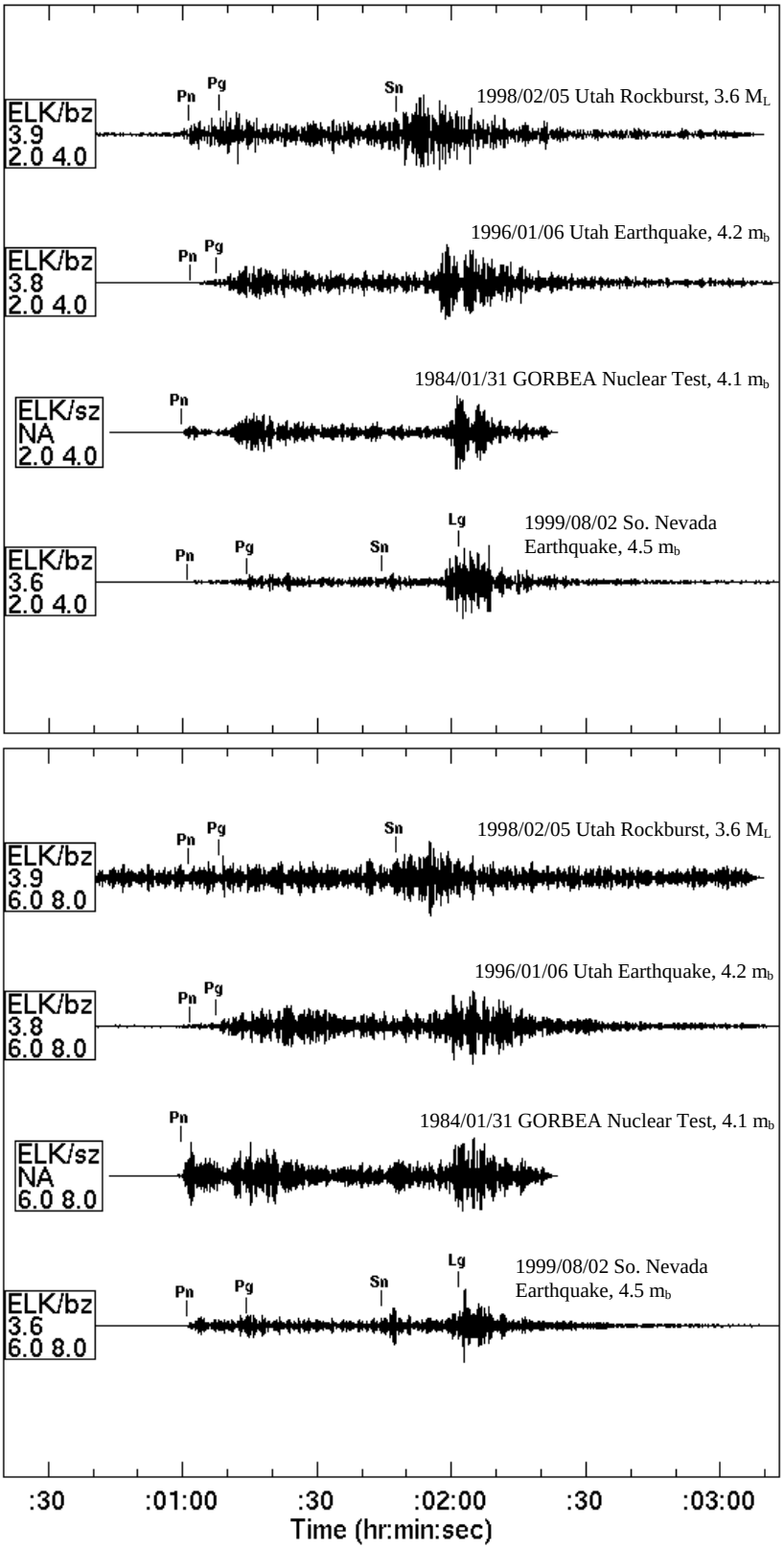

Figure 4. Comparison of regional signals at ELK from Utah rockburst, Utah earthquake, NTS nuclear explosion, and southern Nevada earthquake at similar distances (400 - 435 km) in two passbands: 2-4 Hz (top) and 6-8 Hz (bottom).

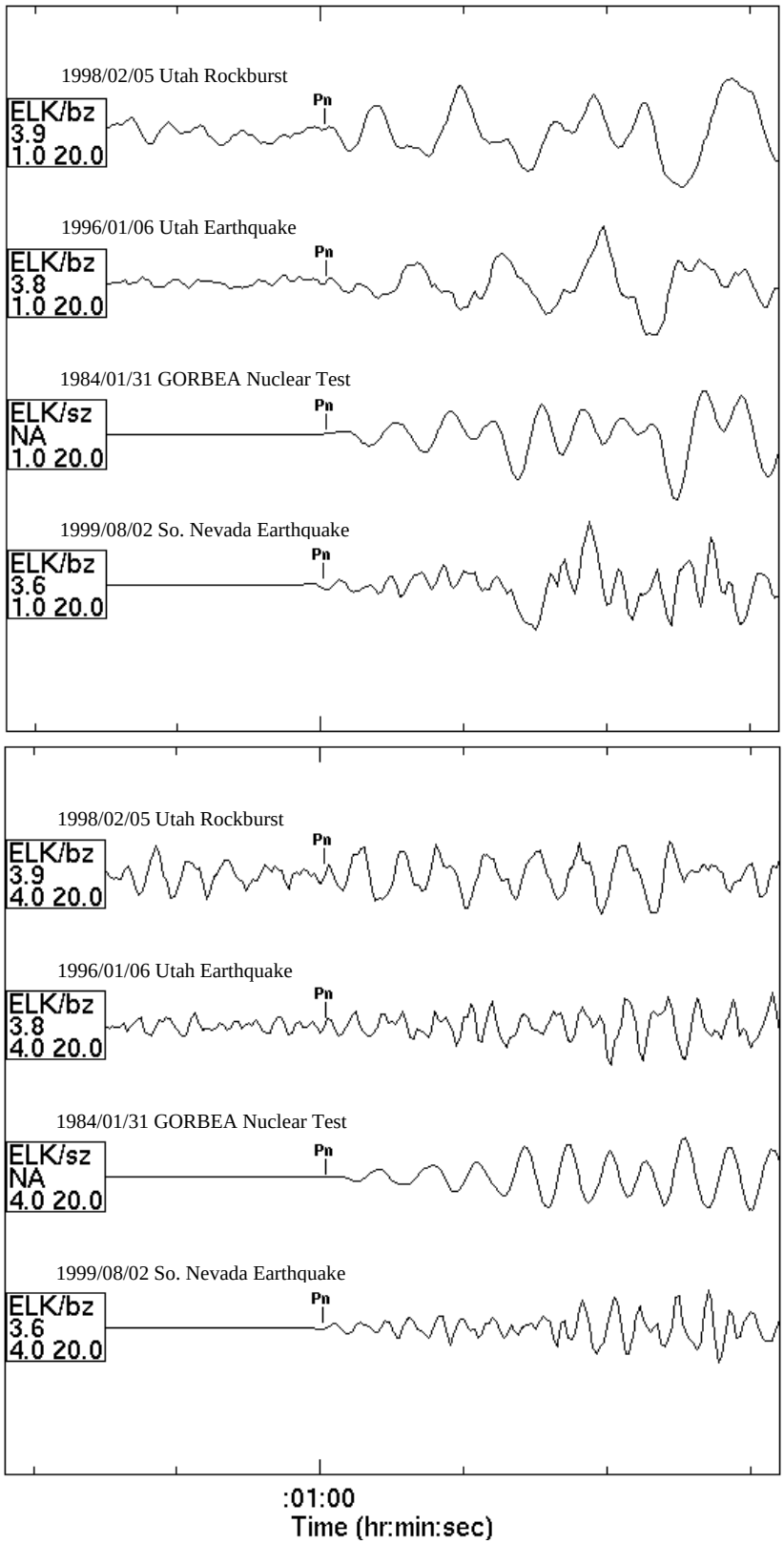

Figure 5. Comparison of initial regional P signals at ELK from Utah rockburst, Utah earthquake, NTS nuclear explosion, and southern Nevada earthquake at similar distances (400 - 435 km) for two highpass filters: 1 Hz corner (top) and 4 Hz corner (bottom).

which might allow discrimination or screening out of the remaining three events. This result does not look promising for screening events in this magnitude ($m_b \leq 4$) and distance ($R \geq 400$ km) range for tectonically active propagation environments like the western U.S. based on P first motions. We also see little evidence of greater complexity in the initial regional P signals for the rockburst and earthquakes compared to the nuclear explosion, although we are continuing to look at these and other events using systematic measures in different frequency bands which might permit some discrimination.

Another regional discriminant which we have been investigating for screening rockbursts and other mining events is relative long period (LP) or M_S excitation. Although our past studies (cf. Bennett et al., 1996) have suggested relatively weak M_S from rockbursts, the majority of mining-induced seismic events are too small to produce measurable LP Rayleigh waves at teleseismic stations; so we lack reliable measurement samples on which to base M_S-versus-m_b screening for rockbursts. We have been continuing to look for observations of LP Rayleigh wave signals at regional distances from rockbursts and other source types which may be useful for screening or determining potential screening problems. Figure 6 shows LP signals for the same four western U.S. events at station ELK after bandpass filtering for the passband 0.03 to 0.10 Hz. In this distance range the two earthquakes appear to have clear LP Rayleigh signals with dominant periods of about 12 seconds. There appears to be little evidence of LP Rayleigh in the corresponding rockburst record; and, unfortunately, the available nuclear explosion signal is cutoff prior to the expected LP Rayleigh wave arrival time. Similar processing of several other Utah rockbursts also showed no indication of LP Rayleigh signals above background noise. However, we have seen LP Rayleigh waves in regional records from some of the southwestern Wyoming mine collapse events, although the LP signals again appear weak relative to m_b. We are continuing to look into better procedures to extract M_S and determine M_S-versus-m_b screening from regional signals for these small events.

In addition to western U.S., we have been looking more closely at the same kinds of regional IMS station measurements from European events with good ground truth. Figure 7 shows a comparison of bandpass filter analyses of regional signals at GERES for an eastern Germany mine collapse (at the top) and an eastern Germany mineblast (bottom). The figure shows roughly similar L_g/P ratios in most frequency

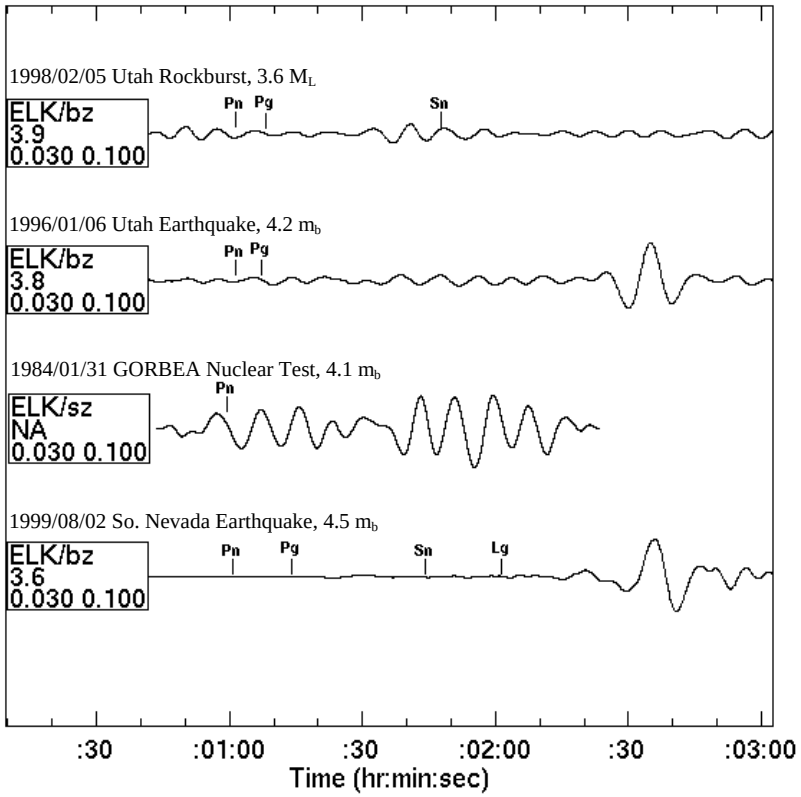

Figure 6. Comparison of LP regional signals (0.03 - 0.10 Hz) at ELK from Utah rockburst, Utah earthquake, NTS nuclear explosion, and southern Nevada earthquake at similar distances (400 - 435 km).

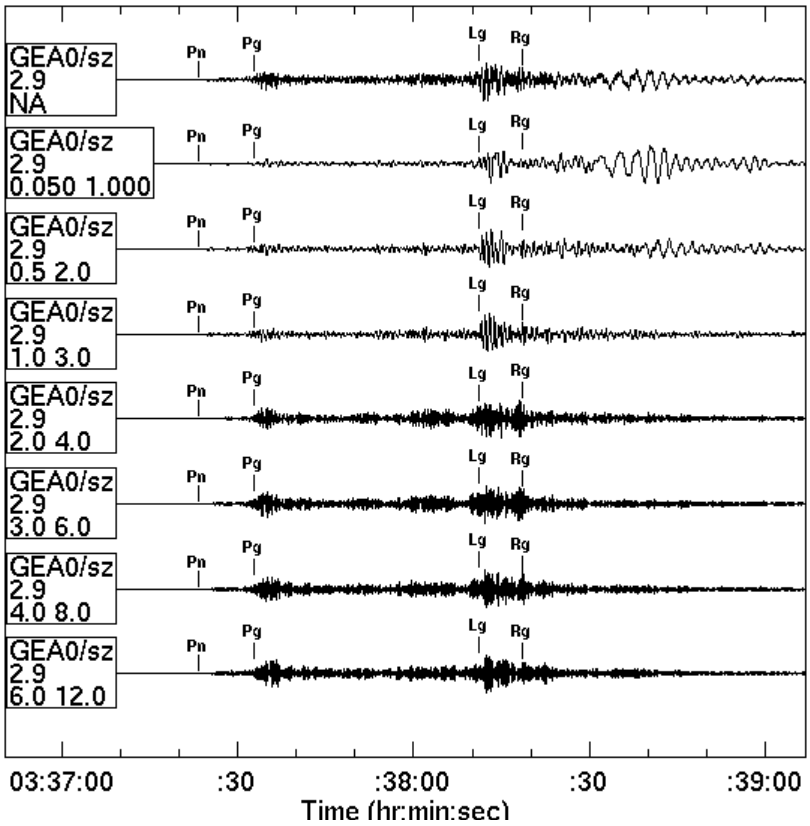

1996/09/11
German Mine
Collapse
4.6 m_b, R = 325 km

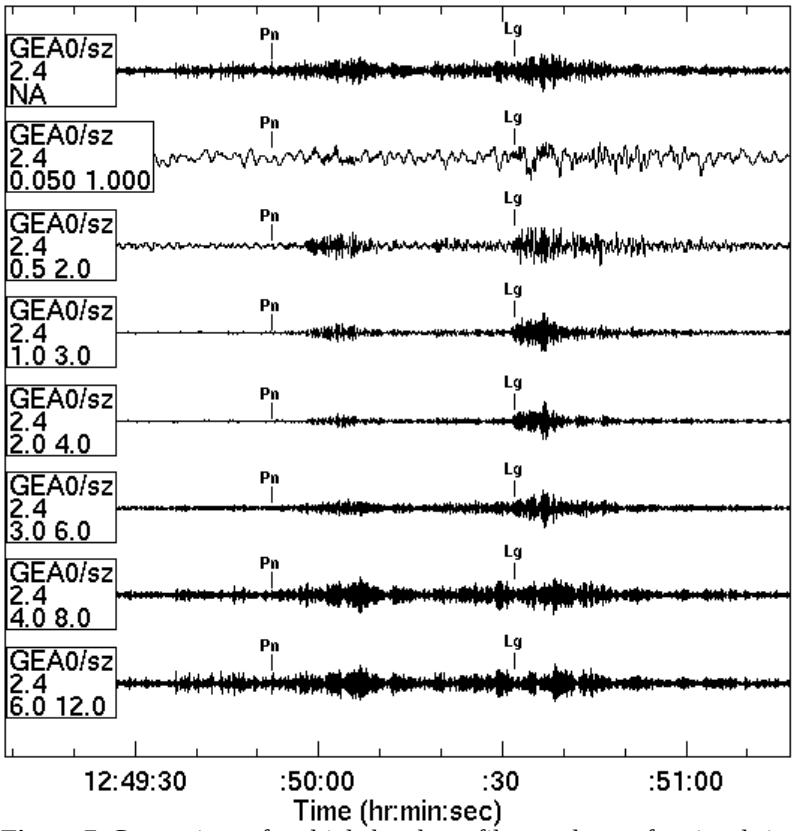

1998/01/30
German Mineblast
3.8 m_b, R = 270 km

Figure 7. Comparison of multiple bandpass filter analyses of regional signals at GERES for German mine collapse (top) and German mineblast (bottom) at similar distances.

bands for the different sources. Based on similar comparisons for other European events, we have concluded that there appears to be little distinction in L_g/P_g ratios for European rockbursts and chemical explosions, although the ratios for both source types tend to be larger than those observed for nuclear explosions in other tectonic regions. We are also continuing to look at some of the alternative regional discriminant measures for use in screening these events. In particular, we see in Figure 7 considerable LP Rayleigh wave excitation for the German mine collapse, which is much larger than for the corresponding mineblast; and such LP Rayleigh signals would not be expected from a nuclear explosion. There also appears to be some evidence of more impulsive character in the initial P_n signals from the mineblast for this region compared to the mine collapse, unlike what we saw above in the western U.S. We are analyzing larger event samples for European events with good ground truth recorded at regional IMS stations to evaluate these alternative discriminants.

CONCLUSIONS AND RECOMMENDATIONS

Nominal PIDC/IDC screening procedures almost always fail in rockburst regions. The reason for failure is usually that the IMS station data at teleseismic distances are insufficient for screening relatively small events. There appear to be some systematic differences in several regional signal parametric measurements at IMS stations between rockburst and non-rockburst areas worldwide. Although regional L_g/P ratios at high frequencies are different on average for rockbursts and underground nuclear explosions, there appear to be some anomalies that require explanation and point to utilization of alternative regional observations for more reliable screening of these and other source types. Finally, some issues raised by event screening of mine explosions in Wyoming suggest that there may be need for more careful application of PIDC/IDC screening criteria in some areas and consideration of other regional discriminants for screening.

REFERENCES

Bennett, T. J., A. K. Campanella, J. F. Scheimer, and J. R. Murphy (1992), Demonstration of Regional Discrimination of Eurasian Seismic Events Using Observations at Soviet IRIS and CDSN Stations, Phillips Laboratory Report PL-TR-92-2090.

Bennett, T. J., M. E. Marshall, B. W. Barker, K. L. McLaughlin, and J. R. Murphy (1996), Investigations of the Seismic Discrimination of Rockbursts, Phillips Laboratory Report PL-TR-96-2184.

Bennett, T. J., R. W. Cook, and J. A. Carter (1997), Seismic Discrimination with Regional Phase Spectral Ratios: Investigation of Transportability, Phillips Laboratory Report PL-TR-97-2140.

Bennett, T. J., M. E. Marshall, and R. W. Cook (1999), Screening of Seismic Events in Rockburst Areas, in Proceedings of the 21st Seismic Research Symposium: Technologies for Monitoring the Comprehensive Nuclear-Test-Ban Treaty, LA-UR-99-4700, 363-373.

Bennett, T. J., M. E. Marshall, and R. W. Cook (2000), Regional Signal Characteristics for Use in Screening Seismic Events in Rockburst Areas, in Proceedings of the 22nd Seismic Research Symposium: Planning for Verification of and Compliance with the Comprehensive Nuclear-Test-Ban Treaty (CTBT), 33-41.

Blandford, R. R. (1993), Discrimination of Earthquakes and Explosions at Regional Distances Using Complexity, AFTAC Report AFTAC-TR-93-044.

Dewey, J. W. and A. L. Leeds (2000), Monitoring Routine Mine Seismicity in the Conterminous United States, in Proceedings of the 22nd Seismic Research Symposium: Planning for Verification of and Compliance with the Comprehensive Nuclear-Test-Ban Treaty (CTBT), 13-22.

Fisk, M., S. Bottone, H. Gray, and G. McCartor (1999), Event Characterization Using Regional Seismic Data, in Proceedings of the 21st Seismic Research Symposium: Technologies for Monitoring the Comprehensive Nuclear-Test-Ban Treaty, LA-UR-99-4700, 427-437.

Fisk, M., S. Bottone, G. McCartor (2000), Regional Seismic Event Characterization Using a Bayesian Kriging Approach, in Proceedings of the 22nd Seismic Research Symposium: Planning for Verification of and Compliance with the Comprehensive Nuclear-Test-Ban Treaty (CTBT), 23-33.

Pomeroy, P. W., W. J. Best, and T. V. McEvilly (1982), Test Ban Treaty Verification with Regional Data – A Review, *Bull. Seism. Soc. Am.*, 72, S89-S129.

Taylor, S. R., N. Sherman, and M. D. Denny (1988), Spectral Discrimination Between NTS Explosions and Western United States Earthquakes at Regional Distances, *Bull. Seism. Soc. Am.*, 78, 1563-1579.

CEPSTRAL F-STATISIC PERFORMANCE AT REGIONAL DISTANCES

Jessie L. Bonner[1], Delaine T. Reiter[1], Anca M. Rosca[1], and Robert H. Shumway[2]

Weston Geophysical Corporation,[1] University of California at Davis[2]

Sponsored by Defense Threat Reduction Agency

Contract No. DSWA01-98-C-0142

ABSTRACT

We have developed a cepstral F-statistic method that attaches statistical significance to peaks in the cepstra of seismic data. These peaks often result from echoes such as depth phases and thus provide a means of identifying possible depth phase candidates. Detections from this method are stacked as a function of their *pP-P* and *sP-P* delay times predicted by IASPEI travel-time tables using a modified version of the network stacking method of Murphy *et al*. (1999). The method detects depth phases with signal-to-noise ratio (SNR) greater than 2, as long as the P wave SNR is greater than 5 to 8, providing a wide range of applicability. We have tested the method on limited datasets from the United States Geological Survey, the Prototype International Data Center, and the International Data Center, and have shown the method to be more reliable at automatically picking possible depth phases than current algorithms. We are now in the process of further testing the method using the extensive datasets at the Research and Development test bed at the Center for Monitoring Research.

We have successfully applied the method to events with epicentral distances greater than 12 degrees and focal depths greater than 15 km. Our focus during the past year has been to examine the technique at near-regional distances for small-to-moderate sized events of varying depths. To accomplish this task, we have acquired a high-quality ground-truth dataset compiled by Ratchkovski and Hansen (2001) using the Alaska Earthquakes Information Center (AEIC) network. We have chosen a subset of the 14,000 events they relocated with magnitudes ranging from 3.5 to 5.1 (M_L), and we are in the process of applying the method to the seismic data recorded for these events at regional distances (using arrays/stations ATTU, BCAR, BMAR, KDAK, ILAR, and IMAR). We are comparing our cepstral depth phase detections at regional distances with depth calculated from data recorded at teleseismic distances (PDAR, MNV, and YKA). For the preliminary analysis at regional stations, the peak created by the *sPn* arrival is the phase most often detected by our cepstral F-statistic method for sub-crustal events. Often, the geometry of the ray paths at regional distances results in *sP* being the only depth phase predicted and observed. We use this *sPn* peak to independently confirm the network-calculated depths for several events of the AEIC dataset. However, in some cases, the improper classification of this peak as *pPn* has resulted in more than doubling the true event depth, thus creating a screening faux pas. Our results thus far show that the method can be applied to regional data with success; however, additional tools may be needed to help determine the true identity of the depth phase (*pP* vs. *sP*).

KEY WORDS: seismic, depth phases, cepstrum, F-statistic, event-screening

OBJECTIVES

The depth of a seismic event is one of the most compelling characteristics seismologists have to determine if an event is man-made or not. Unfortunately, the depth is also notoriously difficult to determine accurately. Some of the methods used to determine focal depth include waveform modeling, beam forming and cepstral methods for detecting depth phases such as *pP* and *sP*. To improve depth estimation using cepstral methods we focused on three primary objectives: (1) formulating a method for determining the statistical significance of peaks in the cepstrum, (2) testing the method on synthetic data as well as earthquake data with well-determined hypocenters, and (3) evaluating the method as an operational analysis tool for determining event depths using varied datasets at both teleseismic and regional distances.

We have successfully completed most of each of the objectives, and we will briefly describe our research to develop and test a cepstral F-statistic. A few additional questions have surfaced during the past year, including:

1. Is there any way to reduce the false alarm rate in the cepstral F-statistic?
2. How are depths determined based upon cepstral F-statistic peaks at different arrays/stations?
3. Can the method be successfully applied to near-regional events?

In the following section, we will provide results of our attempts to answer these three important questions.

RESEARCH ACCOMPLISHED

We have formulated a cepstral F-statistic using a classical approach to detecting a signal in a set of stationary correlated time series (Shumway *et al.*, 1998). The method is particularly suited for regional array analysis (Bonner *et al*., 2000); however, the method can also be applied to three-component data (Shumway *et al*., 2000). Tests on synthetic data show the method works best when the *P* wave arrival has a signal-to-noise ratio (SNR) greater than between 5 and 8 with the depth phase exhibiting a SNR greater than between 2 and 4. These requirements in SNR were validated using events from the Hindu Kush region of Afghanistan with well-determined depths calculated from data recorded on arrays at teleseismic distances.

To test the operational capabilities of this method as a tool for data center use, we analyzed 61 events located by the National Earthquake Information Center (NEIC) and/or the Prototype International Data Center (pIDC). Our method determined statistically significant depths for 41 of 61 events. Ten of the events had low SNR at the recording arrays, while another 10 were either too shallow for analysis or did not exhibit depth phases. The method determined depths between 12 and 90 km for 7 of the 17 events which the pIDC had fixed to 0 km. The scatter between the cepstral F-statistic depths, the NEIC depths and the pIDC depths decreases significantly as the magnitude increases. The F-statistic method works best for teleseismically recorded events with magnitude greater than 4.0; however, similar analysis using far-regional data (12 - 20 degree) has shown success as well. Overall, we believe the method would be most valuable if used as a tool by the analyst to help highlight possible depth phases for further review. During various reviews of our research, several important questions and concerns emerged, and some of these topics are discussed in this paper.

False Alarms in the Cepstral F-Statistic

One of the concerns that arose while developing the cepstral F-statistic method involved multiple peaks that resulted in potential false depth phase picks. Multiple peaks that exceed the 99% confidence level in the cepstral F-statistic will complicate the analysis for the peaks associated with the actual depth phases. Figure 1 shows the cepstral plots for a synthetic event with a depth of 46 km. The *pP-P* delay time should be at 13 seconds, and a large peak in the cepstral F-statistic does indeed correspond to this time. However, at 25.5 seconds, there is an additional smaller amplitude peak that rises slightly above the 99% confidence level. Based upon our detailed analysis, false alarms (i.e. peaks in the cepstral F-statistic not associated with depth phases) result from two different cases. The first is the arrival of post-*P* phases that have similar spectral characteristics to the *P* waves and thus the cepstra stack as if they were depth phases. We have found that changing the pre-processing filter parameters and/or the tapering window in the log spectrum (for the processing flow, the reader is referred to Bonner *et al.*, 2000) at different frequencies may attenuate these peaks; however, in most cases these false alarms will always exist in the cepstral F-statistic and thus must be considered as potential depth phase candidates. In a later section, we will discuss a method of depth phase beam forming that can reduce the impact of these false alarms. Another case of false alarms occurs when the quantities that form the cepstral F-statistic, the beam cepstrum and the total cepstrum, exist in close proximity to each other through random processes. This explains the peak at 25.5 seconds in the F-statistic of Figure 1, where a small peak in the beam cepstrum is accompanied by a decreasing trend in the total cepstrum, resulting in a false alarm. Often, using a slightly different window of data or changing the filter or smoothing components will remove this false alarm, but instead, we search for peaks in all three cepstral quantities prior to classifying it as a cepstral F-statistic detection.

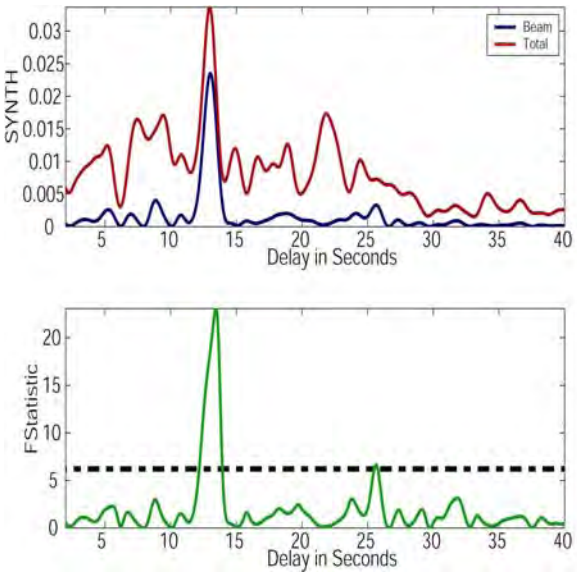

Figure 1. (Upper) Beam and total cepstra for synthetic array data for an earthquake at 46 km depth. The beam cepstrum is formed by summing the detrended and windowed log spectra. The total cepstrum is formed by stacking the individual cepstra. (Lower) The cepstral F-statistic is calculated using both the total and beam cepstra, and shows a large peak above the 99% confidence level (black dashed line) at 13 seconds and a smaller peak at 25.5 seconds.

Depth Determination from Cepstral F-Statistic Detections

During the earliest stages of this research, we were employing a crude and subjective method for determining depth of a seismic event based upon the cepstral F-statistic peaks. Our method was meant to complete the analysis on as many arrays as possible and to visually correlate the depths determined from the cepstral peaks among the different arrays. This may lead to one depth that is consistent at all arrays considered in the analysis, or there may be numerous plausible depths. It became clear that this method introduced the potential for human error into the analysis.

We tested the method of depth phase beam forming as first suggested by Israelsson (1994) and applied by Woodgold (1998). Murphy *et al.* (1999) has modified the method to place one-second boxcar windows centered on post-*P* detections generated by the automatic processing at the pIDC and then stack them as a function of *pP*-*P* or *sP*-*P* delay times predicted by IASPEI travel time tables. This method has shown remarkable success at highlighting depth phases for analyst review. An example of the application of this method for an event in Argentina (IDC Evid 592530) with an IDC reported depth of 107.6 ± 3.9 km is shown in the left panel of Figure 2. We have modified the method to stack cepstral F-statistic detections instead of post-P detections, and we have decreased the boxcar width from 1.0 second (Murphy *et al.*, 2000) to 0.6 seconds in order to decrease the width of the beam-formed peaks. In the right panel of Figure 2, we show the results of stacking the cepstral F-statistic detections for the same pIDC data used to create the left panel. Both plots show large peaks associated with a depth of 108 km; however, note that we find three additional detections among the IMS stations using our method. In this case, three additional stations do not change the results significantly, as this event was large enough (m_b=5) for obvious depth phases to be observed at multiple stations. We present examples in Figures 3 and 4 that show the same analysis on smaller events for which the detection of the depth phase is more difficult. In the example in Figure 3, a Hindu Kush event (pIDC Evid 20085674) depth was determined by network hypocenter determination at 140.8 ± 19.7 km with no depth phases incorporated in the solution. Stacking of the network post-P detections shows two detections that correspond to this depth; however, stacking of the cepstral detections show six peaks at this depth. A third event (Figure 4) from Oaxaca, Mexico (pIDC Evid 20785471) had a pIDC reported depth of 95.8 ± 54.7 km with no depth phases. Our analysis shows five detections that correspond to a depth of 17.2 ± 2.5 km. This depth is more plausible than the pIDC depth, because the epicenter of this event is near the trench of the Mexican subduction zone, where historical data suggest the events are at crustal depths. The results thus far are quite promising that the Murphy *et al.* (1999) method of depth phase beam forming will provide a robust, automated method of translating cepstral F-statistic peaks to a depth.

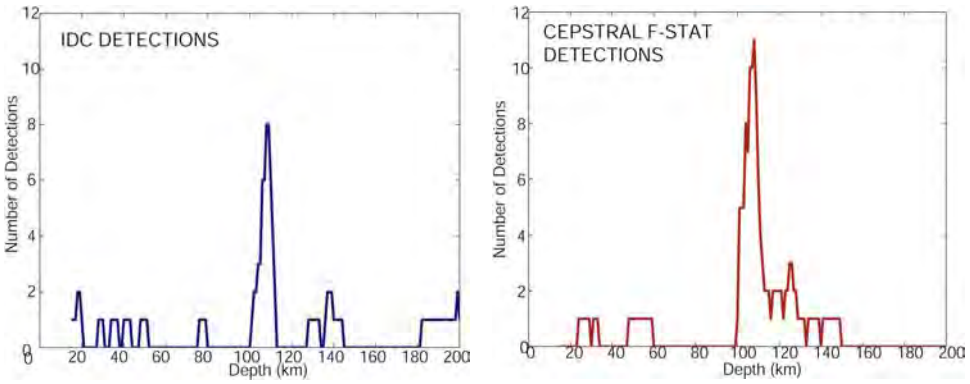

Figure 2. (Left) Network stacking of post-P detections at the IDC for an event in Argentina (IDC Evid 592530). (Right) Network stacking of cepstral F-statistic detections. Both plots show large peaks associated with a depth of 108 km; however, note that we find three additional detections among the IMS stations using our method. The IDC depth for this event is 107.6 ± 3.9 km.

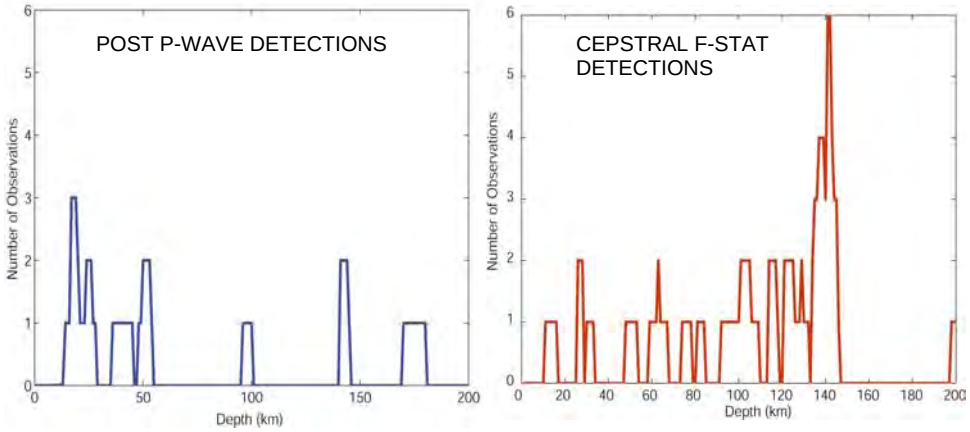

Figure 3. (Left) Network stacking of post-P detections at the pIDC for an event in Hindu Kush (pIDC Evid 20085674). (Right) Network stacking of cepstral F-statistic detections. The cepstral analyses show a six detection peak associated with a depth of 140.9 ± 5.5 km that agrees with the pIDC depth for this event of 140.8 ± 19.7 km with no depth phases reported.

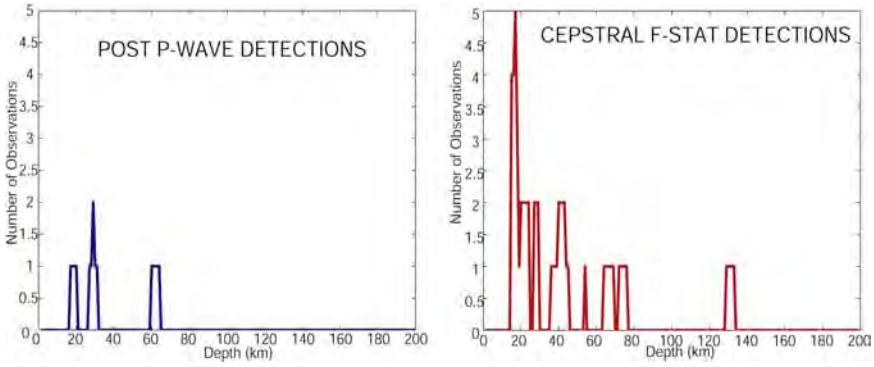

Figure 4. (Left) Network stacking of post-P detections at the pIDC for an event in Oaxaca, Mexico (pIDC Evid 20785471). (Right) Network stacking of cepstral F-statistic detections. The cepstral analyses show a five detection peak associated with a depth of 17.2 ± 2.5 km that disagrees with the pIDC depth for this event of 95.8 ± 54.7 km.

Cepstral F-Statistic Analyses on Regional Data

Near-regional cepstral analysis is complicated by a number of factors, including emergent and low SNR *Pn* arrivals and complicated *Pn* and *Pg* coda. If one is relying upon the cepstral analysis at regional stations for a depth estimate, it is probably because the event has an $m_b < 4.0$, which translates to smaller amplitudes and SNR in some cases. Another complexity is related to the nature of the ray paths for depth phases at near-regional distances. Figure 5 shows the initial distance from an event to a station in which a depth phase (either *pPn*, *sPn*, *pP*, or *sP*) is theoretically predicted to occur as a function of the event depth in the IASPEI91 model (Kennett and Engdahl, 1991). For near-regional distances (< 10°) and crustal events (< 35 km) , IASPEI91 predicts *pPn* and *sPn* may be observed at distances greater than 1°. However, for events that occur deeper than the crust-mantle interface, *sPn* will be the only observable depth phase. For many of the events thus far analyzed at regional distances, *sPn* has been the only depth phase detected by the cepstral analysis. We originally classified these peaks as *pPn* resulting in the events being placed deeper than they actually occurred. The depth phases *pP* and *sP* are predicted at 14° which correlates with our previous studies (Bonner *et al*., 2000) that demonstrated the cepstral F-statistic method can be applied successfully at distances greater than 12°. The question remains as to how the method will work in an operational setting for epicentral distances less than 12 degrees where *pPn* and *sPn* are the predicted depth phases.

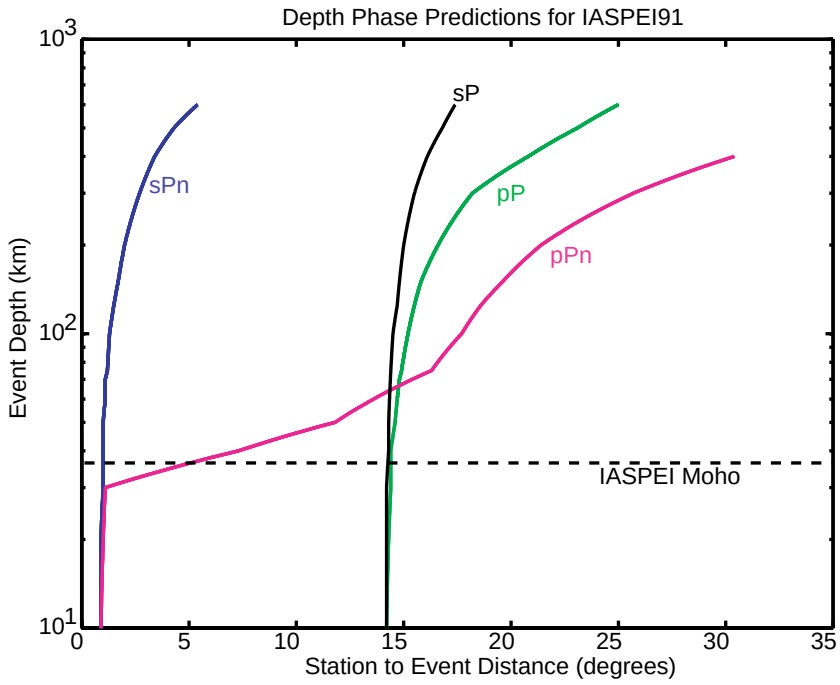

Figure 5. Depth phase arrivals at regional and near-teleseismic distances as a function of epicentral distance and event depth. The plot shows the initial distance from an event in which a depth phase (either pPn, sPn, pP, or sP) is theoretically predicted to occur from IASPEI91 (Kennett and Engdahl, 1991) as a function of the event depth. For the near-regional analysis (< 10°) of the AEIC data, we can only detect sPn and pPn phases for crustal events (<35 km), while deeper events may only have the sPn arrival.

Our focus during the past year has been to examine the cepstral F-statistic technique at near-regional distances for small-to-moderate sized events of varying depths. To accomplish this task, we have acquired a high-quality ground-truth dataset compiled by Ratchkovski and Hansen (2001) (henceforth referred to as RH (2001)) using the Alaska Earthquakes Information Center (AEIC) network. We have chosen a subset

(Figure 7) of the 14,000 events they relocated, and we are in the process of applying the cepstral F-statistic method to the seismic data recorded for these events at regional distances. Data recorded from the Alaskan stations/arrays ATTU, BCAR, BMAR, KDAK, ILAR, and IMAR (Figure 6) are being used in the analysis to determine depth phases, and we are comparing the cepstral depth phase detections at regional distances with depth phase detections recorded at teleseismic distances (PDAR, MNV, and YKA). Preliminary results of these analyses are presented in the following paragraphs.

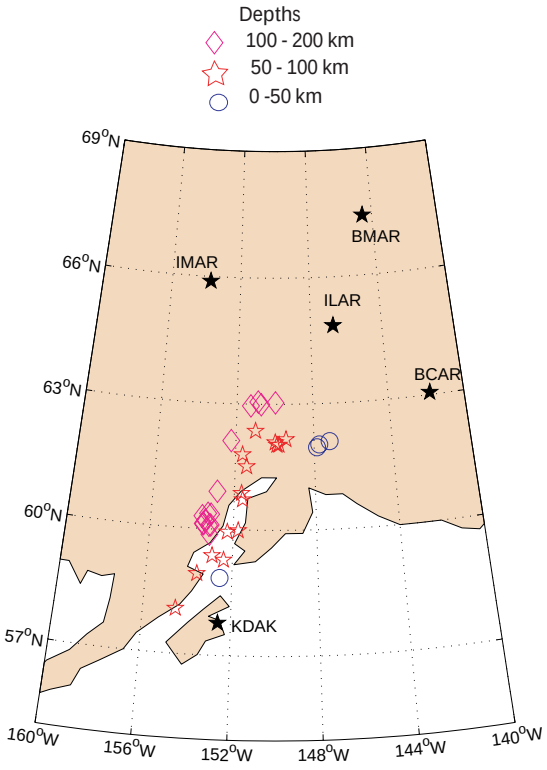

Figure 6. Subset of events from the Ratchkovski and Hansen (2001) database for use in cepstral F-statistic studies at near-regional (black stars) 3-C stations or arrays. The shape of the Alaskan-Aleutian subduction zone can be inferred from the deepening of earthquakes toward the west.

Table 1 provides source data for an event from the RH (2001) subset for which regional cepstral analyses are ongoing. Evid 14888 is a crustal event occurring at 40 km depth in central Alaska. The event was recorded on BCAR, BMAR, ILAR, IMAR, and KDAK (all shown in Figure 7) together with YKA in northern Canada. Data from each event was downloaded from the United States National Data Center, and the cepstral F-statistic analyses were performed (Figure 7). Data at KDAK and IMAR were poor quality and were not used. Several arrays have cepstral F-statistic detections that align with theoretical arrivals for the depth phases calculated using the RH (2001) depth. At BCAR, a peak that rises slightly above the 99% confidence interval aligns with *pPn* while at ILAR (Figure 8), large peaks are noted for both *pPn* and *sPn*. At BMAR, there is a peak just below the 99% confidence level that correlates with the predicted *pPn* arrival, and if the level was reduced to 95%, the peak would have been marked as a detection as would additional peaks that do not correspond to depth phases. Based upon our analyses, the ILAR data provides the strongest argument in support of the RH (2001) depth determined for this event. The number of peaks in the cepstral F-statistic is greatly increased in the regional analyses as compared to the far-regional and teleseismic applications. We believe that the manner in which we have used the technique here as a

secondary tool for verification of network calculated depths may be the most appropriate application of the cepstral F-statistic at regional distances.

EVID	YMD	Origin	Long	Lat	Depth	Mag
14888	980115	05:59:04	-147.74	62.04	39.67	4.1

Table 1. Events from the RH (2001) database discussed in this paper.

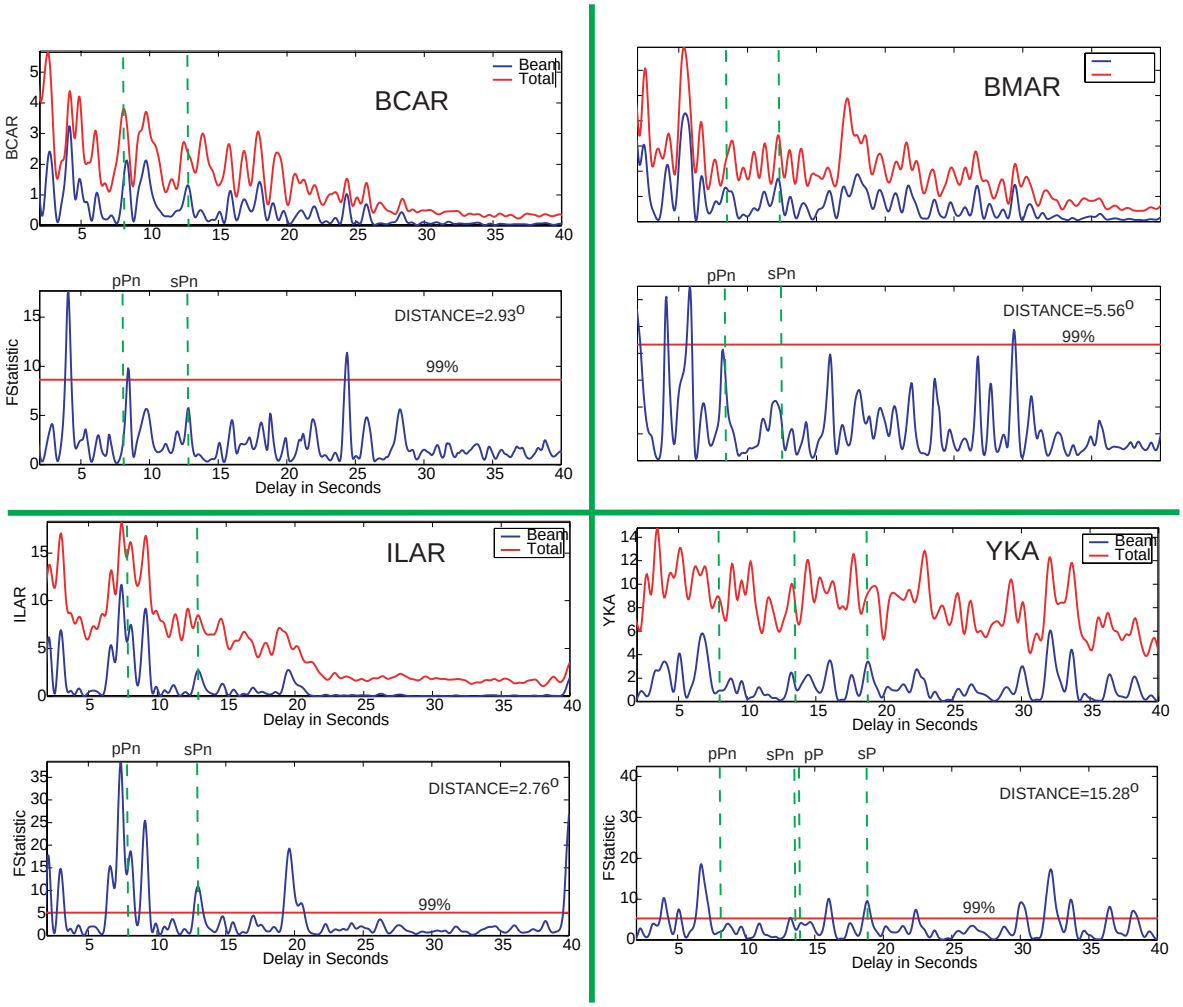

Figure 7. Cepstral F-statistic analyses on regional data recorded at BCAR, BMAR, ILAR, and YKA for event 14888 (Table 1). In the upper plot of each station analysis, the total cepstrum and beam cepstrum are presented. In the lower plot, the cepstral F-statistic is shown together with the 99% confidence level. In each plot, the x-axis represents the delay time (in seconds) between the depth phase candidate and the P wave arrival. The epicentral distance and the predicted arrival times for the depth phases based upon the RH (2001) depth are also provided.

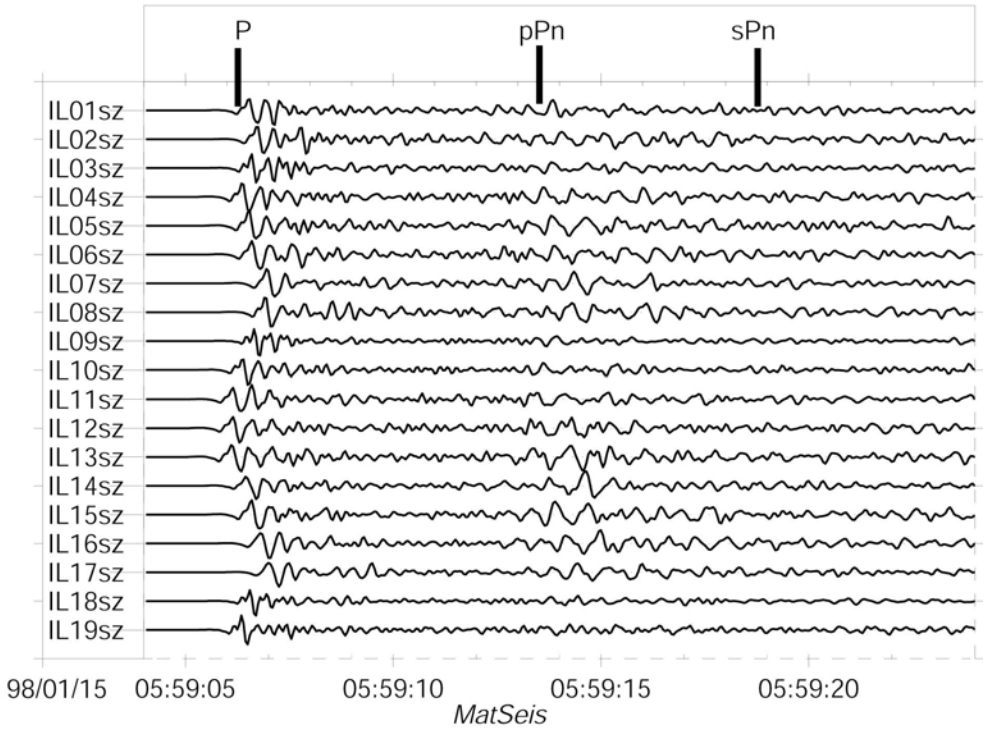

Figure 8. ILAR data for Evid 14888 with the cepstral F-statistic peaks at 7.7 and 12.7 seconds denoted as pPn and sPn, respectively

CONCLUSIONS AND RECOMMENDATIONS

The goals of this study were to determine a statistical parameter to accompany cepstral peaks in seismic data, and to determine if cepstral methods could be incorporated into the daily processing routines at a data center. We have formulated a cepstral focal depth estimation technique that provides a statistical estimate of the significance of the peaks in the stacked cepstrum. This significance measure, which we have termed the cepstral F-statistic, has been missing in previous cepstral estimates of focal depth. We have applied this method to synthetic data and found that the method will detect depth phases with SNR greater than 2 to 4 when the *P* wave SNR is greater than 5 to 8. We have tested the method on USGS, pIDC, and IDC datasets and shown that the method is more reliable at picking possible depth phases than current detection algorithms. We suggest that the Murphy *et al.* (1999) method of network stacking of post-*P* detections be extended to include cepstral F-statistic detections, thus providing an automated method of translating cepstral peaks to seismic event depths. Our results suggest the method is best applied at epicentral distances greater than 12° where *pP* and *sP* are the most commonly observed depth phases. Near-regional analysis is more difficult to accomplish in an operational setting because of the complexity of regional seismograms and the nature of the ray paths for *pPn* and *sPn*. As this research program draws to a close, we plan to begin implementing the program and results into the CMR R&D test bed for additional testing and algorithm development with a goal of including the technique in a future release of IDC software. Our recommendation is for use of this technique in an operational setting such as the United States National Data Center (USNDC), the International Data Center (IDC) and NEIC as a tool to aid an analyst in determining a depth for an event. For teleseismic data, the method can be used in parallel with the standard processing techniques with cepstral F-statistic detections being fed into a network-stacking algorithm for a preliminary depth determination. The analyst could then use the results to verify the existence of the depth phases suggested by the cepstral analyses. For regional data, we suggest a different application. After a

preliminary depth has been determined using standard location techniques with network phase arrival time data, we propose that the cepstral F-statistic technique could be implemented on the regional network data for the event. The peak detection methods would help highlight any possible depth phases that could then be used to verify or alter the initial network-calculated depth. By employing techniques such as the cepstral F-statistic method, statistically valid depths can be assigned to events that only a few stations recorded, leading to more confident event screening. Also, depth determination independent of a network solution will lead to more accurate and reliable event locations, since the depth calculated from the cepstral F-statistic method can be used to constrain a hypocentral solution.

ACKNOWLEDGMENTS

We would like to thank the following people for their help and support on various aspects of this study, including Keith Priestley, Jack Murphy, Jim Lewkowicz, Shelly Johnson, Shirley Rieven, Carolynn Vincent, Bob Woodward, Richard Baumstark and Anca Rosca. We would like to extend thanks to the NEIC, USNDC, and pIDC for their help in acquiring bulletin and waveform data for the events analyzed in this study. Also, we wish to express our gratitude to Natalia Ratchkovski and Roger Hansen for allowing us access to their database of Alaskan events.

REFERENCES

Bonner, J., D. R. Reiter, and R. H. Shumway (2000), Application of a cepstral F-statistic for improved depth estimation. *Proceedings of the 22nd Annual DoD/DOE Seismic Research Symposium on Planning for Verification and Compliance with the Comprehensive Nuclear-Test-Ban Treaty (CTBT)*, p 53-62.

Israelsson, H (1994), Stacking of waveforms for depth estimation, Center for Seismic Studies Final Report C95-02.

Kennett B. L. N. and E. R. Engdahl (1991), Travel times for global earthquake location and phase identification, *Geophys. J. Int.*, **105**, p. 429-465.

Murphy, J. R., R. W. Cook, and W.L. Rodi (1999), Improved focal depth determination for use in CTBT monitoring, *Proceedings of the 21st Annual Seismic Research Symposium on Monitoring a Comprehensive Nuclear Test Ban Treaty*, p 50-55.

Ratchkovski, N. and R. A. Hansen (2001), New evidence for segmentation of the Alaska subduction zone, Submitted to the *Bull. Seism. Soc. Am.*

Shumway, R. H., D.R. Baumgardt and Z.A. Der (1998), A cepstral F-statistic for detecting delay-fired seismic signals, *Technometrics*, **40**, p. 100-110.

Shumway, R. H., J. L. Bonner, and D. Reiter (2000), Nonparametric deconvolution of seismic depth phases. Proceedings of the 2nd International Symposium on Frontiers of time series modeling, December 14-17, 2000, Nara, Japan, Institute of Statistical Mathematics, Tokyo, Japan.

Woodgold, C. R. D. (1999), Wide-aperture beamforming of depth phases by timescale contraction, *Bull. Seis. Soc. Am.*, **89**, p. 165-177.

SEISMIC LOCATION CALIBRATION FOR 30 INTERNATIONAL MONITORING SYSTEM STATIONS IN EASTERN ASIA

Clint Conrad[1], Mark Fisk[1], Vitaly I. Khalturin[2], Won-Young Kim[2], Igor Morozov[3], Elena Morozova[3], Paul G. Richards[2], David Schaff[2], and Felix Waldhauser[2]

[1] Mission Research Corporation, [2] Lamont-Doherty Earth Observatory, [3] University of Wyoming

Sponsored by Defense Threat Reduction Agency

Contract No. DTRA01-00-C-0031

ABSTRACT

We review the progress of a collaborative academic-industry research consortium, comprised of five institutions, that has started an integrated series of projects to improve the capability to locate seismic events based on data acquired by International Monitoring System (IMS) stations in Eastern Asia. This effort is to develop and deliver validated high-resolution travel time grids for operational use.

During the first year of work we have focussed on IMS stations in Central Asia and Northern Pakistan, specifically the stations MAK, BRVK, KURK, AAK, AKTO, ZAL, PRPK/NIL, for which we are obtaining preliminary Source Specific Station Corrections (SSSCs). Each station presents its special problems and opportunities. Thus, although only two of these stations (ZAL and NIL) are currently contributing data to the International Data Centre (IDC), we have broadband high-quality data from surrogate stations at or close to the planned IMS sites for the other five sites. In joint projects with the National Nuclear Centre of the Republic of Kazakhstan (NNCRK) and the Institute of Dynamics of the Geosphere of the Russian Academy of Sciences, regional waveforms from Borovoye (BRVK) have become available for 80 Soviet PNEs, 228 Semipalatinsk explosions and 11 Lop Nor explosions. In a joint project with the NNCRK and the Complex Seismological Expedition based in Talgar, Kazakhstan, regional waveforms from 37 Soviet Peaceful Nuclear Explosions (PNEs) have become available for several other stations in Central Asia. Since 1994 we have operated broadband instrumentation jointly with the NNCRK at MAK, BRVK, KURK, and AKTO — enabling, for example, the recording of regional waves from numerous earthquakes throughout Central Asia, and some nuclear explosions (Lop Nor). We have obtained empirical travel times from all these datasets, using published high-quality ground truth information for the Soviet PNEs.

Other valuable sources of empirical travel time information have been the Deep Seismic Sounding (DSS) profiles carried out with chemical explosions in and near Kazakhstan, and DSS profiles carried out with nuclear explosions in the northern part of the former Soviet Union. We have been able to document the variability of regional travel times with these data, finding in particular that *Sn* and *Lg* waves show significant variability. Preliminary Source Specific Station Corrections have been used for stations MAK, AAK, KURK, ZAL, TLY, ULN, NIL, and BRVK to relocate nuclear explosions at Lop Nor, showing improved accuracy and reduced confidence ellipses. We are extending this process of validation to include PNEs and other underground nuclear explosions in the former Soviet Union, and earthquakes for which we have adequate ground truth.

We are on collecting high-precision hypocenter locations for mainland China by applying a double-difference (DD) earthquake relocation technique to travel time data given in the Annual Bulletin of Chinese Earthquakes (ABCE). In areas with dense seismicity, where the DD technique minimizes model effects without the use of station corrections, we find the relocated events cluster in space and appear to delineate local tectonic features. Analysis of the residuals indicates that the phase picks are of high quality, and that they are best suited to image seismicity with high resolution on a local (several km) scale. Increasing earthquake density by including ABCE data from additional time periods might help to relocate earthquakes over larger distances, such as entire fault systems. Such studies have the potential to increase groundtruth data as well as contribute to a better understanding of the tectonic processes in China.

KEY WORDS: earthquake location, Peaceful Nuclear Explosions, Chinese seismicity.

OBJECTIVE

The goal of this project is to improve the accuracy of estimates of the location of seismic events and to reduce the uncertainty of such estimates on the basis of an interpretation of the arrival times of regional seismic waves observed at 30 stations of the International Monitoring System located in Eastern Asia.

RESEARCH ACCOMPLISHED

Introduction

Following the recommendations of two IMS Location Calibration Workshops held in Oslo, Norway, in 1999 and 2000, our approach is to generate station-specific travel times for each observable seismic phase, as a function of distance and azimuth (and depth, where possible). In practice, such travel times are characterized by Source Specific Station Corrections (SSSCs) to the IASP91 travel times. SSSCs are obtained on the basis of (i) early studies based mainly on earthquake data (e.g. Nersesov and Rautian, 1964), (ii) Deep Seismic Sounding, and (iii) recent studies of nuclear and chemical explosions. We are also using (iv) an empirical approach in which phases are picked at IMS stations (or at surrogate stations near IMS sites that are currently not operating), for so-called reference events whose locations are known quite accurately (to within 5 km GT5 quality) on the basis of data obtained from local and regional networks.

Our project began in March 2000. It is a three-year collaborative academic-industry research project led by Lamont and involving a consortium of five institutions. Details of our work are described in Richards et al. (2000) and at http://www.LDEO.columbia.edu/~richards/consortium.html including the list of 30 stations we are studying, their locations, relevant maps, and description of pertinent datasets. During the first year of work we have focussed on the derivation of SSSCs for seven IMS stations in and near Central Asia. Much of our progress to date has been based on major datasets of waveforms and phase picks for 70 Soviet-era Peaceful Nuclear Explosions (PNEs).

We have obtained preliminary SSSCs using the method of Bond r (1999) applied to a model of eastern Asia composed of 20 different regions within each of which we have defined a set of regional travel times. We find that these SSSCs reduce residuals for the phase picks of numerous PNEs. Use of kriging plus SSSCs further reduces residuals. Validation of a set of SSSCs is best done by demonstrating location improvement, and we have begun this phase of our work with relocation of underground nuclear explosions at the Lop Nor test site in China.

Though we have obtained locations of tens of thousands of seismic events in Eastern Asia, estimated on the basis of regional seismic signals recorded by local and regional networks, it is a time-consuming process to identify and document the subset of these events that can with confidence be categorized as GT5 or better. We are engaged in that process, and are developing sets of reference events for several sub-regions of Eastern Asia. Some of these are in China, where it is proving important to locate numerous earthquakes at once, using modern methods to reduce model error that are insensitive to errors in station location.

First SSSCs

Our first procedure for obtaining SSSCs has used the method described by Bond r (1999), in which our whole study region (Eastern Asia) is first divided into sub-regions within each of which we use available information to obtain travel times as a function of distance for each of the main regional seismic phases (*Pg*, *Pn*, *Sn*, *Lg*). A preliminary regionalization of this type is shown in Figure 1. An assumption underlying Bond r s approach is that structure does not vary laterally within each sub-region. Since travel time (and hence structure) is established for each sub-region, it is conceptually possible to compute the travel time for a path from each point in Figure 1, to each of the 30 IMS stations we seek to calibrate. The correct way to obtain such a travel time, for a path that crosses one or more region boundaries, is to integrate along the actual ray path which in general will be laterally refracted at a region boundary so that the path does not stay in the same vertical plane. However, Bond r (1999) has suggested the following simple formula for obtaining an approximate travel time to distance X:

$$T(X) = \text{sum of } [(x_i / X) \, . \, T_i (X)] \qquad (1)$$

where the index i ranges over all sub-regions crossed by the ray path, and x_i and T_i (X) are the path length and travel time (for the full distance X) in the i-th sub-region. The desired travel time is thus obtained as a weighted average of the travel time in each sub-region, the weights being (x_i / X), which for each i is just the fraction of the total path lying in sub-region i. (A problem with this formula, is that it may be inaccurate for paths of more than 1000 km or more, in application to sub-regions smaller than 1000 km across. An artificial relation between T_i and X is then needed artificial, because the path length here is too long to be fully contained within the sub-region.) Once $T(X)$ is obtained, the source specific station correction (SSSC) is given by

$$T_{SSSC} = T(X) - T_{IASP91}$$

To obtain the regionalization and travel times for each block, in the case of Central Asia, we note first the classic study of Nersesov and Rautian (1964), describing the early work on a big profile carried out by the Complex Seismological Expedition. Khalturin et al. (2001) used observations of small-magnitude underground nuclear explosions at the Semipalatinsk Test Site, and earthquakes with good locations, to obtain a version of the Nersesov and Rautian travel times which is adapted to this test site and surrounding areas. They located several small magnitude events on the test site with accuracy about 5 km using only a few stations. Their results were confirmed by comparison with ground truth information, obtained after the seismically-based locations had been estimated. In addition we have data from 27 Deep Seismic Sounding (DSS) profiles in Central Asia, obtained from Antonenko (1984), Shatsilov (1993), Zunnunov (1985) and the book Seismic Models of the Lithosphere of the main Geostructures in territory of the USSR (1980).

The regionalization indicated in Figure 1 is based on DSS profiles throughout the former Soviet Union, together with many regional studies of China and the Indian sub-continent. Our regionalization is frequently under review within the Lamont consortium. The version we are currently using is described at http://www.LDEO.columbia.edu/~armb.

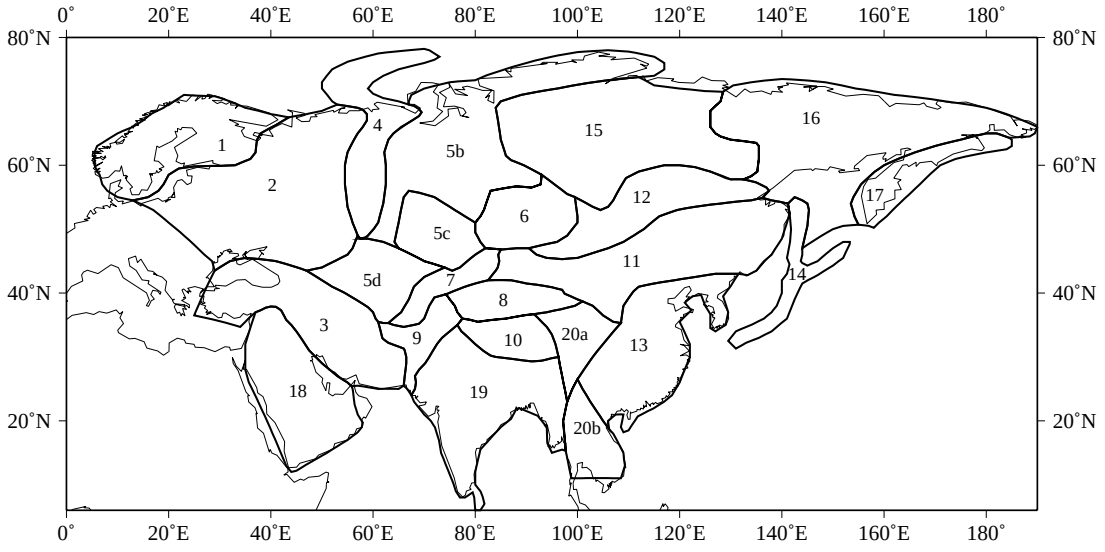

Figure 1. This map shows our preliminary regionalization of most of Eurasia, for purposes of obtaining approximate travel times of regional seismic waves to IMS station in Eastern Asia. For each regional seismic wave of interest (*Pg*, *Pn*, *Sn*, *Lg*), the relationship between travel time and distance is assumed to apply throughout each sub-region.

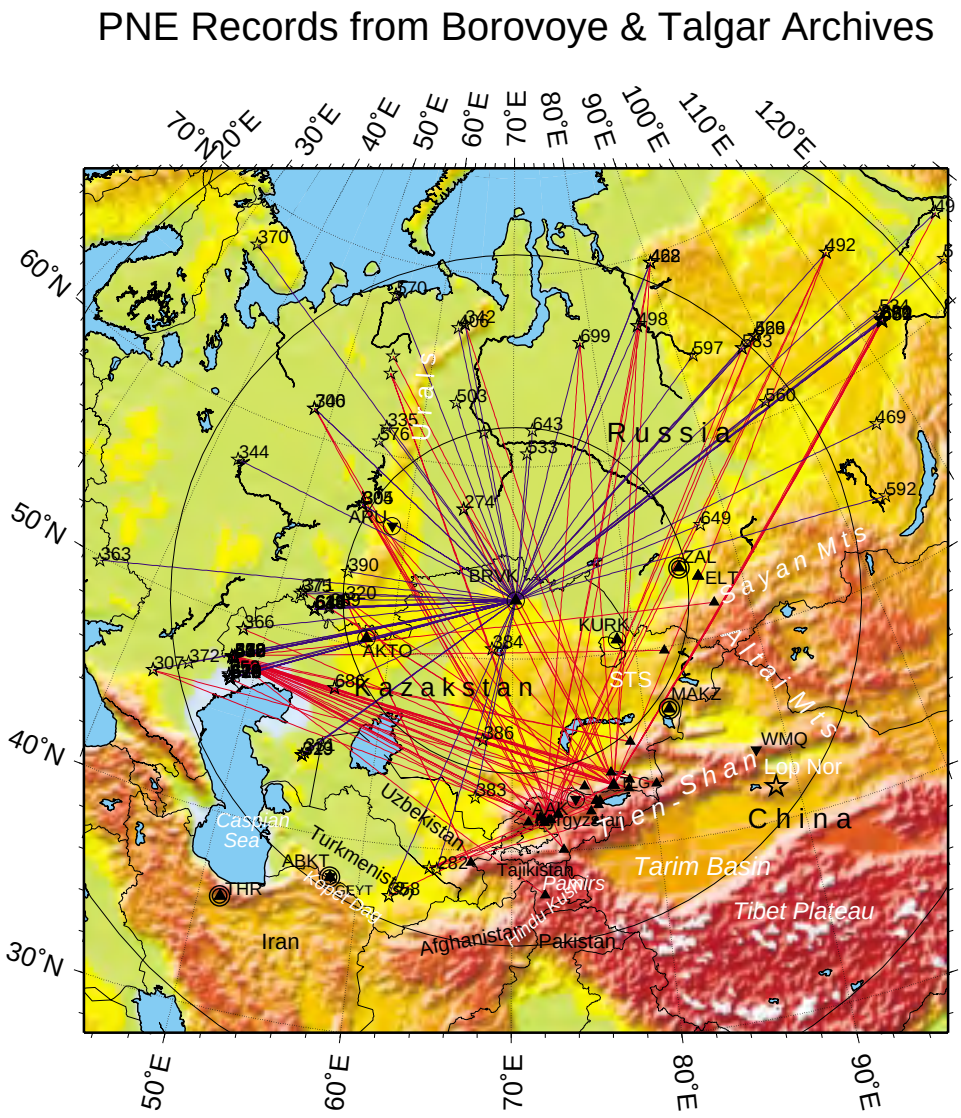

Figure 2. Waveform data from Soviet PNEs (stars) recorded at Borovoye, northern Kazakhstan, and at 26 stations of the Talgar Complex Seismological Expedition, Russian Academy of Sciences, during 1966 to 1988. Paths between 80 PNE sources and Borovoye are indicated by blue lines, while paths of 37 PNEs to Talgar CSE stations are indicated by red lines. Event numbers (Mikhailov et al., 1996) are indicated for each explosion. IMS primary (double circle), auxiliary (single circle), IRIS/GSN (inverted triangle) and Talgar CSE stations (solid triangle) are indicated. Circles centered on BRVK have 1000 and 2000 km radii.

An evaluation of the SSSC for Borovoye (BRV)

The IMS includes an auxiliary station at Borovoye, in northern Kazakhstan. Though not yet operating as an IMS station with data flowing to the Vienna IDC, there has been an Observatory at Borovoye acquiring digital seismic data since 1966. In joint projects between the Lamont-Doherty Earth Observatory, the National Nuclear Centre of the Republic of Kazakhstan (NNCRK), and the Institute of Dynamics of the Geosphere of the Russian Academy of Sciences, regional waveforms from Borovoye (BRVK) became

available early in 2001 for 80 Soviet PNEs, 228 Semipalatinsk explosions and 11 Lop Nor explosions. These data are now available to interested users who may obtain the Borovoye waveforms from the Center for Monitoring Research, and the IRIS Consortium (for further information, see http://www.LDEO.columbia.edu/Monitoring/Data/brv_web/brv_archive_web.html). These waveforms are of course useful for a wide variety of research projects, in particular for evaluating the SSSCs obtained from regionalizations such as that of Figure 1 (and associated travel times for each sub-region).

We picked the arrivals of *P*- and *S*-waves from the Borovoye digital waveforms for 70 PNEs, and made use of the GT1 or better information contained in Sultanov et al. (1999) to obtain empirical travel times at BRV for these events. Figure 2 shows the Borovoye (BRVK) location and Soviet PNEs for which we have picked empirical travel times, and also the location of 26 stations of the Complex Seismological Expedition, based in Talgar, Kazakhstan, for which we have additional empirical data based on digitized waveforms from the same events. Figure 3 shows the residuals for these travel times against the predictions of IASP91, and Figure 4 shows the residuals against IASP91 after the preliminary SSSC for BRV has been applied. We have also carried out a series of kriging exercises, using some of the PNE travel times to BRV for this purpose, and the remaining PNE travel times to Borovoye for an evaluation shown in Table 1.

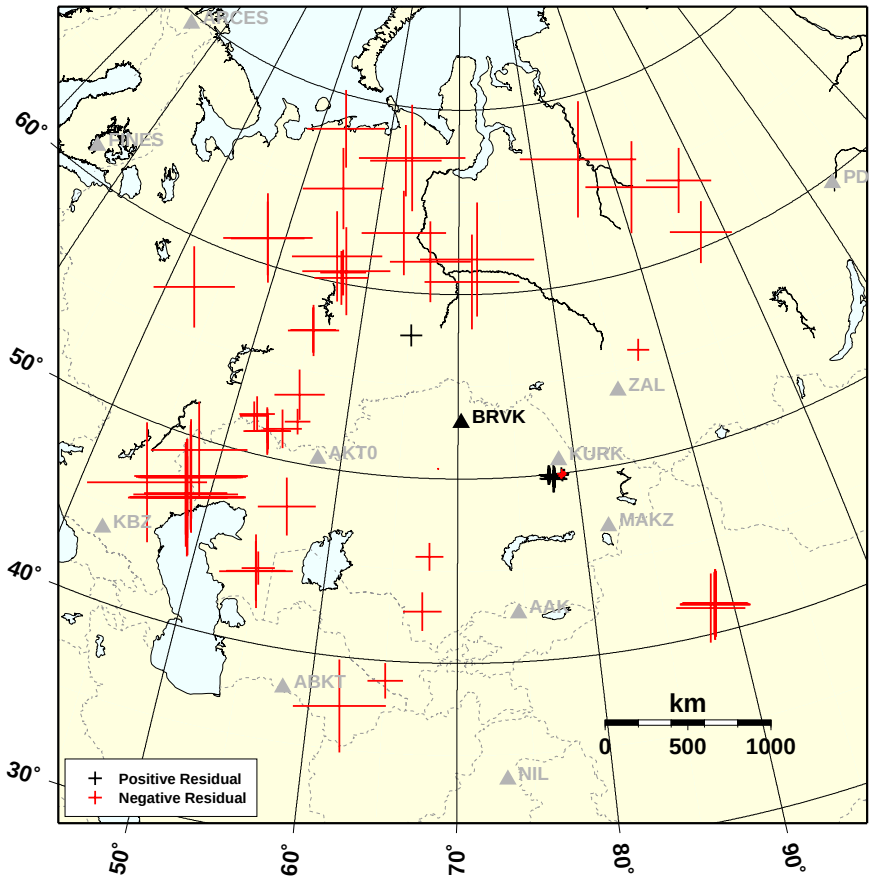

Figure 3. Map of PNE locations for events whose travel time to Borovoye (BRV) has been measured from waveforms in the archive of that observatory. On average, travel times are 3.9 s earlier than IASP91 times and these residuals have a standard deviation of 2.0 s.

Table 1 shows that the mean *Pn* travel time bias for Soviet PNEs is reduced by 3.2 s. The standard deviation of *Pn* residuals is reduced by a factor of about 2. Kriging residuals to SSSCs provides further

improvement, reducing mean *Pn* travel time bias by up to 3.7 s and the standard deviation of *Pn* residuals by a factor of about 3. We emphasize that these are preliminary results, using Bond r s (1999) method. We shall be obtaining SSSCs by different methods, and we are carrying out a direct evaluation of travel times in 3D structures for the specific purpose of comparing with the more primitive evaluation indicated by equation (1).

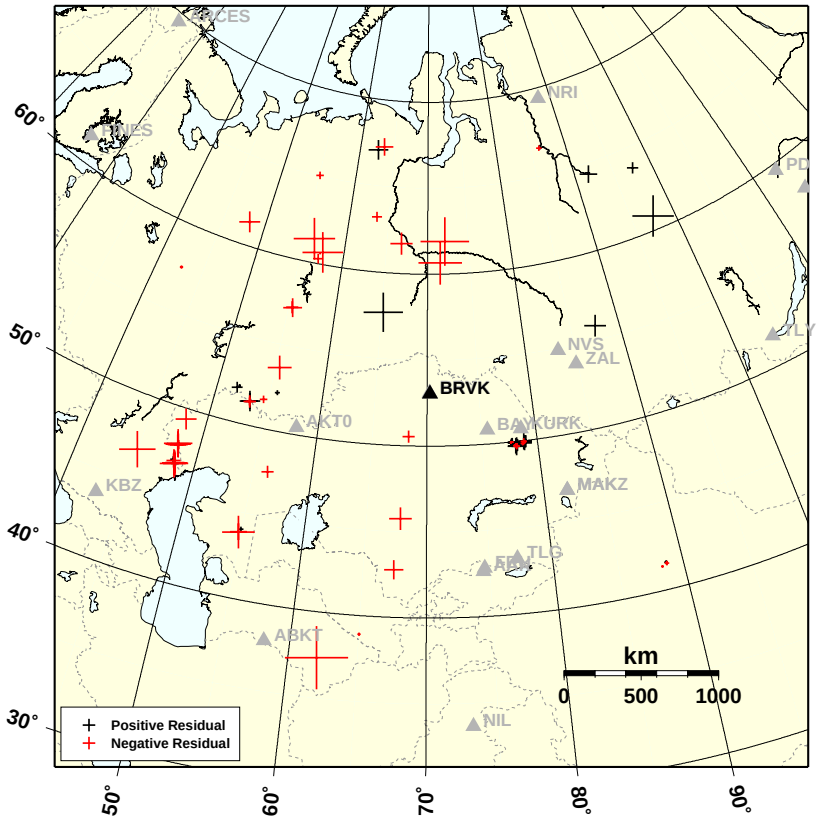

Figure 4. Residuals here are the observed travel time, minus the IASP91 time, minus the SSSC for Borovoye for the appropriate distance and azimuth. On average, observed times are now only 0.4 s earlier that IASP91 times, and have a standard deviation of 1.2 s. Both the average residual and the scatter are significantly improved over Figure 2.

Table 1. Residuals and variances for Pn travel times at Borovoye, for different source regions

Case	IASPEI91		SSSC		SSSC+Kriging	
	$\mu_{\Delta T}$	$\sigma_{\Delta T}$	$\mu_{\Delta T}$	$\sigma_{\Delta T}$	$\mu_{\Delta T}$	$\sigma_{\Delta T}$
STS UNE's	+0.50	0.44	+0.11	0.42	+0.05	0.32
Lop Nor UNE's	-3.78	0.15	-2.05	0.15	-0.04	0.15
Soviet PNE's	-3.91	1.96	-0.67	1.29	-0.40	1.16
Overall	-1.68	2.57	-0.36	1.07	-0.15	0.83

Validation of our preliminary SSSCs

The most direct way to demonstrate that a set of SSSCs is useful, is to see if they can provide improved locations when applied to events whose location is in fact known. For the Lop Nor nuclear explosion of 1995 May 15, which occurred during the first year of GSETT-3, we have arrival times of *Pn* at stations NIL, AAK, MAKZ, BRVK, KURK, ZAL, TLY and ULN. Figure 5 shows five different locations for this event, including ground truth (taken from work of Engdahl and Bergman). The location estimate using regional waves interpreted with IASP91 has considerable uncertainty, significantly reduced when SSSCs for these eight stations are applied. The best location is based on regional and teleseismic signals. Table 2 summarizes the improvement in location given by using our preliminary SSSCs for Lop Nor explosions.

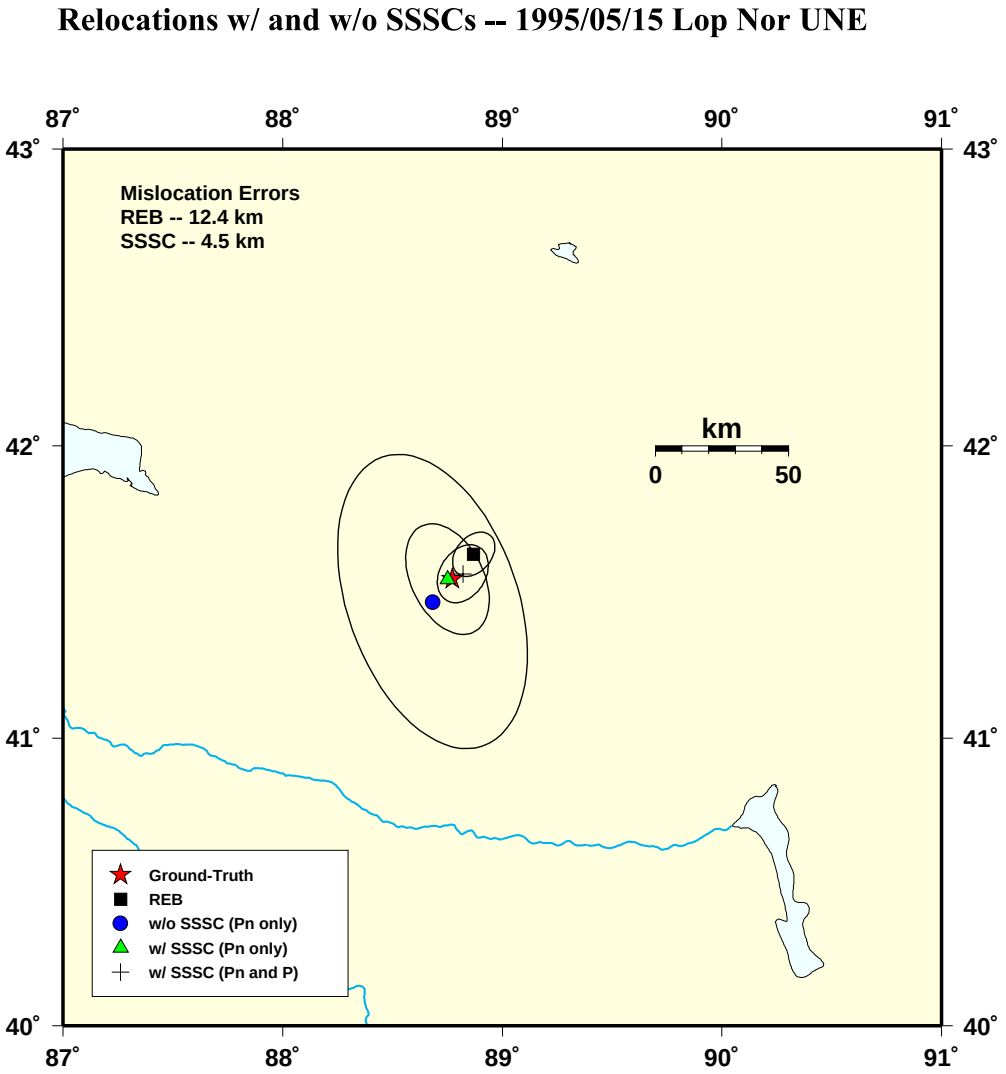

Figure 5. The ground truth location here (red star) is taken from work of Engdahl and Bergman. The REB location (black square) has a small confidence ellipse but it does not include the actual location. A location estimate using regional waves only, interpreted with IASP91 (blue circle) has large uncertainty. The location estimate using regional waves with SSSCs for eight regional IMS stations (green triangle) shows a good result. The location using regional and teleseismic waves gives the best result (black cross).

Table 2. Location performance metrics for Lop Nor explosions

	Pn phases only		P + Pn phases	
	w/o SSSC	w/ SSSC	w/o SSSC	w/ SSSC
Mean mislocation error (km)	112.8	19.1	12.9	7.7
Mean error ellipse size (km^2)	66,389	15,282	950	580

Additional datasets for empirical travel times in Eastern Asia

The Soviet-era PNEs and underground nuclear explosions (UNTs) at weapons test sites were recorded by hundreds of stations within the territory of the former Soviet Union, that typically did not report those arrival times in the open literature. Arrival times of these events were reported to the International Seismological Centre (ISC) by hundreds of stations in Eastern Asia. And of course many of the PNEs and some of the UNTs were very well recorded by hundreds of temporary field stations deployed in long profiles within the U.S.S.R. In addition to the use of Bond r s (1999) method, we are building a dataset of all these travel times that can be used to obtain SSSCs more directly from observations. The principal work of building this dataset, is resolving hundreds of questions on

- what to do when different analysts pick different arrivals from the same waveform, and
- what to do when different station coordinates are listed by different organizations for different stations.

This work is well in hand. For example, for phase data collated by Ivan Kitov of the Institute of Dynamics of the Geosphere (IDG) from 83 PNEs and UNTs from Novaya Zemlya (35 tests) and Semipalatinsk Test Site (80 tests), one question is concerned with the 129 Soviet station locations associated with arrival picks in the data and how these should be merged with the reports of the same events given at 915 stations (east of 20E and north of 5N) for which IDG has also collated phase data derived from the ISC bulletin. These data provide dense coverage, as indicated by Figure 6, but to use these data we needed to resolve the following issues:
1) There are duplicate station "codes" but different locations.
2) The station list file has 1044 stations (129 Soviet + 915 derived from ISC) but 944 stations when duplicate code names are removed.
3) In case of phase picks for PNEs, there are 106 stations with more than 20 observations and 236 stations with fewer than 20 picks. We have examined all of these 106 stations and have used numerous contacts with knowledgeable sources of information in the former Soviet Union to decide the best station locations.
4) The ISC station list and the principal Soviet station list contain different station codes for the same station, as well as the same code for different stations, which must all be resolved.
5) Finally, when the station database is constructed, operation start and end time has to be entered in the case of several stations that were moved, and the best information from station operators has to be used.

The outcome of this major effort, is a groomed list of 355 station coordinates in which we have confidence, for stations that reported the vast majority of the phase pick data for Soviet PNEs and UNTs.

Additional to the nuclear explosion phase-pick databases we have listings of tens of thousands of seismic event locations in Kyrgyzstan, Southern Kazakhstan, and the Altay-Sayan and Baykal regions of Russia. We are working to obtain subsets of these events that are GT5 quality, and preferably events that occurred since January 1995 (the beginning of full-time GSETT-3 operations) with magnitude large enough to give

unambiguous picks at the IMS stations were are studying. For events in Tibet and the Indian sub-continent, our consortium partner at URS Greiner, Chandan Saikia, is providing a small number of GT5 events and a much larger set of GT10 events.

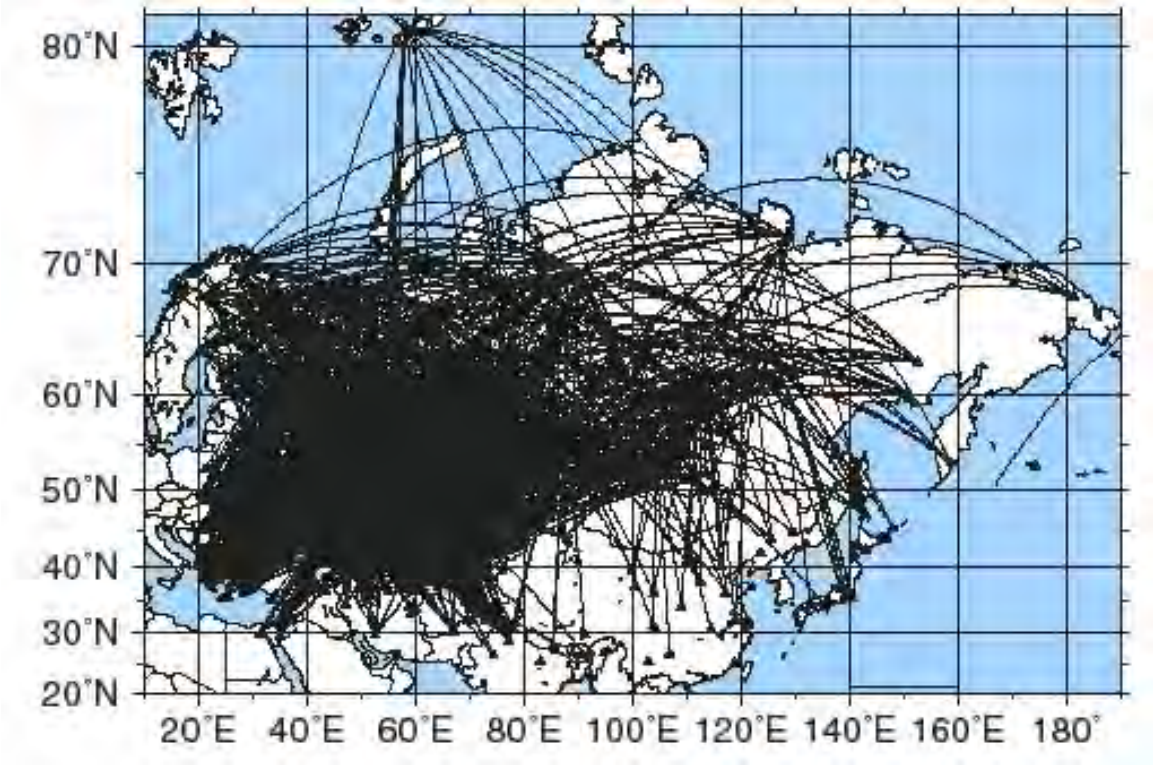

Figure 6. Great circle paths between the PNEs (stars) and stations (triangles) for which phase data are reported from 83 Soviet-era PNEs at standard and regional stations of the former Soviet Union and other stations in Eurasia, as collated by staff of the Institute of Dynamics of the Geosphere (Moscow). We have worked with several sources of information on station operations to resolve numerous questions of the station locations used in this dataset, which is a valuable resource for IMS station location calibration.

Spatial Clustering of Seismicity in China

We have begun to collect high-precision hypocenter locations for mainland China by applying a double-difference (DD) earthquake relocation technique (Waldhauser and Ellsworth, 2000) to travel time data listed in the Annual Bulletin of Chinese Earthquakes (ABCE). This dataset is described by Hearn and Ni (2000). The DD technique uses travel time differences between nearby earthquakes recorded at common stations to solve for highly accurate hypocentral separations between the events. It therefore works best in areas with dense earthquake distribution, where it minimizes effects due to unmodeled velocity structure without the use of station corrections. The method is not sensitive to errors of a few km in station location, unless used to locate events at distances of less than a few tens of km, because it is only the travel time difference that is used, and the azimuth of two events not far apart will be almost the same at each station.

We have formed travel time differences from about 140,000 *P*- and *S*-phases of about 6,000 events (magnitudes 2.7 - 7.1) listed in the ABCE for seven different years. Due to the sparse spatial distribution of the events, and thus the somewhat large average distance between hypocenters, small clusters of up to 70 events could be formed only in areas where the seismicity is dense enough. In these areas the average location accuracy improved after relocation by more than an order of magnitude compared to the ABCE locations.

Figure 7 shows the DD results for four examples, of event clusters that occurred in eastern (Cluster 1), southern (Cluster 2 and 3), and western (Cluster 4) China. The top row of panels indicates the location of the clusters and the stations used to relocate the earthquakes. Panels in the second and third row show the epicenters as listed in the ABCE catalog and after DD relocation, respectively. In Cluster 1 to 3, strong spatial clustering is observed which appears to delineate local tectonic features. In Cluster 4 the relocated events are more diffuse, most likely due to the sparse station distribution.

Analysis of the residuals of travel time differences indicate that the phase picks are of high quality, as noted by Hearn and Ni (2000). Thus this data is best suited to image seismicity with high resolution on a local scale where events locate close together. Increasing earthquake density by including ABCE data from additional time periods might help to relocate earthquakes over larger distances, such as entire fault systems. Such studies would have the potential to contribute to a better understanding of the tectonic processes that take place in China as well as to provide groundtruth data for our location calibration work.

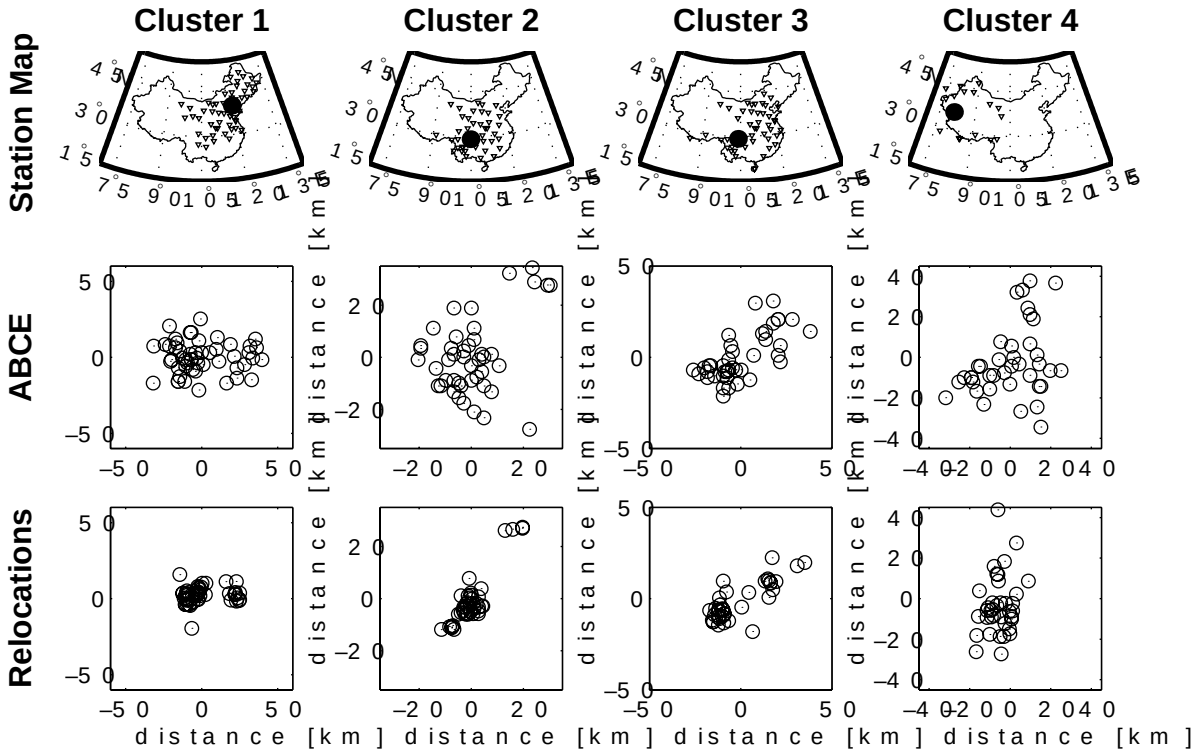

Figure 7. Examples of double-difference locations for four earthquake clusters on mainland China. Top row: location of clusters and stations used in the relocation. Middle row: location of epicenters as listed in the ABCE catalog. Bottom row: location of epicenters after relocating the events with the DD method.

CONCLUSIONS AND RECOMMENDATIONS

We have obtained preliminary SSSCs for IMS stations in Eastern Asia, that demonstrably improve location estimates in the limited number of cases where we have sought this basic validation.

We recommend the use of empirical datasets of travel times from well-documented (GT5 or better) seismic events, (1) to aid in the evaluation of our preliminary SSSCs, (2) to enable kriging residuals on our preliminary SSSCs, and (3) to permit independent derivations of SSSCs using methods other than that of Bond r (1999) on which we are currently relying. We shall be carrying out these three different uses of empirical data.

Since SSSCs can be produced by several different methods, and by different groups of researchers studying the same set of stations, it will be important to develop procedures that enable different SSSCs to be objectively compared, and ranked as to their effectiveness.

ACKNOWLEDGEMENTS

We acknowledge the assistance of numerous operators of local and regional networks in Central Asia; also Tom Hearn and Jim Ni for information on Chinese seismicity and how it is reported, Jack Murphy for helpful discussions of Soviet PNE data, and Bob Engdahl for access to Lop Nor datasets (groomed ISC phase picks, and location estimates based on hypocentroidal decomposition).

REFERENCES

Antonenko, A.N. (1984), The Deep Structure of the Kazakhstan Earth Crust (from seismic data). Nauka Publ. House, Alma-Ata, 242 p. (in Russian).

Bondár, I. (1999), Combining 1-D models for regional calibration, in Proceedings of a Workshop on IMS Location Calibration, Oslo, January 1999.

Hearn, T. M, and J.F. Ni (2000), Tomography and Location Problems in China Using Regional Travel-Time Data, in *Proceedings of the22nd Annual CTBT Monitoring Symposium*, New Orleans.

Khalturin, V.I., T.G. Rautian, and P.G. Richards (2001), A study of small magnitude seismic events during 1961 – 1989 on and near the Semipalatinsk Test Site, Kazakhstan, *Pure appl. Geophys.*, *158*, 143-171.

Mikhailov, V.N. (editor) and 14 co-authors (1996), USSR Nuclear Weapons Tests and Peaceful Nuclear explosions, 1949 through 1990, RFNC-VNIIEF, Sarov, 96 p.

Nersesov, I.L. and T.G. Rautian (1964), Kinematics and dynamics of seismic waves at distances up to 3500 km, *Proc. Inst. Physics of the Earth, Moscow, 32*, 63-87.

Richards, P. G., W.-Y. Kim, and V. I. Khalturin (2000), A Plan for Seismic Location calibration of 30 IMS Stations in Eastern Asia, in *Proceedings of the Annual CTBT Monitoring Symposium*, New Orleans.

Seismic Models of the Lithosphere of the main Geostructures in territory of the USSR, Moscow, Nauka Publ. House, 1980, 311 p. (in Russian).

Shatsiliv, V.I. et al. (1993), Velocity Models of the Earth's Crust in Kazakhstan, Evrasia Publ. House, Almaty, 105 p (in Russian).

Sultanov, D.D., J.R. Murphy, and Kh. D. Rubinstein (1999), A Seismic Source Summary for Soviet Peaceful Nuclear Explosions, *Bull. Seism. Soc. Amer., 89*, 640-647.

Waldhauser, F., and W. Ellsworth (2000), A Double-Difference Earthquake Location Algorithm: Method and Application to the Northern Hayward Fault, California, *Bull. Seism. Soc. Amer., 90*, 1353-1368.

Zunnunov, F.Kh. (1985), Central Asia Lithosphere from Seismic Data, Tashkent, FAN Publ. House, 108 p. (in Russian).

MONITORING OF SEISMIC EVENTS IN THE CENTRAL ANDEAN REGION

Lawrence A. Drake, Rodolfo Ayala and S. Cristina Condori

Observatorio San Calixto

Sponsored by Air Force Technical Applications Center

Contract No. F49620-91-1-0214

ABSTRACT

Where the crust of the earth is very thick, for example in the Andean region of South America, the locations and depths of seismic events given by reporting agencies are systematically wrong, because these agencies use models of the earth with crusts of 24-, 33- and 35-km thickness, whereas the earth's crust in western Bolivia reaches a thickness of 72 km. In addition, the International Data Centre commences its location of events in the central Andean region with a location from the Yellowknife array in western Canada. By this method it is difficult to read accurately the arrivals of events of magnitude less than 4. We have used local seismic stations in the region of Bolivia and a three-dimensional model to locate seismic events in the central Andean region. We use the Podvin-Lecomte method to calculate the least-time paths from points in the grid to the seismic stations and the maximum of the Tarantola-Valette probability density function to calculate the seismic event location. Our grid spacing is 5 km and we make an iteration at one tenth of 5 km. Our assumption of a P- to S-wave velocity ratio of 1.76 means that the least-time paths of P and S waves are the same, but clearly, under the Western Cordillera, this assumption is also systematically wrong. Between latitudes of 15 and 28 degrees S, we have noticed that the larger, active (since the beginning of the Holocene) volcanoes are approximately over the revised 125-km depth contour of the Nazca slab. We are strongly reducing S-wave velocities in this part of the model. Also, recent work with P-to-S converted seismic waves has shown a 10- to 20-km thick intra-crustal low-velocity zone extending from the Eastern Cordillera, where the Brazil Shield is underthrusting, to the Altiplano in Bolivia and the Puna in Argentina. We are reducing P- and S-wave velocities in this extensive intra-crustal region also.

KEY WORDS: earthquake location, central Andean region, Western Cordillera, low velocity zone.

OBJECTIVES

The objectives of this study were: i) to test a proposed three-dimensional P- and S-wave velocity model for the region of southern Peru and western Bolivia; ii) to determine the mislocation for earthquakes of intermediate depth outside the Bolivian seismic network (and including some Peruvian stations); and iii) to compare different velocity models and earthquake location methods for the region.

RESEARCH ACCOMPLISHED

Introduction

The region of study is located above the segment of the subduction zone dipping ENE normally about 30° (Barazangi and Isacks, 1976; Sacks, 1977; Cahill and Isacks, 1992).

The western central Andes region has a morphostructural zonation with two zones: i) the low Pacific lands (altitudes up to 2500 m), comprising the Coastal Cordillera and the Longitudinal Valley; and ii) the high Andes (altitudes between 2500 and 7000 m), comprising the Western Cordillera, the Altiplano, the Eastern Cordillera and the Subandean zone (Figure 1).

The use of worldwide teleseismic data, for example the bulletins of the International Data Centre, permits us to define the general patterns of seismicity (Barazangi and Isacks, 1976, 1979; Chowdhury and Whiteman, 1987; Cahill and Isacks, 1992), but a higher precision of location is obtained by a local network with close azimuthal coverage. However, lateral variations in the Wadati-Benioff zone caused by the descending high-velocity slab introduce location errors and a smaller thickness of the Wadati-Benioff zone than the actual thickness (McLaren and Frohlich, 1985). Commonly, location errors are smaller for events with focal depths less than 50-km depth, because the rays spend only a short time traveling within the slab. In contrast, rays from deeper events may travel long distances in the slab; this causes them to be grossly mislocated by local networks (Engdahl et al., 1977; Fujita et al., 1981; Frohlich et al., 1982).

The permanent Bolivian local seismic network has sparse coverage in the Peru-Bolivia border region (Figure 1) and to find more precise locations we need to include some stations of the Peruvian net.

Data

The data were recorded by the permanent telemetric Bolivian local seismic network (Figure 1) and some stations of Peruvian net; these data cover the period from January 2000 to December 2000, with magnitude mb greater than 3.0.

The uncertainties of picking P arrival times were less than or equal to 0.05 s and the uncertainties of picking S arrival times were less than or equal to 0.10 s (Figure 2). The P to S-wave velocity ratio was taken to be equal to 1.76.

Table 1. Station coordinates of the Bolivian permanent telemetric network, with some Peruvian seismic stations

CODE	LATITUDE °S	LONGITUDE °W	ALTITUDE M
BBOB	16.1443	68.1329	3960
BBOD	16.6374	68.5981	4230
BBOE	16.8127	67.9821	4325
BBOF	16.9740	68.3380	4480
LPAZ	16.7829	68.1307	4740
CON	15.4400	69.4300	3900
LYA	18.1350	70.8500	363
SNG	16.5700	72.7150	161
TAM	13.4780	71.8590	3858
TOQ	17.3070	70.6430	2586

Hypocenter location method

Two different hypocenter location methods were used: i) the conventional method Hypocenter version 3.2 (Lienert et al., 1986); and ii) the 3-DGRIDLOC method (Wittlinger et al., 1993; Ayala, 1997).

This latter method is a combination of two tools: First, the PL method (Podvin and Lecomte, 1991) is used to solve the forward problem, that is, to calculate the first arrival times at the cells of the seismograph stations from each of the cells of a three-dimensional velocity model. This method was inspired by the approach of Vidale (1988; 1990). In the ray approximation, wave propagation is described by the eikonal equation

$$(\nabla t)^2 = s^2$$

where s is the slowness of the medium (inverse of wave velocity) and t represents the arrival time of a wavefront at a point. According to the classical ray approximation (asymptotic approximation of the wave equation at infinite frequency), wavefronts are treated as propagating discontinuities (represented as isochrons). The approach of Vidale (1988; 1990) relies on a finite difference approximation of the eikonal equation. With the PL method, wavefronts rather than rays are propagated in the model. First arrival times are computed relying on a systematic application of Huygens' principle in the finite difference approximation. Such an approach takes into account transmitted and diffracted body waves and head waves. Local discontinuities of the gradient of the time field of the first arrival, for example, caustics, are built as intersections of locally independent wavefronts. As a consequence the PL method provides accurate travel times of the first arrivals in the presence of severe, arbitrarily shaped velocity contrasts.

Secondly, a nonlinear algorithm from Tarantola and Valette (1982) uses a probability density function to solve the inverse problem; that is, from the first arrival times at the seismograph stations, it calculates the cell that most probably contains the earthquake. The process is repeated with cells reduced in volume by a factor of 1000.

By direct methods, such as 3-DGRIDLOC, based on a hypocenter searching in a three-dimensional mesh, when the velocity model is known, earthquake outside the network, where there is sparse coverage of seismograph stations, can be reliably located (Nelson and Vidale, 1990).

Velocity models

To relocate the earthquakes we used two different velocity models: i) a conventional velocity model of flat homogeneous layers (Table 2); and ii) an approximately three-dimensional velocity model for the region, with a descending high-velocity slab, dipping ENE at approximately 30°.

Table 2. Velocity structure

Layer thickness (km)	**P velocity** (km s^{-1})
10	5.0
25	6.0
25	6.6
	8.0

The three-dimensional velocity model corresponds to the western part of the three-dimensional velocity model proposed for the region of the Bolivian Andes (Ayala, 1997; Ayala and Drake, 1997). The model comprised 150 x 100 x 70 cubic cells of approximately 5-km size (Figure 1), defining a cubic volume of 750 km in longitude, 500 km in latitude and 350 km in depth with different velocity structures for each of the morphostructural zones (Schmitz, 1993; Wigger et al., 1994; Romanyuk et al., 1999). The depth of the Moho was taken from the Airy compensation model (Schmitz, 1993; Schmitz et al., 1997). The shape of the slab was taken from the geometry of the Wadati-Benioff zone (Cahill and Isacks, 1992), with a thickness of 80 km and a velocity 2.7 per cent faster than the surrounding mantle velocity (Engdahl et al., 1995; Dorbath et al., 1996). For the mantle, at depths between 200 and 650 km above and below the slab, we took the velocity of the *iasp91* model (Kennett and Engdahl, 1991).

Results

Most of the earthquakes relocated are inside the Bolivian and Peruvian seismic nets along a narrow band of seismicity related to the subducted Nazca plate.

The relocations of the earthquakes using the method Hypocenter, version 3.2, with all stations, are different to locations of the IDC bulletins. The average computed horizontal mislocation is less than or equal to 10 km, and the average computed vertical mislocation is less than or equal to 20 km, compared with the locations of the IDC bulletins. The residuals of all relocations, with and without the Peruvian seismic stations, are similar, and proved to be relatively insensitive to the amount of mislocation, compared with the location of the IDC bulletins. The average computed horizontal and vertical location errors are less than or equal to 15 km. In general, the vector of mislocation is in the northeast-southwest direction.

The relocation of events using the 3-DGRIDLOC method and a three-dimensional velocity model, with and without the Peruvian seismic stations, also proved to be relatively insensitive to the amount of mislocation, compared with the locations of the IDC bulletins, and showed average computed horizontal and vertical mislocations less than or equal to 10 km, compared with the locations of the IDC bulletins. The larger mislocations are in the northern part of the region, while, in the southern part of the region, the mislocations are smaller. When the data of the Peruvian seismic stations are introduced, the residuals increased.

CONCLUSIONS AND FUTURE PLANS

Conventional location velocity models, for example, those of Hypocenter, version 3.2, introduce systematic location errors in subduction zones, both because the structure of the earth is very different from those of the models in these regions, and because, in this particular comparison of locations, we assumed a P- to S-wave velocity ratio of 1.76, whereas clearly, under the Western Cordillera, this assumption is also wrong. The residuals, with and without the Peruvian seismic stations, were similar and proved to be relatively insensitive to the amount of mislocation, compared with the locations of the IDC bulletins.

For the three-dimensional 3-DGRIDLOC method, our assumption of a P- to S-wave velocity ratio of 1.76 meant that the least-time paths of P and S waves were the same, and this saved computing time, but it was a wrong assumption. The three-dimensional velocity model is a more realistic approximation to the velocity structure of the region. The model and the three-dimensional 3-DGRIDLOC method have allowed us to obtain locations more like those of the IDC bulletins, especially in the case of earthquakes outside the network, mainly in the southern part of the Peru-Bolivia border region. The active volcanic chain of the Western Cordillera reduces the S-wave velocities in this part of the model; this fact is reflected when the Peruvian seismic data are introduced, and the locations using 3-DGRIDLOC method and three-dimensional velocity model show larger residuals. The location for the southern part of the region shows smaller mislocations compared with the northern part of the region; this fact shows that the three-dimensional velocity models is more appropriate in the southern part of the region than in the northern part of the region

In future work we will: i) continue to revise the locations of earthquakes in the whole of the Bolivian Andes; ii) quantify more precisely, using the data of temporary seismic nets, the differences of our locations from those of the bulletins of the IDC; and iii) improve the three-dimensional velocity model for the region, in order to take into account the anomalous velocity regions. Besides the difficulties of the S-wave velocities beneath the volcanoes of the Western Cordillera, recent work with P-to-S converted seismic waves has shown an intra-crustal low-velocity zone, of thickness of 10 to 20 km, extending from the Eastern Cordillera, where the Brazil Shield is underthrusting, to the Altiplano in Bolivia and the Puna in Argentina.

ACKNOWLEDGEMENTS

We thank Dr. Johnny Tavera from Instituto Geofísico of Peru, for providing us with the data of some stations of Peruvian permanent local network in order to do this study.

REFERENCES

Ayala, R. (1997). Seismotectonique des Andes de Bolivie et rôle de l'Orocline bolivien, *PhD thesis*, Université Louis Pasteur, Strasbourg, France.

Ayala, R. and L.A. Drake (1997). Earthquake location with a 3-D velocity model for the region of the Bolivian Andes, in *Proceedings of the 19th Annual Seismic Research Symposium on Monitoring a Comprehensive Test Ban Treaty*, Orlando, USA, pp. 191-200.

Barazangi, M. and B.L. Isacks (1976). Spatial distribution of earthquakes and subduction of the Nazca plate beneath South America, *Geology*, 4, 686-692.

Barazangi, M. and B.L. Isacks (1979). A comparison of the spatial distribution of mantle earthquakes determined from data produced by local and by teleseismic networks for the Japan and the Aleutian arcs, *Bull. Seism. Soc. Am*., 69, 1763-1770.

Cahill T. and B.L. Isacks (1992). Seismicity and shape of the subducted Nazca plate, *J. Geophys. Res*., 97, 17503-17529.

Chowdhury, D.K. and S.K. Whiteman (1987). Structure of the Benioff zone under southern Peru to central Chile, *Tectonophys.*, 134, 215-226.

Dorbath, C., A. Paul and The Lithoscophe Andean Group (1996). Tomography of the Andean lithosphere at 20°S: First results of the lithoscope esperiment, *Phys. Earth Planet. Inter*., 97, 133-144.

Engdahl, E.R., N.H. Sleep and M.-T. Lin (1977). Plate effects in north Pacific subduction zones, *Tectonophys*., 37, 95-116.

Engdahl, E.R., R.D. van der Hilst and J. Berrocal (1995). Imaging of subducted lithosphere beneath South America, *Geophys. Res. Lett.*, 22, 2317-2320.

Frohlich, C., S. Billington, E.R. Engdahl and M. Malahoff (1982). Detection and location of earthquakes in the central Aleutian subduction zone using island and ocean bottom seismograph stations, *J. Geophys. Res*., 87, 6853-6864.

Fujita, K., E.R. Engdahl and N.H. Sleep (1981). Subduction zone calibration and teleseismic relocation of thrust events in the central Aleutian Islands, *Bull. Seism. Soc. Am*., 71, 1805-1828.

Kennett, B.L.N. and E.R. Engdahl (1991). Travel times for global earthquake location and phase identification, *Geophys. J. Int.*, 105, 429-465.

Lienert, B.R., E. Berg and L.N. Frazer (1986). Hypocenter: An earthquake location method using centered, scaled, and adaptively least squares, *Bull. Seism. Soc. Am*., 76, 771-783.

McLaren, J.P. and C. Frohlich (1985). Model calculations of regional network locations for earthquakes in subduction zones, *Bull. Seism. Soc. Am.*, 75, 397-413.

Nelson, G.D. and J.E. Vidale (1990). Earthquake location by 3-D finite difference travel times, *Bull. Seism. Soc. Am.*, 80, 395-410.

Podvin P. and I. Lecomte (1991). Finite difference computation of travel times in very contrasted velocity models: a massively parallel approach and its associated tools, *Geophys. J. Int.*, 105, 271-284.

Romanyuk, T.V., H.J. Götze and P.F. Halvorson (1999). A density model of the Andean subduction zone, *The Leading Edge*, 18, 264-268.

Sacks, I.S. (1977). Interrelationships between volcanism, seismicity and anelasticity in western South America, *Tectonophys*., 37, 131-139.

Schmitz, M. (1993). Kollisionsstrukturen in den Zentralen Anden: Ergebnisse refraktionsseismischer Messungen und Modellierung krustaler Deformationen, *Berliner Geowiss. Abh*., B (20), 1-127.

Schmitz, M., W.-D. Heinsohn and F.R. Schilling (1997). Seismic, gravity and petrological evidence for partial melt beneath the thickened Central Andean crust (21-23°S), *Tectonophys.*, 270, 313-326.

Tarantola, A. and B. Valette (1982). Inverse problems = quest for information, *J. Geophys.*, 50, 159-170.

Vidale, J.E. (1988). Finite difference calculation of travel times, *Bull. Seism. Soc. Am.*, 78, 2062-2076.

Vidale, J.E. (1990). Finite difference calculations of travel times in 3-D, *Geophysics*, 55, 521-526.

Wigger, P.J., M. Schmitz, M. Araneda, G. Asch, S. Baldzuhn, P. Giese, W.-D. Heinsohn, E. Martinez, E. Ricaldi, P. Röwer and J. Viramonte (1994). Variation in the crustal structure of the southern Central Andes deduced from seismic refraction investigations, In: *Tectonics of the Southern Central Andes* (K.-J. Reutter, E. Scheuber and P.J. Wigger, eds), Springer-Verlag, Berlin, pp. 23-48.

Wittlinger, G., G. Herquel and T. Nakache (1993). Earthquake location in strongly heterogeneous media, *Geophys. J. Int.*, 115, 759-777.

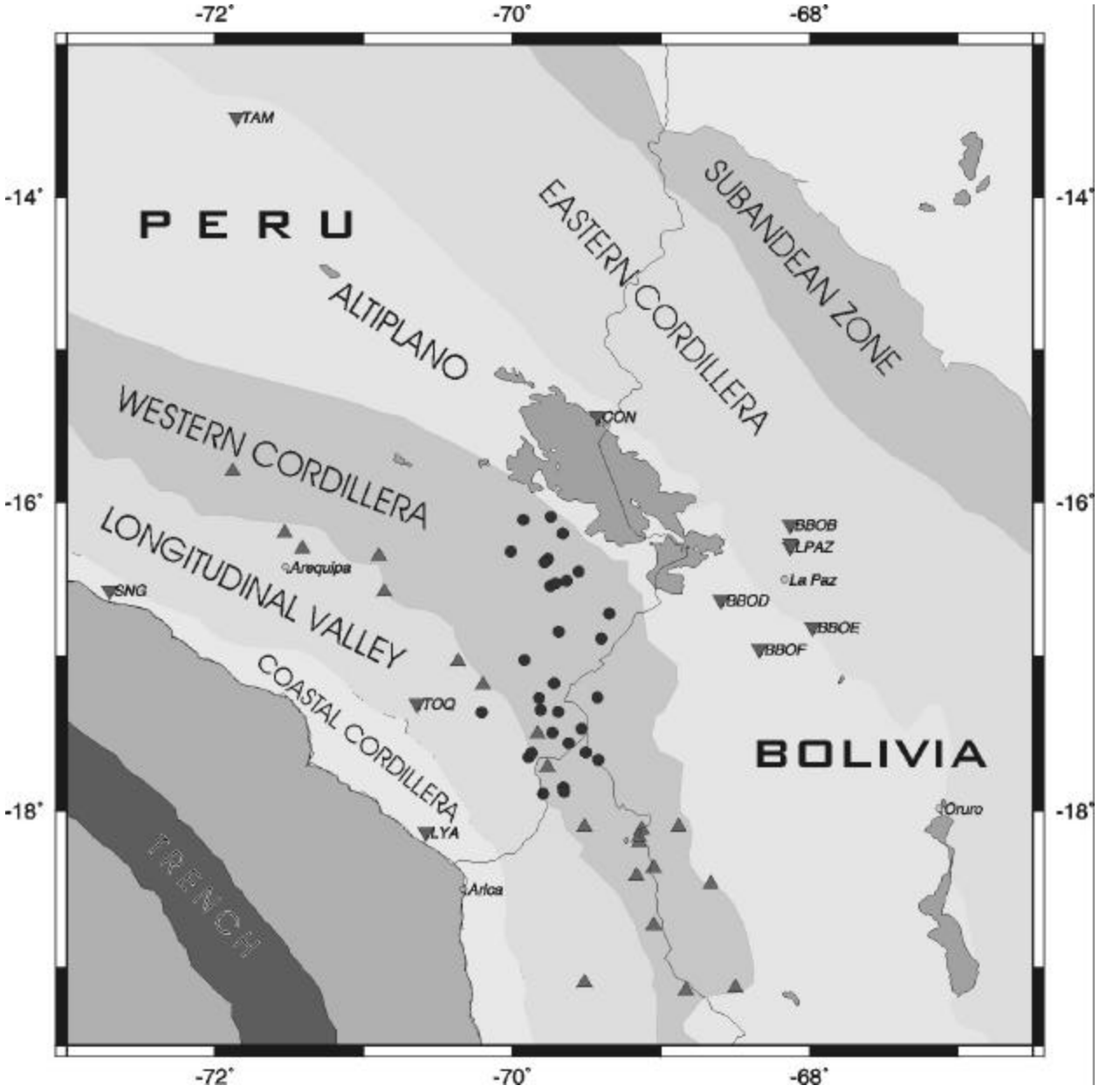

Figure 1. Map of the morphostructural units for the western central Andes and the distribution of seismograph stations of the Bolivian permanent telemetric network, including some Peruvian seismic stations (inverted triangles); the triangles represent the active volcanoes in the region; the white small circles represent the main cities; the dark circles represent the epicenters of the earthquakes recorded during the period January 2000 to December 2000, with magnitudes mb greater than 3.0.

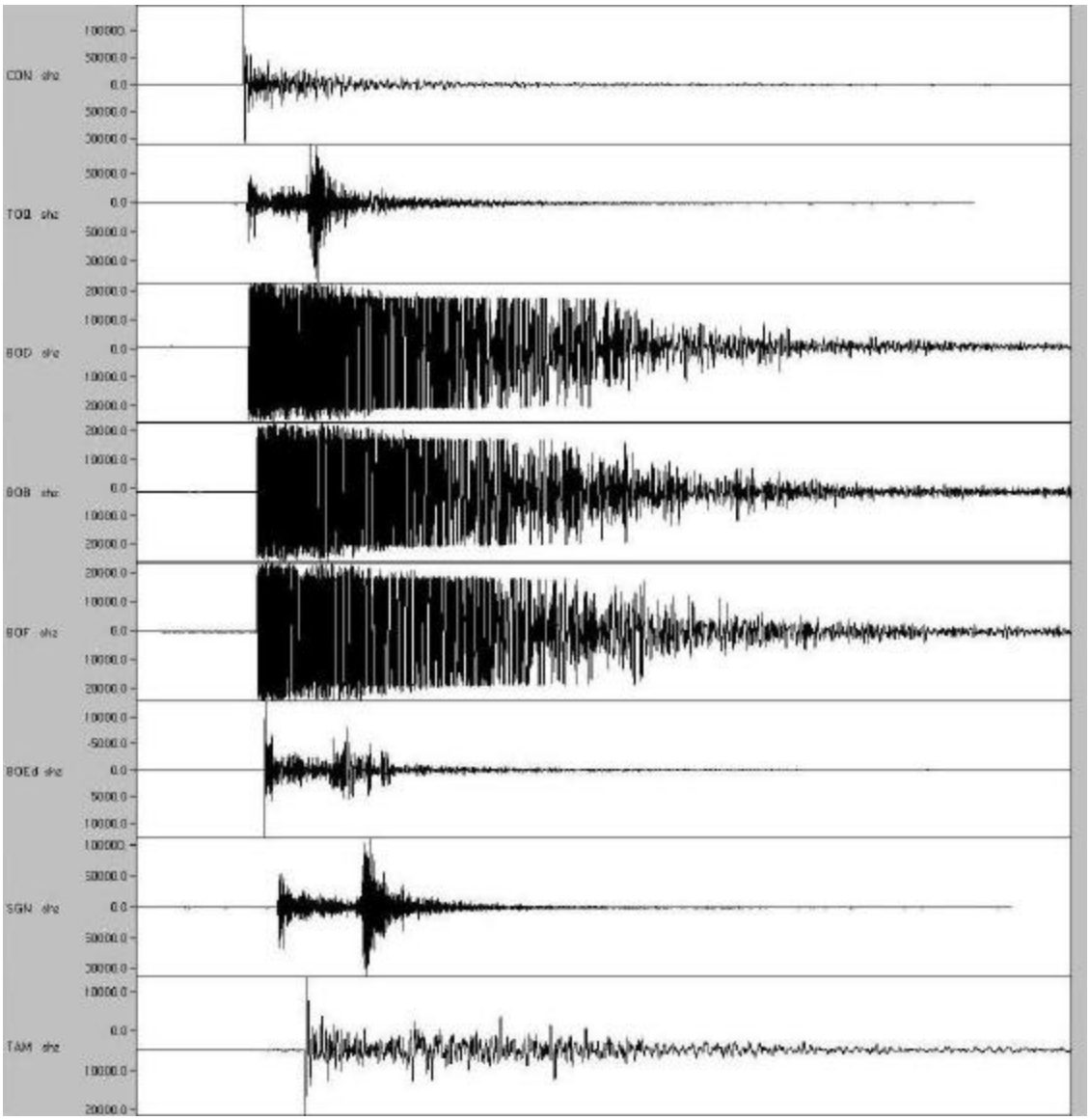

Figure 2. Example of short-period seismographs of 25 April 2000 earthquake recorded by the Bolivian seismic network and the Peruvian seismic station located in western central Andes.

VALIDATION AND GENERATION OF REFERENCE EVENTS BY CLUSTER ANALYSIS

E. R. Engdahl and Eric A. Bergman

University of Colorado, Boulder

Sponsored by Defense Threat Reduction Agency

Contract No. DTRA01-00-C-0032

ABSTRACT

High-resolution cluster analysis (multiple-event relocation) of earthquakes and other seismic sources is developed as a tool for assembling catalogs of reference events, especially those whose locations can be determined with an accuracy of 5 km or better [Ground Truth (GT) 5]. We use the Hypocentroidal Decomposition (HDC) method of Jordan and Sverdrup (1981), which is well suited to the rigorous statistical analysis required for this task. Candidate reference events typically arise from local seismic networks and from temporary deployments for aftershock studies that can yield very high-resolution hypocenters that, nevertheless, must be validated. We utilize arrival time data (as reported to the International Seismological Centre and to the U.S. Geological Survey's National Earthquake Information Center) at regional and teleseismic distances in the cluster analysis to validate candidate reference events, and in some cases, to generate new reference events.

HDC analyses have now been performed on a number of earthquake and explosion sequences in Eurasia and Africa, resulting in reference events with locations known to GT5 accuracy. In this paper we review and evaluate our analyses of these clusters to date, and address problem areas. In particular, we find that some candidate reference events cannot be validated because either the reported local network solutions are in error, or the coverage of reported arrival times used in the HDC analysis is not sufficient to constrain the locations. Some discrepancies may arise when local networks locate small precursors or low-energy early stages of rupture in larger earthquakes, while teleseismic stations record only the main pulse of energy release. We have found several cases in which there appear to be systematic biases in the time base used for local network solutions. In another case, we obtained "reference event" locations from two different sources for the same cluster. The two sets are similar enough that HDC cannot be used to discriminate between them, yet different enough to prevent either set from being accepted at GT5 accuracy. Our experiences highlight the importance of a thorough and many-faceted validation program for candidate reference events.

KEY WORDS: reference events, cluster analysis

OBJECTIVE

The primary objective of this research effort is to develop a comprehensive reference event database with validated travel-time information for regional seismic phases recorded by International Monitoring System (IMS) and surrogate stations in Asia and north Africa. This database can be used to support the calculation of regional travel-time curves and source-specific station corrections.

RESEARCH ACCOMPLISHED

Introduction

In this report, we discuss the results of cluster analyses on earthquake and explosion sequences in Eurasia and northern Africa using phase data reported to the ISC and NEIC. All of the events studied have magnitudes of 3.5 or greater. In most cases, reference event data are available from short-term portable seismograph deployments following the initiation of seismic activity. The HDC analyses produce new locations that are defined by "cluster vectors" in space and origin time, relative to the centroid, which is then located in the traditional manner to yield absolute locations and origin times. If one or more reference events are included in

the cluster, the centroid can be shifted to provide the optimal match to the reference locations, which brings all events in the cluster into close alignment with "ground truth". The expanded set of corrected hypocenters is then available to calculate source-station path corrections relative to the Earth model ak135 (Kennett *et al.*, 1995) for regional seismic phases recorded by IMS and surrogate stations in the region of interest. We follow with descriptions of individual sequences (see Figure 1) that highlight our experience in the analyses to date.

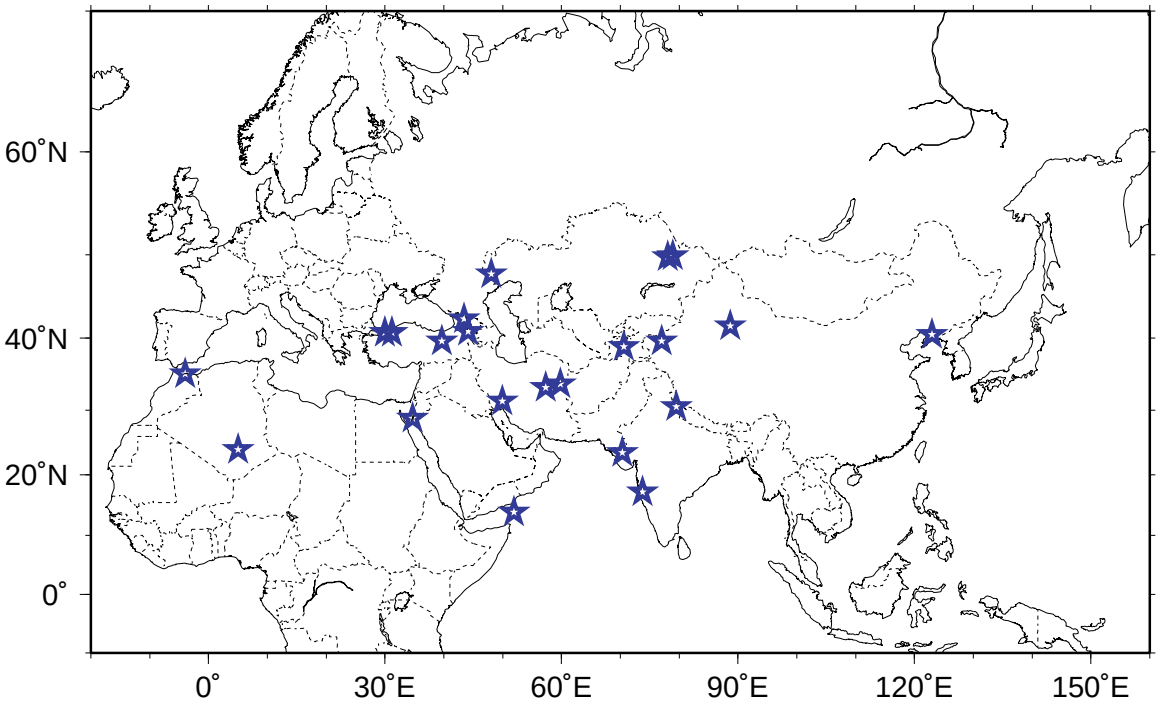

Figure 1. Locations of reference event clusters studied.

Validation Method

The approach being used is based on a high-resolution cluster analysis for relative event location, forming event clusters that contain one or more candidate reference events. The clusters are typically 50-100 km across and contain up to 100 or so events that have occurred since 1964 and that are well recorded at regional and teleseismic distances. The cluster is located in an absolute sense as if all the data were from a single event, using ak135. Obviously, this is subject to bias. To remove the bias, we shift the cluster in space and time to best match the reference events. The degree of consistency between the relative locations as determined by global arrival time data and the relative locations specified by the reference event data is one of the tests we use to validate candidate reference events.

Duezce, Turkey: An example of generation of ground truth events

This is a well-studied event on November 12, 1999, for which we were able to obtain 8 reference events, well recorded at regional and teleseismic distance, from studies made by Milkereit (2000) and Tibi (2001). A cluster of 32 events was formed from the mainshock and aftershocks through December 1999. We found very consistent shift vectors to the 8 reference events, resulting in 16 reference events of GT5 accuracy.

Figure 2 shows the progress in HDC analysis that leads to generation of new reference events.

Figure 2a shows an early relocation of 52 events, before poorly located events are removed and outlier residuals flagged. Green vectors show the change in relative location from the EHB starting locations. 90% confidence ellipses for relative location are shown in blue. Tic marks are at 10 km intervals. Figure 2b shows the final

relocation of 32 well-constrained events. Figure 2c shows only the 8 original reference events (black number), and 8 "promoted" reference events (red number) that meet GT5 criteria.

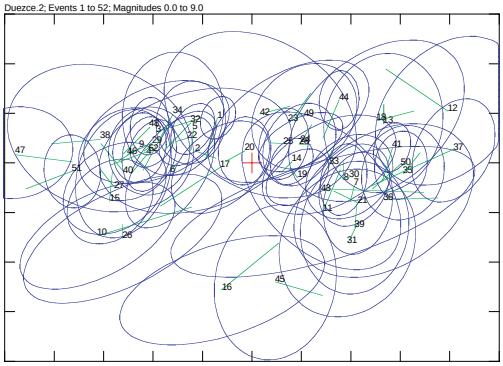

Figure 2a

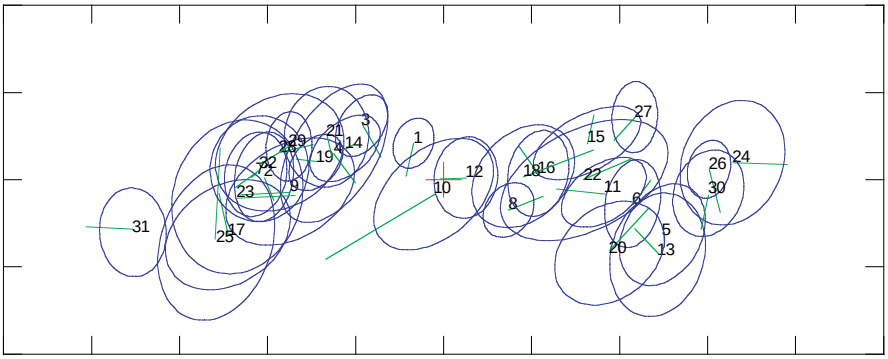

Figure 2b

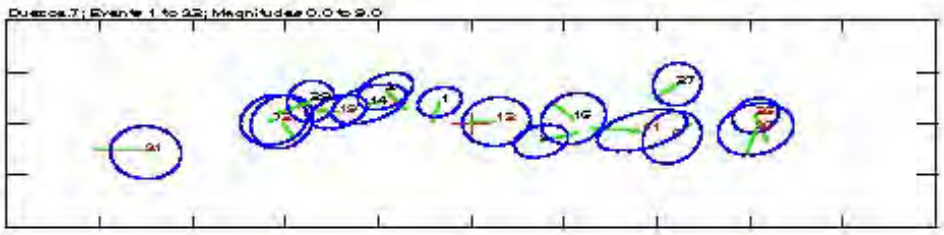

Figure 2c

Zirkuh & Dasht-e-Bayaz

This grouping arose from our study of the Zirkuh (Berberian *et al.*, 1999) earthquake and aftershocks of May-November 1997. The main shock is near the north end of a long fault, and most of the aftershocks, including the ones reported by an aftershock study as "reference events," are in the southern part of the fault zone, as much as 100 km from the main shock. However, several other large earthquakes have occurred near the northern end of the Zirkuh fault, where it intersects with the E-W trending Dasht-e-Bayaz fault (Berberian and Yeats, 1998). There were three major earthquake sequences in a three-week period from mid-November to early December

1979. We formed a cluster of larger events from these three sequences, the 1997 Zirkuh mainshock and a few of its aftershocks, and some individual events from other times, 36 events in total.

Although there are no reference locations available for any of these events, we have placed constraints on the absolute location of the cluster by utilizing the geometric constraints of the Zirkuh and Dasht-e-Bayaz faults, which are orthogonal to each other. The main events have well-constrained strike-slip mechanisms so the requirement that the main shock epicenters locate on the main faults (whose surface ruptures were well mapped right after the quakes) provides a strong constraint on the location of the cluster. Sixteen of the events in the cluster satisfy GT5 criteria on location, although origin times are still unconstrained.

Zirkuh South

The bulk of the aftershocks for the 10 May 1997 Zirkuh earthquake in eastern Iran are in the southern end of the fault zone, and reference locations from an aftershock survey (M. Raeesi, MS Thesis, University of Tehran, 2000) are available for many of them. We analyzed a cluster of 42 events from the sequence and found many inconsistencies between the HDC results and the "reference" locations. Upon a closer reading of the thesis and discussions with the author and his advisor, we believe that further analysis of the aftershock survey data will be required in order to generate true reference event locations. There were numerous logistical problems with the survey (which was in a remote and dangerous part of the country) that may have compromised the results, and the fact that much of the aftershock activity occurred as much as 100 km away from the main shock epicenter led to unfortunate deployment decisions. The available reference material did not adequately document these problems. This is a good example of the need for a validation process for candidate ground truth events. We are pursuing additional data that may yet make it possible to use this sequence for ground truth analysis. There is a possibility to gain additional seismic readings through other agencies, and to use high-resolution maps of surface breakage to help constrain the location of the cluster.

Eilat, Gulf of Aqaba

A list of candidate reference events came from the JSOP project, combining data from several networks in the area. The main events of interest were a large earthquake on November 22, 1995, and its aftershocks. We formed a cluster of 37 events from this sequence and earlier events in the immediate area. As many as 13 events have been presented as reference events (Sweeney, 1998), but our validation exercise indicated numerous inconsistencies, probably because of the different organizations involved. Finally we kept only the main shock on November 22, 1995, as a reference event (using a location provided by A. Hofstetter, Geophysical Institute of Israel). It was the only event whose location from local and regional data met the GT5 criteria and for which HDC analysis provides sufficiently strong location accuracy. The cluster was shifted to best match this location and a total of 12 events in the cluster were promoted to reference event status at the GT5 level. Efforts are ongoing to obtain additional data (especially from Egyptian stations) that might bring some of the other events in the area up to reference event status. This is one of the larger clusters we have used, extending about 100 km in the north-south direction, so it would be especially desirable to obtain additional reference events to ensure that the "common path" assumption for cluster analysis is not being violated.

Garm, Tajikistan

Reference events for this region are obtained from a dense local seismic network (G. Pavlis, Indiana Univ.). We formed a cluster of 23 events between 1975 and 1984. They are all well recorded at regional and teleseismic ranges, and the HDC locations for most of them are close to or better than GT5. There are three good reference events, which give a consistent offset of the cluster. A fourth reference event was rejected because it was very inconsistent with the three others; either the HDC relocation or the reference location is bad. We will include additional events since 1984 to improve the station coverage and statistics.

Hoceima, Morocco

The reference events are part of a major swarm of earthquakes between 1994 and 1996. Most of the arrival time data for these events is at regional distances, however. Cluster analysis cannot be performed with such data, because it violates the assumption of common path errors. Our normal procedure is to use data only beyond 3°.

In this case, the cluster includes only 15 events (from May 1994 to June 1996) that can be located at GT10 or better by HDC, but none of them qualify for GT5. The cluster is very tight, about 20 km by 20 km; therefore, we could re-examine this cluster using data from shorter distances and include more events. Including more events would also improve the cluster vector statistics and reduce the size of the HDC confidence ellipses in some cases.

We used two reference events for this cluster, which were a revision of the locations reported by Sweeney (1998) and which gave very consistent epicenter shifts for the cluster. The difference in OT shifts between the two reference events was rather large, however, over a second. We learned subsequently that—because of timing problems in the network—the reported origin times for these reference events have been normalized (separately) by Department of Energy researchers to the ak135 reference model using reported regional and teleseismic residuals. Using this approach, the normalized origin time for each event becomes highly dependent on the stations reporting data for each event (576 & 200 stations). Therefore, although we can validate the two reference event locations, there is no independent information from this cluster on absolute travel times.

Jiashi, China

This is a massive swarm in western China, beginning in January 1997, that was studied by a temporary deployment of seismometers. We formed a cluster of 83 events that are well located with HDC. Although we were provided with a list of reference locations from the local network that included most of the cluster events, we discovered a serious problem. Only one event had been well located by the network, and the remainder had been located with a master event method that was apparently misapplied, as the pattern of epicenters was in substantial disagreement with the HDC results. Moreover we found a very large difference (nearly 3 seconds) between the reference solution of the master event and the HDC results. This is too large to be plausible as a manifestation of the Earth's heterogeneity. We suspect that there is a problem with the time base used for these Chinese temporary deployments, as we saw a similar phenomenon with the Xiyuan cluster (below). Time-keeping problems might also explain why the Chinese researchers used the master event method. We have recently learned (Wu Zhongliang, personal communication) that the China Seismological Bureau is installing a temporary BB network around Jiashi to study this swarm, and we hope to obtain additional reference event data here. If so, we will be able to promote a large number of events to GT5 status as a result of the HDC analysis.

Koyna Dam, India

Reference locations have been obtained from a local seismic network installed to monitor induced seismicity at the Koyna reservoir in 1967. Many events greater than magnitude 5 have been recorded over the past few decades. We initially worked with a list of 17 reference locations from the National Geophysical Research Institute (NGRI). The first one is the original 1967 event (and of questionable reliability), but the rest are all between 1993 and 2000. We formed a cluster of 31 well-recorded events, and found very consistent estimates of cluster offset from nine reference events.

This should have been one of our better ground truth examples, but soon after finishing the analysis, we learned that there is an alternative set of reference locations for these events, produced by a different group of seismologists in India. We performed the analysis again with the new reference locations (the two sets of reference events have some common events but are not identical) and found equally consistent estimates of cluster offset. The differences are sufficient to deny the possibility of declaring any of these events as GT5 events. We hope that it will be possible to reconcile the differences, but in any case this should be remembered as a cautionary tale about the reliability of so-called "reference events".

Racha, Georgia

The reference events come from a temporary seismic network (Fuenzalida et al, 1977b) that captured aftershocks of a large event in April 1991. The cluster events are from April-October 1991. The cluster included 47 events that could be located to GT10 or better. The cluster is elongated, about 70 km in an E-W direction, and composed of two sub-clusters. Some tests of relocating the sub-clusters separately were done, but we saw no evidence that smaller clusters improved the outcome. We used six reference events that gave a very consistent estimate of the cluster offset and 19 events of GT5 accuracy. We should be able to improve station

coverage and statistics (and provide better coupling to IMS stations and surrogate stations) by adding more recent events to the cluster.

Sahara (Ahaggar Mountains), Algeria, nuclear explosions

This is a small cluster of 5 French nuclear tests in Algeria between 1962 and 1966 with reference event information published by Bolt (1976). As a validation experiment, we perform an HDC cluster analysis of the 5 events. The shifted HDC relocation is very good; the cluster is extremely tight, less than 10 km across; and we obtain a very consistent estimate of the shift vector, 5.6 km at 186°, -0.08 s origin time. The origin times are very close because these data were used with events elsewhere to set the baseline for the IASPI91 travel-time model. It is worth noting the arrival time data sources for these explosions: 620501 - ISS Bulletin: 631020 and 650227 - USC&GS Shot Report (most data read from original seismograms); and 651201 and 660216 - ISC Bulletin.

Spitak, Armenia

This is a small cluster of 11 earthquakes that are very well recorded at regional and teleseismic distances; the HDC locations are almost all better than GT5 quality in relative terms. The three reference locations are derived from a permanent regional network. The cluster consists mainly of an earthquake sequence in December 1988, with aftershocks continuing to May 1990, but there is also one event from January 1967 in the same area. This should have been an excellent ground truth resource, but the relative locations from HDC analysis are inconsistent with the reference locations. No two of the reference events are in agreement. Because of the very strong constraints on the HDC locations, we suspect a problem with the reference locations. As this cluster was formed from an active aftershock sequence, it may be that the local network and the global network (for HDC) are looking at different events which are nearly coincident in time, or the local network is picking up early low-energy precursors to larger events. Further investigation is required, possibly a review of waveform data.

Zagros, Iran

This is a cluster formed of seismicity over a fairly large area of the Zagros Mountains, motivated by a report of three reference events in the Sweeney Report, based on Asudeh (1983). The paper reported locations for three events in September 1976, based on a temporary deployment of seismic stations, but a careful reading indicates that the closest station to any of these events is at a distance greater than 150 km. Hence, the "reference" locations are probably no better than GT15. The HDC analysis for the cluster was very successful, yielding many events with relative locations at the GT5 level, so an effort to obtain true reference locations for a few events in the Zagros would be quite profitable. We are discussing this possibility with researchers of the IISEE in Iran, who operate seismic stations in the area.

Tabas, Iran

The cluster of 35 events is based on the aftershock sequence of the Tabas-e-Golshan earthquake of September 16, 1978, in eastern Iran, plus additional events in the area through 1992. Berberian (1982) discussed the tectonic significance of the locations for hundreds of aftershocks, but the actual hypocentral data are contained only in his thesis. Referring to the thesis, only two events are part of the cluster of larger earthquakes that can be well located with the HDC method. Unfortunately, we discovered inconsistencies in these reference data. The thesis contains a master table of all events and a table of the "best-located" events, but the hypocenters of the two "reference" events are different in the two tables. Moreover, the locations from the master table are in significantly better agreement with the HDC results than the locations from the "best-located" table. Hence, we have used the latter events to shift the cluster, resulting in 12 reference events of (tentatively) GT5 quality. But the origin times also seem to be biased relative to the origin times resulting from the HDC analysis. We are investigating these issues with the help of Berberian.

Erzincan, Turkey

Three reference events were identified in the Sweeney report from a study by Fuenzalida *et al.* (1977a). The cluster events are from October 1976-April 1992 and included only 9 events. However, the reference events

gave a consistent estimate of the shift vector as 9.0 km at 240°, -2.05 s in origin time which yielded 6 events with an accuracy of GT5 or better.

Lop Nor, China, nuclear explosions

Source parameters for Lop Nor explosions that are available from various sources appear to be conflicting. Hence, we decided to perform a careful cluster analysis of 20 events in three closely spaced source regions at the Lop Nor test site. All could be located to GT5 or better and all were tied to the origin times and locations (based on satellite imagery) of four events provided to us by Terry Wallace of the University of Arizona. These events gave us a very consistent estimate of the shift vector as 2.0 km at 289°, +0.82 s in origin time. Of the 11 events in common with Wallace's original JED analysis only 2 events differed by more than 2 km from his locations (94/10/07 at 2.5 km and 96/06/08 at 3.8 km). Of course, all of the origin times agreed to within 0.2 sec. We also compared our results to the JED locations published by Gupta (1995). Of the 13 events in common with his analysis 7 events differed by more than 2 km from our locations, with one differing by 7.7 km. Also, since he used the JB model for his analysis, his origin times were all about 2.5 sec earlier than ours.

Gulf of Aden

These are large events with CMT solutions, whose locations were obtained by a normal non-linear waveform inversion, but with the location constrained to a chosen bathymetric feature (Pan *et al.*, 2000). Cluster analysis provides a means of testing the accuracy of the constrained locations that have the potential for improving our understanding of regional variations in travel times. Probably the largest source of uncertainty comes from the choice of which feature to constrain the location to. This is not easy when there are many like features (ridges and transforms) close together. In addition, there is the problem of intra-plate events that occur close to the plate boundary.

Cluster analysis of 55 events in this region that included six reference events from the Harvard compilation resulted in shifted HDC locations for 18 events with an accuracy of GT5 based on the size of the HDC confidence ellipse. However, since the location of the Harvard reference events is based on sea floor topography with resolution not better than 5 km, the GT5 shifted HDC locations can't really be much better than GT10 in the absolute sense. Most of these 18 events are on the transform segment of the cluster. However, one of the Harvard reference events moves away from the pattern of other nearby ridge-axis events and we suspect that this is actually an intra-plate event close to the ridge.

Azgir, Kazakhstan, nuclear explosions

The HDC procedure is compared to the procedure of Joint Hypocentral Determination (JHD; Dewey, 1972, 1989) using seven closely spaced underground nuclear explosions near Azgir with ground truth information reported by Sultanov *et al.* (1999). In this comparison, as reported by Israelsson *et al.* (2001), HDC and JHD are applied to the same arrival time data to validate computational consistency of event locations and source-station travel time corrections, and to compare the scaling of error ellipses by the different data weighting of the two methods. The resulting HDC and JHD epicenters are generally consistent with a maximum separation of 1.7 km and with error ellipses that overlap ground truth within about 0.5 km. HDC and JHD error ellipses have slightly different orientations and ellipticity, and the JHD ellipses are on average slightly larger than HDC ellipses with the semi axes being about 10% longer. The median of the origin time differences is about 0.1 sec with a maximum difference of 0.2 sec. These analyses confirm that Sultanov's ground truth information for the Azgir explosions is self consistent. The arrival time data, which was provided from sources other than ISC/NEIC, provide especially useful regional travel times.

Balapan/Degelen, Kazakhstan, nuclear explosions

Coordinates for many of the nuclear explosions at the Balapan and Degelen test sites have been determined using a combination of LANDSAT and SPOT images (Thurber *et al.*, 1993; Thurber *et al.*, 1994; P. Richards, Lamont Doherty Geological Observatory). Origin times are also known very well on some of these events. An integration of these sources results in 100 explosions at the Balapan test site and 152 explosions at the Degelen

test site that are of accuracy GT1 or better for which we have assembled the associated reported arrival-time data.

Chamoli, India

Proprietary locations from a temporary network provided six reference events that could be used in cluster analysis. The station azimuth gap for these solutions is less than 100 degrees and independent relocations using the same data are consistent. However, local data from other sources have yet to be integrated, so that our source conservatively estimates the accuracy of these events as GT5-GT10.

A provisional cluster of 48 events yielded 20 events with an accuracy of GT5 based on the size of the HDC confidence ellipse. However, taking into account the uncertainty in reference event locations, we can only provisionally estimate the accuracy of these locations asGT5. Interestingly enough, this recent Chamoli sequence seems to have filled a gap where no previous earthquakes during the 1964-1999 period seem to have occurred.

Bhuj (Republic Day) earthquake; Gujarat, India

Proprietary locations from an 8-station aftershock deployment that are considered accurate to +/- 1-2 km, as reported on at the 2001 Seismological Society of America meeting, have been made available to the project. However, integration of arrival time data from other deployments and permanent network stations operated by Indian institutions, as well as improvements to the local velocity model, need to be made before final reference event locations can be determined. Nevertheless, 6 of the 8 events from the proprietary data set were recorded well enough at regional and teleseismic distances to be included in a provisional Bhuj cluster.

Results of a provisional cluster analysis of 51 events that included the Bhuj main shock and all of the larger aftershocks were quite consistent. HDC locations with respect to the 6 reference events were very systematic. Hence, the shifted HDC locations probably provide the only reliable source of information on the location of events in this sequence that occurred before any temporary networks were installed. In all, 16 of these locations were of GT5 quality, but further improvement can be expected with additional data. The earthquake sequence is unusual in that there is a wide range of depths (8 - 30 km), confirmed not only by local network hypocenters but by depth phases as well. Hence, a final piece of processing could be to assign (for events which were set at an optimal depth of 18 km) more appropriate depths as indicated by the distribution in space of the local network hypocenters.

Izmit, Turkey

There were dense deployments of temporary networks for both the Izmit and Duezce events that occurred along an extended fault system. From locations provided by A. Hofstetter (Geophysical Institute of Israel), we were able to identify three reference events in the Izmit segment of the fault system that included the main shock and two large aftershocks. A cluster of 20 events resulted in 8 events of GT5 quality that are tied to only 2 of the reference events. The inconsistent shift vector and the early offset of the main shock origin time to the cluster result lead us to believe that the reported reference event was a small sub-event of the complex main shock which was not seen at regional distances. Accurate fault maps for the region may help to improve the resolution of these results.

Xiuyan, China

The Xiuyan earthquake occurred in a region where the maximum intensity contours are so tightly constrained that the location accuracy of the main shock could be estimated by the Chinese as GT2. In addition, a local seismic network of analog and digital was being operated during a period that overlapped with the earthquake sequence. Four events reported by Xu (2001) were recorded well enough to be used as reference events, and arrival time information to stations in China were provided to the project by Xu.

Cluster analysis of 30 events across the aftershock region led to the following observations: (1) We cannot validate the reference event locations to any better than GT10 because either there are errors in these locations

or the station coverage used in the HDC analysis is not sufficient to constrain our locations. In most cases, it is a combination of both of these problems; (2) Origin times indicated by our cluster analysis using regional and teleseismic data reported by ISC/NEIC are systematically about 4 sec later than the origin times of the reference events. Hence, the median path anomalies to all stations used in the cluster analysis are positive. Chinese seismological stations have timing synchronous with UNT with an accuracy better than tens of msec. Reconciliation of these origin time differences may be related to inconsistent time standards globally and needs to be investigated.

CONCLUSIONS AND RECOMMENDATIONS

High-resolution cluster analysis is being applied to earthquake sequences and to some nuclear explosion sites in Asia and north Africa for which one or more of the associated events is known to an accuracy of 5 km or better (GT5). These analyses produce new locations (relative to the centroid of the cluster) and 90% confidence ellipses that in some cases, after shifting the centroid to best match reference event locations, sharpen the spatial relationship of earthquake sequences to known faults.

Our initial work with candidate "reference events" suggests that considerable care must be taken to ensure reliable results. Many aftershock studies and temporary seismograph deployments in remote areas suffer from logistical, operational, and analytical difficulties that may compromise the quality of the computed locations. Such problems are seldom apparent in published papers and abstracts. In many cases it will be necessary to gain access to raw data and analysis records—and most importantly, to gain the cooperation of the original researchers—to confirm the reliability of "reference events" offered by the seismological community in these regions.

The Hypocentroidal Decomposition method of cluster analysis has proven to be very well suited to the requirements of ground truth validation exercise, but we have also found a number of areas in which additional development of the method is needed. Enhancements to the algorithm are needed to implement a more appropriate statistical model for reading errors, and for dealing with outliers. A statistically rigorous procedure for optimally matching the HDC cluster with reference event locations is needed. Further research is also needed on some aspects of the application of the HDC method. For example, we need a better understanding of how to choose a minimum epicentral distance for data to be used in HDC analysis, and a protocol for deciding how large a cluster may be without compromising the analysis.

REFERENCES

Asudeh, I. (1983), ISC mislocation of earthquakes in Iran and geometrical residuals, Tectonophysics, 95, 61-74.

Berberian, M. (1982), Aftershock tectonics of the 1978 Tabas-e-Golshan (Iran) earthquake sequence: a documented active 'thin- and thick-skinned tectonic' case, Geophys. J. R. astr. Soc., 68, 499-530.

Berberian, M. and R. S. Yeats (1998), Patterns of historical earthquake ruptures in the Iranian Plateau, Bull. Seismol. Soc. Am.

Berberian, M., J.A. Jackson, M. Qorashi, M.M. Khatib, K. Priestley, M. Talebian, and M. Ghafuri-Ashtiani (1999), The 1997 May 10 Zirkuh (Qa'enat) earthquake (Mw 7.2): faulting along the Sistan suture zone of eastern Iran, Geophys. J. Int., 136, 671-694.

Bolt, B.A. (1976), Nuclear explosions and earthquakes: The parted veil, W.H. Freeman.

Engdahl, E. R., R.D. Van der Hilst and R.P. Buland (1998), Global teleseismic earthquake relocation with improved travel times and procedures for depth determination, Bull. Seism. Soc. Amer., 88, 722-743.

Fuenzalida, H., L. Dorbath, A. Cisternas, H. Eyidogan, A. Barka, L. Rivera, H. Haessler, H. Philip, and N. Lyberis (1977a), Seismic source study of the Racha-Dzhava (Georgia) earthquake from aftershocks and

broadband teleseismic body-wave records: an example of active nappe tectonics, Geophys. J. Int.,130, 29-46.

Fuenzalida, H., L. Rivera, H. Haessler, D. Legrand, H. Philip, L. Dorbath, D. McCormack, S. Arefiev, C. Langer, and A. Cisternas (1977b), Seismic source study of the Racha-Dzhava (Georgia) earthquake from aftershocks and broadband teleseismic body-wave records: an example of active nappe tectonics, Geophys. J. Int.,130, 29-46.

Gupta, V (1995), Locating nuclear explosions at the Chinese test site near Lop Nor, Science and Global security, 5, 205-244.

Jordan, T.H. and K.A. Sverdrup (1981), Teleseismic location techniques and their application to earthquake clusters in the south-central Pacific, Bull. Seis. Soc. Amer., 71, 1105-1130.

Kennett, B. L. N., E.R. Engdahl and R.P. Buland (1995), Constraints on seismic velocities in the Earth from traveltimes, Geophys. J. Int., 122, 108-124.

Pan, J., M. Antolik and A. Dziewonski (2000), Locations of mid-oceanic earthquakes constrained by sea-floor bathymetry, Eos Trans. Amer. Geophys. Union, 81, F868.

Milkereit, C. *et al.* (2000). Preliminary aftershock analysis of the Mw=7.4 Izmit and Mw=7.1 Duezce earthquake in western Turkey, In: The 1999 Izmit and Duezce earthquakes: preliminary results (Editors: A. Barka, Oe. Kozaci, S. Akyuez and E. Altunel), 179--187, Istanbul Technical University.

Sultanov, D.D., J.R. Murphy and K.D. Rubenstein (1999), A seismic source summary for Soviet Peaceful Nuclear Explosions, Bull. Seis. Soc. Amer., 89, 640-647.

Sweeney, J.J. (1998), Criteria for Selecting Accurate Event Locations from NEIC and ISC Bulletins, Lawrence Livermore National Laboratory, Technical Report UCRL-JC-130655.

Thurber, C.H., H.R. Quin, and P.G. Richards (1993), Accurate locations of nuclear explosions in Balapan, Kazakhstan, 1987 to 1989, Geoph. Res. Letters, 20, 399-402.

Thurber, C.H., H.R. Quin and P.G. Richards (1994), Catalog of locations of nuclear explosions at Balapan, Kazakhstan, 1965 to 1985, Bull. Seis. Soc. Amer., 84, 458-461.

Tibi, R. *et al.* (2001), Rupture process of the 1999 August 17 Izmit and November 12 Duezce (Turkey) earthquakes, Geophys. J. Int., 144, F1--F7.

Xu, S. (2001), The Study of the XIUYAN Earthquake on Nv. 29, 1999, as an Example of an Event for Local Calibration (presentation), Third Location Workshop of the IDC Technical Experts Group on Seismic Event Location, Oslo.

DEVELOPMENT OF IMPROVED CAPABILITIES FOR DEPTH DETERMINATION

Mark D. Fisk[1], Clinton Conrad[1], and David Jepsen[2]

Mission Research Corporation[1], Australian Geological Survey Organization[2]

Sponsored by Defense Threat Reduction Agency

Contract No. DTRA01-00-C-0027

ABSTRACT

The objective of this research is to develop improved procedures and criteria for identification and validation of seismic depth phases. This effort includes: (1) inspection of waveforms for events in the Reviewed Event Bulletin (REB) to determine whether depth phases have been identified properly; (2) evaluation of existing procedures and criteria for depth-phase validation; (3) development of statistical methods to quantify the moveout of pP-P and sP-P, accounting for timing uncertainties; (4) investigation of techniques to improve depth-phase identification (i.e., F-detector, optimal frequency/filtering tool, and the relative amplitude (RAMP) technique as a test of whether teleseismic P and depth phases fit a double-couple mechanism); and (5) implementation, testing, evaluation, and delivery of software capabilities for improved depth-phase identification and validation to the Center for Monitoring Research (CMR).

We have implemented a method to compute confidence intervals of pP-P and sP-P moveout. We have applied it to 1342 REB events with observed depth phases to determine the percentage of such events with a 90% confidence interval of moveout greater than various thresholds (e.g., 0.0, 1.0, 1.5 seconds). The results indicate that this method is more effective for determining whether depth phases exhibit moveout than requiring the time difference of pP-P at the nearest station beyond 25 degrees and the farthest station within 100 degrees be greater than 1.5 seconds, a criterion currently used at the CMR. Specifically, 425 of 1342 events (32%) have positive moveout at the 90% confidence level, while 281 of 1342 events (21%) satisfy the latter criterion. In addition, we have found that the moveout confidence intervals are more robust to phase timing errors. For many REB depth-phase events, a limited number of observed depth phases and significant scatter in the pP-P and sP-P travel-time differences often cause the moveout confidence intervals to be too large to confidently determine that the moveout is greater than a given threshold. Also, the overwhelming majority of REB events (about 88%) do not have any associated depth phases. To increase the number of detected depth phases and reduce the scatter associated with timing errors, we have investigated the utility of the F-detector (e.g, Blandford, 1974), a signal processing technique that dramatically amplifies signals that are correlated among array elements, while suppressing uncorrelated noise. Using statistical properties of the F-detector, a probability trace (i.e., time series) may be computed indicating whether filtered signals are significantly correlated across an array at a given time. Preliminary results indicate that the F-detector finds many depth phases that were missed by analysts and may provide a more objective approach for determining onset times of P, pP, and sP. We have also found, as in previous studies of the F-detector, that the frequency bands must be tuned for a given array to account for its aperture and ambient noise characteristics. We have also applied the Relative Amplitude (RAMP) algorithm (e.g., Pearce et al., 1988) to REB events with observed depth phases to determine whether relative amplitudes of teleseismic P, pP, and sP are consistent with double-couple focal mechanisms. We present results of these applications and describe plans to complete these investigations and develop appropriate capabilities into operational analysis tools.

KEY WORDS: seismic, depth phases, moveout, F-detector, relative amplitude technique, RAMP

OBJECTIVE

The overall objective of this work is to develop improved procedures and criteria for identification and validation of seismic depth phases. Initial tasks involve inspection of waveforms for REB events to determine whether depth phases were picked properly, and evaluation of the provisional procedures and criteria for depth-phase validation that are currently used at the IDC, based on recommendations by the IDC Technical Experts on Seismic-Acoustic Event Screening in May 1999 (CTBT/WGB/TL-2/31). The main objective of these tasks is to assess where significant improvements, relative to existing capabilities, are needed and can be made. The third main task is to develop a robust statistical method to quantify the moveout of pP-P and sP-P travel time differences, providing rigorous treatment of the number of observed depth phases, their distance range, and the uncertainties in phase onset times. The fourth task is to investigate methods to increase the number of detected depth phases and to validate candidate depth phases relative to a physical model. Research in this area focuses on use of the F-detector (e.g., Blandford, 1974), as a technique to detect more depth phases, and on the relative amplitude (RAMP) technique (e.g., Pearce et al., 1988) to test whether relative amplitudes of teleseismic P, pP, and sP fit a double-couple focal mechanism. The last main task is to implement, test, evaluate, and deliver software tools for improved identification and validation of depth phases to the CMR.

RESEARCH ACCOMPLISHED

Evaluation of REB Depth Solutions

We have evaluated the existing depth screening procedures and criteria used at the PIDC. Let D be the depth estimate and s_{zz} be the variance of the depth estimate in the REB. An event is screened out based on depth if

$D - 2\sigma_D > 10$ km, where $2\sigma_D = 2\sqrt{s_{zz}} + k$.

This criterion is equivalent to requiring that a one-sided 97.5% confidence interval of the event focal depth is deeper than 10 km. The term k is included in the overall depth uncertainty as an interim measure to compensate for model errors that are not adequately represented by s_{zz}. A value of k = 20 km is used for free-depth solutions. A value of k = 0 km is used for events that satisfy the following depth-phase criteria:

- The signal-to-noise (coda) ratio of the depth phases must be at least 2.0;
- At least three depth phases (of the same type) must be observed for an event (i.e., ndp(pP) ≥ 3 and/or ndp(sP) ≥ 3);
- The moveout of pP–P travel times, for stations in the distance range of 25 to 100 degrees, is greater than or equal to 1.5 seconds and/or 1.3 seconds for sP–P; and
- The travel time difference, T(pP-P) > 12.9 seconds and/or T(sP–P) > 19.0 seconds at the nearest station beyond 25 degrees.

We first examined how many REB events are screened out by the depth screening criteria, using a sample of 5412 REB events above mb 3.5 during July to December 1999. Figure 1 depicts the results. The left panel shows histograms of 2228 events (about 41%) with unconstrained depth estimates (white bars), 1079 events (about 20%) that are screened out by depth (green bars), and 128 events (only about 2%) that satisfy the depth-phase criteria listed above (blue bars). The right panel shows 661 REB events above mb 3.5 with depth-phase solutions (white bars) and the 128 events that satisfy the depth-phase criteria.

We also examined the validity of the REB depth confidence intervals using comparisons to other published depth solutions that are thought to be reliable and independent. For example, Figure 2 (left panel) shows REB free-depth estimates versus PDE (Preliminary Determination of Epicenters) depth-phase solutions, published by the U.S. National Earthquake Information Center (NEIC) for 1086 common events above mb 3.5. Using k = 20 km, only three REB depth confidence intervals are significantly deeper than the corresponding PDE depth estimates. Thus, 99.7% of the REB confidence intervals are consistent with or

shallower than the PDE depth-phase solutions, and none of the events that are shallower than 10 km, according to the PDE, are screened out based on the REB free-depth solutions. Similar comparisons were made of REB depth confidence intervals to depth estimates published by the Japanese Meteorological Agency (JMA), the Chinese National Data Center, and the Southern California Earthquake Center (see Fisk et al., 2000). Using over 1600 events, 99.8% of the REB free-depth confidence intervals are consistent with or shallower than the corresponding depth estimates in the other bulletins.

We also examined REB depth-phase solutions, including a comparison of 903 common events with depth-phase solutions reported in both the REB and PDE. Figure 2 (right panel) shows that the REB and PDE depth-phase solutions generally compare quite well, although several events were examined for which the analysts misidentified depth phases that used to obtain the REB depth estimates. In some cases, the depth-phase criteria (defined above) were not satisfied; hence, these events were not screened out. However, we have found several cases with invalid depth phases for which the depth-phase criteria were satisfied.

These evaluation results indicate significant room for improvement in the performance and robustness of the depth screening criteria, especially with regard to the detection and analysis of depth phases. This motivates the focus of our efforts on methods to detect more depth phases and better validate them.

Confidence Intervals of Depth-Phase Moveout

We have developed a method for computing confidence intervals of the moveout of pP-P and sP-P travel-time differences. The method, based on the *t*-distribution, provides rigorous treatment of the number, distance range, and timing uncertainties of observed depth phases. We have applied this method to a sample of 1342 REB events with observed depth phases to determine the percentage of events that exhibit positive moveout at the 90% confidence level. We have compared the results to those based on the IDC depth-phase criteria, as shown in Figure 3, where the black bars represent the 1342 events with depth phases, binned by depth in 10 km intervals, and the green bars represent the numbers of events that satisfy the alternate depth-phase criteria. The left panel shows that 281 events (about 21%) are screened out by the current IDC criteria, while the right panel shows that 425 events (about 32%) are screened out if we require 90% confidence of positive moveout and T(pP-P) > 6.1 seconds for the nearest measurement beyond 25 degrees. The additional events that are screened out by the latter set of criteria are primarily between 20-40 km deep.

In general, we have also found that the confidence intervals provide a more robust approach for determining whether depth phases exhibit moveout than the current IDC moveout criterion of using the time difference of pP-P or sP-P at the nearest and farthest stations in the distance range of 25 to 100 degrees. For example, the left panel of Figure 4 shows an event that satisfies the IDC moveout criterion because the pP-P time difference between the first and last observations between 25 and 100 degrees is more than 1.5 seconds. However, the scatter and the limited range of the three pP observations do not permit the moveout to be determined accurately. In fact, the 90% confidence interval, depicted by the range of slopes shown (green lines), indicates large uncertainty (including negative values) in the moveout at the 90% confidence level. Alternatively, the right panel of Figure 4 shows an example of an event that does not satisfy the IDC moveout criterion because the first and last measurements of pP-P do not have a time difference of 1.5 seconds. However, the 90% confidence interval of pP-P moveout is entirely positive. The moveout of the event on the right is better constrained, based on the number and distance range of the depth phases; thus, it is a better candidate for screening by depth phases. These results show that requiring 90% confidence of positive moveout is a more robust criterion, and more effective, than the current IDC moveout criterion.

Application of the F-detector

Upon examining many REB events, we found that small numbers of observed depth phases and significant scatter in pP-P and sP-P travel-time differences often cause the 90% confidence intervals of moveout to be too large to confidently determine that the moveout is positive. We have also found that it is often difficult to detect and objectively pick onset times for many depth phases if they are emergent and have significant P coda preceding them. This motivated us to investigate the utility of the F-detector to detect more depth phases and objectively/consistently determine their onset times, so that moveout confidence intervals can be determined more precisely, allowing more events with depth-phase solutions to be screened out.

The F-detector is a signal processing technique (e.g., Blandford, 1974) that dramatically amplifies signals that are correlated among array elements, while suppressing uncorrelated noise and/or spikes on individual element. The algorithm first forms a beam (i.e., a stacked average of signals from the array elements, aligned to the event epicenter). The beam is bandpass-filtered and smoothed over a time window. It is then divided by the difference of this quantity and the average individual channel power, filtered in the same passband and smoothed over the same time window. If the signal is highly correlated among array elements, this ratio, defined as *F*, will be large. Alternatively, the expected value of *F* is unity for equal, uncorrelated noise on all channels. Assuming uncorrelated Gaussian noise, *F* has a non-central F-distribution, which allows a probability to be computed of whether the array signals are significantly correlated at any given time.

Figure 5 shows an example of how the F-detector can help identify depth phases for ASAR (Alice Springs, Australia) recording of an mb 3.6 event near the Lop Nor test site on 4 February 2001. Shown from bottom to top is the array beam, filtered in the 2.0-4.0 Hz band, the value of *F* as a function of time (F-trace), the probability trace, and the derivative of the probability trace with respect to time. Also shown are the P and pP arrivals in the REB, the IASPEI91 predicted pP and sP arrival times (labeled pX and sX), and the onsets of P, pP, and sP, based on the F-detector (labeled p1, p2, p3 in the top panel). The F-trace increases near the onset of the P, pP, and sP phases, where the array signals become well correlated. The probability trace clearly shows onset of P, pP, and sP phases at times close to their theoretical values.

Figure 6 shows the travel-time differences of pP-P (green circles) and sP-P (blue squares) for the same event on 4 February 2001. The solid lines represent least-squares fits to the moveout data and the dotted lines represent the predicted moveout, based on IASPEI91. The left panel shows the depth phases associated in the REB (pP only), while the right panel shows the depth phases that were identified using the F-detector (pP and sP), including additional depth phases at CMAR. Note that the 90% confidence interval of the pP-P moveout for the REB solution is not entirely greater than zero; hence, this event would not be screened out. However, the F-detector results on the right show that the 90% confidence intervals of pP-P and sP-P moveout are both entirely greater than zero. Thus, the additional depth phases obtained from the F-detector provide sufficient evidence of valid depth-phase moveout, which could allow this event to be screened out.

We have applied the F-detector to seven events near the Lop Nor test site since 1 January 1999. All of these events have relatively shallow REB depth-phase solutions (i.e., less than 30 km deep), none of which satisfy the IDC moveout criterion. After applying the F-detector, 5 of the 7 events have 90% moveout confidence intervals that are positive, providing evidence of valid depth-phase solutions for these events. We also applied the F-detector to a global sample of 136 REB events with depth-phase solutions between 50 and 100 km deep. The F-detector found 49 additional (high-confidence) depth phases that were not in the REB.

As in previous studies of the F-detector (e.g., Blandford, 2000; Bowers, 1999), we have found that the frequency band(s) must be tuned for a given array to account for the array aperture and ambient noise characteristics. For some small-aperture arrays, we find that noise can be significantly correlated between array elements (e.g., noise from the North Sea at ARCES), causing the F-trace to be large even when no signal is present. However, it is typically possible to diminish the effects of correlated noise by filtering in a particular frequency band. For example, we found that the 3.0-6.0 Hz band typically works well for small aperture arrays (such as ARCES and FINES), while the 0.5-3.0 Hz band typically works better for larger aperture arrays (such as YKA and CMAR). We plan to examine the effects of different frequency bands for various arrays to optimize the performance of the F-detector for identifying depth phases.

We have also found that the probability trace can saturate to unity, particularly for large events, following the onset of the P phase. This is because the P coda can be sufficiently correlated, obscuring signals from pP or sP phases in the probability trace. One way to enhance the signals of depth phases in this situation is to increase the threshold value used to calculate the probability trace, which corresponds to assuming a greater signal-to-noise ratio. This increases the value of F at which the probability trace saturates, making depth phases more prominent on the probability trace. Blandford (2000) has also suggested dividing *F* by its long-term average to improve its detection performance.

Application of the Relative Amplitude (RAMP) Technique

To validate depth phases by a physical model, we have investigated the utility of the Relative Amplitude (RAMP) technique (e.g., Pearce et al., 1988). RAMP searches a strike-slip-dip parameter space using relative amplitudes and polarities of P, depth phases, and/or 3 components of S phases at a number of stations to determine the range of moment tensor solutions that are consistent with the input data. In our application of RAMP, we restricted the parameter space to double-couple solutions consistent with P, pP, and sP amplitudes measured in observed and predicted windows and filtered in the 0.6 to 4.0 Hz band. A 5x5x5 degree strike-slip-dip grid was used, with a total of 93312 possible solutions. This grid size allows RAMP to process quickly while being dense enough so that solutions can be formed. We did not use the polarities because they are often difficult to determine confidently. As a result, this allowed many more solutions to form, of which many were redundant. Since the amplitudes of can be affected by attenuation (particularly along the two-way depth-to-surface path), seismic noise, complex pulse shape, interfering arrivals, and instrument response, we imposed a 33% uncertainty on the amplitudes to encompass these variations. If small uncertainties are imposed, RAMP will often fail to form events. Alternatively, if the uncertainty is too large, the events may not form well-constrained solutions. We further allow incompatible relative amplitudes at one station, so that a potentially valid solution is not excluded due to anomalous amplitudes at a single station. Last, a simple attenuation model is used, with $Q_\alpha = 250$ and $Q_\beta = 100$.

We applied this version of RAMP to 661 REB depth-phase solutions during July to December 1999, of which 434 events have depth estimates less than 50 km. Note that none of these 434 events satisfy the IDC depth-phase screening criteria. Figures 7 and 8 show examples of waveforms (left) and RAMP solutions (right) for events in the Indian Ocean and South Africa, respectively. Observed depth phases in the REB are labeled as pP and sP, while predicted depth-phase arrivals are labeled as pX and sX. Maximum amplitudes of these phases are calculated in a 3-second time window about these positions. The grids in Figures 7 and 8 represent the slip (across) and dip (down) solution space, with the orientation of the arrow (clockwise) indicating the strike. We consider the Indian Ocean event, with 23 solutions, to be well constrained, and the South African event, with 2024 solutions, to be poorly constrained. Note that the solutions are divided into mirrored regions as a result of not constraining the polarities of the phases.

Of the 661 events, 104 were not compatible with any double-couple solution, while 557 were. Of these, 281 events have 500 or fewer solutions (corresponding to about 0.5% of the parameter space), which we consider to be well constrained. Of the 434 events with REB depth-phase solutions less than 50 km deep, 186 have well-constrained mechanisms, and could potentially be screened out. Although further work is needed, incorporating the use of RAMP to screen out events with well-constrained double-couple solutions could more than double the screening performance based on depth phases. It also has the advantage that the depth phases would be validated by a physical model.

CONCLUSIONS AND RECOMMENDATIONS

The main results obtained thus far under this contract are as follows. First, evaluation of the performance of the IDC depth screening criteria indicates that the criteria are quite conservative and that only about 2% of the events above mb 3.5 in the REB satisfy the depth-phase criteria. Thus, identification of more valid depth phases appears to be the best way to significantly improve event screening (or discrimination) based on depth. Second, the confidence-interval approach we developed is more robust and more effective for testing whether observed depth phases for an event exhibit moveout than the existing moveout criterion currently used at the IDC. The former approach was found to improve the screening performance (32% as compared to 21%) for 1342 REB depth-phase solutions that were examined. Also, numerous cases were found for which the IDC moveout criterion does not properly account for uncertainties in the estimated moveout based on the number, distance range, and timing errors of observed depth phases, while the confidence intervals of moveout do provide rigorous treatment of these factors. Third, we found that the F-detector can help identify many more depth phases, which can help to determine confidence intervals of moveout more precisely, thereby confirming valid depth-phase solutions. Fourth, RAMP can validate depth-phase solutions by fitting relative amplitudes of P, pP, and sP phases to double-couple focal mechanisms. We found that RAMP is

particularly useful for relatively shallow events. For example, RAMP obtained "well-constrained" solutions for 186 of 434 REB events (i.e., about 41%) above mb 3.5 with depth-phase solutions shallower than 50 km, while none of these events could be screened out by the current IDC depth-phase criteria.

During the remainder of this contract, we plan to continue to optimize and evaluate these combined capabilities, to identify and validate depth phases for a greater number of events. Specific efforts will focus on tuning the F-detector for IMS seismic arrays, and on evaluating its performance on a larger sample of REB events. We also plan to further evaluate the utility of the RAMP algorithm on a larger set of REB events, including those with and without observed depth phases. We plan to examine effects of using various attenuation models and provide a more rigorous determination of the number of RAMP solutions that defines a well-constrained focal mechanism for a given event, based on theoretical considerations and applications to ground-truth events. We also plan to examine whether events with mis-labelled depth phases or events without actual depth phases (such as explosions) can form well-constrained RAMP solutions. We also plan to examine whether polarities of P and depth phases provide a significant improvement in constraining the RAMP solution space, and the degree to which this imposes additional burden on the analysts. Last, we plan to deliver software capabilities to perform these functions to the CMR.

REFERENCES

Blandford, R. R. (1974). An automatic event detector at the Tonto Forest seismic observatory, *Geophysics*, **39**, 633-643.

Blandford, R. R. (2000). Private communication.

Bowers, D. (1999). Depth Phase Identification for Event Screening: Future Improvements, in *Proceedings of the IDC Technical Experts Meeting on Seismic-Acoustic Event Screening*, 21-25 May 1999.

CTBT/WGB/TL-2/31 (1999). Report of the IDC Technical Experts Meeting on Seismic-Acoustic Event Screening, 21-25 May 1999.

CTBT/WGB/TL-2/58 (2001). Report of the IDC Technical Experts Meeting on Seismic-Acoustic Event Screening, 10-14 November 2000.

Fisk, M. D., D. Jepsen, and J. R. Murphy (2000). Experimental Seismic Event-Screening Criteria at the Prototype International Data Center, submitted to *Pure and Applied Geophysics (PAGEOPH) Special Volume on Seismic Event Discrimination and Identification Related to Monitoring a Comprehensive Test-Ban Treaty (CTBT)*.

Jepsen D. and M. D. Fisk (1999). Evaluation of PIDC Seismic Depth Estimates and Uncertainties, in *Proceedings of the IDC Technical Experts Meeting on Seismic-Acoustic Event Screening*, 21-25 May 1999.

Pearce, R. G., J. A. Hudson and A. Douglas (1988). On the use of P-wave seismograms to identify a double-couple source, *Bull. Seism. Soc. Am.*, **78**, 651-671.

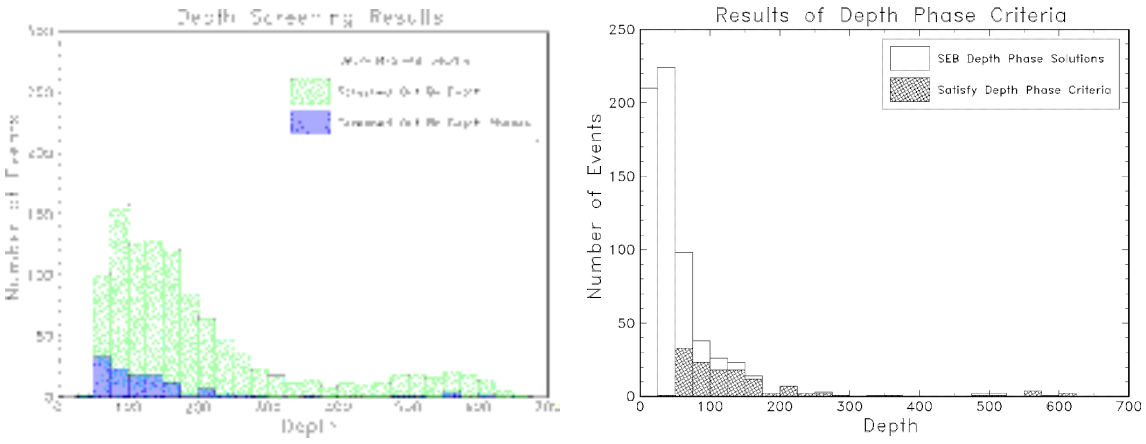

Figure 1. The left panel shows histograms of 2228 REB events above mb 3.5 with unconstrained depth estimates (white bars), 1079 events that are screened out by depth (green bars), and 128 events that satisfy the IDC depth-phase criteria (blue bars). The right panel shows 661 REB events above mb 3.5 with depth-phase solutions (white bars) and the 128 events that satisfy the IDC depth-phase criteria. Only about 2% of the REB events have depth phases that satisfy the IDC depth-phase criteria.

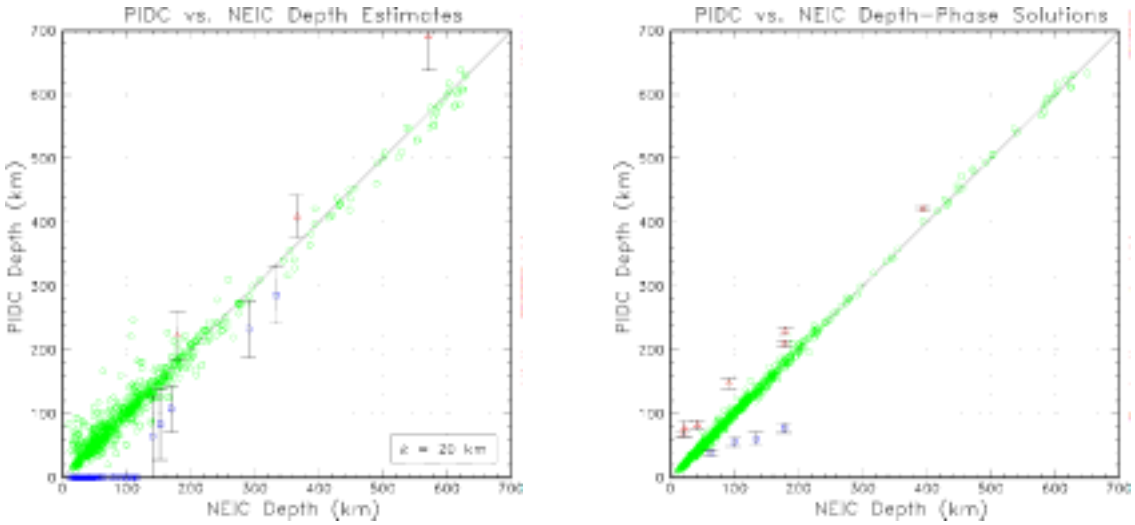

Figure 2. Comparisons of PIDC and NEIC depth estimates for common events above mb 3.5. REB depth confidence intervals are shown only for events with 97.5% confidence intervals that do not contain the NEIC depth estimate. The left panel compares 1086 PIDC free-depth solutions to corresponding NEIC depth-phase solutions; 99.7% of the PIDC free-depth solutions are consistent with or shallower than the NEIC depth-phase solutions. The right panel compares 903 PIDC and NEIC depth-phase solutions; 99.2% of the PIDC depth-phase solutions are consistent with or shallower than the NEIC depth-phase solutions. The seven REB events with depth-phase solutions that are significantly deeper than the corresponding NEIC depth estimates were examined in detail and found to have erroneous depth-phase picks in the REB.

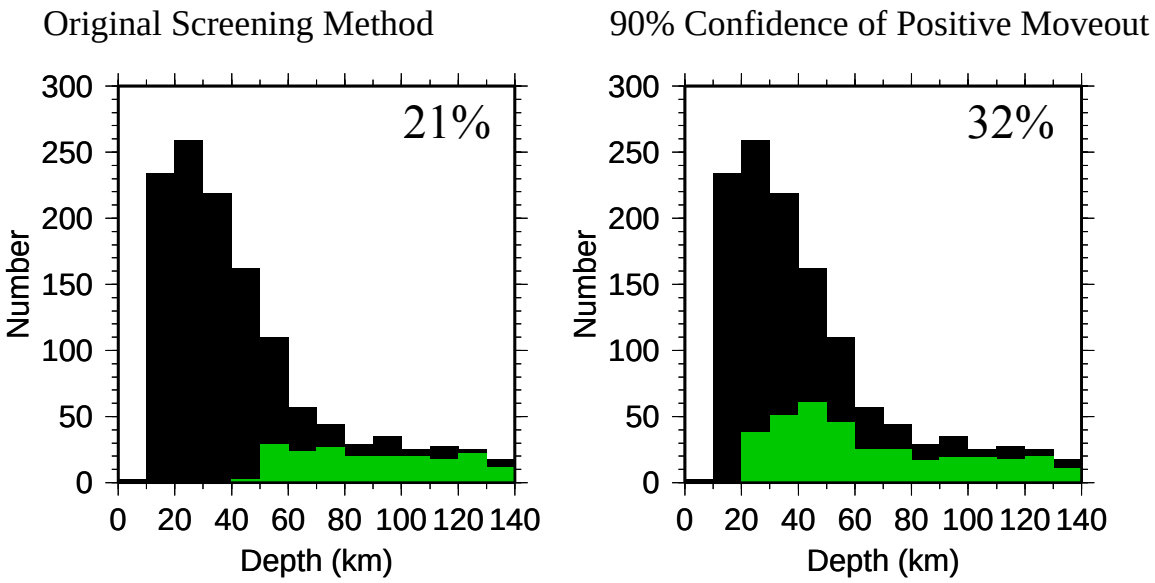

Figure 3. Histograms of 1342 REB events with depth phases (black) and those that satisfy alternate depth-phase criteria (green). The left panel shows the results using the IDC depth-phase criteria, while the right panel shows the results for events with a 90% confidence interval of moveout that is entirely positive, and the pP-P travel-time difference of more than 6.1 seconds at the nearest station beyond 25 degrees.

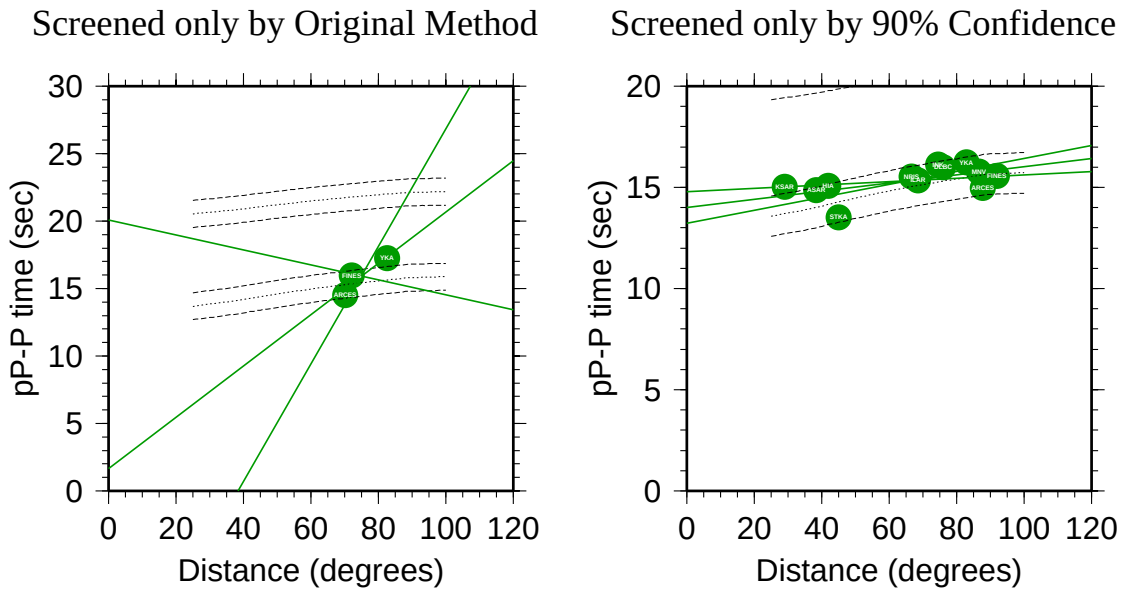

Figure 4. Comparison of alternate moveout criteria for two events with REB depth estimates of 54 km. The event on the left (orid=20336863) satisfies the IDC moveout criterion (>1.5 seconds between extreme pP-P travel-time measurements), but does not have 90% confidence of positive moveout. The event on the right (orid=20296734) does not satisfy the IDC moveout criterion, but does have 90% confidence of positive moveout. Solid lines represent least-squares fits to the data and the range of slopes at the 90% confidence level. Dotted lines are the pP-P travel-time differences predicted by IASPEI91 and ±1 second residuals.

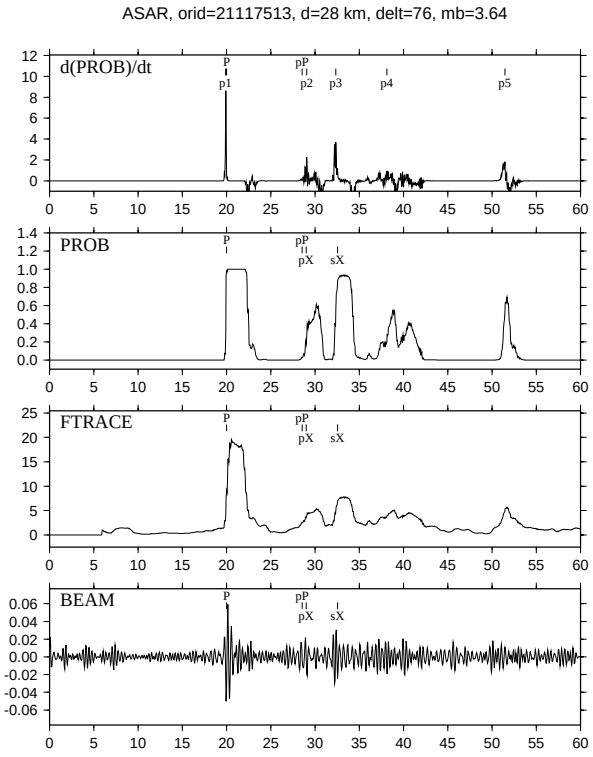

Figure 5. F-detector results for ASAR recording of an mb 3.6 event near Lop Nor on 2001/02/04. Shown from bottom to top are the beam in the 2.0-4.0 Hz band, *F* as a function of time, the probability trace, and derivative of the probability trace with respect to time. Also shown are the P and pP arrivals in the REB, arrivals predicted by IASPEI91 (pX and sX), and onsets of P, pP, sP (p1, p2, p3) based on the F-detector.

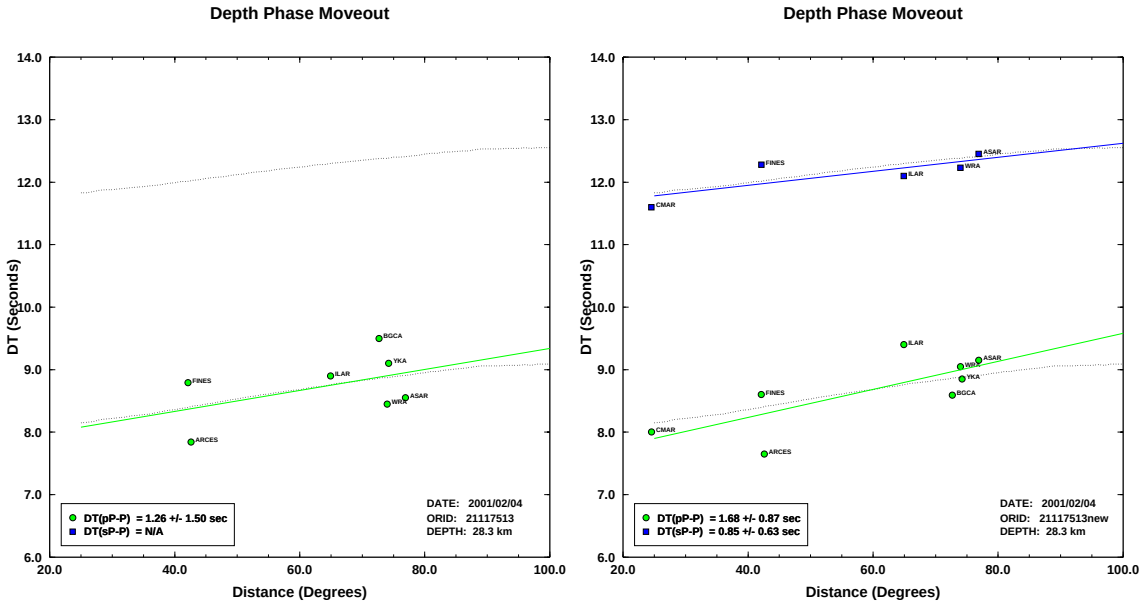

Figure 6. Travel time differences of pP-P (green circles) and sP-P (blue squares) for an REB event near the Lop Nor test site on 4 February 2001. The left panel shows the depth phases associated in the REB, while the panel on the right shows the depth phases that were identified using the F-detector.

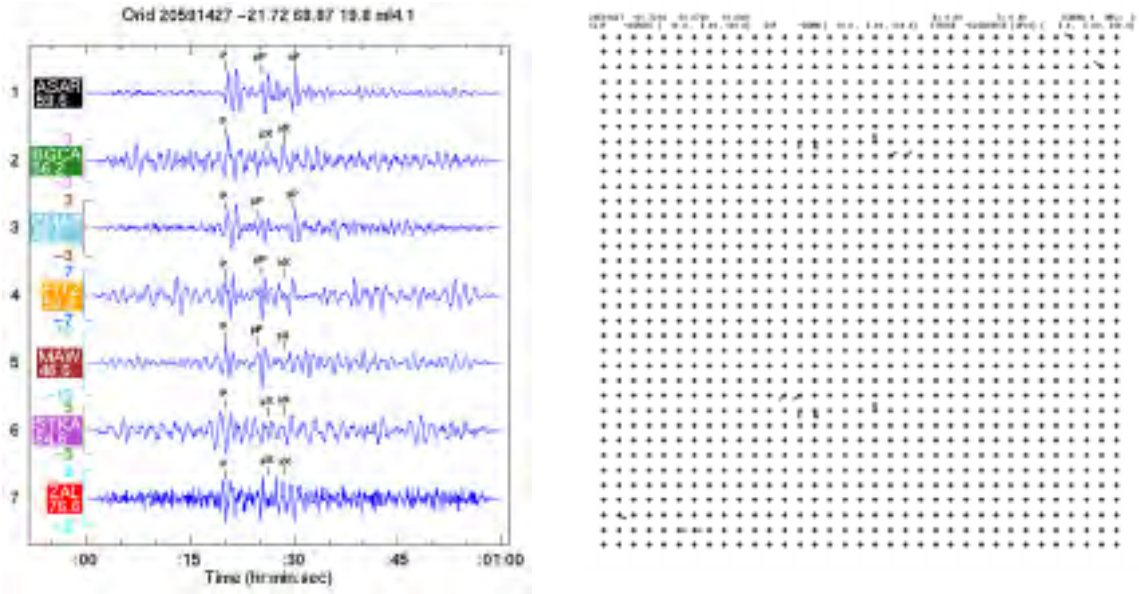

Figure 7. Selected waveforms (left) and the double-couple solutions (right) that are consistent with the relative amplitudes of P, pP, and sP for an Indian Ocean earthquake. This event, with 23 solutions from the RAMP algorithm, is considered to have a well-constrained focal mechanism. The grid represents the slip (across) and dip (down) solution space, with the orientation of the arrow (clockwise) indicating the strike.

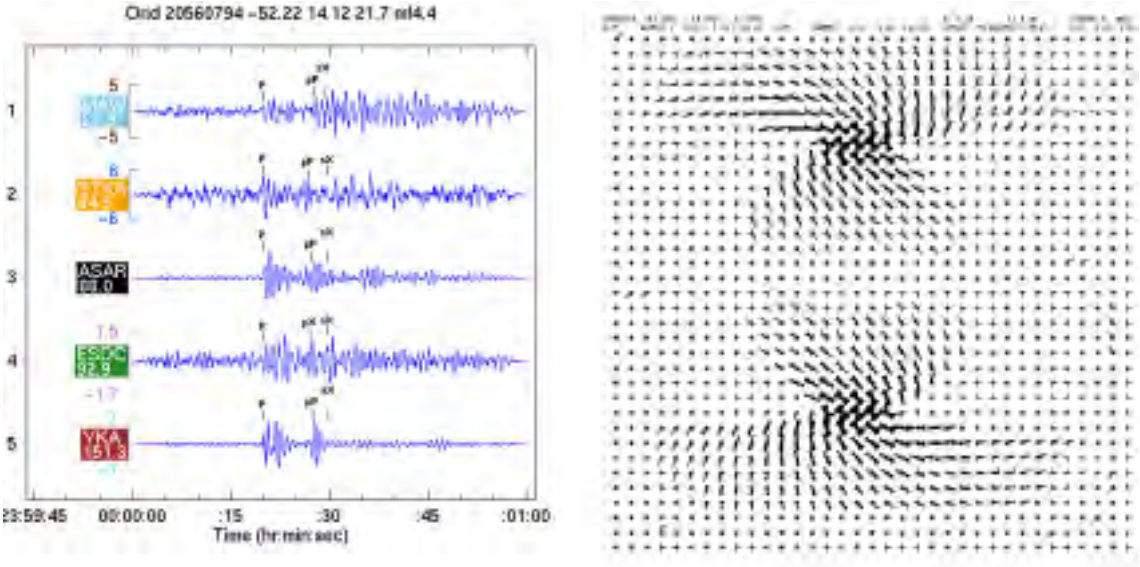

Figure 7. Selected waveforms (left) and the double-couple solutions (right) that are consistent with the relative amplitudes of P, pP, and sP for a South African earthquake. This event, with 2024 solutions from the RAMP algorithm, is considered to have a poorly-constrained focal mechanism.

IMPROVEMENT OF EARTHQUAKE EPICENTRAL LOCATIONS USING T-PHASES: TESTING BY COMPARISON WITH SURFACE WAVE RELATIVE EVENT LOCATIONS

Donald W. Forsyth, Yingjie Yang

Brown University

Sponsored by The Defense Threat Reduction Agency

Contract No. DTRA 01-00-C-0071

ABSTRACT

A deployment of 51 ocean-bottom seismometers (OBS) on the seafloor spanning 800 km across the East Pacific Rise provides a unique opportunity to test the robustness of epicentral location techniques using T-phases. A standard technique for locating events with T-phases is to pick the arrival the time of peak energy, then proceed as if it were an unscattered phase originating at the epicenter. Such an approach has been shown to have no apparent bias in epicentral location. Comparison of waveforms at nearby stations, however, shows that peak energy arrival time can shift to different parts of the wavetrain due to incoherent interference between waves excited or scattered from different locations, even for stations only a few kilometers apart, forcing operator identification of particular features in the waveform. At greater sensor separations, such identification cannot be performed with confidence. We show that a 75% reduction in variance relative to picks of peak arrival times can be achieved by fitting an assumed functional shape to the entire envelope of the T-phase. Since most of the variation in the envelope is caused by scattering and interference of the waves, "noise" is proportional to signal and is log-normal. Best results are obtained by fitting the log of the envelope, which transforms the noise into a nearly constant, Gaussian distributed background and de-emphasizes individual peaks. By fitting the entire long wavetrain of the T-phase, excitation by individual bathymetric features is also de-emphasized.

We test the stability of this approach for events of greatly different size using a mainshock/aftershock sequence of earthquakes at the northern end of the Easter microplate. In addition, for the larger earthquakes, we can compare relative event locations with those determined by cross-correlating waveforms of Rayleigh and Love surface waves recorded teleseismically. The T-phases from the OBSs are supplemented by T-phases recorded at GSN station RPN. Relative event locations show that there is no apparent bias in T-phase locations, as the 95% confidence intervals of locations from the two approaches overlap. Error ellipses are smaller for surface waves than for T-phases, but the T-phase location and detection can be extended to much smaller events.

KEY WORDS: hydroacoustic methods, earthquake location, surface waves, ocean-bottom seismometers

OBJECTIVES

The objectives of this research are

- To explore the synergy between hydroacoustic and seismic techniques for detecting, locating and discriminating between earthquakes and explosions using an array of ocean-bottom instruments,
- To characterize velocity, scattering and attenuation characteristics of T-phases and long- and short-period surface waves in young seafloor in the Pacific using seismograms recorded at an array of OBSs and hydrophones in the MELT Experiment,
- To characterize the excitation characteristics of typical events in the eastern Pacific, including nuclear tests in French Polynesia, based on these ocean-bottom recordings,
- To develop procedures for locating events using a combination of T-phases and surface waves, and
- To develop models for the excitation and scattering of short-period surface waves.

RESEARCH ACCOMPLISHED

The MELT Experiment in 1995/96 (Figure 1) provides a unique opportunity to study the lateral variability of hydroacoustic phases recorded on the seafloor. With such an understanding, we should be able to improve the picking of arrival times for determination of epicenters. The many stations of the array (recording pressure and in many cases three components of displacement) provide redundancy both in terms of location and a variety of paths to assess repeatability of waveforms. Here we focus on a particular earthquake sequence in relatively uniform water depths as a control test. The precision of location is tested by comparing locations from T-phases with relative event locations using surface waves recorded at teleseismic stations, a completely independent data set.

A quick examination of the smoothed envelopes of T-phases from a strike-slip event at the northern end of the Easter microplate recorded at some of the stations of the array illustrates the great variability in waveforms, even at nearby stations (Figure 2). One traditional way of picking arrival times is to pick the peak energy arrival. Closely spaced stations S14 and S16 in figure 2 both have clear, narrow, peak arrivals. The time difference between arrival times, however, is too great to be consistent with a single direct wave traveling to stations whose epicentral distances differ by less than 3 km (the stations are about 10 km apart). Total epicentral distance is on the order of 600 km. The envelopes at other closely spaced station pairs have even less resemblance. This great variability in waveform probably stems from interference of multiple waves traveling from multiple points of excitation or transmission on the seafloor near the source, effectively creating signal-generated noise in the wave shapes.

If the noise in the envelope shape is signal generated, then it should increase in amplitude with increasing amplitude of the signal and it should be approximately log-normal distributed. Figure 3 demonstrates that this is the case; for a typical station, after taking the log of the envelope, noise is approximately constant throughout the record, including background noise. There is an overall gradual growth in amplitude of the log of the envelope, followed by an even slower gradual decay. Specific peaks in amplitude of the envelope correspond to fortuitous constructive interference between waves and should not be assigned any great significance, i.e., should not be viewed as characteristic times to be picked in locating the event (the caveat is that we are looking at events recorded at depths of 3 km or more and thus the hydroacoustic phases are not dominated by fundamental mode propagation in the SOFAR channel). When viewed in log-space, the individual peaks in amplitude appear as nothing more than minor noise fluctuations on the overall pattern of growth and decay of the envelope.

The overall, approximately linear growth and decay of the log of the envelope suggests fitting the signal with an empirical function of exponential growth followed by exponential decay. We are experimenting with other, more complex functional forms that describe the shape somewhat better and are working toward evaluating shapes based on models of the excitation and propagation, but for now we concentrate on the results obtainable with a very simple model that provides a good empirical fit. The envelope is thus described by background noise plus exponential growth followed by exponential decay with a different time constant. Amplitude of envelope, $A_E(t)$, as function of time is given by

$t \geq t_o$

$$A_E = \left[A_0^2 + A_1^2 \exp\left(\frac{-2\{t_0 - t\}}{t_a} \right) \right]^{\frac{1}{2}}$$

$t > t_o$

$$A_E = \left[A_0^2 + A_1^2 \exp\left(\frac{-2\{t - t_0\}}{t_b} \right) \right]^{\frac{1}{2}}$$

where A_o is the amplitude of background noise, A_1 is the maximum amplitude of the signal, t_o is the characteristic arrival time, t_a is the characteristic growth time, and t_b is the characteristic decay time. An additional factor would have to be added for large earthquakes with long-duration sources, but the largest earthquake in this study is m_b ~4.5, for which the source duration is negligible compared to the duration of the hydroacoustic signal.

Thus, instead of basing the pick of the arrival time on a particular peak amplitude which may depend on highly variable wave interference or excitation from a single bathymetric feature, we base it on the overall shape of the signal, identifying the peak of the model shape as the arrival time after optimizing amplitudes and growth and decay times. The least squares fitting of the function is performed to the log of the envelope so that residuals or errors are approximately normally distributed, and undue emphasis is not placed on trying to match an individual peak in amplitude caused by random, constructive interference.

One way to judge the quality of the arrival time picks is to examine the variance of the travel-time residuals. Within the array, travel times are a linear function of epicentral distance (Figure 4) and the residuals from a linear fit are equivalent to travel-time residuals. Arrival times based on the peak of the model function yield a reduction of variance of more than 50% compared to arrival times based on picking the peak amplitude arrival (Figure 5). As expected, model amplitude decreases with increasing epicentral distance, but we find no systematic variation of growth or decay time with epicentral distance or water depth of the receiver (although note that there is limited range of both depth and distance). Because there is no systematic trend and there are trade-offs or covariance in the inversion between growth time, decay time and arrival time, we try fixing the growth and decay times to the average value of all the seismograms. Eliminating the trade-off in arrival time with other factors by fixing the shape in this way yields a further reduction in variance of nearly 50%, for an overall reduction of nearly 75% compared to picking the peak arrival time. Clearly, fitting a functional form to the envelope yields much more stable arrival time picks that should significantly improve estimates of epicentral location based on T-phases.

Further improvement would be possible if the variability in waveforms at individual stations could be predicted. The potential for improvement can be demonstrated by a comparative or relative event study of closed spaced events. We use an earthquake sequence at the northern end of the Easter microplate, consisting of a series of foreshocks and aftershocks; really an earthquake swarm rather than a mainshock sequence. Here we just describe results from the largest or mainshock and two of the aftershocks. Using the fixed-shape approach to picking arrival times, we find arrival times for each event. In addition to picking times at the ocean-bottom seismometer stations, we also pick arrivals at GSN station RPN, which is a similar distance away to the southeast (Figure 1). Taking the time difference between different events at the same station, we find differential times that are used to find relative event locations of the aftershocks relative to the mainshock. The variance from residuals of the relative event locations is much smaller than the travel-time residuals (Figure 5), indicating that there are systematic variations in waveform that are characteristic of particular stations and paths.

The relative event locations using T-phases show epicenters located up to about 30 km apart (Figure 6). This separation is larger than would normally be expected for a swarm on a mid-ocean ridge, calling into question the reliability of these locations. Some investigators have suggested, for example, that particular bathymetric features dominate the T-phase excitation. Could different features affect the excitation for different events in the same general source area, leading to biases in location? To test the precision of location, we have also performed relative event locations using Rayleigh and Love waves observed at teleseismic stations. We use a method of cross-correlating waveforms, employing phase velocities for young seafloor from Nishimura and Forsyth (1989) as the characteristic velocities in the source region for the calculation of locations. Waveforms from different events in the sequence are very similar (see for example, Figures 7 and 8), indicating that the mechanisms and depths are similar. There is a good azimuthal distribution of stations with adequate signal-to-noise ratio (Figure 9), yielding very precise relative locations.

The surface wave locations of these (Figure 6) and other events of the sequence show two sets of events distributed along nearly east-west lines, in accord with the strike of the fracture zones in this area and the left-lateral, strike-slip mechanism of the events inferred from the surface wave radiation patterns. The important point for this study is that the 95% confidence estimates for the locations using T-phases overlaps that of the

surface waves, indicating that there is no apparent bias in T-phase locations based on fitting shape functions to the entire envelope of the signal.

CONCLUSIONS

Fitting a functional shape to the log of the envelope of the T-phase greatly improves the picking of the arrival time compared to simply picking the time of peak energy. In addition, this approach uses the entire signal and is less likely to be influenced by individual bathymetric features affecting the excitation of the hydroacoustic phase. Relative event locations of a mainshock/aftershock sequence using surface waves confirms that there is no apparent bias in relative locations based on T-phases.

REFERENCE

Nishimura, C. E. and D. W. Forsyth (1989), The anisotropic structure of the upper mantle in the Pacific, Geophys. J., **96**, 203-229, 1989.

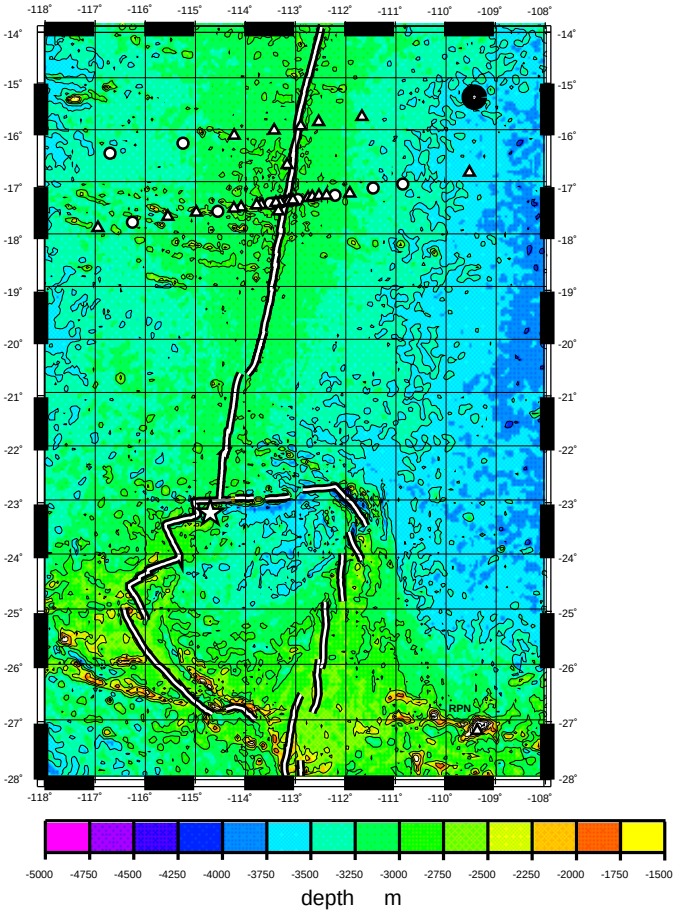

Figure 1. MELT Experiment location. Triangles represent ocean-bottom seismometers (OBS) equipped with 3-component seismometers as well as either hydrophones or differential pressure gauges. GSN station RPN shown in lower righthand corner. Star indicates location of earthquake sequence.

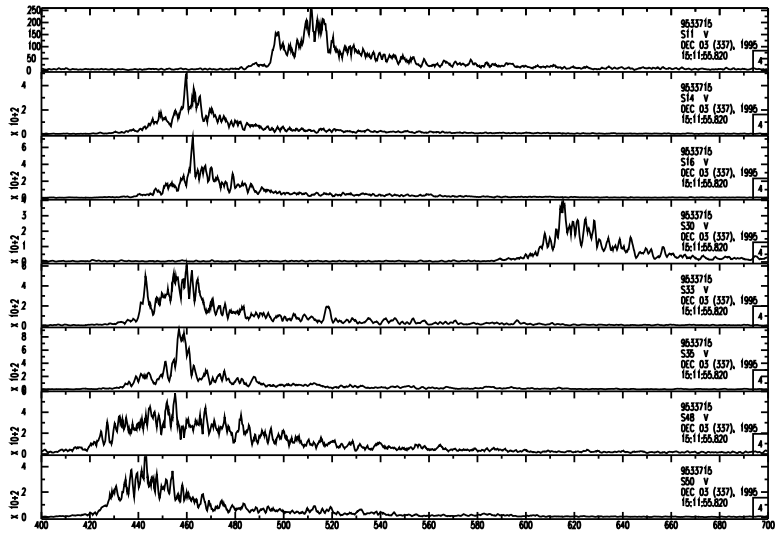

Figure 2. Smoothed envelopes of T phases recorded at several of the stations of the MELT array. These are vertical components, filtered 2 to 6 Hz.

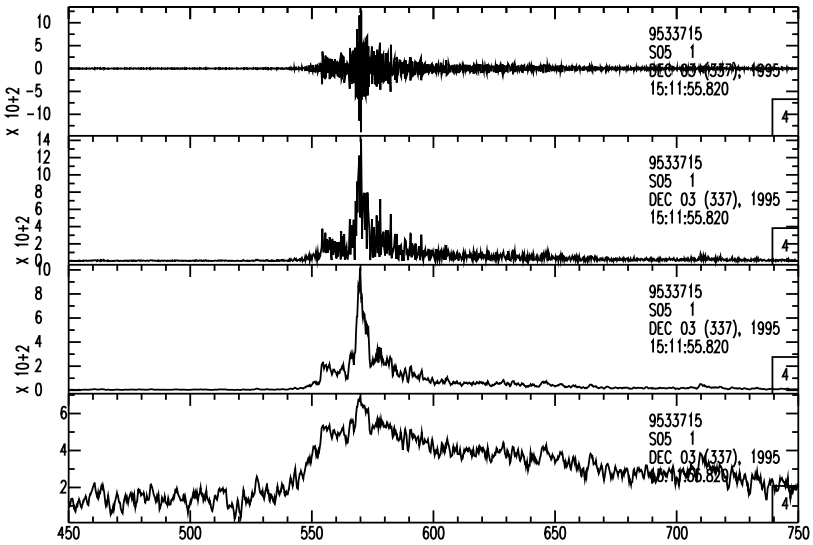

Figure 3. T-phase amplitude, envelope, smoothed envelope, and smoothed log envelope, from top to bottom. Noise is approximately log normal.

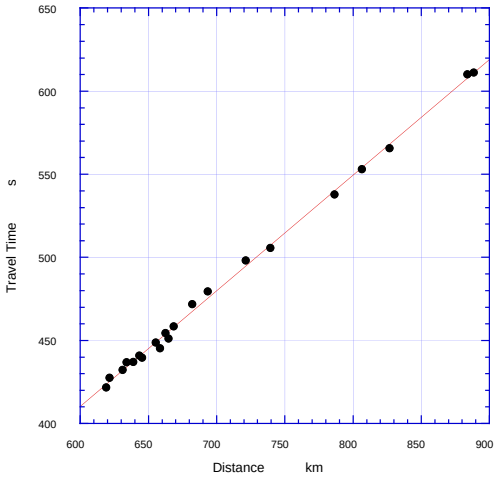

Figure 4. Travel time of T phase versus distance from the epicenter.

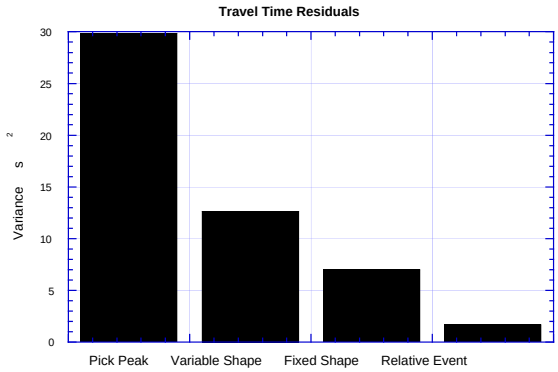

Figure 5. Variances of travel-time residuals estimated for four different approaches to picking arrival times.

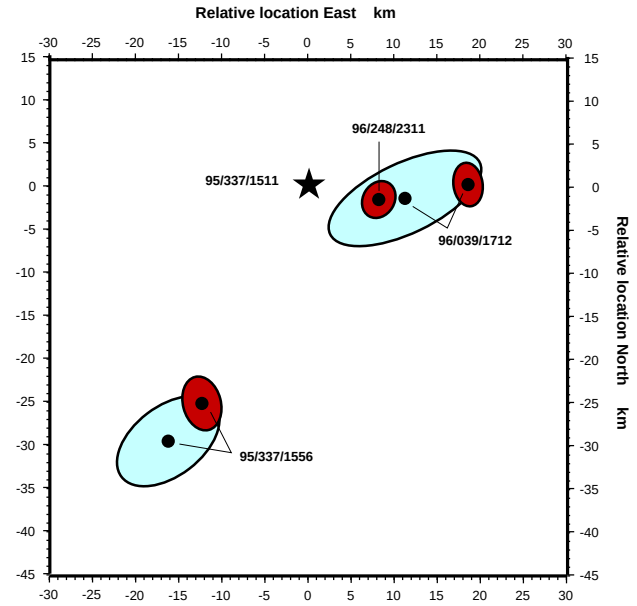

Figure 6. Locations of events relative to mainshock (star). Blue ellipses show 95% confidence ellipses from T phase relocations, red ellipses 95% limits from surface waves. Largest aftershock is located about 30 km to the SSE of mainshock on a parallel fracture zone. There is no apparent bias in T-phase locations based on fitting shape functions to the entire signal.

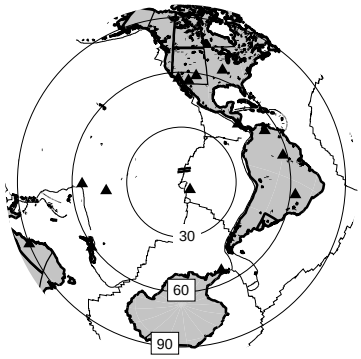

Figure 9. Azimuthal equidistant projection showing distribution of GSN stations (triangles) employed in relative event, surface wave location. Azimuthal coverage is good, with at least one station in every quadrant, i.e., better than the azimuthal distribution of stations recording T phases.

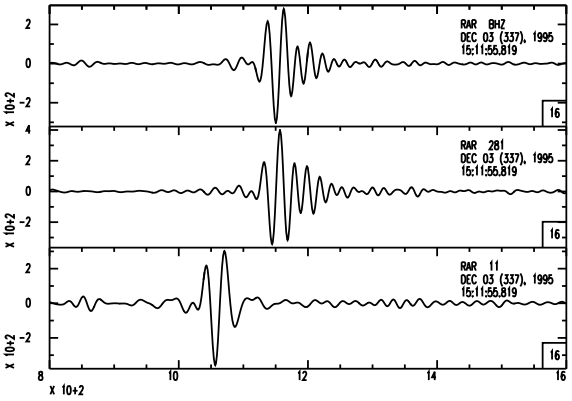

Figure 7. To corroborate relative event locations using T-phases, we use relative event locations determined from surface waves. These panels show vertical, radial, and transverse components, filtered from .02 to .05 Hz, recorded at GSN station RAR in French Polynesia at a distance of about 2800 km from the mainshock.

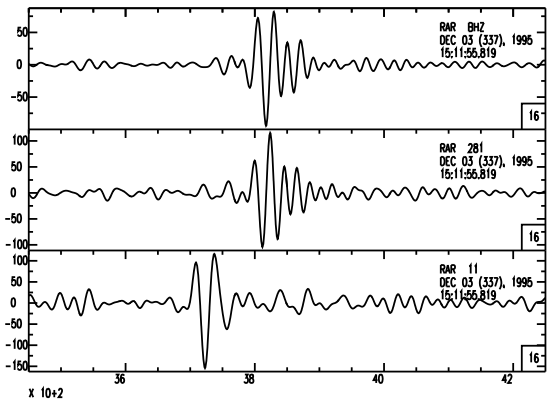

Figure 8. Vertical, radial and transverse components of the largest aftershock recorded at RAR, filtered from .02 to .05 Hz. Both Love and Rayleigh waves are used in the relocation. Note similarity of waveforms to the mainshock, despite differences in amplitude and location.

LLNL DETECTION PROGRAM: BROAD AREA CHARACTERIZATION OF PHASE DETECTABILITY AND EMPIRICAL DETECTORS FOR SPECIFIC SOURCES

David B. Harris, William R. Walter, Arthur J. Rodgers, Alan Sicherman, Stephen Myers and Craig Schultz

Lawrence Livermore National Laboratory

Sponsored by National Nuclear Security Administration
Office of Nonproliferation Research and Engineering
Office of Defense Nuclear Nonproliferation

Contract No. W-7405-ENG-48

ABSTRACT

LLNL detection research addresses two technical issues: detectability of seismic phases over broad regions and specialized algorithms for detecting events originating at specific sources. The detectability of seismic phases underpins the applicability and performance of discrimination and location algorithms by determining which phase observations are likely to contribute to discriminant and event location calculations. Seismic phase detectability is a function of expected phase signal-to-noise ratio (SNR), which, for a particular station, is a function of the phase amplitude spectrum and the noise spectrum at the station. We represent (map) phase amplitudes over broad regions for any given station with empirical (kriged) corrections superimposed on base values determined from an MDAC model. MDAC, which stands for Magnitude Distance Amplitude Correction, is a phase amplitude model that combines a source spectrum model, geometric spreading and attenuation. Ultimately, phase amplitude maps and station noise spectra will determine the geographic distribution of phase observation probabilities. These probabilities, in turn, determine the likelihood that data for particular discriminants will be available and should allow the construction of maps delimiting the geographic range of applicability of those discriminants.

The second technical issue concerns the detection of events occurring at discrete sources, such as mines. This issue is of monitoring interest because mining explosions must be discriminated from earthquakes and nuclear explosions. The need for an efficient screen is particularly acute in mining districts, where explosions dominate event detections at observing stations. The same screening technique can be used to build reference populations of explosions for designing and testing other discriminant algorithms. Frequently, mining sources produce repetitive signals, a signal structure that can be exploited to increase dramatically the probability of detection at a given false alarm rate. The classical solution to problems of detecting known signals is the matched filter, which correlates a template waveform against a continuous data stream to detect occurrences of that waveform. However, signals from repetitive seismic sources often exhibit significant variation that degrades matched filter performance. Our solution to this problem is to use subspace detectors, which replace the matching template with a suite (subspace) of templates that are combined linearly to match occurrences of variable signals from a particular source. We outline template subspace design procedures that maximize the probability of detection for a fixed false alarm rate by varying the dimension of the subspace.

KEY WORDS: seismic detection, phase detectability, signal-to-noise ratio, subspace detectors

OBJECTIVE

Phase Detection and Measurement over Broad Regions

Location and identification of seismic events rely on the ability to detect seismic phases with sufficient signal-to-noise to allow measurements of phase arrival times and amplitudes. However, geometric spreading, heterogeneous attenuation, other variable propagation characteristics of the earth and variations in noise properties cause signal detection characteristics to vary greatly geographically and with frequency.

Seismic identification relies on observations of high-frequency seismic phases to form amplitude, spectral- and cross-spectral ratios for comparison with measurements from events of known source type. Thus, phases must be observed with sufficient signal-to-noise to form meaningful discriminant measurements.

In order to quantify the probability of observing regional phases, we are developing a strategy for characterizing station-specific signal detection as a function of event size, distance, frequency and path. Our characterization depends on the magnitude distance amplitude correction (MDAC) that provides a theoretical model for regional phase amplitudes as a function of frequency, event size (moment magnitude) and distance. Empirical corrections for path effects are estimated by kriging MDAC residuals. The MDAC model parameters, amplitude residual correction surfaces and noise properties at a specific station provide the data from which detection characteristics can be derived.

Subspace Detectors

The objective of subspace detector design is to maximize the probability of detecting variable signals from a particular source for a fixed false alarm rate. Subspace detectors provide a mechanism for detecting signals exhibiting a degree of variation by assuming that the signals to be detected can be represented as a linear combination of basis waveforms. The basis is derived from collections of master event waveforms recorded for events generated by the source of interest and is conveniently represented by a projection operator. The probabilities of detection and false alarm can be traded off by varying the threshold of the detector and the design of the projection operator. Our FY01 research has focussed on determining the statistics of the detector and the dependence of the statistics on the projection operator. This knowledge leads to a projection operator design strategy for maximizing the performance (probability of detection) of a subspace detector.

RESEARCH ACCOMPLISHED

Our seismic detection research is directed in two major areas: regional phase signal-to-noise modeling and source-specific empirical detection. Research accomplished in these areas is described below.

Regional Phase Signal-to-Noise and Detection

Recent advancements in modeling high-frequency (0.5-10 Hz) regional phase amplitudes allows for a predictive model of Pn, Pg, Sn and Lg amplitude spectra for events of a given size and distance (Taylor and Hartse, 1998; Taylor et al., 2002, Walter et al. this Proceedings). This MDAC2 model represents the spectrum of each phase as a convolution of a source spectrum, geometric spreading, attenuation, and site terms. The source model is a generalized Brune (1970) model that accounts for corner frequency -moment scaling. An apparent attenuation law, $Q(f) = Q_0 f^{-\gamma}$ and a geometric spreading exponent, are used for each phase. The theoretical approach has been recently enhanced to allow for non-constant apparent stress and differing P- and S-wave source corner frequencies (Walter and Taylor, 2001). Examples of MDAC2 spectral fits to Nevada Test Site (NTS) earthquake data are shown in Walter et al (this Proceedings).

Using the attenuation parameters discussed in Walter et al (this Proceedings) we can calculate synthetic MDAC2 predicted spectra for a hypothetical earthquake of Mw=3.0 at NTS and ask about its detectability at primary IMS station MNV (~200 km) and auxiliary station ELK (~400km). Taking a ratio of the synthetic MDAC spectra to a noise spectrum at each station we can make predicted signal-to-noise spectra for each phase as shown in Figure 1 below.

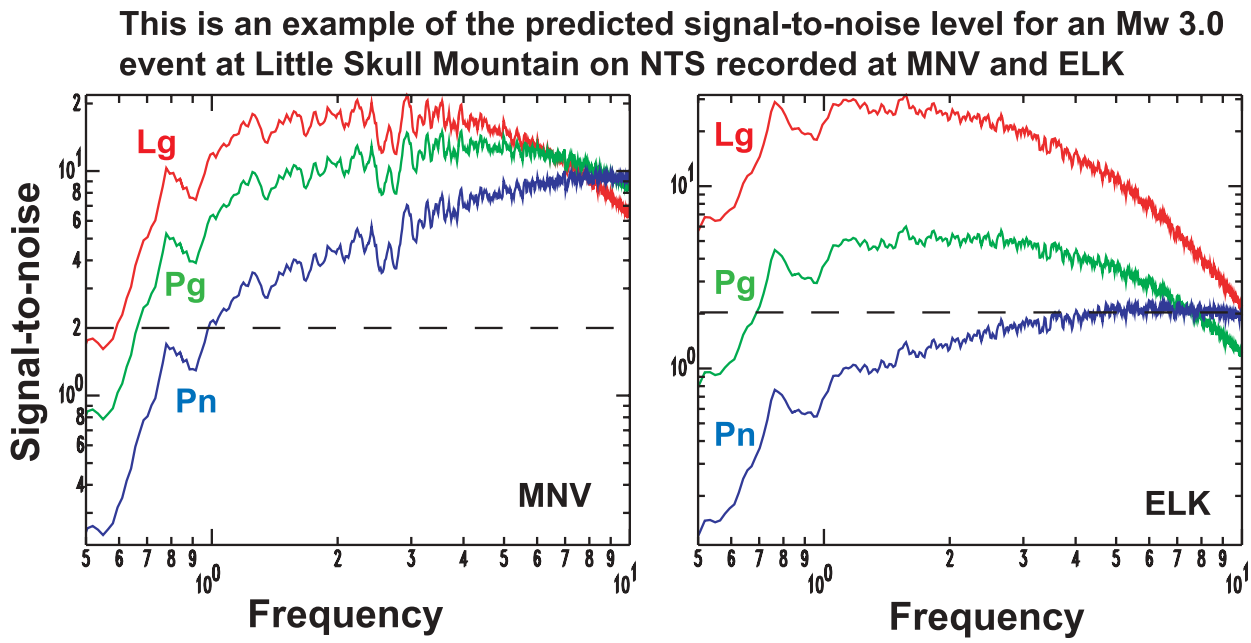

Figure 1. Predicted signal-to-noise spectrum for an Mw=3.0 earthquake near Little Skull Mountain on NTS at station MNV and ELK. The dashed line shows a SNR value of two. Note that at MNV all 3 phases look detectable above about 1 Hz while at the more distant station ELK Pn is probably only detectable above 4 Hz and Pg and Lg may not be detectable above 7 Hz and 10 Hz respectively.

One important caveat to these predictions of signal to noise is that since it was derived from an earthquake source model, it will have to be modified before being applied to explosions. For example, an explosion may generate larger P-waves (Pn,Pg) and smaller S-waves (Sn, Lg) than an earthquake of the same magnitude; if so, this will affect detectability. We are planning to incorporate an explosion source model as an option in future updates of MDAC.

We have applied these techniques to other regions, for example a regional dataset of mb‡3.5 events recorded at station NIL in Pakistan. A subset of high SNR data was fit using MDAC in a grid search routine. After MDAC parameters for all four phases at a station are found, the predicted amplitude in specific frequency bands (e.g. 1-2, 2-4, 4-6 Hz) is subtracted from the observed amplitude to form amplitude residuals. These residuals are projected to the event location and are used to create empirical amplitude correction surfaces with the Bayesian kriging algorithm (Schultz et al., 1998; Rodgers et al., 1999; Phillips, 1999). Figure 2 shows the kriged MDAC residual amplitudes. This figure shows that Lg propagates more efficiently from southern and southeastern azimuths and less efficiently from western and eastern azimuths. Path specific amplitude effects will clearly have a direct impact on phase detection.

We can also estimate the average noise spectrum from this same dataset. The average noise spectra are computed by stacking 565 pre-Pn noise samples, each 35 second long and ending 5 seconds before the analyst picked P-wave arrival. Noise uncertainties are taken as two standard deviations from the mean. Detection of the phase may be possible when the predicted amplitude at a specified frequency falls above the noise model. We combined the MDAC and kriging corrections with the noise model to create laterally varying signal-to-noise surfaces that can then be used as input for probabilistic calculations of signal detection. Figure 3 shows the estimated signal-to-noise for Lg 1 to 2Hz at station NIL for both the laterally homogeneous MDAC correction and the laterally heterogeneous MDAC + kriging path correction. We computed Lg 1- to 2-Hz signal-to-noise as the log base-10 MDAC-predicted amplitude minus the noise. For the noise model we took a conservative approach and used twice the standard deviation above the mean model. For the laterally heterogeneous case, this figure shows that the estimated signal to noise for Lg 1 to 2 Hz is above 2:1 (0.3 log base-10) for distances of nearly 1500 km to the southeast. But for distances greater than 1000 km to the east and west, the estimated signal to noise for Lg 1 to 2

Hz is below 2:1; thus, accounting for the lateral variations is important for more accurate spatial estimates of detectability.

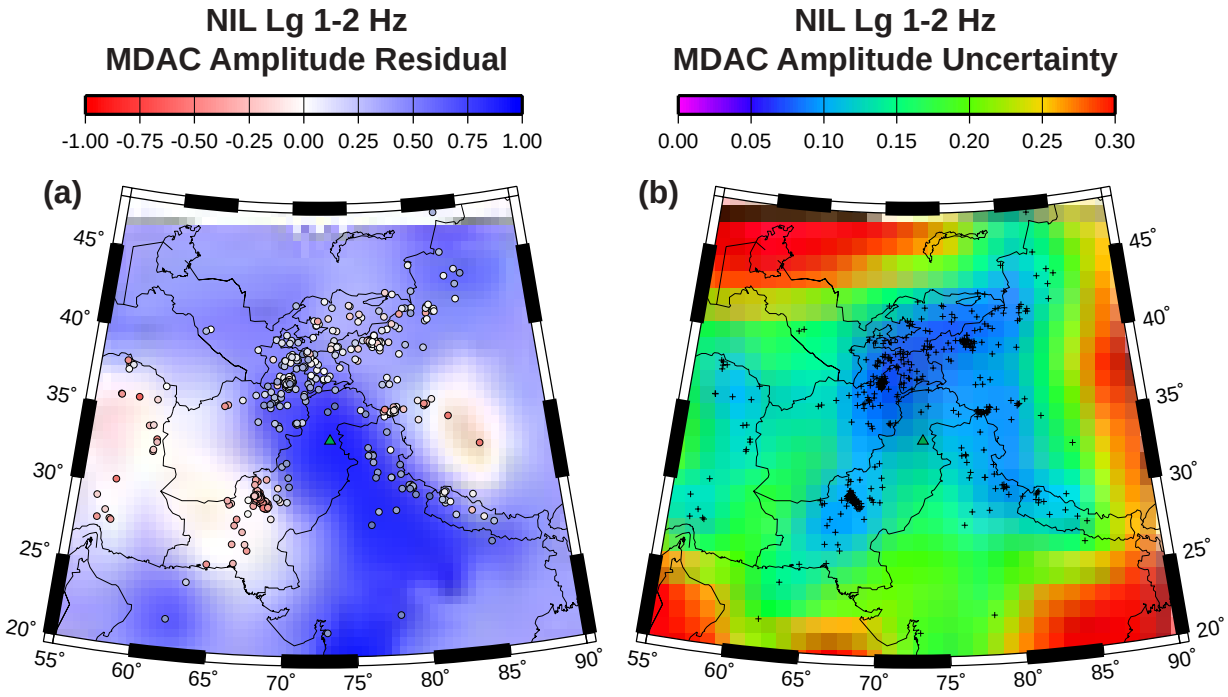

Figure 2 (a) MDAC residuals (circles for Lg 12 Hz at station NIL (Nilore, Pakistan) plotted on top of the amplitude correction surface estimated from Bayesian kriging (Schultz et al., 1998). **(b)** Uncertainty from kriging algorithm.

A more detailed and comprehensive picture of signal detection comes from doing probabilistic calculations in addition to using estimated values. The probabilistic calculations address the uncertainties in signal to noise for an event of a given magnitude and location with respect to a monitoring station. An approach we have employed to address these uncertainties is to take an earthquake data set and use a linear regression model of the following form for any particular phase:

$$\log_{10}(\text{signal to noise}) = A_1 + B_1 M_w + C_2 r + C_3 \log_{10}(r) + \varepsilon$$

where r is the distance to the station, M_w is moment magnitude, and e is assumed to be normally distributed with mean 0 and variance σ_1. The parameters C_2 and C_3 come from the MDAC amplitude model and are treated as known, while the other parameters come from the linear regression fit. This kind of model is similar in spirit to that found in Taylor and Hartse, 1996, and Sereno and Bratt, 1989. The above model is laterally homogeneous (or 1-D) as denoted by the numerical subscript of 1 on the parameters from the regression fit.

We have extended this model concept to address the laterally heterogeneous case as follows:

$$\log_{10}(\text{signal to noise}) = A_2 + B_2 M_w + C_2 r + C_3 \log_{10}(r) + D_2 \text{kriging correction} + \varepsilon$$

where kriging correction is the kriging correction from the MDAC model as illustrated previously in Figure 2, and ε is assumed to be normally distributed with mean 0 and variance σ_2. The subscript 2 on the parameters from the regression fit indicate that this is a 2-D model. Since lateral variability is reflected by the kriging correction term, σ_2 is less than σ_1. As discussed below, this can result in improved confidence in detection.

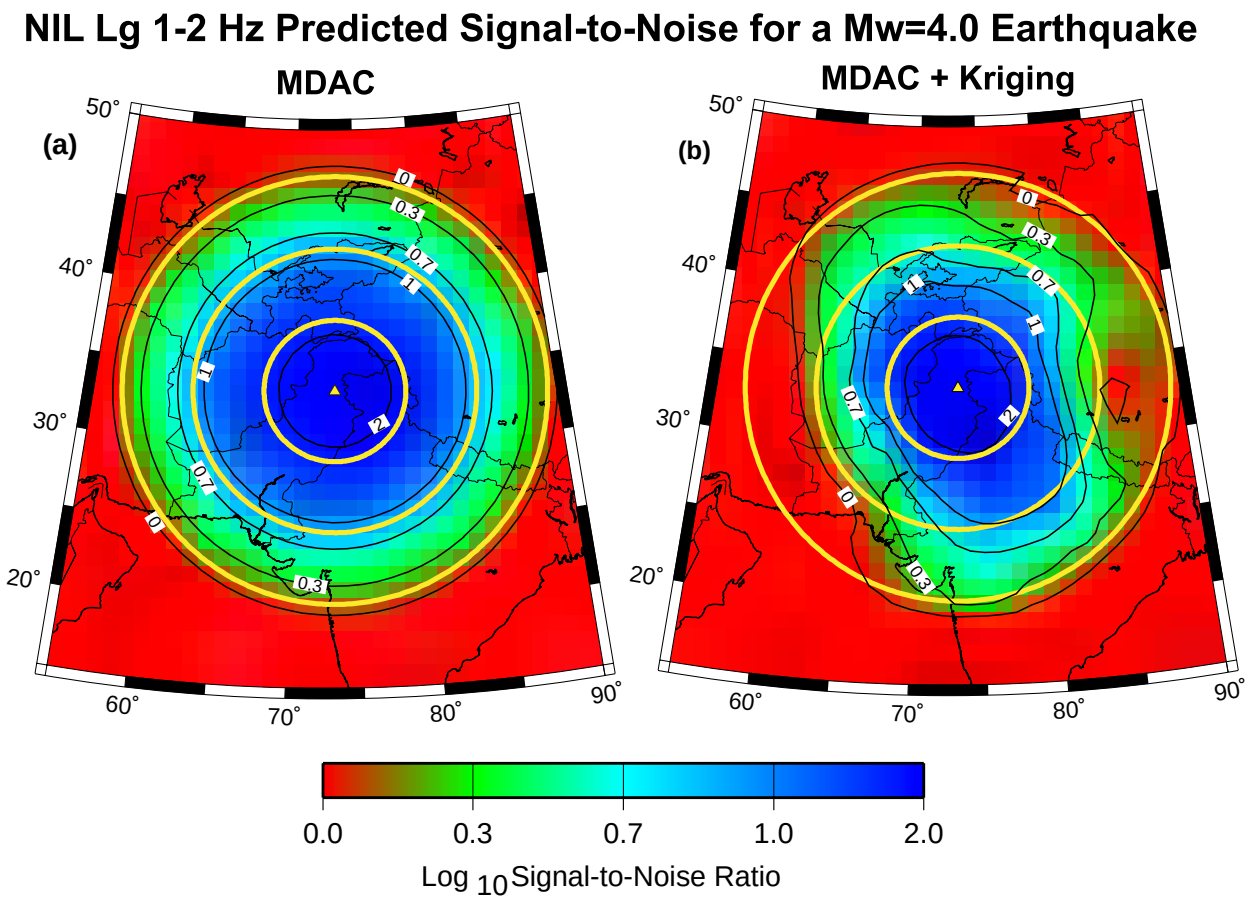

Figure 3. (a) Lg 1-2 signal-to-noise predicted from the MDAC model and the average noise at station NIL. (b) Lg 1-2 signal-to-noise predicted from the MDAC + kriging amplitude path correction. Signal-to-noise ratios less than 1.0 ($\log_{10}$ 0.0) are plotted in red. Yellow circles are plotted at 500, 1000 and 1500 km from station NIL (yellow triangle).

These regression models allow us to construct new figures similar in spirit to the laterally homogeneous and heterogeneous figures above, but which incorporate effects of uncertainties. For example, the regression models can be used to compute the moment magnitude for which we have 90% confidence of detecting a SNR of at least 2:1 as a function of spatial location. The laterally homogeneous model will show radial symmetry about the station, but requires larger moment magnitudes to satisfy the 90% confidence criterion the larger the σ_1. The laterally heterogeneous model has a reduced variance due to the kriging correction term. This can lead to significantly smaller moment magnitudes that satisfy the 90% confidence criterion for the same distance from the station. However, for spatial locations where the kriging correction shows poor signal-to-noise propagation, detection performance will be degraded.

Other insights can be gained by holding different variables fixed and plotting a selected variable as a function of spatial location. In the discussion above, the probability of detection was fixed at 90%, the SNR threshold was set at 2:1, and the moment magnitude was plotted as a function of spatial location. We can also fix the moment magnitude at a fixed level (e.g., 4.0, 3.5, etc.) and plot the probability of detection as a function of spatial location for any selected phase. Comparing the laterally homogeneous and heterogeneous cases reveals insights similar to the example above.

We have also extended the probabilistic models for examining a single phase, to examine the simultaneous detectability of multiple phases such as Pg and Lg both having SNRs, above, say, 2:1. Once the models for individual phases were calibrated, we developed a joint detectability model that is multivariate normal with mean

μ and covariance matrix Σ. The vector μ is the vector mean of the $\log_{10}$ (signal to noise) for each phase as a function of distance and moment magnitude obtained from the regression models for individual phases. The matrix Σ is the covariance matrix of the ε s from those same models. This multivariate normal distribution was used to compute the probability of detecting multiple phases all above a signal-to-noise ratio threshold for a given magnitude and location from a station. Using this model, a figure showing the spatial dependency of probability of detection for, say, both Pg and Lg as a function of magnitude and location can be constructed as was done for a single phase.

In summary, by incorporating kriging corrections into detectability models, we can characterize our capability in a more spatially accurate manner. This increased accuracy can lead to improved confidence for detecting lower magnitude phases at the same distance from a station than would have been estimated without the kriging corrections. We have also extended the models to estimate the joint detectability of multiple phases.

Subspace Detectors

The subspace detector (Scharf and Friedlander, 1994) provides a flexible, yet sensitive detector for signals that exhibit variation within a linear space of basis waveforms. It replaces the single waveform template of the matched filter, with the more general signal representation as a linear combination of a suite of templates. Like all detectors, the subspace detector implements a binary hypothesis test on a window that slides along a continuous data stream (see Figure 4). In the null hypothesis (H_0), the data in the window, represented by vector $\underline{x}$, are assumed to consist of noise, assumed to be a white, zero-mean, stationary Gaussian random process with unknown variance (power level) σ^2. Under the alternative hypothesis (H_1) the data are assumed to consist of signal plus noise. In the subspace detector, the signal is a deterministic mean in the probability model, and is assumed to be the product of a matrix of orthonormal templates (column vectors) $\underline{U}$ and a vector of unknown weights $\underline{a}$. The principal design issue is to choose the number of columns of $\underline{U}$ (dimension d) and to define the column vectors.

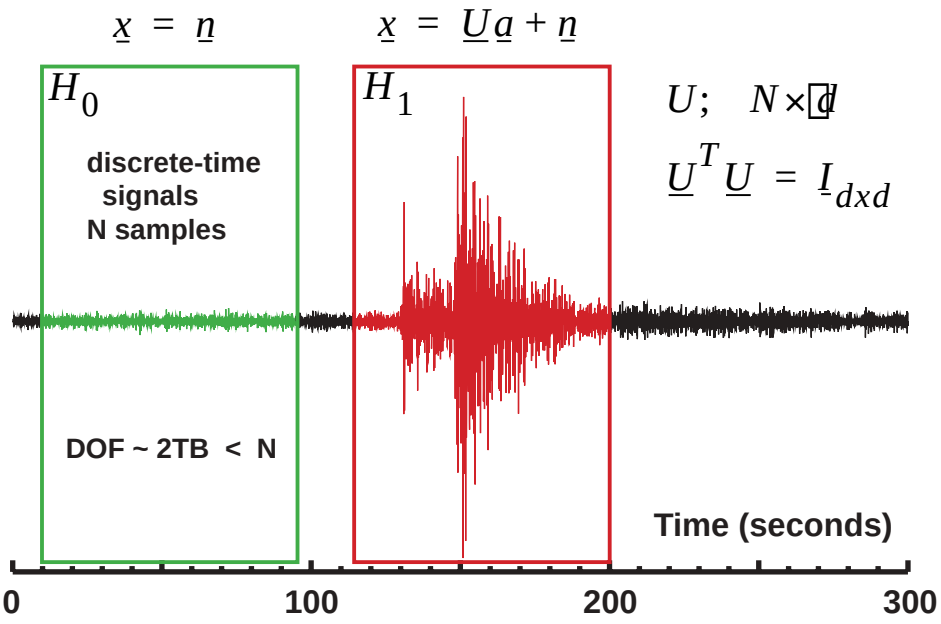

Figure 4 The subspace detector implements a binary hypothesis test on the presence or absence of a signal in background Gaussian noise of unknown variance. The signal is assumed to be a deterministic mean in the probability model and satisfying a parametric model *Ua*, with unknown parameters *a*. The unknown signal and noise parameters are estimated from the data to implement the detector as a generalized likelihood ratio test (GLRT).

A likelihood ratio test is implemented to determine which hypothesis (signal / no signal) is correct. The likelihood ratio contains initially unknown parameters ($\underline{a}$, σ^2), which are estimated from the data. The resulting decision rule is called a generalized likelihood ratio test. The detector implements an intuitive projection operation: the vector of data in the detection window are projected onto the matrix of signal templates. Only when the projection is large is a detection declared. The projection operation is normalized so that the key (sufficient) statistic resembles a correlation coefficient:

$$z = \frac{\underline{x}^T \underline{U}\underline{U}^T \underline{x}}{\underline{x}^T \underline{x}}$$

The operator defining a subspace detector represents a collection of defining waveforms from events at a particular source. Figure 5 displays an example set of 32 aligned signals (vertical channel) observed by Mednet station GFA, and generated by explosions at a phosphate mine near Gafsa, Tunisia. These waveforms were obtained by clustering a larger set of detections with a single link algorithm using a waveform correlation distance measure. The projection operator is a low-dimensional, orthonormal basis for the reference waveforms characterizing the source. To calculate the basis, the reference waveforms are organized as columns of a data matrix $\underline{X}$, an SVD of the matrix is computed, and the matrix of left singular vectors is partitioned into a d-dimensional representation matrix, $\underline{U}_d$, corresponding to the largest singular values and an (N-d)-dimensional matrix, $\underline{U}_e$, spanning residual signals.

The accuracy of the representation provided by the basis waveforms increases with increasing dimension; representation accuracy can be conveniently measured by the fraction (f) of the total signal energy captured by the low-order representation. Figure 6 shows the fractional energy capture for all 32 events in Figure 5 as a function of representation order. Dimension d=10 provides approximately 90% energy capture for all events, and is a suitable representation for the signals generated by this particular source.

Probability distributions for the detection statistic z can be used to compute the subspace detector probability of detection for a fixed false alarm rate. These distributions in turn can be used to optimize the detector by maximizing the probability of detection as a function of the dimension d of the subspace representation. This capability leads to an important design strategy. The detection statistic z can be shown to be central beta distributed with N-d and d degrees of freedom under the null hypothesis (H_0: noise only), i.e. $z \sim \beta(N\text{-}d, d)$. N is the number of degrees of freedom in the data (roughly the number of independent data samples). The distribution is doubly non-central beta under the alternative (H_1: signal + noise) hypothesis when energy capture is less than perfect (i.e. f < 1): $z \sim \beta(N\text{-}d, d, fE/\sigma^2, (1\text{-}f)E/\sigma^2)$.

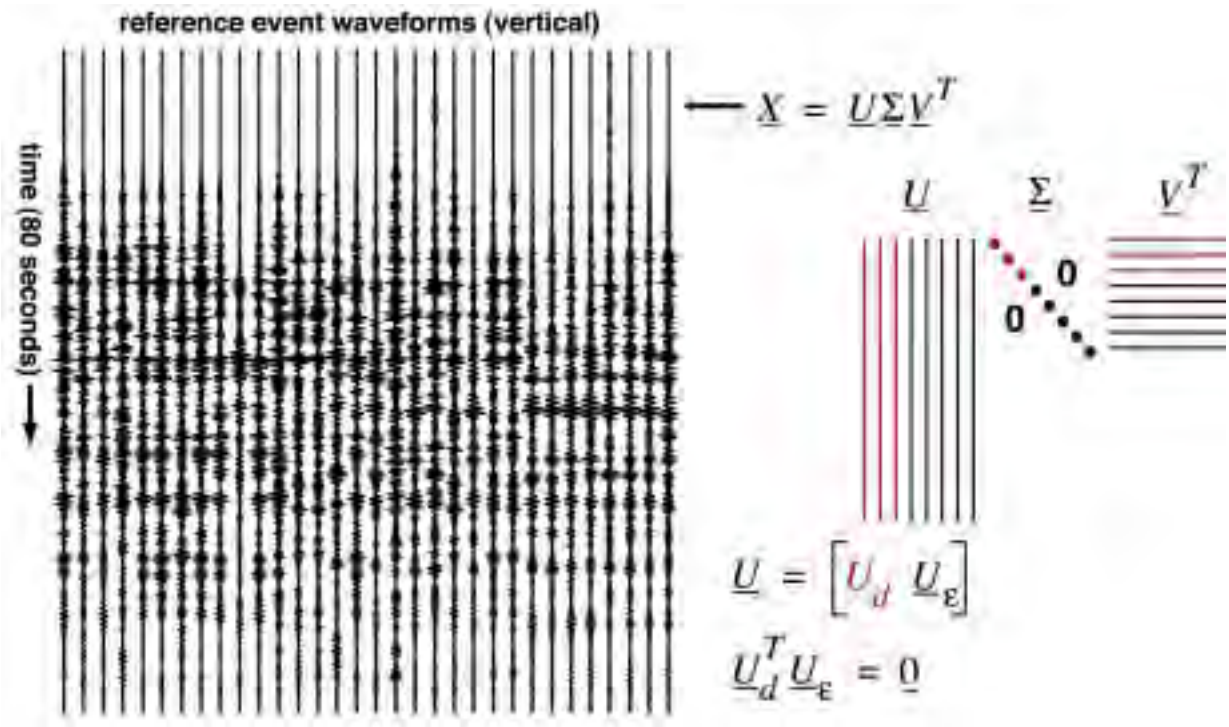

Figure 5 The subspace projection operator U_d is computed from reference waveforms from a particular source. This figure shows 32 waveforms recorded by Mednet station GFA (Tunisia) for explosions at one particular mine in the Gafsa phosphate mining district. The waveforms are aligned and stacked in a data matrix; an SVD is used to extract a lower-dimensional *(d)* matrix of basis waveforms.

The suite of curves in Figure 7 shows how the detection statistic may be optimized to maximize the probability of detection. The figure shows normalized probabilities of detection as a function of post-integration SNR for subspace detectors with dimensions ranging from 1 to 15. These curves are computed using the energy capture curve shown in red in Figure 6 for one of the 32 reference events. The probability curves have been normalized by the probability of detection for a simple energy (STA/LTA) detector operating on the same detection window with the same false alarm rate. Hence, the curves indicate the relative performance of subspace detectors compared to a simple energy detector. Subspace detectors integrate signal energy over all frequencies coherently, whereas the energy detector, with no knowledge of the signal temporal structure, integrates energy incoherently. Consequently, the curves of Figure 7 demonstrate coherent processing gain.

The best performance is attained for subspace detectors with dimensions of 9 or 10, and in a finite range of post-integration SNR. Performance varies as a function of subspace dimension, because more and more signal energy is processed coherently (captured) as subspace dimensions increases. Beyond dimension 10, the subspace operator captures little additional signal energy, but captures more and more noise energy, causing performance to degrade. Processing gain varies dramatically with SNR and is maximized in the threshold-operating region of STA/LTA detectors for the simple reasons that neither detector performs well at SNRs approaching zero, and both perform very well at high SNRs. Subspace detectors perform very well in the crucial region of threshold detection.

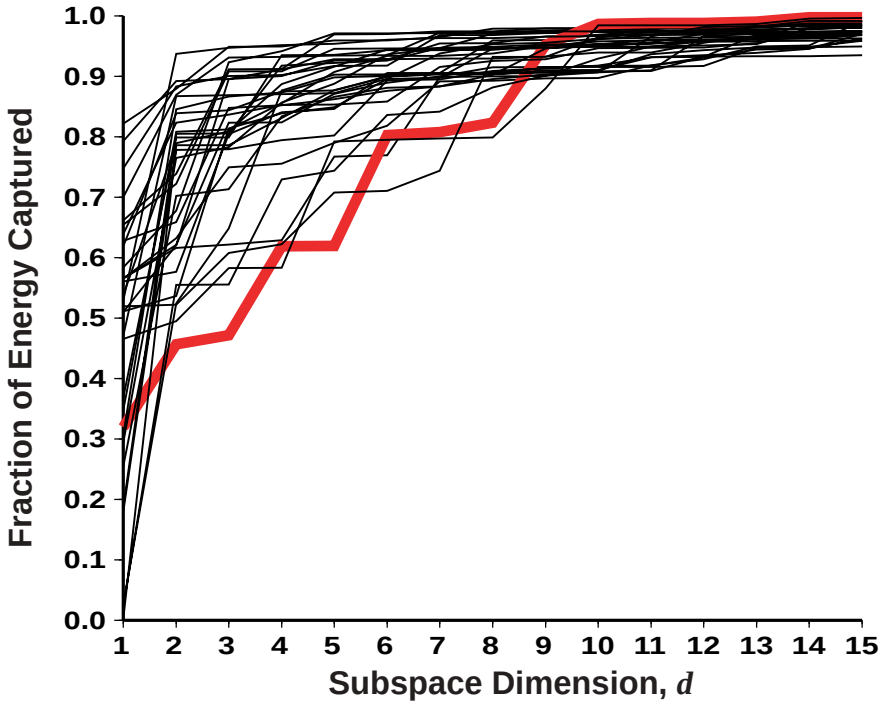

Figure 6 These curves depict the fraction of energy in each of the 32 signals in Figure 5 captured by the low-dimensional subspace representation. The fraction of energy captured by the representation is a function of the dimension *d* of the subspace.

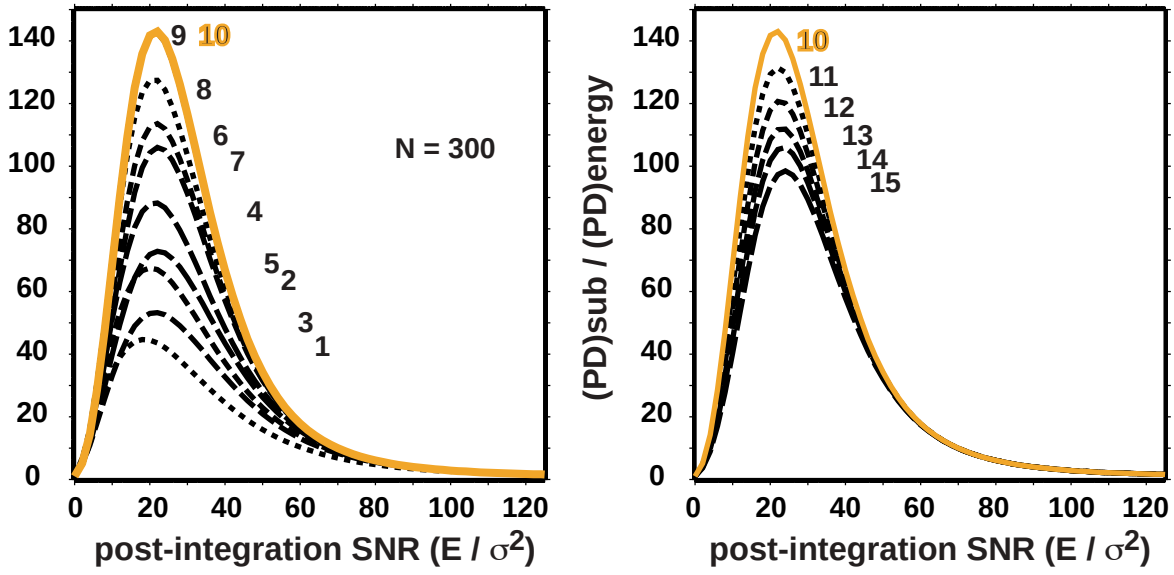

Figure 7 These curves show the normalized probabilities of detection for a range of subspace detectors for a single event waveform (the one indicated in red in Figure 6), at a fixed false alarm probability of 0.0001. The probabilities of detection for the subspace detectors of dimensions *d*=1 through *d*=15 are here divided by the probability of detection for a comparable energy (STA/LTA) detector, and the resulting ratio is plotted as a function of post-integration signal-to-noise ratio. Thus, the curves represent coherent subspace detector processing gain over a simple incoherent detector. The subspace probability of detection is maximum for a dimension of 10, indicating the optimum subspace dimension for this particular event.

CONCLUSIONS AND RECOMMENDATIONS

We have outlined here a methodology to quantify our ability to detect regional seismic phases. The method uses an MDAC spectral model, kriged residuals and a probabilistic model. As MDAC calibration and empirical data collection occurs at each station the detection model will improve. This methodology is important in deciding which phases and frequency bands will be available to locate and discriminate an event at a given station. In turn this procedure guides the choice of particular detection or location algorithms. Finally a quantifiable detection model such as outlined here is crucial for assessing the overall monitoring capability of particular stations.

In addition, we have outlined a method for choosing projection operators in subspace detectors to maximize the probability of detection at a fixed false alarm rate. This procedure provides a rational basis for selecting the order (representation accuracy) of the subspace projection operator. In the future, we plan to deploy this design procedure for the numerous mining sources in northern Fennoscandia and Russia observed by the ARCESS array.

REFERENCES

Phillips, W. S. (1999). Empirical path correction for regional-phase amplitudes, *Bull. Seismo. Soc. Amer*., **89**, 384-393.

Rodgers, A., W. Walter, C. Schultz, S. Myers and T. Lay (1999). A comparison of methodologies for representing path effects on regional P/S discriminants, *Bull. Seismo. Soc. Amer*., **89**, 394-408.

Scharf, L. L. and B. Friedlander (1994). Matched subspace detectors. *IEEE Trans. on Signal Processing*, **42(8)**, 2146-2157.

Schultz, C., S. Myers, J. Hipp and C. Young (1998). Nonstationary Bayesian kriging: application of spatial corrections to improve seismic detection, location and identification, *Bull. Seism. Soc. Am.,* **88***,* 1275-1288.

Sereno, T. and S. Bratt (1989). Seismic detection capability at NORESS and implications for the detection threshold of a hypothetical network in the Soviet Union, *J. Geophys. Res*., **94**, 10,397-10,414.

Taylor, S. and H. Hartse (1996). Regional phase detection thresholds at WMQ, Los Alamos National Laboratory, Los Alamos, New Mexico, LAUR-96-395.

Taylor, S. and H. Hartse (1998). A procedure for estimation of source and propagation corrections for regional seismic discriminants, *J. Geophys. Res*., **103**, 2781-2789.

Taylor, S.,A. Velasco, H. Hartse, W. S. Phillips, W. Walter and A. Rodgers (2002). Amplitude corrections for regional seismic discriminants, *in press PAGEOPH Special Volume on Seismic Discrimination for CTBT Research*.

Walter, W. R., and S. R. Taylor, A revised magnitude and distance amplitude correction (MDAC2) procedure for regional seismic discriminants, Lawrence Livermore National Laboratory, UCRL-ID (in prep.), 2001.

SEISMIC REGIONALIZATION, SIGNAL DETECTOR AND SOURCE LOCATOR

Eystein S. Husebye and Yuri V. Fedorenko

Institute Solid Earth Physics, University of Bergen

Sponsored by Defense Threat Reduction Agency

Contract No. DSWA 01-98-C-0159

ABSTRACT

This class of problems represents a permanent challenge to seismologists despite much ingenuity and efforts over the last decades. The persistent epicenter location problem is illustrative; now as in the 1960 a main research strategy for improved accuracy is tied to an elaborate system of P- and S- travel time and station corrections. For local ranges results would hardly be optimum since the major problem here is that of proper identifying S-phases in largely "chaotic" recordings besides ignoring the information potential in the waveforms themselves. In the simplifying case of spatially stationary signals from a specific mine or quarry it has been demonstrated previously by Fedorenko et al. (1998, 1999) that exploiting waveform information from a network of stations or a single 3-comp. station result in enhanced epicenter locations and source type identification. Corresponding analysis in case of earthquake waveforms are more complex since source type and locations are not necessarily spatially stationary; in essence earthquake records are "deformed" as a function of epicenter distance. The first problem encountered was surprisingly lack of adequate data; for detector research long time intervals are needed while for location station spacing should for a start be between say 15 to 60 km. Instead of wasting much time on local network records, often of poor quality, we deployed our own seismograph network using geophones as seismometers and preamplifier and A/D-converter of our design. Also, our 3-component instrument was tested through joint operation and site sharing with a Kinemetrics Ranger station — not clear which instrument had the best performance. Data transfer often proves to be ruinous in local network operation but not so for us; we simply launched a "school" project with sensor installations in school yards including access to the school's Internet so free data transfer to server in our office. An additional benefit is access to the Internet Time Servers with timing accuracy around 25 msec. Currently 5 stations are operational and 10 more schools scheduled for installation in the Fall of 2001. Firstly, we were somewhat hesitant to start research here since the widely used STA/LTA detector is simple, efficient and robust. However, the long seismic noise records now at hand showed that waveforms and also their envelopes are uncorrelated between components. Exploiting this feature, we designed a 2D-detector jointly incorporating detection statistics both from horizontal and vertical components. 3 filter bands; 1.56 - 3.12, 3.12 - 6.25, and 6.25 - 12.5 Hz were selected from wavelet transform considerations. The 2D-detector is superior to the 1D STA/LTA detector; operating on a RMS threshold level of 3 and still no "noise" triggering. More than 100 detections daily but most of these are traffic "pulses", very local explosions and so on. Detector output, also placed on Internet, is RMS and duration of detection state for the 3 filter bands so we have a "finger feel" of ongoing seismic activity. Since network aperture now is about 35 km we will soon have an event listing and epicenter locations on Internet in order to stimulate science interest among students and future seismologists. Inversion of BB records from large earthquakes is an efficient tool in analysis of source mechanisms including focal parameters. For small events at local distances we are faced with complex and unpredictable waveforms from which mainly P- and S-arrival times are extracted and subsequently used for epicenter determinations. We aim for using waveform envelopes obtained through Hilbert transform for epicenter refinements. First step is to use Lg envelope peaks which are easily pickable and besides have a very consistent (group) velocity of 3.5 km/sec +/- 0.1. The main challenge is that of "'deforming" envelope records in such a manner that we can "predict" them 10 - 30 km away from a given reference station and reference events. In principle, this approach should give excellent results if successful simply because we use dynamic wavefield information for location as compared to conventional kinematic phase information as now.

KEY WORDS: seismograph design, school project, waveform envelope, 2D detector, deformable templates, event location

OBJECTIVE

Progress in seismology is tied to 2 specific factors, namely i) easy access to digital network data of high quality and ii) ensure a continuous influx of talented students to our science for at least maintaining current research activities. These challenges are not particular new and a recent approach of growing popularity is that of launching various kind of seismic school projects as proposed in Husebye and Thorensen (1984). The rational is obvious; earthquakes are a manifestation of the dynamic Earth and as such easily catch the attention and imagination of many high school students at least for the few days such disasters are given media exposure. To capitalize on this albeit short lived interest in natural phenomenon we think that students should become active partners in seismic monitoring that is operate their own school specific 3-component seismograph stations, undertake analyst tasks and also become partners in special research ventures. Ideas and enthusiasm are not enough for launching successful school projects as is clear from many such undertakings. Failures appear to be associated with lack of high-sensitive and inexpensive instrumentation in combination with clumsy data access and lack of interactive analysis software for students. Although educational projects are noble, our launching of a school project in Norway (http://www2.ifjf.uib.no/SEIS-SCHOOL) was and is mainly motivated by a need for high quality data for CTBT research at local and regional distance ranges as shown in Fedorenko et al. (2000). In our experience it is not unproblematic to find small network data of high quality for apertures of 50 - 100 km for which local recordings are easily retrievable. After much efforts with scant success in obtaining data from established international and national data centers we decided to investigate whether we could deploy our own network of inexpensive, high quality stations with a minimum of running costs. As to be demonstrated below, we have been successful in this undertaking (Fig. 1) albeit time and work invested in this enterprise exceeded our initial effort estimate.

RESEARCH ACCOMPLISHED

Instrumentation

A single seismometer costs at least $ 2000 so we looked for cheap geophones (approximately $ 60.) as a substitute. In this way 3-component station may become affordable also for groupings outside the established network operators. However, stations need preamplifiers so we designed our own in order to reshape the original geophone velocity response to a flat acceleration response in the range 0.45 - 45 Hz - symmetric around geophone eigenfrequency at 4.5 Hz. The advantage with a flat acceleration response is that the noise is approximately white above 1 Hz while velocity instruments have response noise fall-off roughly as $1/\omega$. It is also convenient for denoising of seismic records using wavelet transform operations as shown in Fedorenko and Husebye (1999a). The A/D-converter (also own design) has an effective dynamic range of 19 bits achieved through gross oversampling and at a cost of $ 350. Like the preamplifier it is cheaper than those commercial available. Timing; 3 venues are available namely i) radio clock ($ 50.), ii) GPS ($ 300.) and iii) Internet clock (free). For school installations with free Internet connection the latter is preferable as precision is always better than 25 msec. Station sensitivity: The simplest one was that of site-sharing with nearby station ASK (Kinemtrics Ranger) having velocity response. Records are not as expected identical but all local events recorded by ASK was also recorded by our "geophone" station. Since sensitivity depends on pendulum mass there is no point in trying to extend small mass geophones to record the relatively low frequency part of earthquake signal spectra. Station sensitivity also depends on internal and external noise fields. The theoretical investigation here indicates that the sensor internal noise is more than 6 db below the ambient noise at the ARCESS array central site (Z-component) within the 0.25 - 10 Hz band as demonstrated by Fedorenko (2001). The sensor noise model includes voltage and current noise sources at both inverting and non-inverting inputs of OPA2227 operational amplifier, suspension and thermal (Johnson) noise of geophone and also the thermal noise of resistors connected to OPA2227 inputs. For GS11D 4.5 Hz geophones from GeoSpace Corp., Houston, thermal noise dominates being approximately twice larger than the operational amplifier noise. In this case the use of dual geophone sensors will improve SNR by 6 dB. Suspension noise is negligible. Sensors with flat acceleration responses have SNR better than 6 dB (2.0 in r.m.s amplitude) within 0.2-10 Hz band relative to ARCESS noise model as shown in Fig. 2. In other words, our "geophone" instruments may conveniently substitute conventional S-13 seismometer in areas with moderate seismic noise levels, such as Norway.

Signal Detection

Our initial motivation for developing our school station was not 'school' but the need for long strings of high quality records for detector experiments as shown in Fedorenko and Husebye (1999b). Besides, some of the local (national) stations were exceptional spiky. Outcome of these efforts are an anti-spike filter incorporated in the preamplifier design and that our new very efficient 2D-detector operates in the 3 frequency bands 1.563-3.125, 3.125-6.25 and 6.25-12.5 Hz. Also, for better envelope shapes we use a pulse optimal filters which appear to give sharper onsets than frequency optimal filters. The 2D-detector is of the familiar STA/LTA-type but taking advantage of uncorrelated noise between Z- and H- components both for conventional and envelope waveforms as shown by Fedorenko and Husebye (1999b) and Husebye and Fedorenko (2000). A rough distance estimate is obtained through an angle of incident estimate for presumed P- onsets. Operational experiences so far indicate that no false alarms occur even at low threshold levels at 3.0. For ease and school instructions the detection logs are on Internet not lagging behind more than a few minutes relative to arrival time (http://pcg1.ifjf.uib.no). Likewise, with a few additional clicks the corresponding record segments of Z-component are displayed in the 3 filter bands of the 2D signal detector (Fig. 3). Further refinements are under consideration and implementation; as shown by Fedorenko et al. (2000) a few additional clicks would activate the PITSA signal analysis package by Scherbaum and Johnson (1992) for phase pickings, polarization analysis and epicenter locations using grid search techniques. These flexible seismogram and signal analysis options will presumably also be instructive for professional seismologists who often are not quite familiar with observational seismogram analysis. Also, it should not be forgotten that much creative research is aimed at explaining unexplained wavefield features.

Data Transfer and Running Costs

Our interest in school cooperation is partly motivated by access to the permanent school Internet and in this way eliminated an often painful aspect of network operations namely high data transmission costs. Our set up is that of installing the data logger in the respective schools and then transfer data to the network server in our office at the University. In turn, schools download their own and other station data from the server and also application software. So far only the PITSA analysis package is available for data analysis which in near future would be "coupled" to a grid search routine for epicenter location of local events. Presently, data and detector log access and flexible software routines are of highest priorities in our school project. We hope that student teams would undertake routine analysis of local events.

Seis-School Organization

We started simply by installing our prototype sensor in the school yard of Aasane Gymnasium (ASAS) just around 15 km away from the University of Bergen campus. High school student interest was triggered with a local earthquake occurring a few weeks later some 35 km west of Bergen. With good exposure of students and their ASAS recording in local newspapers our school project got a flying start. In another school, Sotra, located in the area with strong shaking from the above local earthquake, a group of students undertook a macroseismic investigation of this event and their findings were rewarded with a prize in a national Young Scientist contest. As of today, 4 schools have seismograph installations while 10 more are waiting for deployments (see Fig. 1). In each school special student teams are (will be) formed who will be partners in appropriate "young scientists" projects and local seismicity monitoring.

School Stations and CTBT

The educational aspects of school projects are noble but reality necessitates that such records are of professional quality. In our case, the original design strategy aimed at data for pure research that is for signal detection and event location experiments. The school "association" becomes very attractive in terms of enthusiastic students and free Internet access equivalent to an elimination of operational costs. The obvious penalty here is that site selection is restricted and hence not optimum in most cases. In other words, how good is our 3-comp. school seismographs and what is their usefulness in CTBT monitoring? As mentioned, a first simple test was site-sharing with a 3-comp. Kinemetrics Ranger station of the national (Norwegian) seismograph network. The outcome here for local events was that the respective event

detection performances were roughly similar or school station slightly better. Since both responses and detectors are different it is difficult to quantify in detail the respective performances of these 2 stations. As part of our station performance evaluation a rigid study of internal instrumentation noise in the preamplifier and geophone and in the A/D-converter has been undertaken. The preliminary outcome of this study (Fedorenko, 2001) is that the internal RMS noise level appears to be a factor of 2.2 less than the ambient ARCESS center sensor (Z-comp.) noise level. In other words, our school station is capable of detecting real seismic signals in the ambient noise as illustrated in Fig. 2. By necessity, the CTBTO monitoring seismic network (IMS) is teleseismic in view of the relatively limited number of arrays and stations deployed. For events of small to intermediate magnitudes the corresponding number of reporting stations will be few - often only 5 or less. To overcome such a drawback there is a provision for extracting data from so called auxiliary stations for improving event locations; travel time corrections for these stations are also in the CTBTO data base. So what about school stations of the type developed by us and described here ? Data quality is no objection (e.g., see record display in Fig. 3,4) and besides timeliness of availability do not pose any hindrance. In our set-up the data are sent server within a minute of end of detection state and then immediately accessible via Internet. Extensive timing corrections are not needed for a simple and effective check of a trial epicenter solution; at local distances an envelope peak should correspond to the universal Lg group velocity of 3.5 +/- 0.1 km/sec as shown by Husebye et al. (1998). In this way location errors exceeding 10 - 12 km are easily detectable.

Deformable Templates — a New Approach to Event Location

Accuracy and robustness in epicenter locations is an outstanding problem in CTBT monitoring. It is complex in the sense that it depends on network configuration relative event location, adequacy of local travel time curves and the analyst's ability to properly identify secondary S-phase onsets. In particular, for small events with few reporting stations relatively large location errors may occur. Currently, an intrinsic time correction scheme is under implementation in the CTBT system for improving epicenter locations tied to alpha and beta stations and arrays. Drawbacks with such a "correction" scheme is complexity in particular as no fixed reference system is available; station correction may be magnitude dependent that is number of reporting stations used is not fixed and that referenced travel time tables are being regionalized. In our opinion, the foremost drawback here is that too little information is extracted from the records - just some kinematic phase arrival times. The local high frequency records are complex so pickings of secondary S-arrivals are often problematic and occasionally error prone. We have previously demonstrated that using waveform envelopes from Hilbert transform operations from a few stations suffice for very accurate locations of stationary and repetitive sources like mining explosions and quarry blasts as shown in Fedorenko et al. (1998; 1999). Other waveform approaches are using optimization techniques for relative accurate pickings of phase times (variant of the JED-scheme) in aftershock sequences, waveform synthetics and so forth. Instructive results have been obtained but techniques are not easily transportable nor flexible for areas with dispersed earthquake activities. The basic problem in waveform location analysis is that we must be able to predict waveform changes as a function of differential epicenter distances; for stationary mining explosions this basic problems are non-existent. Since the high frequency parts of local seismogram appear chaotic and hence unpredictable in contrast to the corresponding envelopes which vary far more smoothly. Also, synthetics are unable to reproduce real local seismograms unless 3D crustal models are used as shown by Hestholm et al. (1994) and Hestholm (1999). With our school network records we have a good data base for waveform location research. As demonstrated in Fig. 4 the original waveforms change fast between the school network station while vary slowly in case of the corresponding waveform envelopes. As shown in Fedorenko and Husebye (1999a), in such case a conventional phase picking may be reduced to nonlinear optimization problem in a 9-dimensional space in which the parameters which minimize the difference between model and observed envelops are sought. The joint use of seismic network data increases number of parameters dramatically. Nonlinear optimization in high dimensional space using standard methods is possible but slow thus being a primary limiting factor for its usage. However, the model and observed envelopes are topologically similar which allows us to develop fast optimization algorithms based on a deformable templates technique. The latter proves to be very useful in pattern recognition problems. As shown in Jain and Zongker (1997), a deformable template approach has recognition rates of the handwritten characters up to 99.25% on a 2000 character subset. This approach can be directly applied to the sequence of envelops from dense seismic networks. Cootes et al. (2000) demonstrate the way to represent an object as complex as a human face by a small number of models.

Basics of shape modeling are shown in Zhu (1999). The essence of our analyzing strategy based on deformable templates methods is:

- Build a set of skeletonized models representing the shape of envelops of seismic events on local distances.
- Develop the method to fit observed envelops to models using a suitable deformable templates algorithm.
- Choose the classifier appropriate for our problem using data from our Seis-School network.
- Develop an epicenter location algorithm using the envelope deformations along time axes from deformable templates methods.

So far, records from our school network have proved both beneficial and very effective in selecting events for our ongoing methodical approach of applying deformable templates techniques for a different methods of seismic event location.

CONCLUSIONS AND RECOMMENDATIONS

Conclusions: Main research efforts have been focused on instrument development, network deployment and operation. Four 3-component stations are now operative in local school yards and event record segments are automatically transmitted via Internet to server in our offices in University of Bergen. Instrument sensitivity using inexpensive 4.5 Hz geophones is good and record quality suffice for CTBTO oriented research problems. School deployments give direct and free Internet connection so operational costs are zero. User access to records are simple and efficient; detection logs are retrieval from Internet including options for PC screen visualization. Password is currently required for extracting data files for further record manipulations. These network recordings have been used for developing a new 2D signal detector and its practical testing over many months of station operations. The 2D detector combines RMS powers on both H- and Z-components permitting an STA/LTA equivalent threshold of only 3 without false alarms (or noise detections). Besides arrival time and signal power estimates the detector also extract rough azimuth and angle of incident estimates. Glitches and other type of record disturbances are not entirely uncommon in station operations; such nuisances are removed by an anti-spike filter incorporated in the preamplifier of our own design. The cost of a complete 3-component instrument based on 4.5 Hz geophones as sensors, exclusive work, amounts to less than US $ 1000. In comparison, a single seismometer of conventional design (like Kinemetrics Ranger or S-13) has a price tag exceeding $ 2000.

Currently, the CTBTO epicenter location approach is tied to an intrinsic set of travel time and station corrections. For local events we are considering a deformable template approach using envelope traces (Hilbert transforms) from our school network. The rational here is that waveforms are more informative than kinematic time corrections and also that envelope shapes are slowly varying with distance re the original waveforms. Thus in principle we should be able to project spatially envelope records between network stations and in this way obtain enhanced epicenter accuracy - we are establishing a data base here from our own network.

Recommendations: CTBTO/IMS monitoring would be more efficient if more auxilary station recordings are used in analysis. We have demonstrated the feasibility of deploying and operating seismic networks where data quality is high and instrument and operational costs are low. Also, we have demonstrated that Internet may be used for almost instantaneous access to a wide class of network recordings. Furthermore, 2D detectors should be more widely used in view of their efficiencies in suppressing false alarms (noise triggers) and alternatives to travel time parameters for event locations should be more vigorously pursued.

REFERENCES

Cootes, T. F., G. V. Wheeler, K. N. Walker, C. J. Taylor (2000), Coupled-View Active Appearance Models, Proc. British Machine Vision Conference, Vol. 1, 52-61.

Fedorenko, Yu. V., E. S. Husebye, B. Heincke and B. O. Ruud (1998), Recognizing Explosion Sites without Seismogramm Readings: Neural Network Analysis of Envelope-Transformed Multistation SP Recordings 3-6 Hz, Geophys. J. Int., 133, F1-F6.

Fedorenko, Yu. V., E. S. Husebye and B. O. Ruud (1999), Explosion Site Recognition: Neural Net Discriminator Using Three-Component Stations, Phys. Earth Planet. Int., 113, 131-142.

Fedorenko, Yu. V. and E. S. Husebye (1999a), First Breaks - Automatic Phase Picking of P- and S- onsets in Seismic Records. Geophys. Res. Lett., 26, 3249-3253.

Fedorenko, Yu. V. and E. S. Husebye (1999b), Simulating Seismic Signal Detectors. Proceedings of the 21st Seismic Research Symposium, Las Vegas, Nevada, Vol. 1, p. 419-426.

Fedorenko, Yu. V., E. S. Husebye and E. Boulaenko (2000), School Yard Seismology, Orfeus Newsletter, Vol. 2, No. 3.

Fedorenko, Yu. V. (2001), Modeling of internal noise of a flat acceleration response seismic sensor. M/S in preparation.

Hestholm, S. (1999), 3-D Finite Difference Viscoelastic Wave Modeling Including Surface Topography, Geophys. J. Int., 139, 852-878.

Hestholm, S. O., E. S. Husebye and B. O. Ruud (1994), Seismic wave propagation in complex crust-upper mantle media using 2-D finite difference synthetics. Geoph. J. Int., 118, 643-670.

Husebye E.S., B. O. Ruud and A. M. Dainty (1998), Fast, robust and reliable epicenter determinations; envelope processing of local network data, Bull. Seism. Soc. Am., 88, 284-290.

Husebye, E. S. and E. Thoresen (1984), Personal seismometry now! EOS, 65, 441-442.

Husebye, E. S. and Yu. V. Fedorenko (2000), 2-D Signal Detectors for 3-Component Seismic Recordings. Proceedings of the 22nd Annual DoD/DOE Seismic Research Symposium, New Orleans, LA, 121-128.

Jain, Anil K. and Douglas E. Zongker (1997), Representation and Recognition of Handwritten Digits Using Deformable Templates. IEEE Transactions on Pattern Analysis and Machine Intelligence 19 (12), 1386-1391.

Peterson, J. (1993), Observations and modeling of background seismic noise, Open File report 93-322, U. S. Geological Survey, Albuquerque, New Mexico.

Scherbaum, F. and Johnson, J. (1992), PITSA, Programmable Interactive Toolbox for Seismological Analysis, IASPEI Software Library, Vol. 5.

Zhu, Song-Chun (1999), Embedding Gestalt Laws in Markov Random Fields-a Theory for Shape Modeling and Perceptual Organization, IEEE Trans. on PAMI, Vol. 21, No. 11.

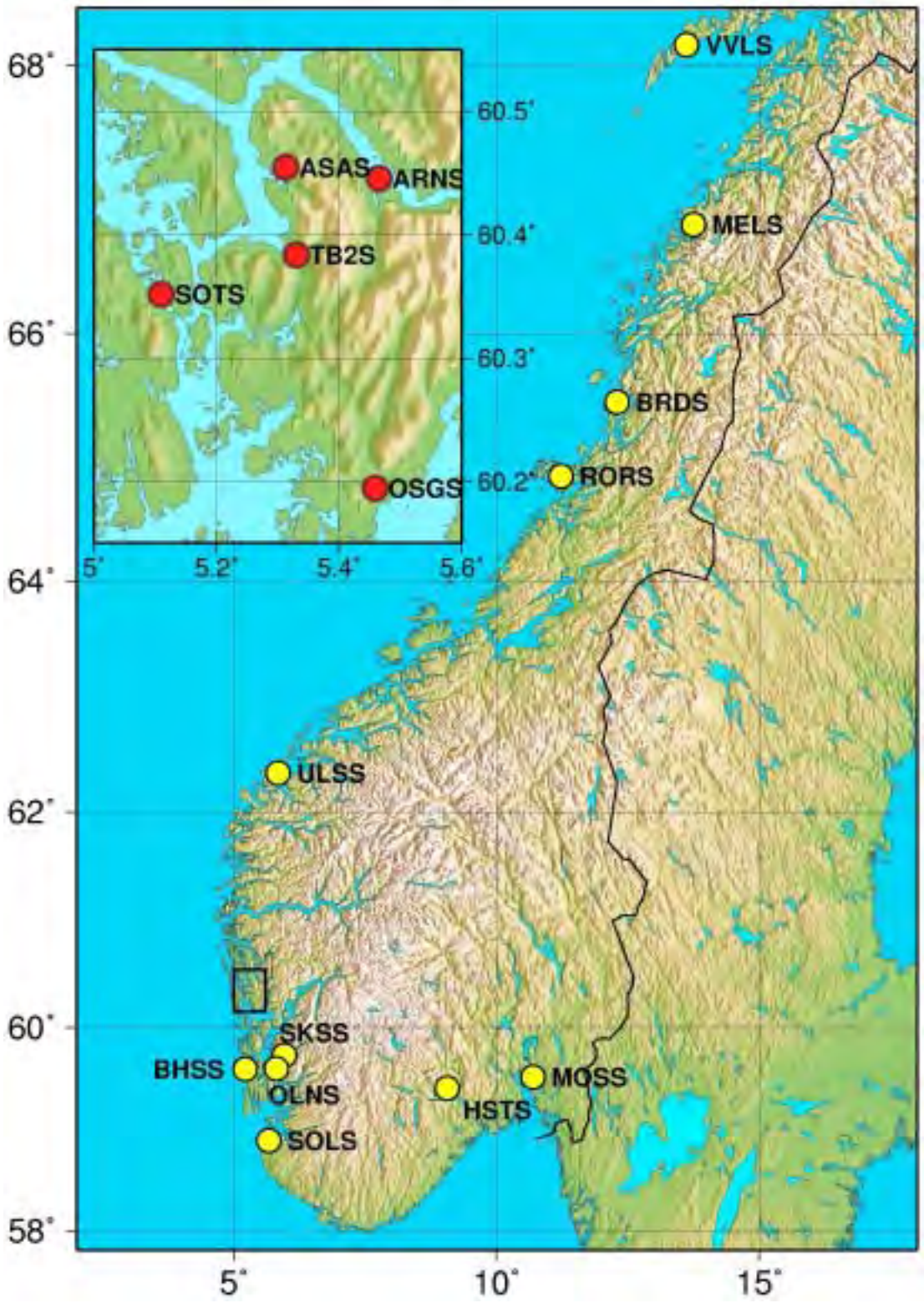

Figure 1. The school network in Norway; insert shows operative stations around Bergen (red dots) while yellow dots are participating school waiting for installation. The ASAS station has been in continuous operation since 1 Nov 2000.

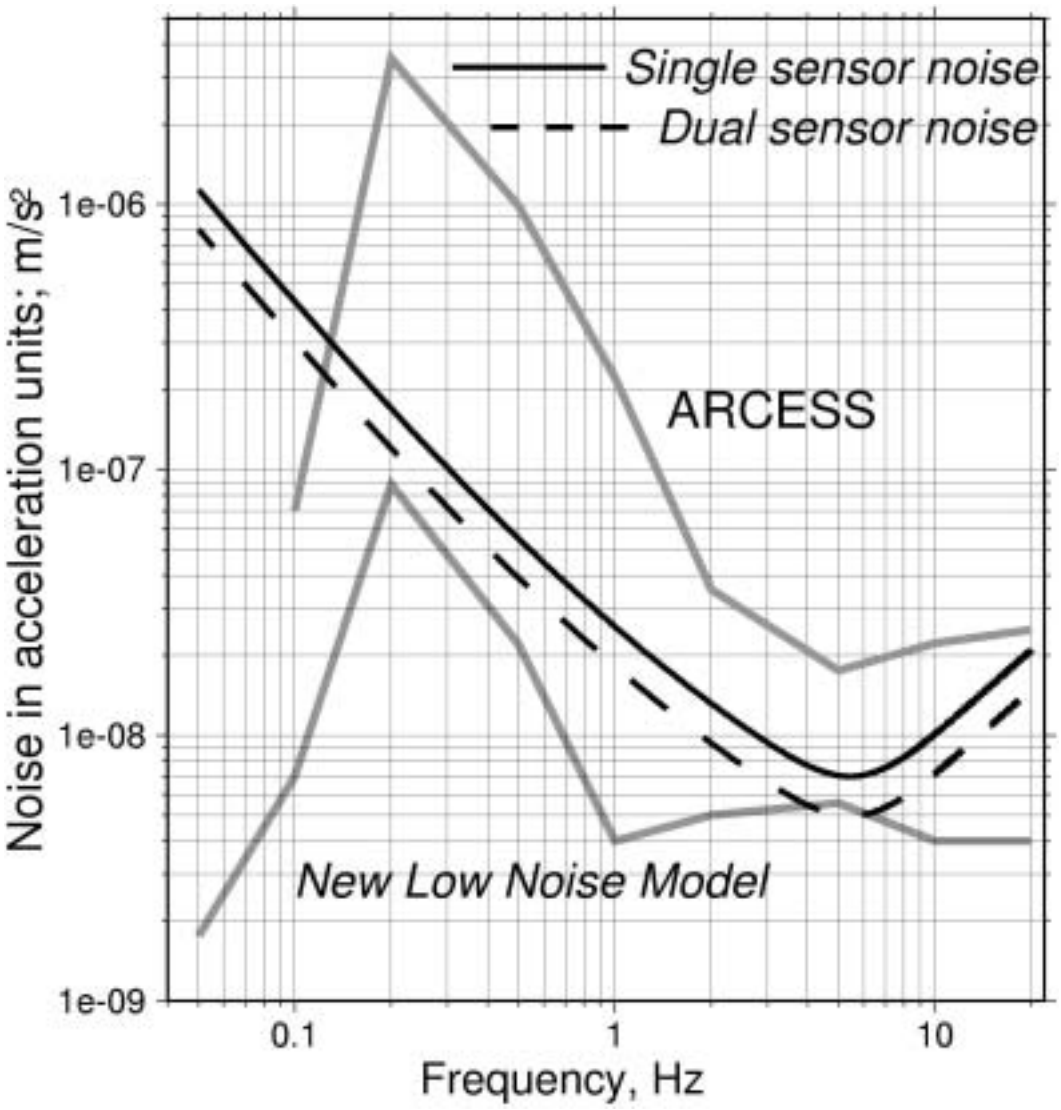

Figure 2. Geophone seismic sensor noise versus the US Geological Survey New Low Noise Model as shown in Peterson (1993) and ARCESS noise recalculated into acceleration r.m.s. units. Solid curve shows equivalent noise acceleration for current single-geophone design; dashed curve represents dual-geophone sensor.

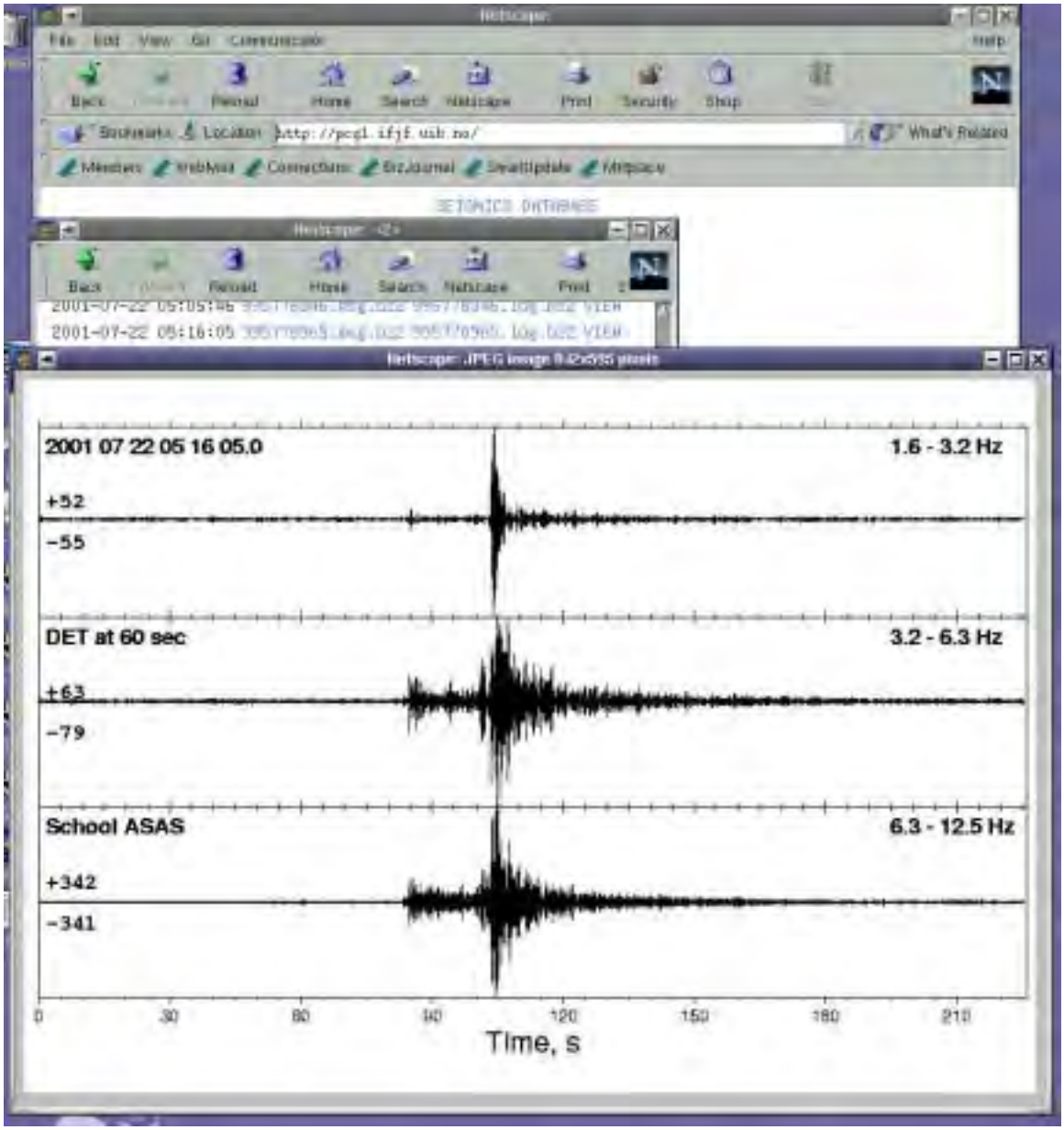

Figure 3. Viewing 'school station' recordings on Internet http://pcg1.ifjf.uib.no/ . The SEISMICS DATABASE appears and a click gives station choice - see insert in Fig. 1. A click then give options of date for viewing; Year/Month/Day. Then the daily detections with view options appear; a click here produce more than 200 seconds of Z-comp. traces in the respective 3 filter bands of the detector. In near future detection logs would also be available for individual stations and multistation detections which will facilitate event selections significantly for school participants. Our efficient 2D detector detects much of garbage signals of very local origin which will be automatically removed from log listings. Waveform data access requires password.

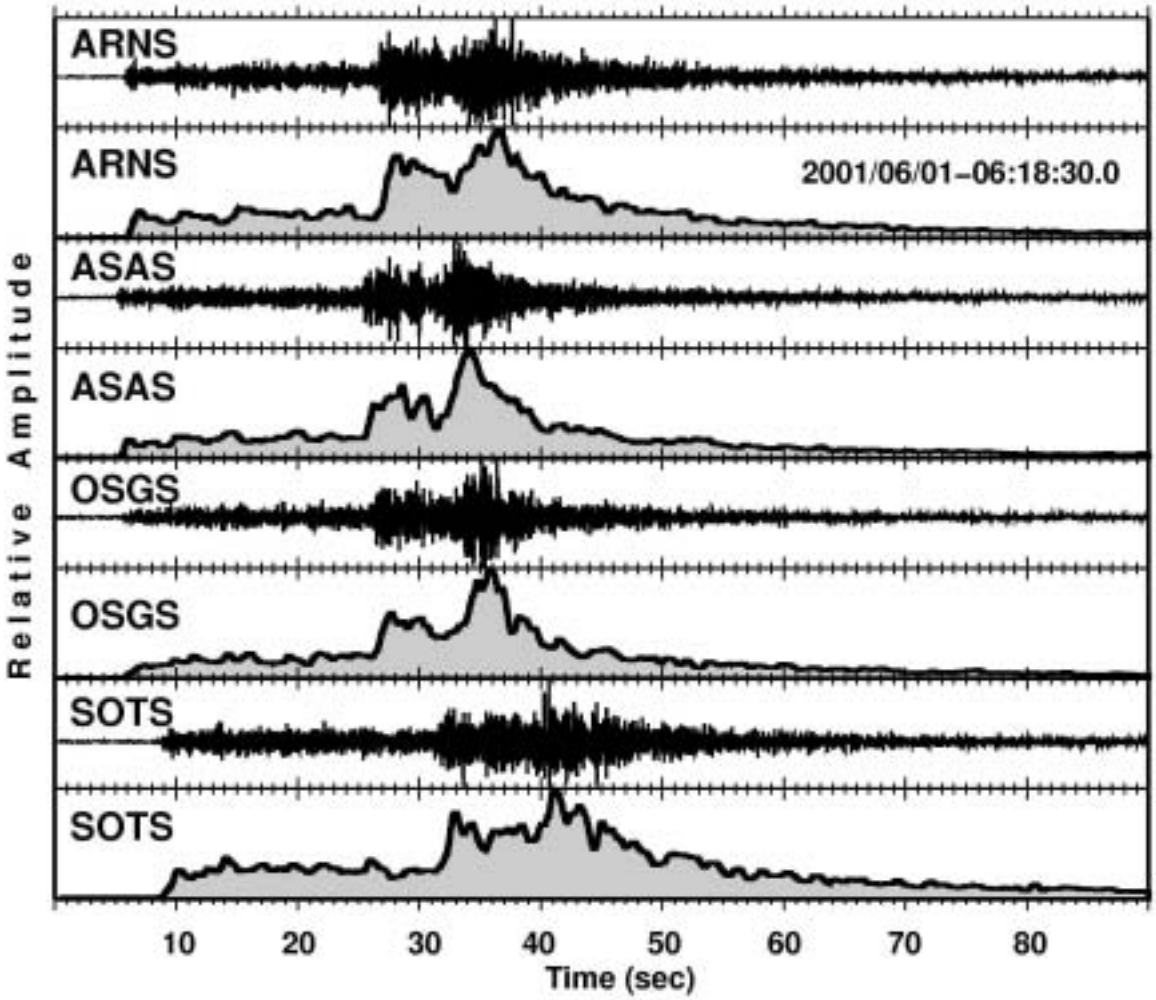

Figure 4. Records from the 4 school stations shown in Fig. 1 from an earthquake in Northern North Sea. Below individual station records are the corresponding envelopes. The outstanding feature here is the fast variation of the original waveforms between the network stations while envelops vary much slower. An essential element of the deformable templates technique is the ability to project the envelope trace of station X so it matches that of station Y. The case of stationary mining explosions is much simpler since spatial waveform projections are not an issue.

THE POTENTIALITIES OF REGIONAL SEISMIC MONITORING

Vladimir V. Kovalenko and Marat S. Mamsurov

Research Institute of Pulse Technique

Sponsored by the Preparatory Commission for the
Comprehensive Nuclear-Test-Ban Treaty Organization

Contract No. 00/20/5020

ABSTRACT

Reliable recording of seismic events at regional distances is a necessary requirement for accurate location of these events, given that the typical spacing of the International Monitoring System (IMS) stations with respect to one another is 1,000 to 2,000 km, i.e., regional distance. Given an IMS system with a detection threshold in the range of 3.0 - 3.5 m_b, equivalent to approximately 0.5 kT of TNT, improving the 90% confidence level in location will be a powerful instrument for constraining potential violators of the Comprehensive Nuclear-Test-Ban Treaty (CTBT). A simple method for assessing travel-time measurement and model errors in seismic location procedures is proposed for the phases Pn, Pg, Sn, and Lg. The estimates may be useful as the first approximation for work on the kinematic calibration of seismic stations.

KEY WORDS: seismic, regional, potentialities

OBJECTIVE

The objective of the work is to examine the potential of the seismic portion of the International Monitoring System (IMS) for accurate seismic event detection and location at the levels required by the CTBT. The estimates may be useful as the first approximation for work on the kinematic calibration of seismic stations.

RESEARCH ACCOMPLISHED

The CTBT is a nonthreshold treaty, but in accordance with paragraph 1, part III of the CTBT Protocol, each State Party shall, on a voluntary basis, provide the Technical Secretariat with notification of any chemical explosion with a yield of 300 T or greater of TNT equivalent detonated as a single explosion anywhere on its territory, or at any place under its jurisdiction or control.

Chemical explosions with yields less than 300 T of TNT equivalent, which are conducted in the interests of the mining industry or others, are so numerous and monitoring for them is so problematic, they are not considered good candidates for IMS calibration or CTBT monitoring. This threshold (>300 T of TNT equivalent) corresponds to the yield of an underground nuclear explosion of 0.5-0.6 kT (m_b=3.7-3.8). Expert opinion in the field of nuclear weapon development holds that the threshold of 1- to 2-kT yield is near the minimum test size useful for military purposes.

The configuration of the seismic stations of the IMS is such that the majority of them register seismic events at regional distances, where signal-to-noise ratio (SNR) is rather large. The connection between magnitude and yield of explosions at regional distances as shown in Archambeau et al (1991) can be approximated by the following formula:

$$m_b = A + B \log Y$$

where m_b = magnitude for body waves, Y = yield of explosion in kT, A and B = coefficients.

The value of $m_b \geq 3.0$ is chosen as a threshold of detection of seismic events by the International Data Centre (IDC) and the value of $m_b \geq 3.5$ is chosen as a threshold for the screening procedure. In this case the assessments for granite (A=3.92, B=0.81) and dry tuff/alluvium (A=3.32, B=0.81) give the following TNT equivalents (Table 1).

Table 1. TNT equivalents for threshold of 3-3.5 m_b

Magnitude	Granite, kT	Dry tuff/alluvium, kT
3.0	0.07	0.40
3.5	0.30	1.70

Thus, the system has high sensitivity for explosions in hard rock (e.g., granite) and sufficiently high for explosions in softer rock (e.g., tuff).

For a TNT equivalent of 0.5 kT, we get the following values for m_b (Table 2) for hard rock, which exceed the threshold of screening, and the following values for softer rock, which also exceeds the detection threshold.

Table 2. m_b values for explosions of 0.5-kT TNT equivalent

TNT equivalent, kT	Granite, m_b	Dry tuff/alluvium, m_b
0.5	3.68	3.08

The seismic portion of the IMS is planned to have a detection threshold of about m_b = 3 - 3.5 and a detection probability of at least 90% for the detection of underground nuclear explosions and other events with a TNT equivalent of at least 0.5 kT as a deterrent to potential violators of the CTBT.

Another important goal for the seismic portion of the IMS is a high degree of accuracy for seismic event location for the purpose of fielding an on-site inspection to confirm the nature of a suspicious event. In accordance with paragraph 3, part II (A) of the Protocol to the CTBT the area of an on-site inspection shall be continuous and its size shall not exceed 1,000 sq. km. There shall be no linear distance greater than 50 km in any direction. The seismic portion of the IMS must satisfy these requirements, but evaluations show that the IMS does not perform at this level for weak sources monitored at regional distances. The basic reason is insufficient accuracy of applied travel-time curves and IASPEI-91 tables, which are calculated chiefly for teleseismic distances. The problem may be resolved by construction of regional travel-time curves and 2-D and 3-D regional velocity models, which provide improvements in event location accuracy and allow us to satisfy the CTBT requirements. But there are certain restrictions, as discussed below.

The probability of locating the event epicenter with a confidence ellipsoid provided by a Gaussian distribution of possible errors could be described by following formula:

$$P_{hit} = 2 [\Phi_o(k) - (1/\sqrt{2\pi}) k \exp(-k^2/2)], \text{ where}$$

$$\Phi_o(k) = 1/\sqrt{2\pi} \int_o^k \exp(-t^2/2)\, dt;$$

$k = a/\sigma_x = b/\sigma_y = c/\sigma_z$ - parameter of distribution;

a, b, c are semi-axes of ellipsoid; and

σ_x, σ_y, σ_z are standard deviations along the axes of the basic coordinate system.

Except for nuclear explosions where $z \cong o$, we move to 2-D distribution, and when the errors are independent along x, y axes, the task can be reduced to two 1-D distributions. In this case:

$$P_{hit} = 1 - \exp(-k^2/2) \text{ where } k = a/\sigma_x = b/\sigma_y$$

In accordance with the requirements of the Protocol to the CTBT, the area of error ellipse must be

$$S = \pi\, a\, b \le 1000 \text{ sq. km}$$

and the large axis of the ellipse must not exceed 50 km ($a \le 25$ km). The probability of locating the event's epicenter within the error ellipse must be at least 90 % ($Phit \ge 0.9$). In this paper, we use an ellipse with the utmost permissible characteristics: a=25 km, $b=1000/\pi a=12.74$ km. For Phit=0.9, k=2.146, $\sigma_x=a/k=11.65$ km, $\sigma_y=b/k=5.94$ km.

Another extreme case is the circular error with $R=\sqrt{1000/\pi} \cong 18$ km, $\sigma_r=18/2.146=8.39$ km. Given an event and using an appropriate basic velocity model of regional phases Pn, Pg, Sn and Lg, we have a root-mean-square (rms) value for the total errors (σ_t), corresponding to a location accuracy for elliptical and circular errors as given in (Table 3).

Table 3. The permissible significance of the total errors (σ_t, sec)

Regional phases	**Phase velocity, km/sec**	a = 25 km	R = 18 km
		σ_t for Phit=0.9/0.7	
Pn	8.00	1.46/2.01	1.05/1.45
Pg	6.00	1.94/2.68	1.40/1.93
Sn	4.62	2.52/3.48	1.82/2.51
Lg	3.50	3.33/4.60	2.40/3.31

The circular case is not very tolerant of errors. When we pass from elliptical to circular error distributions, coordinates along the large and small axes of the ellipse vary in sufficiently narrow limits: $18 \le x \le 25$ km and $12.74 \le y \le 18$ km. The latter indicates that the CTBT goal for accuracy of seismic event location is difficult to meet.

One may use other accuracy estimations for velocity models for regional phases. Figure 1 presents two 1-D velocity models of Pn for the east European platform: A (Mooney, 1999) and B (Dainty et al, 2000). For the calculations, we use the following values for average-weighted velocity (Vaw):

$$Vaw = \sum_i^n \Delta h_i v_i \; / \sum_i^n \Delta h_i \quad \text{where}$$

Δh_i = thickness of i-layer ;

v_i = average velocity in i-layer; and

n = number of layers.

For A, the thickness of the Moho is about 41 km, the path of Pn propagation in the upper mantle is 159 km, and the average velocity is 8.28 km/s; for B - the same characteristics are respectively 40, 160 km and 8.30 km/s. In spite of that, model A is more detailed. As a result average-weighed velocities are practically equal for 7.9 km/s and a corresponding value of $\sigma_t = 1.475$ sec.

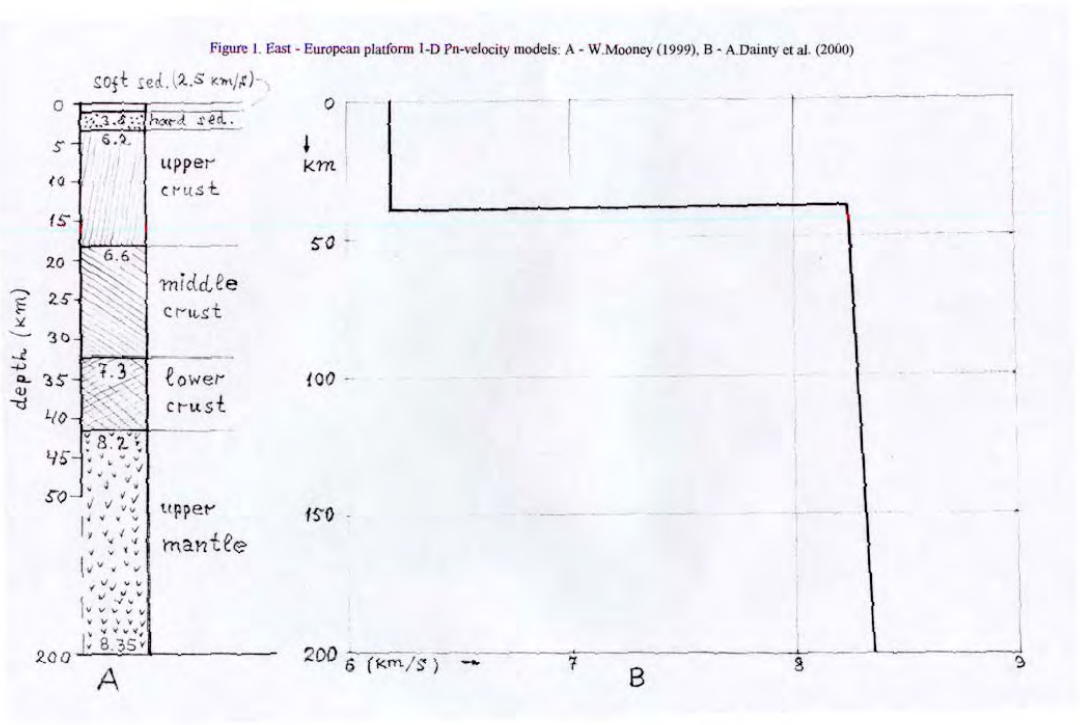

Figure 1. Two 1-D Velocity Models for the east European Platform

The permissible total error σ_t is usually presented in the form of two components: model σ_{mod} and measurement σ_{meas} errors. The first depends on the model chosen for seismic wave propagation and the character of statistical scattering of observed data by means of which the model travel-time curve is built The second is determined by the seismic wave arrival time measurement errors. For the squares of standard deviations, we can write:

$$\sigma_t^2 = \sigma_{mod}^2 + \sigma_{meas}^2 \ .$$

Decreasing of the modeling error is related to improvement of our knowledge of the structure of the earth's crust and upper mantle, and using more reliable velocity models. Decreasing the measurement error substantially depends upon signal-to-noise ratio (SNR). If SNR increases, σ_{meas} could decrease to the required level.

Bondar (2000) represents the dependencies of standard deviations of the measurement error for arrival time of the regional phases Pn, Pg, Sn, Lg versus SNR. At certain SNR values, the standard deviation is not to exceed 1 sec for Lg and 0.5 sec for Pn, Pg and Sn.

For regional phases Pn, Pg, Sn and Lg, Fig. 2 shows the modeling error dependency via distance for global model IASPEI - 91 (1) and two regional models: the Baltic shield (2) and the central part of the east European platform (3). For regional distances of up to 12 degrees, the errors for the Baltic shield model and Pn, Sn, Lg (North et al, 2000; Bondar et al, 1997) approximately correspond to the data in Table 3.

For Pg, the errors exceed the permissible level. This can possibly be explained by the insufficient accuracy of the earth crust model to real conditions (in this case, a 1-D model was used). As Figure 2 shows, when distance increases, the difficulties for providing the required modeling accuracy increase as well.

Figure 2. Pn, Pg, Sn, Lg modeling errors: IASPEI-91 (1), Baltic shield (2) and East - European platform (3)

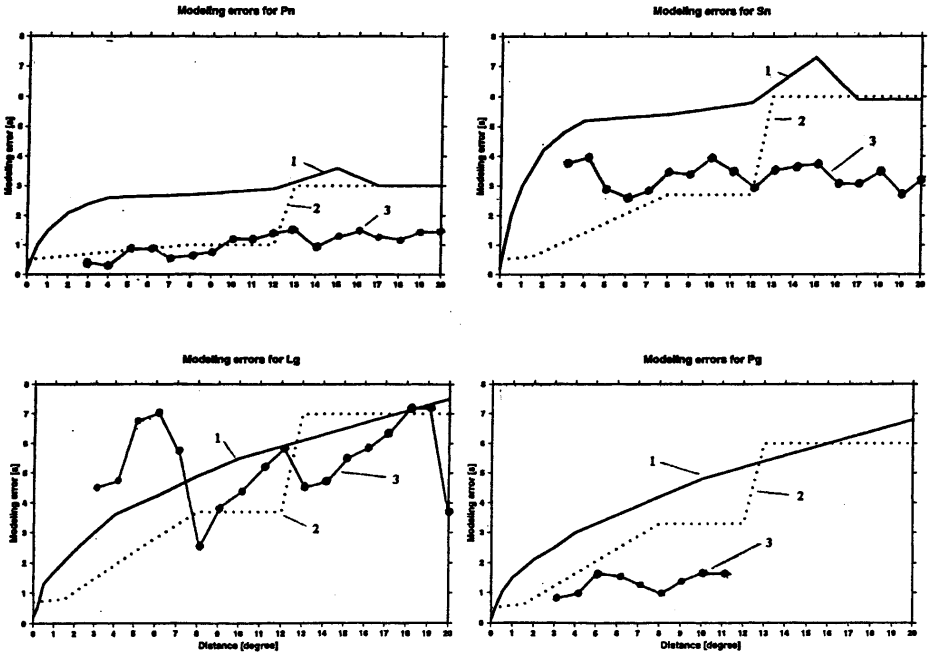

Figure 2. Pn, Pg, Sn, Lg Modeling Errors

Modeling errors from the regional model of the central part of the east European platform (Kirichenko et al, 2000) are essentially differentiated from analogous dependencies for the Baltic shield model, but Pn and Pg correspond considerably better to the Table 3 data. The Baltic shield is a structural uplift of the northwestern part of the east European platform, where its pre-Cambrian folded foundation comes out on the surface. The geological similarity between the provinces also confirms the data, which were generated with the help of 1-D velocity models for northern Eurasia (Dainty et al, 2000). Serious differences in changes in modeling errors for the above models apparently depend on the statistical insufficiency of the observed data and indicate the necessity for further development of the models.

CONCLUSIONS AND RECOMMENDATIONS

For the CTBT to be effective, the IMS requires a detection threshold for ~ 0.5 kT yield or an mb of 3.0 to 3.5 for nuclear and large chemical explosions with at least a 90% confidence level. To satisfy these requirements on accuracy of seismic event location, the mislocation of event epicenters must change from 18 km to 25 km for elliptical errors and from 8 km to 12 km for circular errors.

Selecting the regional seismic wave velocities, which are of interest for us, and comparing them with permissible deviations of the coordinates, we receive permissible standard errors for the required location accuracy. The effectiveness of assessments is enhanced if we use velocity models for the earth's crust and upper mantle and averaged values of seismic wave propagation velocity.

Results obtained should be considered only as a first approximation in the solution of a given problem. For more exact and full assessment of the task of determination of potential possibilities of the IMS, it is necessary to inventory all spectra of magnitude and space-time corrections for stations and arrays for the IMS.

In spite of the opinion of skeptics, the seismic portion of the IMS with well-calibrated stations and lower thresholds of recording of underground nuclear explosions can become a powerful instrument for deterring potential CTBT violations.

REFERENCES

Archambeau , C.B. et al (1991), Scientific and Technical Principles for Treaty Monitoring , *Verification*, Moscow, "MIR".

Mooney, W. D. (1999), Crustal and Upper Mantle Seismic Velocity Structure of the Former USSR, Proceedings of the 21st Seismic Research Symposium, Las Vegas, Nevada.

Bondar, Istvan (1998), Evaluation of PIDC Error Ellipses, Technical Report CMR-98/23, Arlington, VA, USA.

North, Robert, Xiaoping Yang, and Keith Mc Laughlin (2000), Source Specific Station Corrections for Regional Phases at Fennoscandia Stations - A Model for IMS Calibration Efforts, Location Calibration Workshop, Oslo, Norway.

Bondar, Istvan and Vladislav Ryaboy (1997), Regional Travel-Time Tables for the Baltic Shield Region, Technical Report CMR-97/24, Arlington, USA.

Kirichenko, V. V. and Yu. A. Kraev (2000), Development of Regional Travel -Time Tables for Different Geotectonic Provinces of Northern Eurasia, Proceedings of the 22nd Annual DOD/DOE Seismic Research Symposium, New Orleans, USA.

Dainty, A.M. et al (2000), 3-D Modeling Approach to Refine Location of Regional Seismic Events in Western Areas of Northern Eurasia and North America, RF/US Working Group, Third Status Report, CMR, Arlington, USA.

SHORT PERIOD GROUP VELOCITY MEASUREMENTS AND MAPS IN CENTRAL ASIA

A.L. Levshin,[1] M.H. Ritzwoller,[1] M.P. Barmin,[1] and J.L. Stevens[2]

University of Colorado at Boulder,[1] Science Applications International Corporation[2]

Sponsored by Defense Threat Reduction Agency

Contract No. DTRA01-00-C-0026

ABSTRACT

The purpose of this study is to improve group velocity maps designed to advance the detection and discrimination capabilities for the area encompassed by western China, northern India, and Pakistan. These maps may be used to construct sharply tuned phase-matched filters for extracting weak surface wave signals from background noise and to make better estimates of surface wave spectral magnitudes for small events. We are working now to obtain a greatly expanded data set of short-period measurements (7 - 15 s). We have analyzed seismograms following approximately 1,000 events that occurred in and around the studied region from 1996 - 1999. We obtained about 6,000 short-period dispersion curves for Rayleigh and 4,000 curves for Love waves. We added these measurements to existing dispersion curves and estimated a refined set of dispersion maps on a one-degree grid worldwide. Here we present preliminary refined group velocity maps from 10-s to 18-s periods. Improvements produced by the new data set are mostly at the shorter end of this period band in Central Asia.

KEY WORDS: Central Asia, surface waves, group velocities, $M_S{:}m_b$ discriminant

OBJECTIVE

The goal of this research is to improve the ability to detect and discriminate small events over wide areas of Central Asia using regional seismic data. We extend the existing set of Rayleigh and Love wave tomographic group velocity maps to periods shorter than 15 s. Accurate maps at shorter periods would improve signal detection capabilities by advancing signal-to-noise enhancement produced by phase-matched filters. This permits the extension of surface wave magnitude (M_S) estimates to periods shorter than 15 s and to smaller events than current capabilities allow. This is the basis for future tests of $M_S{:}m_b$ discriminant for these events.

RESEARCH ACCOMPLISHED

Introduction

Detection, location, and identification of small seismic events all depend on calibration of source and path effects to ensure maximum efficiency of the monitoring at small magnitudes. The described research, which began in April 2000, is dedicated to advancing detection and discrimination capabilities for small magnitude events by improving calibration information for surface waves in western China, Pakistan, northern India, and surrounding areas. The calibration information will be in the form of short period (7 s - 15 s) Rayleigh and Love wave tomographic group velocity maps and station-specific correction surfaces constructed from these maps. Although we have previously provided similar information in the region of study at intermediate periods (15 s - 50 s; e.g., Stevens and McLaughlin, 1997; Ritzwoller *et al.*, 1998; Levshin *et al.*, 1998), the group velocity maps and correction surfaces at short periods are entirely new (Levshin *et al.*, 2000). This new information will be rigorously tested at the Center for Monitoring Research (CMR) Test bed to quantify the improvement in the ability to estimate surface wave amplitudes and, hence, M_S for smaller events than are currently possible.

The $M_S{:}m_b$ discriminant and its regional variants are the most reliable transportable means of discriminating earthquakes from explosions (e.g., Stevens and Day, 1985, Stevens and McLaughlin, 2001). To measure surface wave amplitudes accurately in order to estimate M_S is challenging for small magnitude events in which surface waves may not be readily identifiable in raw seismograms. Because amplitude spectra of regionally recorded small magnitude events typically peak below 20-s period (where M_S is usually measured) the regional application of the $M_S{:}m_b$ discriminant may be improved if M_S were measured at significantly shorter periods; i.e., 8- to 12-s period. To provide these amplitude measurements, it is crucial to be able to reliably detect small amplitude surface waves and accurately measure the corresponding spectral amplitudes. This goal may be achieved using phase-matched filters (Russell *et al.*, 1988; Herrin & Gofort, 1977; Levshin & Ritzwoller, 2001) that are tuned for all source/station paths of interest. Designing of such filters requires perfect knowledge of surface wave propagation across the regions being monitored. This is the motivation for the current efforts of University of Colorado at Boulder (CU) and SAIC seismologists to obtain new data on short-period surface wave velocities in Central Asia and surroundings. Such measurements will be used for constructing short-period group velocity maps, the refined regionalized 3D crustal model (Stevens and McLaughlin, 1997; 2001), and 2-D group velocity correction surfaces (Levshin *et al.*, 1998) needed for designing the locally tuned phase-matched filters.

CU and SAIC are working collaboratively to:

- obtain a new and vastly expanded set of group velocity measurements in the region of study emphasizing measurements between 7-s and 15-s period;
- convert these measurements into group velocity maps and station-specific correction surfaces using both tomographic and model-based methods;
- cross-validate the tomographic and model-based methods to obtain a set of maps and surfaces that are judged most reliable for the area of study;
- embed these maps and surfaces into global maps and surfaces constructed by the SAIC group;
- test and validate the new maps and corrections surfaces with a rigorous set of tests performed on regional data at the CMR Test bed; and
- deliver documentation and reports of all results with the completed maps and surfaces to customers at DOE, CMR, the U.S. National Data Center (NDC), and the International Data Centre (IDC).

The final results will be provided in a form that can be easily used within operational monitoring systems for surface wave identification and phase-matched filtering.

Improvement of Detection Capabilities Using Phase-Matched Filtering

Recent work done by the SAIC group (formerly Maxwell Technologies) has focused on techniques for improving surface wave measurements and reducing the surface wave detection threshold, and, particularly, on further development of MAXSURF, the code used at the IDC and prototype IDC (PIDC) for automatic identification and measurement of surface waves. MAXSURF is responsible for all surface wave processing at the IDC and the PIDC and runs in the processing stream after events have been identified and located. Surface wave group velocity measurements provided by CU were combined with other available sets of phase and group velocity measurements and used to construct a refined set of global dispersion maps on a one-degree grid. Surface wave detection at the IDC currently compares predicted dispersion curves with measurements from seismograms such as those shown in Figure 1a. The procedure can be improved by using phase-matched filtering, which compresses the signal into a narrow time window improving the signal-to-noise ratio (Figure 1b). Phase-matched filtering requires accurate dispersion measurements at short periods, particularly for low-amplitude arrivals on short paths.

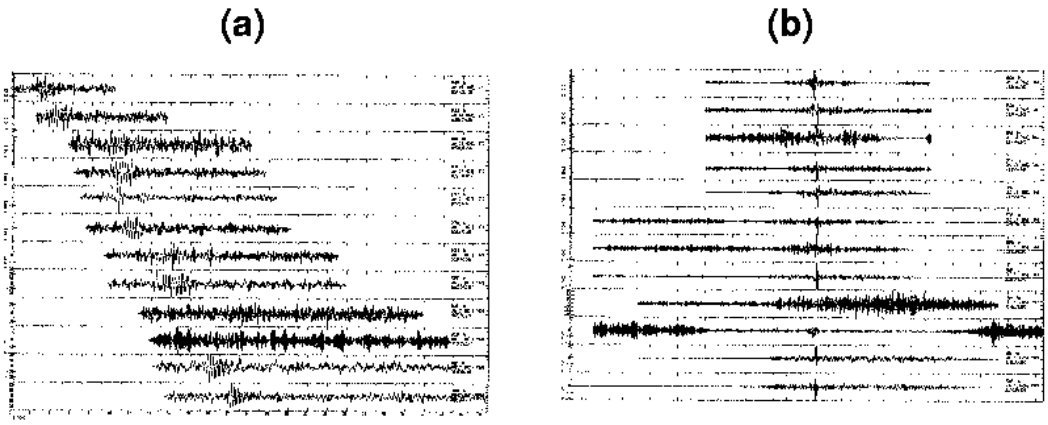

Figure 1. a. Surface wave data from an m_b 3.9 South Pacific earthquake after transformation to a KS36000 instrument. b. Same data after phase-matched filtering.

MAXSURF then examines the arrival window where a surface wave would be expected and applies a dispersion test to see if a surface wave can be identified. If so, then the amplitude is measured and stored in the IDC database. Surface waves are identified in the following way. A set of narrow-band filters is applied to the data over a set of eight periods from 16 s to 50 s. A long-period or broadband beam is formed at arrays with the expected azimuth and slowness. The arrival times at each frequency are then compared with predicted arrival times generated from the regionalized group velocity model (Figure 2a). The efficiency of detection depends on the accuracy. To improve detection, we apply phase-matched filtering first; then we apply narrow-band filters.

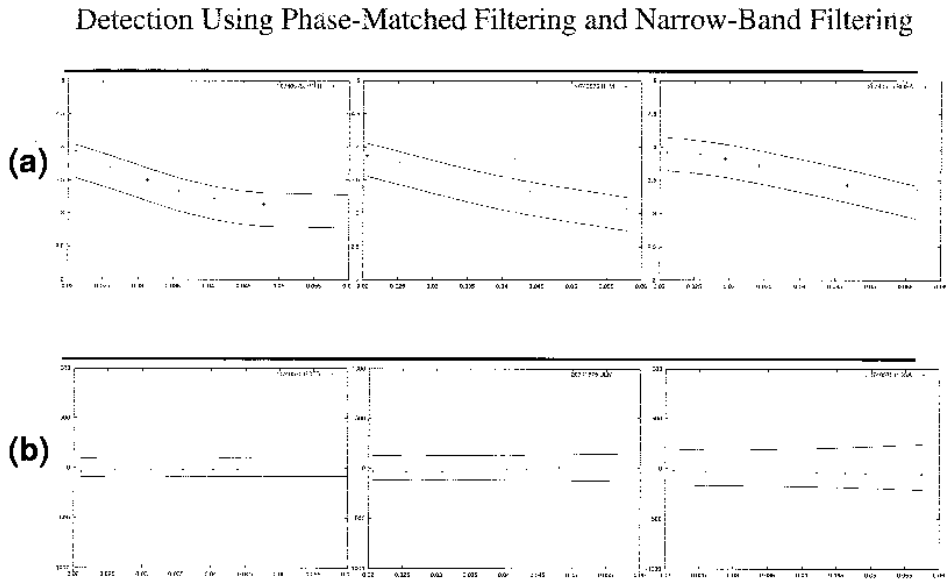

Figure 2. a. Narrow-band filter detection compares measured group velocity with the regionalized model. Measured dispersion data for an m_b 4.2 earthquake observed at 3 stations are shown. b. To improve detection, the data are phase-match filtered, then they are passed through narrow-band filters. The detection test is applied for the same time interval, but the time is now centered around zero.

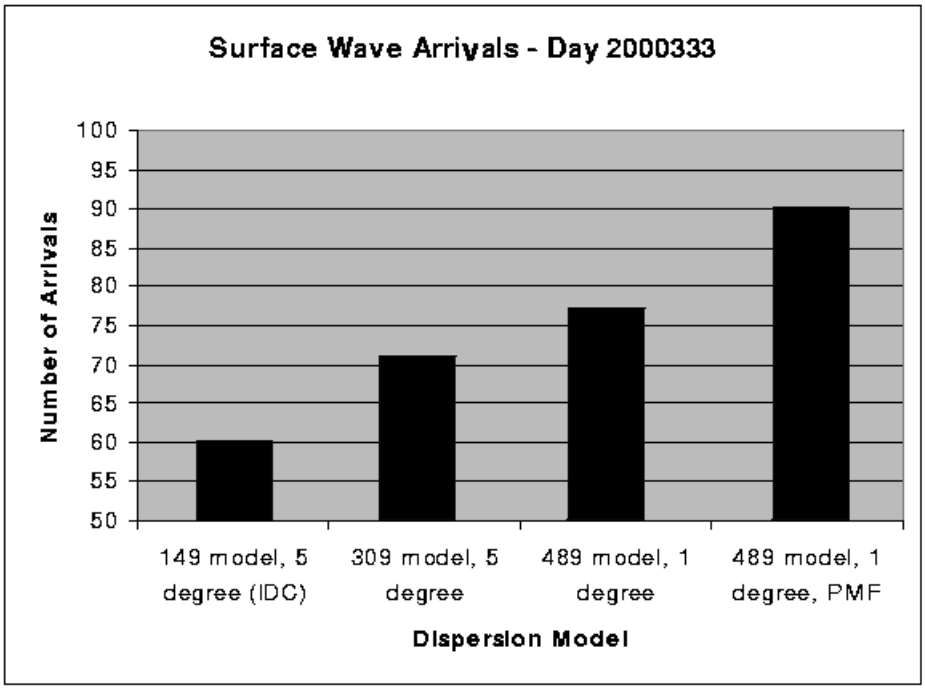

Figure 3. Improvement in the number of detections for a day of data with improvements in the model, and with phase matched filtering.

The number of detections increased by 32% over current IDC detections with phase-matched filtering using the most recent one-degree model. The detection test is applied for the same time interval but the time now is centered around zero (Figure 2b). Improvement in the number of detections for a day using the more detailed ($1^\circ \times 1^\circ$) model and phase-matched filtering (PMF) is demonstrated in Figure 3. The number of detections increased by 32% over current IDC detections with phase-matched filtering using the most recent one-degree model.

This example demonstrates the importance of good group velocity maps. Because surface waves are identified by comparison with predicted arrival times, it is essential that the predicted group velocities are accurate. One way to reduce the threshold further is to increase the frequency band over which surface waves can be measured. The current band of 16-s to 50-s period was found to be a good band for worldwide surface wave data measured at distances of 20-100 degrees, and the global dispersion maps are fairly well defined over this period band. However, at shorter distances, surface waves are dominated by higher frequencies. To improve signal-to-noise ratio and to measure surface waves at close range, the dispersion test and measurement of surface waves should be performed at higher frequencies.

Data and Measurements

Data acquisition. We acquired waveform data from IRIS DMC, GEOSCOPE, and GEOFON data centers for the seismic events that occurred in 1996-1999. Data from 850 events recorded by about 90 stations of the GSN, GEOSCOPE, KNET, KAZNET, CDSN, and GEOFON networks have been obtained. We combined these data with relevant data collected in our previous studies of this region (Levshin & Ritzwoller, 2001). Figure 4 shows positions of stations and events used in this study. Further acquisition of data is in progress.

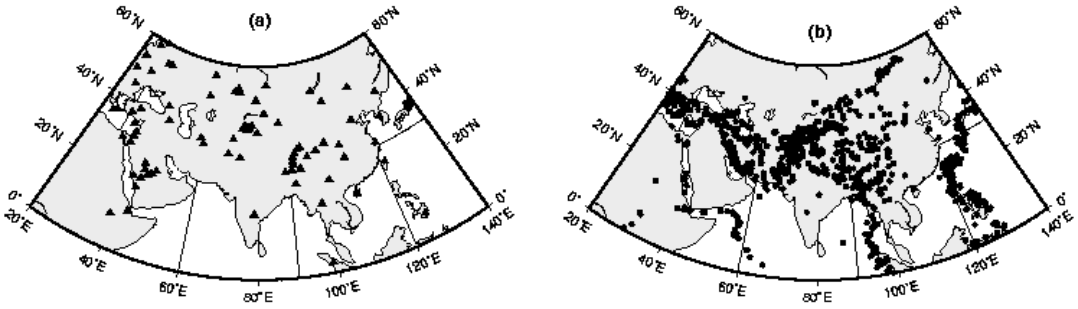

Figure 4. Station and event locations. a. The location of seismic stations used in this study (triangles); b. The locations of the events (circles).

Data processing. All data and corresponding event and station information were converted into CSS3.0 formatted event volumes and processed by seismic analysts in a semi-automatic regime using the frequency-time analysis package developed at CU. We used the Frequency-Time Analysis (FTAN) method (e.g., Dziewonski *et al*, 1968; Levshin *et al.*, 1972; Russell *et al.*, 1988; Levshin *et al.*, 1992; Ritzwoller *et al.*, 1995) to obtain group and phase velocity, and spectral amplitude measurements. As part of FTAN, an analyst interactively designed a group velocity-period filter to reduce contamination from other waves and coda, chose the frequency band for each measurement, and assigned a qualitative grade (A - F) to each measurement. All resulting measurements of group velocities and other surface wave characteristics were preserved in a format that is an extension of the CSS3.0 format. Altogether, more than 6,000 dispersion curves of Rayleigh waves and 4,000 dispersion curves of Love waves were obtained. An example of successful measurements is shown in Figure 5. The event occurred on 8/26/1999 in southeastern Afghanistan with $m_b = 5.2$ and $M_S = 4.4$. Presence of strong higher modes and multiple arrivals interfering with the fundamental modes makes some measurements problematic (Figure 6). Further data processing included data cleaning based on comparison of observed travel times with those predicted by the CU Eurasian model (Villaseñor *et al.*, 2001), and *declustering*, i.e. combining data from very close paths in a single observation (Ritzwoller & Levshin, 1998). These procedures reduce the number of paths used in tomographic inversion by approximately a factor of two.

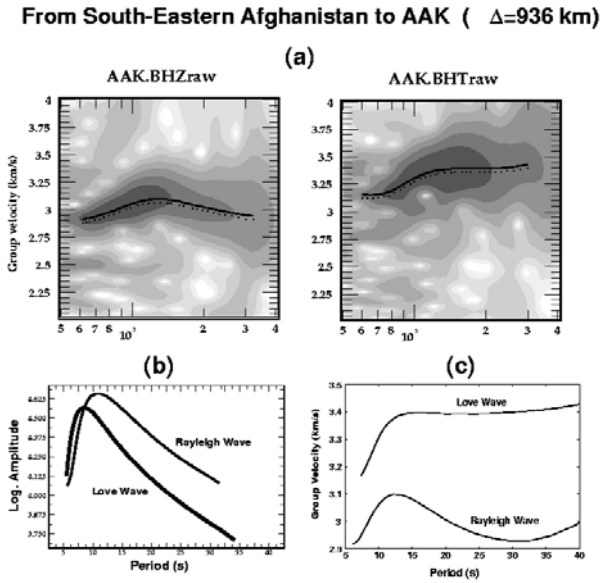

Figure 5. Example of successful short-period measurements: a. Raw FTAN diagrams for Rayleigh and Love waves; b. Spectral amplitude curves of Rayleigh and Love waves; c. Group velocities.

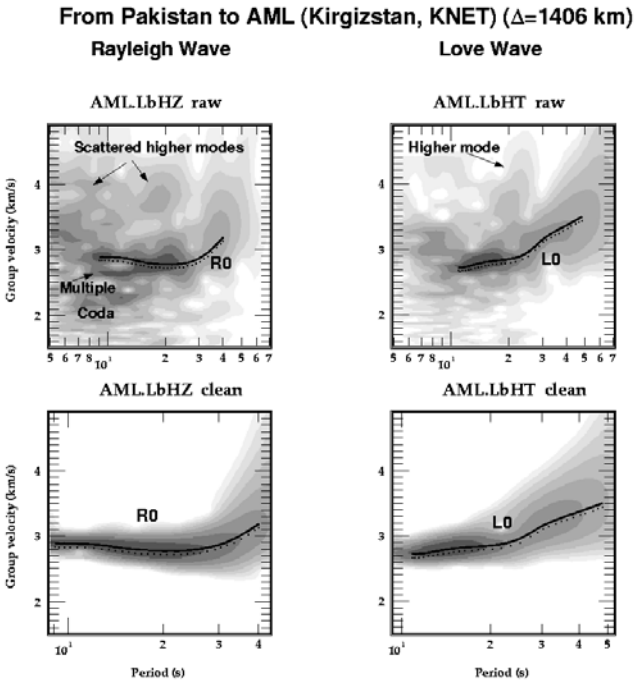

Figure 6. Example of difficulties met in making short-period measurements due to interference with higher modes and multiple arrivals: a. Raw FTAN diagrams for Rayleigh and Love waves; b. Clean FTAN diagrams.

Data coverage. Figure 7 contrasts path density at periods of 10 s, 14 s, and 18 s for our existing data set. Path densities at 14 s and 18 s are much better than at 10 s, partially because at and above 14-s period, measurements can be obtained for paths significantly longer than 2,000 km. Path density for Love waves is significantly less than for Rayleigh waves, mostly due to lower signal-to-noise ratio at the horizontal components and unresolvable interference with Rayleigh waves due to off-path propagation. The densest coverage at short periods is observed around KNET.

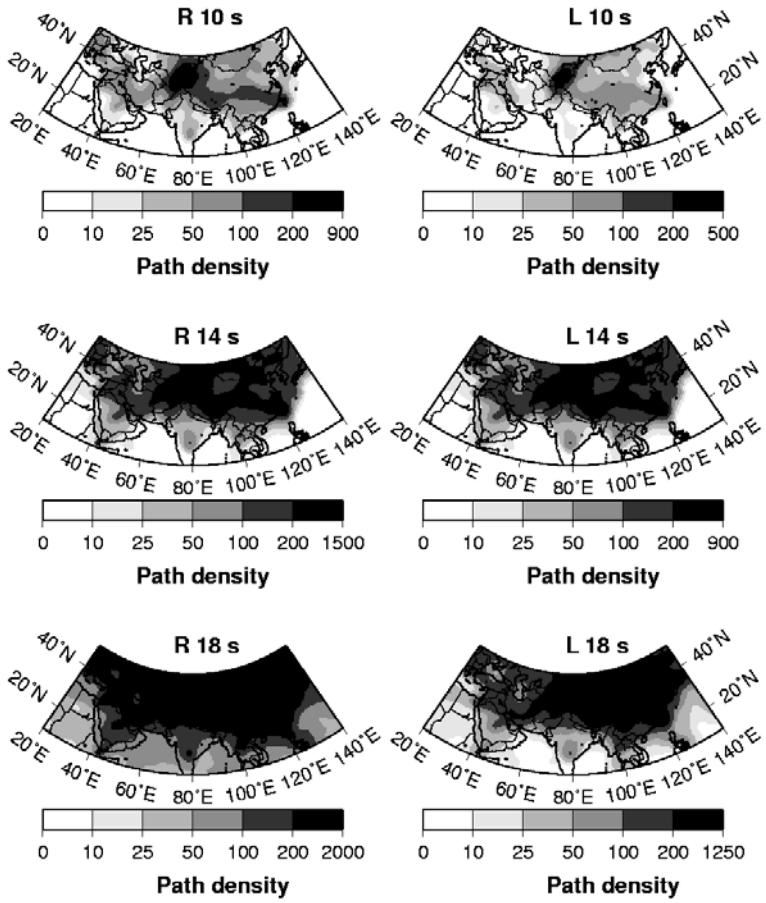

Figure 7. Path density for the current Rayleigh wave (left column) and Love wave (right column) data set at 10 s, 14 s, and 18 s periods. Units are number of paths intersecting each $2^{\circ} \times 2^{\circ}$ cell (50,000 km^2).

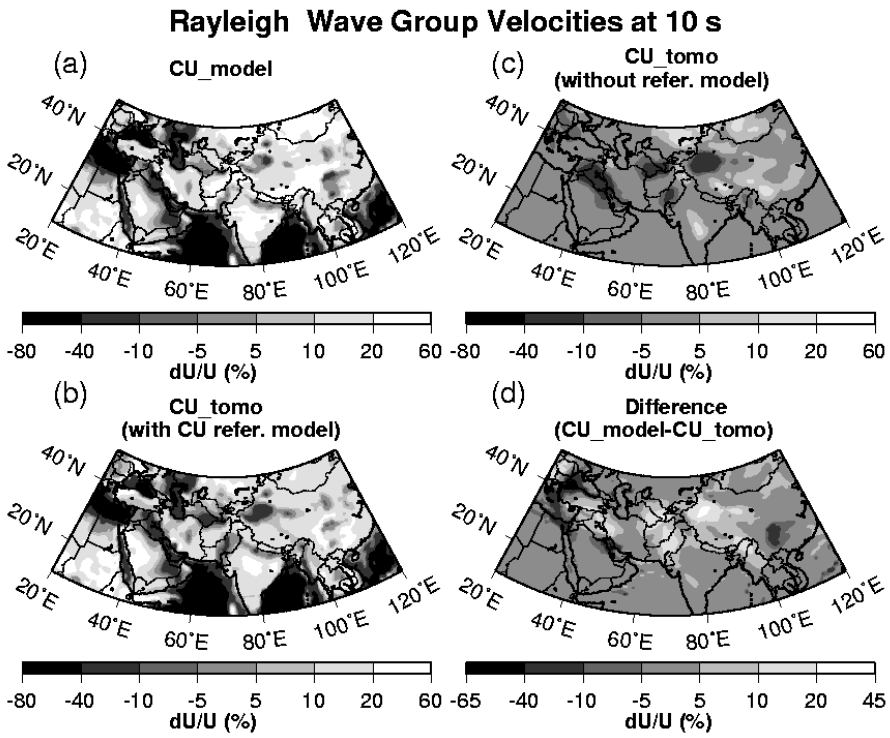

Figure 8. Rayleigh wave group velocities at 10 s. a. Reference map predicted by the CU model; b. Tomographic map obtained using reference map (a); c. Tomographic map obtained without use of reference map; d. Difference between prediction (a) and result (b).

Tomographic Inversion

Method. Our tomographic method is described in (Barmin *et al.*, 2001). At each period, we estimate a group velocity perturbation, $\delta U(\theta, \phi)$, relative to a reference map, $U_\circ(\theta, \phi)$

which itself may be spatially variable so that group velocity at each spatial point (θ, ϕ) is

$$U(\theta, \phi) = U_\circ(\theta, \phi) + \delta U(\theta, \phi)$$

We use our recent CU model (Villaseñor *et al.*, 2001) to compute the reference map. We construct $\delta U(\theta, \phi)$ by minimizing the weighted misfit to the data together with both spatial smoothing and model norm regularization constraints. The spatial smoothing constraint determines the wavenumber content of the estimated map. For data that are inhomogeneously distributed, the model norm constraint is very important, and we use path density to determine the strength of this constraint. Where path density is very low (e.g., in southern India at 10 s in Figure 6), $\delta U(\theta, \phi)$ will be strongly damped and constrained to equal the reference model.

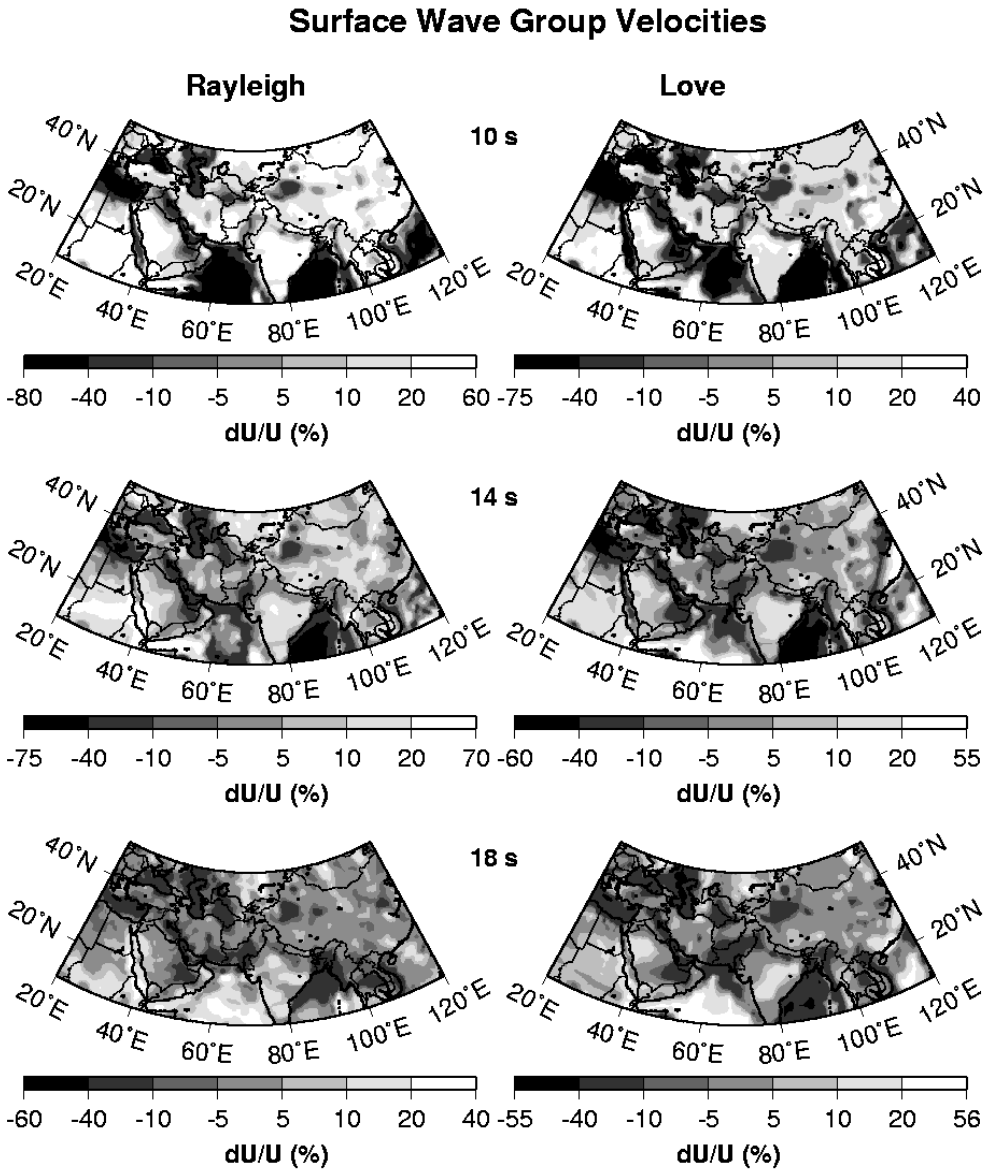

Figure 9. a. Group velocity maps for Rayleigh and Love waves at 8 and 10 s. b. Group velocity maps for Rayleigh and Love waves at 14 and 18 s.

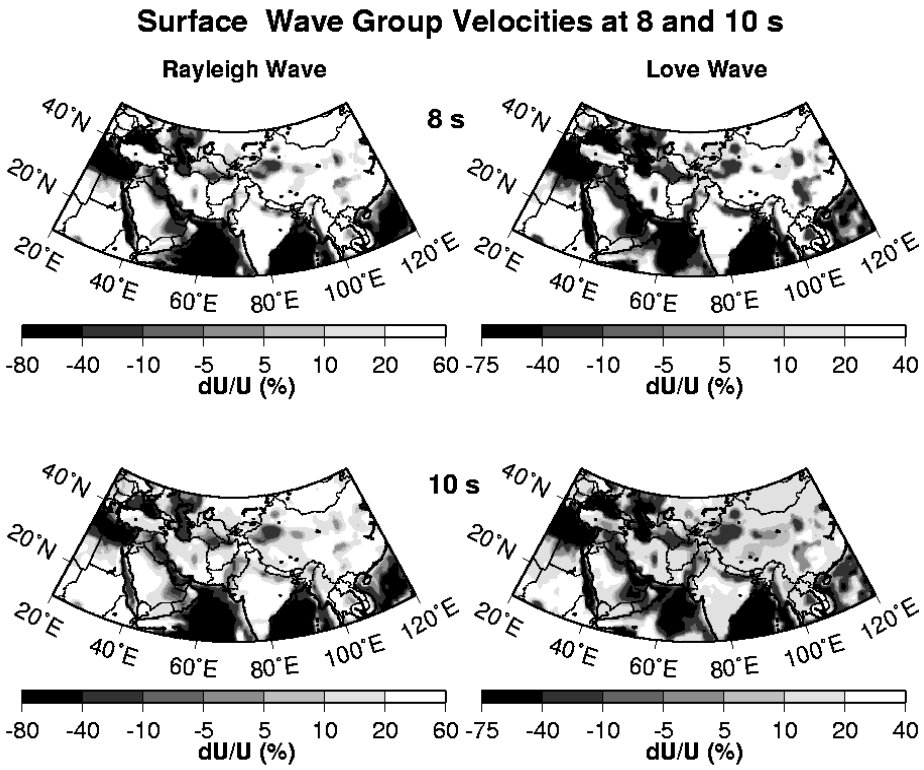

Figure 10. *Preliminary tomographic maps.*

Tomographic maps for a set of short periods obtained using the current data set are shown in Figures 8 and 9. The important role of the reference model is clearly demonstrated by Figure 8. Map (a) presents the prediction from the CU model. Map (b) shows the results of tomography with Map (a) as a reference. Map (c) presents results of tomographic inversion without the reference model. In this case, a mean value of observed group velocities was taken as a reference value across the mapped area. Map (d) shows the relative difference between maps (a) and (b). At first glance, there is no significant difference between maps (a) and (b), and this suggests that tomography does not produce significant new information about the studied area. However, map (c) shows that the data contain signals which could be informative, and map (d) demonstrates significant differences between the prediction and the result of tomography in areas with good path coverage. For example, the low-velocity feature related to the Tarim basin around point $\theta = 80^\circ$, $\phi = 38^\circ$, is much more prominent than in the model prediction. Another feature that is almost absent in the prediction is a low-velocity spot in eastern Pakistan at periods 12 s and above. At the same time, group velocities in areas with poor coverage (like southern India, northeastern Africa) tend to be almost the same as in the reference model. Tomographic maps for four different periods (8, 10, 14, and 18 s) are shown in Figure 9. Sedimentary basins of the Tarim, Dzhungaria, Caspian, Black, and Mediterranean Seas are clearly seen on all maps. Low velocity regions in Pakistan are especially prominent on the 14-s maps. High-velocity regions in Iran, southeastern China and northern India appear on the 8-s, 10-s and 14-s maps. The data fit to tomographic images is two to three times better than to the predictions based on the CU model. This indicates that upper crustal structure in the CU model for this region may be refined using the short-period information obtained in this study. The same is true for the SAIC regionalized model. The values of the group velocity RMS for periods between 10 and 18 s are on the order 0.1 km/s, and the travel time RMS on the order of 20 s.

Resolution and bias. Some means to estimate the quality of group velocity maps are discussed at length by Barmin *et al.* (2001). Two of the most useful qualitative measures are spatially variable resolution and amplitude bias. Figure 10 presents spatial resolution and amplitude bias of the maps in Figure 9 and contrasts the 10-s and 14-s maps with respect to these measures of map quality. Resolution at 10 s is on the order of 200-350 km to the north of latitude 25° and

deteriorates to the south. The amplitude bias in the area with acceptable resolution is less than 20%. The resolution and amplitude bias of the 14 s maps are better than at 10 s due to the more dense coverage.

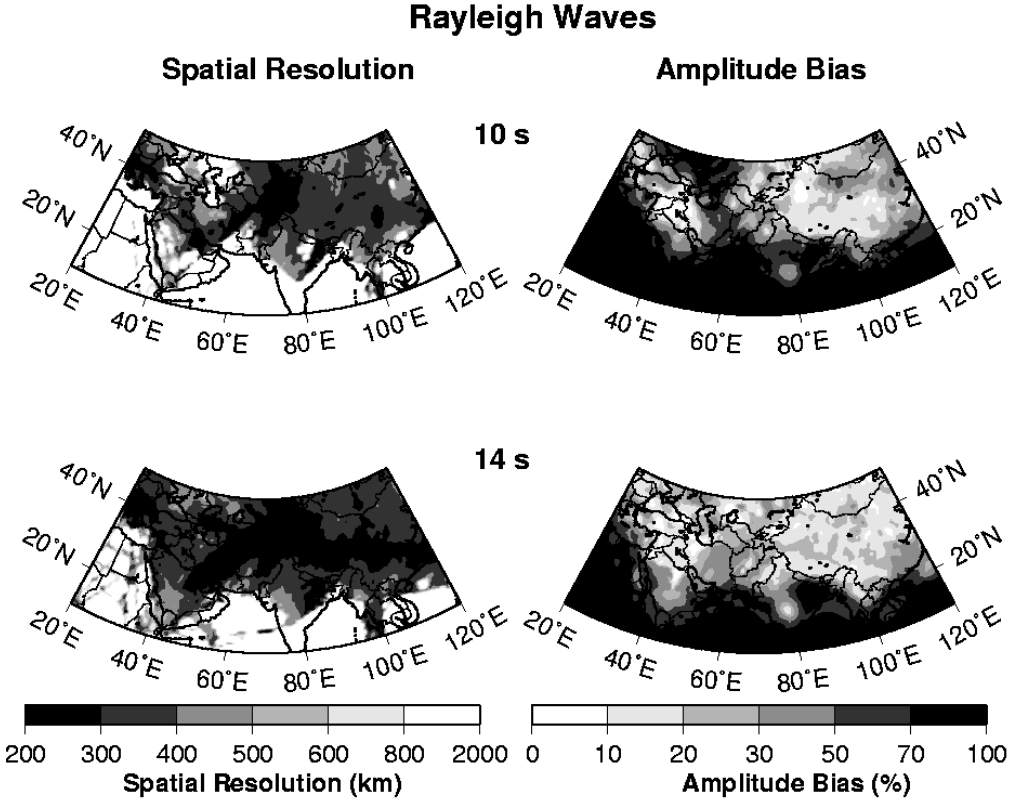

Figure 11. Spatial resolution and amplitude bias of tomographic inversion for the 10-s and 14-s Rayleigh wave data.

CONCLUSIONS AND RECOMMENDATIONS

In future work, we plan to

- Acquire additional data and obtain additional group velocity measurements for about 250 events that occurred in 2000.
- Produce refined Rayleigh and Love wave group velocity maps in increments of 1 s from 8-s to 15-s periods for the region of study by the tomographic method.
- Convert the group velocity maps to station-specific correction surfaces for IMS and other interesting stations in and adjacent to the region of study.
- Incorporate the group velocity measurements into new global group velocity maps by the model-based method developed by SAIC.
- Cross-validate group velocity maps obtained by the tomographic and model-based methods.
- Test and validate the maps and correction surfaces on IMS data at the CMR test bed.

REFERENCES

Barmin, M.P., M.H. Ritzwoller, and A.L. Levshin (2001), A fast and reliable method for surface wave tomography, *Pure and Appl. Geophys.*, **158**, n.7, in press.

Herrin, E. and T. Gofort (1977), Phase-matched filters: application to the study of Rayleigh waves, *Bull. Seismol. Soc. Am.*, **67**, 1259-1275.

Levshin, A.L., L. Ratnikova, and J. Berger (1992), Peculiarities of surface wave propagation across central Eurasia, *Bull. Seismol. Soc. Am.*, **82**, 2464-2493.

Levshin, A.L., M.H. Ritzwoller, and L.I. Ratnikova (1994), The nature and cause of polarization anomalies of surface waves crossing northern and central Eurasia, *Geophys. J. Int.*, **117**, 577-590.

Levshin, A.L., M.H. Ritzwoller, and S.S. Smith (1996), Group velocity variations across Eurasia, *18th Seismic Research Symposium on Monitoring a CTBT, Proceedings*, 70-79.

Levshin, A.L., M.H. Ritzwoller, L.I. Ratnikova, M. Silitch, R. Kelly, and B. O'Sullivan (1997), Intermediate period group velocity maps across Central Asia and parts of the Middle East, *19th Seismic Research Symposium on Monitoring a CTBT, Proceedings*, 67-76.

Levshin, A.L., M.H. Ritzwoller, M.P. Barmin, A. Villaseñor, and C.A. Padgett (2001), New constraints on the Arctic crust and uppermost mantle: surface wave group velocities, P_n, and S_n, *Phys. Earth. Planet. Int.*, **123**, 185-204. Levshin, A.L. and M.H. Ritzwoller (2001), Automated detection, extraction, and measurement of regional surface waves, *Pure and Appl. Geophys.*, **158**, n.7, in press.

Levshin, A.L., M.H. Ritzwoller, M.P. Barmin, and J.L. Stevens (2000), Assessing abilities to estimate short period group velocities in Central Asia, *22nd Annual DoD/DoE Seismic Research Symposium, Proceedings*, I, 67-76.

Levshin, A.L. and M.H. Ritzwoller (2001), Discrimination, detection, depth, location and wave propagation studies using intermediate period surface waves in the Middle East, Central Asia, and the Far East, *Final Report on Contract DSWA01-97-C-0157*, DTRA.

Ritzwoller, M.H., A.L. Levshin, S.S. Smith, and C.S. Lee (1995), Making accurate continental broadband surface wave measurements, *17th Seismic Research Symposium on Monitoring a CTBT, Proceedings*, 482-490.

Ritzwoller, M.H., A.L. Levshin, L.I. Ratnikova, and D.M. Tremblay (1996), High resolution group velocity variations across Central Asia, *18th Seismic Research Symposium on Monitoring a CTBT, Proceedings*, 98-107.

Ritzwoller, M.H. and A.L. Levshin (1998), Eurasian surface wave tomography: Group velocities, *J. Geophys. Res.*, **103**, 4839-4878.

Ritzwoller, M.H., A.L. Levshin, L.I. Ratnikova, and A.A. Egorkin (1998), Intermediate period group velocity maps across Central Asia, western China, and parts of the Middle East, *Geophys. J. Int.*, **134**, 315-328.

Stevens, J.L. and S.M. Day (1985), The physical basis for m_b:M_S and variable frequency magnitude methods for earthquake/explosion discrimination, *J. Geophys. Res.*, **90**, 3009-3020.

Stevens, J.L. and K.L. McLaughlin (1997), Improved methods for regionalized surface wave analysis, *Maxwell Technologies Final Report*, submitted to Phillips Laboratory, MFD-TR-97-15887.

Stevens, J.L. and K.L. McLaughlin (2001), Optimization of surface wave identification and measurement, *Pure and Appl. Geophys.*, **158**, n.7, in press.

Villaseñor, A., M. H. Ritzwoller, A.L. Levshin, M.P. Barmin, E.R. Engdahl, W. Spakman, and J. Trampert (2001), Shear velocity structure of central Eurasia from inversion of surface wave velocities, *Phys. Earth. Planet. Int.*, **123**, 169-184. references

SEISMIC LOCATION CALIBRATION IN THE MEDITERRANEAN, NORTH AFRICA, MIDDLE EAST, AND WESTERN ERUASIA

K. McLaughlin[1], X. Yang[1], I. Bondár[1], J. Bhattacharyya[1], H. Israelsson[1], R. North[1], V. Kirichenko[2], Y. Kraev[2], E. R. Engdahl[3], M. Ritzwoller[3], A. Levshin[3], N. Shapiro[3], M. Barmin[3], M. Antolik[4], A. Dziewonski[4], G. Ekström[4], I. Gupta[5], R. Wagner[5], W. Chan[5], D.W. Rivers[5], A. Hofstetter[6], A. Shapira[6], M.G. Laske[7], and N. Cotte[7]

Science Applications International Corporation[1]
Western Services Inc.[2]
University of Colorado at Boulder[3]
Harvard University[4]
Multimax Inc.[5]
Geophysical Institute of Israel[6]
University of California at San Diego[7]

Sponsored by Defense Threat Reduction Agency

Contract No. DTRA01-00-C-0013

ABSTRACT

The goal of our Consortium's work is to improve event location in the Mediterranean, North Africa, Middle East, and Western Eurasia by calibrating travel times used in the location process by the International Data Centre (IDC). We develop 3-D velocity models and compute predicted regional travel times using ray tracing. The Source-Specific Station Corrections (SSSCs), relative to the IASPEI91, are obtained for regional P and S phases within 20 degrees at each International Monitoring System (IMS) station. SSSCs and modeling errors can be applied in the IDC location process to improve event location in calibrated regions, as demonstrated in previous studies in Fennoscandia and North America (e.g. Yang et al., 2001). We perform validation tests of the SSSCs by comparing them with empirical corrections from cluster analyses and by relocating ground truth (GT) events that possess location accuracies better than 5 km (GT0-GT5). This three-year project, starting in 2000, is divided into two phases, and we are currently at the transition between the two. The 3-D models, SSSCs, and GT events developed in Phase 1 will be delivered to the Prototype IDC this year.

In Phase 1 two separate 3-D velocity models are developed and SSSCs are computed. One is a 3-D hybrid model constructed by combining global mantle models with global crust and upper mantle models using improved group and phase velocity data sets and inversion methodology (Villaseñor et al., 2001). A second is a regionalized crustal model, developed from published tectonic maps and 1-D velocity models, combined with a 3-D mantle model parameterized in terms of radial and horizontal cubic splines using a combination of direct and differential travel times and surface-wave phase measurements (Antolik et al., 2001). The two models are compared for cross-validation and model error evaluation. SSSCs have been computed for the IMS stations as well as for IMS surrogates and other stations for validation testing. GT0-GT5 events collected for the study region are relocated with and without SSSCs applied and results are compared. Detailed evaluations on location improvement are conducted using a suite of evaluation criteria and metrics as recommended by the Oslo Workshop in 1999 (CTBT/WGB/TL-2/18, 1999). Preliminary results show that, when SSSCs are applied, events move closer to their GT locations and error ellipses are reduced without significant loss of coverage.

KEY WORDS: location calibration, SSSCs, travel-times, 3-D velocity models, IASPEI91, GT, IDC.

OBJECTIVE

The objective of this work is to improve IMS seismic event locations in the Mediterranean, North Africa, Middle East, and Western Eurasia using more accurate travel-time information. We develop regional path-dependent travel-time corrections ($\Delta \leq 20^\circ$) for IMS stations in the study region to be incorporated into the PIDC/IDC location process.

RESEARCH ACCOMPLISHED

Introduction

The Group-2 Consortium carries out seismic location calibrations for IMS stations in the Mediterranean, North Africa, Middle East, and Western Eurasia using 3D models. Source Specific Station Corrections (SSSCs) for IMS seismic stations are developed to improve location accuracy and reduce error ellipses. Our goal is to develop SSSCs for Pn, Sn, and Lg phases out to 20° and the Pg phase out to 8° for all IMS stations in the study region (Figure 1). Previous studies have demonstrated that event locations and uncertainties can be improved by applying regional travel time corrections in event location (e.g. Yang et al., 2001a).

This work consists of two phases, preliminary and refined corrections, respectively. In Phase 1 we develop preliminary Pn and Sn SSSCs for a source depth of 10 km. In Phase 2 we will refine and improve the models and methods to obtain final SSSCs, including depth dependence. Pg and Lg SSSCs will also be developed in Phase 2. In both phases, validation testing is conducted using ground truth (GT) events to demonstrate improvement on event locations when using the corrections. In this report we describe preliminary Phase 1 validation testing results which are currently being delivered and tested on the DTRA CMR R&D Testbed.

Two separate 3D models are developed in Phase 1. A 3D hybrid model (CUB model) is constructed by combining global mantle models with global crust and upper mantle models using improved group and phase velocity data sets and inversion methodology (Villaseñor et al., 2001). A second model (SAIC-HRV model) is a regionalized crustal model, developed from published tectonic maps and 1D velocity models, combined with a 3D mantle model parameterized in terms of radial and horizontal cubic splines using a combination of direct and differential travel times and surface wave phase measurements (Antolik et al., 2001). The two models are compared for cross validation and model error evaluation. SSSCs are calculated for a given station using 3D ray tracing. Validation testing of the model-based SSSCs is conducted by relocating GT0-GT5 events. GT10 events may also be used to extend the coverage of the region where GT0-GT5 events are not available. They are recorded at IMS stations and/or surrogate stations as well as other stations, and distributed throughout the study region. We evaluate reductions in mislocations and error ellipses by applying SSSCs in event location. Results discussed in this report are for Pn and Sn SSSCs from the CUB model only.

Regional SSSCs are defined on rectangular $1^\circ \times 1^\circ$ latitude/longitude grids where both a travel-time correction and a modeling error are given at each grid point. The corrections are relative to the IASPEI91 travel times used in the PIDC/IDC location process. Modeling errors, the uncertainty in the predicted travel times, are estimated to ensure 90% ellipse coverage. In Phase 1 modeling errors (Figure 2) are estimated from the variance of the travel time residuals, with respect to the 3D model, in the EHB catalog (Engdahl et al., 1998).

In addition to the relocation testing described in this report, validation testing is also carried out using other methods, e.g. cluster analyses. The JHD/HDC cluster analyses are used to derive path-dependent corrections from event clusters. Comparison are made between these empirical corrections and model-based SSSCs for cross validation (Figure 2). Station corrections and statistical scatter of clusters are used as one source of information in estimating modeling errors.

Validation Testing

Validation testing for regional SSSCs in the Group-2 Consortium region is conducted by relocating events using SSSCs to verify event location improvement relative to the GT and location error ellipse coverage. The events used in validation testing are GT0-GT10 events and are not directly used in the model development.

We evaluate statistics on mislocation, error ellipse area, 90% error ellipse coverage, origin time differences from GT, origin time error, and standard deviation of observations. When SSSCs are applied, event location should be improved and error ellipses should be significantly reduced without loss of 90% coverage.

SSSCs from a large set of stations are applied in event location to validate the models and model errors. To assess IMS location improvement SSSCs are applied to only IMS stations and surrogate stations. The effect of mixing calibrated and uncalibrated regional and teleseismic data is also tested. Four sets of tests are conducted, including calibrated regionals only, calibrated and uncalibrated regionals, calibrated regionals and uncalibrated teleseismics, and calibrated regionals and uncalibrated regionals and teleseismics.

Our major evaluation metrics include those recommended by the 1999 Oslo Location Workshop (CTBT/WGB/TL-2/18, 1999). Additional metrics are also developed to measure the performance of the SSSCs. Both the L1 norm (median, spread, minimum, maximum, 20,40, 60 80 percentiles) and the L2 norm (mean, variance, standard deviation, average deviation) are calculated for the distance from GT, size of error ellipse, 90% ellipse coverage, origin time, origin time error, and misfit obtained with and without SSSCs. Student and Wilcoxon significance tests of paired samples are also applied, and statistics significant at least at 95% level are included in this report. Besides applying the evaluation metrics to an entire data set, we further divide each data set into several classes based on the GT accuracy (i.e. within vs. beyond the GT accuracy when located with and without SSSCs), and on mislocation (i.e. within vs. beyond x km). We also compare the numbers of events in a data set which are located within 1000 km^2 error ellipses that contain the GT and within 25 km distance from the GT with and without SSSCs.

Test Data Sets

Four data sets are used in validation testing of the Pn and Sn SSSCs developed for the study region. They are GT0-GT10 events collected by the Consortium, the Fennoscandian GT events used in a previous study (Yang et al., 2001a), GT10 Mid-Ocean Ridge and Transform (MORT) events, and estimated GT5 EHB events. Since the expected improvement in location is on the order of 10 km, the location of reference events should preferably be within 5 km accuracy or better. We mainly focus on GT0-GT5 events for relocation and error ellipse validation, but other events are also used for validation testing to extend coverage of the region.

The GT0-GT10 events from the Consortium database include nuclear explosions, chemical explosions, and well-located earthquakes, particularly from JHD/HDC cluster analyses (Engdahl and Bergman, 2001). Arrival data are merged from the PIDC REB, EHB catalog, as well as national and local network bulletins in the region. Events with at least three Pn (Sn) arrival data are used in validation testing. There are 11,000 Pn and 860 Sn defining arrivals in the test data set. Figures 3-4 show the GT0-GT10 event locations and Pn and Sn paths.

The Fennoscandia data set was previously used in testing 1D SSSCs for the Fennoscandian stations. It mainly contains 425 GT events in Fennoscandia, originally considered as GT2. Thirty-five MORT events in the Gulf of Aden and North Atlantic are included for testing to extend the coverage. These events are referenced to the bathymetric features and are estimated as GT10. Candidate GT5 events are also selected from the EHB catalog for the study region based on the candidate GT5 selection criteria. Estimated GT5 locations were obtained for 448 events relocated using phases recorded only within 300 km.

Test Results

The Fennoscandian data set and 1D SSSCs serve as a benchmark of the SSSCs developed using the 3D model by raytracing. The location results for the GT events are similar when the CUB and 1D Pn and Sn SSSCs are applied. With the CUB SSSCs 60% of events are improved, and the median ellipse area is reduced by 1900 km^2 (from 3700 to 1800 km^2) without loss of the 90% coverage (99%).

Our major validation testing is conducted using the GT0-GT10 events. To assess the effect of SSSCs in event location, several sets of relocations are done in order to separate factors that affect event location, and in each set there are multiple runs. Depth is fixed to zero in all relocation tests since these events are mostly

shallow. Given the uncertainty in the location accuracy of GT events, at this stage we evaluate the location results for both GT0-GT5 and GT0-GT10 events. To be complete and objective we also include all locatable events in the current evaluation. Events near the boundary of the study region may be poorly located since we do not use any stations outside the region (Figure 1). A total of 571 GT0-GT10 events are relocated using only Pn and Sn phases, with and without SSSCs, for all stations:

- 60% events are improved in mislocation with a median of 8 km, and 47% are improved by more than 20%. 40% events are deteriorated with a median of 6 km, and 31% are deteriorated by more than 20%.
- The median improvement in ellipse area is 2360 km^2 (from 4600 km^2 without SSSCs to 2240 km^2 with SSSCs). The 90% coverages are 97% without SSSCs and 91% with SSSCs.
- 24% of the events are located with less than 1000 km^2 error ellipses that contain the GT locations and within 25 km mislocations, compared to 11% events without SSSCs.
- Origin time errors are reduced for 99% of the events. The median improvement, relative to the "GT" origin time, is 0.8 seconds, and the overall medians are 3.1 seconds without SSSCs and 2.2 seconds with SSSCs. The standard error of observations is improved for 61% events with a median of 0.2 seconds.

In this test, relocation results are similar between all GT0-GT10 events and GT0-GT5 events since there are only 25 GT10 events (all in the Aden and Koyna clusters). The median improvement in mislocation is larger for the GT0-GT2 events (10 km) while smaller for the GT5 events (6 km). Figure 5 compares mislocations with and without SSSCs. There is large improvement in mislocation and error ellipse area for low ndef (number of defining phases used in locating the event) events (Figure 6). Figures 7-10 show some examples of events in this data set using only Pn and Sn phases from all stations with and without SSSCs.

For IMS improvement validation the GT0-GT10 events are relocated using only IMS and IMS/surrogate stations with and without SSSCs. The results are similar to the previous one, but the median deterioration is larger for the case of IMS stations only, indicating that locations may be biased when only few stations with poor station geometries are used. When the SSSCs are applied to both IMS and surrogate stations, 59% events are improved by a median 8 km and the rest are deteriorated by a median 6 km. Error ellipses are reduced by ~60% while maintaining the same 90% coverage. This test shows that the SSSCs will effectively improve regional event locations when the full IMS network is deployed. Further testing using the GT0-GT10 events is also conducted to evaluate the effect of mixing calibrated and uncalibrated regional and teleseismic phases in event location. In general there is small improvement in mislocation and error ellipses.

For better path coverage, we also test the MORT events in validating the regional SSSCs. When the MORT events are relocated using Pn and Sn phases only, the majority of events have significant reductions in both mislocation and error ellipses using SSSCs. However, there are large mislocations and poor ellipse coverage, possibly due to poor station geometry. Relocation of the GT5 EHB events using Pn and Sn phases shows small improvement with SSSCs for all stations due to good azimuthal coverage. Using IMS stations with SSSCs, the majority of GT5 EHB events have large improvement in location and ellipse area, but the ellipse coverage is less than 90%.

CONCLUSIONS AND RECOMMENDATIONS

Validation testing of preliminary Pn and Sn SSSCs is conducted by relocating reference events in the Group-2 study region (Figures 3-4), with and without SSSCs. Four data sets are used in the offline testing, including the Fennoscandian GT events, Group-2 GT0-GT10 events, MORT GT10 events, and GT5 EHB events. To separate various factors that affect event locations, multiple sets of tests are conducted for each data set. Each set of tests is further divided between IMS stations, IMS/surrogate stations, and other stations. We include all events in our evaluation in order to be objective and to reveal potential problems.

Relocation results using SSSCs show overall improvement in event locations and error ellipses. As expected, low ndef events generally have larger improvement/deterioration. When 571 GT0-GT10 events are relocated using only Pn and Sn phases with SSSCs for all stations, 60% of the events are improved with a median

improvement in mislocation of 8 km (10 km for GT0-GT2 events). All events have reduced error ellipses without losing 90% coverage. The median reduction in ellipse area is 2360 km^2 (from 4600 km^2 without SSSCs to 2240 km^2 with SSSCs). The improvement is similar when only calibrated IMS/surrogate regionals are used, but the deterioration is larger when only calibrated IMS regionals are used due to poor station geometry. When mixing calibrated and uncalibrated regionals and teleseismics, relocation results show less improvement in general.

Compared to previous studies, the relocation results are similar to those for Fennoscandia (Yang et al., 2001a), and both are better than those for North America (Yang et al., 2001b). Note that the current results have only used Pn and Sn SSSCs while Pg and Lg were also used for the two other regions. Further, in this report we show statistics for all events, including events along the border of the study region which may be poorly located since we only use regional phases from stations within the study region.

Several lessons have been learned from the validation testing about the data and model. Improvement on these aspects is expected in Phase 2. More details may be found at http://g2calibration.cmr.gov.

- Despite our effort in collecting GT5 or better events throughout the study region, currently the path distribution is still limited. In Phase 2 more data will be collected for better coverage. At present, the data quality in our collections also varies. For instance, within a cluster the reference events may be better than the derived events. Relocation results show better improvement for the reference cluster events when SSSCs are applied. Since the median improvement in event location is less than 10 km using SSSCs, it is important to assess the GT events as accurately as possible. In addition, the event, arrival, and station information is collected and merged from a variety of data sources. Currently inconsistencies may still exist in the data sets. We will continue our effort vetting the information for further studies.

- Some poorly relocated events may be due to poor model predictions in travel times. We are identifying the areas where the model needs improvement. In Phase 2, the emphasis in model development will be placed on improving the model in certain areas and refining the model in general. It is undesirable to mix calibrated and uncalibrated data in event location, particularly to mix calibrated and uncalibrated regional phases for a given station. Developing Pg and Lg SSSCs has a high priority in Phase 2. Teleseismic phase calibration may also be explored since teleseismics play a dominant role in IMS event location. At present the SSSCs are generated for the source depth of 10 km and we mostly fix depth to 0 km in relocating events. In Phase 2 we will explore depth-dependent SSSCs. In addition, the modeling errors currently used are conservative, invariant in azimuth, and station-independent. More realistic modeling errors are expected in Phase 2 that are closely coupled with the 3-D model and stations.

REFERENCES

Antolik, M., G. Ekström, and A.M. Dziewonski, Global event location with full and sparse data sets using three-dimensional models of mantle P-wave velocity, Pure Appl. Geophys., 291-317, 2001.

Engdahl, E.R., van der Hilst, R.D., and Buland, R.P., 1998, Global teleseismic earthquake relocation with improved travel times and procedures for depth determination, Bull. Seism. Soc. Am.,88, 722-743, 1998.

Engdahl, E.R., and E. Bergman, Validation and generation of reference events by cluster analysis, this Volume, 2001.

Villaseñor, A., M.H. Ritzwoller, A.L. Levshin, M.P. Barmin, and E.R. Engdahl, Shear velocity structure of central Eurasia from inversion of surface wave velocities, Phys. Earth Planet. Int., 169-184, 2001.

Yang, X., I. Bondár,, K. McLaughlin, and R. North, Source Specific Station Corrections for regional phases at Fennoscandian stations, Pure Appl. Geophys., 158, 35-57, 2001a.

Yang, X, I. Bondár,, K. McLaughlin, R. North, and W. Nagy, Path-dependent regional phase travel-time corrections for the International Monitoring System, Bull. Seism. Soc. Am., in press, 2001b.

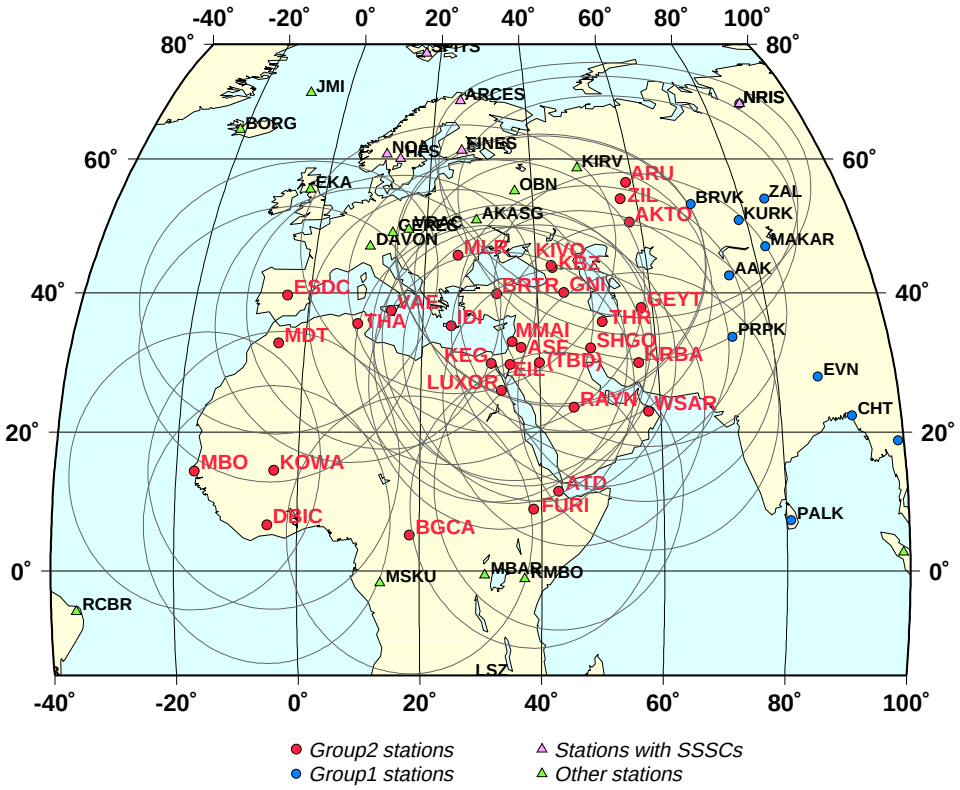

Figure 1. Group-2 Consortium region of interest. There are 6 IMS stations with existing regional SSSCs in this region (Yang et al., 2001a).

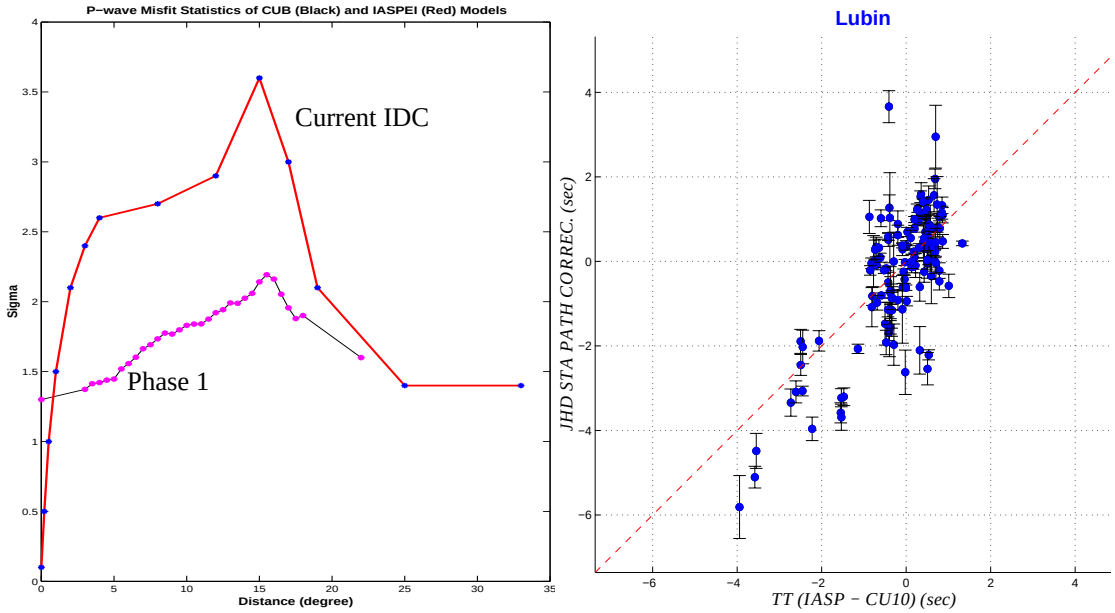

Figure 2.(Left) Modeling errors used in Phase 1 (thin line) compared to that used at the PIDC/IDC currently (thick line). (Right) Empirical path correction comparisons of the Lubin, Poland, cluster and the CUB model. There is good agreement between the empirical JHD path corrections and the model predictions (correlation coefficient of 0.8).

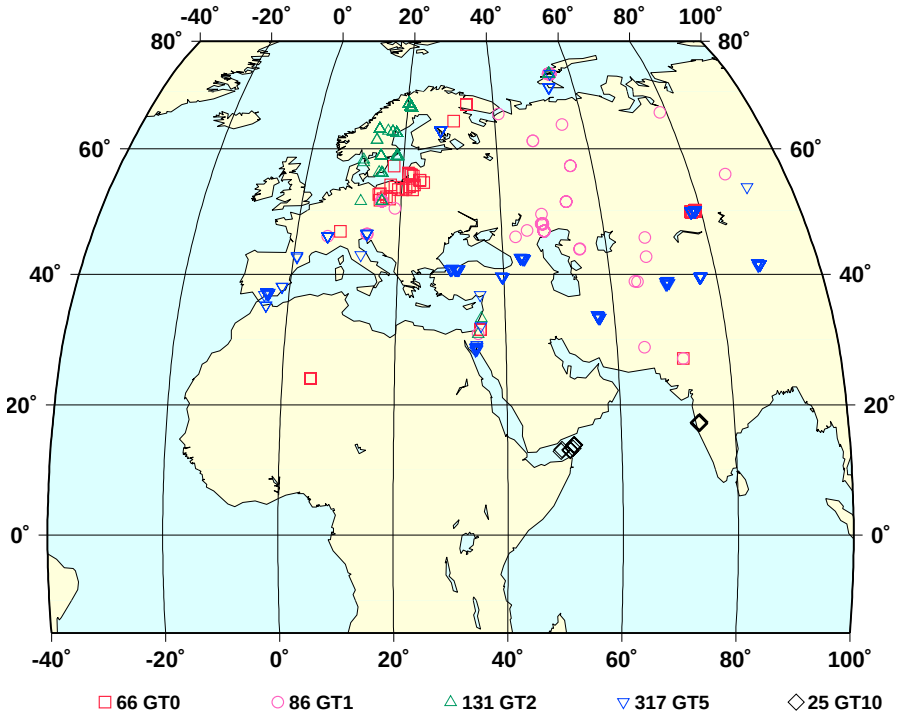

Figure 3. 625 GT0-GT10 events in the Group-2 Database used in relocation (http://g2calibration.cmr.gov).

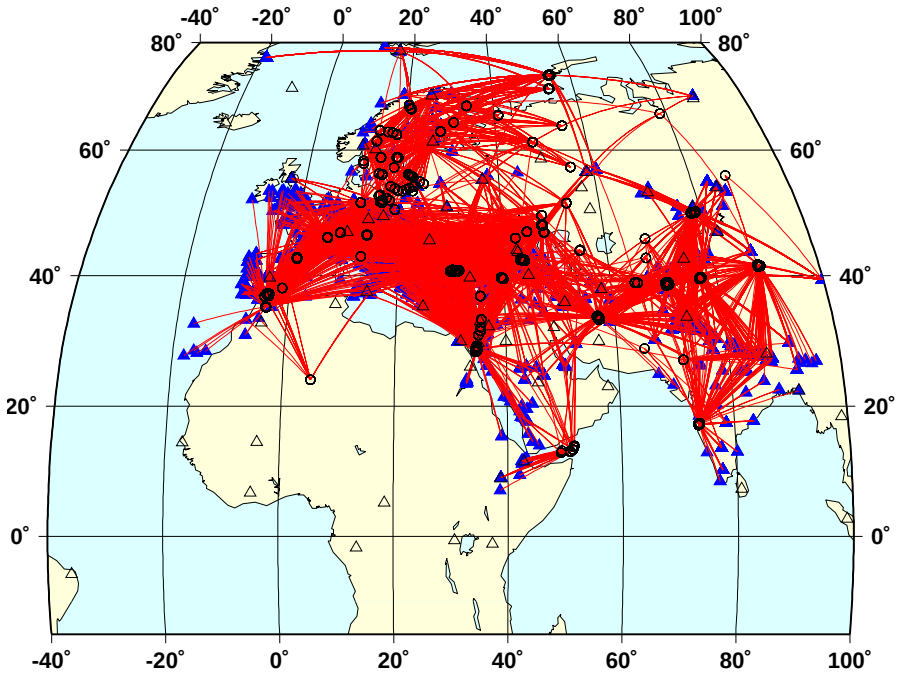

Figure 4. 11,000 Pn and 860 Sn path coverage in the Group-2 GT0-GT10 data set. Events (circles) and stations (open triangles for IMS; solid triangles for other stations) are also plotted.

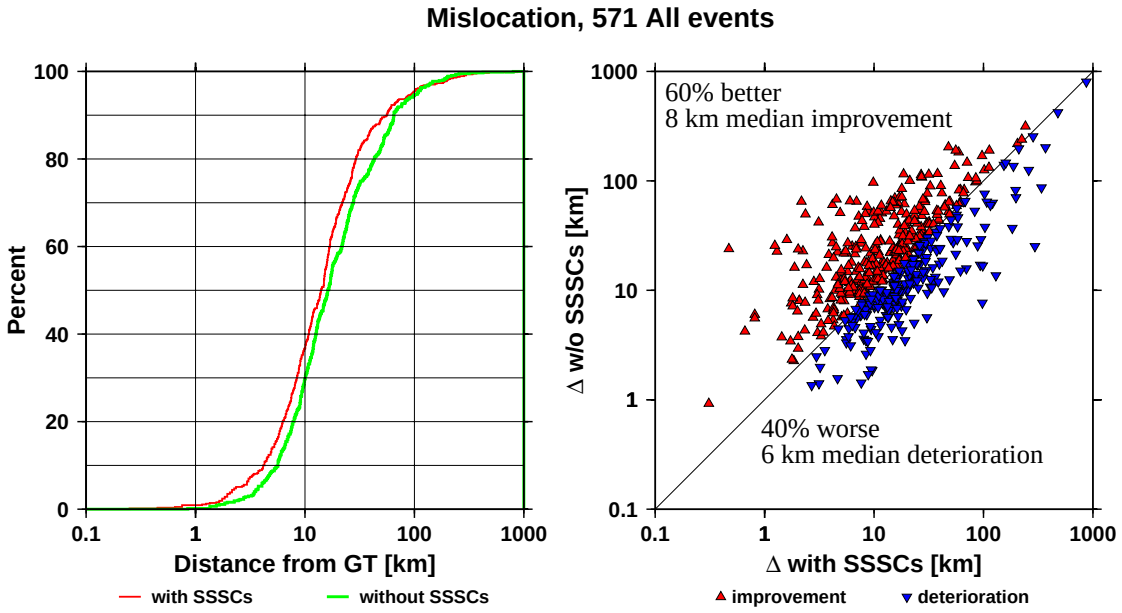

Figure 5. Mislocation comparisons of the GT0-GT10 events with and without SSSCs. (Left) Cumulative plot showing location improvement using SSSCs compared to without SSSCs. The 80 percentile mislocation is reduced from 43.0 to 29.2 km (32% reduction), and the median mislocation is reduced from 16.5 to 14.1 km (15% reduction). (Right) Comparison of mislocations with and without SSSCs. Symbols above the diagonal line indicate improvement with SSSCs.

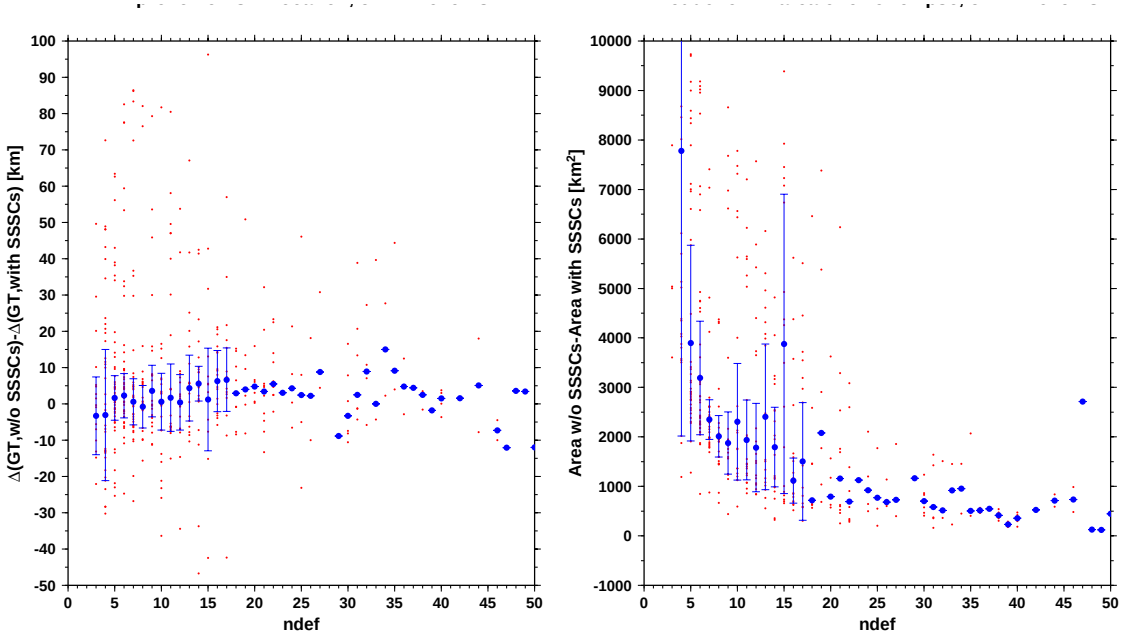

Figure 6. Improvement on mislocation (Left) and error ellipse (Right) vs. ndef for the GT0-GT10 events with and without SSSCs. Positive numbers indicate improvement. Low ndef events show large scatter in improvement/deterioration of mislocation.

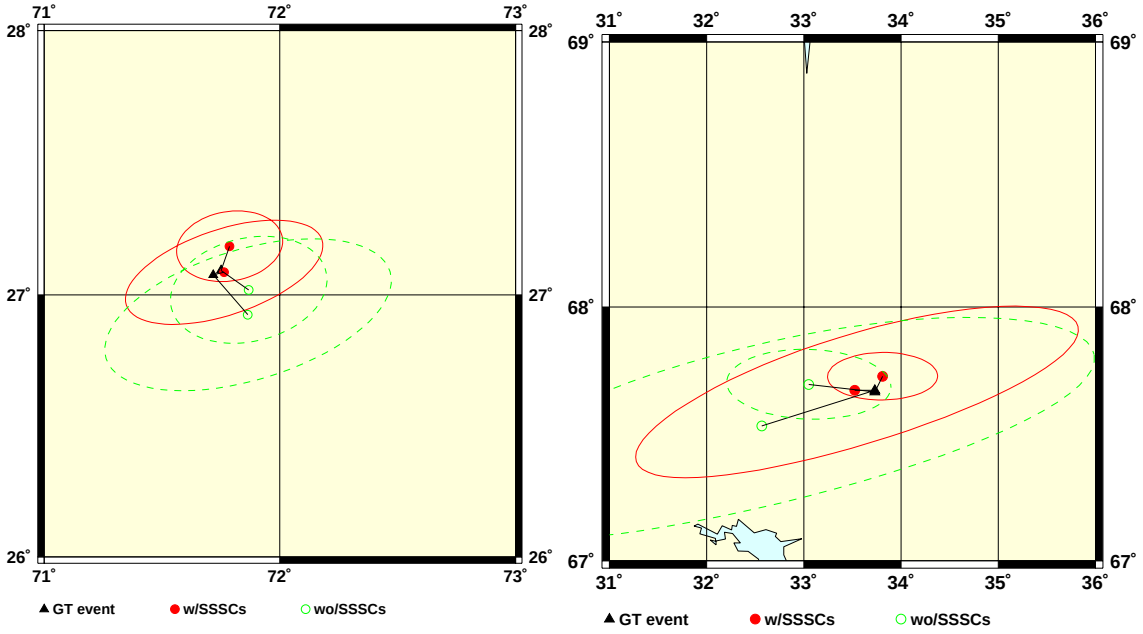

Figure 7. Relocations of the 1974 and 1998 Indian nuclear explosions (Left; GT0) and the 1996/09/29 and 1997/10/12 Kola calibration shots (Right; GT0) using Pn and Sn phases only, with (solid) and without SSSCs (dashed).Using SSSCs the mislocations are 4.6-10.8 km for the former, improved by 3.4 -17.6 km, and 7.6-8.8 km for the latter, improved by 21.4-43.2 km.

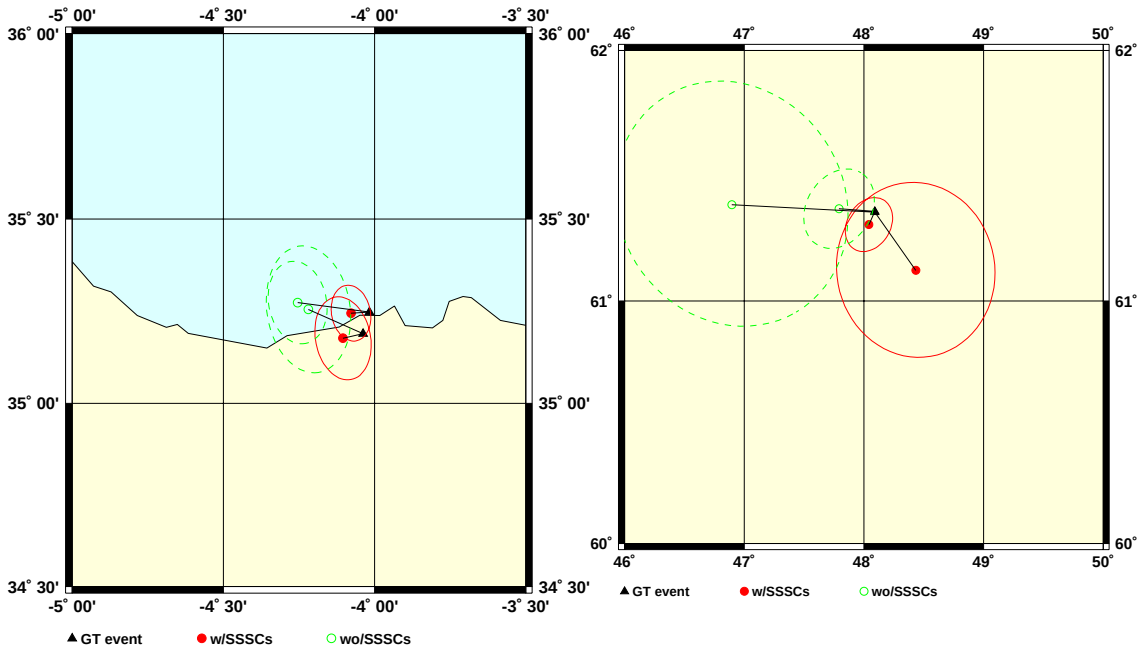

Figure 8. Relocations of the Morocco cluster (Left; GT5) and two PNEs on 1971/10/04 and 1988/09/06 (Right; GT1) using Pn and Sn phases only, with (solid) and without (dashed) SSSCs. Using SSSCs the mislocations are 5.6-6.2 km for the former, improved by 11.8-16.2 km, and 3.7-29.2 km for the latter, improved by 12.4-35 km.

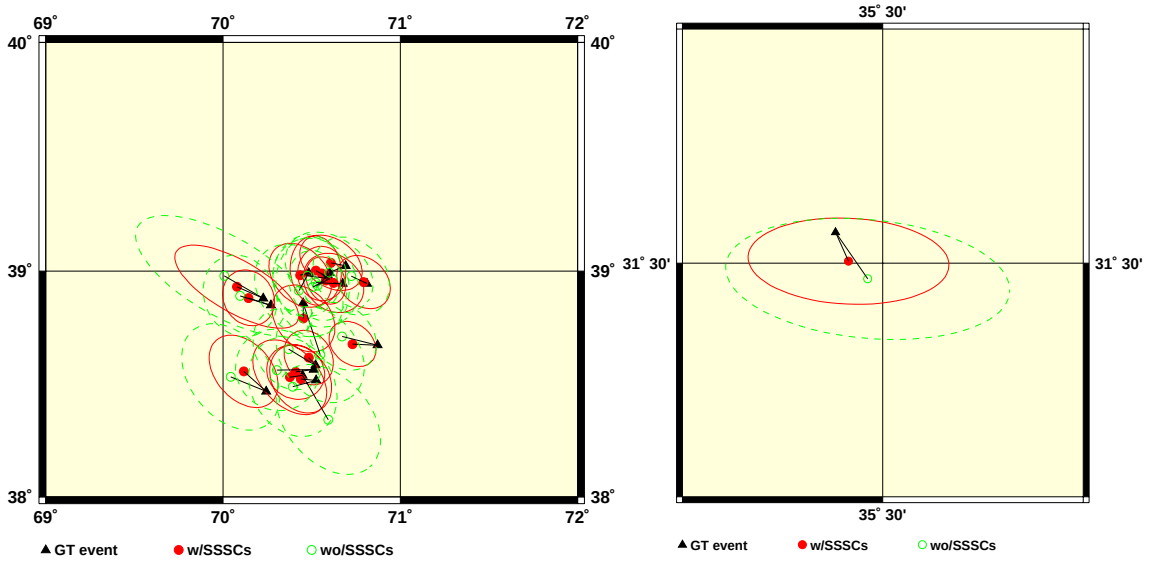

Figure 9. Relocations of the Garm earthquake cluster (Left; GT5) and the 1999/11/11 Dead Sea shot (Right; GT0) using Pn and Sn phases only, with (solid) and without (dashed) SSSCs. With SSSCs the median mislocation is 7.5 km for the former, improved by 5.9 km. The mislocations is 3.8 km for the latter, improved by 2.9 km.

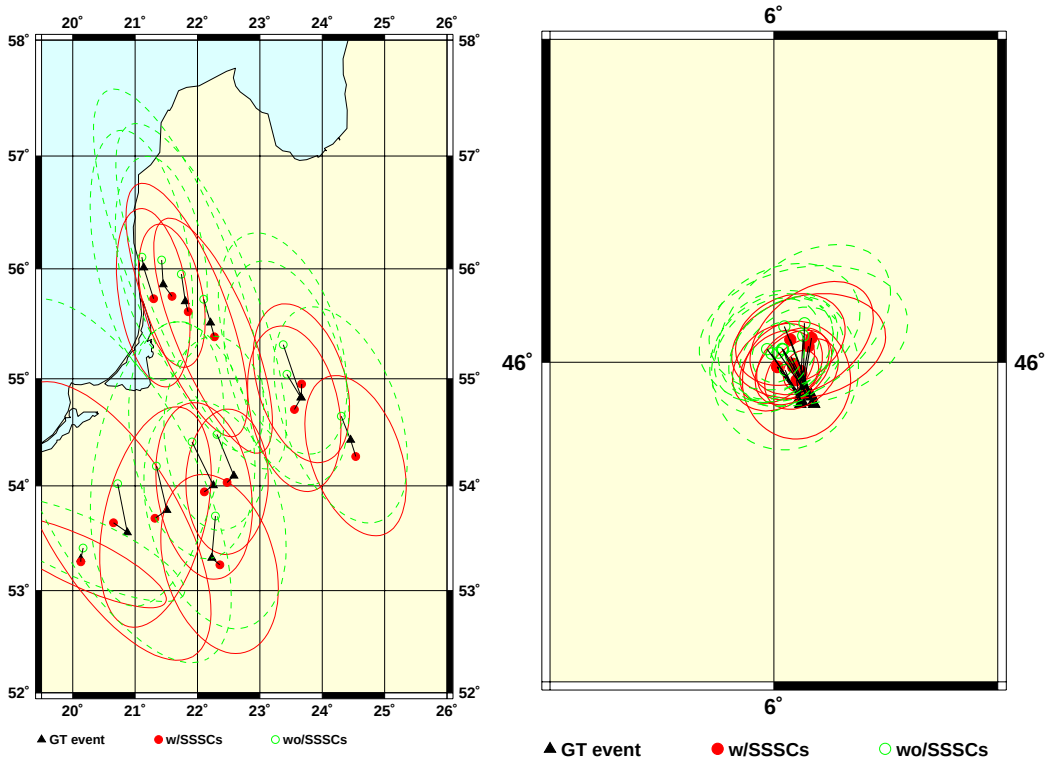

Figure 10. Relocations of the 1997 Polonaise and 1995-1996 Eurobridge shots (Left; GT0) and the French earthquake cluster (Right; GT5) using Pn and Sn phases only, with (solid) and without (dashed) SSSCs. Using SSSCs the median mislocation is 14 km for the former, improved by 24.7 km, and 6.2 km for the latter, improved by 2.8 km.

SEISMIC CALIBRATION OF GROUP ONE INTERNATIONAL MONITORING SYSTEM STATIONS IN EASTERN ASIA FOR IMPROVED EVENT LOCATION

John R. Murphy,[1] William L. Rodi,[2] Michelle Johnson,[3] Ivan O. Kitov,[4] Jamil D. Sultanov,[4]
Brian W. Barker,[1] Carolynn Vincent,[3] Vladimir Ovtchinnikov,[4] and Yuri Shchukin[4]

Science Applications International Corporation,[1] Massachusetts Institute of Technology,[2] Weston Geophysical Corporation,[3] Institute for Dynamics of the Geospheres[4]

Sponsored by Defense Threat Reduction Agency

Contract No. DTRA-00-0024

ABSTRACT

A consortium of institutions that includes SAIC, the Massachusetts Institute of Technology (MIT) Earth Resources Laboratory (ERL), Weston Geophysical Corporation, the Russian Institute for Dynamics of the Geospheres (IDG), and the Chinese Seismological Bureau of Sichuan Province is engaged in a research program directed toward the seismic travel-time calibration of the 30 Group 1 International Monitoring System (IMS) stations of eastern Asia. We have assembled a preliminary 3-D velocity model of the entire region, which is composed of a global background model on a 5°-by-5° grid derived from surface wave analyses, supplemented by more detailed models in regions where they are available. At present, such detailed models have been identified for a large portion of the Former Soviet Union (FSU) for which Deep Seismic Sounding (DSS) data have been used to define a 3-D velocity model of the crust and upper mantle on a roughly 40-km by 40-km grid, and for an approximately 25°-by-30° area centered on the Pakistan/Afghanistan region for which a 3-D velocity model has been defined on a 1° by 1° grid. Regional phase travel times through these 3-D models are being computed using the Podvin and Lecomte finite difference algorithm to obtain preliminary SSSC estimates for the IMS stations in this region. These initial estimates are being tested using various calibration data sets that have been assembled for this study. These include a unique set of regional arrival-time data at FSU permanent network stations from some 60 Soviet Peaceful Nuclear Explosion (PNE) tests, as well as numerous Semipalatinsk and Novaya Zemlya explosions with precisely known locations and origin times. Such data recorded near the Russian IMS stations BRVK, NRI, TIK, YAK, PDY, and AAK have now been carefully analyzed and utilized to produce travel-time residual maps with respect to both the default IASPEI91 travel-time curves and the travel time predicted by our DSS 3-D velocity model. It has been found that, for most of these stations in the stable platform regions of Russia, the travel times predicted by the IASPEI91 model are consistently too slow at distances greater than about 10 degrees by as much as 5 to 10 seconds. However, the corresponding travel-time residuals with respect to our DSS 3-D velocity model were found to be significantly smaller, with most stations showing an average bias near zero. A preliminary event location test has been conducted using data recorded near these IMS stations from 14 Soviet PNE events that were recorded at four or more stations. The results indicate that the DSS 3-D velocity model provides significantly more accurate seismic locations for these ground truth explosions than does the default IASPEI model (i.e. an average mislocation of 11.7 km as compared with 20.4 km).

In an attempt to improve our initial 3-D velocity model of eastern Asia, we are currently applying travel-time tomography to observed regional P wave arrival times from ground truth (GT) events and large earthquakes recorded at IMS and other stations. The velocity model is being parameterized in terms of crust/upper mantle velocity profiles that incorporate sediment/basement and Moho interfaces. The inversion algorithm formulation allows a subset of the model parameters, initially Pn velocity as a function of latitude and longitude, to be updated with other model parameters held fixed. The algorithm determines velocity model parameters jointly with the origin parameters of non-GT events, using grid search and conjugate gradient techniques to obtain the parameter updates. The inversion algorithm is based on the Podvin-Lecomte forward modeling of travel times, and accounts for the nonlinear dependence of travel times on both velocity structure and hypocentral parameters.

KEY WORDS: seismic, calibration, IMS, eastern Asia, SSSC, tomography

OBJECTIVES

The purpose of this effort is to develop improved 3-D velocity models, Site-Specific Station Corrections (SSSCs), and Slowness-Azimuth Station Corrections (SASCs) for eastern Asia, to demonstrate the effectiveness of these models and corrections in improving locations of seismic events, to evaluate the uncertainties associated with these improved models and corrections, and to install these models and corrections at the Center for Monitoring Research (CMR) and evaluate their performance. The specific objectives are four-fold. The first is to collect appropriate calibration data and seismic events occurring in and around the calibration region. The second is to use these data to refine the regional velocity models and to define and refine SSSCs and SASCs for the 30 IMS stations within the region. The third is to use the new velocity models and SSSCs and SASCs with calibration data ["Ground Truth" (GT) data] to evaluate the location capabilities of the system. The fourth is to implement the SSSCs and SASCs into the location system at CMR and to work with the CMR staff to evaluate their performance in that simulated operational environment.

RESEARCH ACCOMPLISHMENTS

During the past year, we have been continuing with our effort to calibrate the 30 Group 1 IMS stations in Eastern Asia for improved seismic event location. The map locations of these stations are shown in Figure 1, where it is indicated that they are composed of 11 primary and 19 secondary stations. It can be seen from this figure that regional distance coverage circles extending to 2000-km radius surrounding these stations would encompass most of the Asian continent, so the area to be calibrated is very large and samples a wide variety of crust and upper mantle environments.

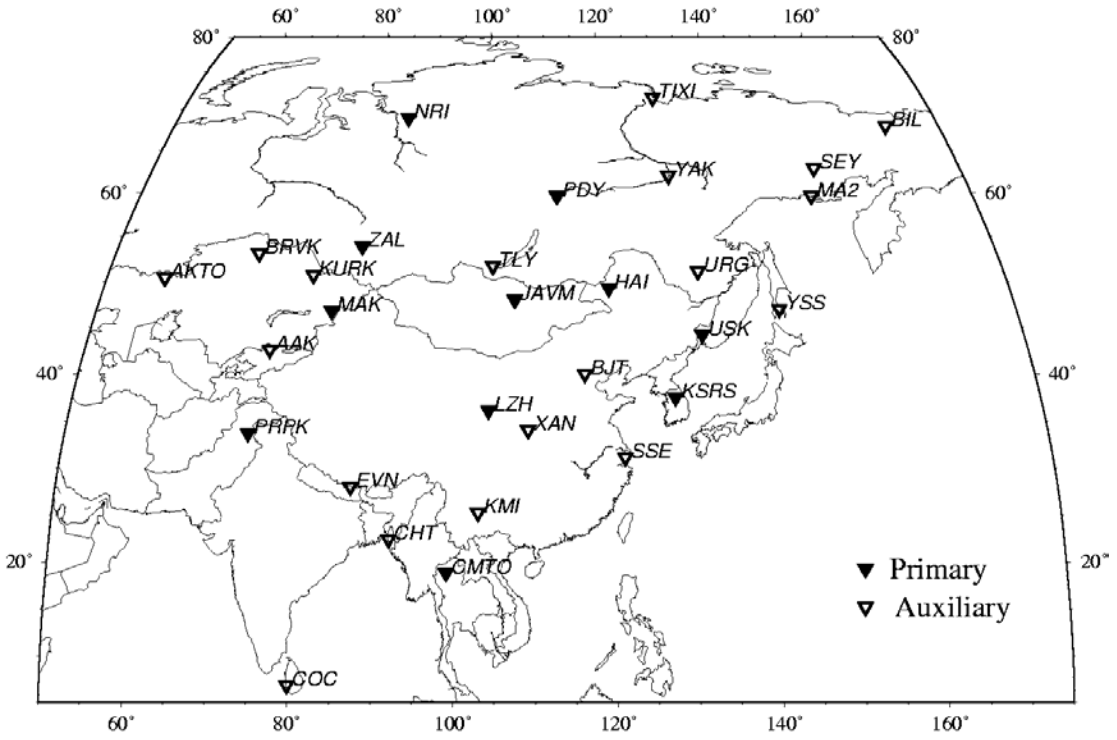

Figure 1. Map showing locations of the Group 1 IMS stations in Eastern Asia.

Our overall approach to this problem centers on the formulation of a 3-D velocity model of the region that can be used to define corrections to the default IASPEI91 model. Thus, an initial velocity model is defined from currently available information and is then refined by performing joint tomography and multiple event locations using arrival time data collected for this region. Once an optimum average model has been developed, source-specific empirical travel-time corrections for each station will be determined by interpolating between observed

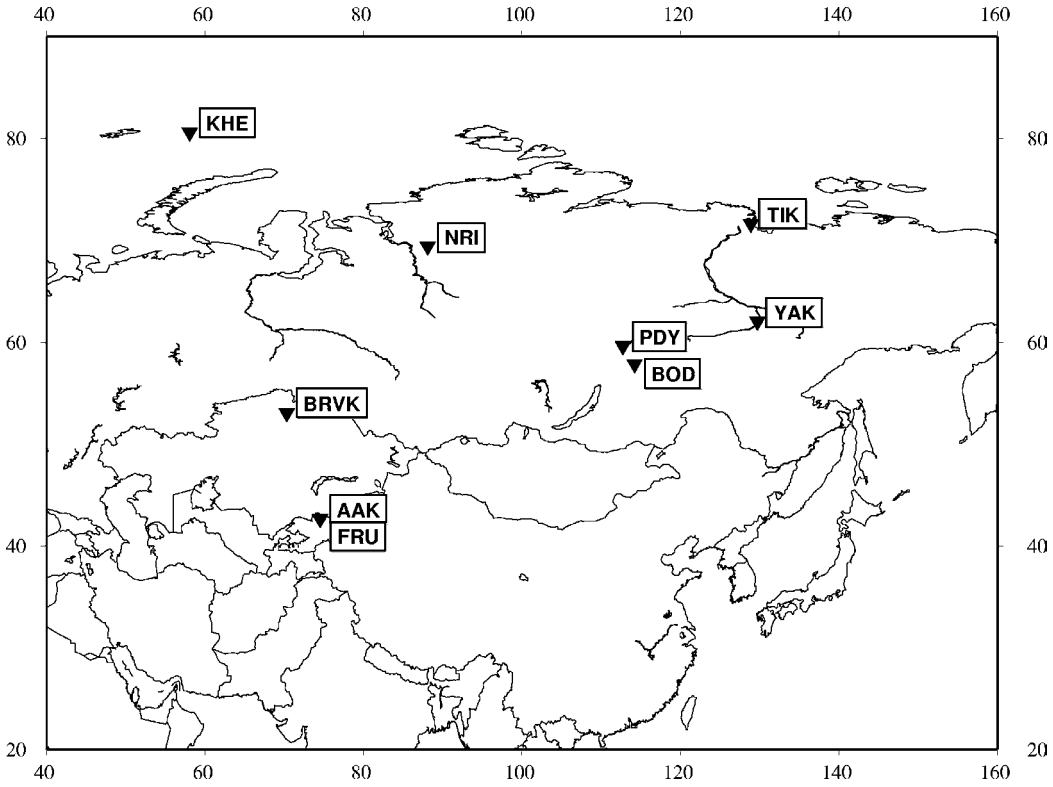

Figure 2. Map locations of seven former Soviet permanent seismic network stations (and associated IMS stations) used in the preliminary evaluation of the DSS velocity model.

calibration event residuals relative to this 3-D model. Model-based travel times determined by ray tracing through the 3-D velocity model will then be combined with these empirical corrections to generate 3-D travel-time tables for each Group 1 IMS station, and these predicted travel times will be differenced against the corresponding IASPEI91 travel times to define the required source-region-specific station corrections (SSSCs) as a function of source location around each station. This process will then be iterated to incorporate data from additional calibration events as they become available, and the final models will be validated based on relocation experiments conducted using travel-time data recorded from ground truth calibration events in the region.

Our preliminary 3-D velocity model for the Group 1 region is composed of a hierarchy of models having different spatial resolutions. A background model defined on a 5° by 5° grid covering the entire study region is derived from the global surface wave inversion results of Stevens and Adams. This background model is superceded by more detailed models in subregions where such information is available. At the present time there are two such subareas: a large region of the FSU for which Deep Seismic Sounding (DSS) data have been interpreted to obtain a detailed model of the crust and mantle on a 1/3° by 1/2° grid, and a large area centered on the Pakistan/Afghanistan region for which Weston Geophysical has been assembling a detailed velocity model (WINPAK3D) on a 1° by 1° grid (Johnson and Vincent, 2001). A software module denoted as QUILT has been developed to transform this composite spherical earth model to flat earth approximations, and to resample them to generate uniform Cartesian block models on 5- x 5- x 5-km grids extending to a range of 2000 km and a depth of 600 km for each selected IMS station. A generalized finite difference ray tracer based on one originally formulated by Podvin and Lecomte (1991) is then used to compute first arrival P wave travel times from each station to every point in the surrounding grid. Corresponding travel times for the same grids are also computed using the 1-D IASPEI model, and these values are subtracted from the 3-D travel times to obtain, by reciprocity, the preliminary SSSC estimates. These estimated corrections to the predicted IASPEI91 travel times turn out to

be quite large for a number of the Group 1 stations, and show complex spatial patterns reflecting the 3-D complexity of our initial velocity models. For example, the computed corrections for the station at Borovoye, Kazakhstan, (BRVK) range from about -10.5 to +2.9 seconds, while those estimated for the proposed IMS station near Nilore, Pakistan (PRPK) range from about -5.2 to +5.2 seconds. Clearly, corrections of this magnitude have the potential to significantly affect seismic location accuracy for regional events recorded by these stations.

Evaluation studies of the DSS velocity model of the FSU conducted to date have focused on analyses of Soviet PNE arrival time data recorded at the seven Soviet permanent network stations whose map locations are identified in Figure 2. Four of these stations (BRVK, NRI, TIK, YAK) are essentially co-located with corresponding IMS stations, while two others (FRU and BOD) are in reasonably close proximity (i.e. approximately 25 and 200 km, respectively) from corresponding IMS stations (AAK and PDY). The seventh station, KHE, located on Franz Joseph Land to the north of the island of Novaya Zemlya, is not the planned site of a future IMS station. However, data recorded at this station from Soviet PNE tests, as well as from underground nuclear tests at the two Novaya Zemlya weapons test sites, provide valuable constraints on the velocity model characteristics in north central Russia and, therefore, they have been included in this preliminary model validation study.

The ground truth regional calibration database that has been assembled for station BRVK is arguably the best available of any seismic station in the world. Support for this assertion is provided by Figure 3, which shows the map locations of some 55 Soviet PNE events within 20° of the Borovoye station for which measured arrival times are available. It can be seen that these explosion locations are remarkably well distributed around the station and, taken together with the travel-time data measured at this station from several hundred Semipalatinsk explosions, provide a unique resource for testing and evaluation studies. For this reason, we have selected BRVK as our benchmark station for the testing and evaluation of all of our proposed calibration procedures.

In the top panel of Figure 3, the symbols plotted at the PNE event locations correspond to the observed P wave travel-time residuals (observed - predicted) computed with respect to the corresponding travel times predicted by the default IASPEI91 travel time curve. It can be seen that almost all of these residuals are negative (i.e.

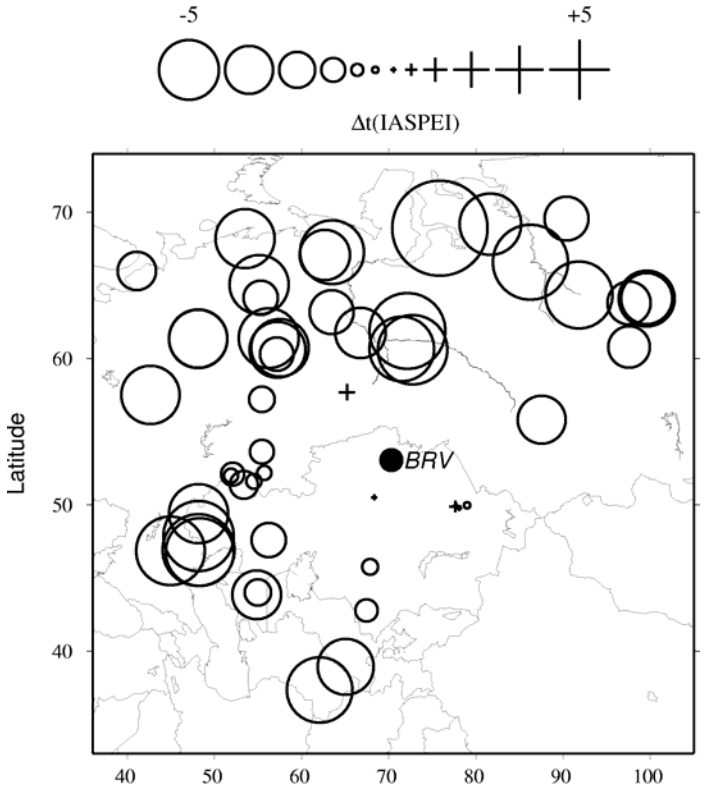

Figure 3. Map locations of the Soviet nuclear explosions recorded at station BRVK. The symbol sizes are proportional to the sizes of the observed BRVK P wave travel time residuals for these explosions, computed with respect to the predictions of the IASPEI91 (top) and DSS 3-D (bottom) velocity models.

circles), indicating that these observed arrivals are early with respect to IASPEI91, as might be expected for this stable platform region. These residuals are as large as -4 to -8 seconds in the 14- to 18-degree distance range and average to about -3.6 seconds over the entire sample distance range extending from 3 to 19 degrees. The lower panel of Figure 3 shows the corresponding map display of the BRVK residuals computed with respect to the travel times predicted by our preliminary DSS 3-D velocity model. It can be seen that these residuals are generally quite small and fairly randomly distributed spatially. The only notable exception to this general conclusion is the cluster of fairly large negative residuals (< -3 seconds) located almost due north of the station at an average epicentral distance of about 8 degrees. Given the systematic nature of this only remaining significant anomaly, it seems likely that it will eventually be accounted for through the tomographic revision of the velocity model and/or the inclusion of supplemental empirical corrections.

A second validation example is presented in Figure 4 for the far-eastern station TIK. In this case, the ground truth data consist of P wave first arrival times observed from 18 Soviet PNE tests and a sample of Novaya Zemlya underground nuclear tests, and it can be seen that the azimuthal coverage is not as complete as for BRVK. However, once again it can be seen that the residuals computed with respect to the 1-D IASPEI91 model (top) are consistently negative and quite large (i.e. average bias of about -4 seconds), while those computed with respect to the 3-D DSS model (bottom) are significantly smaller and fairly randomly distributed spatially. Similar encouraging results have now been documented for the other Russian stations identified in Figure 2 (Murphy et al, 2001), indicating that our initial DSS 3-D velocity model is generally consistent on average with the ground truth data analyzed to date, and that it represents a significant improvement over the default IASPEI91 model in this region.

It now remains to demonstrate the applicability of this new 3-D velocity model to the determination of improved seismic locations. As an initial step in this process, we have conducted regional location analyses of 14 Soviet PNE events whose map locations are displayed in Figure 5. Each of these explosions was recorded by four or more of the stations identified on this figure. In each case, two different seismic

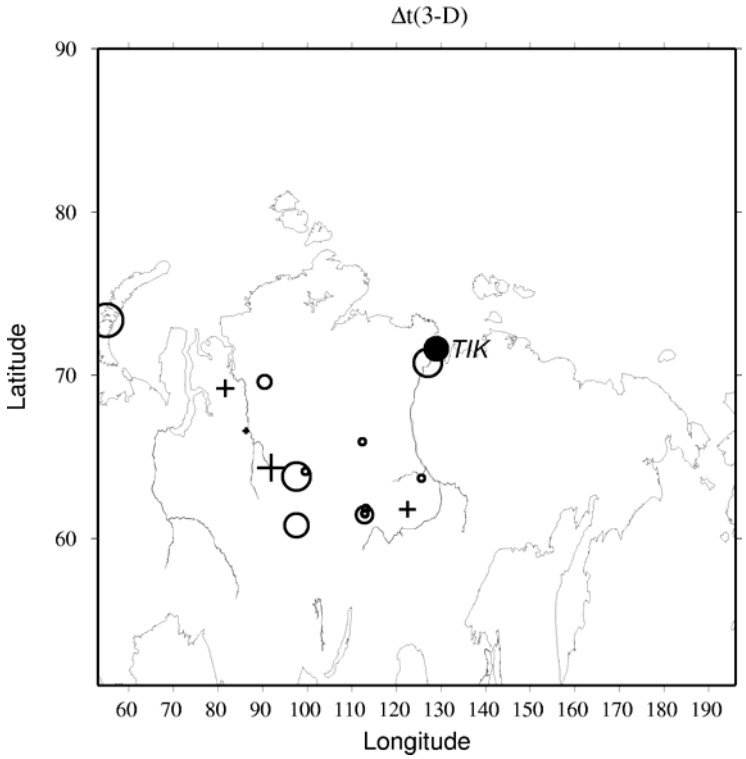

Figure 4. Map locations of the Soviet nuclear explosions recorded at station TIK. The symbol sizes are proportional to the sizes of the observed BRVK P wave travel time residuals for these explosions, computed with respect to the predictions of the IASPEI91 (top) and DSS 3-D (bottom) velocity models.

locations were computed; one using the standard IASPEI91 model and one using travel-time corrections estimated from the DSS 3-D velocity model. That is, predicted corrections to the observed travel times at the stations of Figure 5 were determined with respect to IASPEI91 by ray tracing through the DSS 3-D velocity model, and the explosions were relocated with and without corrections using the same hypocenter inversion code (i.e. LOCSAT). The results of this analysis indicated that the average mislocation for these 14 ground truth events was reduced from 20.4 km to 11.7 km as a result of applying these preliminary station corrections. Since these are predominantly GT1 events, this reduction in average mislocation is highly significant and, therefore, we conclude that the DSS 3-D velocity model does lead to significantly improved seismic locations for this preliminary sample of ground truth events. Similar encouraging relocation results have been documented using our WINPAK3D velocity model of the India/Pakistan region (Johnson and Vincent, 2001), which has led us to conclude that we have formulated a reasonable first order 3-D velocity model for the region which is suitable for refinement via tomographic inversion of suitable independent data sets.

We are currently revising this initial velocity model by applying tomographic inversion techniques to arrival time data observed from well-located explosions and earthquakes. To obtain an initial model for eastern Asia, we have re-parameterized and integrated various global and regional earth models into a universal model. Our parameterization of the universal model is given in terms of a velocity vs. depth profile at each point on a geographic grid. The geographic grid has uniform latitude spacing and, in each of several bands of latitude, uniform longitude spacing. The longitude spacing increases in bands at higher latitude. At each geographic grid-point, the velocity profile is given as velocity/depth pairs at nodes ranging from sea level to a depth of 760 km. Discontinuities in velocity are allowed at the ocean bottom, Moho and the major mantle discontinuities.

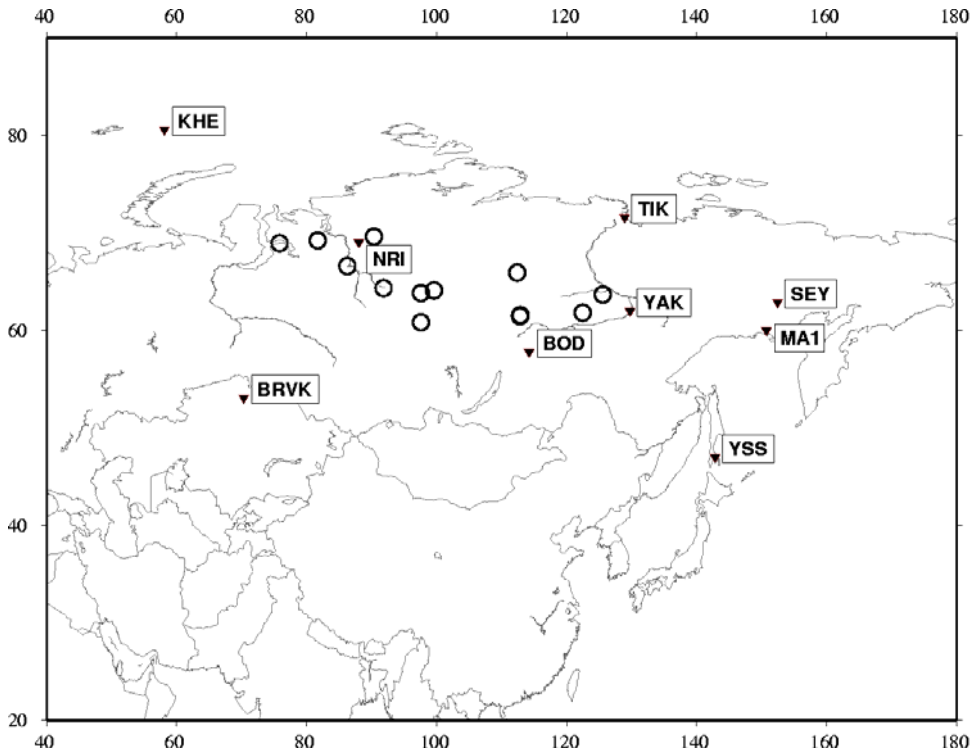

Figure 5. Map locations of 14 selected PNE events (circles), each of which was recorded by 4 or more of the indicated stations (triangles).

Our initial velocity model will be updated to fit regional arrival times observed at IMS and other stations from well-located events. Such events include explosions with known locations, earthquakes located with local networks, or large earthquakes whose locations are well constrained by regional and teleseismic data. To accomplish this, we are developing an inversion algorithm that performs joint velocity tomography and

multiple-event location. The algorithm will relocate the earthquakes in conjunction with revising the parameters of our universal velocity model. Initially, the model update will be restricted to the Pn velocity over a limited geographic region, i.e., the region near Borovoye. The preliminary travel-time data set that have been collected for this region is summarized in Figure 6.

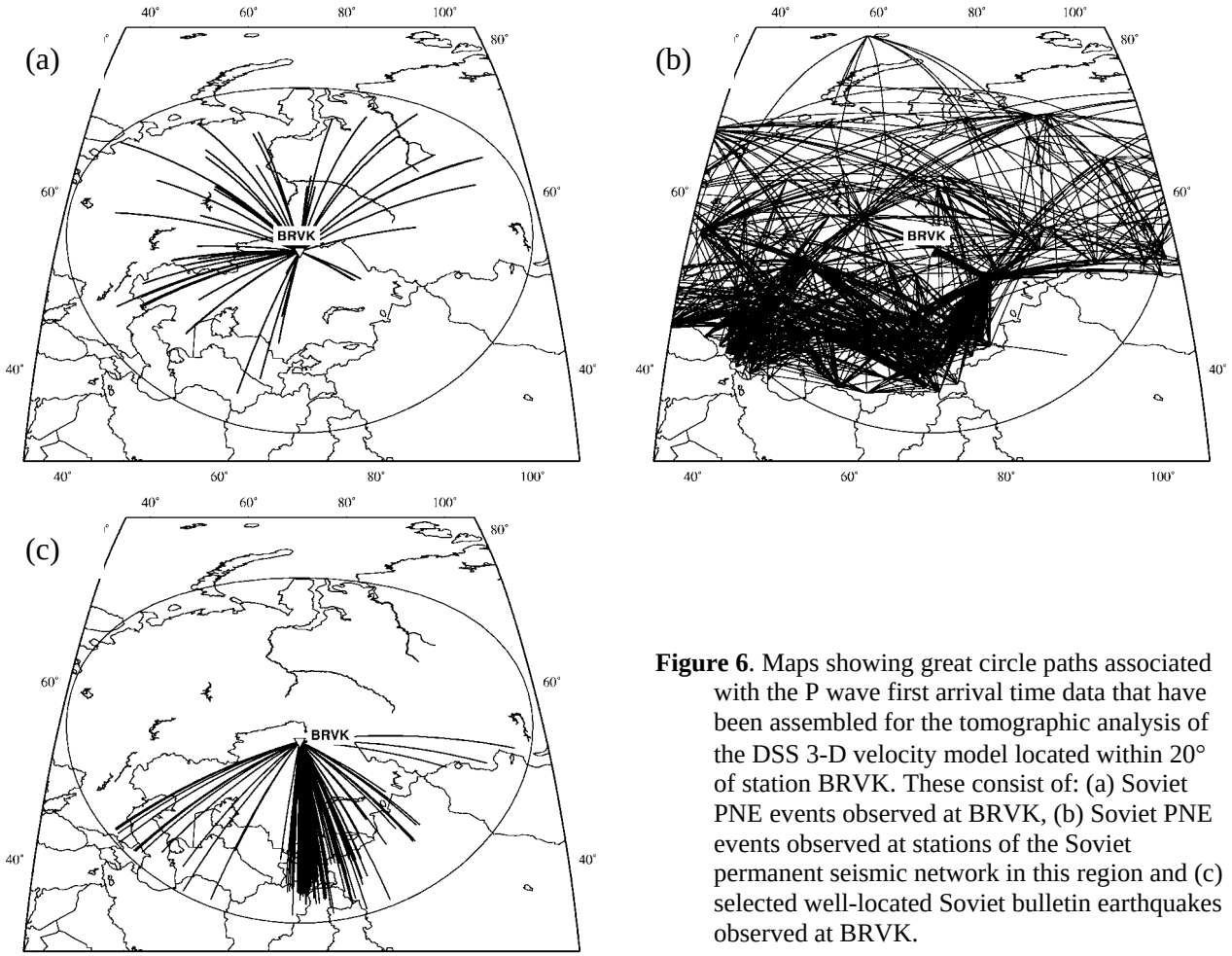

Figure 6. Maps showing great circle paths associated with the P wave first arrival time data that have been assembled for the tomographic analysis of the DSS 3-D velocity model located within 20° of station BRVK. These consist of: (a) Soviet PNE events observed at BRVK, (b) Soviet PNE events observed at stations of the Soviet permanent seismic network in this region and (c) selected well-located Soviet bulletin earthquakes observed at BRVK.

Our inversion approach is formulated as follows. The unknowns are a vector **m** containing the velocity model parameters that are to be estimated (e.g. Pn velocity at each point of the latitude-longitude grid), and the hypocenters and origin times of several events: ($\mathbf{x}_j$, t_j), $j = 1,\ldots,M$. The data are arrival times, d_{ij} , from each event to a subset of stations indexed as $i = 1,\ldots,N$. The data and unknowns are related by

$$d_{ij} = t_j + T_i\left(\mathbf{x}_j;\mathbf{m}\right) + e_{ij}$$

where e_{ij} is the error in d_{ij} and T_i is a function that computes travel time to station i from an event hypocenter $\mathbf{x}_j$. This function depends on the model parameter vector **m**. Our joint inversion criterion is to minimize an objective function of the form

$$\Psi\left(\mathbf{m},\mathbf{x}_1,t_1,\ldots,\mathbf{x}_M,t_M\right) = \sum_{ij}\left|d_{ij} - t_j + T_i\left(\mathbf{x}_j;\mathbf{m}\right)\right|^2/\sigma_{ij}^2 + \tau\left|\mathbf{Lm}\right|^2$$

with respect to all the unknowns. Here, Σ_{ij} is the standard deviation of e_{ij}. The second term of $\mathbf{\Psi}$ imposes a smoothness constraint on the velocity model, with **L** being a regularization operator and τ a regularization parameter. The operator **L** is chosen as a differencing operator with the effect that spatial derivatives of the model velocity are minimized. The parameter τ determines the degree of model smoothness.

Our algorithm performs the minimization of Ψ using a combination of conjugate gradients and grid-search techniques. The conjugate gradients method is used to find **m** iteratively, one projection in model space per iteration step. At each conjugate gradients step, grid search is used to minimize Ψ with respect to the event origin parameters with **m** fixed, thus updating the $\mathbf{x}_j$ and t_j. The grid search for a given event is performed within a specified epicentral radius and depth range from its initial location, allowing us to handle events of varying ground-truth levels (e.g., GT0, GT5, GT15). Our grid search algorithm is described by Rodi and Toks, 2000.

The forward model for this inverse problem is embodied in the travel time functions T_i. For fixed **x**, we evaluate $T_i(\mathbf{x};\mathbf{m})$ by interpolating a travel-time table stored on a 3-D hypocenter grid. The grid is created by applying the Podvin-Lecomte (P-L) finite-difference travel-time algorithm to the earth model defined by **m**, using the location of the *i*th station as the "source" in the calculation. We have developed the necessary algorithms for mapping our universal velocity model to a Cartesian block model needed by the P-L algorithm, and for mapping the 3-D Cartesian travel-time grids to geographic grids. Additionally, the P-L algorithm has been extended to compute the sensitivities of travel times to block velocities, as needed by the conjugate gradients method. The sensitivities are mapped from Cartesian blocks to the universal model parameterization. We note that our joint inversion algorithm is fully nonlinear with respect to both the velocity model and event locations since travel-time modeling and event relocation are performed for each update of **m**. However, this comes at a high computational price and we are also allowing for multiple steps of the conjugate gradients iteration before the P-L modeling is repeated.

Work is also progressing on the definition of more refined starting velocity models for other areas of the Group 1 region. Thus, Chinese earthquake bulletin data are being inverted to define variations of crust and upper mantle structure throughout that country, and currently available published research is being surveyed for other areas of interest. For example, published data on the Korean peninsula are being reviewed and integrated to formulate a velocity model for use in the calibration of IMS station KSRS. Such studies include the waveform analysis of teleseismic pPM and pP phases for an event offshore of North Korea that has provided estimates of Moho depths for five areas in the border regions between northern Korea and northeastern China (Shin and Baag, 2000). These estimates varied from 25 to 35 km, in good agreement with the crustal thickness of 29-36 km over North Korea inferred by Pak et al (1987) using regional gravity and seismic sounding data. Reported velocity profiles for the Korean peninsula vary, with anywhere from 1 to 8 crustal layers, and include an unusual low-velocity crustal layer which has been inferred to lie beneath the Yangsan Fault region in eastern South Korea (Kim, 1999). It is anticipated that the initial regional velocity models determined on the basis of such published data will subsequently be tested using available ground truth data and refined using the joint tomographic inversion and hypocenter relocation techniques which were described above.

CONCLUSIONS AND RECOMMENDATIONS

During the past year we have continued with our comprehensive program to calibrate the 30 Group 1 IMS stations of eastern Asia in an attempt to improve seismic location capability in that area. A preliminary composite 3-D velocity model for the entire region has been formulated and an efficient finite difference ray tracing code for computing travel times through such models has been implemented and tested. Evaluation of the DSS velocity model for the FSU has continued, and ground truth Soviet PNE data recorded at or near the Group 1 IMS stations BRVK, NRI, TIK, YAK, PDY and AAK have been carefully analyzed and used to produce travel-time residual maps with respect to both the default IASPEI91 travel-time table and the travel times predicted by ray tracing through our preliminary 3-D velocity model. It has been demonstrated that the travel-time residuals with respect to our 3-D model are significantly smaller than those computed with respect to the corresponding IASPEI91 model, with most stations showing an average bias near zero for the former model. An initial event location test conducted using data recorded at these "IMS stations" from 14 Soviet PNE tests has been conducted and used to demonstrate that the new 3-D velocity model provides significantly more accurate seismic locations for these ground truth explosions than does the default IASPEI91 model. Similarly encouraging results have been obtained from seismic location analyses of the data recorded from a ground truth earthquake located near the IMS station PRPK in Pakistan, in that the seismic locations determined using our WINPAK3D velocity model with various subsets of the observed data have been shown to be significantly

more accurate than the corresponding locations obtained using the IASPEI91 model. Current effort on the project centers on the development of more detailed velocity models for the remaining Group 1 IMS station areas and on the refinement of the preliminary 3-D velocity models through tomographic inversion analyses. A sophisticated tomographic inversion algorithm has now been implemented which will be applied to a variety of explosion and earthquake travel-time data collected for events in the Group 1 IMS station region. In this approach, a joint inversion will be performed to simultaneously determine earthquake locations, revised velocity model parameters and empirical corrections in a statistically consistent fashion, which takes full account of all available data, as well as the uncertainties in these data. The resulting refined 3-D velocity models and associated empirical corrections will then be used to update the SSSC estimates for the Group 1 IMS stations.

REFERENCES

Johnson, M and C. Vincent (2001), "Development of a 3-D Velocity Model of the India-Pakistan Region for Improved Seismic Event Location," submitted to *Bull. Seism. Soc. Am*., February.

Kim, W. (1999), P-wave velocity structure of upper crust in the vicinity of the Yangsan Fault region," *Geosciences Journal*, **1**, 17-22.

Murphy, J., W. Rodi, M. Johnson, I. Kitov, D. Sultanov, B. Barker, C. Vincent, V. Ovtchinnikov and Y. Shchukin (2001), "Seismic Calibration of Group 1 IMS Stations in Eastern Asia for Improved IDC Event Location," SAIC-01/1021.

Pak, C. S., I.T. O and P. S. Kim (1987), "A study for determination of the crustal thickness of Korea," *Geology and Geography Chosen* (Korea), **6**, 3-7.

Podvin, P. and I. Lecomte (1991), "Finite Difference Computation of Traveltimes in Very Contrasted Velocity Models: A Massively Parallel Approach and Its Associated Tools," *Geophys. J. Int.* **105**, 271-284.

W. Rodi and M.N. Toksöz (2000). Grid-search techniques for seismic event location, *Proceedings*, 22nd Annual DoD/DOE Seismic Research Symposium, New Orleans.

Shin, J. S. and C. E. Baag (2000), "Moho depths in the border region between northern Korea and northeastern China from waveform analysis of teleseismic pMP and pP phases," *Geosciences Journal*, **4**, 313-320.

LLNL CALIBRATION PROGRAM: DATA COLLECTION, GROUND TRUTH VALIDATION, AND REGIONAL CODA MAGNITUDE

Stephen C. Myers, Kevin Mayeda, William R. Walter, Craig A. Schultz, Jennifer L. O'Boyle, Abraham Hofstetter*, Arthur J. Rodgers, and Stanley D. Ruppert

Lawrence Livermore National Laboratory, Geophysical Institute of Israel*

Sponsored by National Nuclear Security Administration
Office of Nonproliferation Research and Engineering
Office of Defense Nuclear Nonproliferation

Contract No. W-7405-ENG-48

ABSTRACT

Lawrence Livermore National Laboratory (LLNL) integrates and collects data for use in calibration of seismic detection, location, and identification. Calibration data are collected by 1) numerous seismic field efforts, many conducted under National Nuclear Security Administration (NNSA) Research Opportunity Announcement (ROA) and Defense Threat Reduction Agency (DTRA) Program Research and Development Announcement (PRDA) contracts, and 2) permanent seismic stations that are operated by national and international organizations. Local-network operators and international organizations (e.g. International Seismic Centre) provide location and other source characterization (collectively referred to as source parameters) to LLNL, or LLNL determines these parameters from raw data. For each seismic event, LLNL rigorously characterizes the uncertainty of source parameters. This validation process is used to identify events whose source parameters are accurate enough for use in calibration.

LLNL has developed criteria for determining the accuracy of seismic locations and methods to characterize the covariance of calibration data sets. Although the most desirable calibration events are chemical and nuclear explosions with highly accurate locations and origin times, catalogues of naturally occurring earthquakes offer needed geographic coverage that is not provided by man-made sources. The issue in using seismically determined locations for calibration is validating the location accuracy. Sweeney (1998) presented a 50/90 teleseismic, network-coverage criterion (50 defining phases and 90° maximum azimuthal gap) that generally results in 15-km maximum epicenter error. We have also conducted tests of recently proposed local/regional criteria and found that 10-km accuracy can be achieved by applying a 20/90 criterion. We continue to conduct tests that may validate less stringent criteria (which will produce more calibration events) while maintaining desirable location accuracy. Lastly, we examine methods of characterizing the covariance structure of calibration data sets. Each data set is likely to be affected by distinct error processes that result in a distinct covariance structure. We present covariance models for select data sets and demonstrate how these data sets can be integrated into one calibration-event catalog.

LLNL has developed a robust magnitude calibration methodology for sparsely distributed regional stations using narrow band coda envelopes. This technique provides stable magnitudes for small events that make detection and identification calibration possible at low magnitudes. This approach has most recently been applied to International Monitoring System (IMS) stations located in Israel, Jordan and Egypt for events that span local and near regional distances. Our preliminary results show that a magnitude estimate from one station using the coda is equivalent to a network average of roughly 9 stations when using traditional magnitudes (e.g., m_b(P), M_L, M_d). The stability of the coda comes from measuring a long length of coda using a calibrated synthetic envelope as an empirical metric. We relate the non-dimensional coda amplitudes to an absolute scale by tying them to independent moment estimates from larger waveform-modeled events. Unlike most narrow band magnitudes, this approach yields an azimuthally averaged, moment-rate spectrum that is completely corrected for path and site effects. The resultant magnitudes from the spectra (e.g., M_w and m_b) are fully transportable and do not suffer from regional bias.

KEY WORDS: calibration events, event location, coda magnitudes, validation.

OBJECTIVE

Introduction

Lawrence Livermore National Laboratory's (LLNL's) seismic calibration program aims to improve prediction of both earth-model-based parameters – such as path-dependent travel time and amplitude – and subsequently determined source parameters – such as location and magnitude. An important component of this effort is the integration and development of accurate calibration (a.k.a. ground truth [GT]) events, for used in the construction or validation of earth models and empirical corrections (Schultz et al., 1998; Myers and Schultz 2000). In our integration effort we collect calibration events from the seismological community, validate location parameters, and in some instances determine parameters that have not been included by the contributor (e.g. origin time or magnitude). Below, we briefly describe our efforts to collect new calibration data. Then we focus on two of the key methodologies that we use in integration, 1) validation of location parameters, and 2) magnitude determination.

Teaming with numerous groups, LLNL has succeeded in obtaining ROA contracts with the object of developing new calibration events. These efforts focus on collection of calibration events in the European Arctic and the Middle East. In several cases temporary stations will be deployed and mine-related or dedicated explosions will be recorded. In other cases the focus is on passive data collection. These projects will provide calibration data with accurate or fiducial hypocenter parameters and regionally determined magnitudes.

As a complement to LLNL's calibration-event collection efforts, we integrate a large number of events from the general seismic community. Contributors range from local network operators and global catalogs, to event relocations from individual researchers. We find that the accuracy of location parameters from these sources varies significantly, and that a rigorous validation effort is required to characterize the uncertainty of each location parameter. For instance, event locations are usually contributed with formal uncertainties only, requiring an assessment of absolute accuracy. LLNL's work has helped to establish network coverage criteria as a means to assess epicenter accuracy, and our ongoing efforts continue to test these criteria. Below, we discuss epicenter accuracy criteria for teleseismic networks and for local networks.

Event magnitude is a crucial parameter in seismic monitoring, yet many contributed events either do not include magnitude or the magnitude determination is preliminary in nature. For events that are recorded teleseismically, the magnitude is generally reliable, due to the number of reporting stations and relatively low variance amplitude observations. However, events that are only recorded on regional networks are typically unreliable, due to the small number of recording stations and high variance amplitude observations. Therefore, LLNL has developed a stable magnitude method based on coda envelope measurements that can be reliably used even for single-station magnitude determination.

RESEARCH ACCOMPLISHED

Seismic Calibration Studies

LLNL is teamed with a number of organizations – domestic and international, academic and private – through the NNSA ROA contracting mechanism, to conduct calibration studies. Figure 1 shows the number and geographic extent of these projects. Projects range from the European Arctic, Turkey, Saudi Arabia, and a broad Middle East calibration effort.

In the European arctic LLNL is working with partners NORSAR and KRSC on the ROA contract to provide ground truth mining explosions for key stations of the IMS network and other stations of interest in northern Fennoscandia and northwestern Russia. In Turkey LLNL is involved in a project to conduct a calibration explosion in Lake Van that will yield calibration and phenomenological data. Also in Turkey and Israel, we are working with in-country collaborators to implement coda-based magnitudes in the routine production of catalogs. Finally, LLNL is working with collaborators in Saudi Arabia to deploy seismic instrumentation for the purpose of calibration event data collection.

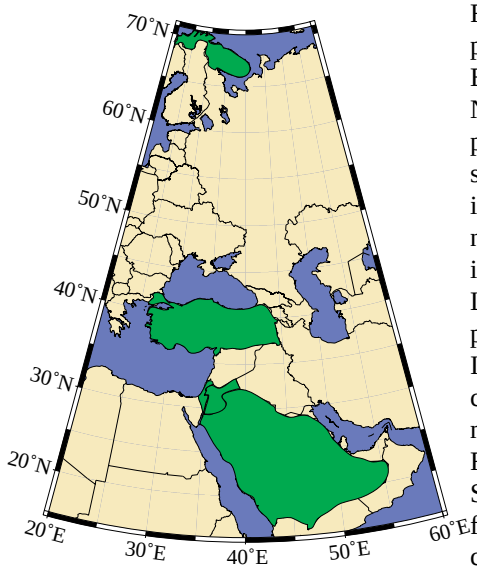

Figure1. LLNL is involved in collaborative projects in Eurasia and the Middle East. In the European arctic LLNL is working with partners NORSAR and KRSC on the ROA contract to provide ground truth mining explosions for key stations of the IMS network and other stations of interest in northern Fennoscandia and northwestern Russia. In Turkey LLNL is involved in a project to conduct a calibration explosion in Lake Van that will yield calibration and phenomenological data. Also in Turkey and Israel, we are working with in-country collaborators to implement coda-based magnitudes in the routine production of catalogs. Finally, LLNL is working with collaborators in Saudi Arabia to deploy seismic instrumentation for the purpose of calibration event data collection.

Epicenter Validation

Accurate event locations are a cornerstone of travel-time calibration. Standard seismic location uncertainty analysis provides an estimate of location precision, but mislocation due to model-based travel-time prediction uncertainty and bias are typically not included in the uncertainty analysis. Therefore, validation of event accuracy is a crucial component of our calibration program. In most instances we cannot validate against fiducial locations. Therefore, we test various location metrics against known locations and assess the accuracy that each metric produces. Of the many potential metrics, we find that a network coverage criterion is the most applicable (Sweeney, 1998). Specifically, we find the azimuthal gap in station coverage to be the most important metric, followed by the number of stations used in the location. We present these criteria as a ratio (e.g. 50/90), where the first number (50) is the number of phases arrivals used in the location and the second number (90) is the largest azimuthal gap in station coverage (in degrees).

Calibration events derived from a teleseismic network (GT15)

The relatively long period covered by global seismicity catalogs (e.g. ISC) provides numerous potential calibration events for use in regional calibration. However, assessing the accuracy of these events can be problematic because the seismic locations are typically the only locations available. In some instances, however, we have locations from other sources that allow us to compare the catalog epicenter with a much more accurate location. Sweeney (1998) compared teleseismic locations to accurate local network locations and found that a 50/90 criterion produced epicenters with 20-km accuracy (GT20). Myers and Schultz (2000) used updated local network locations and found that in all test cases teleseismic locations meeting 50/90 were within 15 km of the reference location (Figure 2).

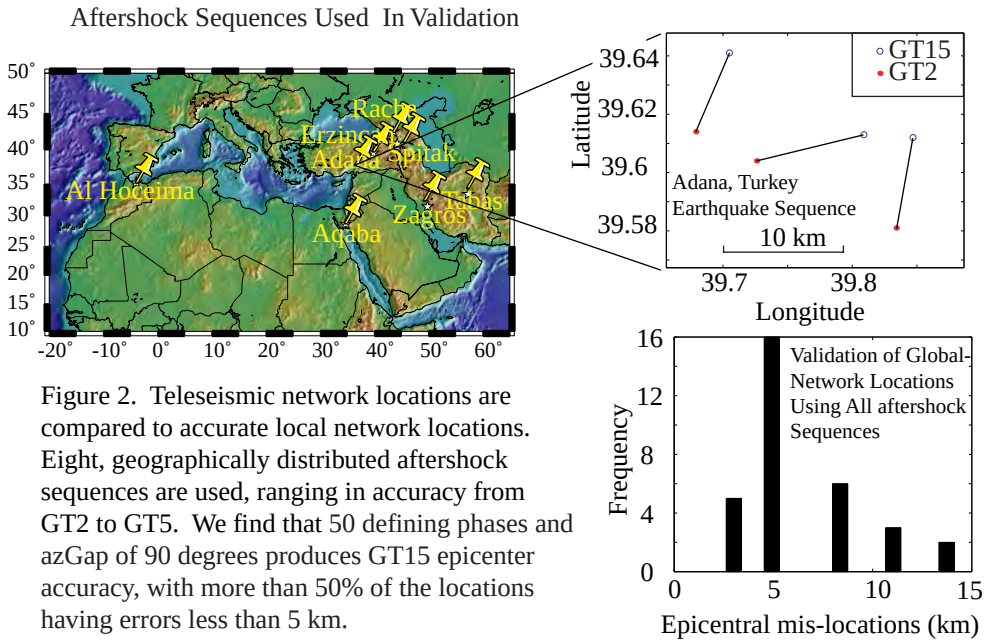

Figure 2. Teleseismic network locations are compared to accurate local network locations. Eight, geographically distributed aftershock sequences are used, ranging in accuracy from GT2 to GT5. We find that 50 defining phases and azGap of 90 degrees produces GT15 epicenter accuracy, with more than 50% of the locations having errors less than 5 km.

By applying the 50/90 criterion to teleseismic catalogs, we identify thousands of calibration events with good geographic distribution throughout Eurasia. Below, we describe criteria for local networks that can produce more accurate calibration events, but the geographic distribution of these events is poor compared to the 50/90 epicenters. By combining 50/90 events with more accurate calibration events, we obtain the high-quality travel-time calibration in limited areas and good calibration and uncertainty characterization over broad areas.

Calibration events from a local-network (GT10)

The most accurate, seismically constrained calibration events come from networks that are 1) close to the event and 2) contain numerous, well-distributed stations. The events can provide improved travel-time calibration because uncertainty associated with the event position is small. For convenience we apply the network coverage criteria (defined above) to local/regional networks.

Recently, a 10/120 local/regional coverage criterion was proposed for GT5 events (Bondar, personal communication), with all stations within 250 km and at least one station within 30 km. In order to test this criterion, we use the 1999 Dead Sea calibration explosions. These events are some of the select few events with fiducial locations that can be used to test epicenter accuracy for a dense local/regional network. There are about 50 stations of the joint Israel/Jordan network within 250km of the Dead Sea shots. To test the regional/local network location accuracy, we repeatedly sampled the network to meet the minimum 10/120 criterion. We located the explosion using 1000 random (non-redundant) network samplings to test the reliability of location accuracy under a variety of circumstances. We find that the resulting locations are accurate to 20 km at the 90% confidence level (Figure3). This test was conducted using a number of 1-dimensional velocity models – including IASPI91 and a local Israeli model (Shapiro, personal communication), and the results did not change significantly. It may be possible to improve upon the location with a 3-dimensional model. However, for the purposes of establishing coverage criteria, we want to minimize the influence of the velocity model because criteria that include the velocity model are not easily portable.

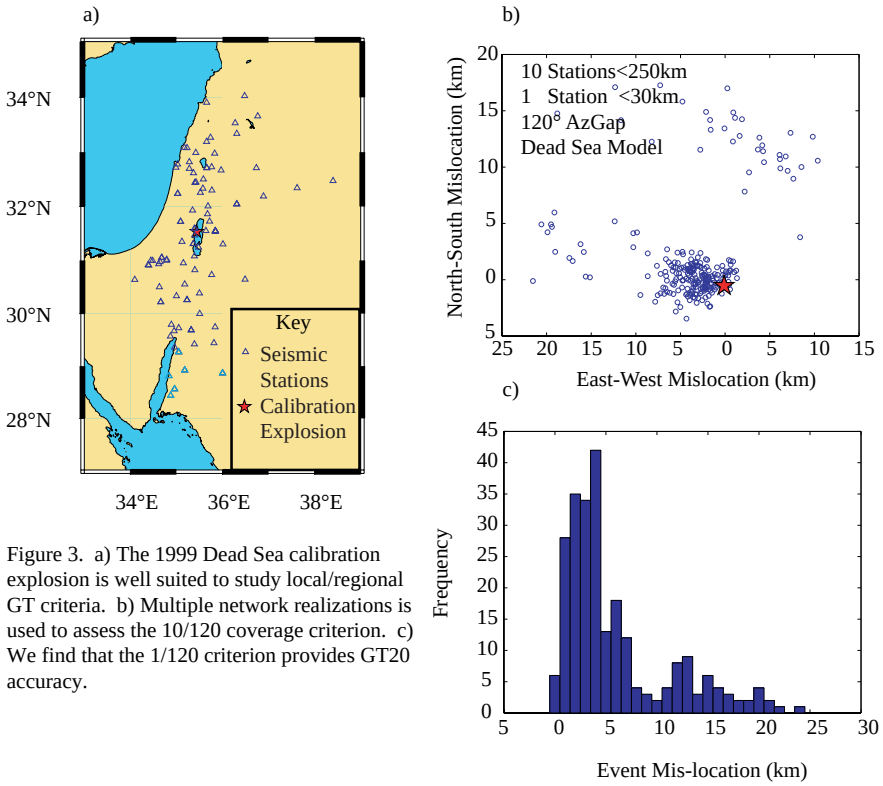

Figure 3. a) The 1999 Dead Sea calibration explosion is well suited to study local/regional GT criteria. b) Multiple network realizations is used to assess the 10/120 coverage criterion. c) We find that the 1/120 criterion provides GT20 accuracy.

In order to establish a local/regional network criterion that improves upon the global network locations, we relocated the largest Dead Sea explosion 1000 times with variable network coverage (Figure 4). The results of this experiment show that – like teleseismic-network locations – azimuthal gap is the most important network coverage parameter, followed by the number of stations. When a 20/90 criterion is met, we locate the Dead Sea explosion to within 10 km of the known location. It is interesting to note that when all of the 50 stations are used, the location error can be as high as 5 km, depending on the velocity model used.

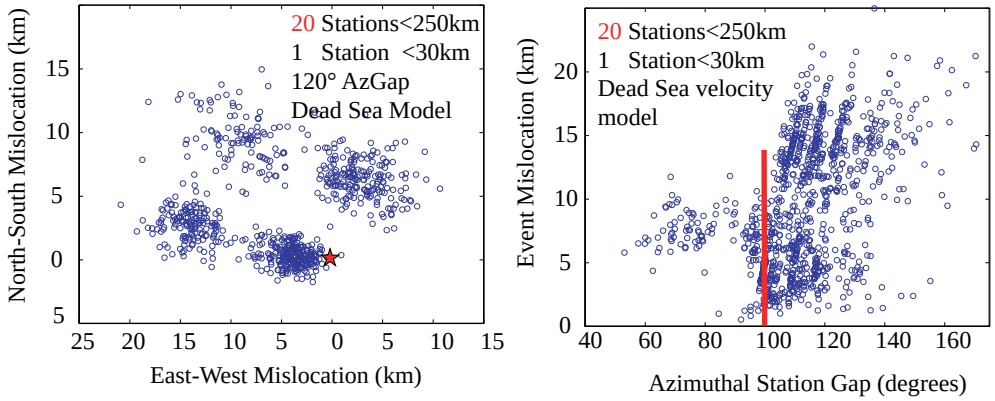

Figure 4. Multiple 20-station-network realizations are used to relocate the largest Dead Sea calibration explosion. a) Realizations show a number of clusters that can be related to which close-in station is present in the realization. b) For a 20 station network, we find that GT10 can be achieved with an azimuthal gap of 100°. A few locations exceed 10km error, but we define GT level as a confidence which allows for outliers.

Coda Magnitude

Magnitude estimation forms an integral part in any seismic monitoring endeavor, especially for nuclear explosion and treaty monitoring. Regional seismic discriminants used in nuclear explosion monitoring are often functions of magnitude such as m_b:M_s, high-to-low spectral ratios, and nuclear explosion yield estimation. Regional magnitudes used in discriminants for small-to-moderate sized crustal events using P_n, P_g, and L_g all suffer from source and path heterogeneity. As a consequence, multi-station averaging is necessary to reduce the amplitude variability. For IMS monitoring, the average station spacing is larger than 1000 kilometers; thus, the ability to measure a stable magnitude for small-to-moderate-sized events becomes difficult because of limited numbers of stations and averaging of measurements. As a result magnitudes for small-to-moderate-sized events cannot be measured teleseismically and require a stable, single-station regional measure of earthquake size. We believe our methodology can provide a "universal" and transportable magnitude based on P and/or S coda that can be easily tied to the already established teleseismic catalogs.

Coda Magnitude Methodology

Following a methodology outlined in Mayeda and Walter (1996), we apply a narrow-band filter for 13 frequency bands ranging between 0.03 and 8.0 Hz for the two horizontal components (Figure 5). This range of frequency bands is chosen such that we can compute M_w. We then take the $\log_{10}$ of envelopes, average the two horizontal envelopes, then smooth them. After forming narrow-band envelopes for all the events, we measure the velocity of the peak S-arrival for each frequency band and plot versus distance. For the longest periods the peak corresponds to the Rayleigh or Love wave, but because we empirically correct for each frequency band, mixing wave types makes no difference on the final results. Since our goal was to calibrate both local and regional-distance earthquakes, we tried different functional forms that matched our data. We found that a simple hyperbola did an excellent job at simultaneously fitting the local and regional phase velocity,

$$v(x) = c0 - [c1/(c2 + x)] \quad (1)$$

where x is the distance and $c0$, $c1$ and $c2$ are constants.

We found that a simple analytic form that resembles the single-scattering model of Aki (1969) generally does a good job at fitting the shapes of both regional and local coda envelopes. The main difference is that we had better fits by forming the envelopes relative to the direct S (or L_g) arrival, not the origin time as is done in nearly all scattering models. The analytic expression that we used to fit the observed narrow-band envelopes at center frequency f is

$$A_c(f,t \mid x) = A_o \bullet H\left(t - \tfrac{x}{v(x)}\right) \bullet \left(t - \tfrac{x}{v(x)}\right)^{-\gamma} \bullet exp\left(-b \bullet \left(t - \tfrac{x}{v(x)}\right)\right) \quad (2)$$

where A_o is a source constant, H is the Heaviside step function, t is the time in seconds from the origin, x is the distance in kilometers, $v(x)$ is the velocity of the peak arrival in km/sec and γ and b control the coda decay. It should be noted, however, that the more complex 2-D and 3-D multiple-scattering models could also be used (see *Sato and Fehler* review, 1999). For our purposes we only want an empirical fit to the data over a range of distances and frequency bands and thus this simple form is completely adequate for this purpose. Furthermore, all the scattering models have implicit assumptions on the attenuation and geometrical spreading, assumptions we feel are inappropriate given that our data span both local and regional distances.

Since we are not explicitly applying a scattering model that has attenuation built into its formulation, we need to find an empirical distance relation for the coda amplitudes. This is preferable since we do not want to make any assumptions about homogeneous coda decay in a region – an assumption commonly made in past coda studies. Instead, we incorporate both geometrical spreading and attenuation (whether it stems from scattering, absorption, leakage etc.) using a strictly empirical form. We use Equation 2 as a means of matching the observed coda envelope shape to extract a coda amplitude measurement. In essence, Equation 2 is used as an empirical metric and thus any functional relationship that fits the data could have been used. The steps described here allow one to measure coda amplitudes, which are initially in dimensionless units, correct for distance and site effects and tie to an absolute measure. The validation of this approach is simple. We verify that we obtain the same source spectra at different stations and distances for the same event (thus confirming

our empirical distance corrections) and then verify that our inferred moments are comparable to those that were independently determined from other means such as long-period waveform modeling.

Coda Shape Factors

Now that we know the velocities for each frequency band, we can fit our simple analytic form to find the coda shape parameter *b*, which controls the coda decay as measured from the direct S (or L_g) arrival. By rearranging Equation 2 and taking the $\log_{10}$ of both sides, we get

$$log_{10}\left[A_c(f,t|x) \bullet (t-\tfrac{x}{v(x)})^{\gamma}\right] = log_{10}\left(A_o \bullet H(t-\tfrac{x}{v(x)})\right) - b \bullet (t-\tfrac{x}{v(x)}) \bullet log(e) \qquad (3)$$

By plotting Equation 3 versus $[t-x/v(x)]$ the slope of the best fitting line is $b\ log_{10}(e)$.

Since we want to fit the coda at all distances, we try to measure the coda over a range of distances to determine if *b* is dependent upon distance. For the higher frequencies *b* is strongly distant dependent whereas for frequencies below ~0.5 Hz the coda shape factor is roughly constant and is smaller (*i.e.*, decays more slowly than the higher frequencies). Again, we found that a simple form of a hyperbola fit the *b* values as a function of distance *x* spanning both local and regional distances.

Simple Distance Corrections

For events in the Dead Sea rift and Gulf of Aqaba region, the Geophysical Institute of Israel routinely performs network locations and assorted magnitudes such as m_b, M_L and M_w. Now that we have the velocities and coda shape factors we set A_o in Equation 2 to unity, take the $\log_{10}$ to be consistent with our observed envelopes, then dc shift the synthetic envelopes to fit the observed envelopes using an L-1 norm. The magnitude of the dc shift is the non-dimensional coda amplitude. This amplitude is analogous to any direct wave measure in the sense that a distance and site correction are still required. Measuring the coda envelope amplitude over a length of time merely provides a more stable measure than using direct waves, which are of short duration and thus considerably more susceptible to interference, path heterogeneity, and source radiation pattern.

For each frequency band we subtract the network-averaged local magnitude, M_L(GII), from the coda amplitude and plot versus distance in kilometers. We used events in a narrow magnitude range for each frequency band (*e.g.*, around +/- 0.25 magnitude units) when determining the distance corrections to avoid potential biases related to corner frequency scaling. Figure 6 shows source-normalized coda amplitude (at 1 Hz) as a function of distance. We tried a number of classic attenuation relations that are routinely applied in direct-wave studies but found that the following empirical form,

$$A(f,x) = \left[c1 + \left(x/c2\right)^{c3}\right]^{-1} \qquad (4)$$

did the best job at simultaneously fitting local and regional distance coda, where *x* is the epicentral distance, *f* is the center frequency, and *c1, c2, c3* are constants. From Figure 6 we observe that the coda-derived amplitude at 1 Hz begins to decay at around 150-km distance, a likely result of local 3-D crustal scattering transitioning to guided 2-D L_g-coda at regional distances. This observation of constant coda amplitude in the local distance range has long been hypothesized in local S-wave coda studies of coda Q and site response. When we apply this to the broader region, we might expect different distant-dependent behavior such as velocity, coda shape factor and attenuation. These are elements of ongoing study.

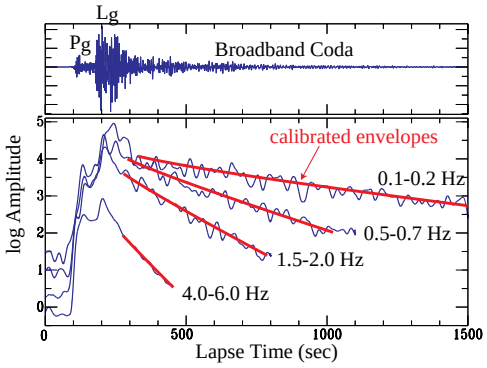

Figure 5. Example of a broadband waveform and selected narrowband envelopes (blue) along with calibrated synthetic envelopes (red).

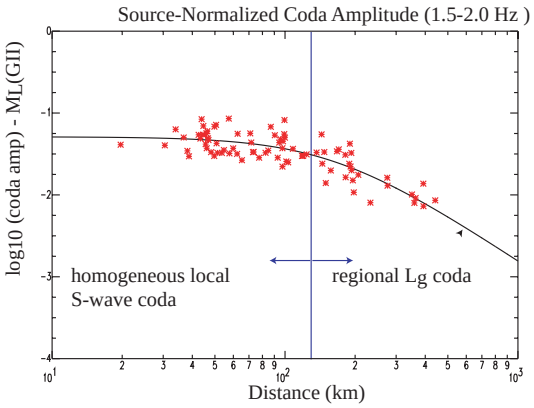

Figure 6. Source-normalized coda amplitudes for events of roughly the same M_L. Notice that the coda is roughly constant for the first 100 to 150 km and then begins to decay after this distance.

Green's Function and Seismic Moment Corrections

Up to this point, we have measured non-dimensional coda envelope amplitudes and corrected for distance. In this section we relate these values to an absolute scale, namely seismic moment, to obtain a moment-rate spectrum. Our only assumption is that the S-wave source spectrum is flat below the corner frequency. We purposely underestimate where the corner frequency lies for our set of calibration events to avoid flattening our spectra unrealistically.

We used a 1-D reflectivity code to waveform model a series of moderate-sized earthquakes in the region to estimate seismic moment. This range of event sizes is needed to define the moment corrections ranging between ~0.03 to ~2.0 Hz, but larger Harvard CMT moments would only allow calibration of the lowest frequencies. As part of the spectral calibration, we add constants to all amplitudes for each frequency band such that the seismic moments, in a least squares sense, agree with the waveform modeled results. Since these are frequency-dependent corrections, independent of distance, the corrections must be uniformly applied to all distance-corrected amplitudes. Detailed analysis shows that with conservative estimates of the corner frequency, we can flatten the spectra for a range of event sizes. For events that are too small to be waveform modeled, we can still estimate moment using periods less than a few Hertz.

Testing and Validation

Figure 7 shows spectra for two events, one is nodal at BGIO, and the other is not. In both cases, the spectra at KEG and BGIO are virtually identical, despite a significant source-radiation pattern difference. If we compare individual amplitudes for a large number of events, we also see that the inter-station variation is also very small. Finally, we verify that our absolute amplitudes are correct by computing M_w from the lowest frequencies of our measured spectra and compare against independent M_w's from waveform modeling (note: we used different events than were used in the moment calibration step). Figure 8 shows that there is excellent agreement between the two approaches.

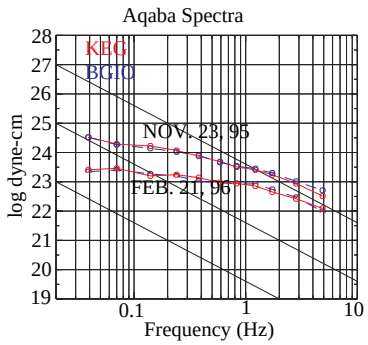

Figure 7. Spectra for two events recorded at BGIO and KEG are practically identical. Though the event of Nov. 23 is nodal at BGIO the averaging properties of the coda eliminate the radiation pattern.

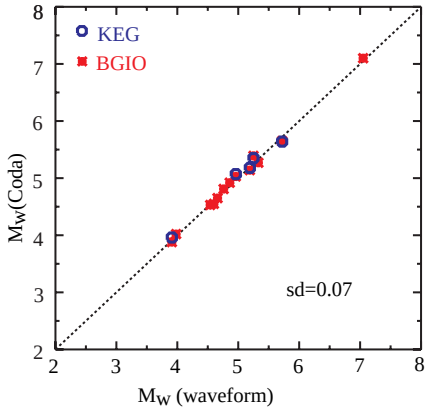

Figure 8. Our single-station coda-derived M_W estimates are in excellent agreement with waveform modeled events, comparable to results from the western United States.

CONCLUSIONS AND RECOMMENDATIONS

Integration of calibration events from external contributors and LLNL's internal efforts requires rigorous validation procedures. We anticipate significant additions to the LLNL calibration database from work conducted under the NNSA ROA contracts. These efforts will provide new benchmark events for testing location accuracy criteria, as well as other events that will require criterion-based validation. The ROA efforts will also produce a catalog of coda-based magnitudes that will aid in subsequent monitoring studies.

We find a network coverage criterion to be best suited for epicenter accuracy validation. For events determined with a teleseismic network we use the 50/90 criterion of Sweeney (1998). After revision of benchmark events, we find that the 50/90 criterion provides 15-km accuracy as opposed to the 20-km accuracy reported by Sweeney. For local networks we test the 10/120 criterion of Bondar (personal communication), and find that this criterion provides 20-km accuracy. By increasing the number of network stations to 20 and reducing the azimuthal gap to 90°, we find that accuracy can be improved to 10 km.

We have developed a code-based magnitude determination that is particularly applicable to sparse regional networks. The method is based on simultaneous analysis of narrow-band coda envelopes. Raw amplitude observations are calibrated using waveform modeling results for large events and assuming a simple source spectral model. We provide tests demonstrating the robustness of the method and favorable comparisons to independent waveform modeling results.

REFERENCES

Aki, K. (1969). Analysis of the seismic coda of local earthquakes as scattered waves, *J. Geophys. Res.*, **74**, 615-631.

Mayeda, K., and Walter, W. (1996). Moment, energy, stress drop, and source spectra of western United States earthquakes from regional coda envelopes, *J. Geophys. Res.*, **101**, 11195-11208.

Myers, S.C. and C.A. Schultz (2000). Improving sparse network seismic location with Bayesian Kriging and teleseismically constrained calibration events, *Bull. Seism. Soc. Am., 90*, 199-211.

Myers, S.C. and C.A. Schultz (2000). Evaluating Reference Events for Seismic Event Location, UCRL-JC-143948 Abs.

Schultz, C.A., S.C. Myers, J. Hipp, and C.J. Young (1998). Nonstationary Bayesian kriging: A predictive technique to generate spatial corrections for seismic detections, location, and identification, *Bull. Seismol. Soc. Am.*, **88**, 1275-1288.

Sweeney, J. 1998) Criteria for selecting accurate event locations from NEIC and ISC bulletins, UCRL-JC-130655,1998.

METHODS OF IMPROVING REGIONAL SEISMIC EVENT LOCATIONS

Delaine Reiter[1], Carolynn Vincent[1], Michelle Johnson[1], and William Rodi[2]

Weston Geophysical Corporation[1]
Massachusetts Institute of Technology[2]

Sponsored by Defense Threat Reduction Agency

Contract No. DTRA-00-C-0098

ABSTRACT

In this paper we investigate the effect that depth-dependent Source Specific Station Corrections (SSSC's) have on improving regional seismic event location accuracy. To accomplish this we have relocated events considered GT5 or less that occur within the region encompassed by Weston Geophysical's regional 3-D model of the India-Pakistan region (WINPAK3D) using different depth-dependent SSSC's. By comparing the hypocenters produced using SSSC's at different depths to the ground truth location, we have gained insight into the minimum number of depth-dependent SSSC's that must be implemented in current automatic processing routines for accurate and efficient regional event location.

For a crustal earthquake, we generated SSSC's for a suite of depths by calculating travel times for WINPAK3D relative to the global IASPEI91 model (Kennett and Engdahl, 1991) to all regional stations. We then estimated the event hypocenter using the International Seismological Center (ISC) location as an initial hypocenter and two different but closely related methods of SSSC application and hypocenter location. For both location procedures, we compared the location derived from application of the different depth-dependent SSSC's to the ISC location in order to determine if there were significant differences in the hypocenters. Our initial results suggest that two SSSC's, one for the crust and one for the mantle, may be the minimum number of SSSC's to achieve the current goal in location accuracy in our study region.

KEY WORDS: depth-dependent SSSC, regional event location, 3-D velocity model

OBJECTIVES

Introduction

The overall objective of this research is to produce a fully 3-D grid-search location algorithm that can more accurately locate seismic events using the International Monitoring System (IMS) network. Our current algorithm implements a regional event location method, one that incorporates 3-D velocity models and travel time predictions with a nested grid-search location technique. When high resolution regional 3-D velocity models are available for an area of interest, they can be used to compute accurate travel times of regional seismic phases such as *Pn*, *Pg*, *Sn*, and *Lg*. Travel times calculated from 3-D models can then be used to develop SSSC's that can be implemented by monitoring organizations to further improve regional event locations. One important question that remains to be answered in the operational usage of SSSC's concerns the role that depth-dependence plays in improving the seismic event location. We know from previous analyses (Rodi and Murphy, 2000) that SSSC's are neither constant nor linear as a function of focal depth. However, it is not clear if producing numerous SSSC's with depth using a small sampling interval will net significant improvement in event location. In this study we have initiated an investigation into the necessity and specifics of utilizing depth-dependent SSSC's. Our objectives are two-fold: (1) We want to determine the most efficient method for utilizing depth-dependent SSSC's in regional event location by considering two different techniques for their implementation, and (2) we want to determine the minimum number of depths for which SSSC's must be generated for efficient and accurate regional

event location in the WINPAK3D region (Figure 1). In the following sections, we present the preliminary results aimed at completing these two research objectives.

Figure 1. WINPAK3D (Weston India-Pakistan 3-D velocity model) study region. WINPAK3D encompasses a variety of different tectonic regimes from stable shield (southern India) to active collisional deformation zones. Crustal thickness varies between 15 km beneath the Arabian Sea to greater than 70 km beneath the Himalayas. The variations in crustal and upper mantle properties in this region provide an excellent testbed for this study aimed at examining the improvement in location accuracy offered by depth-dependent SSSC's.

RESEARCH ACCOMPLISHED

Setting

The Weston India Pakistan 3-D velocity model (WINPAK3D) is a 3-D P-wave velocity model of the crust and upper mantle developed to improve location estimation capability in the India-Pakistan region (Figure 1), especially for small, sparsely recorded regional events. The model was developed by intgrating the results of more than sixty previous studies related to crustal velocity structure in the region. Previous testing demonstrated that this model significantly improves location accuracy in this region, especially for small, regionally recorded events (Johnson and Vincent, 2001; Bernard-Johnson *et al*., 2000). This model has been used to calculate 2-D and 3-D SSSC's for stations within the region, including NIL, for use in regional event location, as described below.

On 14 February 1977, an m_b=5.2 (USGS) earthquake occurred in the region near Nilore, Pakistan. This event was well recorded by two temporary local networks (Tarbela and Chasma) in addition to the array at Nilore, Pakistan (NIL). Based on data from these three local networks, Seeber and Armbruster (1979) published a detailed study of the aftershock sequence and estimated the hypocenter of the event and associated aftershocks. The Seeber and Armbruster location is less than 5 km from the epicenters determined by both the ISC and the USGS using teleseismic and regional phase data. Based on these studies, we have assigned the Seeber and Armbruster location at least GT5 location accuracy. We compared the locations found in our study, calculated using only regional seismic phase data, to this Seeber and Armbruster ground truth location. The event was also recorded at 23 stations at regional distances

(Figure 2), and we used the bulletin data from these stations in the location efforts discussed in the following sections.

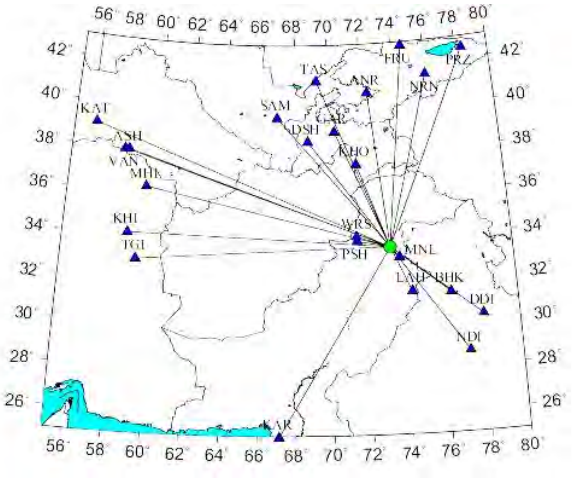

Figure 2. Regional ray coverage for the 14 February 1977 event near Nilore, Pakistan.

Calculation of SSSC's

We generated SSSC's for 23 stations within the India-Pakistan region using the WINPAK3D velocity model. Traveltimes through the WINPAK3D model were calculated from each station to all points in the 3-D space using a finite difference algorithm developed by Podvin and Lecomte (1991), as implemented by Lomax (1999). Traveltime tables were similarly calculated through a 3-D representation of the IASPEI91 velocity model (Kennett and Engdahl, 1991). The IASPEI91 traveltimes were then subtracted from the WINPAK3D traveltimes, resulting in fully 3-D SSSC's for each station. Figure 3 shows constant depth slices of the 3-D SSSC for station ASH in Turkmenistan. Note that there are significant variations in the SSSC's at different depths. 2-D constant depth slices were extracted from the 3-D SSSC's and were applied in two specific ways to the location process to investigate the requirements for applications of depth-dependent SSSC's.

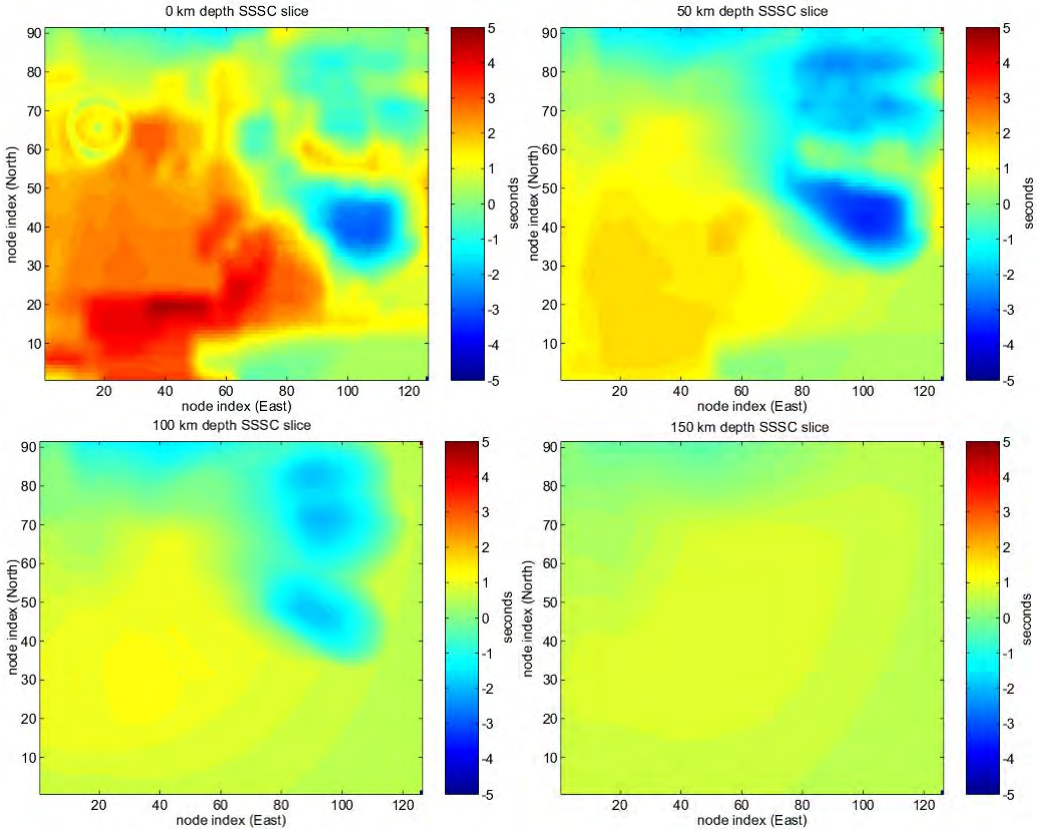

Figure 3. Constant depth slices (0 km, 50 km, 100 km, and 150 km depth) of the 3-D SSSC for station ASH derived from the WINPAK3D velocity model. The effect of the thick crust in the Himalayan region can be observed at depths greater than 100 km (blue region centered near node index 100E and 45N)

Application of SSSC's to Location

We have applied SSSC's to the location process in two different but closely related methods. For the first method, an iterative location procedure similar to current processing techniques at the prototype International Data Center (pIDC) was used to locate the seismic events with SSSC's. First, a preliminary epicenter is obtained using the network phase arrival time data. SSSC's are added to the arrival times based on the preliminary epicenter. The event is then relocated using GSEL, a 3-D grid search location algorithm (Rodi and Toksöz, 2000) and different SSSC's are added to the arrival time corrections to reflect the new location. The process is continued until the calculation converges. For the 14 February 1977 event, the hypocenter stabilized for each SSSC depth after a maximum of six iterations. The ISC hypocenter was used as the initial location.

The second method avoids the iterative process by adding the SSSC's directly to the set of traveltimes through our 3-D model, instead of to the arrival times. This results in a corrected set of travel time tables for input to a location program. GSEL is again used to locate the event within the 3-D corrected traveltime grids. However, for this method of depth-dependent SSSC application, only one computation of the grid search method is needed because the travel time grid itself was modified rather than the arrival times.

Results

We calculated locations for the 14 February 1977 event using the 23 regional *Pg* and *Pn* arrivals together with constant depth SSSC's ranging from 0 km to 180 km depth at 10 km intervals. These locations were calculated using both the one-step grid search and iterative grid search location methods. Figure 4 shows the results of these calculations. For each location, the depth mislocation, epicenter mislocation and hypocenter mislocation are shown (mislocation equals the calculated minus the Seeber and Armbruster (1979) location). For this event, which ground truth places at a depth of 14.46 km (Seeber and Armbruster, 1979), the most appropriate SSSC's range from 0 km to 30 km. For SSSC's 40 km and deeper, there is a marked increase in hypocenter mislocation, dominated by a jump in depth mislocation. This coincides with the Moho depth below the event of between 40 and 45 km. Also note that the epicenter mislocation varies by approximately a factor of 2 (between 6 and 12 km) for the entire range of depth-dependent SSSC's studied. For this event, the epicenter would have still met current CTBT location accuracy requirements of 1000 km^2. In fact, with hypocenter mislocation ranging from about 6 km to 15 km, this event is relatively well-located regardless of which constant depth SSSC is applied. However, it is important to note that the mislocation of the hypocenter calculated using uncorrected arrival times and the IASPEI91 velocity model is only 16.4 km. This is only slightly worse than that found with the least appropriate constant depth SSSC. For other events where the number of regional stations recording the event is significantly decreased, the range of mislocation may be broader, highlighting the potential need for appropriate depth SSSC's. We will continue to analyze events in this manner, particularly those with fewer regional arrivals, to further quantify the minimum number of depth-dependent SSSC's needed for efficient location algorithms.

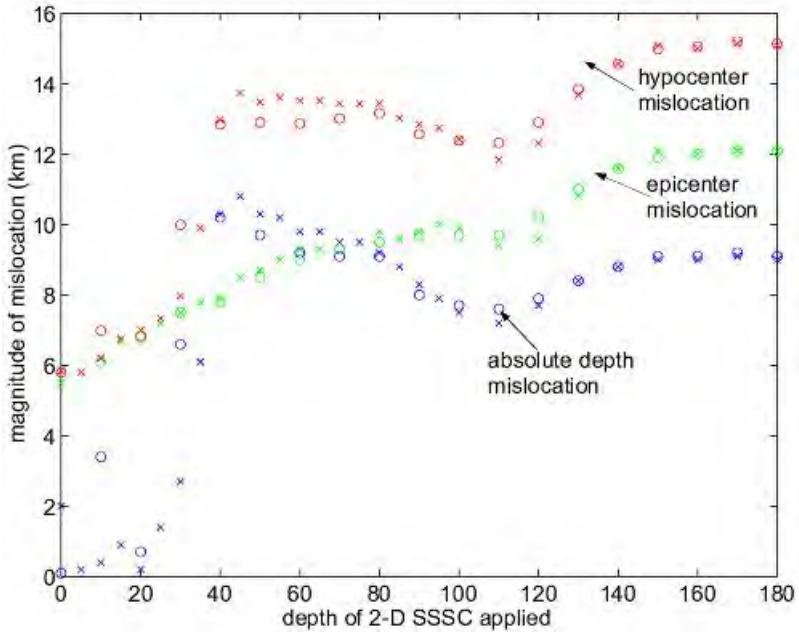

Figure 4. Mislocation of hypocenters calculated using constant depth SSSC's and 23 regional arrivals. Mislocations for hypocenters calculated by the iterative and one-step grid search are shown as circles and x's, respectively.

The differences in locations between the iterative and one-step grid search methods of location and SSSC application are minimal (Figure 4). Neither method produces locations that have consistently smaller errors. Mislocations from both methods follow the same trend, with both showing a significant jump for SSSC's 40 km and deeper. It is important to note, however, that a comparison of the rms norms produced for each hypocenter solution (Figure 5) reveals that the one-step grid search method is more successful than the iterative method at minimizing the residual norm in most cases. The one-step method is also more

efficient in implementation, taking only a fraction of the time to produce a final solution compared to the iterative method used in this study.

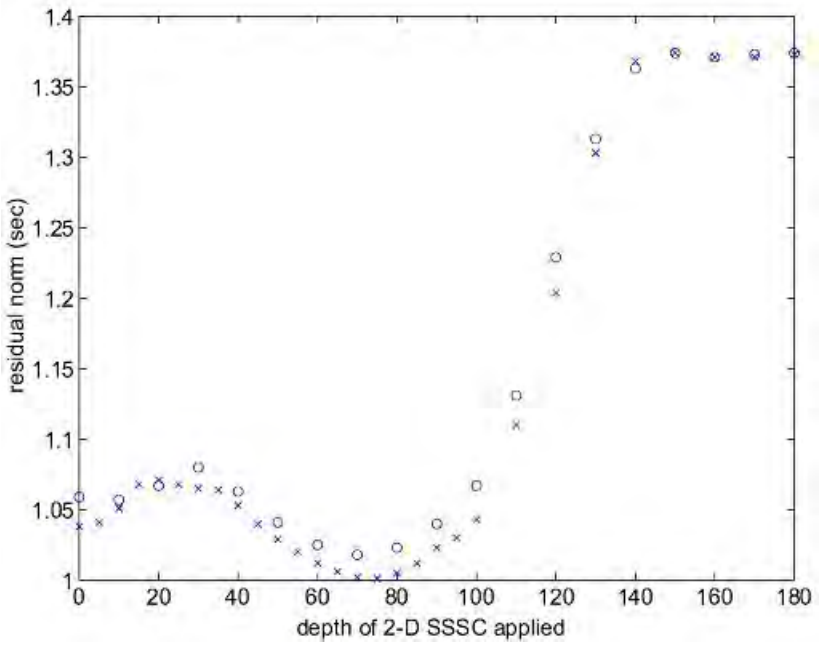

Figure 5. A comparison of rms norms for hypocenters calculated using the iterative grid search method of location plus SSSC application (circles) and the one-step grid search method for location plus SSSC application (x's). The one-step method has lower residual norms for most depths.

CONCLUSIONS AND RECOMMENDATIONS

A primary goal of this research project is the improvement of our 3-D regional grid search location algorithm. In this paper we have investigated the best method for the application of depth-dependent SSSC's. Our preliminary results indicate that by adding the depth-dependent SSSC's directly to the 3-D travel time tables developed from fully 3-D raytracing, we can increase the efficiency of the event location alogrithm while reducing the rms in the hypocenters relative to iterative techniques currently used at the pIDC and IDC. For the crustal event presented in this paper (depth of 14 km), application of a single depth SSSC at any depth between 0 and 40 km leads to a more accurate location compared to the application of a mantle SSSC. Also, we see negligible differences in the hypocenter and epicenter mislocation regardless of which SSSC depth between 0 and 40 km is used. Further study is needed to determine how many depth-dependent SSSC's are necessary to locate both crustal and sub-crustal events with sparse data, and we are continuing research on this topic.

REFERENCES

Bernard-Johnson, M., S. Rieven, C. Vincent, D. Reiter, and W. Rodi (2000), Empirical analysis of a 3-D Pakistan regionalized velocity model for improved seismic event location, *Proceedings, 22nd Annual DoD/DOE Seismic Research Symposium: Planning for Verification of and Compliance with the Comprehensive Nuclear-Test-Ban Treaty*, **02**, 06, 10pp.

Johnson, M. and C. Vincent (2001), Development of a 3-D velocity model of the India-Pakistan region for improved seismic event location, *Bull. of the Seismol. Soc. of Amer*, in review.

Kennett, B. L. N. and E. R. Engdahl (1991), Travel times for global earthquake location and phase identification, *Geophys. J. Int.*, **105**, 429-465.

Lomax, A. (1999), Probabilistic, non-linear earthquake location in 3-D media (An online guide to software), http://iapetus.unice.fr/~lomax/nlloc.

Podvin, P. and I. Lecomte (1991), Finite difference computation of traveltimes in very contrasted velocity models: a massively parallel approach and its associated tools, *Geophys. J. Int.*, **105**, 271-284.

Reiter, D., W. Rodi, M. Johnson, C. Vincent, and A. Rosca (2001), A new regional 3-D velocity model of the India-Pakistan region, *Proceedings, 23rd Annual DoD/DOE Seismic Research Review*.

Rodi, W. and J. Murphy (2000), Depth dependence of SSSC's, SAIC/Maxwell memo, 1 June 2000.

Rodi, W. and M. Nafi Toksöz (2000), Grid-search techniques for seismic event location, *Proceedings, 22nd Annual DoD/DOE Seismic Research Symposium*, **02**, 39, 9pp.

Seeber, L. and J. Armbruster (1979), Seismicity of the Hazara Arc in northern Pakistan: decollement vs basement faulting, in *Geodynamics of Pakistan*, A. Farah and K. A. DeJong (Editors), *Geological Survey of Pakistan*, 131-142.

A NEW REGIONAL 3-D VELOCITY MODEL OF THE INDIA-PAKISTAN REGION

Delaine Reiter[1], William Rodi[2], Michelle Johnson[1], Carolynn Vincent[1], and Anca Rosca[1]

Weston Geophysical Corporation[1]
Massachusetts Institute of Technology[2]

Sponsored by Defense Threat Reduction Agency

Contract No. DSWA01-98-C-0143

ABSTRACT

We have developed a 3-D velocity model for the crust and upper mantle in the India-Pakistan region (WINPAK3D) to improve regional event location. Results of extensive testing demonstrate that the 3-D model improves location accuracy for this region, specifically for the case of small, regionally recorded events, for which teleseismic data may not be available. The initial model for the region was developed by integrating the results of more than sixty previous studies related to crustal and upper mantle velocity structure. During the final year of this effort, we have developed a 3-D joint velocity tomography/event relocation to improve this preliminary velocity model. The algorithm applies an iterative, conjugate-gradients technique to minimize the misfit between calculated and observed travel times from multiple stations and events, subject to smoothness and geologic constraints. Events are relocated using the grid search location method of Rodi and Toksöz (2000) after each update of the 3-D velocity model. Travel times and their sensitivities to the velocity structure are computed with an extension of the 3-D Podvin-Lecomte (1991) method. We are applying our tomography algorithm to a suite of 580 events containing over 7,800 arrivals from the Engdahl *et al.* (1998) database.

A critical aspect of model development is validation, which we have addressed in three ways: (1) cross-validation analysis for a variety of events, (2) comparison of model-determined hypocenters with known event location, and (3) comparison of model-derived and empirically derived source-specific station corrections (SSSC's) generated for the International Monitoring System (IMS) auxiliary seismic station located at Nilore, Pakistan. The 3-D model provides improvement in regional location compared to a global 1-D model. For example, an event with a well-known location had an epicenter mislocation of only 6.1 km for the solution determined using the 3-D model, compared with a mislocation of 15.4 km for the IASPEI91 model (Kennett and Engdahl, 1991). These and other results demonstrate that 3-D models are a prerequisite for achieving improved location accuracies in areas with complex crustal and upper mantle structure.

KEY WORDS: 3-D velocity model, India, Pakistan, tomography, improved event location

OBJECTIVE

Improving seismic event location is particularly important for monitoring the Comprehensive Nuclear-Test-Ban Treaty (CTBT). The treaty requires a location accuracy of better than 1000 km^2 due to the restrictions defined both for on-site-inspections (OSI) and for using location as a discrimination tool. For small events ($m_b < 4.0$), meeting this requirement is problematic because of limited recordings and complicated crustal structure at regional distances not accounted for in the standard global 1-D models such as the IASPEI91 model (Kennett and Engdahl, 1991). Precise regional location of seismic events in the context of the CTBT requires a velocity model that accurately represents the real Earth structure, as systematic biases caused by unmodeled Earth structure are known to play an important role in earthquake location errors (e.g., Douglas, 1967; Dewey, 1972; Engdahl and Lee, 1976; Jordan and Sverdrup, 1981; Pavlis, 1992). Regional 3-D models that better represent the true Earth structure can be used to compute accurate travel times of regional seismic phases such as *Pn*, *Pg*, *Sn*, and *Lg*. Travel times calculated using 3-D models can then be used to develop source specific station corrections (SSSC's) that can be implemented by monitoring

organizations to provide improved regional event locations. Our goal is to develop a regional model of the crust and upper mantle for the India-Pakistan region that will improve event location accuracy and provide a set of improved hypocenter estimates based on that model. We are building an accurate 3-D model for the India-Pakistan region by updating a preliminary model through a joint velocity tomography and hypocenter relocation technique. Here we describe this approach in detail and our progress towards developing an accurate model for the India-Pakistan region.

RESEARCH ACCOMPLISHED

Preliminary Model

We have developed a regional 3-D velocity model of the crust and upper mantle structure, the Weston INdia/PAKistan 3-D model (WINPAK3D), to improve seismic event locations for the India-Pakistan region (Figure 1a). The region of interest has a complex tectonic history exhibited in the diverse geometries of crustal structures across the area. Using the available geophysical literature, we have compiled a detailed 3-D velocity model for the India-Pakistan region (Figure 1b). We synthesized data from approximately sixty published references relevant to the velocity structure, geology, and tectonics throughout the region. These references include data such as seismic reflection and refraction surveys (*i.e.* DSS profiles, *Pn* tomography, *Pnl* waveform inversion), interpretations of gravity data, surface wave studies, and receiver function analyses. Because these data sources vary in spatial coverage, resolution, and the number of constraints, the model varies in a similar manner. The velocity model is defined on a grid of one-degree by one-degree blocks and 5 km depth intervals from 0 to 75 km. We have appended the IASPEI91 model (Kennett and Engdahl, 1991) to the base of the preliminary velocity model, beginning at 80 km depth and extending to 700 km depth, to accommodate raypaths that travel into the upper mantle. See Johnson and Vincent (2001) for additional details on the development of the WINPAK3D model.

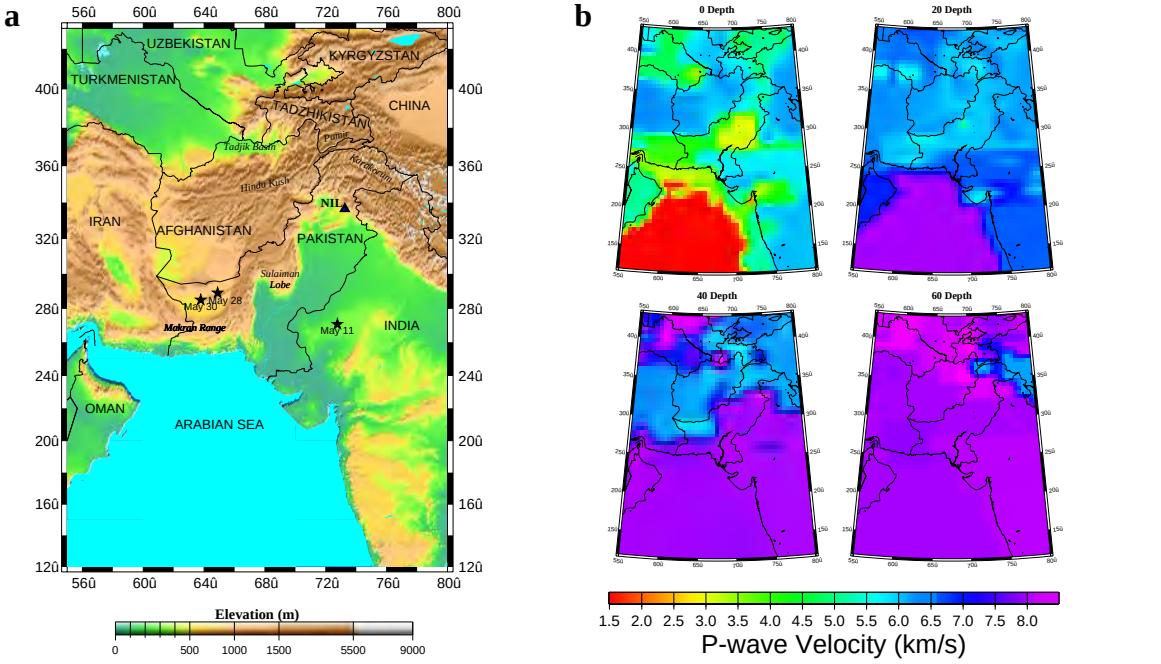

Figure 1. (a) Regional setting of the WINPAK3D velocity model showing the location of seismic station NIL at Nilore, Pakistan (future site of IMS station PRPK) as the black triangle and locations of the India and Pakistan nuclear test sites as black stars. (b) Slices of the velocity model at selected depths show the variability of velocity model resolution, as well as the large range of crustal thickness across this complex tectonic region.

Evaluating the Initial Model

The initial WINPAK3D velocity model was evaluated to ensure a reasonable model as a starting point for tomographic inversion. Testing and validation of a velocity model is a difficult task for several reasons: (1) the paucity of ground truth data, *i.e.*, explosions and earthquakes with known or well constrained location, as defined by Yang *et al.* (2000), (2) the pitfalls of using root mean square (rms) residuals to indicate improved location accuracy , and (3) the need to avoid circularity issues by ensuring that data used to generate the model are omitted from tests to validate the model. We evaluate our regional model's validity by comparing the hypocenter from a well-located event, recorded at a number of regional seismic stations, with model derived hypocenters. In addition, we implement a robust statistical procedure to further examine the validity of our regional model. We compare the performance of the 3-D model to the IASPEI91 model to determine the improvement over the global 1-D model for this region. Since the model was under development at the time of testing, the southern one-third of the current model was not included in the following model evaluation tests.

We begin by comparing our regional 3-D velocity model with the IASPEI91 model using the cross validation technique, a statistical method of evaluating a model. Cross validation obtains nearly unbiased estimators of prediction error in complicated problems (Efron and Gong, 1983). We performed this analysis for 6 events (Figure 2), chosen because they are well recorded and their epicenters are distributed across the model region. Applying the cross validation approach to the location problem, we repeatedly solved for the hypocenter of each event using unique subsets of 5 stations (simulating a sparse array) randomly selected from the set of regional arrivals. For each realization, we predicted the travel times to the omitted stations based on the hypocenter determination derived from the 5 stations. We calculated the average residual of predicted travel times at each station for all realizations and then evaluated the model fit in terms of the rms error for all stations. If the devised model is a physically relevant one, then it will yield accurate predictions for the omitted data.

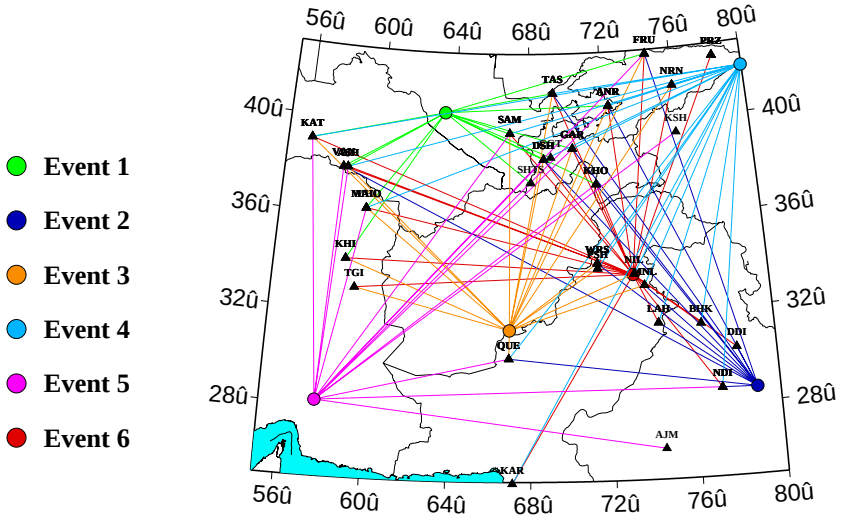

Figure 2. Events used for the cross validation analysis to test travel time prediction capabilities of the WINPAK3D model as compared with IASPEI91. Raypaths to the regional stations that recorded the events are shown.

We performed this analysis for both the WINPAK3D and IASPEI91 models and calculated the rms error for the travel time predictions made from each model (see Table 1). WINPAK3D achieves a smaller prediction error for the India/Pakistan region for 5 of the 6 events, with a large range of improvement in travel time prediction accuracy (22-83%) over IASPEI91. For event one, the prediction was the same for both WINPAK3D and IASPEI91. Although the rms prediction results demonstrate that WINPAK3D improves travel time prediction accuracy over IASPEI91 for events and raypaths throughout the model region, the amount of improvement that the 3-D model provides over IASPEI91 is quite variable. This is likely due to the varying resolution of the model discussed in the previous section. These results suggest

that WINPAK3D will serve as a good starting model for the tomography inversion, yet certain regions of the model will be subject to bigger updates than others.

Table 1. Cross Validation Results: RMS Prediction Error

			Model Prediction Error (seconds)		
Event	**Stations**	**Realizations**	**WINPAK3D**	**IASPEI91**	**Improvement**
1	5/14	2002	2.1	2.1	0%
2	5/13	1287	6.4	8.7	26%
3	5/17	5000	6.8	8.7	22%
4	5/18	5000	5.7	7.4	23%
5	5/14	2002	3.9	6.9	43%
6	5/23	5000	1.3	7.6	83%

Event 6 (m_b 5.2, USGS) in the cross validation analysis occurred on 14 February 1977 in the region near Nilore, Pakistan (Figure 2). This event was well recorded due to the presence of two temporary networks, Tarbela and Chasma, and a subarray of five stations centered on Nilore, Pakistan (NIL), all located in close proximity to the event . Based solely on data from these three networks, Seeber and Armbruster (1979) estimated the hypocenter of the event and conducted a detailed study of the aftershock sequence. Using teleseismic as well as regional data (not including the temporary networks), both the International Seismological Centre (ISC) and the U.S. Geological Survey (USGS) located the event within approximately 5 km of the epicenter reported by Seeber and Armbruster (S-A). The hypocenters of the main shock (depth = 14.46 km; John Armbruster, personal communication, 2000) and the 50 accurately located aftershocks determined by S-A indicate a rupture surface between 12 and 18 km depth. Given the high location accuracy estimated for this event as well as the large number of regional arrivals, we chose this event for a test of our model's location capabilities.

The S-A location (1979) for this event is one of the better constrained locations in the region due both to the local network coverage and to the detailed aftershock study. Though there have been several nuclear tests in the region, classified as ground truth (Yang et al., 2000) with known accuracies of 0 km and 1 km (GT0 and GT1), the regional data availability within our model area is limited. Arrival times for the 14 February 1977 event were reported to the ISC by 23 seismic stations within our model region. This event is additionally important due to its proximity to the seismic station at Nilore, Pakistan (NIL), the future site of the International Monitoring System (IMS) station PRPK.

Table 2. Location accuracy results of the 14 February 1977 Pakistan event

	RMS				Mislocation (km)	
Reference	**Residual (s)**	**Lat.**	**Lon.**	**Depth (km)**	**Epicenter**	**Depth**
Seeber and Armbruster	0.05	33.625	73.208	14.46	-	-
WINPAK3D	1.06	33.57	73.20	11.1	6.1	-3.3
IASPEI91	1.47	33.51	73.11	8.9	15.4	-5.5
NEIC	-	33.595	73.253	33	5.0	18.5
ISC	1.25	33.597	73.267	27	5.2	12.5

We believe that the velocity model should be validated using many source-station pairs prior to assessing model performance with sparse data. Using the 23 regional arrivals, we calculated the hypocenters predicted by both the WINPAK3D and IASPEI91 models (Table 2) for this event. The epicenter determined by WINPAK3D is 6.1 km from the "best" event location as determined by S-A (1979), while the IASPEI91 epicenter is approximately 15 km from the event. The depth is well determined for both models, due to extensive near-regional coverage when data from all stations are used. However, the cross validation results suggest that, in structurally complex regions, global models will be unacceptable for accurate location of small events not recorded teleseismically.

Therefore, we compare the locations for the event as determined by both the WINPAK3D and IASPEI91 models using only four stations, serving as IMS station surrogates. The four surrogate stations and their IMS counterparts are shown in Figure 3. The location determined using WINPAK3D and only arrivals from VAN, FRU, MNL, and TGI (Figure 4a, Table 3) is remarkably accurate (4.6 km). The IASPEI91

solution is within 14 km of the S-A epicenter. However, the surface projection of the 3-D 95% confidence region determined by the Monte Carlo simulation algorithm of Rodi and Toksöz (2000), encompasses the S-A epicenter for the WINPAK3D model, but not for the IASPEI91 model (Figure 5a). Furthermore, the epicenter calculated using the 3-D model and only four regional data is as accurate as the epicenters produced by both the ISC and the USGS (Figure 4a), which included teleseismic as well as regional data.

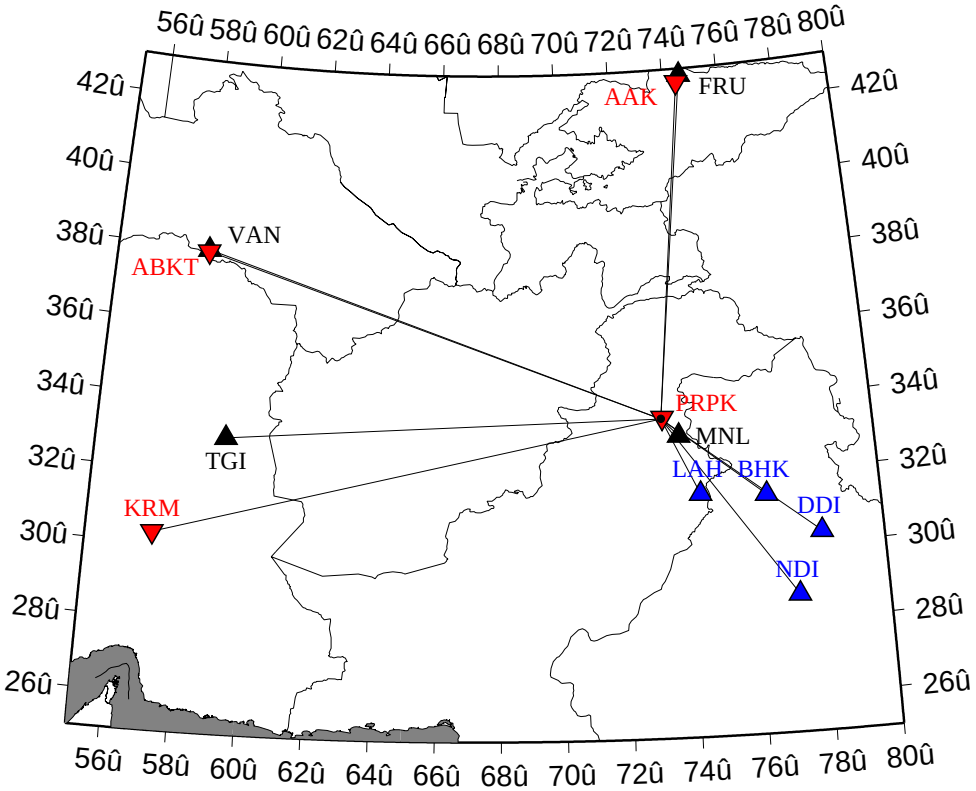

Figure 3. Location of the 14 February 1977 event (small circle plotted on top of PRPK) and the locations of regional stations VAN, FRU, MNL, and TGI (black triangles) used as surrogates for IMS stations (red, inverted triangles) for the sparse array locations. Blue triangles (LAH, BHK, DDI, and NDI) show stations used in the sparse array depth accuracy study.

We used the same four stations to determine the event location while fixing the depth to 15 km, the approximate depth of the S-A (1979) solution. With the hypocenter fixed at the approximate event depth, epicenter mislocation decreases to 2.9 km for the WINPAK3D model while it increases to 17 km for the IASPEI91 model. The confidence regions for fixed depth solutions are smaller, and again, the WINPAK3D confidence region encompasses the S-A location while the IASPEI91 confidence region does not. Interestingly, the solutions determined by both models, for both the fixed depth and free depth cases, lie within the 1000 km^2 region (17.8 km radius) required for CTBT monitoring protocol. We believe this is due to the close proximity of MNL to the event, helping to constrain the event depth.

Next, we next compare depth accuracy between WINPAK3D and IASPEI91 for the 4 station problem where different stations were substituted for MNL, the station closest to the epicenter (Figure 4). Given that the event is known to be a shallow crustal event, the only constraint imposed was to limit depth to less than 100 km depth. The results for the 4 station problem where depth is not controlled by a local station are shown in Table 3. The 3-D model provides much better constraint on event depth than the IASPEI91 model. WINPAK3D determined the depth of the event within 10 km of the S-A (1979) depth for all 4 variations of station coverage. However, all solutions calculated with the IASPEI91 model placed the event at the maximum allowed depth of 100 km. Epicenter mislocation was smaller for the WINPAK3D model as well, and in one case epicenter mislocation for the IASPEI91 solution exceeded the 17.84 km radius required for the 1000 km^2 OSI region. More importantly, the IASPEI91 based solutions could

falsely rule out this shallow event based on the erroneously deep hypocenters. Therefore, for this event, the WINPAK3D model has been shown to be extremely important for achieving the location accuracy required in nuclear monitoring.

Table 3. Location Accuracy for Sparse Arrays

	WINPAK3D Mislocation (km)		IASPEI91 Mislocation (km)	
Stations	**Epicenter**	**Depth**	**Epicenter**	**Depth**
IMS Surrogates	4.6	-14.5	13.5	-14.5
TGI, VAN, FRU, LAH	8.7	0.5	20.5	85.5
TGI, VAN, FRU, BHK	7.1	-9.4	10.5	85.5
TGI, VAN, FRU, DDI	1.9	-9.4	10.5	85.5
TGI, VAN, FRU, NDI	0.8	0.5	11.9	85.5

The International Data Center (IDC) currently uses the IASPEI91 global travel time curves as the default for event location. When the global model is insufficient for characterizing regional geology, the IDC sometimes applies path corrections (Yang *et al.*, 1999) in the form of SSSC's that are a function of source location for any station and phase. We derived SSSC's based on the WINPAK3D velocity model for the India-Pakistan region as described in Reiter *et al.* (2001). To account for the event depth, we calculated the anticipated SSSC for station NIL based on the WINPAK3D model for an event at 15 km depth.

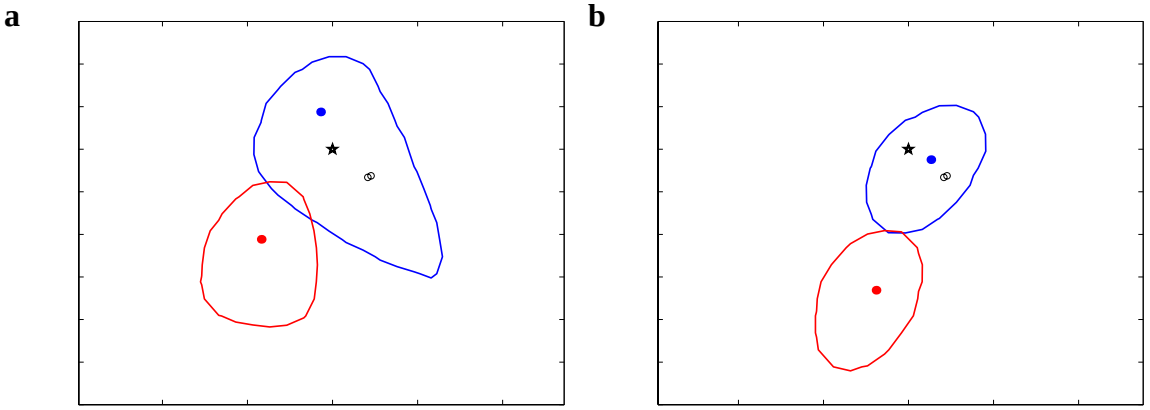

Figure 4. Location of 14 February 1977 event as determined by the WINPAK3D and IASPEI91 models using only arrivals from four stations (VAN, TGI, FRU, MNL) serving as IMS surrogates when (a) solving for hypocenter and (b) solving for epicenter only, with depth fixed to 15 km. The epicenter given by Seeber and Armbruster (1979) is indicated by the star. ISC and NEIC solutions determined using both regional and teleseismic data are shown by the open circles.

The 14 February 1977 event provides a unique reciprocity test of the 3-D velocity model, since it occurred very near the Nilore, Pakistan seismic station (NIL/PRPK). The residuals with respect to IASPEI91 at each station serve as empirical SSSC's. The differences between the empirical and model-based SSSC's at each station are less than 1 second for nearly half of the 23 stations and less than 3 seconds for the remaining stations. Since the SSSC values are as large as +/- 8 seconds in some parts of the region, discrepancies between the SSSC's of around 1 second are relatively small and show that the model-based and empirical SSSC's for NIL/PRPK are in very good agreement.

Tomography

A subset of 580 events were selected from the Engdahl *et al.* (1998) database of well located earthquakes and explosions. The selection criteria and processing of events in the Engdahl *et al.* (1998) data set results in location accuracy of 15 km or better in most continental areas, according to the IASPEI Working Group on Reference Events (http://lemond.colorado.edu/~copgte/). The subset of events were chosen in order to provide the best spatial distribution of events across the region, both in latitude-longitude and in depth.

Additionally, only events with 6 or more regional arrivals were selected from the database to insure sufficient data for hypocenter relocation. These events were recorded at 78 stations within our model region, amounting to over 7,800 arrivals (Figure 5). Travel times from these events will be used in an iterative velocity model tomography and hypocenter relocation procedure (described below) to update the preliminary model.

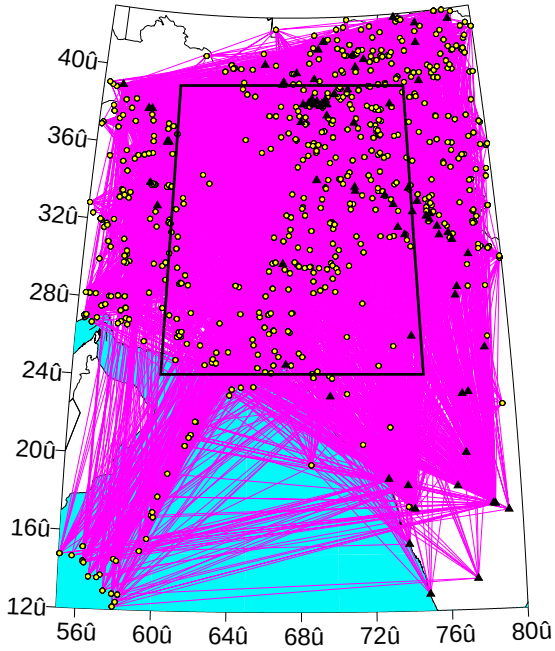

Figure 5. Ray coverage for tomography inversion provided by the 580 events (circles) recorded at 78 stations (triangles). The region outlined by the black rectangle is expected to have the best resolution in the tomographic update. Events and stations beyond this zone were included to provide optimal ray coverage in the primary model region. Ray coverage with depth is also very good.

We have re-parameterized WINPAK3D to reduce the number of model parameters to be solved for in the inversion. Our new parameterization is given in terms of a velocity vs. depth profile at each point on a geographic grid sampled uniformly in latitude and longitude. At each geographic grid-point, the velocity profile is given as velocity/depth pairs at nodes ranging from sea level to a depth of 760 km. Discontinuities in velocity are allowed at the ocean bottom, Moho and the major mantle discontinuities (410 and 660 km in the IASP91 model).

Our initial velocity model will be updated to fit the arrival times data from our database of 580 events. To accomplish this, we are developing an inversion algorithm that performs joint velocity tomography and multiple-event location. The algorithm will relocate the earthquakes in conjunction with revising the parameters of the velocity model. Initially, the model update will be restricted to the *Pn* velocity where we expect the greatest changes. Subsequent inversions will consider updates to the crustal thickness and other parameters.

Our inversion approach is formulated as follows. The unknowns are a vector **m** containing the velocity model parameters to be estimated (e.g. *Pn* velocity at each point of the latitude-longitude grid), and the hypocenters and origin times of several events: $(\mathbf{x}_j, t_j)$, $j = 1,..., M$. The data are arrival times, d_{ij}, from each event to a subset of stations indexed as $i = 1,..., N$. The data and unknowns are related by

$$d_{ij} = t_j + T_i(\mathbf{x}_j; \mathbf{m}) + e_{ij}$$

where e_{ij} is the error in d_{ij} and T_i is a function that computes traveltime to station *i* from an event hypocenter $\mathbf{x}_j$. This function depends on the model parameter vector **m**. Our joint inversion criterion is to minimize an objective function of the form

$$\Psi(\mathbf{m}, \mathbf{x}_1, t_1, ..., \mathbf{x}_M, t_M) = \sum_{ij} | d_{ij} - t_j + T_i(\mathbf{x}_j; \mathbf{m}) |^2 / \sigma_{ij}^2 + \tau | \mathbf{Lm} |^2$$

with respect to all the unknowns. Here, σ_{ij} is the standard deviation of e_{ij}. The second term of ψ imposes a smoothness constraint on the velocity model, with **L** being a regularization operator and τ a regularization parameter. The operator **L** is chosen as a differencing operator with the effect that spatial derivatives of the model velocity are minimized. The parameter τ determines the degree of model smoothness.

Our algorithm minimizes ψ using a combination of conjugate gradients and grid-search techniques. The conjugate gradients method is used to update **m** iteratively along a sequence of computed search directions. At each conjugate gradients step, grid search is used to minimize ψ with respect to the event origin parameters with **m** fixed, thus updating the $\mathbf{x}_j$ and t_j. The grid search for a given event is performed within a specified epicentral radius and depth range from its initial location, allowing us to handle events of varying ground-truth levels (e.g., GT0, GT5, GT15). Our grid search algorithm is described by Rodi and Toksöz (2000).

The forward model for this inverse problem is embodied in the traveltime functions T_i. For fixed **x**, we evaluate T_i (**x**; **m**) by interpolating a traveltime table stored on a 3-D hypocenter grid. The grid is created by applying the Podvin-Lecomte (P-L) finite-difference traveltime algorithm (Podvin and Lecomte, 1991) to the earth model defined by **m**, using the location of the *i*th station as the ``source" in the calculation. The forward P-L time calculation traces the wavefront propagation based on the Huygens' principle in the finite difference approximation. The model is discretized with an equally spaced grid comprised of constant velocity cells. Multiple arrivals (transmitted, diffracted, and head waves) are calculated at each grid node and the first arrival time is chosen. The time *t* at the current node is a function of the times t_n at some (3 or fewer) of the neighboring nodes and the slowness, *s*, in the cell traversed by the wavefront to reach this node. That is, $t=t(t_n, s)$.

We have extended the P-L algorithm to compute the sensitivities of traveltimes to cell velocities, as required for the inversion. When performing the forward calculation, we save the node pattern ("stencil") that shows which of the neighboring nodes were used to calculate the minimum time at the current node. The stencils are used to back-trace from any node of the grid to the source. The ray-tracing is done by identifying all of the grid nodes and the cells (slownesses) that contribute to the calculation of the time at the receiver. As the wavefront propagates away from the source, more nodes (and cells) are involved in the travel time calculation at each step. After the midpoint of the raypath, the propagation region narrows until it reaches the one node at the source location.

The sensitivity of the travel time to the slowness, $\partial t/\partial s$, is calculated at each grid node of the "ray" for the last cell traversed by the wavefront to reach that node. The weight of each neighboring node in the calculation of the time at the current node ($\partial t/\partial t_n$) determines the weight of the subsequent node-to-source subpath in the total travel time calculation for the ray. The sensitivities along each subpath are weighted by this term.

The ray-tracing algorithm and sensitivity calculation were tested by comparing the travel time computed as the sum of the weighted sensitivity-slowness products to the forward P-L calculated times. For rays with 10^5 nodes, the difference between travel times calculated by these two methods is on the order of 10^{-2} s when the calculation is done in single precision. Error of this magnitude for the number of nodes in the ray can be accounted for by the level of precision in the calculation, demonstrating that the ray-tracing technique is accurately tracing the minimum time P-L raypath.

We have developed the necessary algorithms for mapping our universal velocity model to a Cartesian block model needed by the P-L algorithm, and for mapping the 3-D Cartesian traveltime grids to geographic grids. The sensitivities are mapped from Cartesian blocks to the universal model parameterization.

We note that our joint inversion algorithm is fully nonlinear with respect to both the velocity model and event locations since traveltime modeling and event relocation are performed for each update of **m**. However, this comes at a high computational price and we are also allowing for multiple steps of the conjugate gradients iteration before the P-L modeling is repeated.

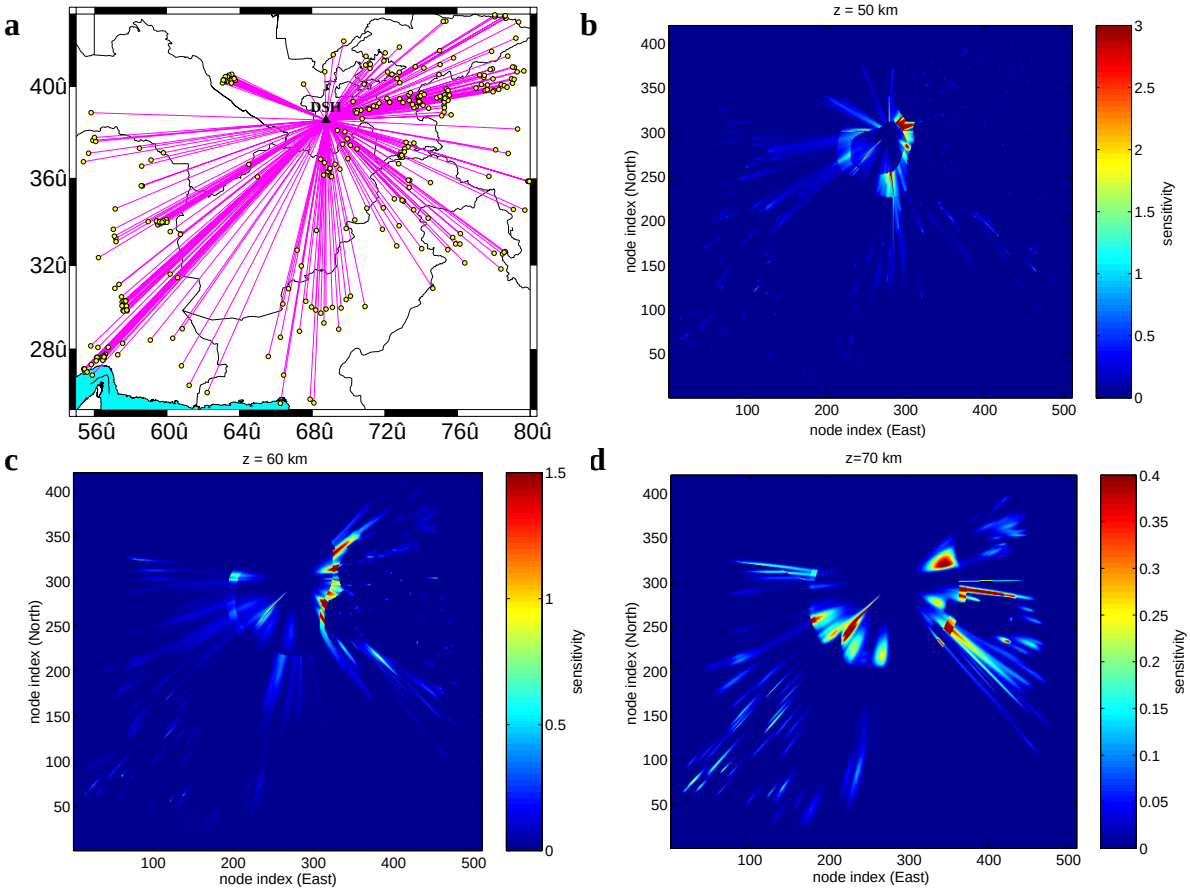

Figure 6. Ray sensitivities for station DSH. (a) Location of station DSH (triangle) and raypaths to events (small circles) within our model region that were recorded at DSH. Sensitivities of rays to model slices at (b) 50 km , (c) 60 km, (d) and 70 km depth.

Preliminary Analysis of Ray Sensitivities

We have performed a test of our ray sensitivity algorithm by computing the sensitivities to cell velocities of all the arrivals from our event database that were recorded at station DSH (Figure 6a). Selected depth slices of the sensitivities for DSH are shown in Figure 6b-6d. The rays have strong sensitivity to the model near the Moho boundary (presumably in the *Pn* velocity depth range). This suggests that updates to the *Pn* velocities as well as the Moho depth will provide the most significant improvement to the velocity model.

CONCLUSIONS AND RECOMMENDATIONS

Validation of the final, tomographically inverted, regional 3-D velocity model (WINPAK3D) will include more extensive application of the methods presented within this paper for testing of the preliminary model. We believe that all three techniques are important to the validation of any velocity model. Cross validation provides a statistical evaluation of the model's travel time prediction capabilities. Evaluation of location accuracy for a number of ground truth events is a very important aspect of model validation, as it will provide estimates of the model's location capabilities for location-based discrimination. Finally, model versus empirical based comparisons such as the comparison of the WINPAK3D SSSC for NIL with the

empirical SSSC derived from data for the 14 February 1977 event will provide a unique opportunity for validation when such events are available. Following the tomographic inversion and subsequent model validation, we believe that the updated WINPAK3D model will provide reliable, high-accuracy locations, for small events with sparse data, which will be critical for CTBT monitoring in the India-Pakistan region.

REFERENCES

Dewey, J. W. (1972). Seismicity and tectonics of western Venezuela, *Bull. Seism. Soc. Am.* **62**, 1711-1751.

Douglas, A. (1967). Joint epicentre determination, *Nature* **215**, 47-48.

Efron, B. and G. Gong (1983). A Leisurely Look at the Bootstrap, the Jackknife, and Cross-Validation, *The American Statistician* **37,** No. 1, 36-48.

Engdahl, E. R. and W. H. K. Lee (1976). Relocation of local earthquakes by seismic ray tracing, *J. Geophys. Res.* **81**, 4400-4406.

Engdahl E. R., R. van der Hilst, and R. Buland (1998). Global teleseismic earthquake relocation with improved travel times and procedures for depth determination, *Bull. Seism. Soc. Amer.* **88** (3), 722-743.

International Association of Seismology and Physics of the Earth's Interior (6/27/00), Working Group on Reference Events (available from http://lemond.colorado.edu/~copgte/).

Johnson, M. And C. Vincent (2001). Development of a 3-D Velocity Model of the India-Pakistan Region for Improved Seismic Event Location, *Bull. Seism. Soc. Amer.* In Review.

Jordan, T. H. and K. A. Sverdrup (1981). Teleseismic location techniques and their application to earthquake clusters in the south-central Pacific, *Bull. Seism. Soc. Am.* **71**, 1105-1130.

Kennett, B.L.N. and E. R. Engdahl (1991). Travel times for global earthquake location and phase identification, *Geophys. J. Int.* **105,** 429-465.

Pavlis, G. L. (1992). Appraising relative earthquake location errors, *Bull. Seism. Soc. Am.* **82,** No. 2, 836-859.

Podvin, P. and I. Lecomte (1991). Finite difference computation of traveltimes in very contrasted velocity models: a massively parallel approach and its associated tools, *Geophys. J. Int.* **105,** 271-284.

Reiter, D., C. Vincent, M. Johnson, J. Bonner, and W. Rodi (2001). Methods of Improving Regional Seismic Event Locations, *Proceedings*, 23rd Annual DoD/DOE Seismic Research Review.

Rodi, W. and M.N. Toksöz (2000). Grid-search techniques for seismic event location, *Proceedings*, 22nd Annual DoD/DOE Seismic Research Symposium, **02**, 39, 9 pp.

Seeber, L. and J. Armbruster (1979). Seismicity of the Hazara Arc in northern Pakistan: decollement vs basement faulting, in *Geodynamics of Pakistan*, A. Farah and K. A. DeJong (Editors), *Geological Survey of Pakistan*, 131-142.

Yang, X., I. Bondár, and C. Romney (2000). PIDC Ground Truth Event (GT) Database (Revision 1). CMR Technical Report CMR-00/15.

Yang, X., K. McLaughlin, and R. North, 1999. Source-Specific Station Corrections for Regional Phases at International Monitoring System Stations. *Proceedings of the 21st Seismic Research Symposium: Technologies for Monitoring the Comprehensive Nuclear Test Ban Treaty* **1**, 333-343.

RESEARCH IN REGIONAL SEISMIC MONITORING

F. Ringdal[1], E. Kremenetskaya[2], V. Asming[2], T. Kværna[1], S. Mykkeltveit[1] , J.I. Faleide[1] and J. Schweitzer[1]

[1]NORSAR

[2]Kola Regional Seismological Center

Sponsored by Air Force Technical Applications Center

Contract No. F08650-01-C-0055

ABSTRACT

This project represents a continuing effort to use data from the regional networks operated by NORSAR and the Kola Regional Seismological Centre (KRSC) to assess the seismicity and characteristics of regional phases of the European Arctic. Recently, seismic instrumentation has been installed inside the mines in the Khibiny Massif of the Kola peninsula in order to provide origin times of the seismic events as well as to contribute to additional validation of the location accuracy. We are now planning to expand this effort by collecting similar ground truth information for other mines in the Kola Peninsula, Spitsbergen and NW Russia. We present some initial ground truth information from rockbursts/earthquakes in a coal mine in Spitsbergen (Barentsburg). A 3-component digital seismometer system was installed in this mine in November 2000, and we present results of locating these rockbursts. The largest of these events are well recorded by the International Monitoring System (IMS) arrays SPITS and ARCES, and can therefore be useful for IMS calibration purposes.

Another area of interest for calibration is the northern Ural Mountains, where there is significant mining activity. The Amderma station, which is operated by KRSC, routinely detects a large number of mining explosions in mines near Vorkuta, and examples of such event recordings are presented. The largest of these events are also observed at the Fennoscandian arrays, especially ARCES, although they are seldom large enough to be included in the Reviewed Event Bulletin (REB), which currently requires P-detection by at least three primary IMS stations. Nevertheless, the detection, location and screening of such small events, even when observed by only a single station, are of interest in a global monitoring situation. The provision of ground truth of selected explosions and/or rockbursts in this area will help in calibrating the ARCES array (and possibly other stations) for such monitoring purpose.

The seismic events associated with the tragic accident of the “Kursk” submarine in the Barents Sea in August 2000 were recorded on several IMS stations. Observations from these stations have proved to be important in determining the sequence, characteristics and timing of these events. During the months following the accident, the Russian Navy carried out a number of underwater explosions in the Barents Sea near the site, and preliminary results from locating these events will be presented.

A workshop was held in Oslo, Norway, during 23-27 April 2001 in support of the global seismic event location calibration effort currently being undertaken by PrepCom’s Working Group B in Vienna. The workshop, which was chaired by Dr. Frode Ringdal, was attended by 65 scientists from 14 countries and the Provisional Technical Secretariat of the CTBTO. Among the contributions were recent results provided by NORSAR and KRSC of our joint regional calibration effort in the European Arctic, which includes ground-truth data and regional models applicable to a number of IMS stations in this region.

KEY WORDS: detection, location, calibration, rockbursts, explosions, earthquakes

OBJECTIVE

This work represents a continued effort in seismic monitoring, with emphasis on studying earthquakes and explosions in the Barents/Kara Sea region, which includes the Russian nuclear test site at Novaya Zemlya. The overall objective is to characterize the seismicity of this region, to investigate the detection and location capability of regional seismic networks and to study various methods for screening and identifying seismic events in order to improve monitoring of the Comprehensive Nuclear-Test-Ban Treaty. An important part of the work is contributions toward the international effort to provide regional location calibration of the International Monitoring System.

RESEARCH ACCOMPLISHED

Introduction

NORSAR and Kola Regional Seismological Centre (KRSC) of the Russian Academy of Sciences have for many years cooperated in the continuous monitoring of seismic events in North-West Russia and adjacent sea areas. The research has been based on data from a network of sensitive regional arrays which has been installed in northern Europe during the last decade in preparation for the International Monitoring System (IMS). This regional network, which comprises stations in Fennoscandia, Spitsbergen and NW Russia, provides a detection capability for the Barents/Kara Sea region that is close to m_b = 2.5 (Ringdal, 1997).

The research carried out during this effort is documented in detail in several contributions contained in the NORSAR Semi-Annual Technical Summaries. In the present paper we will limit the discussions to some recent results of interest in the general context of regional monitoring of seismic events in the European Arctic and also some results relevant to the location calibration effort currently underway for the IMS.

Amderma station

The seismic station at Amderma is a key monitoring resource for the Kara Sea region. We have carried out a study of regional events detected by this station during the years 1994-1998. This study confirms that the occurrence of seismic events in the Kara Sea and adjacent regions is very low, with the notable exception of the Vorkuta area south of Amderma. Most of the events in the Vorkuta area are assumed to be mining explosions. We have found a few previously unknown seismic events in the Kara Sea region, all at magnitude 2.5 or below. We have made no attempt to discriminate the source type of these events.

Our results indicate a detection threshold of about ML 1.8-2.0 for the Amderma station at an epicentral distance of 300-400 km. This is the distance to the two Kara Sea events on 16 August 1997 (toward the north), and also the distance to the Vorkuta mining area south of the station. The study confirms that the Amderma station provides a very useful supplement to the Fennoscandian array network in monitoring the Kara Sea/ Novaya Zemlya region.

The Kursk disaster in August 2000

On 12 August 2000 signals from two presumed underwater explosions in the Barents Sea were recorded by Norwegian seismic stations. The first of these, at 07.28.27 GMT, was relatively small, measuring 1.5 on the Richter scale. The second explosion, 2 minutes and 15 seconds later, was much more powerful, with a Richter magnitude of 3.5. It soon became clear that these seismic events were associated with the sinking of the Russian submarine “Kursk”. NORSAR informed Norwegian authorities after analyzing the recordings, and published selected analysis results on the Internet through NORSAR’s Web page (www.norsar.no).

The large underwater explosion on 12 August 2000 in the Barents Sea was located fully automatically by NORSAR’s Generalized Beamforming process (GBF) with an estimated location only 14 km from the known position of the submarine. The GBF process is running on-line at NORSAR for the purpose of providing trial epicenters of seismic events in Europe and the European Arctic. Later interactive analysis gave a

position that was as close as 5 km from the site of the accident. This high accuracy is due to the travel-time calibration available for the Barents region, as provided by the Fennoscandian/Barents velocity model.

The fact that the large explosion was preceded by a much smaller co-located event was noted by reviewing the GBF automatic output in more detail. It turned out that this smaller event was detected by the ARCES array in northern Norway. For obvious reasons, the automatic location estimate was less accurate than that of the larger event, but still close enough to the Kursk site to be associated with the accident. The similarity of the kinematic parameters of the two events can be seen in Figure 1, which shows f-k analysis results of the Pn and Sn phases of each event. It is noteworthy that the azimuth bias between the Pn and Sn phases are almost exactly the same for the two events. This confirms previous studies indicating that azimuth calibration of each phase should be done individually to obtain optimum location estimates for a given site. It also demonstrates that even very weak events can be located with high accuracy in areas where sufficient calibration information is available.

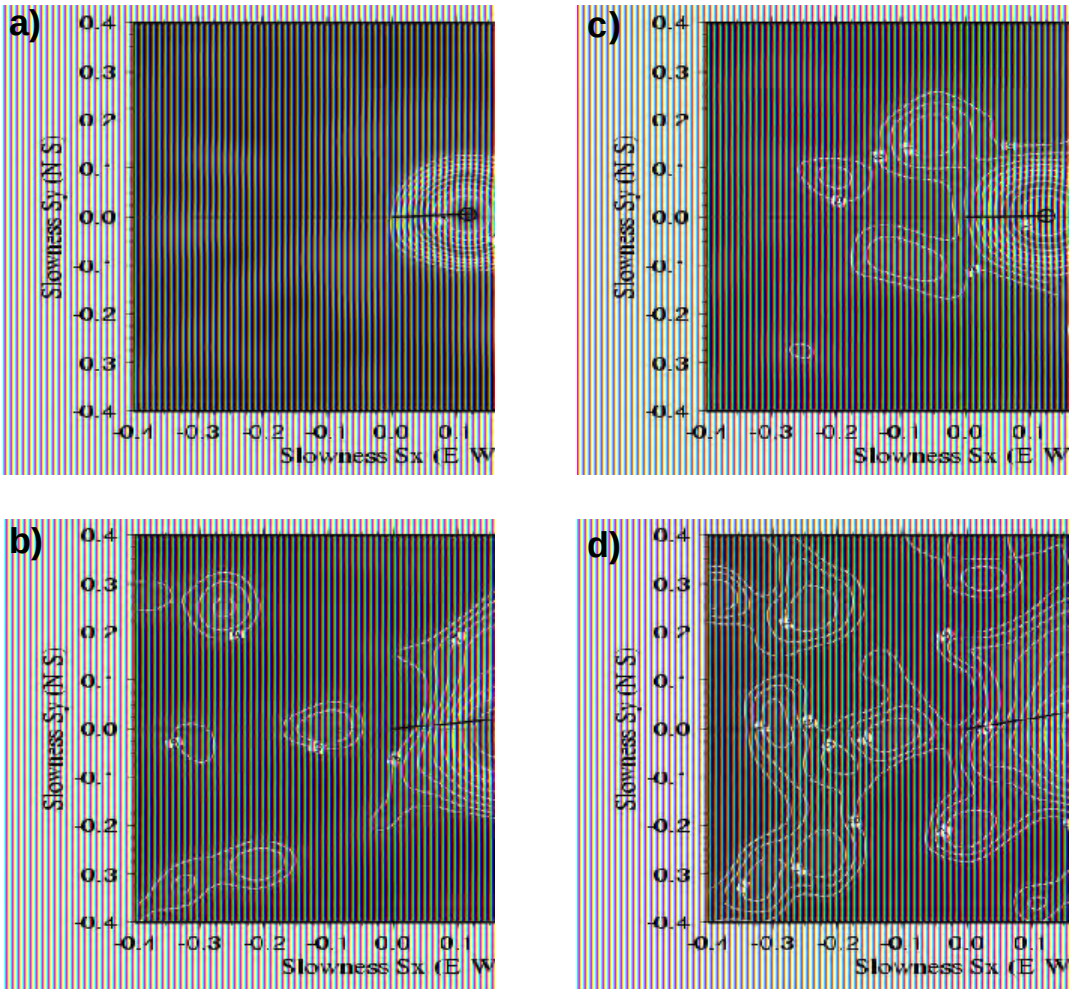

Figure 1. Frequency-wavenumber (f-k) plots of the Pn and Sn phases at ARCES for the two events on 12 August 2000. The labels a) and b) correspond to the Pn and Sn phases for the large event, whereas c) and d) correspond to the small event. Note the similarity of the two cases. In particular, both events show the same difference between apparent P-azimuth and apparent S-azimuth.

The area in the Barents Sea where the Kursk accident occurred has no known history of significant earthquake activity. Beginning in September 2000, numerous seismic events were detected in the area.The circumstances surrounding these events were initially unknown, but on 14 November 2000, the Russian authorities announced that the events were small explosions set off using grenades or depth charges, with the stated purpose to protect the Kursk submarine. Waveforms for six such explosions during 22-24 September 2000 are shown in Figure 2. These explosions were all quite small (around magnitude 1.5 on the NORSAR GBF scale), but were nevertheless seen clearly even on single ARCES seismometer recordings. They were also detected by the FINES and Apatity arrays, with a somewhat lower signal-to-noise ratio.

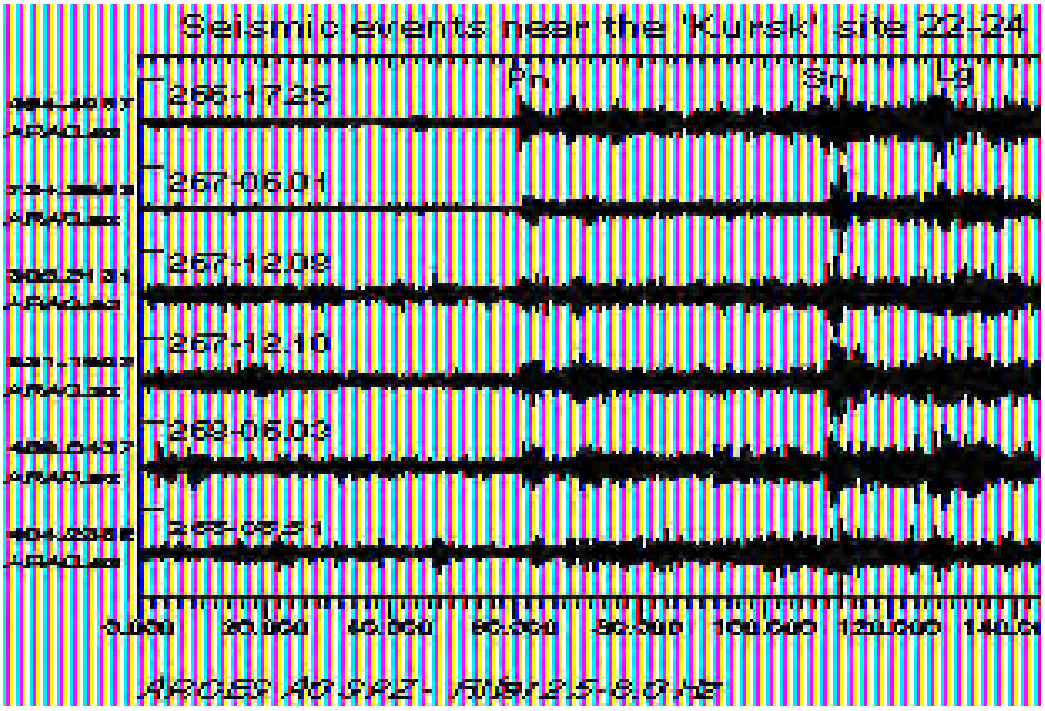

Figure 2. Waveforms for 6 small explosions near the Kursk site, as recorded on the center seismometer of the ARCES array in Finnmark, northern Norway. The data have been filtered in the band 2.5-8 Hz.

Figure 3 shows NORSAR's locations of 117 explosions detected during the period September 2000 - February 2001. The locations are based on interactive analysis of the data, and are therefore more accurate than the automatic GBF-based results. Naturally, the locations of the larger events are more accurate than those of the smaller events, and the majority of well-located events are concentrated in a cluster 10-20 km NW of the Kursk site. The magnitudes according to the NORSAR GBF scale range from 0.8 to 2.5.

The recording of the numerous small explosions near the Kursk site confirms the value of the IMS stations in monitoring seismic activity in the Barents Sea at very low magnitude levels. These explosions were particularly well recorded by the ARCES array (distance 500 km), but also the FINES, SPITS and NORES arrays detected several of the events. In addition, the Apatity array station in the Kola Peninsula (not an IMS station) provided useful recordings.

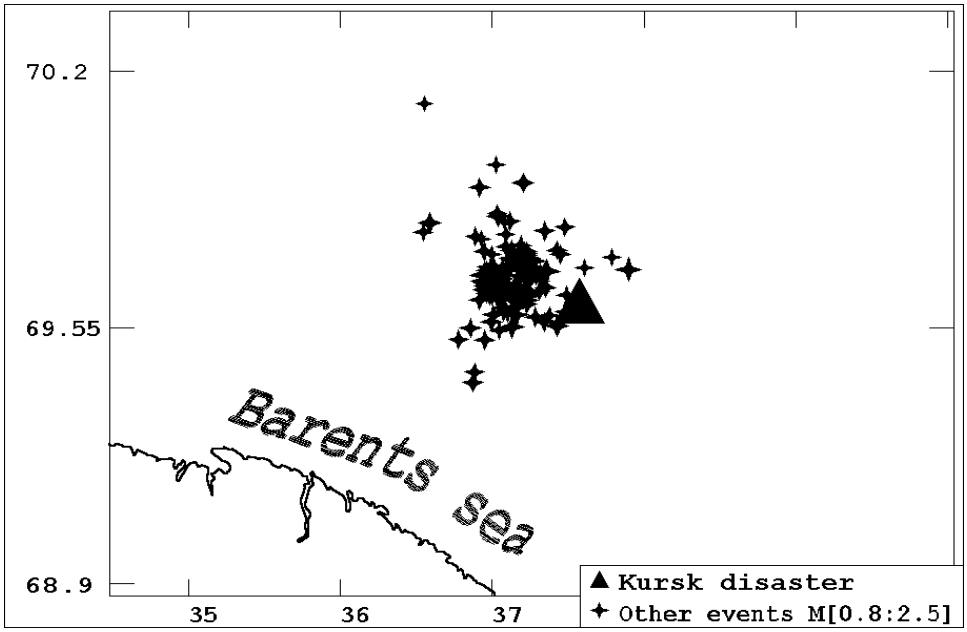

Figure 3. Locations of 117 underwater explosions near the Kursk site from September 2000 through February 2001. The site (true location) of the accident is marked with a triangle.

Spitsbergen mining events

Spitsbergen and the adjacent areas are parts of a geologically complex region with moderate to high seismicity. The main seismicity in the area is associated with the North-Atlantic Ridge, and especially the Knipovich Ridge situated at a distance less than 400 km from the archipelago (Sundvor and Eldholm, 1979). In addition, some coal mines are located in the area of Spitsbergen, causing occasional induced seismicity.

During the last few years an increased occurrence of rockbursts in the mines near Barentsburg, Spitsbergen has been observed. To obtain more information about these events, KRSC and NORSAR installed a digital 3-component seismic station, BRB, in the town of Barentsburg in December 2000. The station is located at a distance of only about 5 km from the mines.

In order to locate the recorded events with only the BRB station, we applied the polarization analysis technique (Asming et al. 1998) for determination of an event azimuth and P and S phase identification. An example of applying the polarization analysis technique is shown in Figure 4. For estimating the distance to the events the time difference between the P and S phases was used. It was necesssary to fine tune the velocity model in order to obtain accurate locations, and to this end, a small calibration explosion was conducted on 18 March 2001 at 11:03:00. The explosion coordinates were 78.067N, 14.36E; yield was 30 kg; the distance to BRB station was 3.12 km. To calibrate the local travel times we estimated local velocities taking into account that Vp/Vs is about 1.73 and we obtained Vp = 4.54 km/s and Vs = 2.62 km/s. A model for more distant stations was obtained by adding a low velocity near-surface layer to the Barents velocity model (Kremenetskaya et. al., 2001).

A total of 541 seismic events were detected near Barentsburg from 01/12/2000 to 19/04/2001. Figure 5 shows that the events can be separated into two groups, corresponding to the northern and southern mine. A closer analysis showed that the parameters of events outside the mines are very different from those occurring in either the South or North mines, whereas the South and North event parameters seem to be quite similar. This leads us to the conclusion that the events outside the mines have natural reasons whereas the events

in the mining areas are mostly technogenic. Thus, the Barentsburg area is unusual in the sense that strong technogenic seismicity is mixed with a significant natural seismic 'background'.

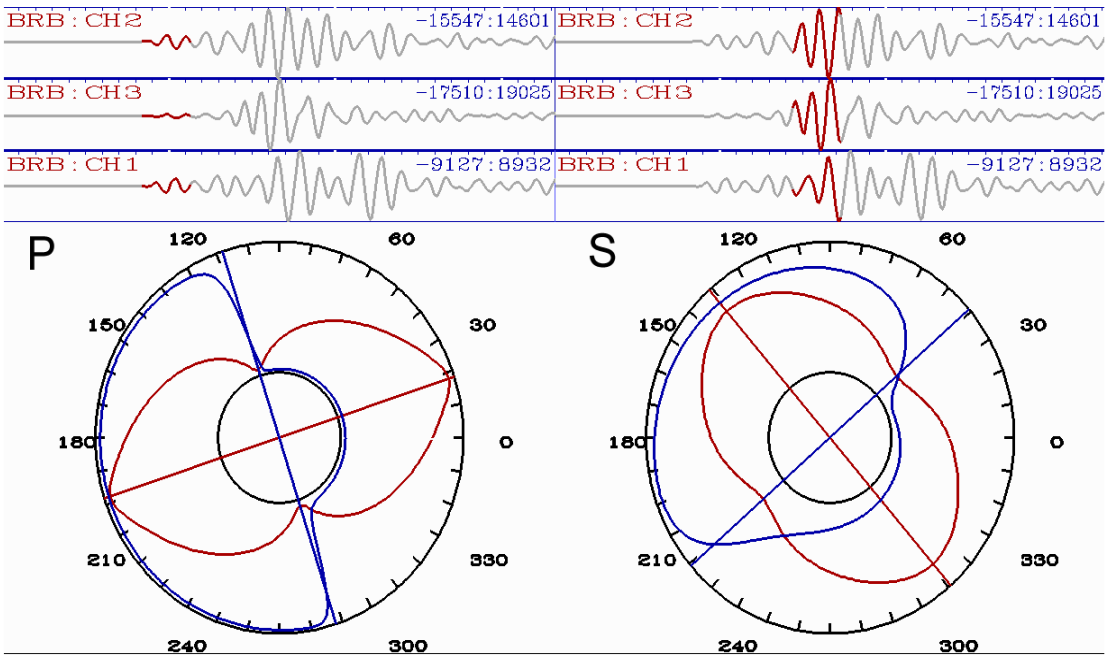

Figure 4. An example of applying the polarization analysis technique to BRB recordings.

Based on reports from the mines about a number of felt rockbursts, we were able to verify that our seismic locations were quite accurate, probably with an error of less than 1 km for the larger events. The majority of events were detected by the IMS station SPITS, and some of the largest events, which had local magnitude (ML) of about 3.0, were detected also at the IMS station ARCES (distance 1000 km). The data could therefore be useful for developing and verifying travel time correction for location calibration purposes.

Location Calibration

Crustal transects across the Barents Sea

In order to develop more precise travel times for regional phases, we have studied synthetic travel times for regional crustal transects across the Barents Sea and the adjacent western continental margin. We have calculated synthetic travel times for the first arrivals along four regional crustal transects across the Barents Sea and the adjacent western continental margin (see Figure 6) and compared these with the corresponding travel times predicted by the Barents regional velocity model which today is used to locate earthquakes in this area. Along one of the transects, between the spreading axis in the Greenland Sea and SPITS on Svalbard, we have also carried out a sensitivity study concerning the effects of uncertainties in the Moho topography on the calculated travel times.

Depending on the offset, travel-time differences of up to 2 - 3 seconds are found when comparing travel-time curves from the four transects to the standard 1-D model (Barents Sea crustal model). This reveals that the Barents Sea crustal model needs to be refined in order to fit the velocity structure established along the regional transects. Because most of the observed events in this region are only observable at regional distances, it will be particularly important within this context to address upper mantle velocities, as a basis for Pn and Sn travel times.

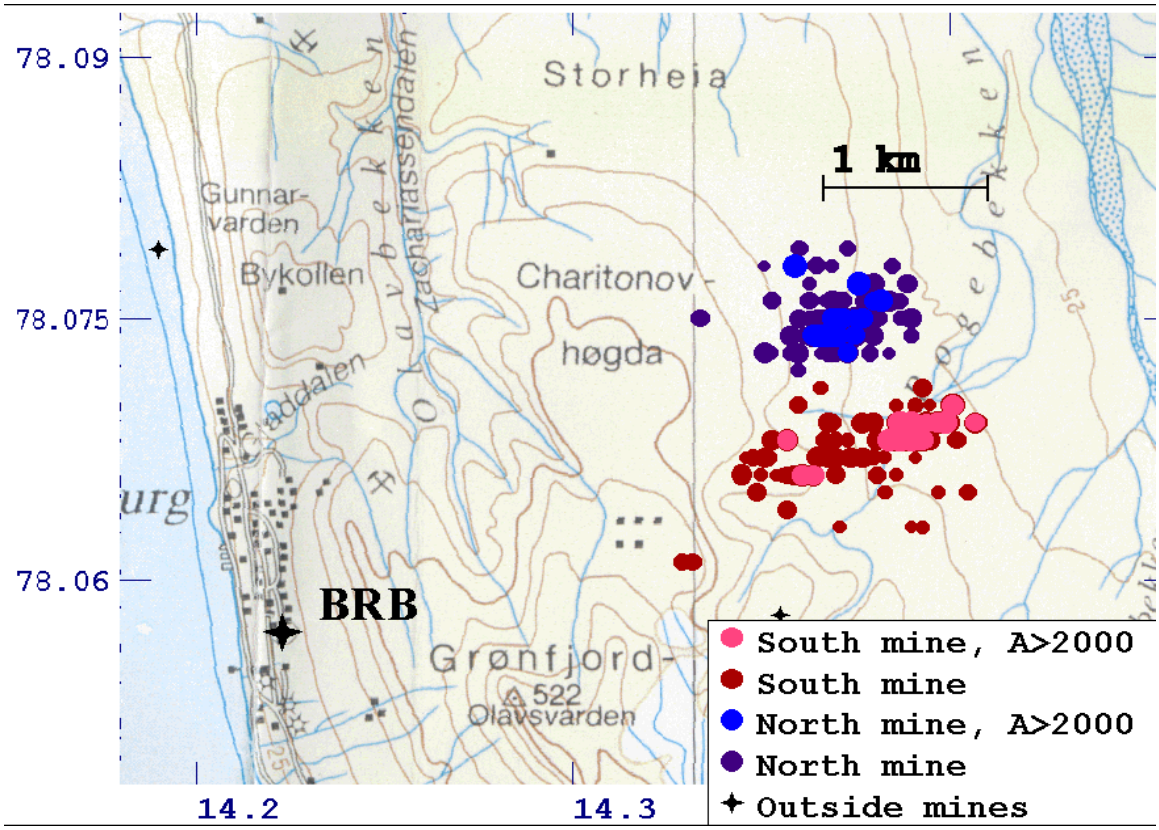

Figure 5. Seismic events near Barentsburg, Spitsbergen occurring from 01.12.2000 to 26.03.2001. The location of the 3-component seismic station BRB is indicated.

Oslo Workshop on location calibration

A workshop was held in Oslo, Norway during 23-27 April 2001 in support of the global seismic event location calibration effort currently being undertaken by Working Group B of the CTBTO Preparatory Commission in Vienna, Austria. Dr. Frode Ringdal chaired the meeting, which was attended by 65 experts from 14 countries and the Provisional Technical Secretariat of the CTBTO The recommendations from this workshop have been provided in the paper CTBT/WGB/TL-2/61, issued by Working Group B of the CTBTO Preparatory Commission.

CONCLUSIONS AND RECOMMENDATIONS

Our studies demonstrate that the regional array network in northern Europe, which comprises stations in Fennoscandia, Spitsbergen and NW Russia, provides an overall detection capability for the European Arctic that is close to m_b = 2.5, using the Generalized Beamforming (GBF) method for automatic phase association and initial location estimates. In selected areas it is significantly better - for example, the capability in the Kursk accident area in the Barents Sea is close to m_b =1.5 (in terms of the GBF scale).

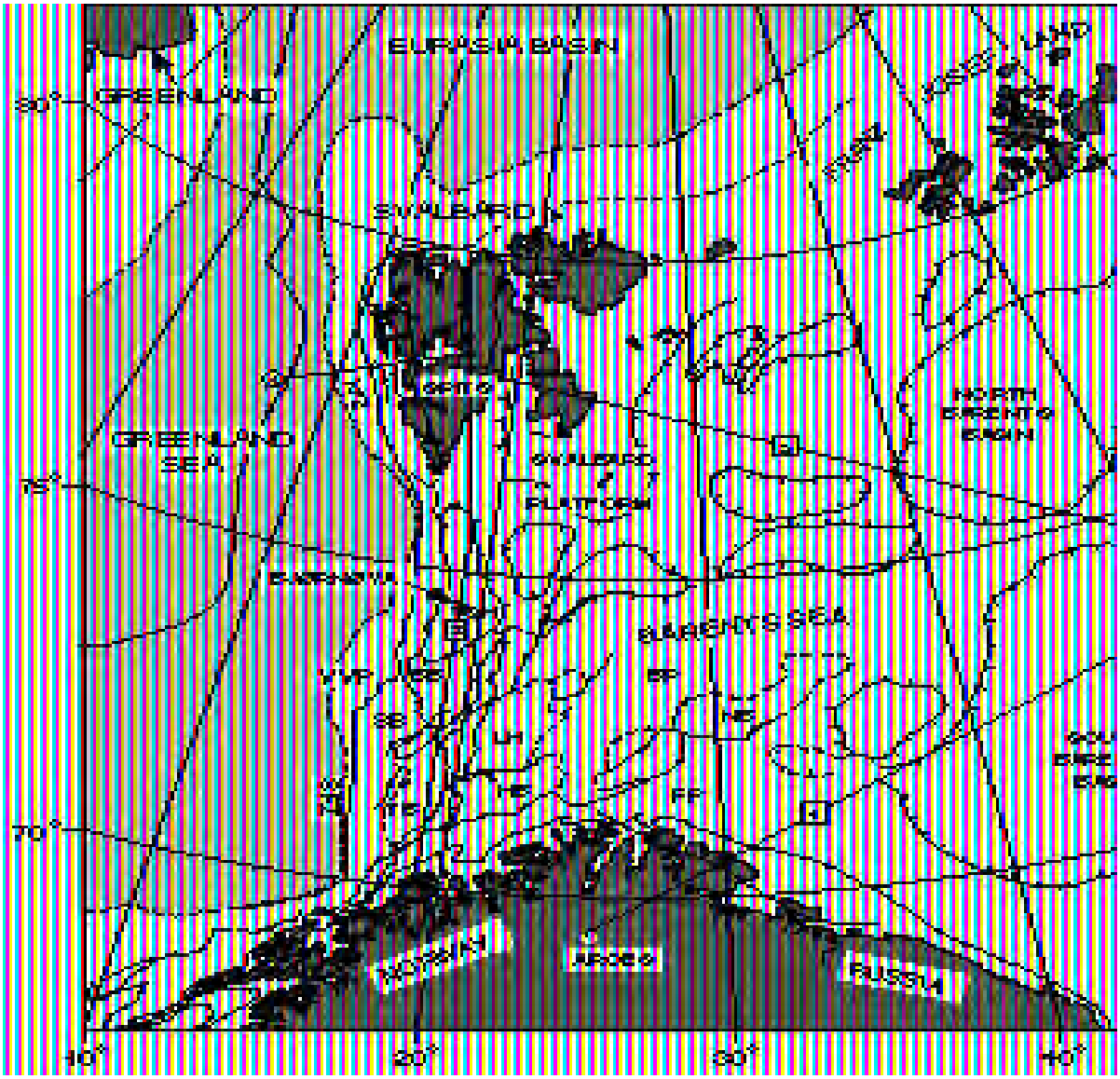

Figure 6. Regional setting - main geological provinces and structural elements in the Barents Sea and surrounding areas. Location of crustal transects and the seismic arrays SPITS and ARCES are shown. BB = Bjørnøya Basin, BP = Bjarmeland Platform, FP = Finnmark Platform, HB = Hammerfest Basin, HFZ = Hornsund Fault Zone, LH = Loppa High, NB = Nordkapp Basin, SFZ = Senja Fracture Zone, SB = Sørvestnaget Basin, SH = Stappen High, TB = Tromsø Basin, VVP = Vestbakken Volcanic province (Faleide, 2000).

We have also demonstrated, both in the case of Kursk events and in other connections, that location estimates by a single array or 3-component station can be provided with high accuracy, assuming that site-specific calibration information is available for the station-site path in question. We recommend that single-station location algorithms continue to be developed and evaluated.

In terms of location calibration, the single most important topic is to obtain accurate "ground truth" locations both for the development of site-specific station corrections and for evaluation of the performance of various

calibration schemes. We recommend that a program to install seismometers inside selected mines be implemented, with associated GPS receivers for accurate timing and location of the mining events. NORSAR is planning to pursue this issue in Fennoscandia and NW Russia in our future research in the European Arctic region.

The global location calibration effort will continue to be an important part of our work. The recommendations provided in the paper CTBT/WGB/TL-2/61 should be followed up by the international community, and the progress of this work will be reviewed in a planned workshop in Oslo in 2002.

REFERENCES

Asming, V.E., E.O. Kremenetskaya and F. Ringdal (1998): Monitoring seismic events in the Barents/Kara Sea region, *Semiannual Technical Summary, 1 October 1997 - 31 March 1998*, NORSAR Sci. Rep. 2-97/98, Norway.

Faleide, J. I. (2000): Crustal structure of the Barents Sea - important constraints for regional seismic velocity and travel-time models. *Semiannual Technical Report 1 October 1999 - 31 March 2000. NORSAR Sci. Report* **2-1999/2000**, Kjeller, Norway, 119-129.

Kremenetskaya, E., V. E. Asming and F. Ringdal (2001): Seismic location calibration of the European Arctic. *Pure and Applied Geophysicas,* 158 No. 1-2, 117-128

Ringdal, F. (1997): Study of low-magnitude seismic events near the Novaya Zemlya nuclear test site, *Bull. Seism. Soc. Am. 87 No. 6,* 1563-1575.

Sundvor E. and O. Eldholm (1979): The western and northern margin off Svalbard. - *Tectonophysics*, 59, 239-250.

UNCERTAINTY ANALYSIS IN SEISMIC EVENT LOCATION

William Rodi and M. Nafi Toksöz

Massachusetts Institute of Technology

Sponsored by Defense Threat Reduction Agency

Contract No. DTRA01-00-C-0102

ABSTRACT

Uncertainty in event locations derived from seismic data is caused by errors in the arrival times of picked phases, misidentification of seismic phases, and errors in the travel-time model used in the location process. The event mislocation induced by these error sources is affected by the number and spatial distribution of stations that record an event. This project is developing a statistical framework and computational techniques for accurately analyzing event location uncertainty. Our statistical approach is based on a maximum-likelihood framework, which defines an optimal location estimate to be that maximizing a likelihood function, and derives confidence regions in terms of hypothesis tests applied to likelihood ratios. An appropriate likelihood function is prescribed in terms of a probabilistic model of the various types of errors in seismic data. With appropriate computational tools, it is possible to implement a general class of error models that allow for non-Gaussian distributions, spatially correlated errors in travel-time tables, and other complexities that conventional location algorithms do not handle. Additionally, the assumption of local linearity of the forward problem (travel-time vs. location) can be avoided. We are developing such computational tools based on grid-search and Monte-Carlo simulation techniques. We have implemented our statistical formulation in a general event location algorithm that finds optimal location estimates from arrival time, slowness and azimuth measurements for regional and teleseismic phases, and computes the non-elliptical confidence regions which follow from a general error model and nonlinear analysis. We have used the algorithm to study the effects of nonlinearity and non-Gaussian error assumptions on the confidence regions of sparsely recorded events, applying it to regional arrival data from the 1991 Racha earthquake sequence, data from local and national networks in Turkey, and from the Reviewed Event Bulletin of the International Data Centre. Our present efforts focus on developing a realistic and practical formulation of the errors in the travel-time tables that are used in locating events ("modeling errors"). We are basing our formulation on empirical methods for estimating travel-time corrections from multiple-event data sets, with the goal of deriving location confidence regions that properly reflect the results of network calibration studies.

KEY WORDS: seismic event location, location uncertainty, confidence regions

OBJECTIVE

The objective of this work is to develop a methodology for seismic event location that provides reliable estimates of location uncertainty that can be used in nuclear event monitoring. Conventional methods for inferring confidence regions on event locations employ assumptions that may not be valid in the case of small, sparsely recorded events. These assumptions include local linearity of the travel time vs. hypocenter forward model and the treatment of errors in arrival time picks and travel-time models as uncorrelated, Gaussian random variables. The linear approximations used in computing standard, elliptically shaped confidence regions are only appropriate when the "true" confidence region for an event is small compared to the distances to stations, and does not include large velocity variations. Gaussian error models do not capture the observational difficulties of correctly identifying and picking low signal-to-noise arrivals (Jeffreys, 1932). Further, they are an ad hoc representation of what is often a larger source of error: the errors in the travel-time tables used in locating an event. We are attempting to address these difficulties by developing a general theoretical framework and computational tools for uncertainty analysis in seismic event location.

RESEARCH ACCOMPLISHED

Theoretical Formulation

Our approach to seismic event location is based on a maximum-likelihood formulation. We define an optimal location for a seismic event to be that which maximizes a likelihood function, constructed on the basis of an assumed statistical model of errors in the seismic data used in locating the event. Confidence regions are defined in terms of hypothesis tests using likelihood ratios as the test statistics. We have formulated and implemented this approach for three types of seismic data used in nuclear monitoring: arrival times, azimuths and slownesses. To simplify the discussion here, we consider only arrival times.

The hypocentral parameters of a seismic event are an origin time t and location $\mathbf{x} \equiv (\theta, \phi, z)$, where θ is latitude, ϕ is longitude and z is depth. Let $\mathbf{d} = (d_1, d_2 \ldots, d_n)$ be an n-dimensional vector of arrival times picked from various seismic phases at a seismic network. The event location problem may be expressed as

$$d_i = t + T_i(\mathbf{x}) + c_i + e_i, \quad i = 1, \ldots, n. \tag{1}$$

T_i is a travel-time function for the ith datum, which in our algorithms is evaluated by interpolating a travel-time table, sampling travel-time as a function of epicentral distance and event depth (for a 1-D earth model) or as a function of $\mathbf{x}$ (for a 3-D earth model). The term e_i denotes the observational, or picking, error in d_i. The term c_i can be interpreted in two ways. First, it is a correction to $T_i(\mathbf{x})$, accounting for the difference between the travel-time function and the true travel times in the Earth. However, if c_i is not known, it can be considered an additional source of error in d_i, and from this view it is sometimes referred to as a "modeling error." In our formulation, we assume that any known corrections have been included in T_i, leaving c_i as an unknown error. The uncertainty analysis for the event hypocenter $\mathbf{x}$ must account for the combined error, $c_i + e_i$.

Our current algorithms assume that the picking errors are statistically independent and, following Billings et al (1994), that each is distributed with an exponential power distribution, whose probability density function (p.d.f.) is given by

$$f(e_i) = \frac{1}{K(p)\sigma_i} \exp\left\{ -\frac{1}{p} \left| \frac{e_i}{\sigma_i} \right|^p \right\} \tag{2}$$

where the scale parameter σ_i is a standard error, $K(p) = 2p^{1/p}\Gamma(1+1/p)$, and Γ is the gamma function. When $p = 2$, then e_i is normally distributed with a mean of zero and variance of $(\sigma_i)^2$. When $p = 1$, it is exponentially distributed. We assume that the standard errors are known in a relative sense and write

$$\sigma_i = \sigma \nu_i \tag{3}$$

where the ν_i are known but the universal scale parameter, σ, is not. For the moment, we will ignore the modeling errors and assume $c_i = 0$.

The joint p.d.f. of the n data is the product of the error p.d.f.'s. Considered as a function of the unknown parameters ($\mathbf{x}$, t, and σ) this joint p.d.f. is the likelihood function we seek to maximize. Denoting it as $L(\mathbf{x}, t, \sigma, \mathbf{d})$ our assumptions imply

$$-\log L(\mathbf{x}, t, \sigma; d) = \sum_{i=1}^{n} \log \nu_i + n \log K(p) + n \log \sigma + \frac{1}{p\sigma^p} \sum_{i=1}^{n} \left| d_i - t - T_i(\mathbf{x}) \right|^p \Big/ (\nu_i)^p . \tag{4}$$

We denote the maximum-likelihood estimates of the unknowns as $\mathbf{x}_{m1}$, t_{m1}, and σ_{m1}. The maximization may be subjected to prior constraints on the parameters. For the applications here the constraints of interest are

$$0 \le z \le z^{\max} \tag{5}$$

$$\sigma^{\min} \le z \le \sigma^{\max}. \tag{6}$$

From the point of view of finding **x** and *t*, maximizing *L* is equivalent to minimizing the last term of equation (4), which is just a norm of data residuals. For example, with $p = 2$ the problem reduces to nonlinear least squares. However, with error models more general than we consider here, allowing for example asymmetric or multi-modal error distributions, the likelihood function would not necessarily be in terms of a simple residual norm.

Given its structure, *L* is amenable to a hierarchical maximization with respect to the unknown parameters. We define a "reduced" likelihood function which, for each fixed hypocenter, is minimum with respect to *t* and σ (subject to prior constraints on σ):

$$\tilde{L}(\mathbf{x};\mathbf{d}) = \max_{t,\sigma} L(\mathrm{x}, t, \sigma; \mathrm{d}). \tag{7}$$

For general $p \ge 1$, this maximization over *t* and σ can be performed with a combination of analytical and root-finding techniques. The location problem reduces to maximization of $\tilde{L}$ with respect to **x**.

Grid Search

Our grid search algorithm computes the reduced likelihood function, $\tilde{L}$ in equation (7), at each point in a 3-D grid of hypocenters. Following previous workers, the hypocenter grid is constructed dynamically through a process of successive refinement. Our procedure for grid refinement resembles that of the "neighborhood" search algorithm developed by Sambridge (1999). If the search is not restricted to a specified region, the first grid covers the entire globe and 0 to 700 km in depth at a coarse spacing: 100 km in depth, 9° in latitude, and 9° in longitude near the equator and increasing at higher latitudes. On each pass of grid refinement, nodes are added as neighbors of a subset of grid points comprising the "best" (largest $\tilde{L}$) points tested thus far. Neighbors are placed at one-third the grid-spacing of the previous pass. The size of the grid subset chosen for refinement is reduced on each pass. The search ends when the grid spacing is less than 0.3 km.

Non-Elliptical Confidence Regions

In conventional event location algorithms, confidence regions on the hypocenter, epicenter and depth of an event are computed under the assumptions that the data errors are Gaussian ($p = 2$) and that the travel-time functions, $T_i(\mathbf{x})$, are well approximated as locally linear near $\mathbf{x} = \mathbf{x}_{\mathrm{ml}}$. These assumptions lead to hypocenter and epicenter confidence regions that are elliptical in shape. The size of the confidence regions, for a given confidence level, is scaled by a critical value of the F distribution for an appropriate number of degrees of freedom, as determined by a prior assumption about the data variance, σ^2. This approach is developed by Flinn (1965), Evernden (1969) and Jordan and Sverdrup (1981) under differing assumptions about σ^2 (unknown, known and partially known, respectively).

We have generalized this approach to avoid the linearity approximation and to allow for non-Gaussian data errors and arbitrary parameter constraints. As in the conventional approach, we define a confidence region in terms of a test statistic, τ, which is a function of the data and parameters being tested. For a hypocenter confidence region, we write the statistic as $\tau(\mathbf{d}, \mathbf{x})$. The confidence region, at confidence level β (e.g., β = 90%), comprises those values of **x** that satisfy the inequality

$$F\left[\tau(\mathbf{d},\mathbf{x})\right] \le \beta \tag{8}$$

where **d** is the observed data vector, and $F[\ ]$ denotes the cumulative distribution function (c.d.f.) of a random variable. Following a well known statistical approach, we define the test statistic as the logarithm of a likelihood ratio:

$$\tau(\mathbf{d},\mathbf{x}) = \log \tilde{L}(\mathbf{x}_{\mathrm{m1}};\mathbf{d}) - \log \tilde{L}(\mathbf{x};\mathbf{d}) = \log\left[\frac{\max_{\mathbf{x},t,\sigma} L(\mathbf{x},t,\sigma;\mathbf{d})}{\max_{t,\sigma} L(\mathbf{x},t,\sigma,\mathbf{d})}\right] \tag{9}$$

That is, for given **x**, τ compares the difference between the maximum likelihood (achieved by $\mathbf{x}_{\mathrm{ml}}$) and the likelihood achieved by **x**. Since the inequality (8) rejects large values of τ, confidence regions will exclude hypocenters that achieve relatively small values of likelihood, i.e., poor fits to the data. We point out that under the Gaussian, linear assumption, the likelihood ratio statistic is equivalent to the variance ratio on which elliptical confidence regions are based.

The statistic for a 2-D confidence region on the event epicenter, (θ,ϕ), is defined by

$$\tau(\mathbf{d},\theta,\phi) = \log\tilde{L}(\mathbf{x}_{\mathrm{m1}};\mathbf{d}) - \log \max_{z} \tilde{L}(\theta,\phi,z;\mathbf{d}) \tag{10}$$

and for a confidence interval on focal depth we use

$$\tau(\mathbf{d},z) = \log\tilde{L}(\mathbf{x}_{\mathrm{m1}};\mathbf{d}) - \log\max_{\theta,\phi} \tilde{L}(\theta,\phi,z;\mathbf{d}). \tag{11}$$

Confidence regions using these log-likelihood statistics could still be defined via the inequality of equation (8), except this inequality presumes that the distribution (c.d.f.) of τ does not depend on the true values of parameters that are not being tested. To address this, we assume the main dependence is on focal depth and σ, and rewrite the c.d.f. of τ as $F[\tau;z,\sigma]$. We generalize the inequality of equation (8) to use the c.d.f. of τ that is minimum with respect to the untested parameters. Thus, the hypocentral confidence region is given by

$$\min_{\sigma} F\left[\tau(\mathbf{d},\mathbf{x});z,\sigma\right] \le \beta. \tag{12}$$

The epicentral confidence region is

$$\min_{\sigma,z} F\left[\tau(\mathbf{d},\theta,\phi);z,\sigma\right] \le \beta \tag{13}$$

and the focal depth confidence interval is

$$\min_{\sigma} F\left[\tau(\mathbf{d},z);z,\sigma\right] \le \beta \tag{14}$$

With these definitions, a confidence region will include the true value of the tested parameters *at least* 100β percent of the time.

Confidence Regions Via Monte Carlo Sampling

Without assumptions like linearity of T_i, it is not possible to derive an analytic expression for the c.d.f. of τ, which is needed to compute confidence regions. However, we can approximate the c.d.f. using Monte Carlo simulation. We outline the technique for hypocentral confidence regions. The basic idea is to estimate the c.d.f. of the test statistic τ by simulation, i.e. computing τ for many randomly generated samples of the error vector. We generate each error, e_i^{mc}, using a pseudo-random number generator in accordance with the assumed error distribution [eqs. (2)–(3)] for some given "true" σ. Then, for given true hypocentral parameters, **x** and *t*, synthetic data are calculated as

$$d_i^{\mathrm{mc}} = t + T_i(\mathbf{x}) + e_i^{\mathrm{mc}}. \tag{15}$$

We apply our grid search algorithm to these data to obtain the maximum-likelihood hypocenter, $\mathbf{x}_{\mathrm{m1}}^{\mathrm{mc}}$. Plugging this into the formula for τ,

$$\tau(\mathbf{d}^{\mathrm{mc}},\mathbf{x}) = \log\tilde{L}(\mathbf{x}_{\mathrm{m1}}^{\mathrm{mc}};\mathbf{d}^{\mathrm{mc}}) - \log\tilde{L}(\mathbf{x};\mathbf{d}^{\mathrm{mc}}), \tag{16}$$

we obtain one sample from $F[\tau;z,\sigma]$. We compare this sample to the observed value of the statistic, $\tau(\mathbf{d},\mathbf{x})$, obtained from the real data. We count a rejection of **x** if

$$\tau(\mathbf{d}^{\mathrm{mc}},\mathbf{x}) < \tau(\mathbf{d},\mathbf{x}) \tag{17}$$

The proportion of rejections after many Monte Carlo trials yields an estimate of $F[\tau(\mathbf{d},\mathbf{x});z,\sigma]$. Performing this simulation for multiple values of σ and then minimizing amongst them gives the *lowest* confidence level such that the confidence region includes **x**.

The process for depth confidence intervals and epicenter confidence regions proceeds in the same manner, except that in the latter case the simulation is performed for multiple values of true depth as well as σ, and the confidence level is minimized over both.

Examples From the Racha and Adana Earthquake Sequences

Figure 1 shows confidence regions computed for an event from the 1991 Racha, Georgia, earthquake sequence, studied by Myers and Schultz (2000). The data set comprises P wave arrival times at six regional stations, obtained from the International Seismological Centre (ISC) with two stations re-picked by Lawrence Livermore National Laboratory (LLNL). We computed confidence regions with our Monte Carlo/grid search algorithm two ways. First, we assumed the picking errors are from a Gaussian distribution, with the standard deviation constrained between 1.0 and 2.0 seconds for the ISC picks and between 0.5 and 1.0 seconds for LLNL picks. Second, we assumed the errors were from an exponential distribution (p = 1), with the same constraints applied to the standard errors. In both cases, we used the travel-time tables for the IASPI91 Earth model.

The results in Figure 1 illustrate the effect of nonlinearity on the confidence regions of sparsely recorded events. Even in the Gaussian case (top), we see that the epicenter and hypocenter confidence regions depart significantly from ellipses. This is due largely to the fact that the event depth is poorly constrained by first arrivals from only six stations covering a limited distance range (6° to 22°). Travel time does not behave as a linear function over the wide range of event depths that is consistent with the data.

Comparing the top and bottom portions of Figure 1, we see that the confidence regions for Gaussian and exponential error distributions are similar, but not identical, in shape. More noticeable is the fact that the exponential ones are bigger at high levels of confidence, above 90%. This is consistent with the larger tails of the exponential distribution. However, only confidence regions at very high confidence levels, particularly in the Gaussian case, include the local network location. This was generally the case for 18 Racha events we analyzed, all of which had six or fewer data. For the 14 of these events whose epicenters were reasonably constrained, the locations were consistently mislocated by roughly 40 km north-northwest of the true location. These results are consistent with those of Myers and Schultz (2000), who showed that the mislocations are due to the need for travel-time corrections as large as 3 seconds at some stations.

As further examples, Figure 2 shows confidence regions determined with Gaussian and exponential error assumptions for the 27 June 1998 M=6.2 Adana earthquake, and Figure 3 shows the same for its largest aftershock on 4 July 1998. The data used in these examples are from the Reviewed Event Bulletin (REB) of the International Data Centre. Only first arrival P times were used in our calculations, which numbered 24 for the mainshock and 20 for the aftershock. For both the Gaussian and exponential error models, the standard error (σ) was bounded between 0.5 and 1.5 seconds.

In the case of Gaussian errors (top of Figures 2 and 3) we do not see strong non-ellipticity of the confidence regions because the confidence regions are small compared to the distances to the stations, and they are contained mainly in the upper mantle where there are no large velocity contrasts (in the IASPI91 model). Despite these factors, though, there is noticeable departure of the confidence regions from ellipses in the case of exponentially distributed errors (bottom of figures).

Once again, only confidence regions at high confidence levels cover the true locations of the Adana events, as inferred from a dense local network that surrounded the events (Aktar et al, 2000). The fact that the mislocation is similar (west and deep) for the two events suggests it is not due to picking errors that were anomalously large compared to our assumed picking accuracy, which was itself rather large (standard error of up to 1.5 seconds).

Modeling Errors

In the examples above, reasonable assumptions about picking errors do not yield valid conclusions about the uncertainty in event locations. The confidence regions do not include the true event locations except at high confidence levels, and the mislocation is similar for different events in the same region, suggesting a repeatable source of error. Errors in travel-time models frequently exceed picking errors and, when they cannot be corrected, must be accounted for in the uncertainty analysis.

A simple, and commonly used, way to do this is to inflate the assumed variance of the data errors, attempting thus to define the probability distribution of the sum of picking and modeling errors [$c_i + e_i$ in equation (1)]. This would be appropriate if modeling errors were independent between stations and seismic phases. Another mechanism is to modify the shape, as well as the width, of the error distribution, e.g., manipulating p as we did in the examples. However, to the extent that modeling errors are correlated between stations and phases, the confidence regions that result might still not be indicative of the true location error. Ultimately, a statistical analysis of actual picking and modeling errors is needed to derive an appropriate error model.

We are currently pursuing a formal approach to the problem by attempting to link the effects of modeling errors in the single event location problem to empirical calibration methods. Such methods fit travel-time residuals observed from many events with parameterized corrections. An analysis of the errors in the correction estimates provides the statistical model of modeling errors that we need.

For example, many approaches to calibration (e.g., Dewey, 1971; Jordan and Sverdrup, 1981; Pavlis and Booker, 1983) assume that travel-time corrections are static at stations (i.e. independent of event location) and then solve the problem of jointly determining the locations of multiple events and the station corrections. The problem can be posed as

$$d_{ij} = t_j + T_i(\mathbf{x}_j) + c_i + e_{ij}, \quad i = 1,....,n;\ j = 1,....,m \tag{18}$$

for m events with origin parameters $(\mathbf{x}_j, t_j)$, $j = 1,....,m$. (We have not denoted it, but we do not assume there are data for all mn possible (i,j) pairs.) Applying our maximum-likelihood formulation to this problem, we can define a solution as maximization of the likelihood function given by

$$-\log L(\mathbf{x}_1, t_1, ..., \mathbf{x}_m, t_m, \mathbf{c}; \mathbf{d}) =$$

$$K_1 + K_2 \sum_{ij} \left| d_{ij} - t_j - T_i(\mathbf{x}_j) - c_i \right|^p / (\nu_{ij})^p \tag{19}$$

where $\mathbf{c} = (c_1,\ldots,\boldsymbol{c}_n)$, $\mathbf{d}$ denotes the vector of data from all events, and K_1 and K_2 are constants. A complete solution of this problem yields a probability distribution of an estimator for $\mathbf{c}$, which could then be used as a modeling error distribution in locating a new event. An even more rigorous approach would be to include each new event in the multiple-event analysis and infer its location uncertainty directly, accounting for the trade-offs amongst event locations and travel-time corrections.

The assumption of source-independent station corrections restricts a calibration analysis of this type to events that are in a tight cluster. To address calibration with events distributed over a wide region, it is necessary to consider the spatial dependence of travel-time corrections. A geo-statistical approach to this problem was formulated by Schultz et al (1998), who applied a kriging method to interpolate observed travel-time residuals between events. We are investigating an analysis of modeling errors using this approach. In this analysis, a travel-time correction is a *path*-dependent term, c_{ij}. A prior error model for the c_{ij} is specified by considering them to be samples of a random field. We are formulating this approach with a universal parameterization of corrections for all stations. A simple example, assuming only P wave data so as to avoid new notation, is to define a single random field, $(\mathbf{x})$, and let

$$c_{ij} = a(\mathbf{y}_i) + a(\mathbf{x}_j) \tag{20}$$

where $\mathbf{y}_i$ is the location of the *i*th station. The uncertainty analysis for an event location now falls out of the joint inversion problem of multiple-event location and kriging.

Approaches such as this provide a rigorous framework for addressing the uncertainty in seismic event locations and the effects of both observational and modeling errors. However, they do not necessarily lead to practical algorithms for accomplishing the analysis. We are investigating the feasibility of applying our grid search and Monte Carlo techniques to the problem, and seeking approximations and shortcuts that can accomplish the basic goals of the approach in a practical way.

CONCLUSIONS AND RECOMMENDATIONS

We have developed a general theoretical and computational framework for characterizing the uncertainty in seismic event locations. Applications to date show that, for sparsely recorded events or poor station distribution, the elliptical confidence regions resulting from a linear, Gaussian analysis do not adequately characterize this uncertainty. The effects appear to be significant when the true confidence region is too large compared to event-station distances, or encompasses significant variations in the Earth's velocity. An example of the latter situation is when the data allow focal depths ranging through the crust and upper mantle, which is a common occurrence when only first arrivals are used. The use of non-Gaussian error distributions can also lead to non-elliptical confidence regions.

As part of our uncertainty analysis, we are attempting to include a realistic model of the errors in the travel-time tables used in locating an event. We are pursuing an approach that links the error model used in single-event location to the results of calibration analyses performed with multiple-event data. To test our ideas, we are preparing a large database of events in Turkey that are recorded by local and national networks spanning the country, many of which are recorded by regional and teleseismic stations. These data will enable us to study the size and spatial dependence of travel-time residuals, and also provide accurate locations for many small events so we can validate the confidence regions we derive from sparse regional networks.

REFERENCES

Aktar, M., M. Ergin, S. Özalaybey, C. Tapirdamaz, A. Yörük and F. Bicmen (2000). A Lower-Crustal Event in the Northeastern Mediterranean: The 1998 Adana Earthquake (M_w=6.2) and Its Aftershocks, *Geophys. Res. Letters, 27,* 2361-2364.

Billings, S. D., M. S. Sambridge and B. L. N. Kennett (1994). Errors In Hypocenter Location: Picking, Model and Magnitude Dependence, *Bull. Seism. Soc. Am., 84,* 1978-1990.

Dewey, J. W. (1971). Seismicity Studies with the Method of Joint Hypocenter Determination, *Ph.D. Thesis,* University of California, Berkeley.

Evernden, J. F. (1969). Precision of Epicenters Obtained By Small Numbers of World-Wide Stations, *Bull. Seism. Soc. Am., 59,* 1365-1398.

Flinn, E. A. (1965). Confidence Regions and Error Determinations for Seismic Event Location, *Rev. Geophys., 3,* 157-185.

Jeffreys, H. (1932). An Alternative to the Rejection of Observations, *Mon. Not. R. Astr. Soc, Geophys. Suppl. 2,* 78-87.

Jordan, T. H. and K. A. Sverdrup (1981). Teleseismic Location Techniques and Their Application to Earthquake Clusters in the South-Central Pacific, *Bull. Seism. Soc. Am., 71,* 1105-1130.

Myers, S. C., and C. A. Schultz (2000). Improving Sparse Network Seismic Locations with Bayesian Kriging and Teleseismically Constrained Calibration Events, *Bull. Seism. Soc. Am., 90,* 199-211.

Pavlis, G. L., and J. R. Booker (1983). Progressive Multiple Event Location (PMEL), *Bull. Seism. Soc. Am., 73,* 1753-1777.

Sambridge, M. (1999). Geophysical Inversion with a Neighbourhood Algorithm - 1. Searching a Parameter Space, *Geophys. J. Int., 138,* 479-494.

Schultz, C. A., S. C. Myers, J. Hipp and C. J. Young (1998). Nonstationary Bayesian Kriging: A Predictive Technique to Generate Spatial Corrections for Seismic Detection, Location, and Identification, *Bull. Seism. Soc. Am., 88,* 1275-1288.

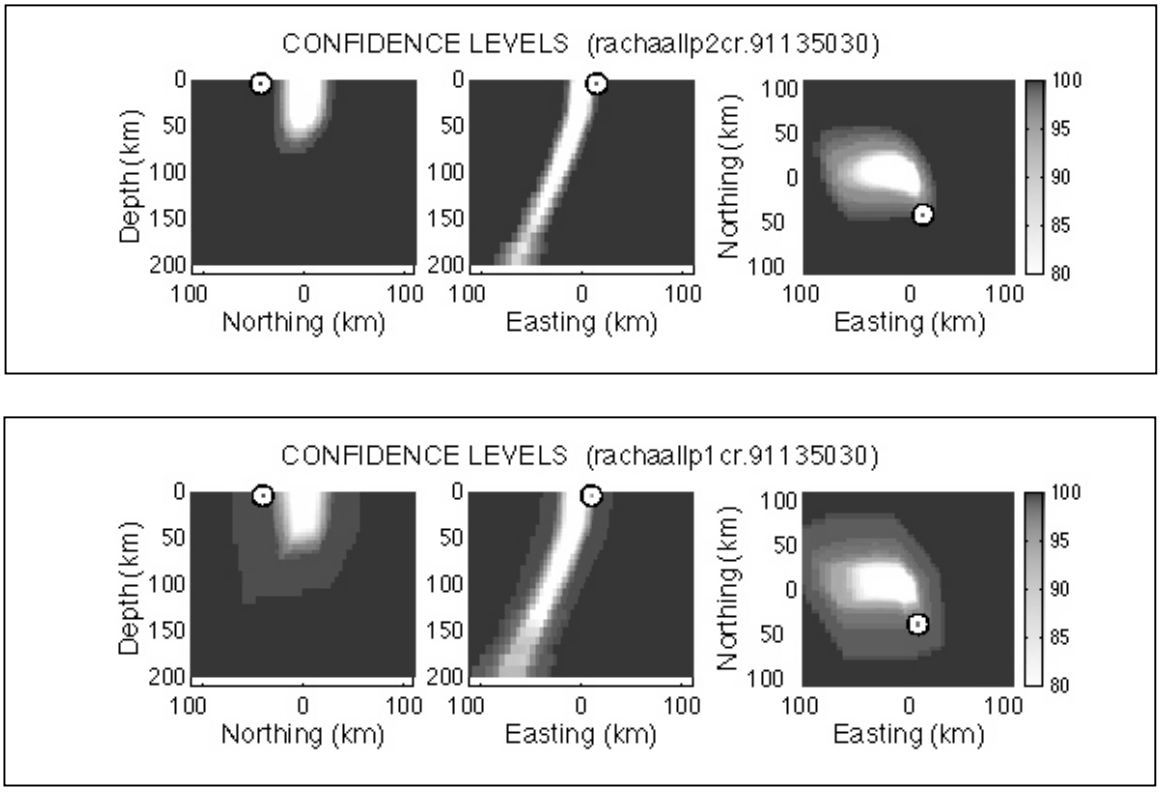

Figure 1: Confidence level vs. location for an event from the 1991 Racha earthquake sequence (ID 91135030). The top panels are based on the assumption of Gaussian picking errors (p=2). The bottom panels assume the errors are from an exponential distribution (p =1). *Left and center:* Cross-sections of confidence level vs. hypocenter taken through the maximum-likelihood location. *Right:* Confidence level vs. epicenter. Each contour of constant confidence level is the boundary of the 3-D hypocenter (left and center) or epicenter (right) confidence region at that level. Note that confidence levels below 80% are all displayed with white. The circles mark the local network location for the event. The maximum-likelihood epicenter is at zero northing and zero easting.

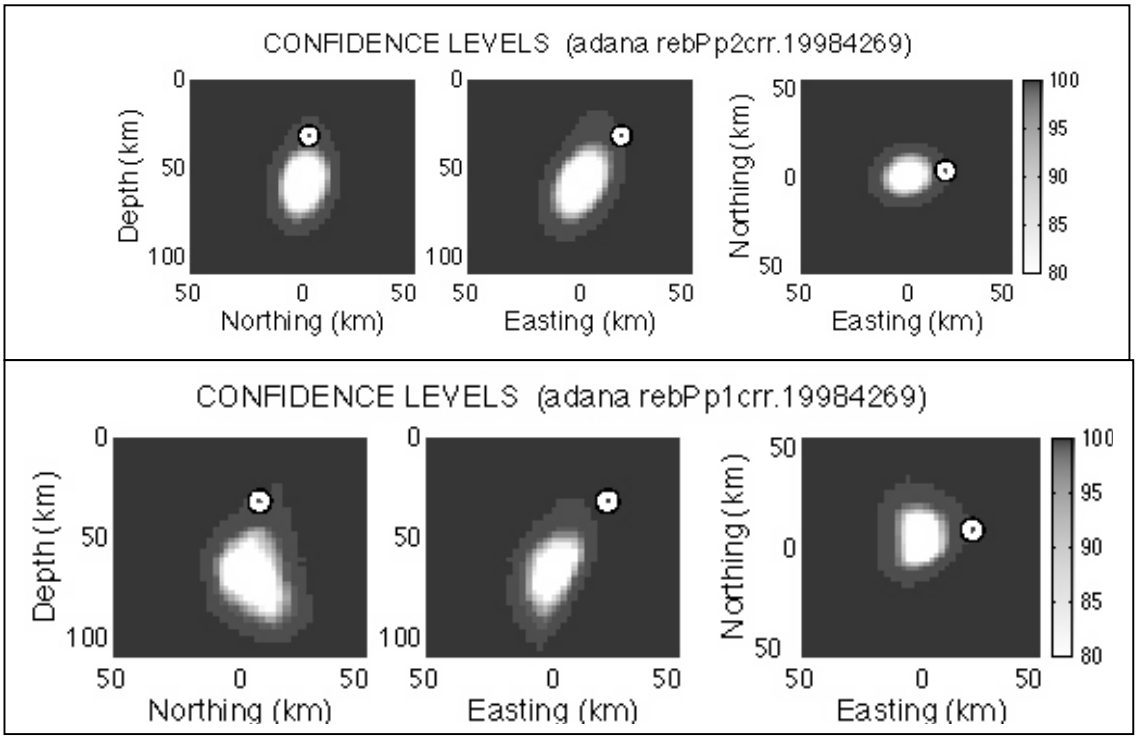

Figure 2: Confidence level vs. location for the 27 June 1998 Adana earthquake, determined with a Gaussian (top) and exponential (bottom) error model. The panels are defined as in Figure 1. The circles mark the local network location for the event.

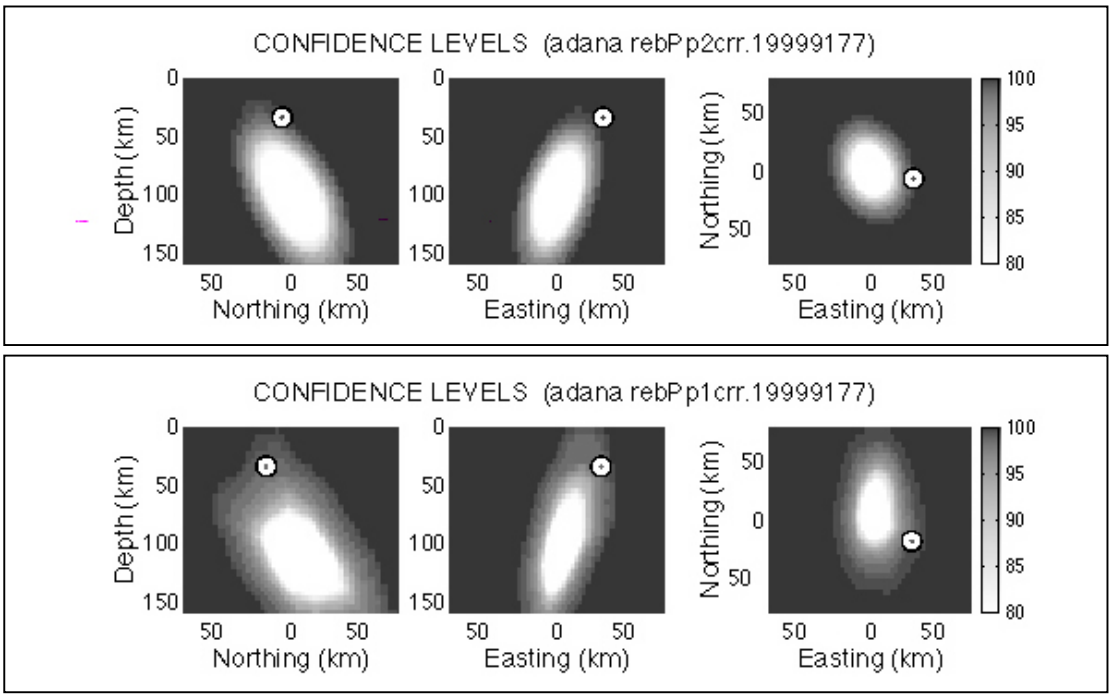

Figure 3: Confidence level vs. location for the 4 July 1998 aftershock of the Adana earthquake, shown in the same format as Figure 2.

INTERNATIONAL MONITORING SYSTEM LOCATION ACCURACY IMPROVEMENT IN NORTH AMERICA AND NORTHWESTERN EURASIA USING SOURCE-SPECIFIC STATION CORRECTIONS (3-D) FOR Pn, Sn, AND Pg PHASES

Russian Federation/United States Calibration Working Group*

Sponsored by Defense Threat Reduction Agency

Contract No. DSWA01-98-C-0032

ABSTRACT

This study was carried out under the United States/Russian Federation (US/RF) Joint Program of Seismic Calibration of the International Monitoring System (IMS) in Northern Eurasia and North America. The main objective of the calibration efforts is to improve the IMS location accuracy of regional seismic events within North America (NA) and Northwestern Eurasia (NWE) utilizing Source-Specific Station Corrections (SSSCs) inferred from 3-D crustal and upper mantle velocity models. These corrections are hereafter referred to as SSSCs(3-D). The methodology for both NA and NWE was: 1). Collection and analysis of Pn, Sn, and Pg travel times and 1-D crustal and upper mantle velocity models, and assigning the 1-D models to tectonic regions to develop 3-D velocity models; 2). Feasibility study of 3-D travel-time modeling for development of SSSCs(3-D) corrections; 3). Relocation experiments for validation of SSSCs(3-D) developed by 3-D modeling. In the regions where no information on deep velocity structure was available, tectonic regionalization was used to extrapolate and/or interpolate seismic data from other regions where the velocity structure was known.

We developed SSSCs(3-D) for Pn, Pg, and Sn phases for IMS stations in NA and NWE and for several additional stations in NWE. Three-dimensional crustal and upper mantle P velocity models for NA and NWE were derived by fitting the models to observed travel-time residuals of Pn waves from ground truth zero (GT0) nuclear and chemical explosions, and from compiled seismic data. A 3-D modeling program "sssc2" developed by Dr. P. Firbas computes SSSCs up to 20 degrees for Pn and up to 8.5 degrees for Pg from these models. Corrections were derived for Sn by using a relationship between Pn and Sn travel times derived from ground truth (GT) events and IASPEI-91 tables. To validate the location accuracy improvement using SSSCs(3-D), we relocated four sets of calibration events for NA and NWE with approximately 90 events (announced chemical explosions and mine blasts from the Prototype International Data Centre (PIDC) GT0-GT2 database, historical nuclear explosions detonated in NWE, and GT10 events supplied by Dewey and others for western areas of the USA territory). These GT events were independent of the GT data that were used to derive the 3-D models. Results of the relocation experiments for GT0-GT2 and GT10 events in different regions of NA and NWE clearly indicate that the event location estimates were improved when SSSCs(3-D) were applied.

Generally we conclude that the application of the SSSCs(3-D) significantly reduces the error ellipse area and improves location accuracy. These corrections for NA have been accepted by the Configuration Control Board (CCB) of the PIDC to calibrate locations for IMS stations in NA. For the Lg phase, we propose that the existing corrections continue to be used. For teleseismic phases, no corrections have been developed for IMS stations in NA.

* The RF members of the Working Group (WG): Colonel V. Gordon (chairman), Colonel V. Shishkov, Colonel V. Yakushevich, and Lt. Colonel D. Bobrov. The US members of the WG: Dr. A. Dainty (chairman), Dr. D. Baumgardt, Mr. J. Murphy, Dr. R. North, and Dr. V. Ryaboy.

KEY WORDS: earth crust, upper mantle, velocity structure, event location.

OBJECTIVE

The International Monitoring System (IMS) is being developed for global monitoring under the Comprehensive Nuclear-Test-Ban Treaty (CTBT). To help fulfill this task, seismic events should be located with high accuracy. To achieve the CTBT goal of 1000 km^2 location accuracy the IMS has to be calibrated, i.e.travel-times of seismic waves used in the location must take into account the 3-D structure of the Earth. This work is focused on calibration of IMS stations in NA and NWE. The main objectives are the following: 1). Pn travel-times data collection and analysis for different tectonic provinces of North America and Northwestern Eurasia; 2). Application of 3-D modeling for location of regional seismic events; 3). Demonstration of improvements achieved in location accuracy when 3-D models are used.

This work was carried out as part of the United States/Russian Federation (US/RF) Joint Program of Seismic Calibration of the International Monitoring System (IMS) in NWE and NA. This cooperation is useful irrespective of the CTBT.

RESEARCH ACCOMPLISHED

Our goal was to derive a 3-D crustal and upper mantle velocity model for continental NA and NWE capable of predicting Pn travel-times with an accuracy of approximately 1.0 s (RMS). The simplest 3-D velocity models were sought from a family of 3-D models that simultaneously fit the observed Pn travel-times for 8 GT0 events (nuclear and large chemical explosions) in NA and 20 GT0 events (nuclear explosions) and Fennolora long-range profile observational data for NWE. Figure 1 (top and bottom, respectively) shows the good coverage by deep seismic studies for southern and central regions of NA and for large parts of NWE.

The computer program “sssc2” (Firbas, 1997) was used to compute the SSSCs(3-D) for Pn and Pg, up to distances of 20 degrees and 8.5 degrees, respectively, based on developed 3-D velocity models. The methodology of location calibration based on 3-D modeling was recently summarized and published (Firbas, 2000; Ryaboy et al., 2001). The parametrization of the 3-D model employs an approach that allows combination of the best velocity information available from multiple sources. Block parametrization (i.e., division of geographic regions into blocks) is combined with a parametrization based on interpolation and permits substantial features of the Earth’s heterogeneities to be represented, including a laterally heterogeneous crust, an arbitrary curved Moho discontinuity, and a heterogeneous upper mantle. The base model covers the entire Earth and thus the SSSCs(3-D) for both regional and teleseismic phases can be consistently computed. All elements of the model (crust, Moho, uppermost mantle, etc.) are represented independently. An advantage of this approach is that the number of parameters to be varied during the iterative search for an improved 3-D model can be kept small and, furthermore, these parameters always have a clear physical interpretation.

As the first step, the initial 3-D models for P-waves for NA and NWE were based on a model of the Earth’s crust, CRUST 5.1 (Mooney et al., 1998), on Moho depths (Braile et al., 1989), and on the upper mantle velocity model RUM (Gudmundsson and Sambridge, 1998). As starting model for western areas of NWE, the 3-D model for P-waves developed by (Firbas, 1997a) was also used. In the search for the simplest 3-D model fitting the available data, the most accurate information (3-D crustal velocity model and the Moho depth) was kept fixed. The 3-D upper mantle velocity models of NA and NWE were then adjusted iteratively by comparisons of calculated and observed Pn travel times. Calculated Pn residuals based on the 3-D velocity models were tested against the maps of observed travel-time residuals and improvements to the 3-D model were made where necessary (Gordon et al., 2001; Ryaboy et al. 2001). This iterative procedure was quite straightforward, as the number of varied parameters could be kept relatively low. First, the 1-D velocity-depth sections were kept fixed and just the boundaries between tectonic units in the upper mantle were moved as needed. When the movement of the boundaries in the 2 x 2 degrees resolution model did not bring any further substantial improvements, new 1-D velocity-depth sections were added and/or existing 1-D velocity-depth sections were modified. We extrapolated 1-D velocity models within regions with similar geological structure. The 3-D velocity models fit the observed Pn travel times with a precision of 1 s (RMS). Figure 2 (top and bottom) shows proposed maps of the upper mantle velocity regionalization of NA and NWE, respectively. The 3-D crustal and upper mantle velocity models developed for NA and NWE (Gordon

et al., 2001; Ryaboy et al. 2001) were used to produce maps of the SSSCs(3-D) for Pn and Pg for IMS stations and for several additional stations in NWE.

The SSSCs(3-D) for Sn waves were calculated from the SSSCs(3-D) for Pn waves using a relationship between Pn and Sn travel-times inferred from the Center for Monitoring Research (CMR) GT database and the IASPEI-91 travel-time tables. It is known that Vp/Vs ratio depends on many factors including depth and tectonic province (Alekseev et al., 1988; Hauser and Stangle, 1990). Since Vp/Vs ratio depends on depth, simple scaling of Pn travel times directly into Sn travel times is not possible as the Vp/Vs dependency on depth implies that Pn and Sn waves for the same station - source pair do not propagate along the same ray-path. Statistically significant correlation was found between ratios TSn/TSn_iasp91 and TPn/Tpn_iasp91, where TSn and TPn are measured travel-times for GT events and TSn_iasp91 and TPn_iasp91 are corresponding IASPEI travel-times. A function was fitted to the distribution of all available points (TPn/Tpn_iasp91, TSn/TSn_iasp91) based on the CMR GT database. The correlation coefficient for this fit was 0.75, high enough to allow usage of this polynomial function for conversion of predicted Pn travel times into predicted Sn travel times. This approach, together with conservative estimates of modeling errors, proved to be successful and the location quality remained on the same level when TSn travel times were added to the locations based on Pn and Pg travel-times only.

We did not use the Lg phase in NWE due to large errors of discovered in arrival-time measurements. However, for NA, in agreement with current Prototype International Data Center (PIDC) procedures, we have used either CMR Lg travel times without SSSCs (for IASPEI-91) or Lg travel-times with SSSCs(1-D) (Yang and McLaughlin, 2000) as appropriate. Figures 3 and 4 show, as examples, the SSSCs(3-D) and modeling errors maps calculated for Pn waves for two IMS stations: PDAR (NA) and OBN (NWE). 1-D velocity-depth sections for the mantle were assigned to every grid point on 2x2 degree grid and the 3-D velocity distribution at any point is the linear interpolation of the four nearest 1-D velocity-depth sections. To obtain a reasonable resolution and size of the SSSCs files even for stations in northern areas, we calculated time corrections and modeling errors with different latitude/longitude grids for each station. SSSCs(3-D) files have grid 0.5 degree for latitude axis. Grid for the longitude axis has a constant value for each station within the range 0.5 degree to 1.2 degree depending on the latitude of the station.

To validate the calculated SSSCs(3-D) we have used two data sets of GT0-GT10 events for NA and two data sets of GT0 and GT2 for NWE. All these events were used only for relocation experiments and were not used for development of 3-D velocity models. We performed a careful analysis of travel times and, on occasion, waveforms to identify outliers at the level of events and at the level of individual arrivals, with the goal of eliminating their undue influence on the relocation experiments. Data quality analysis (visual inspection) of the GT0 and GT2 events for NA using waveforms (Baumgardt et al., 2000) largely confirms our results regarding identification of outliers based on the travel-times analysis. Altogether 15 GT0-GT2 events (mainly announced chemical explosions) were found for NA to have a sufficient amount of reliable regional arrival-time data to be used for the relocation experiments using regional phases only. The second data set for NA includes 29 GT10 events from the US calibration event data set with REB arrivals (Dewey et al., 1999). Figure 5 (top) shows the location of GT events used for relocation experiments in NA. Two sets of GT0-GT2 events were used for relocation experiments within Northern Eurasia. The first set of events includes 31 GT0-GT2 events from PIDC GT database, and the second set of events consists of 17 nuclear explosions detonated within western areas of NWE from 1965 to 1988 (Figure 5 bottom). These explosions were detonated when the IMS network did not exist, and we calculated SSSCs(3-D) and used for relocation experiments additional stations (“surrogate” IMS stations) located at distances of 150-200 km on average from the current IMS stations.

Relocation experiments were performed to evaluate the impact of the SSSCs(3-D) for Pn, Pg, and Sn on regional seismic event locations within NA and western areas of NWE and to asses the improvement both in terms of location accuracy and in the reduction of the size (area) of the 90% error ellipses. In line with the current PIDC procedures we used for NA all phases (i.e. regional Pn, Pg, Sn and Lg as well as the teleseismic phases). However, we used for relocation experiments within western areas of NWE only Pn, Sn, and Pg phases. The approach for the measurement errors used was identical to the current PIDC practice. As we are

not proposing new SSSCs corrections for Lg, we used for North America either uncorrected Lg travel times or SSSCs(1-D) for Lg (Yang and McLaughlin, 2000). LocSAT program was used for the relocation experiments.

Results of the relocation experiments for GT0, GT2 and GT10 events located in different regions of NA and NWE clearly indicate that the event location estimates were improved when the SSSCs(3-D) were applied. For GT0 - GT2 data for NA was found that the median mislocation changed from 9.3 km for IASPEI-91 to 6.2 km for SSSCs(3-D), and the median 90% error ellipse area decreased from 2,011 km^2 for IASPEI-91 to 754 km^2 for SSSCs(3-D). For GT10 events in NA the median mislocation decreased from 16.7 km or IASPEI-91 to 11.4 km for SSSCs(3-D), and the median 90% error ellipse area decreased from 1,802 km^2 for IASPEI-91 to 725 km^2 for SSSCs(3-D). It is very encouraging that when using the initial SSSCs(3-D) fir 31 GT0-GT2 events in NWE the median mislocation decreased from 17.3 km for IASPEI-91 to 7.7 km for SSSCs(3-D), and the median 90% error ellipse area decreased from 4,113 km^2 for IASPEI-91 to 873 km^2 for SSSCs(3-D). For 17 nuclear explosions detonated within NWE the median mislocation decreased from 22.5 km for IASPEI-91 to 8.9 km for SSSCs(3-D), and the median 90% error ellipse area decreased from 2,811 km^2 for IASPEI-91 to 662 km^2 for SSSCs(3-D).

CONCLUSIONS

1. A 3-D crustal and upper mantle velocity models for NA and western areas of NWE based on previous results of deep seismic studies and derived by fitting 3-D velocity models to observed travel-time residuals of Pn waves from GT0-GT2 nuclear and chemical explosions were created to generate SSSCs(3-D).

2. SSSCs(3-D) for IMS stations in N A and for IMS stations and additional stations in western areas of NWE for Pn, Pg, and Sn phases are proposed based on the models in (1). SSSCs(3-D) corrections for Sn phase were derived by using a relationship between Pn and Sn travel-times derived from ground truth (GT) database and IASPEI-91 tables.

3. To validate the location accuracy improvement of the SSSCs(3-D), we relocated for NA a set of 15 GT0-GT2 events (announced chemical explosions and mine blasts) from the PIDC GT database and a set of 29 GT10 events supplied by Dewey et al. (1999). For western areas of NWE we relocated two sets of GT0-GT2 events: first set of the events includes 31 GT0-GT2 events from the CMR GT database, and the second set of events consists of 17 nuclear explosions detonated from 1965 to 1988.

4. The validation of the SSSCs(3-D) based on the comparison of the travel-times for the high quality GT0 events (mostly nuclear explosions) confirms that the predictions of the Pn travel-times using 3-D velocity models are of high quality (RMS 1.0-1.5 s).

5. Generally, we conclude that the application of the SSSCs(3-D) significantly improved location accuracy and reduced 90% error ellipses. These corrections developed for NA have been accepted by the Configuration Control Board (CCB) of the PIDC to calibrate locations for IMS stations in North America. The corrections for NWE are currently under further development and testing.

ACKNOWLEDGEMENTS

The authors are grateful to Dr. Petr Firbas for his “sssc2” program that was used during this study. Dr. Istvan Bondar kindly provided predicted Pn travel-times calculated for two nuclear explosions using his software based on 1-D modeling approach.

REFERENCES

Alekseev A.S., Egorkin A.V., Pavlenkova N.I. (1988), Shear waves in lithosphere studies on the territory of the U.S.S.R., Tectonophysics, 154, 227-239.

Baumgardt D., Ryaboy V., Schneider C., Dainty A. (2000), Validation for North America of model-based travel-time corrections for location using ground truth (GT) databases at the PIDC. Proceedings of the Second Workshop on IMS Location Calibration, Oslo, Norway, March 2000.

Braile L.W., von Freese R.R.B., Keller R.G. (1989), Seismic properties of the crust and uppermost mantle of the conterminous United States and adjacent Canada. In: Geophysical framework of the continental United States (Editors: L.C. Pakiser and W.D. Mooney), Geological Society of America, Memoir, 172, 655-680.

Dewey J., Herron E, Kork J., Recent calibration events in the United States, Memo, December 1999.

Firbas P. (1997), Program SSSC for computation of station-source specific time corrections for 3-D velocity models. Technical report CMR-97/08, Center for Monitoring Research, Arlington.

Firbas P. (1997a), IMS Calibration: 3-D Travel-Time Modeling for Europe (Status Report for the period September-December 1996).Technical report CMR-97/02, Center for Monitoring Research, Arlington.

Firbas P. (2000), Location Calibration Based on 3-D Modeling. In: Advances in Seismic Event Location. (Thurber C.H., Rabinowitz N. - editors), Kluwer Academic Publishers, pp. 135-161.

Gordon V.R., Bobrov D.I., Ryaboy V. (2001), SSSCs based on 3-D modeling for Pn, Sn, and Pg phases at IMS stations in Northwestern Eurasia. Proceedings of the Third Workshop on IMS Location Calibration, Oslo, Norway, April 2001.

Gudmundsson O., Sambridge M. (1998), A regionalized upper mantle (RUM) seismic model. J. Geophys. Res., vol. 103, No. B4, 7121-7136.

Hauser F., Stangl R. (1990), The structure of the crust and the lithosphere in Fennoscandia derived from a joint interpretation of P- and S-wave data of the FENNOLORA refraction seismic profile. Proceedings of the sixth EGT workshop, 71-92.

Mooney W.D., Laske G., Masters T.G. (1998), Crust 5.1: A global crustal model at 5^{o} x 5^{o}. J. Geophys. Res., 103, B1, 727-747.

Ryaboy V., Baumgardt D.R., Firbas P., Dainty A.M. (2001), Application of 3-D crustal and upper mantle velocity model of North America for location of regional seismic events. Pure and Applied Geophysics, 158, 79-103.

Yang X., McLaughlin K. (2000), Regional source specific station corrections (SSSCs) for North American IMS stations. Technical report CMR-00/01, Center for Monitoring Research, Arlington.

NORTH AMERICA

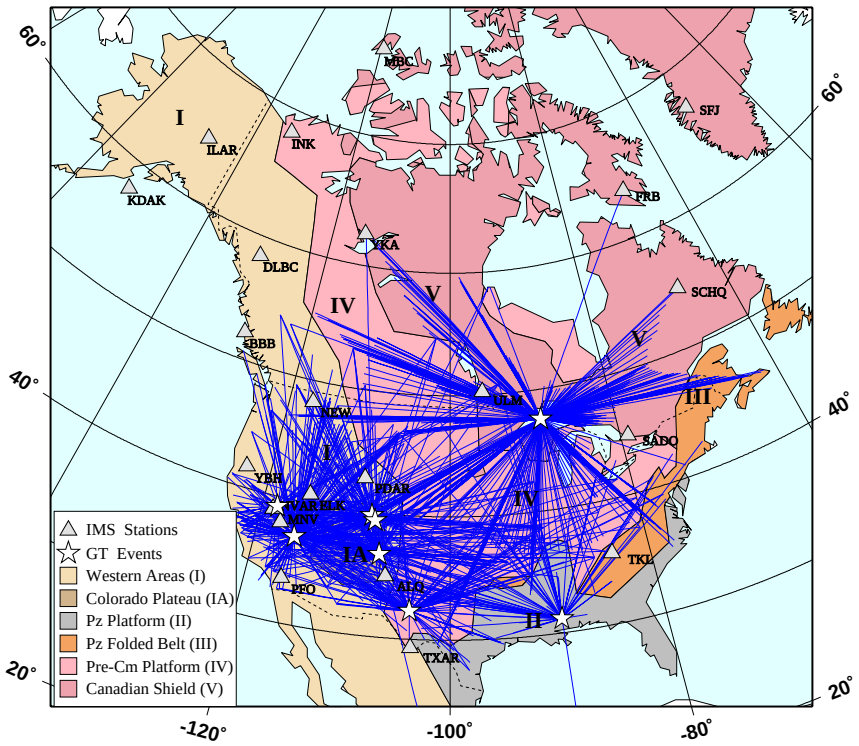

NORTHERN EURASIA

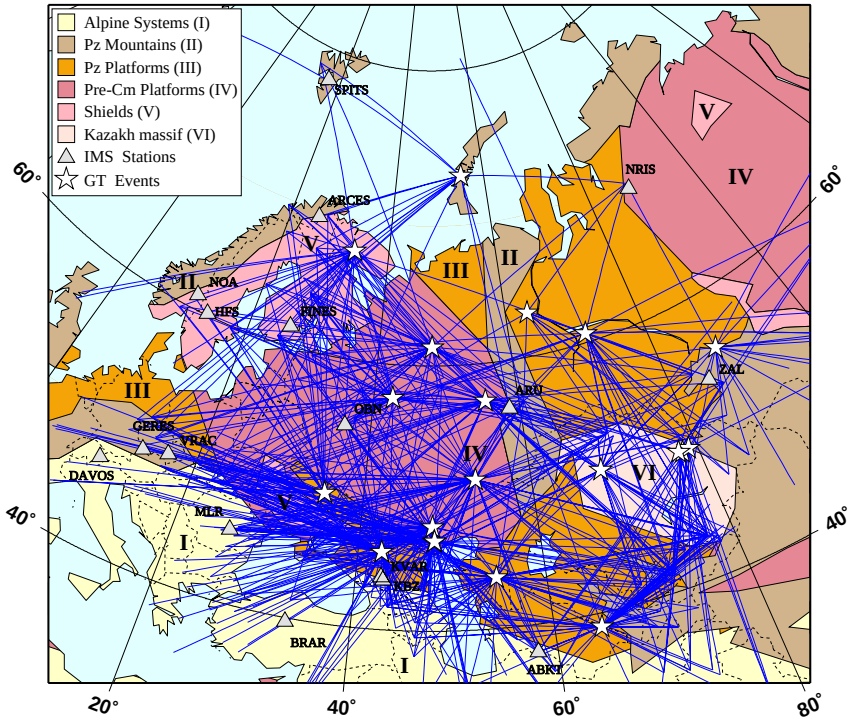

Figure 1. Calibration events used for development of 3-D velocity models. Lines are Pn event-station paths.

NORTH AMERICA

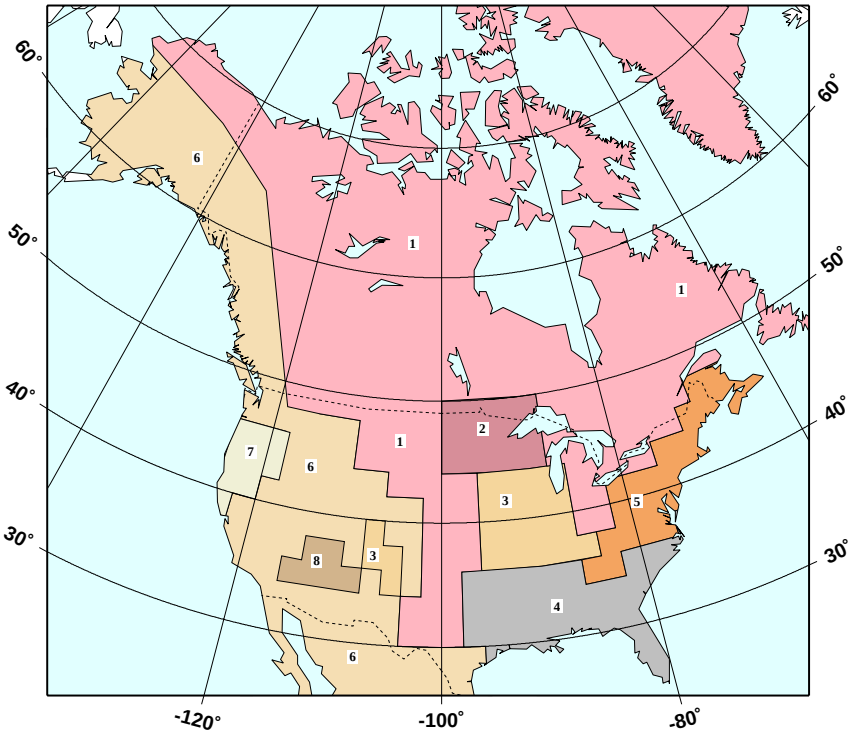

NORTHERN EURASIA

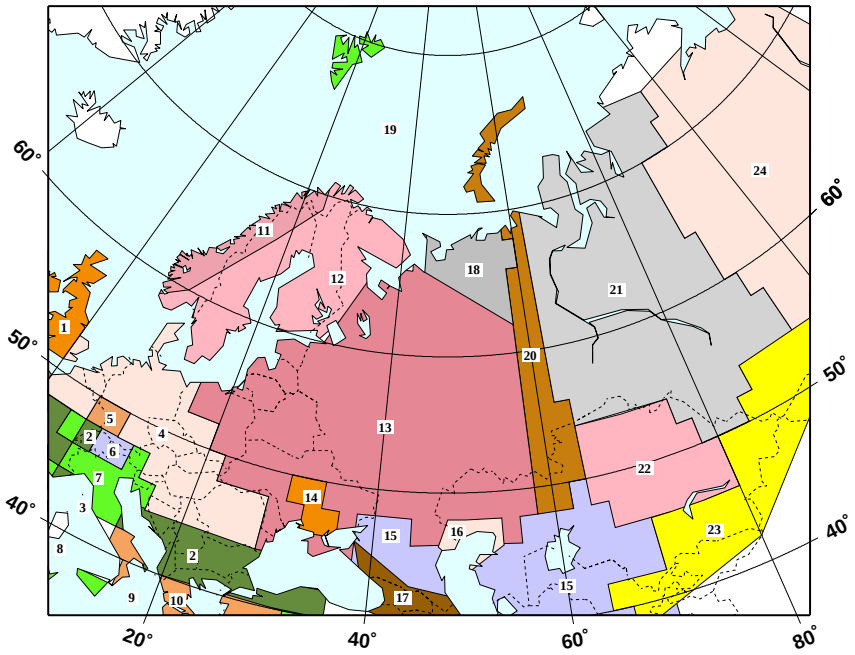

Figure 2. Upper mantle P-velocity regionalization maps. Each region is characterized by 1-D velocity model.

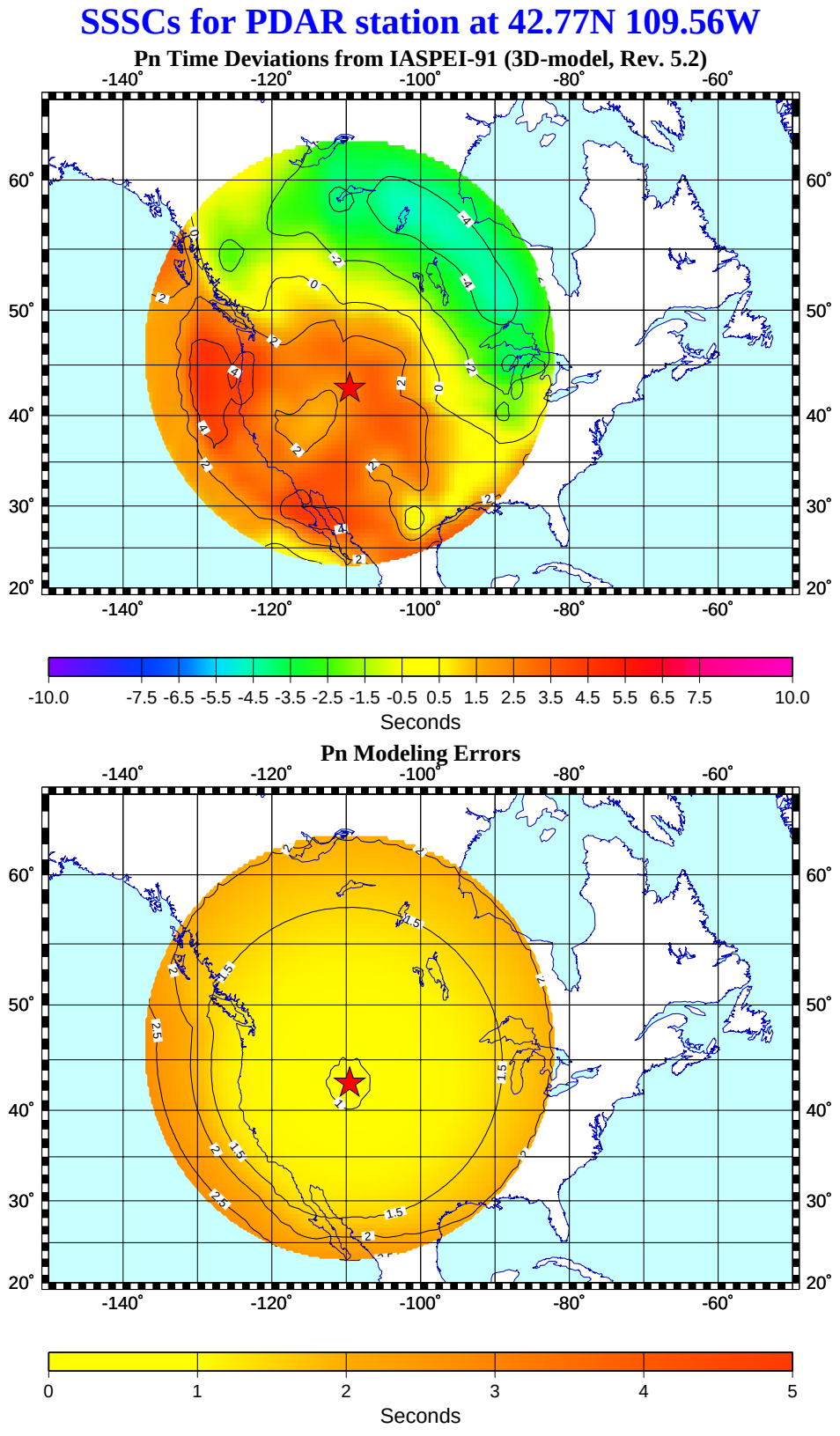

Figure 3. PDAR station, North America. Pn SSSCs and modeling errors.

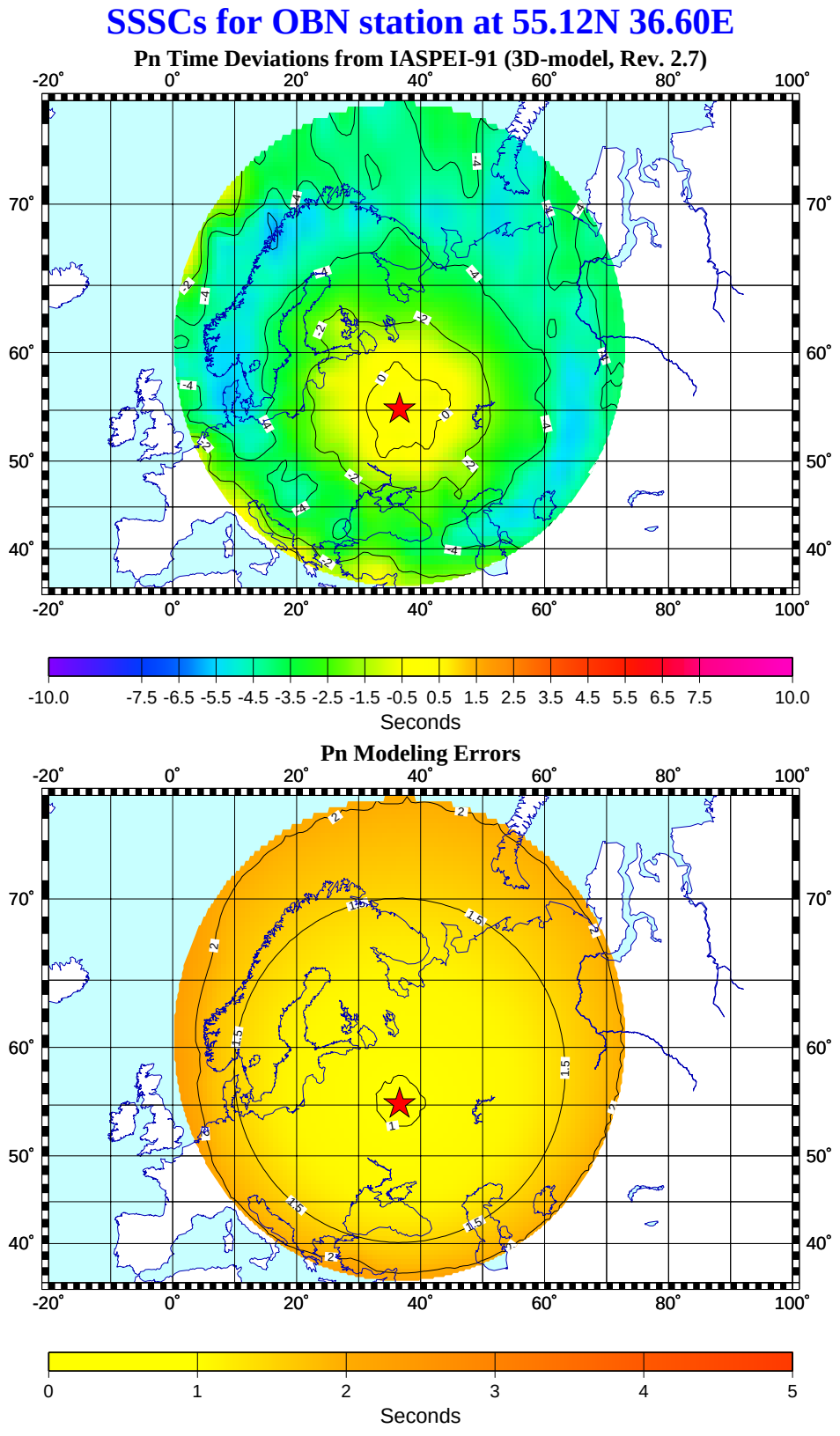

Figure 4. OBN station, Northern Eurasia. Pn SSSCs and modeling errors.

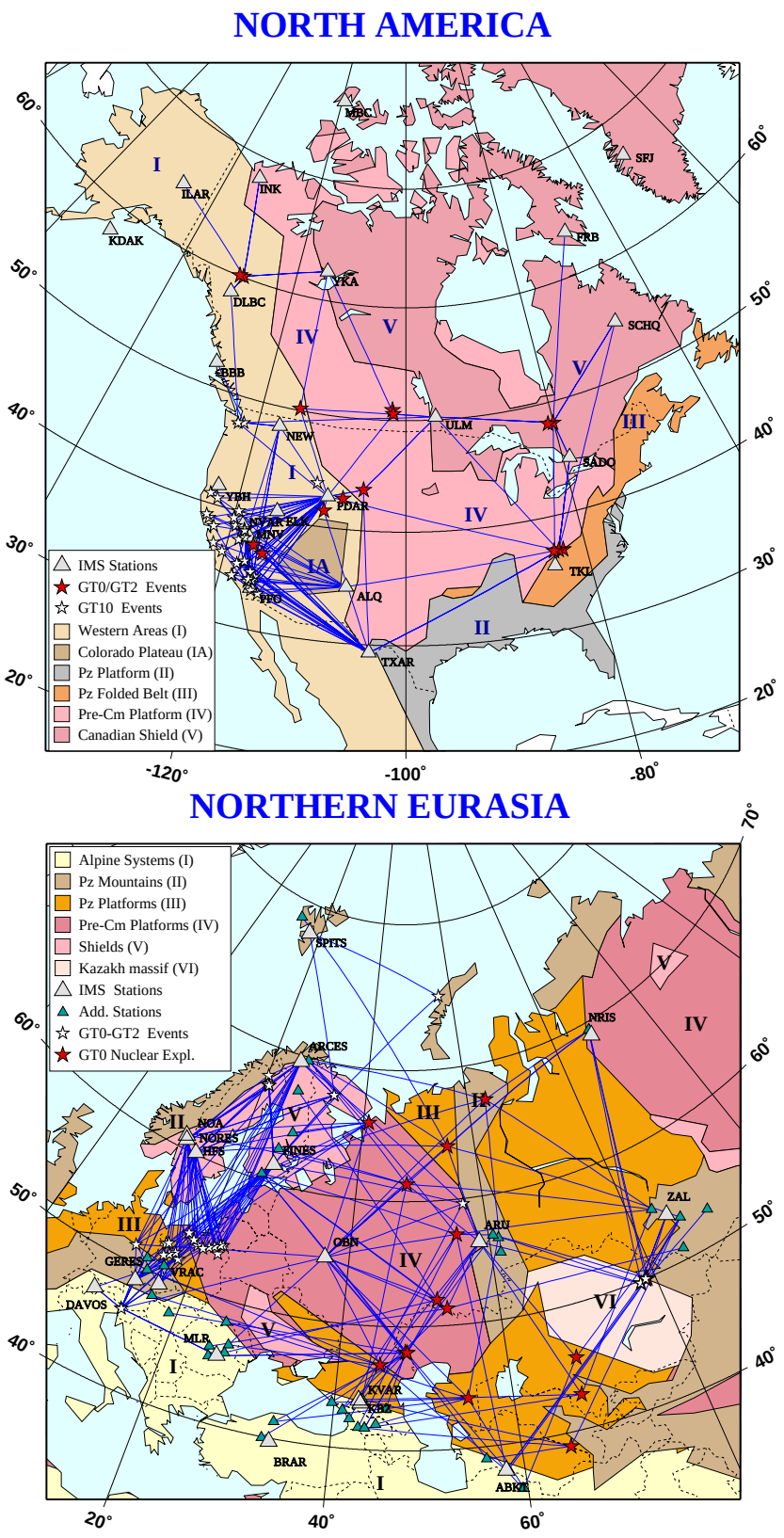

Figure 5. GT events used for relocation experiments. Lines connect the events with seismic stations used for relocation experiments at regional distances.

SEISMIC EVENT LOCATION STRATEGY AND PATH CALIBRATION IN AND AROUND THE INDIAN SUBCONTINENT

Chandan K. Saikia and Gene Ichinose

URS Group, Inc.

Sponsored by Defense Threat Reduction Agency

DTRA01-00-C-0033 and DSWA01-98-C-0146

ABSTRACT

The primary objective of this study is to obtain reliable earthquake locations ($4<M_W<6$) that occur in and around the Indian subcontinent for reliable calibration parameters for the region. Unlike many other regions of the world, our study region often lacks easy access to local seismic data. Thus, it has become essential to establish a procedure that can be used to improve locations of seismic events that satisfy the ground truth (GT25) criteria. To this end, we find that for an event that satisfies GT10 criteria one can remove all the local and regional phase data within 30^o and can still produce locations comparable to the GT10 results when the depth is independently determined. For moderate sized events, locations become biased due to the poor azimuthal distribution of seismic stations. This influences the trade-off between the depth and the origin time. We have examined our approach by applying to events whose locations were also determined using synthetic aperture radar interferometry (InSAR) analysis. We find that seismic locations determined by our approach remained within 5 km of these locations. Though the InSAR locations may not coincide with the dynamic seismic locations for the larger events because of the size of the fault, they are, however, fairly close for moderate sized events ($M_W \sim 5.5$). We have applied this location approach to identify GT10 events that are within 20^o of NIL in Pakistan, EVN in Nepal, and COC of Sri Lanka. In addition, we have also compiled several catalogues of earthquakes occurring along the northern, central, eastern and western Himalayan Mountain surrounding the Indian subcontinent. We have relocated events from two aftershock sequences, one sequence occurring following the Chamoli earthquake of March 28, 1999, and the other following the Jabalpur earthquake of May 21, 1997. We have also relocated earthquakes occurring in northeast India using the JHD (Joint Hypocenter Determination) technique. International Monitoring System (IMS) stations also record many of these events. We have further identified additional aftershocks that followed India's Republic Day Earthquake of January 2001 (M_W 7.7) which meet the GT10 event location criteria. We are now in the process of yielding an empirical travel-time correction surface for the region using these new GT10 events, including the events from the Koyna region. We have developed regional models for various regions of the Indian subcontinent using travel-time data from the in-country scientific studies and regional waveforms recorded in HYB and regional stations in India.

KEY WORDS:: ground truth, synthetic aperture radar interferometry, IMS, JHD, error ellipse, Rayleigh and Love wave dispersion.

OBJECTIVE

The principal objective of this paper is to present results of our ongoing study on the path calibration for the entire Indian subcontinent to provide model-based P-wave travel times in the region. To accomplish this goal, it is necessary to establish a catalog of earthquakes with quantitative estimates of uncertainties in their ground truth locations. In general, nuclear explosions (when announced) and quarry blasts provide the best ground truth accuracy to within 0 and 2 km. It is, however, difficult to ascertain uncertainties in ground truth locations for earthquakes, especially at low magnitude ($M_W< 4.5$)

The primary objective of this study is to obtain reliable earthquake locations ($4<M_W<6$) that occur in and around the Indian subcontinent for reliable calibration parameters for the region. Unlike many other regions of the world, our study region often lacks easy access to local seismic data. Thus, it has become essential to establish a procedure that can be used to improve locations of seismic events that satisfy the ground truth (GT25) criteria. To this end, we want to demonstrate that for an event that satisfies GT10 criteria, one can remove all the local and regional phase data within 30^o and can produce locations comparable to the GT10 results when the depth is independently determined. In this paper, we will first demonstrate the method and then proceed to apply it to earthquakes occurring in the study region. We will also present results from investigations on regional waveforms that are recorded from earthquakes in northeast India at three stations, namely LSA, CHTO and KMI.

RESEARCH ACCOMPLISHMENTS

Unlike many regions in the world where calibration shots are plentiful with ground truth (GT) accuracy from zero to 2 km, there are only a few such documented events in the study region with precisions that include the nuclear explosions of 1974 and 1998 in India and of 1998 in Pakistan. However, many earthquakes spanning a wide range of magnitude and depth occur along the Himalaya Mountain range from the northwest province in Pakistan to the northeast region in India extending toward the Indo-Myanmar orogeny. Many large earthquakes occurring in this seismic belt satisfy the criteria of GT25 events. These earthquakes are recorded by many stations at teleseismic and upper-mantle distances, and often are recorded by many stations lying nearly along one azimuth. Since access to local catalogs for arrival times from stations located within India is not often available, the number reduces when the criteria for the GT10 events are applied. In order that the GT25 event locations are improved to within the level of accuracy expected for the GT10 events, we successfully examined a method for a possible synergy between the seismic and InSAR (Synthetic Radar Interferometry) locations, using earthquakes for which the InSAR locations are available. In general, the InSAR images correspond to the static deformation across the fault, and for large earthquakes the dynamic event location does not often coincide with the location inferred from the static deformation estimated from the InSAR images. As the magnitude decreases, the static location itself becomes reflective of its dynamic location. In general, the pattern of the co-seismic deformation associated with an earthquake varies with a depth and focal mechanism. The shallower the event, the more likely that it will be observable in its co-seismic deformation in the radar data.

Testing of Location Strategy

Seismic Locations of GT25 Events Relative to Seis+InSAR/GT10 Locations

We examined the event location strategy using both seismic and InSAR data from the May 17, 1993,-Eureka Valley earthquake ($M_W\approx6$). The middle panel in Figure 1 shows a comparison of different seismic locations, namely RELOC, GT10nF, GT25nF, EHB and ISC, estimated using travel times of P and S waves from regional and teleseismic stations. These locations are not far from the corresponding InSAR location ($37.111^oN\pm0.5$km and $117.79^oW\pm0.6$km, Massonnet and Feigl, 1995; Peltzer and Rosen, 1995). The EHB location is from the catalog produced by Engdahl and his associates. The GT10nF and GT25nF are our locations which are equivalent to the GT10 and GT25 locations, but in this case we fixed the event depth determined the P wave seismogram modeling (top panel). RELOC is the location determined using travel-time data from portable and local permanent stations from the Northern California Seismic Network (NCSN) after applying average station corrections. The upper circle to the right of the middle panel gives the distribution of stations, indicating that a large number of the stations that recorded this event lie along the azimuth between 90^o and 180^o. A comparison of all locations suggests that these seismic locations lie within 10 km of the InSAR location.

We applied the same location approach to the 1998 Indian and Pakistani explosions. Fixing their depths at the surface, we relocated the two 1998 explosions using travel-time data. Locations shown in Figure 2 are based on different seismic phases. The GT1 location for the Indian explosion (Barker *et al*., 1999) lies within 5 km of the GT25nF location. For the Pakistani explosion, seismic locations from various sources are beyond 10 km from the GT1 location.

In a recent analysis, Lohman *et al.* (2001) were able to recover the InSAR location for the M_w5.4 Little Skull Mountain earthquake. Their Table 1 gives parameters for the InSAR locations along with the locations found through other strategies involving regional broadband seismograms (Figure 3). We have used this event for another benchmark calculation to investigate whether our approach will find location as good as its corresponding GT10 location. Lohman *et al.* (2001) found several locations, one with the InSAR data alone at 36.743^{o}N and 116.242^{o}W and another with a joint analysis of the seismic and InSAR synergy at 36.747^{o}N and 116.283^{o}W using the standard southern California/or Mojave crustal model. Since the InSAR location does not have the desired resolution, the joint seismic and InSAR location (referred to as Seis+InSAR location) is of a better quality. The GT25nF location is about 4 km from the Seis+InSAR location. We obtained the GT25nF location using the IASP91 crustal model, used no travel-time corrections for the teleseismic stations and did not account for the azimuthal bias. Included in the figure are also the EHB and GT25n and GT10n locations, n referring to the free-depth location, estimated by us. The GT10nF location that was estimated using stations up to 10^o is in proximity to GT25nF location, and both are about 5.5 km from the Seis+InSAR location. Thus, we not only have a good calibration for the locations of the GT25nF events, but also for a GT10nF event location. In the past the accuracy of the GT10 and GT25 locations could not be examined without the InSAR location.

Application to the Earthquakes in India - May 21,1999, Jabalpur and March 28, 1999, Chamoli

Previous studies (Saikia *et al.*, 1999; 2000; Saikia, 2000) have demonstrated that the crustal structure in central India consists of two layers on a half space by successfully modeling regional waveforms recorded at regional stations, namely HYB (Hyderabad), BHPL (Bhopal) and Bilaspur (BLSP), from the May 21, 1997 Jabalpur earthquake. Recently our study was extended to include an investigation of broadband waveforms recorded by regional stations in India from the March 28, 1999, Chamoli earthquake (IMD, Indian Meteorological Department 2000). We found that when seismic waves traverse from northern India through the Gangetic basin, they disperse significantly, and the P_{nl} wave travel times relative to the well-dispersed surface waves, including the dispersion characteristics observed in the surface waves, become path dependent (Saikia *et al.*, 2001). These observations do correlate with the varying thickness of the Gangetic sedimentary basin, further confirmed by the modeling of the recorded waveforms. We relocated these two earthquakes using focal depths determined from the teleseismic modeling of depth phases and using the P and S-wave travel-time data collected from local catalogs. The May 21, 1997, earthquake occurred following the installation of a regional broadband network in India, which generated regional seismograms providing an optimal azimuthal station coverage. Using both P and S travel times from catalog (IMD, 1999), we relocated this event, location shown by REG, using a local crustal model.

Next, we relocated the event by removing all stations within 30^o, essentially making it a GT25 event. The earthquake was recorded by a large number of stations worldwide; many stations reporting travel times for the depth phases also. Figure 4 shows all locations determined for this event, including the corresponding error ellipses where all locations cluster to within 3 km. Since information from sources other than seismic are not available, we can only argue based on the analysis of the Little Skull Mountain (M_W 5.4) and Eureka Valley (M_W 6.0) earthquakes that itsGT25nF location is probably accurate to about 10 km. Following the main event, a temporary network of many stations, shown by triangles in Figure 5, was installed in the epicentral region and recorded about 29 aftershocks (M_L<4), all satisfying the GT10 event location criteria. We relocated these events using the JHD (Joint Hypocenter Determination, Figure 5). Each line connecting a square to a circle represents a shift in relocations relative to the IMD locations. Of these, only the largest event was recorded at teleseimic distances. Figure 6 shows the residuals over the Indian subcontinent relative to our new location and IASP91 crustal model. The March 1999 Chamoli earthquake (M_W 6.7) also generated several aftershocks with M_W > 4. We obtained JHD relocations for these events using travel times from local catalogs and estimated travel-times residuals for P waves at all teleseismic distances (Saikia, *et al.*, 2001).

Path Calibration Study Surrounding Northeast India

Figure 7a shows a variation in travel times for P and S-wave first arrivals as a function of epicentral distances taken from monthly ISC (International Seismological Center) bulletins for $\Delta > 3^o$ and from local catalogs for $\Delta < 3^o$. The solid lines are least-squares fit with the Pn, Pg, Sn and Sg velocities inverted from the slope of these curves. Figure 7b shows the earthquakes and stations used in this analysis. We relocated these events using JHD method in which we also perturb through the crustal model. Figure 7c shows the travel time curves relative to our new locations which suggest that the average Pn velocity is 7.8 km/sec, lower than 8.33 km/sec that was obtained from the travel-time data before relocations.

Characterization of Surface Waves Using Seismograms at LSA

We collected broadband regional waveforms recorded at LSA from earthquakes (M_W>5.0) occurring within20^o of station LSA and analyzed both Rayleigh- and Love-wave dispersion curves using Herrmann's computer package, which uses the multiple-filter technique of Dziewonski. The group-velocity dispersion curves are complex in nature, exhibiting scatters at short periods (<10s), which relates to the complexity of the structure in the region. Figure 8 shows some examples of well-dispersed waves. We inverted both Rayleigh- and Love-wave dispersion curves and obtained a crustal model as shown in Figure 9 (upper panel) along a path from the Indo-Myanmar region to the station LSA (bottom right). Although this inversion has yielded a low-velocity layer at depth, we find that waveforms are not sensitive to any variation in the material properties of this layer. To the right of upper figure are shown the resolving kernels at different periods. Bottom left figure indicates the fit between the observed and simulated dispersion curves from the inverted crustal model for both Love and Rayleigh waves. We are continuing to develop more models in this region along various paths to station LSA based on the surface-wave dispersion analysis. To validate the P- and S-wave model, we forward modeled (computed seismograms) using the new model and checked to insure that synthetics were able to match the body and surface wave amplitudes and arrival times observed at LSA. The source was determined independently using regional long period waves by moment tensor inversion of three or more stations, namely CHTO, KMI and LSA, at long period (Figure 10). In the lower panel to the right is shown the crustal model and to the left is shown the agreement between data and synthetic seismograms along the path toward the station LSA. Note that this path to station LSA from the epicenter has a deep sedimentary river basin inside the province of Assam. In our previous studies, such a model was not available and was difficult to obtain this agreement for the seismograms for which seismic waves traverse through the sedimentary basin of the river.

Other Related Investigation

The Republic Day earthquake (M_W 7.7) in India had drawn wide spread attention throughout the world because of the human causalities including the structural damages even at large epicentral distances (≈250 km). The ground motion in the epicentral region sustained for an extended period of 90s, which is long. Following this devastating earthquake, scientists visited the epicentral region to investigate surfacial features related to the earthquake and brought instruments to record aftershocks and seismograms. These temporary stations recorded several aftershocks (M_W> 4) which satisfy GT10 criteria. We are using them for estimating of travel-time corrections for stations located at upper-mantle and teleseismic distances. We have also analyzed local short-period seismograms from northeast India in conjunction with the broadband seismograms recorded at LSA to investigate Q values of the region (Duarah *et al.*, 2000).

CONCLUSIONS AND RECOMMENDATIONS

Finding accurate ground-truth locations for earthquakes occurring in and around the Indian subcontinent is often difficult because of the poor azimuthal coverage of the region. In addition, there are logistic difficulties in accessing local earthquake catalogs. In this study, we have demonstrated that we can, however, alleviate this problem by focusing on earthquakes that are shallow (h<10 km) and have M_W> 5.5. We find that shallow earthquakes leave imprints in the form of co-seismic deformation of the earth's surface. Analysis of synthetic aperture radar images along the line of sight is a new emerging technique and has proven that co-seismic

deformation estimated from the fringes in the synthetic radar interferometry images when inverted in conjunction with the seismic data can yield highly reliable event location (Lohman *et al.*, 2001). This study has further demonstrated that for large earthquakes that are recorded by many teleseismic stations and have depths determined independently, their locations can also be derived to the accuracy level of the GT10 events, and sometimes even better. To obtain reliable locations using the seismic method alone for events of lower magnitude which will often be recorded by upper-mantle stations rather than by the teleseismic stations, it is needed that for some events we have locations with highest reliability. We recommend the processing of the InSAR images in conjunction with the seismic data for some of selected events in areas where seismic monitoring is most warranted. Once these locations are found, they can form the basis for master events to improve locations of other nearby seismic events.

REFERENCES

Barker, B., M. Clark, P. Davis, M. Fisk, M. Hedlin and others (1998). Monitoring Nuclear tests, Science, V281, 1967-1968.

Duarah, R., S. Baruah, and C. K. Saikia (2000). Depth characteristics of Lg waves and estimation of Q values for northeastern India, AGU abstract, San Francisco meeting.

IMD, India Meteorological Department (1999). Jabalpur earthquake of 22nd May, 1997 and its aftershocks, A consolidated document, Government of India, 70p.

IMD, India Meteorological Department (2000). Chamoli earthquake of March 29, 1999 and its aftershocks - A consolidated document, Government of India, 70p.

Lohman, R. B., M. Simons, and B. Savage (2001). Location and mechanism of the Little Skull Mountain earthquake as constrained by satellite radar interferometry and seismic waveform modeling, J. Geophys. Res., in review.

Massonnet, D. and K. L. Feigl (1995). Satellite radar interferometric map of co-seismic deformation field of M-6,1 Eureka Valley, California earthquake of May 1, 1993, Geo. Phys. Res. Lett., 22, 1541-1544.

Peltzer, G. and P. Rosen (1995), Surface displacement of the May 17, 1993 Eureka Valley, California, Earthquake observed by SAR Interferomtery, Science, V268, 1333-1336.

Saikia, C. K., L. Zhu, B. B. Woods and H. K. Thio (1999). Path calibration and source characterization in and around India, 21st Seismic Research Symposium: Tech. For Monit. CTBT, 243-253.

Saikia, C. K. (2000). A method for path calibration using regional and teleseismic broadband seismograms application to the May 21, 1997 Jabalpur, India earthquake, Current Science, Vol 79, 1301-1315.

Saikia, C. K. (2001). Location and focal mechanism of May 21, 1997 Jabalpur earthquake as constrained by regional travel times and seismic waveform modeling, Bull. Seis. Soc. Am., (manuscript in preparation).

Saikia, C. K., G. Ichinose, S. N. Bhattacharya, J. R. Kayal (2001). Location and mechanism of the March 28, 1999 Chamoli earthquake and modeling of regional seismograms to understand the influence of the Gangetic sediment on regional waveforms, Bull. Seis. Soc. Am., (manuscript in preparation).

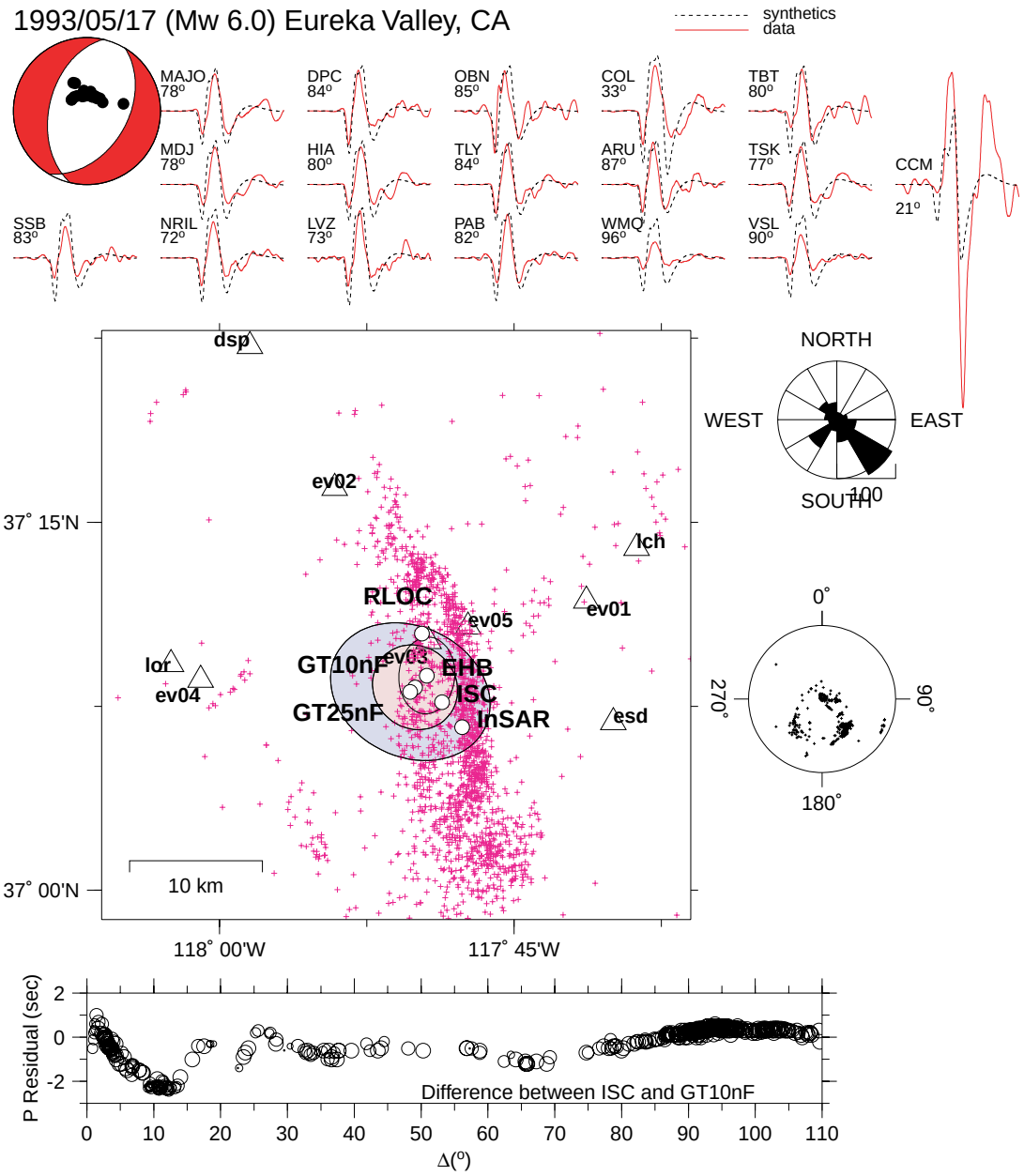

Figure 1. Seismic analysis of the Eureka Valley, California earthquake. (top) Solution and modeled teleseismic P-waves and depth phases (h=14km). The plotted P-waves are shown in velocity, for 42 sec, and at the same amplitude scale. (middle) Location map for portable and permanent seismic stations (triangles) used to relocate the mainshock (RLOC) and over 300 aftershocks (+). Also shown are the GT10nF and GT25nF locations compared to the EHB, ISC, and InSAR locations. The teleseismic station distribution is shown to the right. (bottom) The difference between the ISC and the GT10nF P-wave travel time residuals.

Figure 1. Seismic analysis of the Eureka Valley, California, earthquake (top). Solution and modeled teleseismic P-waves and depth phases (b=14 km). The plotted P-waves are showing in velocity for 42 sec. and at the same amplitude scale (middle). Location map for portable and permanent seismic stations (triangles)used to relocate the mainshock (RLOC) and over 3oo aftershocks (+). Also shown are the GT10nF and GT25nF locations compared to the EHB, ISC, and InSAR locations. The teleseismic station distribution is shown to the right (bottom), The difference between the ISC and the GT10nF P-wave travel-time residuals.

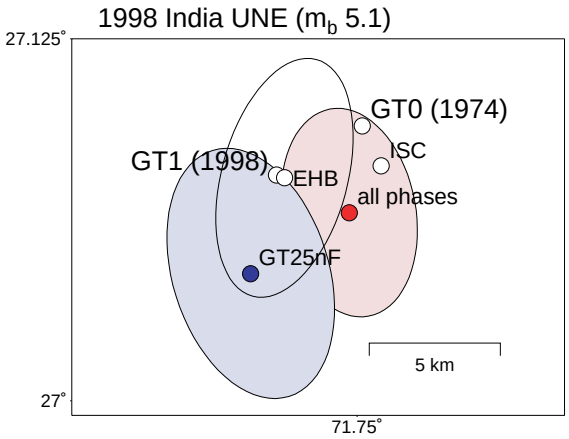

Figure 2a. Location and error ellipses for the 11 May 1998 India nuclear test at the Pokaran test site. The labels "all phases" are given to events which did not fall into the GT10 criteria. The GT25nF location is within 5 km of the GT1.

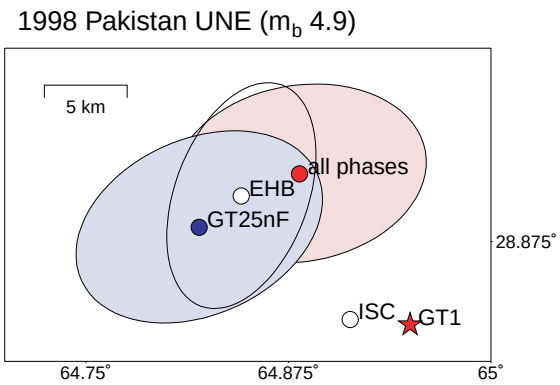

Figure 2b. Location and error ellipses for the 28 May 1998 Pakistan nuclear test. The GT25nF location is within 14 km of the GT1.

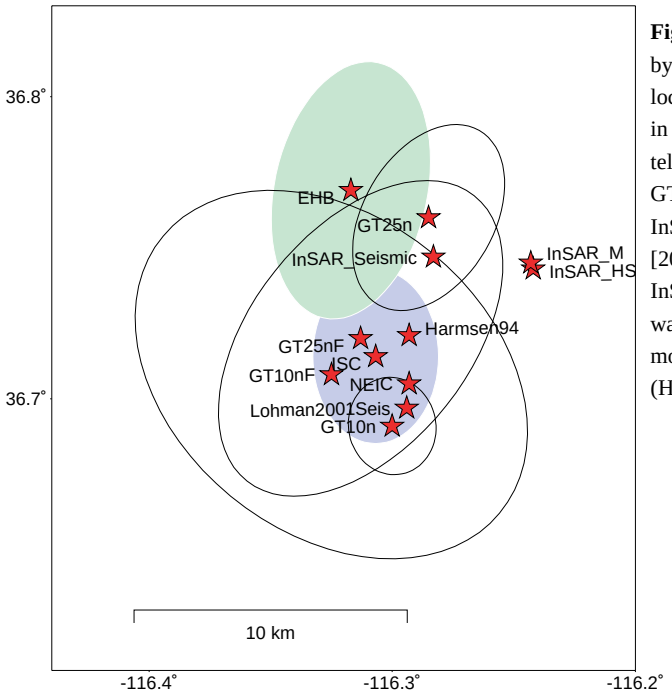

Figure 3. Comparison between locations obtained by seismic and InSAR methods. The GTXnF locations are determined using the criteria described in the text with a fixed depth determined using teleseismic P-waveform inversion results. The GT25nf and GT25n are within 10 km of the joint InSAR and seismic location by Lohman et al. [2000].
InSAR_Seismic location obtained using both seismic waveforms and InSAR with the Southern California model. InSAR_M (Mojave Model), InSAR_HS (Halfspace Model).

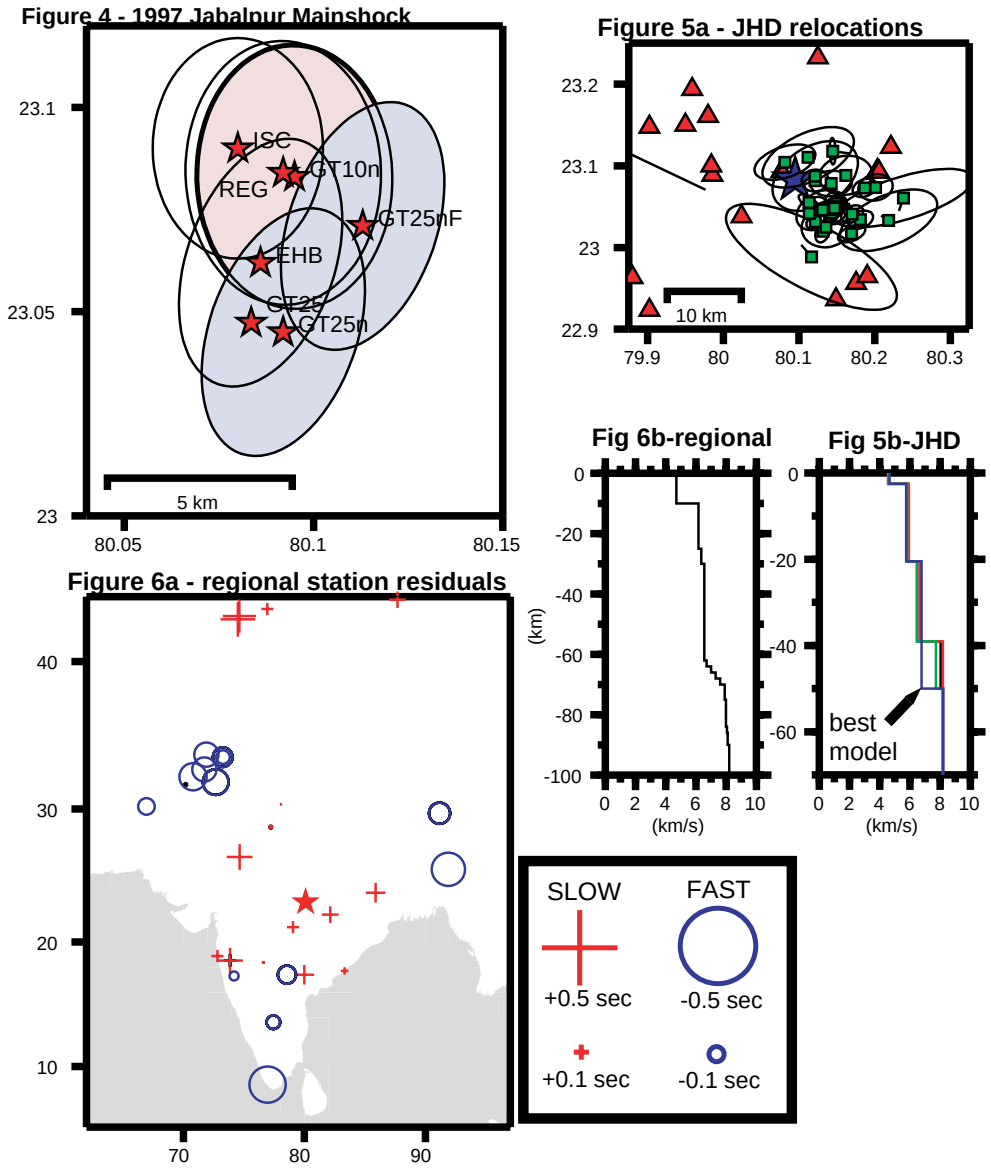

Figure 4. Location map and error ellipses for the 21 May 1997 Jabalpur, India earthquake (Mw 5.8). The REG location is the local IMD location for the mainshock. We relocated the event using free depth (GT10 and GT25n) and fixed depth (GT10nF and GT25nF) criteria. These locate within 5 km of the REG and GT25 (PIDC) locations. The mainshock focal depth, obtained by waveform inversion, was fixed in the relocations [Saikia, 2000]. **Figure 5a** -The aftershock sequence was recored by portable IMD stations and relocated using the JHD method. The relocations are shown as squares and the line points from the IMD location. **Figure 5b** shows the P-wave velocity models obtained from different JHD iterations. **Figure 6a** - The station residuals from the well located Jabalpur mainshock (shown as star) are computed relative to a regional reference P-wave velocity model shown in **Figure 6b.**

Figure 4. Location map and error ellipses for the 21 May 1997 Jahalpur, India, earthquake (Mw 5.8). The REG location is the local IMD location for the mainshock. We relocated the event using free depth (GT10 and GT25) and fixed depth (GT 10nF and GT25nF) criteria. These locate within 5 km of the REG and GT25 (PIDC) locations. The mainshock focal depth, obtained by waveform inversion, was fixed in the relocations (Saikia, 2000). Figure 5a: the aftershock sequence was recovered by portable IMD stations and relocated using the JHD method. The relocations are shown as squares and the line points from the IMD location. Figure 5b shows the P-wave velocity models obtained from different JHD locations. Figure 6a: the station residuals from the well located Jabalpur mainshock (shown as star) are corrupted relative to a regional reference P-wave velocity shown in Figure 6b.

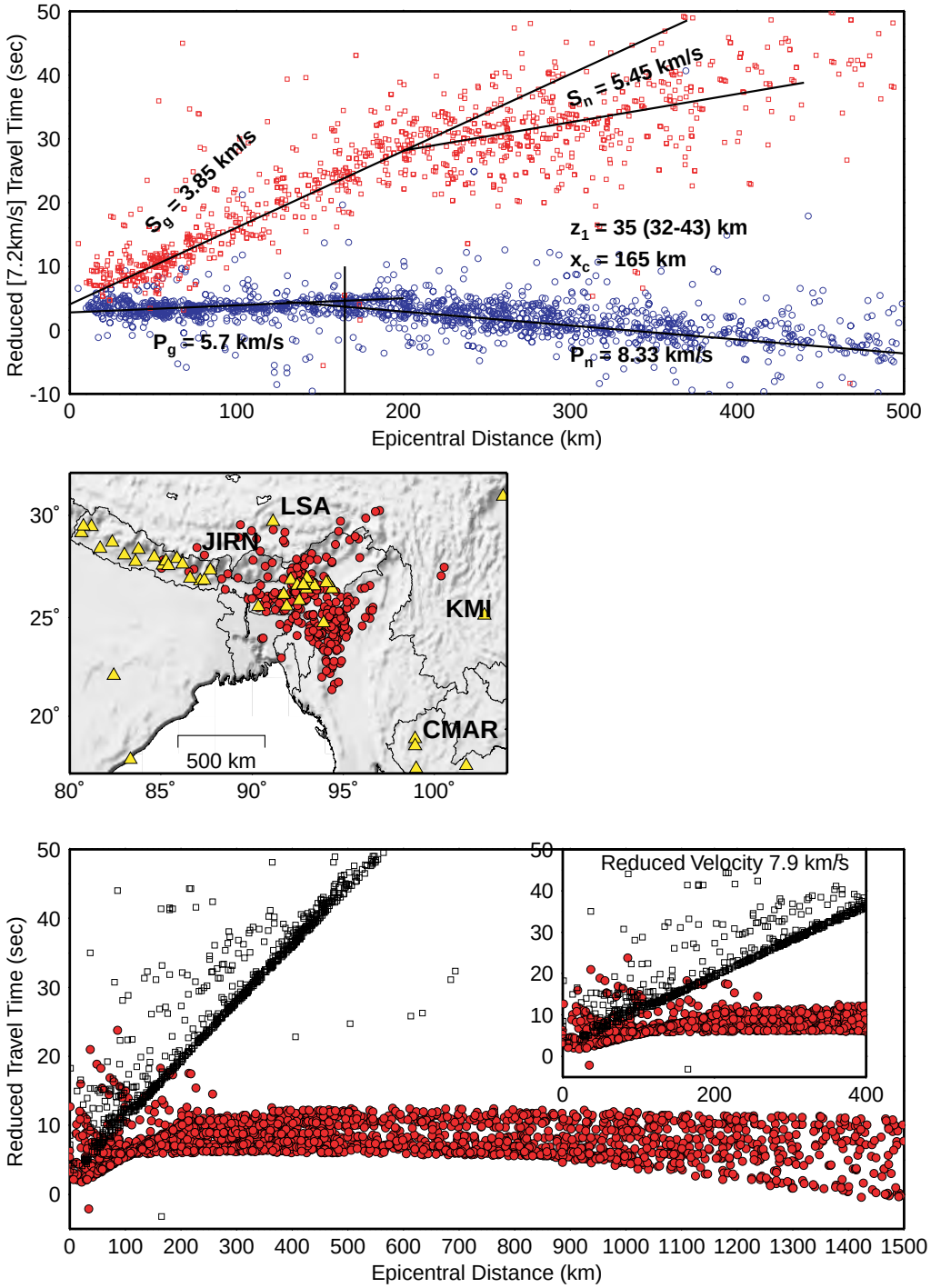

Figure 7. Reduced travel times for north east India earthquakes using phase data from the IMD, NGRI, and stations that report to the ISC. Simple 2-layer interpretations are plotted on the graph. The bottom plot shows the reduced predicted travel times after relocations using station corrections and 1-D model optimization. The times shown are observed travel time plus the residual.

Figure 7. Reduced travel times for northeast India earthquakes using phase data from the IMD NGRI and stations that report to the ISC. Simple two-layer interpretations are plotted on the graph. The bottom plot shows the reduced predicted travel times after relocations using station corrections and 1-D model optimization. The times shown are observed travel-time plus the residual.

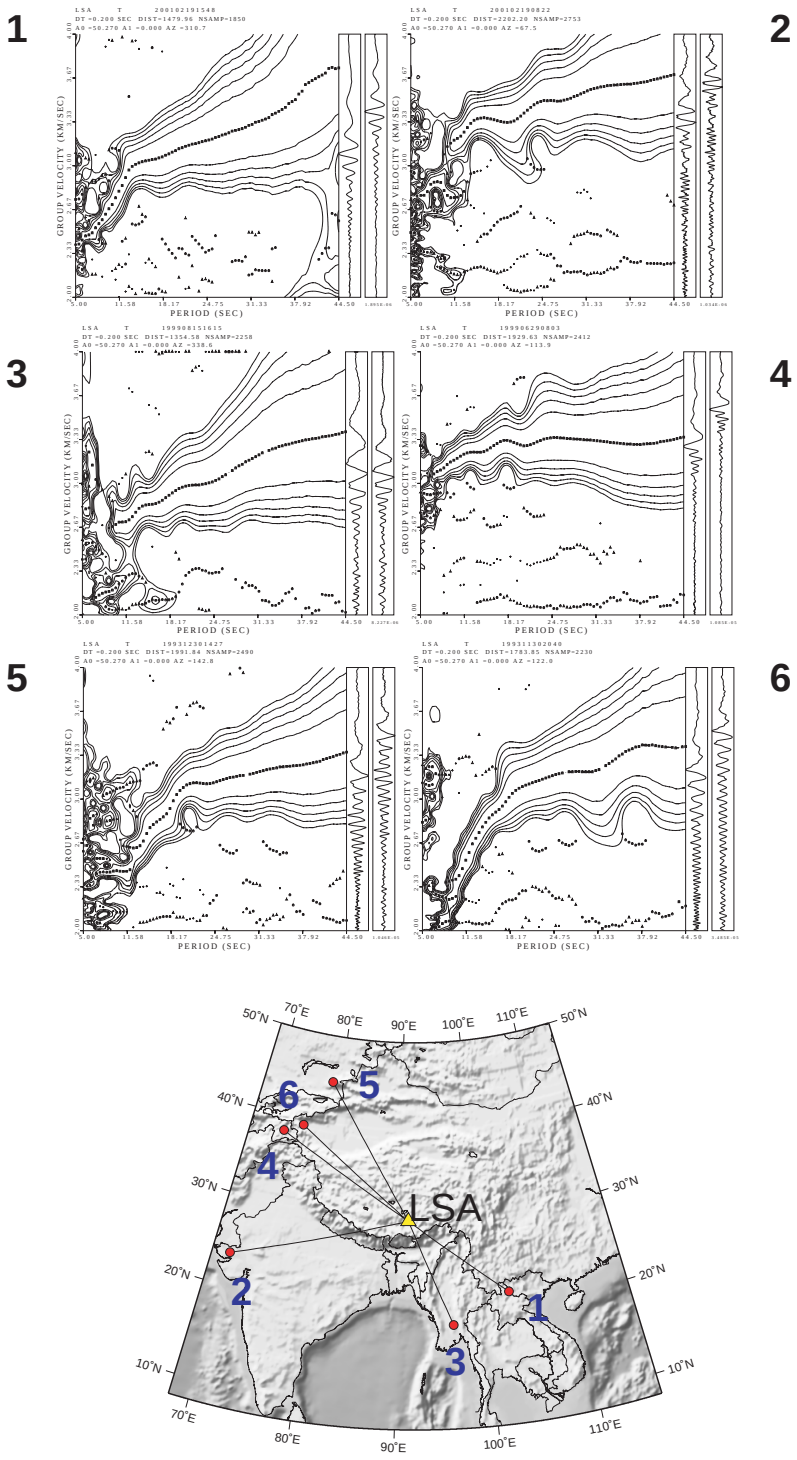

Figure 8. Love-wave dispersion curves for 6 paths from station LSA across southeast Asia.

Figure 8. Love-wave dispersion curves for six paths from station LSA across southeast Asia.

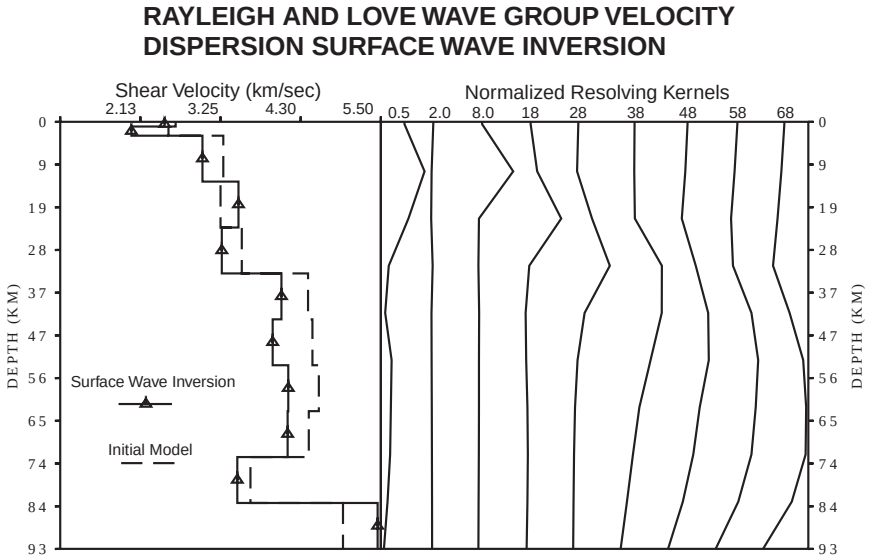

The initial S-wave velocity model was derived from the JHD of P-phase arrivals and Poisson ratio of 0.25. The resolution is best in the middle crust (0 to 28 km) for dispersion measurements between 8 and 28 seconds.

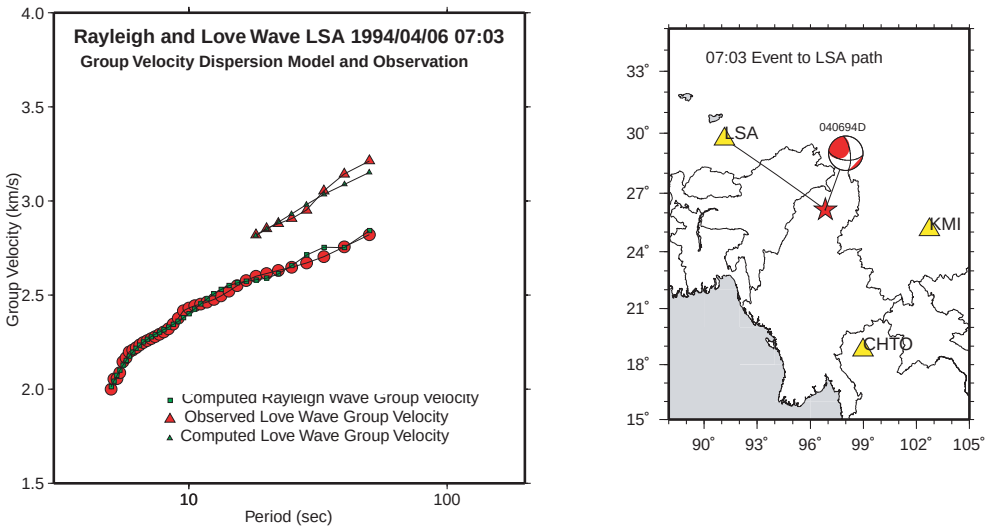

Figure 9. Observed and predicted Love and Rayeigh wave group velocity dispersion curves were inverted for the 1-D S-wave velocity structure for the path between LSA and event 04/06/94 07:03UT.

Figure 9. Observed and predicted Love- and Rayleigh-wave group velocity dispersion curves were inverted for the 1-D S-wave velocity structure for the path between LSA and event 04/06/94 07:03UT.

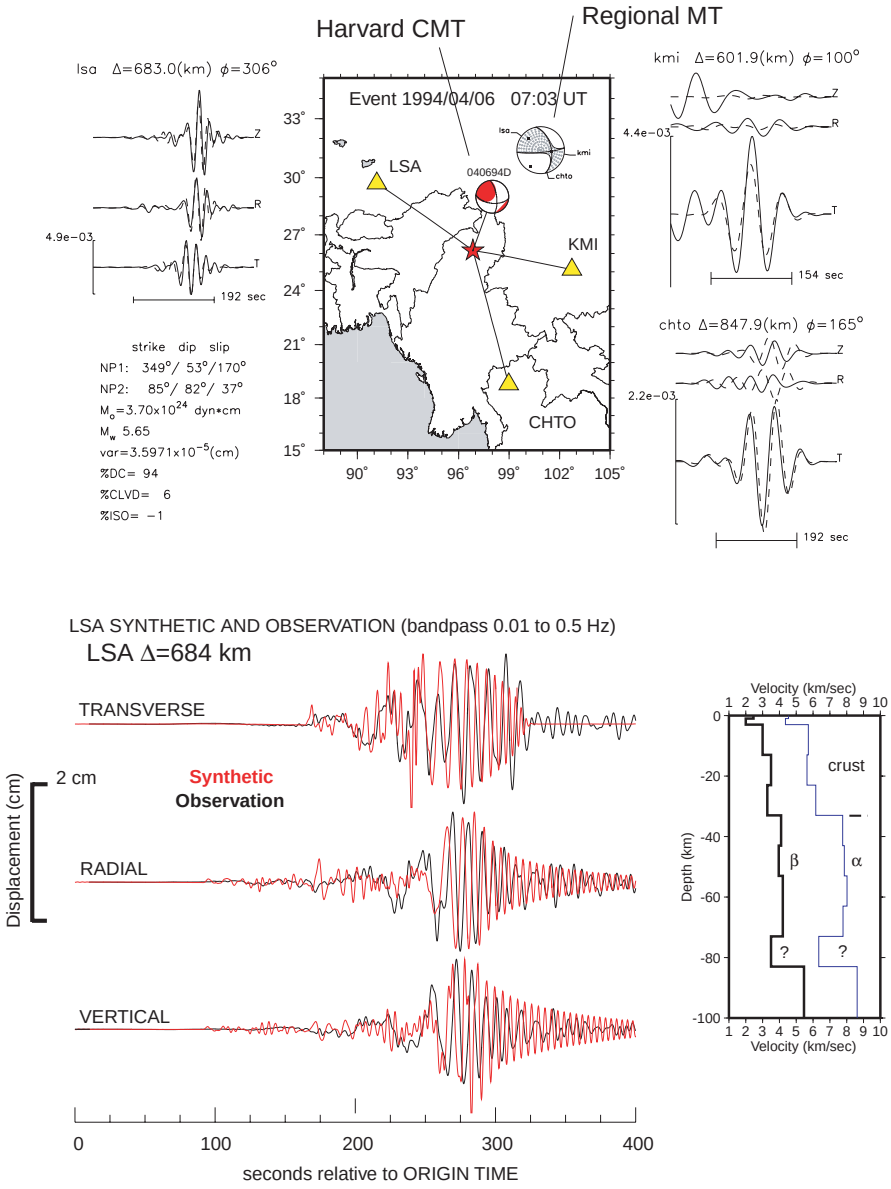

Figure 10. Validation of P- and S-wave velocity model inversion results. We first compute the regional moment tensor solution using long-period waves (50 to 100 sec). The moment tensor is then used to compute synthetic seismograms with the new velocity model. The body and surface waves appear to fit well in the 100 to 2 second period range. The P-wave model is determined using the JHD method on P-phase arrivals. The S-wave model is independently determined by surface wave inversion of group velocity dispersion. The observed waveforms are sensitive to LVZ's in the crust but is not sensitve to the deep LVZ which is not well resoved in the JHD or dispersion analysis.

Figure 10. Validation of P- and S-wave velocity model inversion results. We first compute the regional moment tensor solution using long-period waves (50 to 100 sec). The moment tensor is then used to compute synthetic seismograms with the new velocity model The body and surface waves appear to fit well in the 100- to 2-second period range. The P-wave model is determined using the JHD method on P-phase arrivals. The S-wave model is independently determined by surface wave inversion of group velocity dispersion. The observed waveforms are sensitive to LVZ's in the crust but are not sensitive to the deep LVZ, which is not well resolved in the JHD or dispersion analysis.

REGIONAL LOCATION AND IDENTIFICATION USING SPARSE STATIONS

Brian Savage, Ying Tan, Lupei Zhu, and Don Helmberger

California Institute of Technology, Seismological Laboratory

Sponsored by Defense Threat Reduction Agency

Contract No. DSWA01-98-0010

ABSTRACT

Locating events in Southern California is quite simple since we have about 500 stations, with a large fraction broadband (TriNet). We locate and identify within minutes. Thus, we have an opportunity to test hybrid methods against the full array estimate. Here we report on three projects addressing these issues; (1) locating events using one calibrated station with waveform data plus a few other stations with travel-time and polarity information, (2) particularly complex sub-regions where the depth phases such as pPn and sPn prove ineffective, and (3) calibrating paths using a combination of sparse regional waveforms and radar.

In previous efforts (last years report) we presented results using waveforms from one-station (PAS) and a few polarities from the array (3 to 5). The model employed a grid-search over mechanism (strike, dip and rake) with the depth fixed. Along most paths the method proved effective when comparing against the entire network. Here we present results of letting the depth vary as well so that the single station must use pPn and sPn and the ratio of body waves to surface waves to fix the depth. Only about half the paths still work, but in those situations, the location is greatly improved over just travel-time fitting because of the whole seismogram matching procedure. Our method uses an adaptive grid search over location with calibrated Pnl and surface wave time shifts.

However, the corrections to 1-D models are only applicable to areas in which the velocity structure does not vary drastically. Refracted phases, like Pn, at distances over 200 km provide most P arrival times. When the velocity structure begins to vary drastically near the source, the receiver, or along the propagation path, the arrival times vary greatly. Moreover, the structure modifies the waveform shape such that it makes identification of Pn and its associated depth phases exceedingly difficult. Such an area occurs beneath the high Southern Sierras through Owens Valley and into Death Valley. A low velocity zone, relative to the mantle, exists directly under the Moho and creates extra arrivals. These extra arrivals could be misconstrued as depth phases and thus a mis-location. Steps to identify areas of dramatic velocity variation, such as the one noted previously or in and around the Tibetian plateau, are needed to avoid misinterpretation of direct arrivals and depth phases.

In lieu of robust event locations, regional path calibration and crustal modeling utilizes well-located explosions, such as seismic reflection/refraction experiments or isolated blasts [Kanamori and Hadley (1975)]. In regions that include no well-located seismic events, other methods of path calibration are needed. Using InSAR (Interferometric Synthetic Aperture Radar) data to locate earthquakes provides the necessary ground truth to accomplish regional path calibration, leading to more accurate event locations. By using InSAR data to constrain the location and seismic data to determine the mechanism, the combination characterizes events robustly. As shown by Lohman et al. (2001) for the 1992 Little Skull Mountain event, InSAR data has the ability to locate events to within 0.5 km in the horizontal direction and 1.0 km in the vertical. Even with limited data coverage, this approach provides excellent constraints on location and mechanism, natural or man-made. Corrections to simple 1-D models can be made by using locations derived from InSAR data. These corrections are then used to locate events in an accurate fashion.

KEY WORDS: location, regional model calibration, InSAR, seismic, complex sub regions

OBJECTIVE

The objective of this study is to develop new and improve on existing techniques of locating events, in depth and surface expression. Several problems have been identified with the event location process, such as the trade-off between depth and origin time and the lack of high quailty data due to sparseness of regional seismic networks, which are usually short-period vertical seismometers. Development of new methods within Southern California to coincide with sparse station distribution provides error estimates associated with new methods and ways to reduce these errors. In conjunction, use of ground-truth events to calibrate regional paths, we may readily identify areas of three dimensional structure to accurately locate events further.

RESEARCH ACCOMPLISHED

Issues involving one-station solutions were covered at a recent DTRA workshop (Kansas City, 2001) and will be omitted in this report where we will concentrate on the detailed Pnl wavetrain (Pn, pPn, and sPn). However, we will also address the merits of using both radar (static field) and the seismic-wavefield (dynamic) together to study earthquakes.

Pn Complexity

Through the use of three large events in central California we are able to illuminate areas of regional seismic wave propagation, the crust and upper mantle, to determine appropriate corrections to 1-D models and begin to develop 3-D models.

Data from an event in Santa Rosa, CA is shown, but not modeled as a profile, as it is does not provide a simple 2-D profile due to large azimuth swings. Selected waveform data is shown in figure 1b and time picks from the stations within California are shown as a map in figure 1a. As the arrivals approach the Sierras and the Basin and Range, Pn delays grow larger and then reach a maximum at Mammoth, CA. About 1 second of this delay at Mammoth is a result of local structure. Stations further to the southeast also show late Pn arrivals. The Pn arrivals in the northern portion are longer period than the faster Pn arrivals to the south, suggesting complex structure. The data suggests a very sharp boundary between KCC and MLAC and a gradual increase in velocity, greater than 8.0 km/sec, further to the southeast. As the data suggests and as is also seen by Pn tomography, a slow velocity anomaly appears underneath the Sierra Nevada and areas to the east.

A second event in Mammoth, CA and the locale of TriNet in southern California allows the creation of a record section down the axis of the southern Sierra Nevada. Figure 2 shows stations used for this profile in blue, while figure 3 displays the velocity data. The radial, not shown, and vertical components are similar in nature, indicating little anomalous structure near the receivers. A 1-D record section, shown for reference, incorporates a mantle velocity of 8.0 km/sec and a simple crust of 6.3 km/sec in figure 4. The arrivals in figure 4 are refractions, as they are single sided pulses in velocity, while reflections are double sided. The two single sided pulses are Pn and sPn, with Pn arriving first, as sPn must travel to the surface as an S-wave, then traverse much the same path as Pn. Arrivals propagating down the southern Sierra Nevada axis include an anomalous second arrival with a large downswing following the initial Pn, figure 3. This is either a set of two refractions, with opposite amplitudes, or a reflection off a boundary near the Moho. The arrival is consistently behind Pn by 0.75-1.0 seconds, indicating it travels at the same speed and through the same material.

By adding a slow region on the source side, as shown in figure 5, a second arrival appears behind Pn with the timing adjusted by the velocity and the depth extent of the anomaly, figure 3. We add the anomaly on the source side because the secondary arrival exists across the entire section of data. The velocity of 7.6 km/sec is similar to that seen by (Zhao, 93) and (Carder, 1973). The second arrival is a reflection off the bottom of this feature. At distances over 350 km the reflection travels in the mantle just below the Moho, similar to a refraction in speed but double-sided in shape. At distances less than 350 km the second arrival diverges from Pn as it must travel to the base and back entirely within the anomaly. If the bottom of the

anomaly dips away from the source, figure 5, then the timing of the second arrival, at shorter distances, decreases relative to Pn as it travels a smaller distance than before, as shown in figure 3.

In this section we analyze what a crustal root does to seismograms as they travel down the axis of a mountain chain, in the same orientation as the previous profile. Three models with varying crustal roots are approximations of those in (Pakiser and Brune, 1980). Each crustal root model shows two distinct arrivals independent of the crustal thickness, figure 6. However, the depth of the crustal root directly affects the absolute timing of Pn, pPn, and sPn. Examining the records past the first arrival, the main difference between the crustal and mantle root models is the presence of the large downswing in the mantle anomaly models. Data traveling down the Sierran axis also shows this downswing, giving more credence to the anomalous mantle rather than crustal root model.

Utilizing a third event in Nevada, we produce a profile along Death Valley's eastern edge with station in the red profile in figure 2 and the velocity data in figure 7. Comparing this velocity data with synthetics for the 1-D model in figure 4, the similarities and simplicity in the seismic waveforms at distances up to 600 km appear. For this reason, we interpret the eastern section of data propagating down Death Valley and the California-Nevada border as 1-D. The travel times of Pn and sPn increases as the distance increases relative to a 8.0 km/sec mantle, but the simplicity of the data does not warrant extra structure, only small velocity shifts along the propagation path. Model Eastern Mojave, figure 8, created specifically for this data set, adds additional layers to a layer over a half-space, and accurately predicts the data, figure 7. Addition of the tectonic North America (TNA) (Grand and Helmberger, 1984) mantle, for completeness, adds nothing to the waveforms at these distances for the types of arrivals we consider.

Regional seismic data, through the use of Pnl waveforms, has efficiently identified distinct and separate provinces. A region of one-dimensional structure exists on the border between California and Nevada extending through the crust into the mantle, the area where first-arriving regional travel. A second distinct region to the west beneath the southern Sierra Nevada Mountains exists only within the mantle. The mantle has a velocity of 7.6 km/sec, different than the 7.8-8.0 km/sec normally seen. The anomaly extends down to depths of 75-100 km.

InSAR Locations

InSAR data alone and a combination of InSAR and regional seismic data to locate and determine the source parameters of events was tested for the well-studied 1992 Little Skull Mountain earthquake. We invert using a non-linear technique, the Neighborhood Algorithm, to solve for the location, source, slip and area. Figure 9 shows the Little Skull Mountain earthquake InSAR scene with solutions from previous investigators.

For the InSAR-only inversion we find a large tradeoff between slip and area, figure 10a, whereas the seismic moment is well constrained to be about 4.4 $*10^{17}$Nm (Mw 5.7), figure 10b. Since the area is not well constrained by our data, we adopt a value of 25 km^2 as estimated from aftershock distributions (Harmsen, 1994; Meremonte et al., 1995; Smith et al., 2000) and that is used in previous studies (Wernicke et al., 1998; Savage et al., 1999).

When we invert using only the InSAR data, and assume a fixed fault area of 25 km^2, a search through the entire range of potential mechanisms suggests a best fitting mechanism with a rake of 47^o. This estimate of the rake is much shallower than predictions from previous seismic studies. Figure 10c shows the map view locations of best-fitting fault planes of area 25 km^2 from inversions where we fixed the rake at values between -20^o and -100^o. All of these models have similar misfits to the InSAR data, illustrating the tradeoff between earthquake mechanism and location inherent with this set of InSAR data. If additional InSAR data existed with a different LOS direction, we would be better able to determine the mechanism and thus the location.

Since additional InSAR data is not available we turn to seismic data to tightly constrain the mechanism of the LSM earthquake. However the seismic data contains relatively little information on the location, as accurate as InSAR would procvide. Both layered models, Standard Southern California and Mojave,

predict mechanisms and moments that are well within the range of predictions from previous seismic studies. Both of these mechanisms fit the seismic data very well, but do not fit the InSAR data well.

Our initial attempt at a simultaneous joint inversion calculates misfits to both the seismic and InSAR data, weighted by the RMS value of each data set. This inversion approach results in models that average the parameters from the InSAR-only and seismic-only inversions and fit neither data set well. Using the InSAR data to relocate the best-fitting mechanism inferred from only the seismic data produces a better result. We iterate between seismic-only and InSAR-only inversions multiple times. Figure 11 shows the mechanism for the Mojave elastic model and the associated misfits. This result fits both the seismic and the InSAR data well. Synthetic waveforms calculated from the best-fitting mechanism from the inversion using only InSAR data do not fit the seismic data nearly as well as does the one from the joint inversion figure 11. The joint InSAR/seismic inversion produces a mechanism that is 1km shallower than the InSAR-only inversion and predicts a moment of $4.1*10^{17}$Nm (Mw 5.7).

InSAR data can effectively locate shallow earthquakes that are too small or too distant to accurately locate using traditional seismic methods. In this study, the InSAR data is sensitive to the seismic moment of the earthquake, but suffers from a tradeoff between mechanism and location. The seismic data is sensitive to the mechanism, but not to the location. Both data types are unable to separate area from magnitude of slip, or to distinguish which of the two potential conjugate planes ruptured. The main observational limitations of this study are the availability of only one SAR image before the earthquake and the existence of only one component of deformation.

CONCLUSIONS AND RECOMMENDATIONS

A large anomaly of slow mantle velocity appears underneath the Sierras and the valleys to the east. While, a crustal root is not possible when examining the Mammoth earthquake profile down the Sierra Nevada axis. Results of this type compare well with those of Savage et al. (1994), Carder et al.(1970), and Carder (1973). The lack of a high velocity lid could explain the data shown by Melbourne (2000) and the tomography of Zhao (1993). There also appears to be a large velocity contrast at about 75-100 km depth below the eastern California shear zone. Identification of anomalies such as this are useful, in that they may be accounted for in terms of the first arriving Pn travel times. Future investigations may be accomplished using Pn tomography and simple waveform analysis.

Hopefully, future studies of small events will have more independent interferograms and therefore will permit greater averaging to reduce noise. We must also be able to measure multiple components of the deformation in order to improve the ability of InSAR data to determine earthquake mechanisms. Beyond the discussion of the LSM earthquake, this study supports the feasibility of the formation of a catalogue of earthquakes located using both InSAR and seismic data. This catalogue could support regional path calibration which can benefit from improved bounds on source locations. In many regions of the world earthquake location error is greater than 25 km. For many of these events this uncertainty can be reduced by two orders of magnitude.

REFERENCES

Bolt, B.A. and R. Gutdeutsch, Reinterpretation by ray tracing of a Transverse Refraction Seismic Profile through the California Sierra Nevada, Part 1, *Bull. Seismo. Soc. Am.*, 72, 3, 889-900, 1982

Byerly, P, Comment on "The Sierra Nevada in the Light of Isostasy", *Bull. Geol. Soc. Am.*, 2025-2031, 1937

Carder, D.S. and A. Qamar and T.V. McEvilly, Trans-California Seismic Profile-Pahute Mesa to San Francisco Bay, *Bull. Seismo. Soc. Am.*, 60, 6, 1829-1846, 1970

Carder, D.S, Trans-California Seismic Profile, Death Valley to Monterey Bay, *Bull. Seismo. Soc. Am.*, 63, 2, 571-586, 1973

Eaton, J.P., Crustal structure in northern and central California from seismic evidence, *Bull. Cal. Div. Mines. Geol*., 190, 419-426, 1966

Fliedner, M.M. and S. Ruppert, Three-dimensional crustal structure of the southern Sierra Nvada from seismic fan profiles and gravity modeling, *Geology*, 24, 4, 367-370, 1996

Grand, S.P. and D.V. Helmberger, Upper mantle shear structure of North America, *Geophys. J. Roy. Astr. S.* , 76, 399-348, 1984

Hadley, D. and H. Kanamori, Seismic structure of the Transverse Ranges, California, *Geol. Soc. Am. Bull*., 88, 1469-1478, 1977

Harmsen, S. C., The Little Skull Mountain, Nevada, Earthquake of 29 June 1992: Aftershock Focal Mechanisms and Tectonic Stress Field Implications, *Bull. Seismo. Soc. Am*., 84, 1484-1505, 1994

Helmberger D.V. and G.R. Engen, Modeling the Long-Period Body Waves from Shallow Earthquakes at Regional Ranges, *Bull. Seismo. Soc. Am*., 70, 5, 1699-1714, 1980

Helmberger, D.V. and J.E. Vidale, Modeling Strong Motions produced by Earthquakes with Two-Dimensional Numerical Codes, *Bull. Seismo. Soc. Am*., 78, 1, 109-121, 1988

Jones, C.H., Is Extension in Death Valley Accommodated by Thinning of the Mantle Lithosphere beneath the Sierra Nevada, California, *Tectonics*, 6, 4, 449-473, 1987

Jones C.H. and H. Kanamori and S. W. Roecker, Missing roots and Mantle "drips": Regional Pn and teleseismic arrival times in the southern Sierra Nevada and vicinity, California, *Jour. Geophys. Res.*, 99, B3, 4567-4601, 1994

Jones, C.H. and R.A. Phinney, Seismic structure of the lithosphere from teleseismic converted arrivals observed at small arrays in the southern Sierra Nevada and vicinity, California, *Jour. Geophys. Res.*, 103, B5, 10,065-10,090, 1998

Jones, L. E. and D. V. Helmberger, Earthquake source parameters and fault kinetics in the eastern California shear zone, *Bull. Seismo. Soc. Am*., 88, 1337-1352, 1998

Lawson, A.C., The Sierra Nevada in the Light of Isostasy, *Bull. Geol. Soc. Am*., 47, 1691-1712, 1936

Melbourne, T. and D. Helmberger, Mantle Control of the Plate Boundary Deformation?, In perpetration, 2000

Massonnet, D., and K. L. Feigl, Radar interferometry and its application to changes in the earth's surface, *Rev. Geophys*., 36, 441-500, 1998

Meremonte, M., J. Gomberg, and E. Cranswick, Constraints on the 29 June 1992 Little Skull Mountain, Nevada, Earthquake Sequence Provided by Robust Hypocenter Estimates, *Bull. Seismo. Soc. Am.*, 85, 1039-1049, 1995

Okada, Y., Surface deformation due to shear and tensile faults in a half space, *Bull. Seismo. Soc. Am*., 75, 1135-1154, 1985

Pakiser, L.C. and J.N. Brune, Seismic Models of the Root of the Sierra Nevada, *Science*, 210, 5, 1088-1094, 1980

Romanowicz, B., D. Dreger, M. Pasyanos, and R. Uhrhammer, Monitoring of Strain Release in Central and Northern California using Broadband Data, *Geophys. Res. Lett*., 20, 1643-1646, 1993

Rosen, P. A., S. Hensley, I. R. Joughin, F. K. Li, S. N. Madsen, E. Rodriguez, and R. M. Goldstein, Synthetic Aperture Radar Interferometry, *Proc. of the IEEE*, 88, 333-382, 2000

Sambridge, M., Geophysical inversion with a neighborhood algorithm - I, Searching a parameter space, *Geophys. Jour. Int*., 138, 479-494, 1998

Sambridge, M., Geophysical inversion with a neighborhood algorithm - II, Appraising the ensemble, *Geophys. Jour. Int.* 138, 727-746, 1998

Savage, B. and D.V. Helmberger, The Sinking of the Kursk, *Bull. Seismo. Soc. Am.*, In press, 2001

Savage, J. C., M. Lisowski, W. K. Gross, N. E. King, and J. L. Svarc, Strain accumulation near Yucca Mountain, Nevada, 1983-1993, *Jour. Geophys. Res.*, 99, 18103-18107, 1994

Savage, J. C., J. L. Svarc, and W. H. Prescott, Strain accumulation at Yucca Mountain, Nevada, 1983-1998, *Jour. Geophys. Res*.,104, 17627-17631, 1999

Savage, M.K. and L. Li and J.P. Eaton and C.H. Jones and J.N. Brune, Earthquake refraction profiles of the root of the Sierra Nevada, *Tectonics*, 13, 4, 803-817, 1994

Simons, M. and Y. Fialko, On the efficient use of continuous geodetic imagery, in preparation, 2001

Smith, K. D., J. N. Brune, D. dePolo, M. K. Savage, R. Anooshehpoor, and A. F. Sheehan, The 1992 Little Skull Mountain Earthquake Sequence, Southern Nevada Test Site", U. S. Geol. Surv. Digital Data Series DDS-058, Chapter K, 1-16, 2000

Walter, W., Source Parameters of the June 29, 1992 Little Skull Mountain Earthquake from Complete Regional Waveforms at a Single Station, *Geophys. Res. Lett.* , 20, 403-406, 1993

Wang, C. Y. and R. B. Herrmann, A numerical study of P, SV, and SH-wave generation in a plane layered medium, *Bull. Seismo. Soc. Am*., 70, 1015-1036, 1980

Wernicke, B.and R. Clayton and M. Ducea and C.H. Jones and S. Park and S. Ruppert and J. Saleeby and J. K. Snow and L. Squires and M. Fliedner and G. Jiracek and R. Keller and S. Klemperer and J. Luetgert and P. Malin and K. Miller and W. Mooney and H. Oliver and R. Phinney, Origin of high mountains in the continents: The southern Sierra Nevada, *Science*, 271, 5246, 190-193, 1996

Wernicke, B., J. L. Davis, R. A. Bennett, P. Elosegui, M. J. Abolins, R. J. Brady, M. A. House, N. A. Niemi, and J. K. Snow, Anomalous Strain Accumulation in the Yucca Mountain Area, Nevada, *Science*, 279, 2096-2100, 1998

Zhao, L.S., Lateral Variations and Azimuthal Isotropy on Pn Velocities Beneath Basin and Range Province, *Jour. Geophys. Res*., 98, B12, 22,109-22,122, 1993

Zhao, L. and D. V. Helmberger, Source Estimation from Broadband Regional Seismograms, *Bull. Seismo. Soc. Am*., 84, 91-104, 1994

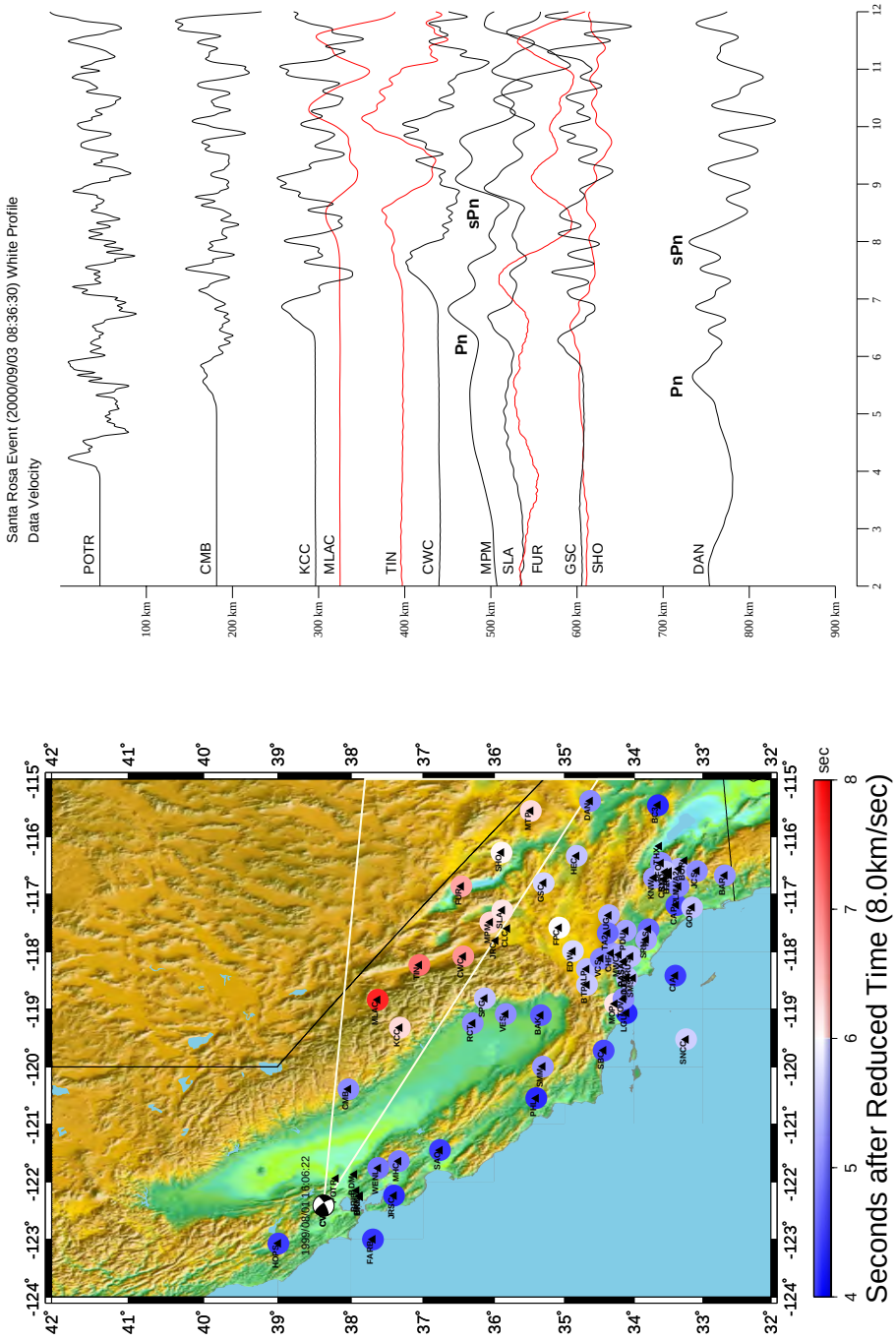

Figure 1. a) Pn time picks where the color is the delay after an arrival of 8.0 km/sec. b)Velocity data from Santa Rosa Earthquake.

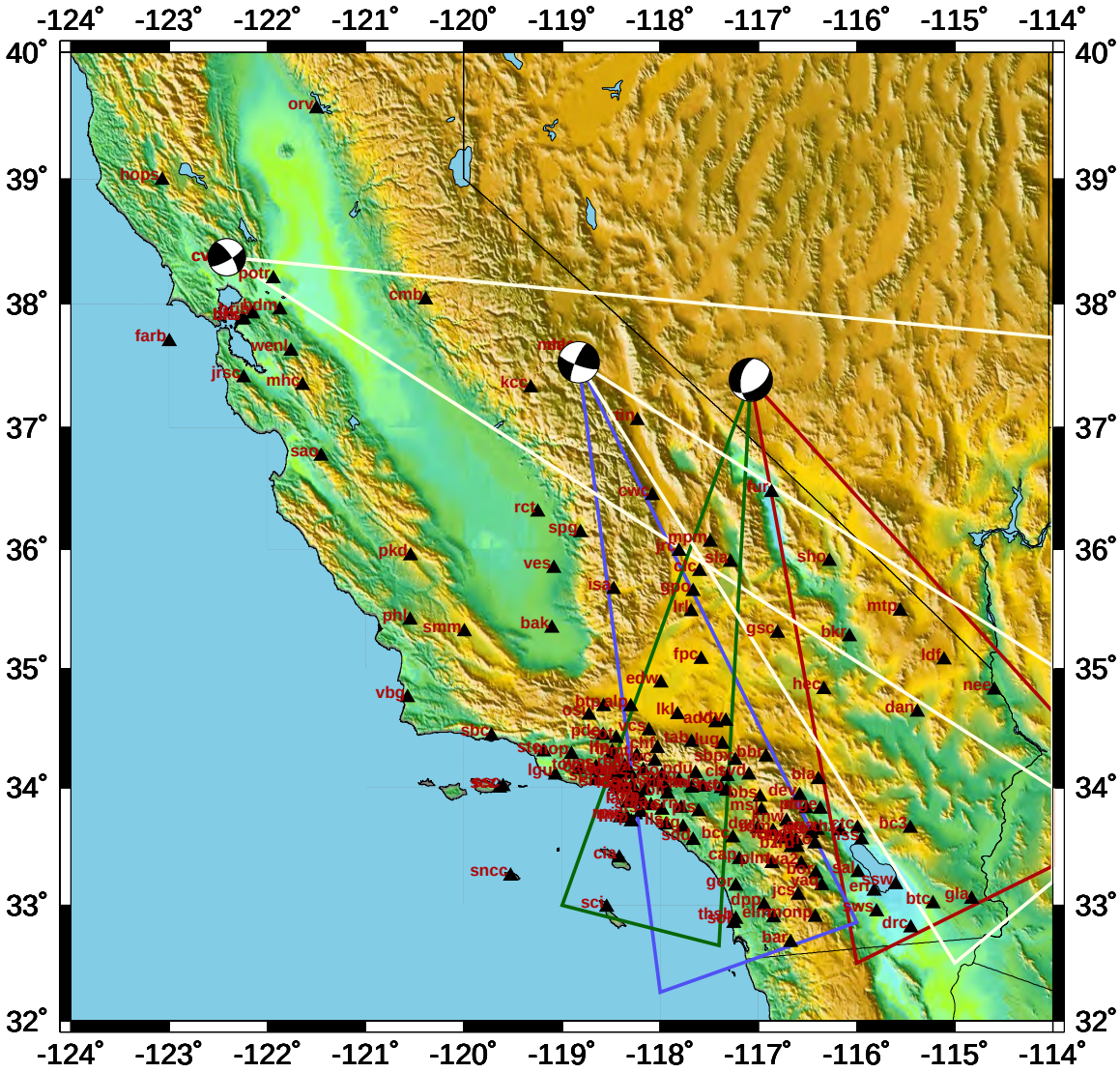

Figure 2. Map of California and Nevada, showing TriNet and BDSN stations as triangles, the focal mechanisms used for this study and the profiles modeled using Pnl waveforms

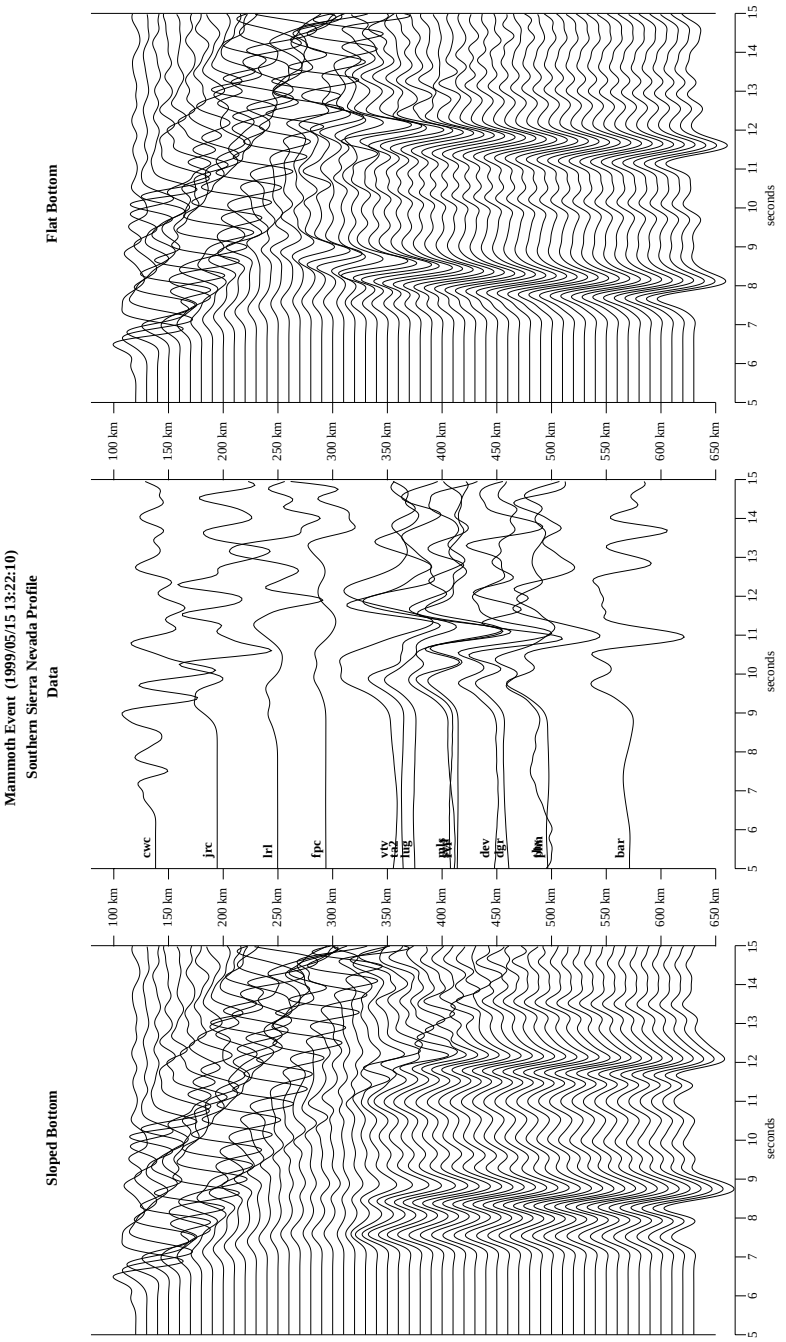

Figure 3. a) Synthetics created from the model in figure 5b with a sloped bottom b) Record section of the Mammoth event traversing the southern Sierra Nevada. The data is reduced using a velocity of 8.0 km/sec. The profile in map view is shown in figure 2 in blue. c) Velocity model synthetics with a flat bottomed bathtub anomaly just below the crust at 7.6 km/sec in figure 5a

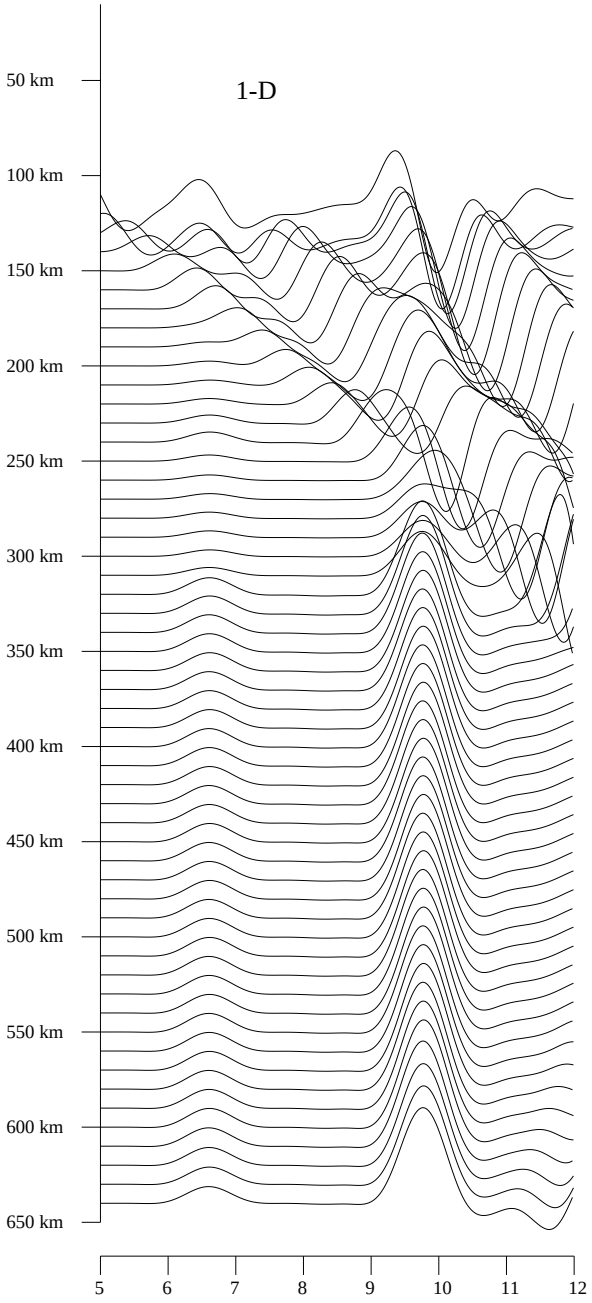

Figure 4. 1-D record section to indicate what Pn and sPn look like in a layer over a half-space.

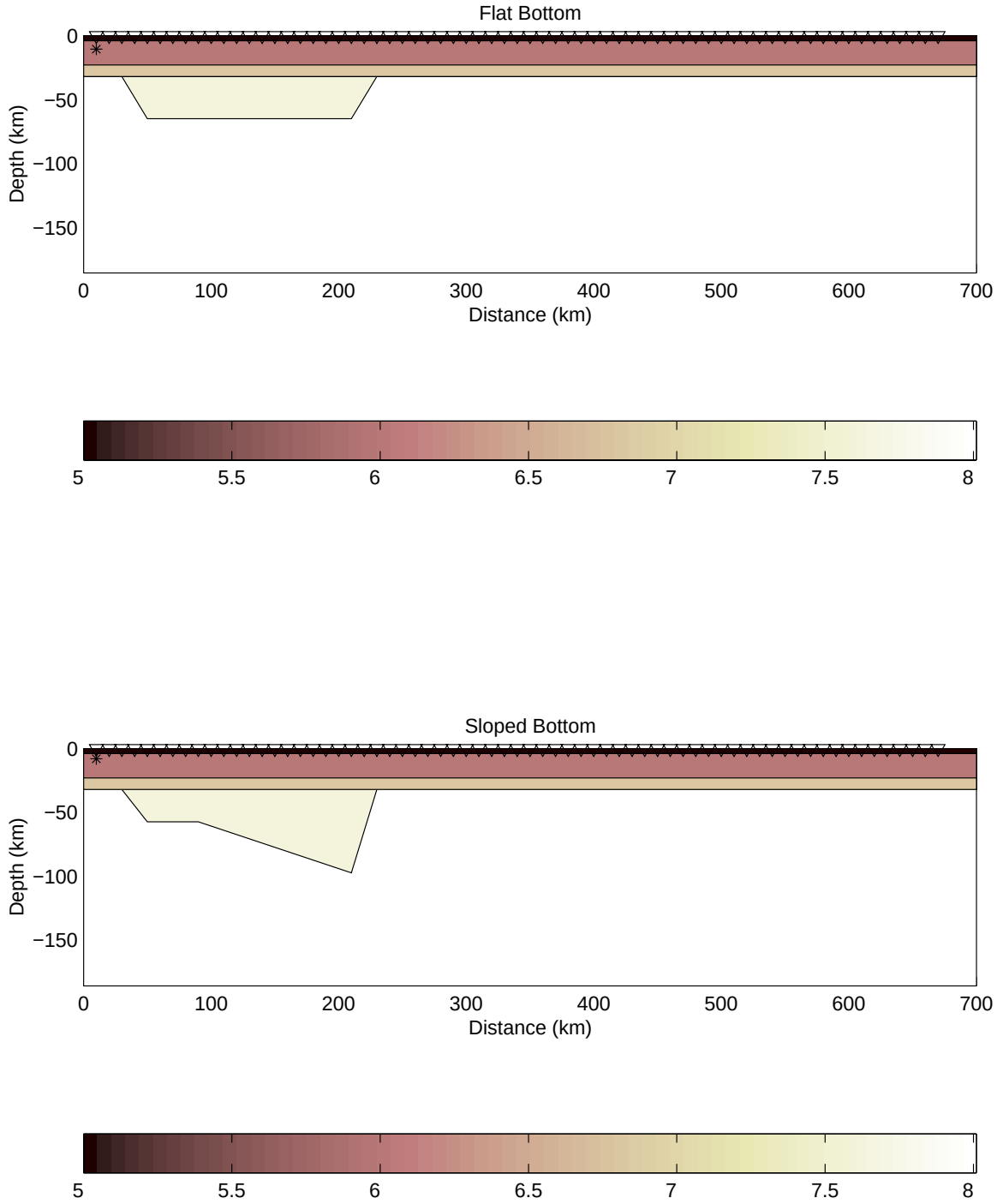

Figure 5. a) Velocity model with a flat bottomed bathtub anomaly just below the crust at 7.6 km/sec b) Model refinement of the model in a) by addition of a sloped bottom to align Pn and Pn?

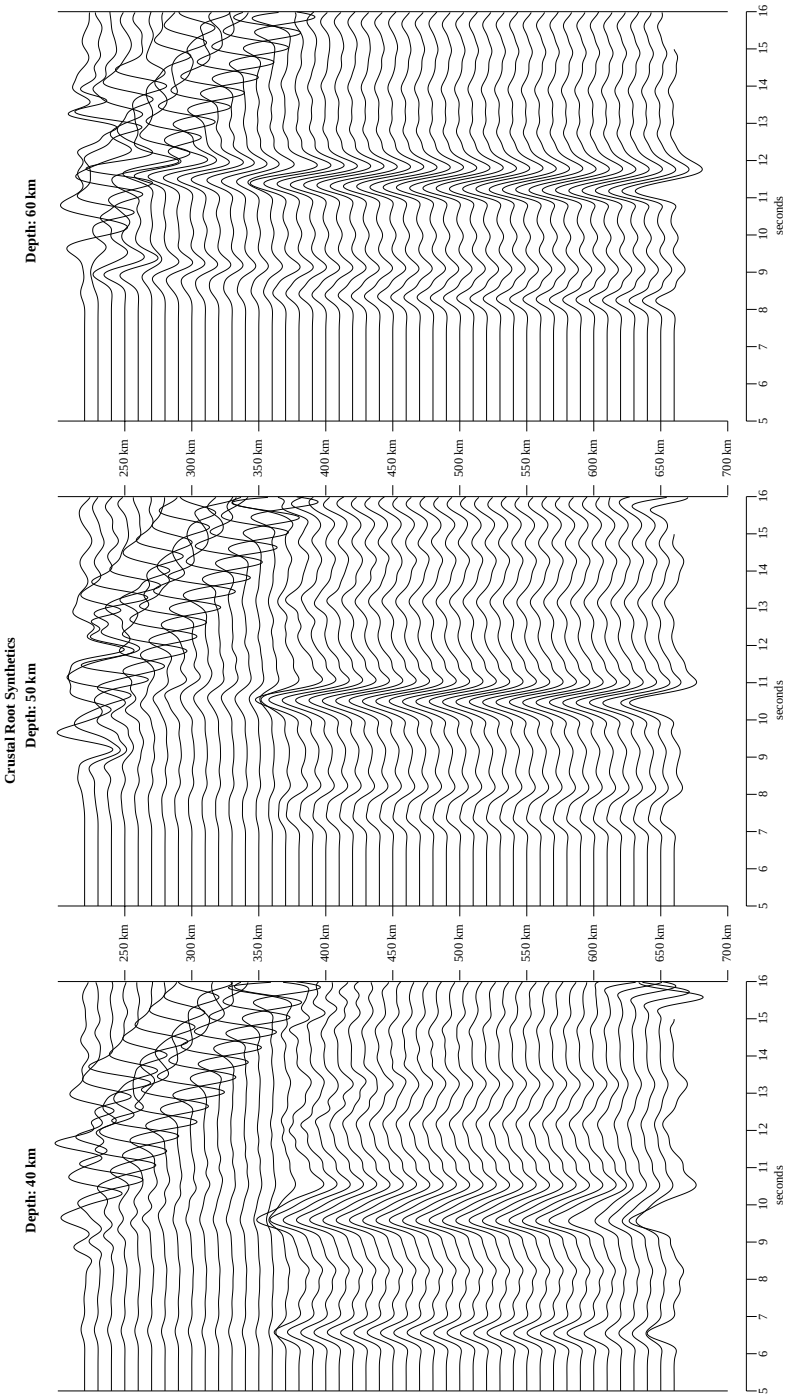

Figure 6. Synthetics for models with crustal roots from 40km to 60 km following Pakiser and Brune (1980)

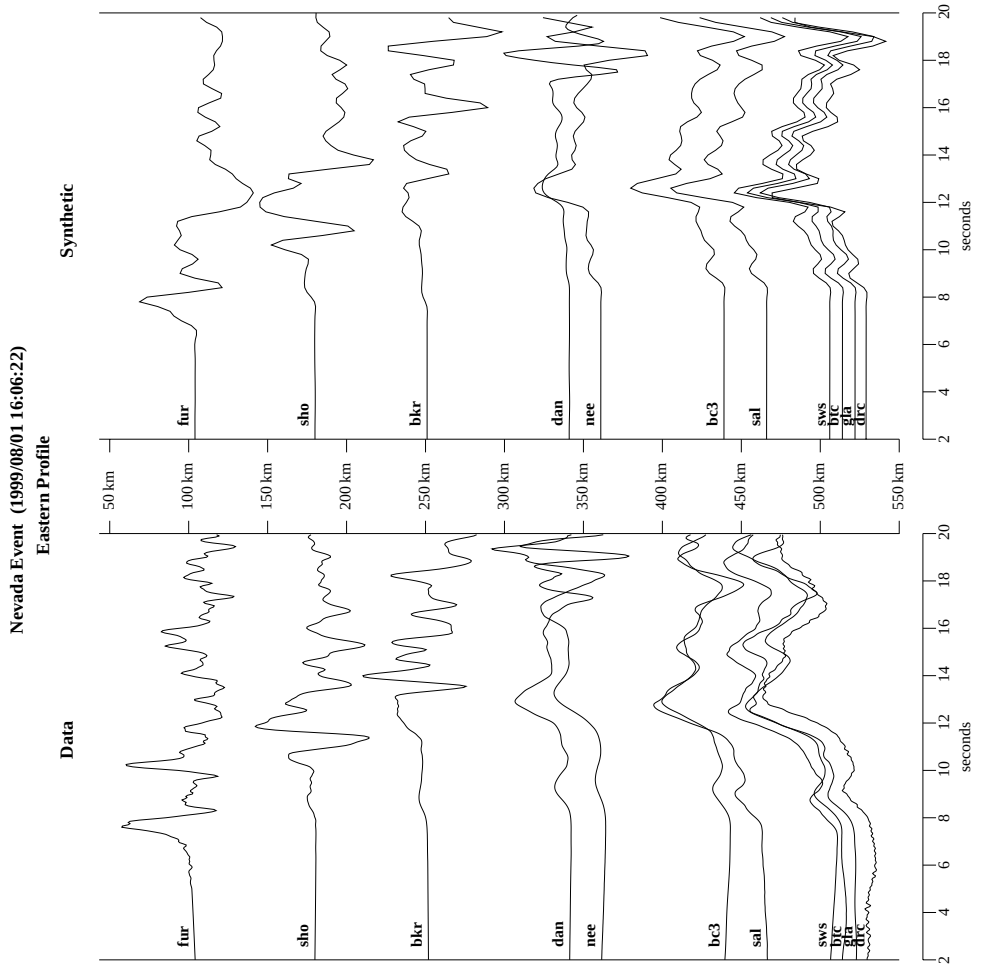

Figure 7. Comparison between data and synthetics for the eastern most profile marked in red in figure 2. The velocity depth section is shown in figure 8.

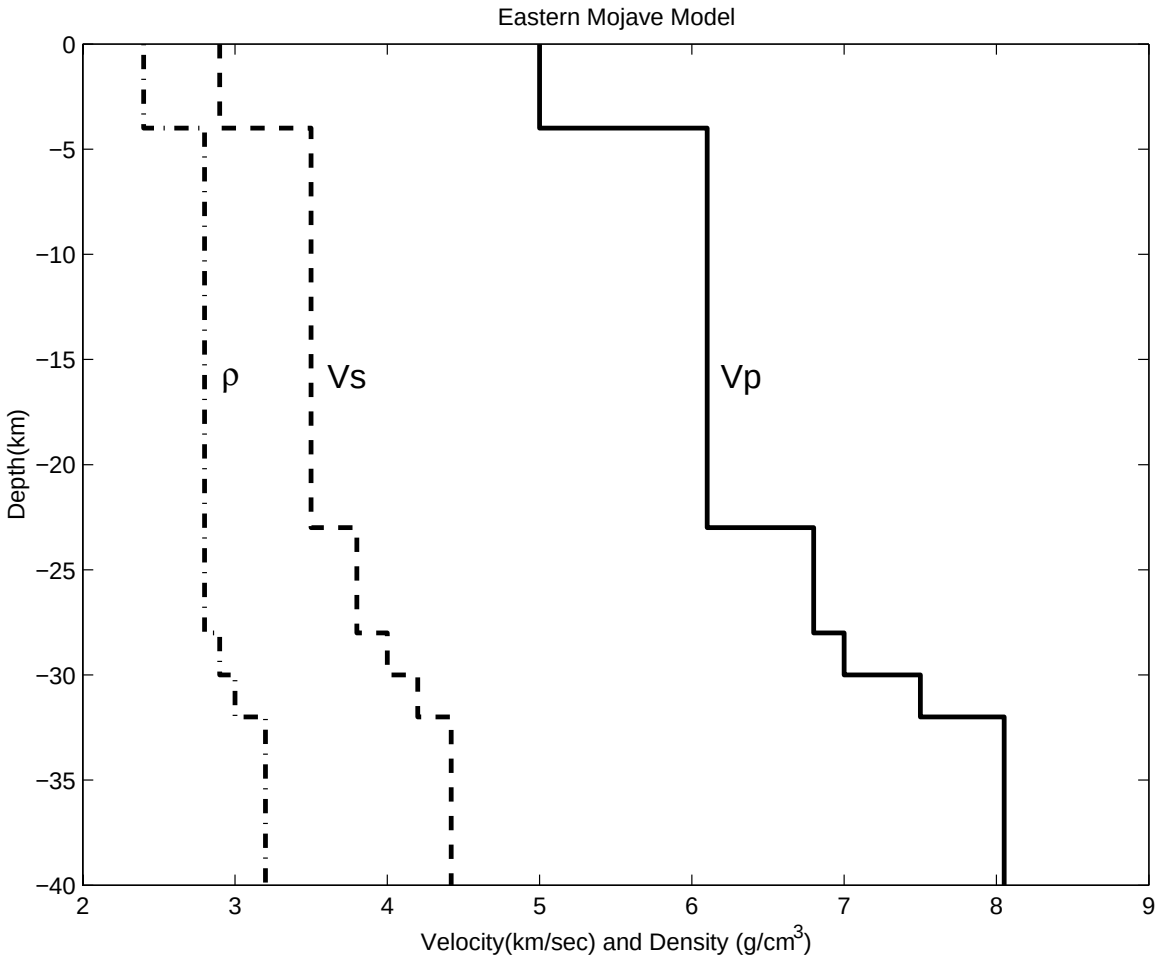

Figure 8. Depth velocity section of the eastern mojave model derived for the red section in figure 2.

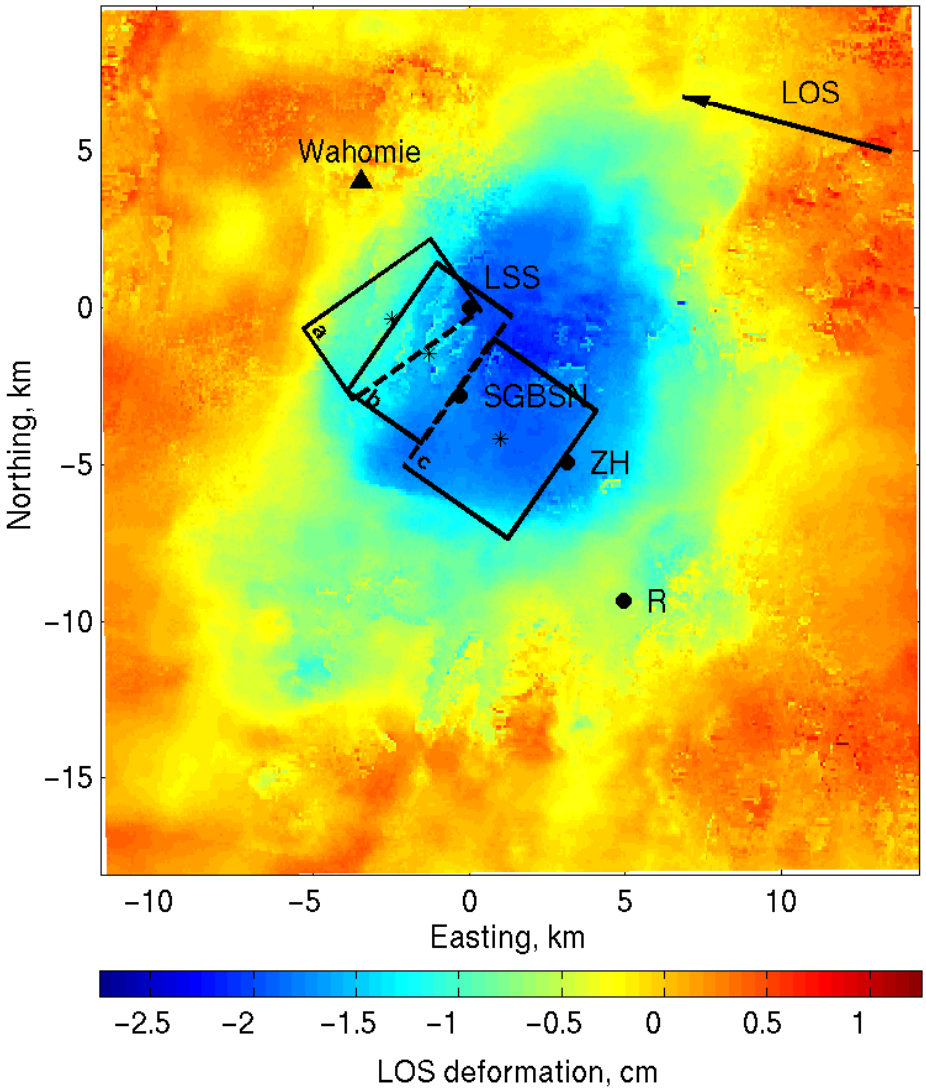

Figure 9. LOS displacement field from the averaged interferogram used in the inversions. The arrow indicates the surface projection of the LOS vector from the satellite to the ground. Note small-scale fluctuations due to tropospheric variations between scene acquisition dates. Geodetic benchmark Wahomie is shown as a filled triangle. LSM locations from Romanowicz et al., (1993) (R), Zhao and Helmberger, (1994) (ZH), and the SGBSN are indicated and labeled as is the best-fitting fault plane from our joint inversion (LSS) using the layered space from Jones and Helmberger, (1998). Rectangles show the fault planes used by (a) Savage et al., (1999), and the (b) SE-dipping and (c) NW-dipping planes in Wernicke et al., (1998). The dashed line indicates the bottom of the plane in all cases. This and all subsequent maps use a UTM (zone 11) projection. The origin (0,0) corresponds to the center of our best-fitting fault plane (LSS).

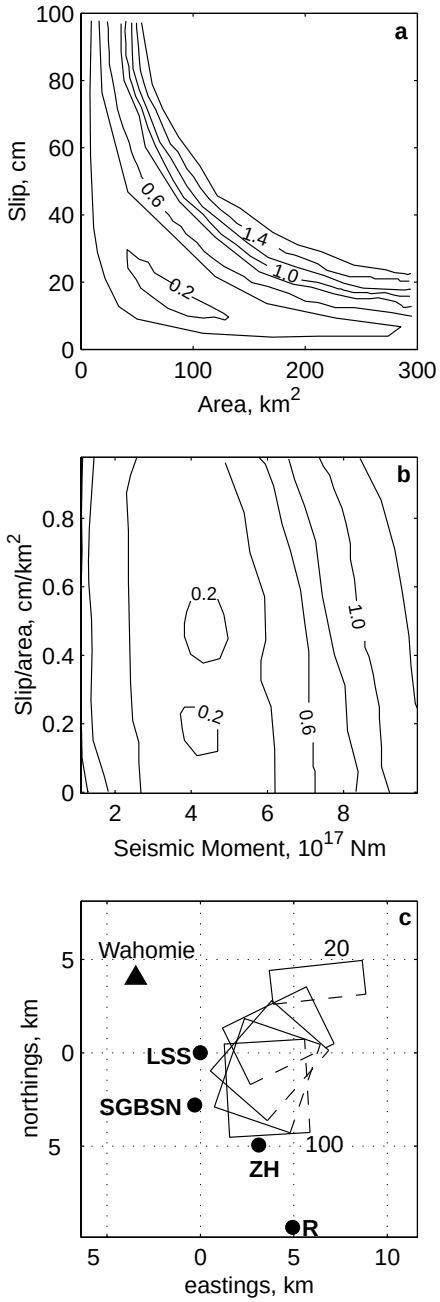

Figure 10. (a) Contours of RMS model misfit versus fault plane area and amount of slip. Misfit continues to increase to the upper right of the panel. (b) Contours of RMS model misfit versus moment and slip/area. Moment is calculated using μ=33 GPa. (c) Map view location of best-fitting planes with area 25 km^2 and rake fixed at values between -20^o and –100^o. Solid circles indicate the seismic locations of our best-fitting mechanism (LSS) from the joint inversion using the Mojave layered model, the Southern Great Basin Seismic Network (SGBSN), Zhao and Helmberger, (1994) (ZG), and Romanowicz et al., (1993) (R). All three panels correspond to inversions using only InSAR data and assume an elastic half space.

Figure 11. Mechanisms as well as observed waveforms and synthetic waveforms from the joint and InSAR-only inversions using the Mojave layered model. Pnl waveforms are filtered from 0.01-0.05~Hz, while full waveforms are filtered from 0.01-0.2~Hz. Data are shown as black lines and synthetics as gray lines. The time scale is shown at the base of each group of plots, with the 20~second bar referring to the Pnl waveforms and the 60~second bar referring to the full waveforms.

LLNL SEISMIC LOCATION: VALIDATING IMPROVEMENT THROUGH INTEGRATION OF REGIONALIZED MODELS AND EMPIRICAL CORRECTIONS

Craig A. Schultz, Megan P. Flanagan, Stephen C. Myers, Mike E. Pasyanos, Jennifer L. Swenson, William G. Hanley, Floriana Ryall, and Douglas A. Dodge

Lawrence Livermore National Laboratory

Sponsored by National Nuclear Security Administration
Office of Nonproliferation Research and Engineering
Office of Defense Nuclear Nonproliferation

Contract No. W-7405-ENG-48

ABSTRACT

Monitoring nuclear explosions on a global basis requires accurate event locations. As an example, a typical size used for an on-site inspection search area is 1,000 square kilometers or approximately 17 km accuracy, assuming a circular area. This level of accuracy is a significant challenge for small events that are recorded using a sparse regional network. In such cases, the travel time of seismic energy is strongly affected by crustal and upper mantle heterogeneity and large biases can result. This can lead to large systematic errors in location and, more importantly, to invalid error bounds associated with location estimates. Calibration data and methods are being developed and integrated to correct for these biases. Our research over the last few years has shown that one of the most effective approaches to generate path corrections is the hybrid technique that combines both regionalized models with three-dimensional empirical travel-time corrections.

We implement a rigorous and comprehensive uncertainty framework for these hybrid approaches. Qualitative and quantitative validations are presented in the form of single-component consistency checks, sensitivity analysis, measures of robustness, and outlier testing, along with end-to-end testing of confidence measures. We focus on screening and validating both empirical and model-based calibrations as well as the hybrid form that combines these two types of calibration. We demonstrate that the hybrid approach very effectively calibrates both travel-time and slowness attributes for seismic location in the Middle East, North Africa, and Western Eurasia (ME/NA/WE). Furthermore, this approach provides highly reliable uncertainty estimates. Finally, we summarize the National Nuclear Security Administration (NNSA) validated data sets that have been provided to contractors in the last year.

KEY WORDS: location, integration, uncertainty framework, validation

OBJECTIVE

This paper discusses the primary focus of the Lawrence Livermore National Laboratory (LLNL) seismic location effort to integrate a diverse set of three-dimensional velocity model and empirical based travel-time products (developed both in house and through external contracts) into one consistent and validated calibration set. Integrating reliable velocity models that correct for systematic travel-time anomalies is critical to providing accurate and reliable estimates of seismic event location. If these anomalies are not accounted for, then the predicted errors will likely misrepresent the true uncertainty of an event's location. At LLNL, we have implemented a unified framework that combines empirical-based kriging with model-based path corrections to remove this type of bias from the location problem, as shown in Figure 1. Our framework incorporates any combination of *a priori* and *a posteriori* one-dimensional, two-dimensional, and three-dimensional models. These error distributions are then propagated into our coverage ellipse estimates. Our focus this year has been on the merging of these models geographically and on developing a validation process that can provide high *confidence* in our confidence estimates.

RESEARCH ACCOMPLISHED

Much of the current university and other external research has focused on developing model-based corrections that work to improve travel-time prediction at both regional and upper-mantle triplication distances. Beyond the upper mantle distances, global Earth models plus a static station correction generally provide excellent travel-time prediction. Thus, we typically merge regional and teleseismic models just beyond the upper-mantle triplication distance. In the regional distance range, we allow for the merging of an optimal combination of regional models. After a merged set of calibration velocity models is applied at a station, we add empirical corrections using the nonstationary Modified Bayesian Kriging algorithm (Schultz et al., 1998) where travel-time residuals for suitably well located calibration events exist. Since the teleseismic errors are quite small, only the highest quality reference events are useful at these larger distances. At regional distances less precise ground truth (GT) is still helpful (e.g. 20-km accurate ground truth). Our approach combines the extrapolative advantages of model-based corrections and the interpolative/statistical advantages of Bayesian prediction (i.e. modified kriging) to produce hybrid travel-time predictions and uncertainty models. For ease of use, model-based and empirical corrections are combined to produce one travel-time correction and uncertainty model that is applied to the optimal global Earth model for a given station. However, any model that can be described by a depth/distance/travel-time file can be utilized in our system.

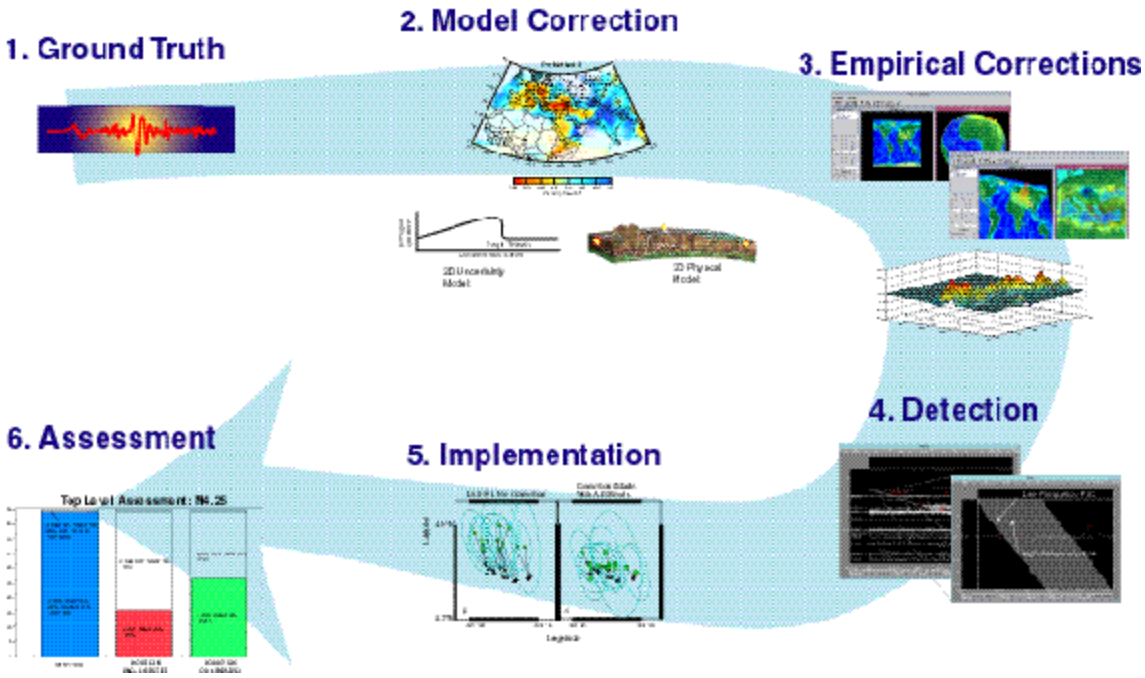

Figure 1: Developing a comprehensive framework for location.

We continue to work closely with Sandia National Laboratories to implement a framework that allows us to design, build, integrate, and visualize the calibrations that are produced by combining our own internal NNSA research with that provided through research associated with external contracts. A large part of our effort at LLNL continues to be concerned with generating standardized detection, travel-time, and amplitude correction volumes on a regional basis.

Development and Validation of 1-D, 2-D, and 3-D Models

We investigate our ability to improve seismic event location accuracy in the Middle East, Northern Africa, and Western Eurasia (ME/NA/WE) region by developing 1-D, 2-D and 3-D velocity models of the crust and upper mantle to account for velocity heterogeneity in the region. Event locations based on 1-D models are often biased, as they do not account for significant travel-time variations that result from spatially heterogeneous crust and mantle structure. Previous studies have shown that event locations and uncertainties can be improved by

applying empirical travel-time corrections relative to the default *IASPI91* 1-D model (e.g., Myers and Schultz, 2000). Empirical corrections and other model optimization methods are well suited to improve travel-time prediction in areas where GT events are available. However, vast portions of the ME/NA/WE region are devoid of GT events; thus, we seek to improve travel-time prediction at regional and near-teleseismic distances in regions without GT calibration.

Our approach here is to develop model-based travel-time correction surfaces derived from several different models which can be used along with empirical travel-time residuals and GT event locations for validation and testing. We explore the degree of improvement in location accuracy and uncertainty achieved by each velocity model using a variety of validation techniques. The velocity models we tested are of three types:

- 2-D radially heterogeneous, station specific models derived from regressing travel times;
- a *Pn* velocity model produced by tomographic inversion; and
- an *a priori* 3-D model based on geophysical studies ranging from seismic reflection to geophysical analogy.

Model-based travel-time predictions remove predictive travel-time residual trends and provide improvement relative to global models, as well as providing the requisite zero-mean distributions for kriging.

2-D Station Specific Velocity Models

In order to improve the travel-time predictions at regional and near teleseismic distances, we develop 2-dimensional, station-specific travel-time models that are optimized to predict travel times from GT events. The data used are a set of teleseismically constrained *P*-phase arrival times from a declustered dataset (described above). We use 100% of the groomed data set to compute our 2-D models. In the model validation phase, we leave 90% of the data out and use a 10% data subset to estimate the prediction uncertainty. The dataset is parsed into three distance ranges -- regional (1°-13°), upper-mantle (13°-30°), and teleseismic (30°-90°) -- based on the depths of the turning rays and therefore upon the portion of the earth sampled by the wavefield.

The first step in creating 2-D radially heterogeneous and azimuthally invariant travel-time models is to create 1-D regionalized travel-time models for each station at each of the distance ranges described above. We developed an adaptive grid search method that efficiently samples and explores the space of reasonable mo dels, allowing the four most influential model parameters (crustal thickness, upper and lower crustal *P*-wave velocity, and upper mantle *P*-wave velocity) to vary. The model parameters we use to describe model space are crustal thickness, upper and lower crustal *P*-wave velocity, upper mantle velocity, sediment thickness, sediment *P*-wave velocity, thickness of the mantle lid, and *P*-wave velocity gradient in the lid. We calculate travel times through each regionalized *P*-wave velocity model using a ray-tracer that employs the single-valued *tau-p* formulation similar to that of Buland and Chapman (1983). An earth-flattening transformation is used to account for the sphericity of the earth, which preserves the kinematic properties of the rays. The resulting travel-time tables are populated with travel times, parameterized by distance and depth.

To test the predictive power of each 1-D regionalized model, we compute the mean residual and an *rms* residual between the declustered *P*-phase arrivals at each station and the arrivals predicted by each 1-D travel-time model. We repeat the calculation for the declustered *P*-phase arrivals at each station and the arrivals predicted by the *IASPI91* model. When we rank the models according to *rms* residual, we find that a suite of models predicts the travel-time arrivals equally well. We choose to further minimize our models against our background model (*IASPI91*) to address distance discontinuities between the regionalized models and to promote a smooth transition to the background model outside the coverage area of our models.

To ensure a smooth travel-time curve, we merge our preferred 1-D regionalized curves smoothly at the distance thresholds to produce 2-D curves. Merging is accomplished using a sine-taper (smoothing) function to reduce distance discontinuities between the individual curves. The sine-taper is applied over a distance range of 1°, so that travel-times are smoothed between 12.5° and 13.5°, and between 29.5° and 30.5°. The result is a radially heterogeneous and azimuthally invariant travel-time curve for both the crust and upper mantle. When we compute travel-times through the 2-D models and compare predicted arrivals with the data, we find that our 2-D models improve travel-time fit (reduction in *rms* residual) and reduce the bias, relative to *IASPI91*. Repeating the process with the 10% validation data set demonstrates that we also improve travel-time predictability with our 2-D models. Results for two representative stations are shown in Figure 2.

Pn Velocity Model

We derive a model of uppermost mantle P-wave velocities throughout the Middle East, North Africa, and Former Soviet Union using regional P-wave travel times from a groomed version of the ISC catalog (Engdahl *et al*., 1998). This catalog was then statistically declustered spatially in order to reduce the size of the dataset and to identify and

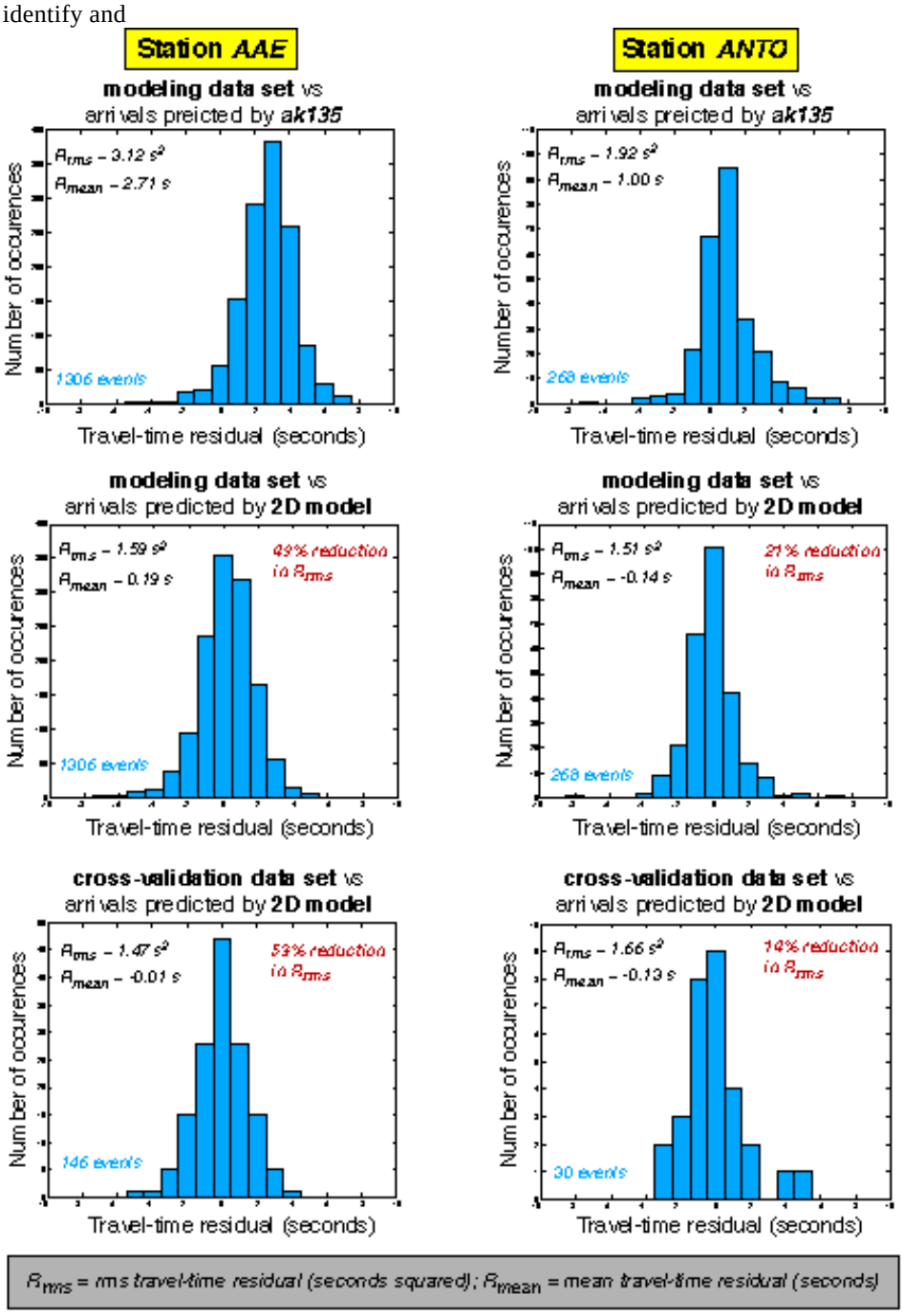

Figure 2. Histograms show the distribution of travel-time residuals at stations AAE and ANTO. Top row: travel-time residuals relative to *IASPI91*, using the modeling data set. Middle row: travel-time residuals relative to our preferred 2-D model, using the modeling data set. Bottom row: travel-time residuals relative to our preferred 2-D model, using the cross-validation data set.

remove outliers. The top panel in Figure 3 shows the path coverage for the inversion. Notice the highly uneven sampling of our study area, with many raypaths in the Mediterranean, Europe, the Middle East and Indian subcontinent and few or no raypaths in Africa, the Former Soviet Union, and the oceans.

We have used a conjugate gradient method for the P-wave velocity tomography. The conjugate gradient technique is a search method that works very well on sparse linear systems like the travel-time problem.

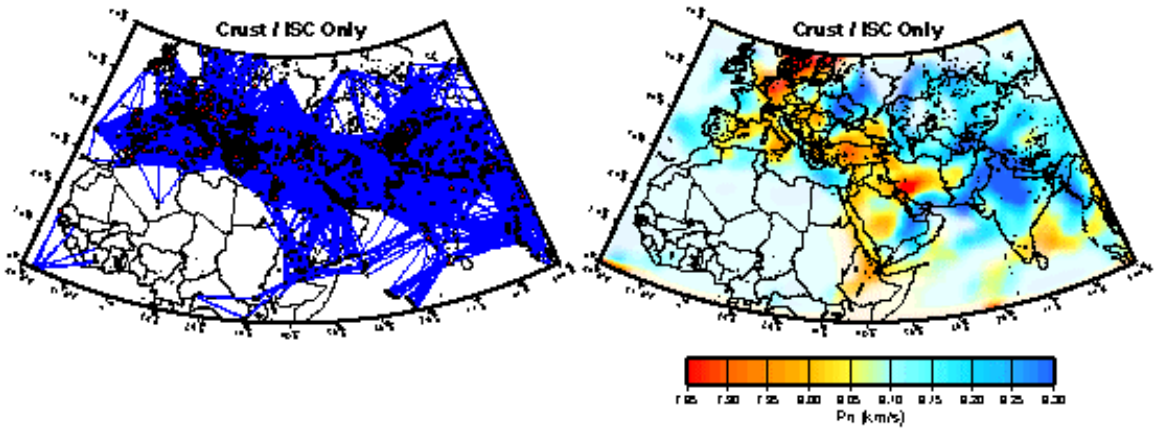

Figure 3 Paths and uppermost mantle P-wave velocities from the P_n tomography. We find slow upper mantle velocities along the Tethys collision zone and Red Sea rift, and fast upper mantle velocities in India and southern Former Soviet Union.

Because there is no matrix inversion involved, it is well suited for large systems of equations. We chose a 2-degree by 2-degree grid for the inversion, and within each grid, we solve for the P-wave velocity in both the crust and upper mantle, assuming a crustal thickness of 35 km (Pasyanos, 2000). We currently provide uncertainty estimates for the P-wave velocities in the crust and upper mantle for the P_n tomography.

From the inversion results, we are able to provide three-dimensional background P-wave travel-time correction surfaces for any seismic station. We can construct the travel times along any given path by integrating the P-wave slowness results from the tomography results. We can then build the surface by calculating the travel times along a regular grid in latitude, longitude, and depth. Travel times in the surfaces are given as residuals relative to travel times predicted by the *IASPI91* model (Kennett and Engdahl, 1991) and are shown in Figure 4.

3-D a priori Velocity Model

We use ME/NA/WE2.0 (Pasyanos, et al., 2001), a self-consistent three-dimensional Earth model for the crust and upper mantle, to compute travel-time correction surfaces for use with our location algorithm. This *a priori*, regionalized model is a preliminary set of geophysically distinct regions that can be used for estimating travel times, surface wave dispersion, and discrimination properties particularly in aseismic regions where calibration data are sparse. The model can also provide a platform for assessing progress in seismic location, discrimination, detection—the entire calibration process—and aid in determining the priority and planning of calibration experiments. Because the ME/NA/WE2.0 model is 3-D, region-specific velocity structure, it can be characterized more accurately than 1- or 2-D models. A representative cross-section through the velocity model is shown in Figure 5.

This *a priori* model specifies geographic boundaries and velocity structures based on geology, tectonics, and seismicity. This regionalization serves as a starting point, and we expect to refine and improve upon it based on such tests as predicting *P* and *Pn* travel times (presented here) as well as surface wave velocities. As the model improves and demonstrates some predictive power, it may evolve into a base model for tomographic inversions as well as a reference model for other CTBT-related research efforts.

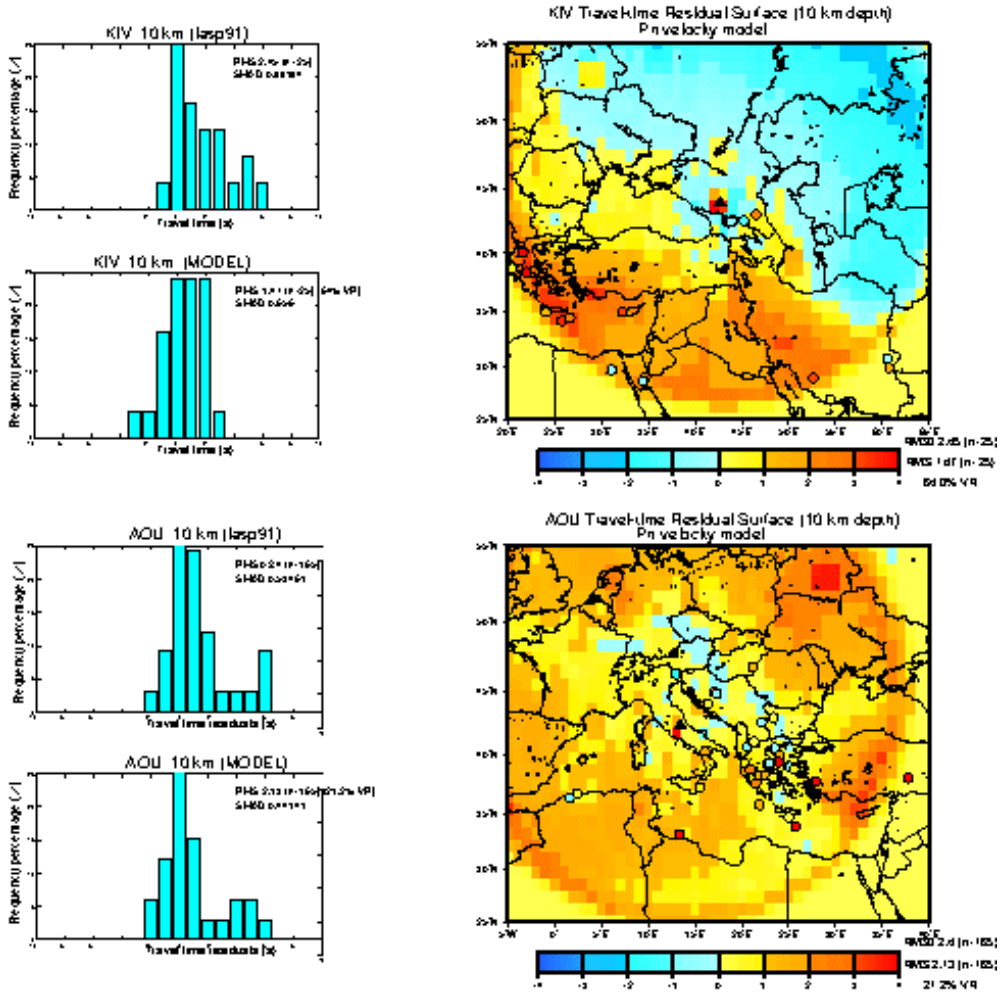

Figure 4. *P*-wave travel-time correction surfaces and histograms for stations KIV and AQU based on our *Pn* tomography model.

To compute travel times through the ME/NA/WE2.0 velocity model, we use an algorithm, originally developed by Vidale (1988) and further refined by Hole and Zelt (1995), which uses a finite difference approximation (FD) to compute first arrival travel times through regularly gridded velocity structures. We modify the original code in two ways. First, we adapt it to read in 3-D velocity models instead of 1-D such that it can compute times through our ME/NA/WE2.0 (or any custom 3-D) model. Second, we apply a Cartesian-to-spherical coordinate transformation to the source and receiver locations that are input to the code [Flanagan et al., 2001]. These modifications are necessary because we need to compute travel times out to regional and near-teleseismic distances (~13° to 30°). The code is run in a volume of dimensions of roughly 25° by 25° laterally and 800- to 1000-km deep with a grid spacing of 3 km. The grid spacing is determined empirically as a trade-off between the accuracy of the travel-time prediction and computer memory limitations, and we find that a grid spacing of 3 km provides a reasonable accuracy (i.e., timing errors of approximately 0.25 s).

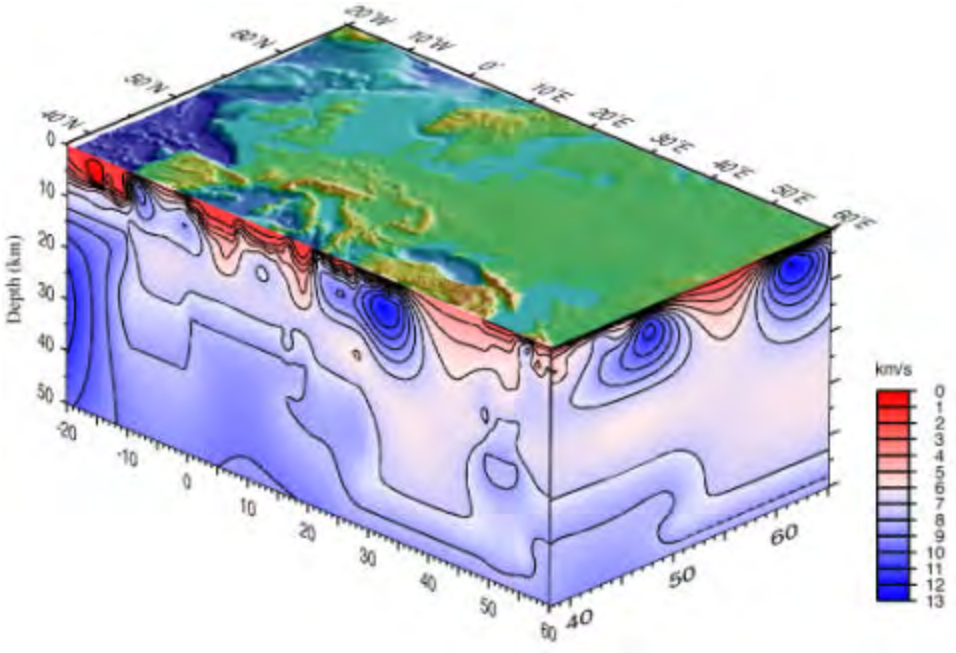

Figure 5. Cross-section of P-wave velocities from our 3-dimensional ME/NA/WE2.0 model.

We compute station-specific correction surfaces based on the P-wave travel times predicted by the FD algorithm. To compute these model-based correction surfaces, we subtract the *IASPI91* predicted time from the ME/NA/WE2.0 predicted time along a regular grid in latitude, longitude and a given depth. Example surfaces at 10-km depth are shown in Figure 7 along with travel-time residuals from a groomed, declustered dataset of GT15 events (Engdahl *et al*., 1998). We find travel-time differences of up to 6 sec relative to *IASPI91*, most in areas of very thick crust or sediment. Note the patterns in these correction surfaces correlate with the structural features in the ME/NA/WE2.0 model; fast predictions are seen to the north on the Russian platform while slow anomalies are seen at the southern Caspian as well as eastern Turkey and the southern Caucasus. These correction surfaces can then be used as additional constraints in the location algorithm to improve regional seismic location.

To test the predictive power of our *a priori* model, we compare the travel times predicted by both our ME/NA/WE2.0 model and the *IASPI91* model with the declustered P arrivals at each station. To compute these travel-time residuals, we interpolate between grid nodes to calculate the predicted travel time for an exact earthquake-station path; then, each predicted time is subtracted from the observed arrival time. These residuals are shown in histogram form in Figure 6. Note for some stations the 3-D ME/NA/WE2.0 model predicts the observations very well, showing a significant variance reduction, while for others it improves the fit given by the *IASPI91* only slightly.

Improving Location: The 1991 Racha Aftershock Sequence

Next we determine the improvement provided by the various models by relocating a set of ground truth events; the improvement in seismic location that is gained by using the different velocity models is the ultimate test of our approach. As a test case, we use a set of GT2 locations determined using regionally recorded aftershocks in the region of Racha, Georgia. In a previous study, Myers and Schultz (2000) demonstrated location improvement using Modified Bayesian Kriging (MBK) to compute empirical correction surfaces for a sparse 6-station test network. The MBK correction surfaces for the test-network stations are based on high-quality teleseismically constrained GT15 hypocenters throughout the Middle East (Engdahl et al., 1998). The 1991 Racha events are then relocated with and without the aid of MBK correction surfaces, and the resulting epicenters are compared to the benchmark GT2 locations determined from a dense local deployment of seismic sensors. When no travel-time correction is applied, the mean horizontal distance between the local and test network locations is 42 km, and there is a distinct bias in sparse-network locations towards the north-northwest.

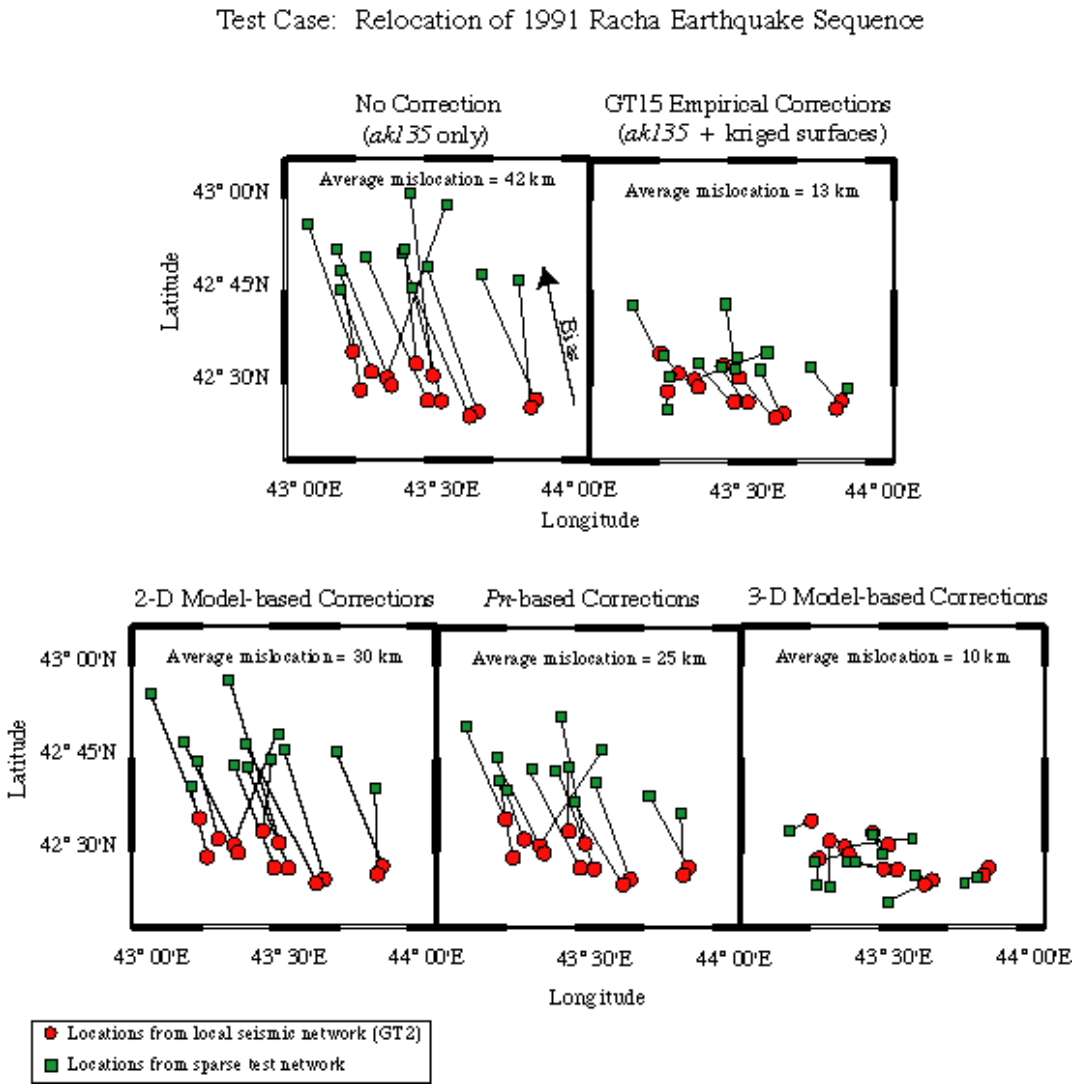

Figure 6. Example correction surfaces at 10-km depth shown along with travel-time residuals from the declustered data set (blue indicates fast regions and red indicates slow). In general, travel-time variance for the ME/NA/WE2.0 model is reduced compared to *IASPI91*. In some instances the mean of the distribution is displaced from zero; however, this may be due to optimization of the event origin times relative to the *IASPI91* velocity model.

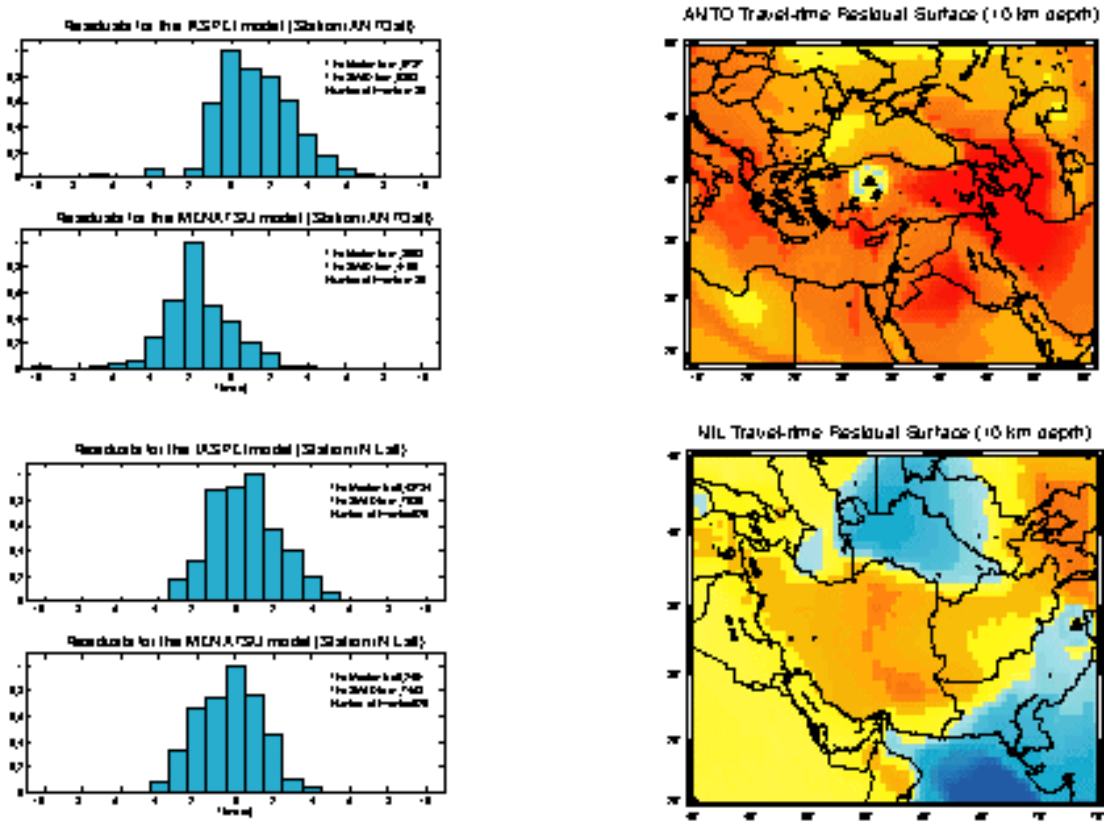

Figure 7. Relocations of the 1991 Racha earthquake sequence with correction surfaces derived from kriging empirical residuals, a 2-D velocity model, Pn tomography, and a 3-D *a priori* velocity model. Location bias is significantly reduced when either empirically derived or model-based corrections are applied to reduce travel-time prediction inaccuracies.

The mean difference between local and sparse network locations is reduced to 13 km when the empirical corrections are applied and the bias in location is significantly reduced (Figure 7, top).

We compute model-based correction surfaces for the six stations (KAS, KVT, GAR, KHO, ARU, and SVE) comprising the sparse test network. We then relocate this same set of events using our model-based correction surfaces and produce an average mislocation bias of 30 km using the 2-D models, 25 km using *Pn* tomography, and only 10 km using the 3-D model. However, of the six stations, only two are regional distance from Racha, two are teleseismic, and two are very far regional distance, so the Pn correction was not always employed. This test case clearly demonstrates the power of applying model-based corrections to improve location capability for small, regionally recorded events. A larger data set of GT0-GT10 events is being collected and will be used to further evaluate the effectiveness of each model for improving event location accuracy. We are also developing a variety of validation techniques (*e.g.*, cross-validation, sensitivity tests) to model the uncertainty process for model-based corrections that will be required to compute representative error ellipses for the new locations.

LLNL Framework for Integrating and Validating Calibrations

The overall goal of our framework is to provide a flexible, interactive environment in which an analyst can produce, test, and manage calibration information for seismic stations. This framework focuses on providing accurate characterizations of location uncertainty given the highly nonstationary and regionally varying nature of seismic travel-time, azimuth, and slowness. To account for variations in regional structure, our framework is designed to account for dramatic variations in travel-times and amplitudes that occur over relatively short distances in the crust - variations that can lead to significant errors in event location.

The ability to accurately locate seismic events rests on the development of reliable uncertainty models and the careful validation of these errors at each step of the process. Figure 1 gives a general overview of the components involved in the calibration of seismic location. These components include: (1) cataloging well constrained ground truth events that can be used to assign and validate the uncertainties in the location process (Hanley and Schultz, 2000); (2) refining one-, two-, and three-dimensional velocity models to better predict travel times (Flanagan et al., 1999; Swenson and Schultz, 1999; Swenson et al., 1999; Flanagan et al., 2000); (3) applying statistical prediction techniques that work together with the travel-time models to extract additional accuracy from the ground truth data (Schultz and Myers, 1998; Myers and Schultz, 1999; Myers and Schultz, 2000); (4) determining detection thresholds and filter phase filter characteristics as a function of magnitude; (5) applying state-of-the-art location algorithms; (6) assessing of our progress in improving seismic location uncertainties.

Validation and Benchmarking of Models and Empirical Surfaces

The one validation technique applied to all these models and associated empirical surfaces is the model-checking cross-validation technique. In this approach events are removed from the data set and an uncertainty model is built by differencing predicted and observed arrival times. Normalizing the difference between predicted and observed arrivals by the predicted (Bayesian Kriging) uncertainty provides validation of the empirical uncertainty model. In this case, the normalized mean, root-mean-square, and histogram are provided as validity measures.

CONCLUSIONS AND RECOMMENDATIONS

In general, we have developed a hybrid approach to location that uses three-dimensional model corrections for a region and then uses reference events when available to improve the path correction. Our approach is to select the best *a priori* three-dimensional velocity model that is produced for a local region and then use this as a baseline correction. When multiple models are produced for a local region, uncertainties in the models will be compared against each other using ground truth data, and an optimal model will be chosen. We are working towards implementing a calibration integration process of combining three-dimensional models on a region-by-region basis and integrating the uncertainties to form a global correction set. The Bayesian kriging prediction combines the optimal model combination and its statistics with the empirical calibrations to give an optimal *a posteriori* calibration estimate. The result is improved location estimates and robust location uncertainties that show significant improvement in calibrated regions (Schultz and Myers, 1999; Schultz et al., 1999).

To aid this process we have developed a general framework to provide a flexible, interactive environment in which a researcher can produce, test, and manage calibration information for seismic stations. This approach allows a general statistical analysis on a regional basis and results in a self-consistent global calibration set.

REFERENCES

Buland, R. and C. Chapman (1983), The computation of seismic travel times, *Bull. Seism. Soc. Am.*, 73, 1271-1302.

Engdahl, E.R., R. van der Hilst, and R. Buland (1988), Global Teleseismic Earthquake Relocation with Improved Travel Times and Procedures for Depth Determination, *Bull. Seismol.. Soc. Am., 88,* 722-743.

Flanagan, M. P., S. Myers, C. Schultz, K. Koper, M. E. Pasyanos, and W. R. Walter (2001), Three-dimensional *a priori* model constraints for improving regional seismic event location, *Bull Seismol. Soc. Am., in preparation.*

Flanagan, M. P., C. A. Schultz, S. C. Myers, M. E. Pasyanos, W. R. Walter, K. D. Koper (2000), Improving Regional Event Locations in the Middle East by Incorporating Model Based Correction Surfaces Derived from 3-D Velocity Structures, SSA Spring Meeting, San Diego, CA, *Seism. Res. Lett., vol. 71, no. 2,* p. 208, *UCRL-JC-137115 abs.*

Flanagan, M. P., C. A. Schultz, and L. J. Hutchings (1999), Development of 3-D Crust and Upper Mantle Velocity Models to Improve Seismic Event Location, AGU Fall Meeting, San Francisco, CA, *EOS Trans. Am. Geophys. Un., vol. 80, no. 46,* p. F656, *UCRL-JC-135476 abs.*

Hanley, W.G., C. A. Schultz, S. C. Myers (1999), Statistical analysis of travel time residuals applied to the analysis of station quality, *Seismological Society of America 94th Annual Meeting.*

Hole, J.A. and B.C. Zelt (1995), 3-D Finite Difference Reflection Travel Times, *Geophys. J. Int., 121*, 427-434.

Kennett, B.L.N. and E.R. Engdahl (1991), Traveltimes for global earthquake reference location and phase identification, *Geophys. J. Int, 105*, 429-465, 1991.

Myers, S.C. and C. A. Schultz (2000), Improving Sparse Network Seismic Location with Bayesian Kriging and Teleseismically Constrained Calibration Events, *Bull. Seism. Soc. Am.*, 90, 199-211

Myers, S.C. and C. A. Schultz (1999), Improvement in seismic location using non-stationary Bayesian kriging, *Seismological Society of America 94th Annual Meeting.*

Pasyanos, M. (2000), Predicting geophysical measurements: Testing a combined empirical and model-based approach using surface waves, *Bull. Seism. Soc. Amer.*, 90, 790-796.

Pasyanos, M. E., W. R. Walter, M.P. Flanagan, P. Goldstein, and J. Bhattacharyya (2001), Building and Testing a Geophysical Model for Western Eurasia and North Africa, *J. Geophys. Res., submitted*, March, *UCRL-ID-142778.*

Schultz, C.A. and S. C. Myers (1999), Improving regional seismic event location through calibration of the international monitoring system, *21st Seismic Research Symposium Technologies for Monitoring the Comprehensive Nuclear Test Ban Treaty*.

Schultz, C.A., S. C. Myers, M. Flanagan J. Swenson, J. Hanley, M. Pasyanos (1999), Improving seismic event location through calibration of the International Monitoring System, *21st Seismic Research Symposium Technologies for Monitoring the Comprehensive Nuclear Test Ban Treaty.*

Schultz, C.A., and S. C. Myers (1998), Nonstationary Bayesian Kriging: A predictive technique to generate spatial corrections for seismic detection, location, and identification, *Bull. Seism. Soc. Am*., 88, 1275-1288.

Swenson, J.L, C.A. Schultz, W.G. Hanley (1999), Using radially heterogeneous and azimuthally invariant travel-time models to improve seismic location in the Middle East and North Africa, *Fall American Geophysical Union Meeting.*

Vidale, J., (1988) Finite-difference Calculation of Travel Times, *Bull. Seismol. Soc. Am., 78*, 2062-2076.

DEVELOPMENT OF A GROUND TRUTH DATABASE FOR IMPROVEMEMENT OF CTBT MONITORING IN THE EASTERN MEDITERRANEAN REGION

Avi Shapira,[1] Vladimir Pinsky,[1], Mehmet Ergin,[2], Yefim Gitterman,[1]
Dogan Kalafat,[3] Kyriakos Solomi,[4] and Rami Hofstetter[1]

Geophysical Institute of Israel,[1]
TUBITAK Marmara Research Center, Earth and Marine Sciences Research Institute, Turkey,[2]
Bogazici University, Kandilli Observatory and Earthquake Research Institute, Istanbul, Turkey,[3]
and Geological Survey Department of Cyprus[4]

Sponsored by Defense Threat Reduction Agency

Contract No. DTRA01-00-C-0119

ABSTRACT

A reliable Ground Truth (GT) database is crucial to improve the monitoring of small seismic events in the Middle East. Therefore, the Geophysical Institute of Israel (GII), Bogazici University, Kandilli Observatory and Earthquake Research Institute, Istanbul (Turkey) (KOERI), TUBITAK Marmara Research Center, Earth and Marine Sciences Research Institute, (Turkey) (EMSRI) and the Geological Survey Department of Cyprus (GSDC) joined their efforts to develop a database using seismic data from the national networks and arrays advantageously placed in the eastern Mediterranean region.

The elaborated GT database includes: 1) GT2-GT5 data for earthquakes and aftershocks that are well constrained by dense local and portable networks; 2) GT2 data of large routine quarry blasts supplied by blast pattern parameters; and 3) GT0 data for controlled routine quarry blasts and special design calibration explosions conducted previously and during project duration, including detailed blast pattern design.

At the first stage of the project, we elaborated the database for calibration of the International Monitoring System (IMS) stations EIL and MRNI relative to local GT events, well located by the Israel Seismic Network (ISN) stations. We collected 27 GT0 events (including the three Dead Sea calibration explosions in November 1999) and 23 GT2 industrial explosions from quarries in the Negev and Galilee (local magnitude M_L = 2.7-3.1); all the explosions are recorded with a high signal-to-noise ratio (SNR) up to 250 km. About 20 accurately located (GT2-GT5 rank) earthquakes in Israel (M_L > 3) were selected.

Next, we accumulated travel times data from earthquakes for correction of the travel-time models from specific areas to the IMS stations within the radius of 2000 km of the chosen seismic networks. After screening of numerous candidate events, we selected 21 earthquakes from different eastern Mediterranean sites within the footprint of the local networks: a) 6 earthquakes of M_L >4 located between the Cypriot Seismic Network and the ISN (GT5 rank); b) 7 Adana-Ceyhan earthquakes (M_L > 4) and 8 Izmit and Bolu-Duzce earthquakes (M_L > 4.5), well covered by the Turkish networks together with portable stations (GT2-GT5 rank). All selected earthquakes were carefully screened, relocated, and checked according to the appropriate GT criteria.

The accumulated GT events were also used to improve event location: a) event relocation based on evaluated travel-time residuals; b) estimation of corresponding 90% confidence ellipsoids; c) verification by the Monte-Carlo simulation. The collected earthquake/explosion data will be used for: a) mapping travel time residuals, azimuth residuals and regional phase attenuation, b) upgrading of the Robust Location Procedure to an automatic bulletin producer; c) development of the grid search procedure for location and confidence volume estimation; d) modification and testing of advanced seismic processing methods: 1) maximum likelihood beamforming applied to the BRAR and MRNAR arrays; and 2) regional multi-station spectral and kinematic discriminants to be adapted to the Turkish Seismic Network.

KEY WORDS: ground truth database, IMS station calibration, eastern Mediterranean, event relocation

OBJECTIVE

The main objective of the project is to characterize and enhance the CTBT monitoring potential of small events in the eastern Mediterranean area, based on jointly collected GT0-GT5 database of earthquakes and chemical explosions and on development and implementation of improved signal processing techniques.

RESEARCH ACCOMPLISHED

On the first stage the main effort for the GII (Israel), the KOERI/EMSRI (Turkey), and the GSDC (Cyprus), was to elaborate a joint database of waveforms and source parameters: 1) GT5 dataset of earthquakes (aftershocks), located within the network foot-print, with an estimated small location error (Pinsky et al., 2001); 2) GT0-GT2 waveform dataset for controlled routine quarry blasts and calibration explosions of special design (Dead Sea, Negev and Galilee). The database was elaborated by screening local bulletins and seismic records of national stations.

Earthquakes and large aftershocks (GT2-GT5) jointly observed by seismic stations in Israel, Cyprus and Turkey.

"Israeli" earthquakes

For the period 1995-2001 we screened 21 earthquakes of magnitude $M_L > 3$ (Fig. 1) located within the Israel Seismic Network (station azimuth gap<210°), which were checked to fit the GT5 criteria (Firbas, 2001). Most of the events are observed also by the Cypriot Seismic Network (CSN). Several earthquakes with M_L>3.5 are expected to be detected by the Cilician Network (Southern Turkey) and we are now looking for their data.

The source parameters of the selected events and their waveform data from the CSN and the ISN are now available. Some of the earthquakes are observed by the IMS stations EIL and MRNI, installed in 1996 and 1997 respectively, and the records will be used in the project for regional source characterization and calibration of the stations. All of the events were relocated to more accurate and more reliable solutions using relevant weights. Corresponding 90% confidence ellipsoids were estimated and checked by the Monte-Carlo simulation, an example is presented in Fig. 2.

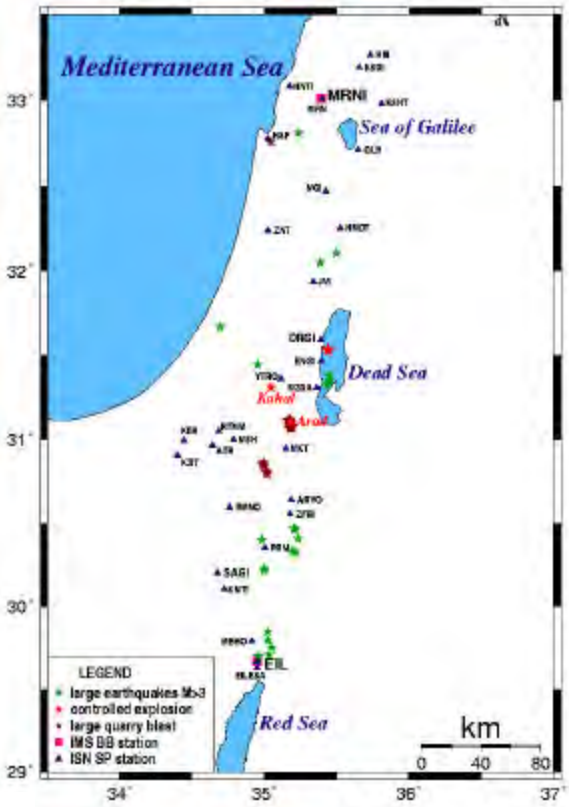

Fig. 1. Map of selected earthquakes with magnitude M_L>3 located within the Israel Seismic Network

Fig. 2. Example of estimating 90% confidence ellipsoid (with axes LMIN, LMAX) for an earthquake 11.03.2000 01:52:31.5. The network configuration used in the estimation is also shown.

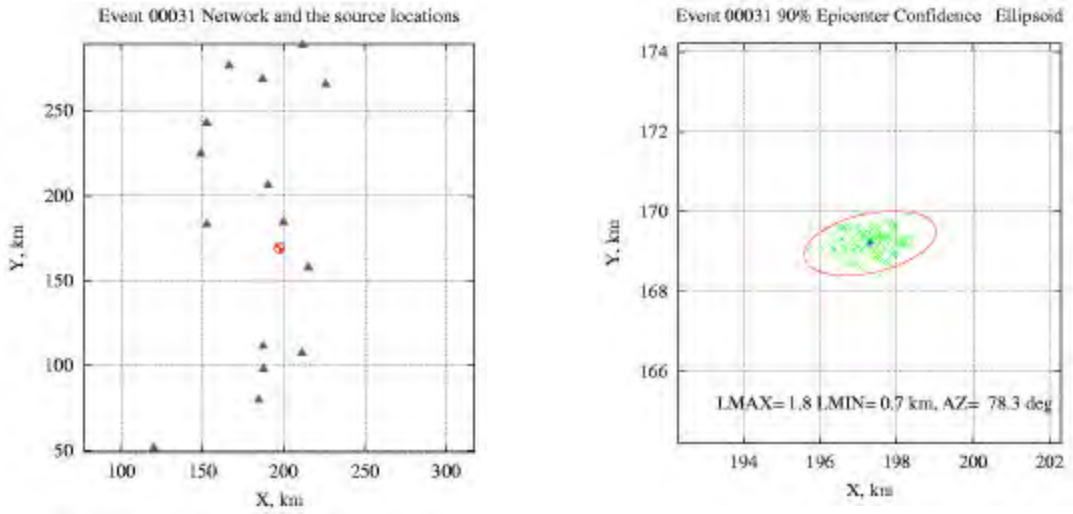

Aftershocks of large earthquakes in Turkey

Three catastrophic earthquakes occurred in Turkey in 1998-1999: the first one in Adana and Ceyhan areas (27.06.98, 13:55:52.08, Mw=6.3) (Aktar et al., 2000); the second was close to Izmit (17.08.99, 00:01:39.13, Mw=7.6); and the third was in the Bolu-Duzce area (11.12.99, 16:57:19.5, Mw=7.3) (Ozalaybey et al., 2000). Origin time and magnitude values are from NEIC. The earthquakes were accompanied by a series of strong aftershocks, recorded by the permanent local Golcuk and Cylician networks, as well as by portable stations, deployed after the mainshock (Ito et al., 2001). The dense observations facilitated location computations with a high location accuracy for some aftershocks, thus meeting the GT5 criterion. All the events were observed by the ISN and CSN. Source parameters and waveform data were collected, screened and stored in the project database for the following analysis.

The KOERI and EMSRI (Turkey) seismological institutions delivered source parameters of numerous aftershocks from the local bulletins, with corresponding waveforms. We selected fifteen GT5 candidate events (magnitude > 4), which are referenced in the pIDC REB bulletins, and presented below in Tables 1-2, and Fig. 3. The tables comprise the mainshocks (N1 and N7 of the Table 1 and N2 of the Table 2). The maps show locations of the stations and the events and demonstrate the excellent azimuthal coverage of these sources. Source locations of three of the Izmit events (N1, N3, N4 in Table 1) are within 3 km. The same is true for the two Bolu-Duzce aftershocks (N3 and N4 of Table 2). These data might be of great value for the accurate travel-time estimation and calibration of IMS and other stations.

Samples of the raw data, representing recordings of the Turkish networks, are shown on Figs. 4-7. Figures 1 and 2 exhibit waveforms of an Izmit aftershock at the 3-component BB station ISK, deployed in Istanbul (Fig. 5), and the farther IMS array BRAR, located in Istanbul (see the map on Fig. 3a), where regional phases Pn, Pg and Sg can be found (Fig. 4). Strong S-waves (high S/P ratio) from the Izmit and Bolu-Duzce events, are recorded at ISK and BRAR (see Figs. 4-6). No distinct S-waves onsets and strong wave scattering for the Adana events are observed at Cilician stations (Fig. 7). The scattering is possibly related to the location of the earthquakes and recording stations within the valley, surrounded by mountain structures (see Fig. 3b).

The source parameters of the events are presented in Tables 1-2. Magnitude estimations are taken from the PDE bulletin. Some recording stations (Nst) located at distances less then 100 km are also shown (in parentheses). Prominent P and S first arrivals and a large number of close (r<100 km) stations (more than 10 in most cases), ensure a high (of GT5 rank) accuracy of source location.

Table 1. Selected IZMIT and BOLU-DUZCE earthquakes.

N	O.T.	Lat. deg.	Long. deg.	H, km	M_{PDE}	Nst (R<100 km)	RMS, sec	Az. gap, deg.	Standard location errors			
									Dt_0, sec	dy, km	dx, km	dH, km
1	**990817 00:01:38.7**	**40.729**	**29.966**	**13.3**	**6.7**	**18 (14)**	**0.3**	**75**	**0.96**	**2.6**	**3.4**	**2.7**
2	990817 02:50:47.0	40.638	30.048	1.0	4.5	7 (10)	0.3	257	0.69	3.4	4.7	4.9
3	990831 08:10:50.9	40.747	29.984	8.4	5.2	36 (34)	0.3	66	0.68	1.8	1.2	2.8
4	990831 08:33:24.8	40.740	29.979	10.0	4.6	36 (34)	0.3	97	0.59	1.5	1.0	2.4
5	990913 11:55:29.3	40.753	30.100	16.7	5.9	36 (34)	0.3	60	0.58	1.7	1.4	1.6
6	990917 19:50:6.9	40.753	30.100	13.9	4.5	42 (40)	0.2	60	0.58	1.3	1.1	1.6
7	**991112 16:57:20.8**	**40.830**	**31.138**	**10.0**	**5.5**	**28 (17)**	**0.4**	**?**	**0.83**	**2.7**	**1.7**	**2.6**
8	991119 19:59:12	40.819	31.005	5.6	4.3	35 (20)	0.5	73	1.22	1.6	2.4	3.1

Table 2. Selected ADANA-CEYHAN earthquakes.

N	O.T.	Lat.	Long.	H, km	M_{PDE}	Nst (R<100 km)	RMS, sec	Az. gap, deg.	Standard location errors			
									dt_0, sec	dy, km	dx, km	dH, km
1	980103 21:15:7.5	37.202	35.766	15.8	4.1	15 (11)	0.4	84	0.94	1.9	2.7	3.7
2	**98062713:55:51.4**	**36.885**	**35.498**	**33.1**	**6.3**	**12 (10)**	**0.2**	**78**	**1.12**	**5.7**	**11.5**	**8.9**
3	980628 03:59:25.9	37.005	35.655	21.2	4.3	13 (9)	0.2	125	0.96	3.0	4.8	6.3
4	980628 15:20:34.7	36.992	35.658	35.1	3.4	14 (8)	0.4	145	1.02	4.0	1.0	3.6
5	980704 02:15:47.9	36.910	35.429	29.5	5.1*	19 (10)	0.8	83	1.92	5.7	5.4	4.5
6	981204 04:59:27.8	36.995	35.568	29.2	4.3	14 (9)	0.3	82	0.91	2.5	2.6	5.0
7	990115 02:04:31.3	37.033	35.850	24.1	4.3	18 (15)	0.4	64	1.1	3.2	3.2	3.9

Golcuk bulletin

Fig. 3. Selected Turkish events (★) and observing stations (▲): (a) Izmit and Bolu-Duzce earthquakes; (b)

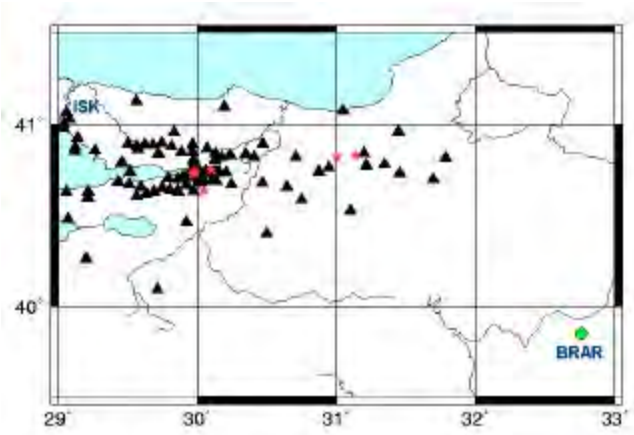

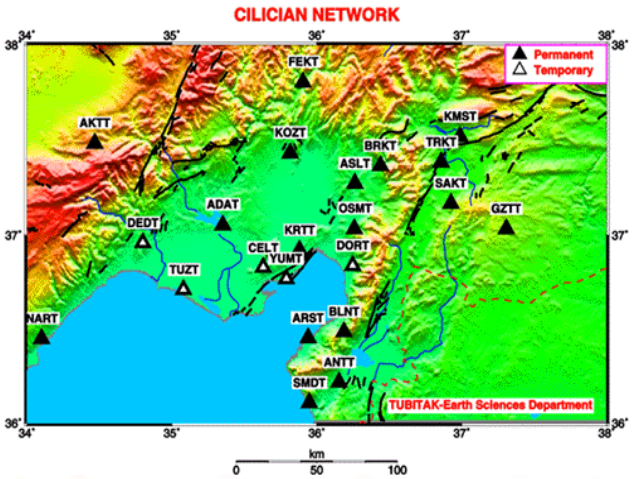

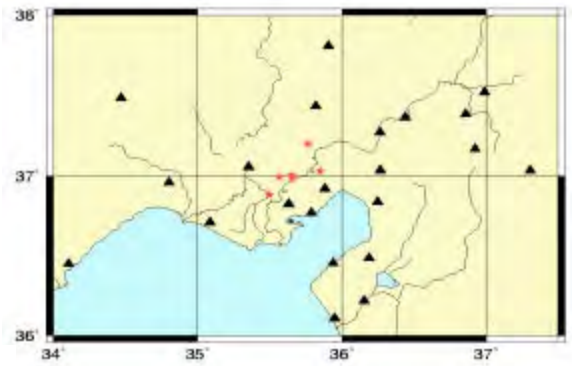

Ci*lician network and selected aftershocks of the Adana-Ceyhan earthquake.

Fig. 4. Waveforms of the 17.09.99 Izmit aftershock (M_{PDE}=4.5) at the IMS array BRAR.

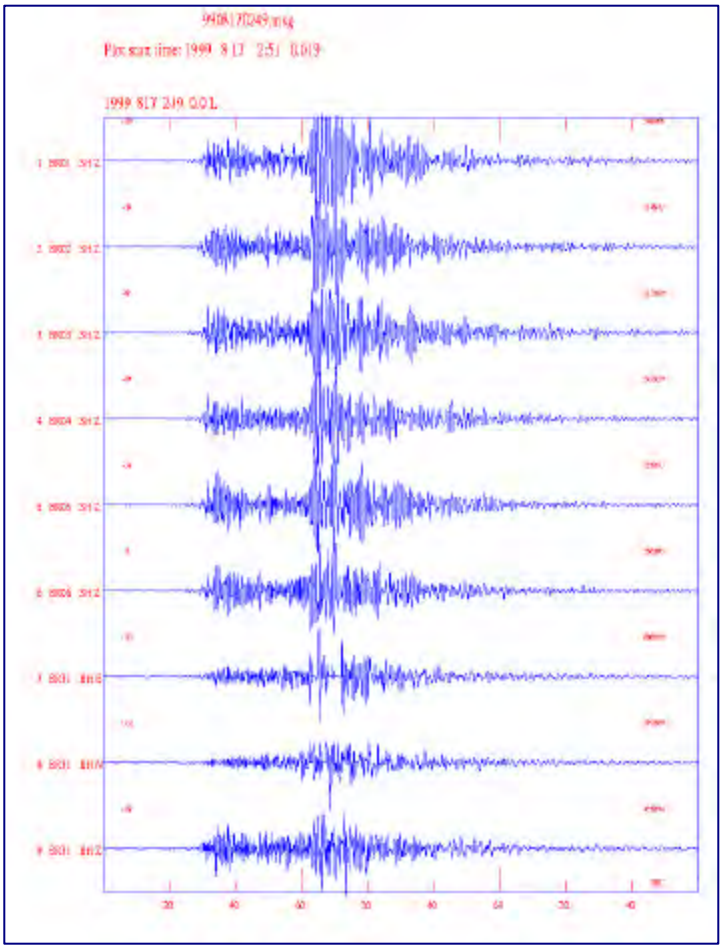

Fig. 5. Waveforms of the 17.09.99 Izmit aftershock (M_{PDE}=4.5) at the ISK BB station.

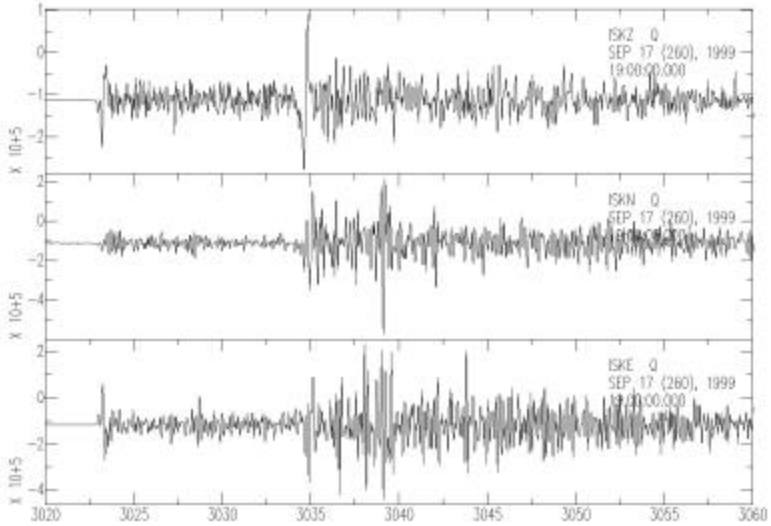

Fig. 6. Waveforms of the Bolu-Duzce aftershock (19.11.99, 19:59, M_{PDE}=4.3) at ISK.

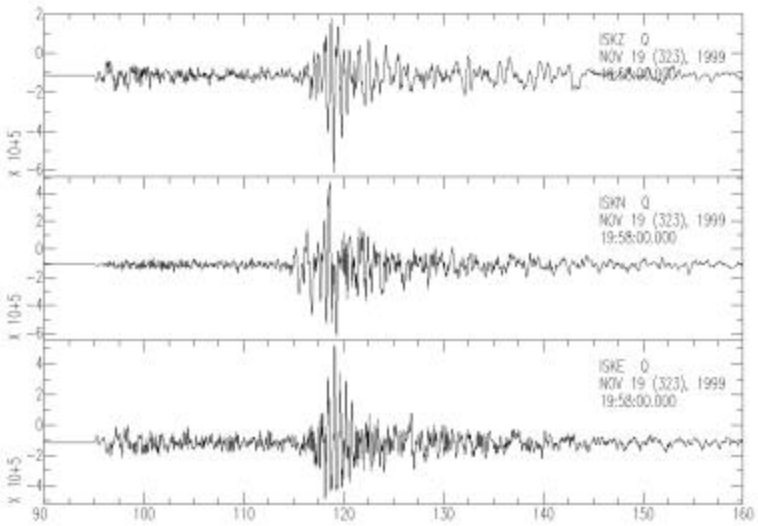

Fig. 7. Waveforms of the Adana aftershock (28.06.98 03:59, M_{PDE}=4.3) recorded at the Cilician network.

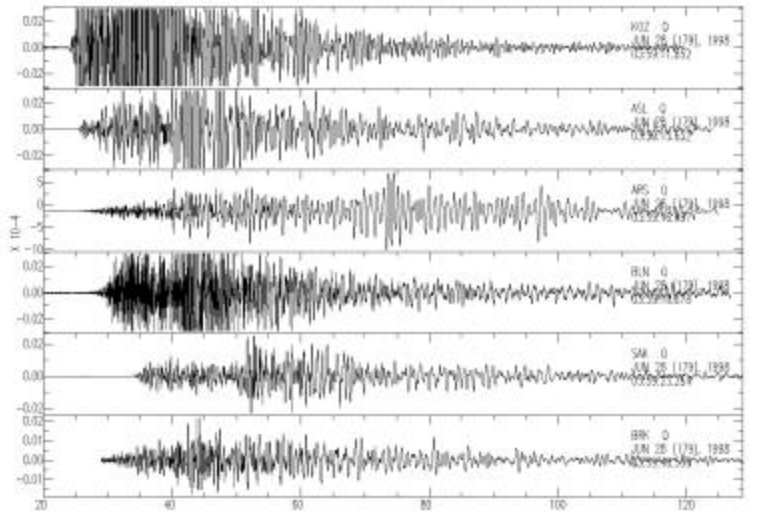

Selected Cyprus Events

From the list of Cyprus earthquakes selected by the GSDC (Cyprus), we found 10 events recorded by all three local networks: the CSN in Cyprus, the ISN in Israel and the Cilician network in Turkey (phase readings are provided by the EMSRI, [Turkey]). Based on estimated standard location errors (see Table 3), we selected six earthquakes (shown on the map in Fig. 8) that meet azimuthal gap and standard error criteria for the GT5 rank. Local duration magnitude M_L is given in the table. Bulletin information and waveform data were collected and screened. Sample seismograms recorded by the CSN are shown in Fig. 9

Table 3. Selected Cyprus events.

N	O.T.	Lat. deg.	Long. deg.	H, km	M_L	Nst (R<100 km)	RMS, sec	Az. gap	Standard location errors			
									dt0, sec	dy km	dx km	dH, km
1	990222 21:06:35.6	34.546	32.844	9	4.7	34 (6)	0.43	182	0.3	1.5	2.4	2.8
2	990729 04:49:44.6	34.439	32.85	9	4.1	38 (6)	0.41	164	0.47	1.5	2.4	4.3
3	990811 01:28:38.7	34.655	33.045	9	4.0	28 (3)	0.66	130	0.51	1.8	3.0	4.3
4	990811 04:27:34.0	34.666	33.035	9	4.0	33 (7)	0.45	129	0.21	1.0	3.0	1.8
5	990811 04:43:25.8	34.693	33.02	9	4.1	25 (6)	0.54	137	0.33	1.3	3.4	2.5
6	990813 15:31:39.1	34.634	33.016	9	4.8	35 (6)	0.8	132	0.34	1.1	2.3	2.0

Fig. 8. Selected Cyprus events, observed by different local networks

Large routine quarry blasts in the Negev and the Galilee (GT2).

We collected data for 23 large (of local magnitude M_L about 3) quarry blasts, including Ground Truth information, which can be related to the GT2 rank. The event location is shown in Fig.1. Origin time, magnitude, coordinates and their corresponding uncertainties (mostly less than 0.3 sec, 0.2 units and 2 km accordingly) are estimated by the Israel Seismic Network. Blast design information is obtained from the quarries and is presented in Table 4. In addition to short-period ISN stations, the blasts were also recorded by the IMS stations EIL and MRNI (or their corresponding surrogate stations). Sample seismograms are shown in Fig. 10.

Table 4. Blast pattern parameters of the selected quarry explosions.

Date	Mag. M_L	Quarry	Total charge, ton	Delays, msec	No. of delays	No. of holes	Hole depth, m	Hole diam., inch
19950322 09:14	2.8	Arad	7.92	25-40	7	111	7	$6^{1/4}$
19950402 08:40	2.9	Arad	9.62	25-40	6	120	7	$6^{1/4}$
19950416 12:08	3.0	Zin	15.5	25-40	5	77	$9\text{-}13^{1/2}$	-
19950426 12:23	2.7	Zin	8.08	25-40	6	64	8	9
19950522 11:56	2.9	Arad	6.50	25-40	-	250	5	$5^{1/8}$
19950523 09:20	2.9	Arad	13.06	25-40	8	110	7	10
19950731 11:14	2.9	Arad	13.26	25-40	8	100	9	$7^{7/8}$
19950803 08:47	2.9	Arad	12.84	25-40	10	96	9	$7^{7/8}$
19950820 12:52	3.0	Arad	12.0	25-40	3	86	9	$7^{7/8}$
19950823 11:49	3.0	Arad	20.6	25-40	20	-	9	-
19970330 08:38	3.0	Oron	20.64	25-40	18	150	9	$7^{7/8}$
19970406 09:39	3.0	Oron	20.0	25-40	11	150	9	$7^{7/8}$
19970521 08:04	2.8	Arad	8.7	25-40	15	87	6.7	$7^{7/8}$
19970609 08:48	2.8	Arad	11.66	25-40	33	90	7	$7^{7/8}$
19970818 09:27	2.9	Arad	7.0	25-40	7	56	9	$7^{7/8}$
19970819 13:51	2.8	Zin	10.0	25-40	8	135	6	$7^{7/8}$
19970820 14:47	3.1	Oron	9.5	25-40	12	98	7	$7^{7/8}$
19970905 07:50	2.9	Oron	13.2	25-40	10	90	8	$7^{7/8}$
19970914 08:28	2.7	Arad	5.92	25-40	5	36	9	$7^{7/8}$
19970915 09:53	2.8	Oron	5.62+4.2	25-40	8+10	47+600	9& 2.5	$7^{7/8}$& $3^{1/2}$
19971223 10:00	2.8	Arad	12.0	25-40	10	90	10	$7^{7/8}\text{-}9^{1/2}$
19980225 09:07	2.8	Arad	11.4	25-40	10	76	9	9
19980705 13:00	2.5	Carmel	8.4	25	12	-	16	4½

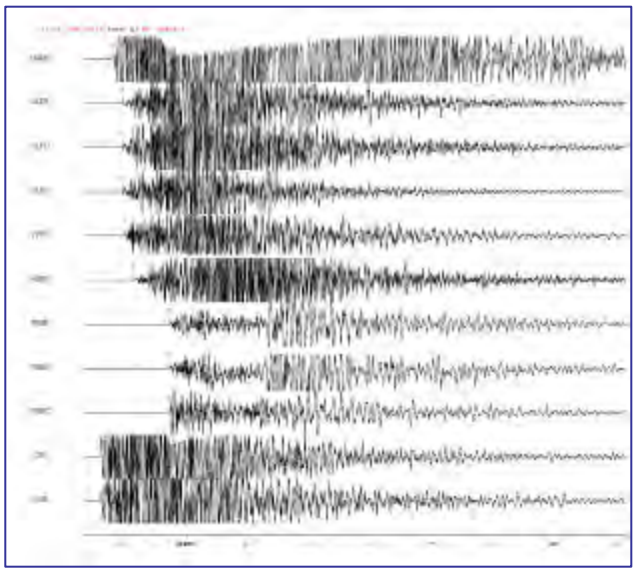

Fig. 9. Waveforms of the Cyprus earthquake (11.08.99 01:28, M_L=4.0) recorded at the Cyprus network

Calibration explosions in the Dead Sea (GT0).

Waveforms from the Dead Sea underwater explosions in Nov. 10, 1999 (2060 kg), and Nov. 11, 1999 (5000 kg), recorded by stations in Saudi Arabia (see Fig. 11 and Table 5), were made available during the RELEMR workshop in Barcelona, May 2001. The records were screened, and a preliminary analysis of the seismograms was made. Waveform samples are presented in Figs. 12 and 13.

Clear regional phases of Pn, Pg and Sg are observed at distances R<500 km (Fig. 12). At remote stations, located at distances 700-1100 km, Pn cannot be observed above the background noise (see Fig. 13). In comparison with the IASPEI91 travel time model, we observe early arrivals of Pg and Sg phases (residuals dt~3-5 sec) (Fig. 13).

Table 5.Selected Saudi Arabia stations with good quality records and observable signals of the Dead Sea explosions

Station	Latitude	Longitude	Altitude, km	Dead Sea expl. site	
				Dist., km	Azim.
QURS	31.3860	37.3240	0.4910	179	95
ALWS	29.3103	35.0650	0.0000	248	188
HAQS	29.0548	34.9297	0.4200	278	190
BDAS	28.4317	35.1014	0.3600	344	185
TBKS	28.2248	36.5485	0.8200	371	163
DBAS	27.2114	35.9773	0.1800	481	174
UMJS	25.2340	37.3119	0.1300	720	165
YNBS	24.3397	37.9922	0.0800	834	162
AFFS	23.9267	43.0005	1.0900	1122	137

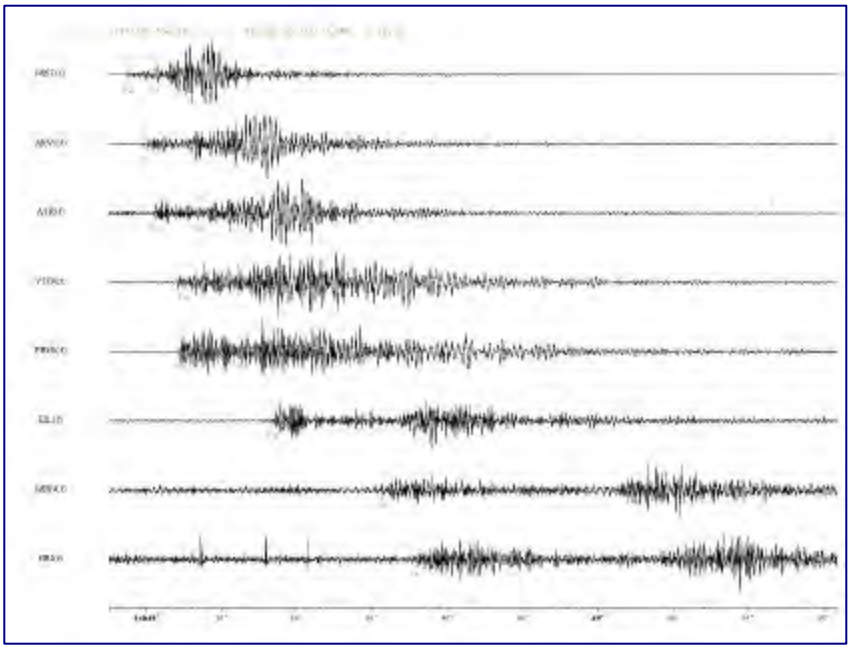

Fig. 10. Sample seismograms of a blast in the Oron quarry, located in the Negev desert, Southern Israel, on Aug. 20, 1997 (M_L=3.1) recorded at short-period stations of the Israel Seismic Network (distance range 17-276 km) including surrogate stations EIL and MRN.

Fig. 11. Location of the Dead Sea shots and selected Saudi Arabia stations

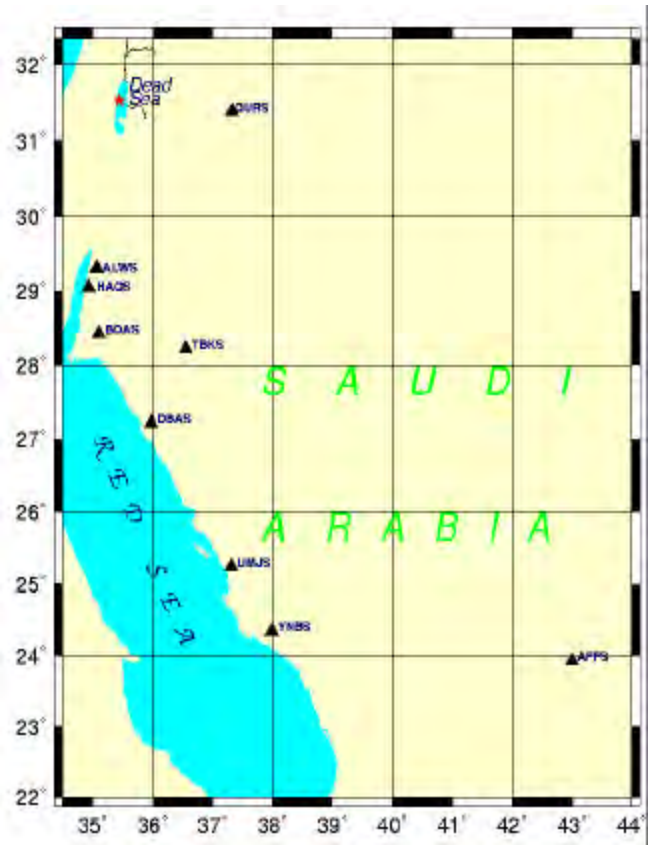

Fig. 12. Vertical seismograms of the second Dead Sea explosion 2060 kg recorded at Saudi Arabia stations in the distance range 179-471 km. Filter 0.5-10 Hz was applied.

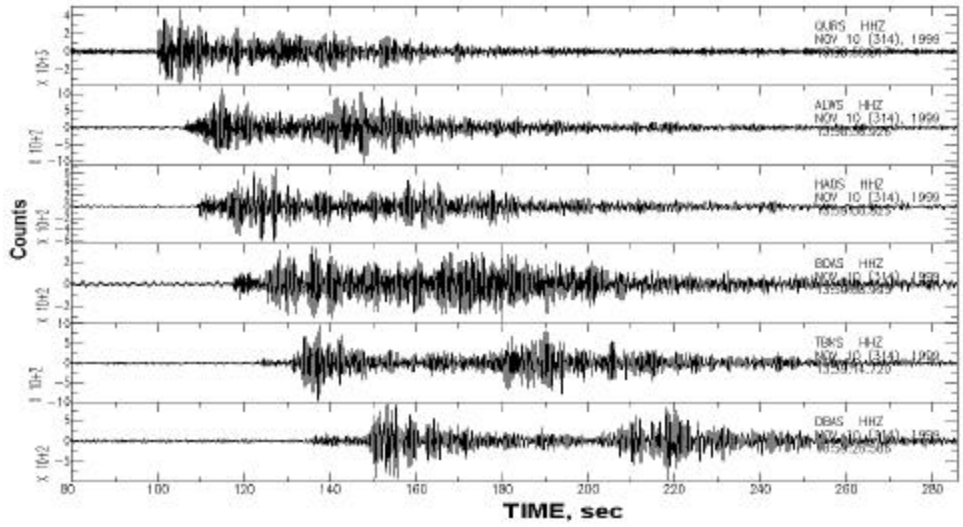

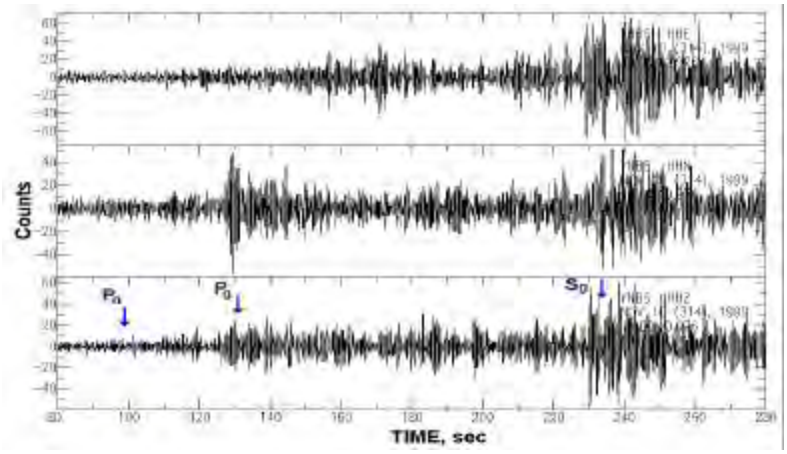

Fig. 13. Three-component seismograms of the second Dead Sea explosion 2060 kg recorded at Saudi Arabia station YNBS, distance 834 km. Filter 1-3 Hz was applied. Arrows show phase arrivals calculated from IASPEI91 model.

CONCLUSIONS AND RECOMMENDATIONS

As the result of joint efforts of the GII (Israel), the KOERI/EMSRI (Turkey), and the GSDC (Cyprus), a database of Middle East-Eastern Mediterranean events is prepared. The database includes: GT2 and GT5 earthquakes in Israel and Cyprus, aftershocks of strong earthquakes in Turkey, routine large quarry blasts (GT2) and controlled explosions (GT0) in Israel. All events were verified in a trustworthy way by a series of relocation experiments, resulting in an improved hypocenter location accuracy.

The elaborated database is intended for: a) calibration of regional IMS stations by verification of travel times and source characterization of local earthquakes and explosions; b) characterization of various regional phases propagation in terms of excitation and attenuation; c) mapping of magnitude thresholds for different observational systems (local networks and subnetworks, and arrays); d) further development and verification of signal processing methods for improvement of detection, location and identification of seismic events in the Middle East and Eastern Mediterranean region.

REFERENCES

Aktar, M., M. Ergin, S. Ozalaybey, C. Tapirdamaz, A. Yoruk and F. Bicmen (2000), A lower-crustal event in northeastern Mediterranean: The 1998 Adana Earthquake (Mw=6.2) and its aftershocks, Geoph. Res. Lett., 27, 2361-2364.

Ito, A., B. Ucer, S. Baris, A. Nakamura, Y. Honkura, T. Kono, S. Hori, A. Hasegawa, R. Pektas and A. M. Isikara (2001), Aftershock activity of 1999 Izmit earthquake, Turkey, revealed from microearthquake observations, BSSA, 2001 (in press).

Pinsky V., Y. Gitterman, A. Shapira. (2001), Collection of Regional Calibration Data Within Area Around the Israel Seismic Network, 3rd Workshop on Location Calibration, Oslo, Technical Expert Group on Seismic Event Location Technical Documentation, Norway, 23-27 April 2001.

Firbas, P. (2001), IDC Calibration Programme – Phase I, 3rd Workshop on Location Calibration, Oslo, Technical Expert Group on Seismic Event Location Technical Documentation, Norway, 23-27 April 2001.

Ozalaybey, S., Aktar, M., M. Ergin, H. Karabulut, M. Boushon, C. Tapirdamaz and A. Yoruk (2000), Aftershock studies following recent earthquakes in Turkey, Abstracts of the XXVII General Assembly of the European Seismological Commission, Lisbon, Portugal, 10-15 September, 2000.

CAPTURING UNCERTAINTIES IN SOURCE-SPECIFIC STATION CORRECTIONS DERIVED FROM A 3-D MODEL

N.M. Shapiro,[1] M.H. Ritzwoller,[1] M.P. Barmin,[1] P.B. Weichman,[2] L.F. Tenorio,[3] W.C. Navidi[3]

University of Colorado at Boulder,[1] ALPHATECH Inc,[2] Colorado School of Mines[3]

Sponsored by Defense Threat Reduction Agency

Contract No. DTRA01-99-C-0019

ABSTRACT

Uncertainties in Source-Specific Station Corrections (SSSCs) arise from several sources. If the SSSCs are constructed directly from empirical travel times, there are errors caused by origin time and hypocenter location errors, measurement errors, and phase misidentification. If a 3-D model is used either to interpolate an empirical surface or to compute the SSSC directly, then uncertainties in the 3-D model will also introduce errors in the SSSC. In order to capture the uncertainties in the SSSC that arise solely from the 3-D model, we trace rays through a large number of random model realizations and catalogue the fluctuations in the computed SSSCs. Each random realization of the 3-D model should fit the data used to construct the model and be drawn from information about the uncertainties at each point in the 3-D model, including both the vertical and horizontal correlation of the model uncertainties. We have made progress in estimating point-wise model uncertainties by performing a Monte-Carlo inversion of broad-band surface wave dispersion. The spatial correlation of uncertainties is more poorly known than the point-wise uncertainties, but we suggest that it is governed largely by the spatial correlation of the Earth itself. Therefore, with reasonable confidence we identify the correlation of the errors with the spatial correlation of the model. We describe the method used to generate the set of random models and report the first results of the application of this method to the CU-Boulder 3D model. Our results show that theoretical estimates of uncertainties are similar to those obtained using empirical information. We also demonstrate that the uncertainties in SSSCs depend strongly on the model properties, in particular the vertical velocity gradient and the horizontal correlation of the model errors.

KEY WORDS: seismic location, SSSCs, 3-D models, error estimates, uncertainties

OBJECTIVES

The principal objective of this paper is to develop a method to estimate uncertainties in Source-Specific Station Corrections (SSSCs) that arise from the uncertainties in a 3-D model and to assess how the uncertainties in SSSCs depend on the vertical velocity gradient and the horizontal correlation of the model errors.

RESEARCH ACCOMPLISHED

Introduction

Most earthquake location methods are based on travel times calculated using 1-D velocity models. However, a 1-D model is only a very rough approximation of the real Earth. Therefore, to improve the accuracy of earthquake location, one needs more accurate predictions of the travel times. This has lead to the idea of Source-Specific Station Corrections (SSSCs). The SSSCs could be estimated directly from the observed travel times, but this approach can work only for a limited number of wave paths concentrated in seismically active regions with good station coverage. Therefore, in many cases, it is useful to have SSSCs based on travel times predicted by realistic 3-D earth models. A complete solution of the earthquake location problem includes hypocenter coordinates, an origin time, and estimates of uncertainties in all these parameters. The uncertainties characterize the quality of the reported earthquake location, and require a knowledge of uncertainties in the predicted SSSCs.

Uncertainties in SSSCs would arise both from errors in the empirical information and from errors in the seismic model. In this paper, we consider the uncertainties in the SSSCs that arise from errors in a 3-D model. One way to estimate these uncertainties is to compare model-predicted travel times with observations. In the absence of observations, theoretical methods are needed to compute uncertainties in the SSSCs. We use average empirical errors to establish certain average trends. In order to understand the geographical variability, however, the errors in the SSSCs will have to be based on model errors.

We estimate the errors in SSSCs with a simple Monte Carlo method. The basic idea is to generate a large number of random model realizations based on the statistics of the model errors. For each model realization, we compute travel times and obtain a statistical ensemble of predicted travel times, which is used to characterize the uncertainties in the SSSCs arising from the model. We consider the SSSCs calculated for the seismic phase Pn using the 3-D model of the crust and upper mantle developed at the University of Colorado (CU) 3D model). This model has been obtained by Monte Carlo inversion of broad-band surface wave dispersion. One of the main advantages of this inversion method is that it provides point-wise estimates of model uncertainties (Shapiro and Ritzwoller, 2001).

We begin the discussion with a brief description of the CU 3-D model. Then we estimate average empirical errors in SSSCs predicted by the CU 3-D model by computing the RMS misfit between the travel times predicted by the CU model and the observed Pn travel times reported in the EHB catalog (Engdahl et al., 1998). We then describe the Monte Carlo method used to estimate the theoretical errors in the SSSCs. We apply this method to calculate theoretical errors in travel times predicted by the CU 3-D model in several locations in Eurasia. Our results show that theoretical estimates of uncertainties are similar to those obtained using the average empirical information. We also demonstrate that the uncertainties in SSSCs depend strongly on the vertical velocity gradient and the horizontal correlation of the model errors.

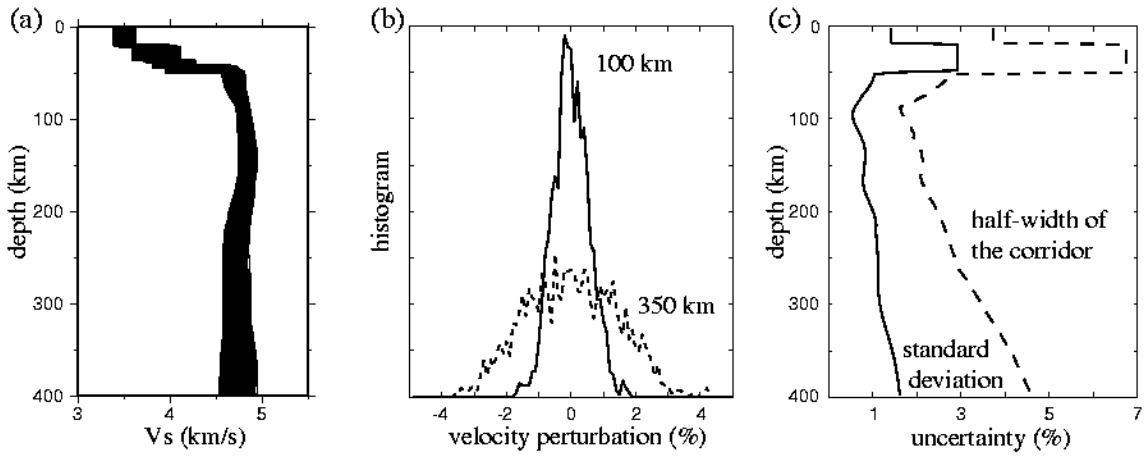

Figure 1. a. Ensemble of acceptable 1-D models obtained during the inversion of broad-band surface-wave dispersion data at a point in a cratonic region, the East European Platform (54N 30E). b. Histograms of velocity perturbations at two depths: 100 km (solid line) and 350 km (dashed line). c. Estimates of uncertainty obtained using the ensemble of acceptable models. Standard deviation of velocity at each depth is shown with the solid line. The half-width of the corridor of acceptable values is shown with the dashed line.

The CU 3-D Model

The 3-D model developed at CU is obtained from inversion of broad-band surface-wave dispersion data. The details of the measurements and the inversion have been described in previous papers (Ritzwoller and Levshin, 1998; Barmin et al., 2001; Shapiro and Ritzwoller, 2001). Here we summarize briefly the procedure of model construction emphasizing

the features relevant to error analysis.
The inversion procedure is divided into two steps: (1) surface-wave tomography (e.g. Ritzwoller and Levshin, 1998; Barmin et al., 2001), which is the construction of 2-D maps characterizing the geographical distribution of surface-wave phase and group velocities, and (2) the inversion of these maps for the velocity structure of the crust and upper mantle. As described by Barmin et al. (2001), the first step (surface-wave tomography) is a nearly linear inverse problem from which we can estimate at each geographical location four dispersion curves: Rayleigh and Love phase and group velocities. In the second step, these dispersion curves at each geographical location are inverted for a local 1-D S-wave velocity model of the crust and upper mantle to depth of 400 km. The P-wave velocity model is obtained by applying a simple scaling relationship:

$$d\ln V_P = 0.5 d\ln V_S \qquad (1)$$

The inversion is performed using a Monte Carlo method that provides a local ensemble of acceptable 1-D models at each spatial node. This ensemble characterizes the statistical properties of the model. Local ensembles of acceptable 1-D models obtained for points located in the East European Platform and in the Caucasus are shown in Figures 1 and 2, respectively.

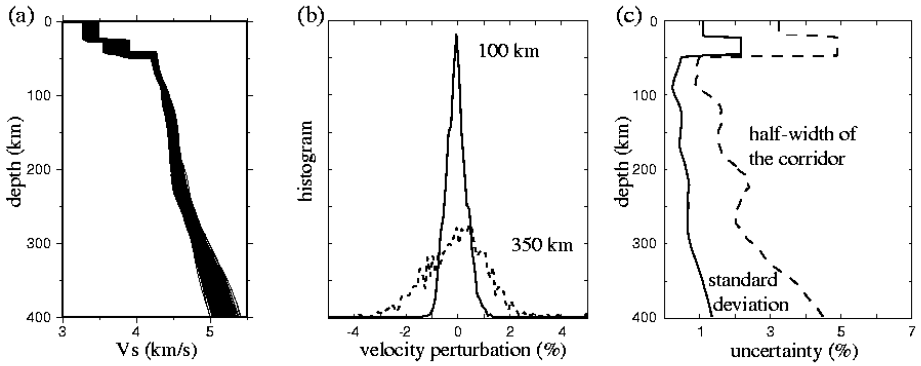

Figure 2. Similar to Figure 1, but for a tectonically deformed region, a point in the Caucasus (40N 44E).

The ensemble of acceptable models at each spatial node is used to define a local average model and model uncertainties. The average model is defined as the median of the velocity distribution at each depth. However, the statistical properties of this distribution are not uniquely defined but depend on multiple choices made during the inversion (i.e. parameterization, acceptance criteria, model space sampling algorithm). As a consequence, the standard deviation of the velocity at each depth underestimates the model uncertainty. A more adequate representation of this uncertainty is given by the half-width of the corridor of acceptable values. A systematic comparison of the standard deviation and the corridor half-width (Figures 1c and 2c) shows that the half-width is about three times larger. Therefore, a useful definition of the model uncertainty is to set it equal to three times the standard deviation of the ensemble of acceptable
1-D models at each depth.

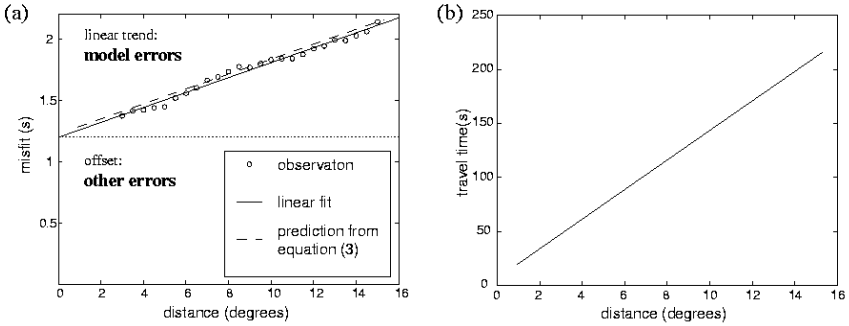

Figure 3. a. Average RMS misfit between Pn travel times predicted by the CU 3-D model and Pn arrival times reported in the EHB catalog (circles).

In Figure 3, the solid line shows the results of linear regression (equation 2 with $E_0 = 1.2s$ and $C_d = 0.061s/degree$). The dashed line shows the values obtained with equation (3) and $C = 0.0044$; b. Pn travel times predicted by the IASPI91 model.

Average empirical errors in SSSCs for reference

In order to characterize average empirical errors in Pn-wave SSSCs computed using the CU 3-D model, we compare Pn travel times calculated using the CU 3-D model with the travel times reported in the EHB catalog (Engdahl et al., 1998). We consider distances between 3 and 15 degrees where the first arrival is normally identified as the Pn wave. Average empirical errors E at different distances Δ are calculated as the RMS misfit between observed and predicted travel times. The resulting function $E(\Delta)$ is shown in Figure 3a. It can be approximated by a linear regression:

$$E(\Delta) = E_0 + C_d \qquad (2)$$

This equation shows that the average empirical error in SSSCs can be subdivided into two parts: (1) an offset $E_0 \approx 1.2s$ and (2) a linear trend with $C_d \approx 0.061s/degree$. We propose a simple model of the errors in which the linear trend results from the error in the model, and the offset E_0 is a combination of errors in travel time picking, phase misidentification, event mislocation, and errors in station corrections.

In Figure 3b, we show Pn travel times predicted by the IASPI91 model (Kennett and Engdahl, 1991). Between 3 and 15 degrees, this is a linear function of distance $t(\Delta)$. Considering this linear behavior of average travel time and equation (2), we can approximate the errors in SSSCs resulting from errors in the 3D model as a linear function of travel time t

$$E_m(t) = C\,t \qquad (3)$$

where $C \approx 0.0044$. This coefficient C is called the "relative travel-time error". Analysis of the RMS misfit has, therefore, established that the relative travel-time error resulting from model uncertainties will be about 0.5 percent, on average. This is a reference value that theoretical estimates should fit.

Theoretical errors in predicted travel times: The method

Uncertainties in a 3-D model will result in uncertainties in predicted travel times. However, the travel-time errors are not controlled by the point-wise model uncertainties alone but also depend on the spatial correlation of these uncertainties and on characteristics of the model itself. We propose to estimate the uncertainties in the SSSCs that arise from the 3-D model with a Monte Carlo approach. This approach is based on ray tracing through a large number of random model realizations followed by a statistical analysis of the fluctuations in the computed travel times. Each random realization of the 3-D model should fit the data used to construct the model and be drawn from information about the uncertainties at each point in the 3-D model, including both the vertical and horizontal correlation of the model uncertainties.

We consider here an application of this approach to the CU 3-D model. The average CU 3-D model is obtained as a combination of the local average 1-D models at all nodes on a $2^\circ \times 2^\circ$ geographical grid. This model is used to calculate the average values of predicted travel times and to construct the SSSCs. The uncertainties in the SSSCs are estimated by considering all local 1-D acceptable models found during the inversion at all locations.

Each random realization of the 3-D model is obtained by selecting one of the members of the ensemble of 1-D acceptable models at each geographical location. This approach allows us to satisfy two conditions: (1) the random model realization fits the data, and (2) the vertical correlation of velocity perturbations in the 3-D model realizations is drawn from the vertical correlation of the model errors. The condition of the horizontal error correlation is more difficult to satisfy. The main problem is that this correlation is not estimated during the inversion. We suggest that it is governed largely by the spatial correlation of the Earth itself. Therefore, with reasonable confidence, we can identify the correlation of the errors with the spatial correlation of the model. In the examples shown below, we demonstrate that taking this horizontal error correlation into account can significantly affect the estimated uncertainty in predicted

travel times.

We trace rays through all random 3-D model realizations and obtain a statistical distribution of predicted travel times for all distances. From this distribution we estimate the standard deviation of the predicted travel times. However, this standard deviation underestimates the uncertainty. Following the approach established during the analysis of the ensemble of 1-D acceptable models, we define the uncertainty in predicted travel times to be three times their standard deviations.

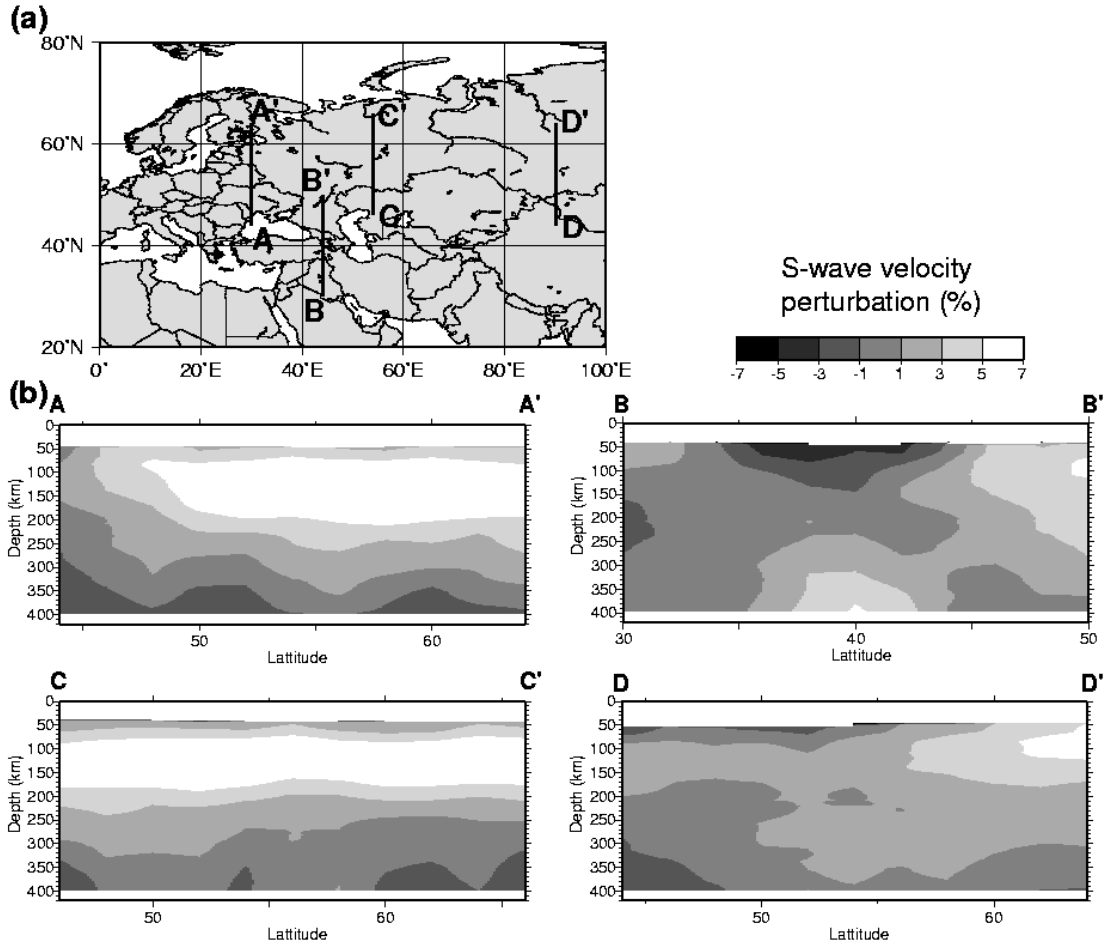

Figure 4. a. Map of West Central Eurasia showing the location of four profiles used in calculation of the uncertainties in model-predicted travel times. All profiles are 20° in length. b. Vertical cross-sections of the S-wave velocity structure beneath the four profiles shown in (a).

Theoretical errors in predicted travel times: Preliminary results

We use the Monte Carlo method to calculate the errors in travel times for four 2-D profiles shown in Figure 4. Two profiles cross the East European Platform (profiles A-A' and C-C'); the other two profiles cross tectonically active regions (profile B-B' goes from Iraq across Eastern Turkey and the Caucasus, profile D-D' goes from the Junggar Basin to Central Siberia crossing the Altay and Sayan mountains). The length of each profile is set to 20°, a typical distance used to calculate the SSSCs for regional phases.

There are important differences in the velocity structures of these four profiles in terms of both vertical velocity gradient and horizontal correlation. The profiles crossing the East European platform are horizontally well correlated

(especially profile C-C') and are characterized by a thick, high-velocity lithosphere. The horizontal correlation is weak for the two profiles crossing the tectonically active regions. The lithosphere is much less prominent beneath profile D-D' and completely disappears beneath profile B-B', which is characterized by a very prominent positive vertical velocity gradient.

We consider two end-member algorithms for generating random model realizations of 2-D profiles. In the first case, at each geographical location on a two-degree grid along each profile, we randomly select one of the members of the local ensemble of acceptable 1-D models. The local models are selected independently at each point and, therefore, the resulting 2-D model realizations are horizontally uncorrelated.

The second algorithm produces maximally horizontally correlated 2-D model realizations. To describe how this algorithm works, remember that each member of the ensemble of 1-D acceptable models is described by a simple function *c(z)*, where *c* is seismic velocity and *z* is depth. At each location, we also define an average model $c_a(z)$. Each individual model can also be described in terms of perturbations relative to this average model, or in terms of errors $e(z) = c(z) - c_a(z)$. The construction of a maximally correlated 2-D model realization begins with the selection of a reference point in the middle of each profile. At this point, we randomly select a local model $e_r(z)$. Then, at all other points, the local models $e_i(z)$ are selected to minimize the one-norm difference with respect to the local model at reference point $e_r(z)$.

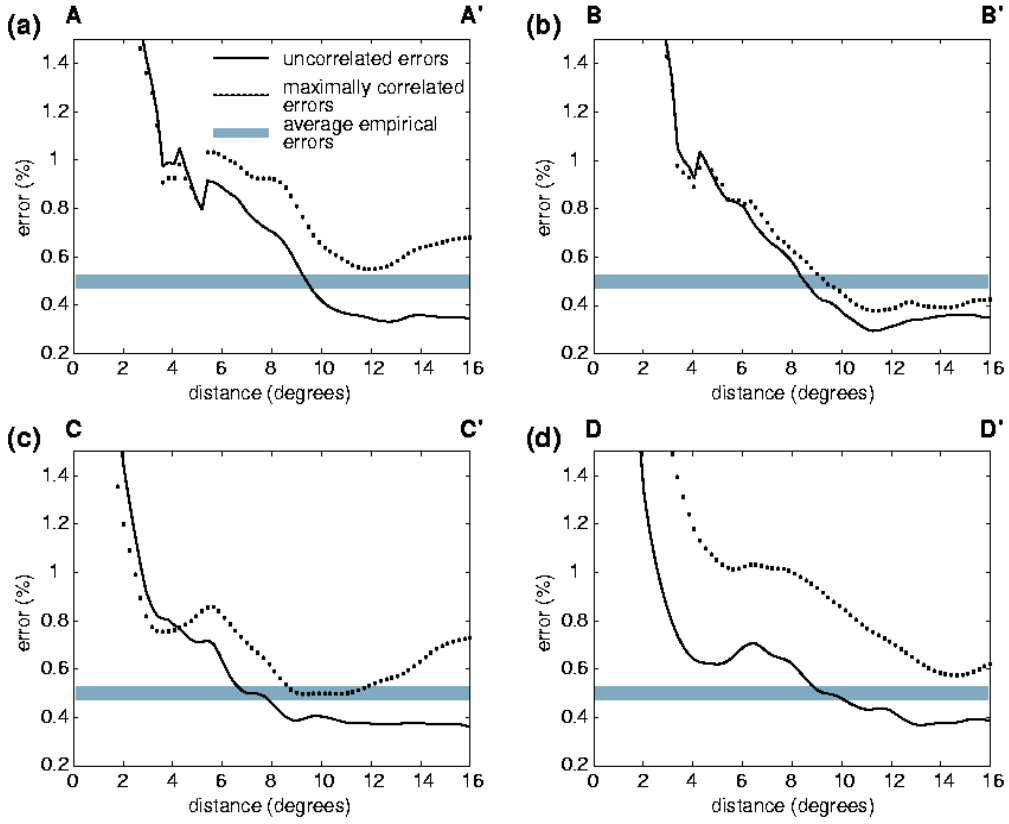

Figure 5. Relative errors in predicted travel times. Solid and dotted lines show the results obtained with completely uncorrelated and perfectly correlated model realizations, respectively. Gray lines show the average relative empirical errors (~0.5%). a. Results for profile A-A'. b. Results for profile B-B'. c. Results for profile C-C'. d.

Results for profile D-D'.

Using the described algorithms, we generate uncorrelated and maximally correlated ensembles of 2-D model realizations for all four profiles. Then, we trace rays through all model realizations and estimate uncertainties in Pn travel times for each of the eight ensembles. The results are shown in Figure 5.

Relative errors predicted by the spatially correlated ensembles are systematically larger than those predicted by the uncorrelated ensembles. This result is not surprising. Correlated velocity perturbations result in larger fluctuations of travel times and, as a consequence, in larger uncertainties. However, the difference between the uncertainties resulting from correlated and uncorrelated models can be very small, as it is for profile B-B'.

We conclude that the horizontal correlation of model errors affects differently the travel times calculated for different velocity models. For example, in the case of profile C-C' that crosses the cratonic area, most of the rays are concentrated in the high velocity continental lithosphere (Figure 6a) and Pn waves propagate quasi-horizontally over long distances. In this case, the horizontal correlation of the model errors significantly increases the travel-time uncertainties. Note that the lithospheric layer is also present beneath profiles A-A' and D-D'. Profile B-B' crosses the tectonically active region characterized by a prominent positive vertical velocity gradient (Figure 2a). In this case, the distribution of rays is much more homogeneous vertically. Seismic waves do not propagate quasi-horizontally, as in the case of the well-developed lithosphere, but dive to greater depths (Figure 6b). Therefore, even when there is a strong horizontal correlation of model errors, the along-ray velocity structure is not correlated and the resulting uncertainty does not increase substantially.

For all four profiles, the distance dependence of the errors in travel times can be roughly approximated by two asymptotics. At short distances ($< 4^{\circ}$), the travel-time errors are significantly affected by large uncertainties in the crustal structure. Therefore, the errors are large but rapidly decrease with distance. At long distances, the relative errors are approximately constant. This long-distance asymptotic behavior is similar to the behavior of the average empirical travel-time error (*C* in equation 3). Moreover, the predicted values of these relative errors are close to the observed value of 0.5%. We also note that the prediction obtained using correlated ensembles of 1-D models tends to underestimate the empirical uncertainty, while the perfectly correlated ensemble tends to overestimate it.

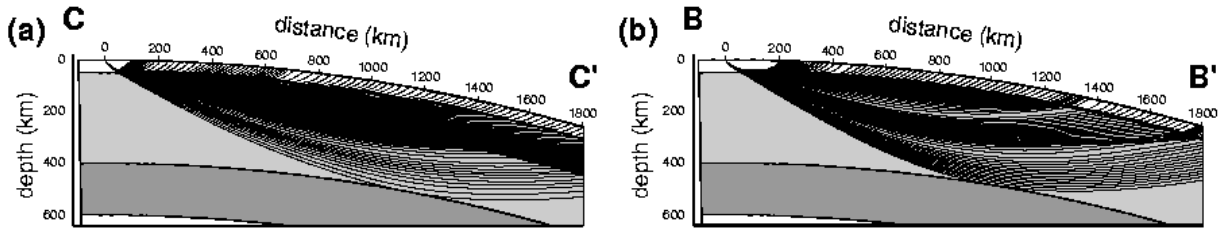

Figure 6. Configuration of Pn rays. The Pn phase is considered to be formed by rays with turning points in the upper mantle (light gray) above the transition zone (dark gray). The ray-tracing algorithm accounts for the sphericity of the Earth. a. Results for the average model beneath profile C-C'. b. Results for the average model beneath profile B-B'.

Discussion

Our results show that the horizontal correlation of the model errors can significantly increase travel-time uncertainties. We have considered here two extreme cases of the behavior of the horizontal correlation of the model errors: maximally spatially correlated and completely uncorrelated models. The spatial correlation of the model uncertainties is more poorly known than the point-wise uncertainties, but we suggest that it is governed largely by the spatial correlation of the Earth itself. Therefore, with reasonable confidence we can identify the correlation of the errors with the spatial correlation of the model. Following this hypothesis, we expect that the approximation of maximally correlated errors is more appropriate for stable cratonic areas where the structure is relatively homogeneous. In

tectonically active areas, the structure is more heterogeneous and the model errors are expected to be poorly correlated. Therefore, surprisingly, we expect the errors in predicted travel times to be larger in stable regions than in tectonically active regions.

In the future, we plan to test the effects of the error correlation more rigorously. Toward this goal, the horizontal model correlation has to be characterized quantitatively to allow us to construct new ensembles of random 3-D model realizations, where the error correlation is governed by the 3-D model correlation.

To quantify the spatial correlation or, more exactly, the similarity of the model at different spatial locations, we introduce the "similarity function" defined as the normalized one-norm difference between two local 1D models:

$$S_{ij} = \int \frac{|m_i(z) - m_j(z)|}{\sigma(z)} dz \qquad (4)$$

where $c_i(z)$ and $c_j(z)$ are the seismic velocities at locations i and j and $\sigma(z)$ is the average model uncertainty. The similarity function is zero when the local models at two points are identical. The difference between two models is weak if the value of S is less than 1. A value of S larger than 1 means that the difference between two models is significant.

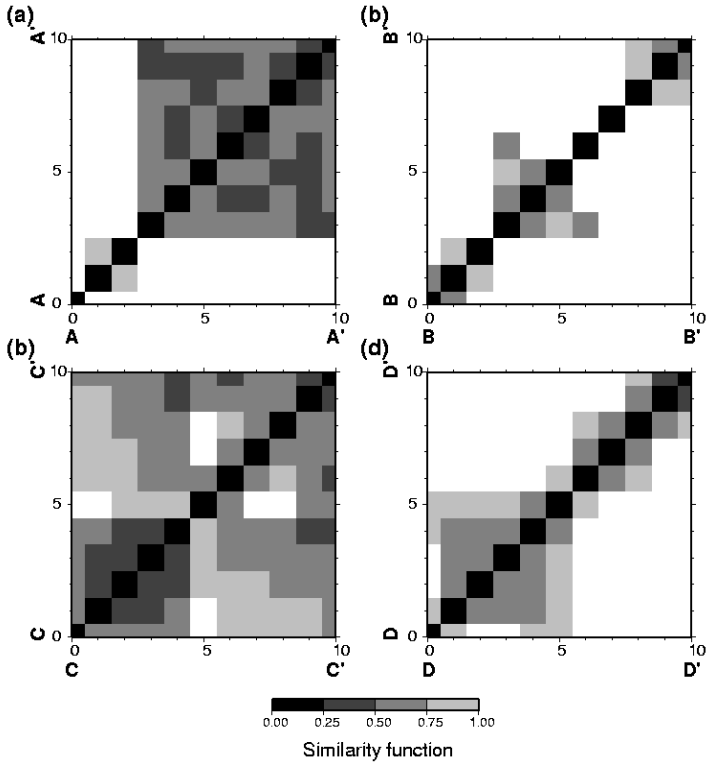

Figure 7. Similarity matrices calculated for the profiles shown in Figure 4. *Similarity function* is defined by equation 4. Dark shades denote high similarity between the 1-D models at the corresponding spatial locations.

The CU 3-D model is defined on a 2^o x 2^o grid. Therefore, each of the 20-degree length profiles shown in Figure 4 is fully described by 11 local 1-D models. For each 2-D profile, the values of the similarity function calculated between the 11 points form a 11x11 "similarity matrix". The similarity matrices computed for the four 2-D profiles are shown in Figure 7. For profiles A-A' and C-C' the spatial correlation is high and most of the off-diagonal elements of the similarity matrices are less than 1. For the weakly correlated profiles B-B' and D-D', most of the off-diagonal elements are larger than 1.

In the future, we will use these similarity matrices to construct random model realizations with realistic spatial correlation. The main idea is to modify the algorithm used to produce the random model realizations so that the model errors will be governed by the similarity matrices.

CONCLUSIONS AND RECOMMENDATIONS

We presented the first estimates of errors in SSSCs that arise from the errors in 3-D velocity models. This work remains in its early stages. However, several important results are clear:

- We developed a Monte Carlo method to estimate errors in SSSCs that arise from the errors in 3-D velocity models.
- The estimated theoretical travel-time errors are similar to the average empirical travel-time errors.
- Strong horizontal correlation of the model errors increases the errors in the SSSCs.

The errors in SSSCs depend strongly on the vertical velocity gradient in the model.

In the future, we plan to improve the algorithm for generating of 3-D model realizations by using a more realistic estimate of the spatial correlation of the model errors based on the correlation of the model itself.

REFERENCES

Barmin, M.P., M.H. Ritzwoller, and A.L. Levshin (2000), A fast and reliable method for surface wave tomography, *Pure and Appl. Geophys.*, in press.

Engdahl, E.R., R. van der Hilst, and R. Buland (1998), Global teleseismic earthquake relocation with improved travel times and procedures for depth determination, *Bull. Seism. Soc. Am.*, **88**, 722 - 743.

Kennett, B.L.N. and E.R. Engdahl (1991), Travel times for global earthquake location and phase identification, *Geophys. J. Int.*, **105**, 469 - 465..

Ritzwoller, M.H., and A.L. Levshin (1998), Eurasian surface wave tomography: Group velocities, *J. Geophys. Res.*, **103**, 4839 - 4878.

Shapiro, N.M. and M.H. Ritzwoller (2001), Monte-Carlo inversion of broad-band surface wave dispersion for a global shear velocity model of the crust and upper mantle, *Geophys. J. Int.*, submitted.

INITIAL RESULTS AT REDUCING SYSTEMATIC ERRORS FOR SEISMIC EVENT LOCATIONS USING A MODEL INCORPORATING ANISOTROPIC REGIONAL STRUCTURES

Gideon P. Smith and Douglas A. Wiens

Washington University in St Louis

Sponsored by Defense Threat Reduction Agency

Contract No. DTRA01-00-C-0103

ABSTRACT

We are utilizing a mapping of the lateral and anisotropic variations in Pn velocities beneath continents across the globe (Smith and Ekstrom, 1999) to predict travel times of P-wave propagation at distances of 2-14 degrees. At such distances the phase Pn is the seismic phase that is most frequently reported and that thus controls the location accuracy. This is important in CTBT applications as many events of interest are only detected at these distances. We are thus working on reducing the systematic errors in Pn travel-times and the resulting seismic event location at regional distances using our mapping.

In our investigations we have begun by establishing a list of ground truth events by which to test locations using our different models. In establishing this list we have endeavored to include a variety of geographic areas and sizes of events. We have also developed a grid-search algorithm to relocate each of these events using isotropic, laterally varying, and full anisotropic models. In our initial studies we have not accounted for ray-path effects which may prove to be significant. Our results from the first stage of this study indicate a progressive improvement in the relocation with increased model complexity. However, significant systematic errors remain in locations where heterogenity is accounted for but anisotropy is not. The most significant results appear to be for events with few stations reporting but with reasonable azimuthal distribution.

KEY WORDS: Pn, anisotropy, regional phases, CTBT, relocation

OBJECTIVE

Introduction

In CTBT applications many events of interest are only detected at regional distances. Our objective is identification and reduction of systematic errors in the location of events determined using regional seismic data. At such distances (2-14 degrees) the phase Pn is the seismic phase that is most commonly reported and which thus controls the location accuracy. In order to accurately locate seismic events, whether natural or artificial, by traditional travel-time methods one must first be able to accurately predict arrival times. Historically travel-times have been calculated using one-dimensional seismic velocity models (e.g. Jeffreys and Bullen, 1940; Herrin et al., 1968; Herrin and Taggart, 1968; Herrin, 1968; Dziewonski and Anderson, 1981; Kennett and Engdahl, 1991). However, the Earth is composed of rocks which vary laterally at varying length scales (e.g. Crosson, 1976; Engdahl et al., 1977, 1982; Engdahl and Billington, 1986; Dziewonski, 1984; Su and Dziewonski, 1993) and can be anisotropic (e.g. Christensen, 1966; Kumazawa and Anderson, 1969; Hess, 1964; Raitt et al., 1969; Forsyth, 1975; Tanimoto and Anderson, 1984), resulting in travel-times which do not match those predicted by these one-dimensional velocity profiles. In addition, at regional length scales global Earth models, which are largely based on long-period surface waves and vertically arriving body waves, provide poor first arrival travel-time predictions. Providing more accurate prediction of P-wave propagation at regional distances is therefore of particular importance in event location. When attempting to satisfy the location requirements of the CTBT it is essential to obtain the most accurate location possible, with the minimum necessary computing time

The question remains as to whether the current generation of regional models can usefully contribute to relocation problems. While it has already been well established that variations in regional phases such as Pn can lead to large mislocations of the epicenter (Herrin and Taggart, 1962), progress has been slow in routinely applying regional models to locations for global catalogs. This is probably because most of the Pn velocity models produced are of a highly local nature (e.g. Hess, 1964; Raitt et al., 1969; Bamford, 1977; Fuchs, 1977; Hirn, 1977; Vetter and Minster, 1981), and no systematic global mapping of Pn velocities has been attempted. In addition although azimuthal anisotropy is a known feature of Pn propagation (e.g. Beghoul and Barazangi, 1990; Hearn, 1996), most previous studies of Pn anisotropy have not mapped lateral variations in azimuthal anisotropy, but instead produced, if anything, a single estimate for an entire region.

In recent work the P.I. has mapped lateral and anisotropic variations in Pn velocities beneath continents across the globe (Smith and Ekstrom, 1999). This work represents the most comprehensive and possibly the most accurate mapping of anisotropic Pn velocities available to date. This provides the first opportunity to truly test the possibility of applying an anisotropic Pn velocity model to calculation of travel-times to improve regional locations for events distributed in different parts of the world. The question remains whether this new mapping can provide, in a practical application, significant reductions in systematic event location at the regional scale. Our work is aimed at applying this new mapping of Pn anisotropic structure to investigate the possible systematic errors produced by lateral heterogeneity and azimuthal anisotropy

RESEARCH ACCOMPLISHED

Grid Search Relocation Algorithm

We have begun our study by developing and applying a grid search relocation algorithm to ground truth events. In this study we use travel-time data from the ISC database. The ISC location is used as a first estimate. The fit of travel times is then calculated for this location and for a set of points on a rectangular grid at 10-km spacing. The minimum in the rms of the travel times is then selected as the new location estimate and the travel-time misfits recalculated using a smaller grid spacing. This is repeated until the travel-time misfit appears to converge. This procedure has been performed for a selection of PNE for isotropic, laterally heterogeneous, and anisotropic structures. In this stage of our study great-circle raypaths were used.

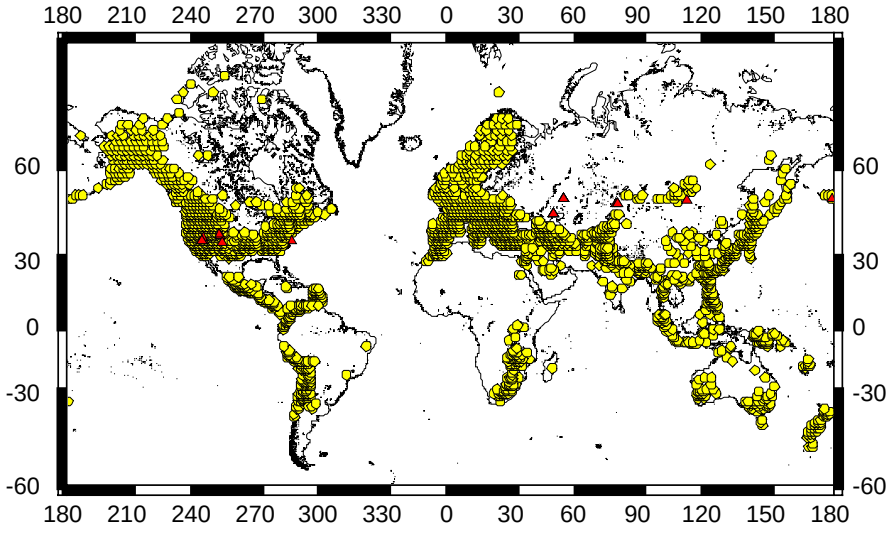

Figure 1. Worldwide distribution of Pn velocity estimates in the model of Smith and Ekstrom (1999). Triangles show the locations of PNEs used in Smith and Ekstrom (1996).

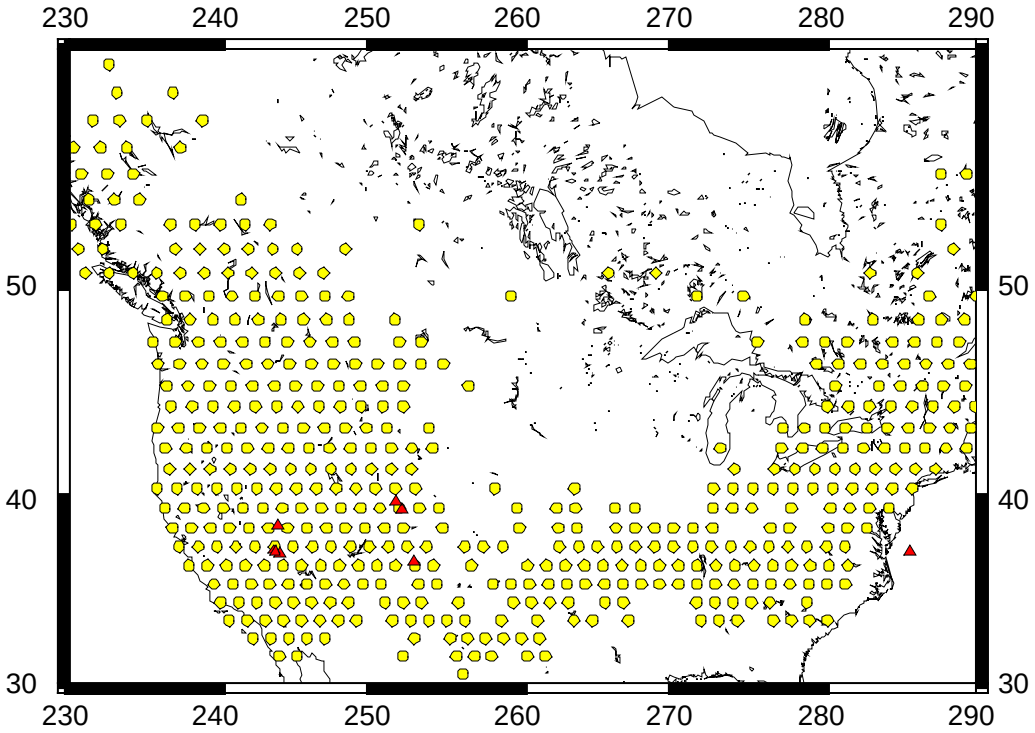

Figure 2. US distribution of Pn velocity estimates in the model of Smith and Ekstrom (1999). Triangles show the locations of PNEs used in Smith and Ekstrom (1996).

Figure 1 shows the worldwide distribution of Pn velocity estimates in the model of Smith and Ekstrom (1999). Triangles show the locations of PNEs used in Smith and Ekstrom (1996). We have used this same list of PNEs as a starting list of ground truth events for the current study. Clearly the geographic area with the best coincident coverage of PNEs and Pn velocity estimates is the United States. Although we are continuing to expand our list of test events the events in this region provide useful insight into effects of our model and algorithm (see Figure 2). Pn anisotropy for this region is shown in Figure 3.

Table 1: Results of relocation using different velocity models

Model	RMS Misfit to Known Location (km)
isotropic	12.1
heterogeneous	11.6
anisotropic	10.9

Table 2: Results of relocation using different velocity models and restricting distance range to arrivals > 6°

Model	RMS Misfit to Known Location (km)
isotropic	14.1
heterogeneous	13.8
anisotropic	11.4

Table 1 shows the RMS misfit using isotropic, laterally heterogeneous, and anisotropic models. Although this table suggests a general location improvement using the anisotropic structures we note that the majority of this improvement is seen in the locations for the western most events. This is explicable by examination of Figures 2 and 3 which demonstrate that for the eastern most event all regional arrivals are from similar azimuths, and so

the 3 models converge to the same answer. It is notable that these improvements are minimal and given the minted test-bed perhaps not statistically significant. Possible explanations for this minimal level of improvement are in use of direct raypaths as opposed to calculating the true raypath predicted by our model, and also dependence on the crustal model. Table 2 shows the results of experiments where we have relocated the events but only using travel-times from more distant stations (> 6 degrees). Although this reduces the number of travel-times the significance of accounting for correct uppermost mantle velocities increases.

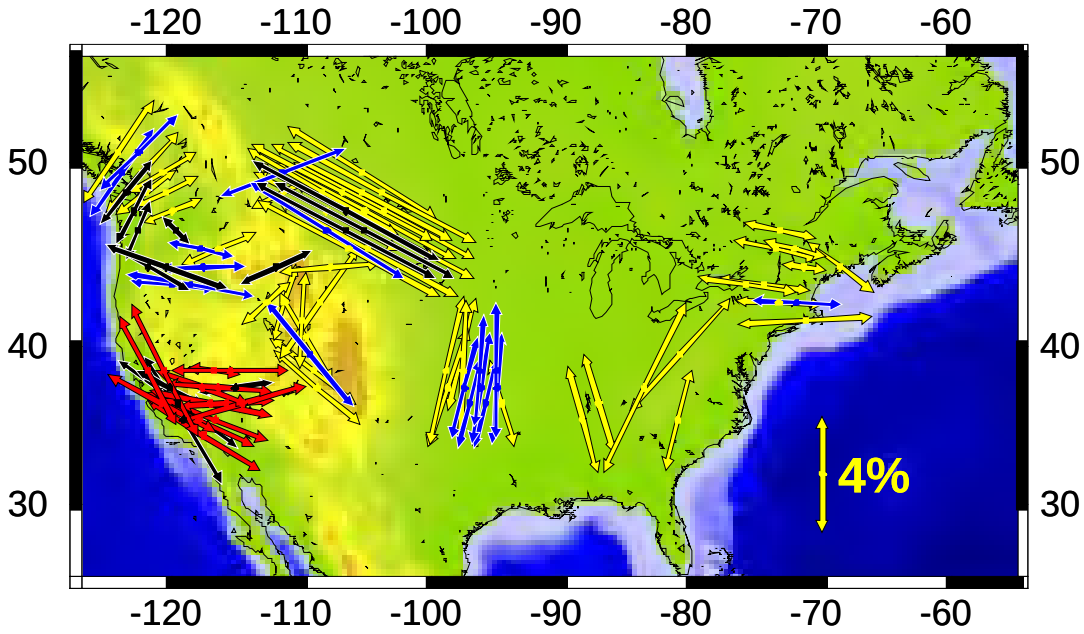

Figure 3. Pn anisotropy estimates in the US. Arrows show the fast anisotropic direction and are proportional to the size of anisotropy. A 4% arrow is shows for scale.

CONCLUSIONS AND RECOMMENDATIONS

Our current study clearly indicates that inclusion of more precise models, incorporating both heterogeneity and anisotropy at the regional scale, can improve the location accuracy. However, the improvements obtained are not as striking as one might expect given the level of anisotropy and heterogeneity in the current models. A variety of explanations for this are possible.

One obvious explanation lies in the use of approximate raypaths as opposed to calculating the raypaths predicted by our model. The second possible source of error is in the calculation of the crustal leg of the travel time. At greater distances this portion of the travel time becomes a less significant percentage of the overall travel time and we are currently examining the fit of travel time versus distance to try to quantify this effect. In addition both the distribution of Pn velocity estimates available, and the azimuthal distribution of travel times for the event being tested appears to have a critical effect on the improvement possible. We are currently examining the effect of azimuthal distribution of travel times to try to quantify at what level application of the anisotropic model becomes useful in a practical sense.

REFERENCES

Bamford, D., (1977). Pn velocity anisotropy in a continental upper mantle, Geophys. J. Roy. Astron. Soc., 49, 29-48.

Beghoul, N., and M. Barazangi, (1990). Azimuthal anisotropy of velocity in the mantle lid beneath the Basin and Range, Nature, 348, 536-538.

Carder, D.S., (1962). The Gnome Symposium. Bull. Seism. Soc. Am., 52, 977-979.

Christensen, N. I., (1966). Elasticity of ultrabasic rocks. J. Geophys. Res., 71, 5921-5932.

Crosson, R. S., (1976). Crustal structure modeling of earthquake data 1. Simultaneous least squares estimation of hypocenter and velocity parameters, J. Geophys. Res., 81, 3036-3046.

Dziewonski, A. M, (1984). Mapping the lower mantle: determination of lateral heterogeneity in P velocity up to degree and order 6, J. Geophys. Res., 89, 5929-5952.

Dziewonski, A. M., and D. L. Anderson, (1981). Preliminary Reference Earth Model. Phys. Earth and Planet. Int., 25, 297-356..

Engdahl, E. R., and S. Billington, (1986). Focal depth determination of Central Aleutian Earthquakes, Bull. Seism. Soc. Am., 76, 77-93.

Engdahl, E. R., N. H. Sleep, and M.-T. Lin, (1977). Plate effects in North Pacific subduction zones, Tectonophys., 37, 95-116.

Forsyth, D. W, (1975), The early structural evolution and anisotropy of the oceanic upper mantle, Geophys. J. Roy. Astr. Soc., 43, 103—162.

Fuchs, K., (1977). Seismic anisotropy of the subcrustal lithosphere as evidence for dynamical processes in the upper mantle, Geophys. J. Roy. Astron. Soc., 49, 167-179.

Hearn, T., 1996. Anisotropic Pn tomography in the Western United States, J. Geophys. Res., 101, 8403-8414.

Herrin, E.,(1968). Seismological tables for P-phases, Bull. Seism. Soc. Am., 60, 461-489.

Herrin, E. and J. Taggart, (1968). Regional variations in P travel times. Bull. Seism. Soc. Am., 58, 1325-1337.

Herrin, E. and J. Taggart, (1962). Regional Variations in Pn velocity and their effect on the location of epicenters, Bull. Seism. Soc. Am., 52, 1037-1046.

Herrin, E., W. Tucker, J. Taggart, D. W. Gordon, and J. L. Lobdell, (1968). Estimation of surface focus P travel times, Bull. Seism. Soc. Am., 58, 1273-1291.

Hess, H. H, (1964), Seismic anisotropy of the uppermost mantle under oceans, Nature, 203, 629—631.

Hirn, A., (1977). Anisotropy of the continental upper mantle: possible evidence from explosion seismology, Geophys. J. Roy. Astron. Soc., 49, 49-58.

Jeffreys, H. and K. E. Bullen, (1940). Seismological Tables, British Association for the advancement of Science, London.

Kennett, B. L. N., and E. R. Engdahl, 1991. Traveltimes for global earthquake location and phase identification, Geophys. J. Int., 105, 429-465.

Kumazawa, M., and O. L. Anderson, 1969. Elastic moduli, pressure derivatives, and temperature derivatives of single crystal olivine and single crystal forsterite, J. Geophs. Res., 74, 5961-5972.

Raitt, R. W., G. G. Shor Jr., T. J. G. Francis, and G. B. Morris, Anisotropy of the Pacific upper mantle, J. Geophys. Res., 74, 3095--3109, 1969

Smith, Gideon P., and Goran Ekstrom, 1999. A global study of Pn anisotropy beneath continents, J. Geophys. Res., 99, NO. B12, 23,787-23,800.

Smith, Gideon P., and Goran Ekstrom, 1996. Improving teleseismic event locations using a 3-dimensional Earth model, Bull. Seism. Soc. Am., 86, 788-796.

Smith, Gideon P., and Goran Ekstrom, 1996b. Regional Phases in global Earth models, abstarct EOS Trans., 77, Fall Meet. Suppl., F489.

Su. W. and A. M. Dziewonski, 1993. Joint 3-D inversion for P- and S- velocity in the mantle, EOS, 74, 557.

Tanimoto, T. and D. L. Anderson, Mapping convection in the mantle, Geophys. Res. Lett., 11, 287--290, 1984

Vetter, U., and J.-B. Minster, 1981. Pn velocity anisotropy in southern California, Bull. Seis. Soc. Am., 71, 1511-1530.

ON THE USE OF KRIGED P-WAVE TRAVEL-TIME CORRECTION SURFACES FOR SEISMIC LOCATION

Lee K. Steck, Michael L. Begnaud, and Aaron A. Velasco

Los Alamos National Laboratory

Sponsored by National Nuclear Security Administration
Office of Nonproliferation Research and Engineering
Office of Defense Nuclear Nonproliferation

Contract No. W-7405-ENG-36

ABSTRACT

Accurate location of seismic events remains a critical issue for global nuclear explosion monitoring. Herein we present some observations on the nature of kriged P-wave travel-time correction surfaces and their application to improving seismic event location in China. We have adopted the correction surface approach due to ease of implementation and the fact that empirical correction surfaces can be constructed without detailed knowledge of crustal structure. However, correction surfaces can be built on any velocity model, no matter how detailed, so that when such models do become available, surfaces can be recalculated for that model. This, in turn, enables prediction of corrections in regions lacking seismicity. We use the modified Bayesian kriging method to construct surfaces for 76 stations around Asia, analyzing travel-time data from seismic events in the United States Geological Survey Earthquake Data Reports (EDR) and the International Seismic Center (ISC) catalog. Due to limited data, we gather residuals for events throughout the crust (as defined by the 1-D global model employed) whose location accuracies range from 2-25 km. The correction surfaces are used with the EvLoc algorithm to perform regional relocations of several thousand events in the region around China.

Correction surfaces dramatically improve the clustering and linearity of regional seismicity and increase the stability of EvLoc. About 50% more events are successfully relocated when surfaces are used. Comparing regional relocations to high-quality ground truth also reveals a significant quantitative improvement in location accuracy. In an effort to further improve our location ability, we are creating a comprehensive merged database for the China region, comprised of EDR, ISC, Reviewed Event Bulletin, and several regional catalogs. This database will provide the most complete record of arrivals for events in eastern Asia, and its location performance will be validated against current databases.

One measure of the robustness of the kriged surfaces is their correlation; nearby stations should have similar P-wave correction surfaces. We find that surface correlation is high for nearby stations but drops off beyond about 250 km, implying that, on average, crustal structure varies rapidly across Asia. This length scale may be useful for assessing whether or not surrogates should be used in developing correction surfaces for new stations. Moreover, this correlation length can also be used to constrain the model correlation length parameter in the kriging procedure.

We have performed a suite of sensitivity tests to examine the effect of depth and epicentral mislocations on travel-time residuals. These tests were performed using four closely spaced high-quality ground truth events as observed by the 76 stations for which we calculate correction surfaces. Fixing the latitude and longitude of the events and letting the origin time and depth vary, we find that there is about 0.13-sec deviation in residuals for every 10 km of depth error. Epicentral mislocations result in P-wave residual errors of about 0.75 sec per 0.1^{o}. When compared to the root-mean-square residual value of about 1.9 sec, effects due to depth errors and depth averaging are minimal.

KEY WORDS: location, validation, calibration, regional

OBJECTIVE

Accurate seismic event location remains a key element for monitoring the globe for nuclear explosions. It is particularly difficult to obtain accurate locations at lower magnitudes using sparse global networks. One approach towards improving location is to use travel-time residuals of well-located events to correct travel times for other events in the same region. This approach, which accounts for inadequate Earth models, has been used to calibrate spatially limited regions of interest, most notably at nuclear test sites in various countries. However, in the present context we must monitor vast regions of the Earth's surface, and hence have begun constructing surfaces of travel-time corrections that will ultimately span entire continents, if not the globe. This aspect of the approach is relatively new, and we present some observations on the use, and nature, of P-wave travel-time correction surfaces, testing their application to improving regional seismic event location in Asia.

We have adopted the correction surface approach for a number of reasons, including ease of implementation and the fact that empirical correction surfaces can be constructed without detailed knowledge of crustal structure. In the implementation we discuss here, empirical travel-time corrections are determined with respect to a 1-D base model, and corrections are not predictable beyond the correlation length of the geologic structure. It is important to note, however, that correction surfaces can be calculated for any base model, no matter how detailed, so that when detailed crustal structure is obtained, surfaces can then be recalculated for that model, in turn enabling travel-time correction prediction in regions without empirical data. To construct our correction surfaces, we use the modified Bayesian kriging (MBK) method of Schultz et al (1998).

The MBK method creates an interpolated surface from residuals using correlation lengths of the background model and the data. The correlation of the data can be determined empirically using variogram analysis, presuming the data are isotropic. The correlation of the background model is more difficult to estimate, but we propose a method below that may prove effective. MBK also produces an error variance surface associated with the correction surface. MBK marks an improvement over standard kriging in that it is able to blend back to the variance of the background model beyond the empirically derived correlation lengths. This method has been applied successfully for *P*-waves travel times for seismic location in the Middle East (Schultz et al., 1998; Myers and Schultz, 1998) and in Asia (Steck et al., 2001), and we refer the reader to Steck et al. (2001) for details of our particular implementation. Certainly, the effectiveness of the correction surface method is dependent on the accuracy of the trave-time residual data used. In this study, we use several levels of ground truth, ranging from events located with an accuracy of 2 km (nuclear tests located with the aid of satellite imagery), to events located to an accuracy of about 20-25 km. The latter range is for events whose locations have maximum azimuthal gaps of less than 90 ^{o} and 180^{o}, and numbers of defining phases greater than or equal to 50 and 30, respectively [E. R. Engdahl, personal communication; Bondar et al (2001); Sweeney (1996)].

RESEARCH ACCOMPLISHED

Empirical Kriged P-wave Travel-Time Surfaces

In this paper we elaborate on the performance of empirical kriged *P*-wave travel-time correction surfaces that were developed by Steck et al (2001). The surfaces cover a region between 20ß-55ß latitude and 65ß-115ß E longitude, and were developed for 76 regional seismic stations around Asia. Figure 1 shows the station locations. The propagation path corrections are source-to-station corrections, where each station has its own set of corrections, and the corrections vary depending upon geographic position of the source. Because we are most interested in surface sources, we have restricted our investigations to crustal events, and the correction surfaces are not applicable to sources below the Moho. For this paper the travel-time residuals are calculated with respect to a regional 1-D velocity model based on results published in Li and Mooney (1998) and reported in Steck et al. (2001).

The best constrained ground truth information available for the region is that from nuclear explosions. We include locations for explosions from two test sites: the Chinese test site at Lop Nor (Gupta, 1995) and the former Soviet Union test site at Balapan, Kazakhstan (Thurber et al., 1993). Because the origin times for these events are not known, these events are considered to be accurate within 2 km, although the reported location error is typically less than 2 km. We also examined 26 events that have independent depth constraints, ultimately using only about a third of them as ground truth to construct our travel-time surfaces. While perhaps

not as valuable as epicentrally constrained ground truth for calibration purposes, these data nevertheless offer some improvement over events for which the depth is poorly constrained, and this is a point that we will return to.

The most abundant data we have are constrained events that have been recorded by at least 30 stations with an azimuthal gap < 180°, and have a sum of depth plus depth error less than the moho depth of the model. Applying the 30/180 criteria results in 917 useable ground truth (GT)20 events for the *China_LM* model. If we instead constrain our data using a 50/90 criterion, the number of useable events decreases to 689; see figure 2 for event locations. From these sets of events we then gather residuals by station, discarding residuals larger than 5 s (for 30/180) or 10 s (for 50/90) in absolute value, and kriging the declustered data to obtain an interpolated surface for each station. Declustering the residual data accelerates and stabilizes the kriging procedure.

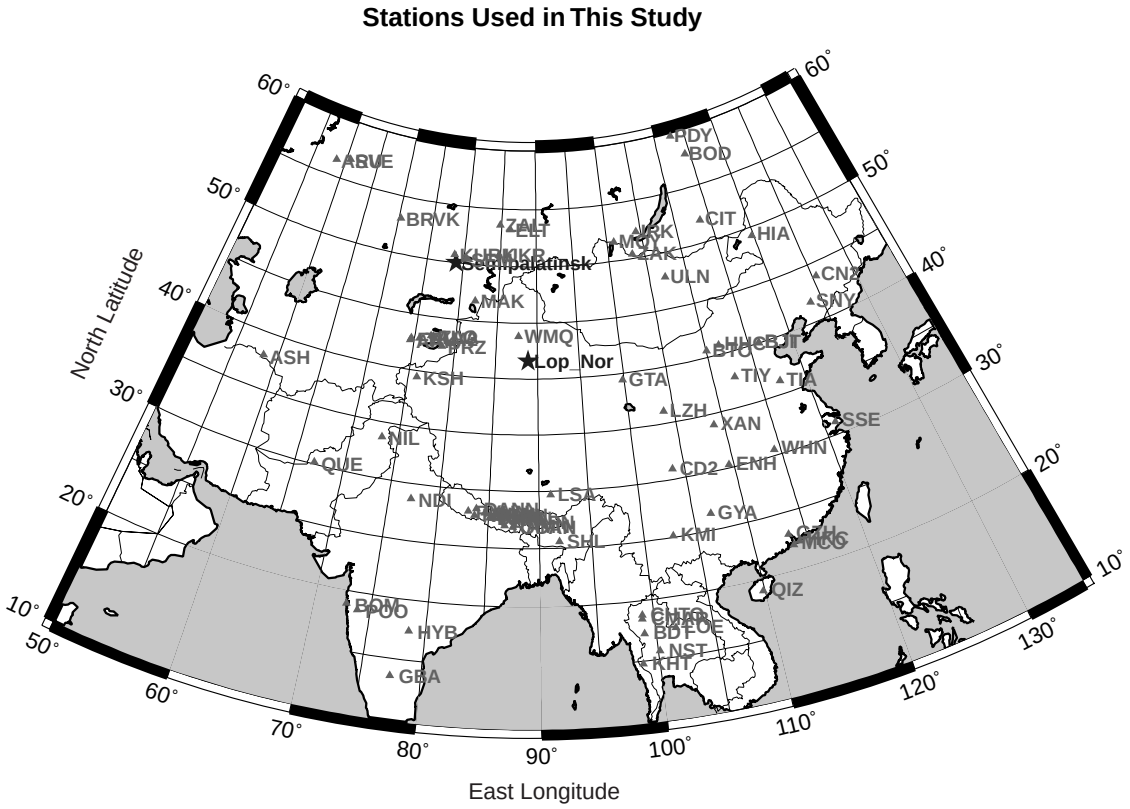

Figure 1. Map of 76 seismic stations used in this study.

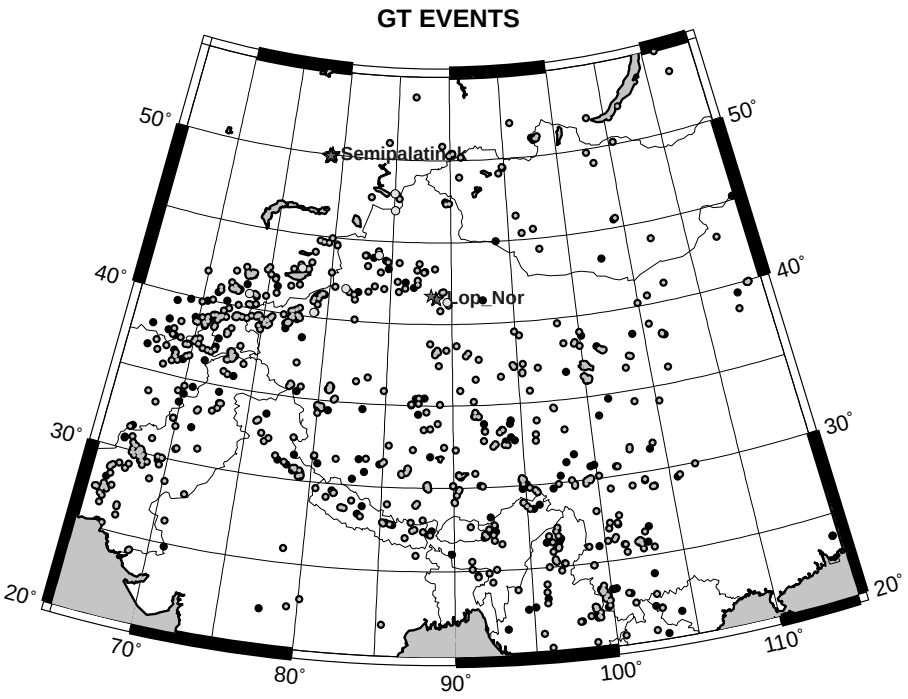

Figure 2. Locations of GT2-20 events used to create correction surfaces. Black dots show the 917 30/180 data, small gray dots within the black dots show 689 50/90 data. Stars show GT2 nuclear tests and larger gray circles indicate depth-constrained events, primarily in the Tien Shan area.

Regional Location Using Kriged P-wave Travel Time Surfaces

Travel-time correction surfaces are used to relocate 6748 events from the United States Geological Survey (USGS) Earthquake Data Reports (EDRs) and the International Seismic Centre (ISC) catalogs, for the region around China, using the EvLoc algorithm (Bratt and Bache, 1988; Nagy, 1996). In this case only stations for which corrections were available are used. Figure 3 shows our relocations without using correction surfaces (top), and relocations with corrections (bottom). While qualitative in nature, comparing these two plots shows that the use of correction surfaces improves the tightness and linearity of events and clusters. The use of correction surfaces improves our ability to relocate events with sparse data by stabilizing the location procedure. When correction surfaces are not applied (and the same stations are used), only about 70% of the original 6748 events converged to a solution. Quantitative location improvement can be obtained for regions having high-quality ground truth. Regional relocations with corrections are better than either corrected or uncorrected teleseismic locations.

Correlation of Kriged P-wave Travel-Time Surfaces

One measure of the robustness of the kriged surfaces is the correlation between surfaces for nearby stations. If the number and locations of events from which the surfaces are derived are similar, one might expect that surfaces for nearby stations would be well correlated, while the correlation would be somewhat random for more distant stations. To investigate this, we look at all possible station pairs for the 76 stations in Asia. Our measure of surface correlation is the simple expression:

$$\rho_{jk} = \mathrm{COV}_{jk} / \sigma_j \sigma_k$$

where ρ is the correlation, COV is the covariance, σ is the standard deviation, and j,k represent the two kriged surfaces (Davis, 1986). Figure 4 shows the correlation, ρ, versus inter-station separation distance, x, for two

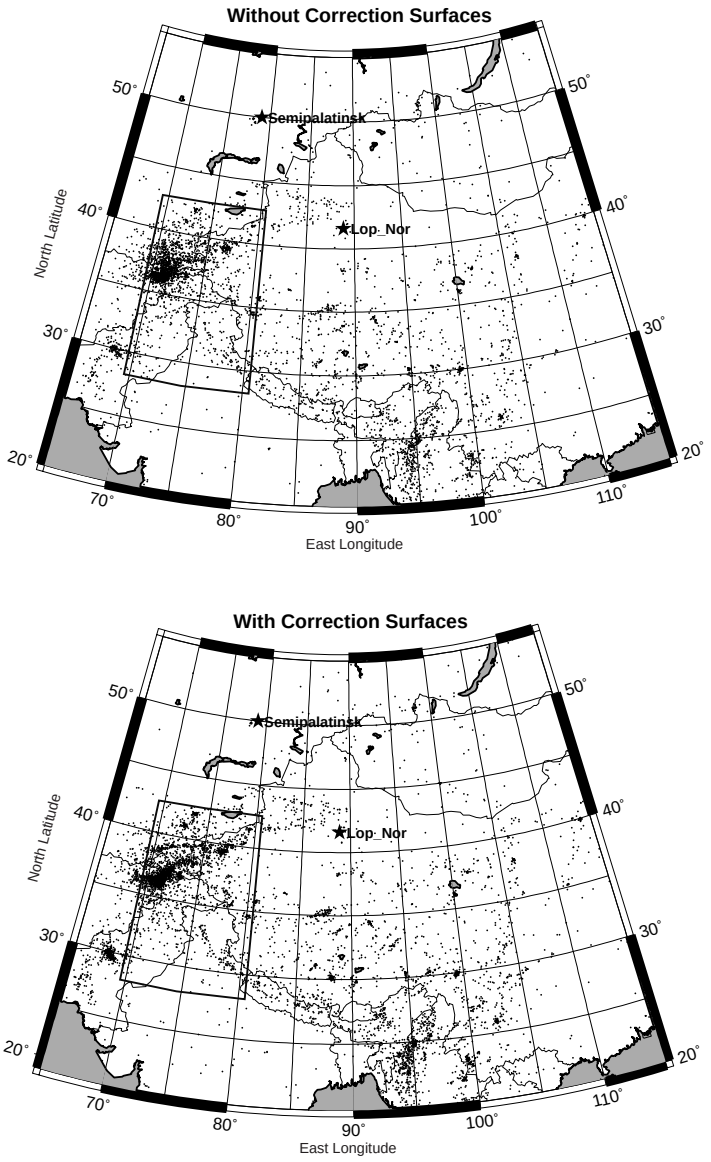

Figure 3. (top) 4630 successful relocations without kriged correction surfaces, (bottom) 6748 successful relocations with kriged correction surfaces based on 30/180 data. In both cases, only stations for which corrections were available were used in the relocations. Note greater event clustering and linearity, particularly within the boxed region.

sets of data, those with 50 stations or greater and an azimuthal gap < 90^o and those with 30 or more stations and an azimuthal gap < 180^o. Curves of the form:

$$\rho = A_0 10^{(A_1 x)} - A_2$$

are fit to the data as well, with very similar results. The y-intercept was slightly higher for the 50/90 data (.8633 versus .8109) suggesting a higher correlation for the better constrained events. Perhaps the most striking observation here is that correlation drops off dramatically beyond 250 km, and even within that distance, there are several largely uncorrelated surface pairs. The lower correlations inside 250 km largely arise from correlating surfaces with little data or from surface pairs with limited overlap in event coverage. The 250-km correlation range agrees qualitatively with results from Shearer (2001) where reciprocity is used to assess a global average correlation range of about 150 km. The swift drop-off in surface correlation suggests that on average, geology varies rapidly in this region, with a structural correlation range of about 250 km. This may be valuable for assessing whether or not surrogates should be used in developing station correction surfaces for new stations, though the inter-station geologic terrain should be evaluated first if at all possible. Since the correlation of the surfaces is really a measure of the correlation of surface geology between stations, we propose that a more effective estimate of model correlation length can be obtained from the surface correlation length, ρ.

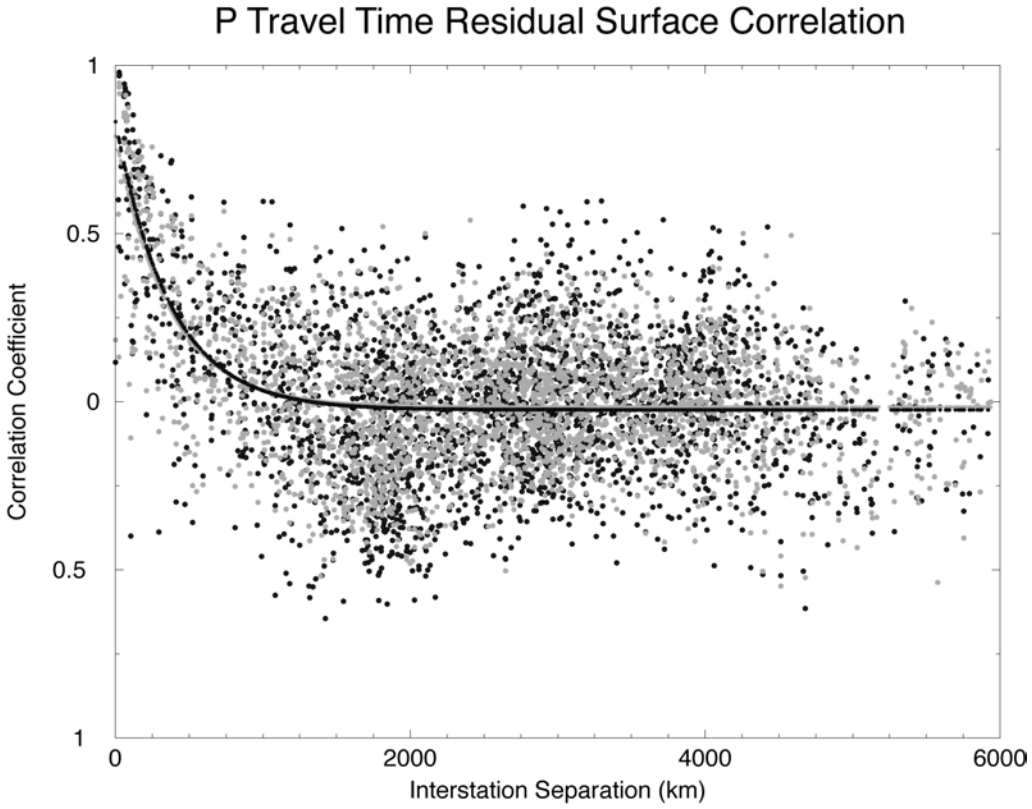

Figure 4. Correlation of kriged surfaces for station pairs, plotted as a function of inter-station distance. Gray circles are for seismic events with 30 or more defining phases (one per station) and maximum azimuthal gap less than 180°; black circles for events with 50 or more defining phases and maximum azimuthal gap less than 90 °. Curves fit to both sets of data are also shown.

Effects of Mislocation on Travel -Time Residuals

To produce our correction surfaces, we use a combination of events located to within 2 km or 20-25 km of their true location, where the former is for nuclear explosions located with JED methods and satellite imagery, and the later is for well-located earthquakes. We also have some earthquakes for which depths have been constrained by a number of different methods, from waveform fitting and inversion, to depth phase analysis. To investigate the value of using depth-constrained events and events whose location is known only to within some

limit, we ran synthetic tests in which either depth or epicenter was perturbed from its initial ground truth estimate. In EvLoc, we then calculate new travel times for the perturbed hypocenters, and solving for a new origin time if depth was perturbed. Travel-time residuals are then calculated and compared to residuals for the unperturbed case. We investigate this using four high-quality ground truth events in western China, as observed by the 76 stations for which we have calculated correction surfaces. For the depth-perturbed events, we fix the latitude and longitude and let origin time vary. For increments of 10 km in depth, we then re-gathered the station residuals, and find the average deviation of the residuals from the residuals at zero depth. These data are shown in Figure 5. One can see that there is about 0.13-s deviation in residuals for every 10 km of depth error.

Epicentral errors are explored by perturbing the epicenter to the north, east, south and west by increments of 0.05^o, 0.1^o, 0.25^o, and 0.5^o. Origin time and depth are held fixed. The differences between the residuals from the shifted epicenters and those at the correct epicenter are calculated and grouped by distance bin. From these a standard deviation is determined for each distance bin, and results are shown in Figure 6. We find about 0.75 s standard deviation in travel time residual per 0.1^o of mislocation.

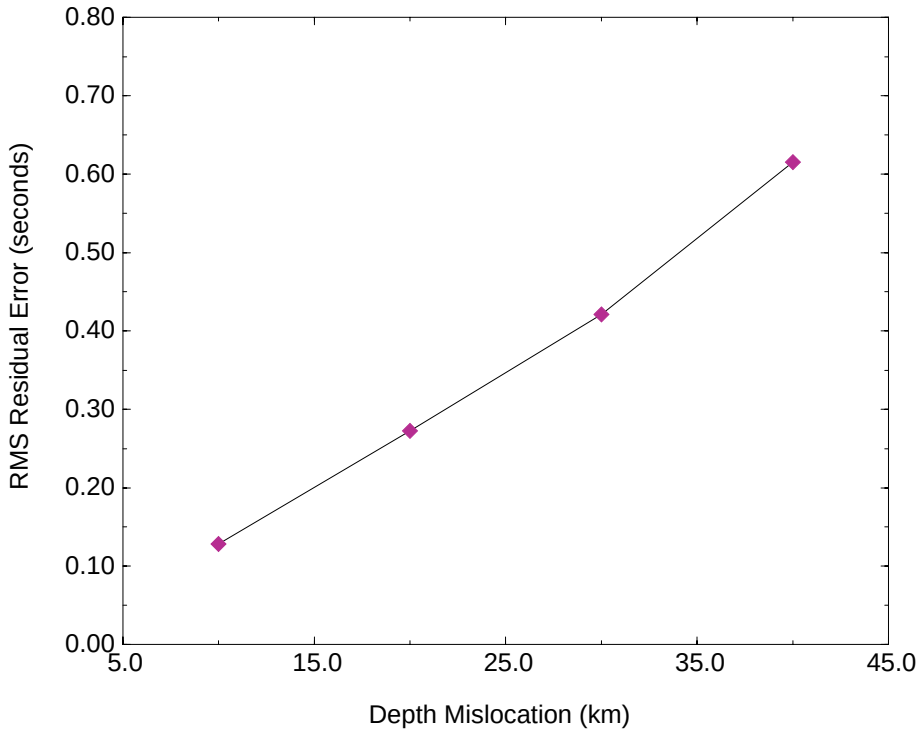

Figure 5. Standard deviation of residuals from those at zero depth, as a function of depth mislocation.

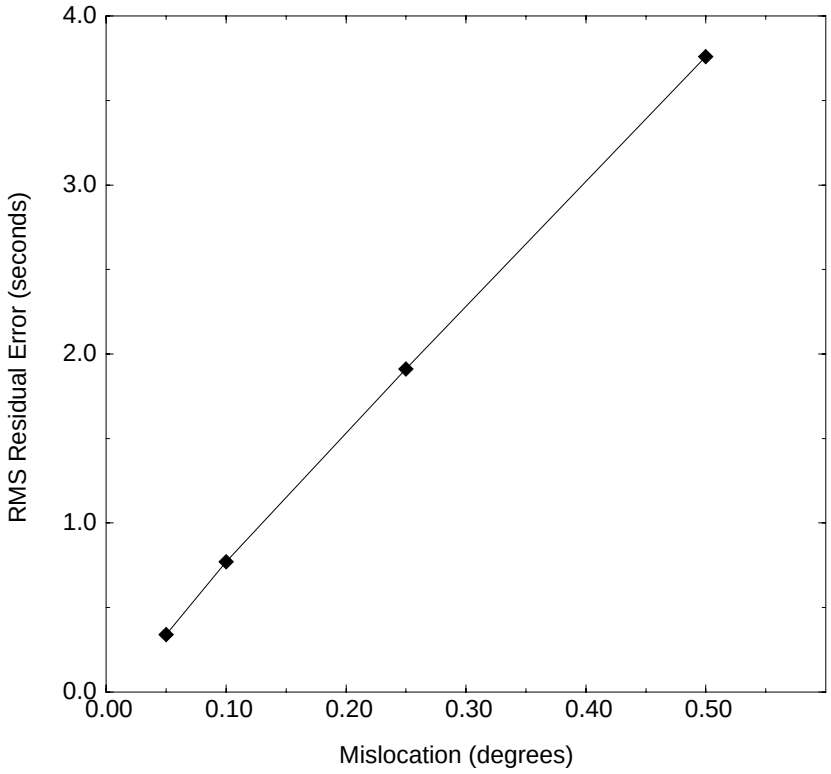

Figure 6. Standard deviation of residuals from those at ground truth epicenter, as a function of epicentral mislocation.

As seen in figure 3, even using travel-time residuals from seismic events having locations accurate to only 20 km can dramatically improve our regional location ability in Asia. In this study we have combined residuals for events located throughout the crust, using all events for which depth plus depth error is less than crustal thickness. This was motivated in part by our need for data but also by the overall lack of strong constraints on depth for this region. Results shown in Figure 5 suggest that the errors introduced by this approach are small, on the order of a few tenths of a second, compared to the overall size of the residuals, which are on the order of a few seconds (see figure 7). This effect has also been reported by S. Myers (Pers. Comm.). Errors in residuals are larger for epicentral mislocation, at about 1.5 seconds for a 22-km location error. While 1.5 s is approaching the size of an average root-mean-square (RMS) residual (1.85 s), it is smaller than the smallest standard deviation assigned to the residuals, and there are nevertheless improvements in our locations using data at, or under, this level of ground truth accuracy. This may result from the larger residuals dominating the improvement, or it may be that we are simply improving the clustering of events, while their absolute location is still off by about 20 km. In either case, this suggests that mislocation biases for regional events are significantly larger than those of teleseismically located events, and that the use of teleseismically located event P-wave residuals can be used to improve regional locations.

Developing Regional Seismic Databases for Improving Event Location and Ground Truth

The use of two-dimensional kriged travel-time correction surfaces requires ground truth information, which can be in the form of known explosion locations and well-located teleseismic events. To develop a ground truth data set, we rely on existing catalogs and our own travel-time information. There are many global and regional seismic catalogs with earthquake information for Asia used in location studies, each containing origin and arrival information that may or may not overlap with the other catalogs. In order to obtain the most accurate earthquake locations, all available arrival information should be combined into a single data set, including derived travel times from digital stations. We have developed a seismic location database for the China region,

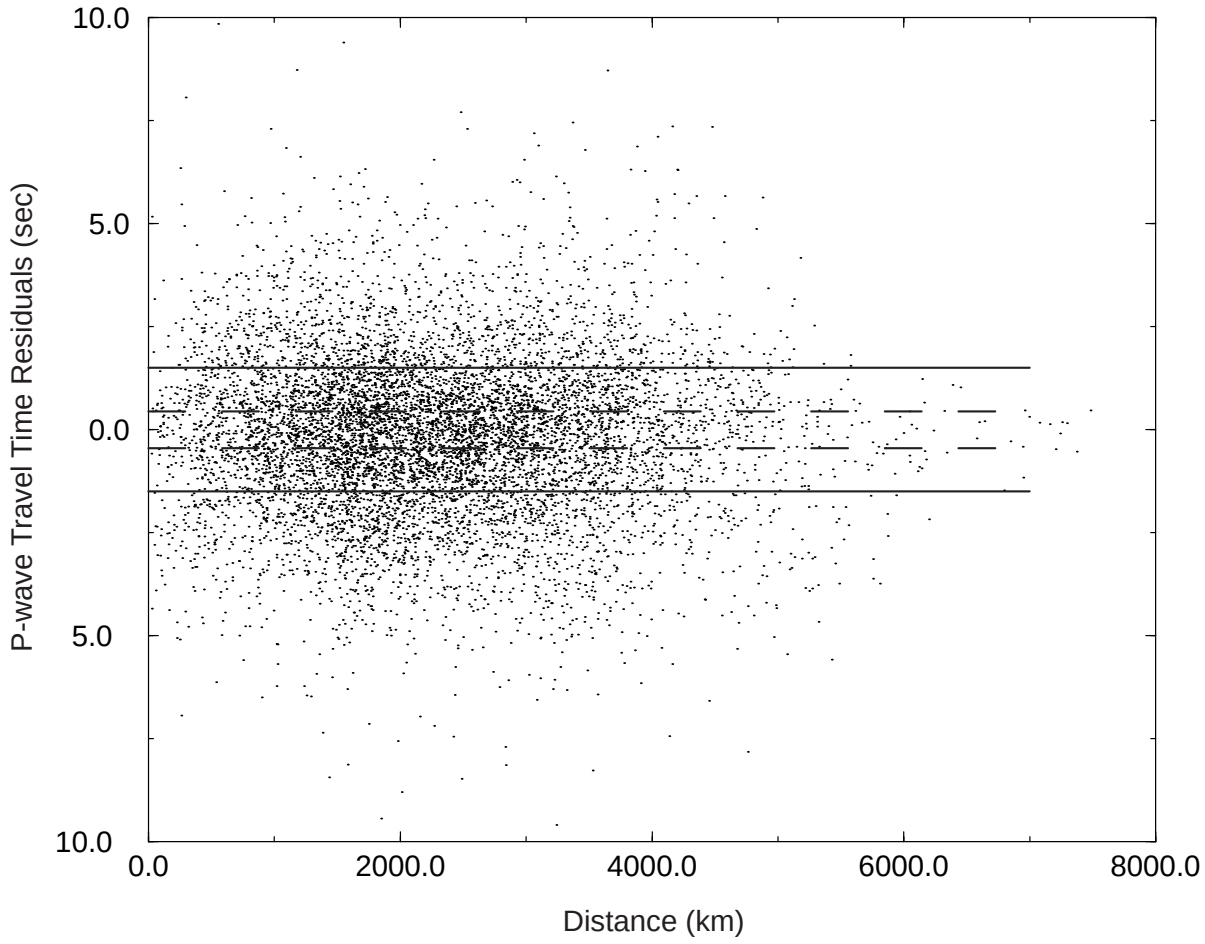

Figure 7. P-wave travel-time residuals versus distance for all 76 stations. The dashed lines represent the RMS residual error for depth mislocation of 30 km (– 0.40 sec). The solid lines are RMS residual error for an epicentral mislocation of 22 km (–1.5 sec). This compares to an RMS residual of –1.85 sec.

combining origin and arrival information from a number of global catalogs, including the prototype International Data Center (pIDC) Reviewed Event Bulletin (REB), USGS Earthquake Data Reports (EDR), International Seismic Centre (ISC), as well as several regional catalogs. Regional arrivals obtained from digital data in Asia are also included. We also include ground truth information from previous research efforts for nuclear test sites and regional mining information. This merged database will provide more arrival data in which to improve location studies such as developing and utilizing empirical travel-time corrections surfaces.

As a first step, the above catalogs are joined based on origin location and time to produce a master table listing common origins by event ID (evid). This master origin table provides the basis for merging the arrival tables from different catalogs and deleting redundant arrivals based on a catalog hierarchy. Certain catalogs are known to have errors in arrival times from truncation and machine versus manual picking. Traits such as this go into determining a suitable catalog hierarchy in which to remove duplicate information. The final location database will thus have the most accurate arrival information available and contain origin, origin error, association, and arrival tables, all without redundant information.

CONCLUSIONS AND RECOMMENDATIONS

We find that kriged P-wave travel-time correction surfaces dramatically improve seismic event locations in Asia. Correction surfaces stabilize the location procedure such that 50% more events are located when surfaces are used, and clustering and linearity of seismicity are more pronounced. Because the input P-wave residuals are derived from events located to only 20-km accuracy, the locations themselves may still contain biases despite improvement in relative locations. If the seismicity used to create the surfaces is in fact unbiased but simply contains random errors on the order of 20 km, then the final locations may not be biased. By perturbing known event depths and epicenters by varying amounts, we are able to assess that errors in depth do not have a significant effect on the construction of the surfaces, being an order of magnitude smaller than typical residuals. Errors in epicenter will contribute significant error to the correction surfaces, but these errors still do not dominate the surfaces' effects on location. This may arise through the averaging effects implicit in our surface construction, or through the corrections being dominated by the larger values present in the surfaces themselves. Nevertheless, the more accurately one knows the locations of the events whose residuals are being used, the more effective the surfaces will be in improving locations. Through investigation of the correlation of our correction surfaces with each other, we find that an average structural correlation length for Asia is about 250 kilometers.

REFERENCES

Bondar, I., X. Yang, R. G. North, and C. Romney (2001), Location Calibration Data for CTBT Monitoring at the Prototype International Data Center, *Pure Appl. Geophys.*, 158, 19-34.

Bratt, S. R. and T. C. Bache (1988), Locating Events With a Sparse Network of Regional Arrays, *Bull. Seism. Soc. Am.*, 78, 780-798.

Gupta, V. (1995), Locating Nuclear Explosions at the Chinese Test Site Near Lop Nor, *Science and Global Security*, 5, 205-244.

Li, S. and W. D. Mooney (1998), Crustal Structure of China From Deep Seismic Sounding Profiles, *Tectonophysics*, 288, 105-113.

Nagy, W. (1996), New Region-dependent Travel-time Handling Facilities at the IDC: Functionality, Testing, and Implementation Details, *Tech Rep. SAIC-96/1179*, 57 pp.

Schultz, C. A., S. C. Meyers, J. Hipp, and C.J. Young (1998), Nonstationary Bayesian Kriging: A Predictive Technique to Generate Spatial Corrections for Seismic Detection, Location, and Identification, *Bull. Seismol. Soc. Am.*, 88, 1275-1288.

Shearer, P. M. (2001), Improving Global Seismic Event Locations Using Source-receiver Reciprocity, *Bull. Seismol. Soc. Am.*, 91, 594-603.

Steck, L. K., A. A. Velasco, A. H. Cogbill, and H. J. Patton (2001), Improving Regional Seismic Event Location in China, *Pure Appl. Geophys*.158, 211-240.

Sweeney, J.J, (1996), Accuracy of Teleseismic Event Locations in the Middle East and North Africa, *Lawrence Livermore National Laboratory report* UCRL-ID-124868.

Thurber, C. H., H. R. Quin, and P. G. Richards (1993), Accurate Locations of Nuclear Explosions in Balapan, Kazakhstan, 1987 to 1989, *Geophys. Res. Lett.*, 20, 399-402.

Thurber, C.H., C. Trabant, F. Haslinger, and R. Hartog. (2001), Nuclear explosion locations at the Balapan, Kazakhstan, nuclear test site: the effects of high-precision arrival times and three-dimensional structure, *Phys. Earth Planet. Int*., 123, 283-301.

IMPROVED SURFACE WAVE DETECTION AND MEASUREMENT USING PHASE-MATCHED FILTERING WITH A GLOBAL ONE-DEGREE DISPERSION MODEL

Jeffry L. Stevens, David A. Adams, and G. Eli Baker

Science Applications International Corporation

Sponsored by Defense Threat Reduction Agency

Contract No. DSWA01-98-C-0154

ABSTRACT

The primary goal of this project is to improve the capability to identify and detect surface waves for the purpose of earthquake/explosion discrimination. We are developing improved, higher resolution earth and dispersion models. The models consist of approximately 600 distinct crust and upper mantle structures, with surface layering and/or ocean depths that vary on a one-degree grid. There are a total of 64,800 earth models and dispersion curves, but the tomographic inversion is performed only for the 600 distinct crust and upper mantle models, with the shallow structure constrained by other information. The data set used in the inversion now consists of approximately 548,000 phase and group velocity dispersion measurements obtained from a variety of sources. Surface sediments are defined using the global sediment maps of Laske and Masters (1997), and ocean bathymetry is defined using the Etopo5 topographic data set.

Automatic identification of surface waves at the International Data Centre is currently performed by narrow-band filtering the data at several frequencies, and then comparing the arrival times with a regionalized dispersion model. We have implemented and tested a new procedure in which we first phase-match filter the data and then apply narrow-band filters to the compressed waveform and use a detection test similar to the current test. This allows us to take advantage of the improved signal-to-noise ratio of the phase-match filtered waveforms, while retaining the robustness of narrow-band filtering for frequency-dependent signal identification. After phase-matched filtering, the predicted arrival time is zero at all frequencies, so we test to see if the arrivals are within a time window similar to that used in the existing test. To test the procedure, we processed the same data set using five-degree and one-degree models with and without phase-matched filtering. Detections using the one-degree model with phase-matched filtering increased by more than 30% compared to the five-degree model currently in use at the IDC without phase-matched filtering.

We use long-period waveforms from historic nuclear explosions to assess the potential of automated Rayleigh wave travel-time picks to improve seismic event locations. The improved accuracy of locations reported by Yacoub (2000), based on 20-second Rayleigh waves, provided the impetus for this work. Although surface wave arrival times cannot be measured as accurately as body wave arrivals, that surface waves are much slower means that accurate locations can be achieved. We find that good locations can be determined with surface waves, which could potentially improve locations made with body waves alone provided that the paths are relatively short and an accurate dispersion model is available for the region. This may be especially important for small events with few total measurements. To assess the value of single surface wave measurements for that purpose, we also estimate the accuracy of single-station distance estimates.

KEY WORDS: surface wave, dispersion curve, phase-matched filter, regionalization, moment, location

OBJECTIVE

The primary objective of this project is to develop improved methods for detection and measurement of surface waves. This is important because the threshold level for surface waves is, in general, the threshold

for the M_s:m_b discriminant. By reducing the threshold for surface wave detection, we can reduce the number of unidentified events and increase the likelihood of identifying smaller nuclear explosions.

RESEARCH ACCOMPLISHED

As stated above, the primary focus of this project is to improve the capability to identify and detect surface waves for the purpose of earthquake/explosion discrimination. This is being accomplished through development of high-resolution earth models constrained by inversion of surface wave observations and auxiliary information, which in turn are used to derive surface wave phase and group velocity dispersion curves on a global grid. These dispersion curves are then used to construct phase-matched filters to improve surface wave detection. The availability of high-resolution group velocity curves also makes it possible to use surface waves to improve event location, as suggested by Yacoub (2000), so we have performed a study to assess under what conditions this technique may be useful. This paper is organized into three parts: improvement of regionalized global earth models and dispersion curves; automatic surface wave identification using phase-matched filtering; and location of events using surface wave observations.

Development of Regionalized Earth and Dispersion Models

The most important information required for improving surface wave detection and measurement is accurate global dispersion maps. Consequently, most of our work has concentrated on the development of three-dimensional velocity models of the earth's crust and upper mantle by tomographic inversion of surface wave dispersion measurements. This work uses an extension of the technique described by Stevens and McLaughlin (2001), in which a global earth model with 149 distinct model types on a five-degree grid was developed. That model is now being used for routine surface wave identification at the International Data Centre (IDC). The technique used at the IDC is to compare predicted group velocity dispersion curves derived from these regionalized models with measured dispersion curves from observed surface waves. As discussed later, phase velocities derived from these earth models can also be used to develop phase-matched filters to improve signal-to-noise ratio and optimize the detection test.

The data used to derive our earth models consist of more than 548,000 measurements of surface wave group and phase velocity dispersion from earthquakes and explosions. These measurements were obtained from various sources and are for frequencies ranging between 0.005 and 0.1667 Hz with the great majority of observations between 0.01 and 0.1 Hz. The data set has been derived from a variety of regional and global studies including the following: global surface wave group velocities from earthquakes derived using PIDC GSETT3 data (Stevens and McLaughlin, 1996), augmented with more recent measurements derived from PIDC data; surface wave phase and group velocity dispersion curves from underground nuclear test sites (Stevens, 1986; Stevens and McLaughlin, 1988), calculated from earth models for 270 paths (test site – station combinations) at 10 frequencies between 0.015 and 0.06 Hz; phase and group velocity measurements for western Asia and Saudi Arabia from Mitchell et al.(1996) for 12 paths at 17 frequencies between 0.012 and 0.14 Hz; the global phase velocity model of Ekstrom et al. (1996) for 9 periods between 35 and 150 seconds calculated for each 5-degree grid block from a spherical harmonic expansion of order l=40; group velocity measurements for Eurasia from Ritzwoller et al.(1996) and Levshin et al.(1996) for 20 frequencies between 0.004 and 0.1 Hz with 500 to 5000 paths per frequency; Antarctic and South American group velocity measurements from the University of Colorado (Vdovin et al., 1999; Ritzwoller et al., 1999); high-frequency Eurasian dispersion measurements from University of Colorado (Levshin and Ritzwoller, pers. comm., 2001), and a large set of dispersion measurements from Saudi Arabia provided by Herrmann and Mokhtar at St. Louis University. We have received a large set of data from LLNL for North Africa and Eurasia (Pasyanos, pers. comm., 2001), but are still reviewing the measurements and have not included it in the inversion results described here.

Development of improved earth models and dispersion curves has proceeded using the following approach:

1. The starting point was the 5-degree IDC 149 model set (Stevens and McLaughlin, 2001), which was based on approximately 90,000 dispersion measurements.
2. New dispersion measurements were added to the data set and the same model set was reinverted with the new data.

3. New model types were added in areas with increased data or where the data misfit indicated that new model types were required and a new inversion was performed with the larger data and model set.
4. A procedure was developed for including shallow structure, particularly sediment thicknesses and ocean depths, on a one degree grid while inverting for a limited set of distinct models, most of which remained on a five-degree grid, in the crust and upper mantle.
5. The locations and boundaries of the underlying model types were redefined, starting with the Crust 2.0 model, so that they follow plate boundaries and other geologic constraints. The inversion technique was also modified to allow small variations in Moho depth and layer thickness to be defined on a one-degree grid for each model type.

So, with our current approach, the inversion is performed for shear velocity structures in approximately 500 distinct crust and upper mantle model types, but the shallow structure, bathymetry, as well as small changes in layer thickness and Moho depth, can vary on a one-degree grid (64,800 distinct models). P wave velocities are constrained via a constant Poisson's ratio of 0.27, and density via Birch's Law. The layers vary in thickness (averaging about 10 km) and reach down to a depth of about 250 km. Below 250 km the Earth model is fixed to match PREM. The top few kilometers of the model (consisting of water, ice and/or sediments) is fixed and matches data from 1-degree bathymetry maps made by averaging Etopo5 5 minute measurements of topography, and Laske and Masters (1997) 1-degree maps of sediments. One advantage of inverting for a fixed set of crust and upper mantle structures is that it reduces the problem to a more manageable size. An earth model consisting of 16200 2-by-2 degree cells and with about 10 layers per cell would have on the order of 10^5 free parameters. Our current model consists of 537 model types that reduce the total number of free parameters to 6494. Other advantages of this type of inversion are that it uses all frequencies (and both phase and group velocity) at once, with different frequencies resolving different length scales; the technique keeps similar structures consistent with each other, avoiding fluctuations in nearby points common in more traditional group velocity inversions; and it allows Moho depths, subcrustal layer thicknesses, and lateral boundaries between geologic regions to be added to the model as fixed *a priori* information. The principal disadvantages are that distinct model types must be chosen carefully and added sparingly if needed, and that there is no smoothness constraint between adjacent structures.

The current model under development consists of 537 model types. There are two main varieties of types, those originating from the Crust 2.0 2x2 degree crustal types (Bassin et al., 2000 and Laske et al. 2001) and those based on ocean ages (Stevens and Adams, 2000). The Crust 2.0 models are an improvement of the Mooney et al. (1998) Crust 5.1 model revised and refined to a 2-degree scale. They may include a layer of ice, water, 1-3 layers of sediments, and 3 crustal layers. Because many of the Crust 2.0 models differ only in shallow structure rather than crustal velocity or thickness, we use a somewhat different set of models. We combine similar model types that vary in shallow structure, since we treat those variations as independent constraints, which has the effect of reducing the number of model types relative to Crust 2.0. However, we also separate models in widely separated regions so that results from a model in North America, for example, do not affect a model of the same type in Eurasia. This increases the number of model types. We also reparameterized the structure of the oceans based on ocean age. Previously ocean structures were based on both age and sedimentary thickness. We formed 17 ocean types based on the Muller et al. (1997) isochron map. There are five types for each of the three major oceans: Pacific, Indian and Atlantic. The five types match the age ranges 0 to 10.9 Ma, 10.9 to 20.1 Ma, 20.1 to 40.1 Ma, 40.1 to 83.5 Ma and 83.5 to 180.0 Ma. The remaining two types are for the Arctic Sea for ages 0 to 40.1 Ma, and 40.1 to 180.0 Ma.

Sedimentary structures, bathymetry and lateral boundaries between different oceanic types are included on a 1-degree level of detail. This parameterization serves as an initial model for a series of 3-D tomographic inversions. Regularization is controlled by two parameters, one for a vertical smoothing condition applied to layers in each model type, and a damping parameter. The tomographic inversion has the form shown in equation 1. S_g is the slowness of the g^{th} one degree cell; m_j is the shear wave velocity of the j^{th} layer where j spans all the adjustable layers of all model types. X_{ig} is the length of i^{th} raypath traveled in the g^{th} cell, $?T_i$ is the travel time residual for the i^{th} raypath. From this equation we can see that 64800 one-degree cells are needed to calculate the partial derivatives. One-degree cells are necessary here to carry the information about sediments and bathymetry. However, the free parameters, indexed with j, span a coarser scale, that of

the model types. These equations, plus equations for dampening and smoothing, are solved using the LSQR method. 20 send phase and group velocity maps are shown in figures 1 and 2.

$$\sum_j \delta m_j \sum_g \frac{\partial \delta_g}{\partial m_j} X_{ig} \approx \delta T_i \qquad (1)$$

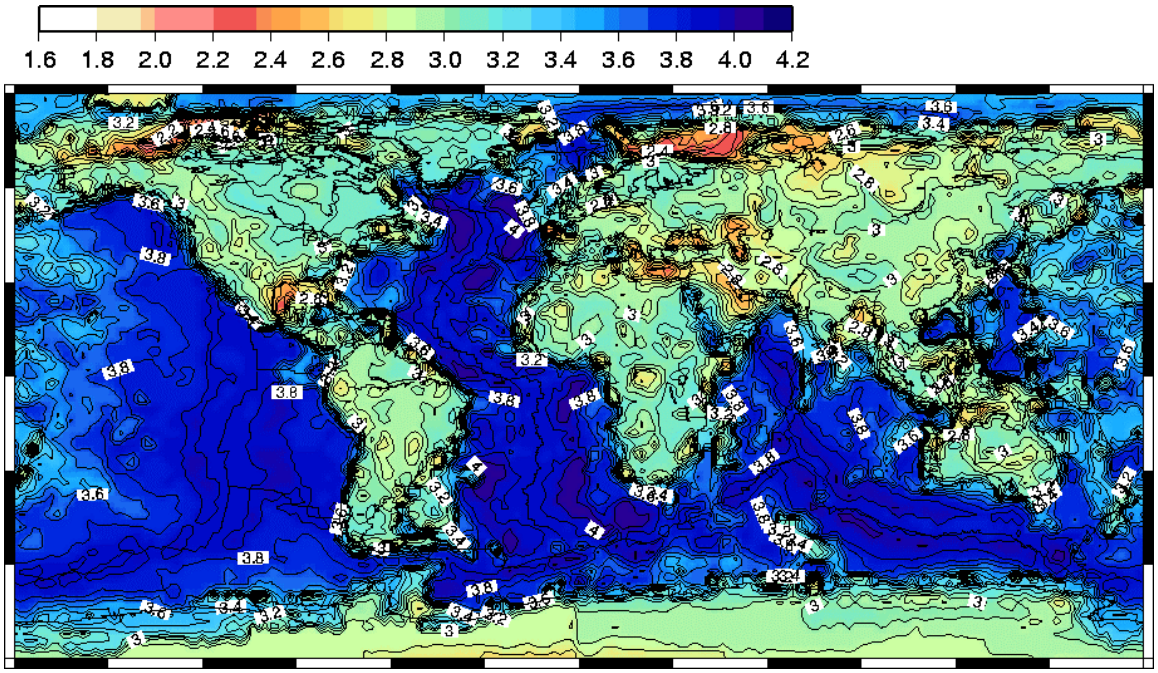

Figure 1. 20-second group velocity map.

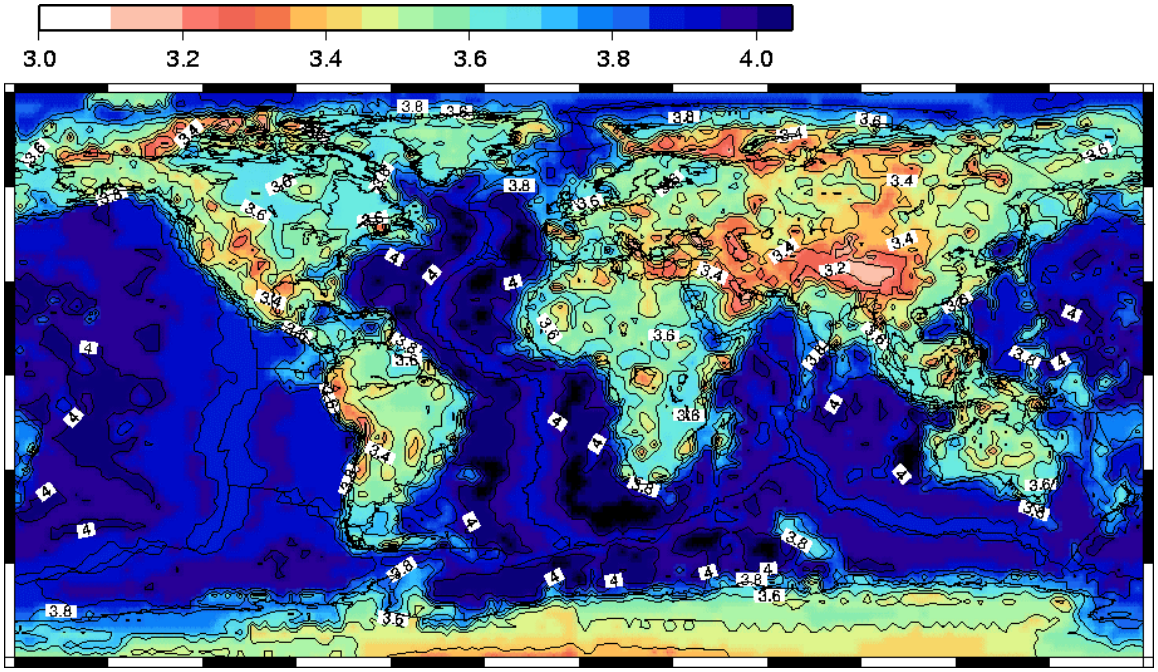

Figure 2. 20-second phase velocity map

The depth profiles of the three main oceanic types are shown in figure 3.

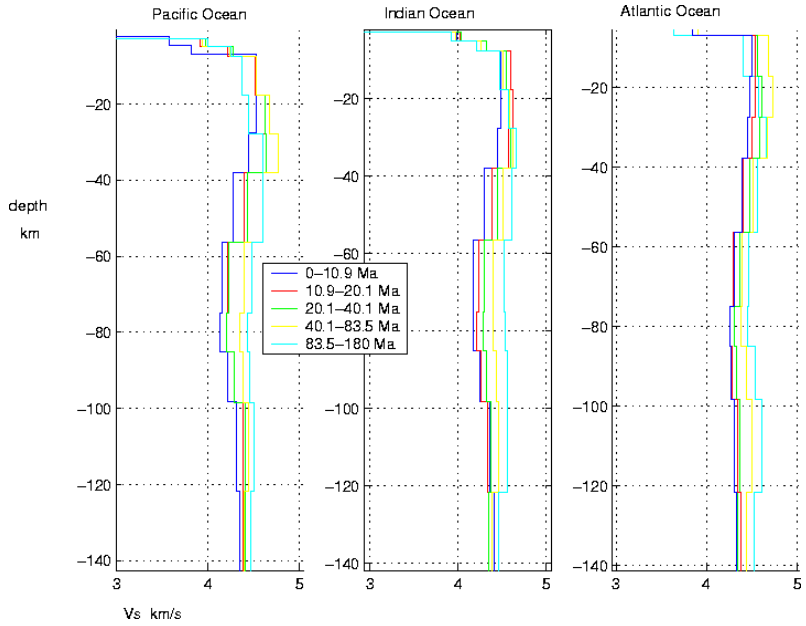

Figure 3. Shear wave velocity depth profiles for the main fifteen ocean types. These results are consistent with thermal models of oceanic lithosphere.

Automatic Surface Wave Detection Using Phase-Matched Filtering

Automatic identification of surface waves at the International Data Centre is currently performed using the processing program Maxsurf by narrow-band filtering the data at several frequencies and then comparing the arrival times with a regionalized dispersion model. An automatic surface wave processing program, Maxpmf, has been developed which is similar to Maxsurf except that it applies phase-matched filtering to seismograms and calculates path-corrected spectral magnitudes in addition to M_s. Maxpmf integrates a regionalized phase velocity model to generate a phase-matched filter that is used to compress the surface wave waveforms. Figure 4 below shows an example of waveform compression after application of phase-matched filters to a data set. Figure 5 shows the recommended way to perform surface wave identification using phase-matched filtering, which is to apply narrow-band filters to the phase-match filtered waveforms and then look for arrival times near zero.

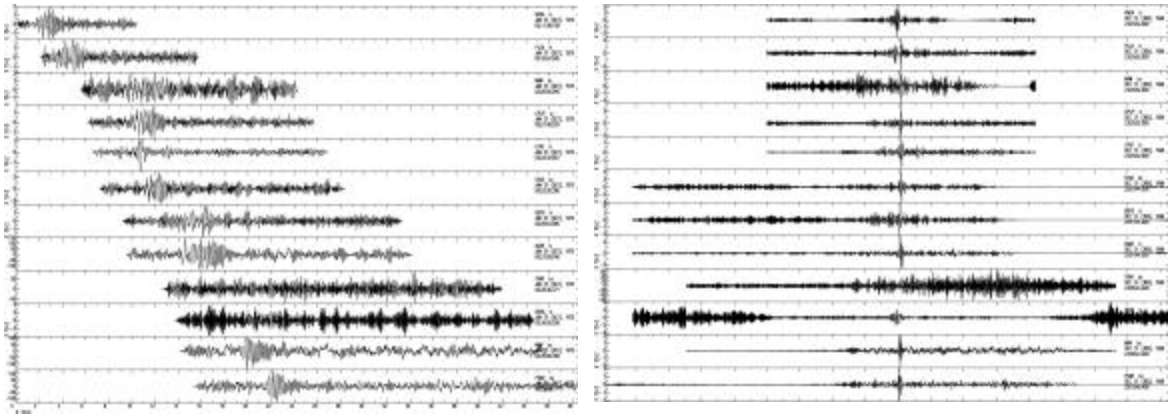

Figure 4. Data in the 5 km/sec to 2 km/sec time window from an m_b 3.9 South Pacific earthquake after transformation to a KS36000 instrument (left) and after compression by phase-matched filtering (right).

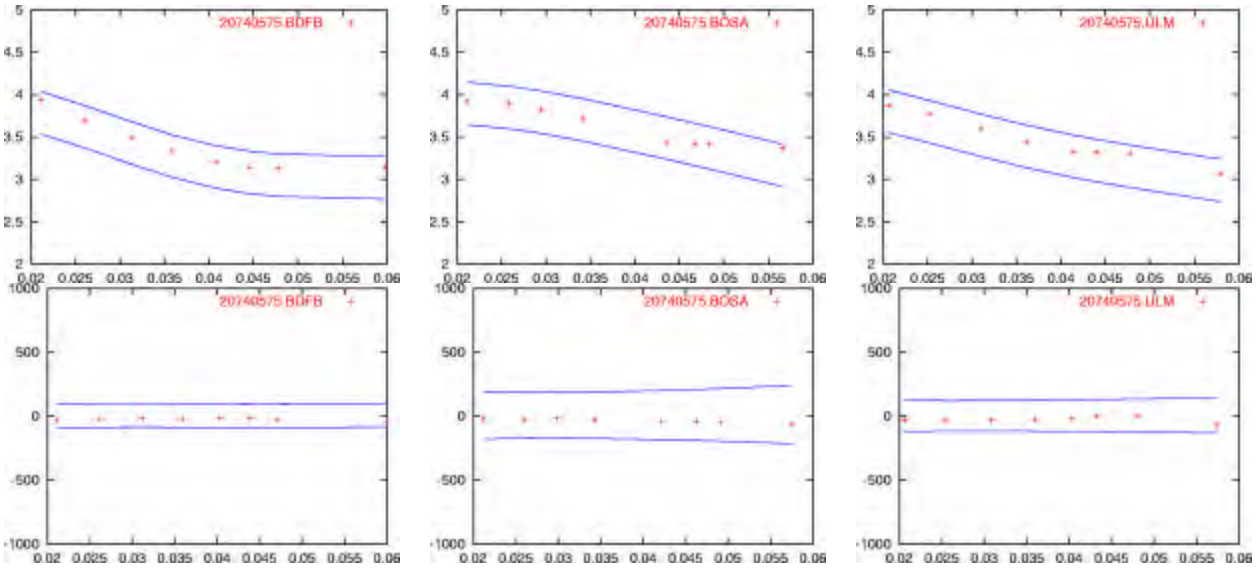

Figure 5. The narrow-band filter detection test (top) compares measured group velocity with a regionalized group velocity model. To improve detection, we phase-match filter the data first, then apply narrow-band filters (bottom). The detection test is applied for the same time interval, but the time is now centered around zero. This example is for an m_b 4.2 South American earthquake observed at BDFB, BOSA, and ULM.

As a test of both the improvement in models and the ability of phase-match filtering to improve detection, we ran Maxpmf on one full day of data and applied both the current narrow-band filtered test and the phase-matched filter test described above to this data set. The results are shown in Figure 6. The four bars show, respectively, the number of detections determined by the current procedure, the number of detections with the best 5-degree model, the number of detections from the current one-degree model, and the number of detections using the one-degree model with phase-matched filtering. Each improved model, and the implementation of phase-matched filtering, shows an improvement. The number of detections increased by 32% over current IDC detections with phase-matched filtering using the most recent one-degree model. The one-degree model used in this test was a modification of the earlier 5-degree model and did not include the modifications discussed earlier to incorporate the Crust 2.0 improvements.

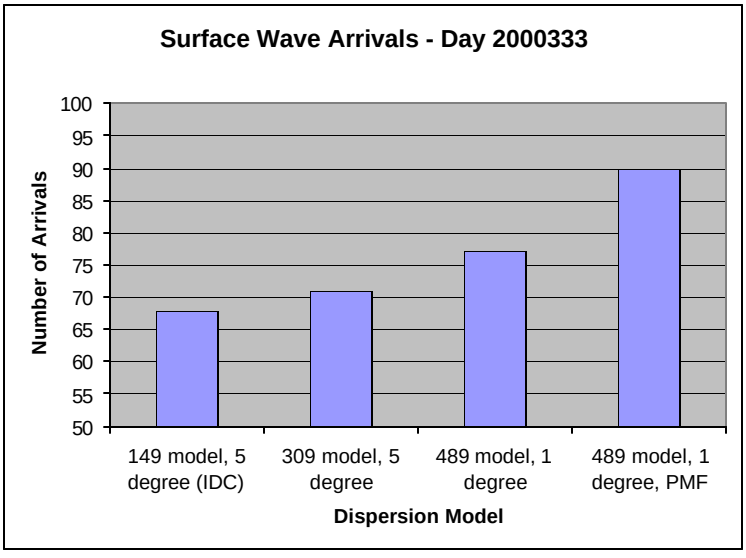

Figure 6. Improvement in the number of detections for a day of data with improvements in the model, and with phase-matched filtering.

As an additional test of the models, we compare observed and predicted dispersion curves for data from nuclear test sites. Tables 1 and 2 show group velocity dispersion residuals and standard deviations in the residuals for periods of 40 seconds and 20 seconds, respectively, for paths from several nuclear test sites. With the expanded data set and 149 models, the results are changed only slightly relative to the inversion with the smaller data set. In fact the results are degraded slightly for the paths from the test sites. This is because the new data caused larger changes in other areas and with the constraint of the small number of models, the data fit became slightly worse in order to allow larger improvements in the areas with concentrations of new data. With 388 models, however, these constraints are relaxed, and the data fit improves for all test sites, and improves quite dramatically for paths in Asia. Curiously, the data fits are not improved with the one-degree model. This result together with the result shown in Figure 8 suggests that the global model is improved, but at the cost of some degradation in paths from the major test sites. We are in the process of investigating the reasons for this now.

Table 1. 40 Second Group Velocity % Average Residuals (Standard Deviations)

Source	IDC 5° 149 Models	5° 149 Models Expanded Data Set	5° 388 Models	1° 489 Models
NTS (59)	0.15 (1.40)	0.22 (1.44)	0.14 (1.20)	-0.17 (1.28)
East Kazakh (40)	0.80 (2.21)	0.85 (2.45)	0.13 (1.11)	0.31 (1.18)
Mururoa (13)	-0.78 (1.43)	-0.73 (1.79)	-0.59 (1.56)	-1.07 (1.48)
Novaya Zemlya (99)	-0.06 (2.06)	0.01 (2.05)	-0.18 (1.81)	-0.10 (1.98)
Amchitka (55)	0.25 (1.39)	0.34 (1.39)	0.35 (1.08)	0.08 (1.18)

Table 2. 20 Second Group Velocity % Average Residuals (Standard Deviations)

Source	IDC 5° 149 Models	5° 149 Models Expanded Data Set	5° 388 Models	1° 489 Models
NTS (58)	-0.47 (2.25)	-0.38 (2.23)	-0.30 (1.88)	-0.08 (2.61)
East Kazakh (40)	-0.75 (1.96)	-0.65 (2.07)	-0.64 (1.44)	-0.05 (1.27)
Mururoa (11)	0.41 (1.43)	0.41 (1.40)	0.53 (1.36)	-0.05 (2.22)
Novaya Zemlya (99)	-0.26 (3.61)	-0.23 (3.66)	-0.43 (3.01)	0.31 (3.28)
Amchitka (54)	0.83 (3.76)	0.70 (3.74)	0.22 (3.23)	0.84 (3.92)

Location Improvement Using Surface Waves

Surface wave arrival times can be used in the same manner as (or together with) P-wave arrival times to determine source location. With a good regionalized group velocity model and well-determined group arrival times, the location could be determined quite accurately, and in cases where P-wave coverage is poor, or azimuthal coverage is limited, using surface wave arrivals has the potential to significantly improve location accuracy. Yacoub (2000) found that he was able to determine the location of 7 Nevada Test Site (NTS) explosions more accurately with surface waves narrow-band filtered at 20 seconds than with P waves. This was done using a constant group velocity of 3.0 km/sec for all paths. This result is attributed to the fact that surface wave group velocities are much slower than P-wave velocities, so that errors in arrival time correspond to significantly smaller errors in distance than the corresponding errors in P wave arrival times, and to the consistency in surface wave arrival times.

We have performed some experiments using our global group velocity models and dispersion measurements to assess the ability to locate events using surface wave arrivals. Table 3 lists location errors from Yacoub (2000) derived using both surface waves and P waves, and the location errors we derived from independent measurements of data at several frequencies from the same events using the regionalized dispersion curves discussed earlier. The results confirm that location estimates are somewhat better than can be obtained from P-wave arrivals at the same stations, although the location errors are somewhat larger than obtained by Yacoub. This may be because Yacoub used a larger and higher quality data set. Also, it should be recognized that Yacoub's P-wave measurements used only data from stations that also had surface wave data, and considerably better results could be obtained from a larger P-wave data set.

Yacoub (2000) found remarkably constant group velocity measurements, all very close to 3.0 km/sec. We cannot confirm this and assume that it must be due either to a particular choice of paths, or some anomaly in the way the measurements were made. Figure 7 shows the distribution of measured group velocities from

all of the explosion data from all test sites. While the mean of the distribution is very close to 3.0 km/sec, there is considerable variation from this value in the data set.

Table 3. Location errors for 3 methods, the number of stations used for each (Yacoub P and surface wave locations used identical sets of stations).

Event	# STA		Location Error (km)		
	Yacoub	IDC	Yac. LR	Yac. P	IDC
Hearts	19	17	11.2	18.3	22.5
Backbeach	19	2	9.7	33.1	NA
Scantling	18	11	25.1	49.9	18.9
Lowball	17	12	16.3	28.3	18.1
Mizzen	14	9	9.8	32.0	34.2
Strake	14	0	13.0	26.0	NA
Sheepshead	12	16	9.2	16.1	13.0
Averages			13 ± 6	29 ± 11	21 ± 7

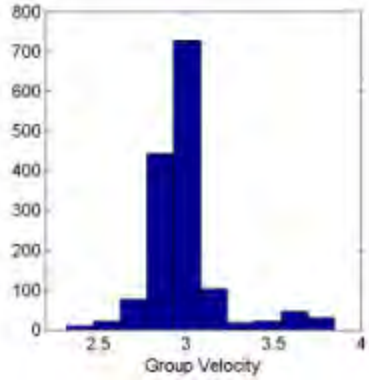

Figure 7. Histogram of measured group velocities of 20-second Rayleigh waves from explosions at all major test sites.

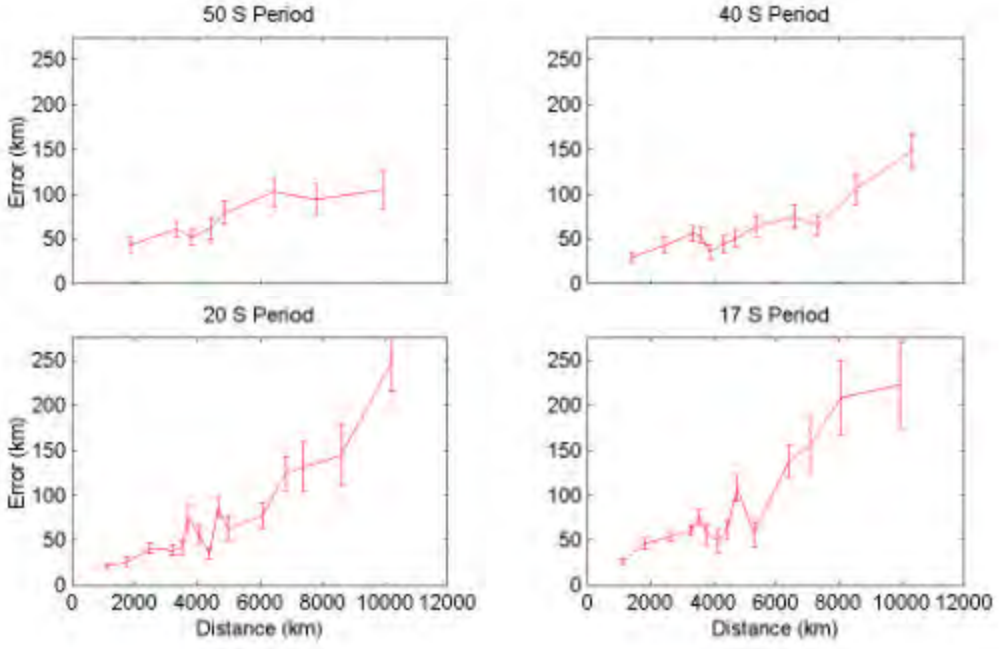

Figure 8. Mean and two standard deviation error bounds of distance estimates from single stations, for different frequencies. There are approximately 100 data per distance bin.

Figure 8 shows the estimated error as a function of distance for single station measurements. In general, the location error increases with distance to the observing station. Lower frequencies, however, degrade much more slowly. However, at shorter distances higher frequency data give more accurate locations.

Figure 9 shows the location error derived from surface wave measurements for the Semipalatinsk test site as a function of the number of recording stations. The results are similar to the NTS results with a typical location error of about 30 km. It is important to note, however, that location accuracy depends as much or more on which stations recorded the event as on how many. Referring to Figure 8, it is clear that surface waves recorded at distances of 3000 km or less provide much better constraints on location than more distant stations. Surface waves are most likely to be useful in constraining location therefore when they are measured at shorter distances and combined with a small number of P-wave measurements. The P-wave measurements on their own may not be very accurate, but even a single surface wave accurately measured at a distance of <2000 km could significantly improve the location.

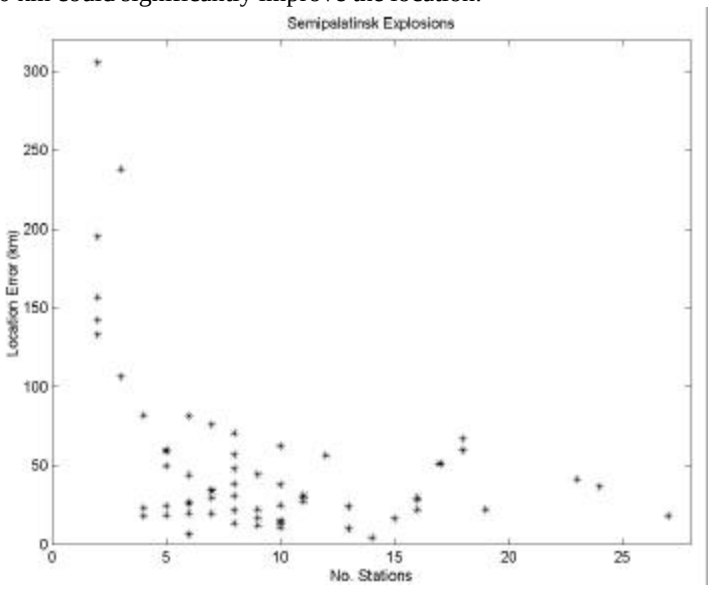

Figure 9. Location errors for Semipalatinsk explosions. The median error for events recorded at 6 or more stations is 30 km.

CONCLUSIONS AND RECOMMENDATIONS

This study has focused on development of improved methods for detection and measurements of surface waves. As part of this effort, we have developed a gradually improving set of global earth models suitable for calculation of phase and group velocity dispersion curves. Over the course of this study, the earth models have evolved from a five-degree model based on 90,000 dispersion measurements to a one-degree model based on over 500,000 measurements. Currently, we are incorporating improvements in boundaries and constraints on shallow structure and Moho depth using the Crust 2.0 models to improve the starting models for the tomographic inversions. We have used phase velocities derived from these models to form phase-matched filters, and developed an improvement on the surface wave detection algorithm that uses phase-matched filtering followed by narrow-band filtering for detection. We performed a test on one day of data at the PIDC with several dispersion models and found a significant improvement using this technique. We have also tested the use of surface waves for location. Although we cannot confirm improvement as significant as suggested by Yacoub (2000), it does appear that surface waves can add an additional constraint that could significantly improve location, particularly in cases where there are only a few P arrivals and the surface waves are measured on short paths.

ACKNOWLEDGEMENTS

We thank M. H. Ritzwoller of Colorado University and M Pasyanos and of Lawrence Livermore National Lab. for providing us with new data.

REFERENCES

Bassin, C., Laske, G. and Masters, G. (2000), The Current Limits of Resolution for Surface Wave Tomography in North America, EOS Trans AGU, 81, F897.

Ekstrom, G., A. M. Dziewonski, G. P. Smith, and W. Su (1996), "Elastic and Inelastic Structure Beneath Eurasia," in *Proceedings of the 18th Annual Seismic Research Symposium on Monitoring a Comprehensive Test Ban Treaty*, Phillips Laboratory Report PL-TR-96-2153.

Laske G. and G. Masters (1997), A Global Digital Map of Sediment Thickness, *EOS Trans. AGU, 78*.

Laske, G., Masters, G. and Reif C., Crust 2.0 (2001), A new global crustal model at 2*2 degrees, http://mahi.ucsd.edu/Gabi/rem.html.

Levshin, A. L., M. H. Ritzwoller, and S. S. Smith (1996), "Group Velocity Variations Across Eurasia," in *Proceedings of the 18th Annual Seismic Research Symposium on Monitoring A Comprehensive Test Ban Treaty,* Phillips Laboratory Report PL-TR-96-2153.

Mitchell, B. J., L. Cong and J. Xie, (1996), "Seismic Attenuation Studies in the Middle East and Southern Asia", St. Louis University Scientific Report No. 1, PL-TR-96-2154, ADA317387.

Mooney, W., G. Laske, and G. Masters (1998), "Crust 5.1: A Global Crustal Model at 5x5 Degrees," *Journal of Geophysical Research*, v. 103, no. B1, pp. 727-747.

Müller, R. D., R. R. Roest, J. Royer, L. M. Gahagan, and J. G. Sclater (1997), "Digital isochrons of the world's ocean floor", *J. Geophys. Res*., 102, 3211-3214.

Ritzwoller, M. H., A. L. Levshin, L. I. Ratnikova, and D. M. Tremblay (1996), "High Resolution Group Velocity Variations Across Central Asia," in *Proceedings of the 18th Annual Seismic Research Symposium On Monitoring A Comprehensive Test Ban Treaty*.

Ritzwoller, M.H., O.Y Vdovin, and A.L. Levshin (1999), "Surface wave dispersion across Antarctica: A first look", *Antarctic J. U.S.*, in press.

Stevens, J. L. (1986), "Estimation of Scalar Moments From Explosion-Generated Surface Waves," *Bull. Seism. Soc. Am.*, v. 76, pp. 123-151.

Stevens, J. L. and D. A. Adams (2000), "Improved surface wave detection and measurement using a global regionalized one degree dispersion model," Transactions Am. Geophys. Union, December.

Stevens, J. L. and K. L. McLaughlin (1996), "Regionalized Maximum Likelihood Surface Wave Analysis," Maxwell Technologies Technical Report PL-TR-96-2273, SSS-DTR-96-15562, September.

Stevens, J. L., and K. L. McLaughlin (1988), "Analysis of surface waves from the Novaya Zemlya, Mururoa, and Amchitka test sites, and maximum likelihood estimation of scalar moments from earthquakes and explosions," S-CUBED technical report SSS-TR-89-9953, September.

Stevens, J. L. and K. L. McLaughlin (2001), "Optimization of surface wave identification and measurement," *Pure and Applied Geophysics*, V. 158, no. 7, in press, July issue.

Vdovin, O. Y., J. A. Rial, M. H. Ritzwoller, and A. L. Levshin (1999), "Group-velocity tomography of South America and the surrounding oceans", *Geophys. J. Int*., 136, 324-330.

Yacoub N. (1996), "Maximum Spectral Energy Arrival Time of Rayleigh Waves for Accurate Epicenter Determination and Location Error Reduction", proceedings *of the 22nd Annual Seismic Research Symposium in New Orleans, LA.*

ASSESSMENT OF SEISMIC AND INFRASOUND SIGNALS IN KOREA WITH GROUND TRUTH

Brian Stump[1], Myung-Soon Jun[2], Chris Hayward[1], Jeong-Soo Jeon[2], Il-Young Che[2], Sara Mihan House[1], and Tae-Sung Kim[1]

Southern Methodist University[1]
Korea Institute of Geosciences and Mineral Resources[2]

Sponsored by Defense Threat Reduction Agency

Contract No. DSWA01-98-C-0131

ABSTRACT

A four-element, 1-km aperture seismo-acoustic array is being operated northeast of Seoul, Korea. Each element of the array consists of a GS-13 vertical seismometer (1 Hz) in a shallow borehole (~10 m) and a low-frequency acoustic gauge connected to an 11-element hose array (7.6 m hoses) at the surface. The array is being used to assess the importance of co-located seismic and acoustic sensors for the purposes of: (1) quantifying wind as a source of seismic and acoustic noise; (2) constraining propagation path effects in the atmosphere and solid earth; (3) locating the sources of the waves; (4) characterizing the source type. Combined analysis of the seismic and acoustic data can be particularly important in identifying sources of industrial blasting. Seismic noise estimates illustrate a level that is only slightly above the low noise model on average. Acoustic noise levels resolve the microbaroms during low noise times but document a nearly 50 dB increase in noise during the windiest periods. Infrasonic noise in the 0.01 to 5 Hz band increases rapidly with wind velocity. The seismic noise shows little or no dependence on wind velocity. Analysis of the data suggests that there are many more acoustic signals than seismic (4-10 times). The majority of the acoustic signals occurs during working hours and are constrained to several narrow azimuth ranges. These observations suggest that the signals are man made. Approximately 1/4 of all seismic signals are associated with an acoustic arrival. The seismo-acoustic observations come from sources in the 30 to 200 km range and occur during working hours, local time. The 30 to 200 km observation distance is surprising in that average atmospheric velocity models predict no acoustic returns in this range. Average atmospheric models modified by meteorological data for the troposphere indicate the possibility of ducting in the troposphere as an explanation for these arrivals. Event location is based upon regional seismic phase identification (P_n, P_g, P_mP, L_g, R_g) using the array and back azimuth estimates from both the seismic and acoustic data. Aliasing for the short wavelength infrasound signals is reduced using broadband back azimuth estimates. Additional infrasound sensors with 100 m offset are planned to further reduce the aliasing problem. Many of the infrasound signals have good signal to noise from 1 to beyond 4 Hz. Despite the small size of the array, event clusters are identified at regional distances. Waveform comparisons of these clusters suggest that the events are from common source areas. The high Q path of the Korean Peninsula results in regional seismograms that have significant energy to frequencies as high as 16 Hz, the corner frequency for the anti-alias filters. Events associated with acoustic signals are presumed to be from mining regions. Ground truth in the form of in-mine observations provides validation of this interpretation. These data are also used to assess blasting practices and their relationship to the observed seismic and infrasound signals. The existence of Rg arrivals and dominance of P energy at high frequency are consistent with this interpretation. There is more event-to-event variation in the acoustic signals than the sesmic signals within the event groups, suggesting the effect of variable atmospheric propagation effects consistent with ray paths in the troposphere.

KEY WORDS: Seismo-acoustic, mining, discrimination, infrasound

OBJECTIVE

The Korean Peninsula (Figure 1) provides a unique laboratory for studying regional seismic wave propagation. Numerous broadband seismic stations in the region and a variety of natural and man-made sources provide opportunities for characterizing wave propagation and source effects within the region. The region includes two

seismic arrays, KSRS and CHNAR, the seismo-acoustic array near Chulwon operated by Korea Institute of Geosciences and Mineral Resources (KIGAM) and Southern Methodist University (SMU). Figure 1 illustrates the seismicity of the region using preliminary event locations made in this study as well as event locations by others.

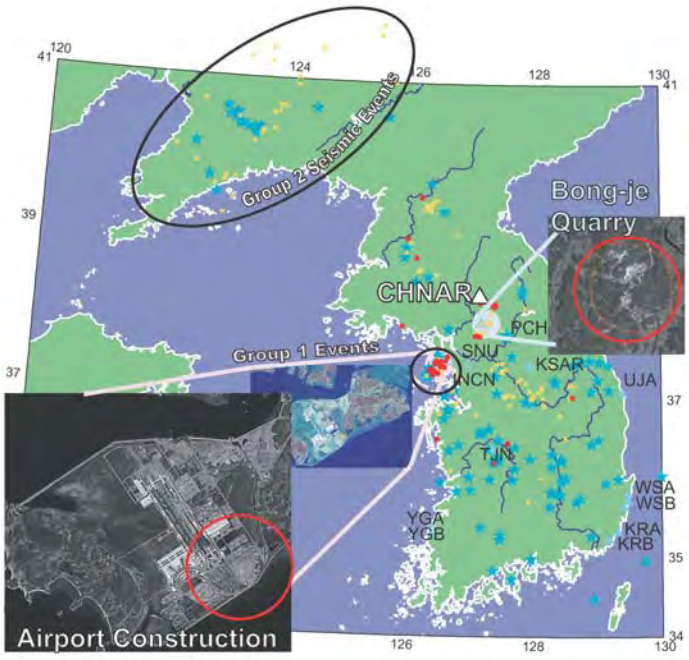

Figure 1. The map shows the events located on the basis of two months of CHNAR data. Seismo-acoustic events are shown as solid red dots; seismic events without acoustic signals are shown as yellow dots; events from the Korean NDC bulletin are marked as blue stars; and ground-truth studies based on event locations are highlighted as solid pink and blue circles. The broadband stations, the existing seismo-acoustic research array CHNAR, and the IMS array KSAR are light blue triangles. The inset images are taken from Landsat-7 satellite imagery and show two of the verified sources. (adapted from Stump *et al.*, 2000)

Intra-plate earthquakes are observed in and around the Korean Peninsula (Jun, 1991; Jun and Kulhanek, 1991; Kim, 1980). Focal mechanisms for 22 of the largest events in the last century (Jun *et al., 1999)* show predominantly strike-slip faulting with a small amount of thrust. The average compressional axis trends ENE to WSW across the entire Peninsula , which suggests the peninsula, is a single tectonic region and possibly single seismic structure. In NE China, the Tan-Lu fault is a particularly active source region. This left-lateral fault system may have originated the 1975 Haicheng earthquake. The peninsula also has an active mining industry. Near-surface mining explosions generate regionally observed seismic and acoustic signals (Hagerty *et al.*, 1999). Sorrels, Herrin and Bonner (1997) have used such acoustic signals recorded at TXAR to identify mining explosions in southwestern New Mexico.

RESEARCH ACCOMPLISHED

In the last year, the work has focused on four areas: (1) Quantifying wind as a source of seismic and acoustic noise; (2) Constraining propagation path effects in the atmosphere and earth; (3) Determining event origins; (4) Characterizing source types. The following discussion is organized into these four areas.

Quantification of Wind as a Source of Seismic and Acoustic Noise

Seismic and infrasound noise analysis was undertaken for a twenty-day period (Day 30-49, 2000) during which the sites were snow covered. The purpose was to quantify the absolute seismic and acoustic noise levels at the array elements, the variation of each with local winds, and the relationship between seismic and acoustic noise.

Infrasound

The infrasound noise estimates for a representative array element (CHN00) are given in Figure 2 (left). Microbaroms show as a noise peak between 4 and 8 s. The effect of wind on spectral noise levels is shown in Figure 2 (right). Wind speed is measured10 m above ground at the array hub (CHN00). Below 4 Hz, noise levels increase with winds in excess of 1-2 m/s. Hedlin *et al*., 1999, have reported similar effects.

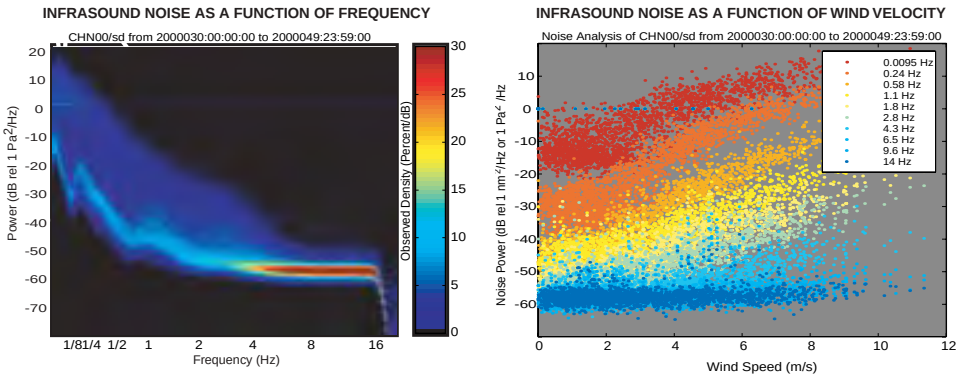

Figure 2: The power-normalized probability density as a function of frequency of 20 days of infrasound noise at CHN00 is plotted to the left. Noise power as a function of wind speed for different narrow band frequencies are plotted to the right.

Seismic

The same methodology was used to investigate wind generated seismic noise. Representative seismic noise plots superimposed on the low and high seismic noise models are reproduced in Figure 3. Although some time periods approach the low noise model levels, the most probable level is at least 10 dB higher, still well below the high noise model.

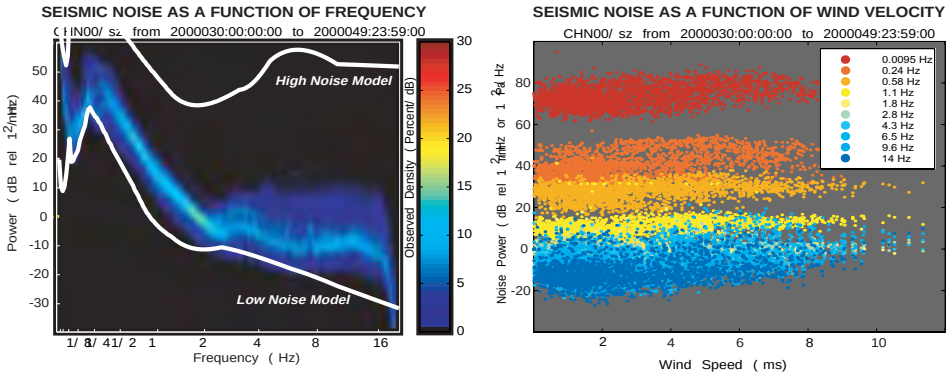

Figure 3: The power normalized probability density for 20 days of seismic noise at CHN00 is plotted as a function of frequency to the left. Noise values for different center frequencies are plotted as a function of wind speed to the right.

The low observed seismic noise is consistent with the borehole seismometer installation in competent rock. The seismic noise to wind velocity dependence is further illustrated in Figure 3 (right). Like the infrasound noise, for any one frequency band the seismic noise varies by 20 dB or less. There is little correlation between seismic noise and wind speed, thus this 20 dB is the controlling factor in the total seismic noise estimates. The lack of noise-wind correlation is consistent with the 10 m borehole and the low coupling the atmospheric pressure variations to seismic coupling in the site s hard rock. The peak in the seismic noise at 5s (Figure 3), the microseisms, occurs at nearly the same frequency as that in the infrasound data, the microbaroms (Figure 2). The similar peak period is consistent with a common cause for low frequency seismic and infrasound noise as suggested by Donn and Posmentier (1967)

Constraining Propagation Path Effects in the Atmosphere and Solid Earth

Seismic

Wave propagation characteristics across the Korean Peninsula must be quantified to interpret the seismograms recorded at CHNAR. Fortunately, there are many seismographs on the Peninsula including KIGAM s broadband network (Figure 1) and the IMS array KSRS. Data from these stations for a preliminary event set (Table 1 and Figure 4) was obtained to constrain estimates of propagation path effects.

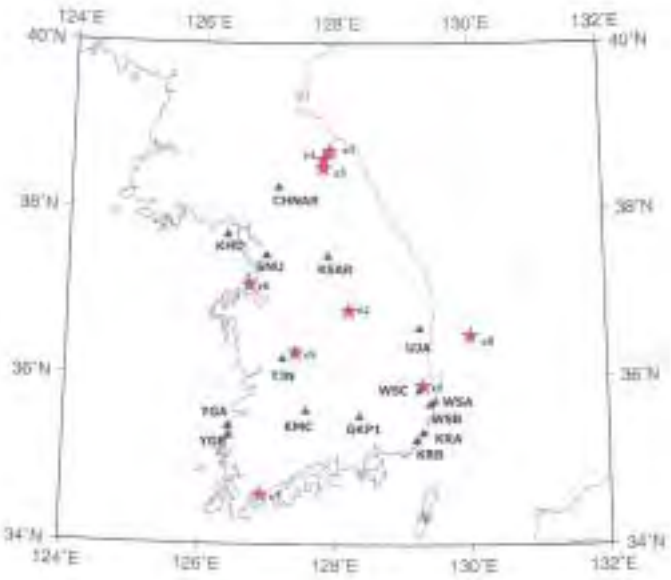

Figure 4: The map shows events (red stars) and seismic stations (blue diamonds) that were used in the preliminary wave propagation effects and source effects study.

Table 1. The table shows origin time and magnitude of 9 events located by KMA (Korea Meteorological Administration) and used to select a seismograms from stations on the Korean Peninsula.

Event No.	Origin time(GMT)		Location (Degree)		Mag.	Focal Depth (km)
	Mon-Day-Year	Hour-Min-Sec	Lat.	Lon.		
E1	9-11-99	20-56-53.0	35.9	129.3	3.2	5.9
E2	12-27-99	03-29-19.9	36.8	128.2	3.0	3.45
E3	01-18-00	06-08-49.5	38.7	127.9	3.0	14.3 ?
E4	05-11-00	06-01-08.4	38.6	127.8	2.9	0
E5	07-23-00	22-00-00.1	38.5	127.8	3.0	0
E6	10-27-00	22-10-11.8	37.1	126.7	2.7	Sea
E7	12-02-00	07-53-40.0	34.6	126.9	3.1	?
E8	12-09-00	09-51-00.0	36.5	130.0	3.7	Sea
E9	12-21-00	23-19-38.5	36.3	127.4	2.7	?

Figure 4 summarizes the event locations for events in Table 1 and shows the location of regional seismic stations. Events 1-2 and 7-8 are associated with earthquakes recognized by the KMA. Based upon associated infrasound signals at CHNAR, events 3-5 are explosions. This event set provides an opportunity to study both wave propagation through the peninsula and waveform characteristics associated with particular source types. As an example, consider the unfiltered record section from event 7 (Figure 5). At nearest stations P_g is the first arrival; beyond 150 km P_n is first. The largest phase associated with this earthquake is L_g. A R_g phase can be identified at stations less than 200 km from shallow events. At about 100 km, PmP is a strong phase. Such data provides important constraints upon regional propagation models. Figure 5 illustrates that modest magnitude (3.1) earthquakes can provide significant waveform data for constraining these models.

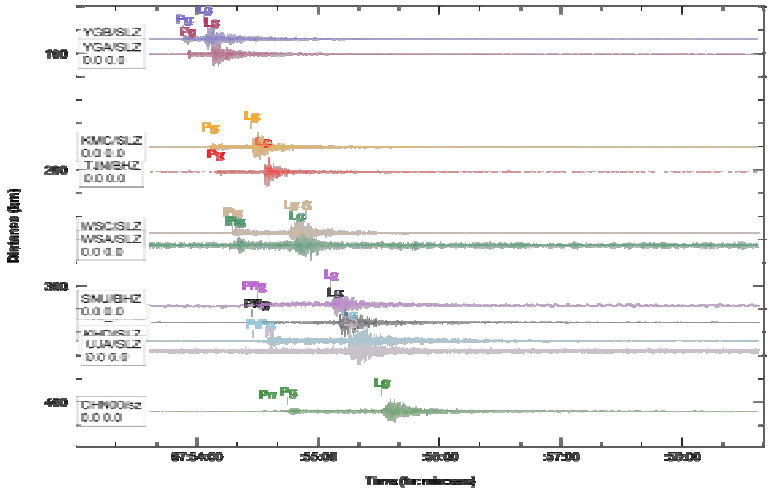

Figure 5: A record section shows waveforms from the stations from the KIGAM broadband network for Event 7 (Table 1 and Figure 4).

Infrasound

Stump et al.(2000) found that approximately one quarter of all seismic events recorded at CHNAR have associated infrasound signals. These events are attributed to mining explosions. At CHNAR they observed an average of three to four seismic events and one seismo-acoustic event per day. Analysis of the acoustic data suggested that there were many more acoustic signals than seismic. This observation motivated a more in depth analysis of the acoustic data at CHNAR in hopes of building a database useful for studying acoustic wave propagation effects. Seven days of CHNAR acoustic data were analyzed for each of October, November, February, April, June and August. Figure 6 summarizes the approach azimuth and time of day of these signals as determined by processing the array data.

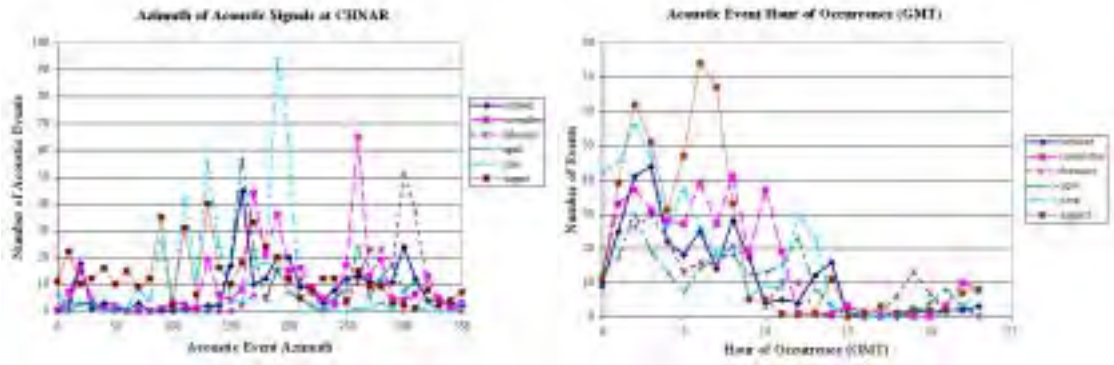

Figure 6: The azimuth of acoustic events from CHNAR as a function of month of year is displayed to the left. One-week periods of data from the months of October, November, February, April, June and August were analyzed. The hour (GMT) at which each of the events occurred is displayed to the right.

An average of nearly 50 coherent acoustic signals per day was observed on the CHNAR array, ten times more than the number of coherent seismic signals. Figure 6 (left), illustrates that the acoustic signals observed at CHNAR come from distinct azimuths that vary with month, possibly reflecting changes in regional wind patterns. For example, a large number of signals were observed between 80 and 140 degrees during June and August but not other months. These events are probably man made since they occur during normal work hours (Figure 6 right).

Locating the Sources of the Waves

Seismic

The network seismic data for the analyzed events (Table 1 and Figure 4) provide an initial resource to develop empirical travel time curves for the Korean Peninsula. Such curves may then be compared to complementary work (Lee, 1979; Kim et al., 1983; Kim et al., 1985; Kim, 1995; Kim et al., 1997; Kim et al., 1998a; Kim et al, 1998b). Using this data in a complete waveform modeling exercise will more fully resolve the distance and source contributions effects in observations. As a first step to understand the propagation in Korea, arrival time picks of all regional phases were made using the KMA event locations. The velocities of P_n, P_g, L_g phase were calculated as 8.2 km/sec, 6.6 km/sec, and 3.8 km/sec (Figure 7) respectively with individual arrival time errors as large as 5-10 s.

Event locations reported in Stump et al., 2000 used the simple relationship distance $X= (t_{Lg} - t_p)$ Æ 8 to produce single array locations from L_g-P time and back azimuth estimates from CHNAR. The data reproduced in Figure 7 suggests that for distances shorter than the P_g to P_n crossover, 155 km, that the simple distance estimate is $X_{<155} = (t_{Lg} - t_{Pg})$ Æ 8.9 and that beyond the crossover distance the simple estimate is $X_{>155} (t_{Lg} - t_{Pn})$ Æ 7.1. As Figure 5 illustrates, P_n is an emergent arrival that is over shadowed by P_g and so for small magnitude events care must be taken that P_n is indeed the identified first arrival used for estimating distance. For single array locations phase velocity measurements from the array can confirm phase identity.

Infrasound

Most seismo-acoustic signals (Figure 1) are 30 to 200 km from the array. These locations are based upon the seismic data and its association with an infrasound arrival (Stump et al., 2000). Locating acoustic-only signals requires an atmospheric velocity model. The first approach is to use an Effective Sound Velocity Structure (ESVS) based upon average seasonal variations in winds. Such a model predicts that between 30 to 200 km from the source, there will be no arrivals.

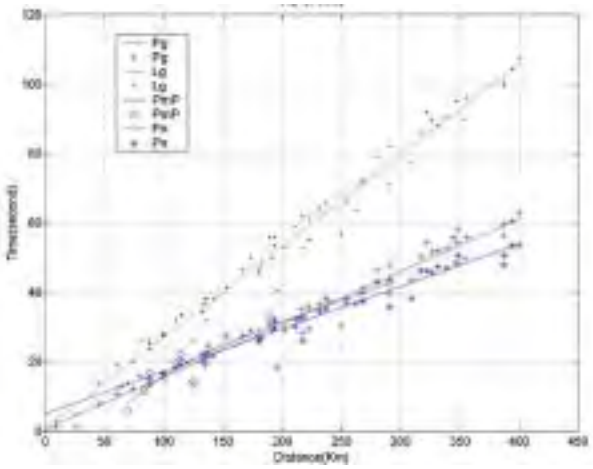

Figure 7: The figure shows arrival time data from the nine events in Table 1 based upon the KMA locations and the estimated travel time for each of the individual phases. A linear least square fit has been made to the picks.

At CHNAR, all observed seismo-acoustic signals fall within this theoretical blind zone. Arrivals in this range can be produced by tropospheric wind generated turning rays (Garc s et al ., 1998). Hagerty et al. (1999) attribute a troposphere duct to the infrasound first arrival from Kazakhstan mining explosions 250 km away. They also report that seasonal variations in troposphere winds lead to significant variations in the signal detectability. Che et al. (2000) have compared acoustic propagation in Korea based a seasonally averaged ESVS and a model with a troposphere based on regional meteorological observations. The seasonally averaged ESVS for October predicts no arrivals out to 220 km for paths traveling from S80W and only a single, low atmospheric arrival at close range from N80E.

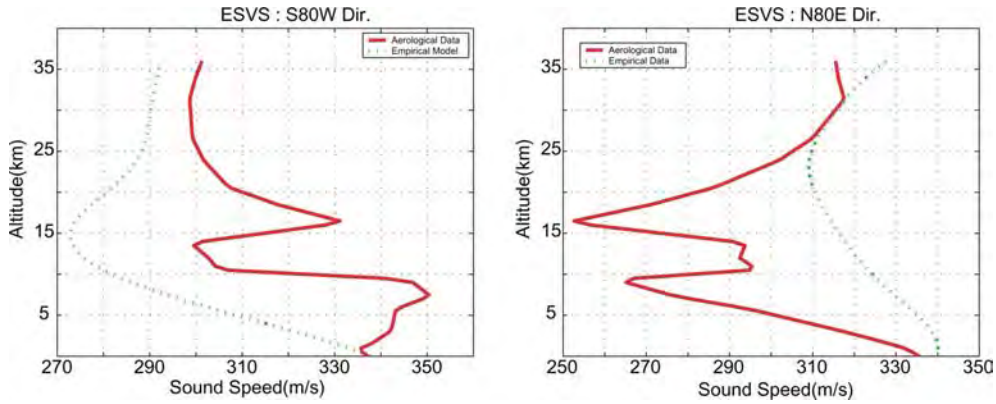

Figure 9. The figure shows a comparison of ESVS model for October in Korea (dotted line) with velocity model developed from meteorological observations in the troposphere. The left figure is for direction S80W and the right figure is for N80E.

Figure 9 compares the average October troposphere model with a model modified by local meteorological observations in October at Osan, Republic of Korea. The strong effect of low altitude winds is illustrated with ray tracing through the troposphere in the modified model (Figure 10). The velocity increase below 8 km for the S80W path provides a duct for the infrasound arrivals from 50 to 250 km away. Such troposphere ducting may result in the reported infrasound observations. This illustrates the importance of using local meteorological data during infrasound interpretation.

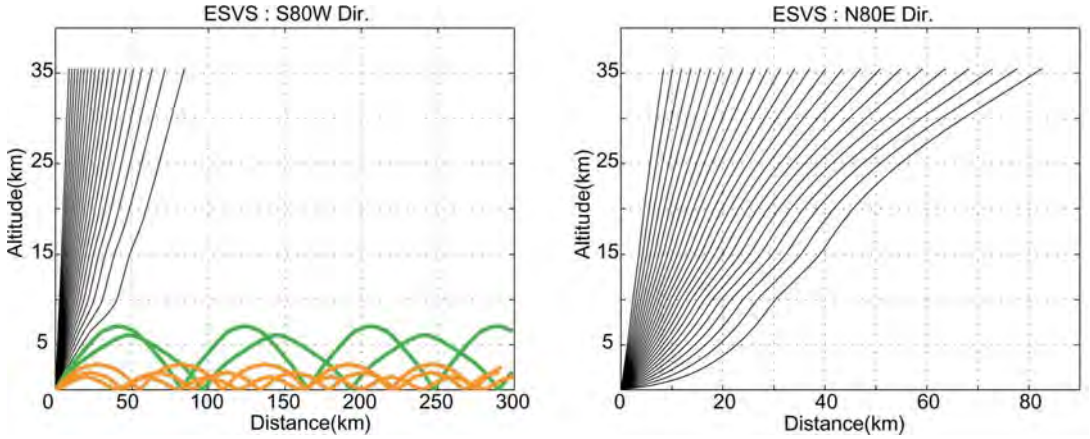

Figure 10. Plots show ray tracing through troposphere model based upon meteorological data. The left figure is for S80W and right figure is for N80E.

Characterizing Source Type

Seismic

Combining seismic and infrasound data can provide improved event characterization and identification. Regional seismic signatures indicative of a shallow explosive source include observations of strong high frequency P wave energy relative to L_g (Hartse et al., 1997) and short period R_g energy although regional attenuation along the propagation path can also affect P to L_g ratios and the R_g propagation degrades beyond 100-200 km . The preliminary data (Figure 4) provides an assessment of these propagation path effects. Figure 11 compares high frequency 8-10 Hz data from Event 7, an earthquake from the far southern tip of Korea and Event 4, an event from the north with an associated infrasound signal (Table 1). For event 4, R_g is observed at close stations such as CHNAR. For event 4, the P energy is dominant while for event 7 L_g dominates over P.

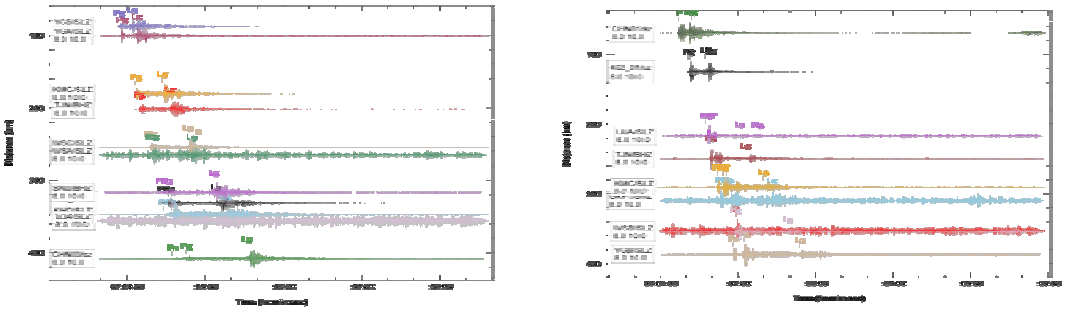

Figure 11: The left record section shows bandpass-filtered seismograms (8-10 Hz) from Event 7 (earthquake) and the right shows Event 4 (explosion based on accompanying infrasound signal).

Based on the network data reproduced in Figure 11, the relationship between P and L_g energy is insensitive to range. Detailed studies of the network data provide additional constraints on the regional Q structure across the Korean peninsula and a more detailed physical assessment of the contribution of propagation path effects to the regional phases.

Ground truth data provide the opportunity to further investigate the characteristics of seismic and acoustic signals and relate them to the source. A cluster of seismo-acoustic events 100 km to the SW of CHNAR was identified (Figure 1) and associated with the construction of Seoul s new Inchon International Airport. Overhead imagery of the construction site is included in Figure 1. Video images of the construction explosion indicate that besides the main blast designed to fracture the material for removal, additional nearly unstemmed explosives may be used to break individual rocks too large to remove mechanically. These additional blasts may radiate significant infrasound energy. The total blast duration is about 300 ms. Ground truth information, including some near-source seismic records, have been obtained from five mining and construction operations across the Republic of Korea. This information is used to assess the source size and characteristics and the associated seismic and infrasound signals. No explosions in this set exceed 3000 kg and many are much smaller, consistent with the small size of seismic signals reported for many of the seismo-acoustic events in Stump et al., 2000. A short event duration, 300 ms for the event at Inchon International Airport, is consistent with a small size explosive.

CONCLUSIONS AND RECOMMENDATIONS

1. Infrasound noise at CHNAR is strongly dependent upon near-surface wind velocity but seismic noise is almost independent of observed wind velocity.
2. The frequency locations of the amplitude peaks are the same for both microbaroms and microseisms.
3. In and around the Korean Peninsula, regional earthquakes and explosions are observed well beyond 400 km and can provide the basis for separating propagation and source effects at regional distances. Energy in excess of 8 Hz from these small events is efficiently transmitted along these propagation paths.
4. KIGAM broadband network data provides data for travel time analysis and waveform modeling. A preliminary velocity model has been developed from this data with Pn, Pg and Lg velocities of 8.2, 6.6 and 3.8 km/s. A modified single array location procedure is proposed based upon this preliminary model.
5. Infrasound signal travel paths in the 30 to 200 km range can be explained by local tropospheric winds and therefore local metrological must be included in the models.
6. There are nearly ten times more acoustic signals observed at CHNAR than seismic. Analysis of selected time windows over one year suggests that signal source location changes with time. Repeated signals are observed over $< -5^{o}$ azimuth bands during certain times of the year.
7. Evidence exists for the efficient generation of high frequency P energy relative to Lg for explosions over a large range of source to receiver distances suggesting that propagation path effects are secondary to this source effect.
8. Ground truth on mining explosions suggests that the majority of industrial explosions are < 3000 kg and < 300 ms total duration consistent with small, high frequency regional signals.

REFERENCES

Che, Il-Young, J.-S. Jeon and M.-S. Jun (2000). Infrasound wave propagation characteristics in Korea.

Donn, W. L. and E. S. Posmentier (1966), Infrasonic waves for the marine storm of April 7, *J. Geophys. Res., 72,* 2053.

Garc s, M. A., R. A. Hansen and K. G. Lindquist (1998), Traveltimes for infrasonic waves propagating in a stratified atmosphere, *Geophys. J. Int., 135,* 255-263.

Hagerty, M.T., W.-Y. Kim and P. Martysewvich (1999). Characteristics of Infrasound Produced by Large Mining Explosions in Kazakhstan, in Proceedings of the 21st Annual Seismic Research Symposium on Monitoring A Comprehensive Test Ban Treaty, 21-24 September 1999.

Hartse, H.E., S.R. Taylor, W.S. Phillips and G.E. Randall (1997). Preliminary Study of Seismic Discrimination in Central Asia with Emphasis on Western China, *Bull. Seism. Soc. Am., 87,* 1464-1474.

Jun, M.-S., J.-S. Jeon and I.-Y. Che (1999). Earthquake Mechanism of Korean Peninsula, *in preparation.*

Jun, M.-S. (1991). Body-Wave Analysis for Shallow Intraplate Earthquakes in the Korean Peninsula and Yellow Sea, *Tectonophysics, 192,* 345-357.

Jun, M.-S. and O. Kulhane (1991). Source Parameters of Earthquakes In and Around the Korean Peninsula Deduced from Spectral Analysis, *Physics of the Earth and Planetary Interiors, 65*, 255-266.

Kim, S. J. and S. G. Kim (1983), A study on the Crustal Structure of South Korea by using Seismic Waves, Jour. Korean Inst. Mining Geol., Vol. 16, NO. 1, P. 51-61.

Kim, S. K. and B. H. Jung, (1985), Crustal Structure of the Southern Part of Korea, Jour. Korean Inst. Mining Geol., Vol. 18, NO. 2, P. 151-157.

Kim, S. K. (1995), A study on the Crustal Structure of the Korean Peninsula, The Journal of the Geological Society of Korea, Vol. 31, No.4, p. 393-403.

Kim, S.G. and S. K. Lee (1997), Determination of Lateral Variations for Pn Velocity Structure Beneath the Korean Peninsula Using Seismic Tomography, Econ. Environ. Geol., Vol. 30, No. 6, p. 625-635.

Kim, S. G. and Z. Wu (1997). Uncertainties of Seismic Source Determination Using a 3-Component Single Station, *J. Phys. Earth, 45,* 1-11.

Kim, S.G. and Q. Li (1998), 3-D Crustal Velocity Tomography in the Southern Part of The Korean Peninsula, Econ. Environ. Geol., Vol. 31, No. 2, p. 127-139.

Kim, S.G. and Q. Li. (1998), 3-D Crustal Velocity Tomography in the Central Korean Peninsula, Econ. Environ. Geol., Vol. 31, No. 3, p. 235-247.

Kim, W. Y., D. W. Simpson, and P. G. Richards (1994). High-frequency spectra of regional phases from earthquakes and chemical explosions, , *Bull. Seism. Soc. Am., 84,* 1365-1386.

Lee, K (1979), On Crustal Structure of the Korean Peninsula, The Journal of the Geological Society of Korea, Vol. 15, No.4, p. 253-258.

McKisic, J. Michael (1997). Infrasound and the Infrasonic Monitoring of Atmospheric Nuclear Explosions: A Literature Review, Phillips Laboratory Technical Report, PL-TR-97-2123, 28 February 1997, Phillips Laboratory, Hanscom AFB, MA 01731-3010

Stump, B., C. Hayward, S.M. House, M.-S. Jun and J.-S. Jeon, 2000. A Small Aperture Seismo-Acoustic Array, Signals Assessment, in Proceedings of the 22nd Annual Seismic Research Symposium in Monitoring A Comprehensive Test Ban Treaty, September 2000, New Orleans, LA.

BAYESIAN TOMOGRAPHY APPLIED TO SEISMIC EVENT IDENTIFICATION PROBLEMS

Steven R. Taylor, Aaron A. Velasco, Xiaoning (David) Yang, Monica Maceria, and W. Scott Phillips

Los Alamos National Laboratory

Sponsored by National Nuclear Security Administration
Office of nonproliferation Research and Engineering
Office of Defense Nuclear Nonproliferation

Contract No. W-7405-ENG-36

ABSTRACT

The advantages of a Bayesian approach to tomography are that large-scale and high-resolution tomographic models available from other well-accepted studies can be used as prior background models. The resulting refined tomographic model blends into these prior background models. Moreover, the error budget is well established in a Bayesian framework. We assume a general linear Gaussian (least squares) model, where the covariance matrix is partitioned into data and prior model components. Uncertain data are naturally down weighted and certain model components will be subject to small perturbations.

Bayesian attenuation tomography (Tarantola, 1987) is being incorporated into the Magnitude and Distance Amplitude Correction (MDAC) methodology used for amplitude corrections to seismic discriminants (Taylor *et al.,* 1999). Because a signal-to-noise criterion is used to select amplitudes for the inversion, the data are left-censored and the resulting Q_0 models will be biased high. We examine the utility of the Expectation Maximization (EM) algorithm to the left-censored data problem (Dempster *et al.*, 1977). In this case, we can define only an upper bound to measured amplitudes based on pre-phase noise. The EM algorithm can be used to fill in the missing data values with their conditional expectation based on the relationship of amplitudes with other related completely observed variables. We have initially chosen a bivariate Gaussian model for filling in missing amplitudes based on the relationship between amplitude and pre-phase noise. The methodology can be extended to the multivariate case by the incorporation of other variables such as magnitude and distance, background noise, and Pn velocity tomography.

We apply the technique to eastern Asia for Pn, Pg, Sn, and Lg signals at 1 Hz using data from 1651 earthquakes recorded at 12 stations. Tomographic patterns correlate well with those expected from geophysical considerations (e.g. high attenuation in Tibet and low attenuation up into the stable regions of Kazakhstan). Interestingly, many of the large cratonic basins surrounding the Tibet Plateau (e.g. Tarim, Junggar) show reduced attenuation. Application of the EM algorithm tends to increase attenuation in Tibet (particularly western Tibet) and the cratonic basins to the north of but not to the east of Tibet.

We are refining regionalized surface slowness models in a number of regions for surface wave magnitude measurements to be used for m_b — M_S discriminants. Regional M_S can be measured at lower magnitudes through the application of phase-match filters. The filters can be constructed from tomographic group velocity maps from which path-specific dispersion curves can be calculated. Global and regional group velocity maps are available from previous studies (e.g., Stevens and Adams, 2000; Levsin et al., 2000) and Bayesian slowness tomography provides a framework for utilizing existing global and regional models as priors on which to improve resolution in specific regions.

Tomography provides only an approximation to the propagation effects a seismic wave may experience. For example, phase blockage can occur over relatively short distances in the absence of any anelastic effects. Station-centric kriged amplitude or slowness correction surfaces on top of the tomographic models may assist in quantifying departures from the smooth tomographic model (Pasyanos, 2000).

KEY WORDS: seismic, attenuation tomography, Bayesian, surface waves, magnitude, discrimination

OBJECTIVE

Our work to date involving MDAC (Magnitude and Distance Amplitude Corrections; Taylor and Hartse, 1998; Taylor *et al.,* 1999) corrections to seismic discriminants has combined simplified one-dimensional propagation models with kriged surface corrections. As pointed out by Taylor and Hartse (1998) the amplitude residuals to the 1D propagation models can be spatially averaged in some way to account for deviations (*e.g.* unmodeled lateral variations in Q and/or geometrical spreading). Bayesian kriging (Schultz *et al.,* 1998; Phillips, 1999; Rodgers *et al.,* 1999) provides a useful way for computing amplitude correction surfaces and propagating errors. However, kriging is a purely empirical approach and provides little or no information in data-poor regions. Thus, it is necessary to refine the 1D models to more realistic, physically based, spatially varying propagation models. One approach we discuss in this report is the incorporation of phase amplitude attenuation tomography into the MDAC procedure.

Attenuation tomography is a well-established method that has been used for many years (e.g. Young and Ward, 1980; Singh and Herrmann, 1983; Mitchell *et al.,* 1997). Phillips *et al.,* (1999) have recently investigated the utility of attenuation tomography for correcting seismic discriminants using 1 Hz Pg/Lg amplitude ratios. In subsequent work, we have tested 1 Hz Lg amplitude tomography (Phillips *et al.,* 2000) with promising results. In this report, we discuss an extension of the amplitude tomography method using a Bayesian framework (Tarantola, 1987). As will be discussed further in the methodology section, Bayesian methods are more general than standard least squares methods. An advantage of the Bayesian approach to tomography is that the posterior model will blend into the prior background model. The prior model can be a well-accepted global model that can contain constraints from detailed studies in specific regions. For example Xie (pers. comm., 2001), included results from PASSCAL experiments within Tibet that suggest attenuation within the plateau is greater than that calculated using data crossing the entire plateau (which may be due to a data censoring problem discussed below).

Importantly, the error budget is very well defined in a Bayesian approach. The covariance matrix is partitioned into data and prior model components. Uncertain data are naturally down weighted and certain model components will be subject to small perturbations. For example, matrix-conditioning problems are handled by inclusion of a prior model and associated uncertainties in the model and data (as opposed the relying on the selection of a poorly constrained ridge or damping parameter).

Because a S/N criterion is used to select paths used in the inversion, the data are left-censored. This means that the points below a certain S/N noise threshold are eliminated from the inversion causing the resulting Q_0 values to be biased high. The data censoring may be due to effects such as phase blockage, phase conversion (e.g. Lg to Sn scattering in a basin) amplitudes below detection thresholds from magnitude and distance effects, or transmission through high attenuation paths. In this study, we examine the utility of the Expectation Maximization (EM) algorithm to the left-censored data problem (Dempster *et al.*, 1977). In this case, we can only define an upper bound to measured amplitudes based on pre-phase noise. The EM algorithm can be use to fill in the missing data values with their conditional expectation based on the relationship of amplitudes with other related completely-observed variables.

In this report, we first describe the Bayesian approach to attenuation tomography where the EM algorithm is used to fill in missing amplitudes with their conditional expectations based on pre-phase noise measurements. We then discuss application to regional phases in central Asia.

RESEARCH ACCOMPLISHED

Bayesian Tomography

The tomographic equations to be solved are given by

$$D_{ij} = S_i + P_j - k\sum_m \alpha_m r_{ijm} \qquad (1)$$

where $D_{ij} = A_{ij} — G(r,r_0)$ is the amplitude from source i to receiver j corrected for geometrical spreading, k is a constant, α_m is the attenuation coefficient and r_{ijm} is the normalized chord length in cell m used to parameterize the imaged area. Equation (1) forms a linear system of equations that can be solved for the attenuation coefficients, source, and site terms. To solve the system of equations (1) we use the Bayesian approach of Tarantola (1984).

Application to Eastern Asia

The Baysian tomographic inversion was applied to a data set of earthquakes and explosions in eastern Asia (Figure 1). RMS measurements from regional seismograms were computed using the processing described in Hartse *et al.,* (1997). We converted the RMS measurements to pseudo displacement spectra using a technique described in Taylor *et al.,* (2001) based on Parseval s Theorem. We preformed the inversion on Pn, Pg, Sn, and Lg signals at 1 Hz and will discuss the Lg results in this report. Data were selected from 12 stations AAK, BRVK, ENH, KURK, LSA, LZH, MAKZ, NIL, TLY, ULN, WMQ, and XAN.

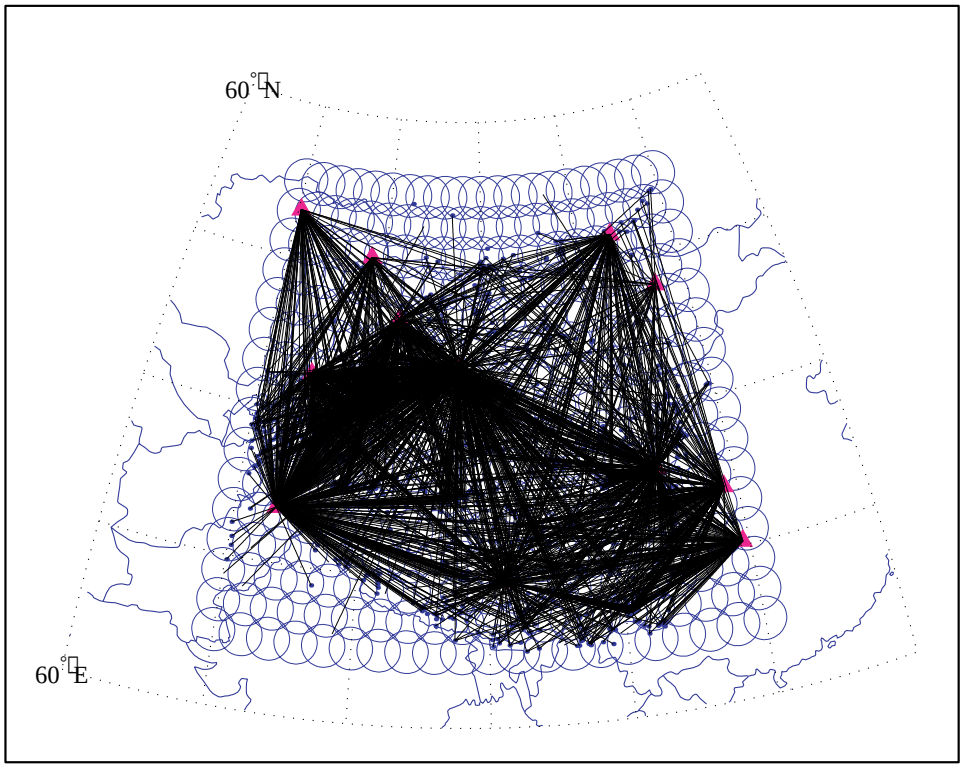

Figure 1. Map showing event-station paths and grid used in tomographic inversion.

Using pre-phase noise, we included spectral values having a signal-to-noise (S/N) ratio greater than 0. This resulted in a total number of 2855 paths from 1651 events shown in Figure 1. The region is parameterized into a grid of small circles evenly spaced at 2-degree increments. To insure complete coverage, the radius of each small circle is given by the grid spacing times $\sqrt{2}/2$. Based on our work in Phillips *et al.,* (2000) we used a 2° grid spacing.

We used the 3° Eurasia Lg coda Q model and associated errors of Mitchell *et al.,* (1997) as the prior attenuation and covariance model. The priors for the site terms, P_j, were set to zero. The prior errors on the site terms can be used as a way to damp the solution. For example, the prior errors on the site terms can be set to zero to fix them. For the source terms, it would be most desirable to have regional seismic moments for each event. Because the moments were not available, we used a regional moment-magnitude scale for Pn of Patton (1999).

As with the site terms, prior errors can be specified for the source terms. Setting the errors to zero will tie directly to m_b. A direct tie to m_b in regional attenuation studies (e.g. Phillips *et al.,* 2000) is undesirable because upper mantle bias may be mapped into the tomographic models. By specifying source term errors, we can allow the source terms to adjust which can absorb some of the problems associated with m_b bias and source scaling. Unaccounted source scaling (e.g. corner frequency) effects can be absorbed in the source terms without having to specify a given source model or scaling relationship. The data errors are used to control the importance (weighting) of each data value. Initially, we have chosen an ad hoc approach to weight the data based on S/N. A more rigorous statistical formulation will be used in future work.

The tomographic map for Lg attenuation is shown in Figure 2. We obtained a variance reduction of 27% over the prior model. The model is similar in many respects to that shown in Phillips *et al.,* (2000). The main differences are on the edges of the model where the Bayesian tomography blends into the background model of Mitchell *et al.,* (1997; Figure 3). As pointed out by Phillips *et al.,* (2000), the tomographic patterns correlate well with that expected from geophysical considerations (e.g. high attenuation in Tibet and low attenuation up into the stable regions of Kazakhstan). Interestingly, many of the large cratonic basins surrounding the Tibet Plateau (e.g. Tarim, Juggar) show reduced attenuation. As discussed by Whitted *et al.,* (1999), it may be that some of these large basins are thought to represent regions of stronger lithosphere relatively undeformed by the Indo-Asian continental collision and thus are regions of lower attenuation.

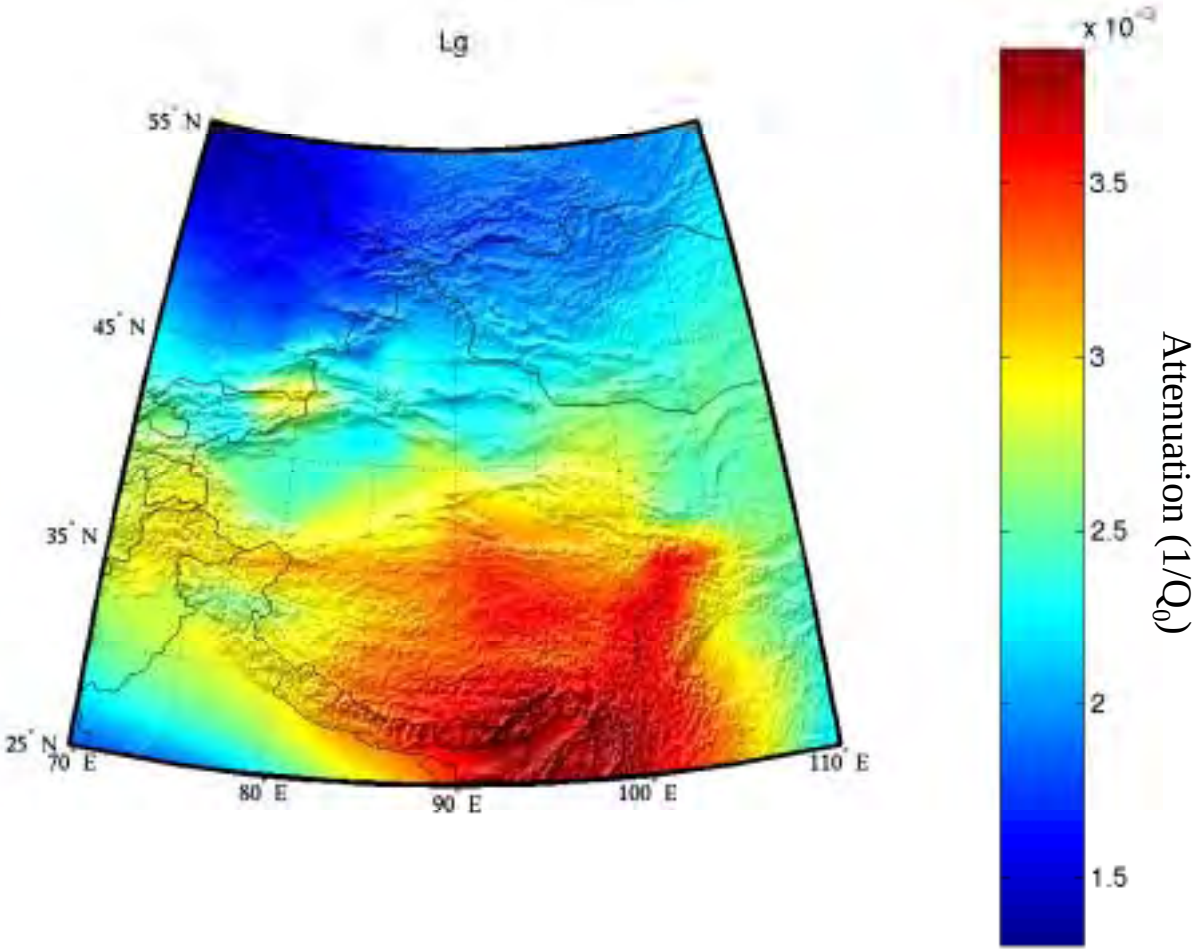

Figure 2. Attenuation tomography map for Lg. Red indicates high attenuation and blue low attenuation.

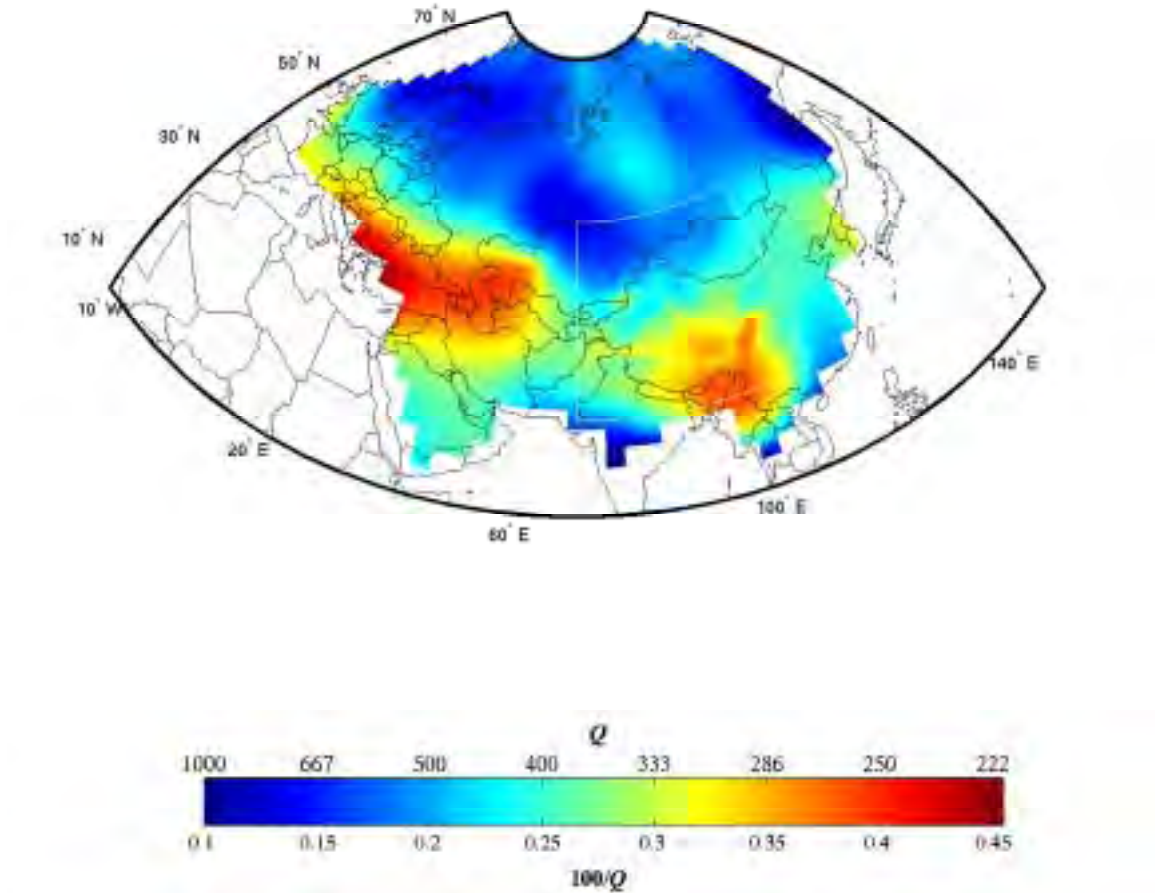

Figure 3. Two degree attenuation tomography map for 1 Hz Lg of Figure 2 (white outline) blending into 3 degree Lg coda Q map of Mitchell *et al.* (1997).

Figure 4 shows Kriged tomographic amplitude residuals at station WMQ using the Bayesian kriging algorithm of Schultz *et al.* (1998). These maps can be used as station-centric amplitude correction surfaces to the tomographic model and can be used to identify phase blockages. A number of interesting features can be observed from these maps. For example, the strong effects of the Tibetan Plateau on Lg can be observed. Also, a region of enhanced Lg amplitudes is observed to the east of the Tsaidam Basin.

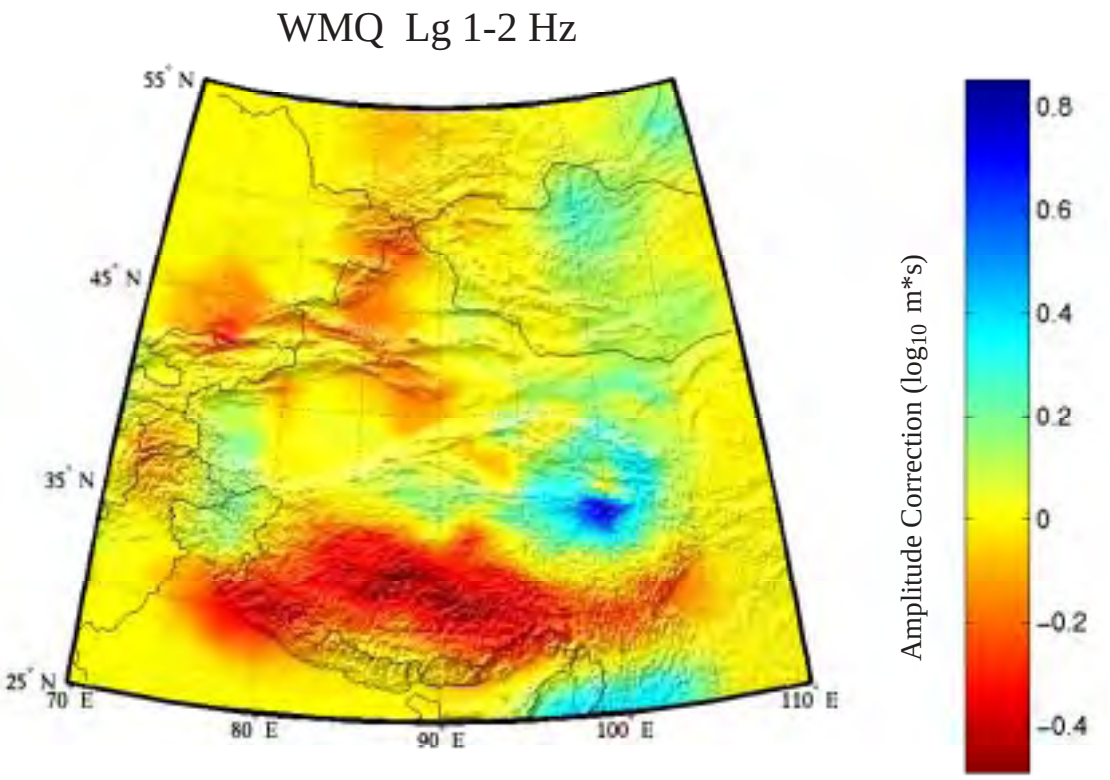

Figure 4. Kriged tomographic residuals for WMQ.

Application of the Expectation Maximization Algorithm to Left-Censored Data

Because a S/N criterion is used to select paths used in the inversion, the data are left-censored. This means that the points below a certain S/N noise threshold are eliminated from the inversion causing the resulting Q_0 values to be biased high. The data censoring may be due to effects such as phase blockage, phase conversion (e.g. Lg to Sn scattering in a basin) amplitudes below detection thresholds from magnitude and distance effects, or transmission through high attenuation paths. In this study, we examine the utility of the Expectation Maximization (EM) algorithm to the left-censored data problem (Dempster *et al.*, 1977). In this case, we can only define an upper bound to measured amplitudes based on pre-phase noise. The EM algorithm can be use to fill in the missing data values with their conditional expectation based on the relationship of amplitudes with other related completely-observed variables. In this example we choose a bivariate Gaussian model for filling in missing amplitudes based on the relationship between amplitude and pre-phase noise. The methodology can be extended to the multivariate case by the incorporation of other variables such as magnitude and distance, background noise, and Pn velocity tomography. An advantage of EM is that the an estimate of the censored data and associated errors can be made prior to the inversion, so that the Bayesian methodology discussed above need not change.

Figure 5 shows the difference in Q_0 for a tomographic inversion with an EM correction and for one without (Figure 2). The Q_0 values are observed to decrease in Tibet and particularly in western Tibet. Also, the Q_0 values decrease in the Tarim Basin while they are relatively unchanged in the Dzungarian Basin and in the large basins to the east of Tibet (such as the Tsaidam and Szechwan Basins).

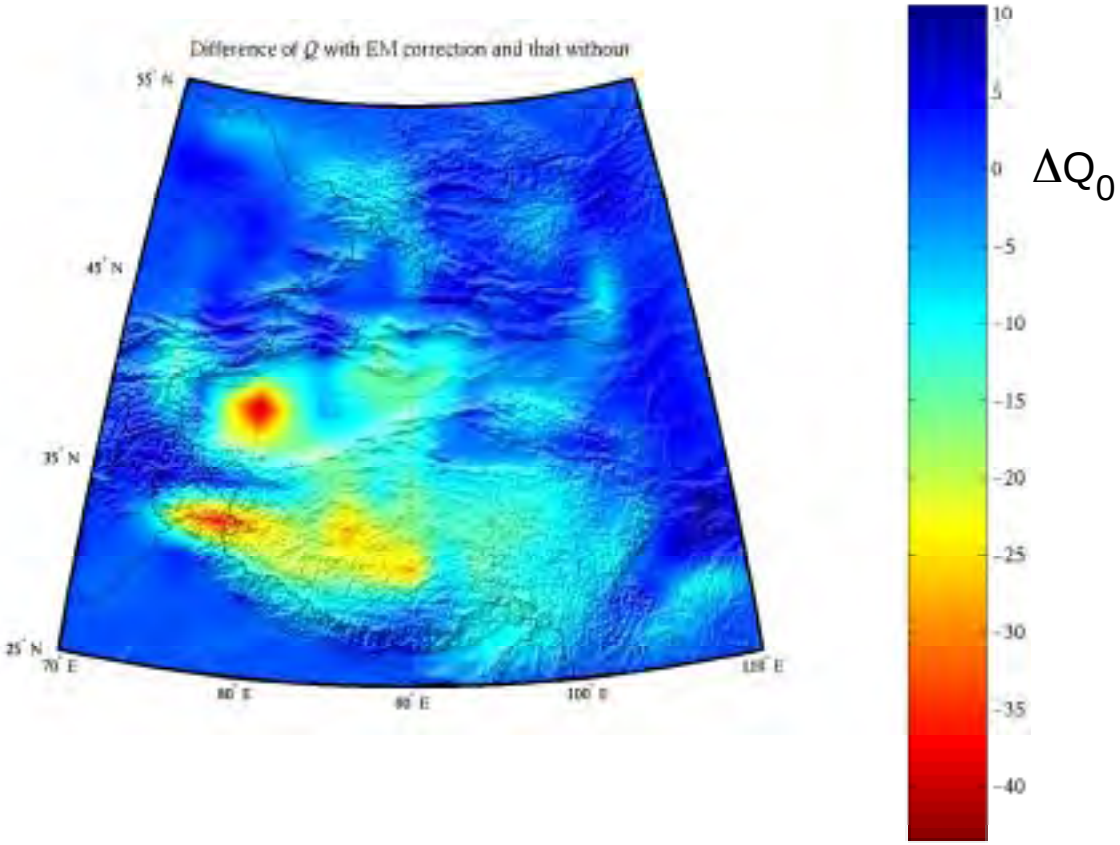

Figure 5. Difference in Q_0 between tomography with EM correction and without (Figure 2).

CONCLUSIONS AND RECOMMENDATIONS

We have begun examining the utility of Bayesian tomography to regional phase attenuation and surface slowness models. The Bayesian approach allows for refinement of available prior models in selected regions. The refined models smoothly blend into the background models. The Bayesian approach also tracks model and data errors very efficiently. We are also investigating the utility of the Expectation-Maximization algorithm for handling censored data in an effort to reduce bias in tomographic models.

REFERENCES

Dempster, A.P., N.M. Laird, and D.B. Rubin, Maximum likelihood from incomplete data via the EM algorithm, *J. Roy. Statist. Soc.,* B39, 1-38, 1977.

Hartse, H.E., S.R. Taylor, W.S. Phillips, and G.E. Randall, Regional event discrimination in central Asia with emphasis on western China, *Bull. Seism. Soc. Am.*, 87, 551-568, 1997.

Levsin, A. L., M. H. Ritzwoller, M. P. Barmin, and J. L. Stevens, Assessing abilities to estimate short period group velocities, in *Proceedings of the 22nd Annual DoD/DOE Seismic Research Symposium*, vol. 1, 67-76, 2000.

Mitchell, B.J., Y.Pan, J. Xie, and L. Cong, Lg coda Q variation across Eurasia and its relation to crustal evolution, *J. Geophys. Res.,* 102, 22,767-22,779, 1997.

Patton, H.J., Regional magnitude scaling, transportabiliy, and Ms:mb discrimination at small magnitudes, Los Alamos National Laboratory, LAUR-99-6705, submitted to PAGEOPH, 1999.

Phillips, W.S., G.E. Randall, and S.R. Taylor, Regional phase path effects in central China*, Geophys. Res. Lett*., 25, 2729-2732, 1998.

Phillips, W.S., Empirical path corrections for regional-phase amplitudes, *Bull. Seism. Soc. Am.,* 89, 384-393, 1999.

Phillips, W.S, H.E. Hartse, S.R. Taylor, A.A. Velasco, and G. E. Randall, Regional phase amplitude ratio tomography for seismic verification, Los Alamos National Laboratory, LAUR-99-1904, submitted to PAGEOPH, 1999.

Phillips, W.S, H.E. Hartse, S.R. Taylor, 1 Hz Lg Q tomography in central Asia, *Geophys. Res. Lett.,* 20, 3425-3428, 2000.

Rodgers, A.J., T. Lay, W.R. Walter, and K.M. Mayeda, Comparison of regional phase amplitude ratio measurement techniques, *Bull. Seis. Soc. Am*., 87, 1613-1621, 1999.

Rodgers, A.J., W.R. Walter, C.A. Schultz, S.C. Myers, and T. Lay, A comparison of methodologies for representing path effects on regional P/S discriminants, *Bull. Seism. Soc. Am.,* 89, 394-408, 1999.

Schultz, C.A., S.C. Myers, J. Hipp, and C. Young, Nonstationary Bayesian Kriging: A predictive technique to generate spatial corrections for seismic detection, location, and identification, *Bull. Seism. Soc. Am.,* 1275-1288, 1998.

Stevens, J. L, and D. A. Adams, Improved surface wave detection and measurement using phase-match filtering and improved regionalized models, in *Proceedings of the 22nd Annual DoD/DOE Seismic Research Symposium*, vol. 1, 145-154, 2000.

Tarantola, A., Inverse Problem Theory, Elsevier Science, Amsterdam, The Netherlands, 1987.

Taylor, S.R., and H.E. Hartse, An evaluation of generalized likelihood ratio outlier detection to identification of seismic events in western China, *Bull. Seis. Soc. Am*., 87, 824-831, 1997.

Taylor, S.R., and H.E. Hartse, A procedure for estimation of source and propagation amplitude corrections for regional seismic discriminants, *J. Geophys. Res.,* 103, 2781-2789, 1998.

Taylor, S.R., A.A. Velasco, H.E. Hartse, W. S. Phillips, W.R. Walter, and A.J. Rodgers, Amplitude corrections for regional seismic discriminants, *Los Alamos National Laboratory, Los Alamos, NM*, LAUR-99-3040, accepted PAGEOPH, 1999.

Xie, J. and H.J. Patton, Regional phase excitation and propagation in the Lop Nor region of central Asia and implications for P/Lg discriminants, *J. Geophys. Res.,* 104, 941-954, 1999.

ASSESSING LOCATION CAPABILITY WITH GROUND TRUTH EVENTS: THE DEAD SEA AND SOUTH AFRICA REGIONS

Clifford Thurber, Haijiang Zhang, and William Lutter

University of Wisconsin-Madison

Sponsored by Defense Threat Reduction Agency

Contract No. DSWA01-98-1-0008

ABSTRACT

We are combining locally derived ground truth (GT) information with analyses of regionally recorded waveform data to derive path corrections to global network stations for earthquakes and explosions in the Dead Sea and South Africa regions. Our strategy is to determine locations that are quality GT5 or better for events using "local" information, and then to treat these locations as known, fixed hypocenters in a regional joint hypocenter determination (JHD) inversion for the path corrections. We are using arrival time picks from all available waveform data from global network stations in the inversion for path corrections.

For the Dead Sea region, we are using data from 53 earthquakes and the 3 Dead Sea calibration explosions to derive local 1-D velocity models and station corrections for about 70 seismic network stations within Israel and Jordan, using JHD. The explosions are treated as sources with known (fixed) location and origin time in the JHD inversion. The resulting locations for the earthquakes are constrained quite well, with estimated 95% confidence regions ranging from 1 to 3 km in both epicenter and depth. Thus, we feel confident in treating these earthquakes as GT5 events. The next step is to use a smaller group of events with data available at regional and teleseismic distances as "master events" with fixed locations in a regional JHD solution for path corrections to global network stations. We also investigate the use of "surrogate" stations to interpolate path corrections at IMS stations without observations. For South Africa, we have obtained ground-truth information on mining-induced earthquakes from the seismology investigators (T. Jordan and D. James) who operated the PASSCAL South African craton broadband experiment. We identified 14 events having regional and teleseismic waveforms that could be used for location calibration purposes, and we were provided with locations (including depths) determined from mine records for these events. As in the case of the Dead Sea investigation, the next step is to use the larger events in our Dead Sea dataset as "master events" with fixed locations in a regional JHD solution for path corrections to global network stations. We present our results for the Dead Sea and South Africa path corrections along with an assessment of the location accuracy that can be obtained via their use. We also examine the ability to estimate IMS station path corrections using path corrections from nearby non-IMS stations. A nearest-neighbor interpolation algorithm performs well at predicting the IMS station path corrections in most cases.

KEY WORDS: location, ground truth, corrections, calibration

OBJECTIVE

We are combining locally derived ground truth (GT) information with analyses of regionally recorded waveform data to derive path corrections to International Monitoring System (IMS) and global network stations for earthquakes and explosions in the Dead Sea and South Africa regions. Our location calibration strategy is to determine locations that are quality GT5 or better for events using "local" information, and then to treat these locations as known, fixed hypocenters in a regional joint hypocenter determination (JHD) inversion for the path corrections. We are using arrival time picks from all available waveform data from global network stations in the inversion for path corrections. We then use the path corrections at non-IMS stations to estimate corrections for nearby IMS stations with no available observations and use the GT event data to assess location accuracy.

RESEARCH ACCOMPLISHED

Dead Sea region

In November 1999, three underwater chemical explosions were conducted in the Dead Sea (Gitterman and Shapira, 2001). According to the authors, the goals of that experiment were "to calibrate the regional travel times and propagation paths of seismic waves across the Middle East and the Eastern Mediterranean region and thus improve location accuracy of seismic events; to calibrate local, regional, and International Monitoring System (IMS) stations; and to provide data for source characterization to improve IMS detection, location, and discrimination capabilities." With the GT information of these three calibration explosions, we have relocated 53 regional earthquakes through JHD analysis using arrival time picks at stations in Israel and Jordan. The P-wave arrival times were determined by us from the original digital waveform data (50 events) or were obtained from the Prototype International Data Centre (pIDC) (3 events).

We performed JHD analysis using the algorithm VELEST (Kissling et al., 1994). VELEST produced a best-fitting layered velocity model, station corrections for 73 seismic network stations within Israel and Jordan, relocated event locations and origin times, and estimated uncertainties of the event locations and origin times. The GT information for these 57 events is provided in Table 1, and the event locations are plotted in Figure 1, along with the local stations.

From the above 53 earthquakes, 10 with available regional data were used in a regional JHD inversion, combined with one calibration explosion (991111) and another earthquake (991028) without ground truth information. These events are indicated with an asterisk in Table 1. Event 991028 was added based on its available arrival time data at many IMS stations. The locations and origin times for the other 11 events were restrained to those from the VELEST GT results in the JHD solution. We used velocity model ak135 in our JHD analysis. We obtained path corrections for many regional stations, including 17 IMS stations, which are presented in Table 2. The number of observations of these events using just IMS stations is too small to allow for a thorough location error analysis.

One important issue is whether or not path corrections for new IMS stations can be estimated from nearby ("surrogate") stations with a longer history of observations. We used non-IMS stations in the region less than 5° away from IMS stations to find the relationship between their path corrections. For example, IMS station HFS has four neighboring non-IMS stations (see Table 3). We interpolated an estimated HFS station correction from its neighboring stations with a two-dimensional "nearest neighbor" (NN) interpolation method. The interpolated path correction using NN is -2.09 s, in excellent agreement with the value in Table 2 (-2.17 s). We also interpolated other IMS path corrections using neighboring stations and various interpolation methods, and compared the results with the known station corrections. From the comparison, we found that the two-dimensional NN interpolation method produced superior results. Using this approach, we can interpolate path corrections at other IMS stations using their neighboring stations. The results are shown in Table 4. We note, however, that variations in station elevations may have a significant effect on this interpolation approach. This problem will receive further investigation.

South Africa region

For the South Africa region, we obtained GT data on events of magnitude 3.5 to 4.5 from T. Jordan and D. James, who had carried out a broadband seismic array study across the region in 1997-1999. These events are mining-induced earthquakes. They obtained event locations from mine operators, who run local seismic networks at the mines but do not use a standard time base, and origin times from the Geological Survey of South Africa or the ISC. The GT locations for the 14 events used are presented in Table 5.

P-wave arrival times were picked from original digital waveform data obtained from the Center for Monitoring Research and from the IRIS Data Management System. Waveform data were obtained for a number of stations in Africa (Figure 2), for stations up to 45° epicentral distance. In parallel, we obtained pIDC picks for the same 14 events to provide a greater sampling of stations. As in the case of the Dead Sea events above, the arrival times of both datasets (digital and pIDC) were used in JHD solutions for path corrections, keeping all events fixed at their GT locations, but fixing just the master event's origin time

(980821). The resulting path corrections are given in Table 6, consolidated from the two solutions, and the origin times from the digital JHD solution are given in Table 5.

We selected the same event, the one with the largest number of observations (980821; 7 observations), to use as the master event for a test of relocation accuracy to simulate a Comprehensive Nuclear-Test-Ban Treaty (CTBT) monitoring scenario, using just the digital dataset. The other 13 events had between 3 and 6 observations. The JHD results were quite good, with 9 events having mislocations of less than 7 km, and the other 4 events having mislocations ranging from 12 to 16 km (Figure 3), despite the small number of observations and poor azimuthal coverage. Thus, all of the events would meet the 1000 km^2 location accuracy criterion of the CTBT (National Research Council, 1997). We note that the larger event mislocations are all shifted towards the east, consistent with an elongation of the confidence ellipses in the east-west direction. Our next step will be to examine the improvement in locations that can be obtained when waveform cross-correlation is used to determine the arrival times.

CONCLUSIONS AND RECOMMENDATIONS

We have utilized "local" GT information in two very different cases, the Dead Sea and South Africa regions, to explore our ability to derive path corrections that can be used to derive relatively accurate event locations. In the Dead Sea case, a "local" JHD analysis was used to derive the GT information, whereas in the South Africa region, we were able to obtain GT location information from a local source. We carried out JHD analyses for both datasets to determine path corrections to IMS and other stations.

We used the Dead Sea results to test interpolation methods for estimating path corrections for IMS stations from those at nearby non-IMS stations. The NN method proved to be effective. We anticipate that kriging would also be effective. One issue requiring further investigation is the effect of varying station elevations on this path correction estimation approach. We used the South Africa results to provide another test of location accuracy using sparse regional-distance data. We found that event locations could be determined to the level of accuracy desired for CTBT monitoring. We also are confident that the accuracy can be improved substantially with the application of waveform cross-correlation for this dataset.

ACKNOWLEDGEMENTS

We acknowledge the assistance of Nitzan Rabinowitz, Xiaoping Yang, and the IRIS Data Management System in obtaining the waveform data used in this study. We are also extremely grateful to Tom Jordan and David James for sharing their information on event locations in South Africa.

REFERENCES

Gitterman, Y. and A. Shapira (2001), Dead Sea Seismic Calibration Experiment Contributes to CTBT Monitoring, *Seism. Res. Lett.*, 72, 159-170.

Kissling, E., W.L. Ellsworth, D. Eberhart-Phillips, and U. Kradolfer (1994), Initial Reference Models in Local Earthquake Tomography, *J. Geophys. Res.*, 99, 19,635-19,646.

National Research Council (1997), Research Required to Support Comprehensive Nuclear-Test-Ban Treaty Monitoring, National Academy Press, Washington, D.C.

Table 1. Ground Truth data for earthquakes in the Dead Sea region: origin time, latitude, longitude, depth (in km), and uncertainties; * denotes events used in the regional analysis.

#	YRMODA	HRMN	SEC	LAT	LON	DEP	?OT	?X	? Y	? Z
1	000327	1505	48.03	31.7296	35.5660	22.2	0.3	1.4	1.5	0.7
2	000328	0103	18.65	31.7325	35.5437	22.7	0.3	1.4	1.5	0.9
3	000412	0047	47.89	31.2774	35.5558	10.0	0.3	1.3	1.3	0.9
4	000705	0333	51.48	31.4870	35.5844	12.8	0.3	1.4	0.9	1.0
5	880303	2339	26.73	31.4737	35.5572	7.1	0.4	0.6	1.3	0.4

6	890218	0019	55.28	31.6869	35.5135	13.0	0.4	0.2	1.1	0.4
7	891218	1133	40.92	31.4490	35.6203	1.6	0.3	0.4	0.8	0.3
8	900326	1352	12.02	31.4678	35.5560	7.1	0.4	0.6	1.1	0.3
9	910623	1302	22.24	31.2920	35.4887	0.9	0.1	1.1	1.1	0.4
10	910623	2222	57.53	31.2924	35.4742	-0.2	0.1	1.2	1.0	0.4
11	910624	2047	10.86	31.5646	35.4959	16.7	0.3	0.8	1.5	0.9
12	910905	0817	5.81	31.7110	35.4344	-0.1	0.1	0.6	1.6	0.4
13	910905	2102	0.60	31.2836	35.4988	1.1	0.3	1.2	1.0	0.4
14	910927	2224	54.13	31.0700	35.4527	1.0	0.3	0.9	0.7	0.3
15	910930	1155	41.56	31.0750	35.4488	0.6	0.1	0.8	0.5	0.4
16	911004	0817	25.12	31.0703	35.4644	1.1	0.3	0.8	0.6	0.3
17	911128	1311	51.06	31.2000	35.3631	-0.4	0.1	1.0	1.3	0.4
18	920102	1837	42.79	31.4325	35.5493	0.6	0.1	0.6	1.5	0.4
19*	920111	0346	31.52	31.2409	35.3843	5.9	0.4	0.9	1.2	0.3
20	920626	1641	35.17	31.0915	35.4129	8.9	0.4	0.3	0.3	0.8
21*	920626	1717	45.23	31.0810	35.4271	9.2	0.4	0.7	0.4	0.8
22	920907	0257	52.74	31.3068	35.4698	1.5	0.3	1.1	1.3	0.4
23	921008	0517	51.62	31.2943	35.4085	10.4	0.3	1.0	0.9	1.2
24	921128	0149	09.20	31.4025	35.4298	7.5	0.4	0.9	1.4	0.4
25	930528	0322	46.61	31.0879	35.4364	0.9	0.1	0.9	0.7	0.4
26	930704	2305	51.42	31.8905	35.4417	0.0	0.1	1.0	1.5	0.4
27*	930802	0912	56.71	31.5025	35.4957	23.5	0.3	0.6	1.4	0.9
28*	930802	2316	53.03	31.3138	35.4089	23.5	0.3	0.9	1.0	1.0
29	931104	2112	29.13	31.4191	35.5424	3.4	0.3	0.4	1.4	0.2
30	931125	0710	33.30	31.8229	35.6046	0.2	0.1	1.0	1.6	0.4
31	950327	2349	46.34	31.5291	35.4990	0.5	0.1	0.7	1.5	0.4
32	950825	0525	05.63	31.3685	35.4785	1.3	0.3	0.8	1.1	0.4
33	950825	0548	52.18	31.4237	35.4113	0.6	0.1	1.0	1.5	0.5
34	951118	1842	28.04	31.4225	35.5512	10.3	0.4	0.7	1.2	0.4
35	960414	1330	34.83	31.3933	35.3437	0.9	0.1	1.5	1.5	0.4
36	960830	0920	42.75	31.3892	35.3977	22.3	0.3	1.4	1.4	1.1
37*	961010	1136	35.36	31.5194	35.4192	0.3	0.1	1.4	1.4	0.3
38	970904	0820	06.48	31.4190	35.4289	1.0	0.2	0.6	1.1	0.5
39	970923	1523	54.70	31.4615	35.4591	10.2	0.3	0.9	1.5	0.5
40	970926	0706	28.77	31.4719	35.4653	5.2	0.4	0.8	1.0	0.1
41	971002	0045	37.58	31.4569	35.4628	11.7	0.4	0.8	1.2	0.4
42*	940916	0318	56.88	32.0599	35.5273	18.8	0.2	1.3	1.3	1.4
43*	840824	0602	23.95	32.7265	35.1350	-0.4	0.1	1.6	1.6	0.3
44	870427	2041	46.71	31.2222	35.5421	8.0	0.3	1.1	1.5	1.0
45	880226	1751	05.31	31.6740	35.5377	20.8	0.3	0.5	1.6	1.2
46	890118	0100	50.96	32.5128	35.4544	3.5	0.2	1.6	1.3	1.5
47	890412	2111	48.37	31.6631	35.5252	16.5	0.2	1.4	1.4	1.6
48	890426	2128	55.45	31.3195	35.4775	4.1	0.3	1.0	1.4	0.2
49	890701	1404	34.21	31.7814	35.5687	4.5	0.2	1.5	1.5	0.2
50	901010	0040	58.52	31.4915	35.5216	6.1	0.2	0.7	1.6	0.5
51*	920729	0530	47.06	32.4029	35.4592	9.1	0.2	1.4	1.2	1.2
52*	920910	1953	43.64	31.9075	35.1281	15.1	0.2	1.5	1.3	1.4
53*	951128	2110	52.59	29.7573	34.9987	3.4	0.3	1.5	1.2	1.3
54*	991028	1539	13.66	30.4500	35.0749	-	-	-	-	-
55	991108	1300	00.33	31.5330	35.4460	0.0	0.0	0.0	0.0	0.0
56	991110	1359	58.20	31.5340	35.4460	0.0	0.0	0.0	0.0	0.0
57*	991111	1500	00.78	31.5350	35.4460	0.0	0.0	0.0	0.0	0.0

Table 2. IMS station path corrections from the Dead Sea regional JHD analysis. Corrections are in seconds.

STA	LAT	LON	CORR
ARCE	69.535	25.506	-4.41
ARU	56.430	58.562	-1.46
BGCA	5.176	18.424	0.50
CMAR	18.458	98.943	-5.98
DAVO	46.839	9.794	-0.01
EKA	55.333	-3.159	-1.79
ESDC	39.676	-3.962	-0.66
FINE	61.444	26.077	-3.57
FRB	63.747	-68.547	5.92
HFS	60.134	13.697	-2.17
INK	68.307	-133.520	3.44
MBC	76.242	-119.360	-1.26
MLR	45.492	25.944	1.05
OBN	55.167	36.600	-2.56
PDY	59.633	112.700	-3.70
SPIT	78.178	16.370	-4.21
YKA	62.493	-114.605	6.47

Table 3. Comparison of Dead Sea path corrections at nearby stations - IMS station HFS example.

STA	LAT	LON	CORR
HFS	60.134	13.697	-2.17
SLL	60.476	13.320	-2.18
KONO	59.649	9.598	-1.76
UPP	59.858	17.627	-1.98
APP	60.539	13.928	-2.05

Table 4. Interpolated path corrections at IMS stations for Dead Sea region events.

STA	LAT	LON	CORR
ABKT	37.9304	58.1189	0.2
BJT	40.0183	116.1679	7.4
BORG	64.7474	-21.3268	3.2
BRAR	39.8535	32.7608	0.3
DBIC	6.6701	-4.8563	-2.2
ILAR	64.7714	146.8866	-1.7
JHJ	33.1200	139.8200	5.3
KBZ	43.7286	42.8975	2.8
KVAR	43.9557	42.6952	2.7
MJAR	36.5247	138.2070	5.3
NOA	61.0397	11.2148	-2.0
NORES	60.7353	11.5414	-1.1
NRIS	69.0061	87.9964	-0.6
PARD	32.9308	35.4343	0.0
SADO	44.7694	-79.1417	8.1
SCHQ	54.8319	-66.8336	-2.5
ULM	50.2486	-95.8755	5.9
VRAC	49.3083	16.5935	-1.3
ZAL	53.9367	84.7981	-1.2

Table 5. Ground Truth data for South Africa events: origin time, latitude, longitude, depth (km).

YRMODA	HR	MIN	SEC	LAT	LON	Depth
970729	11	25	5.35	-27.9577	26.7022	0.68
970801	02	17	26.93	-27.9492	26.6992	-0.03
970925	00	05	23.04	-26.3709	27.5166	-1.26
971212	16	42	46.46	-26.9664	26.7481	-0.63
980821	16	10	53.30	-26.9536	26.7705	-1.24
980925	15	51	31.31	-26.9259	26.8057	-0.59
981002	10	17	53.34	-26.3953	27.4703	-0.48
981117	20	17	59.34	-26.9319	26.7880	-0.88
981118	16	30	5.43	-26.9461	26.7812	-1.19
981205	04	52	44.31	-26.3597	27.6112	-3.11
990107	15	18	55.28	-26.9185	26.7299	-1.30
990202	10	33	21.79	-26.4356	27.4130	-0.81
990226	09	27	47.49	-26.3876	27.4278	-0.39
990422	22	19	37.34	-27.9338	26.7128	0.33

Table 6. Path corrections for IMS and other stations based on the South Africa regional JHD analysis. Corrections (CORR) and estimates uncertainties (ERR) are in seconds.

STA	LAT	LON	CORR	#OBS	ERR
ARU	56.430	58.562	0.38	1	0.67
BDFB	-15.644	-48.014	0.43	6	0.33
BGCA	5.176	18.424	-1.56	11	0.06
BOSA	-28.614	25.256	0.26	14	0.06
BRAR	39.853	32.761	1.58	5	0.35
CMAR	18.457	98.943	0.15	9	0.32
CPUP	-23.331	-57.329	-6.97	3	0.42
DAVO	46.839	9.794	-4.15	1	0.67
DBIC	6.670	-4.856	-0.74	5	0.07
EIL	29.670	34.951	-0.21	1	0.67
ESDC	39.675	-3.962	0.38	14	0.25
FINE	61.444	26.077	0.66	11	0.26
GERE	48.845	13.702	1.15	9	0.29
KBZ	43.729	42.898	1.09	1	0.67
LBTB	-25.015	25.597	1.09	12	0.06
LPAZ	-16.288	-68.131	0.74	7	0.33
LSZ	-15.277	28.188	-2.00	3	0.08
MAW	-67.604	62.871	1.32	6	0.31
MSKU	-1.656	13.612	-1.66	1	0.13
NOA	61.040	11.215	1.37	3	0.39
NORE	60.735	11.541	1.56	4	0.38
PLCA	-40.731	-70.550	0.06	1	0.67
RAYN	23.522	45.503	-0.46	1	0.13
SUR	-32.380	20.812	0.07	12	0.06
TSUM	-19.202	17.584	-1.78	8	0.06
VNDA	-77.514	161.846	1.15	5	0.35

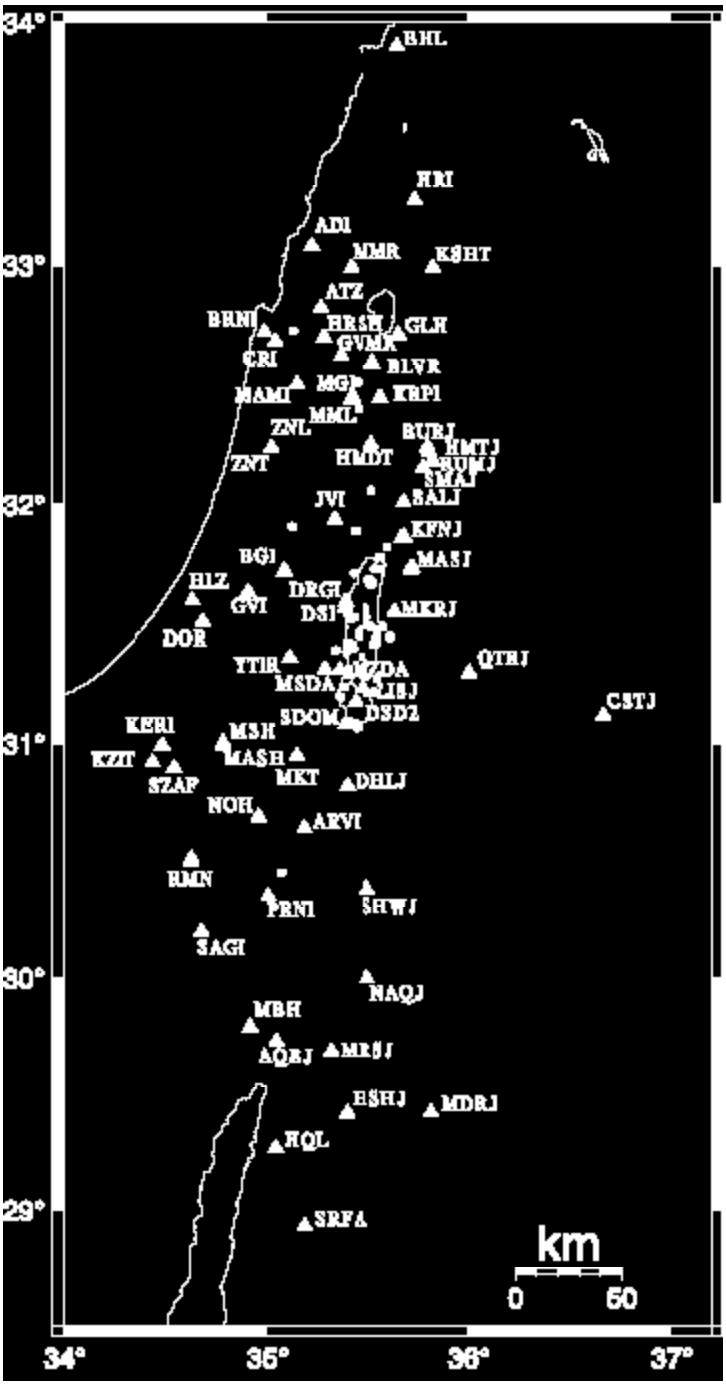

Figure 1. Stations (triangles) and events (circles) used in JHD analysis to derive GT locations for determining path corrections for IMS and other regional stations.

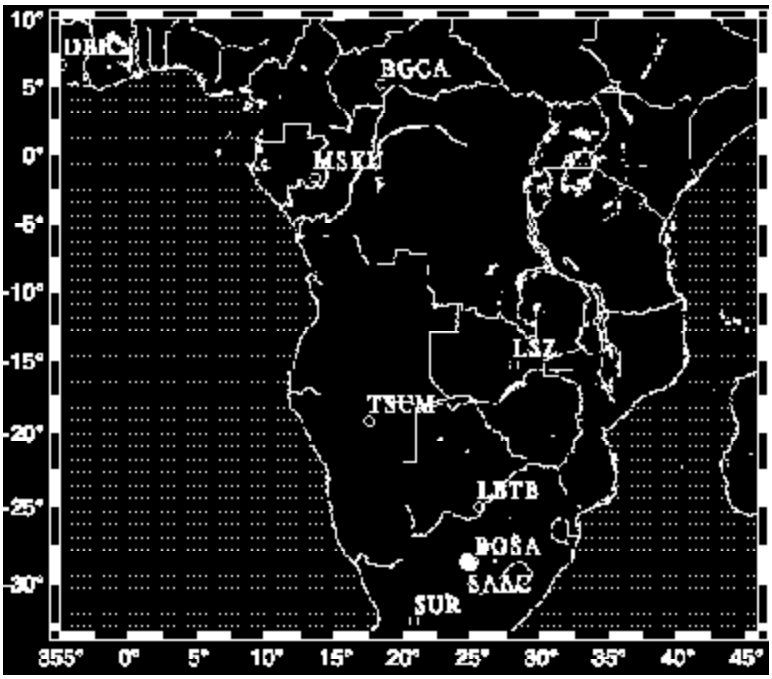

Figure 2. Stations in Africa for which digital waveform data were obtained for events listed in Table 5.

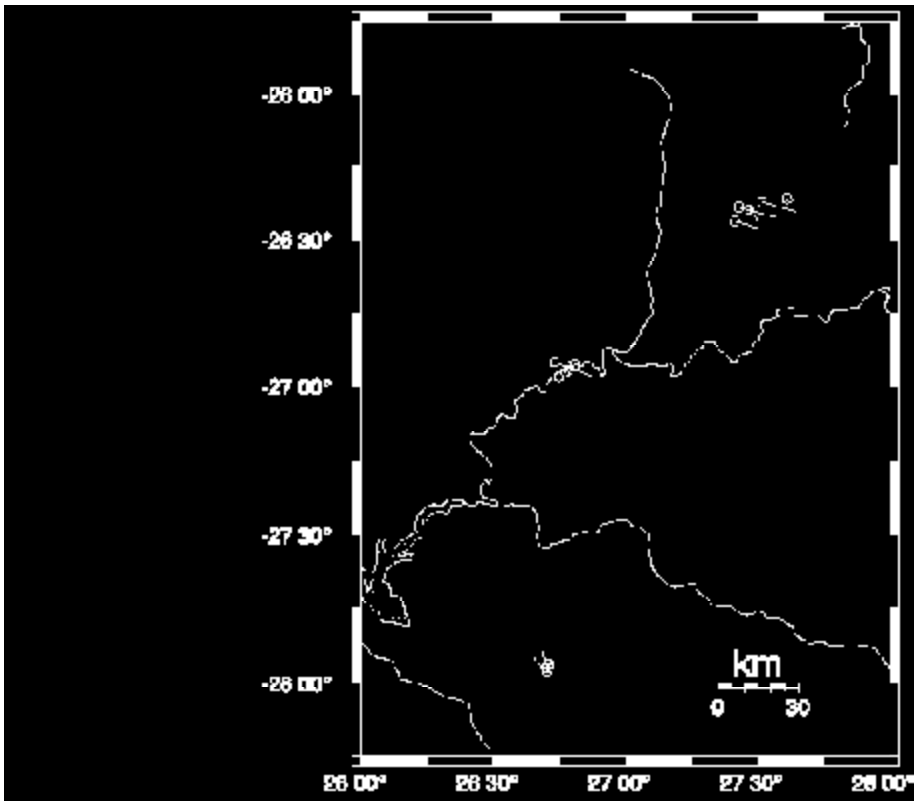

Figure 3. Event mislocations (tails on circles) using one master event (980821) in a JHD solution.

COLLABORATIVE RESEARCH: SEISMIC CATALOGUE COMPLETENESS AND ACCURACY

Frank Vernon[1], Gary Pavlis[2] and Terry Wallace[3]

[1]IGPP, UC San Diego, [2]Geology Dept., Indiana Univ., [3]Dept. Geos., Univ. Arizona

Sponsored by Defense Threat Reduction Agency

Contract No. DTRA01-00-c-0069

ABSTRACT

The single most important goal of seismic monitoring of a nuclear weapons treaty is the detection and accurate location of seismic events of various origins (natural and man made) globally. However, the metric for evaluating the performance of the IMS or other monitoring networks is not easily established since global catalogues, such are the ISC and PDE, have been shown to be incomplete, with large regional variability. Further, the event parameters (location, origin time and magnitudes) are often quite different from catalogue to catalogue. To study these effects we are building a complete catalog of events from open data sources in the Middle East and Central Asia for the time period from 1991 through 2000. Data sources include the GSN, KNET, Geoscope, and Kaznet permanent networks, and data from temporary broadband deployments in Saudi Arabia, Turkmenistan, Pakistan, Tibet, and the Tien Shan. Current progress is centered on building catalogs for each individual dataset. At present over 20,000 events have been located or associated with external catalogs.

To make significant improvements in the locations, we are in the process of testing a new series of computer programs that implement the separated earthquake location method (SELM) for seismic catalogs at any scale. We first build a 3D grid of points inside the earth and associate every event within a region to one or more grid points using a simple distance cutoff criterion. For each grid point that has data associated with it we apply SELM with reference path anomalies computed as the difference between a 3D model and a 1D reference model. Projectors are used to extract only the 4D bias terms from the 3D model with the remaining residuals used to extract other components of the path anomaly vector for that grid point. This provides a mechanism to produce empirical 3D travel time grids that can be updated easily as new data is acquired.

In central Asia a perfect set of test events are the Omega explosions conducted as part of the Kazakhstan-American calibration experiment. In addition to the IMS stations, at least some of the omega events were recorded by 19 additional stations at regional distances. We have conducted a series of experiments to (a) determine optimal station coverage to produce GT-5, (b) develop empirical procedures for optimizing the phase information from regional records, and (3) test several joint hypocenter determination scenarios. Our tests highlight out the importance of calibrated stations and the benefits of using all available data.

KEY WORDS: catalogs, seismicity, location

OBJECTIVE

Seismic event detection and location are the single most important research issues for adequately monitoring a Comprehensive Test Ban Treaty. Confidence in a CTBT relies on the assumption that any underground nuclear weapons test will be detected at an adequate number of seismic stations such that it can be located with sufficient accuracy that the test could be confirmed with an on-sight inspection. Another way to put this is that confidence in seismically monitoring a CTBT is equivalent to confidence in the *seismic catalogue* that is produced by the monitoring system. There are two principle components of a catalogue: (1) completeness in terms of representing all the seismicity within the region of monitoring interest (referred to here as *detection*), and (2) the accuracy of the source parameters for the events within the catalogue.

The present IMS system has a low detection threshold and presumably high location accuracy in the Baltic shield region of Europe. This is due to the presence of various NORSAR arrays, which dramatically enhance the regional detection level. Other areas, in particular the southern hemisphere and Asia, have much higher detection thresholds. The quality of the locations produced by the protype IMS has been assessed by comparing it to other catalogs of seismicity, in particular the NEIC s PDE. However, this comparison can be problematic because the PDE is not complete and suffers from sparse station distribution. Further, the locations in the PDE are not vetted against ground truth nor corrected for known heterogeneity in earth structure. A better gauge of the quality of the IMS catalogue is to measure it against a detailed local catalogue. However, this is a difficult task because individual catalogues are constructed with unique methodology, and thus, are of uneven quality.

We are constructing a catalogue for the region stretching from Saudi Arabia to western China for 1995 to the present. We will use all available data sources which includes several temporary, portable seismic experiments and private or national seismic networks which are not easily available to the researcher. The catalogue construction will have two principle tasks: detecting and associating seismic phase information (the number of expected events within the time frame is in excess of 25,000), and locating these events and assigning realistic location errors. There are several fundamental research tasks that need to be performed before the catalogue can be completed. These include research on locating events which are primarily recorded at regional distances, evaluating both formal and systematic errors, and assessing true detection capabilities. Once the catalogue is constructed, it will provide an excellent test bed for research on strategies for spotlighting regions of enhanced monitoring interest, provide the data base for detailed regional velocity models (which can be incorporated into a general location scheme), and most importantly, assess the quality of catalogues routinely produced for monitoring purposes.

RESEARCH ACCOMPLISHED

Catalogue Production

The geographic region which stretches from the Middle East to central Asia is an area of monitoring interest. It is also a region in which there have been a number of portable seismic experiments mounted in the last few years due to the interest in the structure and dynamics of the India-Asia collision. The total number of stations with continuous broadband data in the area bounded by 10^o to 60^o N and 30^o to 110^o E is in excess of 130. Although some of the data streams are intermittent or only deployed for part of the window of time in which we wish to develop the catalogue, we can estimate the number of events expected on the basis of the performance of KNET and the Saudi experiment is in excess of 25,000. The fact that high quality seismic stations are located near the seisimicity will make the catalogue superior to any other product for the same region.

During the last year (2000-2001) our focus has been constructing a catalogue in Asia, centered on the Tien Shan. The stations used to construct the catalogue in those in KNET, a ten station broadband network in eastern Kyrgystan and the PASSCAL experiment deployed in stages from 1997-2000 in the Tien Shan mountains (23 stations in Kyrgyzstan and 15 stations in China). Figure 1 shows the distribution of the stations which occupy a box 5 x 5 degrees (approximately 300,000 km^2). The total number of events

detected and located is more than 9000. Figure 2 shows the automated locations, with symbols scaled to event size and color coded to event depth.

The event magnitude scale must be calibrated to other catalogues, but preliminary analysis indicates that the detection capability in the 5 degree circle about the center of the array is approximately 2.0. This can be compared to the detection capability of KNET alone. Using the detection threshold technique of Harvey and Hansen (1989, the first step is to filter the broadband data to the traditional narrow frequency band appropriate for estimating m_b (approximately 1 Hz). After filtering, the ratio of the P wave amplitude to the pre-event amplitude noise (snr) is calculated. Using the value of m_b provided by standard catalogues such as the PDE, it is a linear function to scale the m_b by the snr to determine the minimum detection threshold. Eakins et al. (1999) determined that the detection capability for seismicity in the region of Lop Nor recorded at KNET is approximately magnitude 2.5.The experience from KNET is really just a manifestation of the fact that having seismic stations *close* the seismicity increases the detection. The fact that regional networks can greatly improve the monitoring capability for the given region is a central tenet for testing global monitoring catalogues.

Event Location Methodology Development

We have developed a new set of computer codes to process a database of arrival time data to produce improved estimates of two fundamentally different entities: (1) a set of 3D grids of travel time corrections for each seismic station defined in the database, and (2) a set of improved location estimates for each seismic event that are consistent with the 3D travel time surfaces computed in the same procedure. The procedure we use has three steps: (1) cluster association, (2) location and simultaneous estimation of travel time surfaces, and (3) error estimation. At the time of the deadline for this report the computer code to implement our concepts has been written but not yet fully tested. We described the details of the existing or planned implementation of each of these three steps in separate sections below.

Event cluster association. Our objective is to estimate a set of travel time corrections relative to a reference radially symmetric earth model for a 3D volume within the earth. The data we use for this purpose is arrival times of N_p seismic phases recorded at the set of N_s stations for which we have data. Consequently, the complete set of data objects we aim to produce is a set of N_s estimates of a 3D vector field (N_p travel time corrections per grid point) defined on some type of discrete grid. We chose to use a natural grid scheme for regional scale earth science applications that we will refer to as a geographical curvilinear grid (GCLgrid). A GCLgrid is a simple extension of what is commonly called a uniform field in the scientific visualization world. A uniform grid divides a box shaped region into a set of constant sized boxes. A GCLgrid makes the closest equivalent approximation in a spherical earth. That is, we divide a region of the earth into a series of spherical shells of equal thickness and then subdivide the shells into subareas of approximately equal solid angles. To improve the uniformity of the grid at regional scales we translate the intersection of the prime meridian and equator to a specified origin, define a baseline using a great circle path at a specified azimuth, and then define an equal angle grid of latitude and longitudes relative to this baseline and origin. This produces continent scale grids that have properties that do not depend upon the actual location of the grid. Simpler schemes based on the normal geographic reference, for example, commonly have serious distortions at high latitudes that are avoided by this method.

Once we define the geometry of a reference GCLgrid we process a list of associated events within a CSS3.0 database and link each event in the database to one or more grid points using a database relation that is an extension of CSS3.0. The best recipe for assigning an event to a given point in space is an open question, but in the current implementation we use a simple set of rules based on distance. That is, we define a cylindrical region around each target grid point. The radius of this cylinder is initially set to a specified minimum size. We count the number of events within the specified volume. If a specified minimum number of events are not present within this volume the sphere is expanded incrementally until either the hit count exceeds the minimum or the radius exceeds a specified maximum. In the later case no links to the grid point are stored in the database. Otherwise we compute the hypocentroid (center of mass) of the ensemble of events and store the hypocentroid and indices that connect it to all events that form that ensemble.

Location methodology. The approach we use for simultaneous estimation of improved earthquake locations and the ensemble of path corrections is the Separated Earthquake Location Method (SELM) described originally by Pavlis and Hokanson (1985). SELM is an extension of the Progressive Multiple Event Location (PMEL) method of Pavlis and Booker (1983). PMEL/SELM are multiple event location methods that are extensions of the classical Joint Hypocentral Determination (JHD) techniques (Douglas, 1967). The primary distinction between PMEL and JHD is that JHD solves the system of equations for an ensemble as a single, large matrix while PMEL separates the nonlinear location parameters from the linear, station correction terms. In our experience PMEL improves stability through iterative updates of earthquake hypocenter coordinates and through robustness introduced by automated deletions of events that have statistically significant differences in rms misfit compared to the ensemble average. This is not possible with simultaneous methods like JHD where the whole system of equations is inverted all at once.

SELM adds an important second feature that we exploit. Pavlis and Hokanson (1985) show how to construct a pair of complementary, orthogonal projectors, which we will refer to as $\boldsymbol{P}_R$ and $\boldsymbol{P}_N$. We apply these projectors using the relation

$$\boldsymbol{s} = \boldsymbol{P}_R \boldsymbol{s}_{3d} + \boldsymbol{P}_N \boldsymbol{s}_{data}$$

where $\boldsymbol{s}$ denotes a $N_s N_p$ vector of path anomalies. That is, each component of $\boldsymbol{s}$, is a difference, $s_i=(t_{3d})_i - (t_{ref})_i$, between the travel time based on three-dimensional earth model and some 1D reference model. What we call $\boldsymbol{s}_{3d}$ and $\boldsymbol{s}_{data}$ use a different realization of 3D earth structure. Jordan and Sverdrup (1981) introduced the concept we use here in what they called the hypocentroidal decomposition theorem. That is, for an ensemble of events that are localized in space the absolute location of the group is fundamentally indeterminate but precise estimates $\boldsymbol{s}$ can dramatically reduce the scatter in the relative location of events within the group. The J&S method resolves this ambiguity by constructing a projector that annihilates the dependency of the solution on $\boldsymbol{s}$. The projectors we construct are fundamentally different from the J&S approach. The basic difference is that in PMEL/SELM the projectors are constructed to annihilate the dependence of residuals on the hypocentral parameters instead of $\boldsymbol{s}$. This distinction is important to realize since to date the Jordan and Sverdrup approach seems to be the method of choice of various groups working on location problems within the DoD programs. That is, we are using a procedure that differs significantly from those based on the J&S paper.

The key feature SELM adds is that is not possible with the original J&S methods is that we utilize the term $\boldsymbol{P}_R \boldsymbol{s}_{3d}$ to add ancillary information to resolve the absolute location ambiguity. That is, we utilize a 3D model as a secondary reference model used only to resolve the absolute location ambiguity. The data are used directly to estimate the term $\boldsymbol{P}_N \boldsymbol{s}_{data}$ using PMEL. Because the $\boldsymbol{P}_R$ and $\boldsymbol{P}_N$ projectors are orthogonal the two procedures are completely decoupled. The method described in Jordan and Sverdrup s 1984 paper shares this decoupling feature but is incapable of applying the equivalent of $\boldsymbol{P}_R \boldsymbol{s}_{3d}$ exactly.

In the current implementation an ensemble of events and their related arrival times are associated with target points in space that define a GCLgrid (see above). The generalized PMEL/SELM program is then applied to each target point in space. For points with sufficient data we compute the solution as described above. For points with insufficient data our method guarantees that our estimate of $\boldsymbol{s}=\boldsymbol{s}_{3d}$. That is, the computed path anomalies automatically revert to those computed from the reference 3D model when no data is available, but otherwise use all available data to refine the estimated path anomalies. The end result is a set of path anomaly estimates defined on a GCLgrid in space. A final detail is that we distort the GCLgrid by shifting the location of each node point from the target point to the hypocentroid of the final location. This distortion complicates the problem of utilizing a GCLgrid in other applications so we anticipate using an existing GLCgrid mapping algorithm we have developed to interpolate these distorted surfaces onto a regular GCLgrid.

Error Analysis. We have implemented a novel error estimation scheme based on previous work by Pavlis (1986, 1992). The approach we use utilizes the pair of orthogonal projectors described above to separate the errors caused by inadequacies in the velocity model into two terms. First, uncertainties in $\boldsymbol{P}_R \boldsymbol{s}_{3d}$ translates directly into a location bias and can be handled by the absolute error methods described by Pavlis (1986). Secondly, uncertainties in the overall estimate of the path anomaly to a given point in space, $\boldsymbol{s}$, fold into relative location errors. Pavlis (1992) shows that relative location errors can be treated as a term

involving variations in the constellation of stations that record a given event, which scales with the total error ***s***, and a second term that scales with the spatial gradient of ***s***. Future applications to real data should help us understand which of these terms dominate at different scales.

CONCLUSIONS AND RECOMMENDATIONS

We have constructed a catalogue for central Asia. This catalogue is rich in small events that do not appear in other global catalogues, and represent the power of regional monitoring with national resources or portable experiments. At present, the locations are from automated processing; in the next year we will relocate these events using the progressive multiple event methodology which was also developed and enhanced during this contract year.

ACKNOWLEDGEMENTS

We would like to acknowledge Jennifer Eakins (UCSD) who has headed up the automated processing of the KNET and Tien Shan data.

REFERENCES

Douglas, A. (1967). Joint epicentre location, *Nature*, **215**, 45-48.

Jordan, T. H. and K. S. Sverdrup (1981). Teleseismic location techniques and their application to earthquake clusters in the south-central Pacific, *Bull. Seism. Soc. Amer.,* **71**, 1105-1130.

Pavlis, G. L. (1992). Appraising relative earthquake location errors, *Bull. Seism. Soc. Amer.,* **82**, 836-859.

Pavlis, G. L. (1986). Appraising earthquake hypocenter location errors: a complete, practical approach for single event locations, *Bull. Seis. Soc. Amer.*, *76*, 1699-1717.

Pavlis, G. L. and J. R. Booker (1983). Progressive multiple event location (PMEL), *Bull. Seis. Soc. Amer.*, *73*, 1753-1777.

Pavlis, G. L. and N. B. Hokanson (1985). Separated earthquake location, *J. Geophys. Res.*, *90*, 12,777-12,789.

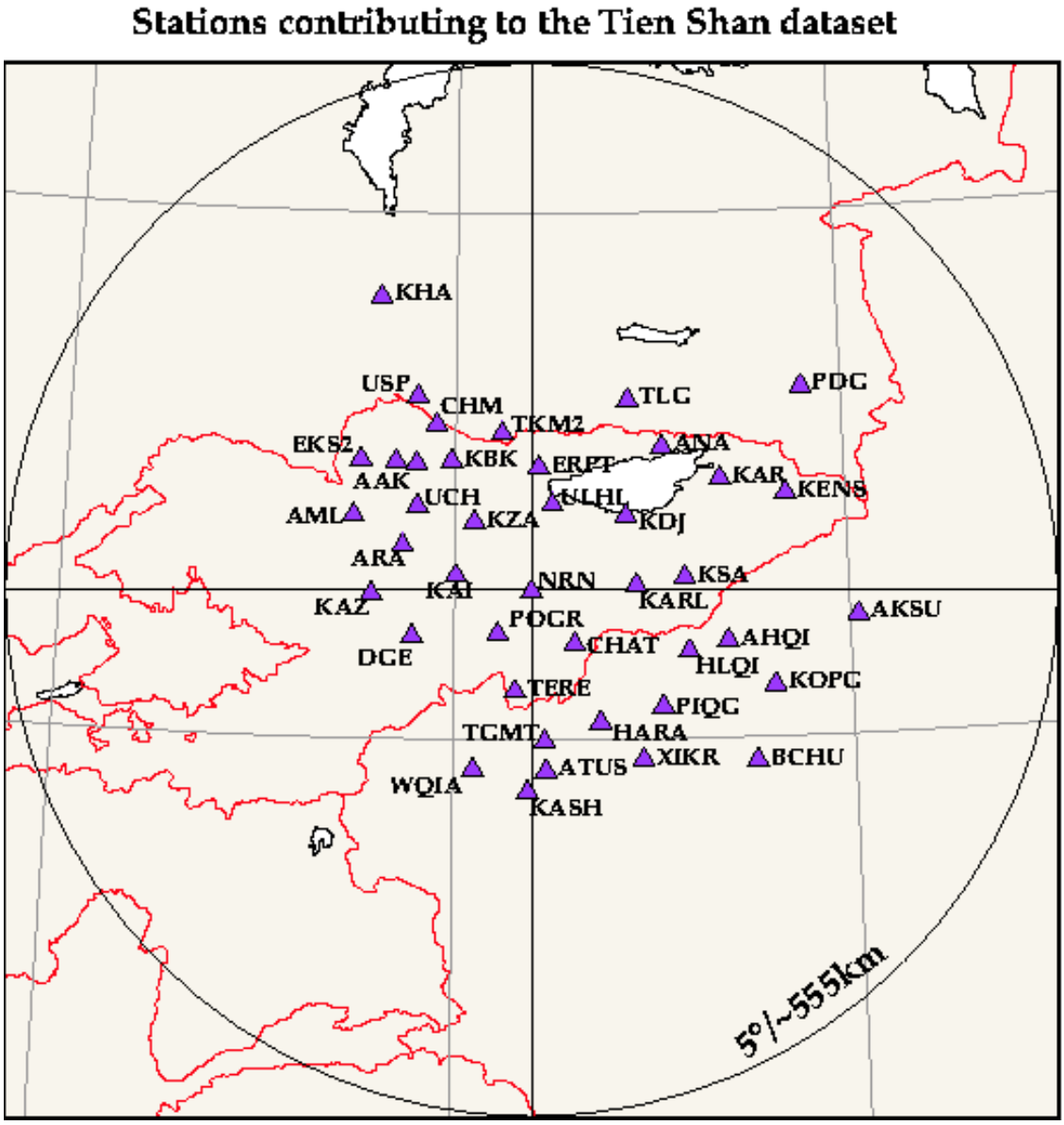

Figure 1. Seismic Stations used to construct the central Asia Catalogue.

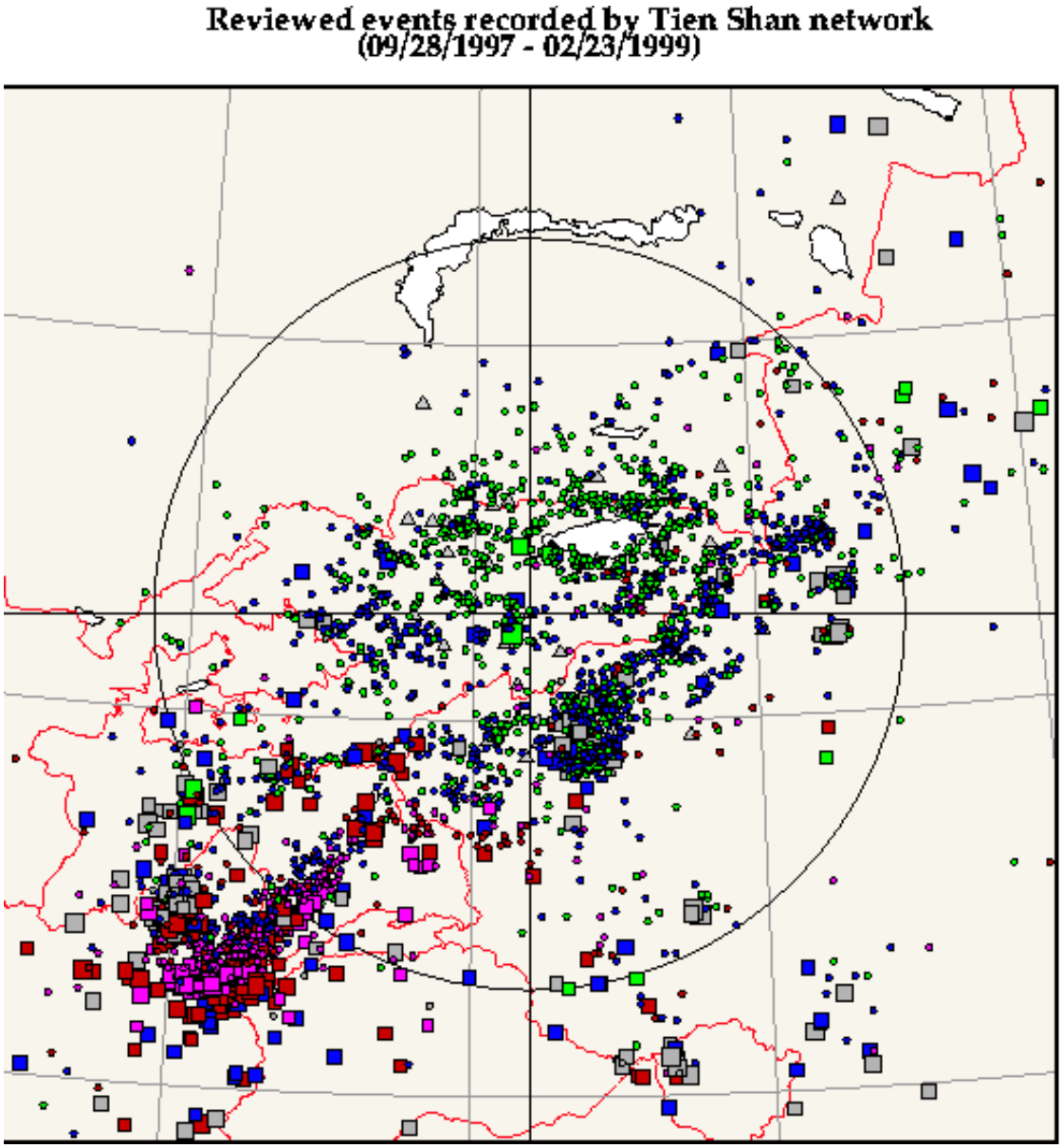

Figure 2: Location of events processed recorded at the stations shown in Figure 1. The epicenter symbols are scaled to event size, and the color is scaled to event depth

LLNL IDENTIFICATION PROGRAM: REGIONAL BODY-WAVE CORRECTION SURFACES AND SURFACE-WAVE TOMOGRAPHY MODELS TO IMPROVE DISCRIMINATION

William R. Walter, Arthur J. Rodgers, Michael E. Pasyanos, Kevin M. Mayeda,
Alan Sicherman and David B. Harris

Lawrence Livermore National Laboratory

Sponsored by National Nuclear Security Administration
Office of Nonproliferation Research and Engineering
Office of Defense Nuclear Nonproliferation

Contract No. W-7405-ENG-48

ABSTRACT

LLNL identification research is focused on the problem of correctly discriminating small-magnitude explosions from a background of earthquakes, mining tremors, and other events. The goal is to reduce the variance within the population of each type of event, while increasing the separation between the explosions and the other event types. We address this problem for both broad categories of seismic waves: body waves and surface waves. First, we map out the effects of propagation and source size in advance so that they can be accounted for and removed from observed events. This can dramatically reduce the population variance. Second, we try to optimize the measurement process to improve the separation between population types.

For body waves we focus on the identification power of the short-period regional phases Pn, Pg, Sn and Lg, which can often be detected down to very small magnitudes. Many studies have shown that particular ratios of these phases, such as 6- to 8-Hz Pn/Lg, can effectively discriminate between closely located explosions and earthquakes. To extend this discrimination power over broad areas, we use our revised Magnitude and Distance Amplitude Correction (MDAC2) procedure. This joint source and path model fits the observed spectra and removes magnitude and distance trends from the data. The MDAC residuals are kriged to provide full 2-D path corrections by phase and frequency band. The MDAC residuals allow the exploration of all possible ratios and multivariate combinations of ratios for their discrimination power. We also make use of the MDAC spectra and the noise spectra to determine the expected detectability of each phase and use that to optimize the multivariate discriminants as a function of location. We quantify the discrimination power using the misidentified event trade-off curves and an equi-probable measure. We evaluate the correction surfaces using a cross-validation technique. The result is an end-to-end validation and discrimination performance measure for each station analyzed, and a set of measurement algorithms and correction surfaces that greatly improves discrimination.

For surface waves we continue to make improvements in our regional group velocity tomography models. We have recently expanded our Rayleigh and Love wave dispersion measurements from the Middle East and North Africa into the European Arctic. The resulting tomography models now cover all of western Eurasia and provide high-resolution maps of group velocity from 10- to 100-seconds period. The maps also provide estimates of the expected phase spectra of new events that can be used in phase-match filters to compress the expected signals and improve the signal-to-noise ratio on surface wave magnitude (Ms) estimates. Phase match filters in combination with regional Ms formulas can significantly lower the threshold at which Ms can be measured, extending the Ms-mb discriminant. We have measured Ms in western Eurasia for thousands of events at tens of stations, with and without phase match filtering, and found a marked improvement in discrimination. Finally we are exploring the Ms-yield relation for the explosions in the dataset with announced yields.

KEY WORDS: seismic, regional, discrimination, identification, explosion

OBJECTIVES

Monitoring the world for potential nuclear explosions requires characterizing seismic events and discriminating between natural and man-made seismic events, such as earthquakes and mining activities, and nuclear weapons testing. We are developing, testing, and refining size-, distance-, and location-based regional seismic amplitude corrections to facilitate the comparison of all events that are recorded at a particular seismic station. These corrections, calibrated for each station, reduce amplitude measurement scatter and improve discrimination performance. We test the methods on well-known (ground truth) datasets in the U.S. and then apply them to the uncalibrated stations in Eurasia, Africa, and other regions of interest to improve underground nuclear test monitoring capability.

RESEARCH ACCOMPLISHED

As part of the overall National Nuclear Security Administration Ground-based Nuclear Explosion Monitoring (GNEM) Research and Engineering program, we continue to pursue a comprehensive research effort to improve our capabilities to seismically characterize and discriminate underground nuclear tests from other natural and man-made sources of seismicity. To reduce the monitoring magnitude threshold, we make use of regional body and surface wave data to calibrate each seismic station. Our goals are to reduce the variance and improve the separation between earthquakes and explosion populations by accounting for the effects of propagation and differential source size. Here, we briefly review two of these efforts: 1) MDAC2 - a revised spectral fitting technique to improve regional body-wave discrimination and 2) high-resolution surface wave tomography to provide structural information in aseismic regions and to improve Ms:mb discrimination.

MDAC2

Effective earthquake-explosion discrimination has been demonstrated in a broad variety of studies using ratios of regional amplitudes in high-frequency (primarily 1-to 20-Hz) bands. When similar-sized earthquakes and explosions are nearly co-located, we can understand the observed seismic contrasts, such as the relative P-to-Lg excitation, in terms of depth, material property, focal mechanism and source time function differences. However, the availability of reference earthquakes, and particularly nuclear tests, to compare to a new event in question is highly non-uniform and limited. Therefore, in real monitoring cases, we are often interested in comparing events that are not co-located and may have quite different sizes. In order to make sure any observed differences between a new event in question and the reference events (or models) are not due to differences in path or magnitude, we must correct for these effects.

For the past several years we have been working with our colleagues at Los Alamos National Laboratory on the best ways to model and remove magnitude and distance trends from regional amplitudes. The original MDAC (Magnitude and Distance Amplitude Correction) procedure involved estimating and removing a simple theoretical earthquake spectrum from the data to remove any magnitude and distance trends in the regional phase amplitudes and any discriminants formed from those amplitudes (Taylor et al., 2002). Recently, we have refined and improved the procedure by generalizing the source model, taking advantage of independent moment estimates and reducing some of the free parameters (Walter et al., 2001, Walter and Taylor, 2001.

The source spectrum depends upon the seismic moment and stress drop and can have additional complications due to non-constant stress drop scaling and differential P/S corner frequency effects. We require the different phases for the same event recorded at the same station to have the same moment and apparent stress (or stress drop) values and other source parameters, such as corner frequencies to be related to each other. This requirement effectively imposes some of the ratio constraints discussed in Rodgers and Walter (2002) on the amplitudes and improves discrimination performance. While such models of source spectra are certainly oversimplified, they have proven track records of providing good first-order fits to real earthquakes. In addition they also provide simple theoretical models to use in aseismic areas.

The MDAC formulation was revised in two ways:

1. We take advantage of the very stable moment magnitude determinations from regional coda envelopes (see Myers et al., this Proceedings). The coda-based technique provides an accurate and independent estimate

of moment from just one station. Using a direct measure of moment also eliminates the need to scale from other magnitudes such as m_b to moment eliminating two fitting parameters from the original formulation (Taylor et al, 2002). The combination of using the more stable coda measure and eliminating two free parameters should reduce scatter in the resulting correction.

2. We generalize the Brune (1970) source spectrum to allow for arbitrary stress scaling and P to S corner frequency ratios. A problem with non-constant stress drop scaling is that the Brune (1970) model is specifically set up as a constant stress drop model. Taylor et al. (2002) have implemented a non-constant scaling, but at a cost of the stress drop becoming a non-physical parameter. This means we can no longer interpret a stress drop in terms of bars (or MPa) in the non-constant scaling case. This is somewhat unsatisfactory both theoretically and practically when we want to use the MDAC formulation in regions without data where parameters like stress drop may be determined from models. Allowing variable P to S corner frequency ratios is also supported by some earthquake studies and gives greater flexibility to the spectral fitting.

The details of the MDAC2 formulation are given in Walter and Taylor (2001). The predicted spectrum is a convolution of the revised source terms and the previously used geometrical spreading, site, and apparent attenuation terms. We can write the log of the MDAC2 predicted spectrum as (Walter and Taylor, 2001):

$$\log P(f,R) = \log(S_o) - \log\left\{1+\left(\frac{\omega}{\omega_c}\right)^2\right\} + \log G(R) + Site(f) - \frac{\pi R}{Q_o c} f^{(1-\gamma)} \log(e) \qquad (1)$$

for a regional phase with velocity c. Here S_o is the source low-frequency spectral level and Q_o is the source corner frequency. These terms are set by the input moment, the apparent stress scaling and material property terms. Apparent stress, geometrical spreading ($G(R)$), site effect, and attenuation (Q_o, γ) terms are typically solved for using a grid search technique that simultaneously minimizes the spectral fit residual and residual magnitude and distance trends. In this way *a priori* information such as previous studies on geometrical spreading or Q-tomography results can be easily incorporated. Finally we can further reduce the MDAC2 residual amplitude variance by using the Bayesian kriging method of Schultz et al (1998) on the results.

Nevada Test Site Examples

The availability in the Western U.S. of many good regional records of earthquakes and nuclear explosions, and much *a priori* information on attenuation and geometrical spreading, make it a good place to test out the MDAC spectral fitting. We use our own geometrical spreading (critical distance R_o, distance exponent η) and attenuation values, which are very similar to those found in prior studies (e.g. Chavez and Priestly, 1986). They are shown in the table below:

Phase	**R_o**	η	**Q_o**	γ
Pn	0	1.1	210	.65
Pg	100.	0.5	190	.45
Lg	100.	0.5	200	.54

An example of the MDAC2 simultaneous fit to Pn, Pg and Lg spectra is shown in Figure 1 for the Little Skull Mountain earthquake mainshock recorded at station KNB in Utah about 300 km distant. This earthquake occurred on the Nevada Test Site (NTS) in June of 1992 with a good aftershock sequence and is only a few tens of kilometers away from the sites of many previous nuclear tests. This figure shows the effect on the spectral fitting of the variable P to S corner frequency ratio. The left hand plot is for equal corner frequency values while the right hand plot is for a higher P corner frequency by the ratio of the wave velocities (1.73). The best fit appears to be closer to equal corner frequency values.

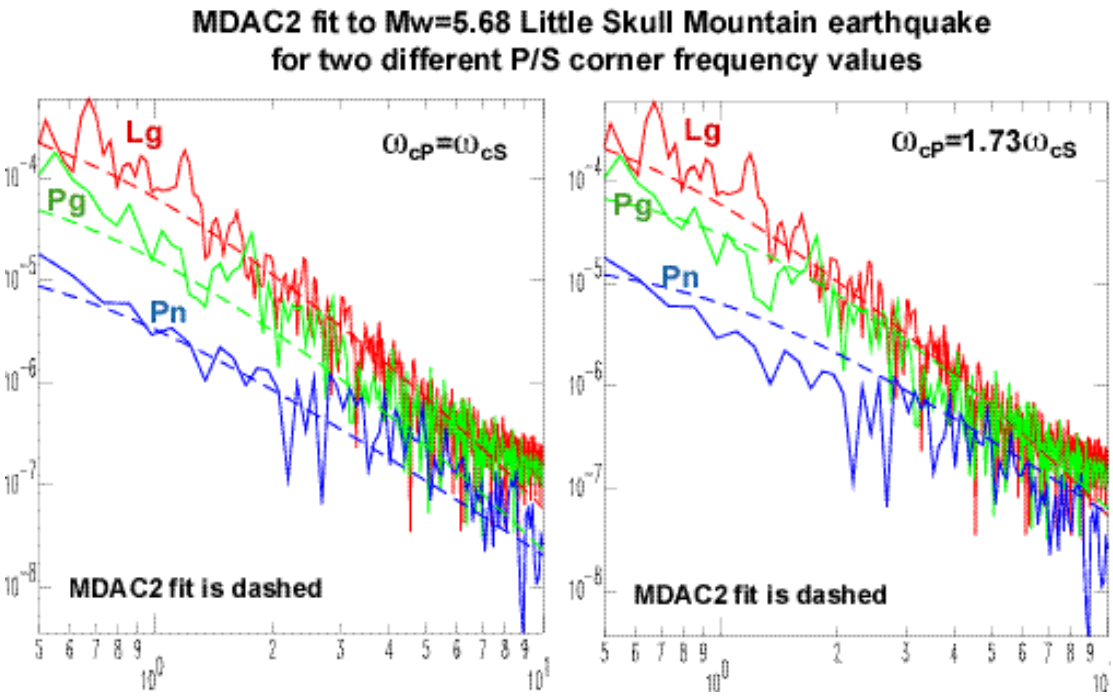

Figure 1. MDAC2 fit to Mw=5.68 Little Skull Mountain earthquake for two different P/S corner frequency values.

Another example of MDAC2 scaling is shown in Figure 2. Here we show Lg spectra for the Little Skull Mountain mainshock and two aftershocks. The coda moment magnitudes are from a previous study (Mayeda and Walter, 1996). Note that the constant apparent stress model on the left does not fit the data as well as the stress scaling with $M_o^{1/4}$ shown on the right. This is consistent with our previous spectral studies using corrected coda envelope measure(Mayeda and Walter, 1996).

One of the major reasons that removing trends from the regional amplitude and discriminant ratios is important is to facilitate the creation of multivariate discriminants. This is the optimal combination of two or more specific amplitude ratios ("features") to improve discrimination. Several studies have shown that the combination of two mediocre discrimination ratios can surprisingly improve performance (e.g. Taylor, 1996). The reason is that combining more features brings more independent information to bear on the problem and also takes advantage of hidden favorable correlation structure between measures. For example, we show in Figure 3 some combinations of three discriminant measures from a previous study (Walter et al., 1995) for NTS.

The magnitude dependent effect of corner frequency scaling is particularly apparent in the Lg coda spectral ratio in Figure 3. We remove this prior to combining ratios. To measure the discrimination performance, we calculate receiver-operator curves (ROC), which can be thought of as the error rates when moving a constant decision line through all possible values. These ROC curves give the tradeoff in performance between the type 1 error (misidentified explosion as an earthquake) and type 2 error (misidentified earthquake as an explosion). A single metric is then given by the equi-probable value, which is defined as the error (point on the ROC curve) where the error rates are equal. In Figure 3 we can see that the best individual ratio is 6-8 Hz Pn/Lg with an equi-probable values of about 2.5%. Surprisingly, though using a linear discriminant analysis (LDA), combination of the two mediocre discriminants 6-8 Hz Pg/Lg and 1-2 Hz to 6-8 Hz Lg coda out-performs the 6- to 8-Hz Pn/Lg. This demonstrates the need to calibrate multivariate discriminants before choosing particular combinations and assessing performance.

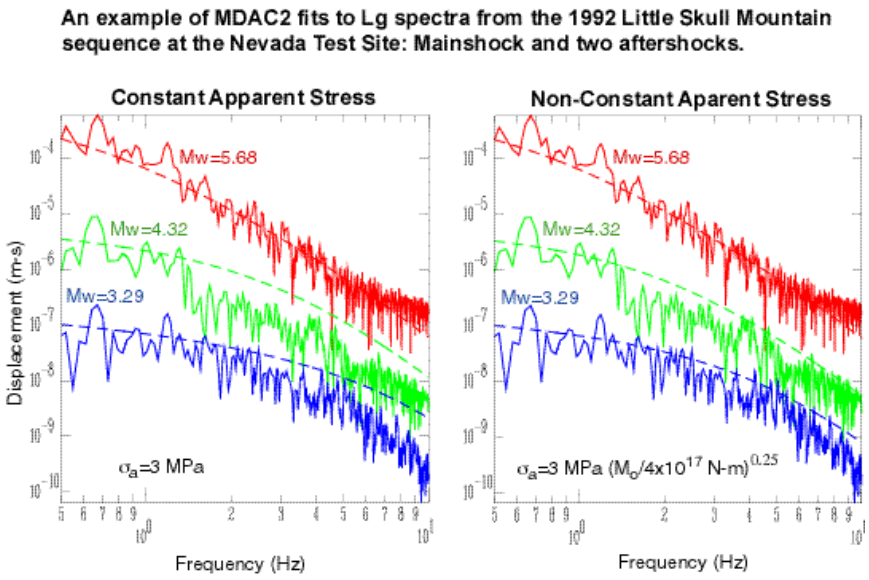

Figure 2. . Example of MDAC2 fits to Lg spectra for constant and non-constant apparent stress cases.

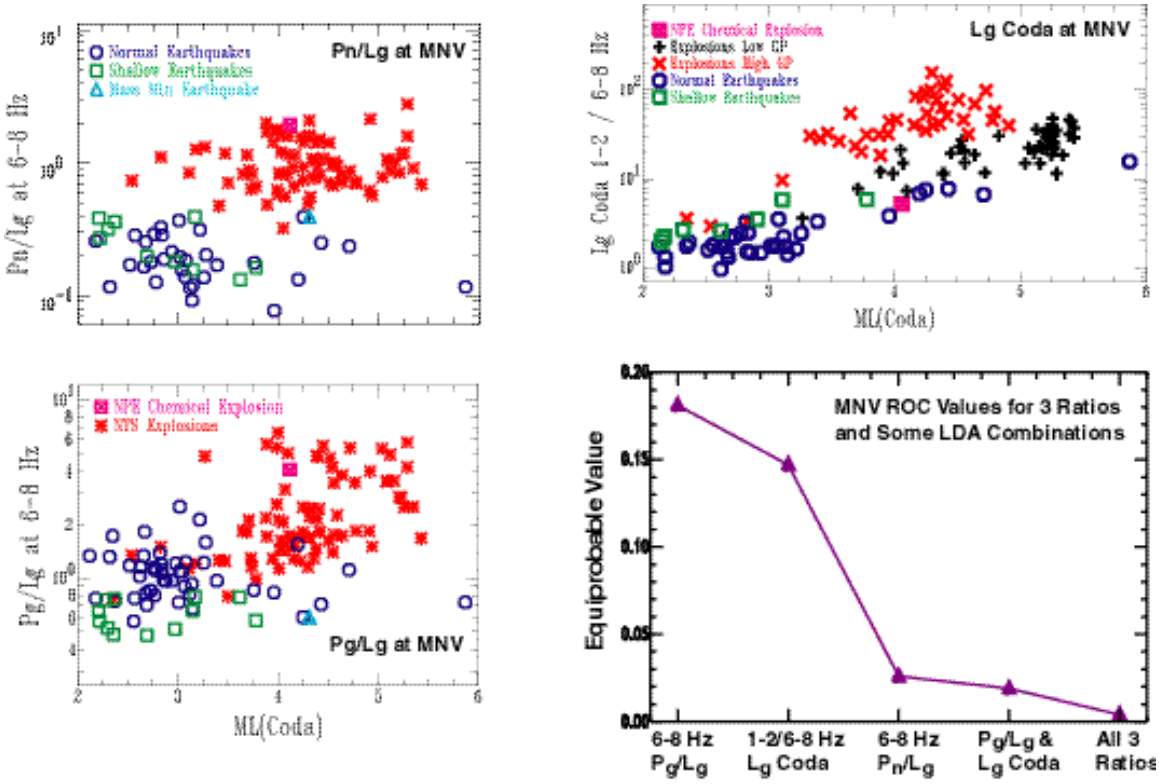

Figure 3. Examples of improving discriminant performance by combining individual measures. Color scatter plots show individual discriminant measures from Walter et al (1995). The lower right figure shows the performance, as measured by equi-probable value, of these individual measures and LDA combinations of them.

An additional consideration in deciding which regional amplitudes to use for individual or multivariate discrimination is their detectability in the frequency bands of interest at a given station. We can use the MDAC2 formulation to estimate this as well as discussed in the paper by Harris et al. (this Proceedings).

Surface Wave Tomography

For the past several years, we have been making regional surface wave group velocity measurements in western Eurasia with the goal of creating a high-resolution tomography model. Such tomography models provide information on velocity structure over broad areas and particularly in aseismic regions such as North Africa and stable Eurasia (e.g. Ritzwoller and Levshin, 1998; Pasyanos et al., 2001a). Last year, we reported on tomography results in the Middle East and North Africa. This year, we have extended the model north to include all of Western Eurasia. In addition, following the guidelines for measurements laid out in the 1998 surface wave workshop (Walter and Ritzwoller, 1998) we have exchanged group velocity curves with groups at the University of Colorado and SAIC/Maxwell. The tomography maps that we have created are thus formed from both our own regional measurements and the broader measurements provided by those two groups. Overall, we have examined more than 20,000 seismograms and made more than 9900 Rayleigh wave measurements and 5400 Love wave measurements at periods from 10-100 seconds. These numbers apply to the middle period range and the number of good measurements decreases at the shorter and longer periods. In addition we have incorporated more than 3000 path measurements from the University of Colorado (Ritzwoller, written communication) and SAIC/Maxwell (Stevens, written communication). An example of the event-station paths measured and the tomography results is shown in Figure 4 for Rayleigh waves at 20-seconds period.

The tomography models can be used to estimate velocity structure directly by inversion. However, because surface waves are most sensitive to S-wave velocities averaged over some depth range, these estimates of P-wave velocity structure can be quite non-unique. To better resolve surface wave inversion trade-off issues, we have recently performed constrained grid searches using these tomography models and incorporating other datasets (e.g. Pn tomography, receiver functions) and *a priori* information (e.g. sediment models, Poisson ratios) to estimate velocity structure (Pasyanos and Walter, 2001). Finally, the surface wave tomography results provide a means to test *a priori* geophysical models and we explore this idea more fully in Pasyanos et al., 2001b, on a Western Eurasia and North Africa (WENA) model. Tests of this *a priori* WENA model for improving location are discussed in Schultz et al. (this Proceedings).

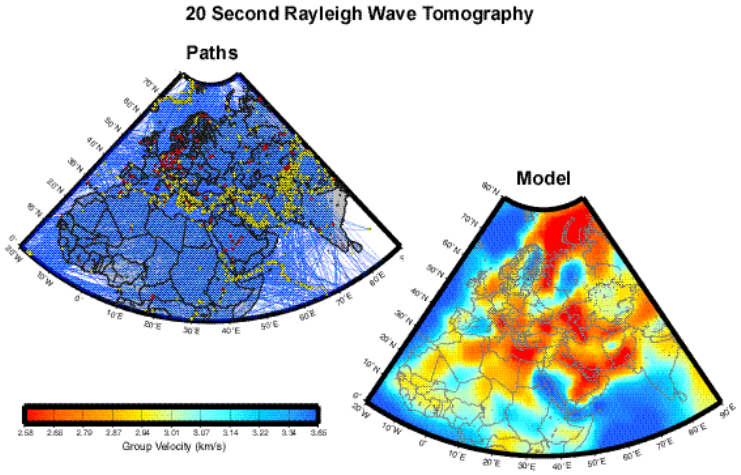

Figure 4. Example of tomography input and results at 20-s period. Top plot shows the events (yellow circles), stations (red triangles) and paths (blue lines) used in the tomography. The path coverage is fairly good in most of the plot, but there are some holes without many crossing paths around the periphery of the plot. The model plot shows the 20-s group velocity. The slower regions match up well with known sedimentary basins and tectonic regions. The faster regions correspond well with oceanic regions and exposed cratons.

Phase-matched M_S and Regional M_S-m_b

The teleseismic discriminant M_S:m_b is one of the best understood and most effective discriminants known (e.g. Stevens and Day, 1985). Several studies have also shown that it appears to be effective down to as small magnitudes as can be measured regionally (e.g., Denny et al., 1987). The problem is that the 20-second surface wave amplitude on which M_S is based can be below the noise even at regional distances. We are researching several ways to allow M_S measurements on smaller magnitude events to be made and used to improve discrimination. One way is to allow regional M_S measurements at periods between 10 and 20 s where the regional Airy phase produces the largest amplitudes (e.g., Denny et al., 1987). Additionally we can improve signal-to-noise by making use of phase-match filters (e.g. Herrin and Goforth, 1977). This is particularly attractive because in addition to reducing the noise level in the signal, it can provide an accurate maximum Ms estimate even on a very noisy trace. For small explosions that have reduced M_S excitation to start with and may not have observable surface waves, this method can still provide some discrimination power relative to earthquakes of the same mb that do have measurable M_S.

The Rayleigh wave group velocity tomography described above can be used to provide predicted group velocity curves for input to a phase-match filtering routine. We can pre-calculate the expected group velocity at a station for any nearby event using the tomography model. In Figure 5, we show such a surface for station KEV in Norway. In addition we can use the measurements to provide an additional refinement to the model predictions using an intelligent interpolation technique. Here we use the Bayesian kriging technique of Schultz et al. (1998) on the measured residuals and add these back to the surface. Pasyanos (2000) previously demonstrated that this model plus a kriging approach provides better estimates of group velocity than either the model or kriging alone. Figure 5 shows an example of a PDE explosion and compares the raw data, a bandpass-filtered signal and a redispersed seismogram from a phase-match filter. Note the improved signal-to noise in the phase-match trace. We previously have compared the impact on the Ms mb discriminant of using phase-match Ms estimates instead of the normal filters in the Middle East and North Africa and found significant improvement. We are now recalculating this comparison for the much larger western Eurasian dataset and will report on Ms:mb results at the meeting

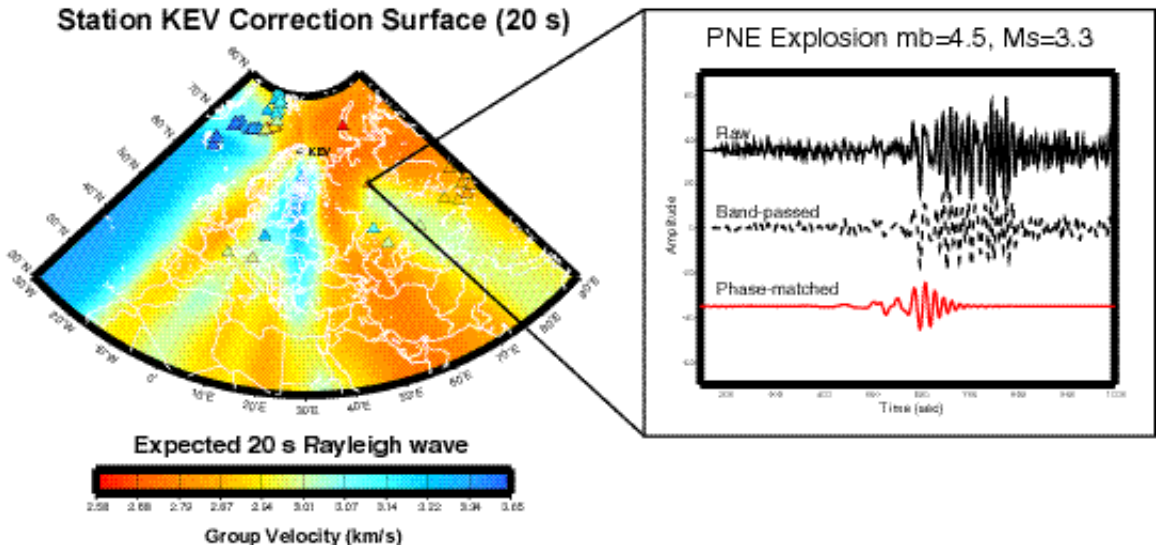

Figure 5. Correction surface for KEV showing predicted 20 second Rayleigh group velocities as a function of event location. The inset compares the results of three different processing on a PNE seismogram. The phase-match redispersed seismogram result comes from using the correction surface.

CONCLUSIONS AND RECOMMENDATIONS

Regional discrimination algorithms require calibration at each seismic station to be used for nuclear explosion monitoring. We have developed a revised Magnitude and Distance Amplitude Correction procedure to remove source size and path effects from regional body-wave phases. This allows the comparison of any new regional events recorded at a calibrated station with all available reference data and models. This also facilitates the combination of individual measures to form multivariate discriminants that can have significantly better performance. We have also developed surface wave group velocity maps and correction surfaces for phase-match filtering to improve Ms-mb discrimination and lower its effective threshold. Calibrating seismic stations to monitor for nuclear testing is a challenging task that will require processing large amounts of data, and collaboration with government, academic and industry researchers and incorporation of the extensive R&D results both within and outside of NNSA.

REFERENCES

Brune, J., (1970). Tectonic stress and the spectra from seismic shear waves earthquakes, *J. Geophys. Res*., **75**, 4997-5009.

Chavez, D., and K. F. Priestley (1986). Measurement of frequency dependent Lg attenuation in the Great Basin, *Geophys. Res. Lett., 13*, 551-554.

Denny, M. D., S. R. Taylor, and E. S. Vergino (1987). Investigation of mb and Ms formulas for the western United States and their impact on the Ms/mb discriminant, Bull. Seism. Soc. Am., 77, 987-995.

Herrin, E. and T. Goforth (1977). Phase-matched filters: Applications to the study of Rayleigh waves, *Bull. Seism. Soc. Amer., 67*, 1259-1275.

Mayeda, K. M. and W. R. Walter, (1996). Moment, energy, stress drop and source spectra of Western U.S. earthquakes from regional coda envelopes, *J. Geophys. Res*., **10***1*, 11,195-11,208.

Pasyanos, M. E. (2000). Predicting geophysical measurements: testing a combined empirical and model-based approach using surface waves, *Bull. Seism. Soc. Am., 90*, 790-796.

Pasyanos, M. E., and W. R. Walter (2001b). Crust and upper mantle structure of North Africa, Europe and the Middle East from inversion of surface waves, *Geophys. J.* (in revision).

Pasyanos, M. E., W. R. Walter and S. E. Hazler (2001a). A surface wave dispersion study of the Middle East and North Africa for monitoring the comprehensive nuclear-test-ban treaty, *Pure. Appl. Geophys*., 158, 1145-1474.

Pasyanos, M. E., W. R. Walter, M. Flanagan, P. Goldstein, and J. Bhattacharyya (2001b). Building and testing a geophysical model for Western Eurasia and North Africa, *J. Geophys. Res*. (submitted).

Ritzwoller, M. H., and A. L. Levshin (1998). Eurasian surface wave tomography: group velocities, *J. Geophys. Res*. 103,4839-4878.

Rodgers, A. J. and W. R. Walter, (2002). Seismic Discrimination of the May 11, 1998 Indian Nuclear Test with Short-Period Regional Data From Station NIL (Nilore, Pakistan), *Pure Appl. Geophys.* (in press).

Schultz, C, S. Myers, J. Hipp, and C. Young (1998). Nonstationary Bayesian kriging: a predictive technique to generate corrections for detection, location and discrimination, *Bull. Seism. Soc. Am., 88* 1275-1288.

Stevens, J. L. and S. M. Day (1985). The physical basis of mb:Ms and variable frequency magnitude methods for earthquakes and explosion discrimination, *J. Geophys. Res., 90*, 3009-3020.

Taylor, S., (1996). Analysis of high-frequency Pg/Lg ratios from NTS explosions and Western U.S. earthquakes, *Bull. Seism. Soc. Am., 86*, 1042-1053.

Taylor, S., A. Velasco, H. Hartse, W. S. Philips, W. R. Walter, and A. Rodgers, (2002). Amplitude corrections for regional discrimination, *Pure. App. Geophys*. (in press).

Walter, W. R., K. Mayeda, and H. J. Patton, (1995). Phase and spectral ratio discrimination between NTS earthquakes and explosions Part 1: Empirical observations, *Bull. Seism. Soc. Am.*, **85**., 1050-1067.

Walter, W. R. and M. Ritzwoller, (1998). Summary report of the workshop on the U.S. use of surface waves for monitoring the CTBT, Lawrence Livermore National Laboratory *UCRL-ID-131835*, 16 pp.

Walter, W. R., A. Rodgers, K. Mayeda and S. Taylor (2000). Regional body-wave discrimination research, in the "Proceedings of the 22nd Annual DoD/DOE Seismic Research Symposium, *Dept. of Defense and Dept. of Energy Report, (three volumes),* Volume II, pages 443-452.

Walter, W. R. and S. R. Taylor (2001), A revised Magnitude and Distance Amplitude Correction (MDAC2) procedure for regional seismic discriminants, Lawrence Livermore National Laboratory internal report.

EXCITATION OF REGIONAL WAVES AND MAGNITUDE DEPENDENCE OF PHASE SPECTRAL RATIOS IN CENTRAL ASIA

Jiakang Xie

Lamont-Doherty Earth Observatory of Columbia University

Sponsored by The Defense Threat Reduction Agency

Contract No. DSWA01-98-1-0009

ABSTRACT

Multiple station recordings of Pn and Lg spectra from a large (m_b = 6.6) nuclear explosion, and several recent chemical explosions ($m_b \leq 3.7$) in central Asia are used to invert for source spectral parameters and path variable Q models. It is confirmed that a simplified, modified Mueller-Murphy source model fits the source spectra of nuclear explosions well. For chemical explosions, the model fits source spectra reasonably well, although the observed Pn source spectra tend to be complicated by event-variable, random fluctuations. The estimated source seismic moments (M_0) and corner frequencies (f_c) are used together with a previous data set to derive source spectral scalings for underground explosions. The new scalings essentially extend the validity of the previous scalings to a wider m_b range of between about 3.7 and 6.6. specifically, the new scalings have the previously reported features of (1) linear correlation between log M_0 and m_b, (2) larger Pn M_0 than Lg M_0 for the same explosions, (3) quarter-root scaling between f_c and M_0, and (4) higher Pn f_c than Lg f_c by factors of 4-5.

A necessary consequence of the scaling relationships is that the Pn/Lg spectral ratio from an explosion should grow rapidly in an intermediate frequency range roughly between the f_c of Pn and Lg. Owing to the scaling of f_c with event size, this frequency range shifts higher for smaller events. This magnitude dependence of the Pn/Lg spectral ratio is directly confirmed by the observation of the above explosions. Further, multiple-event stacking of the Pn/Lg ratios observed at a single station (WMQ), from many Soviet explosions with similar m_b values of about 6.0 are compared with the respective ratio from events with m_b of about 5.0. This comparison verifies the magnitude dependence, which is of great theoretical and practical significance. A simple and efficient procedure is proposed to account for the effect of the magnitude dependence of Pn/Lg ratios in the identification of explosions.

Work is being conducted to invert for source moment, corner frequency and path-variable Q values using Pg from central Asia. Currently I am calculating reasonable geometrical spreading terms of Pg, using synthetics in various velocity models developed for central Asia. I will present resulting source spectra and path Q of Pg.

KEY WORDS: seismic sources, central Eurasia, explosion discrimination, P/Lg ratios, regional wave spectra

OBJECTIVE

The primary objective of this research is to quantify the difference in the excitations of various regional waves, so that we may achieve better, quantitative understanding and criterion of the P/Lg spectral ratio discriminant of explosions. There proposed research is composed of several tasks. The first is to further improve the inverse method for simultaneous determination of source seismic moment (M_0), corner frequency (f_c) and path-variable Q_0 and η (Q at 1 hz and its power-law frequency dependence, respectively)

using regional wave spectra. The second task is to apply the improved inverse method to Lg, Pn, Pg and Sg spectra from many earthquakes and explosions in Eurasia to estimate source M_0, f_c and path Q_0, η. The third task is to analyze source spectral scaling and other source spectral characteristics of seismic events, such as the amount of spectral overshoot of explosions, to explore when, how and why the P/Lg spectral ratios can be used to discriminate explosions from earthquakes.

This research provides important input to the world-wide monitoring of nuclear explosions. The source spectral behavior inferred from this study will help to understand if, when and how the P/Lg amplitude ratio can be used to discriminate explosions from earthquakes.

RESEARCH ACCOMPLISHED

Data

The data used in this study include vertical component Pn and Lg records from many explosions in central Asia. These include (a) a large, m_b = 6.6 underground nuclear explosion on May 21, 1992 in the Lop Nor Test Site (LTS), recorded by IRIS stations AAK, ARU, GAR and OBN, and by the 11 portable Passcal stations deployed during the 1991-1992, passive Tibetan plateau experiment; (b) five chemical explosions detonated in the Kazakhstan Test Site (KTS) between 1997 and 1999, with known yields of 25 or 100 ton (Myers et al., 1999). These explosions are recorded at the Kazakhstan Network (KZNET) stations; (c) fifteen Soviet underground nuclear explosions between 1987 and 1989, recorded at the Chinese Digital Seismic Network (CDSN) station WMQ. Pn and Lg spectra are obtained using the Fast Fourier Transform (FFT) of the time series.

Source spectral parameters of large and small explosions

I inverted for Pn and Lg source spectral parameters of the explosions for which multiple-station recordings are available, using the inverse method of Xie (1998) and Xie and Patton (1999; hereafter referred to as XP99). These explosions include the large ("megaton") LTS and small chemical explosions (event groups (a) and (b) mentioned in the above paragraph). The resulting M_0 and f_c values are listed in Table 1.

Source spectral scalings

XP99 derived scaling relationships among m_b, M_0 and f_c values for Pn and Lg source spectra from underground nuclear explosions at the LTS and KTS, with m_b values between about 5 and 6. Here I extend the scalings with the new results reported in Table 1. Figure 1 shows m_b versus $\log(M_0)$ estimates from Pn and Lg spectra for explosions, obtained in this and previous studies. With m_b treated as the independent variable, linear regression analysis gave the following relations: $\log M_0 = 9.83(\pm 0.20) + 1.10(\pm 0.03)\, m_b$ for *Pn*, $\log M_0 = 9.27(\pm 0.28) + 1.12(\pm 0.04)\, m_b$ for *Lg*; Figure 2 shows the f_c versus M_0 values obtained in this and previous studies. Linear regressions over the logarithm of these values yield the following relations: $\log M_0 = 18.02(\pm 0.29) - 4.05(\pm 0.21) \log f_c$ for *Pn*, $\log M_0 = 15.19(\pm 0.21) - 3.77(\pm 0.12) \log f_c$ for *Lg*. For both the Lg and Pn source parameters, the new scalings in the above equations essentially confirm the respective previous scalings in XP99, with a wider range of validity in terms of m_b (the new m_b range is from about 3.7 to 6.6, expanding the previous range by 1.5). Specifically, the new scalings confirm that at the same M_0 level, Pn f_c is higher by a factor of 4 to 5 than the Lg f_c.

Observed magnitude dependence of Pn/Lg spectral ratios

As suggested by XP99, a necessary consequence of the source spectral scalings is that the frequency range, over which the observed Pn/Lg spectral ratios grow rapidly, must be dependent on the sizes of the

explosions in the study area. This was directly confirmed by XP99 using observed Pn/Lg ratios from nuclear explosions in the m_b range between about 5 and 6. Here I reconfirm this dependence again with the new data that extends the m_b range to between about 3.7 and 6.6. Figure 3 redisplays the observed, station-averaged Pn/Lg spectral ratios for all of the explosions and earthquakes that were shown in Figure 12 of XP99. Also replotted are the generic Pn/Lg ratios for hypothetical explosions and earthquakes of various m_b values, calculated using (a) the source scaling relationships, (b) the modified Mueller-Murphy (MMM) source model, and (c) an average path effect, constructed using the averaged epicentral distance, $\bar{\Delta}$, $\overline{Q_0}$ and $\bar{\eta}$ in XP99. The average path in XP99 is constructed over 13 paths from the LTS to stations of the Kyrghistan and Kazakhstan networks. To compare the previous generic and observed ratios with the new observations, I corrected for the new, different path effects involved for events 052192 and 082298, and plotted the resulting Pn/Lg ratios in Figure 3.

Shapes of the new observed ratios for the large (m_b = 6.6), 052192 and small (m_b = 3.8), 082298 explosions are shifted with respect to the earlier ratios. The frequency range, over which the ratio shows a rapid increase until it reaches the Pn f_c, is shifted lower for the large explosion, and shifted higher for the small explosion. These shifts are exactly as predicted by the scaling relationships. Interestingly, the shift of the ratio from event 082298 is so significant that it falls into the earthquake population in the frequency range of 1-10 Hz. This overlap also exists for the raw ratio from 082298, with no path correction applied (not shown).

To further explore the generality of the observed magnitude dependence of the Pn/Lg ratios from explosions in central Asia, I did an independent, direct calculation of Pn/Lg spectral ratios for fifteen Soviet underground nuclear explosions detonated at the KTS between 1987 and 1989 as recorded at the CDSN station WMQ. I stacked the Pn/Lg spectral ratios for the 10 events with $m_b \geq 6.0$ and for the 5 events with $m_b \leq 5.0$, respectively, resulting in two stacked spectral ratios with mean m_b values of 6.2 and 4.8, respectively. These are plotted in Figure 4, together with the two generic source ratios plotted in Figure 3. The path Pn and Lg Q models from the KTS to WMQ were expected to be similar to those for the average central Asia path used for generating the generic curves. The observed stacked Pn/Lg ratios in Figure 4 are very close to the respective generic ratios, directly confirming the magnitude dependence of the ratios in the study area.

A procedure to account for the magnitude dependence

Had we not known that event 082298 was an explosion and had we not been aware of the magnitude dependence of the Pn/Lg ratios in the study area, we would have mis-identified that event as an earthquake based on the ratio in Figure 3. An important outcome of this study is that, based on the scaling relationships developed in this and previous studies, we can predict how f_c values vary with m_b or M_0 values. For example, according to source scalings for explosions (equations (1) through (4)), we can estimate the factors by which the f_c values for an m_b = 3.8 event increase from those of an m_b = 5.5 event: the factor should be 2.9 for Pn f_c, and 3.2 Lg f_c. If we are in a situation of knowing the magnitude of event 082298, but not its event type, we can plot its Pn/Lg ratio with the frequency axis reduced by a factor of about 3.0 (roughly the median of the Pn and Lg factors), and compare the resulting ratio with the previously observed ratios for larger explosions, as shown in Figure 5. In that figure the new Pn/Lg ratio for 082298, plotted with the frequency normalization, is in the explosion population, and lies between the generic curves for m_b =5.0 and 6.0.

The above normalization procedure is based on scalings for explosions. Alternatively we can choose to use scalings for earthquakes (equations (18), (19), (22) and (23) of XP99). In that case the respective median of predicted frequency shift for Pn and Lg is a factor of 3.7, rather than 3.0. When a frequency-normalization by factor of 3.7 is conducted, the shift of the Pn/Lg ratio of the 082298 explosion is very similar to that shown in Figure 5 (not plotted). Therefore so long as we take into account the magnitude dependence of the Pn/Lg ratios, the event of m_b 3.8 is identified as an explosion regardless of which set of scalings are

used.

CONCLUSIONS AND RECOMMENDATIONS

I would like to clarify two points of this and previous works: first, we think highly of the observations done at the Nevada Test Site (NTS); we have never suggested that the source spectral scalings developed for test sites in central Asia are valid for a test site characterized by a very different geology, such as the NTS. Second, part of our results have been direct observations. For example, the directly observed Pn/Lg ratios plotted in Figure 12 of XP99 and Figure 4 of this paper clearly show statistical trends for the ratios to vary with event magnitude in the two test sites (LTS and KTS). One might argue that our inversions of source spectral parameters are subject to some uncertainties owing to the difficult nature of spectral inversions, but the direct observations are not subject to such uncertainties.

Since it is difficult to find explosions that both span a wide magnitude range, and are well recorded at regional distances over the same (or similar) paths, the number of events that we analyzed so far was relatively small. In particular, there were no explosions in the kiloton range. There was also a lack of data from earthquakes beyond the m_b range between about 4.0 and 5.5, used by XP99. Future research should be directed to remove these limitations. Other worthwhile future research topics, judging from the results obtained so far, include the understanding of (a) whether the scalings are valid for other high-frequency regional waves, such as Pg and Sn, (b) whether the magnitude dependence of the Pn/Lg ratios extend to other types of cross-phase spe ctral ratios, such as Pn/Sn and Pg/Lg ratios in the study region, and (c) how the behavior of regional wave spectra and cross-phase ratios differ from those in central Asia in a drastically different geological environment, such as that in and around the NTS of the western U.S.

REFERENCES

Myers, S.C., W.R. Walter, K. Mayeda and L. Glenn, Observations in support of Rg scattering as a source for explosion S waves: regional and local recordings of the 1997 Kazakhstan depth of burial experiment, Bull. Seism. Soc. Am., 89, 544-549, 1999.

Xie, J., 1998. Spectral inversion using Lg from earthquakes: Improvement of the method with applications to the 1995, western Texas earthquake sequence, Bull. Seism. Soc. Am., 88, 1525-1537.

Xie, J. and H. Patton, 1999. Regional Phase Excitation and Propagation in the Lop Nor Region of Central Asia and Implications for the Physical Basis of P/Lg Discriminants, J. Geophys. Res., 104, 941-954.

Table 1. Explosions used in the multiple-station spectral inversions

Event ID	Origin Time (H:M:S)	m_b	Yield (ton)	Pn M_0† (Nm)	Pn f_c† (hz)	Lg M_0† (Nm)	Lg f_c† (hz)
052192	04:59:57.5	6.6	-	$1.5(\pm0.3)\times10^{17}$	1.7(± 0.1)	$4.3(\pm0.6)\times10^{16}$	0.4(±0.1)
080397	08:07:20.0	-	25	$7.3(\pm0.7)\times10^{13}$	10.0(±0.4)	$1.1(\pm0.3)\times10^{13}$	3.4(±0.1)
083197	07:08:39.2	-	25	$3.5(\pm0.9)\times10^{13}$	13.0(±0.8)	$2.9(\pm1.1)\times10^{12}$	5.3(±0.2)
092897	07:30:15.1	-	25	$1.1(\pm0.2)\times10^{13}$	19.8(±1.5)	$1.2(\pm0.1)\times10^{12}$	6.6(±0.2)
082298	05:00:19.0	3.8	100	$1.1(\pm0.2)\times10^{14}$	9.3(±0.4)	$2.7(\pm0.5)\times10^{13}$	2.9(±0.2)
092599	05:00:05.7	3.7	100	$9.7(\pm2.5)\times10^{13}$	8.7(±0.7)	$3.3(\pm0.5)\times10^{13}$	3.2(±0.1)

Event ID is composed of the month, date and year of the explosion. Event time, location and m_b values are from the U.S. Geological Survey preliminary determination of epicenters (PDE) bulletin, or the International Monitoring System (IDC) bulletin. Event 052192 is a nuclear explosion in the Lop Nor Test Site. All other events are chemical explosions in the Kazakhstan Test Site.

†M_0, f_c values are from spectral inversions of this study.

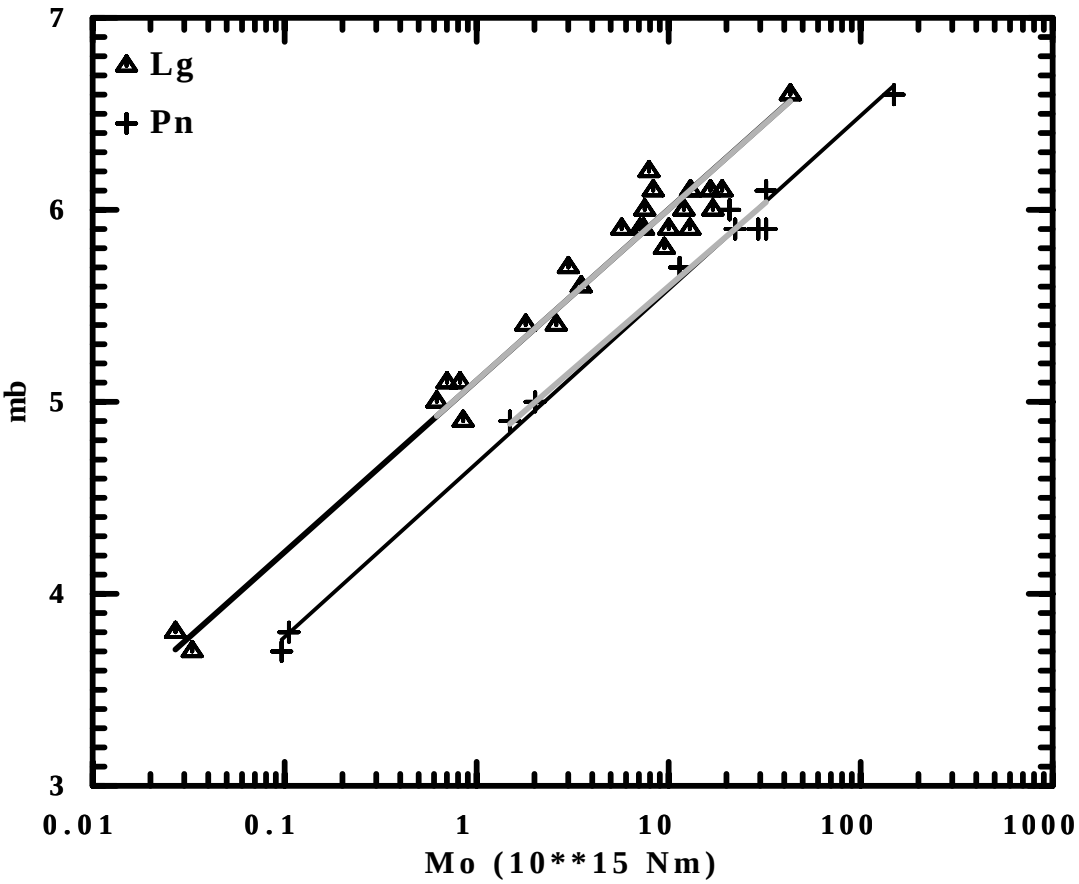

Figure 1. m_b versus logarithm of M_0 for underground explosions in the KTS and LTS. Data points included are those in Figure 7 of Xie and Patton (1999), plus those of the large nuclear underground explosion and two 100-ton chemical explosions obtained in this study. The three 25 ton explosions have no reliable m_b estimates and are not included. New and previous linear regression results are shown by black and gray lines.

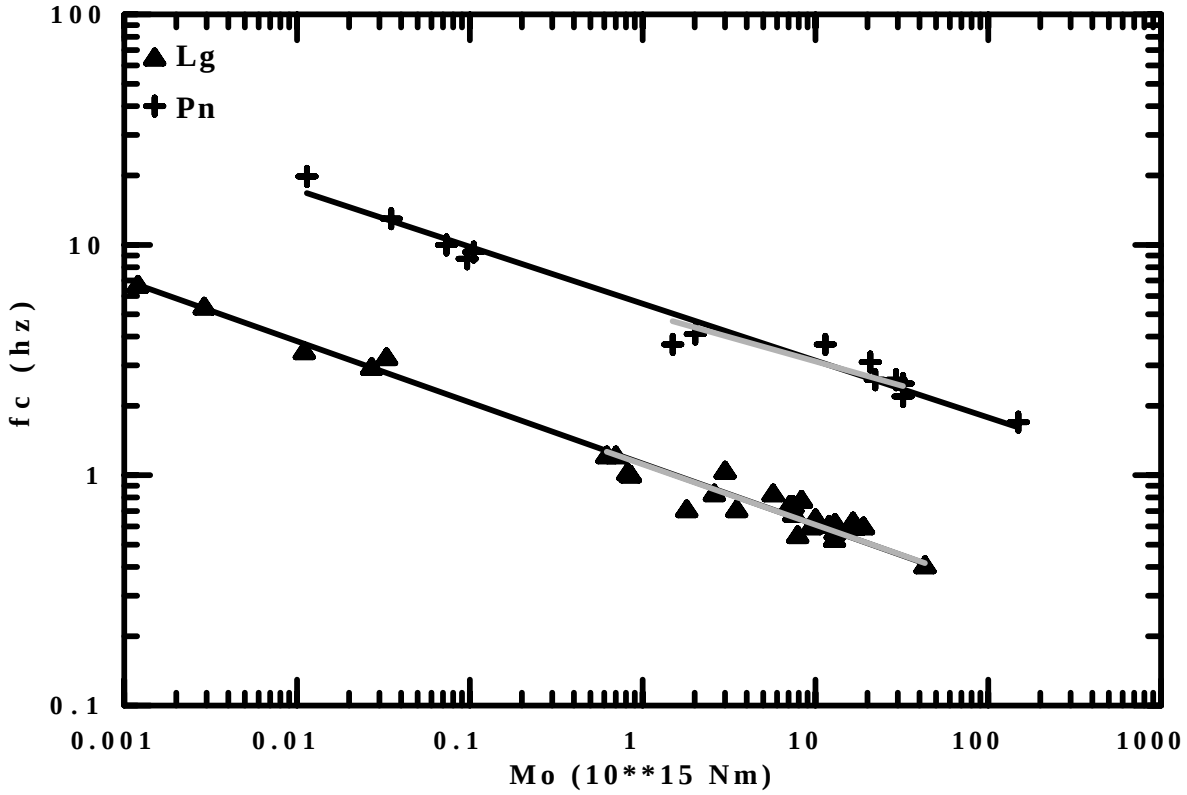

Figure 2. Logarithm of M_0 versus logarithm of f_c values for the explosions. Data points are from this study, and Figure 9 of Xie and Patton, 1999. New and previous linear regression results are shown by black and gray lines.

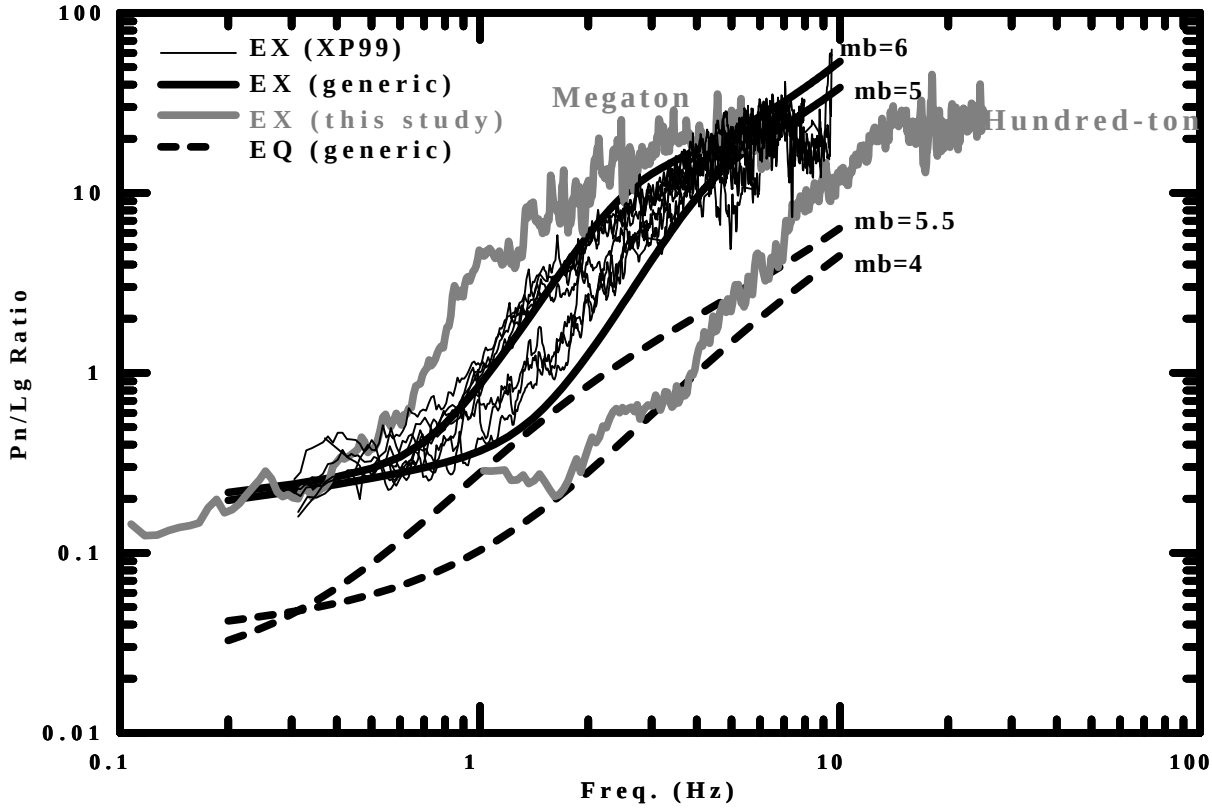

Figure 3. Pn/Lg spectral ratios of ground motion. "EX" and "EQ" denote ratios for explosions and earthquakes, respectively. Continuous smooth curves are generic ratios calculated for hypothetical explosions with m_b of 5.6 and 6.0. Dashed smooth curves are generic ratios calculated for hypothetical earthquakes with m_b of 4.0 and 5.5. All generic ratios are calculated at an average central Asian station about 1000 km away from the sources, and have been shown in Figure 12 of Xie and Patton (1999). Fluctuating, black curves denoted as "EX (XP99)" are station-averages of the observed ratios from explosions with m_b clustered near 5.0 and 6.0, by Xie and Patton (1999). Observed ratios from this study (gray curves) are station-averaged ratios from the 052192 ("megaton") and 082298 ("Hundred-ton") explosions, with path corrections. The path corrections are made by first reducing the observed Pn/Lg ratios to the source using the average Q models for paths from events 052192 and 082298. The resulting ratios are then back-propagated to the average central Asian station by using the Q models mentioned in Figure 12 of XP99. Note that the ratio from the 082298 explosion are well within the earthquake population between 1-10 Hz. This is also true when no path correction is applied (not shown).

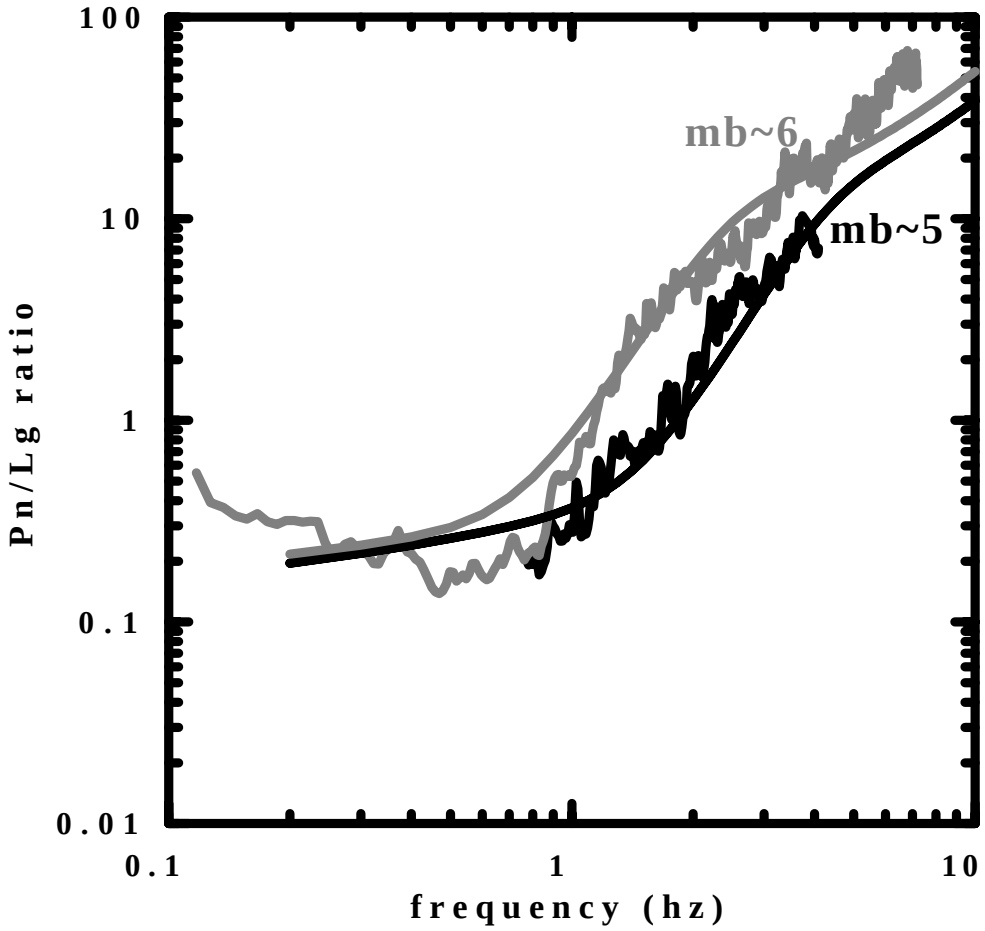

Figure 4. Event-stacked Pn/Lg spectral ratios for Soviet explosions with magnitudes around 5.0 and 6.0, respectively, observed at station WMQ. Superposed are the generic ratios for average central Asian paths (the same as those in Figure 3). The observed ratios are surprisingly close to the generic ratios.

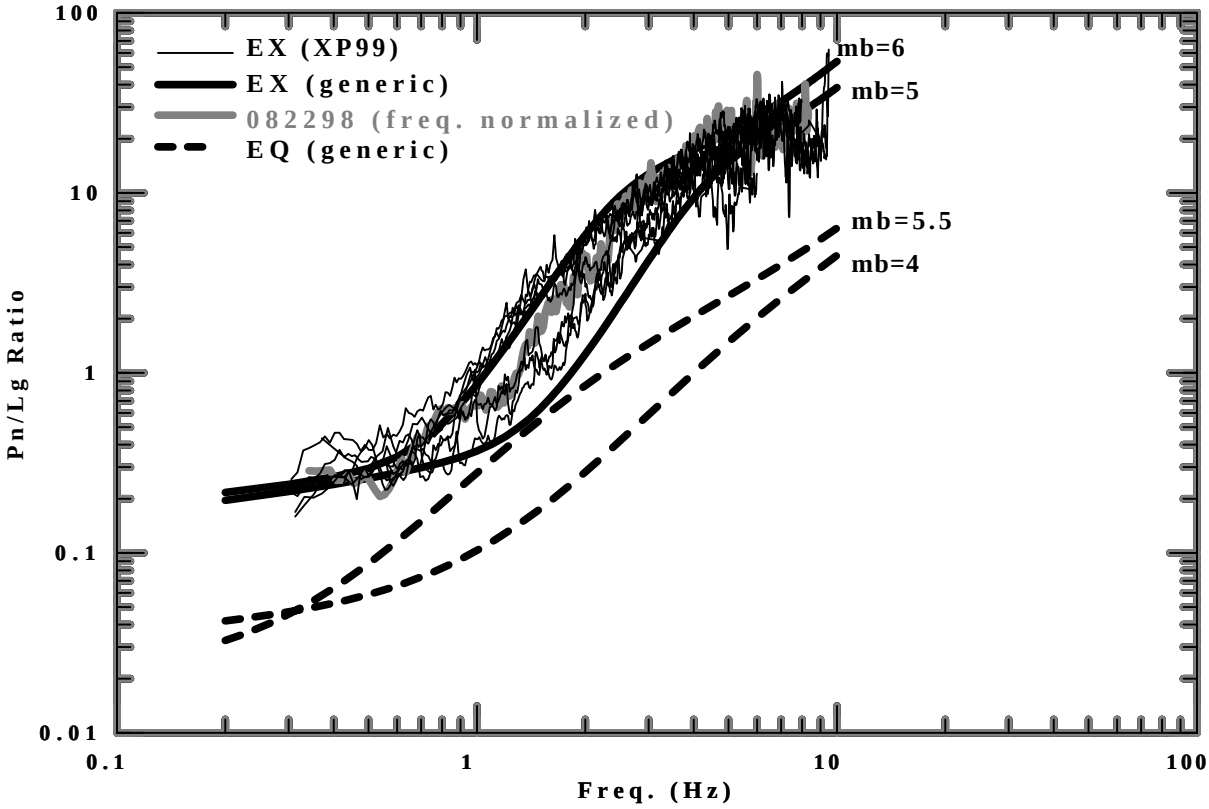

Figure 5. Same as Figure 3 except that ratio for the event of 052192 is not shown, and ratio for the event of 082298 is shown with a frequency reduction of a factor of 3.0. As predicted by the scaling relationships (equations (1) through (4)), the frequency reduction indeed shifts the ratio of 082298 into the position of an m_b = 5.5 explosion.

Seismic Source Characterization

REFINING FAULTING PARAMETERS AND DEPTH ESTIMATES FOR EARTHQUAKES IN EASTERN ASIA

Charles J. Ammon[1], Moira L. Pyle[1], George E. Randall[2], and Aaron A. Velasco[2]

Saint Louis University,[1] Los Alamos National Laboratory[2]

Sponsored by National Nuclear Security Administration
Office of Nonproliferation Research and Engineering
Office of Defense Nuclear Nonproliferation

Contract No. # DE-FG04-2000-AL67054 and W-7405-ENG-48

ABSTRACT

Accurate and stable seismic source parameters for small-to-moderate size events are essential for many aspects of regional nuclear explosion monitoring. For example, magnitude and distance amplitude corrections (MDAC) have been developed for regional discrimination, but they rely on stable moment estimates. We develop a catalog of regional earthquakes in eastern Asia with estimated seismic moments, source mechanisms, and depths using regional seismic data. A catalog of regionally estimated seismic moments, source mechanisms, and depths is also a useful tool for magnitude calibration and regional characterization. We are particularly interested in constraining seismic moments, which are critical for calibrating regional magnitude scales with global catalogs, and in improving depth estimates for Asian events.

A significant challenge of modeling small-to-moderate-size seismic sources is the necessity of relying on short-period signals with long travel paths that have substantial sensitivity to earth structure along the path. When the path effects are unknown or difficult to account for, we must rely on components of seismic signals that are minimally dependent on the structure. Although regional surface-wave phases are strongly influenced by structure, surface-wave amplitude spectra can be modeled adequately with relatively simple earth models, and these spectra carry valuable information on source character. Our efforts build on existing seismic source analysis techniques. We directly model regional seismograms where possible but combine those with surface-wave amplitude spectra observed at more distant regional stations. The inversion is performed using a grid search for strike, dip, rake, moment, and depth. Choosing suitable weights for the different data sets remains a challenge that will only be overcome with experience. Initially, all data are weighted equally by normalizing seismograms and spectra by their uncertainty and the number of observations in each data set. For larger events ($M_W > 5$) we can also include long-period (approximately 40-s period) body-wave trains, which can be modeled reliably using simple stratified earth models. The use of spectra and long-period signals is ideal for estimating the moment and faulting geometry of signals but simple least-squares norms based on these signals do not often provide satisfactory resolution of source depth (when the source is shallow). However, in cases where the long-period mechanism is relatively stable as a function of depth, we can overcome this limitation by exploiting signals more diagnostic of source depth such as teleseismic body-waveforms, broad-band *Pn* waveforms, or select short-period Rayleigh wave spectra. For example, once the mechanism is relatively well known, we can refine depth estimates using short-period P-waveforms using a synthetic seismogram-matching procedure that provides source depth constraints that in some cases span a few kilometers.

KEY WORDS: seismic source characterization, magnitude calibration, regional characterization, regional wave propagation, seismic source depth

OBJECTIVE

Estimating the source type or faulting geometry of small seismic events located hundreds of kilometers from the nearest seismometer can be difficult. Typically one of two classes of modeling approaches is adopted: Spectral, or time-domain. Spectral techniques use the observed variation in surface-wave spectra as a function of azimuth to match the radiation pattern of the source (e.g. Patton, 1976, 1980, 1998; Herrmann, 1976, 1979; Romanowicz, 1982; Patton and Zandt, 1992; Herrmann and Ammon, 1997, and many others). Time-domain methods are straight-forward matches to the observed seismograms and include both amplitude and phase information (e.g. Langston, 1981; Dreger and Helmberger, 1991, 1992, 1993; Lay et al., 1994; Randall et al., 1995; Ghose et al, 1998; Ammon et al., 1998, and others). Spectral methods can be designed to include amplitude only, or amplitude and phase information, while time-domain methods include both. Phase information provides valuable constraints on the source mechanism and depth, but the observed phase is often sensitive to details in Earth structure along the propagation path. Time-domain source inversion methods are usually applied to large events with good long-period signals or short-period signals of small events that have minimal distortion from Earth structure (such as teleseismic P and SH waves) or local and close-regional (less than a few hundred *km*) signals. To use phase in surface-wave spectral analyses works best with a good estimate of the surface-wave phase velocity variations between the source and receiver.

If we consider the problem addressed in Comprehensive Nuclear-Test-Ban (CTBT) work, the best signals from a shallow small event are most likely to be short-period surface waves. But directly fitting the phase of short-period Rayleigh waves (probably the best regionally observed, deterministic signal from a small, shallow event) is challenging because these waves are sensitive to shallow, variable structure along the propagation path. Rayleigh-wave spectral amplitudes are less sensitive to structure variations than the corresponding signal phase, and contain valuable information on the source depth. Thus, it is desirable to combine the part of distant signals that is less sensitive to structure with the amplitude and phase information from the closer stations.

Simultaneous spectral and time-domain seismic source modeling

To achieve this, we combine surface-wave spectral amplitude modeling and time-domain waveform fitting in a grid-search algorithm to estimate the source mechanism (systematically check strike, dip, rake, and depth, & include an isotropic source for comparison). The procedure include surface-wave amplitude information for stations distant from the source and include both amplitude and phase information from the closer observations and teleseismic body waves if the event is large enough for these to be observed (Figure 1). Incorporating observations from more distant stations makes a significant contribution to seismic source studies in two important ways: First, the azimuthal coverage of radiation patterns is improved and second, Rayleigh wave amplitude spectra contain valuable information on the source depth. For shallow events, improved resolution of the depth requires short-period information because the information on shallow depths are contained in the short-period signals. Herrmann (1979) exploited information in intermediate-period surface waves to estimate the faulting geometry and depth of earthquakes in east and central North America from old analog records. He observed signals out to distances of thousands of kilometers and extracted spectral amplitudes suitable for constraining the earthquake parameters. We cannot be certain that observations from such large distances in central Asia will be as simple or robust as those in the stable part of North America. The signal amplitudes may be lower due to scattering and intrinsic attenuation. However, signals from small events may be isolated from background noise and extracted using phase-match filtering exploiting dispersion observations from larger events.

RESEARCH ACCOMPLISHED

The goal of estimating source depth with some precision will require a combination of observations. Particularly valuable in constraining earthquake depth are short-period Rayleigh waves, which may contain a spectral notch indicative of source depth (e.g. Herrmann, 1979). Short-period surface waves can be tricky and when analyzing the signals some form of mode isolation can help simplify their interpretation. Toward-

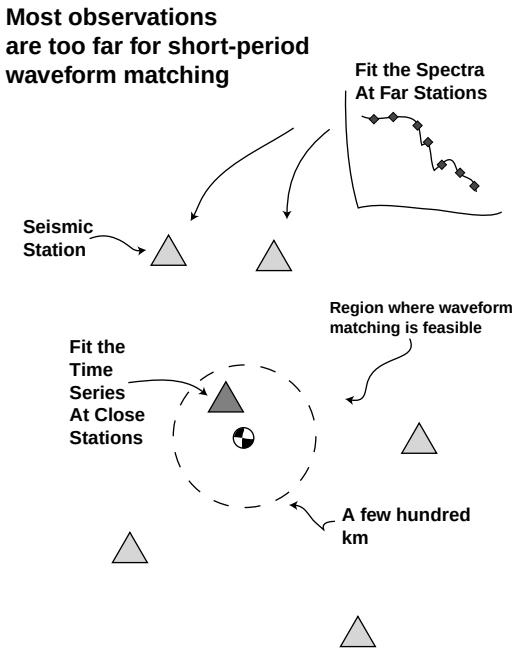

Figure 1. Schematic illustration of the joint source parameter inversion scheme. The triangles represent seismic stations, the focal mechanism represents the source location. The basic idea is to combine observations with a minimal sensitivity to earth structure to produce more accurate estimates of the event mechanism and depth. Since most observations are too far for direct short-period waveform modeling we sacrifice the phase information and use only the more robust spectral amplitudes at those sites. Phase information is included from seismograms recorded at nearby stations, teleseismic P-waves, or regional Pn arrivals.

this goal we have improved and extended software that can be used to analyze and isolate dispersed seismic waves.

Surface-Wave Mode Isolation Software Improvements

In the case of surface-wave analyses, the noise can be background earth noise or signal-generated noise such as body waves, higher modes, multi-pathed arrivals, etc. The dispersed character of surface waves is the key to their identification and extraction from other signals. The computational methods for surface-wave isolation are well established and have been employed for about thirty years (e.g. Dziewonski et al., 1969; Herrin and Goforth, 1977; Levshin et al., 1987, Ritzwoller and Levshin, 1998). An example analysis is shown in Figure 2. We have added a number of minor software improvements to an existing computer application written to perform the surface-wave isolation and group velocity estimation. These enhancements will help ease two aspects of small-event processing. First, we added an option to use pre-event ground motion to estimate the signal-to-noise ratio of the observations. Such information allows quick and easy identification of obviously unreliable observations saving valuable analysts' time for the more subtle observations that require expert knowledge in surface-wave analysis. We have also added the ability to use path-specific group velocities to construct mode-isolation filters (Herrin and Goforth, 1977). Also, higher-mode isolation is now an option. Such higher mode observations can provide valuable constraints on source mechanism and depth, as well as contribute to a better mapping of the regional structure.

Initial Joint Inversion Results

Our early applications of the technique suggest that, in addition to the surface-wave information at greater distance, it can provide better constraints on mechanisms for small events. For larger events, the approach

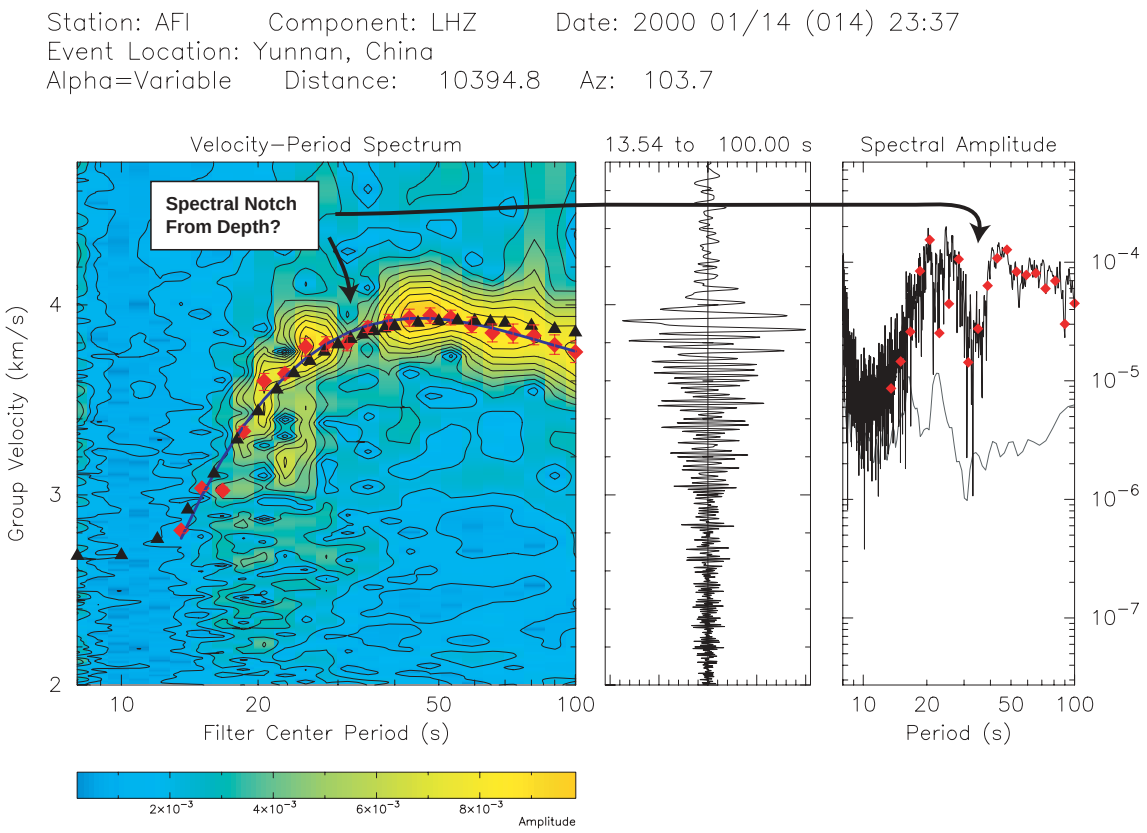

Figure 2. Group-velocity/Mode-Isolation software written for surface-wave analysis. For estimating source properties, the value of the analysis is isolation of fundamental mode surface waves to allow robust spectral amplitudes and to identify waveforms that contain depth relative notches. The above seismogram corresponds to a Rayleigh wave recorded at station AFI at a distance of 10,395 *km* from the *Mw* 5.9 source. The panel on the left shows the signal energy as a function of period and group velocity, the center shows the seismic signal as a function of group velocity, and the last panel shows the seismogram and pre-signal noise spectra.

of Harvard makes more sense since it requires less processing and piecing together of different parts of the seismic wave field. However, the cost of processing simplicity is the fact that the depth of even moderate-size events may be poorly constrained by long-period observations.Thus, we hope to add information even for these moderate-size events by analyzing broad-band or short-period body waveforms (e.g. Langston and Helmberger, 1975). Our initial efforts using waveform comparisons relying on the Harvard mechanisms have resulted in improved depths for a number of events. An example is presented in Figure 4. The Harvard and PDE depths for this event are 33 *km*, but the SH body waveforms observed at station MA2 suggest a slightly shallower depth of about 10 -20 km.

Waveform Collection Efforts

We have assembled long-period displacement seismograms for 50 earthquakes that occurred in the years from 1995-2000 in the Flinn-Engdahl seismic regions 26,27,28, and 41 and which have been modeled as part of the Harvard CMT project. Our plan is to begin modeling these calibrated events to assess the strengths and weaknesses of the joint spectral and time-domain inversion approach. In addition, we have gathered teleseismic P waveforms for the same events to use depth phases to refine depth estimates. Most of the catalog depths for these events are 15 *km* or 33 *km* for Harvard or the USGS respectively.

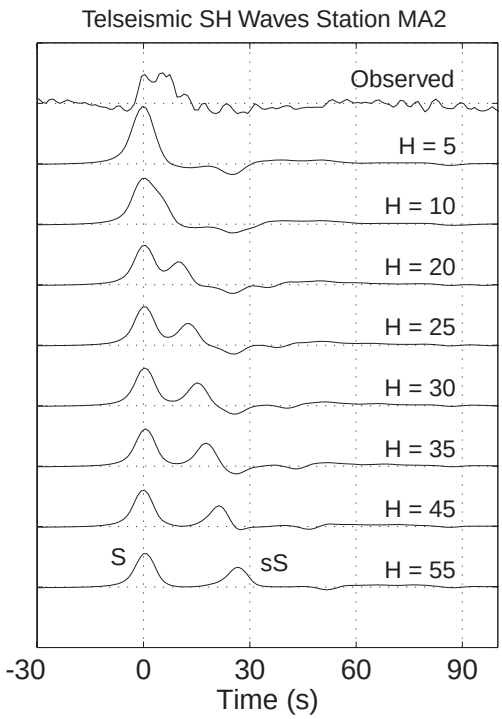

Figure 3. Teleseismic SH-wave comparison for station MA2 ($\Delta = 48$) for a range of source depths. The apparent source depth lies between 10 and 20 *km*. The predicted seismograms were computed using the reflection matrix method for a layered model with a crustal structure appropriate for Asia and a mantle based on PREM. A six-second long trapezoid was convolved with the synthetic seismogram. The signals were aligned on the first peak in the SH waveform.

CONCLUSIONS AND RECOMMENDATIONS

The idea of using teleseismic body waves, surface-wave spectra, or regional Pn waveforms to constrain source depth is not new. Our point is that to constrain the depths of seismic events will require an adaptive approach that utilizes the best data for a particular distribution of observations and a particular focal mechanism. Whenever possible, the combination of these data should be used to assess the reliability of a particular depth. While the approach seemingly lacks elegance or is not easy to implement routinely, the effort is rewarded with improved estimates of source depth, an important parameter for discrimination and for the additional use of the seismograms to estimate such quantities as moment and source mechanism.

REFERENCES

Ammon, C. J., R. B. Herrmann, C. A. Langston and H. Benz (1996), Source parameters of the January 16, 1994 Wyomissing Hills, Pennsylvania earthquakes, Seism. Res. Letters, 69, 261-269.

Dreger, D. S., and D. V. Helmberger (1990), Complex faulting deduced from broadband modeling of the 28 February 1990 Upland Earthquake, Bull. Seism. Soc. Am., 81, 1129-1144.

Dreger, D. S., and D. V. Helmberger (1991), Source Parameters of the Sierra Madre earthquake from regional and local body waves, Geophys. Res. Letters, 18, 2015-2018.

Dreger, D. S., and D. V. Helmberger (1993), Determination of source parameters at regional distances with three-component sparse network data, J. Geophys. Res., 98, 8107-8125.

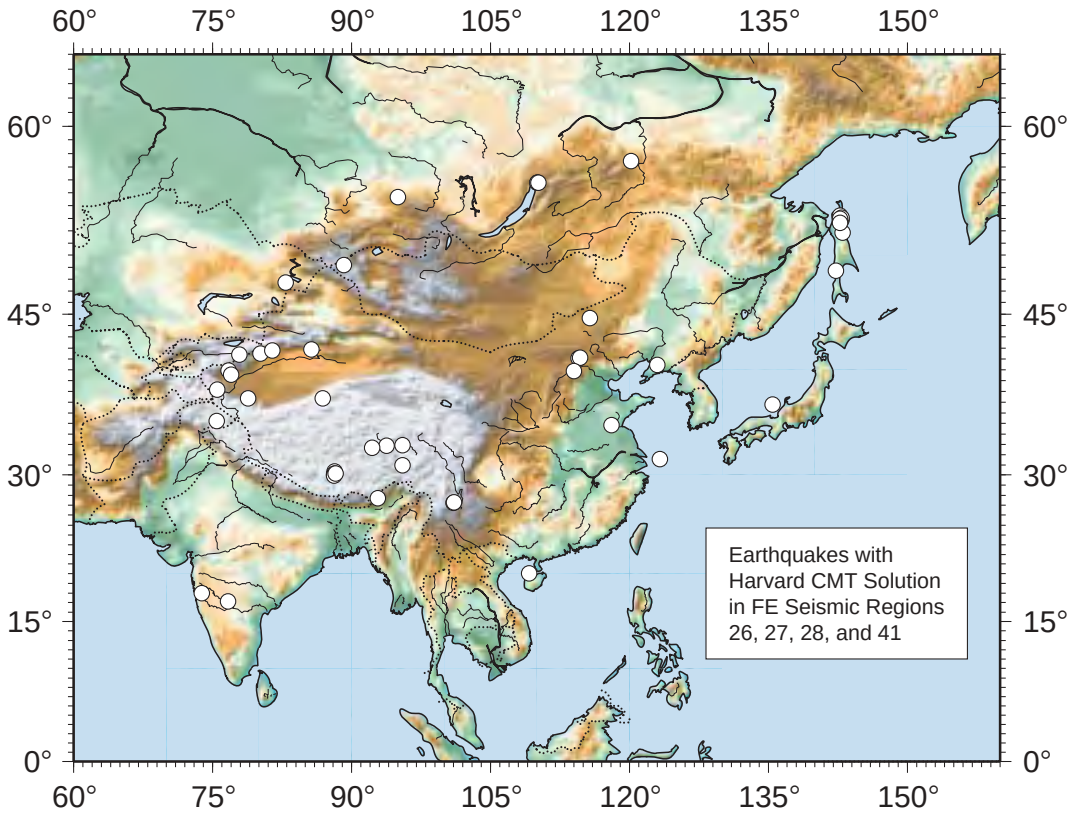

Figure 4. Although the eventual target application for the joint surface-wave spectrum seismogram source estimation procedure are smaller events, the calibration data set is comprised of events with Harvard CMT solutions (shown as circles in the map above). We have selected events within Flinn-Engdahl regions 26,27,28, and 41 for analysis.

Dziewonski, A., S. Bloch and L. Landisman (1969), A technique for the analysis of transient seismic signals, Bull. Seism. Soc. Am., 59, 427-444.

Ghose, S., M. W. Hamburger and C. J. Ammon (1998), Source parameters of moderate-size earthquakes in the Tien Shan, central Asia from regional moment tensor inversion, Geophys. Res. Letters, 25, 3181-3184.

Herrin, E., and T. Goforth (1997), Phase-matched Filters: Application to the study of Rayleigh Waves, Bull. Seism. Soc. Am., 67, 1259-1275.

Herrmann, R. B. (1979), Surface wave focal mechanisms for eastern North American Earthquakes with tectonic implications, J. Geophys. Res., 84, 3543-3552.

Herrmann, R. B. (1986), Surface-Wave studies of some South Carolina earthquakes, Bull. Seism. Soc. Am., 76, 111-121.

Langston, C. A. (1981), Source inversion of seismic waveforms: the Koyna, India, Earthquakes of 13 September, 1967, Bull. Seism. Soc. Am., 71, 1-24.

Lay, T., C. J. Ammon, A. A. Velasco, J. Ritsema, T. C. Wallace and H. J. Patton (1994), Near-real time seismology: Rapid analysis of earthquake faulting, GSA Today, 4, 129,132-134.

Levshin, A., L. Ratnikova and J. Berger (1992), Peculiarities of surface-wave propagation across central Asia, Bull. Seism. Soc. Am., 82, 2464-2493.

Patton, H. (1976), A note on the source mechanism of the southeastern Missouri earthquake of October 21, 1965, J. Geophys. Res., 81, 1483-1486.

Patton, H. (1980), Reference point equalization method for determining the source and path effects of surface waves, J. Geophys. Res., 85, 821-848.

Patton, H. J. (1998), Bias in the centroid moment tensor for central Asian earthquakes: Evidence from regional surface wave data, J. Geophys. Res., 103, 26,963-26,974.

Patton, H. J., and G. Zandt (1992), Seismic moment tensors for western U. S. earthquakes and implications for the tectonic stress field, J. Geophys. Res., 96, 18,245-18,259.

Randall, G. R., C. J. Ammon and T. J. Owens (1995), Moment-tensor estimation using regional seismograms from a Tibetan Plateau portable network deployment, Geophys. Res. Letters, 22, 1665-1668.

Ritzwoller, M. H., and A. L. Levshin (1998), Eurasian surface wave tomography: Group velocities, J. Geophys. Res., 103, 4839-4878.

Romanowicz, B. A. (1982), Moment tensor inversion of long-period Rayleigh Waves: A new approach, J. Geophys. Res., 87, 5395-5407.

SHORT-PERIOD SURFACE WAVES FROM EXPLOSIONS

Jessie L. Bonner[1] and Jeffrey L. Orrey[2]

Weston Geophysical Corporation [1]
GeoVisual Technologies Inc.[2]

Sponsored by the National Nuclear Security Administration
Office of Nonproliferation Research and Engineering
Office of Defense Nuclear Nonproliferation

Contract No. DE-FG02-00ER83123

ABSTRACT

We have examined the generation and propagation of short-period (0.5- to 12-sec period) surface waves from different classifications of explosions. A dataset of local and regional recordings of single-fired chemical explosions (Non-Proliferation Experiment and Balapan Depth of Burial shots), coal-mining explosions (including cast and coal shots from northern Arizona), rock fragmentation shots (SW Arizona), and quarry blasts (Central Texas) has been assembled. The dataset has been complemented with detailed source parameters including origin times, shot patterns, and additional information key to modeling the physics of the various explosions. We are currently completing the initial phases of this project that included database compilation, observational studies, and preliminary modeling of the explosions. During the next phase of the project, we propose to expand on the modeling effort to include complex source models and propagation in 3-D media using Fourier pseudo-spectral approximation (Orrey *et al*., 2001).

The initial focus has been on the modeling of surface-wave generation from two cast blasts of similar yield (~1.6 million pounds ANFO), delay sequence, and near-source structure at a coal mine in northern Arizona. The shots were oriented approximately perpendicular to each other, allowing for interesting comparisons at both local and regional distances. Near-source data (< 5 km) collected by Southern Methodist University and Los Alamos National Laboratory show the dominant surface-wave energy is delayed with respect to the blast initiation time and is better aligned with the onset of horizontal spall impact. Surface wave amplitudes recorded for both shots at regional distances differ by as much as a factor of 2.5, and these differences can be attributed to the orientation of the casting. To test this theory, we completed a preliminary modeling study to investigate the source of the azimuthal radiation patterns using the detailed blasting information obtained from blast engineers and MineSeis1.1 (Yang, 1998). The radiation patterns generated for the blasts were not isotropic as is the case when only vertical spall is modeled, and show larger amplitude lobes perpendicular to the bench, with a small amplitude increase noted for the direction of the delay firing. The overall effect of the horizontal spall is to create amplitudes as much as four times greater in the direction normal to the bench than parallel to the free face. These modeling results support our regional observations. Since equivalent radiation patterns were not observed for the *P* and *Lg* phases, the observation of these radiation patterns at regional distances could act as a cast blast discriminant in regions of monitoring concern.

KEY WORDS: mining explosions, surface waves, discrimination

OBJECTIVES

Introduction

Previous studies have shown that a significant number of small regionally recorded seismic events are mining explosions (Richards *et al*., 1992; Sorrells *et al*., 1997; Leith *et al*., 1996; and Khalturin *et al.*, 1996). Unfortunately, few, if any, validated discriminants exist for any of the wide variety of mine explosions that occur in numerous mining areas, many of which are in regions of high monitoring interest. The objective of this research is to determine if there are unique aspects of short-period (0.2 to 12 seconds) surface wave

generation by mining explosions that will aid in the development of transportable regional discriminants. To complete this goal, we have:

- Collected regional seismic data to examine short-period (0.5 to 12 sec) surface wave generation from different types of chemical explosions in North America and Kazakhstan.
- Determined the propagation characteristics for short-period surface waves generated by explosions in different tectonic settings, and
- Determined additional features unique to surface waves from mining explosions that can be used in the development of a regional discriminant.

In the following sections, we will present results that show the feasibility of modeling explosions of varying classifications in different source regimes using the explosion-generated surface wave datasets.

RESEARCH ACCOMPLISHED

Data Collection

We have collected different data sets to study surface wave generation from different classifications of small explosions, including delay fired mining explosions (cast blasts, quarry blasts, and fragmentation shots) and simultaneously detonated explosions. Table I provides details about the data collected thus far and anticipated datasets that will be acquired shortly. The sources are located in different

Experiment	Explosion	Data Collection
Balapan	Single-fired chemical	9 shots ranging from 25 to 0.1 tons at depths from 2.5 to 550 m. Close-in LANL data from 7-8 stations. Regional data from the Kazahkstan network.
NPE	Single-fired chemical	1 1.07 kt shot at the Nevada Test Site. Regional data from Sandia Net and a University of Arizona Profile. We will also obtain LLNL network data and the Cambridge Univ. profile of seismic stations in upcoming months.
Northern Arizona	Cast Blasts	2 1.5 million pound shots from a coal mine in Arizona. Close-in network (8 stations) and regional recordings (14 stations) ranging from 100 to 700 km. Additional recordings of overburden, parting, cast, and coal shots with blasting parameters.
Arizona	Fragmentation	Copper mining explosions recorded at Tucson (TUC) and other regional stations. Received blasting parameters too late for inclusion in proposal
Indiana	Cast Blasts	Surface waves recorded from coal mining explosions at regional distances by the Billiken network. Currently acquiring source information.
Central Texas	Quarry Blasts	Previous research on azimuthal variation of *Rg* energy from quarry blasts.

Table I. Database of short-period surface wave explosions.

tectonic regimes, ranging from stable continental crust (Central Texas, Indiana, and Balapan) to complex regions suchs as Arizona and Nevada. The data allows for an interesting comparison of the generation and propagation of short period surface waves from explosions. In the upcoming months, we plan to continue data collection in central India and Minnesota.

Classification of Mining Explosions

Cast Blasts. Explosive casting is the technique used by many surface coal mines to control the displacement of overburden (Morhard, 1987) by means of explosive energy. The casting moves 30-80% of the overburden into the mined-out pit, while the remaining spoil is removed by draglines or other machinery. A blasting engineer must consider bench height, pit width, borehole diameter, and geologic formation when designing a cast blast. In most cases, the blaster uses a complicated sequence of downhole and surface delays to minimize the ground roll associated with the large amounts of explosives (between 0.5-8 million pounds of ANFO) used in a cast blast. An example of a cast blast from a mine in northern Arizona is shown in Figure 1. The casting of the overburden into the pit creates both horizontal and vertical spall force components that influence the generation of surface waves (Figure 1; Anandakrishnan *et al.*, 1997).

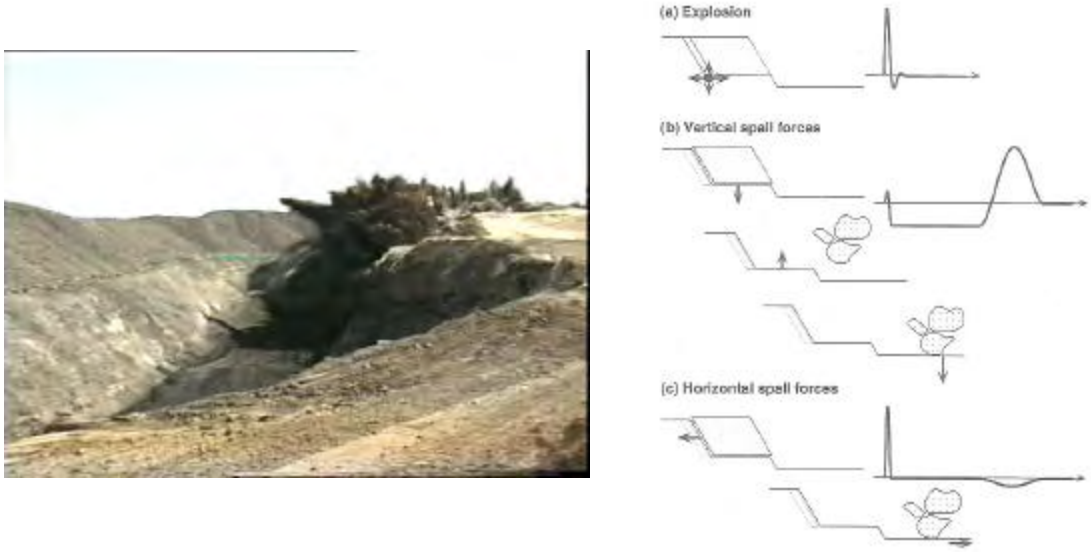

Figure 1. (Left) Cast blast in northern Arizona. (Right) Graphical illustration of the forces resulting from a cast blast into a pit (Anandakrishnan et al., 1997).

Fragmentation Blasts. The majority of hard rock open-pit mines design blasts that will optimize the *in-situ* fragmentation of the material. This is accomplished by loading the holes with two different energy levels: higher energy explosives in the bottom and lower energy near the top. The result is that the material is not thrown into the mined-out pit as in the cast blasts. Instead, the material is fractured in place and removed with shovels and haul trucks. Seismic waves generated from a fragmentation blast should be influenced only by the explosion point and vertical component spall forces.

Quarry Blasts. A third type of explosion used in the mining industry is for quarrying materials such as limestone, gravels, and igneous rocks. On average, quarry blasts (Figure 2) are smaller in spatial extent and explosives content than fragmentation and cast blasts. Since these operations usually involve the crushing of the rock, efficient fragmentation of the rock into small pieces is required for use in a rock crusher. For ease in extraction of the materials, the rocks are usually blasted into the mined-out pit. Quarrry blasts seismograms will thus have both horizontal and vertical spall forces effecting the regional seismograms.

Modeling Mining Explosions

We have completed a preliminary modeling study to investigate the aspects of *Rg* generation from these different classifications of mining explosions using MineSeis1.1 (Yang, 1998) and the model developed by Anandakrishan *et al*. (1997). The model assumes the principle of linear superposition (Stump and Reinke, 1988) to handle the delay firing with the subsurface explosion modeled as a spherical isotropic point source

Figure 2. Quarry blast in central Texas.

(Mueller and Murphy, 1971). The spall model from Barker *et al*. (1993) as modified by Yang (1998) is used to model vertical and horizontal spall components . For a more detailed explanation of the model, the reader is referred to Yang (1998). For this modeling exercise, we considered a simple mining explosion with a single row of charges delay-fired to the north (0° azimuth) with horizontal spall normal to the bench (90° azimuth). We are interested in predicting radiation patterns for mining explosion-generated *Rg* as a function of delay fire direction and horizontal spall trajectory. In Figure 3, we varied the eject angle from 0° (from vertical) to 90° in 15° increments. When the eject angle is 0°, there is no horizontal spall component and the blast is analogous to a fragmentation shot. For quarry blasts, there is some material cast into the pit at eject angles greater than 45°, however, a additional amount of the spalled material is cast into the air at angles between 0 and 30°. Finally, for cast blasts, the majority of the material is ejected at angles greater than 30°. As shown in Figure 3, cast blasts will have the largest deviation from an isotropic source (i.e., a fragmentation blast) with the magnitude of the azimuthal variations being dependent upon the eject angle. In all cases, there is a slight increase in the amplitudes in the direction of the delay-firing. For the cast blasts to take on a more di-polar ("peanut-shaped") radiation pattern, the mass of the horizontal spall must be increased. This plot is meant as an example of the different radiation patterns that can be expected from simple mining explosions (single row without complicated detonation schemes). By adding additional rows of explosives with different interrow and interhole delays, the characteristics can become markedly different.

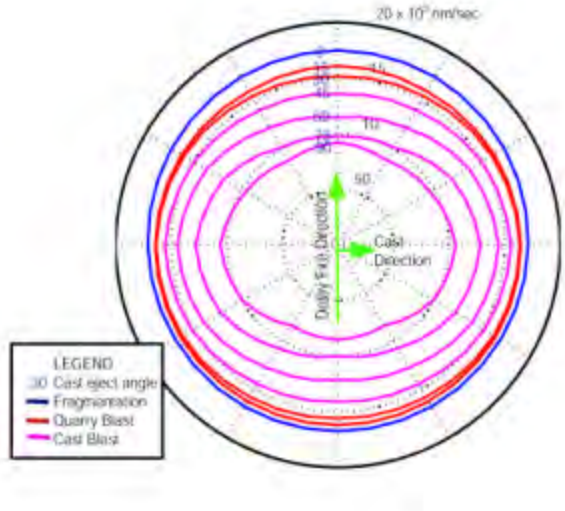

Figure 3. Model results showing azimuthal radiation patterns in Rg amplitudes as a function of spall eject angles for simplified mining explosions. The color scheme highlights typical spall eject angles that can be expected for fragmentation, quarry, and cast blasts. Quarry blasts have components of both fragmentation blasts (efficient fracture of the material) and cast blasts (throwing the rock into the open pit).

Rg Observations

Cast Blasts. We acquired a data set of local and regional recordings of explosions at a large coal mine in northern Arizona (Figure 4). The local recordings were obtained on 24-25 March 1999, when two ~1.6 million pound cast blasts were detonated in a pit (Figure 5) near Kayenta, AZ. Near-source recordings of seismic, acoustic, and videographic data were acquired.

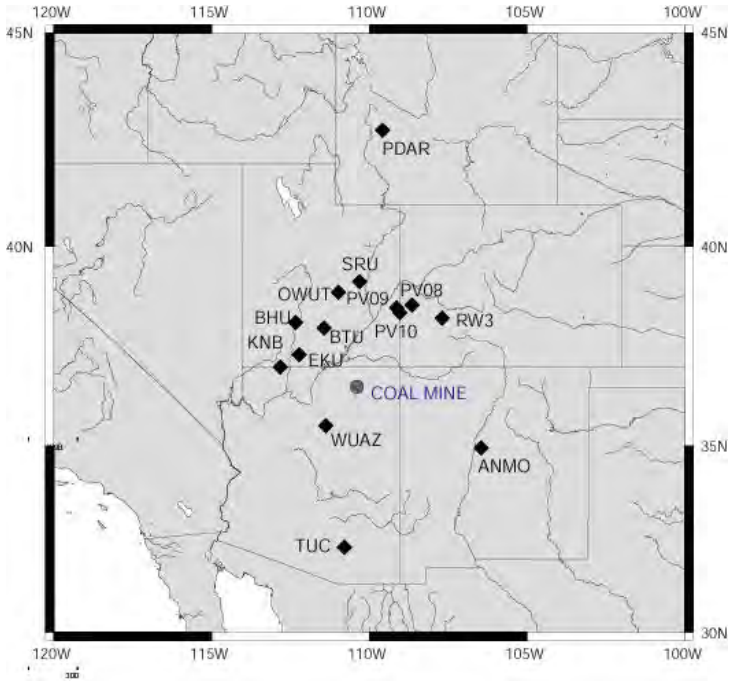

Figure 4. Location of the coal mine in northern Arizona and regional stations that recorded Rg.

Figure 5. The locations of the seismic recording sites of the cast blast experiment for the 24 March 99 (Green) and 25 March 99 (Blue line) cast blasts. Each event was fired from station SB toward the station MID.

Our focus thus far has been on studying surface wave generation from these two cast blasts, given the uniqueness of the dataset. First, both cast basts were of approximately the same total yield (1.6 million pounds) and had a similar blasting design (delay times, explosives per delay, burden, depth of charge, etc). The blasts were detonated in the same pit resulting in less than 1 km difference between the locations of the first hole detonations. And finally, because of the semi-circular nature of the pit, a feature unique to the operations at this mine, the orientations of the blasts were approximately perpendicular to each other, thus allowing for relative amplitude comparisons of the two blasts at local and regional distances.

We completed analysis of the regional *Rg* phase recorded by 17 seismic stations ranging from 135 km to 699 km from the blasts (four examples are shown in Figure 6). The two cast blasts generated *Rg* dominated by 4 seconds-period that was recorded at relatively great distances as a result of efficient propagation in the Colorado Plateau. The four seconds period corresponds to the approximate total duration of the horizontal spall impact on the pit floor. Figure 7 shows the results

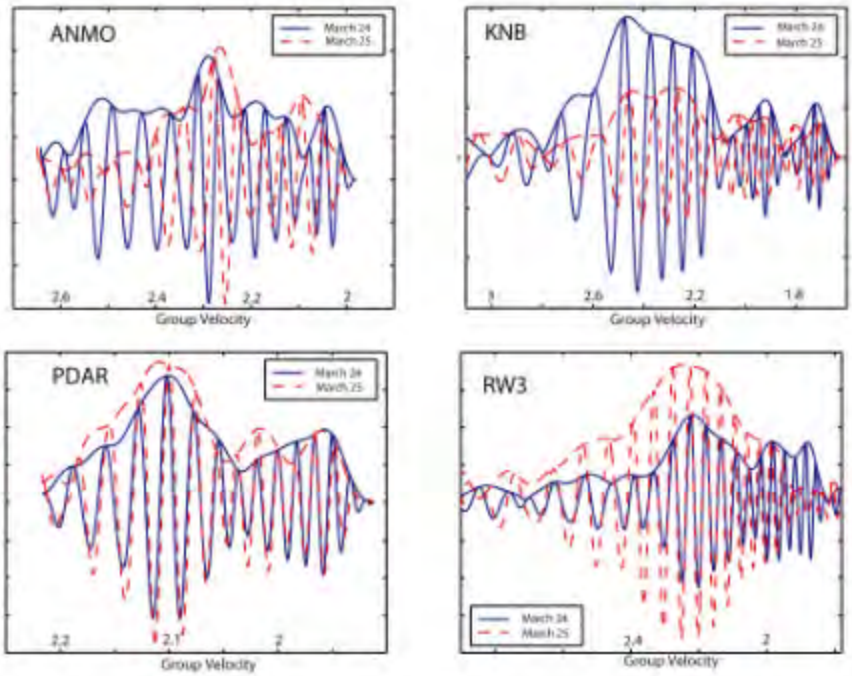

Figure 6. Regional Rg recorded at ANMO, KNB, PDAR, and RW3 for two cast blasts (blue=24 March 1999 and red=25 March 1999) of similar yield (1.6 million pounds of explosives). Differences in the Rg amplitudes can be attributed to radiation patterns for the two blasts that are oriented perpendicular to one another as shown in Figure 5.

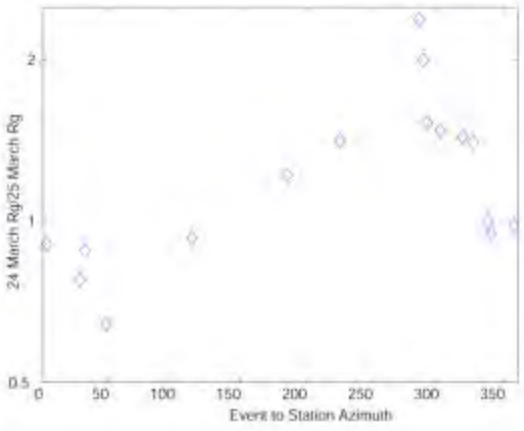

Figure 7. Ratio of the Rg amplitudes for the 24 March 1999 cast blast to the 25 March event.

for all stations and suggests that significant radiation patterns for the two blasts are functions of the orientation of the explosions. The *P* and *Lg* phases did not show the same radiation patterns for these two blasts.

We again used MineSeis1.1 to model these explosions in an attempt to explain the *Rg* observations. We combined seismic velocities measured during the experiment with videographic data to accurately represent the source and spall parameters (Table 2). We generated single-point seismograms using these data and convolved them with Green's functions generated by the reflectivity method (Muller, 1985) for the Colorado Plateau crustal structure. We then convolved these data with comb functions that represent the timing pattern and yield of the individual explosions to represent the superposition seismogram at regional distances. Figure 8 shows the results of using this model to synthesize seismograms for a cast blast as recorded at WUAZ. The model adequately predicts a significant portion of the *Rg* wave packet.

Parameter	Value
Explosive Depth	30 m
Burden	5 m
Face Azimuth	0 (24 March) 90 (25 March)
P-wave Velocity at Depth	7.9
Spall Impact Pulse Width	2
Spall Initiation Pulse Width	1
Spall Yield	22 kT
Yield per hole	8131 kg
Eject Angle	70°
Vertical Falling Distance	30 m
Spacing Between Rows	10 m
Receiver Distance	134.7
Receiver Azimuth	0:15:360
Intershot Delay	17 ms
Interrow Delay	150, 100, 150, 150, 150
Number of Rows	5
Number of Holes per Row	88

Table 2. Source parameters used to model the northern Arizona cast blasts.

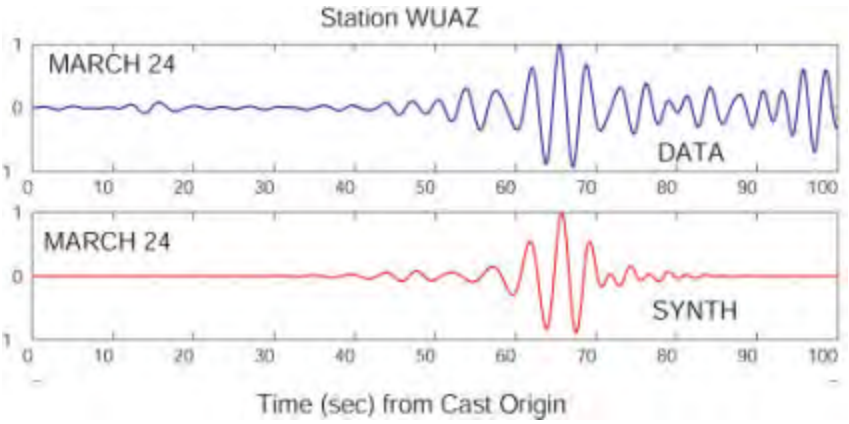

Figure 8. Observed (blue) vs. synthetic (red) cast blast seismograms as recorded at WUAZ. Both the observed and synthetic data are normalized with respect to the largest amplitudes.

The left panel of Figure 9 shows the theoretical surface wave amplitudes as a function of azimuth for the two cast blasts. The radiation patterns are not isotropic, as is the case when only vertical spall is modelled (Figure 3), and show larger amplitude lobes perpendicular to the bench, with a relative enhancement noted for the direction of the delay firing (the arrows shown in the center of the plot). The overall effect of the hoizontal spall is to create amplitudes as much as approximately four times greater in the direction normal to the bench than parallel to the free face. The ratio of the amplitudes from the two theoretical radiation patterns is presented in the right panel of Figure 9, and the *Rg* amplitude ratios (March 24 Rg/March 25 Rg) measured from the regional data are overlain on the plot (red circles). The observed data do support the radiation patterns predicted from the modeling. However, more data are needed to confirm the results, and this study would benefit greatly from stations due east and south of the cast blasts. We are searching for additional data from stations that were not obtained from the USGS AutoDRM during the initial search.

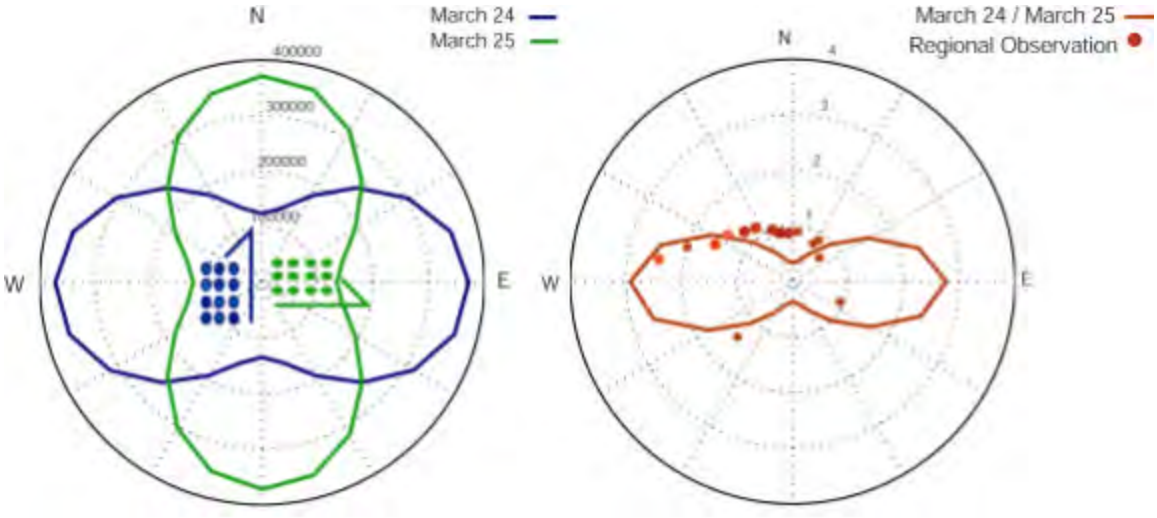

Figure 9. (Left) Radiation patterns for Rg based upon model data recorded at regional distances for two identical cast blasts oriented perpendicular to each other. The delay firing direction is shown by the arrow that is parallel to the bench, thus perpendicular to horizontal spall. (Right) Ratio of the two radiation patterns compared with actual data (red circles) recorded at varying azimuths to the coal mine.

Quarry Blasts. Bonner *et al*. (1994) documented azimuthal *Rg* radiation patterns for quarry blasts in Central Texas. They found that Rg amplitudes are enhanced for (1) paths that do not travel through the quarry pit and (2) paths in the direction of the delay firing. Figure 10 shows the data from one of these quarry blasts, and the radiation pattern does not resemble closely any of the patterns in Figure 3. In a previous modeling study (Barker *et al*., 1997), three-diminsional finite difference calculations and wavenumber integration synthetics were used to interpret near-regional azimuthal variations from quarry blasts in Central Texas. The observational data were compared to the synthetics in relation to the effects of local quarry topography and the spall of the material from the quarry face. The simple explosion plus spall model of Barker *et al*. (1993) predicted the observations better than 3-D finite-difference calculations, however, discrepancies existed between both models and the observations. We plan to further investigate this dataset in the upcoming stages of the project.

Fragmentation Blasts. We have only recently received the detailed blasting records for fragmentation shots at a copper mine in the southwestern United States. We have already downloaded data from 25 shots from this mine as recorded at three to six regional stations. We will use the shot information to perform modeling of fragmentation blasts.

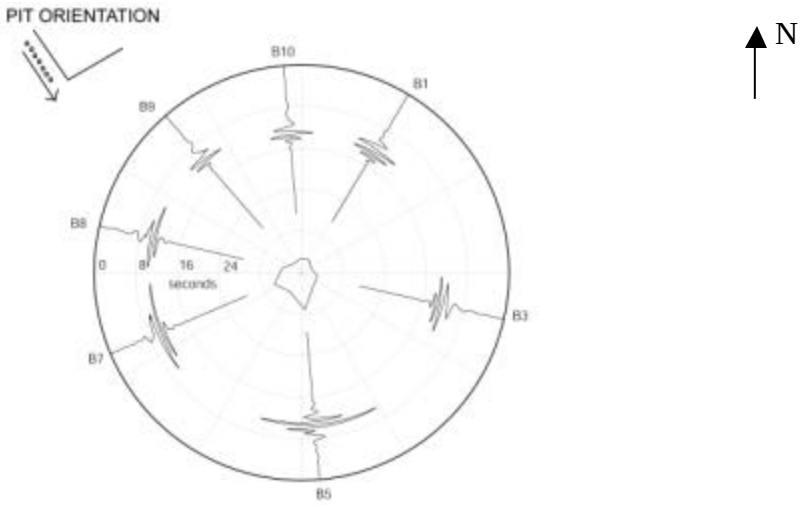

Figure 10. Observed Rg amplitudes from a quarry blast in central Texas (Bonner et al., 1996). Amplitudes for paths that do not traverse the quarry pit as well as paths in the direction of the delay-firing are enhanced.

3-D Modeling of Short-Period Surface Waves

We used a numerical wave field modeling method to generate Green's functions for a 3-D earth model consisting of the northern Colorado plateau, the Uinta Basin, the middle Rocky mountains including the Uinta Mountains, and western Wyoming. The velocity model regionalization was based upon the work of Keller *et al*. (1976) and Prodehl and Lipman (1989). The 3D model was constructed on a 0.5 x 0.5 degree grid and from 35°N to 44°N from 112°W to 107°W with the velocity profile at each point consisting of a 6 layer crust over a 200 km mantle half-space. Numerical methods allow the incorporation of realistic structural features, such as strong lateral velocity variations, anelastic attenuation and surface topography, that affect the propagation of short period surface waves. The particular modeling method we propose to use, called the Generalized Fourier Method (GFM), was developed specifically for regional wave propagation studies (Orrey and Robinson, 2001). Preliminary results of the GFM synthesis of explosion-generated surface waves for our model are presented in Figure 11. For the next phase of this research, we propose to combine the MineSeis code of Yang (1998) with the GFM code of Orrey and Robinson (2001) to model explosions in regional 3-D media.

CONCLUSIONS AND RECOMMENDATIONS

The database we have assembled for this study is unique in its content of local and regional recordings of various classifications of explosions. We have detailed source information from the blasters and in some cases videographic data to help ascertain the physical processes at work during the explosions. We have used the explosion-generated *Rg* to determine upper crust velocity models and attenuation values for the study regions, and will use this information during the upcoming modeling study. During Phase II of the project, we propose to expand the modeling effort to include complex source models and propagation in 3-D media using Fourier pseudo-spectral approximation (Orrey *et al*., 2001). Finally, we have empirical and modeling results that suggest cast blast discriminants can be developed based upon radiation patterns of *Rg*, and we will attempt to transport them to additional datasets during the remainder of the research project.

ACKNOWLEDGMENTS

We wish to thank the many people who have helped collect the data for this project including Brian Stump, Craig Pearson, Bob Herrmann, Howard Patton, Bill Walter, C. L. Edwards, Diane Baker, and Ileana

Tibuleac. We also wish to thank David Yang for developing and tutoring us in MineSeis1.1. We also wish to thank James Lewkowicz and Anca Rosca for helpful comments about the manuscript.

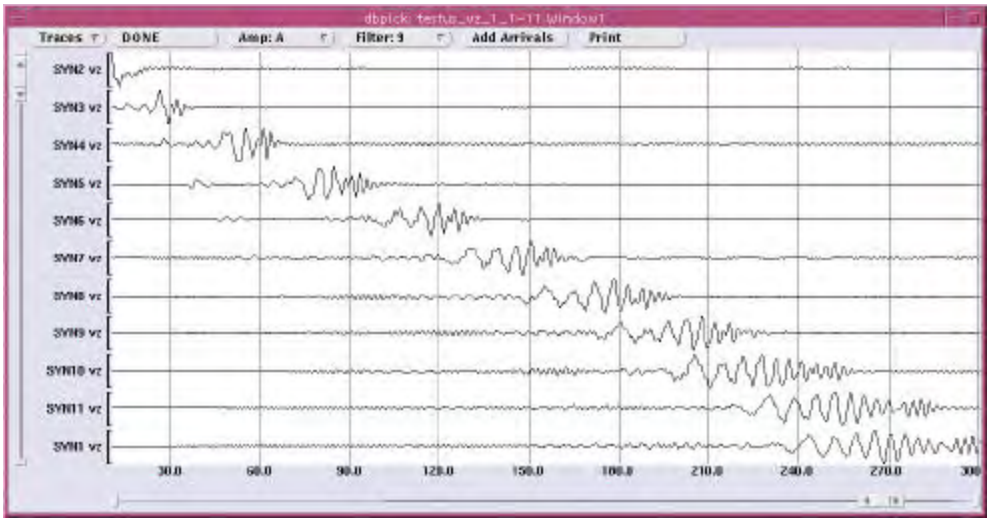

Figure 11. Preliminary resuts for modeling explosion generated short-period surface waves in a 3-D model develped for the middle Rocky Mountians, Uinta Basin, and Colorado Plateau, Each trace is a vertical velocity time series separated by10 km with the last trace representing PDAR data.

REFERENCES

Barker, T.G., K. L. McLaughlin, and J. Bonner (1997), Physical Mechanisms of Quarry Blast Sources, Maxwell Technologies Scientific Report, *MFD-DTR-97-15695*.

Barker, T. G., K. L. McLaughlin and J. L. Stevens (1993), Numerical simulation of quarry blast sources, Technical Report, S-CUBED, La Jolla, Califomia.

Bonner, J., E. Herrin, and T. Goforth (1996), Azimuthal variation of *Rg* from Central Texas Quarry Blasts, *Seism. Res. Letts*, **67**, 43.

Khalturin, V., T. Rautian, P. Richards, and W. Kim (1996), Evaluation of chemical explosions and methods of discrimination for practical seismic and monitoring of a CTBT, Lamont-Doherty Earth Observatory Scientific Report, *PL-TR-96-2172*.

Keller, G.R., R.B. Smith, L.W. Braile, R. Heaney, and D.H. Shurbet (1976). Upper crustal structure of the eastern Basin and Range, northern Colorado Plateau, and middle Rocky Mountains from Rayleigh-wave dispersion, *Bull. Seism. Soc. Am*., **66,** 869-876.

Leith, W., A. Spivak, and L. Pernick (1996), Large mining blasts from the Kursk mining region, Russia, *Proceedings of the 18th Annual Seismic Research Symposium, 12-15 September 1996, PL-TR-96-2153*, Phillips Laboratory, Hanscom AFB, MA.

Morhard, R.C. (1987), Explosives and Rock blasting, Atlas Powder Company, Dallas TX. 622 p.

Mueller, R.A., and J.R. Murphy (1971), Seismic characteristics of underground nuclear detonations, Bull. Seism. Soc. Am., **61**, 1675-1692.

Muller, G. (1985), The reflectivity method: a tutorial. *J. Geophys*, **58**, 153-174.

Orrey, J. and G. Robinson (2001), A parallel implementation of the Generalized Fourier Method for elastic wave simulations, in preparation for submittal to *Geophysics*.

Richards, P.G., D. Anderson, and D. Simpson (1992), A survey of blasting activity in the United States, *Bull. Seism. Soc. Am.* **82**, 1416.

Sorrells, G.G., E.T. Herrin, and J. L. Bonner (1997), Construction of regional ground truth databases using seismic and infrasound data, *Seism. Res. Letts*, **68**, 743.

Stump, B. W. and R. E. Reinke (1988), Experimental confirmation of superposition from small-scale explosions, Bull. Seism. Soc. Am. **78,** 1059-1073.

Yang, X. (1998), MineSeis – A MATLAB GUI Program to Calculate Synthetic Seismograms from a Linear, Multi-shot Blast Source Model, LAUR-98-1486.

DEVELOPMENT OF AUTOMATED MOMENT TENSOR SOFTWARE AT THE PROTOTYPE INTERNATIONAL DATA CENTER

Douglas Dreger[1], Barbara Romanowicz[1], G. Clitheroe[1], Peggy Hellweg[1], Jeffry Stevens[2]

University of California, Berkeley, Seismological Laboratory,[1] SAIC[2]

Sponsored by Defense Threat Reduction Agency

Contract No. DTRA01-00-C-0038

ABSTRACT

We are porting to the Prototype International Data Center (PIDC) seismic moment tensor software used at the Berkeley Seismological Laboratory for the routine monitoring of earthquake strain release (Romanowicz et al., 1993; Pasyanos et al., 1996). The moment tensor software also forms an integral core in our efforts to automatically and rapidly characterize strong shaking from large earthquakes using information derived from sparse regional distance network (e.g. Dreger and Kaverina, 2000). Two separate moment tensor methodologies are employed: a surface wave spectral amplitude and phase method and a three component inverse method. For the purpose of screening seismic events for nuclear treaty monitoring the automatic determination of seismic moment tensors can contribute on several levels. First, seismic moment tensors provide robust estimates of the scalar seismic moment, which is a component of some regional distance discrimination techniques, or is a necessary source parameter for their calibration (e.g. Woods et al., 1993; Patton and Walter, 1993, Mayeda et al., 1993; Mayeda and Walter, 1996). Second, the seismic moment tensor inversions provide estimates of source depth. Finally, the seismic moment tensor may be used to examine the degree that seismic radiation deviates from a pure double-couple model of a tectonic event (e.g. Dreger et al., 2000), thereby providing an additional screening capability. Automated procedures are needed to be able to handle the annual numbers of low magnitude events on a global scale. The objective of our project is to port an automatic system for the analysis of seismic events of Mw≥5.5 on a global scale with the goal of refining capabilities to estimate seismic moment tensors for seismic events down to Mw=4.5. We will present the results of a performance test of the methods using M_W>4.5 data recorded by the IMS primary network for a three-month period. The derived source parameters will be compared against Harvard CMT and regional network solutions.

KEY WORDS: seismic, moment tensor software, PIDC

OBJECTIVE

Introduction

Seismic moment tensor analysis as described in what follows offers improved screening of seismic events. On a global scale approximately 100,000 M4 events occur annually and therefore an automated system is needed to quickly review the seismicity to monitor the CTBT.

The purpose of this project is to adapt and port to the Prototype International Data Center (PIDC) a set of codes developed and routinely used at UC Berkeley (Romanowicz et al., 1993; Dreger and Romanowicz, 1994; Pasyanos et al., 1996) to determine seismic moment tensors and source depth of seismic events automatically and close to real-time. While these codes are being used at UC Berkeley to monitor the strain release in natural earthquakes in northern California, the moment tensor inversion approach provides a potentially powerful event screening procedure in several ways (Pechmann et al., 1995; Dreger and Woods, 1999): (1) by providing estimates of M_w (moment magnitude), a more accurate measure of event size; (2) by providing estimates of source depth, which will help distinguish natural events (depths typically >> 1km) from nuclear explosions and (3) by providing estimates of radiation characteristics (i.e. deviations from the typical double-couple radiation of earthquakes). Indeed, nuclear explosions may display large non double-couple components (>50%) whereas

earthquakes typically exhibit over 70-80% double couple (Dreger and Woods, 1999). Of perhaps greater importance is the ability of moment tensor studies to identify tectonic earthquakes or seismic events at significant source depth, thereby reducing the number of events that must be more closely examined in the monitoring of the CTBT. The initial performance goal of the ported software is the automated determination of moment tensors on a global scale for larger events (M>5.5-6.0) with a reduced threshold in a specifically targeted region. Later releases of the software will incorporate calibration information for several regions of interest, allowing moment tensor determinations at a lower magnitude threshold of approximately M~4-4.5.

The primary issues that are to be addressed during the course of this project are: (1) meeting the real time operational requirements at the PIDC in terms of the degree of automation including the assessment of solution quality; (2) revising the software to perform under the very different operational situation of the PIDC (eliminating the dependence on always available station data at near regional distances in calibrated regions as is the case in northern California, and to develop the capability to analyze data with the very sparse and uncalibrated IMS network configuration). This implies that the seismic moment tensor inversions cannot be expected to run as efficiently and to as low a magnitude as desired without additional effort; (3) and to utilize path calibration information already obtained for regions of interest to improve on capabilities of analyzing low magnitude events in specific target regions.

Moment Tensor Background Information

The use of broadband waveforms, as provided by modern broadband digital seismic stations, through moment-tensor inversion, provides robust estimates of source magnitude (M_w), information about the source mechanism, as well as depth of the source. Thus seismic moment tensors offer a potentially powerful method for screening observed seismicity to potentially identify suspect events, events which deviate from typical source depths and double-couple radiation. Events with anomalous non-double couple radiation patterns (e.g. Patton 1988; Dreger and Woods, 1999) may be flagged to receive more in depth analysis. Previous work has demonstrated that seismic moment tensors of nuclear explosions are anomalous compared to tectonic earthquakes (Patton, 1988; Stump and Johnson, 1984; Vasco and Johnson, 1989), however there is difficulty in resolving a pure isotropic source with regionally recorded long-period data (Patton, 1988). Recent experience with the methods we have developed indicates that anomalous radiation of nuclear explosions and non-tectonic seismic events may be identified with a relatively sparse network of stations (e.g. Dreger and Woods, 1999; Dreger et al., 2000).

The moment tensor formalism was first developed 20 years ago (e.g. Mendiguren, 1977, and has been since applied successfully in various settings, for the study and/or routine cataloguing of moderate to large earthquakes on the global scale, using either a time-domain waveform approach (e.g. Dziewonski et al., 1981) or a frequency domain, surface-wave spectral approach (e.g. Romanowicz, 1982; Romanowicz and Guillemant, 1984). When a good signal/noise ratio is available, it has been demonstrated that data from a single three-component station are sufficient to obtain an accurate moment tensor solution for large earthquakes at teleseismic distances (Ekstrom et al., 1986). At regional distances it has been shown that it is possible to obtain robust estimates of the seismic moment tensor for moderate sized earthquakes with as few as a single station (e.g. Dreger and Helmberger, 1991; Fan and Wallace, 1991; Walter, 1993). For large earthquakes and in global applications, relatively low frequency data can be used, and propagation corrections need not be known with great accuracy, so that standard 1D reference models of the earth, and, more recently, 3D models obtained from global tomography are generally sufficient to obtain acceptable solutions. More recently, with the proliferation of sparse regional broadband networks, moment tensor inversions have been adapted to the case of smaller events observed at regional distances. In this case, propagation corrections for shorter period waves (typically 15-40 sec) that are more sensitive to complex crustal structure, need to be accurately estimated using appropriate regional models. At U.C. Berkeley, we have developed two independent approaches for moment tensor estimation of earthquakes of moderate magnitude at regional distances (Romanowicz et al., 1993). These procedures have been automated and implemented to routinely provide reliable estimates of earthquake size, mechanism and depth in quasi-real time (within 10 minutes of the occurrence of an event, Pasyanos et al., 1996), in the framework of our real-time program (REDI, Gee et al., 1996). The solutions are broadcast over a paging-system to subscribers, as well as over the Internet, to interested scientists and governmental agencies. In our particular application, in addition to providing accurate moment-magnitude (M_w) estimation down to about Mw 3.5-4 within our monitoring region (central and northern California), for larger earthquakes the mechanism

and depth information is critical for the estimation of finite-source parameters, and consequently of distribution of shaking as estimated from a sparse seismic network (Dreger, 1997; Dreger and Kaverina, 2000).

The resulting moment-tensor catalog of 389 moment tensor solutions over the last 8 years includes events to a lower limit of Mw 3.5. The catalog may be accessed from the WWW at:

http://www.seismo.berkeley.edu/~dreger/mtindex.html

The first moment tensor methodology we employ is a time domain waveform fitting procedure that utilizes the entire long-period wavefield (Dreger and Romanowicz, 1994; Pasyanos et al., 1996; Fukuyama et al., 1998; Fukuyama and Dreger, 2000). For the majority of events in northern and central California, three 1D crustal/upper-mantle velocity models are adequate. One model describes the relatively faster wave propagation of the thicker Sierra block, another describes the relatively slower wave propagation in the thinner California Coast Ranges (Pasyanos et al., 1996), and the third has been developed for the offshore Mendocino region. It is clear from our work in California that the complete waveform method operates quite well with only a few calibrated velocity models even in a region as complex as California, and is capable of monitoring seismicity in the 30 to 700 km distance range. The code operates in Japan with a single calibrated velocity model for the entire region (Fukuyama et al., 1998; Fukuyama and Dreger, 2000). With this method data from a single station is often sufficient, however in practice we use three-component data from several stations to improve the azimuthal coverage of the focal sphere (Pasyanos et al., 1996).

The second moment tensor methodology we use is a frequency domain, surface wave approach, adapted from the two-step method of Romanowicz (1982), for which calibrated fundamental mode surface wave phase velocities, in the period range 10-60 sec, are used for propagation corrections (Pasyanos et al., 1996). This method utilizes surface waves, which are the largest of the regional phases allowing for the analysis of smaller seismic events. We are able to analyze events to a magnitude of 3.5 using Berkeley Digital Seismic Network stations in the 100 to 500 km distance range. With sufficient azimuthal coverage this method is found to perform quite well.

In Figure 1 the data fits and solutions that were obtained for a small California earthquake are compared. The very good comparison between the complete waveform approach and the surface wave methods illustrate how two parallel methods can be used to gain confidence in the results. By running two independent seismic moment tensor approaches it is possible to compare the automatic results and to use similarity in the solutions as an indicator of robustness.

RESEARCH ACCOMPLISHED

During the first year of this project we have reached the following milestones.

Both the complete waveform and surface inversion routines have been installed on the Center for Monitoring Research computer system, and are presently undergoing testing and tuning.

The installed software has been modified to obtain parametric event and seismic station information directly from the pIDC database. Additionally, the raw waveform data from primary IMS stations are automatically retrieved. Data from the auxiliary IMS network may be requested and employed during analyst review of the solutions.

We have compiled an IMS data set, which spans the 90 day period from July 19 (day 200) to October 16 (day 290), 1999. The locations of events during this period and IMS Primary stations from which waveform data was collected is shown in Figure 2A. Figure 2B shows the available Harvard CMT solutions, which will be used for calibration purposes. In some regions it will be possible to use other catalogs of moment tensor and first motion solutions for calibration. For this period two data sets have been compiled. One with 30 M>= 5.4 events, and the second with 330 M>=4.4 events. These event lists are used to test the bulk processing capabilities of the two moment tensor methodologies, and to identify and correct software bugs and other problems.

We have begun detailed investigations of the seismic moment tensor inversion results in order to learn how to improve the bulk processing performance and the quality of the inversion results. These investigations have included inversions in three different frequency passbands (0.005-0.02Hz, 0.00714-0.03Hz, and 0.02-0.05Hz), and also the study of body wave, complete waveform and differentially weighted combined inversions. Figure 3 compares waveform inversion results for a Mw5.9 Kamchatka event, which occurred on September 16, 1999. The solution shown in Figure 3b compares very well with the Harvard solution in terms of the relatively deep source depth (50 km vs. 68 km), the non-double-couple nature of the radiation pattern, and in terms of the scalar seismic moment (8.7e24 vs. 1.2e25 dyne cm). This particular solution is derived from the complete three-component displacement waveforms in the 0.02 to 0.05 Hz passband from three stations located at distances between 28^o to 35^o. The Green's functions were computed from the IASPEI91 velocity model. The P and S body wave portions of the seismograms were weighted higher to increase their contribution in the inversion. Figure 3a and 3c compares the complete waveform inversion without differential weighting, and a body wave only result, respectively. In all three cases there is reasonably good agreement with solutions obtained by other researchers. Complete waveforms in the 0.00714-0.03 Hz passband yielded results comparable to that in Figure 3a. These results indicate that complete three-component waveforms from a few distant stations are sufficient for the recovery of the seismic moment tensor and also source depth. At these long-periods however it is expected that shallow source depth resolution will be poor due to the vanishing tractions at the free-surface. In these cases regional distance stations, and shorter periods may be used. These results also show that it will be beneficial to utilize both body and surface waves in the inversions.

At the end of July 2001 we visited the Center for Monitoring Research to coordinate the integration of our software package into the pIDC R&D test bed.

CONCLUSIONS AND RECOMMENDATIONS

The preliminary results we have obtained indicate that it is possible to recover reasonable estimates of the seismic moment tensor using only a few stations and a globally averaged 1D seismic velocity model. Future work will include the bulk processing of the 330 M>4.4 test events, investigating the results for different global 1D-velocity models, the development of an automated method of assessing solution, and the focused monitoring of a region. This later task will involve the use of ground truth and calibration information available at the Center for Monitoring Research. Possible regions for this focused analysis include the Lop Nor and Novaya Zemlia test sites, former Soviet Union, and the Middle East.

REFERENCES

Dreger, D. and D. V. Helmberger (1991) Complex faulting deduced from broadband modeling of the 28 February 1990 Upland Earthquake (M_L=5.2), Bull. Seism. Soc. Am., 81, 1129-1144.

Dreger, D. and B. Romanowicz (1994) Source characteristics of events in the San Francisco Bay Region, USGS Open-file report, 94-176, 301-309.

Dreger, D. (1997), The Large Aftershocks of the Northridge Earthquake and their Relationship to Mainshock Slip and Fault Zone Complexity, Bull. Seism. Soc. Am., 87, 1259-1266.

Dreger, D. and B. Woods (1999) Regional moment tensors as discriminants?, in revision.

Dreger, D. and A. Kaverina (2000). Seismic remote sensing for the earthquake source process and near-source strong shaking: A case study of the October 16, 1999 Hector Mine earthquake, Geophys. Res. Lett., 27, 1941-1944.

Dreger, D. S., H. Tkalcic, and M. Johnston (2000). Dilational processes accompanying earthquakes in the Long Valley Caldera, Science, 288, 122-125.

Dziewonski, A. M., Chou and J. H. Woodhouse (1981), Determination of earthquake source parameters from waveform data for studies of global and regional seismicity, J. Geophys. Res., 86, 2825-2852.

Ekstrom, G., A. M. Dziewonski and J. Steim (1986) Single station CMT:application to the Michoacan, Mexico, earthquake of September 19, 1985, Geophys. Res. Lett., 13, 173-176.

Fan, G. and T. Wallace (1991). The determination of source parameters for small earthquakes from a single, very broadband seismic station, Geophys. Res. Lett 18, 1385-1388.

Fukuyama, E., M. Ishida, D. Dreger, and H. Kawai (1998). Automated seismic moment tensor determination by using on-line broadband seismic waveforms, *Jishin*, 51, 149-156.

Fukuyama, E. and D. Dreger (2000). Performance test of an automated moment tensor determination system, *Earth Planets Space*, 52, 383-392.

Gee, L., D. Dreger, D. Neuhauser, R. Uhrhammer, and B. Romanowicz (1996) The REDI program, Bull. Seism. Soc. Am., 86, 936-945.

Mendiguren, J. (1977), Inversion of surface wave data in source mechanism studies, J. Geophys. Res.., 82, 889-894.

Pasyanos, M., D. Dreger and B. Romanowicz (1996) Toward real-time estimation of regional moment tensors, Bull. Seism. Soc. Amer., 86, 1255-1269.

Patton, H. J. (1988). Source models of the Harzer explosion from regional observations of fundamental-mode and higher mode surface waves, *Bull. Seism. Soc. Am.,* 78, 1133-1157.

Pechmann, James C., et al. The February 3, 1995, ML 5.1 seismic event in the Trona mining district of southwestern Wyoming, Seis. Res. Lett., Vol. 66, No. 3, p. 25-34)

Romanowicz, B. (1982) Moment tensor inversion of long period Rayleigh waves: a new approach, J. Geophys. Res., 87, 5395-5407.

Romanowicz, B. and Ph. Guillemant (1984) An experiment in the retrieval of depth and source parameters of large earthquakes using very long period Rayleigh wave data, Bull. Seism. Soc. Am., 74, 417-437.

Romanowicz, B., M. Pasyanos, D. Dreger and R. Uhrhammer (1993) Monitoring of strain release in central and northern California using broadband data, Geophys. Res. Lett., 20, 1643-1646.

Stump, B. W., and L. R. Johnson (1984). Near-field source characterization of contained nuclear explosions in tuff, *Bull. Seism. Soc. Am*., 74, 1-26.

Vasco, D. and L. Johnson (1989). Inversion of waveforms for extreme source models with application to the isotropic moment tensor component, *Geophys. Journ. Royal Astr. Soc.*, 97, 1-18.

Walter, W. R. (1993). Source parameters of the June 29, 1992 Little Skull Mountain earthquake from complete regional waveforms at a single station, *Geophys. Res. Lett*., 20, 403-406.

Woods, B. B., S. Kedar, and D. V. Helmberger (1993). ML:M0 as a regional seismic discriminant, *Bull. Seism. Soc. Am.*, **83**, 1167-1183.

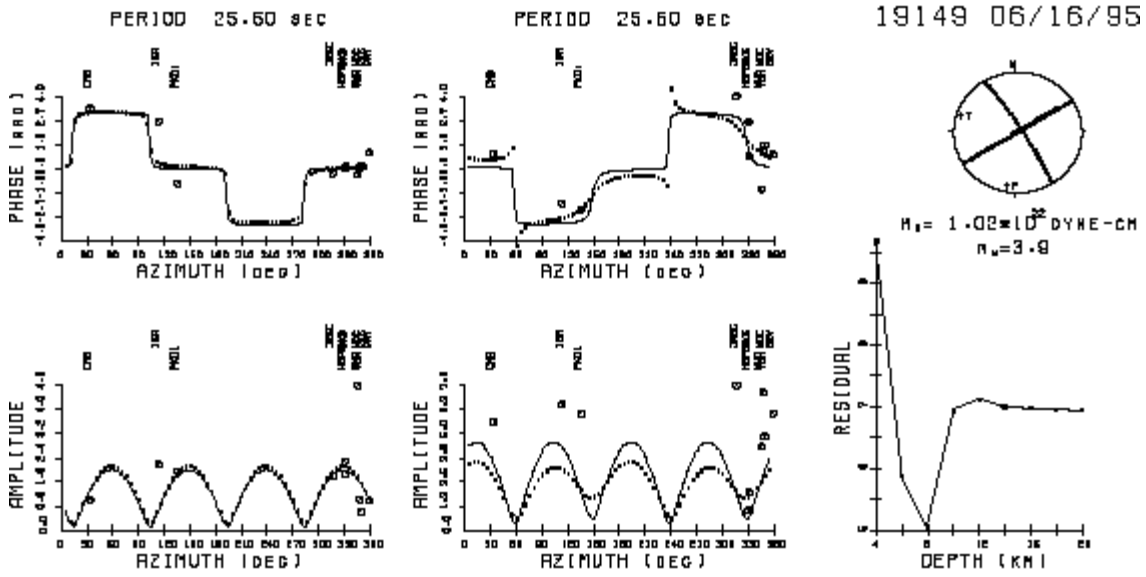

INITIAL	FINAL		
Mo = 1.5e22 dyne-cm	Mo = 1.0e22 dyne-cm	21:20:36	Event origin time
Mw = 4.08	Mw = 3.97	21:27	REDI Page
NP1 238/88/-6	NP1 58/89/6	21:29	Data Extracted
NP2 328/84/-178	NP2 328/84/179	21:31	Inversion Completed
z = 20 km	z = 8 km	21:32:14	MT Page is sent
tau = 1.0 sec	tau = 1.0 sec		

Figure 1A. Example of the regional surface-wave method for an event located near Hollister, California on July 16, 1995. The automatic solution is shown as small circles, the revised as solid lines, and the measured amplitude and phase as large circles. Love wave amplitude and phase are compared on the left, and Rayleigh wave amplitude and phase are compared on the right. The automatic and revised focal mechanism, and source depth as a function of residual are shown to the far right. The text gives the parametric details, and a chronology for the automatic processing and reporting for this event.

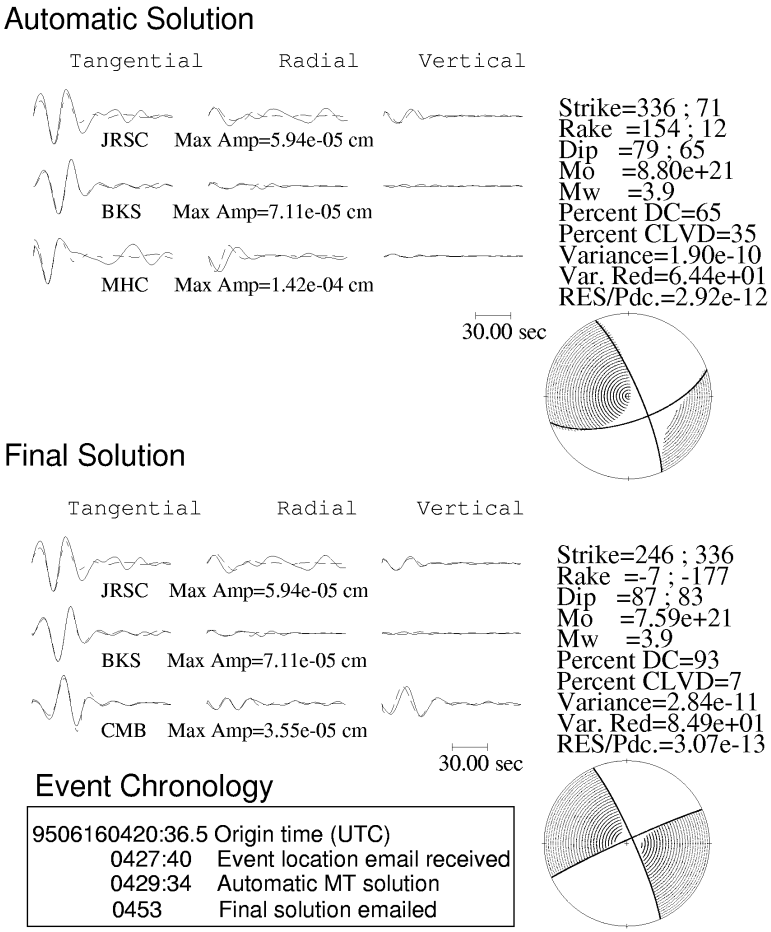

Figure 1B. The automatic and revised solutions for the same event discussed in Figure 1A are compared for the complete waveform method. The analyst review resulted in the removal of the noisy MHC station, and the inclusion of CMB, which provided much better azimuthal coverage. The data is shown as solid lines and the synthetic seismograms as dashed lines. The complete waveforms include phases such as P_{nl}, S_n body waves, and Love and Rayleigh surface waves.

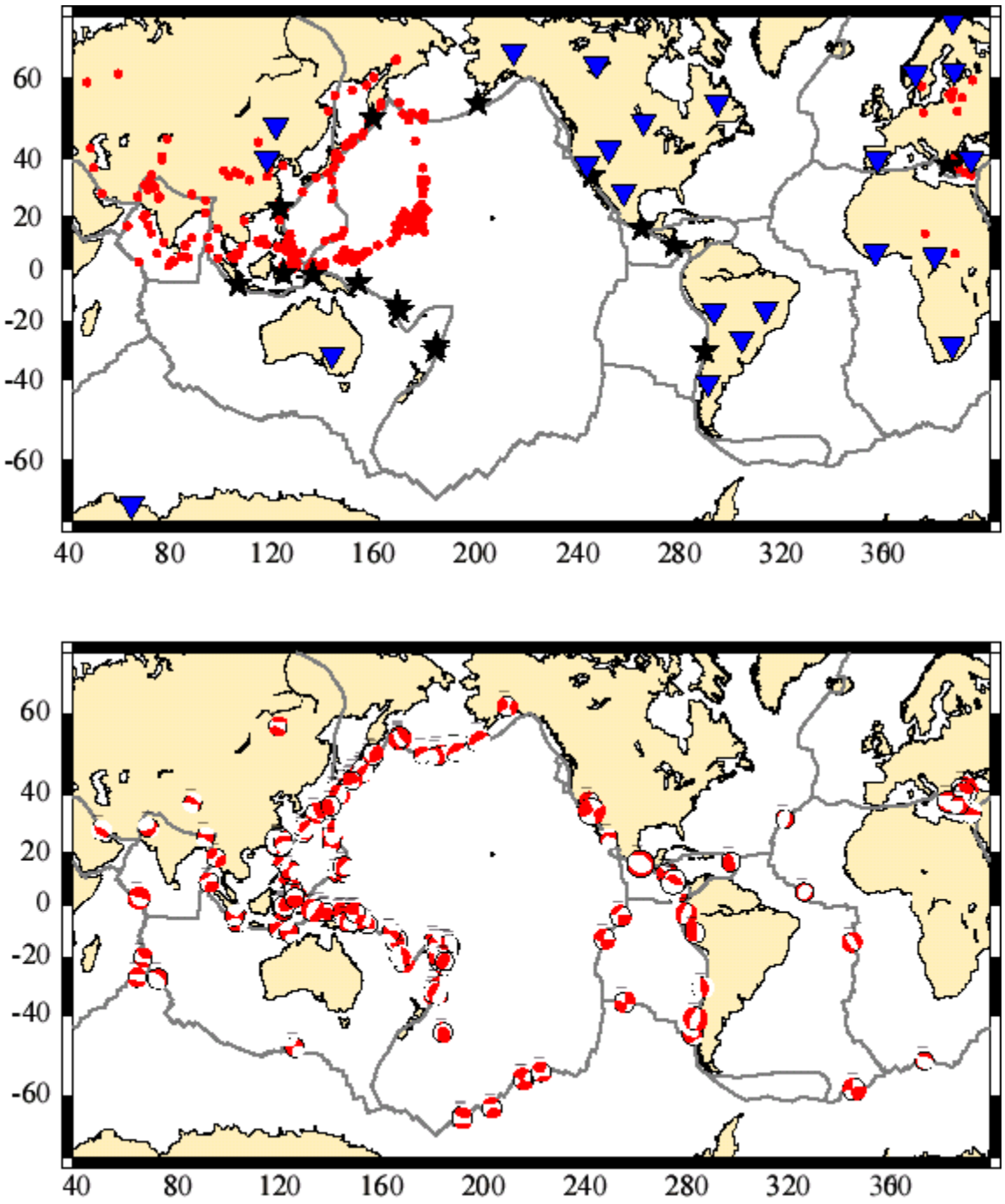

Figure 2. A) Map showing the locations of Mb>4.4 (red circles) and Mb>5.4 (black stars) events from the REB during the 90 day period from July 19, 1999 to October 17, 1999. IMS primary stations from which data was obtained are shown as inverted blue triangles. There are 330 Mb>4.4 events and 28 Mb>5.4 events during this time period. B) Harvard CMT solutions for the same time period.

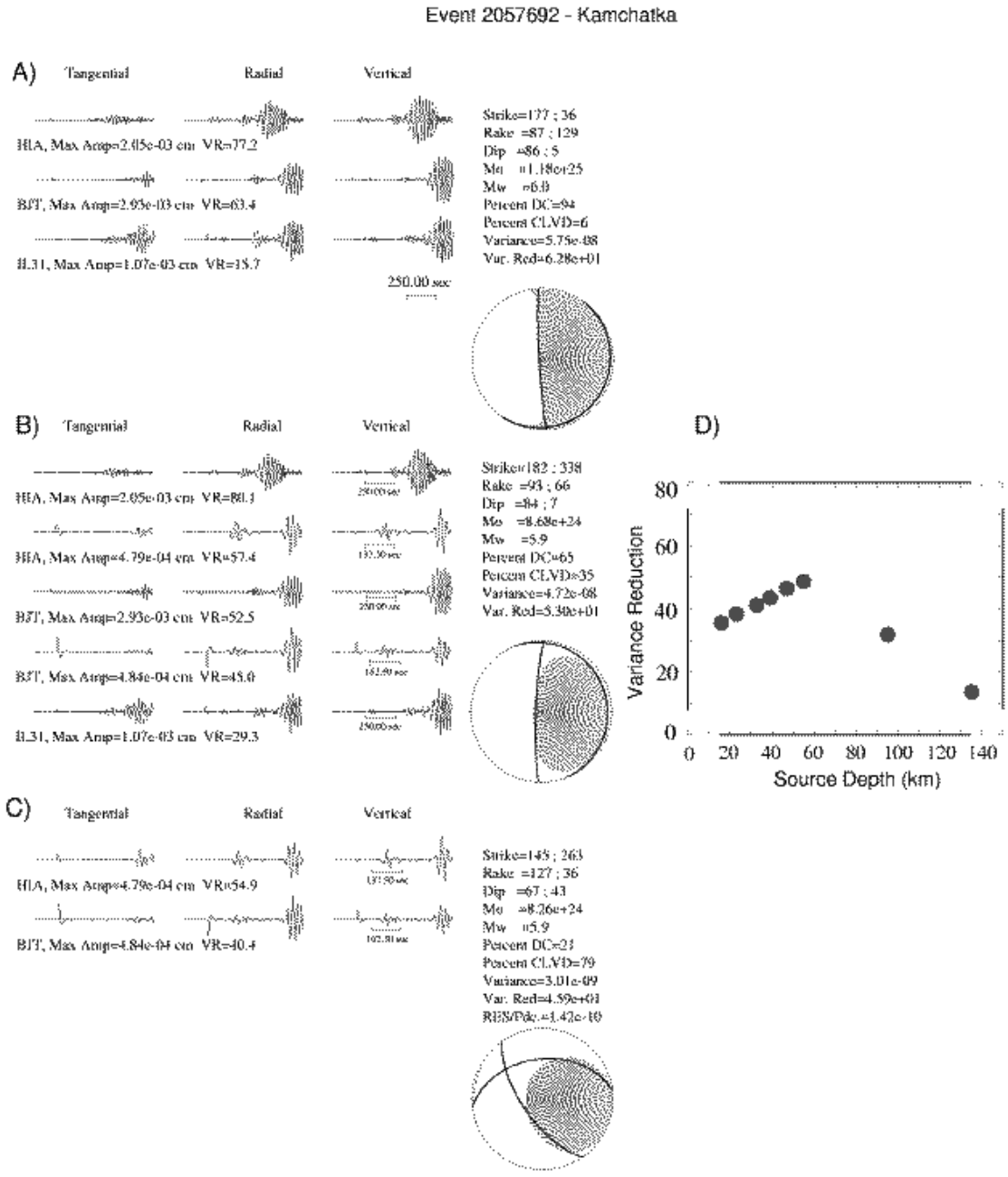

Figure 3. A) Inversion results for the September 18, 1999 Kamchatka event obtained by fitting complete three-component waveforms in the 50 to 20 second period passband from three IMS primary stations located between 28-35 degrees from the event. B) Inversion results for the case when P and S body waves have increased weight. This solution compares very closely with the Harvard CMT. The Harvard CMT resulted in a depth of 67 km, and the variance reduction vs. depth plot shows that a maximum occurs at a depth of 50 km. Only the depths shown were tested and it is possible that a better fit would be obtained if depths between 50 and 100 km were tried. C) Inversion results for the case when only P and S body waves are used.

STUDY OF ANOMALOUS MINE BLASTS

Michael A. H. Hedlin[1] and Vitaly I. Khalturin[2]

University of California, San Diego[1]
Lamont-Doherty Earth Observatory[2]

Sponsored by Defense Threat Reduction Agency

Contract No. DTRA01-00-C-0115

ABSTRACT

The Altai-Sayan mining region located east of Novosibirsk, Russia, comprises over 72 mines which are located between 7 and 559 km from the International Monitoring System (IMS) primary 3-component station ZAL. We have origin time and location estimates of 853 blasts that have occurred in this trend between 1/1/1995 and 6/30/2000. The mines are known to use millisecond delay-fire blasting and had explosive yields ranging from < 10T to > 500 T. We are currently analyzing the range dependence of seismic waveforms from these blasts to prepare for the use of a correlation method to associate individual mine blast recordings with a specific mines and to look for detonation anomalies. Detonation anomalies are of particular interest as the simultaneous release of a significant explosive yield within a routine mine blast shot sequence might be confused with a clandestine nuclear test.

Recent advances in the simulation of seismic signals from delay-fired mine blasts make it possible to study the effects of these complex events provided that ancillary data on the events under study and the medium through which the energy propagates to the receivers are available. Our focus thus far has been on the collection of ground truth data on blasts in the Altai-Sayan region and the crustal structure. We are currently assessing the accuracy of the data and arranging the collection of more complete data in the future.

We have observed surface waves at the Kyrgyz broadband seismic network (KNET) that have been produced by large mine blasts in the Altai-Sayan trend. We are currently assessing the utility of the dense KNET for characterizing sub-kiloton mine blasts from mid- to far-regional range.

KEY WORDS: Altai-Sayans delay-fire mine blasts, detonation anomaly, ground truth data, waveform correlation

OBJECTIVE

Our primary objective is to enhance our ability to identify mining explosions using seismic recordings made at any regional distance and to detect, and characterize, any unusual, large, simultaneous detonations these events might include. The mining technique of choice, worldwide, is delay-firing. Although significant mining operations exist worldwide, we study blasts in the Altai-Sayan region (Figure 1). This mining trend is located east of Novosibirsk, Russia and consists of over 72 open-pit and underground mines. This is the most active mining region in Russia and has produced over 800 significant blasts that have been recorded seismically and located since the beginning of 1995. A much larger number of small blasts have occurred in the trend. We study blasts that have been recorded by IMS stations and by the dense Kyrgyz broadband seismic network (KNET). The mines are located within 6° of the IMS primary 3-Component seismic station ZAL and are12 to 13° from KNET. We study this region because of the frequency of large blasts, the variety of blasting methods employed, the presence of surface and underground mines and the existence of natural seismicity in the near-vicinity of the mines, all within close proximity of ZAL.

Briefly, we are interested in characterizing routine mine blasts in this region to improve our ability to distinguish these events from earthquakes and mine blasts that include significant detonation anomalies. For this purpose, we are planning to use a waveform correlation technique applied to ZAL recordings. We

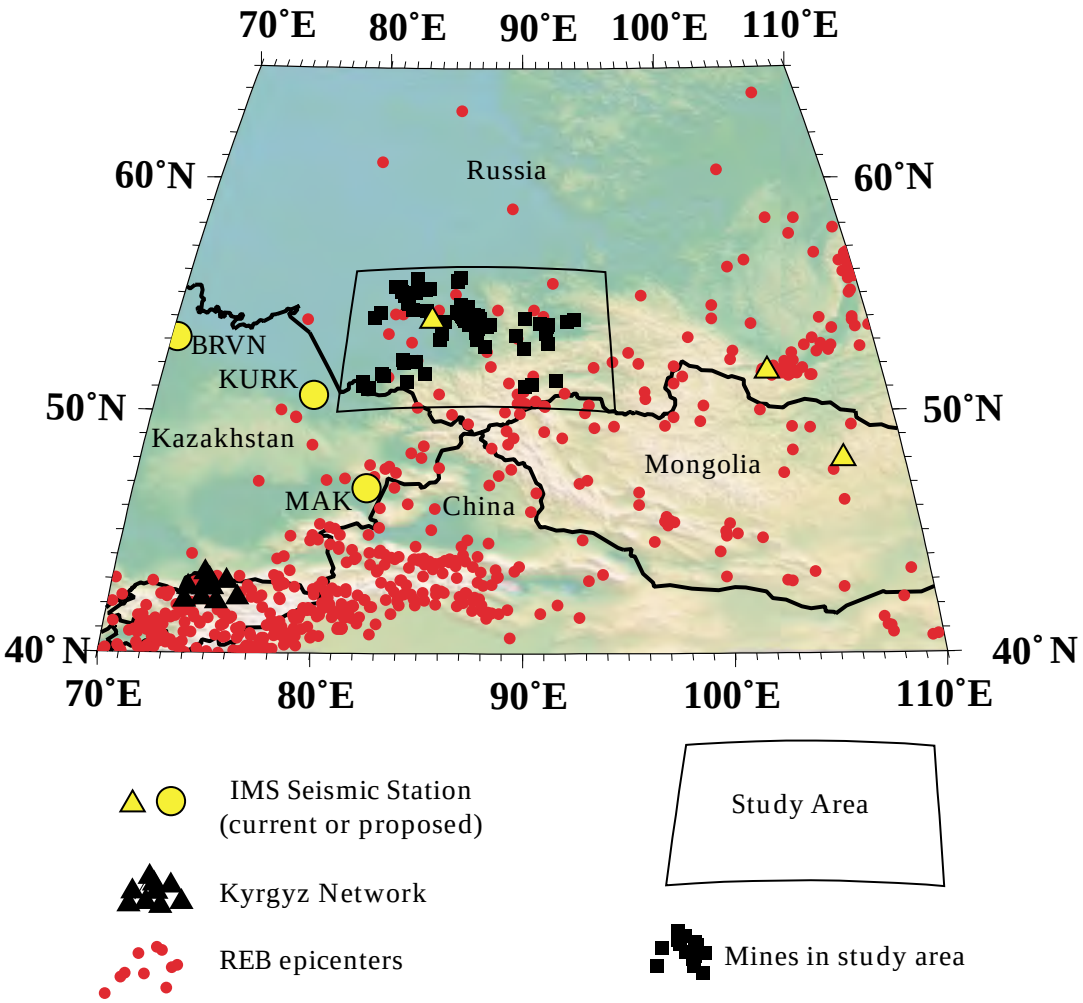

Figure 1. Seismic events reported in the reviewed event bulletin between 1/1/95 and 2/20/2000 are plotted with seismic stations in Central Asia near the study area. The study area includes 72+ surface and underground mines in the Altai-Sayan mining trend.

will also examine spectral rugosity and enhanced surface waves that result from delay-firing. We are collecting ground-truth information on large blasts in this region and information on crustal structure to prepare for modeling of the blasts. We are assessing the accuracy of the ground-truth information. As many of the IMS recordings of mine blasts will be made at mid- to far-regional range, we will also assess the utility of low-frequency seismic signals for characterizing mine blasts. For this purpose, we will use IMS and KNET data.

RESEARCH ACCOMPLISHED

Introduction

The Reviewed Event Bulletin (REB) published by the prototype International Data Centre (PIDC) indicates that large mining explosions are commonly detected by International Monitoring System (IMS) seismic stations at all regional distances; some are seen teleseismically. Khalturin et al. (1997) surveyed over 30 regions worldwide and found that 100 to 200 blasts each year have a magnitude greater than 3.5. Some mining explosions will be difficult to distinguish from single explosions and earthquakes.

Large mining explosions are problematic not just because these events will trigger the IMS, but these large explosions offer a means to obscure nuclear tests. This evasion scenario is particularly troubling because

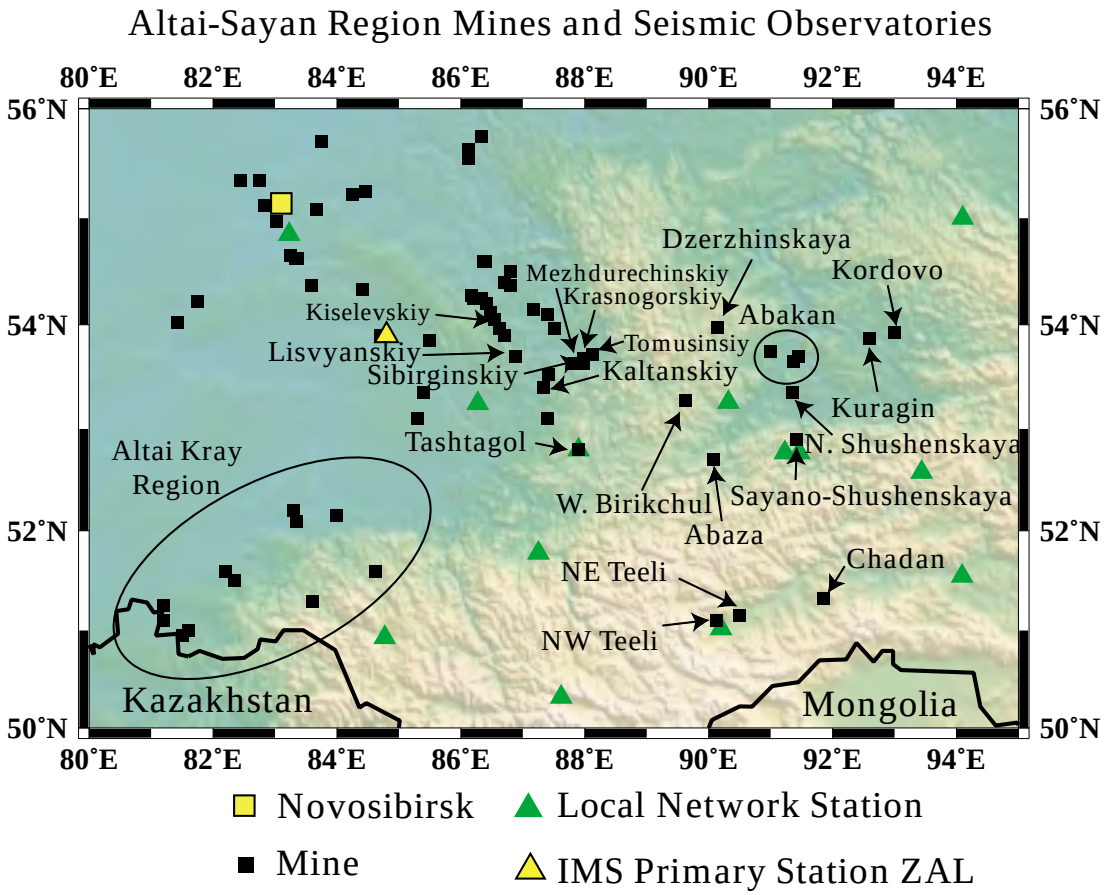

FIgure 2. Mines located in the Altai-Sayan mining region. Most mines are located to the east of Novosibirsk, Russia and are located less than 559 km from the IMS primary 3-component seismic station at Zalesovo. Blast yield and frequency are strongly dependent on the area of the mine. The Altai Kray mining region is responsible for relatively few, small, blasts. Significant blasting is common in the Kuzbass region near the center of the map. The mining region is monitored closely by stations in the Altai-Sayan Seismological Expedition regional network.

blasting anomalies, in which a large part of a mining explosion shot grid detonates simultaneously, are not uncommon. A nuclear test co-located with an industrial explosion might be entirely hidden or mistaken for a detonation anomaly.

Although some industrial explosions are seen teleseismically, most will not be recorded at this range with an adequate signal-to-noise ratio for detailed study. Most will not occur within near-regional range of any IMS seismic stations. There is a pressing need for discriminants that operate at mid- to far-regional range. Low frequency seismic signals have the potential of facilitating mine source characterization from long range, thus have the potential for reducing the cost of monitoring.

In this paper, we describe mining operations in the Altai-Sayan region, which is located east of Novosibirsk, Russia. We report on our preliminary analysis of seismic recordings made by stations in the International Monitoring System (IMS) and by the Kyrgyz Network (KNET). We will describe our efforts to obtain useful ground truth information on large blasts in this region and on the crustal structure as part of our plan to model the events. We are interested in characterizing mining blasts that appear to detonate as planned. We will also examine events that include significant detonation anomalies.

We present seismic recordings made by stations in the IMS and KNET (located at a range of 12 to 13° from

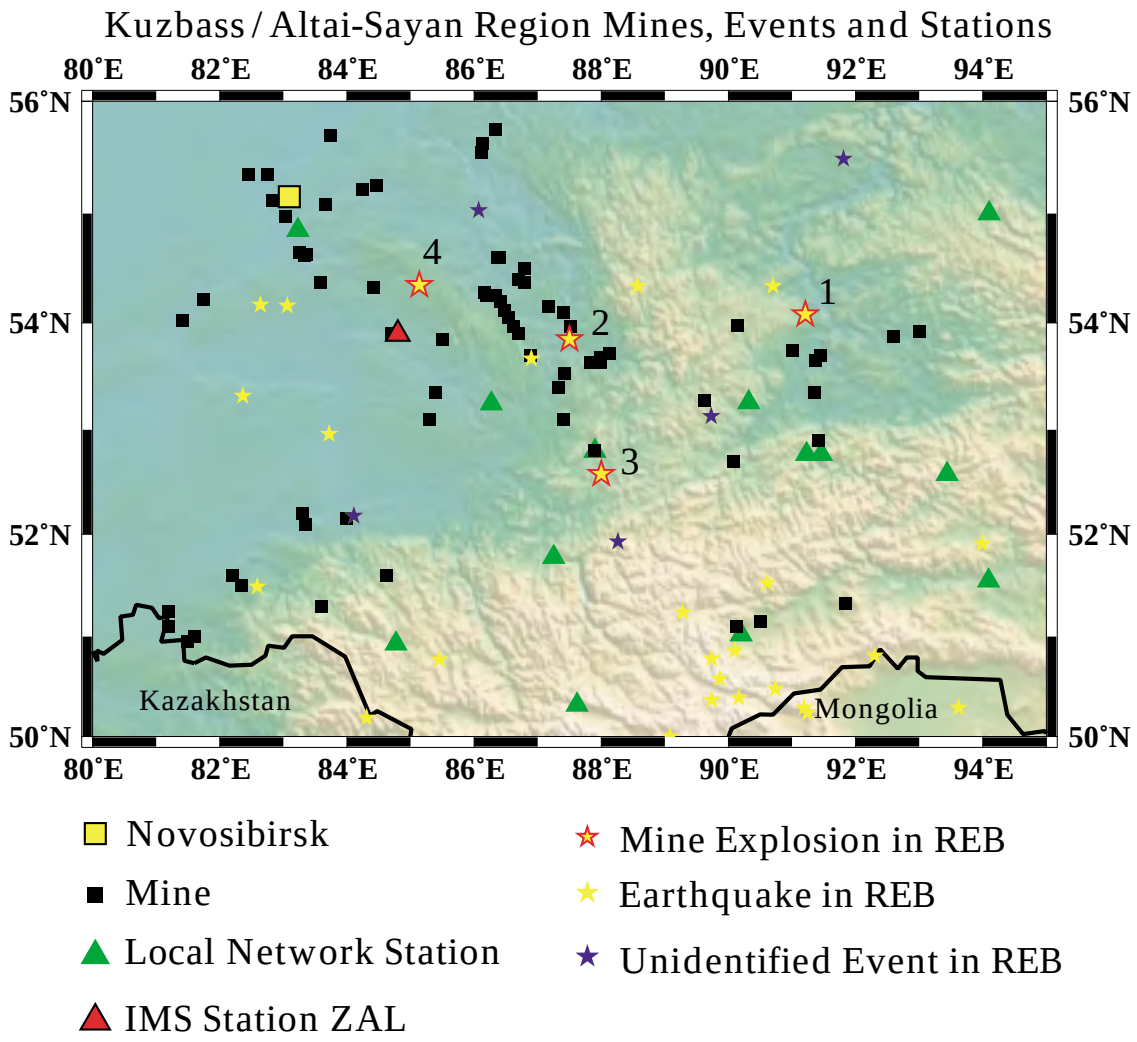

Figure 3. Between 1/1/95 and 2/20/00, 32 events from this region were reported in the reviewed event bulletin. Of these events, 4 are believed to have resulted from mining activity. Some of the REB events are unidentified.

the mines). The KNET data are included in our analysis to determine the utility of a dense network for identifying large blasts from mid-regional range. We also use event locations obtained from the Altai-Sayan Seismological Expedition Network.

Study area

The Altai-Sayan mining region is located in a Paleozoic folded terrain just north of the Mongolian Altai and the Tien Shan (Fotiadi, et al., 1978; Dobretsov, et al., 1995; Zhalkovskii, et al., 1995; Lukina, 1996). The area has remained tectonically active. Over 555 events from the region displayed in Figure 1 were reported in the REB between 1/1/1995 and 2/19/2000. During this time period, 32 of these events occurred in the study area from 50 to 56° N and 80 to 95° E (Figures 2 and 3). The study area includes significant coal mining operations. Mines in the area also produce iron ore, non-ferrous metals (including zinc, copper, lead, molybdenum, and bauxite) as well as precious metals (including gold and silver). We are aware of 72 mines in this region (Figures 1 and 2). There are two large regions of mining activity in the study area. The Kuzbass extends from 53 to 56°N and 86 to 88°E. The Sayans extends from 51 to 54.5°N and 89 to 94° E. The most active mines in the Kuzbass region are in the Mezhdurechinsk area from 53.56 to 53.72°N and 87.68 to 88.10°E. The Krasnogorsky, Tomusinski, Mezhdurechinski, Siberginski and Olzherasski open pits

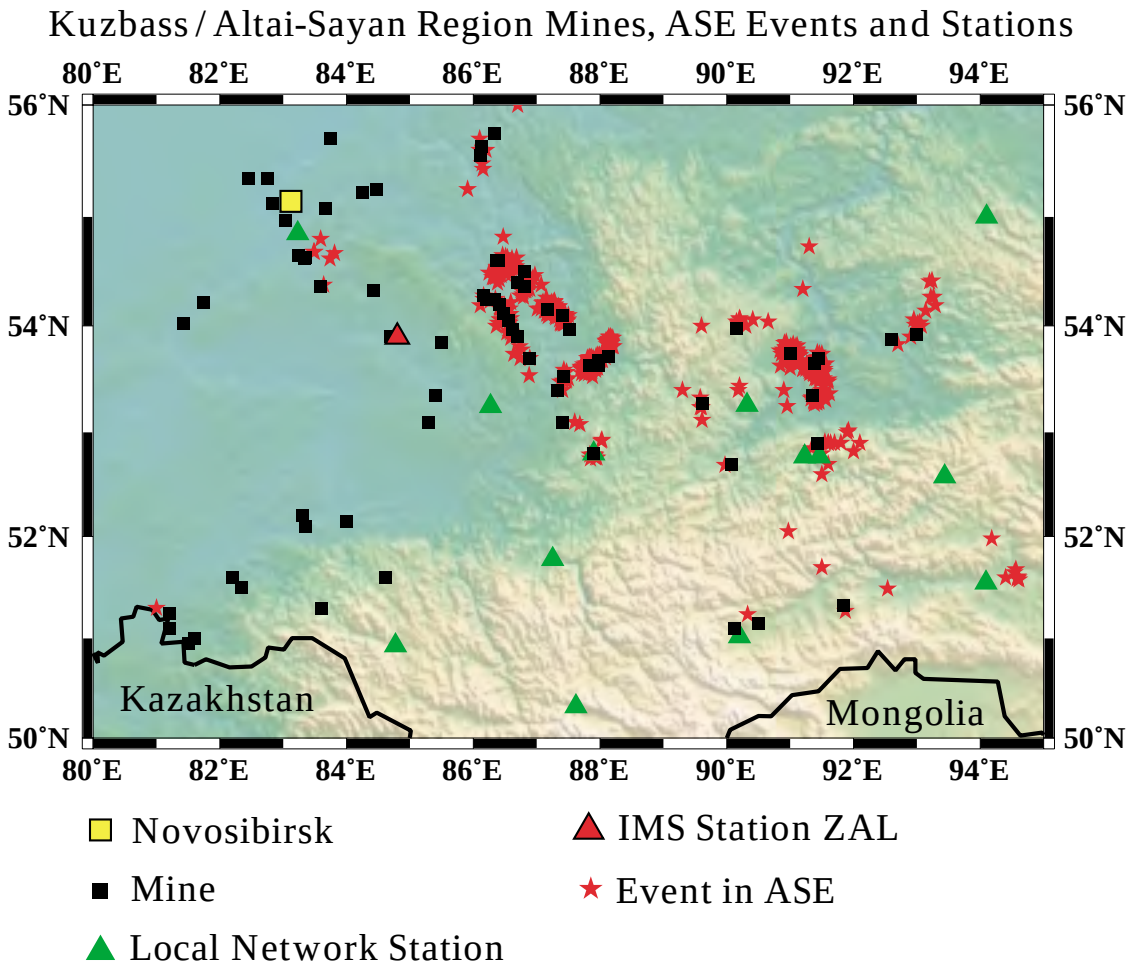

Figure 4. During the time period from 1/1/95 to 2/20/00, over 800 blasts were recorded by the Altai-Sayan Expedition network. The event origins correspond with known mine locations.

are in this area. Each pit is several km long. In the Kuzbass area, over 400 blasts with yield above 100 Tons are known to have occurred in 1999. Of the 28 known mines in the Kuzbass, 26 are open-pit coal mines; two, including Tashtagol, are underground. In the Sayans, there are two active coal open pits near Abakan. These include Chernogorsky and a group of pits collectively referred to as Abakan-2.There are significant construction projects including the Sayano-Shushenskaya hydroelectric power station. In the Sayano-Shuskenskaya area, 1452 explosions occurred between 1990 and 1997 (Dergachev and Filina, 1997).

The IMS primary 3-Component seismic station ZAL and 12 of 17 stations in the Altai-Sayan Seismological Expedition (ASSE) regional network (Figure 2) are located in the study area. The network was deployed by the Altai-Sayans Seismological Expedition of the Siberian Branch of Russian Academy of Science. Each station is equipped with three short-period analog SKM instruments.The magnification is about 30K-50K in the frequency range from 0.7 hz - 15 hz. Some stations also include long period SKD instruments with a pass band between 0.2-18 s. Digital recording equipment was installed at 9 of the sites in 2000. Although seismic recordings from this network are not used in our analysis, source locations and origin times have proved invaluable (Figure 4). Incidentally, the IMS infrasound array, IS46, will be located at Zalesovo.

Five of the events in the study area that were reported in the REB are known to be due to mining activity. Much of the analysis will be based on events that occurred in the same mining trend as the REB events, and were recorded with high signal-to-noise (SNR) at the nearby IMS station ZAL, but did not register on

enough IMS stations to be listed in the REB.

Ground Truth Data

A necessary component of our research is the collection of accurate and detailed information about how, and when, significant blasts have been detonated. Mining blast practice is tailored to local needs and is thus highly variable. During the summer of 2000, Dr Khalturin discussed the collection of ground truth data from mining blasts in the Altai-Sayan region with local experts. Several examples of ground truth information follow:

Table 1: Basic ground truth information

Year	Yr	Dy	Hr	Mn	SS.S	Lat	Long	Energy	Class	Mine	Misc Information	
1999	07	20	07	22	37.6	53.63	86.86	8.1		Listvyan.	Y-239t	35 msec
1999	07	23	06	13	03.5	53.59	87.45	8.7		Kaltansky	Y=244t	
1999	08	11	08	06	33.5	53.68	87.80	10.3		Sibirginsky	Y=549t	35 msec
1999	09	01	07	31	14.3	53.69	87.88	8.2		Krasnogor.	Y=173t	L=467 m
1999	09	28	08	08	28.9	54.07	86.49	9.0		Kiselevsk	Y=224 t	50 msec

Y is total shot yield, L is length of row and, for some events, the inter-shot delay is given.

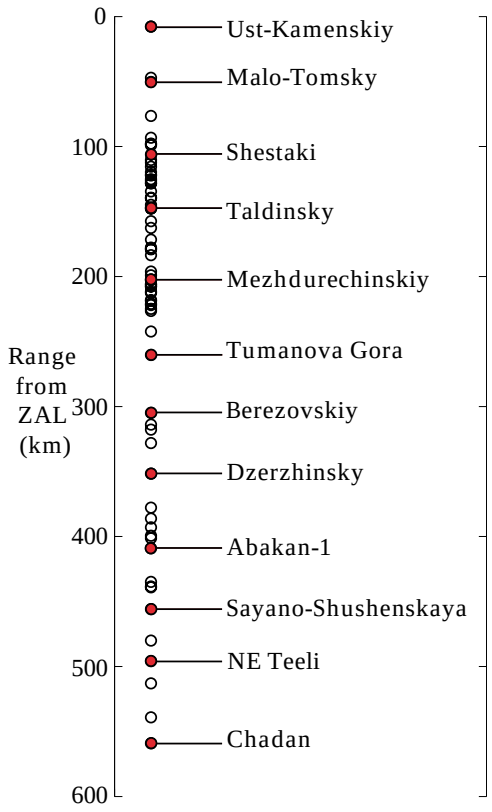

Figure 5. The 72 known mines in the A-S trend are located less than 559 km from the IMS station ZAL. Selected mines at ~ 50 km intervals are highlighted. Most blasting is due to mining activity. The Sayano Shushkenskaya blasts are for construction of a hydroelectric dam.

Much more detailed information is available for a small subset of the blasts. Information pertaining to the 549 ton blast that occurred in the Sibirginsky open pit coal mine on August 11, 1999, was particularly detailed and indicative of the level of detail we might expect in the future. The Sibirginsky mine includes one pit that is ~ 14 km long and 1.5-2 km wide. The event was recorded at 10 stations in the ASSE network and was assigned a coda wave magnitude of 3.2, an origin time of 08:06:33.3 UT and a geographic location of 53.62° N, 87.85° E. The ground truth information indicates that this event included 225 holes and a total of 544,948 kg of explosives arranged in 11 rows. The average hole depth was 41.3 m. The interrow delay was 70 msec, intershot delays were 35 msec. Rows were spaced 8 m, adjacent holes were spaced 5-6 m.

The Sibirginsky blast was relatively large, in comparison with other events in this region, but was otherwise not out of the ordinary. The industry standard blast uses 35 msec intershot delays with yields ranging from < 5 tons to > 500 tons. Most mines use multi-row blasting.

The Sayans region (east of the Kuzbass trend) includes surface (open pit) coal mines. Molybdenum ore is mined in Dzerzhinskaya; Sayano-Shushenskaya is a Hydrostation Dam; Abaza, NW Teeli and NE Teeli are underground iron ore mines. Chadan is an open pit coal mine. Multirow blasting is common at the open pit coal mines and the molybdenum ore mines. Multirow grids most commonly involve 20 —50 msec delays between rowsThe Abaza iron ore mine uses multi row grids with 15 msec delays). The mines in the Altai Kray region produce few large blasts. Typical blasts use 5 to 7 tons of explosives. A few

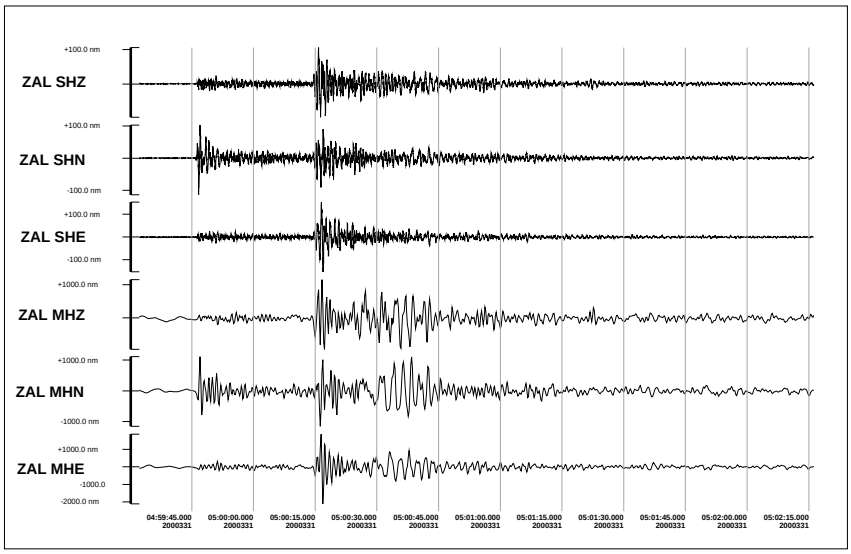

Figure 6. A 690 ton blast occurred in the Tashtagol underground mine on Nov 26, 2000.The MH recordings of this blast made at ZAL reveal a substantial surface wave packet

are greater than 50 tons. The frequency of blasts in each mine ranges from ~ 1/mo to 1-2/yr.

The distances from the mines in the Altai-Sayan region from the IMS station ZAL are given in Figure 5. The trend provides an almost unbroken chain of events from ZAL to > 500 km range.

REB and partially Gr ound Truthed events: Some pr eliminary seismic observations.

The most complete view of seismic activity in the Altai-Sayan trend is given by the ASSE bulletin published by the Altai-Sayan Seismological Expedition (Figure 4). A few of the local mining events are also reported in the REB. Between Jan 1, 1995 and Feb 20, 2000, four events in the REB are known to be mine blasts (ASSE bulletin of explosives).

Table 2. Mine Blasts in study region reported in the REB

Event 1: 1996/01/10 08:14:03.1	54.08N	91.21E	mb 3.2 (Abakan region)
Event 2: 1997/02/20 07:04:00.4	53.85N	87.50E	mb 3.8 (Listvyansky)
Event 3: 1998/02/15 08:51:53.6	52.58N	88.00E	mb 3.6 (Kuzbass)
Event 4: 1998/04/16 04:11:42.2	54.35N	85.14E	mb 3.8 (Abakan region)

Of the 4 events, 2 are known to have occurred in the Kuzbass mining region (Figure 2), the other two occurred in the Abakan mine trend. We have epicentral estimates from the first 3 events from the Altai-Sayan Seismological Expedition (ASSE) bulletin. The average OT difference is 2.0 s. The distance difference average is 55.7 km.

Tashtagol explosion

On Nov 26, 2000, at 04:58:05.8 UT a blast was detonated at Tashtagol (underground) mine at 53.01° N, 87.99° E. The explosive yield has been estimate at 690 tons. The event was assigned an energy class of 9.1 and a coda wave magnitude of 3.1. The details about how this event was detonated are not known yet however it is known to have been delay-fired. ZAL recordings of this event are shown in Figure 6. A significant surface wave packet is evident on the mid-period channels. The short period channels exhibit a clear spectral modulation (not shown).

Kuzbass explosion

A blast detonated in the Kuzbass mine at 2:04 PM local time (07:04 UT) on Feb 20, 1997 was assigned a mb of 3.8 in the REB (and an energy class of 9.2 in the ASSE bulletin). This is the second event listed in

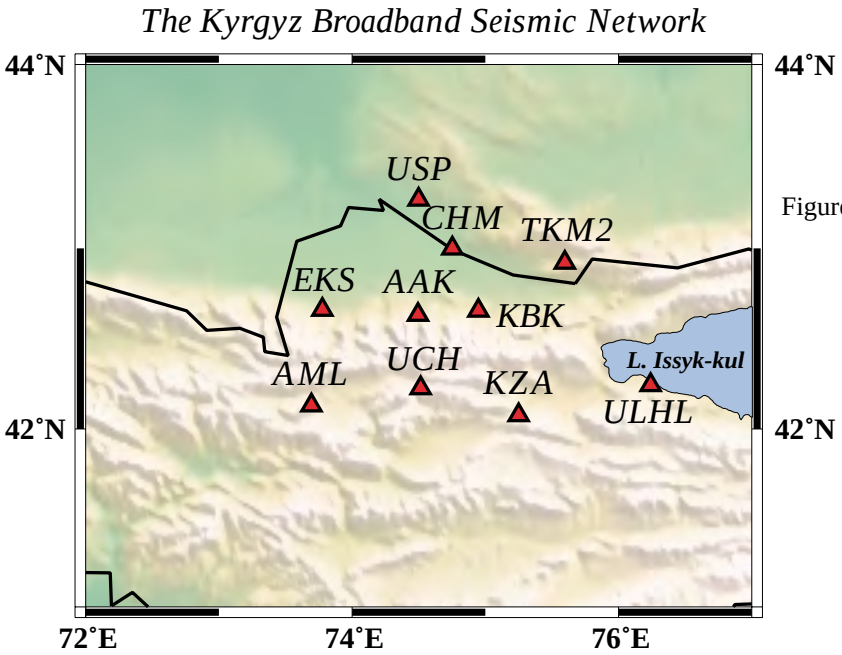

Figure 7. The Kyrgyz broadband seismic network (KNET). The dense KNET comprises 10 stations within an aperture of 200 km.

Table #2. The event was recorded by IMS stations ZAL, HIA, ILAR, YKA, BGCA and DBIC (at 86.06°) and by KNET (Figures 7 and 8). The event was located from 13.47° (TKM2) to 14.90° (AML) from KNET. The arrival at TKM2 at OT+407.4 s gives group velocity of 3.68 km/s.

Planned analysis of ZAL seismic recordings

We study a significant mining region that is covered at near-regional range by one IMS station, and a much greater range by other stations and by the dense seismic network, KNET, in Kyrgyzstan. As the quality, and quantity, of our ground truth data improves, our planned analysis evolves somewhat. We plan to use the high-frequency recordings at ZAL to contrast the spectral rugosity (or roughness) below 10 Hz with that produced by earthquakes from the same region. Our experience with events elsewhere (most notably delay-fired coal mine blasts in Wyoming) is that we should expect significant spectral modulations below 10 Hz, even if the inter-shot delay time is 35 msec. Our experience with Wyoming blasts also leads us to expect enhanced surface waves from the large blasts in the A-S trend. We will examine surface wave amplitudes as a function of event energy class and location using the mid-period recordings at ZAL. We will incoherently stack the > 800 events to define average waveforms as a function of location (or mine) and energy class (e.g. Figure 9). We will compare individual traces to stacked, master, traces to identify detonation anomalies. Our data will be obtained via AutoDRM requests to the pIDC.

Modeling A-S blasts

Once we have adequate knowledge of the crustal structure, and have detailed shot and near-surface information on several blasts that have been recorded well above noise at ZAL, we will attempt MineSeis modeling of the blasts. Physical modeling of normal, and anomalous, mining blasts can be accomplished given the early work of Barker et al. (1990, 93) and McLaughlin et al. (1994) and recent work by X. Yang who has modified the linear elastic algorithm of Anandakrishnan et al. (1997) and packaged it into an interactive MATLAB package (MineSeis; Yang, 1998). The algorithm assumes the linear superposition of signals from identical single-shot sources composed of isotropic and spall components. Both shooting delays and location differences among individual shots are taken into account in calculating delays of the superposition, although the Green s functions are assumed to change slowly so that a common Green s function is used for all the single shots. We used a reflectivity method to calculate the Green s functions. A 1-dimensional velocity model is used (Prodehl, 1979; Anandakrishnan et al., 1997).
An essential step in the modeling of A-S events is the crustal structure. An analysis of seismic recordings

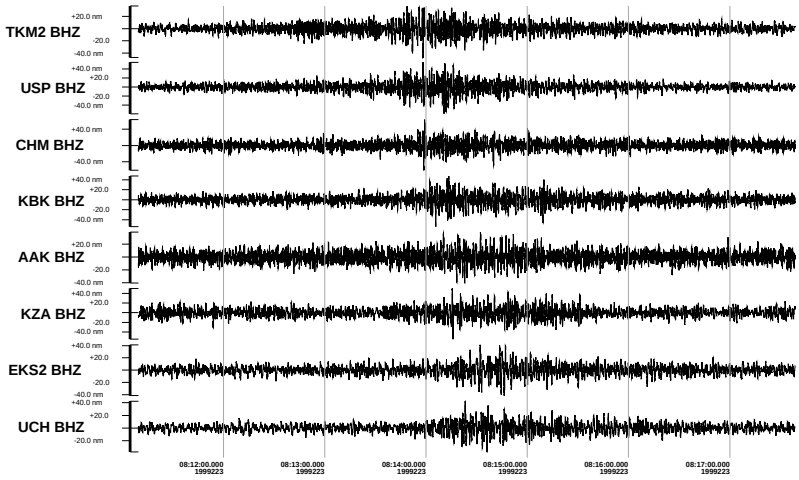

Figure 8. KNET recordings of a surface wave packet produced by a Kuzbass mine blast. that occurred on Feb 20, 1997 .

made by the ASSE network has provided some information on the crustal structure in the Altai-Sayan (Solovyev, et al., 2000). The study of DSS profiles revealsPn velocities ranging from 7.8 to 8.2 km/s. Average upper crustal Pg velocities are ~ 6.0 km/s. Sg velocities range from 3.45 to 3.60 km/s. The depth of the crust ranges from 45-46 km in the northwest corner of the study area to 53-56 km in the southeast.

CONCLUSIONS AND RECOMMENDATIONS

From our preliminary analysis of Altai-Sayan mining events, we believe that there is strong evidence that the methods that have proven to be effective for characterizing large mining events in Wyoming will also be useful in the Kuzbass mining region of Russia. These methods include spectral modulations below 10 Hz and the partitioning of energy between surface and body waves. Most Russian mine blasts produce spectral modulations and surface waves that are recorded by the IMS station ZAL. These observations remain tentative as we do not have enough ground truth information to constrain most events. We have begun a collaboration with Vitaly Khalturin (Lamont) under which we will strive to strengthen communication links between our groups and mining experts in the Kuzbass region.

Observational evidence for the accidental, near-simultaneous, detonation of a large amount of explosives during standard delay-fired explosions comes from other major mining regions. These events have single-fired characteristics and may prove to be problematic in discrimination analysis. The continued study of these unusual events is necessary if we are to minimize the need for on site inspections.

It is important that mining blasts in this significant mining region are properly characterized, despite propagation of the signals across geologically complex structures, to avoid possible false alarms of the monitoring system. A primary thrust of our research will be estimating the frequency and magnitude of detonation anomalies.

ACKNOWLEDGEMENTS

Our main contacts in Russia include Dr Victor S. Seleznev (Head of Siberian Geophysical Survey), Dr Alexy F. Emanov (Chief of the Altay-Sayans Seismological Expedition), and Drs Filina, Kondorskaya and Fedorova. David Yang (LANL) has kindly provided the MineSeis Graphical User Interface (GUI) modeling software.

REFERENCES

Anandakrishnan, S., S.R. Taylor, and B.W. Stump, (1997), Quantification and characterization of regional seismic signals from cast blasting in mines: A linear elastic model, *Geophysical Journal International,* 131, 45-60.

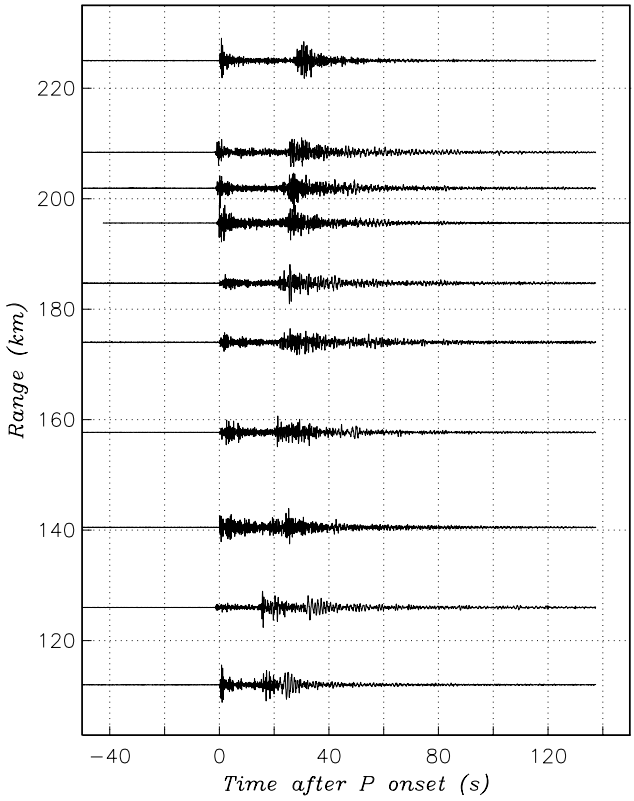

Figure 9. Recordings of Kuzbass mining events made by the short period channel at the IMS station ZAL. Broad spectral modulations are seen most of the events.

Barker, T.G., and S.M. Day, (1990), A simple physical model for spall from nuclear explosions based upon two-dimensional nonlinear numerical simulations, PL report SSS-TR-93-13859.

Barker, T.G., K.L. McLaughlin, J.L. Stevens, and S.M. Day, (1993), Numerical models of quarry blast sources: the effects of the bench, *PL semiannual report, SSS-TR-93-13915.*

Dergachev, A.A., and A.G. Filina (1997), Catalog of seismic events in the area around the Sayano-Shushenskaya GES during 1990-1997, Novosibirsk Nauka Publ. House, 52 pp.

Dobretsov, N.L., N.A. Berzin, M.M. Buslov, and V.D. Ermikov (1995), General aspects of the evolution of the Altai region and the interrelationships between its basement pattern and the neotectonic structural development, *Russian Geology and Geophysics*, 36, 3-15.

Fotiadi, E.E., V.S. Surkov, M.P. Grishin, and O.G. Zhero (1978), Regional Geophysical investigations of the structure of the Earth s crust of Siberia, *Geologiya i Geofizika,* 19, 90-95.

Hedlin, M.A.H., B. Stump, D.C. Pearson, and X. Yang (2000), Identification of mining blaslts at mid- to far-regional distances using low-frequency seismic signals, *in review with PAGEOPH.*

Khalturin, V.I., T.G. Rautian, P.G. Richards, and W.Y. Kim (1997), Evaluation of chemical explosions and methods of discrimination for practical seismic monitoring of a CTBT, *Phillips Lab. PL-TR Final Report.*

Lukina, N.V. (1996), Active faults and seismicity in Altai, *Russian Geology and Geophysics*, 37, 68-71.

McLaughlin, K.L., T.G. Barker, J.L. Stevens, and S.M. Day (1994), Numerical simulation of quarry blast sources, PL final report SSS-FR-94-14418.

Pearson, D.C., B.W. Stump, D.F. Baker, and C.L. Edwards (1995), The LANL/LLNL/AFTAC Black Thunder Mine regional mining blast experiment, *17th annual PL/AFOSR/AFTAC/DOE Seism. Res. Symp.*, 562-571.

Prodehl, C. (1979), Crustal structure of the western United States, *US Geological Survey Professional Paper,* 1034.

Solovyev, V.M., V.S. Seleznev, I.V. Zhemchugova, and A.V. Liseykin (2000), Deep Structure of Altai-Sayans region from the seismmological systems of observations. *Seismology in Siberia at the Millenium Boundary, The proceedings of International Conference, Novosibirsk,* Nauka Publ. House, p222-228.

Yang, X. (1998), MineSeis - A Matlab GUI Program to Calculate Synthetic Seismograms from a Linear, Multi-Shot Blast Source Model, *20th annual Seism. Res. Symp.* 755-764.

Zhalkovskii, N.D., O.A. Kuchai, and V.I. Muchnaya (1995), Seismicity and some characteristics of the stress state of the Earth s crust in the Altai-Sayan region, *Russian Geology and Geophysics*, 36, 16-25.

DISCREPANCIES BETWEEN PIDC, ISC, AND USGS SEISMIC MAGNITUDES

Won-Young Kim, Paul G. Richards, and John Granville

Lamont-Doherty Earth Observatory of Columbia University
Palisades, NY 10964

Sponsored by Defense Threat Reduction Agency

Contract No. DTRA01-00-C-0074

ABSTRACT

We seek first to document and then to explain the well-known systematic differences between magnitudes (m_b) assigned by the PIDC, ISC, and USGS. To do this, we first obtain "classical magnitudes" that as far as possible reproduce the instrumentation and procedures associated with the Veith-Clawson magnitude scale. Though others claim to assign such magnitudes using broadband data, current practice is notably different from the actual Veith-Clawson protocol, and uses measurements made from narrow-band filtered data derived from broadband instruments. We obtain classical magnitudes by making time-domain measurements using WWSSN seismograms simulated from broadband waveforms, thus allowing us to maintain consistency with the original Veith-Clawson magnitude scale.

We have obtained Veith-Clawson body-wave magnitudes using simulated WWSSN short-period signals for 21 earthquakes in 1998 and 1999. All of these events have a Veith-Clawson m_b that is greater than the PIDC REB m_b. The average discrepancy is 0.5 magnitude units. The discrepancy is at least 0.4 m_b units for 71% of the station m_b observations, with several observations having an offset greater than 1 magnitude unit. Note that the same broadband seismograms underlie these discrepant magnitude values, so this is not an issue of scatter in magnitudes derived from different seismograms. The choice of Gutenberg-Richter, or Veith-Clawson, for the distance correction factor does not strongly affect the resultant event magnitude.

The depth assigned to an event by the USGS NEIC in its Preliminary Determination of Epicenters (PDE) is often greater than the depth given by the PIDC REB, especially for shallow events. This is partially due to the fact that the PIDC uses its default depth of 0 km for a significant number of events, rather than solving for an actual event depth. Since an increase in depth will result in a decrease in the magnitude [for a given measurement of log_{10}(A/T) at a given distance, where A is amplitude and T is period], it follows that the discrepancy between REB and PIDC m_b is even greater, if the REB depths are replaced by those of the PDE in the m_b calculation.

KEY WORDS: seismic magnitudes

OBJECTIVE

Main objectives of the study are to document the discrepancy between the four different magnitude scales m_b(REB), m_b(PDE), m_b(ISC), and m_b(Veith-Clawson) for the period 1995–1999 and to investigate the extent to which these discrepancies are dependent on source size, depth and event type (e.g. earthquake or explosion). We also intend to obtain *station corrections* for about 89 IMS primary and auxiliary network stations, to enable the station magnitudes reported in the REB to be used for purposes of obtaining a value on the m_b(Veith-Clawson) scale. The basis to achieve these objectives is to simulate the waveforms of a classical WWSSN instrument, measure amplitude and period of the *P* wave onset for a selected class of groundtruth events that occurred during 1995–1999, and follow the protocol for assigning a classical body-wave magnitude correctly for these events on the Veith-Clawson scale.

Introduction

Almost as soon as the GSETT-3 experiment began to produce daily bulletins of global seismicity in January 1995, it became apparent that for most seismic events the seismic body-wave magnitudes (m_b) assigned by the

Prototype International Data Center (PIDC) were somewhat lower than those assigned for the same events by the US Geological Survey's National Earthquake Information Center (USGS/NEIC). The discrepancy between these two magnitudes extends from magnitude approximately 4 up to above magnitude 6, and has persisted from 1995 to the present day. In this section we describe how big the discrepancy is, why the discrepancy is important, and briefly review the main efforts that have been made to try and explain it.

How big is the discrepancy, and is it persistent?

To address these questions we have compared m_b values published in the Reviewed Event Bulletin (REB) of the PIDC with those published by the USGS in their Preliminary Determination of Epicenters (PDE). We have done this for the first three-month period of 1996, and for every subsequent quarter year up through the first quarter of 1999, for a total of 13 quarters. In Figure 1, we show the first quarter of 1996.

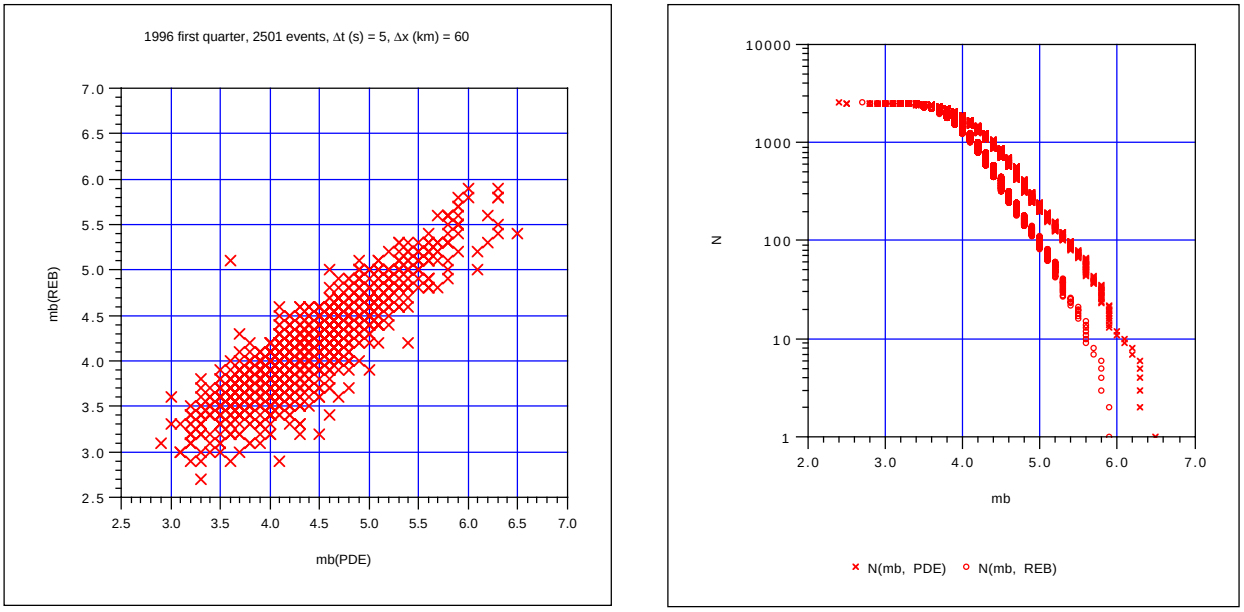

Figure 1. Comparison of m_b values for the events which are in both the REB and the PDE for the first quarter of 1996. Such events are identified by merging the two bulletins, sorting all the events by their origin times, and searching to find events pairs which are separated by not more than a specified time interval (Δt), and are also less than a specified distance apart (Δx). From the lefthand figure, it is clear that most events fall below the line of equal magnitudes, indicating that the REB value of m_b is typically lower than the PDE value. On the right, is shown the cumulative magnitude distribution for the two m_bs, in which it is apparent that the REB value is offset to lower magnitudes but by an amount that decreases at smaller magnitudes.

In Figure 1 on the left we see that most of the 2501 events for this period which are in both bulletins and have their m_b assigned by both organizations fall below the line of equality between REB and PDE magnitudes, and hence that indeed the REB value was typically lower. On the right, we see that if the separate sets of magnitude values are plotted as a display of the a cumulative magnitude distribution, in which N = N(m_b) is the number of events at and above magnitude m_b, then the REB distribution is persistently below the PDE distribution in the range m_b from about 6 down to 4. However, these magnitude distributions, at least for the first quarter of 1996, have different slopes and come together at low magnitudes. A plausible reason for the two distributions coming together at low magnitudes is that during 1995 and 1996 the USGS was accepting PIDC measurements of amplitude and period – and, at low magnitudes, the PIDC was supplying *most* of the

amplitude and period measurements. Therefore, the USGS's bulletin became increasingly dominated by PIDC measurements as m_b decreased.

Similar plots for the later quarters show that m_b(REB) < m_b(PDE). But since the third quarter of 1996, the two distributions N = N(m_b) are essentially parallel for the largest 1000 events. Analysis of all the intervening 7 quarters has shown that the constant offset has been present for each quarter since, in the third quarter of 1996, the USGS stopped using PIDC measurements of amplitude and period, and made their own measurements.

How big is the discrepancy, and is it persistent? It is typically about 0.4 magnitude units, and it has stayed at this value since 1996 up through 1999 with no sign of changing.

Recently, several people (J. Murphy, J. Dewey and R. Willmann) have investigated discrepancy of m_b(REB) against m_b(PDE) and m_b(ISC), using the reported amplitude and period data. Their efforts were quite thorough, yet they could not reach solid conclusion(s) with regard to sources of such discrepancy and any clear remedy to it. It is interesting to note that a few broadband three-component stations and a dozen seismic arrays were major contributing stations to the PIDC for m_b(REB). Only six broadband stations were each reporting magnitude values for more than 10% of the events listed in the REB during January 1996 through July 1998, while 14 arrays were each reporting magnitude values for more than 10% of the events listed on REB in the same period (Murphy et al., 1999). All 89 prototype IMS stations reporting magnitude values are plotted in Figure 2 together with their station corrections determined by Murphy et al. (1999).

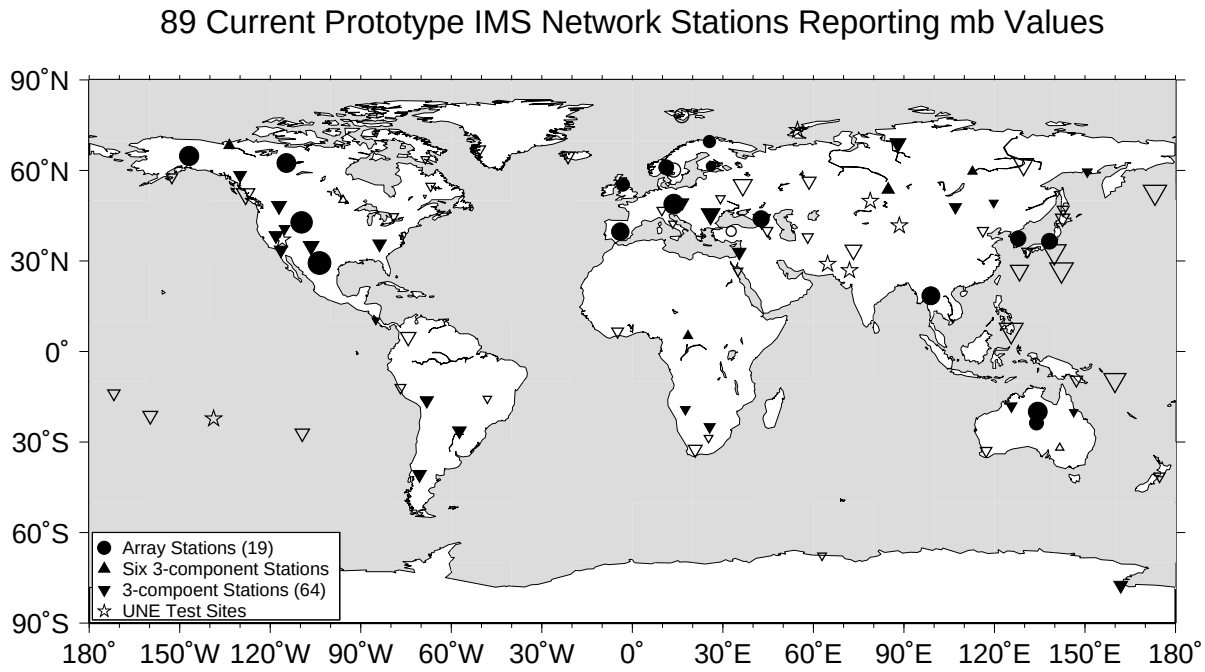

Figure 2. 89 prototype IMS network stations reporting magnitude values are plotted. The symbol size is proportional to the size of stations correction determined by Murphy et al. (1999). Filled symbols are positive station corrections, while open symbols represent negative corrections (*circle*=array stations; *triangle*=six most contributing 3-component stations; *inverted triangle*=64 3-component station).

RESEARCH ACCOMPLISHED

Magnitude of Underground Nuclear Explosions

We analyzed waveform data from underground nuclear tests at Lop Nor Chinese test site, Tuamotu Archipelago (French test site), India and Pakistan test sites. We obtained waveform data from PIDC for these UNTs used by PIDC in generating REB. Figure 3 shows record section of simulated WWSSN short-period seismograms from the Indian UNT on 05/11/1998. There are 51 station magnitudes reported in the REB for this event which has m_b(REB) = 5.0. For this explosion, teleseismic *P* waves at most of the stations in the distance ranges of 28.2 to 94.6° are quite clear and have an average period of 0.77±0.16s.

We reproduced m_b(*P*) as determined by PIDC procedure, except for the array stations, for which we determined amplitude and period from the single reference station instead of calculating the beam trace and measure the amplitude from the beam trace. Figure 4(a) shows comparison between station m_b(REB, *circles*) and m_b reproduced in this study (*pluses*) by following the PIDC procedure. Most of the station m_bs are very close, except few m_bs from array stations. For example, reproduced single station m_bs are more than a factor of two (or 0.3 m.u.) greater than corresponding m_b values from the array beam listed on REB (KVAR, BRAR and MJAR). For other 13 array stations, m_b determined from a single reference station produced fairly consistent results as beam trace. Overall agreement between the two measurements are very close. This exercise ensures that we are using the same data and corresponding instrument responses as used by the PIDC, so that further detailed study would provide us with unequivocal evidence in finding magnitude discrepancies.

We determined Veith-Clawson m_b(VC) using the simulated WWSSN short-period records. We obtained m_b(VC)=4.96±0.35 for the Indian nuclear test. m_bs determined by other agencies are listed in Table 1. Figure 4(b) shows a comparison between m_b(VC) and m_b(REB) at each station. Arrows indicate sign and size of the m_b(REB) – m_b(VC). Though there are substantial differences at some station m_bs reported on REB and this study, the average m_b from the two methods are very close (see, Figure 4(b)).

Table 1: **Body wave magnitudes (m_b) reported by various agencies for the Indian nuclear test**

REB (m_b/N)	WWSSN/V-C (m_b/N)	PDE (m_b/N)	ISC (m_b/N)
5.0/51	4.96/51	5.2/104	5.1/149

Magnitude of Earthquakes

Magnitude determination for earthquakes introduces additional factors such as focal depth. We analyzed 21 earthquakes and excerpts results in some detail here for one of these earthquakes, the Luzon, Philippine Islands event on 12/11/1999 (18:03:36), h=19 km, m_b(REB) = 5.9/21 for detail in order to identify basic questions.

We obtained waveform data from PIDC for this earthquake used by PIDC in generating REB. We reproduced m_b(REB) as determined by PIDC procedure, except the array stations, for which we determined amplitude and period from the single reference station instead of calculating the beam trace and determining the amplitude. m_b(REB)=5.9 from 21 records from the earthquake, whereas the reproduced m_b is 5.85±0.42/21 stations. Figure 5(a) shows m_bs reported by REB (*circles*) and reproduced in this study (*pluses*). Reproduced m_b at ILAR is about 0.3 m.u. greater than REB m_b, whereas at DLBC reproduced m_b is 0.6 m.u. smaller than REB m_b. Extremely small m_b at HIA suggests that the amplitude of the *P* phase is much smaller than other stations, due to the source radiation pattern. Overall agreement between the two measurements are very close, indicating that data and instrument responses used are consistent with PIDC in most but not all cases.

We determined Veith-Clawson m_b(VC) using simulated WWSSN short-period records. We obtained m_b(VC) = 6.23±0.40, whereas USGS/NEIC reported m_b(PDE)=6.5/132. Figure 5(b) shows comparison of the station m_b(VC) and m_b(REB). Arrows indicate sign and size of the m_b(REB) – m_b(VC). The average difference between these two magnitudes is 0.33 m.u. which is somewhat smaller than the m_b(PDE) – m_b(REB) = 0.6 m.u. The mean period in REB is 0.85±0.32 s, whereas it is 1.09±0.29 s from the simulated WWSSN short-period records.

An obvious source of REB and PDE m_b discrepancies is the time window used to measure amplitude and period of *P* phases. The m_b(REB) is determined from the maximum amplitude phase in the 5.5 second time window following the *P* onset arrival. Such short time window may catch large part of seismic energy carried by sharp *P* wave signals from surface focus explosive sources, such as underground nuclear explosions. However, it is too short a window to capture major amplitudes associated with source corner frequency from larger earthquakes. For a certain class of events, mostly shallow crustal earthquake with oblique fault plane, frequently the direct arrival *P* phases have much smaller amplitude than *pP* or *sP* surface reflected depth phases due to orientation of particular source radiation pattern nodal plane. For instance, for earthquakes occurring at a depth greater than about 15 km, depth phases arrive after the 5.5 s time window used to measure amplitude of *P* onset signals to calculate m_b(REB) magnitude. Most of the amplitude measurements used to calculate m_b(ISC) and m_b(PDE) magnitudes are obtained allowing time window of up to 15 s following the onset *P* arrival.

A traditionally used protocol to measure the amplitude and associated period appears in the Manual of Seismological Observatory Practice (Willmore, 1979): "Usually, the largest amplitude is measured within the first few cycles after the *P* onset, but not later than 15 seconds after it. The corresponding period is taken as the time difference between two neighbouring crests."

For example, *P* phases on the vertical records from the shallow earthquake (h=19.5 km) on 12/11/1999 indicate that peak amplitude of *P* phase in the 5.5s PIDC processing window is smaller than the peak amplitude in the PDE m_b window on most of the records (Figure 6). The m_b(VC) is 6.48 and 6.42, respectively for stations FITZ (Δ =34.1°) and VNDA (Δ =96.2°), whereas m_b(VC) from the PIDC window is 6.27 and 6.38, respectively for stations FITZ and VNDA. Hence, the shorter time window used in PIDC process underestimates m_b by 0.21 and 0.04 m.u., respectively for FITZ and VNDA. Average over four stations indicates that m_b(REB) bias due to the short time window is about 0.05 m.u. m_b(REB) is 6.0 and 6.1, respectively for stations FITZ and VNDA, and indicates that m_b(WWSSN, REB window) – m_b(REB) = 0.27.

CONCLUSIONS AND RECOMMENDATIONS

We determined m_b(*P*) (the teleseismic body wave magnitude) by using the simulated WWSSN short-period records and employing the conventional protocol (see, Willmore, 1979) to the waveform data used to generate m_b(REB) at PIDC. We believe that this is the best way to discern the sources of the known magnitude discrepancy which indicates that m_b(REB) is typically about 0.4 magnitude units smaller than m_b(PDE) or m_b(ISC). The Veith-Clawson magnitude, m_b(VC), at each station determined by using the simulated WWSSN short-period records and Veith-Clawson (1972) amplitude-distance curve for the Indian underground nuclear test on 05/11/1998 indicates that network m_b(REB) = 5.0 is very close to the network m_b(VC) = 4.96 determined in this study. This may suggest that the method used by PIDC for m_b may be suitable for shallow, underground explosions. However, the PIDC m_b(*P*) procedure is not adequate for shallow earthquakes occurring at depth ranges 20 to 50 km. Analysis of data from the large, shallow earthquake on 12/11/1999 (h=19 km) indicates that bias due to PIDC's short time window is about 0.05 magnitude units. This analysis also suggest that m_b(VC) – m_b(REB) is about 0.33 magnitude units for the earthquake on 12/11/1999, which is somewhat smaller than m_b(PDE) – m_b(REB) = 0.6 magnitude units.

We are continuing our effort to find sources of such m_b discrepancy and any clear remedy to it by analyzing waveform data from hundreds of events. We will also analyze m_b(single station) vs m_b(beam) for all array stations of the IMS.

REFERENCES

Dewey, J. (1999). A review of hypotheses proposed to explain the discrepancy between PIDC m_b and USGS m_b: Implications for computation of PIDC m_b, unpublished ms. presented at the Annual SSA meeting (22 pages with 17 figures), May, 1999.

Gutenberg, B. and C. F. Richter (1956). Magnitude and energy of earthquakes, Ann. Geof. (Rome), 9, 1-15.

Kim, W. Y. (1998). The M_L scale in Eastern North America, Bulletin of the Seismological Society of America, 88, 935951.

Murphy, J., T. J. Bennett, B. W. Barker and R. W. Cook (1999). Revised global distance corrections and station corrections for use in the estimation of IDC m_b magnitude, unpublished ms., 45 pages with 26 figures, January 1999.

Vank, J, A. Ztopek, V. Krnk, N.V. Kondorskaya, Yu.V. Riznichenko, Ye.F. Savarensky, S.L. Solovev and N.V. Shebalin (1962). Standardization of magnitude scales, Izvest. Acad. Sci. U.S.S.R., Geophys. Ser., 2, 108.

Veith, K. F. and G. E. Clawson (1972). Magnitude from short-period P-wave data, Bull. Seism. Soc. Am., 62, 435-452.

Willmore, P.L. (1979). Manual of seismological observatory practice, Report SE-20, WDC-A for Solid Earth Geophysics, U.S. Dept. of Commerce, National Oceanic and Atmospheric Administration, Boulder, CO. USA and International Seismological Center, Edinburgh, Scotland (1970).

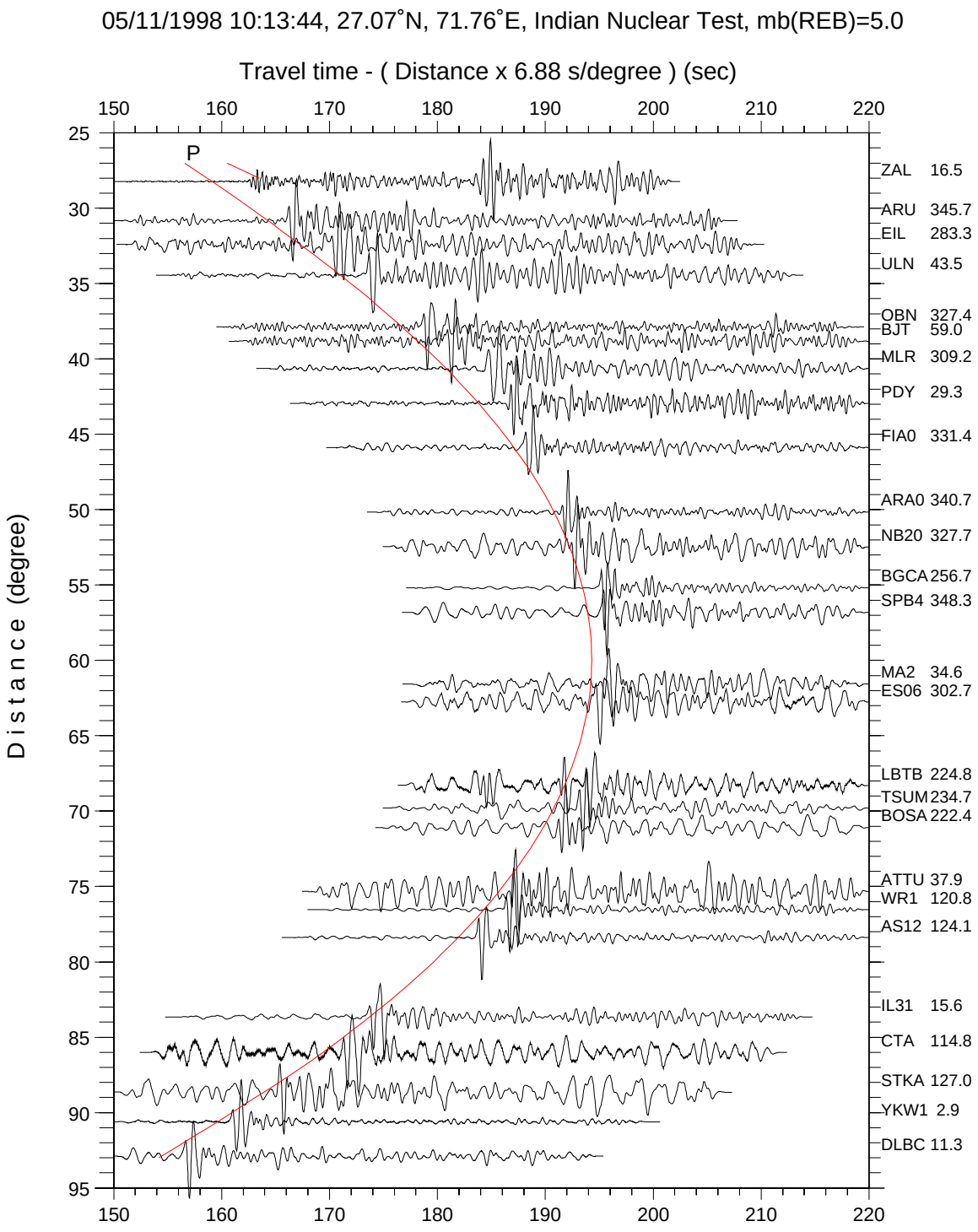

Figure 3. Record section of simulated WWSSN short-period records from the Indian UNT on 05/11/1998. Seismograms are plotted with reduced velocity of 6.88 s/degree and *P* wave arrival times from IASP91 travel time curve are indicated by red line. Station code and azimuth in degrees are indicated at the end of each trace.

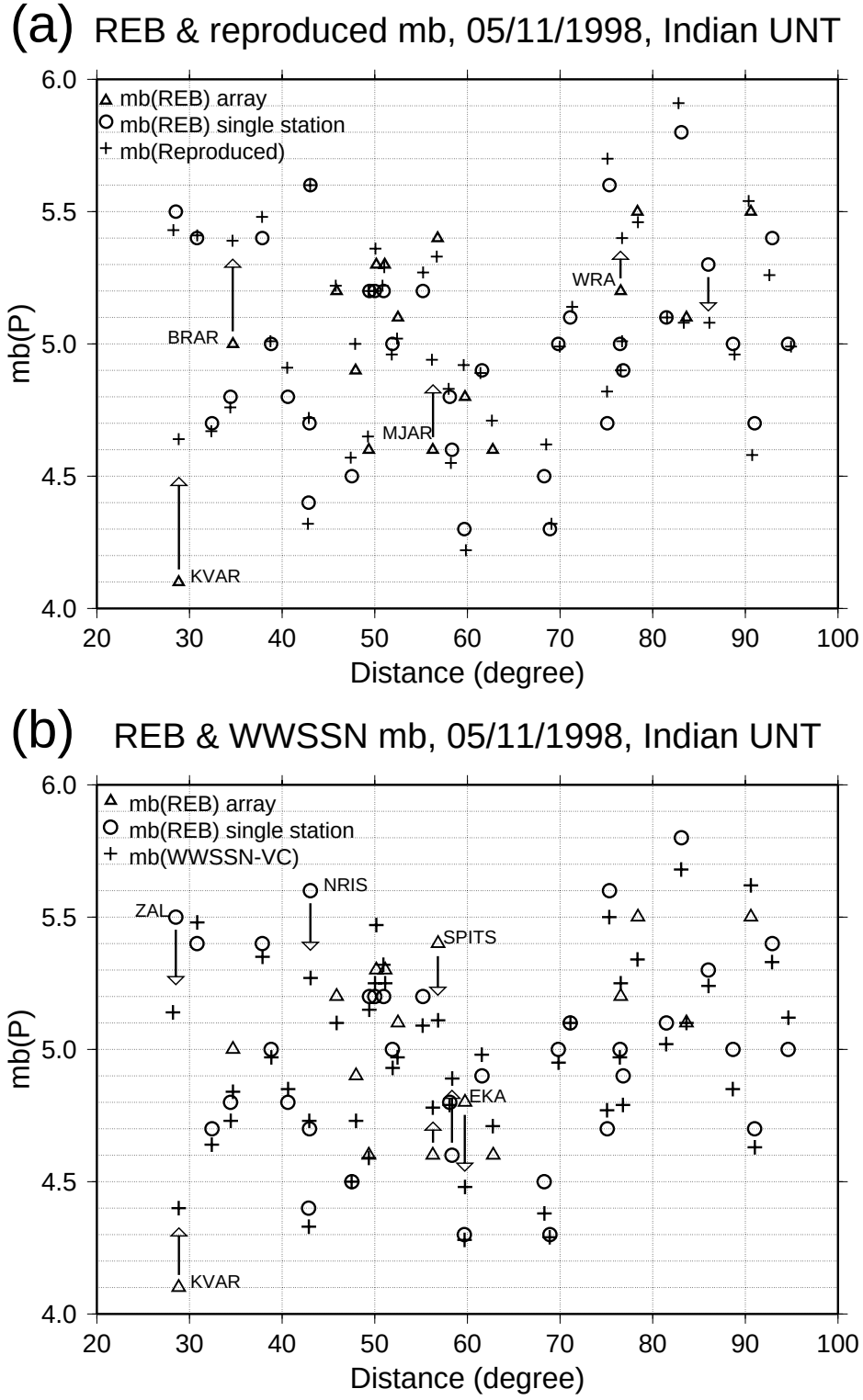

Figure 4. (a) Comparison m_bs reported by REB (*circles* and *triangles* for array stations) and reproduced in this study (*pluses*). Notice that reproduced m_b at array stations are somewhat greater than REB m_b, (b) Comparison of the station m_b(VC) and m_b(REB). Arrows indicate sign and size of the m_b(REB) – m_b(VC). The average difference between these two magnitudes is only 0.04 m.u.

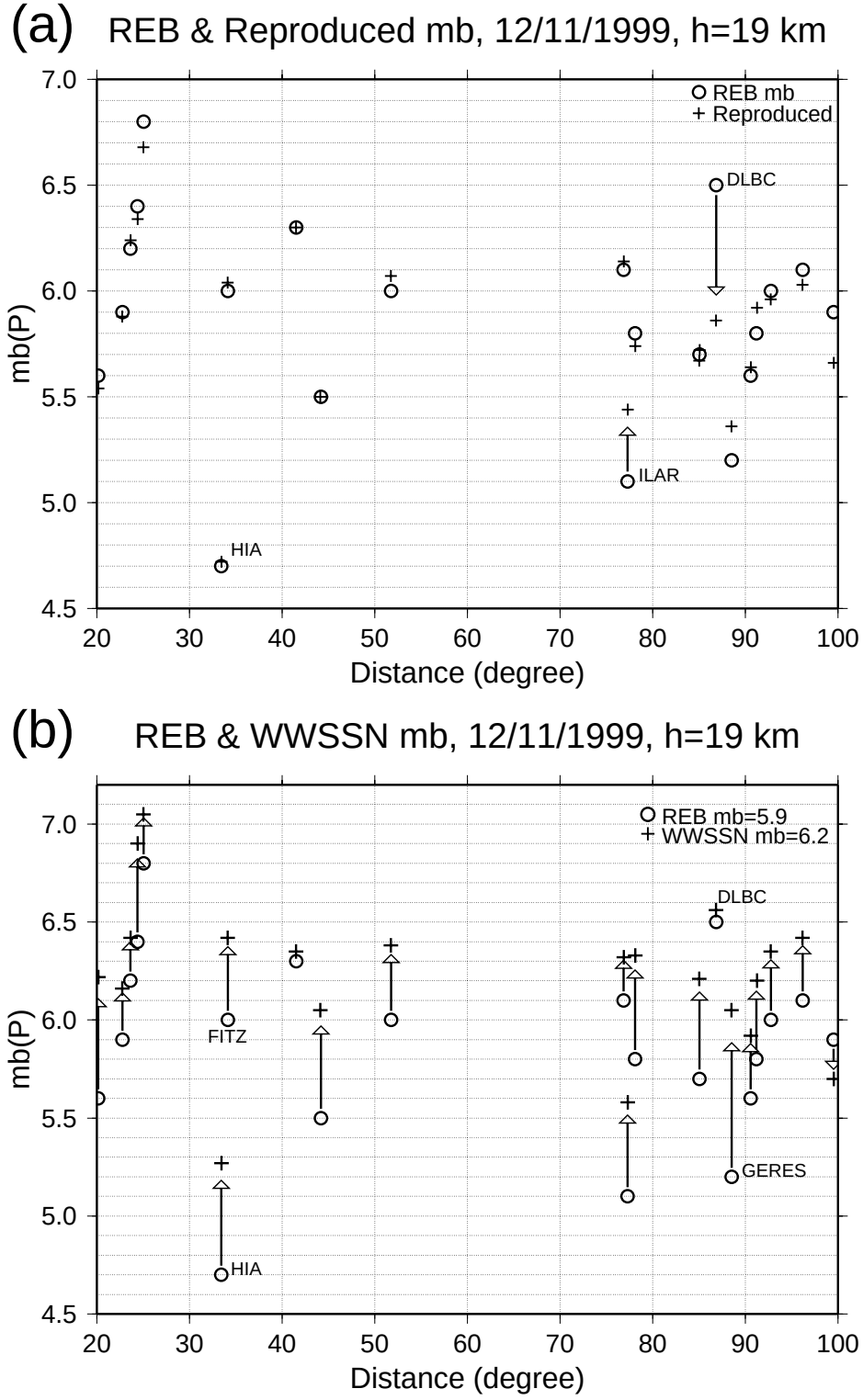

Figure 5. (a) Comparison m_bs reported by REB (*circles*) and reproduced in this study (*plus*). Notice that reproduced m_b at ILAR is about 0.3 m.u. greater than REB m_b, whereas at DLBC reproduced m_b is 0.6 m.u. smaller than REB m_b, (b) Comparison of the station m_b(VC) and m_b(REB). Arrows indicate sign and size of the m_b(REB) – m_b(VC). The average difference between these two magnitudes is 0.33 m.u.

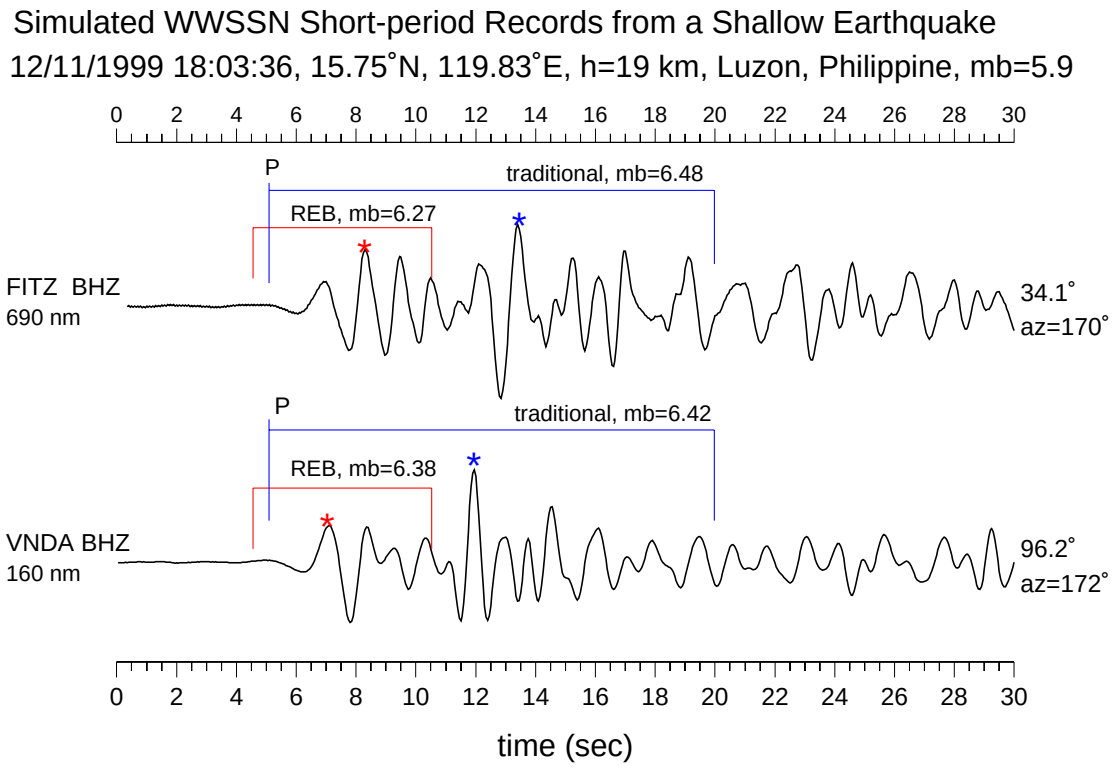

Figure 6. Simulated WWSSN records showing differences in m_b determined from 5.5s PIDC window and 15s traditional window. Largest amplitude phase on both records is *pP* phase (star).

IMPROVING DISCRIMINANTS FOR SOURCE IDENTIFICATION

Thorne Lay and Guangwei Fan

University of California, Santa Cruz

Sponsored by Defense Threat Reduction Agency

Contract No. DTRA01-00-C-0211

ABSTRACT

The ability to correct regional phase discriminant measurements for propagation effects is strongly influenced by the nature of the propagation phenomenon. As an example, blockage of Lg phases by waveguide disruption may lead to enhanced Sn amplitudes, allowing effective discrimination to proceed by interchanging P/Sn ratios for P/Lg ratios, or the corresponding use of Smax measurements. However, if the Lg phase is strongly damped out by intrinsic attenuation, there will be no compensating flux of energy into the Sn wavefield (or vice versa). In addition, the theoretical nature of corrections for amplitude loss for regional phases is expected to assume distinct functional forms for attenuation versus scattering phenomena, and interpolation and extrapolation of empirical corrections should differ for diverse propagation phenomena. The research project that we are pursuing involves exploration of hybrid methods of kriging, parametric regression analysis, and modeling to develop optimal capabilities for correcting for propagation effects. The overriding challenge within central Asia appears to be how to account for, or at least recognize, strong losses of Lg amplitudes for propagation paths within the Tibetan Plateau. Motivated by earlier results from other groups which reported relatively moderate attenuation values for Lg phases within and traversing the Plateau, we assembled a large database which persuasively demonstrated to us that Lg amplitude decay was more rapid than predicted by published attenuation models. One possible cause was a blockage effect associated with loss of Lg energy upon crossing the Plateau margins, but our analysis suggested that the data are more consistent with progressive energy losses proportional to path length within the Plateau, only at a much more severe rate of attenuation than published work would lead us to expect. We developed a differential spectral approach using multiple events with common paths outside of the Plateau but different path lengths in the Plateau to robustly estimate broadband Lg spectral decay. Rather phenomenal evolution of the Lg spectra with path length is observed, with a strong systematic shift of the Lg 'corner' frequency from 2 Hz to 0.2 Hz as a function of increasing path length in the Plateau. Spectral ratios for various path geometries across Tibet indicate that attenuation values for 1-Hz Lg are on the order of 80-90 in the northern central area of Tibet where strong Sn attenuation has previously been mapped, and on the order of 130-150 in most other areas of Tibet. These values are as much as 3 to 4 times lower than published values, but are consistent with (and derived from) the observed progressive extinction of broadband Lg energy. Reanalysis of earlier attenuation estimates has recently been conducted by J. Xie, and he also reports much lower Lg attenuation values within Tibet, consistent with our own estimates. The conclusion is that so-called blockage of Lg energy for paths in Tibet is in fact due to very strong crustal attenuation, of a magnitude likely to be linked to the presence of partial melt in the lower crust (as has been invoked for the upper mantle to account for Sn attenuation). Thus, there is no compensating transfer of energy from Lg to Sn via scattering that would enable a robust Smax solution to the discrimination problem for Tibet events. The observed internal heterogeneity of attenuation within the Plateau makes it difficult to develop alternate lower frequency Lg amplitude measures that might reflect source type as well. Reliance on alternate discriminant measures for Tibetan events appears mandatory.

KEY WORDS: seismic discriminants, regional seismic phases, amplitude corrections, regional wave propagation

OBJECTIVE

We seek to understand the absence of high-frequency *Lg* arrivals for paths traversing the northern boundary of the Tibetan Plateau. The regional signals for events within the Plateau recorded at stations outside the Plateau often appear rather explosion-like due to the weak *Sn* and *Lg* arrivals. Ruzaikin et al. (1977) found that a path length of 200 km within the Plateau is sufficient to attenuate 1-Hz *Lg* signals down to noise levels for observing stations located north of the Plateau. Those authors suggested that either strong attenuation or scattering by a thinning crustal waveguide was responsible, but they stated that their narrowband data did not resolve a progressive shift of *Lg* spectral content to lower frequencies with increasing path length in Tibet, as would be expected if attenuation is primarily responsible. They did note that very low Q values of 20-40 would be required to attenuate 1 Hz *Lg* energy by a factor of 100 over 100- to 200-km path lengths, as observed. Qualitative analysis of *Lg* propagation efficiency relative to *P*-wave coda for stations west and south of Tibet indicated that *Lg* signals are strongly attenuated within central and northern Tibet while the phase does propagate along the Himalayan mountain belt (Ni and Barazangi, 1983). This inefficient *Lg* propagation was again attributed to either strong crustal attenuation within Tibet or to waveguide disruption on the southern margin. Rapine et al. (1997) found inefficient *Lg* propagation across most of Tibet, with no *Lg* from western Himalayan events reaching either station WMQ to the north of the Tarim Basin or station LSA within Tibet (LSA did record *Lg* on some paths from events in the eastern Himalayas and eastern Tibet, suggesting internal variations in propagation efficiency within the Plateau).

McNamara et al. (1996) analyzed data recorded at 11 broadband stations in eastern central Tibet, finding that high frequency *Lg* is generated by events within the Plateau, and can propagate to distances of at least 600 km; however, the phase was not observed for paths traversing western or central Tibet or for events in the Himalayas. For eastern Tibet, where sufficient *Lg* signal to noise ratios were observed, a frequency-dependent Q function given by $Q(f) = (366–37)f^{(0.45–0.06)}$ was estimated for the passband (0.5-16 Hz) (McNamara et al., 1996). This is comparable to the estimate of $Q(f)=(448–82)f^{(0.426–0.157)}$ estimated for 1-6 s *Lg* waves traversing Tibet by Shih et al. (1994). This latter value is likely also dominated by eastern Tibet paths, as 'blocked' observations were omitted from the calculation. Similar Q_{Lg} value was also estimated to be 340 for events north of LSA using spectral methods by assuming a constant Q_{Lg} model (Reese et al., 1999). These attenuation values are typical of tectonically active areas, and are not low enough to cause rapid extinction of 1 Hz *Lg* over just a few hundred kilometers, as observed for paths traversing the northern margin of Tibet. One could then infer that waveguide disruption must cause extinction of *Lg* in the latter regions; however, this is not a secure interpretation because Q_{Lg} may vary laterally within Tibet. Indeed one might expect this to be the case, for it is true of *Sn* attenuation, which is strongest in northern central Tibet. The possibility of stronger *Lg* attenuation in northern and central Tibet is suggested by the lack of high frequency *Lg* detections for events to the west of the broadband stations in the data set of McNamara et al. (1996).

Our presentation resolves this issue, demonstrating the presence of very strong attenuation in the region of north-central Tibet, an area where other work has demonstrated the presence of partial melt in the crust. We also find average *QLg* values for the Plateau of about 150, much lower than proposed in earlier work.

RESEARCH ACCOMPLISHED

Our main data are regional waveforms recorded at broadband station WMQ, the westernmost station of the Chinese Digital Seismic Network. This station lies just north of the Tarim Basin, about 650 km from the northern boundary of the Tibetan Plateau (Figure 1). While three-component data were obtained, we restrict our analysis to the vertical component seismograms due to the attenuated nature of the *Lg* phases traversing Tibet, which leads to confusion with fundamental mode Love wave energy on the transverse components. We examine energy in the standard *Lg* group velocity window of 3.6 to 3.0 km/s, which precedes short and intermediate period fundamental mode Rayleigh wave energy. We analyze recordings for 90 earthquakes with magnitudes of $4.4 \le m_b \le 6.4$ that occurred between 1987 and 1999 in the Tibetan Plateau and around its margins. A few events with paths well removed from Tibet (Figure 1) were also analyzed.

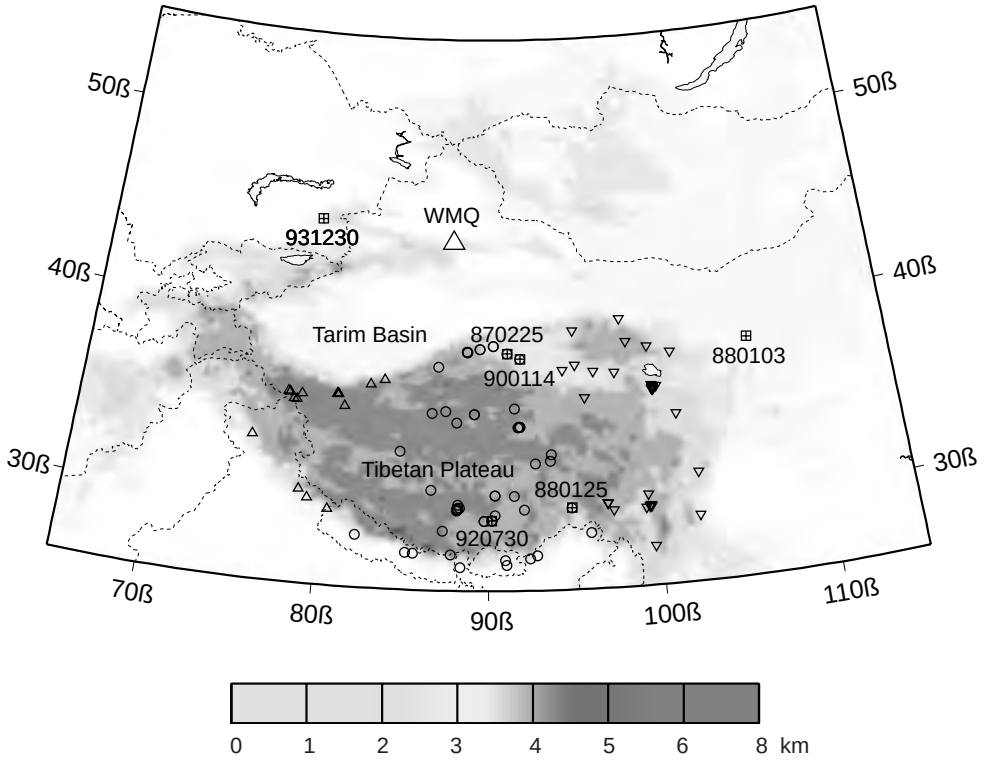

Figure 1. Topography in Western China and its vicinity. The location of station WMQ is shown. The squares, circles, triangles, and inverted triangles indicate the epicenters of the events for which spectra are shown. The events within Tibet are grouped into eastern (inverted triangles), central (circles) and western (triangles) groups.

The recorded seismograms show great variability in broadband waveforms, and our analysis is constrained to qualitative relative measures because we use only one station and cannot fully account for source effects. For events prior to 1998 the source parameters are taken from the International Seismological Centre (ISC) bulletin. For more recent events the source parameters are from the USGS Preliminary Determination of Epicenters (PDE) catalog. Only events with catalog focal depths less than 50 km are included. While catalog source depths in this region are subject to tens of kilometers of uncertainty, this criterion probably ensures that all events analyzed are crustal events, given that the crustal thickness in the central Tibetan Plateau is about 65 to 75 km. All selected events have signal-to-noise ratios greater than 2 for broadband measurements of the *Pn* signal and pre-*Pn* noise.

Figure 2 demonstrates the predominant feature of high frequency *Lg* propagation across the northern Tibetan Plateau boundary first documented by Ruzaikin et al. (1977). The records shown are for a roughly northwest to southeast profile of events, with the signals filtered in the bandpass 1.0-5.0 Hz. The first three records are for events located near the 4000 m topographic contour along the northern boundary of the Plateau. These show typical earthquake-like high frequency signals, with predominant *Lg* energy that is much stronger than the *Pn* arrivals. The lower two records are from events 250-400 km further to the southeast, and the maximum relative amplitude ratio of *Lg* to *P* energy is about a factor of ten lower than for the northwestern events, giving these signals explosion-like character. The distribution of events in Tibet (Figure 1) presents a challenge in that there is not a continuous distribution of events from the Plateau margin to the interior; this makes it difficult to separate possible waveguide disruption effects from strong crustal attenuation effects as causes for the high frequency *Lg* energy blockage. However; we can consider behavior of *Lg* at lower frequency on longer profiles to assess the role of attenuation in the Plateau, as this should be manifested in a progressive shift of the frequency content of *Lg* with propagation length across the Plateau as suggested by Molnar (Ruzaikin et al., 1977).

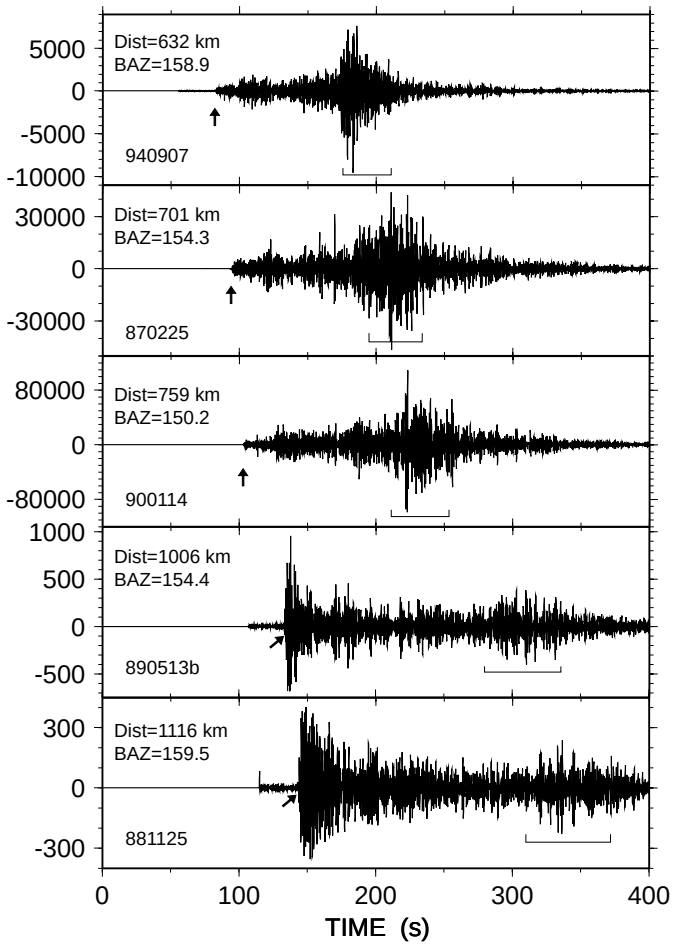

Figure 2. Demonstration of the rapid decrease of Lg energy near the northern Tibetan Plateau boundary. WMQ records are shown for a short NW-SE profile of events, with bandpass filters isolating the 1.0-5.0 Hz passband, for events near the northern boundary (top 3 records) and a few hundred kilometers into the Plateau (lower 2 records). The Lg group velocity window is indicated by the bracket below each seismogram. Small arrows represent the Pn arrivals after the onset of visible signal in each trace. There is about a factor of 10 decrease in the Lg/Pn amplitude ratio common to all events several hundred kilometers south of the Plateau boundary.

Figure 3 shows a longer profile of records, retaining the full broadband energy with amplitudes normalized relative to the 20 s Rayleigh wave energy in each signal. The dramatic shift of frequency content in the *Lg* group velocity window over the first few hundred kilometers is again apparent, but now it is apparent that there is also a progressive shift of frequency content and decrease of relative amplitudes in the *Lg* window for lower frequencies as path length across the Plateau increases.

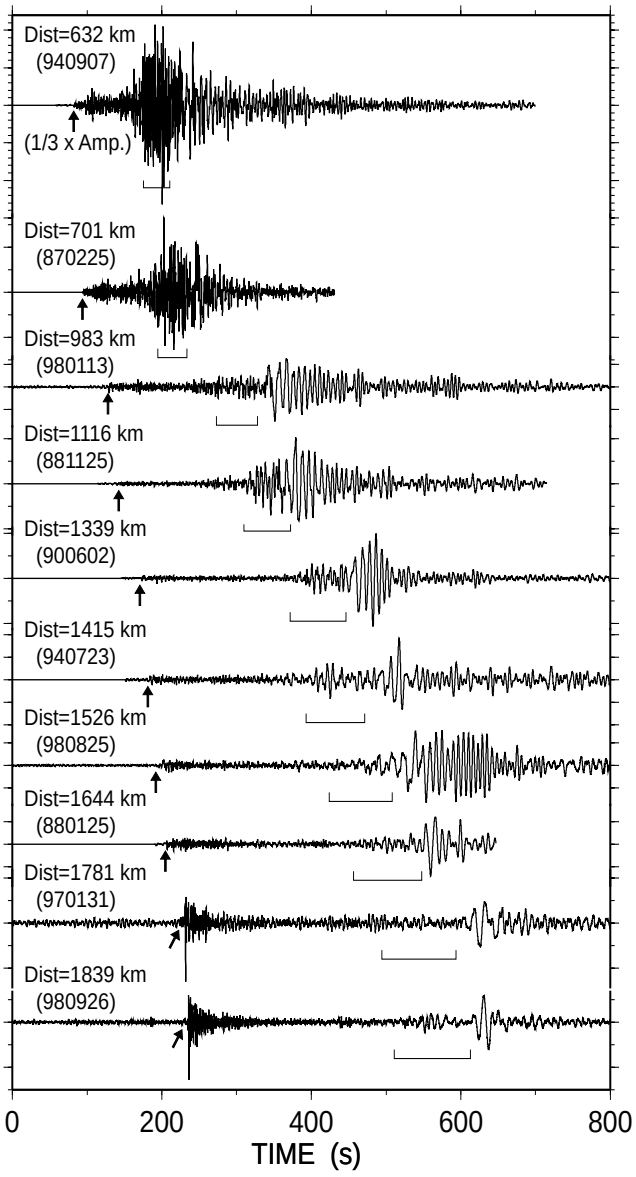

Figure 3. Broadband recordings at WMQ for events traversing the entire central portion of the Plateau. Each record has been amplitude-normalized relative to the 20 s Rayleigh wave energy.

We lack detailed knowledge of the source process and radiation effects for our events, and the station coverage is not adequate to enable empirical separation of source and propagation effects. However, our broadband digital data indicate that propagation effects dominate in shaping the *Lg* window.

Determination of *Lg* Attenuation

Our observations of *Lg* spectral content shifting to lower frequency with increased path length in Tibet demonstrate a strong, progressive *Lg* attenuation in the crust beneath the Plateau. Using a modified two-event method, we estimate *Lg* attenuation coefficient $\gamma(f)$ for the paths crossing several sectors of Tibet. Some constraints are placed on regional heterogeneity of *Lg* attenuation. The displacement spectral amplitude of the *Lg* wave arriving from a source at a distance *d* can be expressed in the form

$$A(f, d) = S(f)R(f, q)G(d)G(f, q)I(f)SS(f), \quad (1)$$

where *f* denotes the frequency, *q* the station azimuth, *S(f)* is the source excitation function, *R(f, q)* is the source radiation pattern, *G(d)* is the *Lg* geometrical spreading function, *I(f)* is the instrument response, *SS(f)* is the station site response, *G(f, q)* is anelastic attenuation function which can be written by

$$G(f, q) = e^{-\gamma d} \quad (2)$$

where γ is the attenuation coefficient, which is related to the quality factor Q and the group velocity U as

$$\gamma = (pf)/(QU). \quad (3)$$

Assuming two events lie within a few degrees of the great-circle path connecting the receiver and the two epicenters, we obtain the ratio of *Lg* wave spectral amplitude for event 2 (the distant event) to that for event 1 (the nearer event) as

$$A(f, d_2)/A(f, d_1) = [S_2(f)/S_1(f)][G(d_2)/G(d_1)]\exp[-\gamma\Delta], \quad (4)$$

Where the indices 1 and 2 represent event 1 and event 2, respectively, and Δ is the distance between the two events. Note that the source radiation pattern $R(f, \theta)$ does not show up in (4) because source radiation and is assumed to be azimuthally independent to first order in *Lg* signals (Sereno, 1990; Shih et al., 1994). The site amplification term canvels out for small difference in back azimuth. For geometrical spreading function *G(d)*, we adopted $G(d) = d^{-0.5}$ for *Lg* wave in the frequency domain (Shin and Herrmann, 1987). To solve for the attenuation coefficient , we need to estimate the effects of the source excitation term *S(f)*, which can be represented by the ω^{-2} model as

$$S(f) = S_0/(1+f^2/f_c^2), \quad (5)$$

where S_o is a constant for a given event, and f_c is the corner frequency. The corner frequency f_c is related to the stress drop, $\Delta\sigma$, the shear wave velocity at the source, υ_β, and the seismic moment of the event, M_0 (Brune, 1970). If the difference in f_c for the two events is small, then, as a first order approximation, (5) can be simply reduced to $S(f) \cong S_0$. One can assume constant stress drop and scale corner frequency with moment, but this is rather arbitrary given observed scatter in measured stress drops. Since our spectral ratios are bandwidth limited by low *Q* values, we ignore small high frequency corrections and restrict our analysis to frequencies below 0.5-1.0 Hz. Thus, we can rewrite (4) as

$$A(f, d_2)/A(f, d_1) = [S_{02}/S_{01}][d_2/d_1]^{-0.5}\exp[-\gamma\Delta], \quad (6)$$

and solve for the attenuation coefficient $\gamma(f)$. Our simplified source correction is approximately equivalent to shifting the spectral ratio to a zero base line for its low-frequency limit. We found that use of the seismic moments from the Harvard CMT solutions provided spectral ratios with small scatter for different event pairs with about the same magnitudes. Because not all of the events studied have Harvard CMT solutions available, we first constructed a reference spectral ratio curve by averaging all spectral ratios after source corrections. Other spectral ratios were shifted relative to the reference spectral ratio by correlating over the frequency band of 0.2-0.5 Hz. Finally, a stacked average is calculated from all spectral ratios for all event pairs to provide a representative *Lg* attenuation, $\gamma(f)$, along a profile.

We constructed four profiles approximately in the north-south direction. Figure 4 shows the locations of selected events used for estimating *Lg* attenuation. The first three profile are positioned in the western, central, and eastern parts of the Tibetan Plateau, respectively, with events near the southern and northern margins and the associated paths crossing the Plateau. The fourth profile covers a relatively small area in the central part of northern Tibet, where strong *Lg* attenuation was observed. In order to approximate great circle paths, only events with back azimuths within 30 degrees are used in calculating $\gamma(f)$. The number of events used for each profile is 4x3, 7x8, 4x7, and 5x6, respectively, where the first number represents the number of events in the north and the second is the number of events in the south. The reference *Lg* attenuation curves were usually the average of many event pairs. 15 event pairs were used for profiles II and III, and 8 event pairs for profile IV. For profile I, the reference *Lg* attenuation curve was calculated using only three event pairs, and is less reliable. The spectral ratios are calculated out only to 1 Hz, given the low signal-to-noise ratio at higher frequencies.

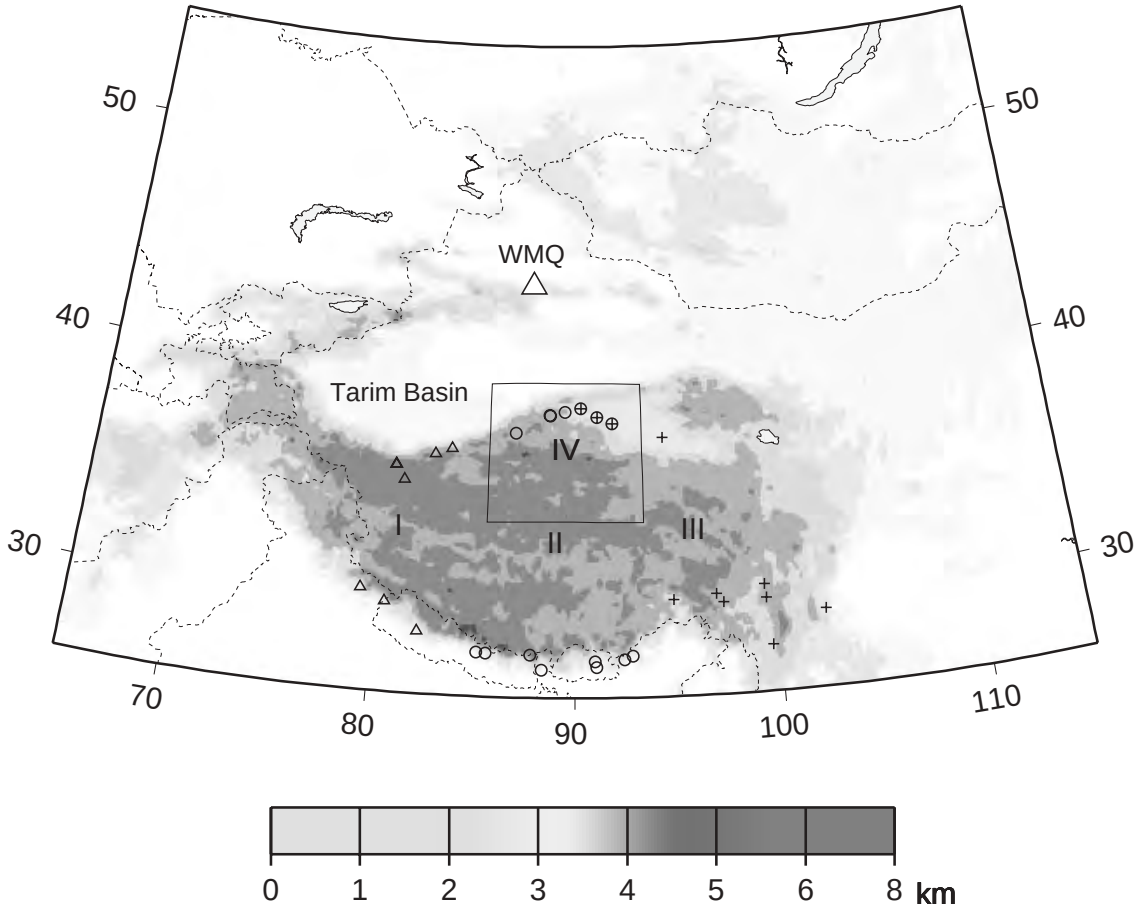

Figure 4. Map indicating the corridors for which 2-station estimates of Lg attenuation are made. The events are either on the northern or southern margin of the Plateau, or for the case of corridor IV, the northern and central Plateau.

The *Lg* attenuation coefficients γ(f) for each profile show clear frequency dependence across the band of 0.1-1.0 Hz. Scatter in the 0.2-0.5 Hz band was minimized by our processing. The largest scatter is observed for profile IV. In general, the *Lg* attenuation γ(f) increases with frequency up to about 1Hz for profiles I, II, and III and up to about 2 Hz for profile IV, then it gradually drops off. This drop off may be caused in part by lack of high frequency source corrections, but mainly is due to high frequency *Sn* coda in the *Lg* window at large distances. The rate of increase in *Lg* attenuation γ(f) is not a constant function of frequency and differs for each profile. The highest attenuation and the best linearity for LOG[γ(f)] of *Lg* are observed in profile IV, where rapid attenuation is observed across a short distance range.

Assuming a power-law frequency dependent model, *Lg* attenuation can be written in terms of quality factor Q_{Lg} as

$$Q_{Lg}(f) = Q_0 f^{\eta}, \qquad (7)$$

where Q_0 is the value of Q_{Lg} at 1 Hz, and η is the power-law frequency dependence. Based on equations (3) and (7), we fit a Q_{Lg}(f) model to observed γ(f) to estimate the value of *Lg* attenuation in various areas of the Tibetan Plateau. The logarithmic *Lg* attenuation coefficients γ(f) are fit to a Q_{Lg}(f) model by least-squares linear regression in two frequency bands, 0.2-0.5 Hz and 0.2-1.0 Hz, for each profile. Figures 5a-d show our results. The numerical values of the best-fit model parameters *Lg* Q_0 and η are listed in Table 1. Previous research on *Lg* attenuation in Asia indicates that η is very sensitive to lateral heterogeneity in the

Table 1. The values of *Lg* attenuation in different parts of Tibet.

		Profile I	Profile II	Profile III	Profile IV
0.2-0.5 Hz	Q_o	146±20	149±14	122±20	90±10
	η	0.67±0.12	0.20±0.09	-0.19±0.15	0.15±0.10
0.2-1.0 Hz	Q_o	160±5	224±9	195±14	85±2
	η	0.75±0.04	0.58±0.06	0.24±0.08	0.10±0.04

crust, thus reliable η estimates are difficult to obtain [Shih et. al., 1994], so we limit our discussion mainly to the quality factor Q_0.

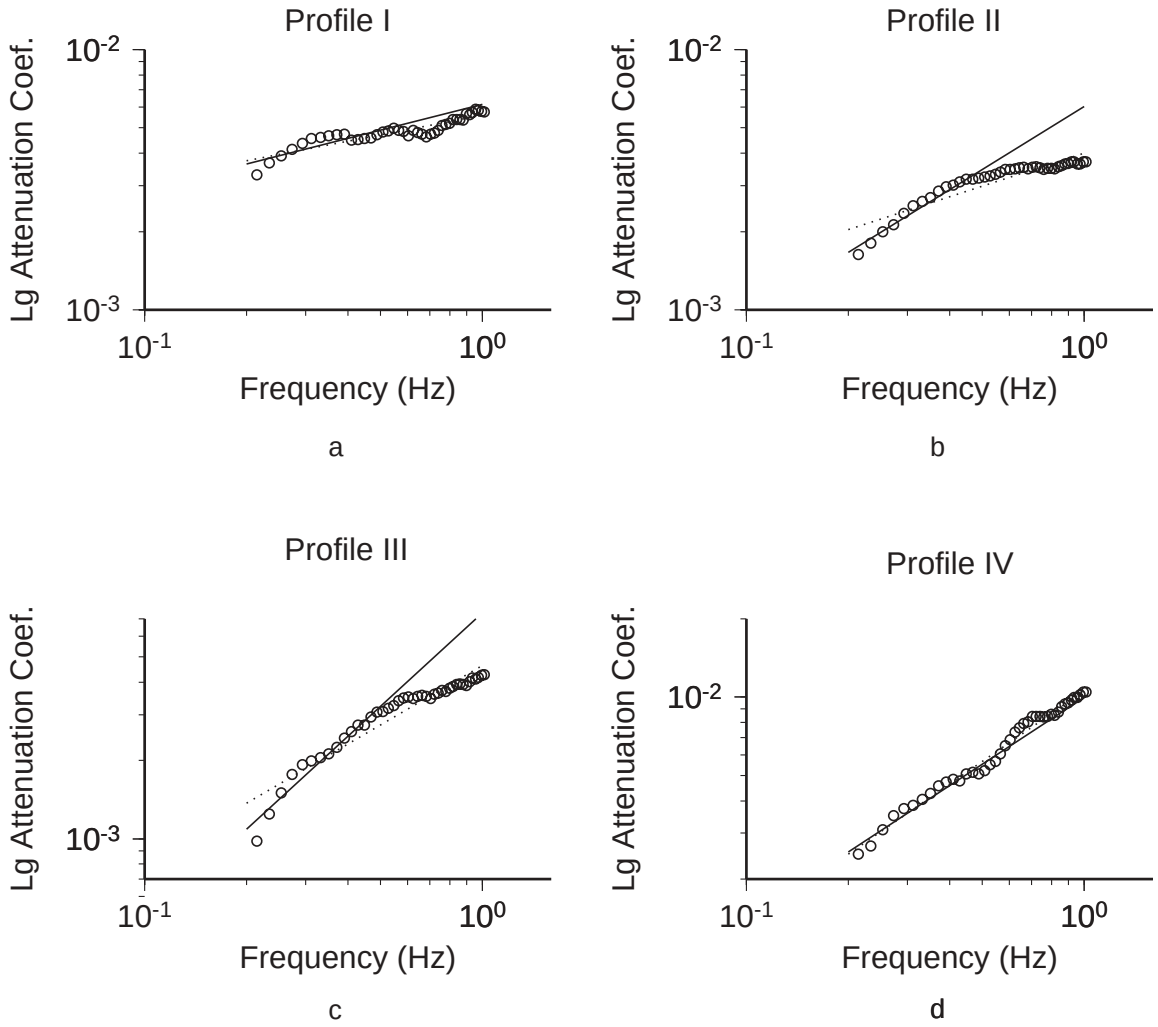

Figure 5. Lg attenuation coefficient *g(f)* and the best fit Q_{Lg} models (straight lines) for each profile. Circles are mean values estimated from stacking multiple spectral ratios in each profile. Solid and dashed lines represent the best fit Q_{Lg} models in frequency bands of 0.2-0.5 Hz and 0.2-1.0 Hz, respectively.

We found that Q_0 values differ for each profile. There is little difference in Q_0 for profile IV between the two best-fit models because the logarithmic spectra are very linear. However, there are variations in the Q_0 estimates for the other profiles between the 0.2-0.5 Hz and 0.2-1.0 Hz bands. Profiles II and III show a reduced slope in logarithmic γ(f) commencing at about 0.5 Hz. Thus, broader band estimates give higher Q_0 values. We believe that this is likely due to contamination at higher frequencies (above 0.5 Hz) by increased contribution of high frequency *Sn* coda rather than true *Lg* signals. The Q_0 value of *Lg* for the Tibetan Plateau as a whole is in a

range of about 120-150 for the 0.2-0.5 Hz band, and in a range of 160-230 for the 0.2-1.0 Hz band based on the results for profiles I, II and III. Our observations indicate that a region in northern central Tibet close to the Plateau margin is characterized by very strong *Lg* attenuation, with a Q_0 value of 85-90. This is consistent with observed high frequency amplitude decay by a factor of ten or more in that region (see Figure 2).

CONCLUSIONS AND RECOMMENDATIONS

The Tibetan Plateau appears to have very strong attenuation of *Lg* phases for paths within and traversing the northern boundary of the Plateau. This is demonstrated by the broadband spectral behavior of *Lg*, which undergoes a systematic shift of apparent corner frequency from 2 to 0.2 Hz as a function of path length. The *Lg* attenuation estimates obtained here are much lower than those in the literature, most of which are for eastern Tibet. Recently, Xie (2001) has reanalyzed the *Lg* spectra data used by McNamara et al. (1996), obtaining a Q_{Lg} model with $Q_0 = (126\pm9)$ and $\eta = (0.37\pm0.02)$, which is very consistent with our estimates in profiles II and III, where the data overlap. Xie s estimate is for the 0.2-3.6 Hz band, with the extension to higher frequency being viable due to the short path lengths involved. This extrapolates smoothly up from our 0.2-0.5 Hz band prior to the decrease in slope of LOG[γ(f)]. Phillips et al. (2000) obtain tomographic models of Q_{Lg} with values of 200 in Tibet south of the Qaidam and Tarim basins. Their results give $Q = 500$ for the Tarim Basin, compatible with our observation of efficient propagation there. Their coverage of western Tibet is very limited due to constraining the data to 0.75-1.5 Hz, which is strongly attenuated over longer paths in Tibet.

We resolve a region in northernmost Tibet with much lower Q than previously reported by any study of Tibet. Figure 6 summarizes our Q estimates, illustrating the localized region with Q values of 85-90. Profile II gives overall Q values of 149 for the 0.2-0.5 Hz band, which requires that Q increase in southern central Tibet to a value of 265 or higher for a northern Q of 90. Phillips et al. (2000) also indicate such an increase in Q from north to south, but they have high values approaching 500 near LSA, which is consistent with Q value of 85 in the northern part of Tibet.

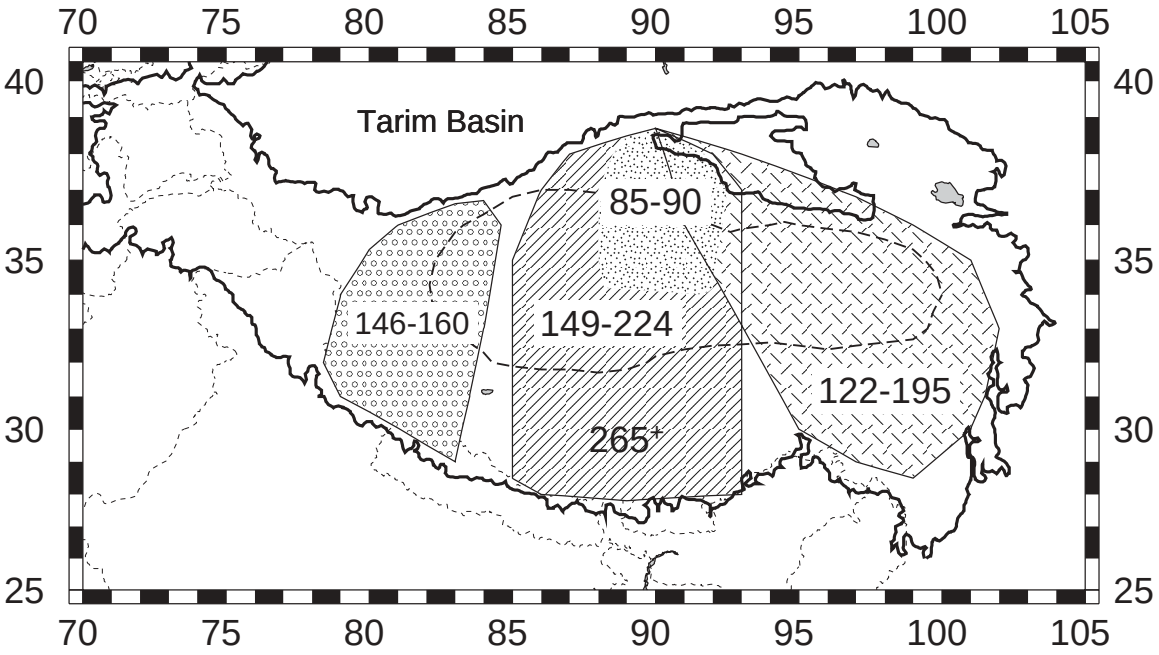

Figure 6. Summary map indicating Qo values for different corridors. The lower values are preferred.

Our values of Q_{Lg} of 100-200 are found in other tectonically active areas, such as California (Herrman, 1980; Nuttli, 1986) and Iran (Nuttli, 1980). In general, the mechanisms of intrinsic attenuation are very sensitive to temperature conditions, and the very low Q_{Lg} of 85-90 may be associated with partial melting in northern Tibet. Owens and Zandt (1997) presented evidence for a lower crustal low-velocity zone likely to involve partial melt

in northern Tibet. This region has inefficient *Sn* propagation (Ni and Barazangi, 1983; McNamara et al., 1995), low *Pn* velocity (McNamara et al., 1997), and high Poisson s ratios of 0.34-0.35 over a 30 km thickness (Owens and Zandt, 1997). Figure 7 shows a north-south profile through Tibet adapted from Owens and Zandt (1997), indicating the coincidence of the partial melt zone in the deep

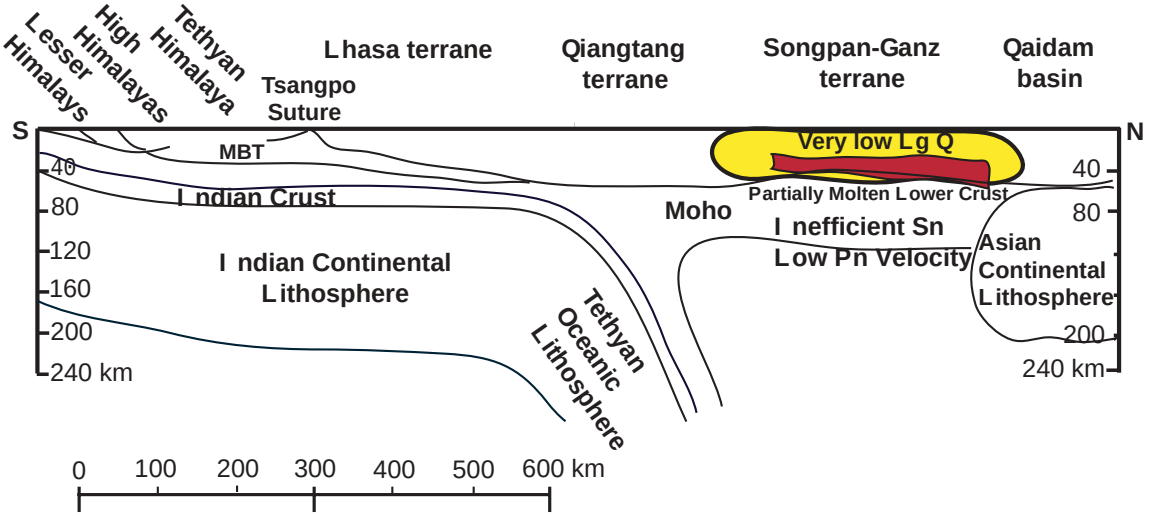

Figure 7. Cross-section through Tibet indicating the coincidence of the region of very low Q_{Lg} and partial melt in the crust, as well as Sn inefficiency and low Pn Velocity.

crust of northern Tibet and the region of low *Lg Q*. Further analysis is required to constrain the spatial extent of the very low *Q* region affecting *Lg*, but it is clear that Tibet can not be viewed as a region with uniform *Lg* attenuation, nor as a region with extensive *Lg* attenuation values in the range of 340-450 as previously indicated. There is some evidence for partial melt and crustal low-velocity zones existing north of the Tsangpo suture in southern Tibet (Nelson et al., 1996; Kind et al., 1996; Cotte et al., 1999). This low-velocity zone may also relate to a localized low Q_{Lg} region, however, it is not yet resolved by our data set due to lack of resolution in southern Tibet.

REFERENCES

Brune, J. N. (1970), Tectonic stress and the spectra of seismic shear waves from earthquake sources, *J. Geophys. Res., 84*, 2262-2272.

Cotte, N., H. Pedersen, M. Campillo, J. Mars, J.F. Ni, R. Kind, E. Sandvol., and W. Zhao (1999), Determination of the crustal structure in southern Tibet by dispersion and amplitude analysis of Rayleigh waves, *Geophys. J. Int*., *138*, 809-819.

Herrmann, R. B. (1980), Q estimates using the coda of local earthquakes, *Bull. Seism. Soc. Am*., *70*, 447-468.

Kind, R., et al. (1996), Evidence from earthquake data for a partially molten crustal layer in southern Tibet, *Science*, *274*, 1652-1654.

McNamara, T. J. Owens, and W. R. Walter (1995), Observations of regional phase propagation across the Tibetan Plateau, *J. Geophys. Res., 100*, 22215-22229.

McNamara, W. R. Walter, T. J. Owens, and C. J. Ammon (1997), Upper mantle velocity structure beneath the Tibetan Plateau from Pn travel time tomography, *J. Geophys. Res., 102*, 493-505.

McNamara, D. E., T. J. Owens, and W. R. Walter (1996), Propagation characteristics of L_g across the Tibetan plateau, *Bull. Seism. Soc. Am*., *86*, 457-469.

Nelson, K. D., et al. (1996), Partially molten middle crust beneath southern Tibet: Synthesis of project INDEPTH results, *Science*, *274*, 1684-1688.

Ni, J. and M. Barazangi (1983), High-frequency seismic wave propagation beneath the Indian Shield, Himalayan Arc, Tibetan Plateau and surrounding regions: high uppermost mantle velocities and efficient S_n propagation beneath Tibet, *Geophys. J. R. astr. Soc.*, *72*, 665-689.

Nuttli, O. W. (1980), The excitation and attenuation of crustal seismic phases in Iran, *Bull. Seism. Soc. Am*., *70*, 469-485.

Nuttli, O. W. (1986), Yield estimates of Nevada test site explosions obtained from seismic *Lg* waves, *J. Geophys. Res., 91*, 2137-2152.

Owens, T. J. and G. Zandt (1997), Implications of crustal property variations for models of Tibetan plateau evolution, *Nature, 387*, 37-43.

Phillips, W. S., H. E. Hartse, S. R. Taylor, and G. E. Randall (2000), 1 Hz *Lg* Q tomography in central Asia, *Geophys. Res. Let*., *27*, 3425-3428.

Rapine, R. R., J. F. Ni, and T. M. Hearn (1997), Regional wave propagation in China and its surrounding regions, *Bull. Seism. Soc. Am*., *87*, 1622-1636.

Reese, C. C., Rapine, R. R., and J. F. Ni (1999), Lateral variation of Pn and Lg attenuation at the CDSN station LSA, *Bull. Seism. Soc. Am*., *89*, 325-330.

Ruzaikin, A. I., L. Nersesov, V. I. Khalturin, and P. Molnar (1977), Propagation of *Lg* and lateral variations in crustal structure in Asia, *J. Geophys. Res*., *82*, 307-316.

Sereno, T.J., S. Bratt, and T. Bache (1990), Frequency-dependent attenuation in eastern Kazakhstan and implications for seismic detection thresholds in the Soviet Union, *Bull. Seism. Soc. Am*., *80*, 2089-2105.

Shih, X. R., K.-Y. Chun, and T. Zhu (1994), Attenuation of 1-6 s *Lg* waves in Eurasia, *J. Geophys. Res*., *99*, 23859-23874.

Shin, T.-C. and R. B. Herrmann (1987), *Lg* attenuation and source studies using 1982 Miramichi data, *Bull. Seism. Soc. Am*., *77*, 384-397.

Xie, J. (2001), *Lg* Q in the Eastern Tibetan Plateau, submitted to *Bull. Seism. Soc. Am*.

NEAR FIELD AND REGIONAL MODELING OF EXPLOSIONS AT THE DEGELEN TEST SITE

J. L. Stevens[1], N. Rimer[1], H. Xu[1], J. R. Murphy[1], G. E. Baker[1]
G. G. Kocharyan[2], B. A. Ivanov[2], and S.M. Day[3]

[1]Science Applications International Corporation
[2]Institute for the Dynamics of the Geospheres
[3] San Diego State University

Sponsored by Defense Threat Reduction Agency

Contract No. DTRA01-00-C-0050

ABSTRACT

The objective of this research program is to improve the capability to predict the seismic source characteristics of underground explosions in rock. This is being accomplished by development of improved dynamic failure models that are constrained by a large unique data set of near-field waveforms and parametric data from both U.S. tests and historic Soviet explosions at the Degelen Test Site. In addition, we are analyzing regional seismic data along a seismic line located north of the Degelen Test Site that recorded data at 9 stations spaced approximately evenly from the test site to a distance of about 100 km. This project is a collaborative effort between SAIC and the Russian Institute for the Dynamics of the Geospheres (IDG).

IDG is in the process of digitizing data from 25 nuclear tests at Degelen. The complete data set consists of 81 near-field waveforms recorded underground at shot depth and 124 near-regional seismic records. Most seismic records include both a vertical and radial waveform. This data set provides a rare opportunity to observe and model the seismic wavefield of the explosions as they evolve from the near field of the explosion out to regional distances. To date, IDG has digitized 27 near-field waveforms and 122 seismic waveforms. We are in the process of defining the optimum procedures to model this data. The goal is to develop material models that are consistent with the data and have a realistic physical basis. Work to date at SAIC has focused on implementation and testing of improved numerical modeling procedures and simulation of near-regional data. We are testing acoustic fluidization as a physical mechanism for strength reduction in nonlinear explosion simulations. Near regional data is being modeled using wave number integration. We are also comparing the Degelen data with similar data from NTS explosions. The near-field Degelen data received to date is lower in amplitude than would be predicted based on NTS experience. Although both the NTS explosions being reviewed and the Degelen explosions were in granite, the material properties of the rock are significantly different. The most significant difference is higher porosity in the Degelen granite. The data set of near-field and regional waveforms will be delivered to the Center for Monitoring Research upon completion of this project.

KEY WORDS: rock mechanics, Degelen, explosion, numerical modeling

OBJECTIVE

The main objective of this research program is to improve the capability to predict the seismic source characteristics of underground explosions in rock. This is being accomplished by development of improved dynamic failure models for hardrock that are constrained by a large unique data set of near-field waveforms and parametric data from both U.S. tests and historic Soviet explosions at the Degelen Test Site. In addition, we are analyzing regional seismic data along a seismic line located north of the Degelen Test Site that recorded data at 9 stations spaced approximately evenly from the test site to a distance of about 100 km. This project is a collaborative effort between SAIC and the Russian Institute for the Dynamics of the Geospheres (IDG).

RESEARCH ACCOMPLISHED

Introduction

Empirical and numerical models of explosion sources do a fairly good job of matching observed seismic signals, but the physical basis for the explosion source is still not well understood. In particular, numerical models of explosion sources developed using laboratory measurements of rock properties predict particle velocity pulse widths that are roughly a factor of 3-5 smaller than those observed near field in hardrock events such as PILEDRIVER. The basic problem is that the strength of the rock measured in the laboratory is much larger than the apparent strength of the rock as determined from the near field ground motion.

A number of solutions to these problems have been proposed over the years, including the effective stress model (Rimer, et al, 1984), and various types of damage models. These models all have the characteristic that the material strength is reduced dynamically to a very low level when the rock fails. The effective stress model says that the weakness comes from water within the rock matrix, and that the broken rock in effect floats on water that is squeezed out of pores or fractures when the rock fails. Although there are questions about the realism of this physical model, it works fairly well to explain the near field waveforms. Figure 1 shows a comparison of the PILEDRIVER waveforms with waveforms calculated using the effective stress model. The agreement is quite good, particularly at the closer two stations. Furthermore, when the PILEDRIVER solution was scaled to the appropriate yield and compared with other US explosions in granite (Hardhat and Shoal), agreement with the observed waveforms was also quite good (Stevens, et al, 1986).

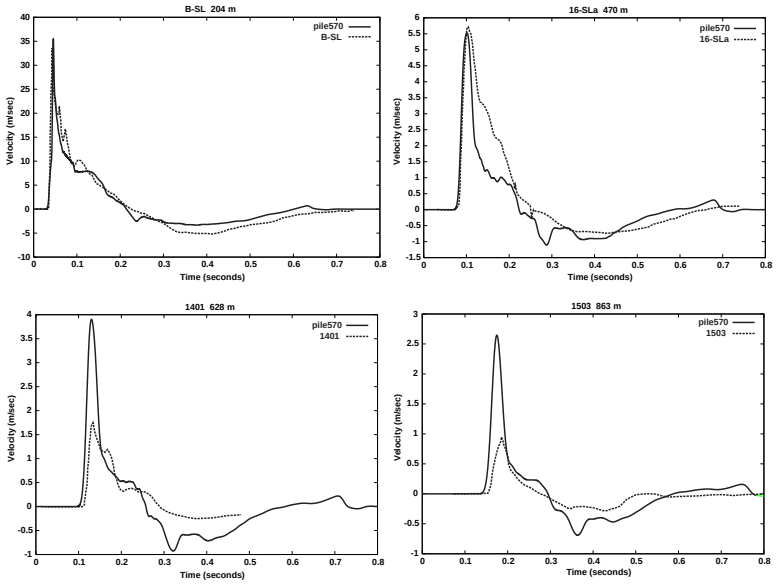

Figure 1. Particle velocity measurements at working point depth from PILEDRIVER compared to numerical simulation pile570 using the effective stress law.

Under a previous DTRA contract, SAIC (at the time Maxwell Technologies) worked together with the IDG and the University of Southern California (USC) to develop improved material models. IDG provided extensive measurements of material properties close to nuclear and chemical explosions both before and after the explosions were detonated (Rimer, et al, 1998). In addition, we implemented the micro-mechanical damage mechanics model for the growth and coalescence of cracks in brittle rocks under compressive loading which was developed by Prof. Charles Sammis of USC into SAIC's nonlinear finite difference codes and then used this model to simulate the observed explosion damage and a small set of near field waveforms that were also provided by IDG. The results of this work are discussed in detail in the final report (Rimer et al, 1999). Since the Sammis damage model does not predict what happens to the rock after unstable brittle failure occurs, the calculations introduced a friction law model post-failure. However, realistic values of friction did not provide enough strength reduction to match the near field data. We were more successful in matching the data by dropping the coefficient of friction to very low values (as low as 0.02) for rubbleized rock, but this again leaves the question of what physical mechanism could be responsible for these very low values and corresponding low strength.

A possible answer initially proposed by Melosh (1979) is "acoustic fluidization". The physics behind this mechanism is that there is a complex dynamic acoustic wavefield that causes high frequency vibrations in the broken rock. These vibrations cause rapidly changing regions of high and low normal stress, and remove the frictional normal stress from parts of the rock as it moves. Consequently parts of the rock are not confined by the frictional stress and in effect have much lower strength. Acoustic fluidization has been used to explain other phenomena such as landslides and craters (Melosh and Ivanov, 1999), which have been similarly difficult to explain because of anomalously low apparent friction. Initial efforts to include acoustic fluidization in our numerical models are described later in this paper.

Degelen Near Field and Near Regional Seismic Data

The numerical modeling component of this project is being constrained by a much better data set than has been available in the past. Near field waveforms are only available from a small number of U.S. nuclear tests, and until recently, none have been available from the testing program of the former Soviet Union. IDG has near field records from a number of nuclear explosions at the Degelen test site that are being digitized for this project. IDG will also be providing near source material properties measurements from these events. In addition, IDG has data from a seismic line located north of the Degelen test site that was maintained with consistent instrumentation for many years during the Soviet testing program. Figure 2 shows a map illustrating the location of the test sites and the seismic stations.

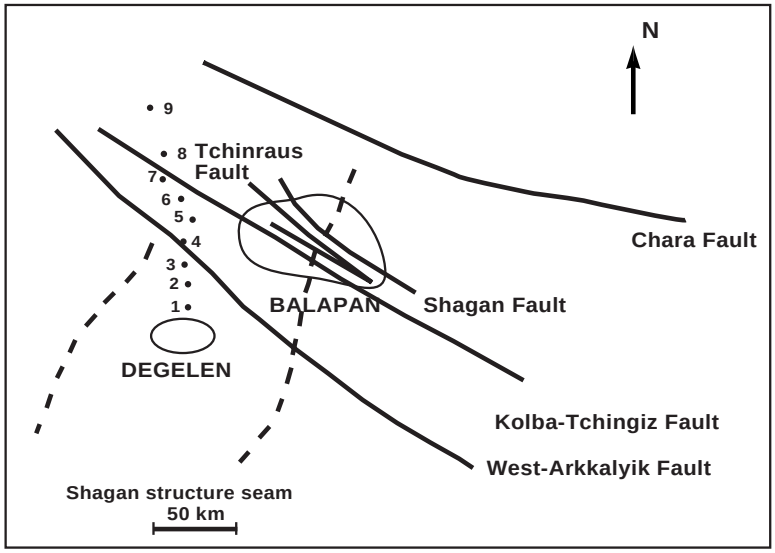

Figure 2. Map showing the locations of the former Soviet Degelen and Balapan test sites, faults, and seismic stations in the region.

The 9 seismic stations are spread out at approximately even intervals from the Degelen test site out to a distance of about 100 km. IDG is also digitizing seismic data from these stations for all of the events that have near field records. This provides a rare opportunity to observe and model the seismic wavefield of the explosions as they evolve from the near field of the explosion out to regional distances. The data that IDG has identified for digitization, and the data digitized as of this writing are listed in Table 1. Figure 3 shows waveforms from one of these explosions.

Table 1. Degelen events with near field and/or seismic records, and waveforms digitized to date. (The total number of digitized records including multiple recordings at some stations, are shown in parentheses. Explosion yield and ISC m_b are shown for events digitized to date.)

Date	Yield (Kt)	m_b	Number of near field records	Waveforms Digitized	Distance range, m	Number of seismic records	Waveforms Digitized	Distance range, km
1988/04/22	2.3	4.9	2	2	69-183	3	3	57-81
1988/11/23	19	5.4	4	3	280-475	9	9	14-83
1987/07/17	78	5.8	14	14	170-900	7	7	14.5-84
1987/10/16	1.1	4.6	4	4	55-132	8	8 (27)	20-76
1989/10/04	1.8	4.7	4	4 (5)	45-285	8	8 (24)	16-85
1981/07/17	9.3	5.1	3	3	115-310	8	8 (27)	15-80
1965/02/04	.001-20	-	4	4	147-750	9	peaks	14-83
1964/05/16	20-150	6.2	4	4	150-600	9	peaks	13-80
1966/03/20			4		300-600	9		15-84
1966/02/13			4		350-600	9		14-80
1973/12/31			4		110-230			
1974/12/16			4		100-200			
1978/03/26			5		76-270			
1980/06/25			3		155-310			
1982/12/25			4		90-190			
1984/10/18			4		35-110			
1968/07/12			2		80-90			
1968/12/18			3		200-510			
1970/06/28			2		200-240			
1980/09/25			3		100-160			
1971/12/15						9		7.5-85
1987/05/06						9		13-83
1987/12/20						9		13-83
1988/10/18						9		11-77
1989/02/17						9		10-77

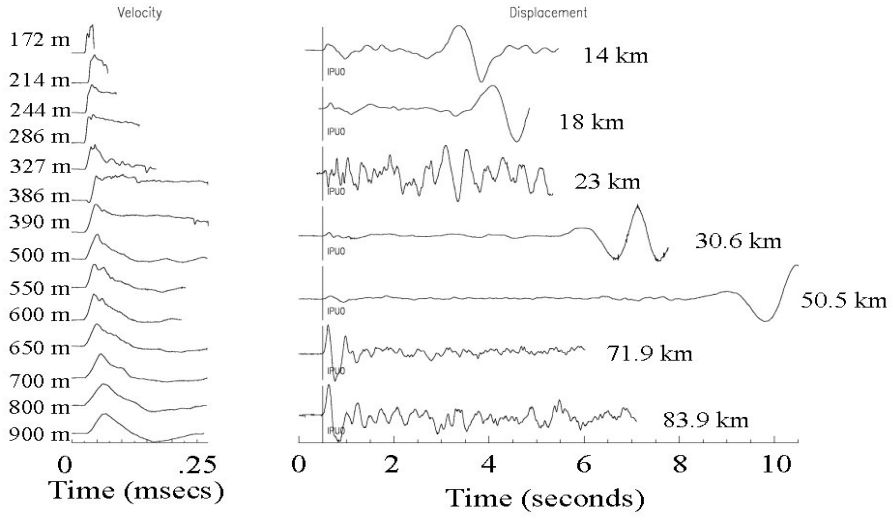

Figure 3. Near-field (left) and near regional seismic (right) waveforms from the 1987/07/17 event.

The near field records in Figure 3 show the evolution of the waveform from the nonlinear to linear regions. Unfortunately, the absolute times are not known for the records. The near regional records show the evolution of the waveform from 14 to 83 km. A strong Rg phase is present in several seismograms that persists to quite a long distance. Some of the records end before the start of the Rg phase and therefore do

not show it. Figure 4 shows a comparison of synthetic and observed seismograms for three of the near regional waveforms from the 1987/07/17 event. The synthetic seismograms were constructed using wavenumber integration (Luco and Apsel, 1983) using the East Kazakh structure from Stevens (1986). The synthetic seismograms were low-pass filtered at 2 Hz. The persistence of Rg calls into question the explanation of Rg scattering as the source of Lg since that mechanism requires most of Rg to scatter into Lg within a few kilometers of the source.

Figure 5 shows a comparison between peak velocity measurements from the first three explosions listed in Table 1 and peak velocity measurements from other explosions in granite. The Degelen velocities are near the lower bound of the other velocity measurements.

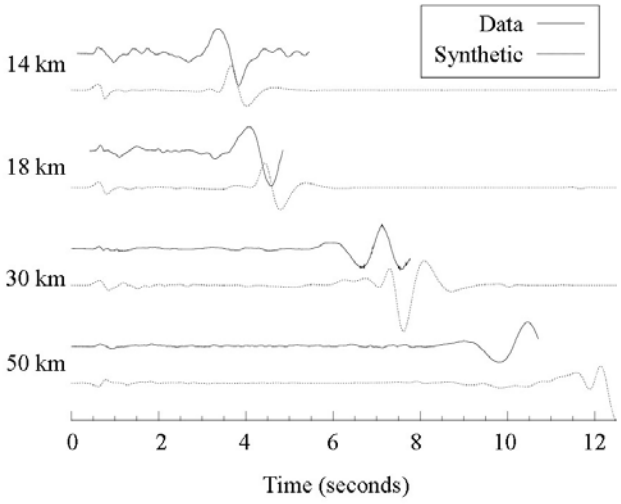

Figure 4. Synthetic and observed seismograms for the 1987/07/17 event. Synthetics were created using wavenumber integration and were low pass filtered at 2 Hz.

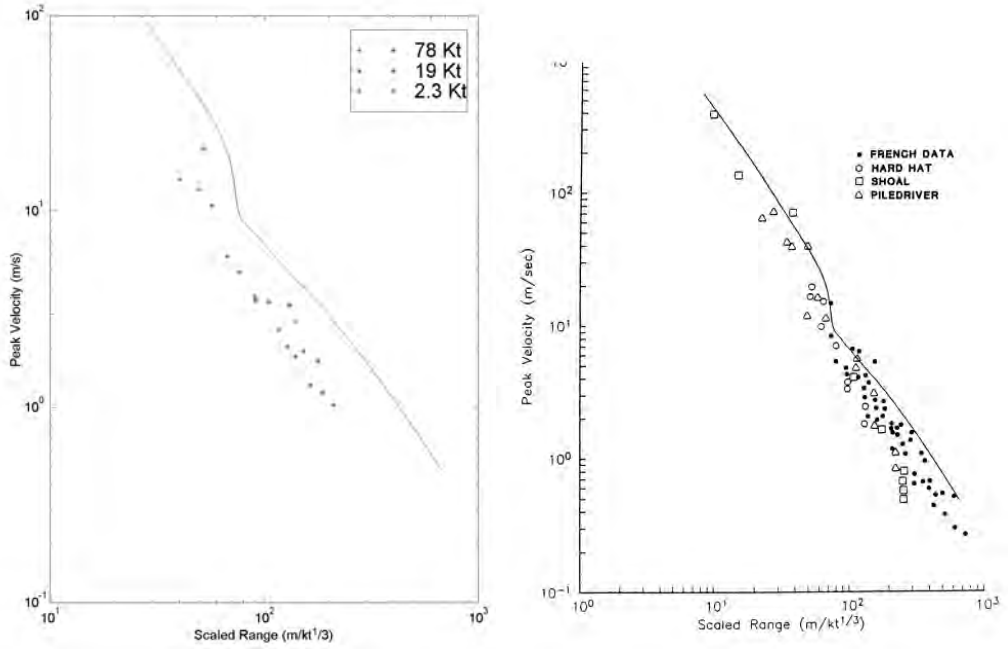

Figure 5. Peak velocity vs. scaled range for the first three Degelen explosions (left) and for historic data from U.S. and French explosions. The solid line is the prediction from the PILEDRIVER simulation discussed in the next section and shown earlier in Figure 1. The Degelen velocities are near the lower bound of the historic data set.

Numerical Modeling of Explosions

The parameters used in numerical simulations of underground nuclear explosions are constrained by laboratory material properties tests and by direct observations of ground motion from underground explosions. Laboratory measurements of strength for brittle hardrocks seem to be very inconsistent with *insitu* strength as inferred by modeling of underground explosions. In particular, finite difference calculations of ground motion in granite, made using the laboratory measurements of shear strength, have invariably given much narrower particle velocity pulses and much smaller displacements than those measured in the field. Constitutive models have been developed (Rimer and Lie, 1982, Rimer, et al., 1984) which attribute this weaker behavior of *insitu* granite and other rocks under explosive loading to ground-motion-induced rock damage or pore fluid pressure increases. Comparisons have already been made in Figure 1 between the particle velocity measurements at working point depth from the 62 kt PILEDRIVER event and the results of the pile570 numerical simulation, made using the effective stress model discussed in Rimer, et al (1984). Numerical results from pile570 are also in good agreement with the measured cavity radius and with the estimated seismic source function given in Table 2.

Table 2. United States Explosions in Granite

Explosion	Yield (kT)	Measured Cavity Radius (m)	Calculated (570) Cavity Radius (m)
PILEDRIVER	62.0	40.1/44.5	42.5
HARDHAT	5.9	19.4	19.4
SHOAL	12.5	26.8	24.9

For this simulation, effective stress model parameters were calibrated to best match the velocity peak and pulse shape at the closest-in gauge station (B-SL). This required a rapid buildup of pore pressure during the loading, leading to a large strength reduction very near the propagating shock front. Note that the pulse shapes at all four stations are rather consistent, with all including a long duration shallow negative velocity pulse. The peak velocities at the two smallest ranges agree very well with the simulation, but the measured peaks at the two larger ranges are a factor of two or more lower than the calculated peaks. The two closest PILEDRIVER gauges were located along roughly a 180 degree different azimuth than the other more distant gauges. However, a connection between possible site anisotropies and the measured ground motions has never been established. It should be noted that the 5.9 kt HARDHAT event, which was detonated in similar rock, near the later PILEDRIVER event, but at a shallower depth of burial, gave particle velocity pulses that were more similar to the PILEDRIVER pulses at the larger ranges. (See Rimer, Stevens, and Day, 1987, for a comparison between the results of the pile570 simulation and the HARDHAT measurements.)

The constitutive models used in these simulations are phenomenological in nature and do not explicitly account for the dynamic response of the *insitu* fractures in the crystalline rock. The Sammis micro-mechanical damage model for brittle rocks under compressive loading (see Ashby and Sammis, 1990) has been incorporated into our numerical simulation codes. This model introduces a damage parameter, related to the increase in flaw size from its pre-shot average value. Damage accumulates as the flaws extend during the compressive loading and reaches some maximum value at which the rock fails unstably. Since unstable compressive failure of a rock element is calculated using this model to occur relatively early in the dynamic motions of interest here, i.e., usually near the propagating shock front, additional modeling was incorporated to complete the description of the stress field after this failure. Limiting the magnitude of deviatoric stresses in a failed rock element through the use of a standard friction law was shown to not provide sufficient strength reduction to simulate the ground motion measurements. In particular, calculated particle velocity time histories were still much narrower than the measured pulses for all reasonable choices of initial flaw size.

The additional strength reduction required to sufficiently broaden the particle velocity pulses was obtained by using a shear damage model originally developed for soft rocks such as tuff, described in Rimer and Proffer (1991). As discussed in Rimer et al (1999), this shear damage model was applied here only for rock elements that had experienced the onset of unstable compressive failure. Thus, a rock element was allowed to undergo significant damage before application of this treatment. The post-failure shear damage model performs an interpolation between the standard coefficient of friction of 0.60 and much lower “effective

friction" values of 0.02-0.20 in the friction law used to limit deviatoric stresses. This linear interpolation is based on the maximum shear strain experienced by the failed rock element.

A series of calculations were made using the Sammis modeling, quantifying the effect of model parameters on particle velocity pulse shapes, cavity radius, and RDP. Calculated particle velocity pulse widths were sensitive to the choice of shear strain magnitude required for full strength reduction, with lower values of this parameter resulting in longer pulse duration and larger RDP. The simulation which best fits all of the PILEDRIVER ground motion data is Run PD10. Comparisons with measured particle velocities are shown in Figure 6. In contrast with the results of pile570, Figure 1, made with the effective stress model, PD10 provides a much better fit to the PILEDRIVER data at the two larger ranges, while underestimating peak velocities at the closest ranges. Subsequent analyses showed that the timing of the strength reductions for the two models were somewhat different, with the effective stress model providing an earlier reduction than the present damage model. However, calculated cavity radius and RDP with the new model are in as good agreement with the measurements as were those with the effective stress model. It is important to emphasize that while the shear damage model (or some other post-failure strength reduction model) is crucial to successful simulation of the ground motion data, it is the micro-mechanical damage mechanics model that primarily determined the size of the central core of low strength rock around the cavity.

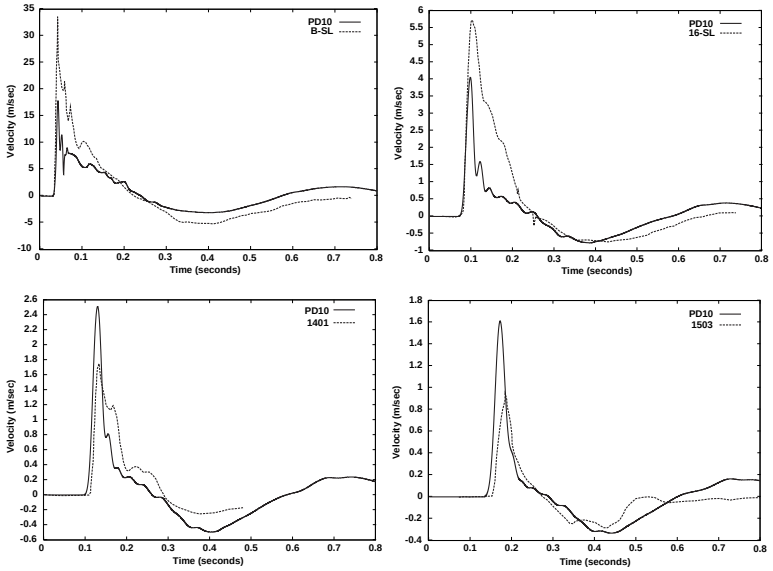

Figure 6. Calculated particle velocity pulses at four ranges for Run PD10 and PILEDRIVER measurements

Acoustic Fluidization

A possible physical mechanism for the strength reduction and very low coefficients of friction discussed in the previous section is the "acoustic fluidization" concept proposed by Melosh (1979) to explain the low strengths (or very low angles of internal friction) apparent in a number of geologic processes, such as seismic faulting, impact crater slumping, and long runout landslides. The main concept of this proposed mechanism is that "sufficiently strong acoustic waves in rock debris can momentarily relieve the static overburden in limited regions of the rock mass, thus allowing sliding to occur in the unloaded region. If this happens frequently enough, flow of the entire rock mass results." In terms of the explosively-induced ground motions of interest here, only the mass of failed or fractured rock would have the potential for acoustic fluidization. The dynamic fracturing process, by itself, provides enough energy to generate sufficiently strong oscillations post-failure to reduce the "effective normal stress/effective friction" to the low values required in the weak core region near the cavity.

We are implementing an approximate representation of acoustic fluidization within our nonlinear finite difference code and have applied it to simulation of PILEDRIVER. Two different schemes are being

implemented, both of which have the following characteristics in common: 1) Acoustic fluidization occurs only after failure has occurred in the cell, and 2) Acoustic fluidization is related to the kinetic energy of each cell. So the basic assumptions of the calculation are that once a cell has failed, it is subject to acoustic fluidization, and that the acoustic fluidization occurs only after the kinetic energy reaches some critical threshold level. The second assumption is not quite right – acoustic fluidization is related to acoustic vibrations within each cell, but it is reasonable to expect these vibrations to be approximately related to the kinetic energy of the cell. We also introduce a decay constant to simulate the decaying acoustic vibrations in each cell that satisfies the equation $\tau \frac{d\theta}{dt} + \theta = \frac{\rho v^2}{2}$

where τ is the decay time, ρ is density, v is particle velocity, and θ is the kinetic energy. Acoustic fluidization occurs if θ exceeds a threshold level in the rubbleized cell. The effect of this equation has been shown in preliminary calculations to: 1) by delaying the onset of θ, smooth the large strength reduction introduced by acoustic fluidization (and to smooth the velocity pulses), and 2) slow the rapid decrease in θ at the end of the step function. An additional modification has been introduced recently to allow the onset and decay times to occur at different rates, since it was found that the equation above causes too long a delay in onset time. In the example below, we discuss only the case for τ=0 which corresponds to an instantaneous onset time and abrupt stoppage of acoustic fluidization. Additional calculations with varying onset and decay rates are currently being conducted.

Implementation 1 – Failure and acoustic fluidization defined by damage model

First-principles implementation of the strong vibrational mode of the acoustic fluidization mechanism is beyond the capabilities of the finite difference continuum code that computes the ground motion. However, we have included some of the observed phenomenological features of the acoustic fluidization mechanism in our computational model. Application is restricted to rock elements that have both previously been reduced to rubble (using the Sammis brittle failure model) and been driven to a sufficiently large kinetic energy. These rock elements are then assigned lower shear strengths through the use of a reduced effective pressure or an increased "acoustic fluidization pressure" in the standard friction law.

We implement this mechanism in terms of the specific kinetic energy density ($\rho v^2/2$) level, called Ek. When this kinetic energy goes above some threshold level, Afonke, acoustic fluidization occurs and the effective pressure consequently drops down. In the finite difference code, the effective pressure field is given by $P_{acf}=P-P_f$, where P is pressure and P_f is the acoustic fluidization induced pressure.

The stress difference, $Y=b* P_{acf}$, is related to Pacf using a friction law where b is the friction coefficient. We assume that acoustic fluidization induced pressure is proportional to both pressure and the kinetic energy density in the mass element through the relation, $P_f=Ek/Afkemx *P$, where Afkemx is a normalization factor. The effective pressure Pacf would drop to zero if the kinetic energy is greater than afkemx. Note that P_f decreases as the particle velocity and kinetic energy in a cell become smaller behind the shock front. Thus, the strength reduction due to acoustic fluidization decreases with time in the cell.

This section contains finite difference simulations of the PILEDRIVER explosions that were made to evaluate both the Sammis micro-mechanical damage mechanism model and the acoustic fluidization mechanism by comparing synthetics and observations. We start first with a series of runs, aiming to find the best parameters, afonke, afkemx, according to the above mechanism, to approximate the observations.

Table 3 shows results such as failure extent, damage extent, acoustic fluidization extent, final cavity size (Rc) and maximum cavity size and RDP different combinations of the two parameters, afonke and afkemx. We notice that the final scenarios are quite sensitive to these parameters, and generally the greater value of afonke and afkemx corresponds to the smaller damage zone and smaller failure zone. We find that the combination Afonke=afkemx=1e6 (erg/cm^3) (Case Pa04 in Table 3) better fits the cavity size and RDP for PILEDRIVER. The particle motion observations and synthetics with this combination of parameters at four locations are shown in Figure 7.

Table 3 Parametric studies of acoustic fluidization.

RUN-ID	Afonke (erg/cm^3)	Afkemx (erg/cm^3)	Failure extent (m) (ifdam=4)	Damage extent (m) (ifdam=1)	Extent of A.F. (m)	Rc (final) (m)	Rcmax (m)	RDP, phi (10^3 m^3)
Pa03	1e6	1e7	367.6	552.4	212.2	47.391	48.31	23
Pa04	1e6	1e6	436.8	630.1	212.2	42.748	56.95	16
Pa05	1e6	5e6	394.1	590.1	212.2	50.045	51.19	26
Pa06	1e6	2e6	436.8	609.8	220.6	49.202	54.98	25
Pa09	1e7	1e7	367.6	552.4	129.0	46.457	47.19	21
Pa10	1e5	1e7	367.6	552.4	342.7	47.480	48.40	22
Pa11	2e5	1e6	451.9	630.1	319.2	43.090	58.49	17

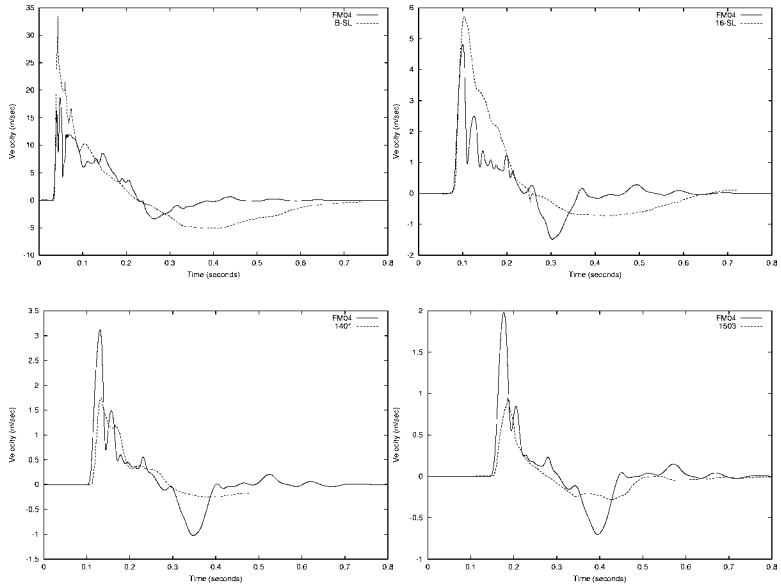

Figure 7. Comparison between observations (dashed lines) and synthetics (solid lines) made with acoustic fluidization. afonke=afkemx=10^6 erg/cm^3.

The simulated waveforms shown in Figure 7 match some of the characteristics of the measured waveforms but are not as good a fit to the data as were those shown earlier in Figure 1 (for the effective stress model) or Figure 6 (for the Sammis model augmented by a post-failure shear damage model). In particular, the very simple model for acoustic fluidization outlined above results in larger negative pulse amplitudes and shorter negative pulse durations than those measured. Part of this is due to a problem in the implementation – as velocity changes from positive to negative the kinetic energy reaches zero and acoustic fluidization abruptly turns off, which is clearly incorrect. Introduction of a decay time into the above acoustic fluidization algorithm to correct this problem has shown the potential for increasing negative pulse durations and bringing the acoustic fluidization results into better agreement with the measurements.

However, the noise in the waveforms produced using the Sammis brittle failure model (Figures 6 and 7) is a consequence of the large strength reduction for failed rock compared to the elastic (infinite strength) deviatoric behavior required for compatibility with the model in the damaged rock outside of it. (See Rimer, et al, 1999, for a discussion of the effects of numerical smoothing of the discontinuity between failed and damaged rock elements for the PD10 model.)

Implementation 2 – Failure and start of acoustic fluidization defined by laboratory strength model, followed by plastic flow

The simulations described in the previous section are noisy, in large part due to incompatibilities both between the brittle failure model and possible plastic behavior near the explosive source and between the elastic pressure-volume relation for undamaged rock and the nonlinear loading relation measured on small samples of granite in the laboratory. In order to incorporate these nonlinear rock behaviors, we removed the Sammis model and instead used the laboratory failure surface for damaged granite as the trigger point for

acoustic fluidization. Calculations were run with this failure surface and the polynomial EOS for granite developed from compressive loading tests on Piledriver rock samples. We assume plastic yielding and a non-associated flow rule (radial return) and use the plastic work (epw) done on a rock element as the threshold to determine if the cell is rubbleized (to initiate the acoustic fluidization model). The acoustic fluidization threshold is set to the same value as implementation #1. These calculations are in progress.

CONCLUSIONS AND RECOMMENDATIONS

IDG is in the process of digitizing data from 25 nuclear tests at the Degelen test site. The complete data set consists of 81 near field waveforms recorded underground at shot depth and 124 (unique) near regional seismic records. IDG has digitized 27 near field waveforms and 122 seismic waveforms (including multiple records of the same signal), and will complete digitization of the remainder of the data set over the duration of this project. The data set of near field and regional waveforms will be delivered to the Center for Monitoring Research upon completion of this project.

We are in the process of defining the optimum procedures to model this data. The goal is to develop material models that are consistent with the data and have a realistic physical basis. Work to date at SAIC has focused on implementation and testing of improved numerical modeling procedures and simulation of near regional data. We are testing acoustic fluidization as a physical mechanism for strength reduction in nonlinear explosion simulations. Preliminary results are promising, but additional work is required to improve the realism of the models. This initial study has focused on modeling of the PILEDRIVER data set with new material models. During the next year, we will continue this modeling effort and also focus on modeling the Degelen data set. Near field data will be modeled with our nonlinear finite difference code as described in this report with improved material models. Near regional data will be modeled using wave number integration.

REFERENCES

Ashby, M.F. and C.G. Sammis (1990), "The Damage Mechanics of Brittle Solids in Compression," *PAGEOPH*, Vol. 133, No. 3.

Luco, J. E. and R. J. Apsel (1983), "On the Green's functions for a layered half-space. Part 1.," *Bull. Seism. Soc. Am.*, 73, 909-929.

Melosh, H.J. (1979), "Acoustic Fluidization: A New Geologic Process?," *J. Geophys. Res*., 84, 7513, December.

Melosh, H.J., and B.A. Ivanov (1999), "Impact Crater Collapse," *Annual Rev. Earth Planet Science*, 27, pp385-415.

Rimer, N. and K. Lie (1982), "Numerical Simulation of the Velocity Records from the SRI Grout Spheres Experiments," S-CUBED Topical Report DNA-TR-82-54, September.

Rimer, N., S. M. Day, G. A. Hegemier, H. E. Read, S. K. Garg, and S. Peyton (1984), "Effect of Pore Fluid Pressure on Explosive Ground Motions in Low Porosity Brittle Rocks," DNA-TR-85-245, July.

Rimer, N., J. L. Stevens, and K. H. Lie (1986), "Effects of Pore Pressure and Fractures on Ground Motion in Granite," S-CUBED Final Report DNA-TR-86-227, June.

Rimer, N., J. L. Stevens, and S.M. Day (1987), "Effects of Pore Pressure, Fractures, and Dilatancy on Ground Motion in Granite," S-CUBED Final Report AFGL-TR-87-0136, April.

Rimer, N. and W. Proffer (1991), "Containment Phenomenology Using a New Shear-Strain-Based Computational Damage Model for Tuff," S-CUBED Report SSS-DTR-91-12612, September.

Rimer, N., K. Lie, J.L. Stevens, J.R. Murphy, and G.G. Kocharyan (1998), "A Micro-Mechanical Damage Model for Estimating Seismic Source Characteristics of Underground Explosions in Hardrock," Maxwell Technologies Technical Report MFD-DTR-98-15985, January.

Rimer, N., J.L. Stevens, J.R. Murphy, and G.G. Kocharyan (1999), "Estimating Seismic Source Characteristics of Explosions in Hardrock Using a Micro-Mechanical Damage Model," Maxwell Technologies Final Report MTSD-DTR-99-16423, July.

Stevens, J. L. (1986), "Estimation of scalar moments from explosion-generated surface waves," *Bull. Seism. Soc. Am.*, v. 76, pp. 123-151.

Stevens, J. L., N. Rimer, and S. M. Day (1986), "Constraints on modeling of underground explosions in granite," S-CUBED annual report, AFGL-TR-86-0264, SSS-R-87-8312, October.

UTILIZATION OF SEISMIC AND INFRASOUND SIGNALS FOR CHARACTERIZING MINING EXPLOSIONS

Brian Stump[1], Chris Hayward[1], Claus Hetzer[2] and Rong-Mao Zhou[1]

Southern Methodist University[1]
Baylor University[2]

Sponsored by Defense Threat Reduction Agency

Contract No. DSWA01-98-C-0176

ABSTRACT

This empirical study is designed to quantify mining explosions as sources of seismic and infrasound signals. The study focuses on the Western US, where a variety of different types of mining operations exist, ranging from surface coal cast blasting to hard rock fragmentation blasting in porphyry copper mines. The study is extended to the taconite mines of the Mesabi Range of Minnesota. Newly installed instrumentation, including in-mine equipment for ground truth as well as regional seismo-acoustic deployments to complement existing resources in the region, is a key component of the study. In-mine monitoring is ongoing at the Morenci Mine in Arizona and the Tyrone Mine in New Mexico. The seismo-acoustic station at Ft. Hancock, Texas, and the infrasound upgrade to Tucson, Arizona, and WUAZ will also be illustrated.

Data from this study have been used to address coupling and source characterization issues for both seismic and infrasound signals. The seismic coupling of large-scale cast blasts in Wyoming, copper fragmentation blasts in Arizona and New Mexico, and taconite fragmentation blasts in Minnesota are compared. For all these event types, there is no relation between total explosive yields and peak amplitude either in the mine or at regional distances. A series of contained, single-fired explosions of varying yield was conducted in the coal mine. At regional distances these events, in contrast, show a definitive magnitude-yield relation that follows the relationship for nuclear explosions. These data and an extensive modeling exercise suggest that the complete characterization of the delay firing process, including a spall contribution, can explain the regional observations.

Acoustic data from within the mine indicate that a relation exists between total explosive weight and peak acoustic amplitudes. At regional distances, under optimum wind conditions, approximately 25% of Morenci Mine shots are observed out to 500 km. The shots that are observed are among those with the largest total explosive yield conducted at this mine.

The acoustic data from within the mine can be used in developing ground truth. Unlike coal cast or taconite blasts, Morenci Copper Mine often shoots several explosive patterns within a short time interval (less than 5 s). The in-mine acoustic data can be used as ground truth to identify the occurrence of those complex explosive events and contribute to the interpretation of the accompanying regional signals.

KEY WORDS: Seismo-acoustic, mining, discrimination, infrasound

OBJECTIVE

This study focuses on seismic and infrasound signals from the following three types of mining operations:

Coal overburden casting (Black Thunder, WY) where explosions are designed to remove overburden to expose coal;
Rock fragmentation for copper recovery (Morenci, AZ) where moderate sized explosions are designed to break the rock for further processing; and
Rock fragmentation in hard rock for iron recovery (Minntac, MN) where large-scale explosions are used to pulverize the taconite for further processing.

Each mine has distinctive blasting practices that are reflected in regional seismic and infrasound signals that are illustrated in this paper.

This paper reports work in four areas:
1. Quantification of coupling of energy from mining explosions into regional seismic waves;
2. Development and constraint of physical models of mining explosions that are applicable to regional seismic signals;
3. Quantification of coupling of energy from mining explosions into infrasound signals; and
4. Characterization of seismic and infrasound signals from a number of unusual sources. Data from the three types of mining explosions listed earlier were used in developing these four work areas.

RESEARCH ACCOMPLISHED

Seismic Coupling

In all three types of mining operations, peak amplitude of regional seismic signals is independent of the total explosive weight (Figure 1 coal cast blasts, Figure 2 taconite (iron) fragmentation, and Figure 3, right, copper fragmentation blasts). In-mine peak amplitudes are also independent of total explosive weight (Figure 3, left). A series of contained, single-fired explosion experiments with total explosive weights from 5,000 to 50,000 lbs. was conducted in the coal mine to further investigate coupling. Regional phase amplitudes of P_n, P_g and L_g increase with a power law relation to total explosive weight (Figure 1, ~W^b).

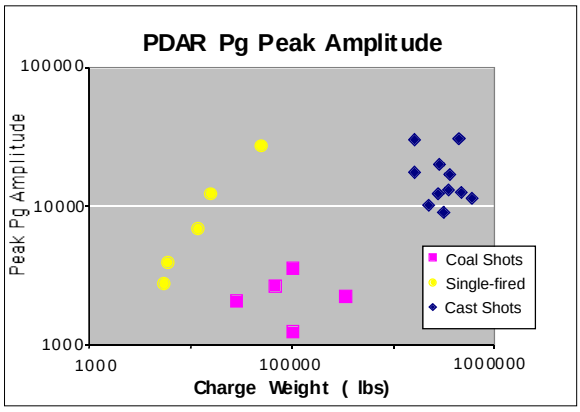

Figure 1: Peak P_g amplitudes observed at array element 03 of PDAR (360-km range) from contained single-fired explosions, delay-fired cast blasts and delay-fired coal shots

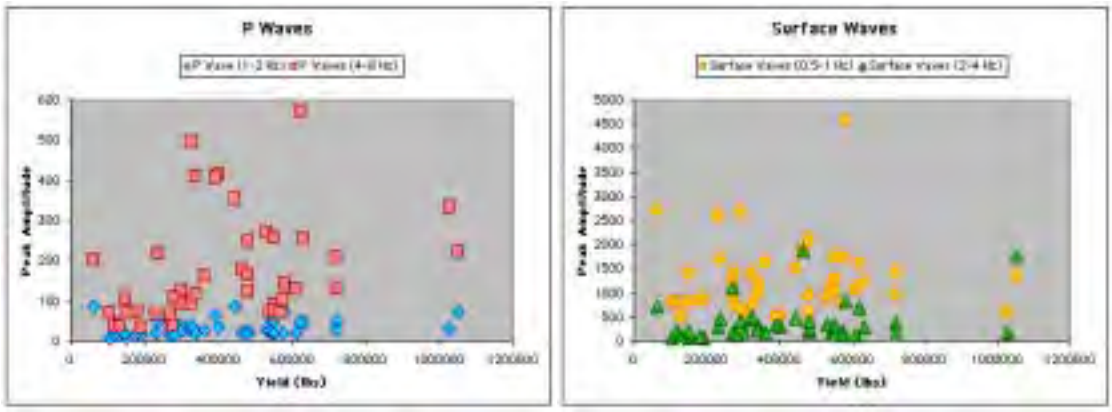

Figure 2: Peak P and R_g amplitudes observed at EYMN (Ely, Minnesota) from taconite fragmentation explosions approximately 110 km to the southwest of the station.

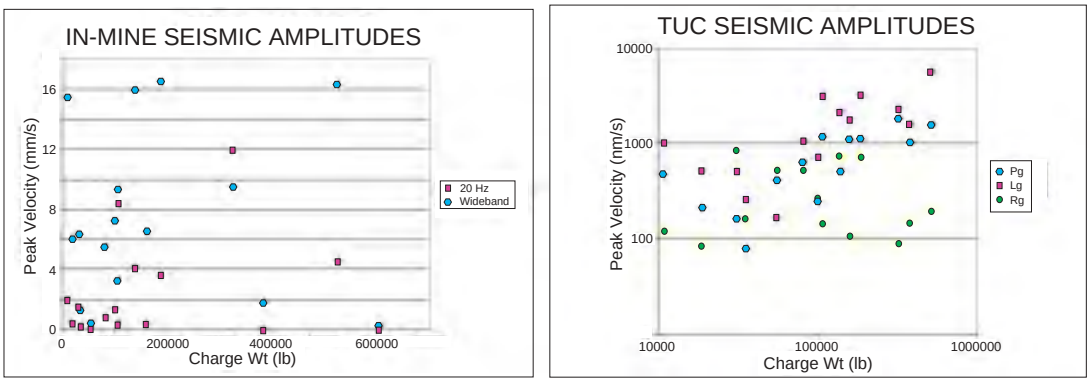

Figure 3: Peak amplitudes of in-mine recordings at Morenci are compared to total amount of explosives used in copper fragmentation blasts (left). Peak P_g, L_g and R_g amplitudes observed at the regional station TUC plotted against total amount of explosives used in the Morenci copper fragmentation explosions (right).

The scaling parameters (the b in $W^{b)}$ determined for these chemical explosions were 0.84 (–0.14) for P_n, 0.84 (–0.09) for P_g, and 0.91 (–0.08) for L_g. These b values are in close agreement with the scaling relations of Vergino and Mensing (1983) for P_n waves from nuclear explosions in Nevada. This comparison of contained, single-fired explosions with standard mining explosions suggests that delay-firing, casting and fragmentation are responsible for the independence of peak regional and close-in amplitudes and total amount of explosives.

Seismic Modeling

Following Anandakrishnan et al (1997) and Yang s (1998) implementation in MATLAB,¤ an equivalent elastic source model for the mining explosion was used to develop regional synthetic seismograms. The source model components shown in Figure 4 include: (a) explosion; (b) vertical spall; and (c) horizontal spall. The purpose of modeling was to investigate why peak regional amplitudes are insensitive to total explosive weight in delay-fired explosions (Figures 1-3) and how mid-frequency surface waves (2-12 s) are generated from large-scale cast blasting.

a) Explosion Source

Mueller-Murphy model

b) Vertical Spall

Opening of horizontal crack

Unloading

Slapdown

Pit Depth

c) Horizontal Spall

Opening of vertical crack

Horizontal slapdown in pit

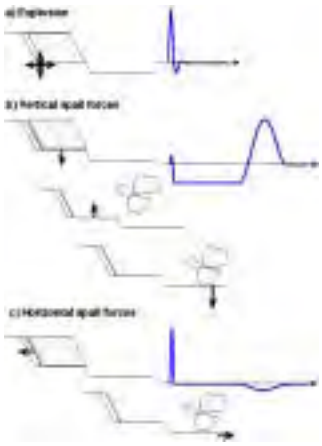

Figure 4: The three components of the equivalent mining explosion source model are represented pictorially. They consist of (a) the directly coupled energy from the contained explosion modeled as a Mueller-Murphy source function, (b) vertical spall due to the tensile failure of near-surface materials and (c) horizontal spall accompanying cast blasting when overburden is cast horizontally into a pit.

In addition to the three-source components, the temporal and spatial finiteness of the explosive array is included in the model. Collaboration with the three mines used in the study provided the necessary information to model the source and generate synthetic seismograms.

Hetzer (2000) investigated the effect of delay firing at the Taconite Mine in Minnesota (Minntac). The mine provided shot details that could be incorporated into the source model (Figure 4). Hetzer set total spall mass, one of the important parameters in the model, as equal to the mine's report of total mass of rock blasted. This same technique was applied to large-scale coal cast blasts in Wyoming. Figure 5 plots the average spall mass per hole versus the average charge weight per hole for the Minntac data (open triangles) and the single cast blast data point. Spall scaling relations developed for nuclear explosions (Viecelli, 1973; and Sobel, 1978) are included in the figure for comparison. The Minntac data relation falls between the Sobel and Viecelli scaling models and is consistent with the coal cast data (red star). This empirical spall scaling relation was used in the mining explosion source model.

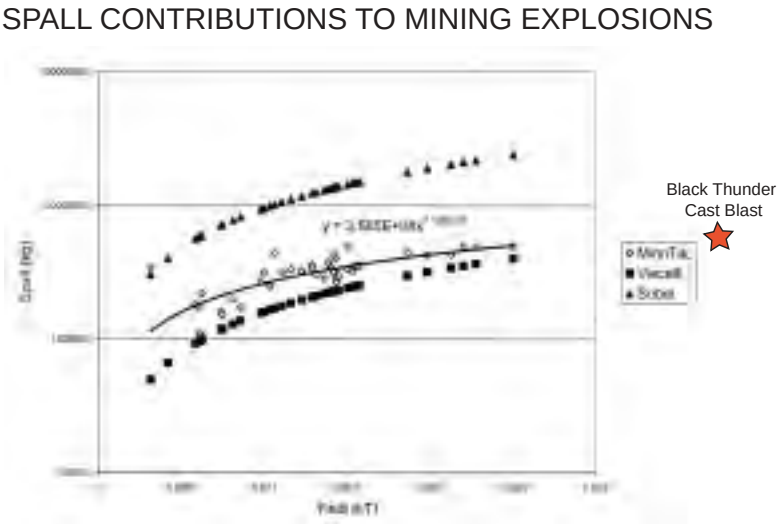

Figure 5: Spall mass (per hole) for the taconite hard rock explosions (open diamonds) and a single coal cast blast (star) were estimated from blasting logs. These empirical estimates from mining explosions are compared to the Viecelli and Sobel spall mass scaling relations developed for underground nuclear explosions.

Near-regional observations from the Minntac fragmentation blasts were made at EYMN approximately 110 km to the NE of Minntac near Ely, Minnesota. These observations provide the basis for the empirical and modeling studies of Hetzer (2000) and are summarized here. The shots ranged from 63,000 lbs to 1,050,000 lbs total explosive weight. Peak body (P_g) and surface wave (R_g) amplitudes showed little relation to total explosive weight (yield) as shown in Figure 2. The previously described source model and a regional propagation model were used to produce synthetics for the Minntac taconite fragmentation blasts. The models replicate the independence of regional signal peak amplitudes to total yield and replicate the order of magnitude scatter in amplitudes for a given yield. The modeling suggests that the average individual charge weight in the explosive array may control the absolute amplitudes of the regional phases. The observed body wave peak amplitudes in the 2-4 Hz band are plotted against average charge weight per hole in Figure 6 (solid symbols) and indicate a slight increase in peak amplitude with increasing single hole yield. For nine of the shots in the observational data set peak amplitudes on synthetic seismograms were compared with observations. The model amplitudes (open circles) are compared to the observations in the 2-4 Hz band in Figure 6 and replicate the increase in peak amplitude with increasing charge weight per hole. The synthetics also replicate the scatter in the peak amplitude values for any given average charge weight.

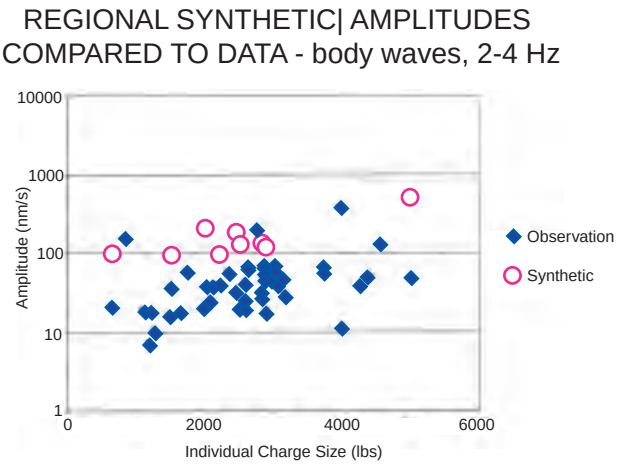

Figure 6: The mining explosion source model (Figure 4) was used to produce synthetics for a distance and crustal velocity model appropriate for EYMN. Synthetics were produced for a number of mining explosions of different average charge weight per borehole. Peak amplitudes of the synthetics are compared to the observations from the same explosions.

A second modeling exercise was completed for the large-scale cast blast associated with the coal mines in Wyoming. Peak P_g, P_n and L_g amplitudes from these blasts show little relation to total explosive yield as well (Figure 1). These large, one to eight million lbs, explosions use many boreholes and as a result have long time durations. They are designed to cast the overburden and so material is moved horizontally and then drops vertically into a pit. As demonstrated in Figure 7 (left), these events generate significant regional surface waves in the 2 to 12 s band. From the surface wave dispersion analysis, a regional velocity model was developed and combined with the above mining source model to produce the synthetic regional surface waves (Figure 7, right). This study suggests that a long duration source in combination with a large-scale casting operation can generate the mid-period surface waves observed with this coal mine.

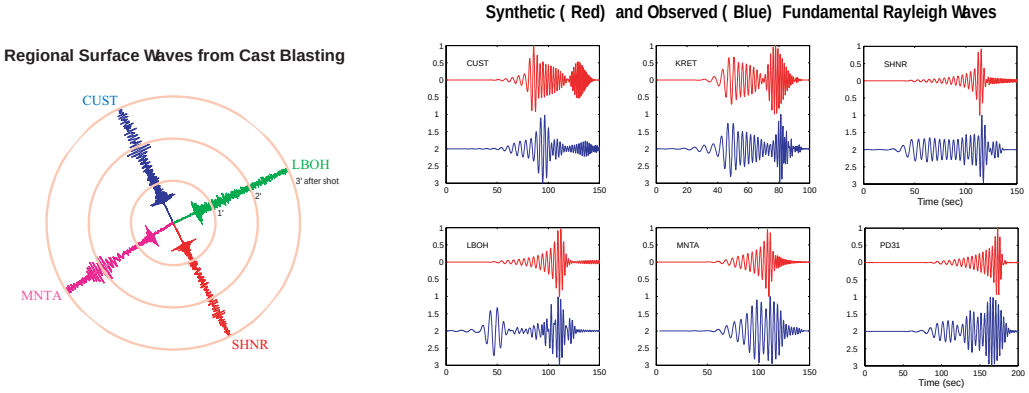

Figure 7: The mining explosion source model was also used to compute synthetics for the large-scale cast blasts. The focus in this modeling exercise is on the long period surface waves.

Infrasound Coupling

Infrasound signals have been reported to accompany mining explosions and may provide a source diagnostic (Sorrells et al, 1997; Hsu and Stump, 1997). Critical analysis of infrasound observations requires associated regional seismic observations and source information (such as blasting practices or designs). Coupling issues must be assessed, as well as models related to atmospheric propagation and source physics. Ground truth from the Morenci and Minntac mines provides source constraints. Preliminary results from Minntac (Figure 8 and Table 1) and Morenci (Figures 9 and 10) are illustrated below. Operations at both mines regularly generate seismic and infrasound signals.

Recorded infrasound data from Lac du Bonnet, Manitoba, were examined for Minntac-originated infrasound signals during August 2000 and November 2000. Four explosions were chosen for each time period. For detected signals, back azimuth estimates were within 5 degrees of the actual (Table 1). Signals included significant energy from 1/10 to several Hz (Figure 8). All explosions over 500,000 lbs generated detectable infrasound. The effects of seasonal winds on the infrasound propagation have not been taken into account.

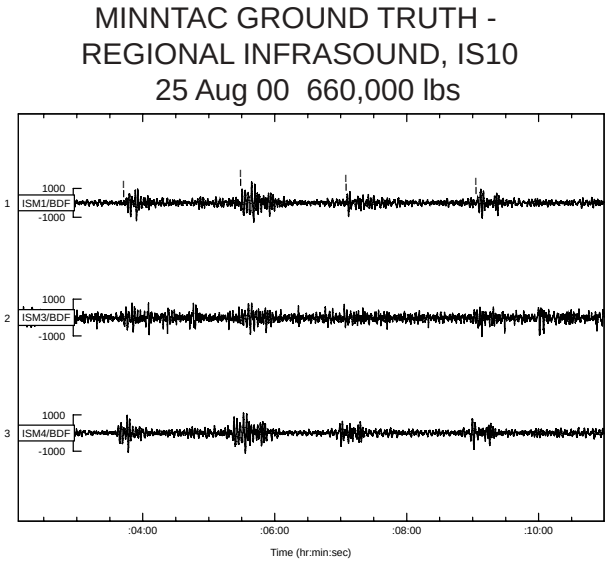

Figure 8: Example infrasound arrivals observed at IS-10, Lac du Bonnet, Manitoba, from a hard rock fragmentation blast at Minntac. Back azimuth estimates from these data were within 5 degrees of the ground truth location.

MINNTAC GROUND TRUTH -
REGIONAL INFRASOUND DETECTIONS AT IMS10

Date	Yield (lbs)	Detection
17 Aug 00	545,932	Yes
23 Aug 00	550,000	Yes
25 Aug 00	660,000	Yes
30 Aug 00	500,000	Yes
14 Nov 00	425,000	No
15 Nov 00	380,000	No
21 Nov 00	275,000	No
28 Nov 00	810,000	Yes

Table 1: Ground truth data from two one-week time periods were used to investigate the detection of infrasound signals at IS10. Five out of eight of the blasts were detected.

Regional infrasound signals from 7 of 25 ground truth events at Morenci in February 2000 were observed at the Los Alamos infrasound array (Figure 9). Every observed explosion was over 100,000 lbs although not every large explosion was observed (Figure 10). The dominant energy in the infrasound signal was in the 1- to 3-Hz band. Back azimuth estimates using f-k analysis were within 5 degrees of the ground truth.

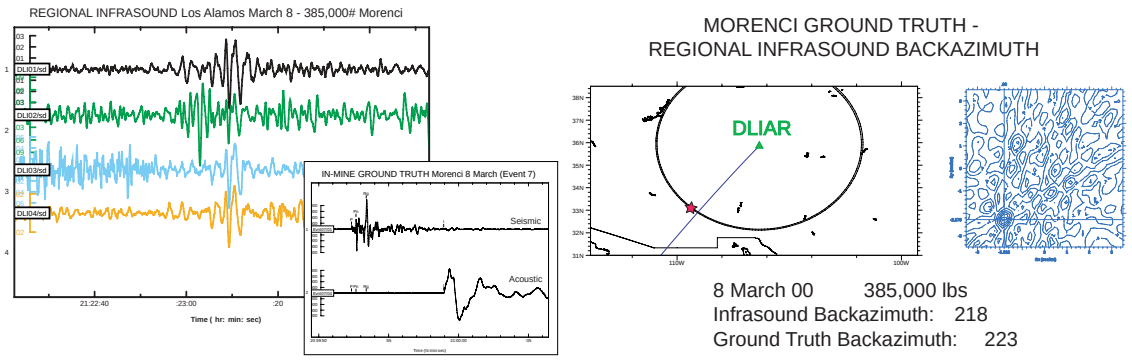

Figure 9: Mining explosions from the hard rock copper mines in southeastern Arizona generate infrasound signals as exemplified by the records from DLIAR in Los Alamos (left). Ground truth for this event was provided by close-in seismic and acoustic records of the blast (left, inset). Frequency-wavenumber estimates were used to make the backazimuth estimate shown to the right.

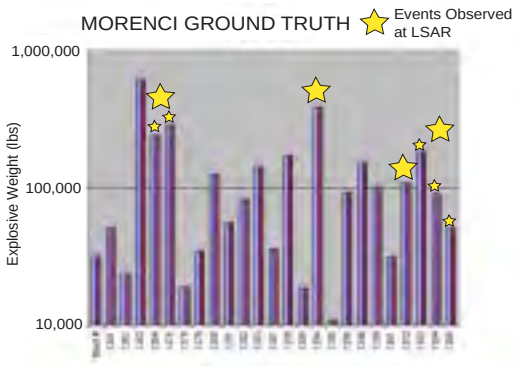

Figure 10: A number of the ground truth mining explosions from the copper fragmentation blasts in SE Arizona were observed at Los Alamos. Detected events were among the largest of the blasts.

Unusual Events

Close-in observations provide source constraints that can be used to interpret regional seismic and infrasound signals. An example of how in-mine monitoring can illuminate unusual blasting practices is provided by data recorded on a seismo-acoustic system that is deployed in the Morenci Mine. A three-component broadband seismometer and three acoustic gauges in a tripartite configuration have been installed in the center of the mine. The combined seismic and acoustic data set provides a quantification of daily blasting in the mine with little or no impact on the mining operation.

Analysis of this in-mine data set has illustrated that it is not uncommon for the blaster at this mine to detonate two or more explosive patterns within a few seconds. Such a blasting practice can produce complicated regional signals. In-mine seismic and acoustic records (top six waveforms) from two closely spaced patterns and the resulting complex regional seismograms observed at TXAR are reproduced in Figure 11.

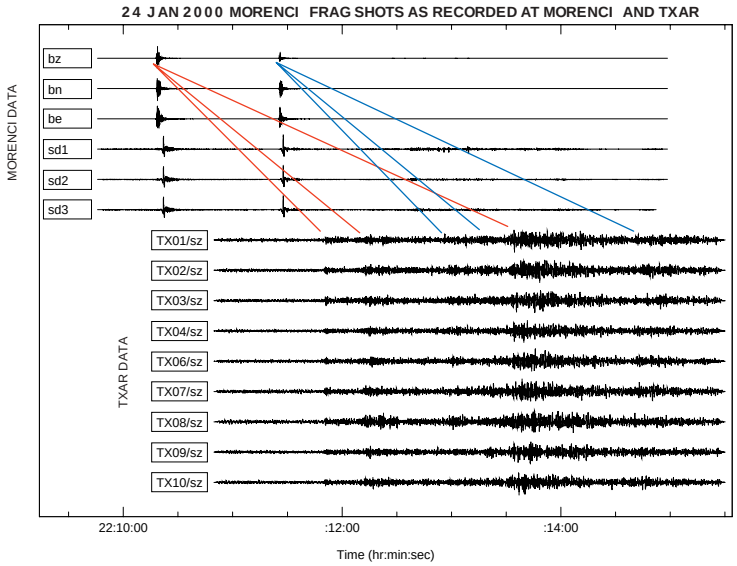

Figure 11: Seismic and acoustic instrumentation from within the cooper mine was used for ground truth. The upper six traces represent the three seismic and three acoustic gauges deployed in the mine. The bottom nine traces are the array elements of TXAR. The close-in seismic and acoustic signals document two mining explosions detonated over a short time period providing a complex regional seismogram.

Infrasound signals were recorded at the seismo-acoustic station outside of El Paso, Texas (Ft. Hancock) from the explosion and subsequent burning of a gas pipeline in New Mexico. Data from all three acoustic and one seismic sensor in the array are displayed in ten-minute segments (Figure 12). As documented by the data, the pipeline burned for over 40 minutes. Details of the infrasound signal are compared to near-source seismograms (Figure 13) illustrating that the complex nature of the explosion is reflected in the infrasound and seismic data. The gas pipeline explosion produced no regional seismic signals at the TXAR (Lajitas, TX) regional seismic array.

Natural Gas Explosion and Burn in New Mexico

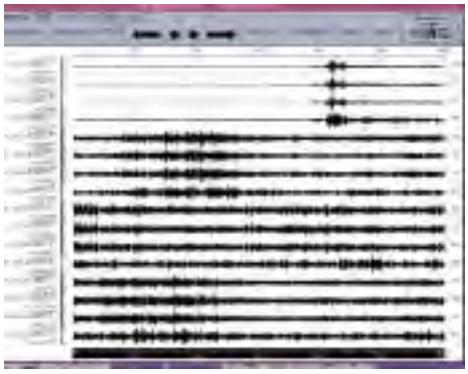

T. Wallace

19 August 2000

180 km NE of site

No Seismic at TXAR

Figure 12: Infrasound (channels 1,2, 3) and seismic data (channel 4) from a seismo-acoustic station installed outside El Paso, Texas (Ft. Hancock). Each horizontal section represents 10 minutes of data. This seismo-acoustic signal that extends for over 30 minutes represents the explosion and burning of a natural gas line in New Mexico (photo: Terry Wallace, University of Arizona).

Natural Gas Explosion and Burn in New Mexico

T. Wallace

Regional Seismic Wave Propagation

PHASE TIME INVERSION: A SIMPLE METHOD FOR REGIONAL WAVEFORM INVERSION

Charles A. Langston

University of Memphis

Sponsored by National Nuclear Security Administration
Office of Nonproliferation Research and Engineering
Office of Defense Nuclear Nonproliferation

Contract No. DE-FC04-00AL66883

ABSTRACT

Broadband regional waveforms from earthquake and explosion sources contain a wealth of information on crustal and upper mantle velocity structure. Arrival times, amplitudes, and frequency content of individual seismic phases can be affected by many details of structure that include velocity gradient, average velocities, and velocity heterogeneity as well as source type, depth, and time function. Major characteristics of the regional seismogram are also controlled by the simple parameter of receiver distance from the source. Inversion of the regional waveform for source parameters (for use in seismic discrimination) strongly depends on the velocity model assumed and has proven to be a difficult task for broadband seismograms. Typical waveform fitting schemes often employ seismogram differences or correlations that are dominated by the largest amplitude or lowest frequency phases within the wave train such as surface waves. It is difficult to match smaller body-wave-type arrivals or to unravel the interference between phases that traverse many different paths in the structure. Small time differences between observed and synthetic arrivals can thwart the usual methods of waveform matching but are important pieces of data in determining an appropriate velocity model. The "phase time" inversion method utilizes a direct but biased comparison of data and synthetic seismograms to model the arrival time of any phase on the regional seismogram. Phase time differences are incorporated into a stable generalized inverse to obtain earth structure parameters of "ideal" parameterized velocity structures. The method is used to model a large suite of regional seismograms from an earthquake in Africa to obtain a simple 1-D velocity structure that can explain regional waveforms between 200- and 800-km distance. The "Lg" phase is seen to be composed of high phase velocity, multiple shear waves that propagate throughout the crust. Apparently low Lg group velocities are caused by the kinematic effect of progressive crustal multiples undergoing post-critical reflection at the Moho to produce high phase amplitudes, then cutting out because of the positive crustal velocity gradient.

KEY WORDS: waveform inversion, regional wave propagation, crustal structure, mantle structure, Lg

OBJECTIVE

Regional waveforms are a challenge to understand because they are produced by many different wave propagation mechanisms. Even for 1-D structure these may include, for example, surface wave excitation and propagation, head wave propagation, tunneling (as in the production of S*), post-critical reflection, near-surface site resonances, frequency-dependent attenuation effects, and a variety of wave interference effects caused by source type and source placement in the structure. The problems become compounded when regional seismic structures are allowed to vary in two and three dimensions. The objective of this research is to develop a straightforward method to model regional waveforms to obtain estimates of the earth model that can then be used to infer nuclear-explosion-monitoring-relevant source parameters such as source type and depth. The method developed here, the "phase-time inversion" method, is an intuitive technique for matching observed and calculated waveforms. In principle, it can be applied to determining earth structure in two and three dimensions as well as in the 1-D example shown in this paper, as long as accurate synthetic seismograms can be computed for the structure of interest.

RESEARCH ACCOMPLISHED

We utilize a high-quality waveform data set from earthquakes recorded by the 1994-1995 Tanzania Broadband Experiment (Owens et al 1995) to derive a velocity model of the crust and upper mantle of the Archean age Tanzania craton and surrounding Proterozoic mobile belts (Figure 1) that are presently undergoing rifting. The 1994-1995 Tanzania Broadband Experiment consisted of a 20-station broadband seismic network arranged in a skewed cross pattern across Tanzania (Figure 1) with the Archean Age Tanzania craton being the primary target of the experiment (Owens et al 1995; Nyblade et al 1996). We use the broadband waveforms from the 18 August 1994 Lake Rukwa earthquake to first infer the character of regional wave propagation within the crust and mantle and then to quantify the arrival times and amplitudes from a variety of observed seismic phases to produce a velocity model. The Lake Rukwa event was recorded at teleseismic distance and was the subject of a detailed source study by Zhao et al (1997), who determined its source mechanism, source function, and depth. Because the source parameters are known for this event, it can be used to decipher the regional wave propagation across the network.

An initial model of crustal structure was constructed using results from teleseismic receiver functions and short-period surface wave dispersion analysis performed by Last et al (1997). We constrained upper mantle P and S wave velocities by performing travel-time studies of first arrival Pn waves from other regional events and Sn waves from Rukwa event waveforms. Pn velocity within the network is quite high at 8.2 - 8.5 km/s with the higher velocities found within the craton. Sn velocity, using picks from the Rukwa waveforms, is 4.75 km/s and is consistent with the high average Pn wave velocity (8.3 km/s) in the mantle.

Simply plotting the vertical and radial displacement waveforms in a reduced time section using the average Pn and Sn velocities yields important information on the nature of wave propagation across the network. Figure 1 shows a reduced time section for vertical component arrivals before Sn. Clearly, these phases generally travel at Pn velocities and can be interpreted as Pn, sPn and multiples. Figure 2 shows the S wave train in a reduced time section using the average Sn velocity across the network. There is a remarkable succession of Sn and multiple Sn phases that can be traced across the network.

Identifying each phase in the Rukwa data was a straightforward matter involving calculating theoretical travel-time curves in an ideal crustal model. Travel-time curves were computed for an earth model parameterized with a linear gradient in the crust over a homogeneous mantle (Figure 3). Parameters for this model are given in Table 1. The Rukwa source was located at 25-km depth within the lower half of the crust so that the P waveforms of Figure 1 are dominated by Pn, sPn phases and their multiples. The apparent low-velocity move-out of the later arriving energy in the P waveform data is the beginning of the regional PL wave (Helmberger and Engen, 1980).

Early versions of the final earth model shown in Table 1 were successful in predicting the general behavior of the broadband waveforms when synthetic seismograms were calculated using the Rukwa source parameters. Relative amplitudes and times of the different head waves and crustal multiples were roughly correct showing good similarity between data and synthetic. However, it proved difficult to devise a method to use all the data simultaneously to find an optimum structure model.

Several schemes were attempted to refine the velocity model. Because the wavenumber integration algorithm is computationally intensive (Barker 1984), multi-mode surface wave summation was used initially to construct an accurate synthetic for the S wavetrain (e.g., Harkrider 1964; 1970). Because this is a much faster process (by two orders of magnitude in speed), many more earth models could be tested. We used a normalized cross-correlation function to determine the fit between data and synthetic (e.g, Wallace and Helmberger, 1982). However, the multi-mode summation we used was not appropriate for the P wave part of the wavetrain. Furthermore, it was difficult to fit important, relatively high-frequency pulses in the wavetrains of many records because there were significant time shifts between the data and synthetic pulses when the fit was dominated by the longer period portions of the seismogram.

An attempt was made to calculate wavenumber integration synthetics using a coarse grid search algorithm in the crustal structure parameters to regain the P wavetrain portion of the seismogram. Normalized cross-correlation was then used on specific time windows in the data and synthetics in an attempt to model various individual phases. Again, modest time shifts between data and synthetic arrivals placed these arrivals outside of the

correlation time window even though the pulse shapes were not very different. We also discovered that there were consistent absolute time shifts between the data and synthetic waveforms that were probably due to details in the Rukwa source time function or errors in the origin time. These time shifts compounded the problems with the correlation operator windows. Clearly, the similarity of data and synthetics showed that the basic wave propagation was understandable, yet it was difficult to quantify the earth model using features of the data waveforms.

The regional waveform consists of multiple body waves and surface waves, many of which interfere with each other in complex ways. Whichever way the amplitudes work out, travel times of these waves are straightforward functions of crustal velocity structure and thickness. We noticed that many synthetic seismograms for differing earth models often looked similar with the major differences occurring in arrival time for the various component phases within them. Since these features changed their travel time when model parameters changed, we decided to use these time differences as data in a formal generalized inversion for velocity parameters.

Figure 3 illustrates implementation of the process using vertical component data from station MTOR. The earth model is parameterized as shown at the bottom of the figure as a linear velocity gradient in the crust defined by surface P wave velocity, v_1, a basal P wave velocity, v_2, and crustal Poisson's ratio, σ_c. Crustal thickness, h, is also a parameter. Mantle P and S wave velocities are fixed by the travel-time regression of the Rukwa Pn and Sn data. Using an initial guess for the earth model, a synthetic seismogram is constructed (the "reference model" synthetic in Figure 3) and compared to the original. Note that the source parameters are fixed.

"Phase times" are defined as the arrival time of some easily recognizable peak or trough associated with a particular seismic phase arrival. For example on Figure 3, T_j is associated with the trough of Sn and T_{j+1} with the peak of sSn. Because the reference model is not perfect, corresponding peaks and troughs on the synthetic (T^o_j T^o_{j+1} etc.) do not occur at the same times for these phase time picks.

An iterative inversion problem can be set up to simultaneously solve for a new set of model parameters using the phase time misfits. The phase times for the data waveforms, starting model synthetic, and model perturbation synthetics are all picked manually using an interactive graphical interface (Figure 3). This has both drawbacks and natural efficiencies. Obviously, this process introduces biases in the interpretation of the data and synthetics. A choice is made to fit a particular arrival in the data and it is assumed that wave shape for the arrival does not change appreciably across the synthetics. Picking the wrong phase in the synthetics will create problems since the inversion system will have inconsistent data. Another drawback is that picking the phase time manually introduces some error in the time estimate that will affect estimates of the model parameters. Furthermore, this process is not easily made automatic since each iteration of the system requires picking a new set of phase times for the updated model and perturbation synthetics.

However, fitting the phase times directly is *the* intuitive process that a waveform analyst attempts when fitting data with synthetic seismograms. The phase time itself is just a generalization of ray arrival time applied to some consistent feature of the waveform. Reduction of a highly sampled time series with thousands of points to a few pieces of data is a great economy in setting up the inversion problem. For example we applied this technique to 56 broadband waveforms with ~3000 points each from the Rukwa event. Using only unambiguous picks of phase times between data and synthetics, these ~180,000 data points were reduced to 91 phase time picks. There is also an economy in the computation of synthetic seismograms since synthetics for only 5 different models need to be computed to form the reference synthetic seismogram and the perturbation seismograms. Implicit in the formulation are smoothing constraints imposed by the form of the crustal model. Rather than parameterizing a model with many thin layers, simple "ideal" velocity profiles, like the linear gradient used here, can be investigated. This simplifies the inversion set-up and reduces likely problems in parameter resolution when velocity and thickness parameters of many thin layers in a model trade off with one another. If a more complicated model is needed to fit the data, the model can be made incrementally more complex.

Synthetic tests of the technique worked remarkably well by yielding the correct velocity model in a single iteration. Relatively large perturbations of the earth structure parameters produced stable partial derivatives. The method also worked quite well for single-station synthetic tests. Errors in picking the phase times were found to be a minor problem and did not degrade the model parameter estimates significantly. Picks could be

made to within 0.5 sec for the synthetic data with the model parameter variance being, at most, 0.01 km^2 in crustal thickness. Variance for the other parameters was a little larger than numerical noise levels.

Figure 4 shows a subset of results from applying the phase time inversion to the Rukwa waveform data. Table 1 displays the starting model and final inversion model parameters. The strategy used in picking phases was to use clear, isolated peaks in the vertical waveforms and a few of the tangential waveforms. Phase time picks from the radial waveforms are redundant since they contain the same arrivals as on the vertical components. Because the tangential waveforms were more affected by azimuthal radiation pattern effects in the Rukwa source (SH wave nodes for both up and down going waves sweep through the network), we generally avoided picking details in the tangential waveforms and attributed tangential waveform complexity to the influence of scattering and to the greater effect unknowns in the source mechanism have on amplitudes near wave nodes. We also did not pick phase times from complicated regions of the vertical waveforms where it was obvious that many arrivals were interfering with each other. It was heartening to see after inversion that these complex portions of the seismogram at certain stations improved in fit.

One iteration was required to produce a stable model. Table 1 shows that there were only small changes in the earth structure parameters and origin time needed to improve the alignment of numerous phase picks. A variance of 1 s was assumed for the phase time picks for the estimate of model parameter variance. Figure 3 shows a typical misfit between the data and starting model synthetic.

Returning to Figures 1 and 2, it is apparent that the P and S wave trains at regional distances are dominated by critical reflections and head waves from discrete up- and down-going reflections in the Tanzanian crust. The depth of the Rukwa source and its normal fault mechanism combine to create a succession of discrete Sn-type head waves on vertical and radial components of the S wave train. Figure 2 shows how high-amplitude critical S-wave multiple reflections apparently decay in amplitude with distance as the head wave propagates away from the critical distance. This happens over and over as progressively higher-order multiples pass beyond the critical angle of incidence.

This observation has interesting implications for the propagation mechanism for the higher frequency "Lg" phase. Lg is a phase which is of interest in nuclear explosion monitoring since it often travels great distances in the crustal waveguide, is the largest phase seen in high-frequency regional seismograms, and can be used to estimate seismic moment and magnitude (e.g., Herrmann and Kijko, 1983; Kennett, 1986; Hanson et al 1990; Campillo 1990). The study of Lg has an extensive literature, but its propagation mechanism has been difficult to understand because of unknowns in crustal structure and use of relatively limited, single-station data sets.

In the Rukwa data Lg is a high-amplitude S phase with a velocity indicative of the upper crust, here at 3.5 km/s. If the empirical travel-time curve is superimposed on the travel-time curves for multiple S waves, we see that the beginning of Lg is composed of post-critical Moho reflections with later portions of Lg composed of higher order post-critical Moho reflections. Phase velocity for these post-critical reflections is high, being ~4.2 km/s, since they have near-grazing incidence angles at the Moho. This explanation reinforces empirical array studies of the Lg phase performed by Vogfjord and Langston (1990; 1996) using high-frequency data from the Norwegian seismic arrays. Using array beams, they decomposed the Lg wave field to show that low group velocity Lg waves were composed of high phase velocity turning waves and post-critical reflections within the Scandinavian crust.

CONCLUSIONS AND RECOMMENDATIONS

It was possible to derive a crust and mantle velocity model from regional waveform data recorded from the Lake Rukwa earthquake and from first arrival time data picked from other large regional events. The model is very simple, consisting of a crust characterized by a linear velocity gradient over a mantle half-space and is consistent with previous crustal structure studies in the area. The crust and mantle velocity structure of the Tanzania craton is similar to velocity structure in other Archean cratonic areas in that it has high average crustal velocities, high velocities near the Moho, and relatively high upper mantle velocities.

A simple, intuitive method for inverting large data sets of regional waveform data has been developed and is called "phase time" inversion. This method minimizes the misfit between the arrival times of discrete phases on observed and synthetic seismograms. It is similar to tomographic methods except that there is no reliance on ray travel times or explicit formulations of ray geometry. Any seismic phase can be used as long as accurate synthetic seismograms can be computed. Application to the Rukwa regional waveform data showed that, in this case, the inversion problem behaved in a linear fashion. Earth models can be parameterized in terms of simple "ideal" systems to minimize the number of model parameters while preserving basic understanding of the wave propagation involved. "Phase time" inversion should be useful in many other studies of broadband waveforms where there is interest in wave propagation mechanisms and determining earth structure parameters.

REFERENCES

Barker, J.S. (1984), A seismological analysis of the May 1980 Mammoth Lakes, California, earthquakes, Ph.D. thesis, Pennsylvania State University, State College, PA.

Campillo, M. (1990), Propagation and attenuation characteristics of the crustal phase Lg, *Pure Appl. Geophys., 132*, 1-19.

Hanson, R.A., F. Ringdal, and P.G. Richards (199), The stability of RMS Lg measurements and their potential for accurate estimation of the yields of Soviet underground nuclear explosions, *Bull. Seism. Soc. Am., 80*, 2106-2126.

Harkrider, D.G. (1964), Surface waves in multilayered elastic media: I. Rayleigh ad Love waves from buried sources in a multilayered elastic half-space, *Bull. Seism. Soc. Am., 54*, 627-679.

Harkrider, D.G. (1970), Surface waves in multilayered elastic media. Part II. Higher mode spectra and spectral ratios from point sources in plane layered earth models, *Bull. Seism. Soc. Am., 60*, 1937-1987.

Helmberger, D.V., and G.R. Engen (1980), Modeling the long-period body waves from shallow earthquakes at regional ranges, *Bull. Seism. Soc. Am., 70*, 1699-1714.

Herrmann, R., and A. Kijko (1983), Modeling some empirical vertical component Lg relations, *Bull. Seism. Soc. Am., 73*, 157-171.

Kennett, B.L.N. (1986), Lg waves and structural boundaries, *Bull. Seism. Soc. Am., 76*, 1133-1141.

Last, R.J., A.A. Nyblade, and C.A. Langston (1997), Crustal structure of the East African Plateau from receiver functions and Rayleigh wave phase velocities, *Jour. Geophys. Res., 102*, 24,469-24,483.

Nyblade, A.A., C. Birt, C.A. Langston, T.J. Owens, and R.J. Last (1996), Seismic experiment reveals rifting of craton in Tanzania, *EOS Trans. AGU, 77*, 520-521.

Owens, T.J., A.A. Nyblade, and C.A. Langston (1995), The Tanzania Broadband Experiment, *IRIS News Letter, XIV* (1).

Vogfjord, K.S., and C.A. Langston (1990), Analysis of regional events recorded at NORESS, *Bull. Seism. Soc. Am., 80*, 2016-2031.

Vogfjord, K.S., and C.A. Langston (1996), Characteristics of short-period wave propagation in regions of Fennoscandia, with emphasis on Lg, *Bull. Seism. Soc. Am., 86*, 1873-1895.

Wallace, T.C., and D.V. Helmberger (1982), Determining source parameters of moderate-sized earthquakes from regional waveforms, *Phys. Earth and Planet. Int., 30*, 185-196.

Zhao, M., C.A. Langston, A.A. Nyblade, and T.J. Owens (1997), Lower-crustal rifting in the Rukwa Graben, East Africa, *Geophysical Journal International*, *129*, 412-420.

Zhu, L., and D.V. Helmberger (1996), Advancement in source estimation techniques using broadband regional seismograms, *Bull. Seism. Soc. Am.*, *86*, 1634-1641.

Table 1. Inversion Model Parameters

	v_1 (km/s)	v_2 (km/s)	σ_c	h (km)	t_0 (s)
Starting model	5.80	7.00	0.250	38.0	0.0
All stations	5.84±0.04	7.09±0.06	0.250±0.005	40.4±0.6	2.2±0.2

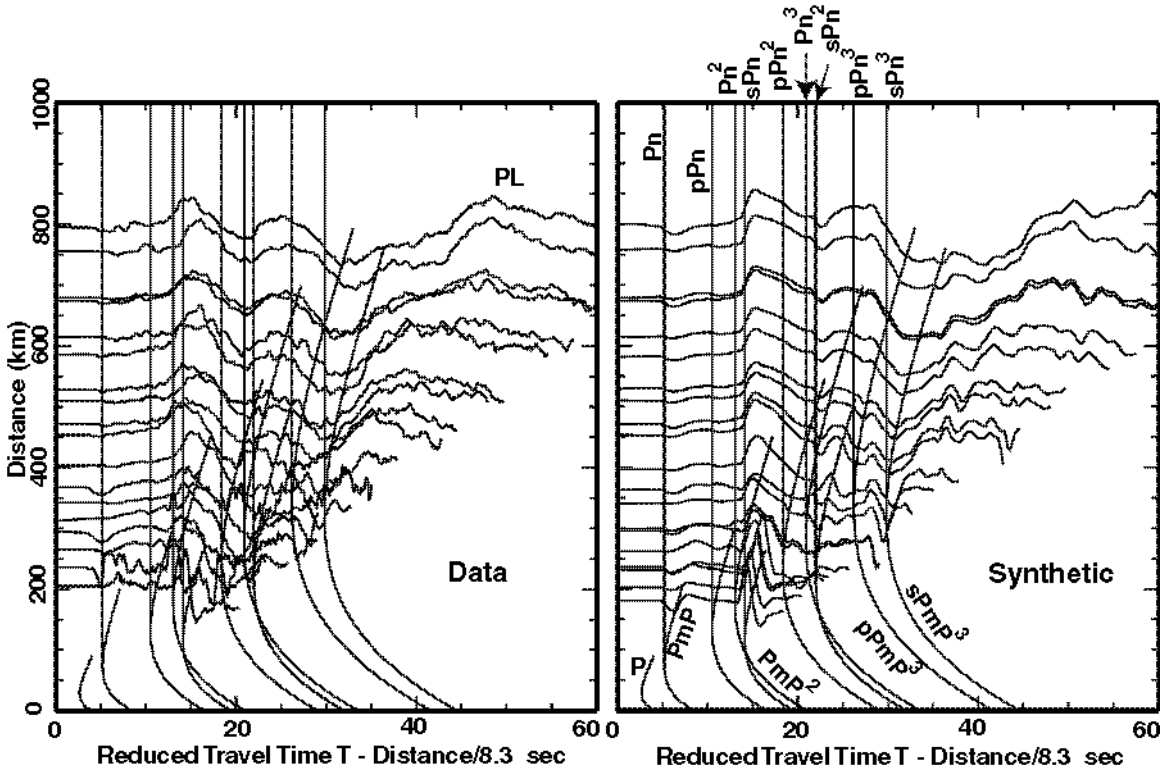

Figure 1. Reduced velocity profiles of vertical displacement data from the Rukwa earthquake and synthetic waveforms from the final inversion model. The data and synthetics have been windowed to exclude the S wavetrain. Note how all waveforms are dominated by waves that travel at Pn velocity. Travel-time curves for major P and sP waves are superimposed on the plot. The largest amplitude phases in the data are sPn-type head waves. Refer to Figure 6 for ray path diagrams. Pn^2 and Sn^2, for example, are mantle head waves associated with PmP^2 and SmS^2 crustal multiples, respectively. All wavenumber synthetic seismograms in this paper were computed using 2048 time points with a 5sps sampling frequency.

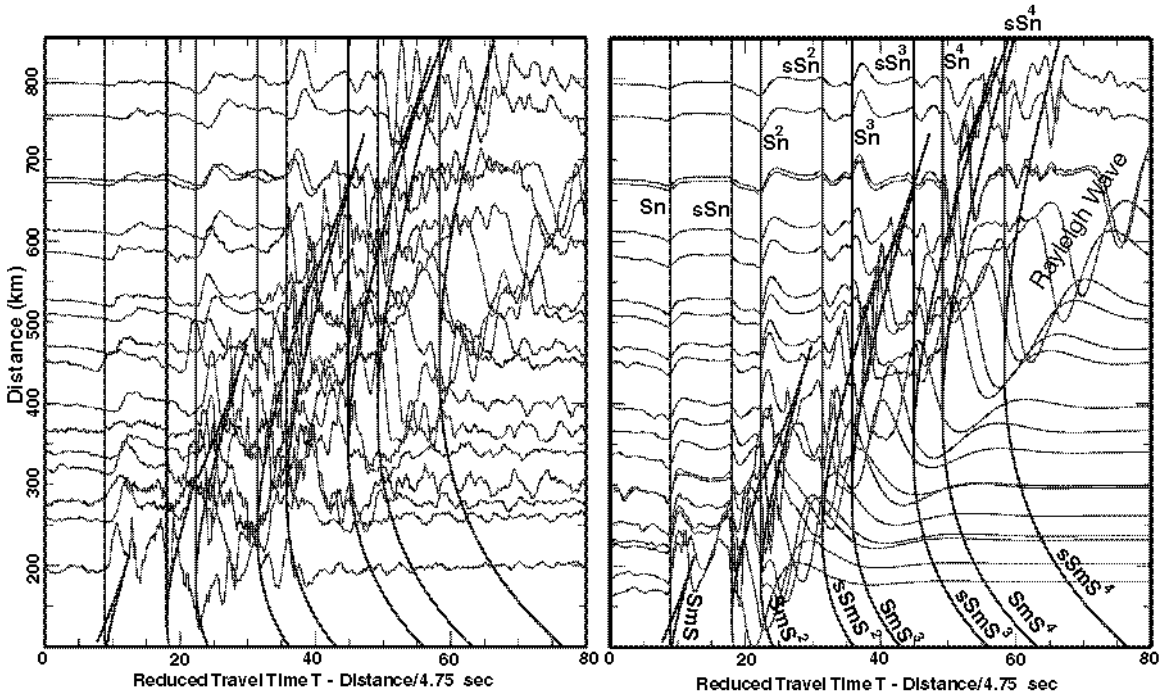

Figure 2. Reduced velocity profiles of vertical displacement data from the Rukwa earthquake and synthetic waveforms from the final inversion model for the S wave train. Travel-time curves for important S wave ray paths are superimposed on the waveform sections. These waveforms contain both Sn-type head waves and post-critical angle multiple S wave reflections.

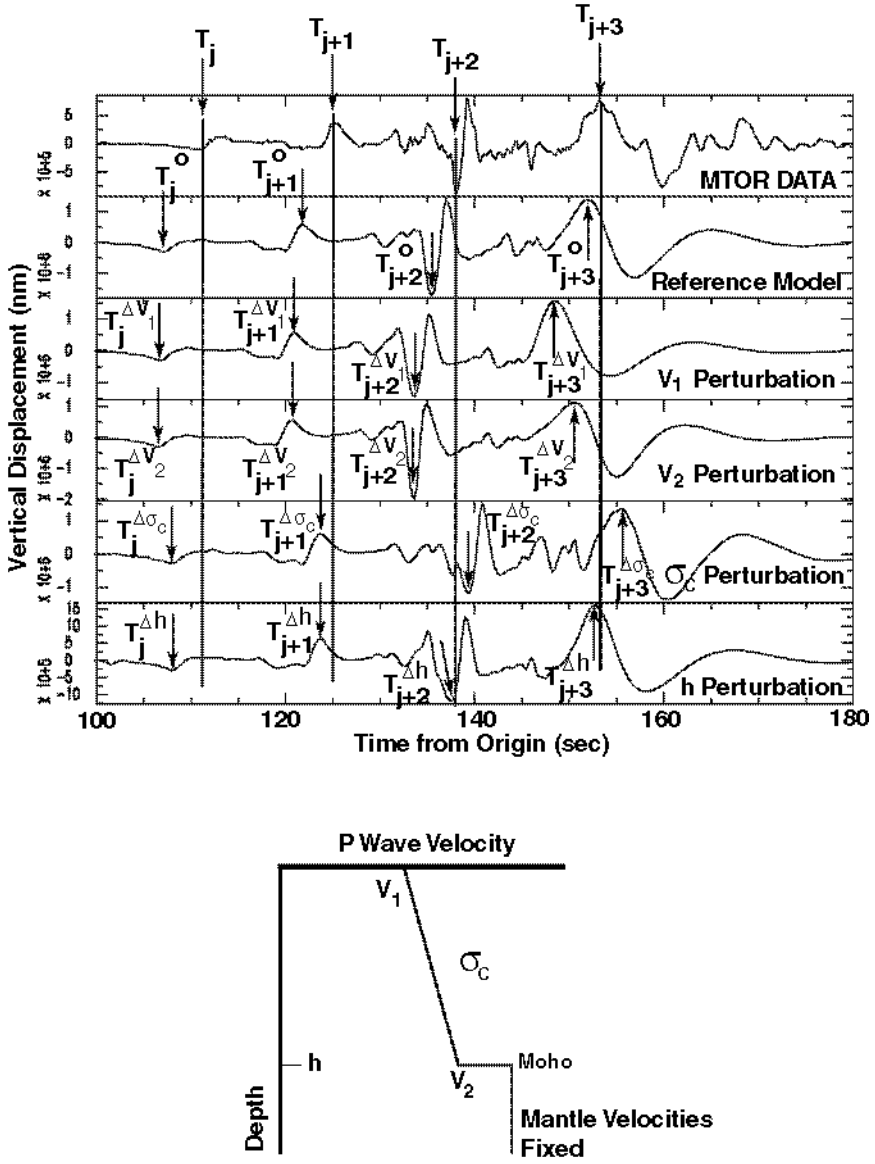

Figure 3. Illustration of picking phase times from observed and synthetic regional waveforms (top panel). Vertical component data from Kwa Mtoro (MTOR) station is shown at the top. A synthetic seismogram is shown just below ("reference model") computed using the starting earth model, and four other synthetics below that are computed using perturbations of the starting earth model. The earth model is parameterized by a linear gradient in the crust over a mantle half-space as shown in the lower panel and arrival times are a function of the assumed source and structure parameters. "Phase times" are picked using obvious peaks or troughs for various arrivals in the data. For example, each phase time shown in the figure corresponds to Sn (T_j), Sn^2 (T_{j+1}), $sSmS^2$ (T_{j+2}), and the Rayleigh wave (T_{j+3}). The corresponding peak or trough is picked on the synthetic waveforms to form the phase time residual and partial derivatives.

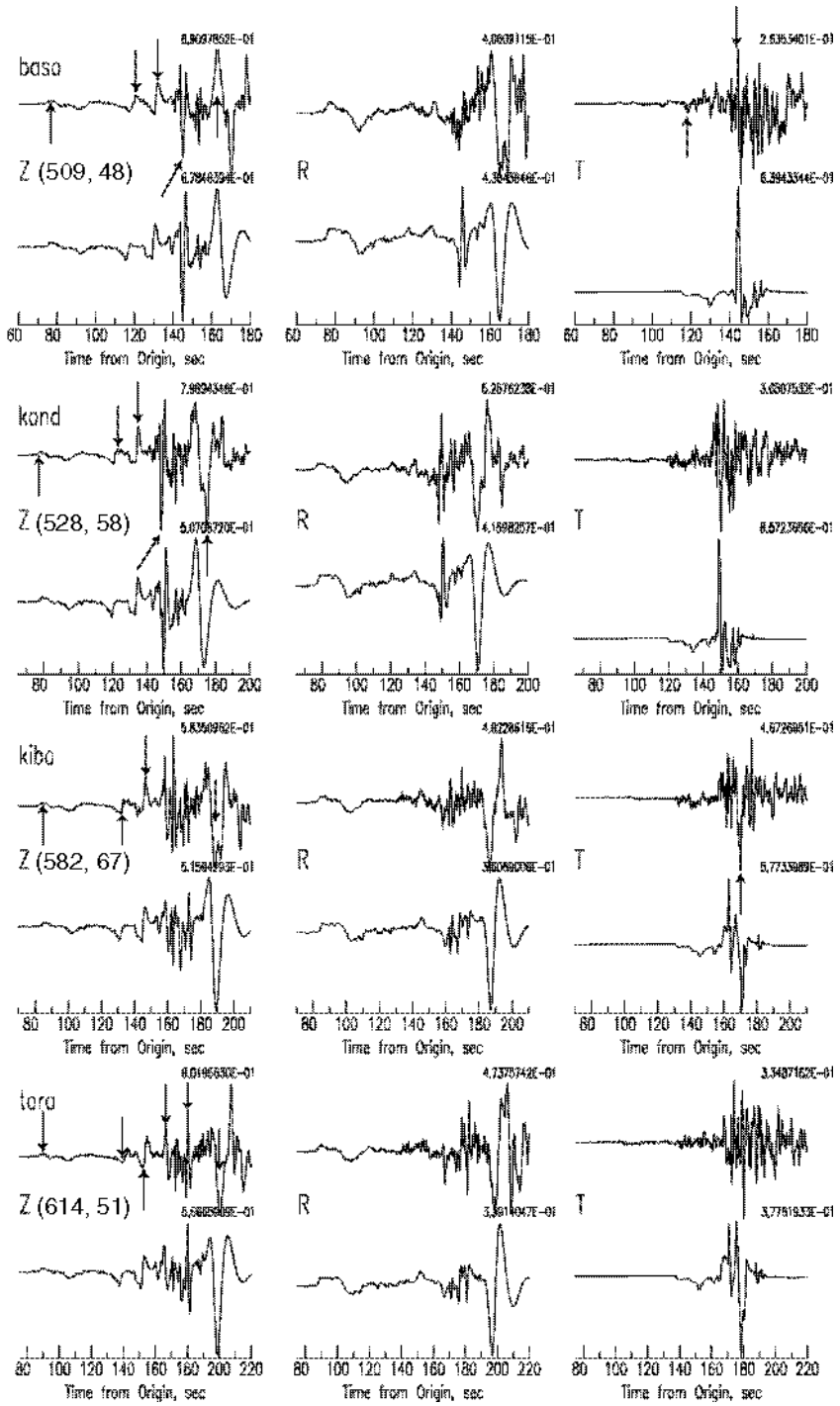

Figure 4. Observed (top) and synthetic (bottom) regional seismograms for the Lake Rukwa earthquake. Vertical (Z), radial (R), and tangential (T) waveforms are shown for each station. Station distance (km) and azimuth from the source (degrees) are shown in parentheses. Seismograms have been normalized for plotting and the absolute amplitude (microns) is given in the upper right of each seismogram. The arrows denote phase time picks used in the inversion. Note that the time scale generally changes with station distance.

A DATABASE OF DEEP SEISMIC SOUNDING PEACEFUL NUCLEAR EXPLOSION RECORDINGS FOR SEISMIC MONITORING OF NORTHERN EURASIA

Igor B. Morozov,[1] Scott B. Smithson,[1] Elena A. Morozova,[1] and Leonid. N. Solodilov[2]

University of Wyoming[1]; Center CEON, Moscow, Russia[2]

Sponsored by Defense Threat Reduction Agency

Contract No. DSWA01-98-1-0015

ABSTRACT

The database of seismic recordings of Peaceful Nuclear Explosions (PNEs) at the University of Wyoming now includes 19 PNEs recorded along 7 long-range refraction/reflection profiles: QUARTZ, CRATON, KIMBERLITE, RIFT, METEORITE, and two lines of project RUBY. The data from RUBY also include recordings of two Kazakhstan nuclear tests. This grid of reversed profiles (also with fan recoding for RUBY) covers the East European Platform, the Ural Mountains, the West Siberian Platform and the Siberian craton, and the Baikal Rift. Dense, 3-component, short-period recordings along these profiles provide practically the only reliable source of seismic information for seismic calibration of these vast aseismic regions. These recordings offer unique opportunities to study propagation effects of regional seismic phases, to examine their correlation with geologic and tectonic features, and to develop new constraints on the structure of the crust and upper mantle.

We are delivering databases of travel-time, spectral, and amplitude attributes of *P*, *S*, and *Lg* phases from PNE recordings. Dense observations of these phases at about 10- to 20-km spacings allow unusual, nearly continuous representation of the variations of their spectral properties over about 0- to 3200-km propagation ranges. Our preliminary analysis has uncovered numerous indications of strong *Lg* and other regional phases variability within the region. In order to increase robustness and versatility of the database, we provide spectral data in several forms, including the traditional (Fast Fourier Transform), multi-taper, and multi-component spectra.

We summarize our recent findings from the analysis of PNE arrivals in Northern Eurasia. These results include (1) unusually detailed velocity and attenuation structure of the crust and uppermost mantle, (2) characterization of crustal attenuation through coda measurements, (3) constraints on seismic scattering, and (4) detailed imaging of the crustal basement using receiver functions. All of these factors are of primary importance for modeling of crustal guided phases, such as the P_g and L_g. We discuss further possible extensions of this database, including a simple empirical technique for regionalization of seismic travel times and for building the source-specific station corrections for a large part of Northern Eurasia. With further analysis facilitated by the developed database, travel-time, amplitude and waveform information from PNE records will provide valuable quantitative constraints and realistic structural data for modeling of L_g and other regional phases, contributing to the development and calibration of regional seismic discriminants.

KEY WORDS: Russian Eurasia, Peaceful Nuclear Explosions, regional seismic phases

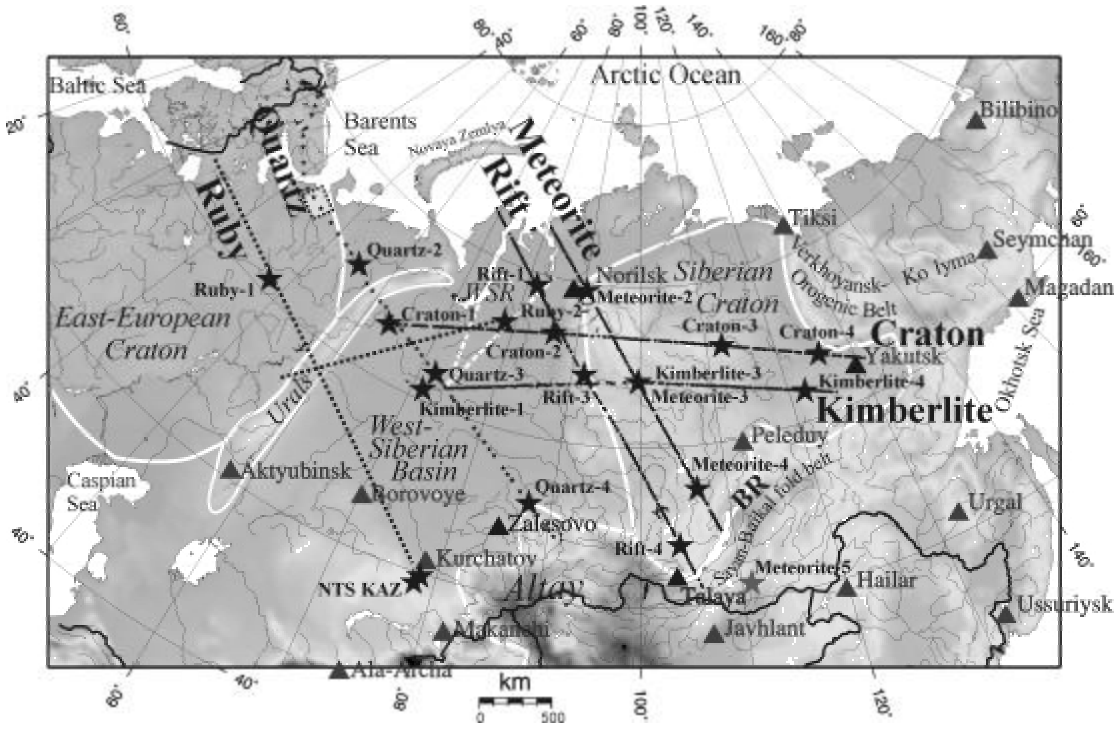

Figure 1. DSS PNE profiles under study at the University of Wyoming: QUARTZ, CRATON, KIMBERLITE, RIFT, METERORITE, and RUBY (two lines, obtained recently). Large stars are the PNEs; small stars (for profile QUARTZ only) are the chemical explosions. Profile RUBY is shown schematically. The coordinates and other parameters of the PNEs used in these profiles were reported by Sultanov et al (1999). White contours show the major tectonic units (labeled: WSR – West Siberian Rift, BR – Baikal Rift). Note the extent of systematic, continuous profiling, with PNEs detonated at the intersections of the 3000- to 4000-km-long profiles. The profiles are close to some of the IMS stations (labeled triangles). The profile QUARTZ has been studied extensively for the upper mantle and crustal structure, for seismic coda effects and crustal reverberations. The box NW of PNE QUARTZ 2 indicates the area where crustal attenuation was measured using coda amplitude analysis.

OBJECTIVE

In cooperation with Center GEON, Moscow, Russia, the University of Wyoming has obtained a substantial part of the unique Deep Seismic Sounding (DSS) data including systematic and continuous profiling of Peaceful Nuclear Explosions (PNEs) in Northern Eurasia (Figure 1). Along with reversed recording of the PNEs to over 3000-km ranges, 30 to 80 chemical explosions were recorded in each of the ultra-long profiles (Figure 1), making these datasets unparalleled in terms of both detailed coverage of the crust and upper mantle and also as comprehensive collections of seismic recordings of explosions at regional distances.

In this study, these unique seismic data are being investigated for their potential use in nuclear explosion monitoring. The importance of this research is emphasized by the great variety of the tectonic structures covered by the profiling and also by the fact that DSS recordings cover largely aseismic regions of Northern Eurasia where virtually no other data are available for seismic calibration (Figure 1). The DSS data sets contain abundant 3-component recordings of the full spectrum of regional phases that can be used in seismic calibration and discrimination.

RESEARCH ACCOMPLISHED

The discussion below can be separated into three inter-related main lines:

1. Analysis of the crustal and upper mantle structure and its effects on the propagation of seismic phases. This includes unusually detailed imaging of the velocity and attenuation structure of the crust and upper mantle and constraining of scattering properties of the crust, and development of approaches that could take advantage of the unusual properties of the DSS PNE data sets.
2. Characterization of seismic phases from the PNEs and assembling a database of parameters of these phases in a form suitable for nuclear explosion monitoring. This effort is focused on uniform treatment of the entire PNE data set and preparing grounds for regionalization of seismic discriminants computed from the different profiles.
3. As a first step of the advanced analysis in (2), empirical regionalization (at present, by interpolation) of the seismic attributes observed in different profiles and by relating these attributes to regional tectonics and to the structures revealed by seismic observations

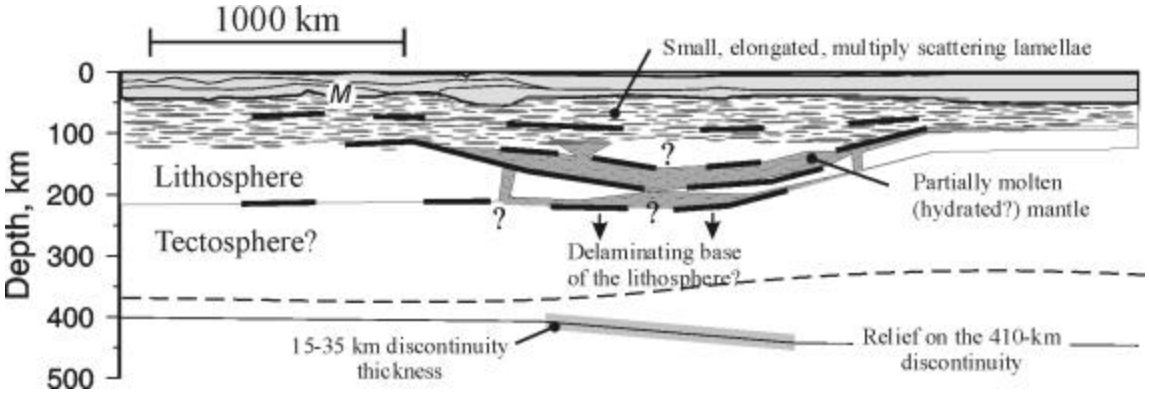

Figure 2. A collage of the recent models of the uppermost mantle derived from controlled-source seismic investigations in Northern Eurasia. The lithosphere varies in thickness between 120-220 km (Morozova et al, 1999), with significantly higher velocity than in the IASP91 model, three groups of reflecting boundaries (bold lines), and potential regions of mechanical instability of its base (Morozov et al, 1998b). The upper about 80 km[1] of the lithosphere are pervasively heterogeneous, modeled as stochastic medium with about 0.5-km vertical correlation length, ±2% to 5% velocity fluctuations, and aspect ratio of up to 50-100 (Ryberg et al, 2000; A. Ryberg and Wenzel, 1999; A. Gorman et al, in review). Due to such strong heterogeneity, seismic waves at frequencies above 5 Hz do not penetrate below this layer but form "high-frequency scattering waveguide" (SWG) modes propagating through it by means of multiple scattering[2] (Tittgemeyer et al, 1996; Ryberg and Wenzel, 1999). Below about 100-120 km, seismic scattering and increased attenuation suggest a layer of partial melting, probably initiated by the presence of fluids (Thybo and Perchuc, 1997; Morozov et al, 1998b; Nielsen et al, 1999). Both of these scattering layers are often viewed as typical in a continental lithosphere (Enderle et al, 1997; Tittgemeyer et al, 1999b; Thybo and Perchuc, 1997). An analysis of topside reflections from the transition zone discontinuities suggests their gradational character and about 20-30 km relief of the 410-km discontinuity (Priestley et al, 1994; Morozova et al, 1999).

In recent years, due to increased availability of the DSS PNE profiles, the **heterogeneity of the crust and upper mantle**, and particularly of the continental lithosphere, has been convincingly documented. Wide-angle refraction,

[1] 100-120 km in a recent 2-D modeling by Ryberg et al (2000).

[2] Probably a better name for such mantle structure would be a “diffusive screen.”

reflection, receiver function, and attenuation studies revealed strong velocity gradient and reflecting boundaries within the continental lithosphere, with broad zones containing pockets of partial melts, topography and gradational character of the transition zone discontinuities (Figure 2). Of particular importance for regional phase propagation are the abundant reflecting boundaries within about 60-150 km below the Moho and the pervasive, strong (±2-5% in velocity), small-scale ($a_z \approx 0.5$-2 km, $a_x \approx 10$-20 km) heterogeneity of the uppermost mantle (Figure 2) recently suggested from investigations of short-period seismic scattering (Ryberg et al, 1995). If confirmed, these findings could overturn both the existing petrophysical models of the upper mantle, and our understanding of the very nature of the upper-mantle seismic phases (*Pn*, *P*, *Sn*, *S*) used as the basis for nuclear test discrimination (e.g., Tittgemeyer et al, 2000). It appears that the present understanding of seismic wave propagation within the uppermost mantle is still limited and far from being mature. Predictions of *Pn* amplitudes in structures like the one shown in Figure 2 can vary by orders of magnitude and be frequency dependent, requiring sets of "source-specific amplitude corrections" for computing discriminants. Notably, for many years to come, the DSS PNE data will still represent by far the most comprehensive and insightful datasets for testing the hypotheses of short-period regional wave propagation and calibrating the discrimination models.

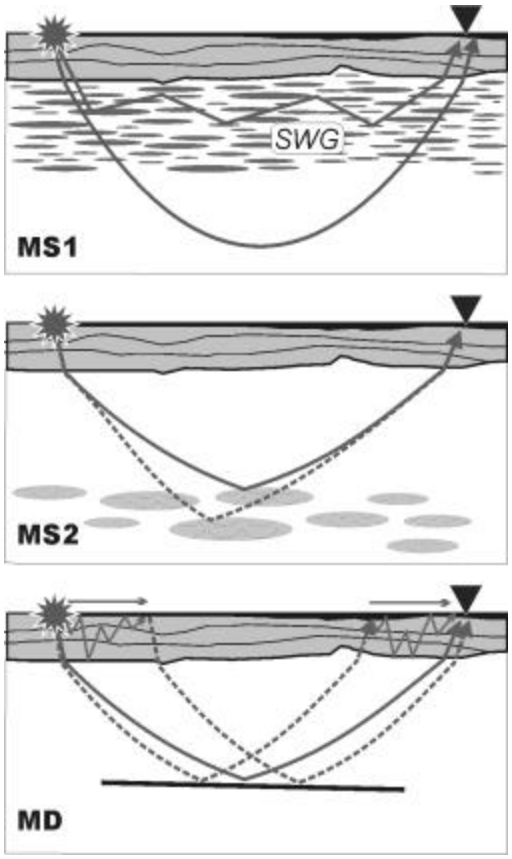

Figure 3. Three competing models of seismic scattering observed in the records from long-range refraction profiles (Figure 1): MS1: strongly scattering mantle lid; high-frequency phases reach the receivers by a diffusive scattering-waveguide (SWG) propagation (blue ray), the phases penetrating deeper lose their high-frequency energy in this layer (red ray) (Ryberg et al, 1995); MS2: the upper 80 km of the mantle is relatively transparent, single scattering occurs (possibly) on pockets of partial melt between 120-200 km; this scattering is causes an increased complexity of the first arrivals (Thybo and Perchuc, 1997); MD: the observed coda is mainly due to crustal scattering at both source and receiver ends, the mantle is "deterministic" in the sense that possible mantle scattering layers may be resolved only as apparent reflecting boundaries (Morozov and Smithson, 2000).

Until recently, PNE records were analyzed primarily with an emphasis on travel-time modeling and inversion. In this study, we switch our attention on the amplitude and waveform pattern of the PNE wavefield. By challenging the broadly accepted view of a relatively featureless upper mantle, amplitude patterns of PNE recordings make a strong impact on our understanding of wave propagation through the uppermost mantle. However, no consistent theory of the scattering and attenuation properties of the uppermost mantle was established, and the models that have been put forward often contradict each other.

A well-known controversy of this kind is the explanation of is the long-range (~2000-3000-km) *Pn* phase observed in the records from profiles QUARTZ and RUBY (Ryberg et al, 1995). Frequency content of this phase is leading to fundamental conclusions about the fine-scale structure of the upper half of the lithosphere (Figure 2). *Pn* in the $f < 5$ Hz, band is largely described by ray theory, whereas for $f > 5$ Hz, the signal appears significantly more complex.

Ryberg et al (1995) interpreted this frequency separation of the long-range *Pn* as an indication of a strongly scattering uppermost mantle, with ±5% RMS velocity fluctuations[3] having ~0.5- to 2-km vertical correlation length and a Gaussian-like spatial correlation function (Figure 3, top; Ryberg and Wenzel, 1999). However, Morozov (in press) argued that there was *no* such frequency separation, and Morozov et al (1998a,b; Morozov and Smithson, 2000) showed that a whispering-gallery (WG) model of this phase, based on a mantle velocity gradient, reflectivity, and crustal scattering could give a better explanation for the observed wavefield and could also help constrain details of the lithospheric structure. Independently of this discussion, Thybo and Perchuc (1997) and Nielsen et al (1999, and two papers in review) analyzed perturbations of the first arrivals from explosions between the offsets of 800 – 1400 km and suggested a source of scattering below about 100 – 140 km within the mantle (Figure 3, middle) in general agreement with the findings by Morozov et al (1998b). Similar models of mantle scattering were also derived from the North American Deep Probe data (Gorman et al, in review); nevertheless, these models were also criticized for their disregard of crustal scattering (Morozov and Smithson, 2000).

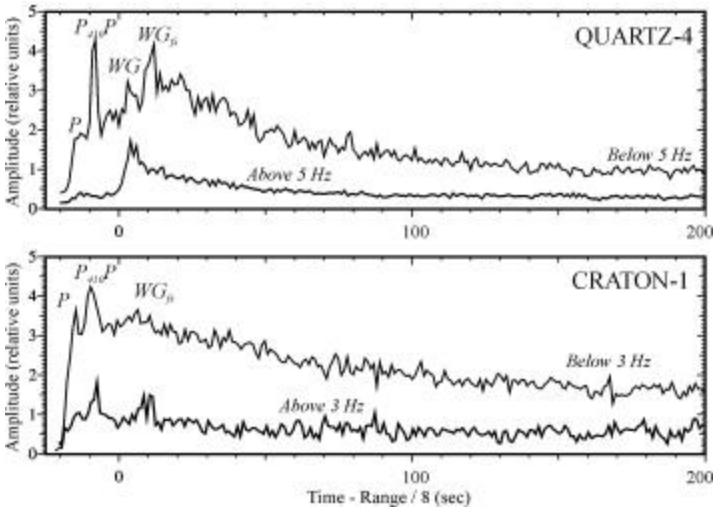

Figure 4. Amplitude of the high-frequency and low-frequency (filter corner frequency is 5 Hz for QUARTZ and 3 Hz for CRATON) records within the offset range 2500 - 2600 km from PNE QUARTZ-4 and CRATON-1 (modified from Morozov and Smithson, in press). Time reduction is 8 km/s, and 7 three-component instantaneous trace amplitude records were averaged within a 2-s sliding time window and within the offset range (Morozov and Smithson, 1996) was used. First arrivals, a reflection from the 410-km discontinuity, and two whispering-gallery phases (*WG* and WG_{fs}) are indicated. Note the difference of the codas following the free-surface multiple refraction WG_{fs} at low frequencies and the Moho multiple *WG* at high frequencies. Note the about 150-sec-long codas following the arrivals; also note the differences in these codas between the high- and low-pass filtered records.

Crustal scattering, however, appears to be a primary factor in the observed PNE wavefield (Figure 3, bottom; Morozov and Smithson, 2000). Crustal $Q_P \approx 270 \cdot f^{0.3}$ accounts for the frequency-dependent codas following the PNE arrivals at about 2500 km from the PNE QUARTZ-4 (Figure 4), confirming our association of the PNE coda effects with crustal, preferably $P \rightarrow L_g$ or $L_g \rightarrow P$ scattering (Singh and Herrmann, 1983; Dainty, 1990). Such comparatively low values of *Q* might be related to the effect of the thick sedimentary cover of the Pechora basin sampled by the part of the profile used in this analysis (Morozova *et al*, 1999). Figure 4 also shows that the two whispering-gallery (*WG*) multiples forming the long-range P_n are clearly distinct in the character of their codas. The first, Moho multiple labeled *WG* in Figure 4 is followed by a coda that dominates the high-pass filtered record. However, in the low-frequency band, the strongest phase is the free-surface P_n multiple (WG_{fs}) followed by its coda. The higher amplitude of the WG_{fs} event is consistent with higher reflectivity of the free surface compared to the Moho. The longer and low-frequency coda of WG_{fs} suggests a predominance of surface waves that propagate efficiently at lower frequencies and are progressively more attenuated as the frequency increases; this observation points again to a crustal origin of the coda. Moreover, the coda decay rates for QUARTZ-4 and CRATON-1 appear to be different

[3] This estimate was recently reduced to ±2% variations, but with a thicker scattering layer (100-120 km), based on 2-D simulations (Ryberg et al, 2000). However, this new modelling is still based on unrealistic, featureless upper crust, and does not take into account the high-velocity, high-gradient upper mantle under the East European Platform that is strongly different from the upper mantle in Siberia and from the global average.

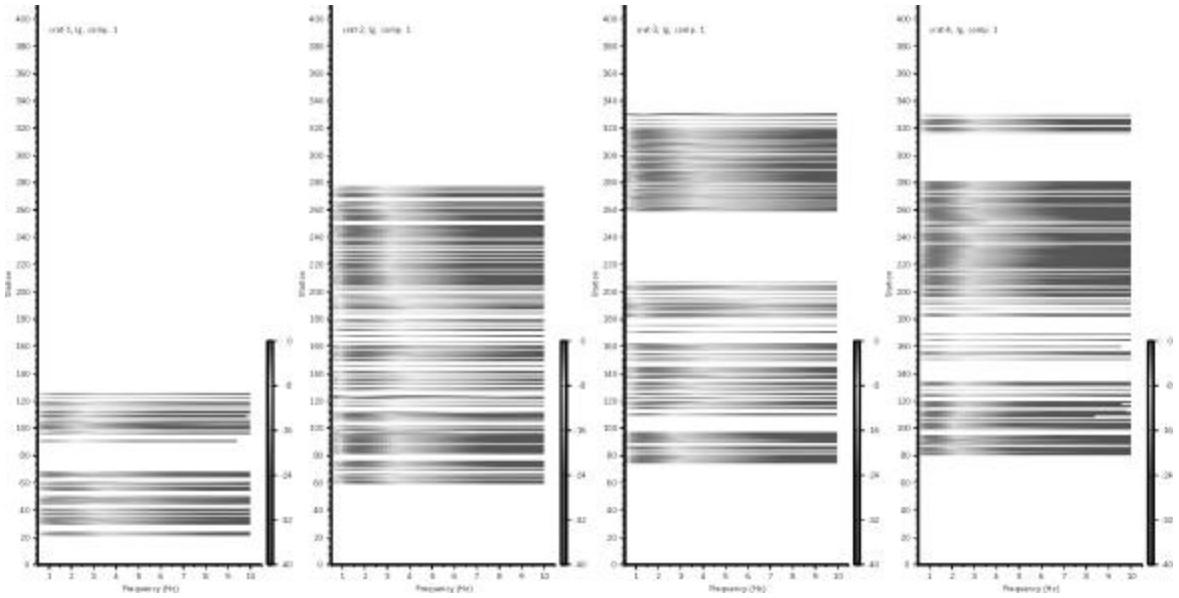

Figure 5. Lg spectra from the four CRATON PNEs from individual recording stations and for the inline component of recordings. Gray-shade levels correspond to the amplitude levels below the RMS values within the same windows, in dB.

indicating a variation in crustal properties along the profiles (Figure 1); this difference will be quantified in a detailed study in the future.

With much more DSS PNE data available for analysis than before, **a database of amplitude and spectral parameters** derived in a uniform manner is required. Such a database is being built at present using a set of approaches and tools designed in our analysis of the QUARTZ data set. The attributes stored in this database include:

1. Travel times of the *S* waves and *Lg* picked from the PNE sections.
2. Instantaneous amplitude envelops of the individual components and 3-component instantaneous polarization vectors of the corresponding windowed arrivals (Morozov and Smithson, 1996). The 3-component amplitude measures produce amplitude estimates that are more stable in respect to near-receiver scattering (Kennett, 1993).
3. Spectra of the *P*, *S*, and *Lg* waves. We provide both Fast Fourier Transform (FFT) spectra and smoothed, multiple taper spectra (Atkinson and Mereu, 1992). The multiple taper spectra are known to provide statistically stable spectral estimates. Both types of spectra are computed for all three individual components of ground motion and for 3-component amplitudes, thereby further increasing their stability (Figure 5).
4. Estimates of pre-shot and end-of-the-record noise (>300-sec after the first arrivals). These are measured using the same amplitude and spectral estimators as applied to event windows.

We expect that this database will serve as a primary source of data for discrimination studies using these PNE data before the full records become broadly available[4]; however, even after that, the database would provide useful additional attributes that can be directly used in computing seismic discriminants.

Utilizing high density and large number of recordings, the spectral data can be presented not only in its conventional form, as spectra recorded at the individual channels (Figure 5), but also as a nearly continuous spectrogram of the

[4] With funding provided by DTRA and NSF, full PNE and chemical explosion records from 9 DSS long-range projects including all of those shown in Figure 1 will become broadly available through IRIS DMC within the next four years.

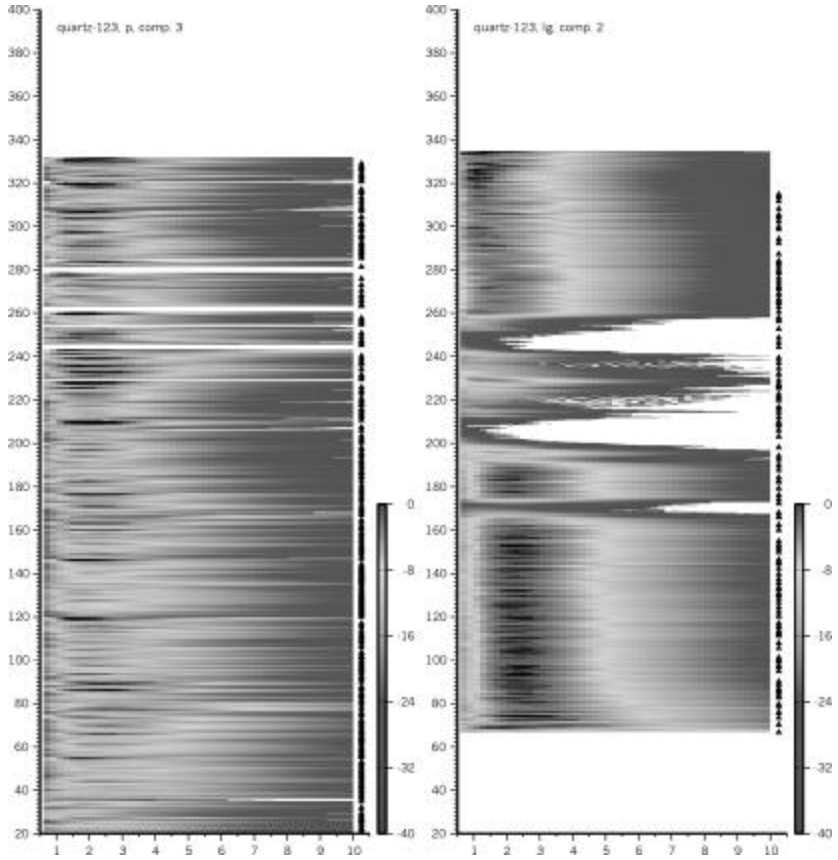

Figure 6. Three-component spectrograms for *P*-wave and *Lg* waves from PNE QUARTZ-2. The triangles on the right of each of these plots indicate the starts of the event windows used for spectral analysis. For each of these windows, a spectrogram was built using multiple Butterworth filtering. Because of the high density of the records, the resulting spectrograms overlap in time, resulting in a nearly continuous, time-frequency representation of wave propagation.

entire wave propagation (Figure 6). Such representation of wave propagation might be particularly useful for comparisons with numerical modeling, which is planned for a future study.

Uniform geographic coverage of the profiles crossing a broad range of tectonic provinces suggests **direct methods of seismic regionalization**. The existing empirical (as opposed to model-based) travel-time regionalization techniques usually rely on (1) classification of the target region in terms of tectonic provinces; (2) assignment of a single regional travel-time curve (TTC) to each of these provinces; (3) using an heuristic interpolation formula to interpolate between these 1-D TTCs when the source and receiver are located in different regions. Although this procedure is simple and robust, offering an efficient way to interpolate between a few 1-D TTCs, its greatest weakness lies in propagation of constant shallow velocity structures across vast regions. In contrast, dense DSS recordings result in numerous high-quality first-arrival TTCs associated with the areas of Northern Eurasia (Figure 1), and we can formulate a regional *P*-wave travel-time model honoring the regional variability of the travel times.

To derive a regional travel-time model, we perform direct spatial interpolation of the travel-time data, also employing heuristic interpolation rules. Interpolation is performed within common-offset sections, and therefore our regionalization is offset-dependent. For any given source-receiver offset, each travel-time pick is associated with the corresponding source-receiver midpoint, and the travel times are interpolated between these midpoints, resulting in a common-offset travel-time field (Figure 7). Computed for a range of offsets, these travel-time fields form a 3-D travel-time cube in latitude/longitude/offset space comprising our regional first-arrival travel-time model. Note that

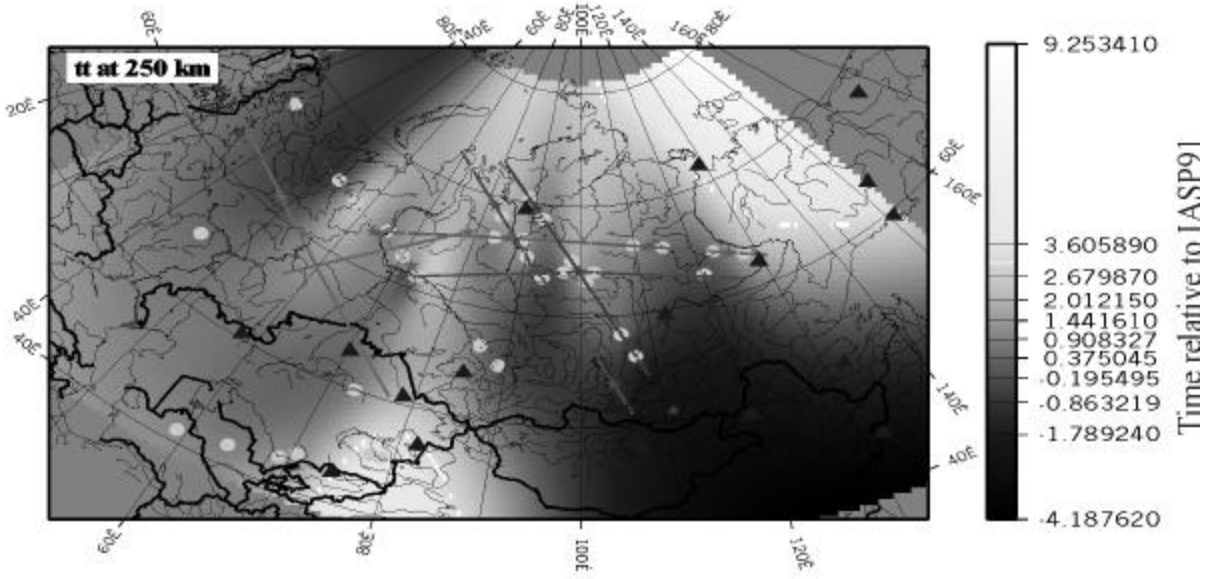

Figure 7. Interpolated travel-time field for offset equal 250 km from DSS travel-time picks. The travel-time data used here include the first-arrival travel times from the PNEs (without RUBY) and from published DSS interpretations of regional DSS profiles, primarily in Kazakhstan (compiled by V. Khalturin, personal communication). Gray dots indicate the positions of the midpoints. A set of similar surfaces built for a range of offsets forms a 3-D travel-time cube that can be used as a regional travel-time model. Black triangles indicate the IMS stations.

such regionalization is more detailed at shorter offsets; in particular, the zero-offset travel-time section corresponds to station statistics.

For a selected station location, by making a conical slice through this travel-time cube, we obtain predicted travel times from any point within the region to that station. These predicted travel times form the source-specific station correction (SSSC) that can be used in station calibration; Figure 8 shows such a surface for a station at Borovoye in Kazakhstan. An advantage of such a way of obtaining SSSCs is in its straightforward manner, its ability to build a correction surface for any location, and on its honoring the observed regional travel times rather than the IASP91 model (which is known to be grossly unsatisfactory at regional distances in Northern Eurasia). With an inclusion of the travel-time picks made at the station, the SSSC can be further improved.

In future research, we plan to improve the above interpolation procedure in several ways: (1) by reducing propagation of the near-offset travel-time perturbations (caused by the near-source and near-receiver structures) to large offsets; (2) by introducing a stochastic mechanism of error estimation; (3) by extension of the procedure to mapping other attributes, such as the values of seismic discriminants.

CONCLUSIONS AND RECOMMENDATIONS

1. DSS studies of the ultra-long-range profiles have demonstrated strong crustal and upper mantle heterogeneity that may be of primary importance for explaining the amplitudes and spectra of regional phases used in seismic monitoring.
2. The database of amplitude and spectral attributes of the seismic phases from 19 PNEs recorded in 7 ultra-long refraction profiles would provide a comprehensive source of information for regionalization of *Lg*, *P*- and *S*-wave, and crustal scattering properties in Northern Eurasia.
3. Joint analysis of the data from the entire PNE dataset results in a straightforward, empirical scheme of travel-time regionalization that can be extended to regionalization of seismic discriminants.

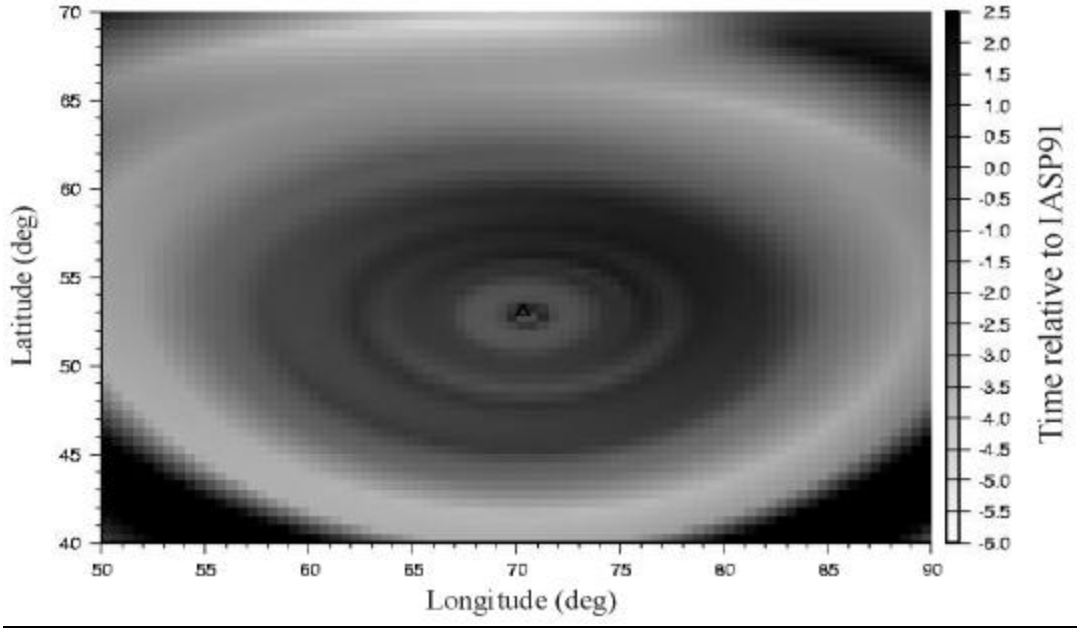

Figure 8. Preliminary source-specific station correction surface for station at Borovoye, Kazakhstan, extracted from the 3-D travel-time cube illustrated in Figure 7.

REFERENCES

Atkinson, G. M., and R. F. Mereu (1992), The shape of ground motion attenuation of curves in Southeaastern Canada, Bull. Seism. Soc. Am., 82, 2014-2031.

Dainty, A. M. (1990), Studies of coda using array and three-component processing, PAGEOPH, 132, 221-244.

Gorman, A.R., R.M. Clowes, R.M. Ellis, T.J. Henstock. G.D. Spence, G.R., Keller, A.R. Levander, C.M. Snelson, M.J.A. Burianyk, E.R. Kanasewich,, I. Asudeh, Z. Hajnal and K.C. Miller (2001). Deep Probe - Imaging the roots of western North America. Canadian Journal of Earth Sciences. In review.

Kennett, B. L. N. (1993), The distance dependence of regional phase discriminants, Bull. Seismol. Soc. Am., 83, 1155-1166.

Kennett, B. L. N. (1987), Observational and theoretical constraints on crustal and upper mantle heterogeneity, Phys. Earth Planet. Interiors, 47, 319-332.

Morozov, I. B. (2001), Comment on "High-frequency wave propagation in the uppermost mantle" by T. Ryberg and F. Wenzel, J. Geophys. Res., in press.

Morozov, I. B., and S. B. Smithson (1996), Instantaneous polarization attributes and directional filtering, Geophysics, 61, 872-881.

Morozov, I., B., E. A. Morozova, and S. B. Smithson (1997), Observation of Lg and S wave propagation along the ultra-long profile "Quartz", Russia, in: Fuchs, K. (Ed.) Upper mantle heterogeneities from active and passive seismology, Kluwer, pp. 147-154.

Morozov, I., B., E. A. Morozova, and S. B. Smithson (1998a), On the nature of the teleseismic Pn phase observed in the recordings from the ultra-long profile "Quartz", Russia, Bull. Seism. Soc. Am., 88, 62-73.

Morozov, I., B., E. A. Morozova, S. B. Smithson, and L. N. Solodilov (1998b) 2-D image of seismic attenuation beneath the Deep Seismic Sounding profile QUARTZ, Russia, Pure Appl. Geoph, 153, 311-343.

Morozova, E. A., I. B. Morozov, S. B. Smithson, and L. N. Solodilov (1999), Heterogeneity of the uppermost mantle beneath the ultra-long range profile "Quartz," Russian Eurasia, J. Geophys. Res., 104 (B9), 20,329-20,348.

Nielsen, L., H. Thybo, and L. Solodilov (1999), Seismic tomographic inversion of Russian PNE data along profile Kraton, Geoph. Res. Lett., 26, 3413-3416.

Enderle, U., M. Tittgemeyer, M. Itzin, C. Prodehl, and K. Fuchs (1997), Scales of structure in the lithosphere - Images of processes, Tectonophysics, 275, 165-198.

Ryberg, T., and F. Wenzel (1999), High-frequency wave propagation in the uppermost mantle, J. Geophys. Res., 104, 10,655-10,666.

Ryberg, T., K. Fuchs, A. V. Egorkin, and L. Solodilov (1995), Observations of high-frequency teleseismic P_n on the long-range Quartz profile across northern Eurasia, J. Geophys. Res., 100, 18151-18163.

Ryberg, T., M. Tittgemeyer, and F. Wenzel (2000), Finite-difference modelling of *P*-wave scattering in the upper mantle, Geophys. J. Int, 141, 787-800.

Morozov, I. B., and S. B. Smithson (2000), Coda of long-range arrivals from nuclear explosions, Bull. Seism. Soc. Am., 90, 929-939.

Thybo H. and E. Perchuc (1997), The seismic 8º Discontinuity and Partial Melting in Continental Mantle, Science, *275*, 1626-1629.

Priestley, K. F., J. Cipar, A. Egorkin, and N. I. Pavlenkova (1994), Upper-mantle velocity structure beneath the Siberian Platform, Geophys. J. Int., 118 (2), 369-378.

Singh, S., and R. B. Herrmann (1983), Regionalization of crustal coda *Q* in the Continental United States, J. Geophys. Res., 88, 527-538.

Sultanov, D. D., J. R. Murphy, and Kh. D. Rubinstein (1999), A seismic source summary for Soviet Peaceful Nuclear Explosions, Bull. Seism. Soc. Am., 89, 640-647.

Tittgemeyer, M., F. Wenzel, K. Fuchs, and T. Ryberg (1996), Wave propagation in a multiple-scattering upper mantle—observations and modeling, Geophys. J. Int., 127, 492-502.

Tittgemeyer, M., F. Wenzel, T. Ryberg, and K. Fuchs (1999), Scales of heterogeneities in the continental crust and upper mantle, Pure and Applied Geophysics. 156, 1-2, 29-52.

Tittgemeyer, M., F. Wenzel, and K. Fuchs (2000), On the nature of *Pn*, J. Geophys. Res., 105, 16,173-16,180.

REGIONAL CODA MAGNITUDES IN CENTRAL ASIA AND *mb(Lg)* TRANSPORTABILITY

W.S. Phillips, H.J. Patton and H.E. Hartse
Los Alamos National Laboratory

K.M. Mayeda
Lawrence Livermore National Laboratory

Sponsored by the National Nuclear Security Administration
Office of Nonproliferation Research and Engineering
Office of Defense Nuclear Nonproliferation

Contract No. W-7405-ENG-36

ABSTRACT

Local and near regional coda have been shown to provide accurate and precise estimates of source, path and site effects. Using empirical methods, we investigate the use of coda to determine moments and magnitudes using regional distance (to 2500 km) data from 21 stations in central Asia and China. We find source levels for bands between 33 s and 8 Hz from events recorded at Urumchi (WMQ) to be a factor of two more consistent for coda than for direct waves, for bands outside the microseism range. However, the anticipated path averaging of regional coda is insufficient to remove bias in all but the lowest frequency bands. We correct for path bias by spatially interpolating coda levels relative to m_b(PDE). For higher bands (1 Hz), the spatial correction patterns vary by an order of magnitude and are similar to patterns obtained using direct L_g. For the lowest band (20-33 s) the maximum spatial variation shrinks to under a factor of 4 and changes sign, reflecting effects other than crustal Q. Thus, the low frequency coda could be useful for correcting for source effects in empirical or tomographic path studies, which is currently performed using m_b. After removing path bias from coda measurements, we find that amplitude measurement consistency between all 21 stations varies considerably from pair to pair (σ = 0.12 to 0.37), with longer interstation distance, low-Q surroundings and poor site conditions yielding the least stable measurements. CMT based moments (Mw) derived from 20-33 s WMQ coda are verified by comparing with moments derived from waveform fitting studies (σ = 0.18).

We continue investigations into the transportability of regional magnitudes using the $m_b(L_g)$ scale devised by Nuttli. Previous work has shown that $m_b(L_g)$ is portable for earthquakes provided that L_g attenuation is well calibrated for propagation paths. In this study, our focus shifts to explosion sources, and the question of transportability of $m_b(L_g)$ for different test sites. We revisit Nuttli's results, which were based on observations at far-regional and teleseismic distances, and depended critically upon accurate knowledge of the L_g Qo. In this paper, measurements of $m_b(L_g)$ are reported for stations within 1000 km, and as such, errors due to uncertainties in the path correction are smaller than was the case for Nuttli's measurements.

KEY WORDS: magnitude, regional monitoring, $m_b(L_g)$, coda

OBJECTIVES

We test the ability of coda methods to reliably estimate moment and magnitude at regional distances in central Asia and China. The methods of Mayeda *et al*. (2000) are extended to account for regional path variation and relative site terms in a multiple station approach. Further, we study the applicability of M_s-m_b discrimination to regional distances through investigations of $m_b(L_g)$ transportability and physical basis.

RESEARCH ACCOMPLISHED

Coda Studies. The stability of coda, with respect to path, has been well documented at local distances. The stability, or uniform coda shape, is consistent with the model of coda as the superposition of waves backscattered from random heterogeneities in the earth's crust and upper mantle (Aki, 1969). Thus, coda reflect path-averaged properties of a given region. The coda stability allows the isolation of relative, radiation-pattern averaged source

effects apart from site and path effects. The numerous independent measurements that can be made in the coda result in a high precision, allowing a single station to yield results comparable to a network average. These techniques were used to estimate absolute source spectra and study source scaling using data from analog, spectral analyzing seismographs (Aki and Chouet, 1975; Chouet *et al*., 1978; Rautian and Khalturin, 1978; Tsujiura, 1978). In addition, coda duration was found to give stable magnitude estimates (Bisztricsany, 1958) and its use became widespread in local network operations. Furthermore, Aki (1980) proposed the use of coda amplitudes, rather than duration, to obtain higher precision magnitude estimates.

The success of coda methods with dense network, local earthquake data occurs because data in the late, or path-averaged, portion of the coda is generally available. The late coda is loosely defined to begin at twice the S-arrival time (Rautian and Khalturin, 1978), taken from observations of the point at which coda shapes begin to coalesce. This poses a problem for the use of coda at regional distances because less data is available at twice the *S* (or L_g or surface wave) arrival, so sufficient path averaging may or may not have occurred to make coda useful for estimating source spectra. However, Mayeda (1993) showed that magnitudes of NTS explosions based on regional L_g coda were a factor of 5 more stable than magnitudes based on direct L_g. In addition, Hartse *et al*. (1995) demonstrated that spectral ratio discriminants were effective using far local to near regional coda data from NTS explosions and nearby earthquakes. Finally, Mayeda and Walter (1996), showed that a Green's function technique could be used to obtain absolute spectra and study source character using regional coda from western U.S. earthquakes and explosions.

In previous work (Phillips *et al*., 2000a), we applied the empirical techniques of Mayeda *et al*. (2000) to study regional coda in the 1 Hz band at stations Makanchi (MAK), Kazakhstan, and Urumchi (WMQ) and Lanzhou (LZH), China. While the consistency between coda measurements at MAK and WMQ was found to be a factor of two better than for direct L_g, biases were noted in the measurements due to differing propagation paths.

Because we measure the coda close to the L_g arrival, we might expect path effects to be present in the results. To examine this, we interpolated distance-corrected 1 Hz coda source factors after subtracting m_b (PDE) using kriging (Phillips et al., 2000a; also included in Figure 4). Results show strong laterally varying effects that correlate well with known L_g path effects in this region (Phillips, 1999). These effects can be corrected, but the inter-station consistency improves little due to correlated adjustments.

Inter-station consistency is often used to demonstrate the stability of coda amplitude measurements. However, based on the path bias we observe and the lack of improvement in consistency after the bias is corrected for, we conclude that the interstation consistency is not sufficient to demonstrate the accuracy of coda measurements, but can be a good indicator of precision. To demonstrate accuracy, we must, instead, compare coda results with independently derived moment and magnitude results (Mayeda *et al*., 2000).

In the current study, we apply coda techniques to 13 bands, from 33 s to 8 Hz, and 21 stations in China and central Asia (Figure 1). As before, we follow the method of Mayeda *et al*., (2000). After smoothing envelopes of bandpassed seismograms, coda decay, b, is determined for a suite of records

$$A(t)=A_0\, t^{-0.7} \exp -b(\Delta)t,$$

and then expressed as a function of distance, Δ, via a hyperbolic fit. The time origin is placed at the peak envelope, accommodating different phases and group velocities for varying distance and frequency. We then obtain coda source factors (A_0) by re-fitting the coda decay data with the predicted $b(\Delta)$. The coda source factors are further corrected based on a linear fit of A_0-m_b (PDE) versus distance prior to kriging to obtain regionally varying path corrections. Kriged corrections are obtained using all data except for the measurement being corrected. Absolute spectra are then obtained using a frequency-dependent correction that produces flat low-frequency spectra below the estimated corner frequency in an average sense for a suite of events, followed by a tie to independently determined moments (CMT and/or literature values). Relative site terms are introduced based on common event measurements throughout the network, which avoids interstation discrepancies that result from poor spatial and temporal distributions of calibration events.

We obtain highest precision, in terms of interstation amplitude scatter, in bands near 1 Hz (σ = 0.13 for MAK-WMQ; Figure 2). Coda provide more consistent measurements than direct phases in nearly all bands, including the

lowest band we examined (20-33 s), with low frequency bands near the microseism range the worst performers in terms of scatter relative to direct phases and the number of measurements that pass signal-to-noise criteria. Examining all pairs of stations, we find that interstation scatter is quite variable. For example, preliminary results show 1 Hz scatter measures 0.12 between Enshi (ENH) and Xian (XAN), and 0.37 between Kunming (KMI) and LZH (Figure 3). Scatter generally increases with interstation distance, reflecting more diverse path effects, which may not have been completely accounted for. Some of the best pairs of stations lie in high-Q regions (1 Hz L_g Q > 600 from tomographic imaging; Phillips *et al*., 2000b). Recall that we have attempted to remove path effects using interpolation (kriging) methods, but this will be most successful for events from areas of high activity. Certain stations, such as LZH, yield higher scatter in many combinations, indicating the influence of site effects such as reverberation, which could contaminate the coda and cause the coda measurements to reflect amplitudes of direct waves more closely.

To validate the accuracy of coda measurements, we must compare with independently derived quantities. After calibrating 20-33 s WMQ coda using CMT moments, we compare to a collection of moments derived from waveform modeling studies, obtaining a scatter of 0.18 (Mw units).

As mentioned above, interpolated (kriged) path correction surfaces for 1 Hz coda are qualitatively similar to those of direct L_g (Figure 4). This results from inadequate path averaging of the scattered waves in the coda, causing coda amplitudes to reflect anelastic properties of the crust over a limited region surrounding the direct path. This holds for nearly all bands; however, at the lowest frequencies, the path corrections become subtle and in the lowest band (20-33 s) the pattern flips sign and is nearly anticorrelated with the 1 Hz pattern (Figure 4). The low frequency pattern cannot reflect crustal attenuation, because it is opposite to what is expected. Instead, it reflects bias in m_b, which will be affected by regionally varying attenuation in the upper mantle, or a Rayleigh wave generation term that systematically varies throughout the region. In either case, the variation is small, indicating a level of stability independent of path that could be taken advantage of in source and path studies in this region.

$m_b(L_g)$ Transportability. A major goal of regional magnitude development is to extend the applicability of M_s-m_b discrimination to smaller events. An ideal regional M_s-m_b discriminant is (1) effective at small magnitudes, (2) transportable to all geological environments, and (3) supported by a sound physical basis. Because L_g amplitudes are often the largest on regional seismograms, this phase offers the best opportunity to monitor small explosions near the detection threshold. Furthermore, O. Nuttli claimed in the 1980's that $m_b(L_g)$ is transportable to all continental areas, a claim that was never tested at the time but was generally accepted by the monitoring community by virtue of its role solving the test-site bias problem. At Los Alamos, we are continuing to develop $m_b(L_g)$ by carrying out studies of its transportability and by building a data base of calibration data for areas of monitoring interest.

It is important to stress that the development of a regional M_s-m_b discriminant represents a major paradigm shift. Instead of basing m_b on the amplitude of a *P*-wave pulse, as in the classical teleseismic discriminant, we are proposing the use of regional m_b based on mainly *S*-energy carried by L_g or coda waves. Furthermore, L_g and coda waves are complex wave trains exhibiting random spectral phase, unlike a pure pulse. For these reasons, regional M_s-m_b relationships might scale quite differently from the classical discriminant. This calls for empirical and theoretical studies to investigate scaling behavior at small magnitudes and to develop a physical basis.

For the past few years, we have studied the transportability of $m_b(L_g)$ for earthquakes and explosions. Results of earthquake studies have been presented in numerous papers, and are summarized only briefly here. Nuttli's claim of transportability depends on two factors: (1) accurate corrections for geometrical spreading and region-specific attenuation, and (2) a region-independent calibration constant used to tie the $m_b(L_g)$ scale to $m_b(P)$. The latter was calibrated only once, for central U. S., where it was found that an earthquake with $m_b(P)$ 5.0 produces a hypothetical, 1-Hz L_g amplitude of 110 microns at a reference distance of 10 km. The studies we have carried out have validated this region-independent constant, 110 microns for m_b 5, for crustal earthquakes in eastern North America, western U. S., central Asia, and central Europe (Patton and Schlittenhardt, 2000; Patton, 2001).

Our approach for testing transportability is given in Figure 5. Earthquake source and propagation phenomena are summarized inside the box in Figure 5(a). Outside the box, data analysis steps are shown: the regional wave forms are passed through a World-Wide Standard Seismographic Network response, and 1-Hz L_g waves are then corrected for Airy phase propagation and region-specific attenuation. M_w:$m_b(L_g)$ scaling relationships are developed using

independent estimates of seismic moment M_o, and statistical tests are run to see if the scaling observations in each region are consistent with a single, unifying relationship. This approach is actually more rigorous than need be since Nuttli claimed transportability of the calibration constant only, not that $m_b(L_g)$ should scale similarly too. Nevertheless, a single scaling relationship satisfies the observations for M_w 4.3 to ~6.0 in all regions tested to date. Provided that path calibration data are accurate for each region, these tests validate a region-independent calibration constant. This remarkable result suggests that excitation amplitudes of 1-Hz L_g waves are relatively insensitive to source radiation patterns and the gross physical properties of the continental crust.

It is noteworthy that a better test would have employed source "potency" instead of seismic moment since potency involves only the parameters that scale with source size, namely fault area and slip. To the extent that source region rigidity varies from one earthquake to the next, this is expected to add variance in M_w:m_b observations, but probably not enough to nullify the transportability results, at least for earthquakes located at seismogenic depths in the crust. On the other hand, the issue of potency versus seismic moment is very important for explosions, as discussed below.

Figure 5(b) summarizes the explosion source as it relates to our transportability studies. The assumption is that far-field propagation should be similar for earthquakes and explosions, and the data analysis is identical. We are faced with three candidate parameters with which to test the portability of $m_b(L_g)$ for explosions: source potency, which is simply the reduced displacement potential, Ψ_∞, seismic moment, and explosive yield, W. In the 1980's, transportability was considered with respect to (*wrt*) yield to solve the test-site bias problem, and this approach was favorable from the standpoint of yield estimation. However, to put the test "on par" with tests already conducted on earthquakes, Ψ_∞ or M_o should be used.

If we elect to test transportability on equal footing with earthquake tests, the choice between Ψ_∞ and M_o will make a difference in the outcome of test results. This is because the source medium can vary greatly for explosions, and the calculation of M_o introduces another dependence on material properties ($\rho\alpha^2$). Ψ_∞ is the fundamental seismic parameter equal to the long-period level of the explosion source spectrum, and this is the reference that should be employed to test portability of $m_b(L_g)$ for explosions detonated in different source media. Just as the choice of Ψ_∞ or M_o will make a difference in the outcome of test results, so will the choice of W or Ψ_∞. Significant differences in material strength and coupling for different media precludes the possibility of $m_b(L_g)$ from being transportable *wrt* both W and Ψ_∞. These issues about testing the portability for explosions are summarized in Figure 5(c).

Figure 6 illustrates the dependence of scaling relationships based on Ψ_∞ and M_o for explosions in hardrock environments versus explosions at the Nevada Test Site (NTS). M_w:$m_b(L_g)$ relationships compare favorably for the two testing environments, and might suggest transportability for explosions, as this was the basis for such conclusions for earthquakes. Ψ_∞:$m_b(L_g)$ relationships lead to quite the opposite conclusion. The method used to derive Ψ_∞:$m_b(L_g)$ relationships is explained in the figure caption. The Ψ_∞:$m_b(L_g)$ relationship for NTS explosions was confirmed using cavity radius information (see caption).

Comparisons between Ψ_∞:$m_b(L_g)$ relationships suggest that, for the same long-period level of the source spectrum, 1-Hz L_g waves from hardrock explosions are over a factor of 3 larger than L_g waves from NTS explosions. This result is counter-intuitive since the excitation of *P*- and *S*-waves is larger in weaker, more compliant materials. Thus, elastic theory would predict that amplitudes should be larger for NTS explosions. Explosion source phenomenology (Figure 5(b)) is complex, and spectral differences or secondary sources might be significant enough to explain this anomaly. However, for a number of reasons not discussed here because of length restrictions, we believe that effects of spectrum and secondary sources are probably insufficient to offset effects of elastic excitation and account for an additional factor of 3 in amplitude.

CONCLUSIONS AND RECOMMENDATIONS

Coda estimates show up to a factor of 2 improvement in inter-station consistency relative to direct L_g, for most bands (33 s to 8 Hz) and are best for closely spaced central Asia and Chinese stations located in areas of high crustal Q. The interstation consistency reflects the precision of the coda measurement, but not necessarily its accuracy. Accuracy is verified by comparing with independently determined moments; we obtain a scatter of 0.18 (Mw) for moments from low frequency coda at station WMQ. For purposes of calibration, additional independently derived moments for low magnitude events are critical to the success of the coda method.

Studies of M_w:$m_b(L_g)$ scaling relationships for regions around the world have validated the transportability of $m_b(L_g)$ for earthquakes. For explosions, we are faced with testing portability *wrt* yield or *wrt* Ψ_∞. Using measurements of $m_b(L_g)$ reported by Nuttli for explosions in hardrock environments, the Ψ_∞:$m_b(L_g)$ relationship is anomalous compared to the relationship for NTS. The problem could be with Nuttli's measurements since they were taken on old analog data for stations at teleseismic distances, and for such long distances, path calibration data had to be known very accurately. We are continuing our investigations of explosion transportability with regional data for stations much closer to the explosion source and with better calibration data.

REFERENCES

Aki, K. (1969), Analysis of the seismic coda of local earthquakes as scattered waves, *J. Geophys. Res.*, **74**, 615-631.

Aki, K., (1980), Physical basis of the duration magnitude and recommended practice for coda magnitude determination, *Proc. 17th Ass. ESC, Budapest*, 73-77.

Aki, K., M. Bouchon and P. Reasonberg (1974), Seismic source function for an underground nuclear explosion, *Bull. Seism. Soc. Am.*, **64**, 131-148.

Aki, K. and B. Chouet (1975), Origin of coda waves: Source, attenuation and scattering effects, *J. Geophys. Res.*, **80**, 3322-3342.

Bisztricsany, E.A. (1958), A new method for the determination of the magnitude of earthquakes, *Geofiz. Kozlem.*, **7**, 2.

Chouet, B., K. Aki and M. Tsujirua (1978), Regional variation of the scaling law of earthquake source spectra, *Bull. Seism. Soc. Am.*, **68**, 59-79.

Hartse, H.E., W.S. Phillips, M.C. Fehler and L.S. House (1995), Single-station spectral discrimination using coda waves, *Bull. Seism. Soc. Am.*, **85**, 1464-1474.

Mayeda, K. (1993), MbLgcoda: A stable single station estimator of magnitude, *Bull. Seism. Soc. Am.*, **83**, 851-861.

Mayeda, K., A. Hofstetter, W.R. Walter and A. Rodgers (2000), Stable source estimates using regional narrow band coda envelopes: Application to CTBT monitoring and seismic hazard prediction in the Middle East region, *Seism. Res. Lett.*, **71**, 209-210.

Mayeda, K. and W.R. Walter (1996), Moment, energy, stress drop and source spectra of western United States earthquakes from regional coda envelopes, *J. Geophys. Res.*, **101**, 11195-11208.

Phillips, W.S. (1999), Empirical path corrections for regional phase amplitudes, *Bull. Seism. Soc. Am.*, **89**, 384-393.

Phillips, W.S., H.E. Hartse and K.M. Mayeda (2000a). Regional coda magnitudes in central Asia, *22nd Seismic Research Symposium*, New Orleans, 107-113.

Phillips, W.S., H.E. Hartse, S.R. Taylor and G.E. Randall (2000b). 1 Hz Lg Q tomography in central Asia, *Geophys. Res. Lett.*, **27**, 3425-3428.

Patton, H.J. and J. Schlittenhardt (2000). Network measurements of Nuttli's mb(Lg) in central Europe: Tests of regional transportability and comparisons with teleseismic mb. *EOS Trans. AGU*, **81**, F845, (also LAUR-00-4163).

Patton, H.J. (2001). Regional magnitude scaling, transportability and Ms:mb discrimination at small magnitudes, *Pure Appl. Geophys., Special Volume on Monitoring a Comprehensive Nuclear-Test-Ban Treaty*, **in press** (also LAUR-99-6705).

Rautian, T.G. and V.I. Khalturin (1978), The use of the coda for determination of the earthquake source spectrum, *Bull. Seism. Soc. Am.*, **68**, 923-948.

Tsujiura, M. (1978), Spectral analysis of the coda waves from local earthquakes, *Bull. Earth. Res. Inst., U. Tokyo*, **53**, 1-48.

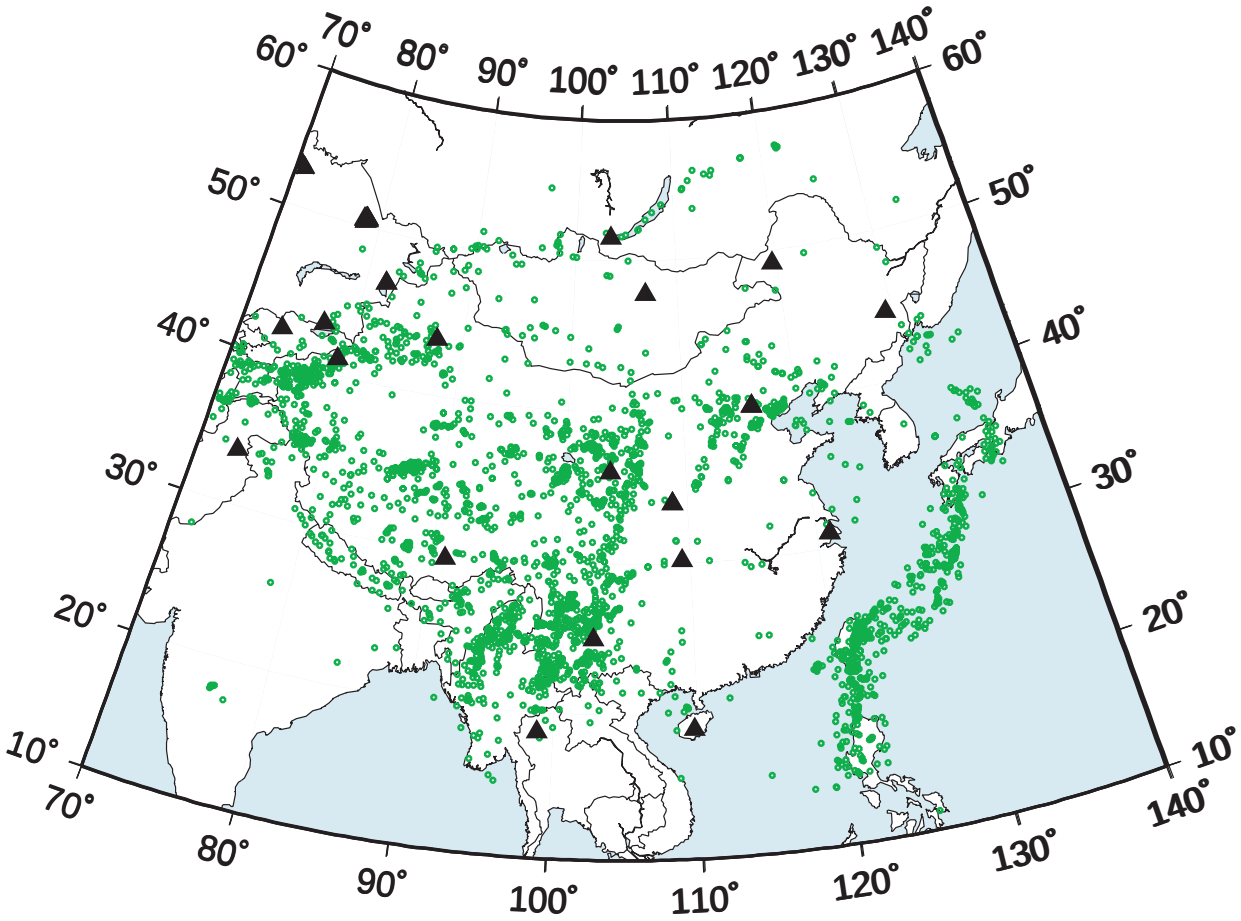

Figure 1. 21 Stations (triangles) and 7400 events (dots) used in the coda study. This data set yielded over 14,000 records, or approximately two per event on average.

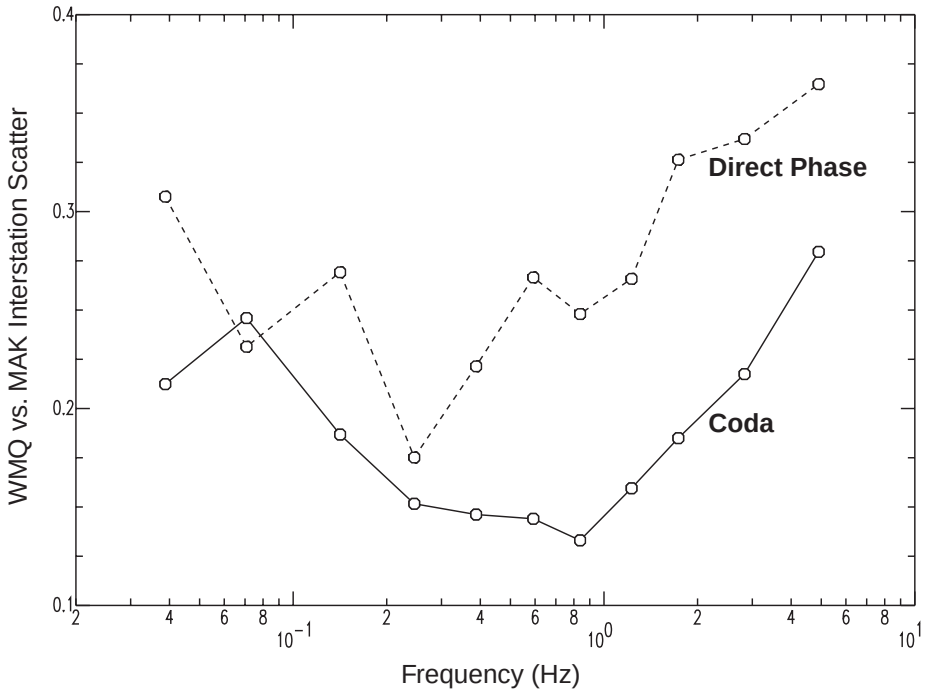

Figure 2. Interstation amplitude scatter for coda (solid line) and direct phases (S, L_g, surface waves; dashed line). Scatter is quantified by the standard deviation of differences between measurements made for common events at stations MAK and WMQ.

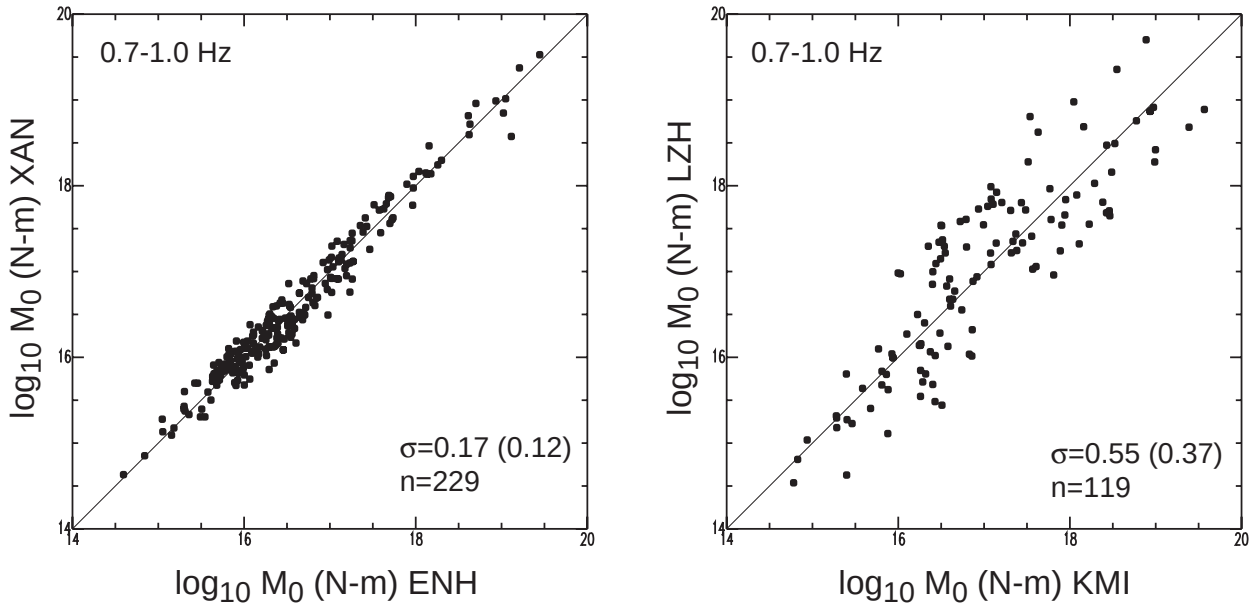

Figure 3. Consistency of coda amplitude measurements between stations ENH and XAN (left) and stations KMI and LZH (right), representing best and worst case pairs in our data set, respectively. These measurements are for the 0.7-1.0 Hz band, and amplitudes have been converted to moment estimates using scaling formulae based on m_b before calibration via CMT estimates. Scatter (see Figure 2 caption) is noted for log Mo and Mw (in parenthesis) quantities, along with the number of common events.

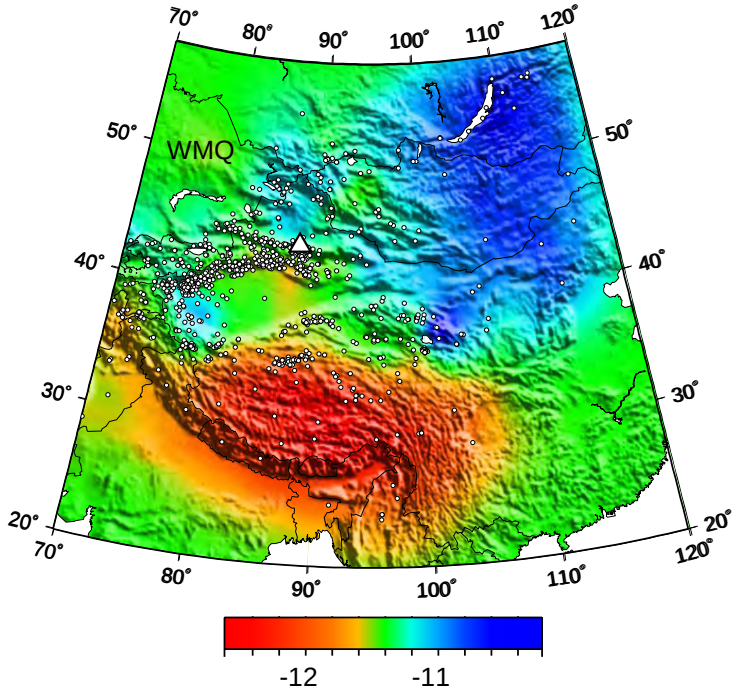

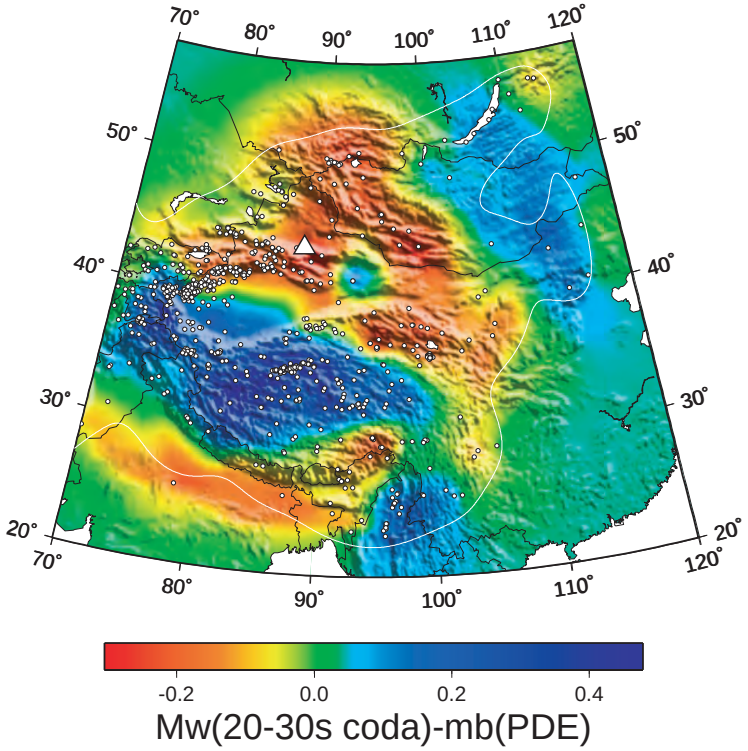

Figure 4. WMQ Coda amplitude (0.7-1.0 Hz; top) and coda Mw (20-33s; bottom) relative to m_b(PDE) obtained by kriging. Color bars represent different scales. Station WMQ is represented by a triangle, and events are represented by small dots.

Testing Portability of mb(Lg) –

(a) **Earthquake** Source and Regional Wave Propagation

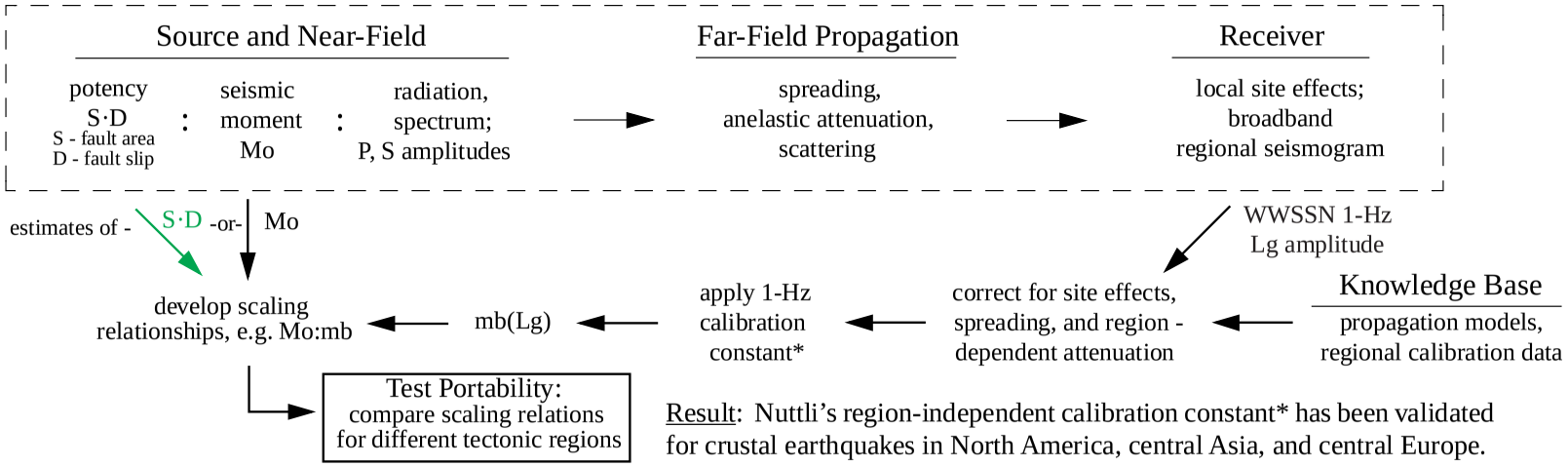

Result: Nuttli's region-independent calibration constant* has been validated for crustal earthquakes in North America, central Asia, and central Europe.

(b) **Explosion** Source Phenomena and Propagation (same as above)

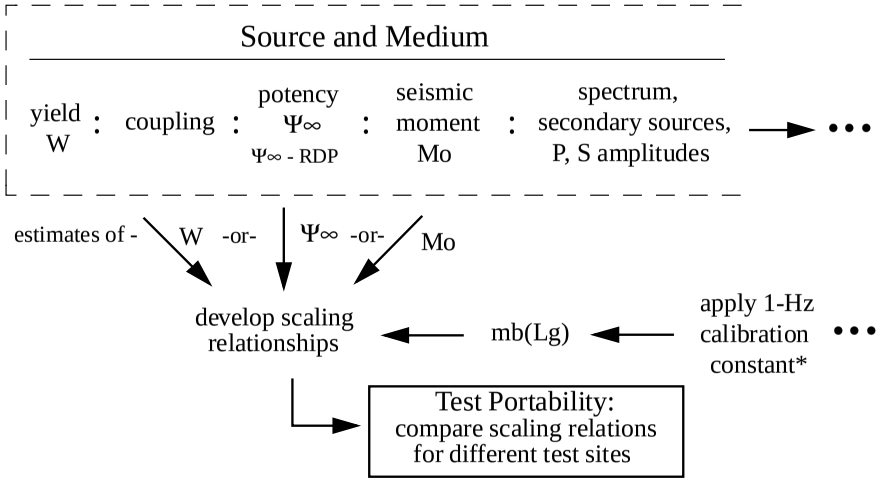

(c) Testing Portability for Explosions: W - or Ψ∞ - Scaling?

- yield estimation - W
- test "on par" with earthquakes - Mo or Ψ∞
- and if large material contrasts - Ψ∞
- variations in coupling and material strength preclude portability *wrt* both W and Ψ∞

Figure 5: (a) Earthquake source and propagation phenomena (inside box) and data processing and analysis steps; (b) the same for explosion source; (c) considerations in the choice between W and Ψ∞ for testing portability

Explosion m_b(Lg) Scaling Relationships: Moment Magnitude M_w and Potency Ψ_∞

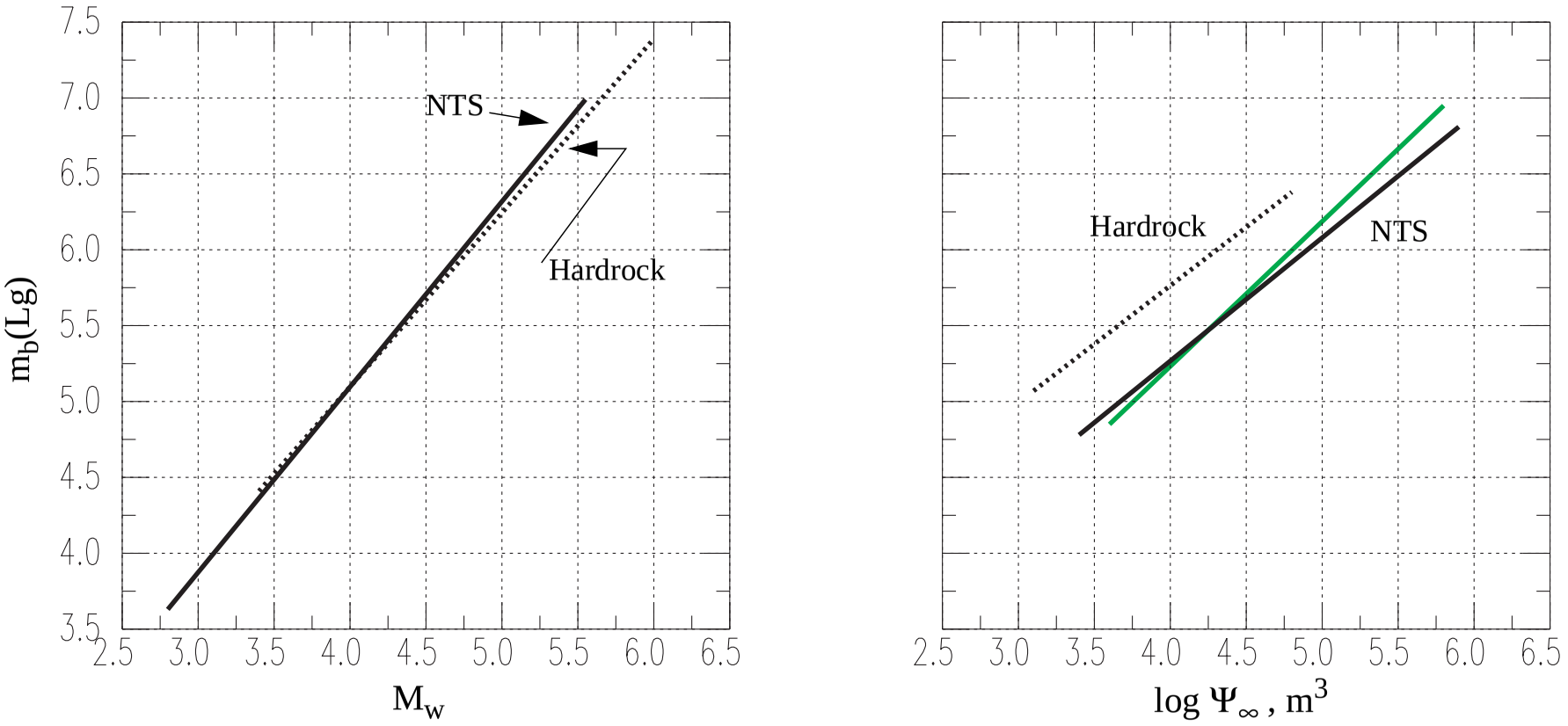

Figure 6: On the left, M_w : m_b(Lg) scaling relationships for NTS and hardrock environments (after Patton, 2001); on the right, log Ψ_∞ (potency) scaling relationships. Potency scaling for hardrock was derived using the M_w : m_b(Lg) relation and Aki et al.'s (1974) formula, $M_o = 4\pi\cdot\rho\alpha^2\cdot\Psi_\infty$, where ρ = 2500 kg/m^3 and α = 5000 m/s. For NTS, the black line was obtained by the same method where ρ = 2000 kg/m^3 and α = 2700 m/s. The relationship shown as grey line is for shots below the water table and was obtained from a regression of m_b(Lg) versus $1/3\cdot r_c^3$, where r_c is measured cavity radius in m. Values of m_b(Lg) for hardrock explosions were measured by O. Nuttli.

ATTENUATION OF LG WAVES IN THE EASTERN TIBETAN PLATEAU

Jiakang Xie

Lamont-Doherty Earth Observatory of Columbia University

Sponsored by The Defense Threat Reduction Agency

Contract No. DSWA01-98-1-0006

ABSTRACT

In the past year I have been processing a large amount of regional/teleseismic data from various broad-band seismic stations in eastern Eurasia. Fourier spectra of Pn, Lg and Pg waves were computed for many events and paths to study path attenuations. Among the data collected and processed are Lg spectra collected from the 1991-1992 Tibetan Plateau Passive Experiment. Using these spectra and a standard two-station method that virtually eliminates source and site effects, I obtain a model of $Q_0 = (126 \pm 9)$ and $\eta = (0.37 + -0.02)$ in a frequency range between 0.2 and 3.6 Hz, where Q_0 and η are Lg Q at 1 Hz and its power-law frequency dependence, respectively. The estimated Q_0 value is among the lowest ever reported for continental areas; it qualitatively supports the observation by McNamara *et al.* (1996) that Lg can not be observed inside the plateau beyond about 700 km, a limiting distance that is much shorter than those in the other low Q_0 (~ 200) regions, such as Iran and the western U.S.

Quantitatively, the estimated Q_0 value is lower by a factor of 3 than the values of 366 estimated by McNamara *et al.* (1996), who used data from the same experiment. Since there are several differences in the data processing and inversion procedures used in this and the previous studies, I investigated the effects of these differences on the Q estimates. I conclude that the most probable cause of the discrepancy is in the different inverse methods used. This is so because the previous inversion allowed the source and site terms to be free parameters solved for. Since 20 events, 8 stations and 5 frequency bands were used, the unknown source and station terms should be more than 100. In this study only two free parameters (Q_0 and η) are solved for, thus avoiding the instability caused by parameter trade-offs.

This research suggests that the previously observed Lg blockage for paths crossing the northern boundary of the plateau may be partially or entirely caused by the abnormal low Lg Q. Further research on lateral and depth variations of crustal Q in and around the Tibetan Plateau is highly recommended.

KEY WORDS: Lg Q, Tibetan Plateau, Lg blockage, Central Asia.

OBJECTIVE

The primary objective of this research is to quantify path attenuation of regional waves in continental areas, such as Eurasia, by developing digital tomographic Q maps. The proposed research include (a) various improvements of the methods for measuring path-variable Q_0 and η (Q at 1 Hz and its power-law frequency dependence, respectively) using regional wave spectra, (b) applications the improved methods to regional waves paths in Eurasia to measure Q_0, η, and (c) to input the measured Q values to a computerized tomographic algorithm, to obtain laterally varying Q maps for Lg and other regional waves.

This research provides important input to the world-wide monitoring of nuclear explosions. The tomographic Q maps can be used for the calculation of source spectral characteristics of any future seismic event to infer the nature and size of the event. These Q maps can also be used for estimating the detection

threshold of the existing seismic stations located within the area studied.

RESEARCH ACCOMPLISHED

Over the past I have continued data collection and inversion for Lg Q in Eurasia. In this paper I report analysis of a data set that consists of Lg spectra from 11 broadband PASSCAL seismic stations deployed during the 1991-1992, passive Tibetan Plateau experiment (McNamara et al., 1996). In an effort to invert for source spectra, I found that the data required that the Lg Q in eastern Tibet be re-measured.

A robust, two-station method is used. Ideally the method uses stacked spectral ratios (SSR, see equations (10)-(17) of Xie and Mitchell, 1990) that are calculated using two-station pairs that are aligned to the same event-to-station azimuths. In practice the SSRs are obtained by requiring that, the differences between the azimuths from the same events to the two stations are smaller than a preset maximum allowable value, $(\delta\theta)_{\max}$. The choice of $(\delta\theta)_{\max}$ is less restrictive for the Lg than for many other phases, since the Lg contains a minimal source radiation pattern in 3D structures. In this study two different values of $(\delta\theta)_{\max}$ of 30° and 12° are used. These values result in 37 and 22 two-station pairs from the data set, respectively. SSRs are formed and used to fit $Q_{Lg}(f)$ models. Figure 1 shows the path coverage by the two sets of SSRs, and Figure 2 shows the SSRs and the fit of the $Q_{Lg}(f)$ models. SSRs obtained with $(\delta\theta)_{\max}$ = 30 ° are fitted by

$$Q_{Lg}(f) = (126 \pm 9) f^{(0.37 \pm 0.02)} \qquad 0.2 Hz \le f \le 3.6 Hz \ .$$

SSRs obtained with a $(\delta\theta)_{\max}$ of 12° are very similar to those with a $(\delta\theta)_{\max}$ of 30° (Figure 2), and are fitted by a $Q_{Lg}(f)$ with Q_0 of (134 ± 10) and η of (0.32 ± 0.02), respectively. These values are virtually the same as those in equation (1), but are theoretically more subject to random errors and bias owing to a smaller dataset. $Q_{Lg}(f)$ in equation (1) is therefore my preferred model. This model is in agreement with the short limiting distance of about 700 km for Lg observation in the study area reported by McNamara et al (1996), and the recent Q_0 estimates by Fan and Lay (2001).

Xie (2001) discussed in detail about several possible reasons why the Q model in this paper differs from a previous one, and concluded that the most likely cause is a parameter trade-off in certain inverse schemes.

CONCLUSIONS AND RECOMMENDATIONS

The Q_0 value of about 126, estimated for the eastern Tibetan plateau in this study, is among the lowest ever documented for any continental areas. An implication of this low value is that the well-known "blockage" of Lg for paths crossing the boundaries of the plateau (e.g., Ruzaikin et al., 1977; Ni & Barazangi, 1983) may be largely, or even entirely, attributed to the low Q_0 values in the plateau (see Figure 3 for a detailed discussion). Another implication of the low Q_0 is that the crust in Tibet may be characterized by higher-than-normal temperature and fluid content, which are responsible for the low Q_0 values. These are in line with the electral conductivity measurements, and suggests that Lg Q should vary laterally, sometimes drastically, in the Tibetan plateau.

Future research should be directed to analyzing more seismic data from recent seismic experiments in the plateau, to resolve details of the lateral variations of $Q_{Lg}(f)$ in the plateau.

REFERENCES

Fan, G.W. and T. Lay, (2001), Characteristics of Lg attenuation in the Tibetan Plateau, J. Geophys. Res., submitted.

Kennett, B.L.N., (1986), Lg waves and structural boundaries, Bull. Seism. Soc. Am., 76, 1133-1141.

McNamara, D.T., T. J. Owens and W.R. Walter (1996), Propagation characteristics of Lg across the Tibetan Plateau, Bull. Seismol. Soc. Am., 86, 457-469.

Ni, J. & Barazangi, M. (1983), High-frequency seismic wave propagation beneath the Indian shield, Himalayan arc, Tibetan plateau and surrounding regions: high uppermost mantle velocities and efficient Sn propagation beneath Tibet, Geophys. J. R. Astr. Soc, 72, 665-689.

Ruzaikin, A.I., Nersesov, I.L., Khalturin, V.I. & Molnar, P. (1977), Propagation of Lg and lateral variation in crustal structure in Asia, J. Geophys. Res., 82, 307-316.

Xie, J. and B.J. Mitchell (1990), Attenuation of multiphase surface waves in the Basin and Range Province, part I: Lg and Lg coda, Geophys. J. Int., 102, 121-137.

Xie, J. (2001), Lg Q in the Eastern Tibetan Plateau, Bull. Seism. Soc. Am., submitted.

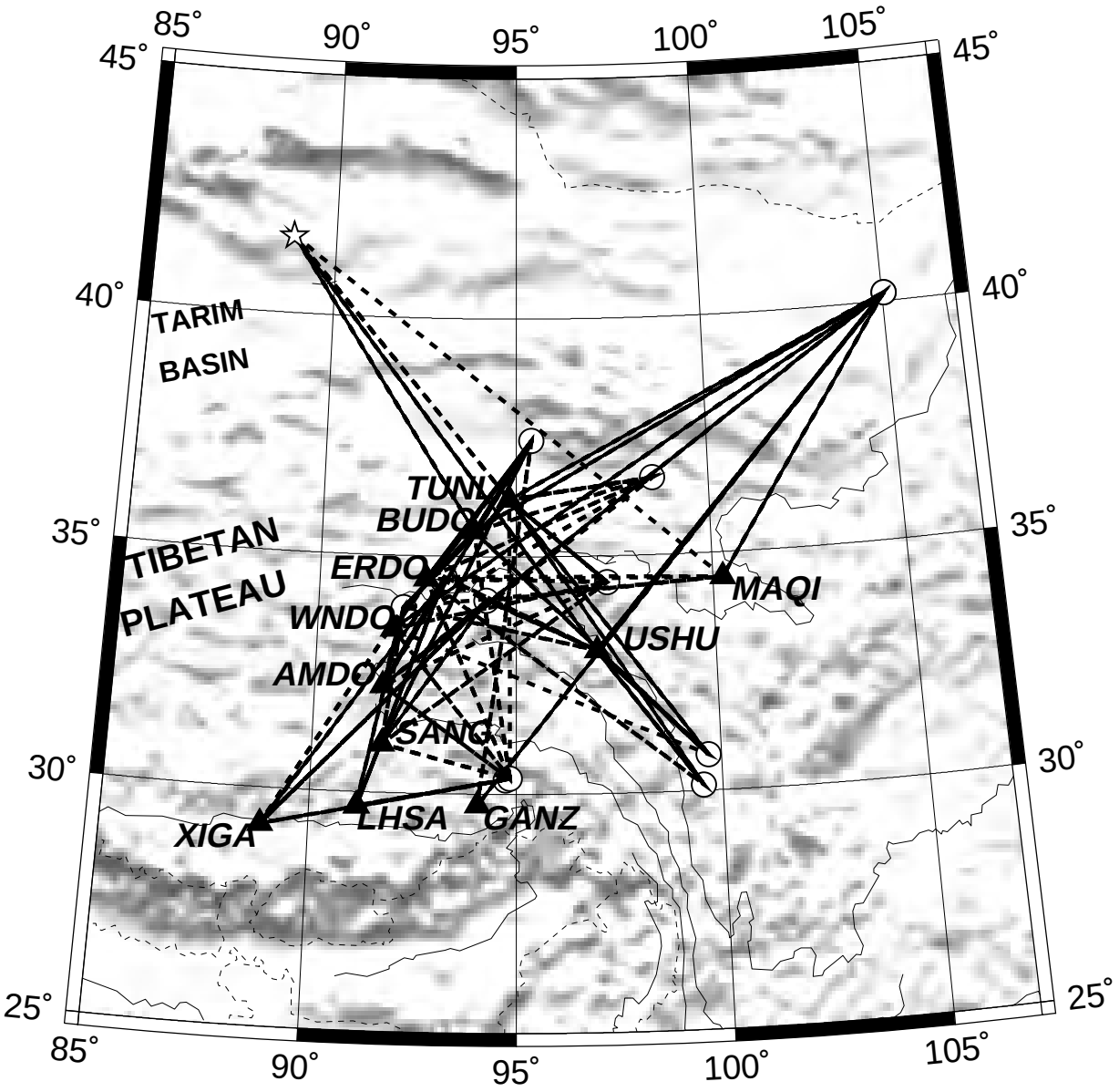

Figure 1. Locations of the PASSCAL stations deployed during the 1991-1992, passive Tibetan Plateau experiment (solid triangles), earthquakes (open circles) and explosion (star) used in this study. Solid paths are those satisfying a $(\delta\theta)_{max}$ (the maximum allowable difference between the event-to-station azimuths of two stations; see text) of 12° when two-station pairs are selected. Dashed paths are those satisfying a $(\delta\theta)_{max}$ of 30°. More information of the stations and events can be found in McNamara *et al.* (1996).

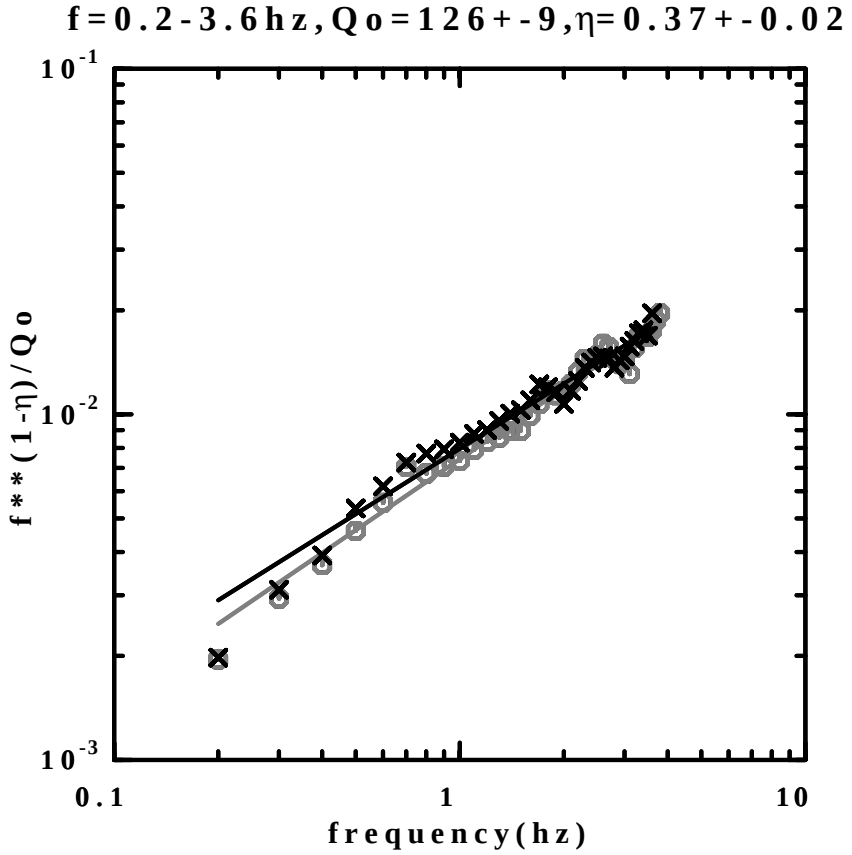

Figure 2. Stacked spectral ratios (SSRs) from many two-station pairs plotted in Figure 1, and the fit of best Q models (straight lines). Black and gray symbols are SSRs obtained using a $(\delta\theta)_{max}$ of 30° and 12°, respectively. The Q models from fitting both sets of SSRs are similar. The Q model written on the top of the panel is from fitting the black symbols.

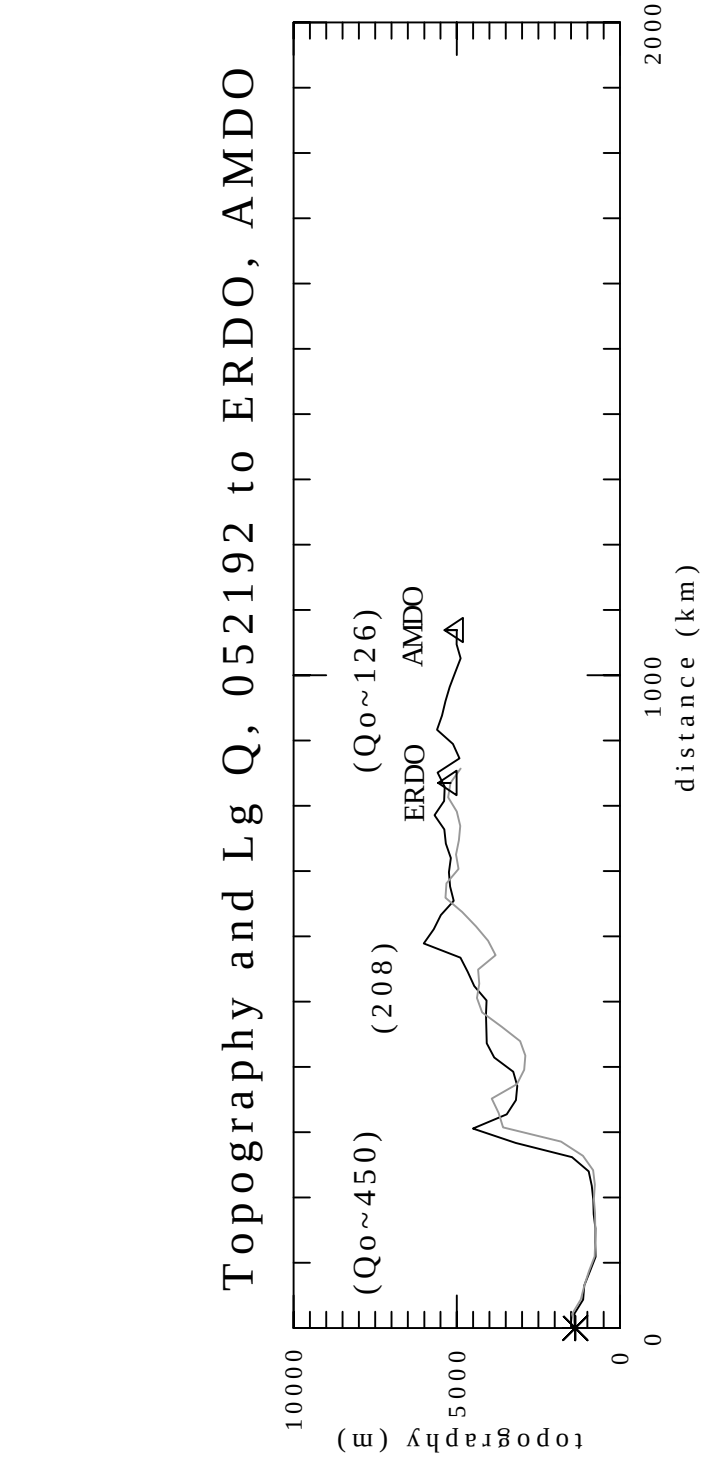

Figure 3. Figure showing a scenario for the Lg blockage across the northern boundary of the Tibetan Plateau. Plotted are topographic profiles from the 052192 Lop Nor explosion (asterisk; also see star in Figure 1) to stations ERDO (curve in gray), and AMDO (curve in black). The observed Lg amplitudes show a partial blockage at ERDO, and complete blockage at AMDO. The numbers in parentheses are Lg Q_0 values. The left segments of the profiles are in the Tarim Basin where Q_0 should be about 450 or higher from previous works. Between stations ERDO and AMDO, Q_0 should be close to 126 (this study). Using these Q_0 values and the spectral amplitude in the expected Lg window at AMDO, I estimate that Q_0 between the topographic boundary and station ERDO is 208 or lower. This means a low average Q_0 value in the plateau of between 126 and 208 is capable to block Lg at AMDO. Therefore, a strong scattering at the topographic boundary is not required. This is consistent with the simulation of, e.g., Kennett (1986), who shows that the scattering is unlikely to fully account for the blockage.

2001

Proceedings of the 23rd Seismic Research Review:
Worldwide Monitoring of Nuclear Explosions

Proceedings of the
23rd Seismic Research Review:
Worldwide Monitoring of Nuclear Explosions

October 2--5, 2001

Jackson Hole, Wyoming

Volume II

Hydroacoustic Monitoring
Radionuclde Monitoring
Infrasound Monitoring
Data Processing and Analysis
Other Topics

Approved for Public Release; further dissemination unlimited

To view these Proceedings online, visit

http://www.nemre.nn.doe.gov/review2001/ .

Vol. II

LA-UR-01-4454

Table of Contents - Volume II

Infrasound Monitoring, cont.

Data Processing and Analysis 179

Other Topics 239

Hydroacoustic Monitoring

THREE-DIMENSIONAL MODELING OF THE HYDROACOUSTIC TO SEISMIC T-PHASE TRANSITION

Catherine D. de Groot-Hedlin, John A. Orcutt
Scripps Institution of Oceanography

Sponsored by The Defense Threat Reduction Agency

Contract # DSWA01-98-0004

ABSTRACT

Plans call for five T-phase stations to be installed as part of hydroacoustic segment of the International Monitoring System (IMS), for use in detecting nuclear explosions in the oceans. The ability to detect T-phase signals at the seismic T-phase stations relies on an understanding of the transition from ocean-borne acoustic energy to seismic energy. Observations of the seismic T-phase indicates that the hydroacoustic energy may convert to either compressional or shear body waves, or to highly-attenuative interface waves that can be observed near the ocean/land boundary. Previous 2-D modeling efforts have shown that T-phase amplitudes depend strongly on the velocity structure of the seafloor and land portion of the propagation path, as well as the depth of the source within the water column. However, Snell's law indicates that 3-D effects, i.e. the angle of incidence to the coast, must also be considered in modeling the acoustic-to-seismic transmission. In this paper, we model upslope propagation of acoustic energy at a sloping wedge using a 3-D finite-difference time-stepping (3D-FDTD) method. We synthesize both vertical and horizontal velocity waveforms for sources at varying angles of incidence to the ocean/land boundary. We investigate the dependence of signal characteristics on both seismic velocities and source direction.

Although the 3-D model simulations are both simple and small-scale, the following conclusions may be made based on this work. For high slopes at the ocean/land interface, T-phase amplitudes on land increase with increasing seafloor slope. This contradicts previous results computed using 2D modeling at lower slope values. T-phase amplitudes on land are strongly dependent on seafloor velocity, with lower amplitudes resulting from higher seafloor velocities. T-phase amplitudes on land drop off rapidly with increasing angle of incidence of the acoustic phase to the shoreline, then level off past the critical angle. For reflected waves recorded on hydrophones, the amplitude ratio of the reflected to the direct acoustic arrivals increases with both increasing angle of incidence at the shorelineand with increasing impedance mismatch between ocean and land.

KEY WORDS: hydroacoustic, T-phase, finite difference time domain (FDTD),modeling

OBJECTIVE:

The hydroacoustic component of the International Monitoring System (IMS) is a sparse network that will ultimately consist of six hydroacoustic stations and five T-phase stations located on oceanic islands or on a continental coastline (as in the case of VIB, in Canada). The main objective of this project is to model hydroacoustic to seismic coupling in order to develop improved methods of interpreting recorded data at T-phase stations. In this paper, we model the 3-D transmission of acoustic energy at a sloping wedge.

T-phase stations are significantly less sensitive than hydrophones to ocean-borne acoustic energy. Furthermore, analysis of data recorded at T-phase stations is considerably more complex than for the corresponding data at hydroacoustic stations due to complications introduced by the coupling of acoustic to elastic energy. Two-dimensional numerical modeling results obtained using a parabolic equation modeling method (de Groot-Hedlin and Orcutt, 2000) and a finite difference modeling (Stevens et.al, 2000, 2001) both suggest that, for a source in the sound channel, the slope of the ocean/land interface is not important in determining the amplitude of the T-phase arrival. However, it was shown that the slope angle is significant for either very deep or shallow sources that excite higher order acoustic modes, since the acoustic to seismic conversion point is further from shore at shallow slopes. In this case, shallow slopes yield lower velocity T-phase arrivals. Two dimensional modeling also indicates that the on-shore velocity model has a significant effect on T-phase amplitudes; a low velocity surface layer results in comparatively high T-phase amplitudes (Stevens et.al, 2000). Furthermore, the partitioning between T- to P- and T- to S-wave coupling has been shown to be strongly dependent on the velocity structure along the slope (de Groot-Hedlin and Orcutt, 1999).

Comparing T-phase arrivals at a seismic station on Ascension Island to corresponding arrivals at the offshore MILS hydrophones, Hanson (1998) noted that the transfer function (i.e. the relative amplitudes recorded at the land-based and hydroacoustic stations) was azimuthally dependent. Although there was some evidence that this result might be due to differences in the underwater portion of the slope of Ascension Island, it was noted that these results were inconclusive as there were too many other variables complicating this result. These variables include varying distances between the seismometer and the acoustic to seismic conversion region, as well as differences in modal structure of the incoming acoustic phases. Recordings of T-phases at stations in northern California also indicated that T-phase amplitudes depend on the azimuth of the acoustic arrival (de Groot-Hedlin and Orcutt, 2001). Arrivals from events near Hawaii arrived at nearly direct incidence to coast and were easily detectable at Berkeley stations; arrivals from French nuclear tests at high grazing angles were mainly deflected from the coast and were thus far less detectable on land.

RESEARCH ACCOMPLISHED

3-D Acoustic Modeling

In this paper, we examine the effects of off-axis scattering to quantify 3-D transmission effects. We use the 3-D finite difference time domain (FDTD) modeling method using a grid staggered in both time and space domains. This method was first developed by Yee (1966) to solve problems in electromagnetism, and has been widely adapted for use in modeling both acoustic and elastic transmission. One difficulty with this method is that it is memory intensive – about 10 grid points per wavelength are required at the highest frequencies in order to maintain adequate numerical accuracy. Another difficulty is that a method of terminating the computation at the grid boundaries is required to eliminate false reflections from the edges of the computational domain. These problems are related in that, without an adequate absorbing boundary condition (ABC), the grid size must be increased to attenuate the false reflections and separate their arrival in time.

To eliminate reflections from outgoing waves at the edges of the computational domain, and thereby model an unbounded region, we introduce a boundary region in which fields are attenuated. We use the perfectly matched layer

(PML) absorbing boundary condition (ABC) introduced by Berenger (1994), which results in absorption over a wide range of angles and frequencies. We modify Berenger's PML ABC by "splitting" the pressure into components p_x, p_y, and p_z, and introducing loss terms in the boundary regions. It can be shown that, for a uniform boundary, the resulting coefficients can be made arbitrarily small (Hastings et.al., 1996). In the simulations that follow, the inhomogeneous medium intersects the edges of the simulation region, however reflections are still negligible.

A schematic diagram of the physical model is shown in figure 1. The entire model consists of 170x175x90 blocks, with each block measuring 25m on a side. The boundary regions each have a thickness of 8 blocks. The water velocity profile used corresponds to the annual average sound speed profile at 53N, 226E (near VIB). An explosive source is located at 400m depth, at the sound channel minimum. Results are shown for 3 slopes: 90°, 45°, and 30°. The slopes are modeled as stair-steps, rather than smooth gradients. However, the roughness scale is about one tenth of a wavelength at the highest frequencies, so scattering effects should be secondary. The sampling rate is every 0.005 seconds, thus we have very high time resolution. In the following computations, we neglect intrinsic attenuation within the main grid in order to simplify the interpretation of the results. The source function is shown in figure 2, and has a 1-7Hz bandwidth.

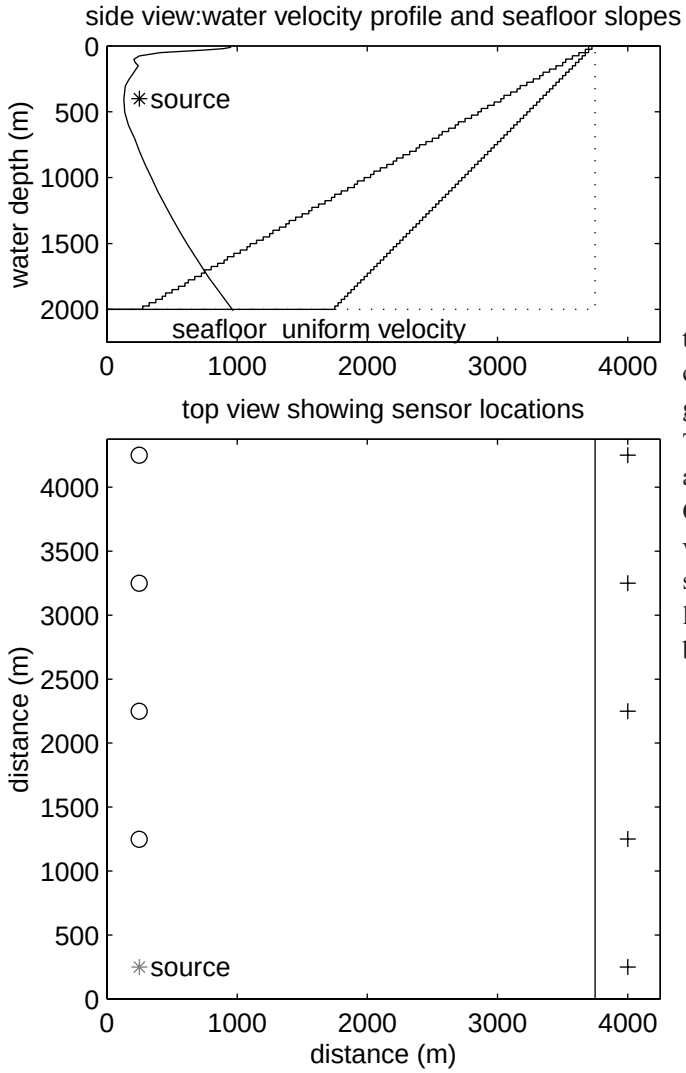

Figure 1. The physical model. a) side view of the model. Velocity and pressure waveforms were computed for 3 slopes: 90°, 45°, and 30°. The gradients are modeled as stair-steps of 25m height. The water velocity profile corresponds to the annual average velocity profile at 53N, 226E, near VIB on Queen Charlotte island. The seafloor is of uniform velocity. b) Top view of the model setup. Pressure sensor locations are indicated by circles; the locations of 3 component seismometers are marked by pluses, and are located 250m inshore.

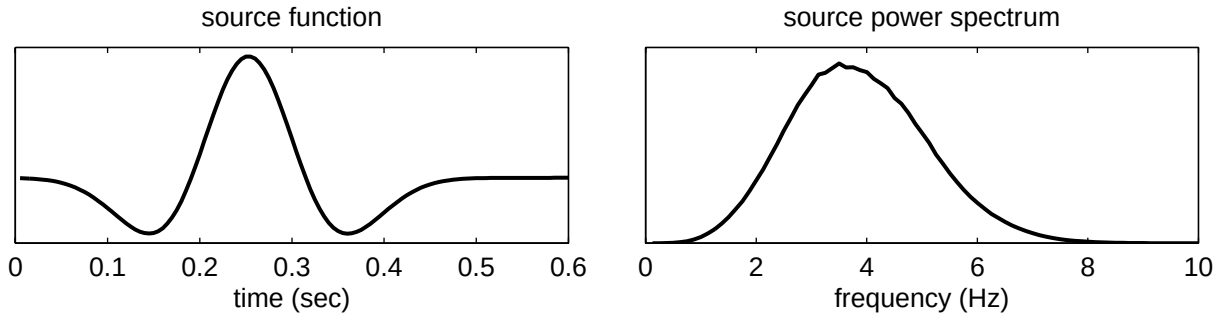

Figure 2. Source function and power spectrum. As shown, the source has a bandwidth from 1-7Hz.

3-D Modeling Results

Top and side views of the pressure field at 1 second, shown in figure 3, indicate how effective the absorbing boundary is. Most absorbing boundaries operate most efficiently at direct incidence, and result in small reflections at other angles. The lack of reflection at the grid boundaries confirms that we can have confidence in the waveform results.

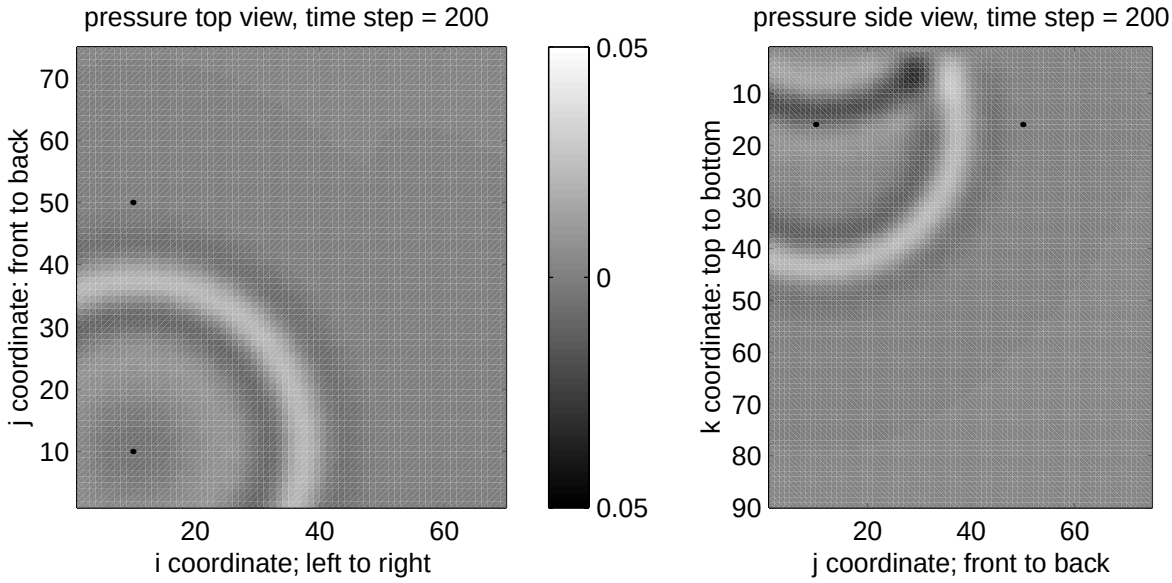

Figure 3. The pressure waveform at t=1 second. No reflections from the grid side boundaries are apparent in the top view (left) or side view cross-section through the receiver location (right). Note that the reflection from the ocean surface, seen in the side view, has the correct (opposite) polarity with respect to the direct arrival. The black dots indicate the location of the source and one of the hydrophones

The velocity waveforms "recorded" at each seismometer location, for each of the three test slopes are shown in Figure 4 slopes for a seafloor velocity of 2500m/sec. The results show that the largest waveforms correspond to the higher slope values. This contradicts previous results which were based on slope values from 2-7^{o} (de Groot-Hedlin and Orcutt, 2000) and 10-30^{o} (Stevens et.al , 2000). Horizontal components of motion have much smaller amplitude for all slope angles, as shown in the results for v_x and v_y. For these models, the variations in amplitude are due to the combined effects of increasing distance and varying angles of incidence at the shoreline. To examine these effects, we plot, in figure 5, the maximum vertical amplitude for each slope values vs. distance from the source. The azi-

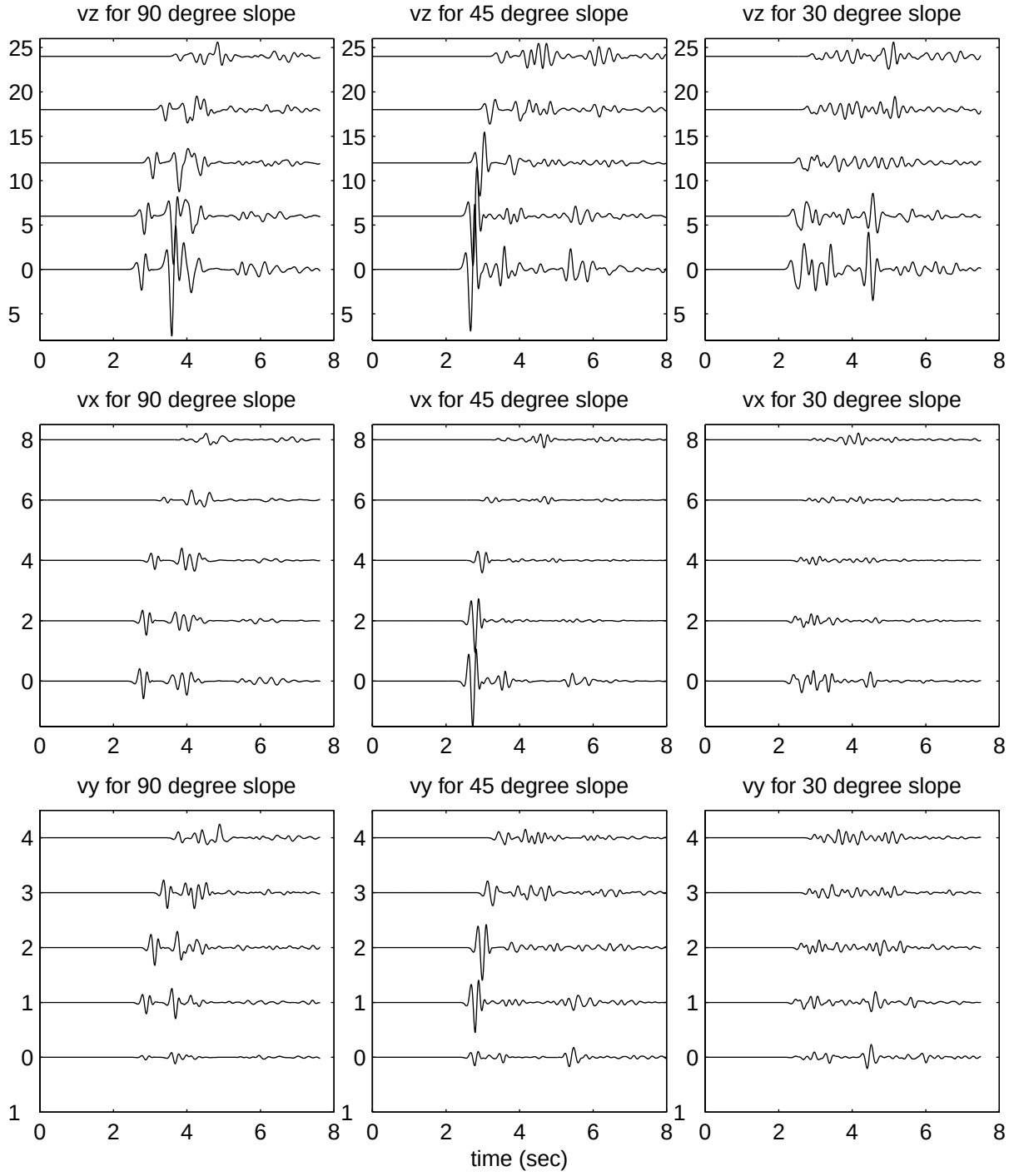

Figure 4. Velocity waveforms for seismometer locations marked by "+" in figure 1. The seafloor velocity in 2500m/sec. Amplitudes are consistent within each direction of motion, ie. amplitudes may be compared between slopes, but note the scale change between components of motion. The distance from the source increases going from bottom to top.

muths from the source to each receiver are also marked. The distance range spans less than a factor of two, yet the amplitudes vary by up to a factor of eight. This suggests that the modeled amplitudes depend more on the azimuth from source to receiver than on the source range. As shown, the amplitude decreases rapidly with increasing azimuth, then levels off at azimuths beyond 39°. The critical angle at this velocity contrast is 31°. For comparison, similar computations were performed for the model with a 45° slope and seafloor velocity of 3500m/sec. Corresponding maximum amplitudes are marked by the triangles in figure 5. Amplitudes are lower at all distance values, and level off at azimuths beyond 28° - the critical angle at this velocity contrast is 23°.

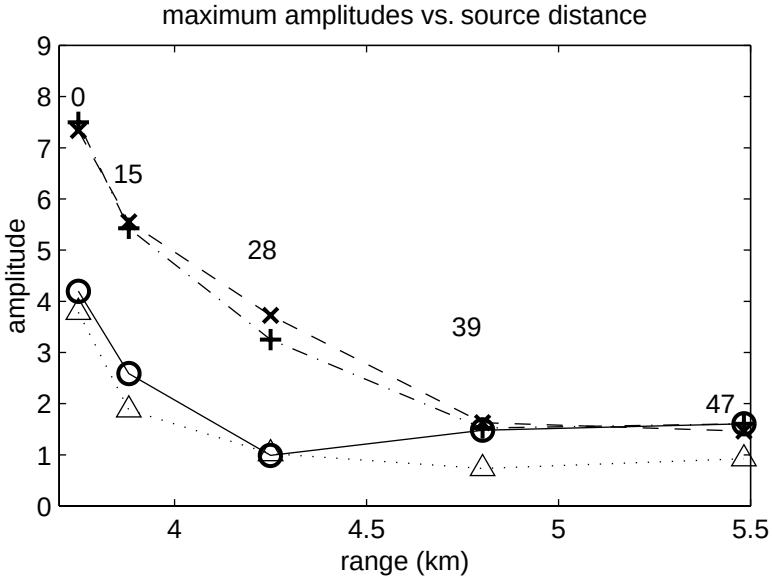

Figure 5. Maximum absolute values of the vertical amplitudes vs. source distance. The back azimuths to the source are also indicated. Results for the 30° slope are indicated by the circles, results for the 45° slope are marked by x'es and the results for the 90° slope are indicated by +'es. For comparison the corresponding results for a model with a 45° slope and a seafloor velocity of 3500m/sec are shown by the gray triangles.

The pressure response at the "hydrophones" at the locations given in figure 1 were derived with no additional computational effort for each model, and are shown in figure 6. The three main wave packets on each waveform correspond to: 1) a combination of the direct and surface reflected arrivals, 2) the reflections from the seafloor at 2.5 to 4 sec, and 3) the reflected arrival from the water/land boundary at 5 to 6 seconds. As expected, the amplitude ratio of the shore-reflected arrival to direct arrival increases with increasing distance from the source (since the reflection coefficient increases with decreasing grazing angle).

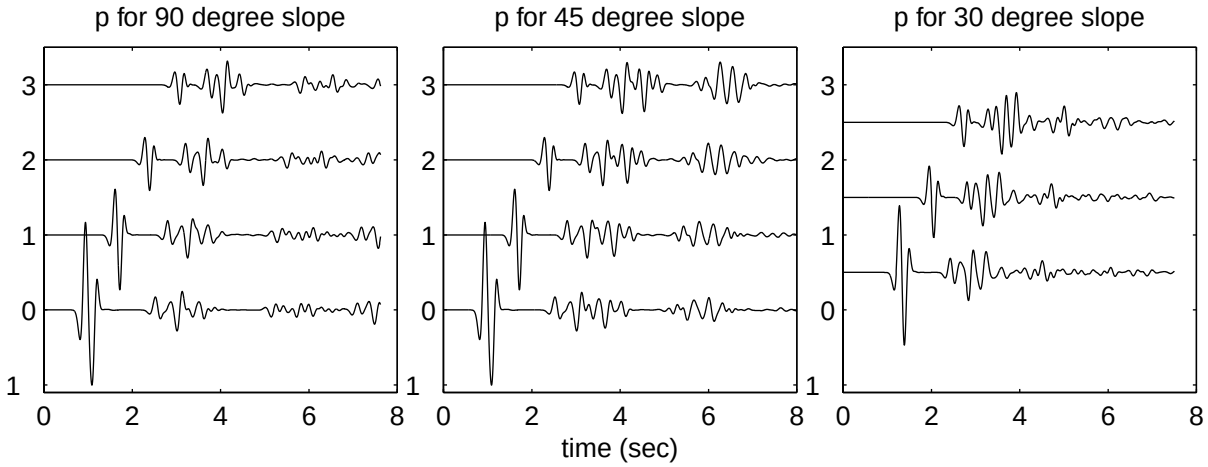

Figure 6. Pressure waveforms for seismometer locations marked by circles in figure 1. For the 30 degree slope, responses were computed at only 3 hydrophones, at locations halfway between those shown in figure 1.

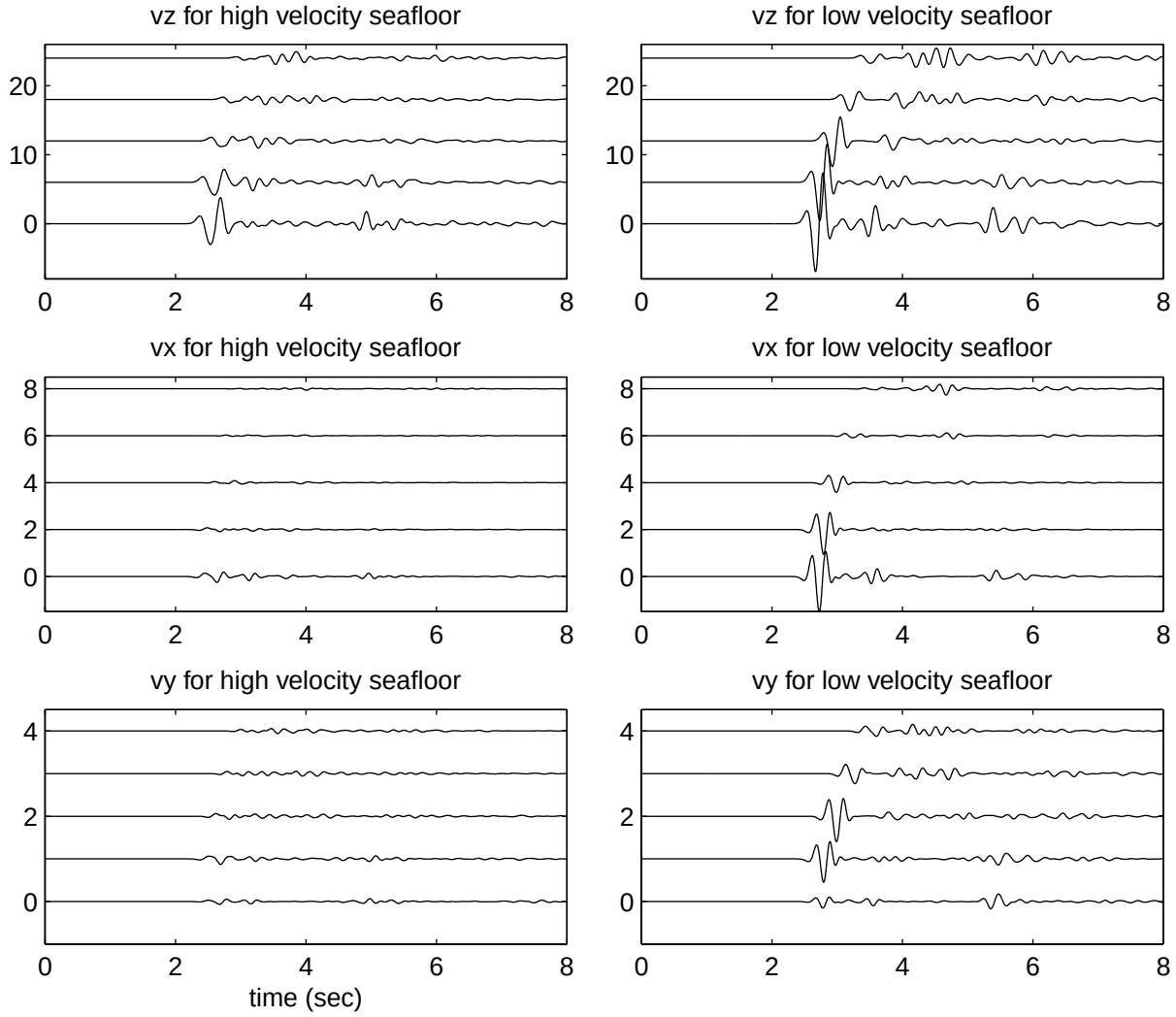

Figure 7. Comparison of velocity waveforms for model with 45° slope and seafloor velocities of 3500m/sec (right) and 2500m/sec (left). T-phase amplitudes are much smaller for the model with the high velocity seafloor.

For comparison, the velocity responses for the model with 45° slope, with a seafloor velocity of 3500m/sec are shown in figure 7. The pressure responses for this model are shown in figure 8. In both figures, these are compared to the previous results for a model with a seafloor velocity of 2500m/sec. Figure 7 shows that the velocities recorded on land are significantly lower for the higher velocity seafloor. As shown in figure 8, the ratio of the reflected arrival to the direct arrival is greater for the larger impedance mismatch.

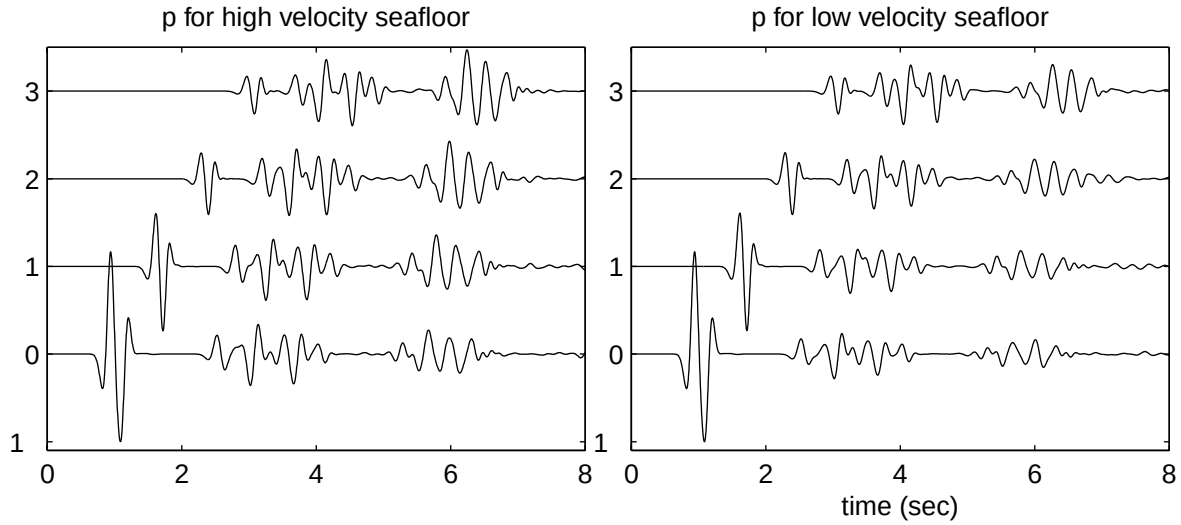

Figure 8. Comparison of pressure waveforms for model with 45° slope and seafloor velocities of 3500m/sec (right) and 2500m/sec (left). Both the seafloor bounce phases (the second arrivals) and the arrivals reflected from the slope (the third arrivals) are larger for the model with the greater velocity contrast.

CONCLUSIONS AND RECOMMENDATIONS

Although the 3-D model simulations are, by necessity, both simple and small-scale, the following conclusions may be made based on this work.

-T-phase amplitudes on land increase with increasing seafloor slopes. This contradicts previous results computed using 2D modeling at lower slope values.
-T-phase amplitudes on land are strongly dependent on seafloor velocity, with lower amplitudes resulting from higher seafloor velocities.
- T-phase amplitudes on land drop off rapidly with increasing angle of incidence of the acoustic phase to the shoreline, then level off past the critical angle.

For reflected waves recorded on hydrophones, the amplitude ratio of the reflected to direct arrivals

-increases with increasing angle of incidence at the shoreline
-increases as impedance mismatch between ocean and land increases

However, this ratio has a complicated dependence on slope at which the acoustic phase is reflected. Reflections have higher amplitude at 45^{o} than at both the 90^{o} and 30^{o} slopes.

These conclusions hold for sources located in the sound channel minimum, and for models with no intrinsic attenuation in the land portion of the travel path. Further work needs to be done using elastic modeling.

References:

Berenger, J.-P., "A perfectly matched layer for the absorption of electromagnetics waves", *J. Comput. Phys*., **114**, 185-200, 1994.

de Groot-Hedlin, C, and J. Orcutt, Comparison of T-phase observations at northern California Seismic Stations and the Pt. Sur hydrophone, 21st annual seismic research symposium, 1999.

de Groot-Hedlin, C, and J. Orcutt, Detection of T-phases at Island seismic stations: dependence on seafloor slope, seismic velocity, and reoughness, 22nd annual seismic research symposium, New Orleans, 2000.

de Groot-Hedlin, C, and J. Orcutt, T-phase observations in northern California; Acoustic to seismic coupling at a weakly elastic boundary, *PAGEOPH*, **158**, 513-530, 2001.

Hastings, F.D., J.B. Schneider, and S.L. Broschat, "Application of the perfectly matched layer (PML) absorbing boundary condition to elastic wav propagation*", J.Acoust.Soc.Am.*, **100**, 3061-3069, 1996.

Hanson, J.A., Seismic and hydroacoustic investigations near Ascension Island, University of Califoria, San Diego, 1998.

Stevens, J.L., G.E. Baker, H. Xu, G. D'Spain, and L.P. Berger, Finite difference modeling of T-phase propagation from ocean to land, 22nd annual seismic research symposium, New Orleans, 2000.

Stevens, J.L., G.E. Baker, R.W. Cook, G.L. D'Spain, L.P. Berger, and S.M. Day, Empirical and numerical modeling of T-phase propagation from ocean to land, *PAGEOPH*, **158**, 531-565, 2001.

Yee, K.S., "Numerical solution of initial boundary value problems involving Maxwell's equation in isotropic media", *IEEE Trans. Antennas Propagat*. **AP-14**, 302-307, 1966.

INITIAL ANALYSIS OF DATA FROM THE NEW DIEGO GARCIA HYDROACOUSTIC STATION

Jeffrey A. Hanson

Science Applications International Corporation

Sponsored by Defense Threat Reduction Agency

Contract No. DTRA01-99-C-0025

ABSTRACT

The Prototype International Data Center (PIDC) began standard processing of data from the first of the new International Monitoring System's (IMS) hydrophone stations in November 2000. The station (designated HA08) is located off the Chagos Archipelago in the Indian Ocean (Lawrence et al, 2000). This is the first IMS hydroacoustic station that allows for coherent multi-sensor waveform processing. It provides better azimuthal arrival determination than was possible with the older IMS hydroacoustic stations. The station is not a classical hydrophone array, and standard array processing techniques may not produce the best results. Soon, two more stations, similar in design, will become operational in the Indian Ocean. It is important that we learn how these stations can best contribute to the Comprehensive Nuclear-Test-Ban Treaty's (CTBT's) hydroacoustic monitoring program.

The new station consists of six hydrophones arranged in two triads. The northern triad is 190 km northwest of the Diego Garcia atoll, and the southern triad is 30 km south of the atoll. The hydrophones are arranged in near equilateral triangles with sides approximately 2.5 km in length. The hydrophones are tethered to the sea floor and are suspended near the sound channel axis depth by subsurface buoys. The archipelago forms a large bathymetric obstruction between the two triads so signals observed at one triad are often completely or partially blocked at the other triad.

Each hydrophone produces on the order of 50 detections/day. The automatic system classifies the detections into three categories (N - noise, T - earthquake-generated signals, and H - signals that appear to be generated from an impulsive in-water event). The azimuth of arrival is determined for most detections. Because we lack ground truth, determining the accuracy of estimated azimuths is difficult. From earthquake locations, the southern triad's azimuth residuals have a standard deviation of approximately 2°. The northern triad detections have much greater residuals (often 50° or more), but most of the large outliers are from signals with partially blocked paths. Reflected acoustic waves appear to interfere with the direct signal. Establishing accurate error estimates for the azimuths as well as other signal features is a primary goal of this research.

KEY WORDS: hydroacoustics, prototype International Data Center, Diego Garcia, azimuth estimation

OBJECTIVE

This research attempts to establish a baseline of performance of the Diego Garcia hydrophone station. The new station has many advantages over previous IMS hydrophone stations such as those at Wake and Ascension Islands. The new hydrophones are well calibrated and use modern electronics to digitize and transmit the hydroacoustic data. In addition each triad has hydrophone spacing on the order of 2.5 km. Diego will soon be joined by two more stations in the Indian Ocean of similar design (Cape Leeuwin and Crozet). An accurate baseline will aid in determining where best to allocate resources to improve the monitoring capability of the new hydroacoustic stations the most.

There are several aspects to the stations that are new and require analysis. Although ocean acoustics is a mature field, the hydroacoustic global monitoring problem has only recently received attention and has gen-

erally suffered from a lack of high-quality data. The new stations are in a different ocean basin than the previous stations used at the PIDC. Although the signals are similar, there are differences probably caused by the source region. The triads are not typical hydroacoustic arrays. The stations consist of a minimum number of elements (3) and the element spacing is greater than several wavelengths. The element spacing causes the array to be spatially aliased. However, this can be overcome because the phase velocity can be restricted, and the signals we are interested in have a large bandwidth. The signal coherency between sensors is not known, which makes error estimation difficult.

Our previous experience is primarily with the U.S. Air Force MILS (Missile Impact Locating System) type hydrophone stations in the Pacific and Atlantic Oceans (Hanson et al., 2001). These consist of 1 to 3 hydrophones generally separated by hundreds of kilometers. The data also suffered because the old instrumentation severely restricted the dynamic range of the signals. The distance between hydrophones in the old stations required incoherent array processing techniques in order to determine azimuth of arrival.

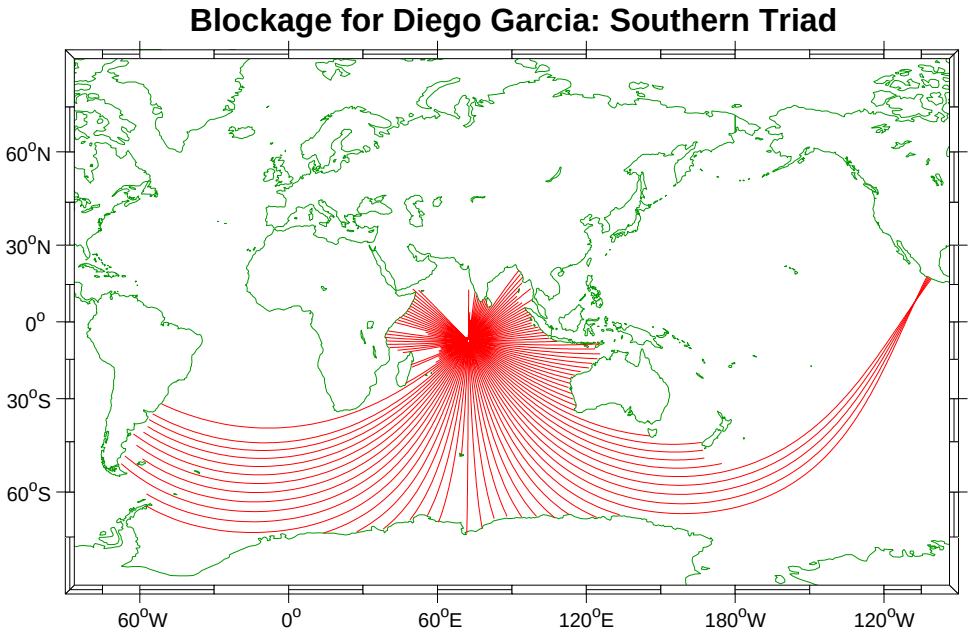

Figure 1. Example ray paths to Diego Garcia South. The northern triad has similar ray coverage but is not blocked to the northwest. Signal blockage maps are predicted from these ray paths (the actual blockage maps use a higher density of rays than shown here). The unblocked paths into the Pacific are real. In March of this year, T phases from earthquakes off Mexico's coast were recorded at Diego Garcia.

An additional objective of this research is to develop new algorithms that improve azimuth estimation with the new hydroacoustic array design. The small number of elements and the long baselines between elements (many wavelengths) cause problems with typical F-K analysis due to spatial aliasing and lack of data redundancy. Determining an unique direction of arrival relies on the signal's bandwidth and temporal duration. We have discovered weighting techniques that improve the estimated azimuths.

RESEARCH ACCOMPLISHED

Detection Processing

Automatic detection processing is handled by the PIDC's DFX application. DFX processes each hydrophone independently. Features are measured for each frequency band that reaches an established energy

threshold level. The frequency bands are the standard bands used for the other hydrophone stations (2-4, 3-6, 4-8, 6-12, 8-16, 26-32, 32-64, 2-80 Hz). A second process, StaPro, determines an initial phase identification. It currently uses a set of default rules that were developed for hydrophones in the pacific. It is anticipated that neural weights will be determined when enough data has been collected to form a training set.

Each hydrophone produces on the order of 50-100 detections/day (see Figure 2). The automatic system classifies the detections into three categories (N - noise, T - earthquake-generated signals, and H - signals that appear to be generated from an impulsive in-water event). The automatic system declares on average 20 T-phases/day for both the southern and northern triads. The southern triad records 1 to 3 H-phases/day. However, there are on the order of 10 H-phases/day at the northern triad. Most of these "H-phases" are believed to be signals from local earthquakes that have shorter duration and a greater frequency content than T-phases from distant sources. Reducing this clutter is an important objective for reducing false alarms that may overburden analysts. Additional tuning of the parameters used in classification may be enough to lower false alarms to an acceptable rate.

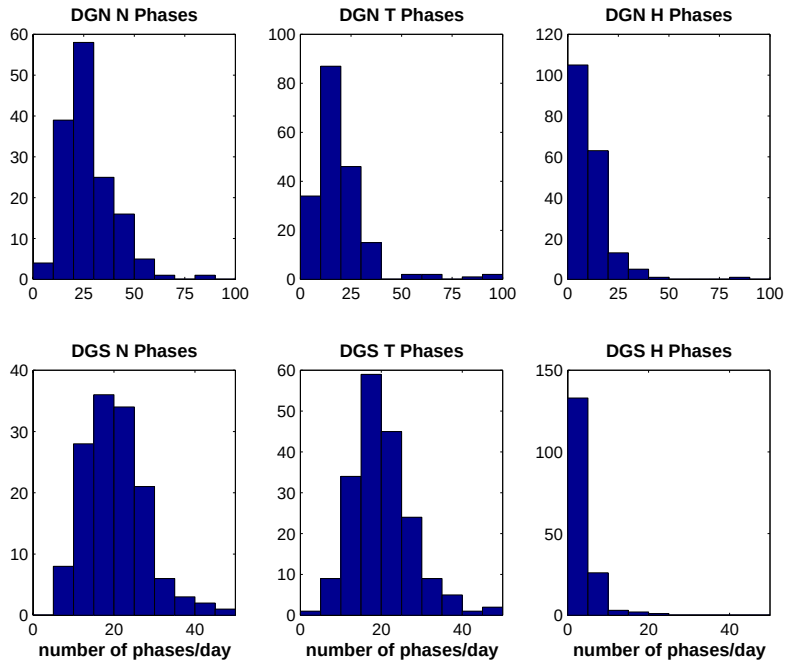

Figure 2. Automatic detections at the northern (top) and southern (bottom) triads. The noise phase (N) and T phase detection rates are comparable between triads. However the northern triad has many more H phase detections than the southern triad. These signals are generally due to local seismicity which are more impulsive and have higher frequency content than the typical T phase. These characteristics make classification more difficult at Diego than was the case for Wake or Ascension.

Average noise levels at the two triads are within normal bounds (Figure 3). The southern triad's ambient noise is somewhat higher than the northern triad. This is not surprising since the southern hydrophones are in a shallower environment and closer to shore. The noise level fluctuates on a daily and seasonal time scale (Figure 4).

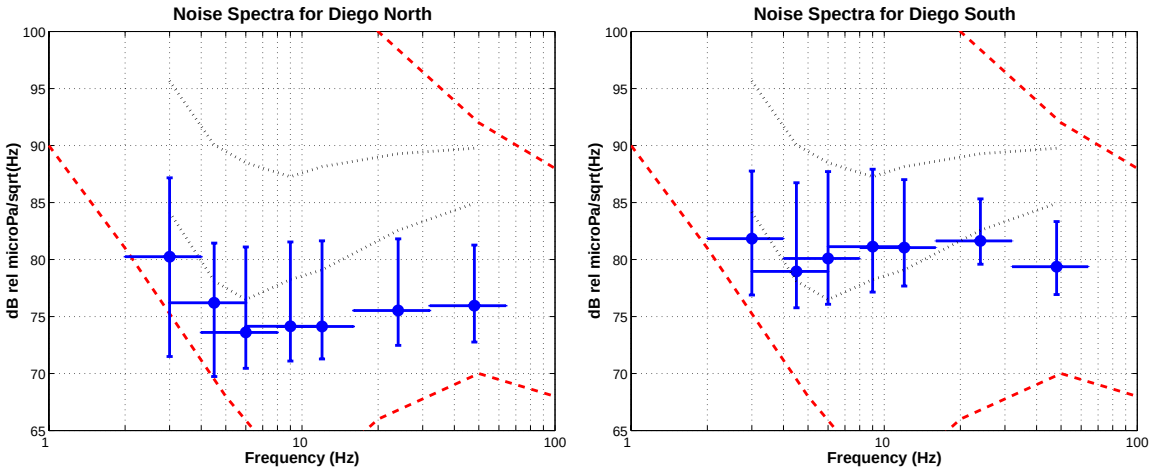

Figure 3. Average noise level (solid dots) at the two triads. The vertical error bars represent the range of noise levels observed over a half year's worth of data (about 9,000 measurements in each). The horizontal error bars indicate the bandwidth each measurement covers (although the measurement covers the whole band, the values are normalized so that the units are Power/Hz). The dashed line represents high and low noise values for a deep ocean environment (from Wenz, 1962). The dotted lines are similar high and low values observed at WK30 (the Wake Island hydrophone station).

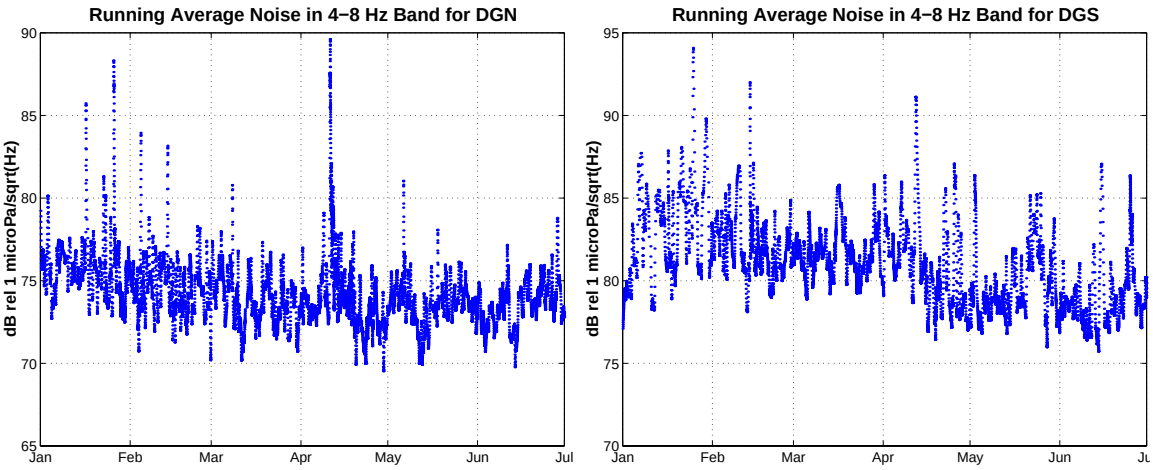

Figure 4. Noise in the 4- to 8-Hz band for the first half of 2001. The values have been smoothed using a 20-point low-pass filter window. There is a 3- to -dB decrease from January to July, which appears to be correlated between triads. Increased noise levels due to ships, marine seismic experiments, and storms have been observed.

The azimuth of arrival is determined for most detections. Because we lack ground truth, determining the accuracy of estimated azimuths is difficult. From earthquake locations, the southern triad's azimuth residuals have a standard deviation of approximately 2° (Figure 5). The northern triad detections have much

greater residuals (often 50° or more), but most of the large outliers are from signals with partially blocked paths. Reflected acoustic waves appear to interfere with the direct signal.

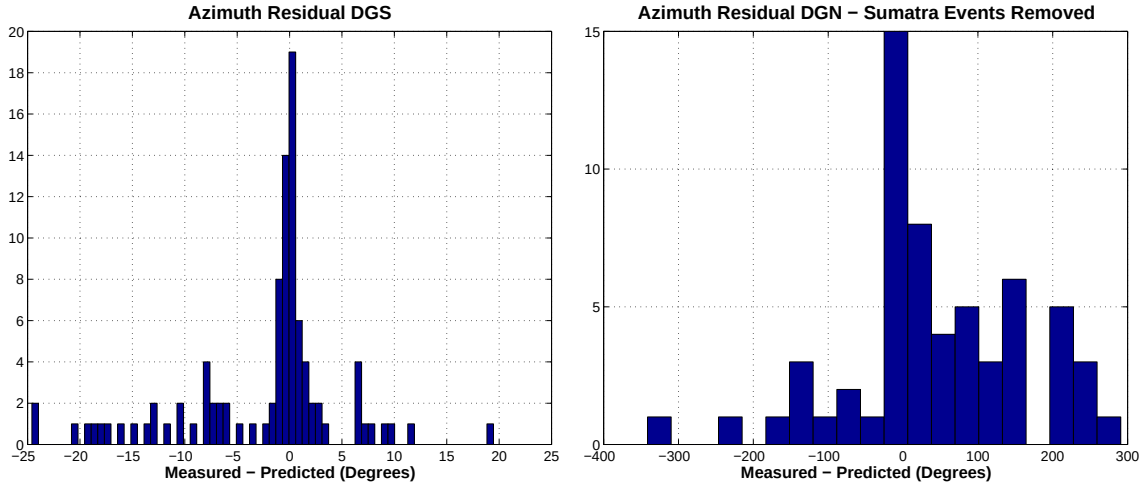

Figure 4. Residuals between measured and predicted azimuths. The predictions are from earthquake locations. The associations in this case were made strictly on time of arrival so some of the large errors may be due to incorrect associations. However, the incorrect association rate does not appear to be greater for the northern triad and does not explain the large residuals.

Array Processing

As previously mentioned, the triads are spatially aliased arrays. This is caused by the 2.5-km spacing between hydrophones while the wavelengths of interest range from 750 meters to as short as 15 meters. However, in hydroacoustic processing we have the advantage that the phase velocity is essentially known (~1.5 km/s). This reduces the spatial aliasing problem, but does not eliminate it (Figure 6).

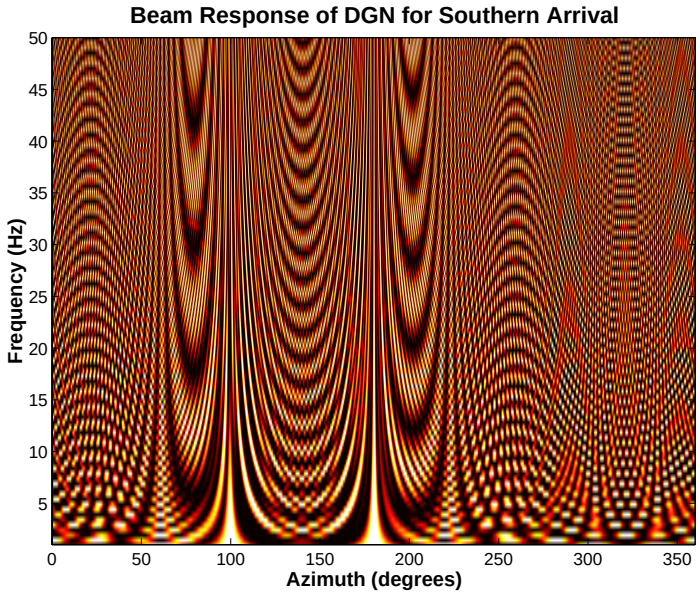

Figure 5. The beam response of the of the northern triad for a plane wave arriving from 180° azimuth. The phase velocity is fixed at 1.5km/s. The strong spatial aliasing is evident especially at an azimuth of 100°. Summing the response over a range of frequencies removes most of the aliasing.

The response pattern shown in Figure 6 demonstrates that the aliasing problem can be overcome by summing over frequency. This is because the array response varies with frequency except at the actual arrival bearing. A broadband signal should not have side lobes with the same amplitude as the main lobe. However, there are side lobes whose frequency dependence is weak (for example, at 100° in Figure 6). Therefore, it is important to take advantage of as much frequency content as possible.

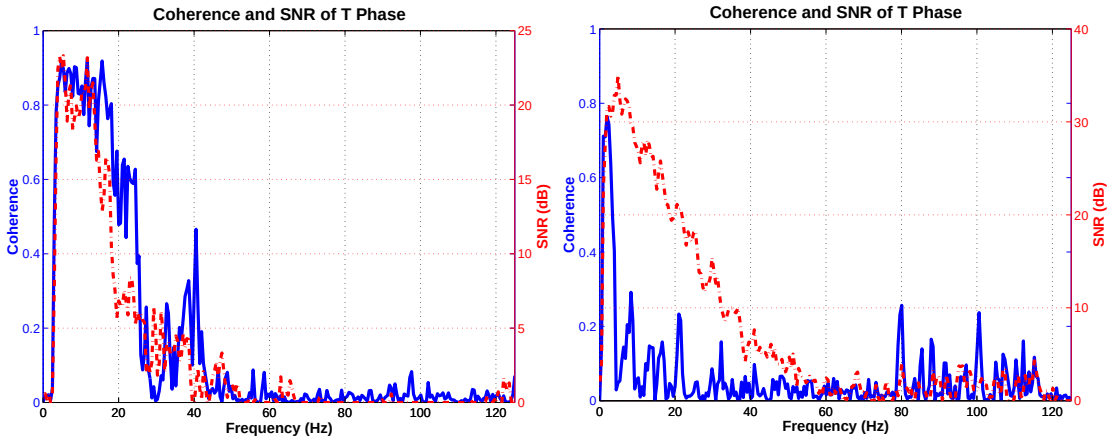

Figure 6. Coherence between two sensors for two T phases. The left vertical axis corresponds to the solid blue line (coherence), and the right vertical axis corresponds to the dashed red line (SNR). The SNR of the two signals are similar, but the T phase on the right loses coherence above 5 Hz while the coherence of the left T phase appears to be controlled by its SNR. Considering many other observations, the amount of coherent energy in a T phase appears to be azimuthally dependent. However, this may be more a function of source area than interference at the receiver. The signal on the right is from a trench earthquake, and the left signal is from a shallow mid-ocean ridge earthquake.

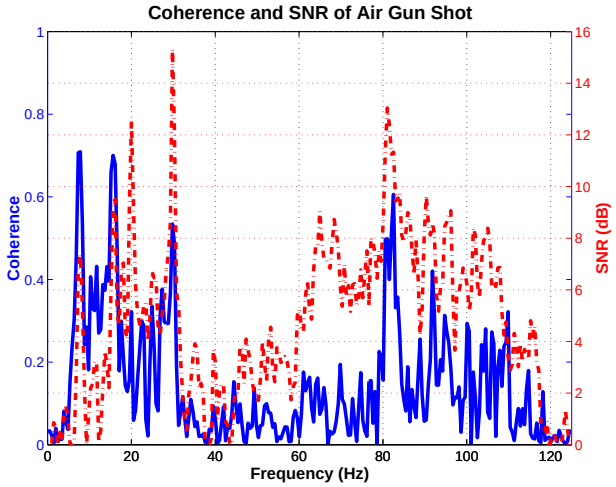

Figure 7. The coherence between two sensors for a series of signals from air gun shots. The left vertical axis corresponds to the solid blue line (coherence), and the right vertical axis corresponds to the dashed red line (SNR). The signals arrive from the northeast. The distance to the ship is not known. There is coherent energy from 5 to 30 Hz and from 90 to 110+ Hz, even though the SNR is relatively low. This suggests that the lack of coherence in some of the T phase signals may be source effects rather than interference from local reflections.

The useful frequency content of a signal for azimuth estimation is obviously dependent on the signal-to-noise ratio, but the energy must also be coherent between sensors. We have examined the coherence of waveforms between sensors within a triad. Most of our signals are earthquake-generated T phases whose characteristics may not be similar to explosion-generated signals. For a given signal, the coherence is generally equivalent for any given pair of sensors within the triad. However, the coherence of one signal can greatly differ from another (Figure 7). T phases from one azimuth may be coherent over their entire band width, but T phases from another azimuth may have very little coherent energy. It remains to be seen if this is a source or receiver end effect.

On the receiver end there could be near-sensor reflectors that are more efficient for waves propagating from one direction than the other. The reflections could interfere with the direct arrival breaking up the signal's coherence. But for the earthquake-generated T phases, the azimuth is directly related to the region that the signal was generated. The incoherent signals seem to come from trench events off of Sumatra while the coherent arrivals seem to be generated from shallow mid-ocean ridge seismicity. The T phases from trench events may emanate from multiple regions (de Groot-Hedlin et al., 1998) creating interfering signals at the receiver end.

There are few examples of in-water sources recorded at Diego Garcia. However, the signals that are recorded appear to be coherent between sensors over the entire bandwidth of the signal (Figure 8). This suggests that the coherence is related to the source, and one needs to be careful when using earthquake-generated T phases as a proxy to explosion data. However, this is based on only a few examples, and therefore we cannot rule out coherence loss due to effects at the receiver end of the path.

Optimizing Azimuth Estimates

The accuracy of azimuth estimation for the hydroacoustic network is especially important because of the network's sparse design. Given good coverage, travel-time estimates will generally constrain an event location much better than azimuth estimates. This is because a small uncertainty in azimuth can become a very large spatial uncertainty as you back project from the hydroacoustic station to the event. But because of the sparse network, there may not always be adequate coverage for event location based on travel times alone. With the earlier IMS hydroacoustic stations (like Wake and Ascension), the accuracy in azimuths was not

sufficient to be of much use in location estimation. However, the triads appear to produce much more accurate azimuths.

Because there are only three elements in a triad which are widely spaced, there may be better ways to process the data than standard array techniques. The geometry of the northern triad is shown in Figure 9. It is essentially an equilateral triangle. Cross-correlating signals is usually not done for arrays with many elements. However, because a 3-element array only has 3 pairs of sensor to cross-correlate, it is quite feasible in this case. In our algorithm, we estimate the F-statistic from an average of the cross-correlations (Katz, 2001). This can be shown to be equivalent to estimating the F-statistic from the beam.

The sensitivity of the cross-correlation function for a given pair of sensors can be easily calculated as a function of azimuth. We do not have to calculate the sensitivity in the slowness direction because we know the phase velocity. The sensitivity can be used to weight the cross-correlations when averaging. Intuitively one can see that the cross-correlation will be particularly insensitive for azimuths that are near parallel to the baseline between the sensors. These sensitivities provide a sophisticated method for weighted data that is not directly possible in beam formation. The effect of this weighting is to narrow the main lobe (improve the resolution). However in doing so, we increase leakage and side lobes in the 'FK' spectrum. This is probably not a significant problem for the type of signals we are interested in. In Figure 9 we demonstrate that modest gains in resolution are achievable. Improvements to the weighting scheme may improve the resolution gain.

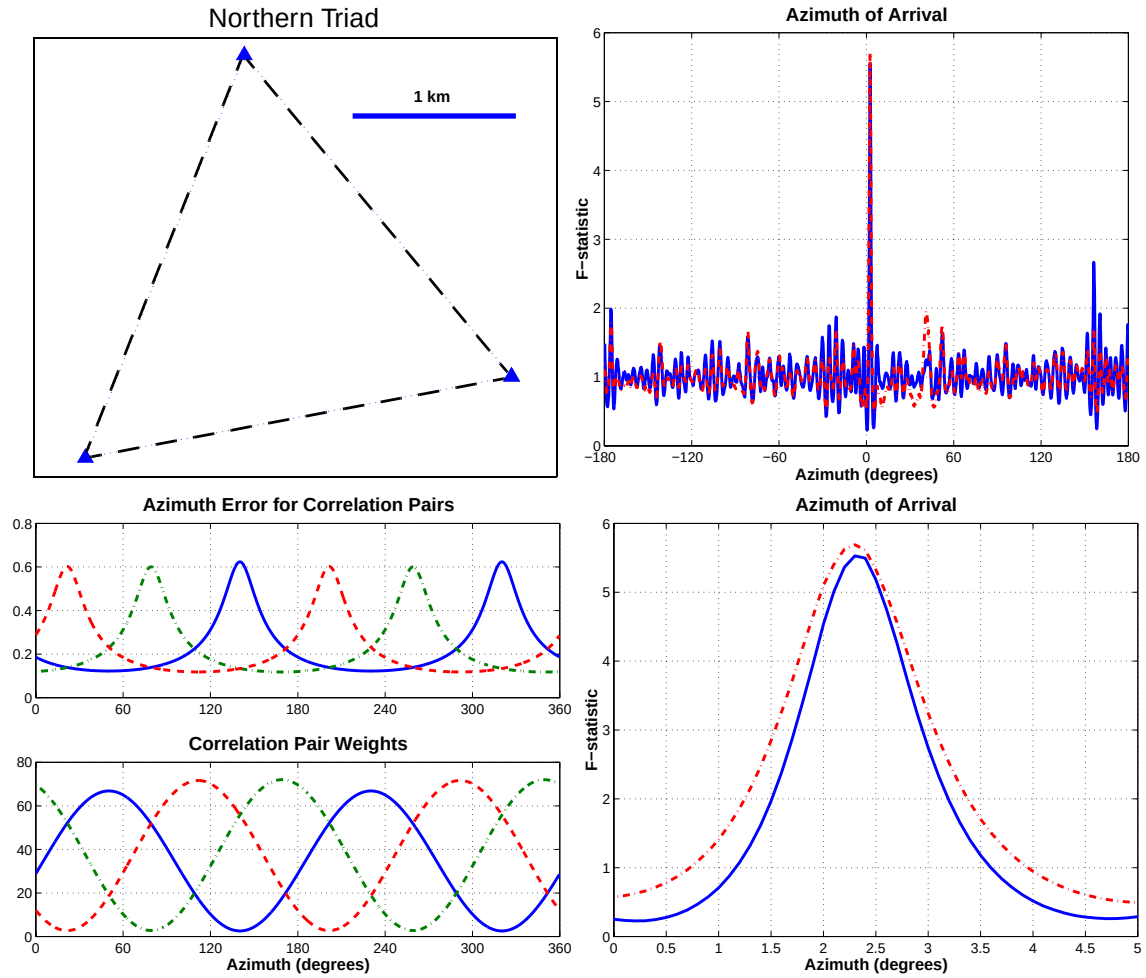

Figure 8. Determining Azimuth from Correlation Pairs. Azimuths are determined from lag times between sensors determined from cross-correlating waveforms. There are 3 pairs of sensors in a triad and

therefore 3 correlations. Because the phase velocity is known, the lag between two sensors is a function of azimuth only. More specifically, it is a function of the angle between the arrival azimuth and the baseline between sensors. By weighting the correlations, it is possible to improve the azimuth resolution. The trade-off is an increase in the side lobes (here at 150°). It may be possible to optimize the weighting functions beyond what is done here.

Explosion Data

The hydroacoustic network has generally lacked ground truth, which has hampered both improvements to the network processing as well as validating the current system. The most important type of data is, of course, explosion data. There are plans for a preliminary calibration experiment in the Indian Ocean for the fall (Blackman 2001), and perhaps a more comprehensive experiment a few years later. In the meantime, any explosion data will greatly help in answering some of the questions identified in this paper.

We have identified a few signals recorded at the northern triad that appear to be from in-water explosions (Figure 10). The signals arrive from the north, but we are unable to locate them since the southern triad is blocked. However these data are still important because they help validate (or show deficiencies in) current processing techniques. The coherency of these signals can improve our understanding of how best to estimate azimuth. They can also be used to estimate the precision of azimuth estimates if not the overall accuracy.

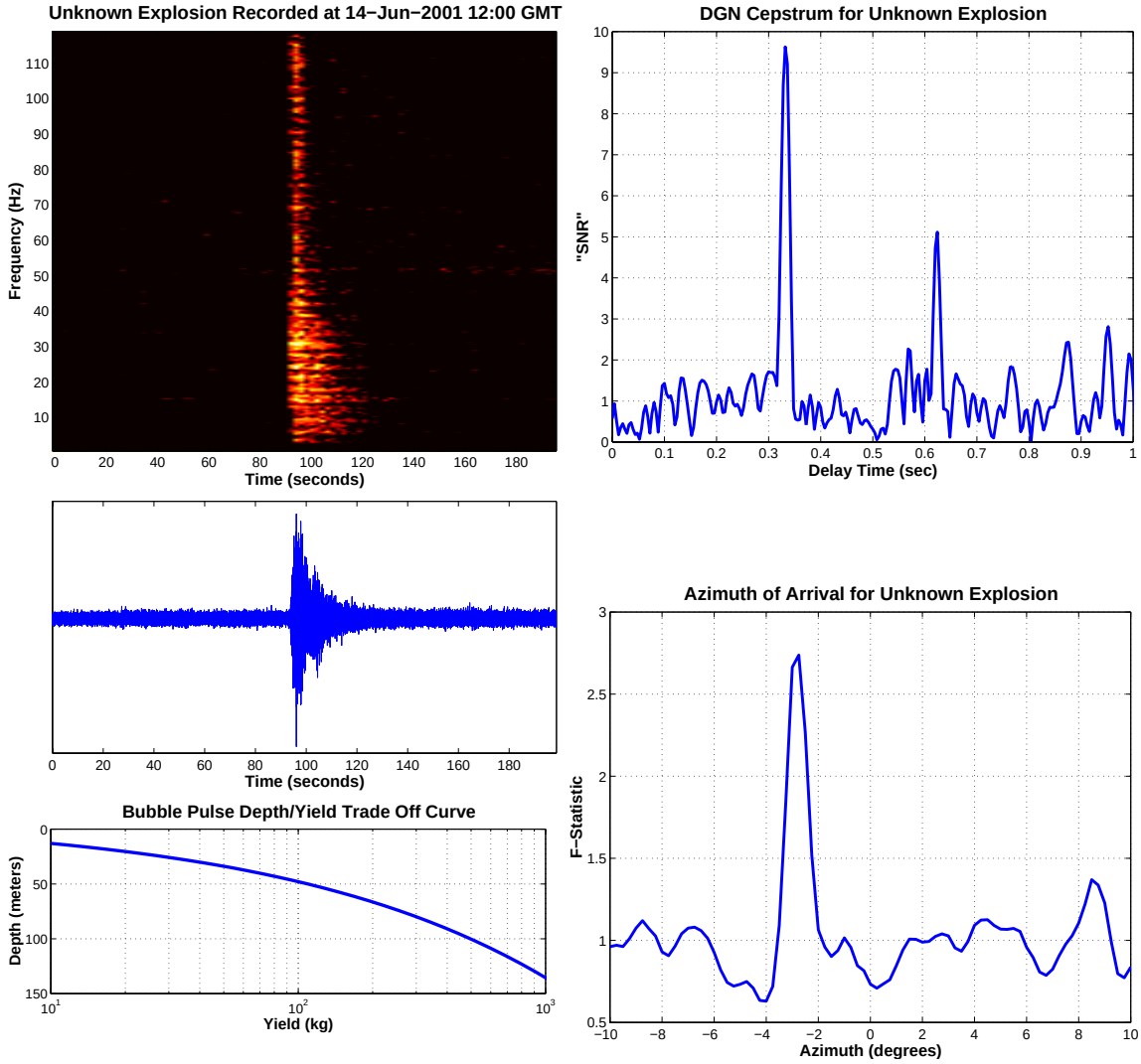

Figure 9. A signal recorded at northern triad that appears to be from an explosion. The scalloping in the spectrum from the bubble pulse is evident in the spectrogram and results in the strong peaks in the cepstrum. The first two peaks in the cepstrum correspond to the first and second collapse of the gas bubble created by the explosion. As expected, the second peak is at a delay time value slightly less than twice the first peak. The depth/yield trade-off curve shows what size explosion it would take to produce a bubble pulse with the observed delay time as a function of source depth (Cole, 1948). The source is almost due north of the northern triad.

CONCLUSIONS AND RECOMMENDATIONS

The PIDC has processed data from the new Diego Garcia hydrophone station for over six months. The station provides high-quality data that provide many opportunities not possible with the older hydroacoustic stations. The noise levels at the two triads are within expected values for deep water locations. The new instrumentation at Diego exhibits a minimum 50-dB gain in dynamic range over the older stations. Hundreds of signals are detected each day at the Diego hydrophones. The current algorithm used to classify signals identifies many to be of “in-water” origin (H), but these are usually signals from local earthquakes. The signals recorded at sensors within a triad can be coherent almost up to the nyquist frequency, but this is not always the case. Some T phases lose coherence at frequencies above 5 Hz.

Azimuth estimation relies on the signal coherence and bandwidth to remove the spatial aliasing inherent in the triad design. Azimuths accurate to within a few degrees are generally achievable, but can fail due to lack of coherence. More investigation needs to be conducted to understand what contributes to this. The ability to achieve very accurate azimuths appears possible and could greatly improve the sparse hydroacoustic network's location ability. The network localization ability based on a more comprehensive understanding of azimuth and arrival time uncertainty needs to be conducted.

REFERENCES

Cole, R.H. (1948) Underwater Explosions, Princeton U Press. Princeton, New Jersey.

de Groot-Hedlin, C., D. Blackman, and J. Orcutt (1998) Observations and Numerical Modeling of T-Phase Coda, Proceedings of the 20th Seis. Res. Sym., 657-665.

Hanson, J., R. Le Bras, P. Dysart, D. Brumbaugh, A. Gault, and J. Guern (2001) Operational Processing of Hydroacoustics at the Prototype International Data Center, Pure Appl. Geophys., 158, 425-56.

Katz, C.N. (2001) personal communication.

Lawrence, M., M. Galindo, P. Grenard, and J. Newton (2000) The Hydroacoustic Network, International Monitoring System: Status and Plans, Proceedings 22nd Seis. Res. Sym., vol. 3, p 51.

Jensen, F.B., W.A. Kuperman, M.B. Porter, and H. Schmidt (1994) Computational Ocean Acoustics, AIP Press, Woodbury, New York.

Wenz, G.M. (1962) Acoustic ambient noise in the ocean: spectra and sources, J. Acoust. Soc. Am., 34, 1936-56.

IMPLOSION SOURCE DEVELOPMENT AND DIEGO GARCIA REFLECTIONS

Philip E. Harben and Carl O. Boro
Lawrence Livermore National Laboratory

Sponsored by
National Nuclear Security Administration
Office of Nonproliferation Research and Engineering
Office of Defense Nuclear Nonproliferation

Contract No. W-7405-ENG-48

ABSTRACT

Calibration of hydroacoustic stations for nuclear explosion monitoring is important for increasing monitoring capability and confidence from newly installed stations and from existing stations. Past work at Ascension Island has shown that ship-towed airguns can be effectively used for local calibrations such as sensor location, amplitude and phase response, and T-phase coupling in the case of T-phase stations. At regional and ocean-basin distances from a station, the calibration focus is on acoustic travel time, transmission loss, bathymetric shadowing, diffraction, and reflection as recorded at a particular station. Such station calibrations will lead to an overall network calibration that seeks to maximize detection, location, and discrimination capability of events with acoustic signatures.

Active-source calibration of hydroacoustic stations at regional and ocean-basin scales has not been attempted to date, but we have made significant headway addressing how such calibrations could be accomplished. We have developed an imploding sphere source that can be used instead of explosives on research and commercial vessels without restriction. The imploding sphere has been modeled using the Lawrence Livermore National Laboratory hydrodynamic code CALE and shown to agree with field data. The need for boosted energy in the monitoring band (2-100 Hz) has led us to develop a 5-sphere implosion device that was tested in the Pacific Ocean earlier this year. Boosting the energy in the monitoring band can be accomplished by a combination of increasing the implosion volume (i.e. the 5-sphere device) and imploding at shallower depths.

Although active source calibrations will be necessary at particular locations and for particular objectives, the newly installed Diego Garcia station in the Indian Ocean has shown that earthquakes can be used to help understand regional blockages and the locations responsible for observed hydroacoustic reflections. We have analyzed several events with a back azimuth from Diego Garcia between 100 and 140 degrees. The Diego Garcia records show a pronounced reflection that correlates in travel time and back azimuth (calculated using the waveform cross-correlation of the tri-partite array elements to determine lag time across the array) with a reflector at the Saya de Malha Bank, on the Seychelles-Mauritius Plateau. We also show that to accurately predict blockage and reflection regions, it is essential to have detailed bathymetry in relatively small but critical areas.

KEY WORDS: calibration, hydroacoustic

OBJECTIVE

Results from the Ascension Island experiment show that for a local hydroacoustic station calibration, an airgun array can accomplish a number of calibration objectives:

1. Accurate location of sensors using numerous precise shot locations (Harben, 1999).
2. Amplitude and phase calibration of the sensors based on good source repeatability (Harben, 2000).
3. Acoustic-to-seismic coupling calibration in the case of T-phase stations (Rodgers, 2000).

Although local station calibrations are necessary to understand the response of a given station, they are not sufficient to understand and characterize the hydroacoustic network performance. Ideally, ocean-basin scale network calibrations with controlled sources would give the network capability assurance that is ultimately desired. Toward this end we have been investigating two issues that have bearing on full network capability assessments. These issues are: long-range acoustic sources for active calibrations and ground truth and reflections and the use of reflected data in network capability assessment. We first present work accomplished on an imploding glass sphere source with the objective of producing an effective long-distance in-band SOFAR (Sound Fixing and Ranging) axis source free from the safety hazards of explosives. Next we present an example of a specific acoustic reflection observed for several earthquakes recorded at Diego Garcia, assessing the back azimuth estimation capabilities of the tri-partite arrays and suggesting how these reflections may be used to improve hydroacoustic monitoring capabilities.

RESEARCH ACCOMPLISHED

The two calibration topics discussed are *implosion source development* and *Diego Garcia reflections*. It should be noted that these studies have their place in a future ocean-basin scale network calibration, the former being one potential source of a number of possibilities that have yet to be tested, the latter being quantified and optimized to improve network detection and location accuracy.

Implosion Source Development

The implosion concept and prototype-controlled imploder have been discussed in a previous paper (Harben et al, 2000). Briefly, an implosive acoustic source is desirable because it offers the potential for SOFAR-depth sources with the acoustic energy release of a small explosion (nominally 1-5 pounds equivalent) but without any of the hazards of explosives. A controlled implosion system developed at Lawrence Livermore National Laboratory (LLNL) uses a cylinder and piston-ram assembly affixed to a 22-liter glass sphere. One end of the cylinder is capped with a pressure-calibrated rupture disc. The other end of the cylinder faces the glass sphere with an external ram attached to the internal piston. When the rupture disc fails, the in-rush of high-pressure seawater drives the piston and external ram into the sphere with sufficient force to shatter it and initiate the implosion.

Implosion results from earlier studies and presented in last year's symposium proceedings (Pulli et. al., 2000) have shown that a 22-liter sphere imploded at a nominal SOFAR channel depth (700 meters) results in a fairly high-frequency acoustic pulse, with the bulk of the acoustic energy out of the monitoring band (2-100 Hz). Two methods that will tend to enhance energy at lower frequencies are: 1) to implode at a shallower depth and 2) to implode a larger sphere volume. Imploding at a shallower depth has the drawbacks of producing a less energetic acoustic pulse due to the lower implosion pressures at shallower depths and producing less efficient coupling of the energy into the SOFAR channel due to the unfavorable ray geometry for trapping energy in the SOFAR channel. A larger implosion source has cost and design implications that require modifying the implosion system. We have looked at both these methods and conducted a field test to determine if we can pump more energy into the frequency band of monitoring interest.

Imploding at a shallower depth was tested using the same single-sphere system used in a test conducted last year. The depth of implosion was 340 meters, half the depth of the previous test. The waveforms of the two tests are shown in Figure 1. Both tests show the characteristic waveform of an imploding sphere: an initial rarefaction pulse during the implosion/compression stage of the collapse followed by a very sharp pressure spike at the instant of complete collapse and motion reversal. A small bubble pulse is also evident. In comparing the two time histories, it is evident that the shallower test had a lower peak pressure, longer collapse time and a longer bubble pulse period. The bubble pulse oscillations from an implosion are analogous to the oscillations from an explosion; however, the details of the physics are quite different. Qualitatively, an explosion generates a shock wave as the explosive rapidly burns and expands. The gas globe consisting of the explosion products expands beyond the diameter of equilibrium pressure with the

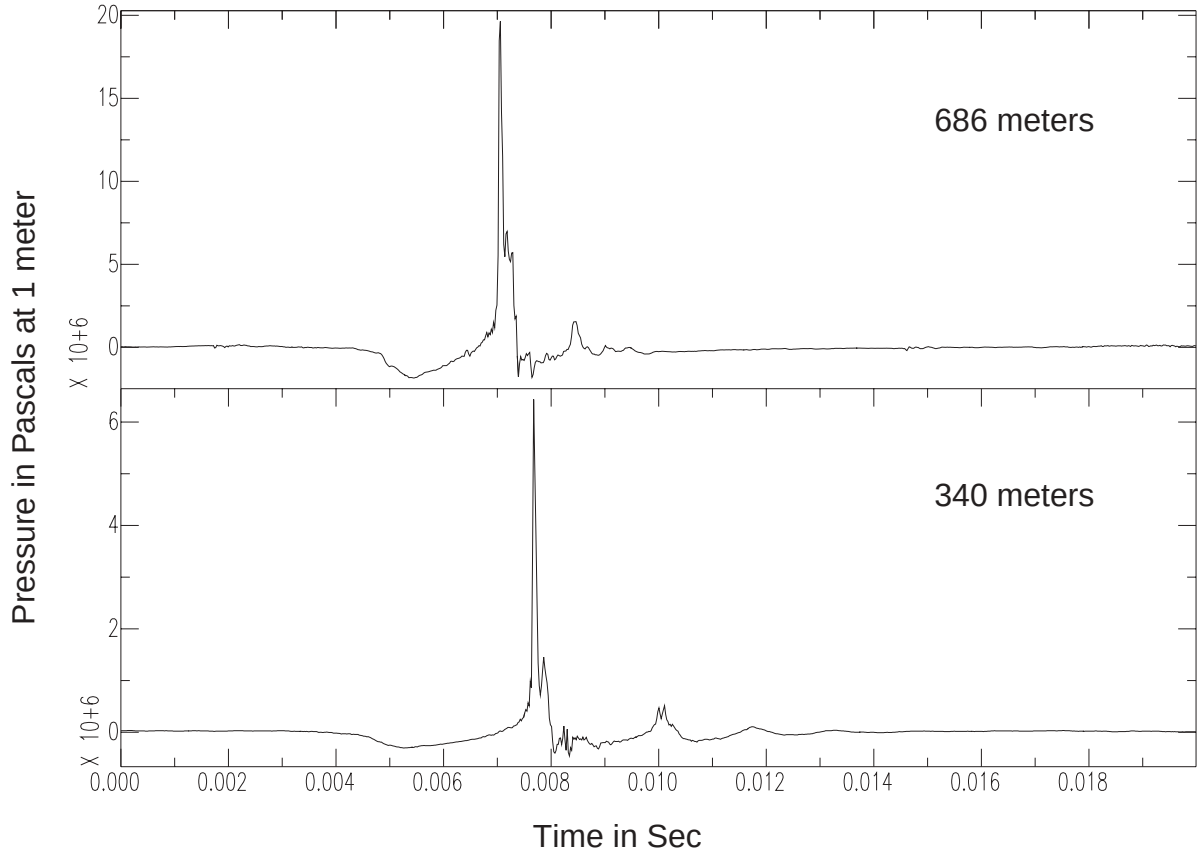

Figure 1. The recorded waveforms from two single-sphere implosion tests. The top test was conducted at 686-meters depth, the bottom at 340-meters depth. Recording is by a ship-suspended hydrophone at nominally 12-meters depth.

ambient seawater then contracts, to oscillate about the equilibrium globe size, giving a bubble pulse at each instant of expansion from a minimum globe size. The implosion begins with a rarefactional pulse as the sphere collapses then generates a shock wave at minimum sphere volume, expanding to oscillate about the ambient pressure. The imploding sphere, however, has a very low gas density relative to the explosion and hence bubble pulses are not pronounced or persistent. The measured values for collapse time, bubble pulse period, and peak pressure are shown in Table 1 below. The values in the table also show results for a single-sphere implosion at 130 meters. This was taken from the initial record of the 5-sphere collapse shown in Figure 3.

	686 meters	**340 meters**	**130 meters**
Peak Pressure (Pa)	2.0×10^7	6.5×10^6	5.0×10^5
Collapse Time (msec)	2.7	4.4	6.9
Bubble Pulse Period (msec)	1.3	2.4	----

Table 1. Measured Values for Implosion Experiment

The bubble pulse period has been shown for explosions to be inversely proportional to (see Urick, 1983) $d^{5/6}$ for depth, d, greater than 100 meters. This is consistent with the observed bubble pulse period differences between 686 meters and 340 meters. A bubble pulse period could not be determined for the 130-meter test because of the interference created by the collapse of the other four spheres.

The pressure peak and collapse time were calculated using the LLNL hydrodynamics code CALE (see Tipton, 1991) by Clark, 2001, for the 686-meter case and found reasonable agreement in peak pressure (1.18×10^7 Pa calculated vs 2.0×10^7 Pa actual) and collapse time (2.0 msec calculated vs 2.7 msec actual). As of this writing, model predictions of peak pressure and collapse time at other depths have not been conducted. It should be noted that implosion collapse modeling of the acoustic frequency spectrum has been conducted by Guerin et al, 2001. Because we could not record at a high enough sample rate on the ocean bottom hydrophone, we cannot compare our results directly to these models.

Increasing the implosion volume by increasing the diameter of the implosion sphere is impractical from a cost and operational standpoint. The 22-liter spheres we used are about the largest we have found commercially. To produce a significantly larger sphere would require special development and substantially thicker walls. Such a sphere would be costly, heavy, and large. We chose instead to cluster a number of the spheres together and thereby increase the overall volume of the implosion. A photograph of the prototype device is shown in Figure 2. The device consists of orthogonal steel planar forms that serve to hold the spheres in place, the same smashing cylinder as used in the single sphere system, and the five spheres. The idea is simple: smash one sphere and the rest will shatter in sympathy once the shock wave from the first implosion develops.

Figure 2. The prototype 5-sphere implosion system is shown next to the 1-sphere system. The smashing cylinder is the same for both.

We tested the 5-sphere system at 130-meters depth. The implosion test was about as large and as shallow as deemed likely in any hydroacoustic monitoring calibration scenario that would use such sources and hence shows about the best that can be easily achieved in pumping more relative acoustic energy into the monitoring frequency band. The 5-sphere implosion waveform, shown in Figure 3, was recorded at a sample rate of 16 kHz on the near-surface hydrophone, fast enough to capture many details of the implosion.

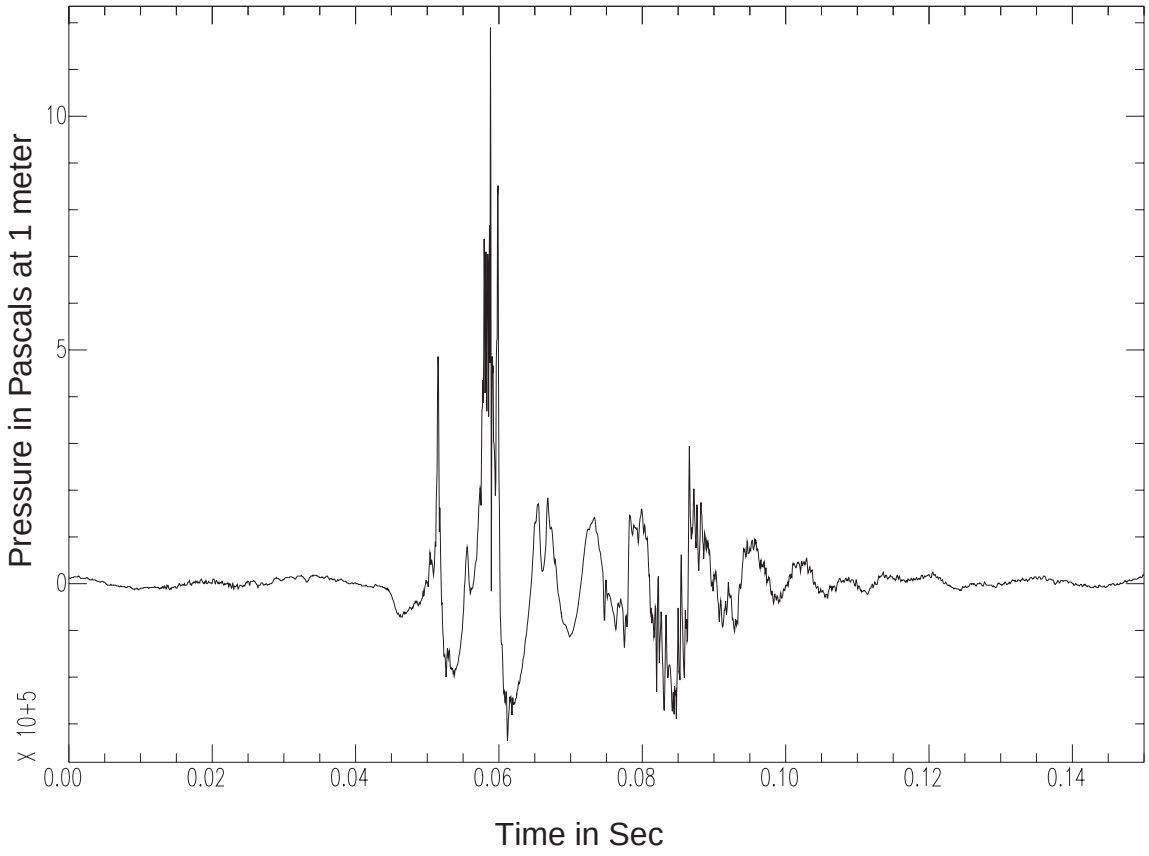

Figure 3. The recorded waveform for the 5-sphere implosion conducted at 13-meters depth. Recording is by a ship-suspended hydrophone at 12 meters nominal depth.

The characteristic collapse of a single sphere is seen in the beginning of the record. The peak pressure and collapse time from this were used to fill in the 130-meter column within the table above. After the peak pressure spike from the first imploding sphere, a larger collapse event is evident followed by a complex pressure spike. We believe this to be the nearly simultaneous collapse and peak pressure spikes from the other four spheres. A complex bubble pulse interference follows with high-frequency hash arriving at about 0.08 sec, consistent with a reflection of the acoustic energy from the free surface.

Unfortunately, the near surface hydrophone recording is not a quantitative indicator of the low-frequency content in the acoustic signal because of interference from the reflection off the ocean surface. It is best to record the signal as deep as possible. This was done during the recent series of sea tests by deploying several Ocean Bottom Seismometers (OBS) with associated hydrophones. Although the hydrophone record obtained at 1.2-km depth was only sampled at 125 Hz with an anti-alias filter at 33 Hz, the 5-sphere recording showed over 80 Db S/N in the acoustic energy density between 3 and 33 Hz. Based on cylindrical spreading in the sound channel and the very low attenuation at these low frequencies, this signal level coupled in the sound channel should be observable thousands of kilometers from the source. What we have failed to determine in these tests is how effectively we couple signal into the sound channel and how this coupling changes as the depth of the source is varied. To conduct these experiment we will need

hydrophones in the SOFAR channel at large distances from the source. Upcoming experiments will allow us to make these measurements.

Diego Garcia Reflections

The observation of hydroacoustic reflections off topographic features is not new (see Kibblewhite et al, 1969 and Northrop, 1968). A recent study by Pulli et al, 2000, has revisited some historical explosions that exhibit topographic reflections and concluded that there is a potential for using reflections to enhance hydroacoustic monitoring capabilities. Since this study, the Diego Garcia (DG) station has come on-line. The north arm of the new Diego Garcia (DGnorth) station was operational by the middle of 2000 and the south arm (DGsouth) of the station near the end of 2000. This is the first International Monitoring System hydroacoustic station that conforms to specifications and has been certified. Many research teams are now examining this new data set and are finding interesting things that will be reported elsewhere. Of particular interest in this study is the potential for using the tri-partite arrangement of hydrophones to calculate a back azimuth and thereby provide an automated method to associate and pinpoint reflected phases. We examined four large (greater than M 4.5) oceanic earthquakes that vary in bearing from about 100 degrees from DG to about 140 degrees (see Figure 4). Three of the four earthquakes occurred before DGsouth was on-line. We analyzed the T-phases recorded by the station to see if accurate back azimuths could be determined and to determine if arrivals after the direct T-phase could be reflections of the direct phase off some bathymetric obstacle.

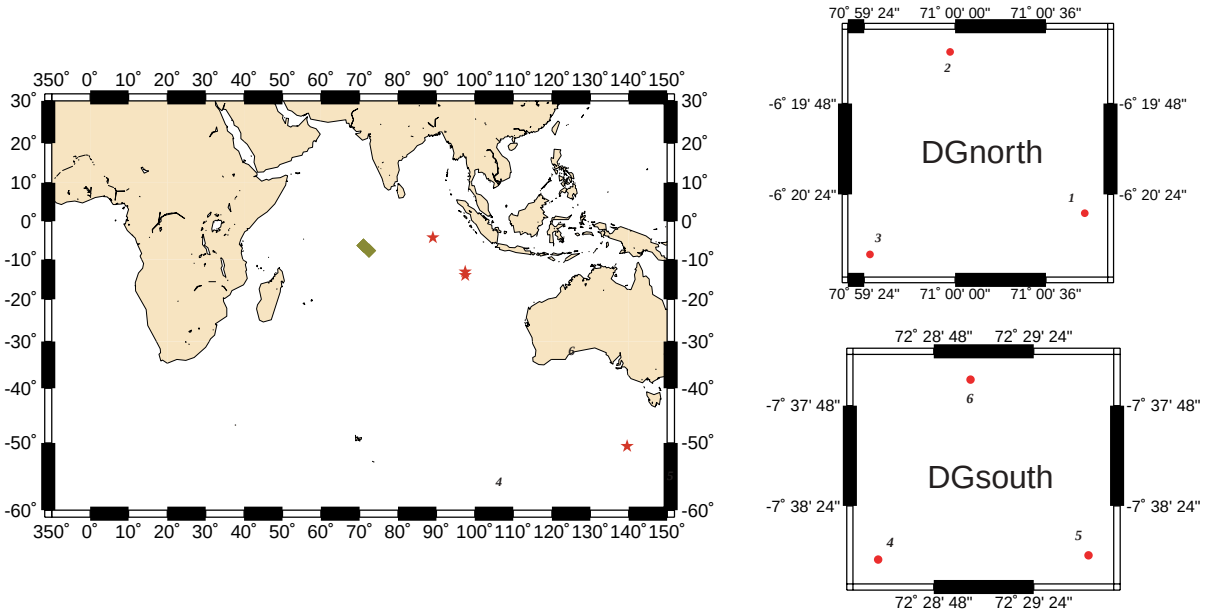

Figure 4. The left map shows the four earthquakes analyzed (stars) and the two Diego Garcia station arms (diamonds). The right maps show the sensor layout for the north (top) and south (bottom) arms of the station.

The spacing of the north-arm hydrophones is about 2.5 km, too large to use standard array processing given that the nominal frequency band of these earthquake generated T-phase signals is 2-12 Hz. Instead, we assumed a coherent plane wave and looked for the lags in the peaks of the signal cross-correlations among sensor elements. We used a 40-second time window that encompassed the bulk of the signal. The windowed waveforms were band-passed with lower and upper corners of 2 Hz and 12 Hz, respectively. These signals were then cross-correlated to determine the lag in the cross-correlation peaks and derive a back azimuth. The same process was applied to all the direct and reflected phases discussed herein. The process is shown in Figure 5 for both the direct phase and a specific reflected phase of a June 18, 2000, Mb 6.8 earthquake located in the South Indian Ocean (the nearly over-plotted stars in the Figure 4 map). This earthquake was about 3010 km from DGnorth on a bearing of 108 degrees from the station. The lags in the cross-correlation peaks of the direct T-phase (the left plot on Figure 5) give a back azimuth of 111 degrees, only

3 degrees from the true value. Notice the relatively poor S/N of the cross-correlation peaks as compared to those from the reflected phase (the right plot in Figure 5) even though the S/N of the direct phase is much larger that the reflected phase. We will discuss the likely cause for this observation at the end of this section. The bearing from DGnorth to the

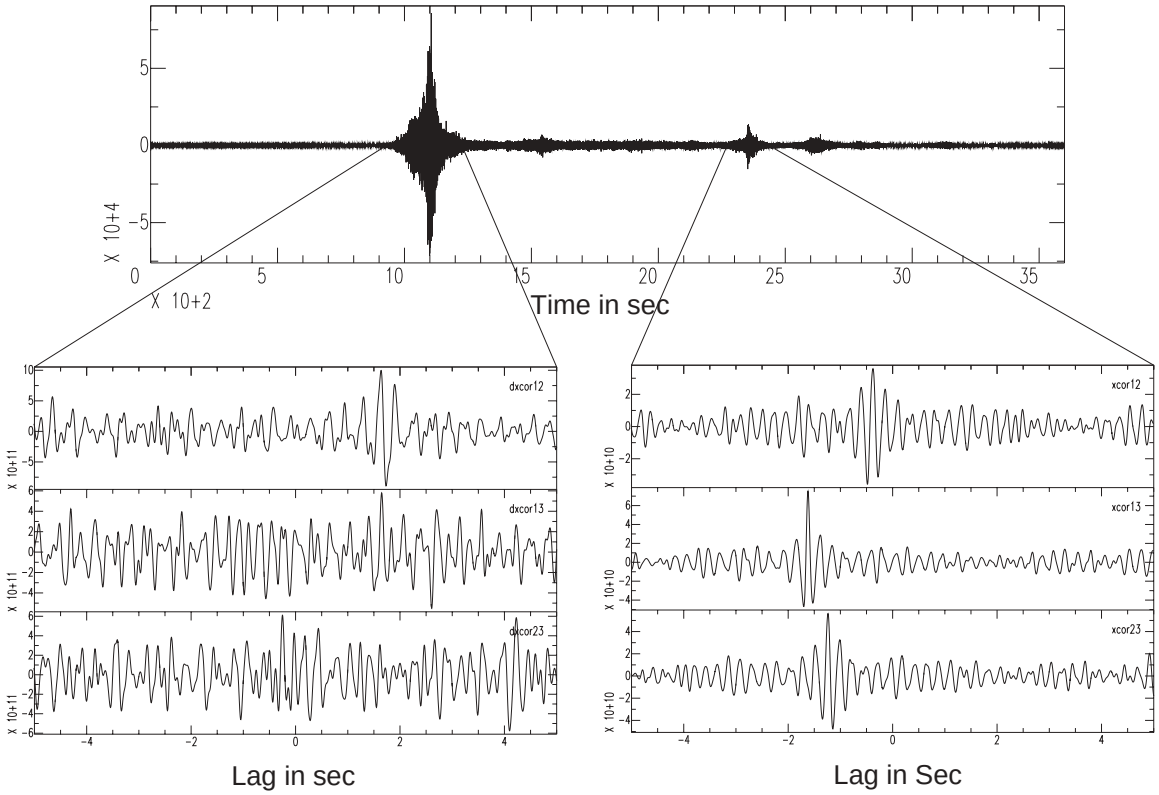

Figure 5. The 6/18/2000 M 6.8 Indian Ocean earthquake is shown at top as recorded by DG01. The waveform cross-correlations of the three north-arm elements are shown for the windows indicated. Notice the direct T-phase (left) has relatively poor cross-correlation peaks compared to a reflected phase (right) despite the much larger S/N of the direct phase.

reflection source as determined by the lags in the cross-correlation peaks is 246 degrees. If we plot the paths of the direct T-phase from the earthquake to DGnorth and the path 246 degrees from DGnorth to the nearest possible bathymetric reflector, we get the presumed reflected T-phase path as shown in Figure 6. The arrival time of such a reflected path is consistent with the observed arrival time, and spectrograms of both the direct and reflected phase are remarkably similar in frequency content and duration. We conclude that the Saya de Malha Bank of the Seychelles-Mauritius Plateau is the likely T-phase reflector for this earthquake.

We analyzed a number of other phases arriving after the direct T-phases for the earthquakes shown in Figure 4. Some gave the same back azimuth as the direct T-phase and consequently may have been aftershocks. Others gave different bearings. We will only focus on the one particular reflection source determined in Figure 5 and Figure 6, the Saya de Malha Bank, and see if other earthquakes on similar bearings produce an observable reflection off the same reflector.

A South Indian earthquake on 9/17/2000, shown nearly over-plotted with the 6/18/2000 event in Figure 4, is a Mb 4.7 presumed aftershock. Although the ratio of signal to noise (S/N) of the direct phase from this event is high, we could not determine a back azimuth because of poor correlation among the tri-partite hydrophones. A phase barely above the noise with arrival time consistent with the same reflection path of Figure 6 was analyzed and found to have surprisingly high correlation among the tri-partite hydrophones with good agreement for the cross-correlation peaks. The back azimuth was 246 degrees, consistent with a reflection off the Saya de Malha Bank.

Finally, an Mb 5.9 earthquake from the West Indian Ocean/Antarctic Ridge (lowest right in Figure 4) on June 11, 2000, was analyzed in the same way as the previous events. The back azimuth of the direct T-phase was calculated from the array elements to be 141 degrees compared to an actual back azimuth of 141 degrees. A reflected phase with poor S/N was identified on the time history recordings with an arrival time consistent with a reflection off the Saya de Malha Bank on the Seychelles/Mauritius Plateau. The back azimuth calculated with the tri-partite hydrophones for this phase had a bearing of 244 degrees, consistent with a reflection off the Bank. We conclude that for this event a reflection off the Saya de Malha Bank is observed. It should be noted that, as in the previous events, the S/N of the peak in the cross-correlation function was also far higher for the low-S/N reflected signal than for the high-S/N direct T-phase.

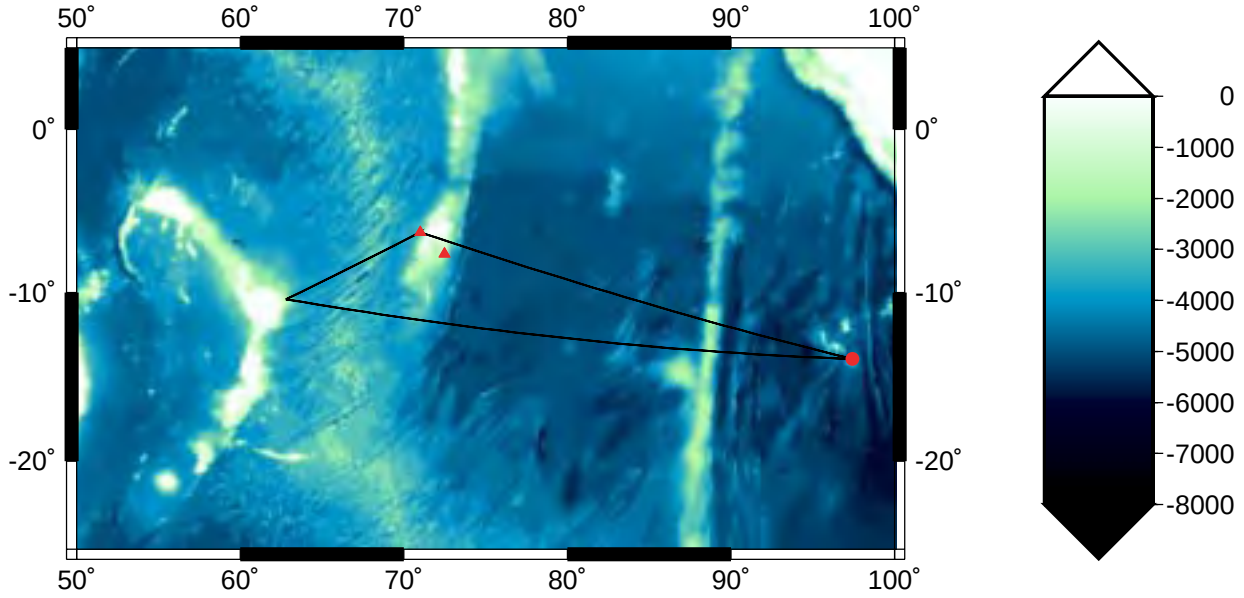

Figure 6. The regional bathymetry with the Diego Station arms (triangles) with the direct and reflected path from the 6/16/2000 earthquake (circle) to the north arm of the Diego Garcia station.

The reason for the poor S/N of the direct T-phase cross-correlation peaks when compared to the reflected cross-correlations is probably due to local Diego Garcia bathymetric scattering of the plane wave along the direct path. The scattering presumably results in poor spatial coherence of the signal when it reaches the sensors, even though the S/N is still quite large. No such bathymetric obstacle (other than the reflector) exists on the reflected path. This does not rule out the possibility that the modal composition of the direct T-phase is changed upon reflection to produce a more spatially coherent signal. A recent event (Mb 4.9 on 3/11/2001, after the south arm of DG became operational, the northernmost on the map of Figure 4) pretty much rules out modal composition change as the main reason for the observed S/N differences of the sensor cross-correlation peaks. That event had poor S/N for cross-correlation peaks of the direct T-phase signal at the north arm but excellent S/N of the cross-correlation peaks of the direct T-phase at the south arm where there were no bathymetric obstacles along the path. If complex modal composition of the direct T-phase was the cause of poor S/N of the cross-correlation peaks, then we would expect it on both the north and south arms.

CONCLUSIONS AND RECOMMENDATIONS

A large-scale calibration experiment that tests a number of sources against the various calibration objectives is a first step in defining what an ocean-basin-scale calibration of the hydroacoustic monitoring network will consist of. It is clear at the outset that no one source will accomplish all of our objectives. Implosion sources, airguns, explosions, and other sources will be tested during the next two years to determine the range scale and calibration objective each is suited for. Our recent work on implosion sources indicates that we can boost energy in the monitoring frequency band and that such a source may be useful for inexpensively and safely gathering travel-time, transmission loss, and

blockage calibration data on a regional to ocean-basin scale. Tests will soon be conducted in the Indian Ocean that will determine just what range-scale the implosion source will be applicable to. One point is clear: the implosion source is far too small to be used for any type of reflection calibration. Such calibrations will have to use special purpose low-frequency sources or fairly large explosions.

Data from the Diego Garcia station --with the tri-partite sensor arrays-- have been full of surprises that beg a rethinking of just how to process hydroacoustic data in a monitoring context and how far we can go in squeezing more capability out of a sparse sensor network. We have documented that consistent reflections occur for sources at particular bearings from the station. In addition, we showed that fairly accurate (within a few degrees) back azimuth estimates of the direct and reflected signal could be determined by examining broadband cross-correlations of the signals across the array elements. Using active sources and natural events, a database of the reflection zones in the Indian Ocean can be developed. If the reflection zones can be sufficiently localized, reflected phases may be able to enhance network location capability. At the very least, reflected phases may be the only path that reaches a particular station arm that is otherwise blocked by topography and hence the only way for that particular station to be used in a detection, location, or discrimination scheme.

ACKNOWLEDGEMENTS

We thank Leroy Dorman and Allen Sauter of the Scripps Institution of Oceanography for support during the field test aboard the R.V. Sproul, provided by the National Science Foundation under grant OCE 97-12605. Doug Clarke provided the CALE simulation of the implosion. Richard Baumstark of the Air Force Technical Applications Center supplied the Diego Garcia recordings.

REFERENCES

Guerin, J-M and P-F Piserchia (2001), Analysis of the Hydro-acoustic Energy Released by an Implosion of a Glass Sphere, Commissariat a l Energie Atomique, DAM DIF DASE.

Hanson, J.A. and P.E. Harben (2000), Acoustic-to-Seismic Wave Coupling Study at Ascension Island, Proc. SSA Annual Mtg., April, 2000.

Harben, P.E., J.R. Hollfelder, and A.J. Rodgers (1999), Experimentally Determined Coordinates for Three MILS Hydrophones near Ascension Island, UCRL-ID-136507.

Harben, P.E., D.K. Blackman, A.J. Rodgers, C. Turpin, and J.R. Hollfelder (2000), Calibration Factors for Three MILS Hydrophones Near Ascension Island, UCRL-ID-138036.

Harben, P.E., C. Boro, L. Dorman, and J. Pulli (2000), Use of Imploding Spheres: An Alternative to Explosives As Acoustic Sources At Mid-Latitude SOFAR Channel Depths, UCRL-ID-139032.

Kibblewhite, A.C. and R.N. Denham (1969), Hydroacoustic Signals from the Chase V Explosion, J. Acoust. Soc. Am., 45, 944-956.

Northrop, J. (1968), SubmarineTopographic Echos from Chase V, J. Geophys. Res., 73, 3909-3916.

Pulli, J.J., Z. Upton, R. Gibson, J. Angell, T. Farrell, and R. Nadel (2000), Characterization of Reflected Arrivals and Implications for Hydroacoustic Test-Ban-Treaty Monitoring, BBN Tech. Memor. W1380.

Pulli J.J. and P.E. Harben (2000), Hydroacoustic Calibration with Imploding Glass Spheres, in 22nd Annual DoD/DOE Seismic Research Proc., Vol. III, pp. 65-74.

Tipton, R. (1991), CALE User s Manual, Version 920701, Lawrence Livermore National Laboratory, Livermore, CA.

Urick, R.J. (1983), Principles of Underwater Sound, Peninsula Publishing, Los Altos, CA.

ARRIVAL STRUCTURE OF LONG-RANGE PROPAGATION EXCITED BY A FINITE AMPLITUDE SOURCE

W. A. Kuperman[1], B. E. McDonald[2] and G. L. D Spain[1]

[1]University of California, San Diego, [2]Naval Research Laboratory

Sponsored by Defense Threat Reduction Agency

Contract No. DTRA-00-C-0084

ABSTRACT

We have studied the group and phase speed structure of long-range acoustic arrivals using linear acoustics. Here we present a preliminary study of some of these same paths but now we consider a higher amplitude source necessitating a nonlinear acoustic treatment. This research involves the eventual coupling of the Nonlinear Progressive Wave Equation (NPE) with an Adiabatic Normal Mode (ANM) Model. We use the ANM model (which has limited range-dependent capability) because our previous treatment for the linear problem was very revealing with respect to the physics of the arrival structure.

KEY WORDS: acoustic arrival, nonlinear progressive wave equation, hydroacoustic

OBJECTIVE

The objective of this work is to derive new technologies, based on the physics of underwater sound propagation (both linear and nonlinear), for localizing underwater sound sources using data from single hydrophone stations that are part of the International Monitoring System.

RESEARCH ACCOMPLISHED

Introduction

According to linear acoustic theory, the arrival structure of a pulse propagating a long distance in the ocean is a result of the relationship between group speed and phase speed of its various components, the latter often characterized as the frequency dependent normal modes, or more simply, acoustic multipaths (Kuperman et al, 2001). In particular, it is the appropriately integrated group speed over the individual acoustic/geographic paths that are important, and the arrival structure therefore contains source property information including its location. This group-vs-phase speed property is, in linear acoustics, independent of source amplitude. Even though the nonlinear or amplitude-dependent regime becomes more complicated, the original nonlinear nature of the source may remain as a scar in the received long distance linear arrival. The goal of this research is to address the possibility of this potential diagnostic. This paper outlines some of the basic linear-vs-nonlinear issues and presents some initial calculations illustrating these points.

Group Speed vs Phase Speed in Linear Acoustics

Though global acoustic propagation can occur only in deep water, we must include coastal or shallow water, bottom reflecting environments because of the potential location of a high amplitude source. The classic group/phase speed representation in shallow water is the so-called Pekeris curves (Jensen et al, 1994) shown in Figure 1 for modal propagation:

We are basically interested in the regime to the right of the minimum (Airy phase) of the group speed curves. Here we see that when phase speed increases, group speed decreases corresponding to a positive waveguide invariant β (Chuprov, 1982; Brekhovskiskh and Lysanov, 1991; D'Spain and Kuperman, 1999). Physically, this can be easily explained in terms of paths with higher angles with respect to the horizontal, and therefore, large

(horizontal) phase speeds, propagate energy at lower speeds.

On the other hand, the set of deep water paths shown in Figure 2 have more diversity in their group-vs-phase speed dependence. Bottom bounce paths have the same relation as above, but the deep refracting paths, such as the RR and RSR paths typically have the opposite group-vs-phase speed dependence. That is, group speed increases with increasing phase speed ($\beta < 0$) because the deep paths refract in water column regions of higher speed as opposed to the bottom reflection case in which a reflection occurs before a path can reach a sufficiently higher speed region in which the net effect over the path is to increase the group speed. In realistic ocean environments, the sound speed varies with range such as the climatology data associated with recent ATOC experiments (Worcester et al, 1991; ATOC Consortium, 1998; Worcester et al, 1999; Colosi, et al, 1999; Heaney and Kuperman, 1998) shown in Figure 3. We must then calculate the effective group speed over the whole path. An adiabatic normal mode computation (Jensen et al, Heaney et al, 1991) is often adequate, where, in addition, we approximate the phase speed to be a continuous variable because of the typically large number of modes, whereas in reality there is a discrete distribution of modes.

The local phase speed of the nth mode at the source location (which corresponds to a launch angle) is related to the modal wavenumber k_n,

$$c_{pn}(\omega) = \frac{\omega}{k_n}, \tag{1}$$

where ω is the angular frequency of the propagating acoustic mode. In a range-dependent environment, we must derive an effective average modal group speed, u_n, from the range-averaged slowness. That is, we note that the pulse observables at range r are arrival times that are given by r/u_n. Hence, for a range-dependent environment we are concerned with $1/u_n \equiv \bar{s}_{gn}$ where the overbar denotes range averaging and s_{gn} is referred to as the (local) modal group slowness. Since the adiabatic mode approximation has a range-averaged modal wavenumber associated with each term, it follows that (Jensen et al, 1994)

$$\overline{s_{gn}(r,\omega)} = \frac{\partial}{\partial\omega}\left(\frac{1}{r}\int_0^r k_n(r',\omega)dr'\right) \tag{2}$$

and the range-dependent effective group speed is,

$$< u_n(r,\omega) >= \frac{1}{\overline{s_{gn}(r,\omega)}} \tag{3}$$

Hence, the range-dependent effective group speed is obtained from the harmonic average:

$$\frac{1}{\langle u_n(r,\omega)\rangle} = \frac{1}{r}\sum_{\Delta r'_n}\frac{\Delta r'_n}{u_n(r',\omega)} \tag{4}$$

where the sum is taken over the approximate n range-independent subintervals, $\Delta r'_n$, of the propagation path. Finally, we note that we can interchange the partial with the integral sign in Eq. 2 and can use the modal formula for the (local or range-independent) modal group speed (Jensen et al, 1994),

$$\frac{\partial k_n}{\partial\omega} = \frac{1}{u_n(\omega)} = \frac{\omega}{k_n(\omega)}\int_0^\infty \frac{p^2{}_n(\omega;z)}{\rho(z)c^2(z)}dz, \tag{5}$$

where $p_n(\omega; z)$ are the normal mode eigenfunctions of the pressure field in the ocean waveguide and $\rho(z)$ and $c(z)$ are the density and sound speed profiles as a function of depth.

Applying Eq. (4) to the data in Figure 3, we obtain the effective group speed (at a final specified range) vs phase speed (g-v) curves parameterized by frequency shown in Figure 4. These curves are actually a summary of the expected pulse arrival structure. Thus, for example, we should see three dominant features in the arrival structure. At the lowest phase speed, we note that all the modal group speeds are independent of frequency and these components have the same and lowest group speed. Hence, there should be a high-intensity last arrival since all components arrive at the same time. Next there should another high-intensity arrival (RR/RSR) region

corresponding to a phase and group speed of (1516 km/s, 1483.6 km/s). At this coordinate there is a stationary region for a group of modes (Kuperman et al, 2001). Finally, there is the region on the upper right that cuts off (to dispersive, lossy bottom interacting modes. This high group speed region, which describes the fastest paths (earliest arrivals) should be low in amplitude. The above is descriptive of the experimental results for this ATOC path shown in Figure 5.

Finally, with respect to linear acoustics, we mention that, as described above, since shallow and deep water propagation have different g-v curves, a transition from shallow to deep water will have a profound effect on the arrival structure. This can be seen from Eq. (4), which states that the effective group speed is an average over group slowness. That is, group speeds add like parallel resistors and so a small continental shelf region will have a large effect on the arrival structure. Hence, we have a linear diagnostic for sources originating in shallow vs deep water regions.

Nonlinear Propagation Effects

Large amplitude sources produce nonlinear effects in which super-position principle breaks down and new frequencies are generated. These effects, even after decay to the linear acoustic regime, remain as possible diagnostics of high-energy sources. In this section, we summarize some of the nonlinear waveguide effects that we expect will be useful. We will base the discussion on the Nonlinear Progressive Wave Equation (NPE) (McDonald and Kuperman, 1985; McDonald and Kuperman, 1987).

The NPE is based on a first-order nonlinear wave equation bearing the same relation to hydrodynamic compressional waves that the Korteweg - de Vries (KdV) equation bears to weakly nonlinear incompressible waves in water. The NPE is cast in a pulse-tracking frame of reference translating at a speed approximating the speed of sound (see Figure 6), and includes lowest order compressional nonlinearity along with diffraction and refraction. For appropriate environments, it possesses similarity solutions (McDonald and Ambrosiano, 1988) analogous to the solitary wave solutions of the KdV equation.

Normally we use pressure in linear acoustics, but it has been convenient to derive the NPE in terms of density; let $R_1(\mathbf{r}, t)$ be a linear baseline acoustic solution, then the NPE for quadratic nonlinearity is given by

$$(c_0^{-1}\partial_t + \partial_r + \frac{1}{2r})R_2 = -\alpha R_1 \partial_r R_1; \tag{6}$$

where, $\propto$ is the coeffcient of nonlinearity. With the modal sum expressed in the time domain

$$R_1(r,z,t) = \sum_n A_n(r)\psi_n(z)\cos(k_n r - \omega t + \phi_n), \tag{7}$$

we obtain, after substantial mathematical manipulation, a nonlinear modal propagation equation for the depth integrated field,

$$\int dz R_2 = \alpha \sum_n \frac{a_n(r)^2 k_n}{2} Q(\theta_n)\sin 2(k_n r' + \varphi_n) \tag{8}$$

where the actual form of Q is given elsewhere (McDonald, 2002). The important point here is the generation of harmonics. This result is a particular simple form obtained by restricting the background environment to an analytical, convergence zone generating sound speed profile. Here we begin to see solutions that exhibit the modal behavior that must accompany nonlinear acoustic propagation; that is, the emergence of harmonics. This idealized result, shown in Figure 7, indicates that the vertically integrated second harmonic maximizes near odd number convergence zones and represents an example of the expected departure from linear results of the previous section.

The nonlinear tendency toward greater bottom interaction has been documented elsewhere (Ambrosiano et al, 1990) using the NPE. This would alter the modal excitation spectrum toward bottom interacting acoustic modes. That is, wavefront steepening shifts the source spectrum toward higher frequency, while Mach reflection increases bottom interaction. A schematic modal frequency - arrival time diagram, shown in Figure 8, illustrates that bottom interaction gives rise to clustered low-frequency arrivals before the final deep water axial cutoff (the lowest group speed). Figure. 9 shows a plot for another ATOC example to be considered in the context of Figure 8. Thus, one evidence of a nonlinear event in the water column could be the appearance of

another focal spot at low frequency in Figure 9 corresponding to the arrival of the bottom interacting modes vs the already existing surface interacting focal region at 2010 seconds. This suggests that we may be able to fold nonlinear effects into a g-v, albeit amplitude dependent, type summary of the propagation conditions.

CONCLUSIONS AND RECOMMENDATIONS

We have shown that the group speed dependence on phase speed (g-v curves) is diagnostic of the arrival structure of a long -distance propagating pulse governed by linear acoustics. Further, we have shown that the effective group speed results from averaging slowness. The different g-v structure in shallow and deep water will show up in the received arrival structure of a pulse traveling between shallow and deep water. Finally, we have also demonstrated that nonlinear modal propagation redistributes the modal acoustic energy and hence the integrated group speeds. Our next goal is to cast these nonlinear results in the analogous g-v structure we have set up for the linear case.

REFERENCES

Ambrosiano, J., D. R. Plante, B. E. McDonald, and W. A. Kuperman (1990), Nonlinear Propagation in an Ocean Waveguide , *J. Acoust. Soc. Am*. 87, 1473 - 1481.

ATOC Consortium (1998), Ocean Climate Change: Comparison of Acoustic Tomography, Satellite Altimetry, and Modeling , *Science* 281,1327-1332.

Brekhovskikh, L. M. and Y. P. Lysanov (1991), *Fundamentals of Ocean Acoustics*, 2nd ed., Springer-Verlag, New York (1991).

Chuprov, S. D. (1982), Interference structure of a sound field in a layered ocean, in *Ocean Acoustics, Current State*, ed. by L. M. Brekhovskikh, I. B. Andreevoi: Nauka, Moscow, 71-91.

Colosi, J. A., E. K. Sheer, S. Flatte, B. D. Cornuelle, M. A. Dzieciuch, W.H. Munk, P. F. Worcester, B. M. Howe, J.A. Mercer, R.C. Spindel, K. Metzger, T. G. Birdsall and A.B. Baggeroer (1999), Comparisons of measured and predicted acoustic fluctuations for a 3250-km propagation experiment in the eastern North Pacific," *J. Acoust. Soc. Am*., 105(6), 3202-3218.

D'Spain, G. L. and W. A. Kuperman (1999), Application of waveguide invariants to analysis of spectrograms from shallow water environments that vary in range and azimuth , *J. Acoust. Soc. Am*., 106(5), 2454-2468.

Heaney, K. D. and W. A. Kuperman (1998), Very long-range source localization with a small vertical array , *J. Acoust. Soc. Am*. 104(4), 2149-2159.

Heaney, K. D., W. A. Kuperman and B. E. McDonald (1991), Perth- Bermuda sound propagation (1960): Adiabatic Mode Interpretation, *J. Acoust. Soc. Am*. 90, 2586-2594.

Jensen, F. B., W. A. Kuperman, M. B. Porter and H. Schmidt (1994), Computational Ocean Acoustics, AIP Press, Woodbury, N.Y.

Kuperman, W. A., G. L. D Spain and K. D. Heaney, (2001), Long range source localization from single hydrophone spectrograms, *J. Acoust. Soc. Am*. 109, 1935-1943.

McDonald, B. E. and W. A. Kuperman (1985), Time Domain Solution of the Parabolic Equation Including Nonlinearity *J. Comp. Math. w. Appl.* 11, 843 - 851.

McDonald, B. E. and W. A. Kuperman (1987), Time Domain Formulation for Pulse Propagation Including Nonlinear Behavior at a Caustic, *J. Acoust. Soc. Am*. 81, 1406 - 1417.

McDonald, B. E. and J. Ambrosiano (1988) Similarity Solution for Low Mach Number Spherical Shocks , *J. Acoust. Soc. Am*. 84, 1497 -1503.

McDonald, B. E. (2002), Nonlinear Effects in Source Localization , in *Ocean Acoustic Interference Phenomena*, eds. W. A. Kuperman and G. L. D Spain, AIP Press, NY.

Worcester, P. F., B. D. Cornuelle, J. A. Hildebrand, W. S. Hodgkiss, T, F. Duda, J. Boyd, B. M. Howe, J. A. Mercer, and R. C. Spindel (1991), A comparison of measured and predicted broadband acoustic arrival patterns in travel time-depth coordinates at 1000 km range , *J. Acoust. Soc. Am*., 95(6), 3118-3129.

Worcester, P. F., B.D. Cornuelle, M.A. Dzieciuch, W.H. Munk, B. M. Howe, J.A. Mercer, R.C. Spindel, J.A. Colosi, K. Metzger T. G. Birdsall and A.B. Baggeroer (1999), A test of basin-scale 13 acoustic thermometry using a large-scale vertical array at 3250-km range in the eastern North Pacific , *J. Acoust. Soc. Am*., 105(6), 3185-3201.

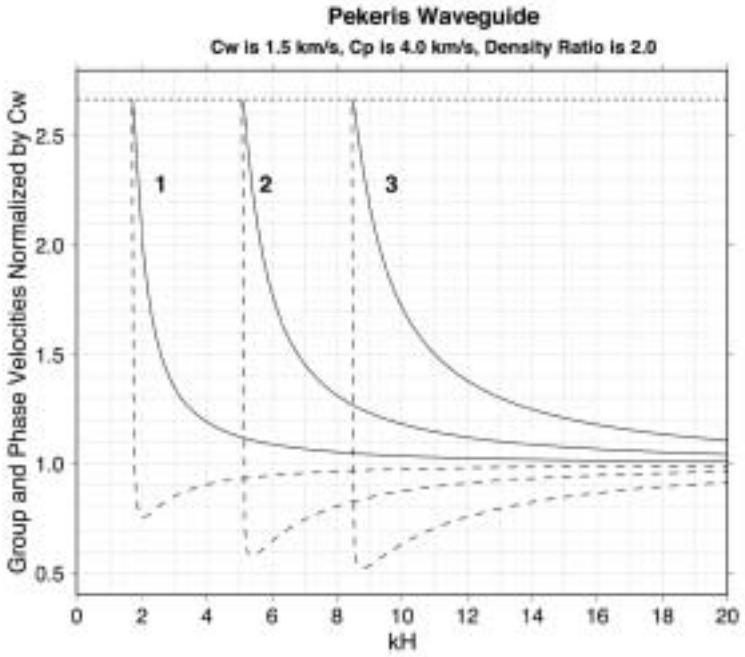

Figure 1: Dispersion curves for Pekeris waveguide.

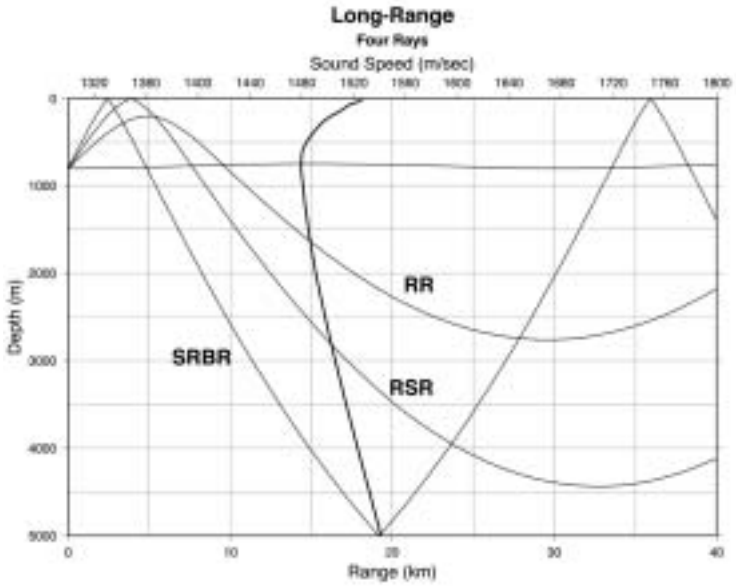

Figure 2: Schematic of deep water paths.

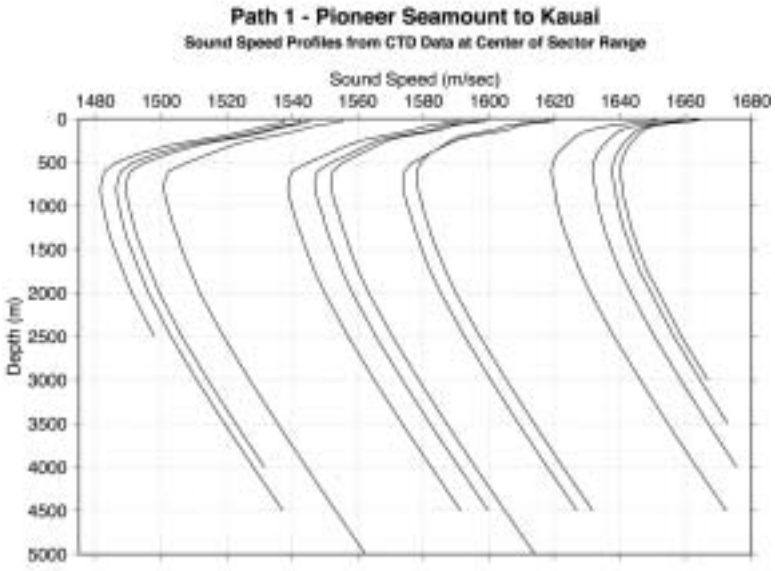

Figure 3: Sound speed profiles for a 3500 km ATOC propagation path as obtained from a climatology data base.

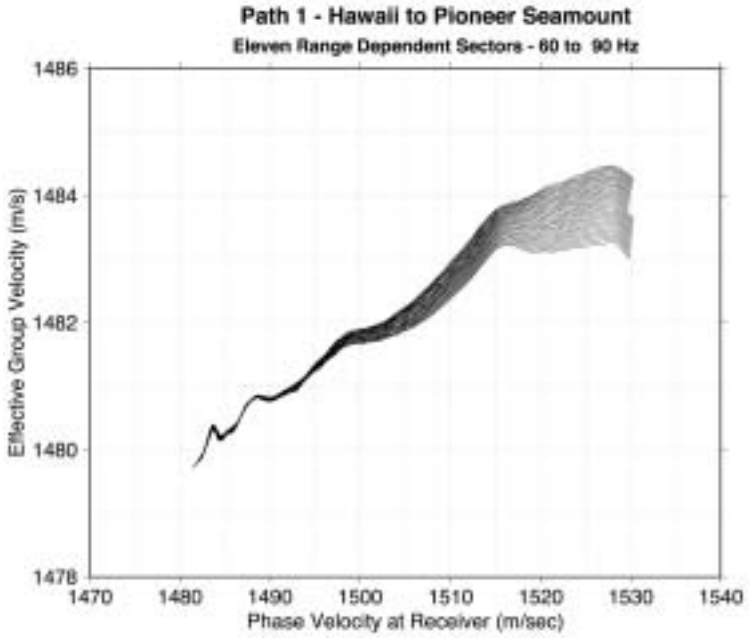

Figure 4: Group speed vs phase speed (g-v) curves for the climatology derived sound speeds of Figure 3.

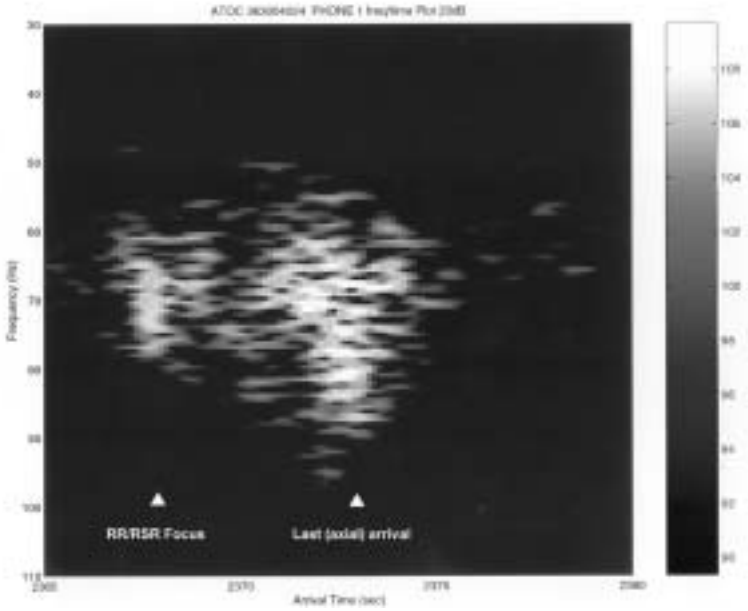

Figure 5: ATOC data: The pulse arrival structure corresponding to Figs. 4 and 5.

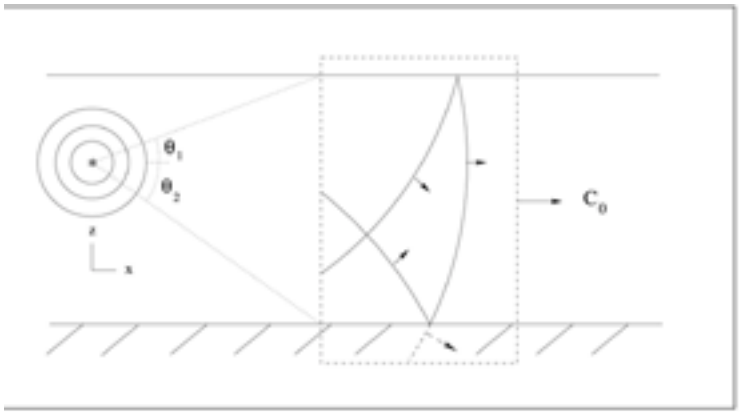

Figure 6: The geometry for the Nonlinear Progressive Wave Equation (NPE)

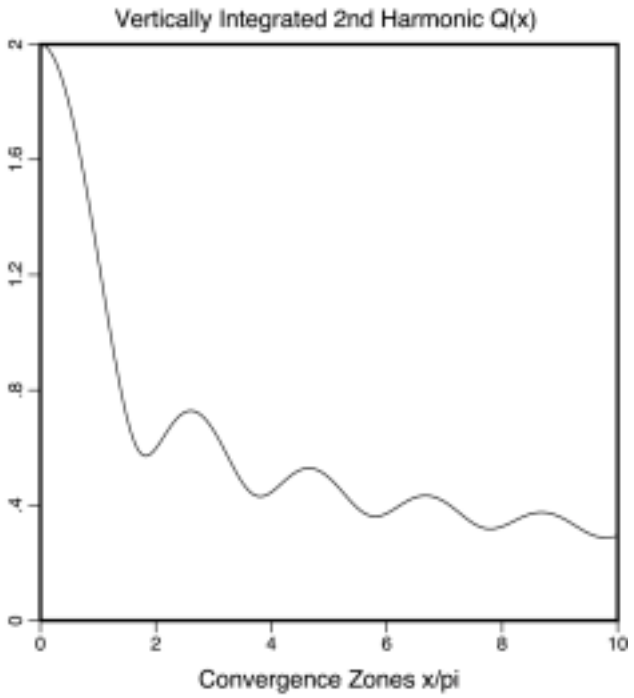

Figure 7: Second harmonic of a high amplitude source for the particular case of a parabolic slowness profile has local maxima near odd number convergence zones

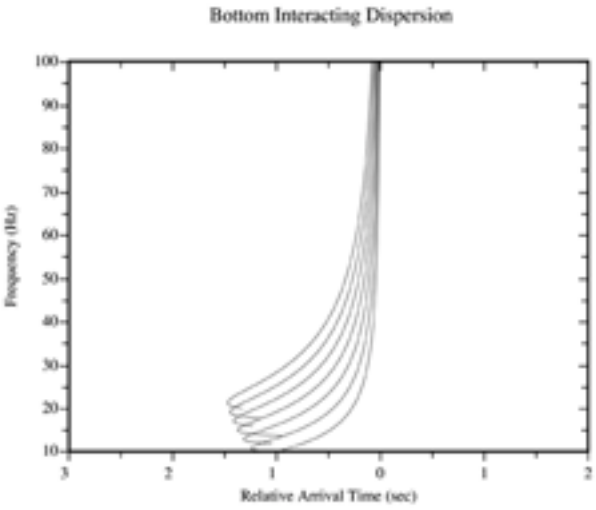

Figure 8: Dispersion curves for a set of bottom interacting modes

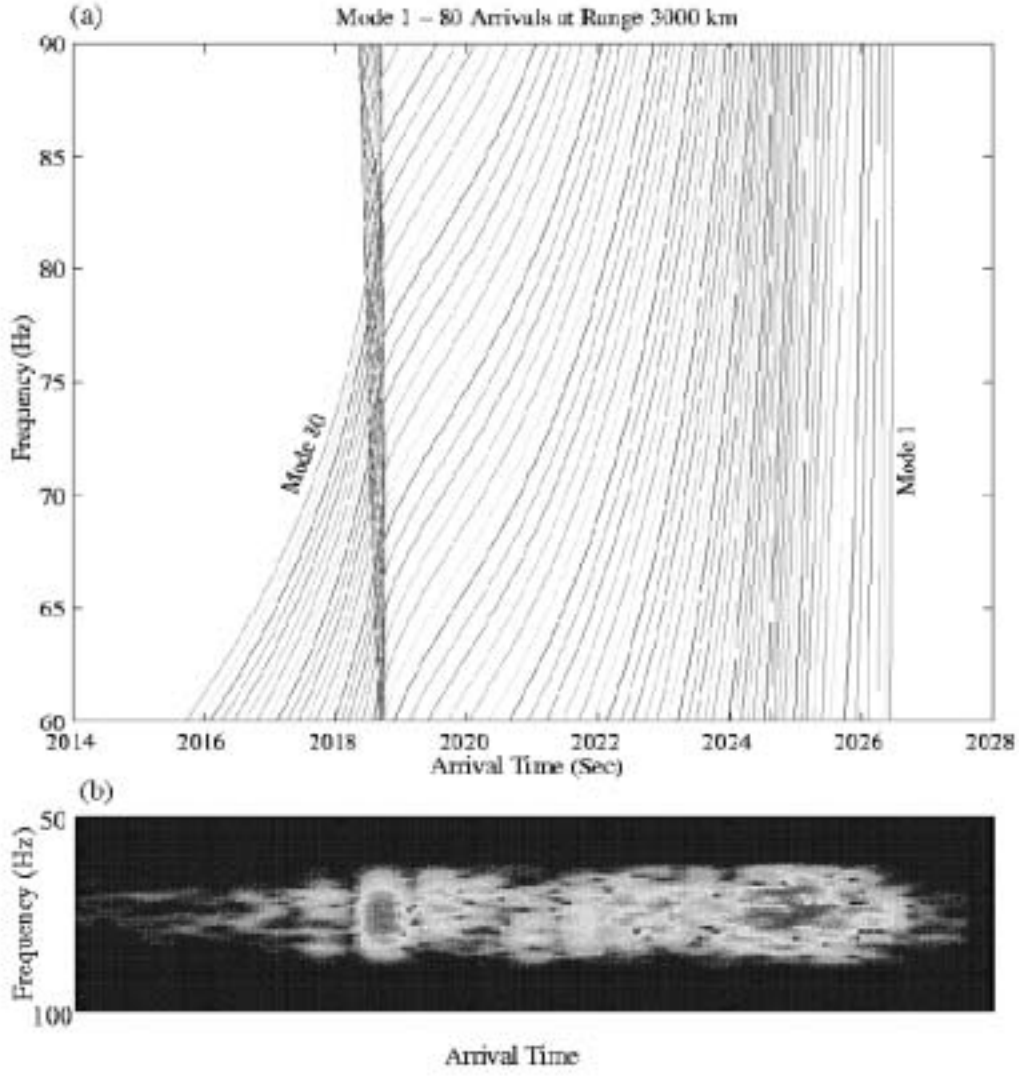

Figure 9: Modal dispersion and arrival structure for an ATOC propagation example.

T-PHASE DETECTION AND IDENTIFICATION OF LARGE EXPLOSIONS AT TELESEISMIC DISTANCES IN THE PACIFIC

Emile A. Okal

Northwestern University

Sponsored by the Defense Threat Reduction Agency

Contract Number DTRA01-00-C-0065/01

Jacques Talandier

Commissariat à l'Energie Atomique

ABSTRACT

We analyze T-phases of very large amplitudes recorded at a number of Pacific sites in 1969 and 1970. We interpret these signals as generated by explosions, which we assume to have been part of the CHASE experiments. Specifically, we study signals from three sources reported in various bulletins (USGS, ISC, etc.), on 13 August 1969, 01 October 1969, and 28 May 1970, and which were assigned earthquake magnitudes of m_b = 4.6, 4.7, and 4.9 respectively. In addition, we detected two similar events on 09 September 1969 and 04 September 1970, unreported in the seismological literature. All events locate off the coast of Washington State, south of Vancouver Island. Abundant T phases were detected by stations of the Polynesian network, by land-based stations of the Hawaiian Volcano Observatory, and were also detectable on island stations such as KIP, RAR, and AFI of the WWSSN, despite mediocre short-period magnifications at the latter (as low as 6250). We also include in our dataset records of the 04 Sept. 1970 shock at a Wake Island hydrophone, as described by R.H. Johnson.

We carry out a systematic relocation of the sources of the T waves, using a variable velocity model based of the regional acoustic speeds of Levitus, and including station corrections accounting for the land propagation of the wave, following conversion at the receiving shore. Finally, we correct for the dispersion of the wave with frequency over the oceanic path. The sources of the T waves are found to be generally incompatible with the published seismic epicenters, the latter leading to negative residuals (meaning the T waves would arrive early), as large as 20 to 30 seconds. Rather, the acoustic epicenters are found to lie approximately 40 km to the west of the seismic ones. A similar discrepancy is not observed in the case of the larger CHASE shots, such as the 1966 event off California, and the 1968 one off the Aleutians. While the seismic epicenter may be grossly in error, we speculate that, under favorable conditions, the acoustic and seismic sources may actually be separated in space and time. We note in this respect that all seismic epicenters are located on the slope of the continental shelf, where water depth corresponds to the SOFAR axis.

The signals are interpreted as explosive in nature, based on the amplitude duration criterion introduced by Talandier and Okal (2001), and it is estimated that their yield could be on the order of 100 tons. The timing of the events in 1969-1970 makes it probable that they were part of the CHASE experiments. Additional characteristics of the T wave signals, such as a strong frequency dispersion, also suggest an explosive origin.

We will also report on other, smaller presumed explosions detected in the Pacific, notably two events off the coast of Oahu on 13 April 2000.

KEY WORDS: T phases, Pacific Ocean, explosions, hydroacoustic detection.

HYDROACOUSTIC BLOCKAGE AT DIEGO GARCIA: MODELS AND OBSERVATIONS

Jay J. Pulli and Zachary M. Upton

BBN Technologies

Sponsored by National Nuclear Security Administration
Office of Nonproliferation Research and Engineering
Office of Defense Nuclear Nonproliferation

Contract No. DE-AC04-2000AL66933

ABSTRACT

Hydroacoustic blockage occurs when a bathymetric feature (island, atoll or seamount) is in the path of propagating acoustic energy. An understanding of hydroacoustic blockage is essential when planning an array location, mapping detection and localization coverage, and interpreting hydroacoustic reflection data. The new hydroacoustic array at Diego Garcia, which actually consists of two sub-arrays on either side of the atoll, provides an excellent opportunity for evaluating model predictions of blockage using the recordings of T-waves from shallow earthquakes in the Indian Ocean.

The latest release of HydroCAM, our long-range hydroacoustic modeling program, includes the Sandwell and Smith 2-minute-resolution bathymetry database. To model hydroacoustic blockage at Diego Garcia, we used this capability to perform a series of fan-ray calculations for both sub-arrays at 2-degree azimuth increments. These rays were compared with previous calculations using the ETOPO5 5-minute grid, both to verify the database integration and to compare the two databases. We used two criteria for hydroacoustic blockage:

- The bathymetry is shallower than 50 meters (thereby blocking most propagating acoustic energy).
- The bathymetry is shallower than the Sound Channel Axis depth in the region (thereby blocking acoustic energy in the SCA).

These criteria result in binary blockage evaluations; that is, either the ray path is blocked or it is not. However, observations indicate that the process of blockage is more complicated. For example, ray paths coming from the north should be blocked by the atoll and not be observed at the south array. Acoustic data from the south array shows that although the energy is attenuated, arrivals can easily be identified.

In order to resolve some of the modeling issues, we have compiled a waveform database of about three dozen shallow earthquakes in the Indian Ocean recorded by the Diego Garcia subarrays. These events cover nearly all azimuths around Diego Garcia. Using this dataset, we have computed a 360-degree blockage chart for Diego Garcia that shows the frequency dependence of energy attenuation around the atoll. We have also suggested some improvements to the models that will improve our blockage prediction capability.

KEY WORDS: hydroacoustics, Diego Garcia, Indian Ocean, blockage

OBJECTIVE

The objective of this research is to model hydroacoustic blockage around Diego Garcia. An understanding of hydroacoustic blockage is essential when planning an array location, mapping detection and localization coverage, and interpreting hydroacoustic reflection data. Model predictions were made using the latest version of our program HydroCAM with two different path blockage criteria. These predictions were then compared with actual observations using a dataset of earthquake sources around the Indian Ocean. A methodology was developed to correct each observation for earthquake magnitude and distance from Diego Garcia.

RESEARCH ACCOMPLISHED

Model Predictions of Blockage Using HydroCAM

Hydroacoustic blockage was modeled at both Diego Garcia subarrays using the latest version (3.3) of the program HydroCAM. We performed a series of fan-ray calculations for both sub-arrays at 2-degree azimuth increments using two bathymetric databases. The first database was the ETOPO5 5-minute resolution grid; the second was the Sandwell and Smith 2-minute resolution grid. Two criteria were used to determine blockage: one was when the bathymetry is shallower than 50 meters (thereby blocking most propagating acoustic energy); the second was when the bathymetry is shallower than the Sound Channel Axis depth in the region (thereby blocking acoustic energy in the SCA). Results of these eight combinations are shown in Figures 1 and 2.

Although the gross features of the predictions are similar, there are important differences. For both of the sub arrays, the widest azimuthal coverage is predicted by the ETOP5 bathymetry database and the 50-meter stop criterion. The smallest azimuthal coverage is predicted by the ETOP5 bathymetry database and the SCA stop criterion These varying results point to either the need for higher resolution bathymetry around Diego Garcia, better stop criteria, or both. Our goal here to compare these predictions with actual observations.

Observations: Events Analyzed

As of this writing, hydroacoustic data from 27 events in the Indian Ocean area have been analyzed. A list of these events is given in Table 1 and a corresponding epicentral map is shown in Figure 3. The event distribution in distance and azimuth is shown in Figure 4. Clearly, we have gaps in the azimuthal coverage for the northeast, southeast, and west directions from the array. We hope to fill these gaps as time goes on and more events are recorded. For each event, 2-3 hours of waveform data (starting at the origin time) were obtained for all six hydrophones at Diego Garcia. The waveform data are sampled at 250 Hz. The analysis process consists of three steps. First, the waveform data are converted to waveform envelopes, from which the amplitudes of the T-waves are measured. Next, these amplitudes must be scaled to account for the fact that the events are of varying magnitude. Finally, the amplitudes must be corrected for propagation losses, given that the events are of varying distances from Diego Garcia. Once these steps are accomplished, an assessment of blockage around Diego Garcia can be undertaken.

Data Processing

Data processing for this analysis consisted of the conversion from full band calibrated waveform data to waveform envelopes. This was accomplished by first detrending the data, then filtering in the passband of 3 to 30 Hz. (Noise dominates the signal below 3 Hz and there is little energy above 30 Hz.) The filtered data were then rectified(absolute value) and smoothed over a 2-second window that was stepped down the time series one sample at a time. This smoothed envelope was then subsampled to a rate of one sample per second. The waveform envelopes for each of the three sensors at each sub array were then averaged. T-wave amplitudes were measured at the peak of the envelope, which corresponds to the arrival time of Mode 1 (sound channel axis propagation). An example is shown in Figure 5. In order to measure blockage, we must first scale the measured T-wave amplitudes to account for differences in event magnitudes and distances from the arrays.

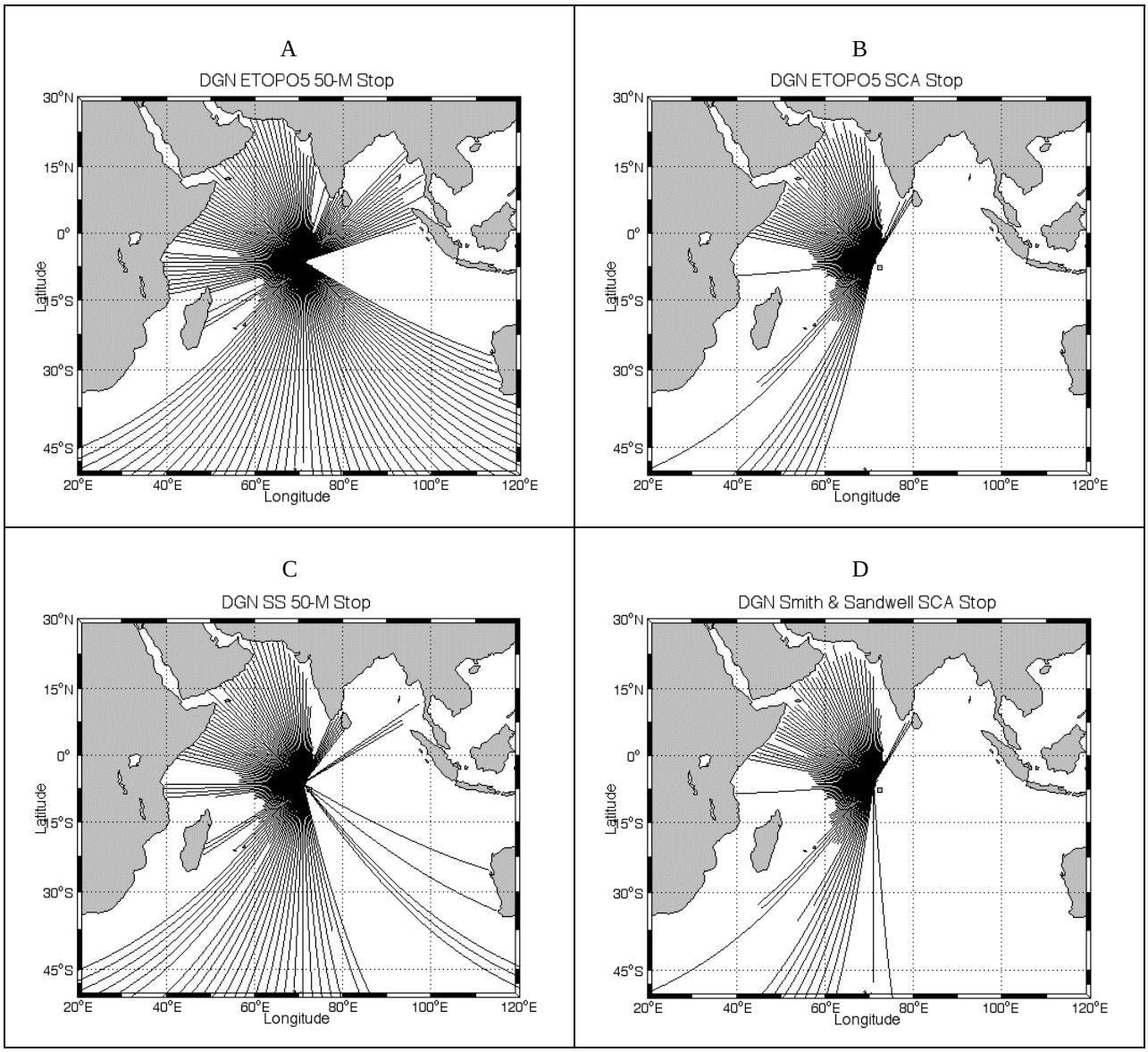

Figure 1. Four fan-ray calculations at Diego Garcia North using HydroCAM: A) ETOPO5 bathymetry database with a ray stop criterion of 50-m depth. B) ETOPO5 database with a ray stop criterion of the Sound Channel Axis (SCA) depth equaling that of the bathymetry. C) Smith and Sandwell bathymetry database with a ray stop criterion of 50-m depth. D) Smith and Sandwell database with a ray stop criterion of the SCA depth equaling that of the bathymetry.

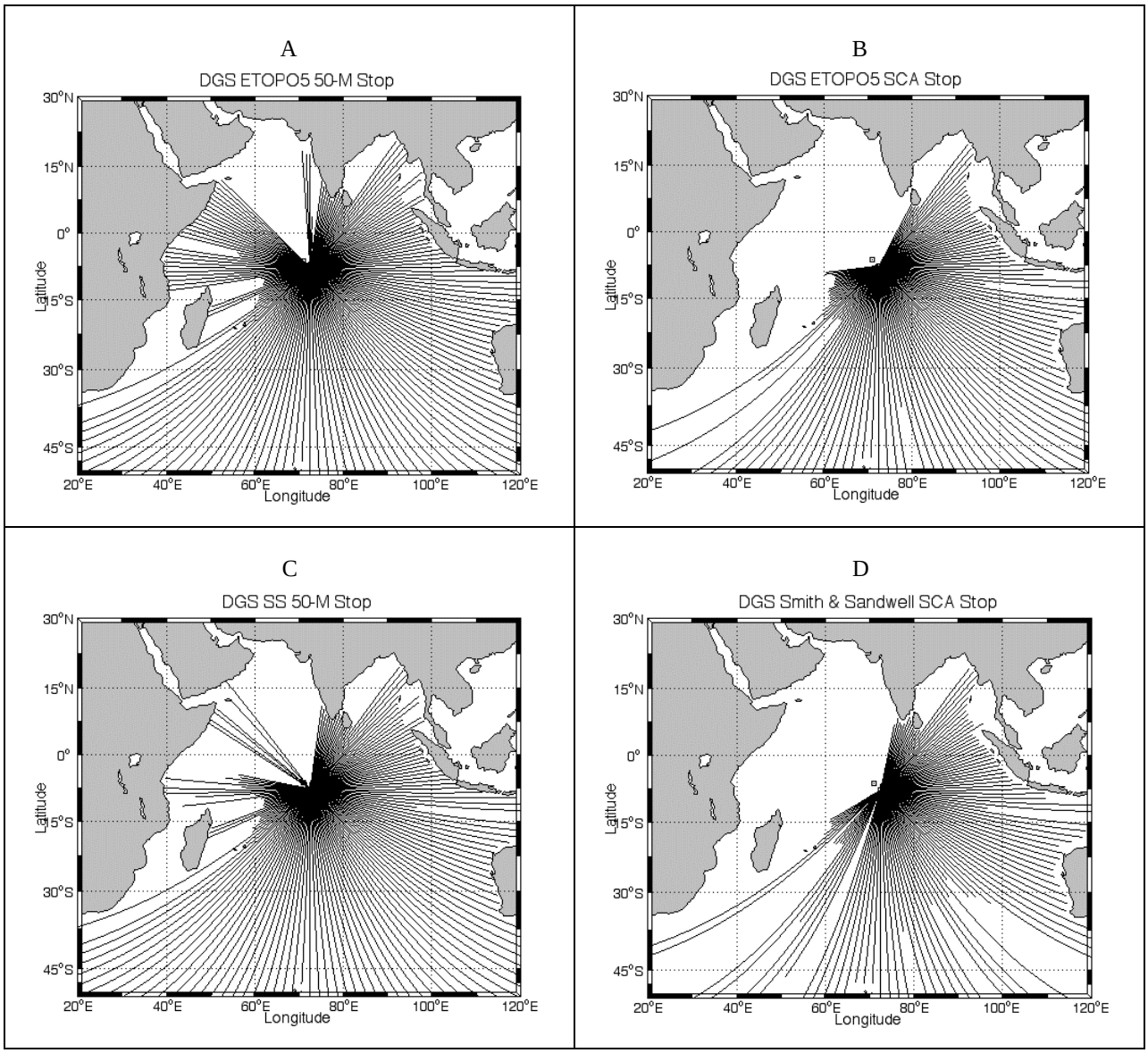

Figure 2. Four fan-ray calculations at Diego Garcia South using HydroCAM: A) ETOPO5 bathymetry database with a ray stop criterion of 50-m depth. B) ETOPO5 database with a ray stop criterion of SCA depth equaling that of the bathymetry. C) Smith and Sandwell bathymetry database with a ray stop criterion of 50-m depth. D) Smith and Sandwell database with a ray stop criterion of the SCA depth equaling that of the bathymetry.

Yr/Mo/Dy	Hr:Mn:Sc	Lat.	Long.	Depth km	Mag m_b	Geographic Area
2001/01/26	03:16:40	23.42	70.23	16.0	7.8	Gujarat, India
2001/01/26	07:32:28	23.42	69.98	10.0	5.5	Gujarat, India
2001/01/28	01:02:10	23.51	70.52	10.0	5.9	Gujarat, India
2001/02/14	19:28:03	-4.68	102.56	36.0	7.2	Sumatera
2001/02/15	10:04:36	23.27	70.29	10.0	4.7	Gujarat, India
2001/03/11	07:06:03	-4.28	89.06	10.0	4.9	South Indian Ocean
2001/03/13	13:48:19	23.73	69.56	10.0	3.7	Gujarat, India
2001/03/25	07:14:08	14.09	53.46	10.0	4.9	Owen Fracture Zone
2001/03/30	07:24:19	-41.98	88.44	10.0	5.1	Southeast Indian Rise
2001/03/31	02:26:30	3.99	95.94	33.0	5.2	W Coast of N Sumatera
2001/04/04	07:26:32	-34.26	55.46	10.0	5.0	Southwest Indian Ridge
2001/04/04	13:06:13	-34.38	55.43	10.0	5.6	Southwest Indian Ridge
2001/04/08	19:26:43	-11.76	65.98	10.0	5.0	Mid-Indian Ridge
2001/04/08	10:54:09	-25.12	67.65	10.0	5.1	Indian Ocean Triple Junction
2001/04/16	14:25:59	23.44	70.12	10.0	4.1	Gujarat, India
2001/04/19	00:44:10	-14.63	66.21	10.0	4.9	Mid-Indian Ridge
2001/04/23	16:35:35	13.21	50.50	10.0	5.2	Eastern Gulf of Aden
2001/04/25	21:02:43	-8.92	106.47	33.0	5.5	South of Jawa, Indonesia
2001/05/04	01:10:48	-33.59	57.19	10.0	5.0	SW Indian Ridge
2001/05/11	22:18:02	0.67	98.58	33.0	5.4	Northern Sumatera
2001/05/18	02:05:34	0.47	97.80	33.0	5.9	Northern Sumatera
2001/05/25	05:05:59	-7.91	110.26	33.0	5.9	Jawa, Indonesia
2001/05/31	20:23:42	9.80	57.68	10.0	4.6	Carlsberg Ridge
2001/06/15	16:19:07	13.76	51.69	10.0	5.7	Eastern Gulf of Aden
2001/06/21	14:19:19	22.93	69.65	10.0	4.5	Gujarat, India
2001/06/28	03:46:27	-6.91	108.30	33.0	5.0	Jawa, Indonesia

Table 1. List of events used for the blockage analysis. An epicentral map is shown in Figure 3. Epicentral data sources include the NEIS and IRIS databases.

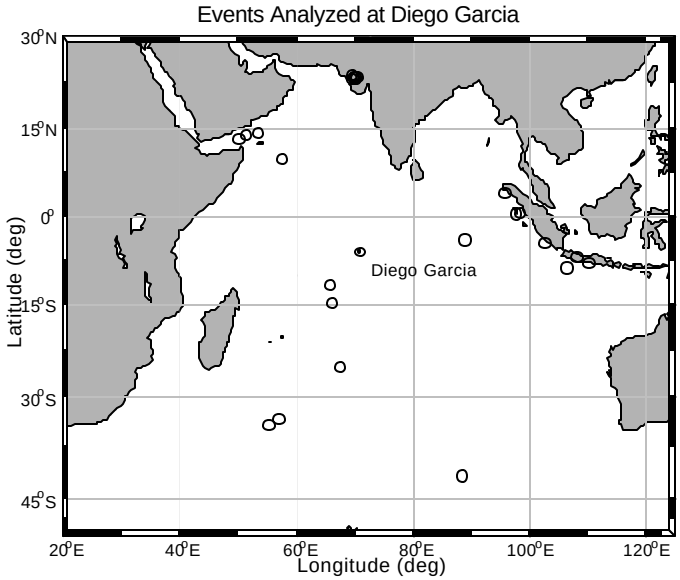

Figure 3. Epicenters of the events measured in this study. See Table 1.

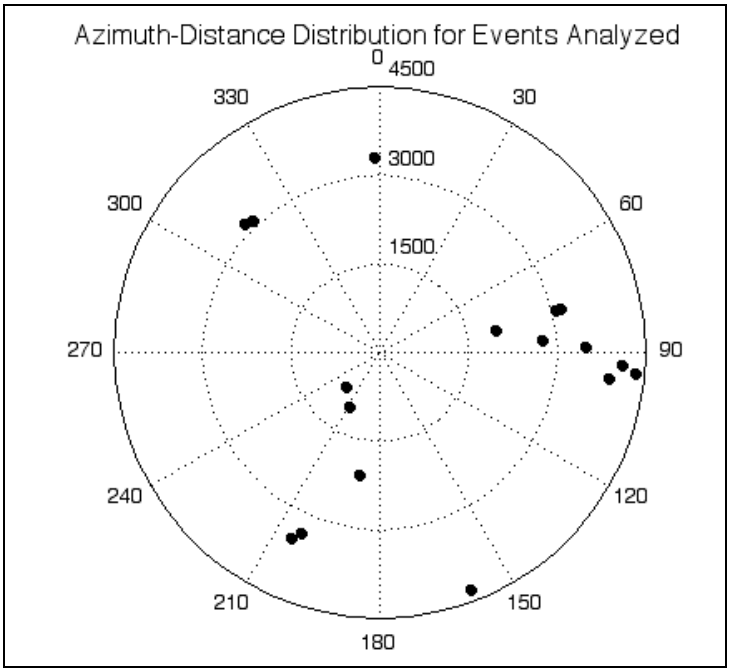

Figure 4. Azimuth-distance distribution for the events studied at Diego Garcia. As of this writing, there are gaps in the azimuthal coverage to the northeast, southeast, and west of the array.

T-Wave Amplitude vs. Seismic Magnitude

The next step in the analysis is the conversion of the measured T-wave amplitudes to their equivalent amplitudes for an event of a given magnitude. To accomplish this, we used the measured T-wave amplitudes for the January 26, 2001, western India earthquake and its aftershocks. Since all of these events are roughly the same distance from Diego Garcia (3280 km), transmission losses will be the same for each event; hence, amplitude differences will solely be the function of earthquake magnitude. (This, of course, ignores any amplitude variation due to differences in source mechanism or source depth.) T-wave amplitudes at the Diego Garcia north array for ten events in the western India source zone are plotted in Figure 6. Seismic magnitudes were taken from NEIS epicenter lists. As expected, there is a linear relationship between T-wave amplitude in dB and seismic magnitude. This relationship, for the fixed epicentral distance of 3280 km to Diego Garcia, is

$$dB = 54.7 + 12.4\, m_b$$

Note from Figure 4 that with a measured background noise level of 95 dB at Diego Garcia, we would expect to observe T-waves from events in the source region as small as magnitude 3.2. Based on this result, we can now derive a correction factor that will scale the measured T-wave amplitudes to those of an earthquake of a given seismic magnitude. Here we chose magnitude 5 as our standard event magnitude. This relationship is

$$dB(m_b=5) = dB - 12.4 + 54.7\, m_b$$

T-Wave Amplitude vs. Distance

Once the T-wave amplitudes have been scaled to a common event magnitude, they must next be corrected for propagation losses to a common distance. This can be accomplished using the equation (Urick, 1983)

$$TL = 60 + 10\log_{10} r + 0.00333r$$

for Mode-1 transmission loss (TL) in the sound channel axis. Here, TL is in dB, and r is the distance in kilometers. This equation accounts for both geometrical spreading and attenuation. (Attenuation losses are very small in the sound channel axis, amounting to only 3.3 dB per 1000 km of propagation.)

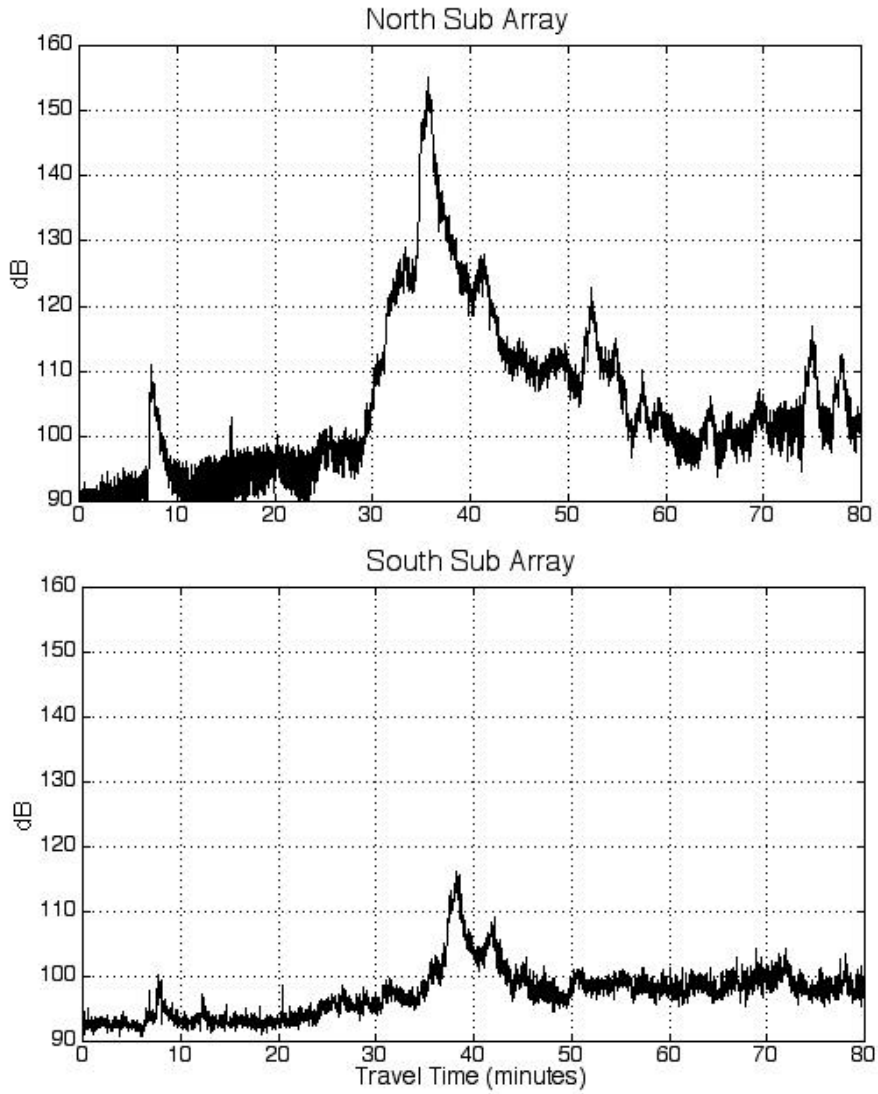

Figure 5. T-wave envelopes computed from Diego Garcia data for January 26, 2001, Guinart, India. The T-wave travel time is approximately 37 minutes to Diego Garcia North (top). The arrival at 8 minutes is the conversion from seismic P-wave below the array to acoustic energy (see Pulli and Upton, 2001). Three of the four predictions for Diego Garcia South indicate that T-waves will be blocked from this azimuth; however T-wave energy is recorded at the South array, albeit at a level that is approximately 40 dB below that at the North array.

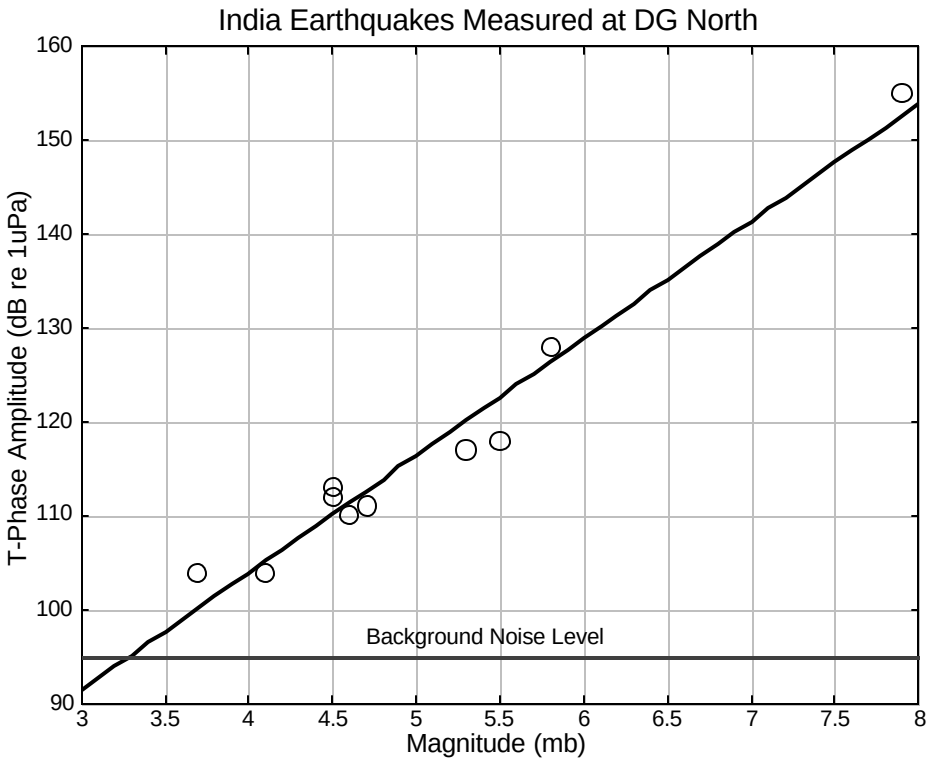

Figure 6. Amplitudes of T-waves in dB measured at the Diego Garcia north array for the January 26, 2001, western India earthquakes and some of its aftershocks. All events are 3280 km from the array.

T-Wave Amplitudes Around Diego Garcia

The measured T-wave amplitudes, corrected to a common magnitude 5 event and scaled for transmission loss, are plotted as a function of azimuth in Figure 7 (for the north array) and Figure 8 (for the south array). Note that transmission losses were not applied to signals that were completely blocked, which would only serve to artificially increase amplitudes at a given subarray. For the north subarray, the most important observation is that we see T-waves coming from the east, whereas all of the predictions from Figure 1 indicate that paths to the east should be blocked. For the south subarray, we see T-waves coming from the northwest, whereas all of the predictions from Figure 2 indicate that paths to the east should be blocked.

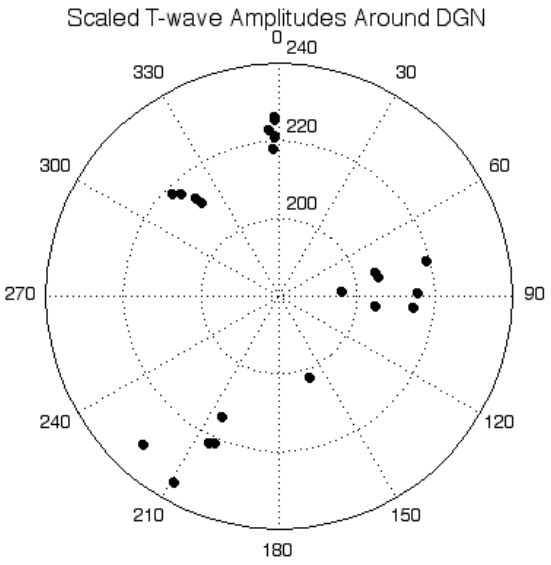

Figure 7. Observed T-wave amplitudes at Diego Garica North subarray. The amplitudes have been scaled to a common event magnitude (5.0) and corrected for transmission losses.

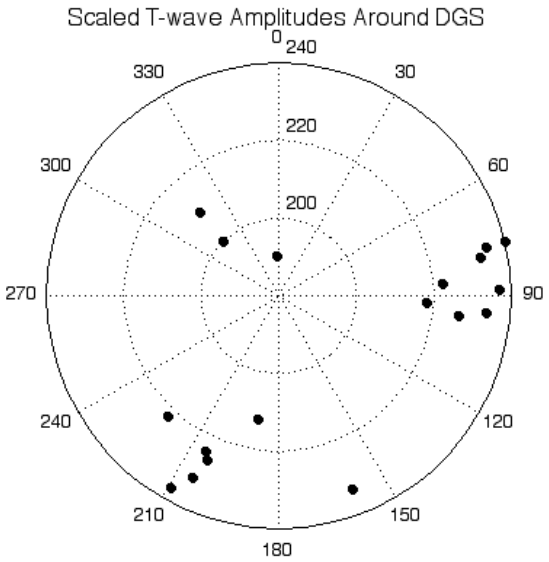

Figure 8. Observed T-wave amplitudes at Diego Garica South sub array. The amplitudes have been scaled to a common event magnitude (5.0) and corrected for transmission losses.

CONCLUSIONS AND RECOMMENDATIONS

Our studies of the prediction of hydroacoustic blockage at Diego Garcia, and our observations based on T-waves from earthquakes in the Indian Ocean area, lead us to draw the following conclusions:

1. The predictions of hydroacoustic blockage around Diego Garcia vary, depending on the resolution of the bathymetry used and the criterion for blockage.
2. In some cases, we observe T-waves at a Diego Garcia sub array where the predictions indicate that none should be observed.
3. A better definition of "hydroacoustic blockage" is required which goes beyond the binary blocked/unblocked

We recommend:

1. Continued accumulation of waveform data at Diego Garcia in order to fill in the coverage gaps that exist in our analysis. Recordings of events in the northeast, southeast, and west directions from Diego Garcia are required.
2. As higher resolution bathymetric databases become available for this region, they should be integrated into HydroCAM.
3. Modeling of the diffraction and scattering of hydroacoustic energy around Diego Garcia should be undertaken.
4. Further acoustical analysis, in the form of modal or PE modeling, should be conducted to discover and evaluate better blockage criteria.

REFERENCES

GDEM (1995), Database Description for the Master Generalized Digital Environment Model (GDEM) Version 5.0, OAML DBD-20F, Naval Oceanographic Office, Stennis Space Center MS. September 1995.

Pulli, J.J. and Z. Upton (2001), Hydroacoustic observations of the January 26, 2001 Western India earthquake and its aftershocks, presented at the Spring Meeting of the American Geophysical Union, Boston, MA.

Smith, W. H. F. and D. T. Sandwell (1997), Global Sea Floor Topography from Satellite Altimetry and Ship Depth Soundings, *Science*, **277**, p. 1956-1962.

Urick, R.J. (1983), Principles of Underwater Sound, 3rd ed., McGraw-Hill Book Company, NY.

Radionuclide Monitoring

RADIONUCLIDE MEASURMENTS FOR NUCLEAR EXPLOSION MONITORING

R. J. Arthur, T. W. Bowyer, J. C. Hayes, T. R. Heimbigner, J. I. McIntyre, H. S. Miley and M. E. Panisko

Pacific Northwest National Laboratory

Sponsored by National Nuclear Security Administration
Office of Nonproliferation Research and Engineering
Office of Defense Nuclear Nonproliferation

Contract No. DE-AC06-76RLO-1830

ABSTRACT

The Automated Radioxenon Sampler/Analyzer (ARSA) and Radionuclide Aerosol Sampler/Analyzer (RASA) are radionuclide detection technologies developed by the Department of Energy (DOE)/National Nuclear Security Administration (NNSA) Program at the Pacific Northwest National Laboratory for monitoring for radionuclides in the atmosphere for signs of atmospheric and underground nuclear explosions.

In March 2001,the ARSA completed an 18-month field test in Freiburg, Germany, as part of the International Noble Gas Experiment (INGE). During this test, the ARSA

- made over 1,200 automated measurements of ^{131m}Xe, ^{133}Xe, ^{133m}Xe, and ^{135}Xe,
- had an up time of approximately 95%,and
- achieved a minimum detectable concentration of about 0.10 to 0.15 mBq/m^3 3 times per day for ^{133}Xe.

By measurement of the relative concentrations of the xenon isotopes, we were able to determine with high confidence that reactors were the source of the radioxenon observed during this test.

Analysis of nearly 1,700 RASA samples has shown that ^{7}Be is the only radionuclide with good quality-assurance properties likely to be detected at an International Monitoring System (IMS) radionuclide analysis laboratory. Concentration of ^{7}Be in ~70% of samples is adequate for an effective quality assurance program. The ^{7}Be half-life, energy, and typical atmospheric concentrations allow precise and relevant follow-up laboratory measurements. These results highlight the importance of station-to-station calibration and emphasize the need for inter-laboratory comparison exercises.

KEY WORDS: ARSA, noble gas, RASA, ^{7}Be, ^{133}Xe, ^{135}Xe, ^{133m}Xe, radionuclide, aerosol, fission, isotope, atmospheric, Radionuclide Laboratory, International Monitoring System, quality

OBJECTIVE

A key function of the radionuclide portion of the IMS includes monitoring the atmosphere for radionuclides emitted as fission or activation product aerosols or gases (radioxenons), since detection of appropriate isotopes can discriminate nuclear from non-nuclear events.

RESEARCH ACCOMPLISHED

A first international demonstration of the ARSA xenon noble gas collection and analysis capabilities (Bowyer, 2001) and other xenon noble gas systems was performed in Freiburg, Germany, in 1999 and 2000. This paper describes the measurements obtained by the ARSA (Bowyer, 1999). Also, since 1998, the RASA system has been collecting and analyzing automated aerosol measurements in Richland, WA, USA to, among other things, determine useable radionuclides for quality assurance/quality control (QA/QC) monitoring for the IMS. The results of these measurements are shown below.

Noble Gas Demonstration

Starting in 1999, a noble gas equipment test was conducted to assess the state-of-the-art of the current equipment available for radioxenon measurement and to assess its suitability for the International Monitoring System (IMS) radionuclide network. In addition to the ARSA, three other technologies were selected for evaluation, including: the ARIX from the V.G. Klopkin Radium Institute in St. Petersburg, Russia, the SAUNA from the Defense Research Establishment — FOI 41, in Stockholm, Sweden, and the SPALAX from the Commissariat l'Energie Atomique, Direction des Applications Militaires, D partement Analyses Surveillance Environnement (CEA/DASE) in Paris, France. The test location at the Institute for Atmospheric Radioactivity (IAR) in Freiburg, Germany, has an average activity concentration of ^{133}Xe, a few mBq/m_ (Stockburger, 1977) due its proximity to many operating nuclear reactors.

The ARSA system measures all of the relevant xenon isotopes from nuclear detonations; ^{131m}Xe, ^{133}Xe, ^{133m}Xe, and ^{135}Xe, by measuring the energies of both emitted particles (betas and gammas) from each decay (Reeder, 1998). The ARSA system measured all of the radioactive xenon concentrations reliably without operator intervention for nearly 18 months. The ARSA automatically measured over 1,200 atmospheric samples of radioactive xenon 3 times per day. In addition, several weeks were dedicated to manually injecting xenon isotopes into the air stream to measure isotopic ratios and for comparison to other xenon systems. The results obtained by the ARSA were compared to an independent analysis of the samples performed by IAR personnel from the xenon stored by the ARSA after measurement. There was a good agreement between the automated ARSA results (~10%), and the independent analysis (Bowyer, 2001).

The calculated up time for the ARSA was approximately 95% (Bowyer, 2001), defined as the total number of cycles that the equipment was not producing, collecting, and subsequently analyzing coincidence spectra divided by the total number of cycles available, minus time taken for spike tests, travel time of personnel, and delays from part availability or customs delays. It is notable that the system down time was mainly due to a single failure mode not repaired during the test. This failure mechanism was traced to a poor connection inside a line replaceable unit that was not replaced during the test due to lack of spares.

Xe-131m was measured occasionally at a few mBq/m^3 level with a few runs where there was nearly pure ^{131m}Xe without accompanying high concentrations of ^{133}Xe. Although this was not expected and more data are necessary, there are mechanisms that could account for a nearly pure (without ^{133}Xe) ^{131m}Xe. The possibilities include medical sources of radioxenon, and old reactor xenon that could have been held up at reactors before release, and hence the long-lived ^{131m}Xe is the only radioxenon present.

Xe-133 was detected nearly every day during this test averaging 1 to 2 mBq/m^3, though levels exceeding 100 mBq/m^3 were observed with plume passage times of <10 hours (Bowyer, 2001). Figure 1 shows a plot of the measured ^{133}Xe concentration in Freiburg for the last 12 months of the 18-month test. There are several locations on the plot where no data are shown, corresponding to down times of the equipment for spike tests, maintenance, or equipment failure. The high concentrations near the end of the test were measured after spike testing was completed, and are most likely due to radioxenon spikes being collected by the ARSA from the room. Other systems being tested in Freiburg also saw the elevated levels with substantial amounts of ^{133m}Xe, indicating that the spikes were the cause of the elevated levels.

Xe-133m was not observed during most of the test, with the exception of the final week, which was probably due to the preparation of very high activity radioxenon spikes used in spike calibration testing (Bowyer, 2001).

Xe-135 was detected nearly a dozen times during the testing period at levels as high as 4 mBq/m^3. These concentrations of ^{135}Xe were usually accompanied by ^{133}Xe concentrations of several tens of mBq/m3, with one notable exception in which the ^{135}Xe/^{133}Xe concentration ration was 2:1. This ratio is only expected following a nuclear detonation or during reactor startup. The ^{133m}Xe/^{133}Xe activity ratio for this period was consistent with reactor startup.

Figure 2 shows the distribution of the concentration data collected in Freiburg during the year 2000. The distribution of concentrations shows an approximately lognormal shape. A three-parameter lognormal distribution,

$$f(x) = \frac{1}{(x-a)\sigma\sqrt{2\pi}} e^{-\frac{1}{2}\left[\frac{\ln(x-a)-\mu}{\sigma}\right]^2}$$

fits the data quite a bit better than the two-parameter lognormal function, which could be due to the fact that the minimum detectable concentration of ^{133}Xe is near 0.1 to 0.15 mBq/m^3 (McIntyre, 1999), or close to the cut-off parameter, *a*, in the lognormal distribution.. This behavior is not inconsistent with other atmospheric dilution observations (Mage, 1974; Ott, 1995).

Laboratory Quality Assurance Measurements

Members of the international community have discussed the role of Radionuclide Laboratories for performing a network-wide quality assurance function. However, the details of this function have been lacking. The recent effort to determine the financial resources needed for the labs has driven an analysis of the nature and frequency of QA measurements. The work reported here is the analysis of aerosol samples in a scenario that represents the expected field and laboratory sample measurement sensitivity and timing. Timing is quite important, because most of the isotopes embedded in the aerosol filter are short-lived and cannot therefore survive the transit time of the aerosol samples to the laboratory.

To simulate realistic field-lab measurement timing, a RASA filter taken in Richland, WA, was allowed to decay for 10 days. Both the field and lab systems were counted for 1 day. The field system employed a 90% relative efficiency P-type detector while the lab system was an ultra-low background 40% P-type. Figure 3 shows the spectrum from the field measurement (the red or highest spectrum), the typical blank from the same RASA (in blue with diamonds at each point, or the second highest spectrum) and the lab system measurement of the same filter with 10 days decay (the green spectrum with triangles at each point, or the lowest spectrum). The filed measurement of the filter shows ^{7}Be, a cosmic-ray product in the upper atmosphere, as well as many common natural isotopes (^{212}Bi, ^{212}Pb, ^{214}Bi, ^{214}Pb, ^{208}Tl, and ^{40}K, for example). Natural isotopes are found in the detector background, but the ^{7}Be is not. The ^{7}Be is found in the lab measurement, but the natural isotopes are mostly not.

The conclusions that could be drawn from this figure are that natural isotopes will have decayed away by the time a lab measurement is made and thus have no constructive role in QA functions. Beryllium-7, whose half-life, T_ is 53.4 day, and which has a primary gamma-ray energy at 477.6 keV, may be the only isotope that is dependably present whose source is certainly on the filter and not the field or lab background. While it would be preferable to have several isotopes present in the lab measurement from ubiquitous airborne radioactivity, ^{7}Be is not an altogether unfortunate isotope to be the only survivor since it has a good half-life and a primary gamma-ray energy reasonably close to that of ^{140}Ba (primary gamma ray energy at 537.4 keV), the isotope used to act as the standard for field and lab system sensitivity.

To make effective comparisons between field measurements and lab measurements, the statistical uncertainty of measurable isotopes must be reasonable. To objectively assess the quality of the nuclide information in the spectra in Figure 3, all were subjected to an automatic analysis. The results in Table 1demonstrate that the only reliable isotope is ^{7}Be and that the statistical uncertainty of the ^{7}Be determination were less than 2%. (Systematic biases such as efficiency calibration errors have not been taken into account, but must eventually be controlled by the use of intra-lab calibration and careful certification of station efficiency.)

While the above example shows that reasonable uncertainties may be sometimes achieved, the question remains as to what fraction of the samples taken in the IMS network will have reasonable ^{7}Be activity such that the statistical uncertainty in the field and the lab are similarly reasonable. To determine this fraction, approximately 1700 RASA daily samples were analyzed using an automated analysis code. The ^{7}Be activity and the corresponding statistical uncertainty were tabulated and histogrammed on a frequency chart with a logarithmic x-axis. Figure 4 shows the fraction of the spectra with ^{7}Be uncertainties in bins from 1% error to 100% error. The sum of the fractional bins from 1% to 100% is also shown. It can be seen that approximately 70% of the spectra have ^{7}Be uncertainties below 3%.

CONCLUSIONS AND RECOMMENDATIONS

Even though automated, high-sensitivity noble gas monitoring is relatively new, our recent demonstration has shown that reliable long-term operation of a system to collect and analyze the xenon isotopes ^{131m}Xe, ^{133}Xe, ^{133m}Xe, and ^{135}Xe is now possible. Recent data collected are consistent with normal reactor operations during start-ups and at equilibrium; however, more data should be collected to characterize radioxenon concentrations in parts of the world where radioxenon levels have never been measured. These data are important to determine the background that will be encountered for radioxenon monitoring on a world-wide scale.

In addition, it has been shown that ^{7}Be will be the major focus of the radionuclide lab QA function, due to the lack of other reasonably long-lived and reasonably active isotopes in the atmosphere. The uncontrolled quantities of other natural backgrounds preclude the use of typical natural isotopes, even if they have not totally decayed by the time of the lab measurement. This leads to the final conclusion that routine samples collected from IMS stations should be quite simple to analyze presuming the backgrounds of the lab measurement system are sufficiently low.

ACKNOWLEDGEMENTS

The authors would like to thank members of the International Noble Gas Experiment (INGE) for useful discussions and a successful noble gas experiment, and the operators of the US National Data Center for access to RASA data from partially installed RASA sites.

REFERENCES

Bowyer, T.W., K. H. Abel, C. W. Hubbard, M. E. Panisko, P. L. Reeder, R. C. Thompson, and R. W. Warner, R.A. (1999). Field testing of collection and measurement of radioxenons for the Comprehensive Test Ban Treaty, *The Journal of Radioanalytical and Nuclear Chemistry*, 240, 109-122.

Bowyer, T.W., J. C. Hayes, T. R. Heimbigner, J. I. McIntyre, M. E. Panisko, (2001). Performance of the Automated Radioxenon Sampler-Analyzer (ARSA) in Phase 2 of the Provisional Technical Secretariat s Noble Gas Demonstration, In preparation, Pacific Northwest National Laboratory Report.

Mage, D.T., On the lognormal Distribution of Air Pollutants, Proceedings of the Fifth Meeting of the Expert Panel on Air Pollution Modeling, NATO/CCMS N.35, Roskilde, Denmark, Jun 4-6, 1974.

McIntyre, J.I., T. W. Bowyer, and P. L. Reeder (1999). Calculation of minimum-detectable-concentrations of xenon isotopes using a beta-gamma coincidence counting system, Pacific Northwest National Laboratory Report #PNNL-13102.˚

Ott, W.R. (1995). Environmental Statistics and Data Analysis, Lewis Publishers, New York.

Reeder, P.L. T. W. Bowyer (1998). Xe isotope detection and discrimination using beta spectroscopy with coincident gamma spectroscopy, Nuclear Instruments and Methods in Physics Research A, 408, 582-590.

Stockburger, H., H. Sartorius, and A. Sittkus (1977). A method for measurement of the Krypton-85 and Xenon-133 content in the atmosphere, Zeitschrift f rNaturforsch, 32, 1249-1253.

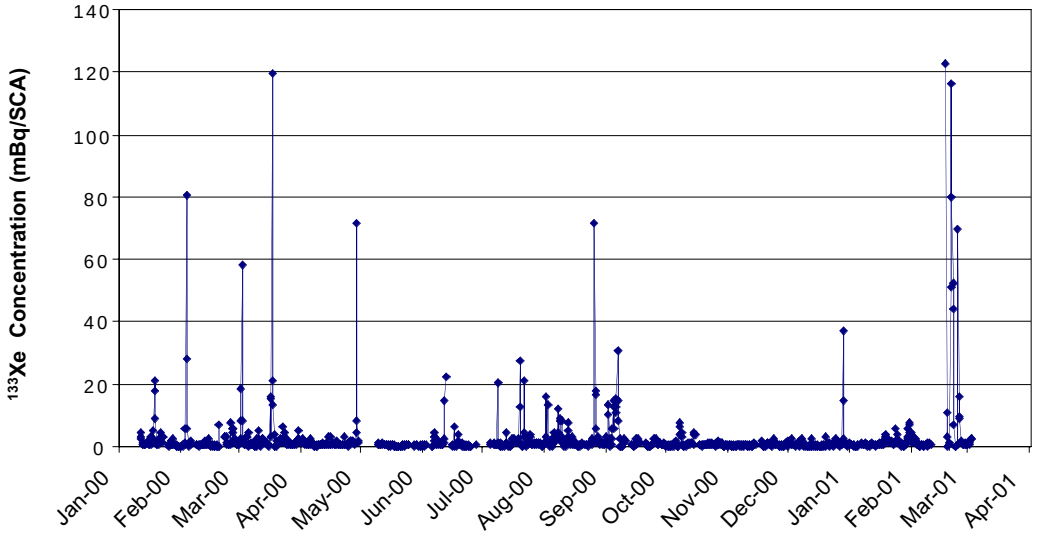

Figure 1. Plot of the concentration of ^{133}Xe taken by the ARSA throughout CY 2000.

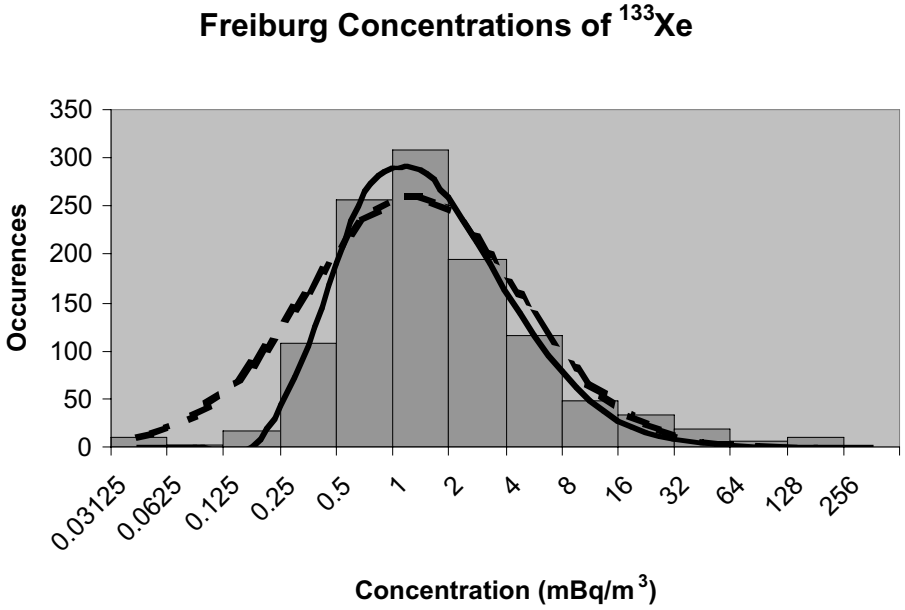

Figure 2. Distribution of the observed concentrations of ^{133}Xe during the year 2000 and fits of this distribution to two different lognormal distributions. The bars show the number of occurrences of a given measured concentration, the dashed line is a fit of a two-parameter lognormal distribution, and the solid line is a fit of a three parameter lognormal distribution.

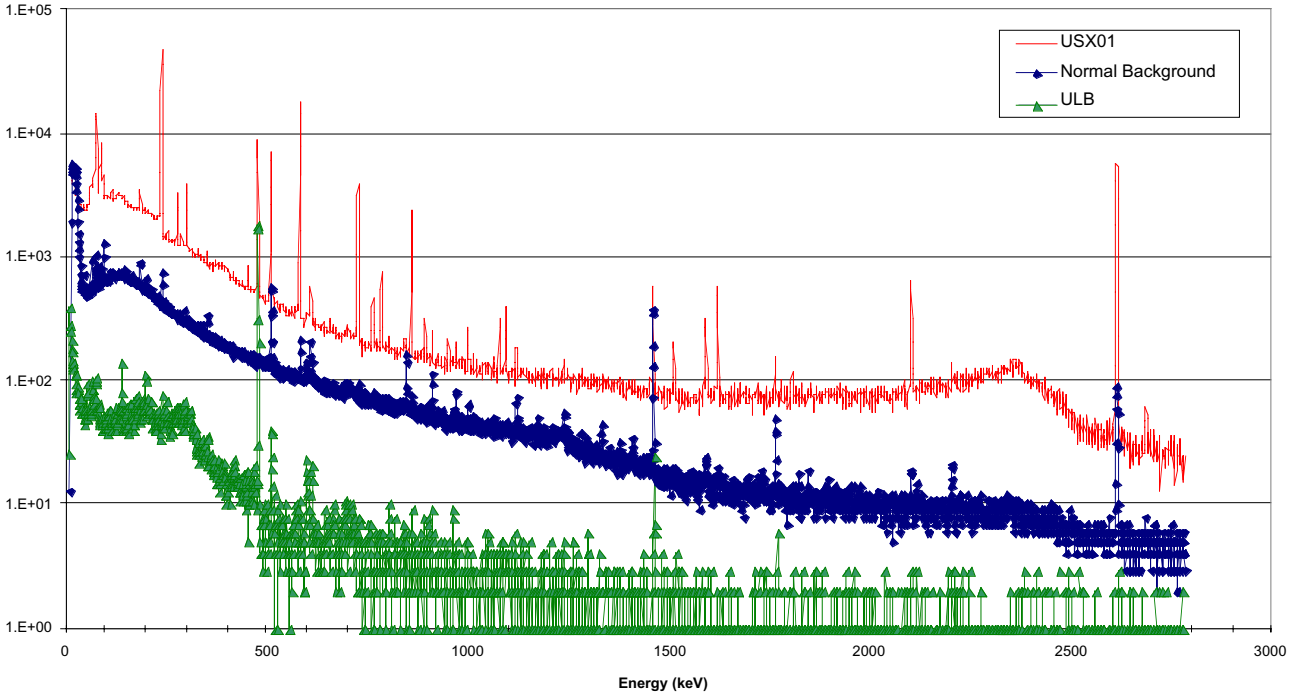

Figure 3. Gamma ray spectrum obtained under three conditions. A RASA field measurement (USX01) is shown in red, or is the highest spectrum. The detector background for that RASA is shown as the blue spectrum with diamonds at each point. The re-measurement of the same filter ten days later with an ultra-low background (ULB) detector is the green spectrum with triangles at each point, or is the lowest spectrum.

Isotope	***Station***	°	°	°	***Lab***	°
	(Bq)	error			(Bq)	error
Be-7	31.72	1.32%			27.85	1.88%
Pb-212	40.21	2.98%		<	0.2067	
Bi-212	43.64	3.20%		<	2.163	
K-40	7.054	3.37%			1.101	17.12%
Tl-208	15.39	5.95%		<	0.07066	
U-235	0.7126	6.05%		<	0.1106	
U-238	20.62	13.34%		<	11.66	
Ac-228	0.3922	15.19%		<	0.3593	
Pb-214	0.2822	18.55%		<	0.03777	
Bi-214	0.534	20.42%		<	0.09837	

Table 1. The results of automatic analysis of the original RASA spectrum and the lab spectrum. The only positive detection isotopes in the lab were ^{7}Be and ^{40}K.

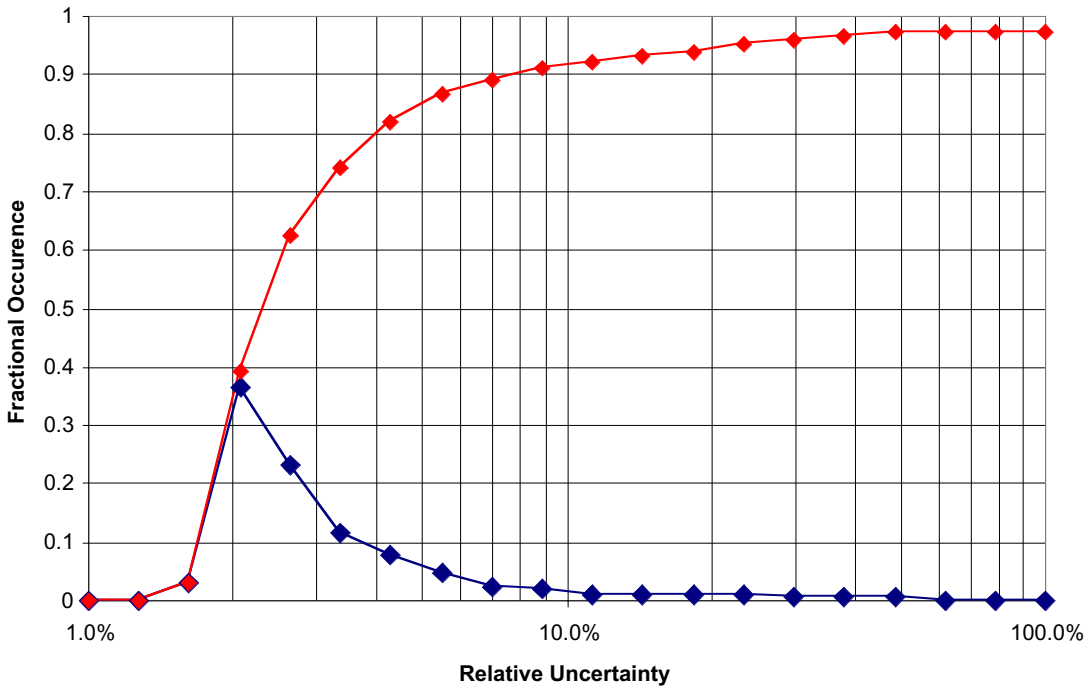

Figure 4. Frequency chart showing the fraction of 1700 RASA spectra with ^{7}Be activity uncertainties in bins from 1% 10 100% uncertainty. The sum of the fractional occurrences from 1% to 100% is also shown. This demonstrates that about 70% of observed ^{7}Be activities have a 3% uncertainty or less.

USING ATMOSPHERIC ^{137}CS MEASUREMENTS AND HYSPLIT TO CONFIRM CHERNOBYL AS A SOURCE OF ^{137}CS IN EUROPE

Erik L. Swanberg[1] and Steven G. Hoffert[2]

Veridian Systems[1], Autometric[2]

Sponsored by Defense Threat Reduction Agency

Contract No. DTRA01-99-C-0031

ABSTRACT

The Chernobyl nuclear reactor accident released considerable amounts of radioactive material into the environment, including a large amount of ^{137}Cs. A large fraction of the ^{137}Cs was deposited on the ground in the surrounding areas. Two atmospheric monitoring stations that contribute data to the Prototype International Data Centre (PIDC), one in Stockholm, Sweden, and the other in Helsinki, Finland, routinely measure ^{137}Cs. It is believed that the source of this ^{137}Cs is the ground contaminated by the Chernobyl accident. The PIDC routinely uses HYSPLIT (HYbrid Single-Particle Lagrangian Integrated Trajectory) atmospheric modeling software to determine probable source locations of radionuclides detected during normal operations. In this paper, HYSPLIT was used in conjunction with the data from the PIDC to more firmly establish the link between Chernobyl and ^{137}Cs measurements. The results indicate that an air mass containing ^{137}Cs has a higher likelihood of having recently been in the Chernobyl area than an air mass that does not contain ^{137}Cs. The inverse seems true also: an air mass that does not contain ^{137}Cs is far less likely to have been in the vicinity of Chernobyl in the recent past. These results, while not definitive, are very encouraging. The results also improve the confidence in HYSPLIT.

KEY WORDS: Chernobyl, Cesium, PIDC

OBJECTIVE

In 1986, the Chernobyl accident released large amounts of many different radionuclides into the atmosphere. Starting with its first sample in 1996, the Prototype International Data Centre (PIDC) has measured ^{137}Cs at radionuclide monitoring stations in Europe. This paper attempts to link ^{137}Cs re-suspension in the vicinity of Chernobyl to the ^{137}Cs regularly measured by monitoring stations. To this end, HSYPLIT (HYbrid Single-Particle Lagrangian Integrated Trajectory) atmospheric modeling software was used in conjunction with radionuclide concentration measurements to show that the Chernobyl region is likely the source of ^{137}Cs.

There are about 150,000 km^2 of land contaminated with ^{137}Cs at greater than 37 kBq/m^2 (UNSCEAR, 2000). It is not surprising that conditions exist that re-suspend this ^{137}Cs. One example is a forest fire in the Chernobyl area that re-suspended measurable amounts of ^{137}Cs, that was detected by the PIDC in May, 2000. Once airborne, the ^{137}Cs is transported considerable distances in the atmosphere. In particular, the ^{137}Cs is transported to European atmospheric monitoring stations before the ^{137}Cs concentration falls below the minimum detectable concentration.

There are four PIDC monitoring stations in Europe, all of which regularly measure ^{137}Cs. Two of these, one in England and the other in Germany, sample air for seven days. For the purposes of this study, these measurements are too long to make reasonable predictions about the origin of the ^{137}Cs re-suspension. Two other stations, one in Stockholm, Sweden, and the other in Helsinki, Finland, sample air for 24 hours. This shorter sampling time allows better estimation of an air mass's previous position. This study, therefore, only uses data from the Swedish and Finnish stations.

To model atmospheric transport, the PIDC runs HYSPLIT daily and generates a Field of Regard (FOR). The FORs show areas where it is most likely a parcel of air originated during a specified time period, and hence help

to indicate possible sources of radionuclides detected. These FORs were used to show a link between ^{137}Cs measurements and Chernobyl. About 18 months of FOR data was used for this study.

RESEARCH ACCOMPLISHED

This section begins by describing the data that was used from the PIDC. It then covers conditions that are favorable for transporting ^{137}Cs from Chernobyl to the monitoring stations. It also describes how HYSPLIT was used to generate FOR data. Then the link between ^{137}Cs measured at the monitoring stations and Chernobyl is established.

PIDC Data

The PIDC receives data from a global system of atmospheric monitoring stations. The Swedish and Finish systems are two of these stations. The stations send High Purity Germanium (HPGe) gamma-ray spectra to the PIDC on a regular basis, usually daily. The spectra are analyzed to determine which radionuclides are present and what their concentrations are. This includes concentrations for ^{137}Cs. The Swedish and Finish stations have been providing the PIDC with this data since 1996.

The PIDC uses atmospheric data and atmospheric modeling software to estimate previous locations of air that was sampled by a monitoring station. The model is run daily. This allows the PIDC to estimate the source of any unusual radionuclides that are observed at a station. The modeling software results were available from May 1999 to September 2000, which are the dates included in this study.

^{137}Cs Transport

In order for ^{137}Cs to travel from Chernobyl to a European monitoring station located over 1000 kilometers away it must first be re-suspended in the air. Then atmospheric conditions must be such that the ^{137}Cs is transported to the monitoring station. Some possible mechanisms for re-suspension include high winds stirring up contaminated soil (Gillette and Porch, 1978), burning of contaminated vegetation (Garger et al, 1998), or perhaps a disturbance in the sarcophagus surrounding the reactor. Atmospheric conditions consist mostly of prevailing winds blowing in the correct direction. This study did not attempt to look at processes that could re-suspend the ^{137}Cs. Hence discrepancies could result where HYSPLIT indicates air transport in the correct direction but no ^{137}Cs was detected. On the other hand, if ^{137}Cs from the Chernobyl region was measured, then both of the above conditions must have been met.

HYSPLIT

The PIDC uses HYSPLIT atmospheric modeling software to simulate particle trajectories in the atmosphere. These trajectories are then used to create FORs as follows. Simulated particles were released every hour from a 2° X 2° grid formed from points located at the intersection of even lines of latitude with even lines of longitude. HYSPLIT used measured atmospheric data to simulate the trajectories real particles would follow if released under the same conditions. If a particle passed near a station in the simulation, its point of origin was noted as having a particle reach the detector. The simulations were run for 24, 48, and 72 hours. After a run was complete, the number of particles that reached the detector was totaled, and the grid point tallies were normalized so that the sum of all grid point values in an FOR is one.

A few remarks are in order. First, the 2° X 2° grid square is somewhat coarse, resulting in coarse resolution. Second, the model was only run for 72 hours. The distance between Chernobyl and the monitoring stations is large enough that it could easily take more than 72 hours for an air mass to travel between the two. Therefore, some ^{137}Cs measurements were possibly not associated with Chernobyl because the air mass took longer than 72 hours to reach the station. Also remember that the atmosphere is a complex system and no model is perfect.

Combining HYSPLIT and ^{137}Cs Concentrations with Atmospheric Transport

Because FORs are normalized, combining them is accomplished by simply adding them together. The figures that follow were created with three different objectives in mind. Figure 1 is an average of all FORs that were

available for the Swedish station. It serves as a baseline and allows any unusual features to be seen. Figure 2 only includes FORs for days when the concentration of ^{137}Cs was above 4 μBq/m^3, which indicates likely origins of high ^{137}Cs concentrations. Figure 3 only includes FORs for days when ^{137}Cs was not measured, indicating where ^{137}Cs does not originate. The FORs are drawn as contour plots. Figures 4 through 6 are corresponding FORs for the Finnish station.

The figures show that when ^{137}Cs was measured, air was much more likely to have come from Chernobyl. In figures 2 and 5, high likelihood regions are near the stations and Chernobyl. There are other regions where the air might have originated, but they have smaller associated probabilities. Since the stations sample air for 24 hours, it is possible for more than one air mass to pass over a station and be included in a sample. Also, air in transit for more than 72 hours is not included in the FORs. Data from both stations indicate Chernobyl as being the most likely source for ^{137}Cs.

It is also interesting to note where the air originates when no ^{137}Cs is detected (Figures 3 and 6). Air appears to come from similar places as the average (Figures 1 and 4) but with lower probabilities of originating near the Chernobyl region. This is what would be expected if Chernobyl were the source of ^{137}Cs. Since none of the other places where air normally reaches the stations from are a source of high ^{137}Cs concentrations, Chernobyl must be the source of the elevated measurements.

Instead of selecting FORs based on whether or not ^{137}Cs was measured, they can be selected based on having a high probability of air reaching a radionuclide monitoring station from the Chernobyl area. This was done using four grid points near Chernobyl. For Sweden, ^{137}Cs was seen 11 out of 13 times when one of these four points had a probability of greater than .05. For Finland the same analysis yields 6 of 9 times. The days with higher likelihood also include the highest measurements of ^{137}Cs made at both stations. Table 1 contains a list of probabilities and ^{137}Cs concentrations.

For several particularly high concentrations of ^{137}Cs, HYSPLIT trajectory models were run. Figure 7 shows the result for one of these runs. It can clearly be seen this day (which was the highest concentration measured to date at the Swedish station) that the air mass goes almost directly from the Chernobyl region to Stockholm.

Table 1. Probabilities of air originating at a grid point near Chernobyl and ^{137}Cs concentrations actually measured.

Sweden		Finland	
Probability	Concentration (μBq/m^3)	Probability	Concentration (μBq/m^3)
0.053	0.59	0.065	Not Detected
0.053	0.58	0.071	0.86
0.055	Not Detected	0.071	0.86
0.065	1.9	0.14	5.7
0.065	1.9	0.17	3.3
0.067	1.8	0.17	3.3
0.069	6.4	0.19	Not Detected
0.069	6.4	0.21	5.7
0.11	45	0.22	Not Detected
0.17	16		
0.19	Not Detected		
0.32	45		
0.39	16		

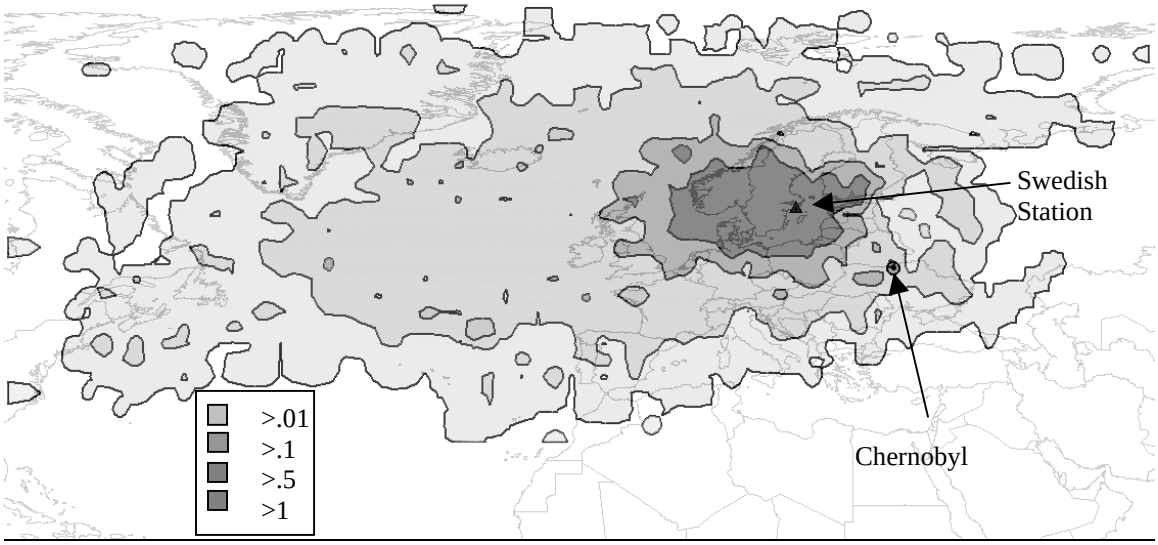

Figure 1. Average of all available FORs for the Swedish station.

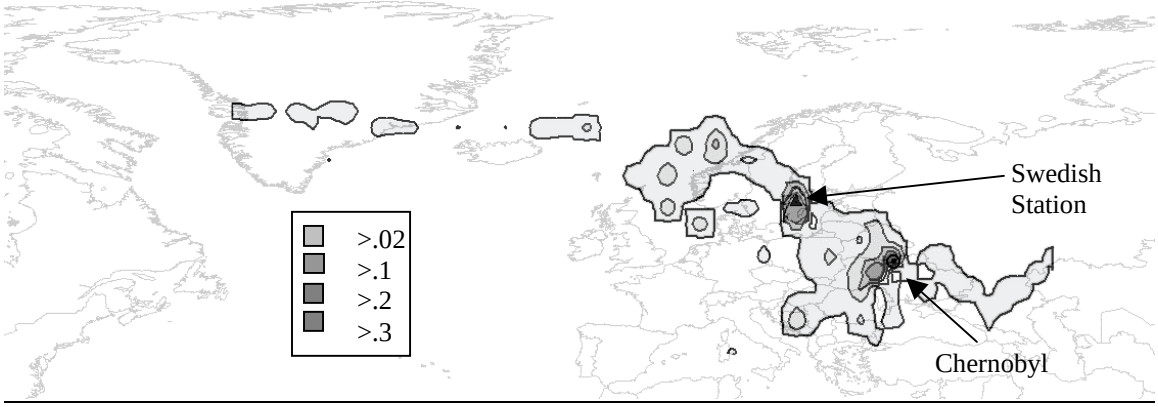

Figure 2. FORs for the Swedish station when the concentration of ^{137}Cs was greater than 4 $\mu Bq/m^3$.

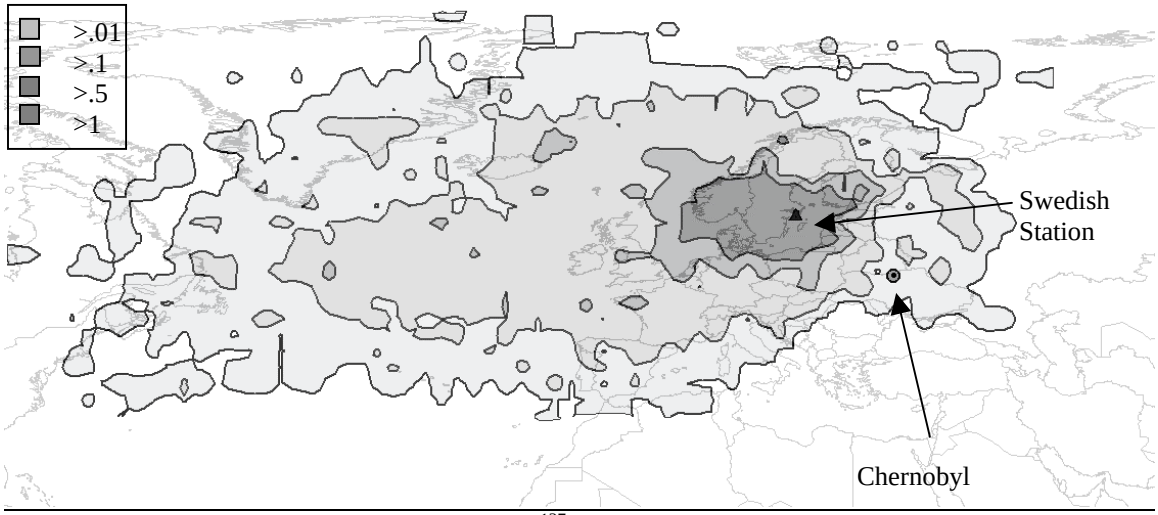

Figure 3. FORs for the Swedish station when no ^{137}Cs was measured.

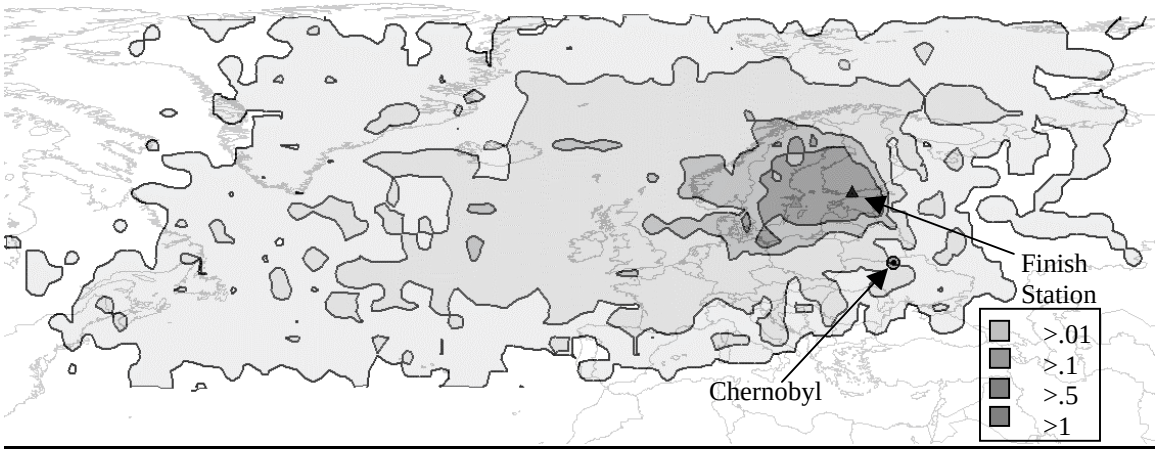

Figure 4. Average of all available FORs for the Finish station.

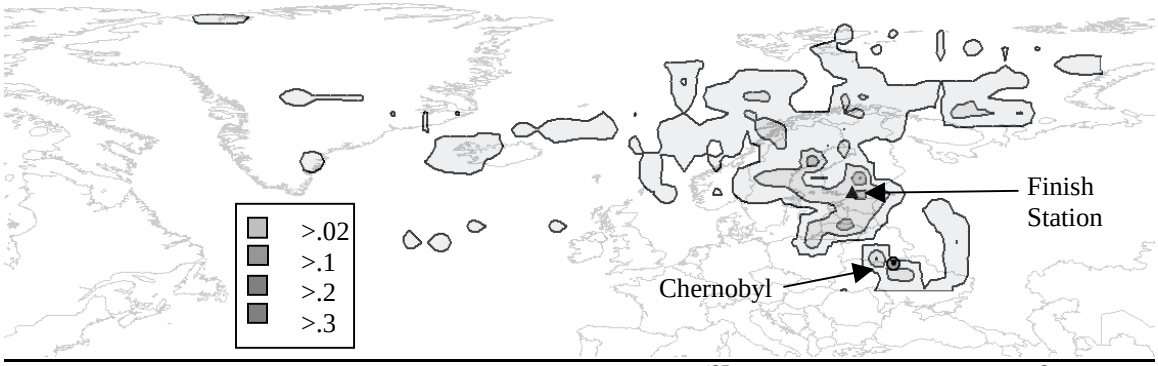

Figure 5. FORs for the Finish station when the concentration of ^{137}Cs was greater than 4 $\mu Bq/m^3$.

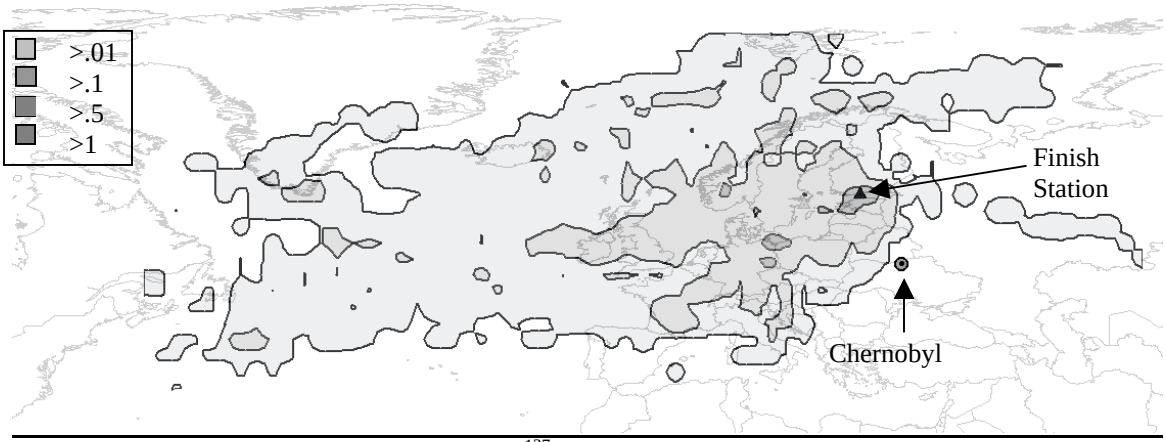

Figure 6. FORs for the Finish station when no ^{137}Cs was measured.

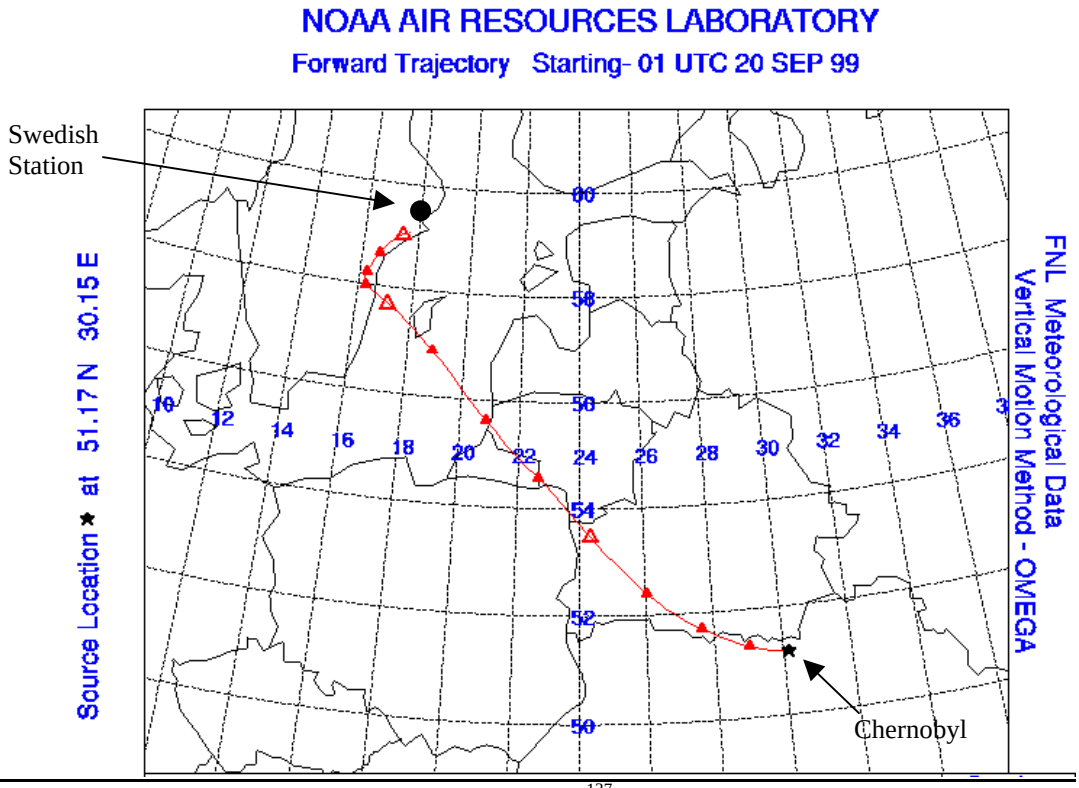

Figure 7. Trajectory for the day the highest concentration of ^{137}Cs was measured in Stockholm.

CONCLUSIONS AND RECOMMENDATIONS

A link was established between ^{137}Cs re-suspended in the Chernobyl region and ^{137}Cs measured by two European monitoring stations in several ways. First, it was shown that when ^{137}Cs was measured, it was more likely for the air that was sampled to have come from the Chernobyl region. Secondly, when no ^{137}Cs was measured the sampled air was much less likely to have been in the Chernobyl region. Likewise, if air did not come from the Chernobyl region, ^{137}Cs wasn't seen. It was also shown that if air did move from the Chernobyl region to a monitoring station, it was likely to contain detectable concentrations of ^{137}Cs. While these results are qualitative in nature, the evidence strongly suggests that a correlation exists.

Another benefit of this study is an increased confidence in the tools used and the manner in which they are used. Data analysis using two different stations yielded equivalent results. These results agree with what common sense dictates, namely that re-suspension of ^{137}Cs in the Chernobyl region is the source of ^{137}Cs in Sweden and Finland. One can thus conclude that using radionuclide concentrations obtained with currently fielded systems in conjunction with HYSPLIT produces good results.

If more conclusive evidence of the link between ^{137}Cs re-suspension near Chernobyl and high ^{137}Cs concentrations is desired, there are a couple of investigations that could be performed. First, ^{134}Cs was also released during the accident. In fact, several of the earlier samples measured by the PIDC contain both ^{137}Cs and ^{134}Cs. Due to its 2-year half life, almost all of the ^{134}Cs will have decayed. But it might be possible, using a detection methodology with reduced minimum detectable concentrations, to measure the ratio of ^{137}Cs to ^{134}Cs in both soil in the Chernobyl region and in the samples from the monitoring stations. If the ratios match, this would be strong evidence for one causing the other. Also, determining conditions good for the re-suspension of ^{137}Cs into the atmosphere could help to improve the data used in this study.

REFERENCES

Gillette, Dale A. and William M. Porch (1978), The Role of Fluctuations of Vertical and Horizontal Wind and Particle Concentration in the Deposition of Dust Suspended by Wind, J. of Geophysical Research, January 20, 1978, 409-414

Garger, E. K., V. Kashpur, H. G. Paretzke, and J. Tschiersch (1998) Measurement of Resuspended Aerosol in the Chernobyl Area Part II. Size Distribution of Radioactive Particles, Radiation and Environmental Biophysics Vol 36 Number 4, 275-283

HYSPLIT4 (HYbrid Single-Particle Lagrangian Integrated Trajectory) Model (1997). Web address: http://www.arl.noaa.gov/ready/hysplit4.html, NOAA Air Resources Laboratory, Silver Spring, MD.

United Nations Scientific Committee on the Effects of Atomic Radiation, UNSCEAR 2000, Sources and Effects of Ionizing Radiation, Volume II: Effects, Report to the General Assembly, with Scientific Annexes.

Infrasound Monitoring

STUDIES OF MICROBAROMS USING MULTIPLE INFRASOUND ARRAYS

Henry E. Bass and Kenneth Gilbert[1], Milton Garces[2] , Michael Hedlin and John Berger[3],
John V. Olson , Charles W. Wilson and Daniel Osborne[4]

[1]University of Mississippi,[2] University of Hawaii, [3]Scripps Institute of Oceanography,
[4]University of Alaska, Fairbanks

Sponsored by Defense Threat Reduction Agency
Contract No. DTRA01-00-C-0078

US Army Space and Missile Defense Command
Contract No. DASG60-99-C-0018

The Preparatory Commission for the
Comprehensive Nuclear-Test-Ban Treaty Organization
Provisional Technical Secretariat
Contract No. 00/30/6021

ABSTRACT

Microbaroms, known to be produced by marine storms, are a prevalent infrasound signal due to the presence of strong storms over the oceans. Often the microbarom wave trains last for tens of hours allowing us to track the storm. When we perform a least-squares fit to plane-wave arrivals on the data we find the apparent source azimuth points to the center of the storm low-pressure center. Early research has shown that microbarom signals are associated with wave height in storms but the theoretical description for the coupling between water waves and acoustic waves in the atmosphere is not complete. Studies of microbaroms from multiple locations are better able to identify the source of microbaroms in the storm and to give an indication of the propagation paths from the storm center to the receivers. We have also begun to study the spatial coherence of microbaroms using the Hilbert Transform technique. We find that the mean packet length is of the order of 2 to 5 wavelengths. With this information we plan to break the wave trains into individual packets in order to explore the extent to which the source is localized.

KEY WORDS: Microbaroms, Marine Storms, Hilbert transform

OBJECTIVE

The objective of our study is to perform multiple detections of microbarom signals from marine storms using multiple infrasound sites. This exercise serves as a test of the data collection and analysis procedures used by each array site as it comes on line. As multiple detections of signals from a storm are made we expect to gather information about the sources and propagation paths of the infrasound generated by the storm.

RESEARCH ACCOMPLISHED

Introduction

Infrasound Arrays that are part of the International Monitoring System of the Comprehensive Nuclear-Test-Ban Treaty are operating at several sites in the United States. During the installation and testing phases of these arrays, natural signals from many sources have been detected. Microbaroms are continuous signals that are associates with severe weather in the ocean. In this report we will describe the microbarom signals from several marine storms with special emphasis on tropical storm Barbara that traversed the Pacific near Hawaii in mid-June of 2001. Microbarom signals from Barbara were especially strong in the IS59 infrasound array located near Kona, HI. The infrasound array in Fairbanks, AK observed signals from

several marine storms in the Pacific during this time and the azimuths of one group of signals was consistent with the location of Barbara.

Microbarom signals are observed worldwide with periods in the 3-8 second 0.12 – 0.33 Hz) range and amplitudes of a few tenths of a Pascal. Due to their pervasiveness, they routinely set the noise levels and thus determine the detection thresholds in that band. They have been extensively studied and it is well known that their generation depends upon the amplitudes of ocean waves produced by storms. Posmentier (1967) and Gossard and Hooke (1975) have given comprehensive reviews of microbarom generation and propagation. Recent studies by Arendt & Fritts (2000) show that the acoustic radiation results from a non-linear coupling of atmospheric waves with the ocean wave spectrum.

RESEARCH ACCOMPLISHED

Tropical Storm Barbara

Tropical storm Barbara began as a low-pressure area off the west coast of Mexico in mid-June, 2001. By June 17 the system was producing microbarom signals detectable by the Hawaiian infrasound station. As it moved westward and northward the system deepened and was officially identified as tropical storm Barbara on June 20. At this point it was producing winds of over 60 mph with gusts up to 70 mph. By June 22 the storm weakened to a tropical depression with winds below 35 mph. Details are available on the NOAA web site: http://www.nhc.noaa/gov/archive/2001. Figure 1 shows the storm track from June 20 through June 23 as Barbara moved toward the Hawaiian Islands.

Observations from the IS59 infrasound station in Hawaii

Even before Barbara achieved tropical storm status it contained winds large enough to produce sizeable ocean waves and the concomitant microbaroms. The infrasound station, IS59, near Kona, Hawaii, observed these microbaroms. Figure 2 shows the June 17and June 18 detections of the microbarom source obtained from frequency-wave number (FK) analyses. The radial line from the center to the maximum provides the slowness and azimuth of the detection. The storm continued to produce microbarom signals and was tracked continuously for the next 5 days by the Hawaiian station. Figure 3 shows the results of array processing of the microbarom signals from Barbara for 24 hours on June 19. The data were band-pass filtered between 0.1 and 0.5 Hertz for this analysis. The top panel shows the inverse of the apparent horizontal phase speed, or slowness; the middle panel shows the azimuth of arrival of the microbaroms and the bottom panel shows the waveform indicating a steady presence of microbaroms over this 24 hour period

Observations from the prototype infrasound station in Fairbanks, Alaska

As is evident from the map in Figure 1 the north Pacific was under the influence of several storm systems during June 2001. Observation of the microbarom signals from Barbara at the Fairbanks station was made difficult because of the clutter of signals from other storms. Figure 4 shows three maps with estimates of wave heights in the north Pacific (obtained from the web page supported by the Fleet Numerical Meteorology and Oceanography Center: http://152.80.49.205). As can be seen in the top panel, showing wave heights and wind directions on June 19, there was major activity in the Gulf of Alaska. The middle panel, showing the winds and wave heights for June 20 continues to show activity, although somewhat diminished. The bottom panel, showing the winds and wave heights for June 21 shows that the major activity has shifted west of the Gulf of Alaska.

Figure 5 shows the microbarom signals detected at the Fairbanks infrasound array for June 19 through 22. The diagrams are polar plots with apparent speed in km/sec as a radial coordinate and the azimuth as the angular coordinate. Microbarom signals are seen each day. The straight-line bearing from Fairbanks to Barbara lies at an azimuth between 158^{o} and 162^{o}. Note that only on June 20 are microbaroms observed in the sector between 150^{o} and 180^{o}. Signal amplitudes during this interval were in the range of a few tenths of a Pascal. Signals from this azimuth lasted several hours during the local afternoon of June 20, the day

that Barbara's winds grew to tropical storm status above 40 mph. The other diagrams in Figure 5 show microbaroms associated with the various storm centers then present in the north Pacific.

CONCLUSIONS AND RECOMMENDATIONS

The infrasound wave field, in the period range between 3 and 8 seconds (0.12 – 0.33 Hz), is populated by microbarom signals. These signals, generated by marine storms, form the background against which detection in the CTBT program must be made. We have shown that a wide variety of marine storms can be producing microbarom signals simultaneously and that they can be detected from a distance of several thousand kilometers from the source. Once detected marine storms can be tracked for days using the microbarom signals from several infrasound stations.

REFERENCES

Arendt, S. and C. Fritts (2000), Acoustic Radiation by Ocean Surface Waves, *J. Fluid Mech*., **415**, 1.

Gossard E. and W. Hooke (1975), Waves in the Atmosphere, *Elsevier*.

Posmentier, E (1967), A Theory of Microbaroms, *Geophys. J. R. Astr. Soc*., **13**, 487.

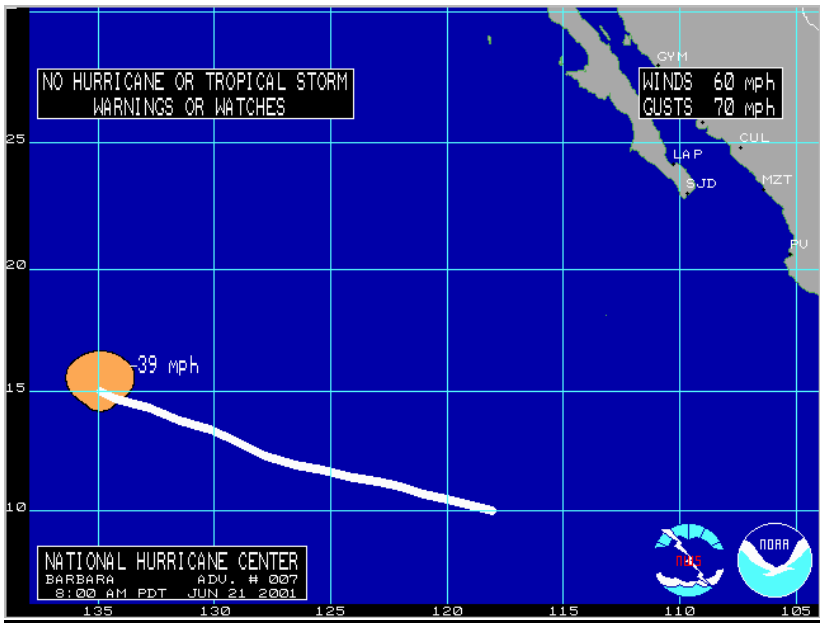

Figure 1a. Track of tropical storm Barbara during the period from June 17 to June 22, 2001.

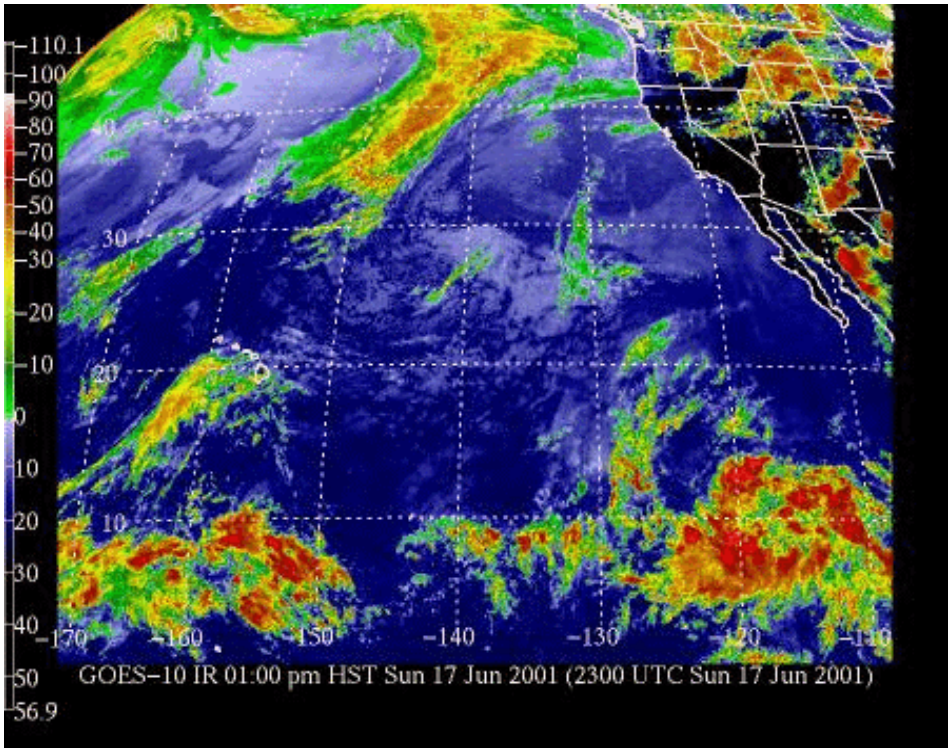

Figure 1b. Infrared image of the conditions in the north Pacific on June 17, 2001.

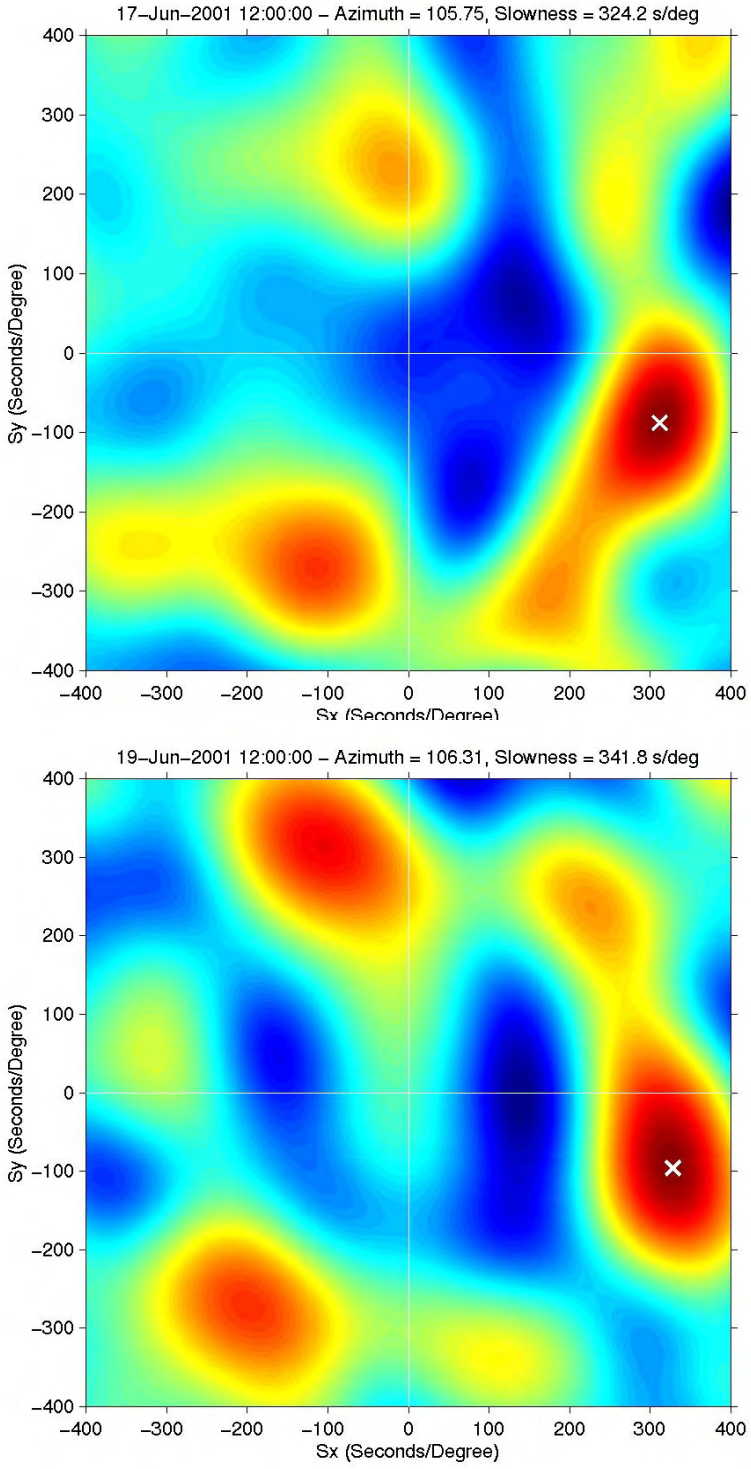

Figure 2. FK detection of the microbarom source by IS59 on June 17 and June 19, 2000, several days before the disturbance grew to tropical storm status.

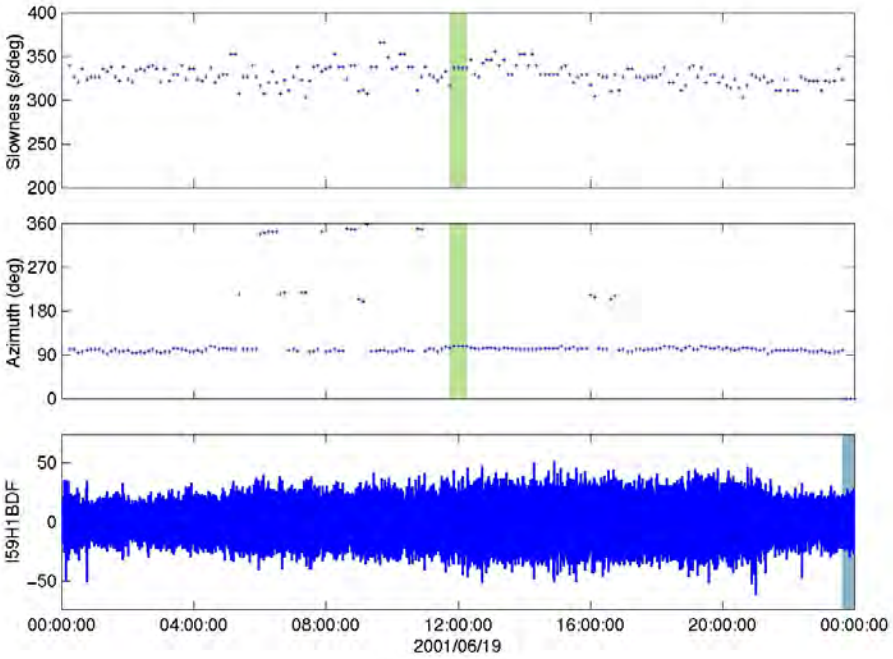

Figure 3. This figure shows the continuous microbarom waveform during the 24 hour period on June 19, 2001. The top panel shows the slowness of the wave train with the maximum correlation, the middle panel shows its direction of arrival (measured clockwise from North), and the bottom panel shows the waveform filtered in the 0.1 – 0.5 Hz frequency band.

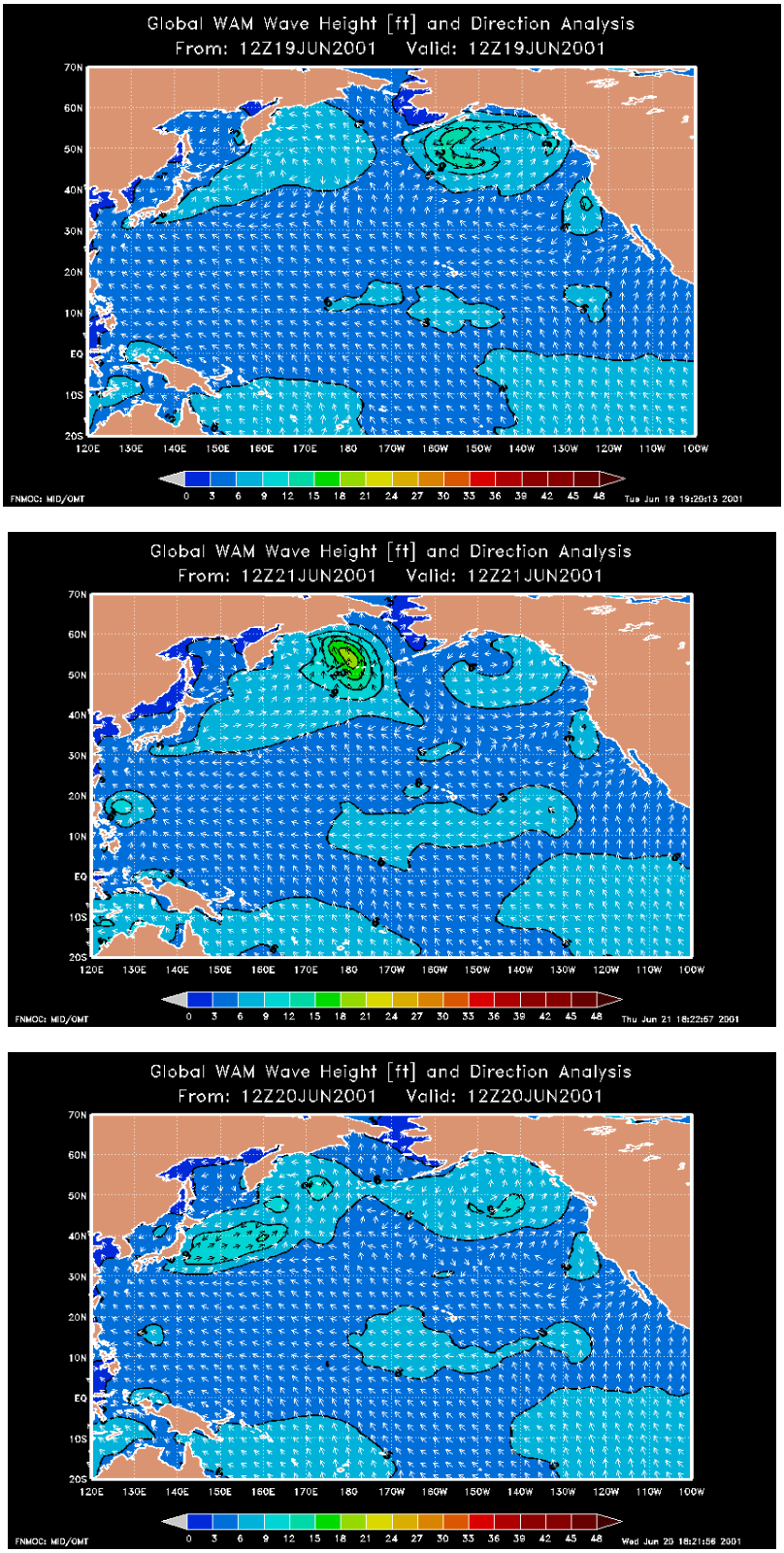

Figure 4. The top panel shows the wind and wave heights in the north Pacific for June 19, 2001. The middle panel shows the wind and wave heights for June 20 and the bottom panel shows the wind and wave heights for June 21. Note the steady activity in the Gulf of Alaska during this period.

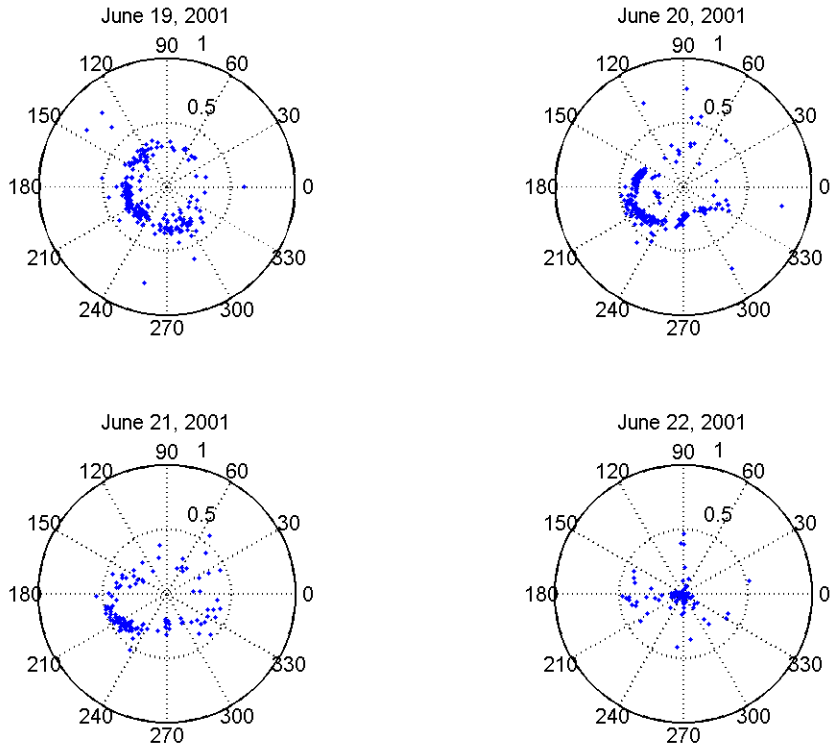

Figure 5. This figure shows four panel each containing the microbarom arrivals for one day from June 19 to June 22, 2001. The polar diagrams are created with the apparent phase speed as the radial component and the azimuth of arrival as the angular component. See the text for details.

THE PACIFIC INFRASOUND EVENT OF APRIL 23, 2001

David J. Brown[1], Anna K. Gault[1], Riley Geary[1], Pierre Caron[1], and Relu Burlacu[2]

Science Applications International Corporation (SAIC)[1]
Mission Research Corporation[2]

Sponsored by Defense Threat Reduction Agency

Contract No. DTRA01-99-C-0025

ABSTRACT

For the past several years, the Defense Threat Reduction Agency's (DTRA) Center for Monitoring Research (CMR) in Arlington, Virginia, has been developing and testing software to extend the International Data Centre nuclear explosion monitoring system to include infrasound monitoring of the atmosphere. This system can form infrasound-only events, or form fused events using any combination of infrasound, seismic, and hydroacoustic data. Evaluation of the performance of the infrasound processing system is hampered by the scarcity of major infrasound events.

On April 23, 200, a significant infrasound event occurred, providing a good test case for the system. Signals from this event, subsequently confirmed by optical observations to be a bolide impact over the Northern Pacific Ocean, were recorded on a number of infrasonic arrays in North America and Hawaii. Using arrival information from several International Monitoring System (IMS) infrasound arrays, an acoustic-only event was built automatically as part of standard event processing at the Prototype International Data Center (PIDC). After optical confirmation it was determined that the infrasound and optical locations differed by 3 minutes in origin time and 80 km in location, which is within the estimated error of the infrasound location. This paper presents the Prototype IDC analysis of this event and the subsequent studies undertaken at CMR to refine the hypothesized source location and evaluate the infrasound processing system.

A number of signal characteristics, such as duration and dominant period, make the April 23 event significant for evaluating nuclear explosion monitoring capability. To provide a better understanding of what characteristics constitute significant signals and to provide a better discrimination capability, CMR has been compiling a collection of infrasonic signals that, for various reasons, are considered to be noteworthy. This infrasound waveform library is being made accessible to researchers for independent research by the CMR Research and Development Support System (RDSS). The infrasound library is divided into several subsections that include a ground-truth database, the ENSCO collection compiled by the University of Alaska, as well as a collection of synthetic-signal data. A web-based interface has been developed to allow easy access to the waveforms. This paper provides a summary of the waveform library and how it may be accessed.

KEY WORDS: infrasound, infrasonic event, infrasound waveform library.

OBJECTIVE

The objective of this research is to improve the current infrasound source location and discrimination capability of the fused seismic-hydroacoustic-infrasonic-radionuclide data processing system being developed at the CMR. The occurrence in the last 12 months of two large bolide (meteorite) events with acoustic signals that were recorded on numerous IMS-style infrasound arrays, provides an opportunity to gauge performance of the automatic infrasonic detection and source location system, as well as an opportunity for system refinement. In this investigation, various velocity models will be used with acoustic arrival information from each of the bolide events, in conjunction with a nonlinear source location procedure to determine the merits of each velocity model.

During event analysis, various characteristics of the recorded waveforms suggested that these events were significant from a monitoring perspective. However, the infrasound source characterization and discrimination procedures are still rudimentary and at an early stage of development. As an aid to improving discrimination, and automatic detector design, developmental work on an infrasound waveform library has commenced at CMR as part of the RDSS. This data collection will be invaluable to independent researchers and is being made available to the research community via a web-based interface.

RESEARCH ACCOMPLISHED

Optical source location information as provided by Los Alamos National Laboratory (LANL, 2001a; LANL, 2001b) for the two bolide events considered in this investigation are listed in Table 1.

Table 1: Bolide events considered in the present study.

Name	Lat	Lon	Time	Energy (J)
Acapulco	14.45	-106.13	2000/08/25 01:12:25	1.4×10^{12}
North Pacific	27.90	-133.89	2001/04/23 06:12:35	4.6×10^{12}

In what follows, each bolide event will be considered independently.

Acapulco Event

Location information for the recording arrays for this event are shown in Table 2 as well as source to receiver backazimuth, θ, and distance, Δ, along the great-circle.

Table 2: Geographical information for the recording arrays.

Station	Lat	Lon	Location	θ (deg)	Δ (km)
DLIAR	35.8667	-106.3342	Los Alamos, New Mexico, USA	179.5	2381
IS59	19.5917	-155.8934	Hawaii, USA	88.0	5304

Arrival information for the IMS-style arrays for this event are shown in Table 3. Azimuth variances, $\delta\theta$, of around 2.5 degrees were found for both stations. A time variance, δT, of 5 sec were used for both stations as this corresponds approximately to one wave period. This value for δT may be too small and the effect on source location of larger values needs to be investigated.

Table 3: Arrival information for the IMS-style recording arrays for the Acapulco Event.

Station	Observed Signal Time T	δT (sec)	Arrival Azimuth θ (deg)	δθ (deg)	F-stat	Signal Duration (min)	Dom. Freq. (Hz)
DLIAR	2000/08/25 03:28:52	5.0	181.3	2.5	21	11.4	0.20
IS59	2001/08/25 06:05:27	5.0	89.2	2.5	43	18.3	0.17

Although the signal from this event was automatically detected at the DLIAR array, maintenance work prevented automatic detection at the IS59 array. An automatic source location was therefore never formed. Subsequent analysis, however, was performed.

Following Jordan and Sverdrup (1981), and Bratt and Bache (1988), a least-squares inversion procedure was applied to the arrival information contained in Table 3. Both azimuth and time were made 'defining' for this algorithm, but slowness was set as 'un-defining' so that it played no role in the source location procedure.

Travel-time information for these location exercises was provided by one of two different methods. The first uses travel-time information assigned via travel time-tables generated using a seasonal propagation model (based on the MSISE-90 temperature model of Hedin, (1991), and the HWM-93 wind model of Hedin et al., (1996)), and the second assumes a constant average horizontal signal propagation speed. Several different propagation speeds were used. The following variances were assumed for the respective travel-time models where *s* is distance in km:

$$\Delta\mathbf{T} = 1462\sqrt{\mathbf{s}/10000} \quad \text{(sec)} \quad \text{Constant velocity model appropriate for stratospheric signals.}$$

$$\Delta\mathbf{T} = \begin{cases} 1800\dfrac{\mathbf{s}}{2500} & ; \quad s < 2500 \\ 1800 + (7200 - 18000)\left(\dfrac{\mathbf{s} - 2500}{21000 - 2500}\right) & ; \quad s > 2500 \end{cases} \quad \text{(sec)} \quad \text{Seasonal model}$$

Although large, the variances for the seasonal model were designed to accommodate the possible phase misidentification when stratospheric phases were assigned thermospheric travel-times or vice-versa.

Observed and seasonally-predicted values for the average horizontal velocity, *V,* are shown for each array in Table 4. Clearly, thermospheric travel-times are predicted for the signals at DLIAR and stratospheric travel-times for the signals at IS59. This is significantly what one would expect for the particular season and geographic location of the arrays. In the summer, the stratospheric winds will be predominantly toward the west, strongly influencing the signal at IS59. The azimuth of arrival at DLIAR, however, is directed largely toward the north and so the signals will not benefit from the seasonal stratospheric winds. The observed average horizontal velocity at each array, of course, implies stratospheric signals at each array.

Table 4: Observed and predicted average horizontal velocities.

Sta	V (observed)	V (predicted)
DLIAR	291	253
IS59	302	313

Shown in Table 5 are the hypothesized source locations for various velocity models Also shown are the spatial and temporal mislocations and size of the 90% confidence ellipse for each model.

Table 5: 90% confidence source location results for various velocity models. Model number indicates constant velocity (in m/s) used. Semi-major axis is indicated by Smaj, Semi-minor axis is indicated by Smin.

Model	Lat	Lon	Time	Spatial mislocation Δ (km)	Temporal mislocation ΔT (min)	Smaj (km)	Smin (km)
290	13.6	-106.9	01:05	124	7	387	195
295	13.7	-106.9	01:09	116	3	162	82
300	13.8	-106.8	01:12	107	0	58	29
summer	14.7	-106.6	01:04	62	8	2606	1294

The constant velocity source locations have clearly benefited from phase identification where a substantially refined variance for the travel-times was possible. The apparent improvement in spatial mislocation in the case of the seasonal model is simply a manifestation of the fact that large variances on the travel-times were used, and only two stations were used to form the source location. In such a case, the source location algorithm will tend to locate the source at the great-circle intersection as defined by the backazimuth at each array. A representative example of the signals recorded from this event (IS59) is shown in Figure 1.

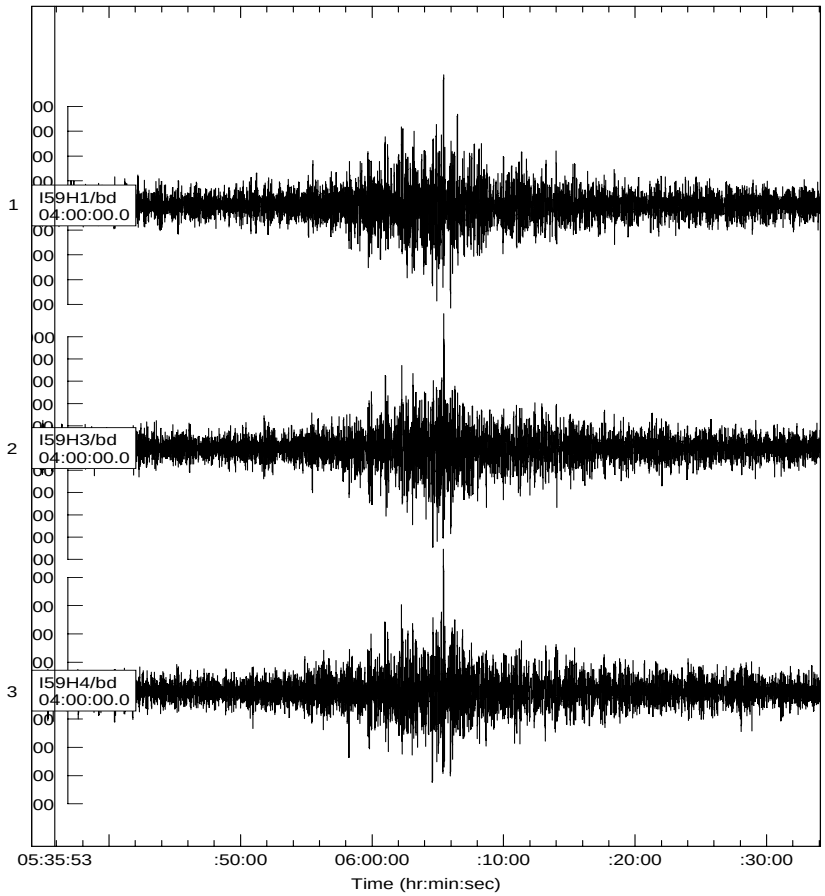

Figure 1: Signal recorded at IS59 (Hawaii) - 5304 km from the Acapulco event. No data were available for channel H2. Time is UTC.

North Pacific Event

This event was formed automatically at the CMR using detections on two IMS infrasound arrays. The Hawaii array (IS59) and the Lac du Bonnet, Manitoba array (IS10) were the closest IMS arrays contributing to standard event formation at the time of the event, and detections from these arrays were used to build the event in the Standard Event List 3 (SEL3). The signal was also detected at a number of other infrasound arrays. The most distant station to record the signal is located in Freyung, Germany (IS26), 10800 km from the estimated source location. The Pinon Flat array, California (IS57), Windless Bight, Antarctic array (IS55), and the IMS prototype array in New Mexico (DLIAR) operated by LANL, were not transmitting data to the PIDC at the time of the event. IS55 and IS57 are newly installed arrays and at the time of the event were not providing data feeds for all PIDC processing. Data from both the DLIAR array and IS57 array were later recovered and transmitted to the PIDC.

Location information for the recording arrays for this event are shown in Table 6 as well as source to receiver backazimuth, θ, and distance, Δ, along the great-circle.

Table 6: Geographical information for the recording arrays.

Station	Lat	Lon	Location	θ (deg)	Δ (km)
IS57	33.6056	-116.4544	Pinon Flat, California, USA	253.9	1781
NVIAR	38.4295	-118.3037	Nevada, USA	235.7	1836
IS59	19.5917	-155.8934	Hawaii, USA	63.5	2408
DLIAR	35.8667	-106.3342	Los Alamos, New Mexico, USA	259.0	2737
IS10	50.2010	-96.0270	Winnipeg, Canada	246.5	4002
IS26	48.8516	13.7131	Freyung, Germany	331.4	10837

Arrival information for these stations is shown in Table 7.

Table 7: Arrival information for the bolide of 2001/04/23.

Station	Observed Signal Time T	δT (sec)	Arrival Azimuth θ (deg)	$\delta\theta$ (deg)	F-stat	Signal Duration (min)	Dom. Freq. (Hz)
IS57	2001/04/23 07:51:48	5.0	254.7	3.00	290	11.5	0.25
NVIAR	2001/07/23 07:56:25	5.0	239.7	2.02	35	7.0	0.22
IS59	2001/07/23 08:28:05	5.0	62.4	2.05	43	15.8	0.25
DLIAR	2001/07/23 08:44:51	5.0	261.9	2.00	81	13.8	0.24
IS10	2001/07/23 09:58:52	5.0	244.4	2.50	128	15.5	0.21
IS26	2001/07/23 16:26:28	5.0	324.9	2.00	27	8.0	0.15

A representative example of the signals recorded from this event (IS57) is shown in Figure 2.

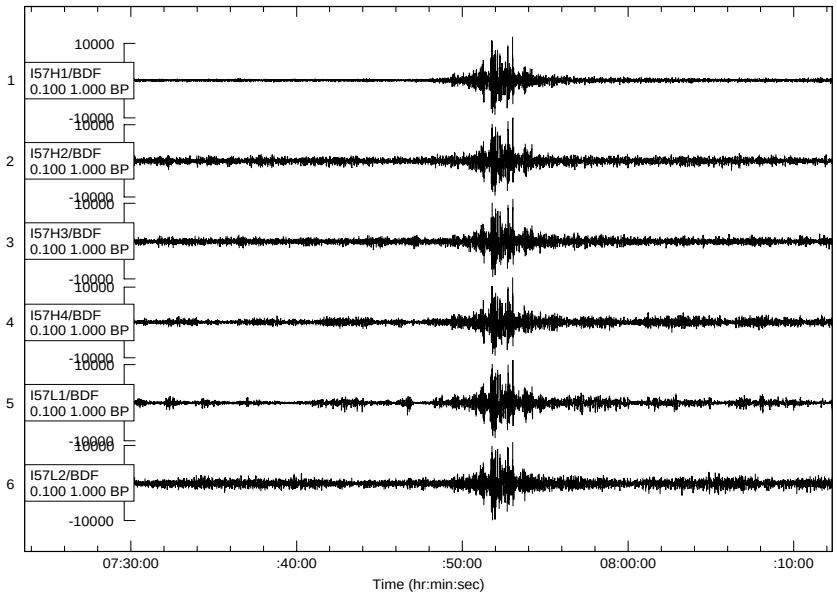

Figure 2: Signal recorded at IS57 (Pinon Flat, California) - 1781 km from the North Pacific event. No data were available for channels L3 and L4, as the station was not yet fully installed. Time is in UTC

Observed and seasonally-predicted values for the average horizontal velocity, *V,* are shown for each array in Table 8.

Table 8: Observed and predicted average horizontal velocities.

Sta	V (observed)	V (predicted)
IS10	295	273
IS26	294	292
IS57	299	265
IS59	296	262
DLIAR	300	256
NVIAR	295	270

The seasonal model clearly predicts thermospheric arrivals at all stations, except IS26. This is completely consistent with the time of year and geographical location of the stations. In the northern hemisphere, strong stratospheric winds from the east are associated with the summer months, and strong stratospheric winds from the west are associated with the winter months. April, in between, is representative of the change of seasons, with generally weak to non-existent stratospheric winds and predominant thermospheric returns. However, for this event, observed horizontal velocities indicate stratospheric arrivals at all stations. The constant velocity source locations as indicated in Table 9 show smaller mislocations and confidence ellipses, as one would expect since the constant velocity travel-times were developed preferentially favoring stratospheric signals. The azimuth and time residuals shown in Table 10 also favor the constant velocity model, as one would expect.

Table 9: 90% confidence source location results for various velocity models. Model number indicates constant velocity (in m/s) used. Semi-major axis is indicated by Smaj, Semi-minor axis is indicated by Smin.

model	lat	lon	Time	Spatial mislocation Δ (km)	Temporal mislocation ΔT (min)	Smaj (km)	Smin (km)
290	28.5	-134.3	06:09	78	-3	147	55
300	28.5	-134.3	06:13	78	1	151	55
spring	28.5	-134.5	05:55	90	17	177	61

Table 10: Azimuth and time residuals at each station

station	290 m/s		spring	
	azimuth residual (deg)	time residual (sec)	azimuth residual (deg)	time residual (sec)
IS59	0.9	47.8	0.8	10.8
IS10	-3.3	-52.2	-3.3	-111.3
NVIAR	1.4	86.7	1.3	357.0
IS57	-1.5	-9.7	-1.4	145.2
DLIAR	1.0	-131.2	1.1	-669.6

The source locations for both the 290 m/s model and seasonal velocity model are indicated in Figure 3 together with the 90% confidence ellipses.

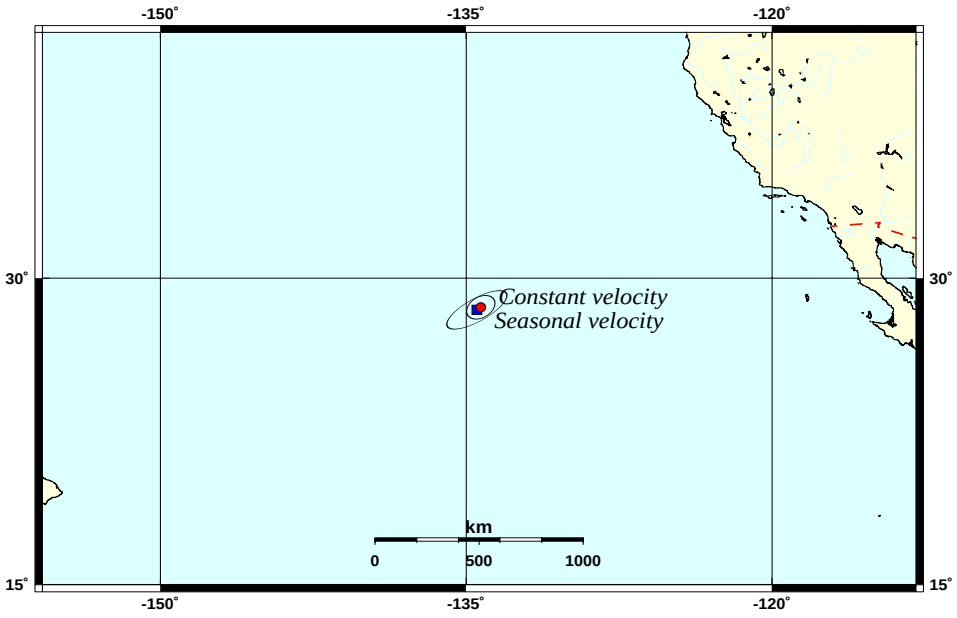

Figure 3. Source locations and 90% confidence ellipses for the 290 m/s model and seasonal velocity model.

These infrasonic source location exercises with both constant and seasonal velocity models show that the constant velocity models appear to perform better, providing smaller mislocations. This, however, should be expected since the velocity models were developed to preferentially favor stratospheric signals and knowledge of the ground-truth source information indicates stratospheric signals at each station, contrary to what one would expect based on seasonal information alone. These results strongly indicate that source location without phase identification can lead to larger than necessary mislocations and confidence ellipses.

Infrasound waveform library

Various signal characteristics were used to establish the significant nature of the Acapulco and North-Pacific events. Signal duration and dominant period are two such characteristics. To provide a better understanding of what constitutes a significant signal, and to provide a better discrimination capability, CMR has been compiling a collection of infrasonic signals that, for various reasons, are considered to be noteworthy.

The 'Infrasound Waveform Library' is composed of several data collections:

1. The Infrasound Ground Truth Database

2. The ENSCO infrasound waveform library compiled by the University of Alaska (Hutchenson, 1997).

3. A synthetic waveform library

4. The IDG-Russian Academy of Sciences/Maxwell collection of acoustic signals from Soviet Union Nuclear detonations, 1961 (Stevens, 2001)

When compiling the Infrasound Ground Truth Database, some attention is paid to establishing the most accurate source location. As such, each event is being assigned a 'GT' number that reflects the uncertainty in kilometers of the known source location. In addition, some effort is being made to trace the originator of the location information. This information is contained in a flat ascii file identified by an event number with a '.txt' extension. The infrasound waveform library is being made accessible to researchers for independent research by the CMR RDSS. A web-based interface allowing researchers access to event information and signal data has been constructed. An example, taken from the Infrasound Ground Truth Database is shown in Figure 4. In this example, one chooses the appropriate GT value for the event (Screen 1) and the source type and then submits the query. All events satisfying the query are then listed in the next screen (Screen 2).

screen 1

Source Type

ro	rocket launch
bo	bolide
ce	chemical explosion
gp	gas pipe
eq	earthquake
vo	volcano

screen 2

Figure 4. Web-based interface for the Infrasound Ground Truth Data Base.

The user has the option of selecting a tar image, where data for the event resides, or displaying an image of the waveform, or learning about the originator of the location information by selecting the 'Source' column.

An example of the sort of discrimination studies possible with the Infrasound Waveform Library is shown in Figure 5. Displayed here is the dominant period versus signal duration for various sources including bolides, historical nuclear detonations, rocket launches and earthquake generated infrasonic signals. Clustering between the large impulsive detonations and less impulsive rocket-type signals is obvious.

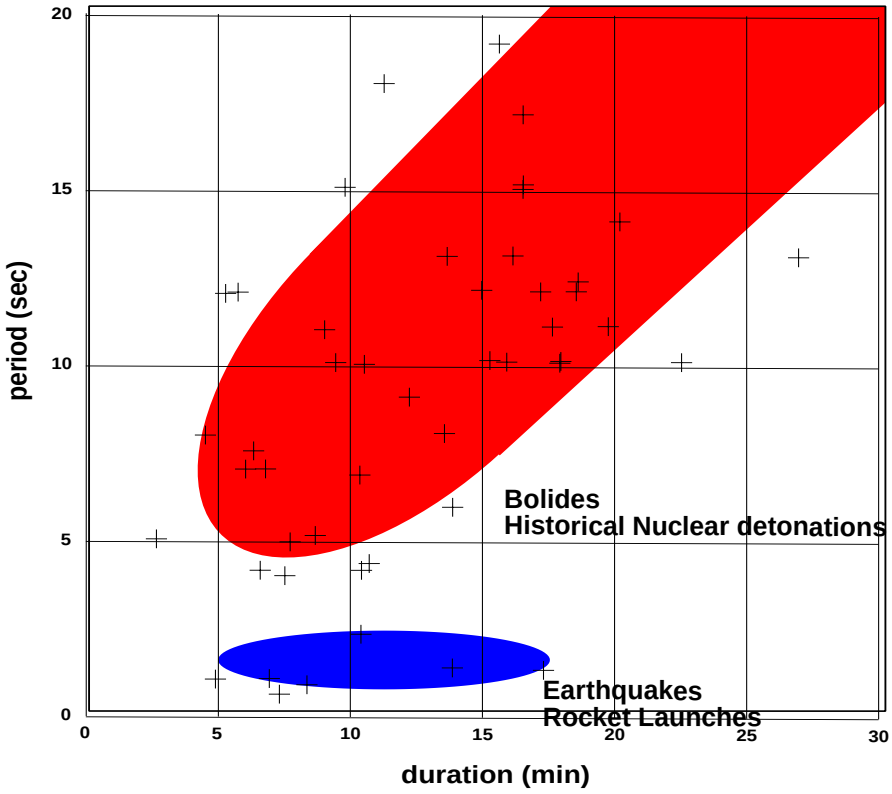

Figure 5. Signal duration versus dominant signal period for various sources. The upper shaded red area corresponds to the bolide and historical nuclear detonation signals, and the lower blue area corresponds to the earthquake and rocket launch signals.

CONCLUSIONS AND RECOMMENDATIONS

Acoustic signals from large bolides provide an excellent source of data to test and refine the detection/location capability of the developing fused seismic-infrasonic-hydroacoustic-radionuclide system at the CMR. The fact that, for these two events at least, the constant velocity models yielded a better mislocation strongly suggests that phase identification is necessary in order to refine variances on travel-time information prior to source location. The fact that stratospheric arrivals were found where thermospheric arrivals were expected suggests that it may be necessary to incorporate updated meteorological data above the seasonal information to correctly predict the likely phases. The use of updated meteorological data needs to be explored further as does the extent to which local meteorology causes azimuthal deviation and thus influences source location. It is clear from the basic discrimination exercises performed here that large explosive sources generate signals with different characteristics to those of the less impulsive, but equally long duration, rocket and earthquake generated acoustic signals. These source characterization and discrimination investigations need to continue and will be enhanced by access to the CMR RDSS Infrasound Waveform Library.

REFERENCES

Bratt, S.R, and T. C. Bache (1988), Locating Events With a Sparse Network of Regional Arrays, Bull. Seism. Soc. Am. 78, No. 2, 78-798.

Hedin, A.E. (1991), Extension of the MSIS thermosphere model in the middle and lower atmosphere", J. Geoph. Res. 96, 1159-1172.

Hedin, A.E., E.L. Fleming, A.H. Manson, F.J. Schmidlin, S.K. Avery, R.R. Clark, S.J. Franke, G.J. Fraser, T. Tsuda, F. Vial, and R.A. Vincent, (1996) Empirical wind model for the upper, middle and lower atmosphere, J. Atmos. Terr. Phys. 58, 1421-1444.

Hutchenson, K. D., (1997) Acquisition of Historical Infrasonic Data. Final Technical Report. ENSCO Inc. Contract No. F08650-95-D-0033.

Jordan, T. H, and K.A. Sverdrup.(1981), Teleseismic location techniques and their application to earthquake clusters in the South-Central Pacific. Bull. Seism. Soc. Am, 71, No 4., 1105-1130.

LANL 2001a. Los Alamos National Laboratory, Press release, May 23, 2001.

LANL 2001b, Los Alamos National Laboratory, Press release, May 23, 2001.

Stevens, J. L., (2001) Infrasound Excitation and Propagation Research (Draft Report), Contract No. DSWA01-97-C-0129.

APPLICATION OF PHYSICS-BASED UNDERWATER ACOUSTIC SIGNAL AND ARRAY-PROCESSING TECHNIQUES TO INFRASOUND-SOURCE LOCALIZATION

Gerald L. D'Spain, Michael A. H. Hedlin, John A. Orcutt, William A. Kuperman,
Catherine de Groot-Hedlin, Lewis P. Berger, and Galina L. Rovner

Scripps Institution of Oceanography

Sponsored by Defense Threat Reduction Agency

Contract No. DTRA01-00-C-0061

ABSTRACT

The purpose of this project is to apply physics-based signal and array processing techniques, recently developed in the area of underwater acoustics, to atmospheric infrasound data and co-located seismic field data. The source of the infrasound data is the newly installed International Monitoring System (IMS) infrasound station at Pinon Flat (PFO). The seismic data are being collected by the Southern California ANZA seismic network. Installation of the eight sensors that comprise the infrasound station at PFO was completed by mid April of this year. The space filters of the array (18 m for the inner centered triangle elements and 70 m for the outer centered triangle elements) also are nearly all in place. Preliminary data collected by this array contain some signals with significant spatial coherence across the array aperture. In particular, a large event with high signal-to-noise ratio was recorded on 23 April. Analyses of the arrival structure of this signal are presented in this paper. In addition, the spatial and temporal properties of the background noise in relation to the local environmental conditions are discussed. A focused experiment involving the temporary installation of additional infrasound sensors to provide larger array aperture is being planned for this summer. A description of the planned experiment is presented below.

KEY WORDS: IMS, infrasound, localization, ambient noise, spatial coherence, seismic

OBJECTIVE

The hypothesis to be tested is that advanced underwater acoustic signal and array processing techniques, with some modifications, can provide more accurate source locations and source signature estimates of low-level events of interest in the enforcement of the Comprehensive Nuclear-Test-Ban Treaty (CTBT) than conventional methods. In addition, the joint use of infrasonic and seismic data from co-located sensor systems has the potential to significantly increase phase identification and source localization capability, and reduce unwanted background noise.

Basic research questions to be addressed in this project include:

- What are the effects of range-dependent, heterogeneous, and time-variable media on infrasound propagation and source localization?
- How can the location of caustics in infrasound be exploited for source localization? Can the location of these caustics be predicted accurately with available environmental data?
- Can waveguide invariant techniques, which have proven to provide robust and simple approaches to analyses of underwater waveguide propagation, be used effectively with infrasound data?
- What are the important sources of infrasonic noise and signals in the southern California environment? How will these measurements be translated into other areas of the world?

- What acoustic propagation codes (e.g., ones based on a parabolic equation (PE) solution to the acoustic wave equation which includes the effect of winds) incorporate the important propagation physics and so can be used for effective forward modeling in the inverse problems of localizing sources and inferring atmospheric properties?

- A question related to the inverse problem is how effective are sources of opportunity, e.g., mining and quarry blasts and bolides, in calibrating the atmospheric propagation characteristics?

- What are the spatial correlation lengths of various infrasound signals and noise at frequencies of interest scientifically and operationally? How do these correlation lengths vary with topography, weather, humidity, background noise, and other environmental variables?

- How can seismic and acoustic data be used in parallel to understand infrasonic wave excitation and propagation and to localize the source? In particular, how do seismic and acoustic waves couple at the interface between the earth and atmosphere and can this coupling be used to both identify the many wave types observed and infer source location?

RESEARCH ACCOMPLISHED

Array Geometry and Description of Data

Infrasound data for this project are being collected by the newly installed International Monitoring System (IMS) station at Pinon Flat Observatory (PFO). This station is located in the high desert region 125 km northeast of San Diego, California. It is deployed on land that is part of, and adjacent to, the geophysical observatory operated by the Institute of Geophysics and Planetary Physics, University of California, San Diego (IGPP-UCSD). The PFO lies between the San Andreas and San Jacinto faults, the two most active faults in Southern California. Co-located with the IMS infrasound station is an IRIS (Incorporated Research Institutions for Seismology) 3-component broadband seismic station that is part of the auxiliary seismic network of the IMS. The sensor locations for these two stations are shown in Figure 1.

The infrasound station is composed of an array of eight MB2000 microbarometers, plotted with circles. Four of these microbarometers, plotted with the large-diameter circles labeled L1 through L4, are connected to 70-m-diameter space filters and form a centered triangle with nominal 1.4-km spacing. The other four microbarometers, the small-diameter circles labeled H1 through H4, have 18-m-diameter space filters and a 100-200 m spacing. The IRIS 3-component seismic station is plotted with a triangle.

Near the end of the installation of the infrasound station at PFO, on 23 April, 2001, (JD 113), a bolide exploded off the west coast of Baja, California (ReVelle, 2001). This event was recorded by nine infrasound stations. The estimated location of the event, obtained by triangulation, was 29.9° N, 133.9° W and its estimated origin time was 06:12:35 GMT (ReVelle, 2001). At this time, only six of the eight infrasound sensors were connected and recording data; no data were being acquired by sensors L3 and L4. The hour's worth of PFO data encompassing this event, starting at 07:30 GMT, 23 April, are the focus of this paper.

Figure 2 shows a spectrogram over this 60-min period from sensor H1. The arrivals from the bolide event, traveling over an epicentral distance of about 1700 km, contain broadband energy that exceeds 2 Hz. The spectral peak occurs near 0.3 Hz. The effective group velocity of the first arrivals over the source-to-receiver path is about 290 m/sec, given the reported epicentral distance and origin time. This value is consistent with propagation in the stratospheric waveguide (e.g., D'Spain, Kuperman, Orcutt, and Hedlin, 2000). The event lasts for 15 min or so with the coda evolving to lower frequency with time. The time series from all six recording infrasound sensors over a 6-min period starting before the first arrival are shown in Figure 3. The arrivals are very coherent across the aperture of the array. Note also that wind-generated contamination is quite low during this period of time due to the early morning hour (local PDT is 7 hours behind GMT) of the event's occurrence.

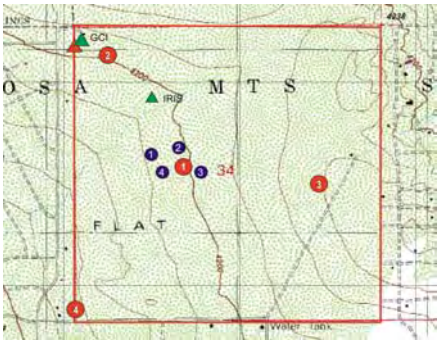

Figure 1. Map showing the geometry of the newly installed IMS infrasound station at Pinon Flat Observatory along with the IRIS 3-component broadband station. The eight microbarometer locations are plotted with circles and labeled L1-L4 (70 meter spaced filters) and H1-H4 (18 meter space filters), and the IRIS station is plotted with a triangle.

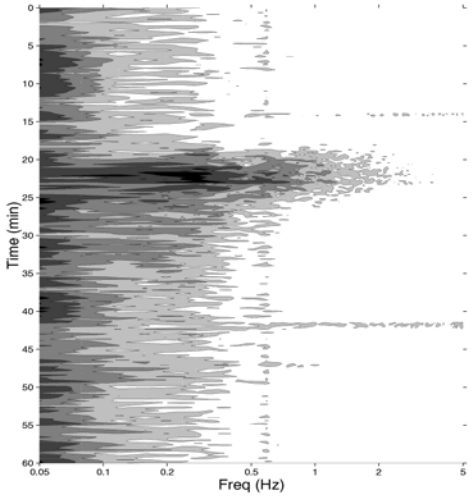

Figure 2. 60-minute spectrogram starting at 07:30 GMT, 23 April, 2001, over the 0.05 to 5 Hz band from data collected by microbarometer H1.

Adaptive Frequency/Wavenumber Processing

Given the estimated epicentral location of the bolide event, its back azimuth from PFO is 261°, Figure 1 shows that, since L3 and L4 were not yet operational at the time of the event, the resulting 6-element array has very little aperture in the radial direction. Therefore, only rough estimates of the wavenumber content of the bolide arrivals can be expected to be obtained. However, given the high signal-to-noise ratio of the arrivals, some useful results may come from data-adaptive beamforming techniques. This section is devoted to presentation of the preliminary results of applying white-noise-constrained adaptive plane-wave beamforming (Gramann, 1992; Cox, Zeskind, and Owen, 1987) to the arrivals.

In the estimate of each data cross-spectral matrix, the time series was divided into consecutive, non-overlapping, 45-sec segments. An fft length of 128 points was used with a 50 percent overlap, allowing 13 realizations within the 45-sec segment to be averaged in making the estimate. Since a Kaiser-Bessel window with an alpha of 2.5 was used to window the time series prior to the fft, the resulting statistically independent realizations in the estimate is 12.7. Several white-noise-constrained values were used, starting from 10*log(N) where N is the number of array elements (equivalent to conventional beamforming). The value used in the results to be presented is 6 dB down from 10*log(N).

The 2-D array frequency/wavenumber processing output is a function four variables, i.e., frequency, time, wavenumber (or slowness), and azimuth. Figure 4 presents a plot of frequency vs wavenumber for a time period at the beginning of the arrival sequence and for an azimuth of 74°, i.e., a back azimuth of 254° which is the direction most of the arriving energy is propagating from (compared to a back azimuth to the estimated location of 261°). The output energy falls along a line passing through the origin with a slope of nearly 330 m/sec. This energy possibly followed ray paths that turn in the stratosphere at 40- to 50-km altitude. The other lines of energy at multiples of approximately 0.04 rad/m are the result of the sidelobe (nearly grating lobe) character of the array response.

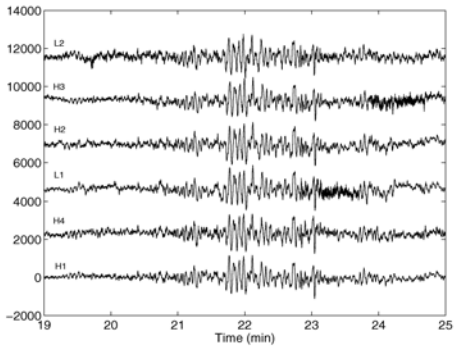

Figure 3.

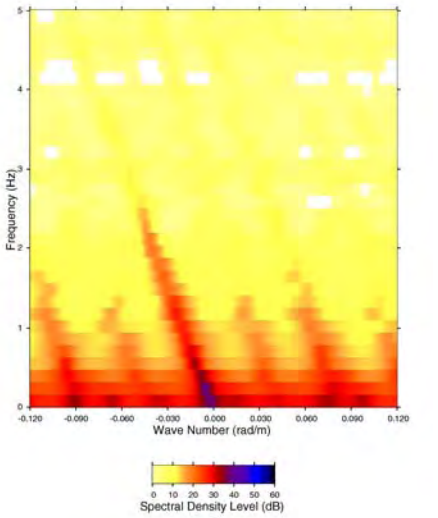

Figure 4. Frequency vs wavenumber.

The 3-panel plot in Figure 5 shows the adaptive beamforming output as a function of time and phase slowness over a 15-min period starting at 07:48 GMT for the three lowest center frequencies of 0.156 Hz, 0.313 Hz, and 0.469 Hz. The middle panel contains a slight hint of an evolution from lower to higher slowness values (faster to slower phase velocity) over the 8-min period of the main arrival. However, a more significant departure from the expected arrival structure is shown in Fig. 5c where the energy in the 0.469 Hz bin arrives at distinctly smaller slowness values than at lower frequencies. Work is continuing on this phenomenon to understand the physical cause of this effect after verifying that it is not the result of bias associated with the adaptive beamforming process.

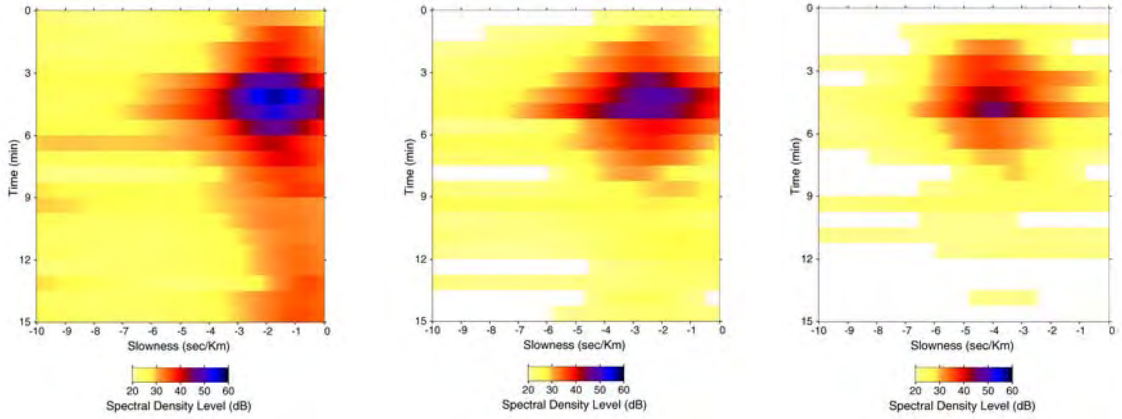

(a) **(b)** **(c)**

Figure 5. The white-noise-constrained adaptive plane wave beamforming output as a function of time and slowness for a fixed azimuth of 74°. The left panel is for a center frequency of 0.156 Hz, the center panel for 0.313 Hz, and the right panel for 0.469 Hz. The 15-min period of the plots starts at 07:48 GMT.

Vector Intensity

Vector acoustic intensity techniques can be applied to the analysis of the data collected by the PFO infrasound array. They are most applicable to the study of fields created by the sum of a large number of contributing sources such as the ambient background field. This section describes the preliminary work done in this area.

Vector intensity is the magnitude and direction of acoustic energy flux. It equals the product of acoustic pressure and acoustic particle velocity. Two types of acoustic intensity exist in a sound field. The active component measures the net flux of acoustic energy through the medium (i.e., the propagating part), whereas the reactive component is a measure of the energy flow required to support the spatial structure of the field (i.e., the standing wave part). In acoustic waveguides, the reactive component typically is significant only in the cross-waveguide direction; i.e., the direction perpendicular to the boundaries and parallel to the predominant direction of spatial variability of the waveguide properties. In the plane parallel to the waveguide boundaries, e.g., at the earth-air interface in atmospheric acoustics, only the active intensity typically is important.

The development of fft-based methods for the estimation of active intensity using data from two closely spaced microphones (e.g., Chung, 1978) led to the rapid growth of vector intensity techniques in air acoustics. The technique originally proposed by Chung (1978) is the one employed here. The component of the vector active intensity in the direction of the separation between the pressure sensors, $I_r(\omega)$, is proportional to the imaginary part of the cross spectrum between the time series recorded by the two microphones, i.e.,

$$I_r(\omega) = \frac{1}{2\rho\Delta r\,\omega}\,\mathrm{Im}\left\{S_{12}(\omega)\right\} \qquad (1)$$

The ambient air density is ρ and Δr is the separation between microphones.

The expression above is valid for frequencies such that $k\Delta r < 1$, where k is the acoustic wavenumber. At the other end of the spectrum, phase and amplitude mismatch between the microphone responses limit the usefulness of this approach. Examination of Figure 1 shows that the separation between H1 and H2 is nearly parallel to the radial direction towards the bolide and the separation between H1 and H4 is nearly transverse to this direction. The distance between H1 and H2 is such that the expression for the active intensity is valid for frequencies less than 0.36 Hz and between H1 and H4, it is valid below 0.48 Hz.

Figire 7 shows the amplitude and sign of the active intensity along the line between H1 and H2 (left panel) and between H1 and H4 (right panel). Positive values represent energy flux from H1 to H2, and from H1 to H4, respectively. The spectrograms are plotted only up to the maximum frequency for which Eq. (1) is valid. The bolide arrivals create large flux in the direction from H1 towards H2 and significantly less along the H1-H4 direction, as expected. In fact, the bolide event can be used as a calibration event to correct for phase mismatch between the three microbarometers. The large energy flow around 0.07 Hz is of the same sign and approximately the same amplitude in both plots, indicating flux from the northwest to the southeast.

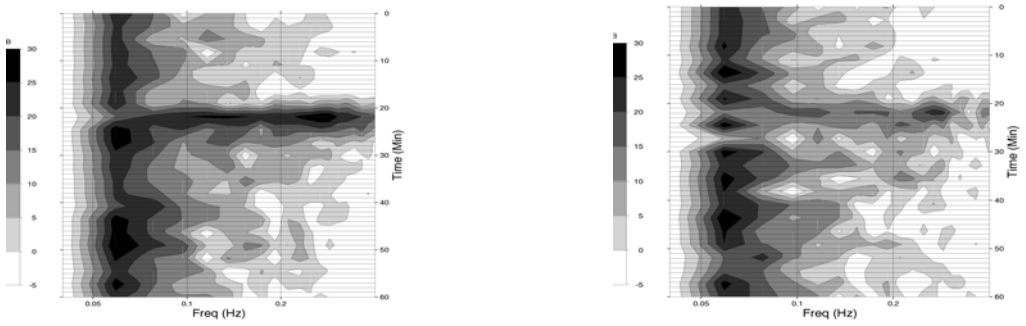

Figure 6. Coherence squared versus frequency and time over the 60-min period starting a 07:30 GMT between microbarometer L2 and two seismometer components of the IRIS station. The left plot is for the vertical component and the right plot is for the east-west component.

Infrasonic/Seismic Coupling

The hour's worth of data starting at 07:30 GMT, 23 April (JD 113), were obtained from the IRIS 3-component seismic station at PFO. The location of this sensor system is about half-way between the microbarometer L2 and the remaining cluster of microbarometers about L1, along a line approximately transverse to the direction towards the bolide; refer to Figure 1. As part of the preliminary analysis of these data, coherence squared estimates between each of the microbarometers and the three seismic components over the hour period have been calculated. A sufficient number of statistically independent realizations were included in the estimates so that the true population coherence squared is greater than zero at the 90 percent confidence level if the estimate exceeds 0.21. The minimum value in the two panels in Figure 6 is set to this 90 percent threshold level of 0.21.

Figure 6a shows the coherence squared between the time series from microbarometer L2 and the vertical seismometer component time series, and Fig. 6b shows the coherence squared between L2 and the east-west seismometer component. The location of L2 is 328 m from the IRIS station. The coherence squared between the vertical component and L2 is quite high in the 1-3 Hz band at the time of the bolide arrivals. It is also statistically greater than zero between L2 and the east-west component (re Figure 6b) over the 1.5- to 2.5-Hz band at this time. The east-west component is nearly aligned along the radial direction to the bolide source; the coherence squared between L2 and the north-south component show no statistically significant values associated with the bolide arrivals. Surprisingly, the high coherence squared estimates below 0.5 Hz in both panels, probably associated with microseism/microbarom energy, disappears at the time of arrival of the bolide signals.

The coherence squared estimates for the bolide arrivals in Figure 6a are higher than for any other seismometer/microbarometer pair. However, those between the vertical component and all other microbarometers still are statistically greater than zero. In contrast, no statistically significant coherence for the bolide arrivals occurred between the horizontal seismometer components and the microbarometers other than the pair shown in Fig. 6b. Also, the coherence between the vertical and east-west seismometer components is significant, but the values for the other two seismometer pairs involving the north-south component are not.

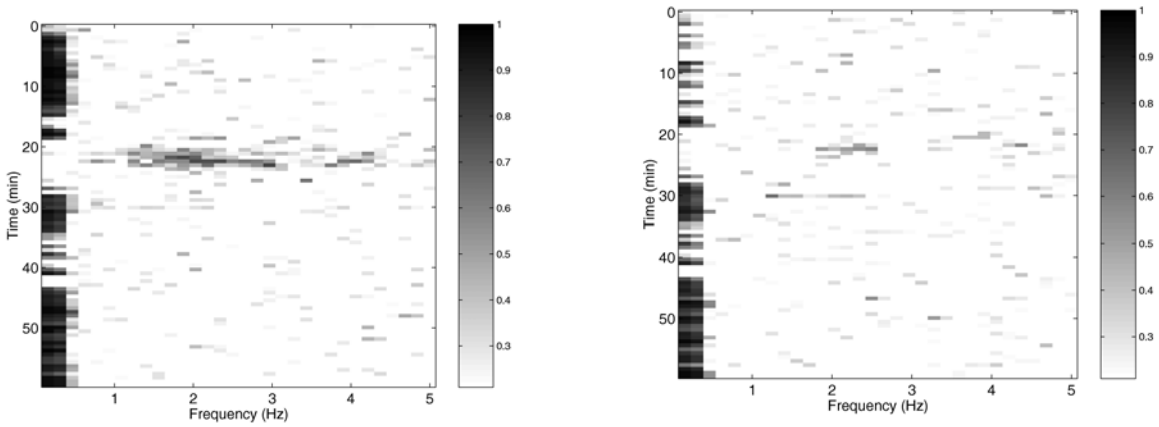

Figure 7. The amplitude and sign of the active intensity as a function of frequency and time over the 60-min period starting at 07:30 GMT, 23 April. The frequency band extends up to the maximum limit of the validity of Eq. (1) in the text. The left plot is for the active intensity component along the line between H1 and H2, and the right plot is the active intensity along the line between H1 and H4.

Relative Dispersion Ranging

One of the approaches that will be studied with the data to be collected in a focused experiment at PFO is the estimation of the range to a broadband source using the relative change in arrival times of multipath arrivals along the propagation path. The ideas behind this technique now will be described. The extremely limited aperture of the partially installed PFO infrasound array in the direction along the propagation path prevent this technique from being applied to the data from the bolide event.

The concept of using relative dispersion across an array aperture to obtain an estimate of source range can be illustrated with a simple model of a source impulse in time that excites two wave types with different group velocities. Assuming initially that each wave type is non-dispersive and arrives with identical amplitude, *A*, then the received signal at range *r* can be modeled as an even impulse pair:

$$x(t,r) = \frac{A}{2}\delta\left[\frac{t - t_c(r)}{\tau(r)} + \frac{1}{2}\right] + \frac{A}{2}\delta\left[\frac{t - t_c(r)}{\tau(r)} - \frac{1}{2}\right] \qquad (2)$$

The quantity, $t_c(r)=r\overline{S}_g$, is the average of the times of arrival of the two pulses, where $\overline{S}_g$ is the average group velocity of the two pulses. The quantity, $\tau(r)$, the time difference between the two arrivals, is equal to:

$$\tau(r) = r\Delta S_g \qquad (3)$$

and ΔS_g is the difference in group slownesses. The range to the source can be estimated from Eq. (3), given that prior knowledge of the environment (i.e., the difference in group slownesses) is available, as done in estimating the range to an earthquake by matching travel time curves to seismograms. In ocean acoustics, this approach recently has been applied to single element spectrograms from very long range propagation experiments (Kuperman, D'Spain, Heaney, 2001).

At range $r+\Delta r$, the time delay between the two pulses, $\tau+\Delta\tau$ can be determined by applying Eq. (3). Combining the two equations to eliminate ΔS_g (assuming it remains constant over Δr)gives:

$$\frac{\Delta r}{r} = \frac{\Delta\tau}{\tau}$$

This equation shows that measurement of the change in arrival times of the two pulses, $\Delta\tau$, between two receivers can be used to obtain source range information without apparently requiring *a priori* environmental information. That is, using the evolution with range of the received signal properties in Eq. (4) requires less environmental information than using the properties of the signal at a single point. The actual source range is not estimated, but rather a combination of source range and source bearing since the quantity, Δr is, determined by the separation between the two receivers, q, and the direction towards the source, θ, i.e., $\Delta r = q\ cos\ (\theta)$.

Similarly, this information can be obtained in the frequency domain, i.e., the Fourier transform of the received signal in Eq. (2) yields

$$\begin{aligned} X(\omega, r) &= (A\,\tau)\,\exp[-i\,\omega t_c]\,\cos(\tau\omega/2) \\ &= (Ar\,\Delta S_g)\,\exp[-i\,\omega r\bar{S}_g]\,\cos(\Delta S_g\,\omega r/2) \end{aligned} \tag{5}$$

The phase terms in this expression are of two types, an imaginary term containing the average of the pulse travel times, t_c, and a second phase term involving τ, the received signal duration. Complex phase terms, arising from delays/advances in the time domain (re the shift theorem in Fourier analysis), are lost in the calculation of the autospectrum:

$$S_x(\omega, r) = \frac{1}{2}[A\,\tau(r)]^2\cos^2(\tau(r)\omega/2) \tag{6}$$

However, the term involving the *difference* in travel times, τ, is retained. Simulations of the spectra in the range/frequency plane for this simple two-pulse model display a set of striations that tend from higher to lower frequencies as the source/receiver range increases. The condition for following along one of these striations, i.e., keeping the phase term in Eq. (6), $\Phi \equiv \tau(r)\omega/2$, stationary, is:

$$\Delta\Phi = 0 = \frac{\partial\Phi}{\partial\tau}\Delta\tau + \frac{\partial\Phi}{\partial\omega}\Delta\omega = \frac{\partial\Phi}{\partial\tau}\frac{\partial\tau}{\partial r}\Delta r + \frac{\partial\Phi}{\partial\omega}\Delta\omega \tag{7}$$

resulting in:

$$\frac{\Delta\tau}{\tau} = -\frac{\Delta\omega}{\omega} = \frac{\Delta r}{r} \tag{8}$$

Therefore, the behavior of the striation pattern in the range/frequency plane contains the same information on source location as the changes in pulse spreading in the time domain, as would be expected from the similarity theorem in Fourier analysis. This information is available by phase incoherent processing since it is obtainable from the spectra of the received signals rather than just their Fourier transforms. The negative sign in Eq. (8) indicates that the frequency content of the striations evolves to lower frequency with increasing range. The two-pulse model can be extended to a set of N pulses each traveling with its own group velocity. Simulations show that, although the widths and relative amplitudes of the individual striations change, the slopes of the striations in the range/frequency plane in this extended case remain unchanged. The reason is that the relative spreading/compression of the arriving signal with change in range remains the same.

For source time functions, $s(t)$, that are finite in duration, the received signal is a convolution of $s(t)$ with Eq. (2), and the resulting autospectrum is the product of the autospectrum of $s(t)$ with Eq. (6). Therefore, the results just presented are still valid as long as the character of the source autospectrum (e.g., its bandwidth and the

smoothness of its variation with frequency) allows the striation pattern in the received spectra to remain visible. This requirement is equivalent to requiring that the doublet arrival structure still be visible in the time domain so that both $\Delta\tau$ and τ in Eq. (4) can be measured.

The constant in Eq. (8) relating a fractional change in frequency of the striation pattern to a fractional change in range is -1. This value is a consequence of the fact that the group velocities of the two pulses were assumed to be independent of range and frequency. However, in those cases where the pulses are dispersive so that the time difference between their arrivals is dependent upon frequency as well as range, then application of stationary phase gives

$$\frac{\Delta r}{r} = -\left[1 + \frac{\partial\tau}{\partial\omega} \Big/ \frac{\tau}{\omega}\right] \frac{\Delta\omega}{\omega} \tag{9}$$

Information on the environment, as represented by the term in brackets in Eq. (9) that measures the change in signal spreading (duration) with frequency, now is required to obtain the source range information. The term in brackets is a constant, $1+\gamma$ independent of τ and ω given that $\frac{\partial\tau}{\partial\omega} \Big/ \frac{\tau}{\omega} = \gamma$.

The solution to this differential equation indicates that the required functional dependence of $\tau(\omega)$ with ω is of the form ω^{γ}. From Eq. (3), the fractional change of τ with frequency is the same as the fractional change in ΔS_g with frequency. D'Spain and Kuperman (1999) show that ΔS_g is proportional to frequency raised to the $-(1+1/\beta)$ power, where $1/\beta$ is the waveguide invariant. Therefore,

$$\frac{\partial\tau}{\partial\omega} \Big/ \frac{\tau}{\omega} = -(1+1/\beta) = \gamma \tag{10}$$

Plugging this result into Eq. (9) gives the expression for the range/frequency dependence of striation patterns in single element spectrograms (Brekhovskikh and Lysanov, 1982; D'Spain and Kuperman, 1999).

In summary, the information on source range obtained from temporal broadening (or compression) of a multi-component arrival as range increases is equivalent to that obtained by examination of the striation pattern of the corresponding autospectra in the range/frequency plane. The behavior of the striation pattern is derived by a stationary phase analysis of the appropriate phase term. The relevant information is extractable by phase incoherent processing. If phase coherent processing between stations also can be done, then range and bearing can be estimated with data from just two stations.

CONCLUSIONS AND RECOMMENDATIONS

The 23 April, 2001, bolide over the northeast Pacific Ocean has provided an interesting event for a first look at the data from the newly installed IMS infrasound station at PFO. The effective group velocity and the predominant phase velocity across the array aperture determined by white-noise-constrained adaptive beamforming techniques is consistent with propagation in the stratospheric waveguide. However, the array aperture along the direction towards the source was limited because two of the eight microbarometers, both part of the outer centered triangle, did not record the event. Phase identification and source localization will certainly be aided by data from these sensors in future events. In particular, a formulation for estimating the range to an impulsive event using relative dispersion across the array aperture is presented, but cannot be effectively applied to the 23 April PFO recordings because of this limitation in aperture. Vector intensity techniques can be used with the PFO data at frequencies below 0.3 Hz and show net energy flux from the bolide event in the expected direction. Finally, the bolide arrivals create statistically significant coherence between the vertical component of the IRIS seismic station at PFO (an auxiliary IMS seismic station) and each of the six recording infrasound sensors. This coherence exists even though the IRIS station is over 300 m from the nearest microbarometer.

Preparations for a 2-week focused experiment in September 2001 at the Pinon Flat Observatory presently are underway. Four MB2000 infrasound sensors with space filters will be installed temporarily at four ANZA seismic station sites to create large horizontal aperture. These temporary installations will take place the first week of September with continuous data recording beginning by the 10th of September. This recording period was selected to encompass four planned rocket launches from Vandenberg Air Force Base; 2 Minuteman III launches, a Delta II rocket, and a Titan IV B launch. These events will provide known infrasound signals for focused study (e.g., McLaughlin, Gault, and Brown, 2000).

REFERENCES

Brekhovskikh, L. M. and Y. P. Lysanov (1991), *Fundamentals of Ocean Acoustics*, 2nd ed.New York: Springer-Verlag, 140-145.

Chung, J. Y. (1978), Cross-spectral method of measuring acoustic intensity without error caused by instrument phase mismatch, *J.Acoust. Soc. Am.* 64, 6, 1613-1616.

Cox, H., R. M. Zeskind, and M. M. Owen (1987), Robust Adaptive Beamforming, *IEEE Transactions of Acoustics, Speech and Signal Processing* ASSP-35 (10).

D'Spain, G. L., W. A. Kuperman, J. A. Orcutt, and M. A. H. Hedlin (2000), Long Range Localization of Impulsive Sources in the Atmosphere and Ocean from Focus Regions in Single Element Spectrograms, Proc. of 22nd Annual Seismic Research Symposium: Technol. for Monitoring the Comprehensive Nuclear-Test-Ban Treaty.

D'Spain, G. L. and W. A. Kuperman (1999), Application of Waveguide Invariants to Analysis of Spectrograms from Shallow Water Environments that Vary in Range and Azimuth, *J. Acoust. Soc.Am.* 106, 5, 2454-2468.

Gramann, R. A. (1992), ABF Algorithms Implemented at ARL-UT,ARL Tech. Letter ARL-TL-EV-92-31, Applied Research Laboratories, The University of Texas at Austin, Austin, TX.

Kuperman, W. A., G. L. D'Spain, and K. D. Heaney (2001), Long Range Source Localization from Single Hydrophone Spectrograms, *J. Acoust. Soc. Am.* 109, 5 pt. 1, 1935-1943.

McLaughlin, K. L., A. Gault, and D. J. Brown (2000),Infrasound Detection of Rocket Launches, Proc. of 22nd Annual Seismic Research Symposium: Technol. for Monitoring the Comprehensive Nuclear Test-Ban Treaty, 219-230.

ReVelle, D. O. (2001), Global Infrasonic Monitoring of Large Meteoroids, *J. Acoust. Soc. Am.*, 109, 5, 2371.

INFRASONIC SIGNALS DETECTED BY THE KONA ARRAY, HAWAII

Milton A. Garcés and Claus H. Hetzer

University of Hawaii, Manoa

Sponsored by Defense Threat Reduction Agency

Contract No. DTRA01-00-C0-0106

ABSTRACT

International Monitoring System (IMS) infrasound array IS59, also known as the KONA array, has been operating since May 25, 2000, and is scheduled for certification into the IMS in September of 2001. A catalog of observed infrasound signals is routinely produced for IS59 and includes Phase, Date and Time UT, Azimuth, Slowness, and Remark fields, as well as Amplitude in millipascals after February 20, 2001. Selected events have been characterized and tentative source identifications made through a combination of field inspections, collaborations with government personnel or agents, and improvements in data analysis. Most of the events have been observed only at KONA, but some have been recorded by two or more arrays.

Sources for infrasonic events recorded at KONA include aircraft noise from nearby Keahole International Airport, surf impact, earthquakes, offshore activities, severe weather, and meteors. Other unidentified local signals are also catalogued. Phase names based on source identification have been devised to aid in classification. From June 19, 2000, to July 2, 2001, 1280 events were recorded, of which 0.31% were confirmed to be telesonic. Approximately 31% were surf-related, 19% associated with weather, and 16% associated with aircraft. More than 59% of recorded events were identified as local.

Various useful analysis tools and techniques have been acquired or developed by Infrasound Laboratory (ISLA) personnel include modified versions of Sandia National Laboratories' MatSeis and Los Alamos National Laboratory's InfraTool, which determines instantaneous azimuth, trace velocity and correlation, as well as a simple STA/LTA-based automatic detector and the Tau-P software of Garcés et al. (1998). Currently the STA/LTA detector is used to detect more impulsive events and InfraTool to detect longer-duration arrivals, and traditional FK analysis as implemented within MatSeis is used to determine back azimuth and trace slowness.

KEY WORDS: infrasound, IS59, KONA

OBJECTIVE

The primary objective of assembling the KONA events catalog is to identify trends in the background infrasonic field in Hawaii. Knowledge and recognition of recurrent events allows the analyst to efficiently screen incoming data and discriminate trivial events from high-priority detections. The establishment of a library of identified arrivals is the first step toward automated identification of suspect events. The catalog also allows events to be selected for research on sound propagation and source identification. Over 1200 events have been recorded and assigned phase names based on tentative source identification.

RESEARCH ACCOMPLISHED

Analysis Techniques

Most of the tools currently in use work with the Sandia National Laboratories' (SNL's) MatSeis software platform. ISLA personnel have modified and customized some of the functions of MatSeis in order to optimize its use for infrasonic analysis, and renamed the result MatSound. MatSound is currently the main analysis tool used at ISLA, as it offers a graphical user interface (GUI) to many powerful functions and is easily extendable to new tools.

For local signal detection, a waveform record is passed through a Butterworth zero-phase 2nd order high-pass filter above 1 Hz to remove microbarom contamination, and the resulting traces are examined for arrivals. Any arrivals seen by the analyst are subjected to FK analysis to determine arrival azimuth, which is used in conjunction with waveform characteristics such as onset quality, duration, and amplitude to identify local phase. A simple STA/LTA-based detector has been developed to automatically identify local arrivals. The detector first computes a 3-second/27-second STA/LTA value for a 4-hour CSS database record, then scans through the result using a 20-second window with 75% overlap. If an STA/LTA value greater than a preset threshold value, currently 1.8, is detected in that window on at least three of the four channels, the average normalized cross-correlation coefficient of the channels is calculated. If the average coefficient is greater than another preset threshold (currently 0.4), the window is marked as an arrival and flagged for analyst attention. FK analysis is performed on the marked window, and the event is automatically assigned a preliminary azimuth and slowness. The detector takes approximately 8-20 minutes (depending on CPU load) to analyze a 4-hour data segment. The false alarm rate of the detector is very low due to the coherence requirements, but the detector is less sensitive to long emergent arrivals, probably because STA/LTA values for emergent events tend to be lower than those of short-duration events with impulsive onsets.

Long-duration, emergent arrivals are identified using the Los Alamos National Laboratory's (LANL) InfraTool program (Figure 1), which has been integrated into the MatSound toolbox. InfraTool steps through array data using a window of adjustable length and overlap and computes an instantaneous azimuth, trace velocity and correlation coefficient for each segment. ISLA personnel have modified the original InfraTool so that slowness is displayed instead of velocity, and an additional display window has been added for the F-statistic. The InfraTool controls have been moved to a separate panel (Figure 2) to facilitate addition of buttons and controls for new tools as they are developed. The original InfraTool allowed a time-window to be selected within the azimuth axes and a mean value computed; functionality has been added to place similar windows in the slowness and F-statistic axes as well, and the windows can be moved simultaneously. The InfraTool control panel can be used to zoom the main MatSound display to the selected time-window, to initiate an FK analysis, and to mark an arrival. Long-duration arrivals such as ITS (see below) are indicated by periods of constant azimuth and slowness along with increased correlation and F-statistic. The InfraTool detector has performed well even in cases where the signal-to-noise ratio is close to unity.

Once an arrival has been identified and cataloged, the Tau-P software of Garcés et al. (1998) can be used to begin epicentral location. The Tau-P code calculates range, travel-time, and several other travel-path parameters for the first infrasonic skip based on meteorological data (for example Figure 3). The original code has been modified to not only compute parameters for the entire slowness plane but to separate out arrival areas within the slowness plane that correspond to different turning heights and therefore to different infrasonic phases. The code can then be used to help calculate origin times for arrivals detected on various arrays, thus allowing an over-all origin time to be estimated by minimizing time residuals (Garcés et al., this Proceedings).

Over the time period from June 19, 2000, to July 2, 2001, over one thousand infrasonic events have been identified at KONA. Each arrival is recorded as an entry in a CSS .arrival database. Sources have been identified through a combination of field inspection, cooperation with government sources, and improvements in data analysis. At present the main sources of these events are severe weather, surf, and unidentified offshore activities. A more detailed discussion of each phase follows.

Aircraft Signals: "IA"

Aircraft signals are generally extended, emergent events with signal-to-noise ratio (SNR) of ~2-4 and durations between 30 and 120 seconds. They are identified based on these waveform characteristics and a back azimuth corresponding to Keahole International Airport. Back azimuth is variable due to different take-off and landing approach paths, but averages to 316.49°. These signals can be confused with certain IN events (see below), which are often detected at similar azimuths. Generally IA events can be recognized by a smoother amplitude taper (Figure 4). During the time period under consideration, 204 signals were identified as IA.

Surf Signals: "IK" and "IWS"

Surf signals are generally sets of impulsive events with variable SNR and single-cycle duration (Figure 5). The frequency content of these signals is between 2 and 5 Hz. They tend to be present in groups of pulses and can occur for hours at a time. Early IK detections were recorded at the analyst's discretion; currently surf signals are recorded only if marked by the STA/LTA detector, and only the first such signal from each azimuth is actually recorded. The number of signals marked by the detector is indicated in the comment field of the CSS database. Two phases are currently used for identification of surf signals, and the distinction is based on back azimuth. The most consistent surf signal comes from Kualanui and is characterized by a back azimuth of about 232.7°. Over the course of the analysis 263 IK signals have been identified.

The IWS phase (also previously called INW) is used to indicate apparent surf noise from any other direction, but is seen most often from a back azimuth of about 320 and may be produced by surf in Makako Bay. At present 139 IWS signals have been identified.

Weather Signals: "IM"

IM signals are generally found within the microbarom passband of 0.1-0.4 Hz. Comparison of recorded back azimuths with regional wave-height diagrams generated by the U.S. Navy's Fleet Numerical Meteorological and Oceanography Center suggests that the signals are generated by strong weather patterns that can be several thousand kilometers away. Occasional inability to correlate strong weather with IM signals suggests that local weather conditions can overwhelm distant signals. FK analysis of these events has been used to track nearby tropical storms. Because the signals are generated by regional weather patterns, there is no typical back azimuth. Over the course of the analysis 242 IM signals have been identified.

Earthquake Signals: "IEP"

Although KONA is an infrasound (not a seismic) array, several local earthquakes have been recorded by the instrument. IEP signals are characterized by very low slowness and the presence of two distinct impulsive arrivals (Figure 6). Although several researchers (e.g. Young & Greene, 1982; Cook, 1971) have shown that surface waves can be coupled into the atmosphere, the arrival time and recognition of both P-wave and S-wave arrivals suggests that in these cases the microphone is sensing ground vibration from the incident seismic body waves. Deep (>20-30 km) earthquakes appear to be preferentially recorded, probably because P-waves from these earthquakes tend to displace the sensor vertically. The array has detected 14 local earthquakes, with a magnitude detection threshold of $M_D = 2.7$.

Waveform appearance in Figure 6 varies significantly across the array due to differences in wind-noise-reducing filter configuration. When this earthquake occurred, sites H1 and H3 were equipped with PVC wind-noise-reducing filters, while H2 and H4 were equipped with porous-hose wind-noise-reducing filters. The extra mass of the PVC filters in contact with the ground improves body wave coupling into the instrument and tends to increase signal-to-noise for the earthquakes on H1 and H3. Also, coupling at H3 is more efficient than at H1 because the filter assembly at H3 is more firmly attached to the ground. The diameter of the H1 filter system is 18m, whereas the diameter of the H3 system is 12 m.

Offshore Signals: "IN"

These signals are normally characterized by slightly lower slowness and a dispersed appearance, and can range in appearance between sharp, impulsive arrivals and long emergent arrivals (Figure 7). The impulsive IN events can be mistaken for surf but are generally higher amplitude and more irregular. Emergent IN events can resemble airplane signatures but tend to arrive from azimuths not associated with local airports and are less smooth; some resemble a series of pulses that have been broadened by propagation. The frequency band is variable, and may extend from 0.5 Hz to 6 Hz. Although 177 IN events have been marked, specific activities that produce these signals remain unidentified.

Pohakuloa Training Area Signals: "IP"

IP signals generally arrive from a back azimuth between 30° and 90°, encompassing an area occupied by the Pohakuloa Training Area. Typical IP events feature a series of sharp, impulsive arrivals at irregular intervals, but some bear a resemblance to IA signals. ISLA has identified 138 signals as IP.

Telesonic Signals: "ITS"

Telesonic signal identifications are based on long durations (generally >2 minutes), generally low SNR (< 3), possible dispersion, and confirmation from other stations. Because of these characteristics, they do not lend themselves to time-domain detection and can be difficult to detect by simple visual examination. A modified version of LANL's InfraTool has proven efficient for detecting these signals, even in cases of SNR close to unity. Four ITS events have been selected. At least two ITS events have been identified as bolides (Figure 9); sources of the other events remain unconfirmed but it seems most likely that they too are related to bolide events.

Unidentified Local Signals: "IW"

This category is a general term for local events that cannot be easily associated with any of the above sources. Often IW events resemble IA signals but arrive from azimuths not associated with an airport, or resemble isolated surf events from azimuths along which the nearest coastline is 50 or more kilometers away and therefore an unlikely source. As analysis techniques improve, designation of signals as IW has become less frequent, but is still necessary. Thus far, 99 events have been designated IW.

CONCLUSIONS AND RECOMMENDATIONS

The KONA Event Catalog is the result of extensive work and has prompted the development of several useful software tools. Analysis techniques at ISLA have evolved and improved over time. A basic understanding of the background infrasonic field of the central Pacific Ocean and the Kona area has been accomplished and the characteristics of many common signals have been determined. This information is essential for the development of automatic, real-time event detection and identification algorithms.

REFERENCES

Cook, R.K. (1971), Infrasound radiated during the Montana Earthquake of 1959 August 18, Geophysical Journal of the Royal Astronomical Society, v. 26, p. 191-198.

Garcés, M.A., R.A. Hansen & K.G. Lindquist (1998), Traveltimes for infrasonic waves propagating in a stratified atmosphere, Geophysical Journal International, v. 135, p. 255-263.

Young, J.M. & G.E. Greene (1982), Anomalous infrasound generated by the Alaskan earthquake of 28 March 1964, Journal of the Acoustical Society of America, v. 71, p. 334-339.

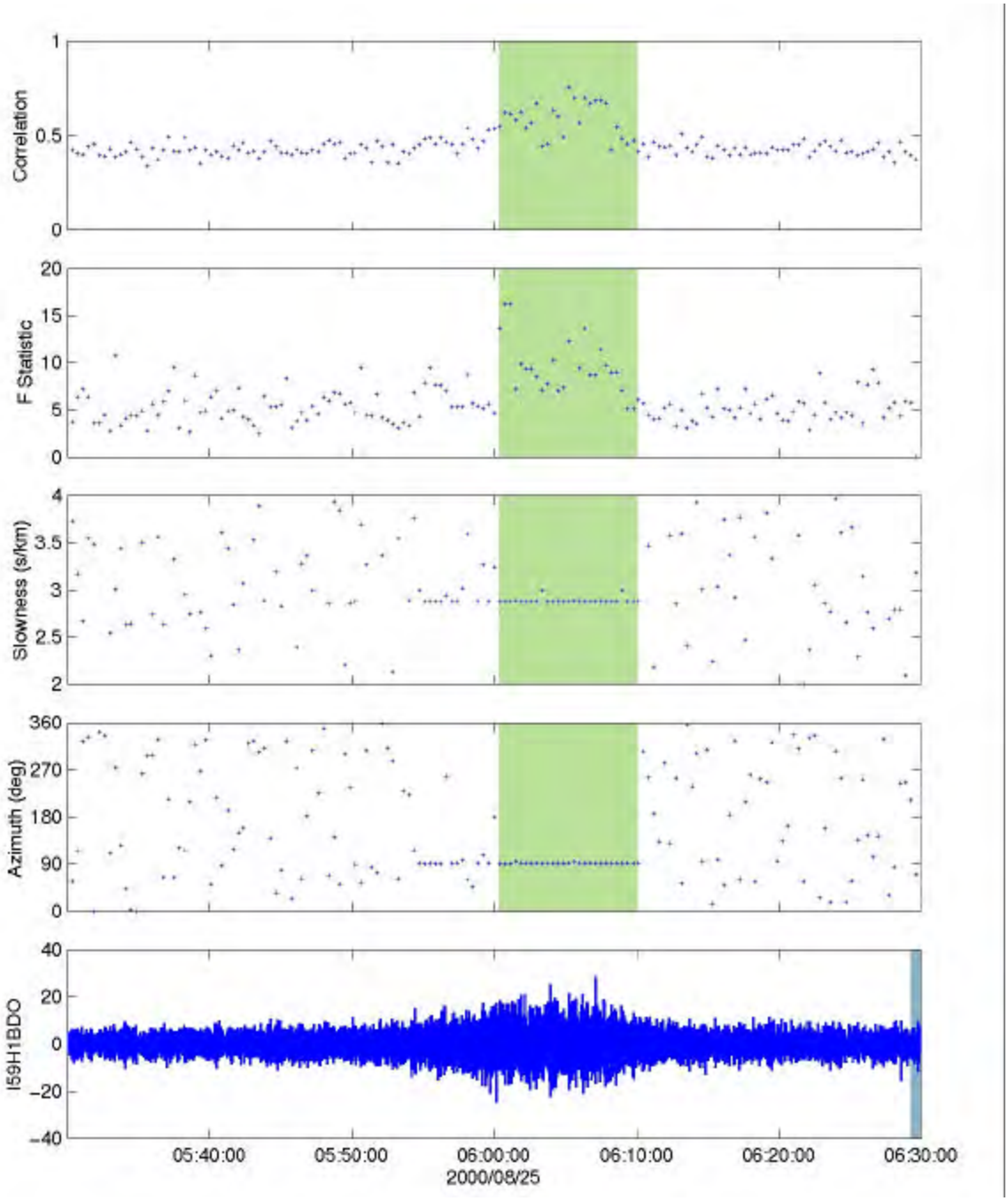

Figure 1. Main InfraTool window showing analysis of an ITS bolide arrival on 8/25/00. Boxes in Azimuth, Slowness, Correlation, and F-Statistic windows correspond to time segments over which mean azimuth and slowness were calculated (Figure 2).

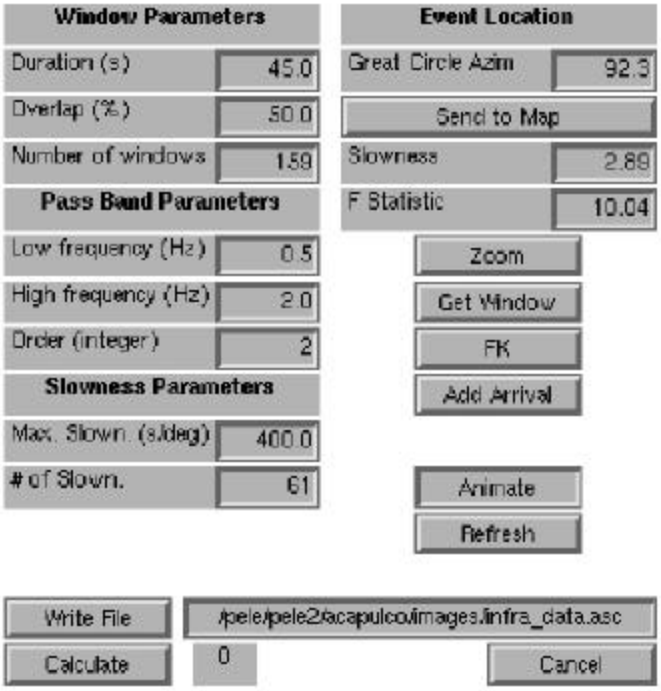

Figure 2. InfraTool control panel showing typical ISLA analysis parameters, mean azimuth and slowness, and available tools.

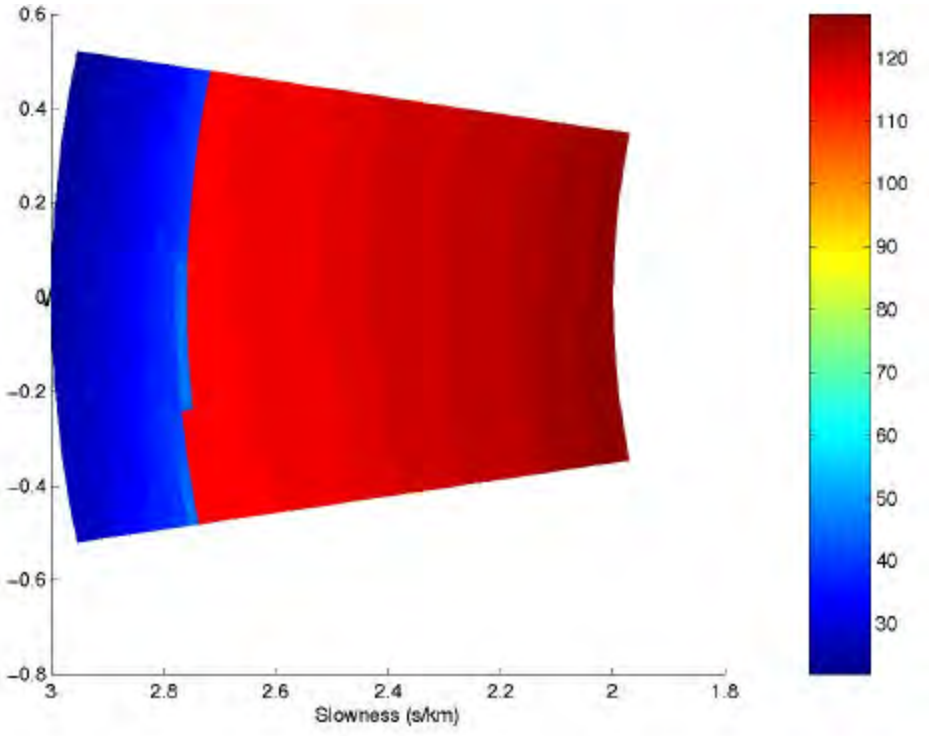

Figure 3. Plot showing turning height for first-skip infrasonic waves for a segment of the slowness plane as calculated by the Tau-P software of Garcés et al. (1998). The outer portion corresponds to a stratospheric phase, the inner to a thermospheric phase.

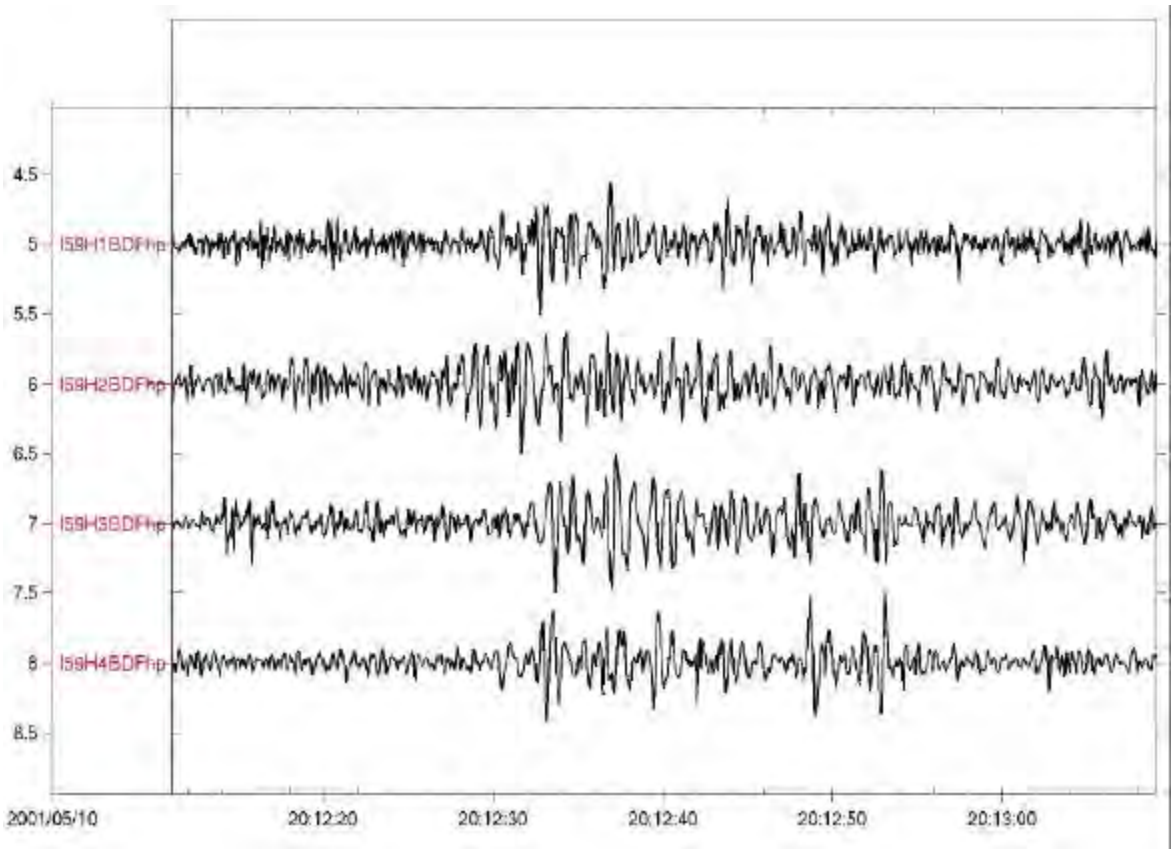

Figure 4. High-pass-filtered waveform showing typical IA arrival.

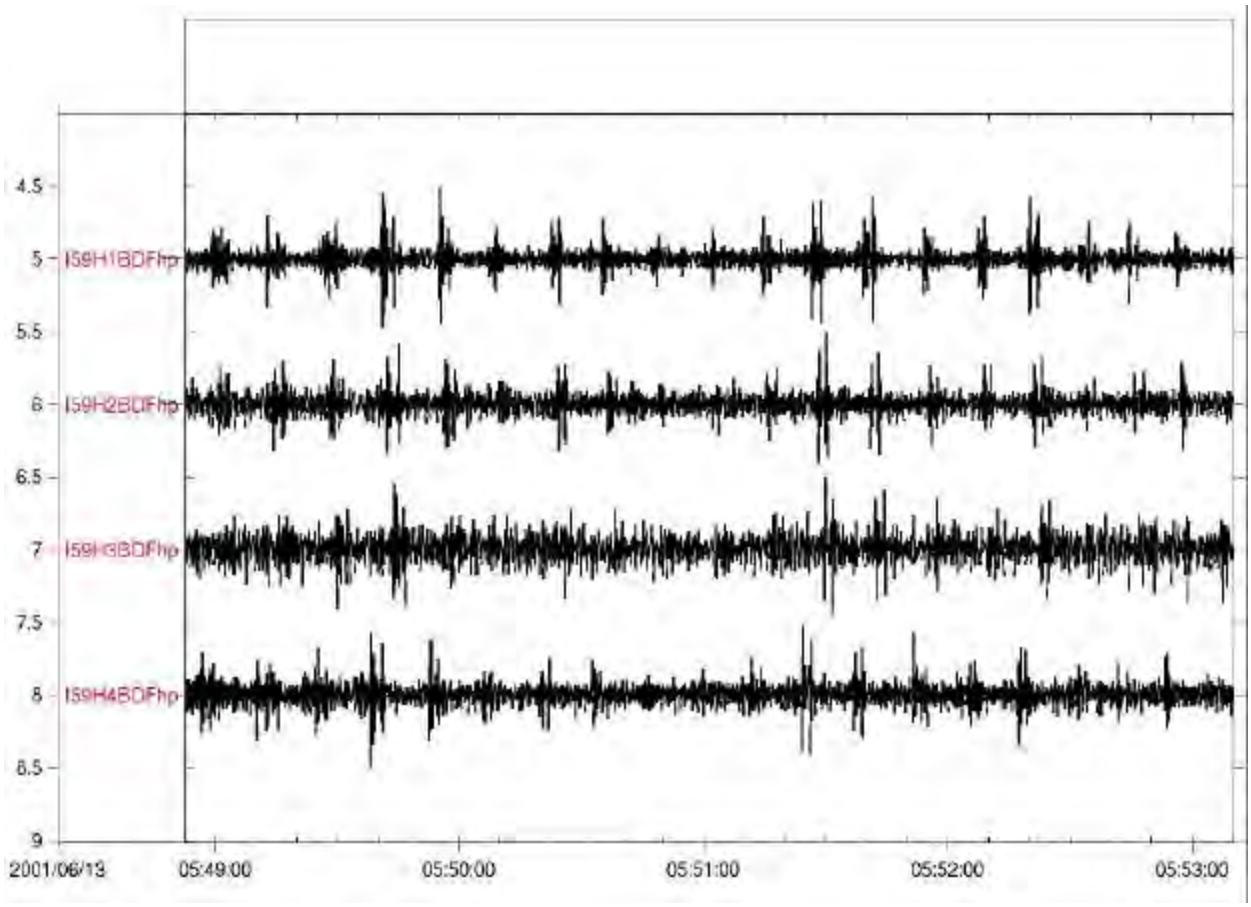

Figure 5. High-pass-filtered waveform showing typical IK arrivals.

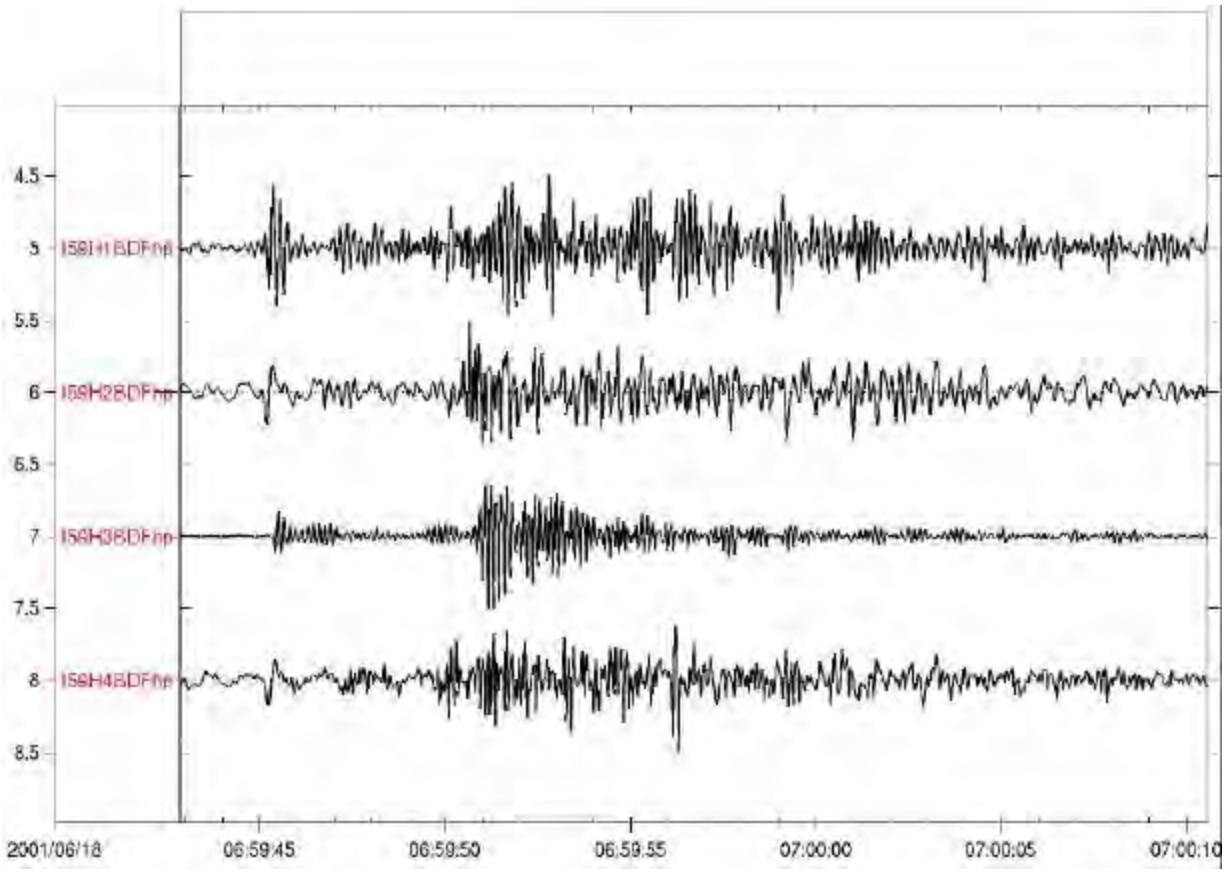

Figure 6. High-pass-filtered waveform showing typical IEP arrivals. Note severely increased signal-to-noise ratio on channel I59H3BDF due to presence of PVC wind-noise-reducing filter in contact with the ground.

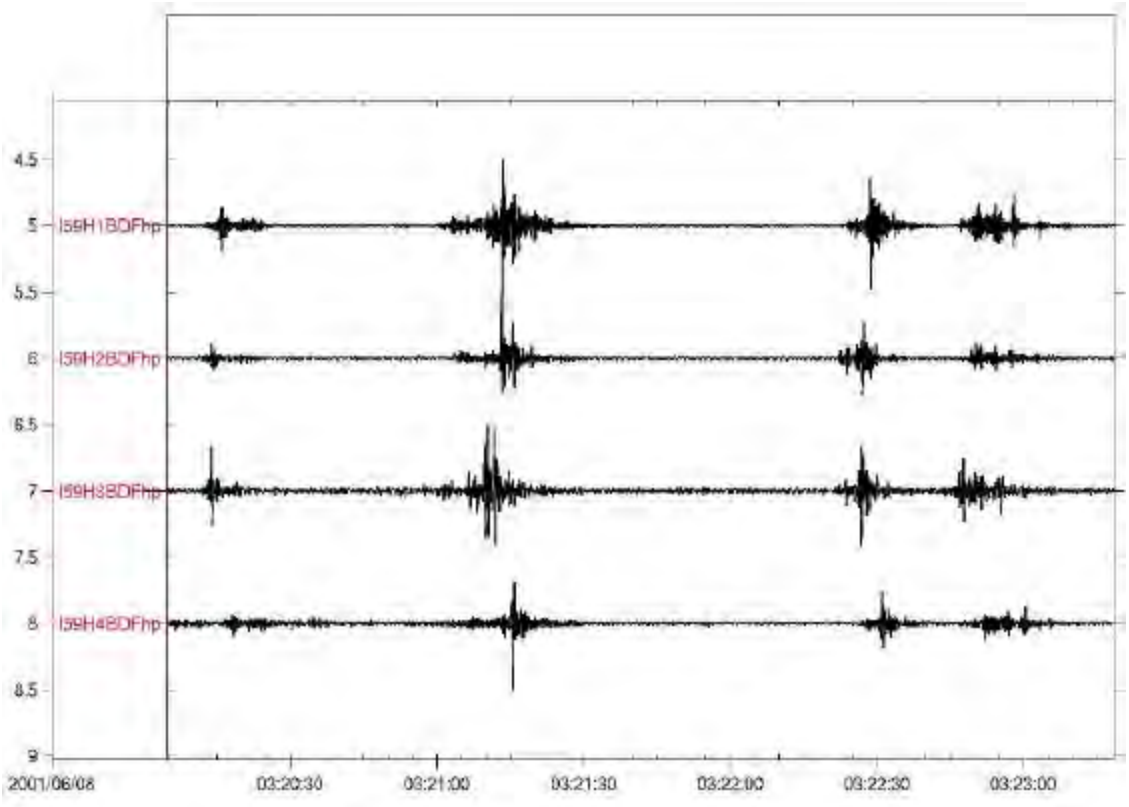

Figure 7. High-pass-filtered waveform data showing typical IN arrivals.

INFRASONIC SOURCE LOCATION OF THE APRIL 23, 2001, BOLIDE EVENT

Milton Garces[1], Claus Hetzer[1], Kent Lindquist[2], Roger Hansen[2], John Olson[3], Charles Wilson[3], Douglas Drob[4], and Michael Hedlin[5]

University of Hawaii, Manoa[1], University of Alaska, Fairbanks [2,3]
Naval Research Laboratory[4], and University of California, San Diego[5]

[1,2,4]Sponsored by National Nuclear Security Administration
Office of Nonproliferation Research and Engineering
Office of Defense Nuclear Nonproliferation

Contract No. DE-FC04-98AL79801

ABSTRACT

An infrasonic event with a 10- to 15-minute duration was detected by multiple infrasonic arrays on April 23, 2001. Data from infrasound arrays IS59 (Hawaii), FAI (Fairbanks), and IS57 (California) are selected for the determination of the origin time and the location of the infrasonic source. The bolide was not observed by infrasonic stations operating in South America or the South Pacific. There were also no confirmed detections from ocean-bottom seismometers and hydroacoustic sensors near the epicenter. A preliminary location was obtained from array back azimuths, and this location was used as a seed for the source iteration process. We compare the estimates obtained for the source location and origin time using different atmospheric models and different stations. The tau-p method is used to estimate theoretical travel times, and we estimate the source position by reducing the time residuals. The variability in the locations may be due to errors in the atmospheric models, the propagation models, or the array estimates. We outline the algorithm used for the location of infrasonic sources, and assess the accuracy of two- and three-station epicentral determinations.

KEY WORDS: infrasound, source location

OBJECTIVE

The aim of this work is to evaluate the precision of infrasonic source locations from multiple array detections. We consider possible modifications to the atmospheric models that may yield consistency between infrasonic locations and satellite-based locations.

RESEARCH ACCOMPLISHED

Introduction

On April 24, 2001, Rod Whitaker of the Los Alamos National Laboratory reported that an interesting event had been detected by DLIAR on the previous day, April 23. Shortly thereafter, David Brown of the Center for Monitoring Research, issued a message corroborating associated detections by IS10, DLIAR, and IS59. Michael Hedlin and Jon Berger confirmed detection at IS57, Pinon Flat. Charles Wilson, John Olson, and Kent Lindquist provided results from the FAI research array, which will soon become IS53. French stations in Bolivia, French Guyana, and Tahiti did not observe the event, and no evident detections were reported by the seismic sensors and hydrophones deployed at the Hawaii-2 Observatory at 28^{o} N 142^{o} W.

Dr. Brown promptly made available to Defense Threat Reduction Agency (DTRA) researchers CSS data for stations IS10, DLIAR, IS57, IS59, and SGAR, and the Infrasound Laboratory (ISLA) of the University of Hawaii used Matseis, from Sandia National Laboratories, and Infratool, from Los Alamos National Laboratory, to produce rapid estimates of the arrival time, azimuth, and slowness of the signal at these arrays. Preliminary locations were made using the tau-p code presently under development at the ISLA. The authors did not know the source of the April 23 event until June 2001, when the Department of Energy (DOE) issued an official information release.

According to the DOE release, infrared sensors aboard US Department of Defense (DOD) satellites detected the impact of a bolide on 23 April 2001 at 06:12:35 UTC (988006355 Epoch time). The bolide appeared to explode at an altitude of 28.5 km above the coordinates of 27.9 North and 133.89 West. The impact was simultaneously detected by space-based visible wavelength sensors operated by the US DOE. The total energy in the visible band was 4.6 X 10^{12} joules. The location for the April 23 event determined by the optical systems is referred to as LO1.

Some discrepancies exist between the satellite and the infrasonic locations that would be expected for these events. There are two possible explanations for these discrepancies: either there was more than one bolide impact within a ten-minute window, or our infrasonic and atmospheric models need to be reviewed. We consider the second explanation, and investigate what modifications to the atmospheric models would produce infrasonic travel-time results consistent with the LO1 location. It is also possible that the sound propagation models are incomplete, and that scattering in the troposphere and stratosphere has an important effect.

Array Processing of the Infrasonic Data for Selected Stations

The locations of selected arrays that detected the April 23 event and used in this study are given in Table 1 and shown in Figure 1. These stations were selected because they are the three closest International Monitoring System (IMS) stations to the event. Based on the epicentral location issued by the DOE release, the range of each station to the source and the expected azimuth of the incoming signal can be readily computed. We used a modified version of Infratool and frequency-wavenumber (FK) analysis to estimate the arrival information of the signals observed at each array (Table 2). To obtain these estimates, we first band pass the signal with a Butterworth zero-phase 2nd order filter between 0.1 and 1 Hz, and use FK analysis with 101 slowness values on successive 45-second Hamming windowed segments of data. We also compute the correlation and the F-statistic for each window (Figures 2-3). We thus obtain estimates of the incidence azimuth (measured clockwise from North), slowness (in seconds/degree), and onset time of the signal. The onset time is determined from an increase in the F-statistic and correlation, as well as from the time at which azimuth values become stable. The arrival estimates are dependent on the choice of frequency band and time window, and we use the same parameters on all arrays to ensure consistency. Further, the azimuth and slowness of the detected infrasonic waves change with time. Thus, we restrict our estimates to the first arrivals, demarcated by the vertical bar in Figures 2 and 3. The apparent slowness of the signal (travel time divided by range), the apparent speed (range divided by travel time), and the azimuth deviation in the signal (expected azimuth – observed azimuth) are provided in Table 3. A positive azimuth deviation corresponds to a correction to the right of the arrival azimuth.

The azimuth and high slowness values observed at FAI are not very precise because the position of the array elements are only accurate to +/-15 m, and we have data from only three of the four elements. For an array aperture of 1 km, this leads to a maximum error in the apparent horizontal phase velocity of ~6%. Such relatively small errors would still not account for the strong discrepancies in the expected and observed array estimates. The azimuth values obtained at IS59 and IS57 (both arrays have an aperture of ~2 km) are reasonable, but the slowness values at IS57 fluctuate quite a bit. This variability in the slowness at IS57 may be due to its relative proximity to the source, and to possible interference of superposed wave trains. Some of the errors in the slowness and azimuth values obtained at IS59 may be attributed to site effects. At the edge of the slowness plane, the 3-D effects of the array element locations are negligible, but the mountains around IS59 may alter the geometry of the propagating wavefronts. Until these site-specific issues are resolved, the arrival time of the signal provides the most robust parameter for performing the source location.

Initial Infrasonic Location Procedure for the April 23 Event

A preliminary location was made by using intersecting back azimuths from five infrasonic arrays: IS59, IS57, FAI, DLIAR, and IS10. However, the epicenter given by the area of intersection of these lines yielded arrival times inconsistent with atmospheric model predictions. We obtained SAGE meteorological data from the Naval Research Laboratory for the day of April 23, 2001, at most of the sites except DLIAR, which is not near any IMS station. We used the meteorological data for IS57 to infer the arrival times for DLIAR. We then used the tau-p method of Garces et al., (1998) to compute predicted travel times (T), ranges (X), azimuth deviation (in degrees, where positive means a correction to the right of the direction of arrival), effective slowness (T/X), and the height of the atmosphere where the selected rays turn. We then use the Geiger method to reduce the residuals in the arrival times. Various assumptions went into these computations. First, the observed slowness

values in most of the arrays were higher than expected, as some of them did not correspond to acoustic velocities. Such arrivals are not predicted by ray theory, and suggest that scattering may have been significant. We use the highest slowness values that are allowed by the ray models for the specified arrival azimuth at each site. Second, we use the local meteorological conditions at the epicenter to trace rays along a rather long transect, where we know we may experience varying conditions. We expect the first skip to be reasonably accurate, and further skips to degrade in precision. Despite these approximations, self-consistent results were obtained for the epicenter and origin time of the source. However, although the infrasonic location (LA1) was close to the satellite location (LO1), the origin times did not agree. The infrasonic inversion yielded an origin time of 05:58 UT at 29.5 North, 134.9 West, whereas LO1 has an origin time of 06:12:35 UT at 27.9 North and 133.89 West.

Modification of the Atmospheric Model

The discrepancy of 00:12:37, 1.6^o in latitude, and 1^o in longitude may be explained by inaccuracies in the atmospheric models, as well as by inadequacies in the ray-tracing formulation. The epicentral location inferred from the infrasonic data is relatively close to LO1, but the origin time is too early. We explore the possibility of modifying the atmospheric models to account for these differences. We concentrate on the travel times, and attempt to match the effective propagation speeds of the arrivals.

The atmospheric profiles used to compute LA1 predicted stratospheric winds that were too weak. As a result, no stratospheric arrivals were predicted for any of the stations, and the location was computed using only the predicted thermospheric arrivals. New atmospheric models were used for this paper, where meteorological estimates up to 55 km were obtained from the NASA Goddard Spaceflight Center (GSFC) Data Assimilation Office. The propagation model parameters are shown in solid lines in the upper panel of Figure 4. Using these profiles, new effective speed values were used to obtain a location and origin time, and this solution is referred to as LA1b. Table 4 shows the propagation model results for this scenario, and the upper panel of Figure 5 shows the location of LA1b.

As shown in Table 4, the apparent speeds for IS59 and FAI computed with an unperturbed atmosphere are too slow to explain the observed arrivals. The source location has also been degraded. The apparent propagation speeds for IS57 are consistent with predictions, which suggest that the atmospheric and sound propagation models along the dominant stratospheric wind direction are adequate. We consider modifications to the upper atmosphere models to account for the discrepancy in the locations. After various iterations, it was observed that the most effective modification involved an increase in the atmospheric sound speed, which implies an increase in the temperature and/or a decrease in the molecular mass.

To modify the atmospheric profiles, a cosine taper was constructed to add a bias at specified height ranges to the wind and temperature profiles. The cosine taper ensures a smooth transition between the unperturbed profile and the perturbed region. The atmospheric profile used in this study was provided by the Naval Research Laboratory (NRL) and was evaluated using a procedure described in Garces et al. (2000). We only concern ourselves with atmospheric heights below 120 km, as most of the rays corresponding to the first arrivals are predicted to turn below this level. In addition, the atmospheric estimates up to 50 km have been validated by various means, and are more accurate than the empirical estimates for heights above 50 km. Thus, we concentrate on the region between 50 km and 120 km, also known as the Mesosphere and Lower Thermosphere (MLT). The selected cosine taper increases from 60 km up to 100 km, where it remains at a constant value. We used the atmospheric profile at the epicenter for our tests. This simplification is reasonable for the E-W line between IS59 and IS57, as the latitude does not change drastically. However, between Fairbanks and the epicentral location, the atmosphere changes quite dramatically. Various perturbations to the atmospheric profile were attempted, and a reasonable fit for all three azimuths was obtained for a 10% increase in the sound speed, with the wind velocity profiles remaining unperturbed. The upper panel of Figure 4 shows the perturbed sound speed profile as a dashed line.

The ratio of the temperature to the molecular mass of the atmosphere is directly proportional to the square of the sound speed. Thus, if the sound speed is increased by a percent δ_c so that the new speed is $c(1+\delta_c)$, the ratio of the temperature to the molecular mass must increase by a percent $(1+\delta_c)^2-1$. A 10% increment in the sound speed corresponds to a 21% increase in the ratio of temperature to molecular mass, and it may occur as a temperature increase from 60 km to 100 km, with a mixture of density decrease and temperature increase above

100 km. The lower panel of Figure 4 shows the effective speed predicted for the perturbed model, and Table 5 shows the predicted propagation parameters. Note the trim of high speed on the outer edge of the slowness plane, which corresponds to the first arrivals for the April 23 event. The 10% correction in the sound speed is about 8% higher than would be expected for temperature corrections in the MLT. We conclude that our assumptions on the path of propagation to IS59 and FAI are in error, and that the heterogeneity of the atmosphere may play a significant factor in the scattering of sound waves during long-range propagation.

We can still use the effective propagation speeds to compute the robustness of the location algorithm. Using the three stations, a new location and origin time are computed from the new propagation speeds, and this location is referred to as LA2. Using the same values provided in Table 5, we also compute locations using only two stations. LA3 was computed using IS59 and IS57, and LA4 was computed using IS57 and FAI. Table 6 provides the origin time and location of these solutions. Solutions LA2, LA3, and LA4 are almost identical, differing by a few seconds and only a tenth of a degree in latitude. However, the nature of the solution for the location is quite different. The aim of computing the residues is to extract the minimum, and although the residue surface for LA2 has a clearly defined minimum, the minimum for LA3 is a linear feature. This topology of the LA3 solution for the residue surface, caused by a lack of constraint perpendicular to the line between the stations, leads to instability in the location algorithm.

The only difference in the procedure used to compute the location solutions LA1, LA1b, and LA2 is in the atmospheric models. LA1 used a model where the stratospheric winds were not sufficiently strong, and this led to slow propagation and thus a predicted origin time that was too early. The predicted epicentral location was not too far off, but this match was fortuitous. LA1b had a stronger stratospheric wind, which produced a good match for IS57 and brought the origin time closer to the LO1 values, but placed the source too far northwest because of the relatively slow propagation speeds of the thermospheric phases. Solution LA2 obtained with the modified atmospheric profiles provided the best fit to LO1, as expected. The difference between LO1 and LA2 is 202 s, 0.20^{o} in latitude, and 0.61^{o} in longitude. This would correspond to an epicentral range of ~70 km from the source location observed by the satellites. However, the LA2 location was obtained with perturbations in the sound speed that are unrealistic, and thus we are compelled to consider alternative explanations for the rather fast propagation speed for the IS59 and FAI arrivals.

Figure 5 shows the effective propagation speed surfaces computed at every height and slowness bin for propagation to IS59 and to IS57. A duct exists in the upper troposphere and lower stratosphere, and in a homogeneous, perfectly stratified atmosphere energy would be trapped in this duct. However, heterogeneity in the troposphere may induce scattering of the ducted energy into the ground. This hypothesis may explain the fast effective propagation speeds, the slow apparent phase speeds, and the azimuth deviations observed in directions opposite to the dominant stratospheric winds (Kulichkov, 1998). Thus, a combination of ray and scattering theories may provide a reasonable explanation for the observed arrivals.

CONCLUSIONS AND RECOMMENDATIONS

Arrival times for infrasonic propagation along the dominant stratospheric winds matched well the predicted arrivals, but unreasonable modifications to the sound speed profile in the upper atmosphere were needed to match the arrival times of possible thermospheric phases. Ongoing studies concentrate on the propagation of acoustic energy in leaky ducts in the troposphere and stratosphere. Further work should also quantify the scales of inhomogeneity and the degree of acoustic scattering in the atmosphere up to heights of 150 km.

REFERENCES

Garces, M, D. Drob, M. Picone, K. Lindquist, and R. Hansen (2000). Characterization Of Infrasonic Waves Observed In Hawaii During Summer, 22nd Seismic Research Symposium: Planning for Verification of and Compliance with The Comprehensive Nuclear-Test-Ban Treaty, New Orleans.

Garcés, M. A., R. A. Hansen, and K. Lindquist (1998). Travel times for infrasonic waves propagating in a stratified atmosphere, Geophys. J. International, 135, 255-263.

Kulichkov, S. N. (1998). On problems of infrasonic monitoring of small energy explosions, Proceedings of the Informal Workshop on Infrasound, Bruyers-Le-Chatel, France.

Table 1. Station location, range from LO1, and azimuth from LO1 for April 23, 2001 bolide event.

Station	Latitude	Longitude	Range, km	Azimuth, deg
IS57	33.60	-116.50	1777.7	253.8262
IS59	19.59	-155.9	2419.0	63.4996
FAI	64.87	-147.84	4228.7	159.7367

Table 2. Observed array parameters: arrival azimuth, slowness (ray parameter) in s/km, and estimated time of arrival of the first coherent energy packet.

Station	Azimuth, deg	Slowness (s/degree)	ETA (UT)
IS57	249.0	316.8	07:48:40 +/- 45 s
IS59	65.6	338.4	08:20:14 +/- 45 s
FAI	143.1	423.0	10:12:13 +/- 45 s

(Used conversion factor of 111.1949266 km/degree)

Station	Slowness (s/km)	Speed (km/s)	ETA (Epoch time)
IS57	2.8491	0.3510	988012120 +/- 45 s
IS59	3.0433	0.3286	988014056 +/- 45 s
FAI	3.8041	0.2629	988020733 +/- 45 s

Table 3. Apparent slowness, apparent speed, and azimuth deviation of infrasonic detections for LO1.

Station	App. Slowness (T/X, s/km)	App. Speed (X/T, km/s)	Azimuth deviation
IS57	3.2430	0.3084	4.8262
IS59	3.1835	0.3141	-2.1004
FAI	3.4001	0.2941	16.6367

Table 4. Predicted apparent slowness, apparent speed, and azimuth deviation for unmodified meteorological model.

Station	App. Slowness (T/X, s/km)	App. Speed (X/T, km/s)	Azimuth deviation	Turning Height (km)
IS57	3.27	0.305 (Is)	0.8	48
IS59	3.57	0.280 (It)	-1.0	117
FAI	3.70	0.270 (It)	-0.5	115

Table 5. Predicted apparent slowness, apparent speed, and azimuth deviation for modified meteorological model.

Station	App. Slowness (T/X, s/km)	App. Speed (X/T, km/s)	Azimuth deviation	Turning Height (km)
IS57	3.27	0.305	0.8	48
IS59	3.33	0.300	-1.3	112
FAI	3.48	0.287	-0.5	112

Table 6. Source Origin Time and Location.

Source ID	Origin time	Latitude (N)	Longitude (W)
LO1	988006355	27.9	133.89
LA1	988005598	29.5	134.9
LA1b	988005878	29.6	136.0
LA2	988006153	28.2	134.5
LA3	988006152	28.1	134.5
LA4	988006167	28.2	134.5

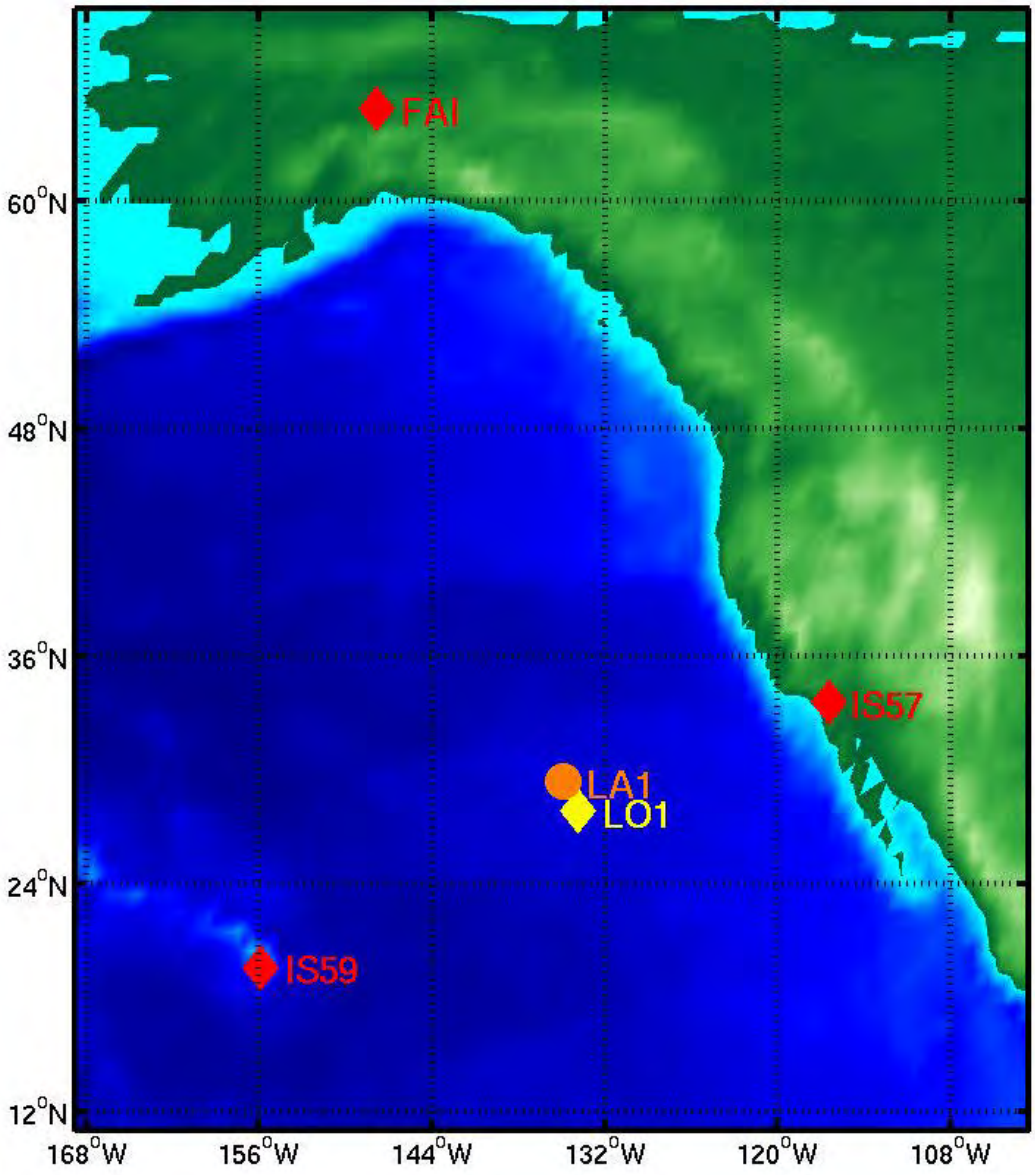

Figure 1. Location of infrasound monitoring station IS59, IS57, and FAI. LO01 shows the source location determined by US satellites, and LA01 shows the first location determined from ray tracing within one week of the event detection. In addition to the three arrays shown, the LA1 location used DLIAR and IS10.

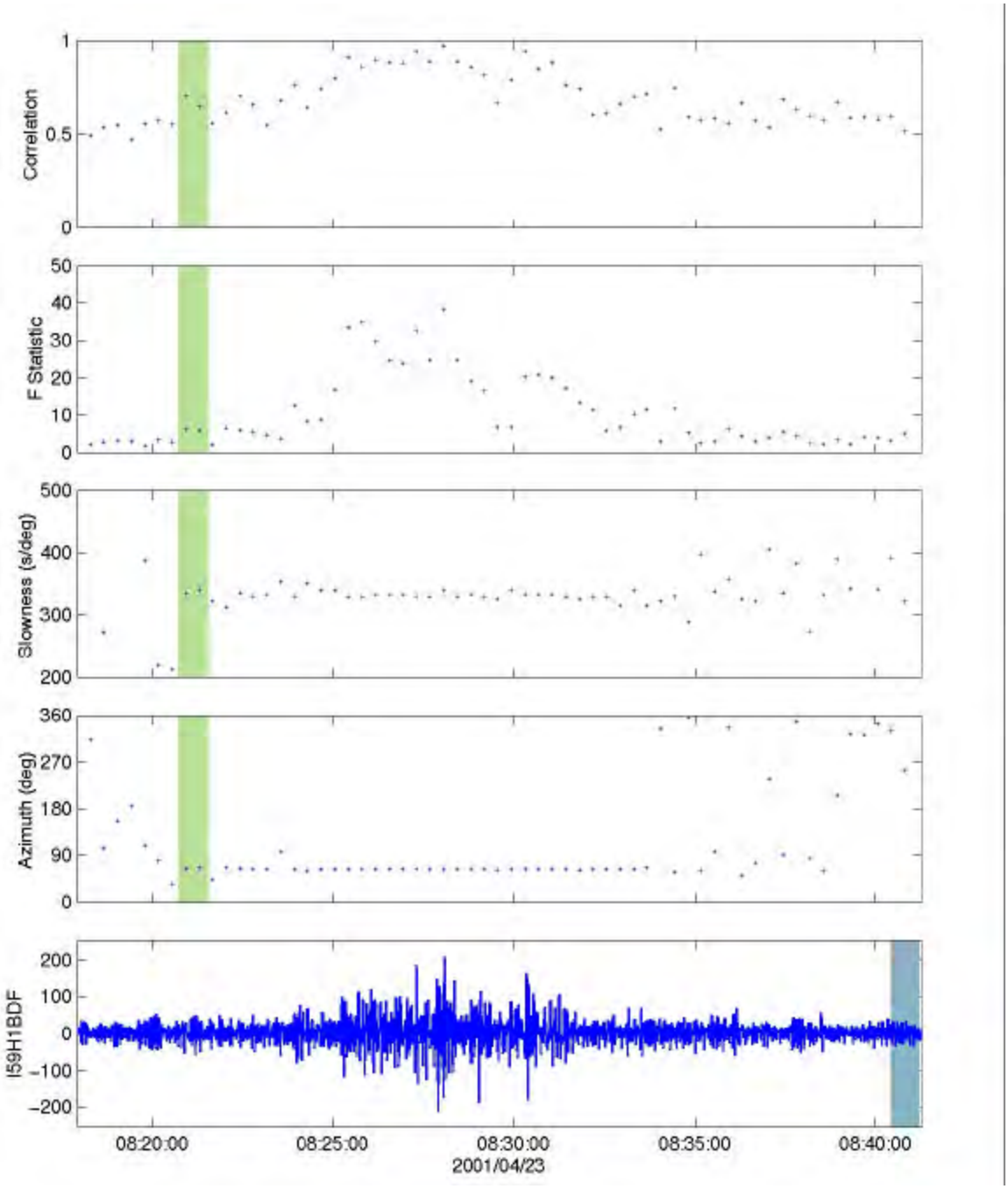

Figure 2. Detection of the April 23 bolide at IS59, Hawaii.

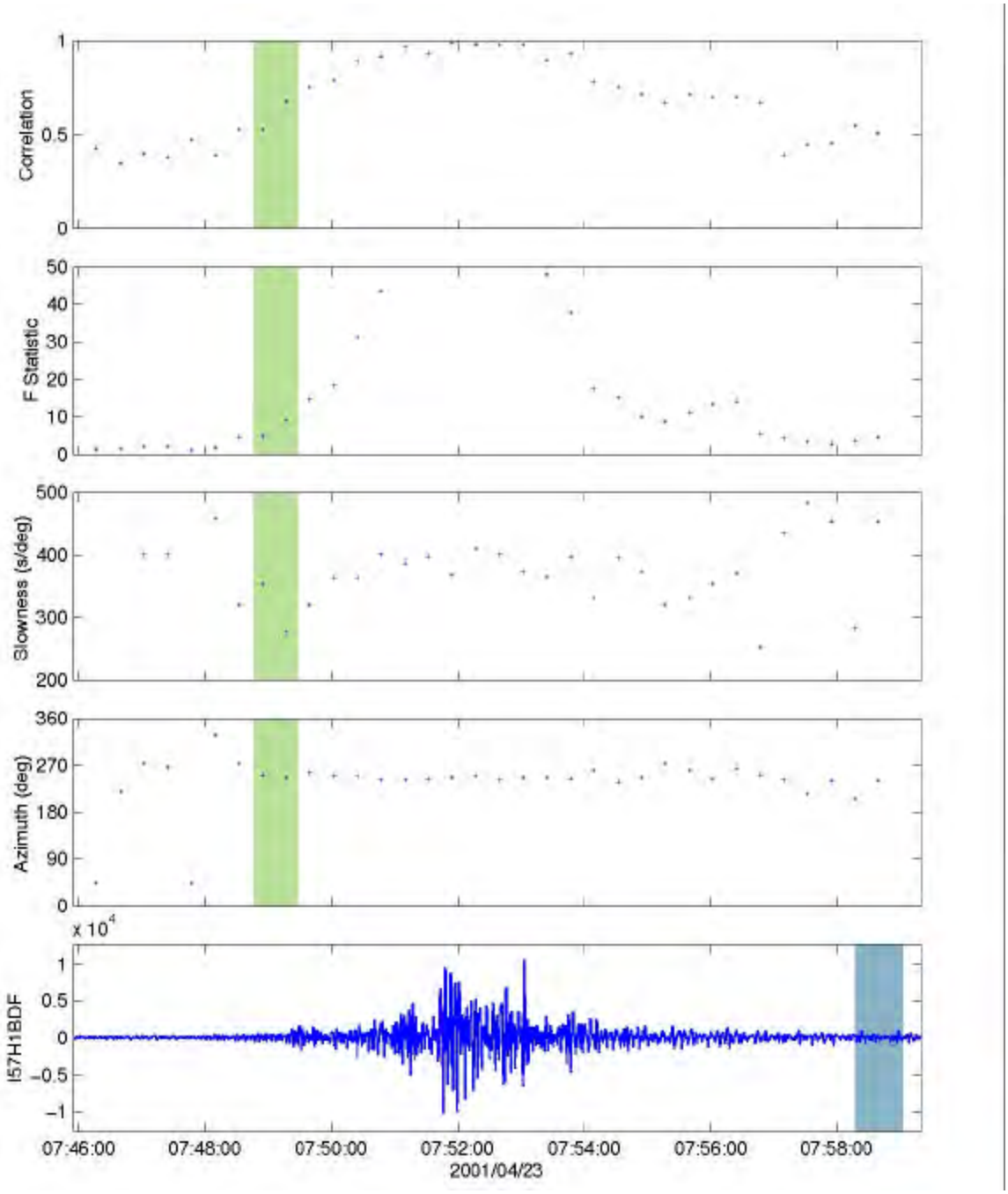

Figure 3. Detection of the April 23 bolide at IS57, Pinon Flat, CA.

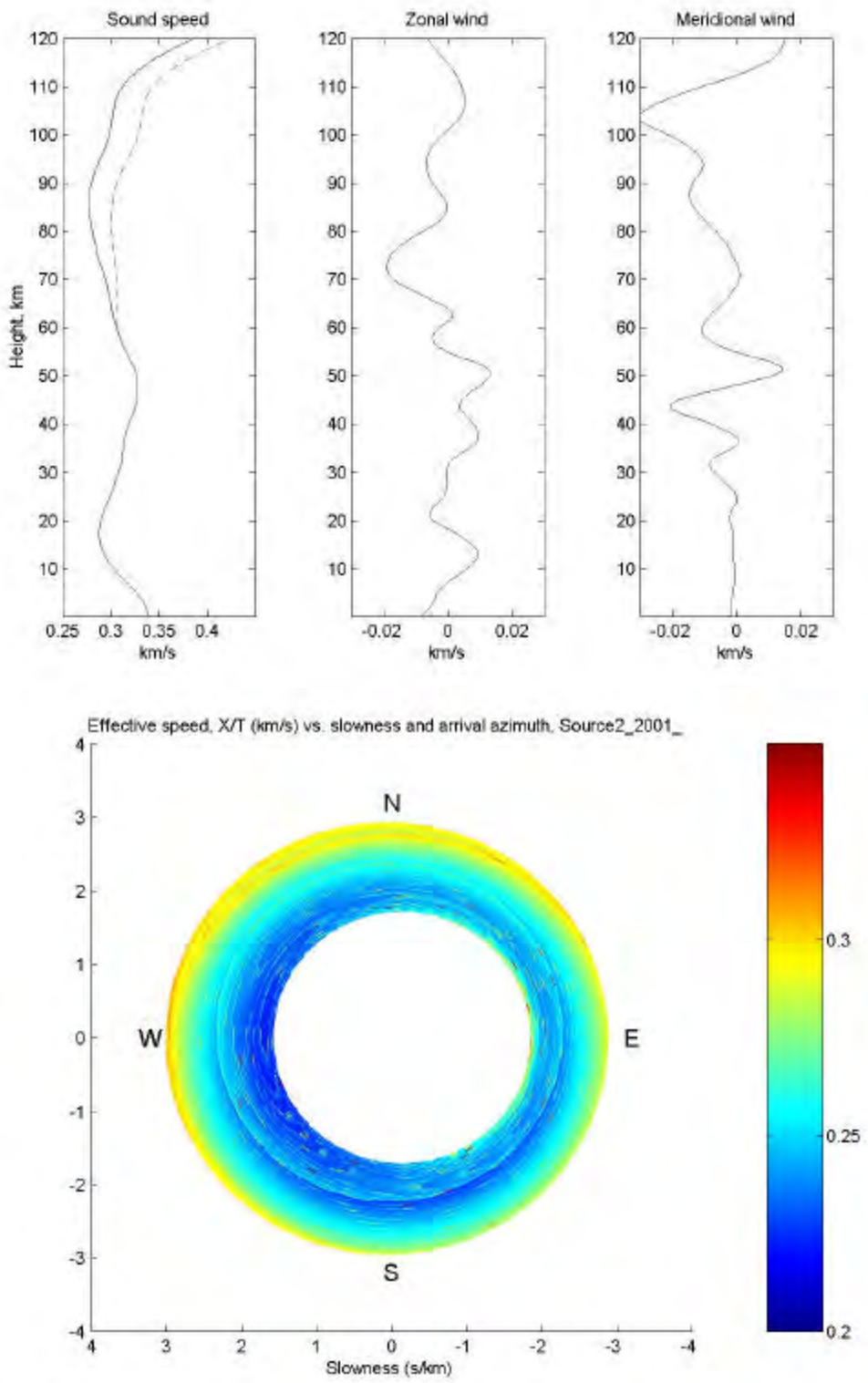

Figure 4. Atmospheric profiles and predicted effective propagation speed. The dashed line denotes the modified atmospheric sound speed, and the effective speed is computed using the perturbed profiles. Note the high-speed trim on the edge of the slowness plane.

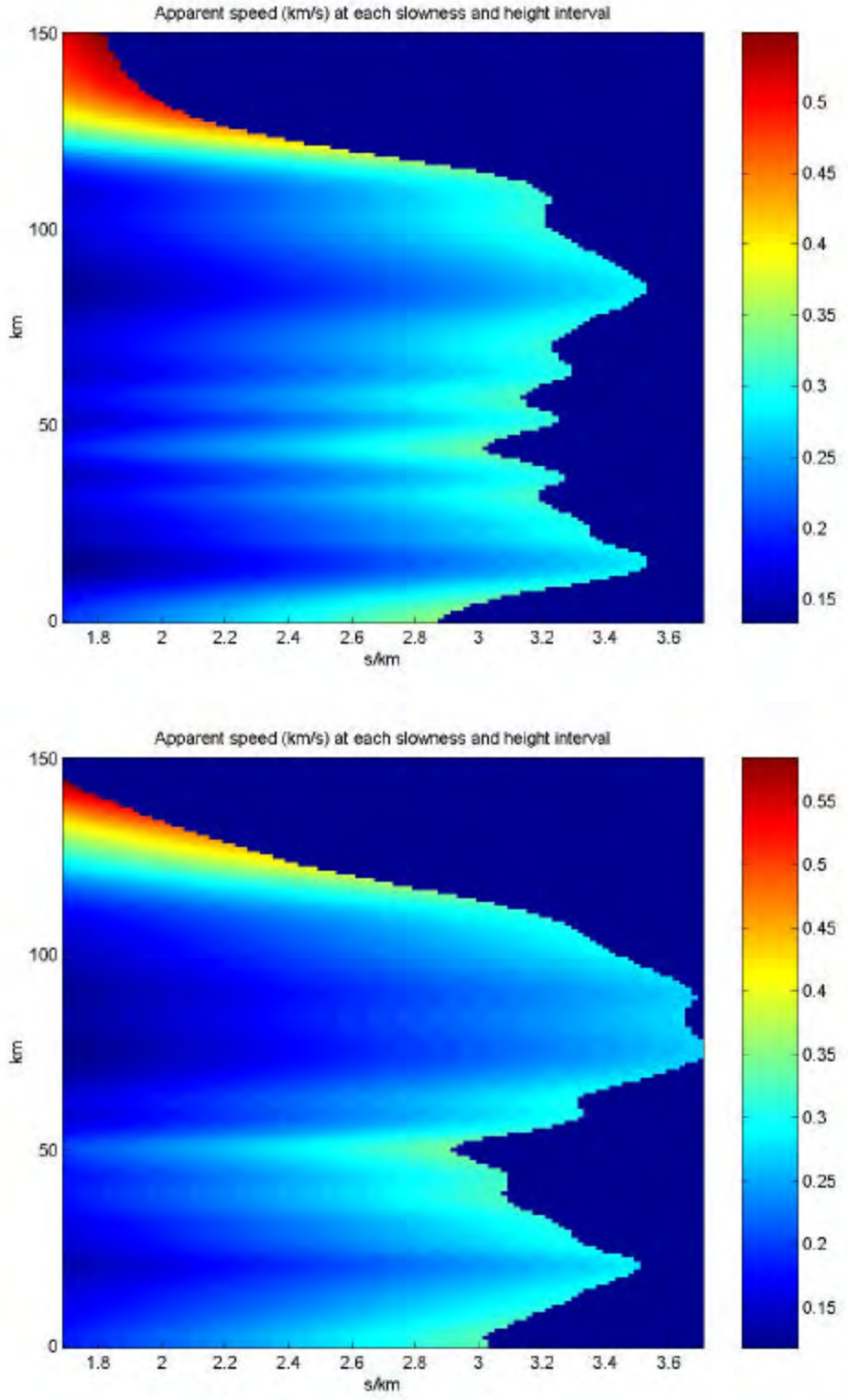

Figure 5. Effective speed (range over travel time) at each height and slowness interval for IS59 (above) and IS57 (below). The stratospheric phase for IS57 at 3 s/km is well defined. A duct exists between 10 and 50 km, and that this energy may be scattered into the ground.

EVALUATION OF INFRASONIC NOISE REDUCTION FILTERS

Michael A. H. Hedlin and Jon Berger

University of California, San Diego

Sponsored by Defense Threat Reduction Agency

Contract No. DTRA01-00-C-0085

ABSTRACT

It is generally accepted that the study of acoustic signals in the atmosphere requires suppression of noise due to atmospheric turbulence. Most acoustic signals of interest arrive with longer spatial wavelengths than the noise that originates near the receiver. As a result, integration of acoustic energy across an area will attenuate spatially de-correlated noise and increase the signal-to-noise ratio. A second approach employs a barrier to reduce wind speeds and small-scale turbulence at the location of the sensor. We are investigating the utility of the various noise-reduction devices that have been proposed or are currently in use. Toward this end, we conduct noise suppression experiments at the Pinon Flat Infrasound test bed in Southern California. This test bed has proved to be ideal for this kind of research as wind speeds vary from near zero to > 15 m/s. The test bed is the site of the 8-element infrasound array IS57 and experiments involving the new fiber optic infrasound sensor. A second goal of our contract is to model the observations and propose remedies for observed shortcomings of the filters.

In our first experiment at Pinon, we tested a wind fence against a 30-m-aperture array of microporous hoses. These data were collected concurrently with unsuppressed noise sampled by a reference port. This test revealed that a 50% porous 2-m wind fence coated with a fine wire mesh reduces infrasonic noise above 0.5 Hz by up to 30 dB. The porous wind fence is not effective at longer periods.

Our second experiment compared the wind fence with an array of 144 open-air ports distributed across an area 70 m in diameter. This is the design favored by the Provisional Technical Secretariat of the Comprehensive Nuclear-Test-Ban Treaty Organization (PTS-CTBTO) for use at locations where wind speeds are commonly above 3 m/s. In this experiment we also compared these filters with an 18-m-aperture multi-port filter (recommended by the PTS for use at relatively calm areas). After > 1 month of recording at wind speeds ranging from near zero to above 15 m/s, we observed significant (15 dB) resonance peaks in the 70-m system at 2.65 and 7.95 Hz. These are the first two eigenfrequencies of an organ-pipe mode inside the nonporous pipes that connect the open ports to the microbarometer. The anti-aliasing filter near 10 Hz removes energy at the higher eigenfrequencies, which are predicted by resonance theory. The peaks become evident at wind speeds below 0.5 m/s. The fundamental resonance peak in the 18-m filter is observed at 9.5 Hz, beyond the band of interest to the monitoring community. Our noise experiment has verified the utility of the 70-m filter for suppression of long-period noise. Noise suppression depends on local wind speeds but will reach 15 to 20 dB between 0.1 and 1.0 Hz. Noise suppression is observed from 50 seconds to above 1 Hz. The 18-m filter is superior to the 70-m filter at frequencies above 0.5 Hz.

How the mechanical noise suppression devices compare with the new fiber optic sensor and with a sensor buried in a shallow porous medium (as proposed by the Southern Methodist University (SMU) group) has not yet been determined.

KEY WORDS: spatial averaging, turbulence, organ-pipe mode

OBJECTIVE

Our objective is to build and test infrasonic noise reduction systems to assess the utility of the different devices as a function of frequency and wind speed. We use chi-squared statistics to assess the significance

of any observed differences in the performance of the different devices. Our goal is to test systems that are being deployed at International Monitoring System (IMS) array sites and to test new devices (such as the new fiber optic sensor under development at UCSD) and spatially compact filters (such as the wind fence, a sensor buried in a porous medium) in our search for systems that are more economical and/or superior to currently preferred designs. We identify shortcomings of filters (e.g. resonance in large pipe filters) and will propose possible remedies.

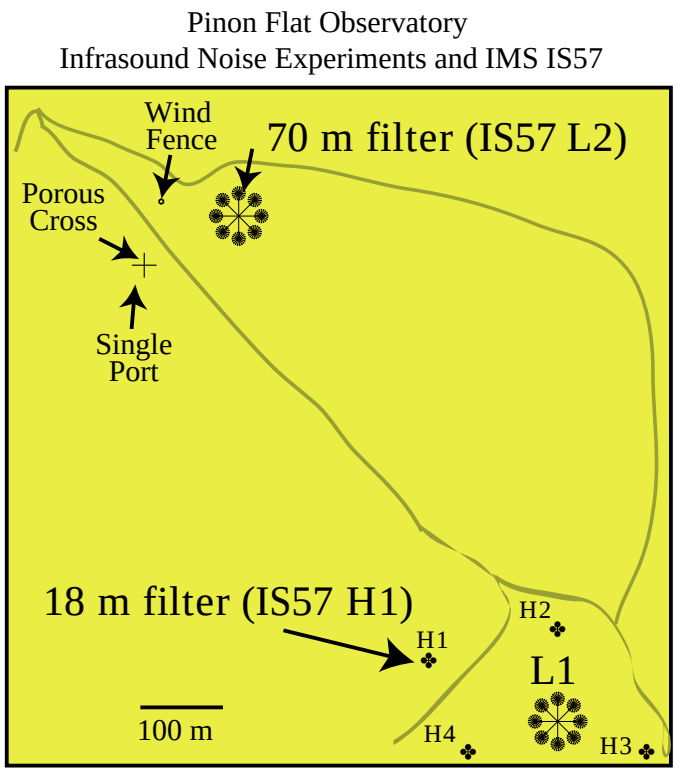

Figure 1. Relative locations of the noise reduction systems at the Pinon Flat Observatory.

RESEARCH ACCOMPLISHED

The Pinon Flat Observatory

All of our experiments have been conducted at the Pinon Flat Observatory (PFO). As an environment for testing the efficacy of the various spatial filters, PFO offers a variety of wide wind conditions. The observatory is located in the Anza Borrego desert ~ 50 km to the southwest of Palm Springs in the coastal ranges. Pinon pine trees and essentially no low-lying ground cover cover much of the area. Wind speeds are often near zero at night and sometimes exceed 15 m/s during the day. Northwest and southeast winds are most common. The observatory is accessible at all times of the year. The International Monitoring System (IMS) infrasound array IS57 is located at PFO (Figure 1). The array comprises 8 instruments distributed across 2km and includes both high-frequency, 18 m, noise reduction systems and low-frequency, 70 m aperture, systems. An IMS auxiliary 3-Component seismic station is located at the NW corner of the observatory. There is essentially no cultural noise in the area.

Noise reduction experiments

For our experiments we used the MB2000 aneroid microbarometer fabricated by the French Departement Analyse et Surveillance de l Environnement (DASE) and now by Tekelec. These sensors provide a filtered signal between 0.01 and 27 Hz (low-passed below 9 Hz by our anti-aliasing filter) with an adjustable sensitivity. We deployed the low sensitivity (20 mV/Pa) version. The electronic noise of the sensor is 2 mPa rms, between 0.02 and 4 Hz, which is well below natural background noise (DASE technical manual, 1998). Each sensor was placed in an insulating case. Each sensor was deployed with ultrasonic wind velocity, air temperature and humidity sensors. The temperature and humidity sensors were located 1 m above the ground. The wind sensor was 2 m above the ground at all sites except within the wind fence. This sensor was located at 1 m, the height of the microbarometer. In all experiments, the infrasound and meteorological signals were digitized at 20 and 1 sps respectively using a 24 bit Reftek 72A-08 data acquisition system. Each system was run on solar power. The experiments were preceded by calibration tests in the field at PFO, and in the laboratory at IGPP in La Jolla, California. The tests were conducted to ensure all field systems were robust and yielded equal digitized signals for equal input.

We have conducted two wind noise experiments since the summer of 2000. For the first experiment, we constructed a 50% porous, 2 m tall, hexagonal wind fence, a 30 m aperture, 4 arm, porous hose filter. Data were also recorded through a single reference port located 5 cm above the ground to indicate the level of

unsuppressed noise at the observatory. The second experiment involved a reference port, a screened wind fence, a 70 m multiport filter and an 18 m multiport filter. The filters are described in greater detail below.

Porous Hose
This simple filter is easy to deploy and, as a result, commonly used to conduct infrasound site surveys. The filter (typically micro-porous garden hose placed on the ground) integrates pressure variations along its entire length. Uncorrelated pressure variations, such as those due to wind turbulence, sum incoherently and are attenuated. Although noise and the signal of interest might have the same time-frequency, the noise, which is most commonly due to wind turbulence, is incoherent over shorter length scales. There are a few, notable, shortcomings of this filter. The signals are integrated with time delays that become significant as the aperture of the filter increases. The microporosity is known to degrade with time with exposure to UV radiation.

The Wind Shelter.
The wind shelter is akin to a forest as it reduces wind speeds inside the shelter and reduces the scale of the atmospheric turbulence so that much of the acoustic energy that results is displaced beyond the frequency band of interest. The design we have chosen to test has been used by Ludwik Liszka at the Swedish Institute of Space Physics and was forwarded to us by Doug Revelle (LANL). Our fence is shown in Figure 2. The design features of a fence (including the shelter height and porosity) are dependent on conditions at the site (Doug Revelle, personal communication). For example, the height of the shelter is dependent on the roughness of the surrounding topography and local mean wind speeds. A wind speed experiment we conducted at the observatory, in which we collected wind velocity at 1.0, 2.0 and 5.0 m, indicates that a 2 m tall fence is appropriate for this site. In our first two experiments, we tested a wind fence that had 50% porosity with and without an additional wire mesh. In our upcoming experiment, we will test a wind fence that has 0% porosity on the sides and is covered by a wire mesh. In all experiments, the sensor in the wind fence is enclosed in foam inside a porous aluminum shell.

Multiport filters
A new design which employs discrete low-impedance ports was conceived by Benoit Alcoverro at the Departement d'Analyse et de Surveillance de l'Environnement (DASE). This space filter distributes low-impedance ports spatially and signals are summed at a central manifold after propagation through impermeable pipes. The key features of this design is that the propagation distance, and thus the time delay, from each port to the summing manifold is equal and thus phase delays are eliminated. The impedances between the ports and the primary summing manifold are the same for all ports. Doug Christie (PTS, CTBTO) has proposed several innovative space filters based on this idea. The space filters range from 92 ports distributed over an area 18 m across to 144 ports covering an area 70 m across (Figure 2). The smaller filter is considered to be effective at high frequencies. The 70 m aperture filter is considered appropriate for windy sites that require long-period noise suppression.

The aim of all mechanical filters is to sample the atmosphere at a series of points and add their pressure signals mechanically by joining many tubes to a single microbarograph. Because of the finite sound velocity, there are phase delays along the lengths of the pipes, limiting the area that can be averaged over with mechanical filters. Further, because of the size of these spatial filters there is no practical way of measuring their response.

An Optical Fiber Sensor.
Work on an entirely new kind of infrasound sensor - an Optical Fiber Infrasound Sensor (OFIS)- is now underway at IGPP. The OFIS consists of a long optical fiber whose optical path length is sensitive to the ambient atmospheric pressure. The OFIS integrates pressure variations that occur along the line in space defined by the optical fiber s path. The averaging characteristics are governed by the speed of light, so we can make the line over which pressure is averaged extremely long (many km). The distributed sensor approach has many advantages.

In this paper, we will focus on the second experiment. A test of the fibre optic sensor is planned for the

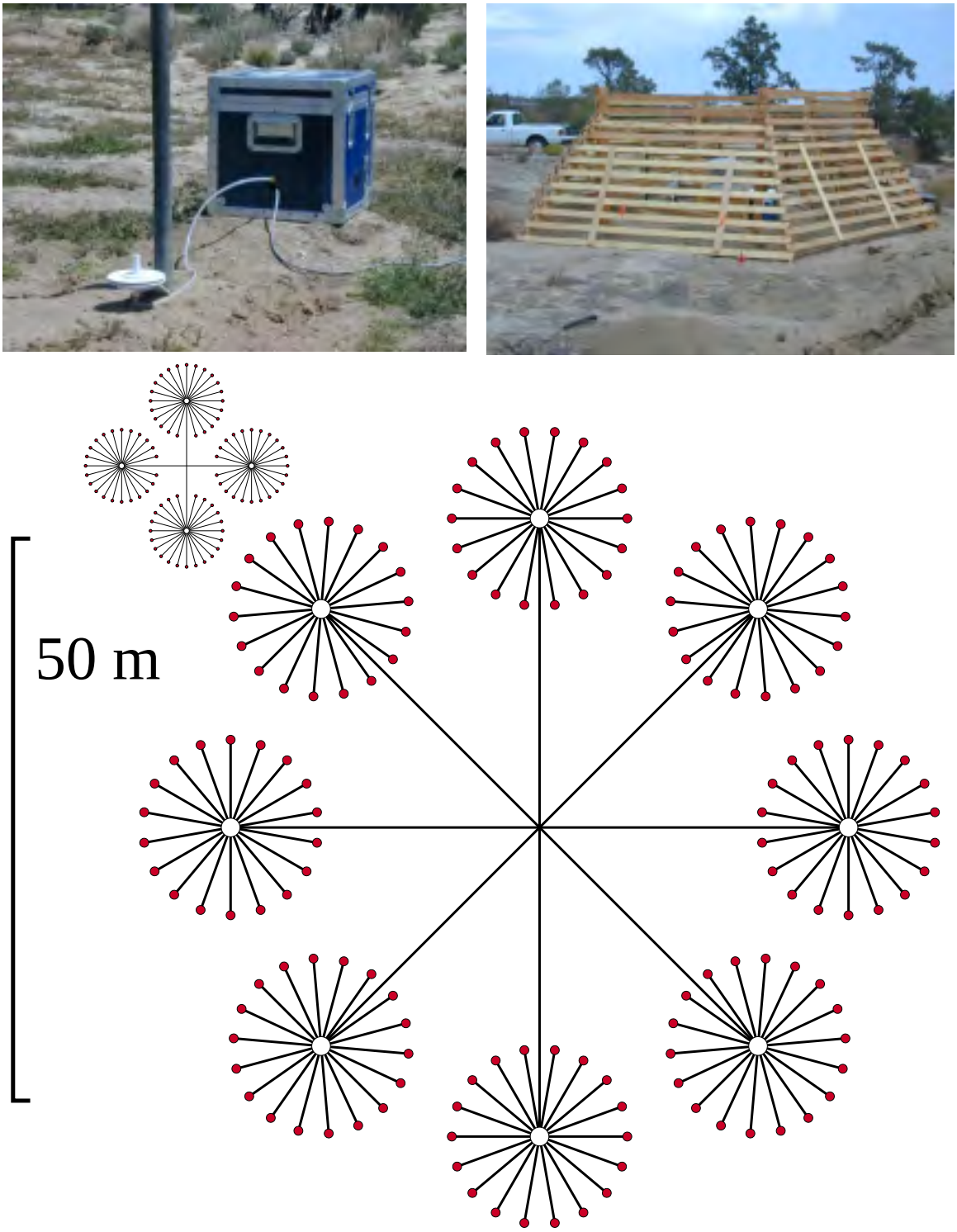

Figure 2. The reference port (upper left), the unscreened 50% porous wind fence (upper right), the 18 m multiport filter and 70 m filter were tested at PFO. In two separate experiments, we tested the wind fence as shown above and coated with a fine wire mesh. The 18 m diameter noise-reducing pipe array is recommended by the Provisional Technical Secretariat for use at high-frequency IMS array elements at stations located in higher wind areas or at all array elements at stations located in low wind areas. The 70 m diameter filter is recommended for use at low-frequency elements in high wind speed areas. The 18 m filter has 92 open-air ports, the 70 m filter has 144 ports.

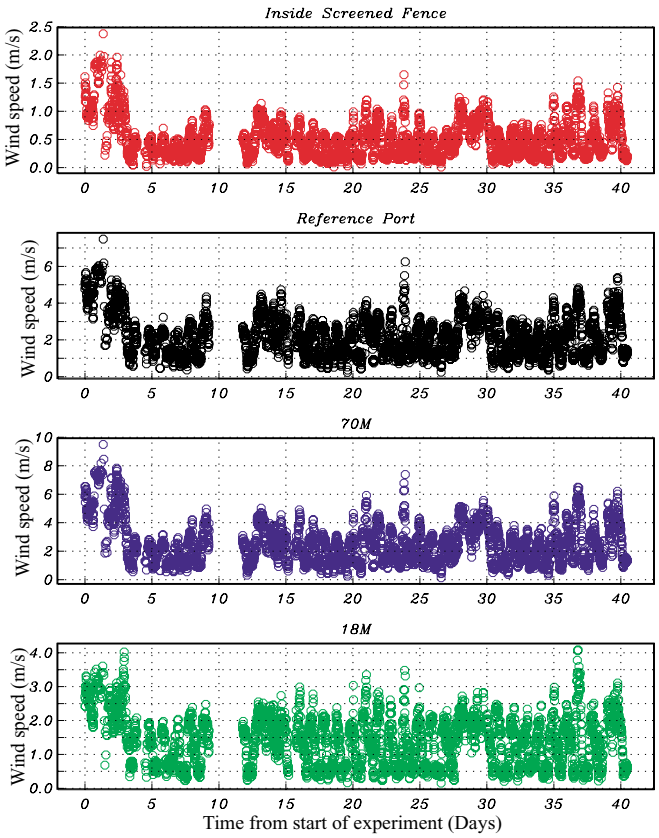

Figure 3. 15 minute average wind speeds taken every 15 minutes during the experiment. Ultrasonic wind sensors were located at 1 m elevation inside the wind fence and at 2 m at the other sites.The data were telemetered in real time to our lab in La Jolla. The break in coverage around day 10 of the experiment resulted from a temporary break in this link.

summer of 2001.

Wind Speed

An essential component of any noise reduction experiment is wind speed data. In Figure 3 we plot wind speeds collected during the main, second, experiment averaged over 15 minute time intervals. Instantaneous wind speeds outside the wind fence occasionally exceed 15 m/s. Diurnal variations are evident at all sites. Wind speeds are lowest in the wind fence and at the site of the 18 m filter, which was located in a sparse Pinon pine forest. We have observed that the screened wind fence reduces wind speeds by up to 90%.

Stacked Spectra

At the heart of our analyis of recorded data is the calculation and stacking of power spectral estimates. Stacking is necessary to reduce the statistical uncertainty inherent in the spectral estimation process and clearly reveal the dependence of average noise levels on wind speeds. We divide the filtered pressure records at each site into 15 minute intervals. The second experiment spanned > 768 hours and thus yielded 3074 time intervals. From each 15 minute segment of data, we calculate a Welch time-averaged power spectrum. Although we collected wind speed data at all sites, for the purpose of comparing data collected at the same time at the different sites, we used just the wind speed data collected at 2 m at the reference port. The wind speeds in the wind fence were reduced sharply by the walls of the fence. The wind speeds at the 18 m element were also reduced by the forest (Figure 3). To describe the increase of infrasonic noise at the different sites with increasing wind speed, we bin the spectral estimates into 0.5 m/s wind speed intervals. The result is shown in Figure 4. In this figure, each curve in each panel represents a single bin. The lowest curve in each panel corresponds to estimates taken when the wind at the reference site was < 0.5 m/s. At the four sites, we see infrasonic noise increases at all frequencies with increasing wind speed. The microbarom peak is most clearly resolved at the 70 m filter. The peak is seen clearly at wind speeds up to 1.5 m/s and in some individual spectra at wind speeds up to 2.5 m/s. The effectiveness of this filter at reducing infrasonic noise below 1 Hz is evident however the resonance peaks above 1 Hz are significant at all wind speeds (Figures 5 and 6). We observe peaks at 2.65 and 7.95 Hz. The frequency of the second resonance peak is 3.0042 times the first (Figure 5). The frequencies of the two observed peaks are nearly independent of wind speed (Figure 5) and temperature. From 0 to 35°C, the frequency of the first peak rises 1.5%, the second rises 0.8%. The pipes in this filter were buried ~ 0.60 m. The temperature was measured 1 m above the surface. The resonance peaks depend on the acoustic velocity in the pipes, which depends strongly on the temperature. The independence of the resonant frequency on temperature indicates the level of insulation provided by the ground. The separation between the resonance peaks is equal to 1/T, where T is the travel time between reverberations. This equals V/L, where V is the acoustic velocity and L is the distance. From 0 to 35°C, the separation in the resonance peaks is estimated to change from 5.2924 to 5.3064 Hz. As

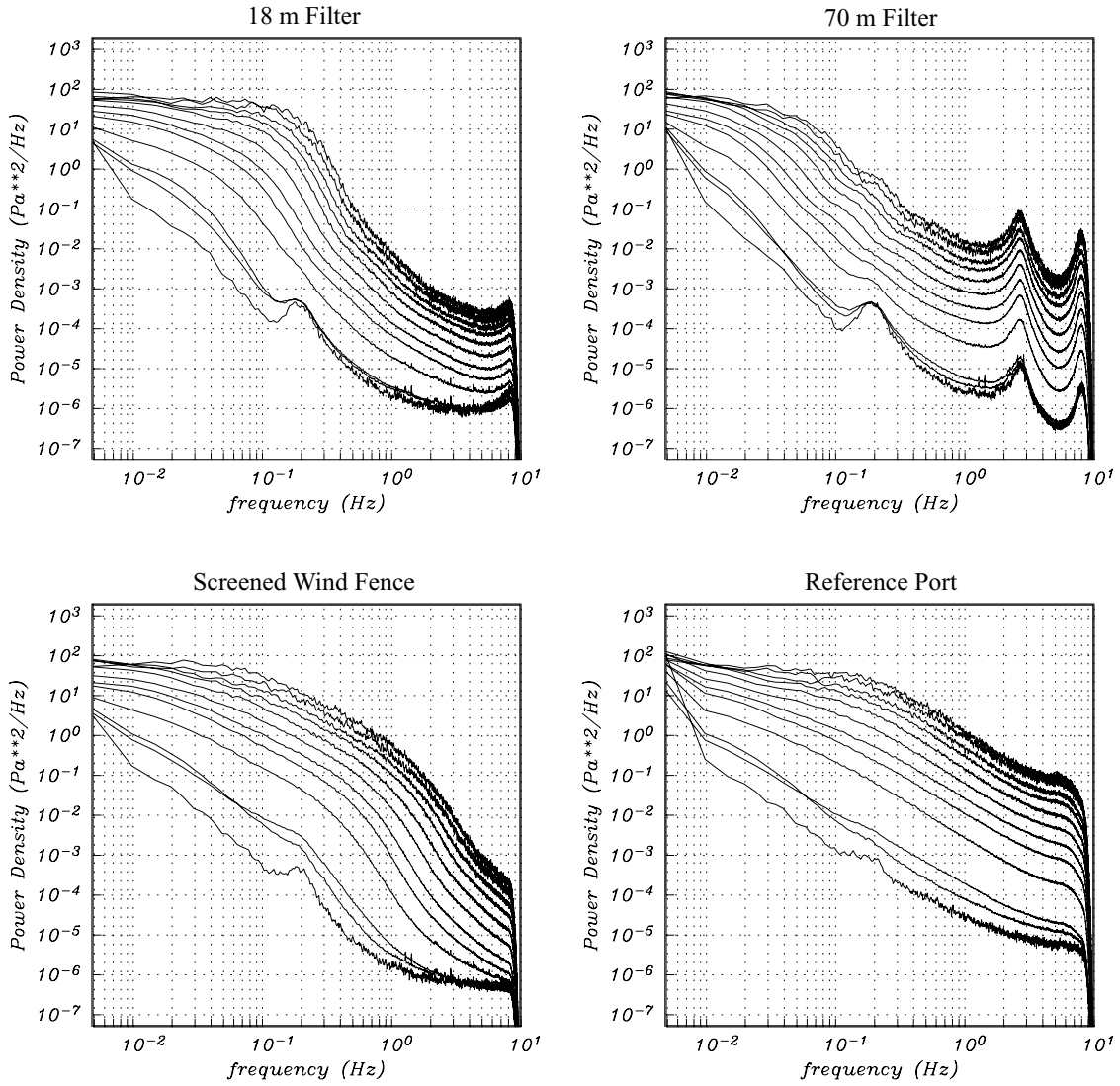

Figure 4. Average power spectra as a function of wind speed. Each curve represents the average power density determined from an unweighted stack of individual power spectral estimates. Estimates were binned by wind speed measured at a height of 2 m at the reference site. Each bin spanned 0.5 m/s in speed, with the first bin beginning at 0.0 m/s.. Power spectral estimates were taken from 15 minute intervals of data.The microbarom peak is seen most clearly at the 18 and 70 m filters at wind speeds below 1.5 m/s. Infrasonic power at all four sites rises rapidly between 1.5 and 2.0 m/s. Resonance peaks are seen in the data from the 70 m filter at ~ 2.67 and 7.95 Hz.In total, there were 3074 spectral estimates from 768.5 hours of recording. The bin from 1.0 to 1.5 m/s included > 800 spectral estimates.

L is unchanged, the frequency change implies a velocity change of 0.26%. As the acoustic velocity (in dry air) is ~ 20.07 (K)^0.5 (McKisic, 1997), where K is temperature in °K, this indicates that the temperature varied in the pipe by 1.4°C, well below the temperature variation at 1 m of 35°C.

Modeling Resonance in the multiport filters

Resonance enriches the spectrum at certain, equipspaced, frequencies and produces substantial coda. Following Sereno and Orcutt (1985), who observed resonance in recordings of seismic energy that propagates in the oceanic water column and sediment, we model resonance in multiport pipe systems as follows. We consider a wavelet, w(t), resonating in a simplified pipe system that consists of a single pipe, open at

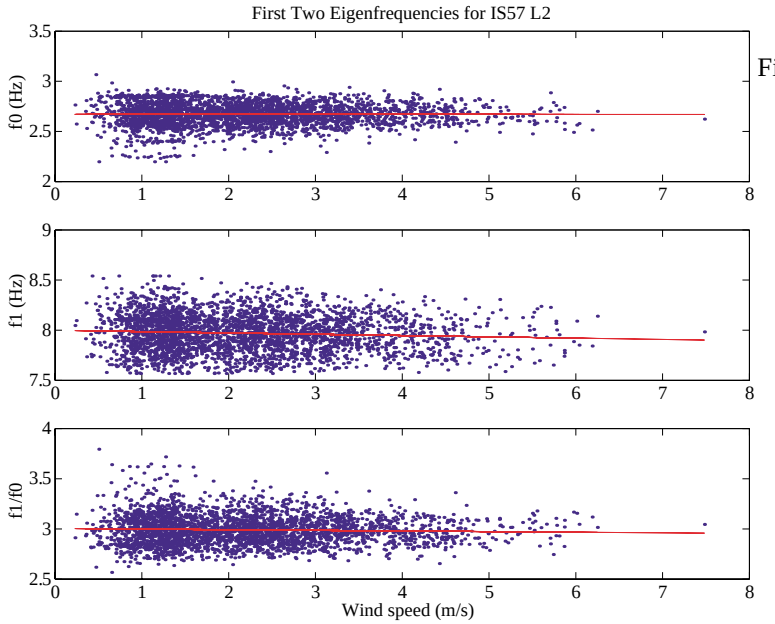

Figure 5. Resonance peaks in data from the 70 m filter at IS57 L2 as a function of wind speed. Only a very weak dependence on wind speed is observed. The linear fit indicates that the first peak, f0, is given by .0001V + 2.6701 (where V is wind velocity). f1 = 0.013V+7.9985. The ratio of the two peaks is 3.0042. The dependence on temperature, T, is f0 = 0.0013T+2.643; f1 = 0.0017T+7.9354 where T is temperature in °C.

both ends. The linear sum of all reverberations at the half-way point of the pipe (where the microbarometer is located) is given by:

$$x(t) = w(t) * \left[\tfrac{1}{T} III\ (\tfrac{t}{T})\ e^{-\alpha|t|} H(t) e^{-i\pi \frac{t}{T}} \right]$$

where T is the time between successive reverberations and is equal to L/V where L is the length of the pipe and V is the acoustic velocity in the pipe. The shah function is tapered exponentially to simulate the effect of attenuation due to propagation in the pipe and leakage at the reflection points. The Heaviside step function, H(t), excludes any acausal energy. The final exponential is required by the p phase shift incurred by reflection at each end of the pipe. By Fourier transforming this equation, we see that the spectrum of the original wavelet is multiplied by an infinite set of staggered tapering functions which decay at a rate determined by the attenuation parameter a. The amplitude spectrum of the sum of wavelets is given by:

$$|\tilde{X}(f)| = |\tilde{W}(f)||III(fT + \tfrac{1}{2}) * \ \tfrac{\alpha - i2\pi f}{(\alpha^2 + 4\pi^2 f^2)}\ |$$

The theory predicts spectral modulations at $f_n = (2n+1)/(2T)$ - the eigenfrequencies of an organ-pipe mode (Aki and Richards, 1980). The longer the pipe, or equivalently the slower the acoustic wave propagation in the pipe, the more closely spaced the spectral highs will be. In the 70 m filter, the first and second resonance peaks are predicted, and observed, at 2.67 and 7.95 Hz respectively (Figure 5). Without the phase shift at the reflection points, the second spectral peak would be observed at double, not triple, the frequency of the first. Using the recording from the single reference port as the basic wavelet, we find that the spectral peaks observed in the 70 m filter are accurately reproduced by this simple theory (Figure 7). We are preparing a more complete theory that describes resonance in the full pipe system shown in Figure 2 and uses attenuation and acoustic velocity parameters constrained more accurately by observation.

Comparison of different noise reduction systems

Figure 8 summarizes the intercomparison of the 18 and 70 m multiport filters with the screened wind fence and the reference port. The 12 panels show the binned and averaged spectral estimates from all four sites and the 95% confidence limits from a chi-squared analysis at wind speeds ranging from 0 to 0.5 m/s (first panel) to 5.5 to 6.0 m/s (lower right panel). We observe the growth of infrasonic noise at all sites with

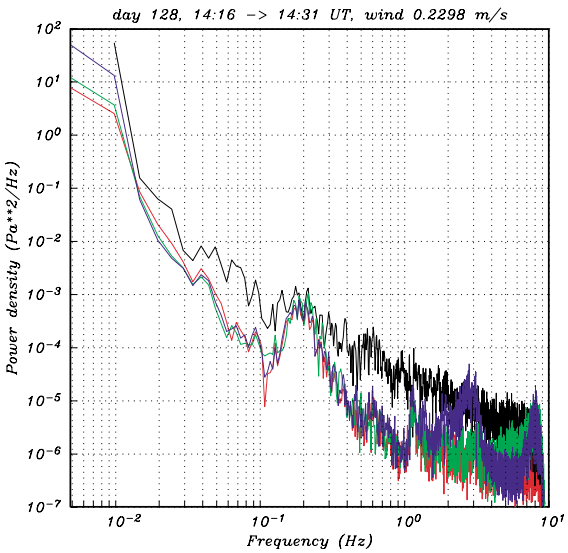

Figure 6. Power spectral estimates taken from the 4 filters at the lowest wind speed observed during the experiment. The resonance peaks in the data from the 70 m filter (blue curve) are clearly observed at a time when wind speeds average 0.23 m/s.

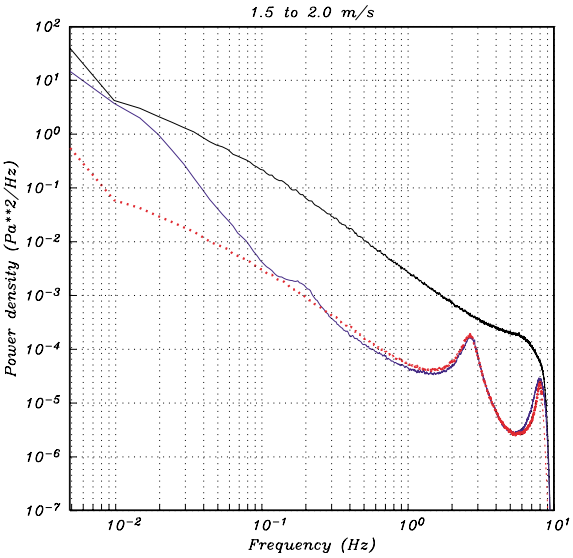

Figure 7. Linear superposition theory accurately reproduces the resonance peaks. In this figure, we show the average spectral estimate from the reference port (black), and the 70 m filter (blue) for the bin between 1.5 to 2.0 m/s. The simulation is shown in red.

increasing wind speed. The confidence limits are broadest at the highest and lowest speeds as we have relatively few spectral estimates in those bins. The bin from 1.5 to 2.0 m/s represents stacks of > 800 spectral estimates. At this wind speed, the confidence limits are indistinguishable from the averages. We observe statistically significant differences in the noise levels between all sites at all wind speeds. All filters reduce noise levels except at the longest periods. Presumably, noise reduction at periods above 50 s is beyond any practical mechanical noise reduction scheme. The 70 m filter provides the most significant noise reduction at long periods. The microbarom peak is not seen in the recordings made via the reference port or in the wind fence except at the lowest wind speeds (Figures 6 and 8).

Signals from the April 23 meteor explosion

The widely reported explosion of a large meteor west of Baja California on April 23, 2001 was recorded by the IMS array IS57 and by all sites in our noise experiment. The large signals provide an opportunity for us to determine the extent, if any, to which signal is degraded by the different filters. Preliminary results are shown in Figure 9. The timeseries from the 18 and 70 m filters are indistinguishably eye from the one obtained via the reference port. The latter, presumably, gives the truest representation of a signal that is significantly above noise. The power spectral estimates, however, show the extent to which resonance distorts the high frequency end of the signal spectrum.

CONCLUSIONS AND RECOMMENDATIONS

Planned wind noise experiments

Our third noise reduction experiment will occur during the summer of 2001. We will test a wind fence that has solid walls, and a screen across the top, against the fibre optic sensor. We will also bury a sensor in a fine gravel pit following specifications developed by the SMU group. Two sites at the IMS array use 70 m filters that are located in insulating pipes at the surface. We will test one of these filters to assess the effectiveness of the insulation at moderating temperature variations in the pipes and reducing convective

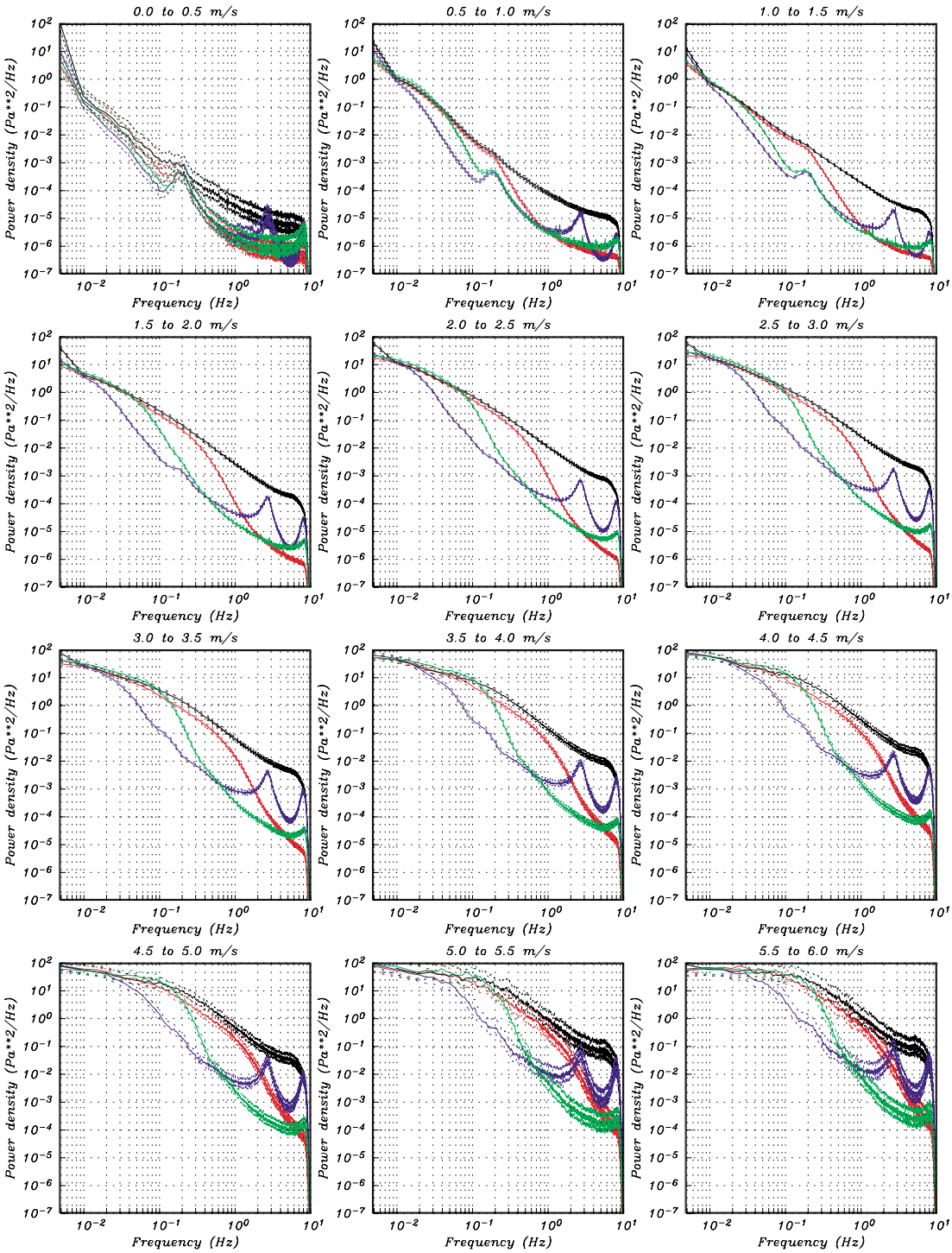

Figure 8. Average power spectral estimates taken from noise recordings at the reference port (black), the screened wind fence (red), the 18 m multiport filter (green) and the 70 m filter (blue). Wind speeds were taken at 2 m at the reference site and averaged over 15 minutes. Plotted with the average spectral estimates are 95% chi-squared confidence limits. The limit curves are indistinguishable from the averages at wind speeds between 2 and 5 m/s. At low and high wind speeds, the coverage is low and the uncertainty is relatively large. The resonance peaks in the 70 m filter are seen to be significant at all wind speeds however this filter is highly effective at long periods. No filter suppressed noise at periods beyond 50 s to 100 s.

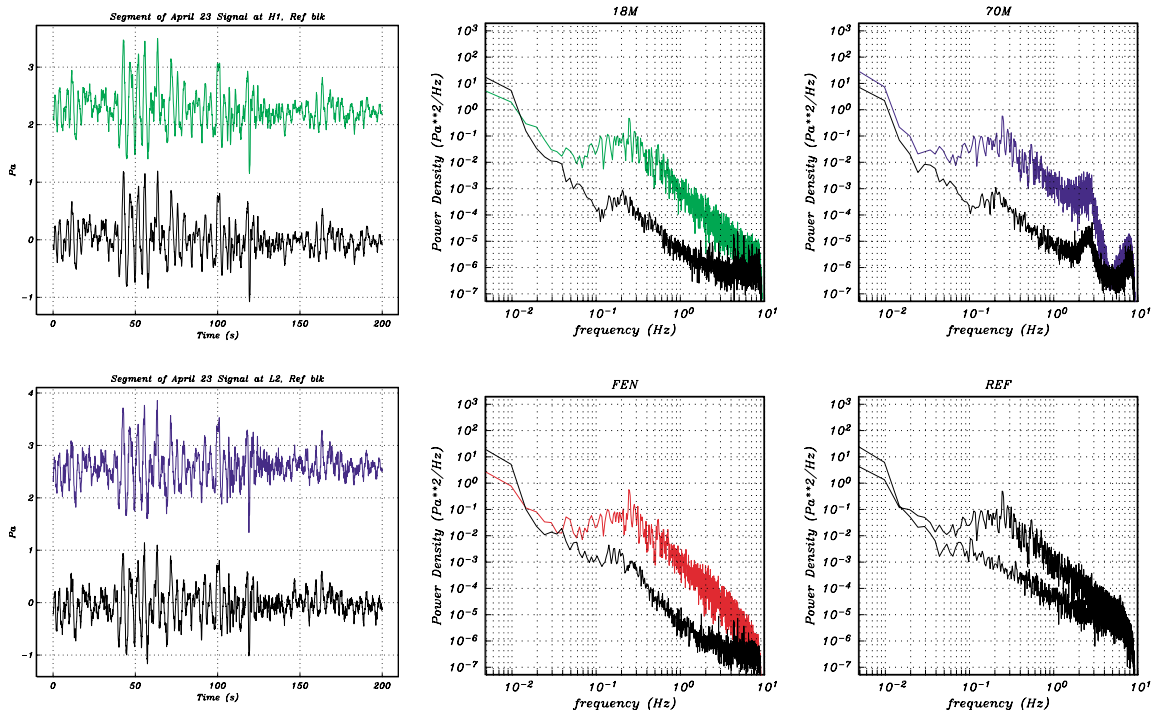

Figure 9. The widely reported explosion of a large meteor off the coast of California was recorded by the IMS array IS57 at PFO and by sensors in our wind noise experiment. On the left, we show recordings from the reference port (black) and from the 18 m filter (green-top) and 70 m filter (blue). Spectral estimates from the four sites are shown to the right. The 18 m filter, 70 m filter, wind fence and reference port are shown to the right in the upper left, upper right and lower two panels respectively.

noise in the acoustic pipes.

The resonance problem

We are considering a number of solutions to the resonance problem observed in the 70 m filter. The first step in our analysis of this problem is modeling the reverberations. Our first attempt at modeling the resonance peaks was presented in this paper. We will now extend this theory to cover resonance in a pipe filter with an arbitrary number of arms (8 are used in the 70 m filter) and secondary resonance in the clusters of shorter pipes. The primary and secondary pipes produce separate sets of resonance peaks. The theory will allow us to experiment with any combination of secondary and primary pipe lengths. We will seek designs in which resonances are less significant. We will also explore mechanical changes to the port design that might limit the amplitude of the reflections.

We will transmit controlled signals in pipes to measure the phase shift at the reflection points and the attenuation of the signal with time as well as the acoustic velocity.

REFERENCES

Aki, K., and P.G. Richards (1980), Quantitative Seismology: Theory and Methods, W.H. Freeman, San Francisco, Calif.

McKisik, J.M. (1997), Infrasound and the infrasonic monitoring of atmospheric nuclear explosions: A literature review, Final report submitted to the DOE and Phillips Lab, PL-TR-97-2123.

Sereno, T.J., and J.A. Orcutt (1985), Synthesis of realistic oceanic Pn wave trains, *J. Geophys. Res.*, 90, 12755-12776.

COMPARATIVE EVALUATION OF SELECTED INFRASOUND NOISE REDUCTION METHODS

Eugene Herrin,[1] G. G. Sorrells, [2] Petru Negraru, [1] J.G. Swanson, [1] Paul Golden, [1] and Carl Mulcahy [1]

Southern Methodist University, [1] Seismic Diagnostic, Inc. [2]

Sponsored by Defense Threat Reduction Agency

Contract No. DTRA01-00-C-0093

ABSTRACT

The objective of this project is to identify and characterize potential low-cost alternatives to the conventional pipe array wind-noise-reduction method. Initial efforts have focused upon the use of a porous medium as a wind noise filter. A simple theoretical model of wind-generated noise in a rigid, porous medium has been developed. This model predicts that the attenuation, A_w , of the noise in this type of medium is related to the observation depth, *d*, by an equation of the form;

$$A_w = \exp(-\alpha_w d) \qquad 1$$

where

$$\alpha_w = \mathrm{Re}\left(\frac{\omega^2}{c^2} + i\frac{\sigma\omega}{P_0}\right)^{\frac{1}{2}} \qquad 2$$

and, c, is the convection velocity of the wind-generated pressure field, σ, is the effective flow resistance of the medium, and P_0 is the static atmospheric pressure at the elevation of the observation point. The results of a small-scale field trial are described in the main body of this report. They validate the predicted exponential attenuation of the wind noise. They also indicated that a finite, porous body would act as a half-space for wavelengths that are less than 3-4 times its horizontal dimensions.

The theoretical model of Attenborough et al (1986) has been adopted to predict the attenuation of airborne sound in a porous medium. This model predicts that the attenuation, A_i , of the infrasound signal in this type of medium is related to the observation depth, *d*, by an equation of the form;

$$A_i = \exp(-\alpha_i d) \qquad 3$$

Sabatier et al (1993) have shown that in the bandwidth of interest to the infrasound community

$$\alpha_i \approx \mathrm{Re}\left(i\frac{\sigma\omega}{P_0}\right) \qquad 4$$

The combined wind noise and infrasound signal models therefore predict that infrasound signal-to-noise ratios will exponentially increase as a function of the observation depth in a frequency range defined by the constraint that;

$$f > \frac{\sigma c^2}{4\pi P_0} \qquad 5$$

where f is the frequency.

The preliminary results of a field experiment to test this constraint and a discussion of its practical implications are summarized in the main body of this report.

KEY WORDS: infrasound, wind noise, attenuation

OBJECTIVE

Atmospheric pressure changes generated by the local surface are the primary factor limiting the infrasonic detection threshold in the 0.02-to 5.0-Hz bandwidth. Two-dimensional spatial filters are used to combat this problem. In the currently favored approach, the filters consist of acoustically coupled, hollow, rigid tubes that contain or permit access to a distribution of small inlet ports. These filters are commonly referred to as "pipe" arrays. The maximum linear dimensions of a "pipe" array are chosen to yield a flat response to infrasonic signals below some selected cut-off frequency; whereas its spatial configuration is chosen to provide an azimuthal response to infrasound signals that is approximately isotropic. Finally, the inlet port distribution is chosen to promote the cancellation of those components of the local atmospheric pressure field that are characterized by relatively short correlation lengths. The "pipe" arrays recommended by the Provisional Technical Secretariat (PTS) for use at stations in the International Monitoring System (IMS) infrasound monitoring network are the most recent examples of this particular type of spatial filter.

While the 'pipe" array approach has been used with success in the past to enhance infrasound signal-to-noise ratios (SNR) in the bandwidth of interest, it is expensive to implement. For example, it is conservatively estimated that the fabrication and deployment costs for the installation of one of the PTS-recommended "pipe" arrays at each of the elements of an IMS infrasound array will account for as much as 25-35 % of the total expenses incurred for sensor element deployment. The objective of this project, therefore, is to identify and evaluate alternative approaches to infrasonic spatial filtering that have the potential to yield SNR improvements equivalent to or better than the "pipe" array approach, but at a substantially lower implementation cost.

RESEARCH ACCOMPLISHED

Prior research has identified two low-cost alternatives to the "pipe" array approach for infrasonic spatial filtering. These are:

- The use of a porous medium as a spatial filter; and
- The use of compliant tubing for the configuration of infrasonic spatial filters.

Project research to date has focused exclusively on the evaluation of the porous medium alternative. The essential results of this research are summarized in the following paragraphs.

Theory

It is a common observation to note that airborne sound is attenuated by its passage through a porous medium. Sabatier et al (1986) have shown that in a semi-infinite poroelastic solid such as porous ground, this phenomenon is both frequency and wavelength dependent. Attenborough et al (1986) have also demonstrated that in the audible frequency range, the attenuation of airborne sound in a porous medium is dominated by the wavelength dependent term. However, arguments offered by Sabatier et al (1993) imply that in the infrasonic frequency range of interest to the nuclear explosion monitoring community, the attenuation of airborne sound is dominated by the frequency dependent term. In particular, the results of the research cited above imply that if the inlet port to a microphone or microbarograph is placed at a depth, $\boldsymbol{d}$, beneath the surface of a semi-infinite porous solid, then the attenuation operator, $\boldsymbol{A_I}$, is of the form;

$$\boldsymbol{A_i}(\boldsymbol{d}) = \mathbf{exp}(-\boldsymbol{\alpha_i d}) \qquad \mathbf{1}$$

where $\boldsymbol{\alpha_i}$ is referred to as the infrasound dissipation function and in the infrasound bandwidth of interest;

$$\boldsymbol{\alpha_i} \approx \mathbf{Re}\left(\sqrt{\boldsymbol{i}\frac{\gamma\sigma\omega}{\rho_o c_o^2}}\right) \qquad \mathbf{2}$$

The variables and parameters appearing on the RHS of equation 2 are defined as follows:

γ = specific heat ratio for air
σ = effective flow resistance of the porous solid
ω = angular frequency
ρ_o = density of air at the observation point
c_o = sound speed in air at the observation point

Sorrells (2001) has shown that a similar operator describes the attenuation of wind-generated atmospheric pressure changes in a semi-infinite porous medium. Specifically he has shown that if A_w is this operator, then;

$$A_w(d) = \exp(-\alpha_w d) \quad (4)$$

where α_w is the wind noise dissipation function and is given by

$$\alpha_w = \mathrm{Re}\left(\sqrt{k_w^2 + i\frac{\sigma\omega}{P_o}}\right) \quad (5)$$

The variable, k_w , that appears on the RHS of equation 5 represents the horizontal wavenumber characterizing the wind generated pressure field and may be treated as a complex number to account for its correlation scale. The parameter, P_o , is defined to be the standard atmospheric pressure at the elevation of the observation point. It therefore follows that if $\Delta SNR(d)$.is the change in the infrasonic SNR at depth, d, relative to observations made at the surface, then

$$\Delta SNR(d) = \exp[d(\alpha_w - \alpha_i)] \quad (6)$$

It is seen from equation 6 that the SNR increases exponentially as a function of increasing depth provided that $\alpha_w > \alpha_I$. Now, for the purposes of illustration, it will be assumed that k_w is real. Therefore,

$$k_w = \frac{\omega}{c_w} \quad (7)$$

where c_w is the horizontal advection speed of the wind generated pressure field. Furthermore, it may be reasonably assumed that the ideal gas law describes the equation of state for air. Therefor

$$\frac{\rho_o c_o^2}{\gamma} = P_o \quad (8)$$

Then using these definitions and expressing the change in SNR in dB relative to the surface it follows that

$$\Delta SNR_{dB}(d,\omega) = 20\,Log(e)\left[d\left(\mathrm{Re}\left(\sqrt{\frac{\omega^2}{c_w^2} + i\frac{\sigma\omega}{P_o}}\right) - \mathrm{Re}\left(\sqrt{i\frac{\sigma\omega}{P_o}}\right)\right)\right] \quad (9)$$

By inspection of equation 9 it is seen that if f is the frequency in hertz then for

$$f << \frac{\sigma c_w^2}{2\pi P_o} \quad (10)$$

$$\Delta SNR_{dB}(d,\omega) \approx 0 \quad (11)$$

and for

$$f >> \frac{\sigma c_w^2}{2\pi P_o} \quad (12)$$

$$\Delta SNR_{dB}(d,\omega) \approx 20\,Log(e)\frac{\omega d}{c_w} \quad (13)$$

Clearly then, given the assumption of a real advective wavenumber, and assuming that the advective speed does not increase as a function of increasing frequency, there is always some "cross-over" frequency that satisfies the constraint implied by equation 12. It then follows that above this critical frequency, the use of a porous medium spatial filter will always increase the infrasound SNR. Whether or not this frequency can be placed near the lower end of the bandwidth of interest, through the choice of the material properties for the porous medium, is an issue of considerable practical significance.

An experimental project has been undertaken to address this issue as well as to validate the theoretical arguments presented above and to test the qualifying assumptions. In addition, a literature search is underway to identify low-cost materials with relatively low flow resistances that can be used as an effective infrasonic spatial filter. The results of these studies to date are briefly summarized in the following paragraphs

Experimental results

Equations 12 and 13 predict that any meaningful improvements in the infrasound SNR resulting from porous medium spatial filtering, are dependent only on the ratio of the installation depth to the advective wavelengths characterizing the wind generated components of the atmospheric pressure field. An important practical implication of this prediction is that the lateral dimensions of a porous medium spatial filter need only be large enough to accommodate the 'semi-infinite" assumption inherent to the theoretical model. Prior experience acquired during studies of wind generated seismic noise suggested that as a "rule of thumb", the "semi-infinite" assumption will be valid for all wavelengths that are less than 2-4 times the maximum horizontal dimensions of the porous medium spatial filter. A small-scale field experiment was planned to test this assumption. It was implemented in the fall of 2000 at the TXAR seismic array to take advantage of existing data acquisition and transmission assets. The configuration of the data acquisition elements used for the initial experiments is illustrated in Figure 1.

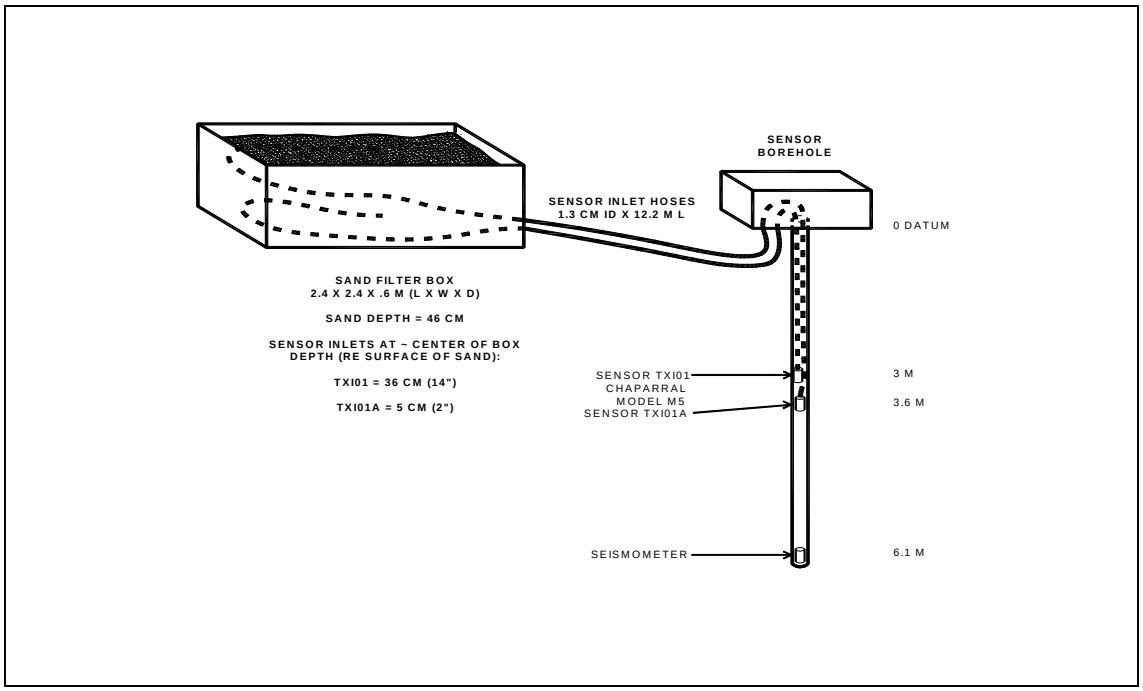

Figure 1. Configuration of the infrasound data acquisition system for the initial porous medium spatial filter field test.

The experimental porous medium spatial filter is simply a rectangular box filled with sand dredged from a nearby dry creek bed. The horizontal and vertical dimensions of the box are 2.4 and 0.6 meters, respectively. The thickness of the sand fill is approximately 0.5 meters. The inlet port of a flexible hose is placed at a depth of approximately 0.3 meter beneath the sand surface to couple the porous medium spatial filter to a Chapparal

model MS microphone installed in a nearby bore-hole. This system is designated as TXI01. An identical system configuration is used to provide data referenced to the surface of the sand fill. This system is designated as TXI01A . The flexible hose inlet port for this system is placed at a depth of about 0.05 meters to avoid "whistling" noise during windy periods. It is also placed directly above the lower hose inlet port. Given this configuration, it is readily seen that the modulus of the transfer function relating observations acquired by TXI01 to those acquired by TXI01A yields the attenuation operators for this particular realization of a porous medium spatial filter. The data from the two systems are sampled continuously at the rate of 40 SPS and transmitted in real time to the Southern Methodist University (SMU) Geophysics Laboratory for permanent storage and analysis.

Prior to the porous medium spatial filter trials, the two flexible hoses were placed side by side to test for differences in the response characteristics of the two systems. The data for these tests were acquired during selected windy periods. Sample records, 15 minutes in duration, were simultaneously extracted from the windy period data and processed to yield power spectral density estimates and the transfer function characterizing the data recorded by the two systems. An example of the results obtained during these tests is shown in Figure 2. These results indicate that apart from a slight difference in gains, the response of the two systems is essentially identical. The gain correction factor derived from these tests is about 2 dB and has been incorporated into the data processing codes used for the porous medium spatial filter trials.

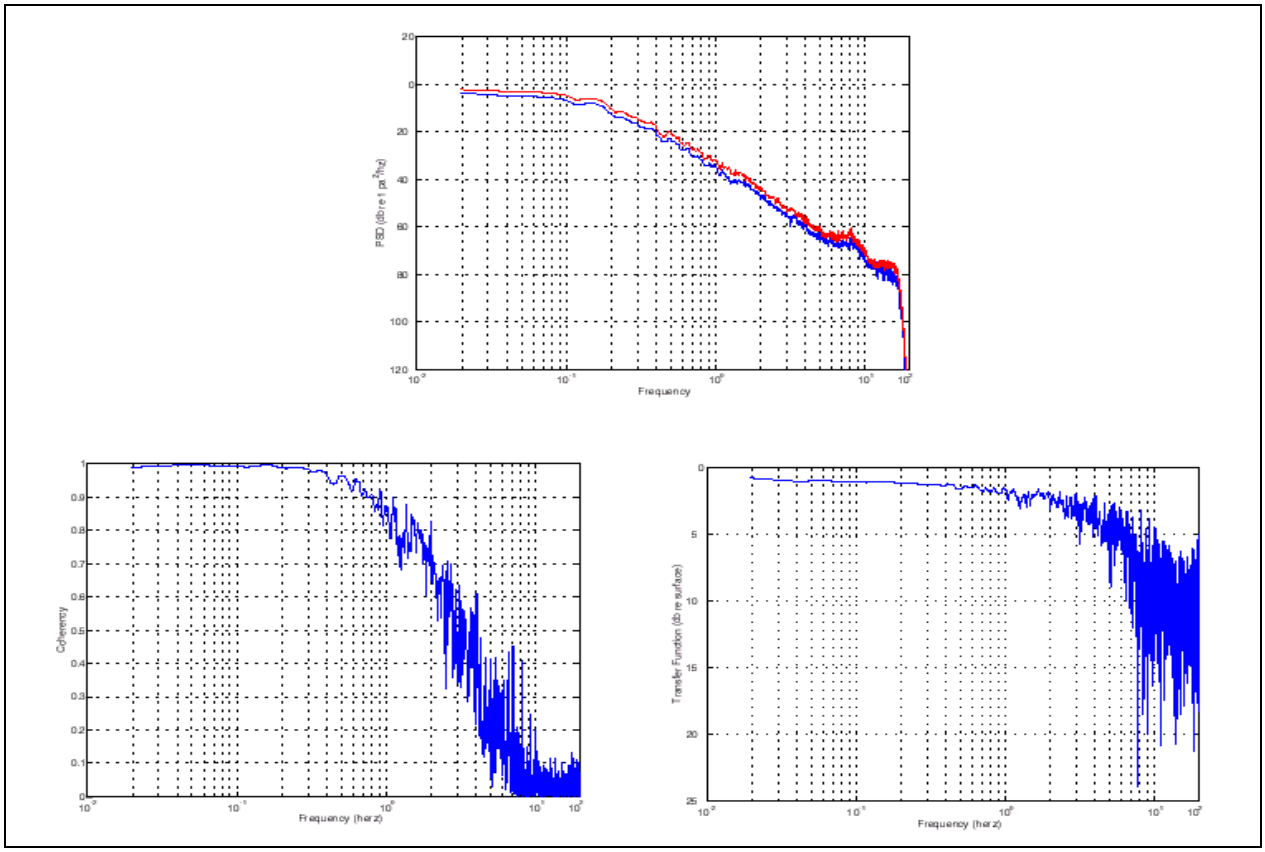

Figure 2. An example of one of the trials of the side-by-side system response tests. The upper panels compare the spectral estimates of noise recorded by the two systems during a fifteen-minute windy period. The lower left panel shows the coherence between the outputs of the two systems. The lower right panel shows the modulus of the transfer function relating the two outputs.

The data sampling and processing procedures used for the initial porous medium spatial filter trial were identical to those described above with the exception that sample data records were acquired during both low and moderate surface wind conditions and separated into two different files. The basis for this segregation is

the reasonable expectation that the advective speeds characterizing the wind generated pressure field under low and moderately windy conditions will differ by a factor of 2 or more. Therefore, significant differences between the experimental attenuation operators characterizing the two different data sets are to be expected provided that:

- Equation 4 above adequately describes the attenuation of wind generated pressure changes in a porous medium;
- The wavelength dependent term appearing on the RHS of equation 5 above dominates the frequency dependent term, at least during low wind conditions;
- The horizontal dimensions of the experimental porous medium spatial filter described above satisfy the qualitative "semi-infinite" assumption identified above over some observable frequency range.

The experimentally determined attenuation operators showed considerable sample-to-sample variation in both data sets. The logarithms of these operators were averaged to reduce this variation. The resultant average attenuation operators characterizing low and moderately windy conditions are shown as irregular solid lines in Figure 3. The smoothly varying solid lines seen in this figure are the "best fit" predicted attenuation operators. Equation 4 was used for their calculation, given the assumption of a real advective wavenumber. The corresponding "best fit" average advective speeds were found to be 6 meters/sec for the low wind data set and 12 meters/sec for the moderate wind data set. The clear separation between the two experimentally determined operators at frequencies above 1 Hz is interpreted to mean that the experimental porous medium spatial filter approximates a semi-infinite porous solid for advective wavelengths shorter than about 6-12 meters.

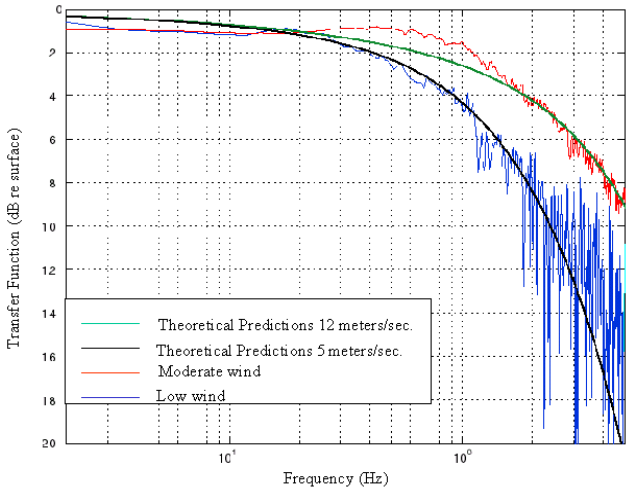

Figure 3. A comparison of the experimentally determined attenuation operators for time periods characterized by low and moderately high surface wind speeds. The irregular curves identify the experimentally determined operators. The solid lines identify the "best fit" predicted attenuation operators for both cases.

The success of the initial experiment encouraged the decision to expand the field test to evaluate the theoretical predictions and qualifying assumptions listed above. Accordingly, the vertical dimensions of the experimental porous medium spatial filter were doubled to 1.2 meters, and the thickness of its sand fill was increased to approximately 0.9 meters in early April 2001. The inlet port for the flexible hose component of the TXI01 system was placed at a depth of 0.84 meters relative to the surface of the sand fill. The inlet port for the flexible

hose component of the TXI01A system was placed at a depth of 0.1 meters relative to the surface of the sand fill and directly above the TXI01 inlet port. In addition, a Texas Electronics Instrumentation Package, containing a Model TD-104D Wind Direction Sensor and Model TV-114 Wind Speed Sensor, was coupled to a REFTEK Model 72A-08 data acquisition system and deployed near the experimental porous medium spatial filter to provide the off-line capability to record wind data during this field trial. Since the completion of the augmentation of the experimental porous medium spatial filter, 67 sample data records have been acquired, using procedures identical to those outlined above. However, at the time for submission of this report, the processing and analysis of the wind data for the corresponding time periods was not complete. Therefor, no attempt has been made to segregate the sample records into wind related categories. The logarithmic mean of the existing sample population of experimental attenuation operators is shown as the solid line in figure 4. The curves formed by discrete stars (*) seen in this figure define the standard deviation bracket of the sample population. It is clear from these results that the current configuration of the experimental porous medium spatial filter effectively attenuates wind noise. Before it intersects the system noise threshold near one hertz, The mean attenuation is about 40 dB. The increase in the mean attenuation operator above two hertz is attributed to the to the finite box dimensions. While this appears to be a significant feature of the experimentally derived transfer functions, actual contributions to the attenuated wind noise spectrum are negligible. The substantial expansion of the width of the standard deviation brackets that is seen to occur at frequencies greater than about 0.25 hertz should also be noted. We believe this phenomenon reflects;

- The location of the so-called "cross-over" frequency, where according to equations 5 and 12 the wavelength dependent term exceeds the frequency dependent term in the wind dissipation function characterizing the porous medium spatial filter.
- An increasing contribution of wind generated pressures changes to the background noise at frequencies greater than 0.25 hertz, and;
- The variability of the advective speeds and correlation states of the wind generated pressure field sampled by our data acquisition procedures.

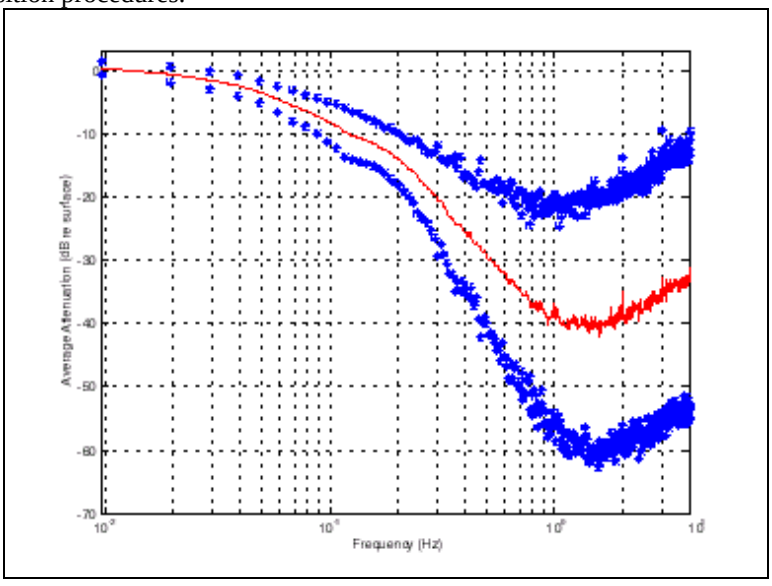

Figure 4. Wind noise attenuation data. The mean wind noise attenuation operator characterizing the augmented experimental porous medium spatial filter for a sample population containing 67 fifteen-minute records is shown as the solid line. The curves identified by stars(*) are the mean values + and - the standard deviation of the sample population.

The corresponding infrasound attenuation operator for this particular realization of a porous medium spatial filter has yet to be defined experimentally. Despite a careful visual search of the TXAR infrasound and seismic records since the beginning of the second field trial in April 2001, we have been unable to confirm the detection of any infrasound signals. However, assuming the validity of equations 2 and 8, and given a reliable measurement of the effective flow resistance of the sand fill, a theoretical infrasound attenuation operator can be derived with the aid of equation 1. The ubiquitous occurrence of microbaroms in the 0.15- to 0.3-Hz

bandwidth provides the experimental basis for the measurement of the effective flow resistance of the sand fill, since they are, insofar as we are concerned, a narrowband infrasonic signal. Observations made during calm periods indicate that the microbaroms are attenuated by about 8-10 dB by the current configuration of the porous medium spatial filter. Assuming a mid-point frequency of 0.2 hertz for the microbarom band it may be found from the use of equations 2 and 8 that this value implies an effective flow resistance of ~200,000 n-sec/m^4. The predicted infrasound attenuation operator for a porous medium with a flow resistance of this magnitude and an observation depth of 0.8 meters is compared to the mean wind attenuation operator for the experimental porous medium spatial filter in figure 5. It is seen from this comparison that the predicted average SNR enhancement provided by this particular configuration of a porous medium spatial filter reaches a maximum of ~20 dB at 1 hertz. It should be pointed out, however, that this maximum is achievable only if the surface amplitudes of the infrasound signals are at least 18-20 dB above the system noise level at frequencies less than 1.0 hertz.

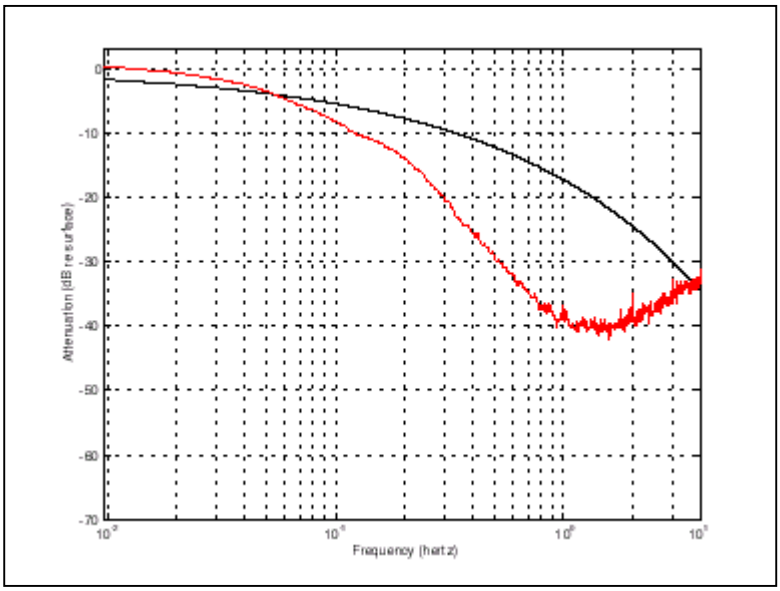

Figure 5. A comparison of the mean wind noise attenuation operator with the predicted infrasonic signal attenuation operator for the experimental porous medium spatial filter.

CONCLUSIONS AND RECOMMENDATIONS

The results of this project to date demonstrate that a relatively simple, low-cost configuration of a porous medium spatial filter effectively reduces wind noise in the infrasound bandwidth of interest. Moreover, if the existing theory correctly predicts the attenuation operator for the experimental spatial filter, then average gains of about 20 dB at frequencies near 1 Hz are possible. Therefore, the experimental confirmation of the predicted infrasound attenuation operator assumes a high priority for future studies.

It is also important to recognize that since a porous medium spatial filter attenuates both signals and wind noise, the relative magnitude of the system noise can impose an important constraint upon the realizable SNR gain. It appears that this problem can be partially resolved by choosing fill materials with much lower effective flow resistances than the dredged creek sand used in this experiment. Examples of granular materials with effective flow resistances of the order of 10^4 n-sec/m^4 or less may be found in Sabatier et al (1993) and Attenborough (1983). The use of a fill material with an effective flow resistance of this order of magnitude is expected to reduce the predicted attenuation of infrasonic signals for a given observation depth, as well as reduce the "cross-over" frequency for the wind dissipation function. Consequently, any future studies in this area should be designed to assess the value of using low effective flow resistance materials in porous medium spatial filters.

REFERENCES

Attenborough, Keith (1983), Acoustical characteristics of rigid fibrous absorbents and granular materials, J. Acoust. Soc. Am. 73, 783-799.

Attenborough, Keith, James M. Sabatier, Henry E. Bass, and Lee N. Bolen (1986), The acoustic transfer function at the surface of a layered poroelastic soil, J. Acoust. Am., 79, 1353-1359.

Sabatier, James M., Henry E. Bass, Lee N. Bolen, Keith Attenborough, and V. V. S. S. Sastry (1986), The interaction of airborne sound with the porous ground: the theoretical formulation, J. Acoust. Am., 79, 1345-1352.

Sabatier, James M., Richard Raspet, and Carl K. Frederickson (1993), An improved procedurefor the determination of ground parameters using level difference measurements, J. Acoust. Am., 94, 396-399.

Sorrells, G. G. (2001), A theoretical expression for the attenuation of wind generated pressure changes in a rigid porous medium.

INFRASOUND DETECTION OF LARGE MINING BLASTS IN KAZAKSTAN

Won-Young Kim

Lamont-Doherty Earth Observatory

Sponsored by Defense Threat Reduction Agency

Contract No. DTRA01-00-C-0077

ABSTRACT

Since October, 1997, we have recorded infrasound signals at Kurchatov, Kazakstan, from large mining blasts in Kazakstan and the Altay-Sayan region, Siberia. Kurchatov is an ideal site for research on infrasound and application of synergistic (seismic and acoustic) methods of event discrimination. This is because it operates a 21-element short-period seismic array and a three-component broadband seismographic station and because of its close proximity to large (100+ ton) mining operations.

Several large mines in the region routinely carry out large explosions that are detected seismically and with infrasound. The mines range in distance from 80 to 750 km from the infrasound array. The Ekibastuz mine, 250 km west of the array, regularly produces 4-6 seismic detections per day. The corresponding number of infrasound detections is found to be dependent upon the season and the local winds. During the winter months, when the direction of the zonal component of the stratospheric wind is from west to east, a strong stratospheric duct develops between Ekibastuz and Kurchatov and the number of infrasound detections is high. During this period the infrasound signal consists of two arrivals separated by about 60 s. A preliminary interpretation of these signals is that the first arrival at 250 km distance propagates through the troposphere and is followed 60 s later by a stratospheric arrival. During the summer months, when the zonal winds reverse direction, the number of infrasound detections is low.

In March 1999, we installed a three-element infrasound array with about 2-km sensor spacing at Kurchatov. Two of the elements consist of Globe microphones connected to noise-reduction hose and pipe arrays, while the third is actually a small array comprised of several Soviet-built, low-frequency microphones (K-301A) connected to various noise-reducing pipe configurations. In the winter of 2000, we also installed a three-element infrasound array with about 2-km sensor spacing at Borovoye, northern Kazakstan. We have compiled infrasound signals from mine blasts since 1999 at these sites in Kazakstan in order to understand the character of infrasound signals produced by regional mine blasts and the nature of infrasound propagation at high latitudes. We are currently analyzing signals from 1999 recorded by the new large arrays. Preliminary analysis of signals recorded during spring, 1999, by the larger aperture array suggests that the larger array results in improved infrasound detection of Ekibastuz mine blasts and improved discrimination of non-acoustic noise. The data from the new large aperture arrays also confirms identification of infrasound signals believed to be produced by events in the Kuzbass mining region of Siberia, over 700 km away from Kurchatov.

KEY WORDS: infrasound, mining blast, Kazakstan

OBJECTIVE

The goal is to improve event location and screening for CTBT monitoring by using infrasound and seismic methods. To achieve this goal, we carry out ground-truth calibration studies in northern Kazakstan and southwestern Siberia, and quantify seasonal variations in infrasound characteristics at high latitudes.

RESEARCH ACCOMPLISHED

Installation of Kurchatov Infrasound System

Since October, 1997, we have conducted infrasound observations at the Kurchatov Geophysical Observatory in Kazakstan using available microphones coupled with existing noise reduction systems in order to address some of the infrasound monitoring issues outlined above. The Kurchatov Observatory (Figure 1) is an ideal site for research on infrasound and on the application of synergistic (seismic and acoustic) methods of event discrimination as it operates both a 21-element short-period seismic cross-array (Figure 2) and a three-component broadband seismic station, and because of its close proximity to several large (100+ ton) mining operations (Figure 1). In addition, conditions appear to be favorable for long-range infrasound propagation in Kazakstan, where infrasound signals have been detected out to 2,000 km distance [Al'Perovich et al., 1985].

A large aperture infrasound array with three elements is constructed in the spring of 1999 at the Kurchatov Geophysical Observatory. The infrasound noise reduction configuration utilized at each element of the large aperture array consists of six, 70 m long underground pipes extending radially from a central chamber and referred to as "spider" (Figure 2). There are two spiders at the central recording site, Ch26 and Ch27, in Figure 2. We presume that this system, which was constructed during the Soviet era, was designed to be functional during the severe local winters, when snow covers the ground for five months each year and prohibits the use of conventional plastic hoses. Two types of capacitor microphone - Globe and Soviet K301 - have been utilized with the pipe arrays described above. The K301s were originally installed at Kurchatov in the early 1970's by the Russian Ministry of Defense and recorded on paper. Since February, 1995, the analog signal from a K301 sensor has been digitized and recorded by a 16-bit A/D system together with the seismic channels from the cross array. Since spring of 1999, 1–2 microphones connected to the spider noise reduction system have been simultaneously recorded, forming a large aperture acoustic array.

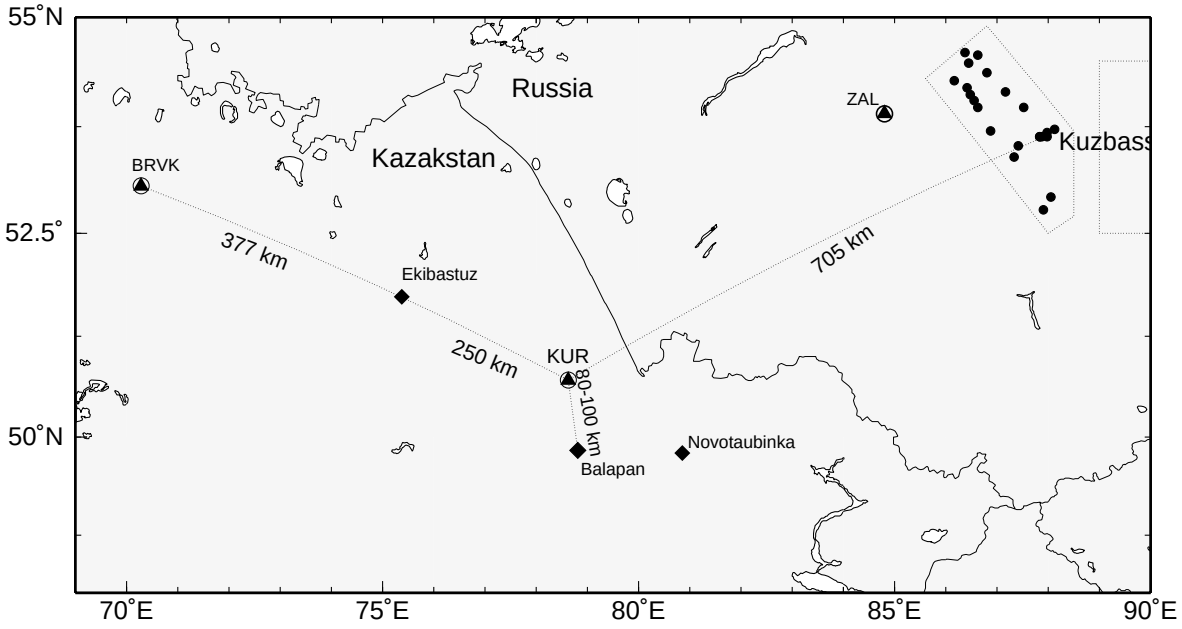

Figure 1. Map of Kazakstan and southwestern Siberia showing locations of broadband seismic stations (solid traingles), active mining areas (diamonds), Kuzbass and Abakan mining areas, and the Kurchatov Geophysical Observatory (KUR), where the seismic and infrasonic observations were made.

Spring 1999 Large Array Observations

Preliminary analysis of signals recorded since spring, 1999, by the large aperture acoustic array indicate an improved ability to detect mine events and to reject non-acoustic "noise" compared with use of the small array alone. An example one-hour window of data recorded during peak mining hours (07:00-10:00 GMT) is shown

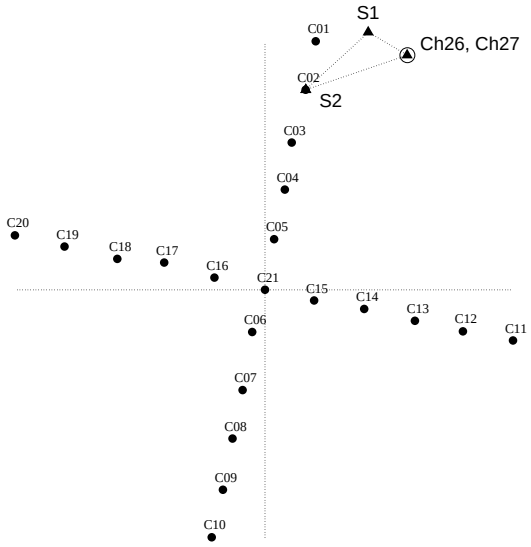

Figure 2. Plan view of the 21-element seismic borehole array (cross array) at Kurchatov and locations of the infrasound array elements (S1, S2 and Ch26). Notice that the spacing between the seismic array element is constant and 2.25 km.

in Figure 3. During this hour we are able to identify 7 Ekibastuz events in the seismic channels; for all but one of these we can also identify associated infrasound signals. The first infrasound arrival for each event has a travel time of 760 s and is followed 90 s later by a second arrival that consists of two pulses separated by 10 s. The estimated back-azimuth for these arrivals is 302°, close to the expected value. The character of the infrasound arrivals is so regular on this day, that we are able to identify two Ekibastuz events (one of these is indicated by the "?" in Figure 3), for which no seismic detection was made, solely on the basis of the infrasound detections. During this period we are also able to identify infrasound signals generated by mine explosions near the Kuzbass region in Siberia (Figure 1), over 700 km away. Example data from the large-aperture infrasound array for the infrasound records (band-passed) and corresponding spectrograms of Ekibastuz explosions and for infrasound arrivals from a Kuzbass event is shown in Figure 4. Note that since August, 1998, we have operated a broadband seismometer near the town of Eltsovka, close to the Kuzbass region, in order to aid identification of Kuzbass events.

Ekibastuz comprises a number of coal mines centered about (51.67N, 75.40E) as determined by satellite photographs [Thurber et al., 1990]. The infrasound wavetrain generated by Ekibastuz explosions can be classified into two categories. The first, shown in Figure 5, consists of 1 or 2 simple pulses, with travel times of approximately 740 and 810 s with respect to the seismically estimated origin time. The second arrival is observed in about 60% of the events from Ekibastuz; when present, it generally follows the first by 50-70 s, though this can range anywhere from 24 to 85 s (see Figure 5). The travel time of the first arrival exhibits great variation and probably reflects varying atmospheric conditions such as transient propagation ducts. The second type of infrasonic wavetrain associated with Ekibastuz events consists of a series of pulses of growing amplitude lasting some 20–30 s. There is no evidence for multiple cast firing within these blasts, hence, the multiple phases observed in the infrasound data must be produced by propagation effects. We applied a beamforming procedure to the acoustic traces shown in Figure 5 to estimate the apparent phase velocity (0.23 km/s) and back-azimuth (304°). The estimated back-azimuth is 7°off that predicted from the seismic location (297°) (see Figure 6).

Table 1: **Large Mining Blasts in Kuzbass and Abakan Region with Groundtruth Data**

Date year-mo-dd	Time (hh:mm:sec)	Lat (°N)	Long (°E)	K	Yield (ton)	name
1999-07-07	08:54:02.9	53.65	87.82	8.7	473	Mezhdurechinsk
1999-07-10	09:51:31.8	53.73	91.03	9.4	297	Chernogorsky
1999-07-14	07:29:27.0	53.66	87.84	9.5	430	Sibirginsky
1999-07-23	08:04:13.6	53.72	87.82	8.8	209	Sibirginsky
1999-08-11	08:06:33.3	53.62	87.85	9.5	550	Sibirginsky
1999-08-18	07:32:48.6	53.71	87.79	8.8	203	Mezhdurechinsk
1999-08-18	08:46:48.0	53.73	91.01	9.0	138	Chernogorsky
1999-08-20	08:20:34.6	53.74	87.88	8.6	222	Mezhdurechinsk
1999-09-01	07:31:14.3	53.69	87.88	8.2	173	Krasnogorsk
1999-09-03	08:37:16.6	53.77	91.02	9.9	378	Chernogorsky
1999-09-10	07:16:14.5	53.64	87.79	9.0	278	Mezhdurechinsk
1999-09-10	07:21:00.1	53.62	87.80	8.8	241	Krasnogorsk
1999-10-18	08:57:31.3	53.67	87.81	9.4	231	Krasnogorsk
1999-10-19	06:49:08.6	53.74	87.92	8.6	335	Tomusinsky
1999-10-29	05:26:01.9	53.69	87.93	8.8	284	Krasnogorsk
1999-11-15	08:59:50.5	53.80	88.02	8.9	257	Sibirginsky
1999-11-23	09:47:19.7	53.70	87.90	8.2	403	Mezhdurechensk
1999-11-23	10:28:40.4	53.67	87.83	8.3	403	Mezhdurechensk
1999-11-24	09:58:29.6	53.67	87.98	8.5	107	Sibirginsky
1999-11-29	09:40:10.4	53.67	87.85	9.7	458	Sibirginsky
1999-12-07	09:01:20.3	53.64	87.86	8.9	235	Krasnogorsky
1999-12-10	08:33:09.0	53.70	87.79	9.1	109	Sibirginsky
1999-12-17	09:01:09.9	53.60	87.49	8.6	161	Krasnogorsky
1999-12-17	09:17:19.8	53.68	87.85	9.2	300	Mezhdurechensk
1999-12-17	09:41:55.8	53.61	87.71	8.6	300	Mezhdurechensk
1999-12-30	05:59:56.5	53.61	87.75	9.0	319	Krasnogorsky
1999-12-30	07:05:02.2	53.90	88.16	8.9	17	Olgerassky
2000-01-17	08:46:19.1	53.70	87.91	8.7	210	Krasnogorsky
2000-01-18	09:53:44.3	53.66	87.85	8.7	122	Sibirginsky
2000-01-20	08:46:45.9	53.61	87.73	8.8	419	Mezhdurechinsky
2000-02-11	08:46:23.1	53.84	88.18	9.2	144	Olzherassky
2000-04-14	06:14:57.0	53.84	88.16	8.8	114	Olzherassky

Ground Truth Data from Large Mining Blasts in Southwestern Siberia

The Kuzbass and Abakan region in southwestern Siberia, Russia are very unusual in being the site of blasting activity that includes numerous explotions which can be detected teleseismically (Figure 7). In terms of size of seismic signals, these may be the largest routinely conducted blasting operations in Eurasia. This extensive mining region, which is close to the tectonically active Altay-Sayan, is also subject to frequent earthquakes. During July, 1999 – April, 2000, we obtained groundtruth data (date, location and total charge size) for several hundred large mining blasts in Kuzbass-Abakan region. 32 of these blasts are also located by Altay-Sayan Experimental and Methodical Seismological Expedition (ASEMSE), Siberian Branch of Russian Academy of Sciences in Novosibirsk, Russia from its local network which consists of about 15 stations with short-period seismometer (SKM) and analog recording. The events located by ASEMSE have location errors ranging from about less than 5 km to up to about 10 km (Table 1).

Table 2: **List of Mines in Kuzbass and Abakan region**

Id	Name	Type
a	Kolmogorovsky-1	open pit coal mine
b	Kolmogorovsky-2	open pit coal mine
c	Kiselevsk	includes Bachatsky, Krasnobrodsky & Novosergeevsky open pit coal mine
d	Taldinsky	open pit coal mine
e	Badaevsky	open pit coal mine
f	Oldgerasky	open pit coal mine
g	Mezhdurechensk	includes Mezhdurechensky, Tomusinsky, Krasnogorsky & Sibirginsky open pit coal mines
h	Kaltansky	open pit coal mine
i	Listvyansky	open pit coal mine
j	Tashtagol	open pit coal mine
k	Abakan-1	
l	Abakan-2	includes Chernogorsky and Izychsky open pit coal mines

CONCLUSIONS AND RECOMMENDATIONS

We have presented here an initial interpretation of the characteristics of infrasound propagation observed in northern Kazakstan and Siberia. During the winter, the infrasound signals associated with Ekibastuz events can be classified into two types. The first type consists of two pulses spaced 50–70 s apart, while the second type consists of multiple pulses arriving within about a 20–30 s window. Infrasound arrivals from both Ekibastuz (Δ=250 km) and Kara-Zhyra (Δ=80 km) explosions support the existence of a tropospheric duct, produced by a temperature inversion and/or a westerly jet in the troposphere. The multiple arrivals characteristic of the second type of infrasound wavetrains likely result from strong positive sound speed gradients in the troposphere and, especially, in the upper stratosphere. The large variability in the character of infrasound signals generated by Ekibastuz events over short time scales (hours to days) is indicative of the rapidity of atmospheric fluctuations.

REFERENCES

Al'Perovich, L. S. et al., (1 9 8 5) The acoustic wave of an explosion, *Izvestiya Academy of Sciences USSR, Physics of the Solid Earth (USA)*, **21(11)**, 835–842.

Georges, T. M., and W. H. Beasley, (1 9 7 7) Infrasound refraction by upper-atmospheric winds, *J. Acoust. Soc. Am.*, **61** (1), 28–34.

Thurber, C., H. Given, and J. Berger, (1 9 8 9) Regional seismic event location with a sparse network: application to Eastern Kazakstan, USSR, *J. Geophys. Res.*, **94**, 17,767–17,780.

Valley, S. L. (editor), (1 9 6 5) *Handbook of Geophysics and Space Environments*, McGraw-Hill, New York.

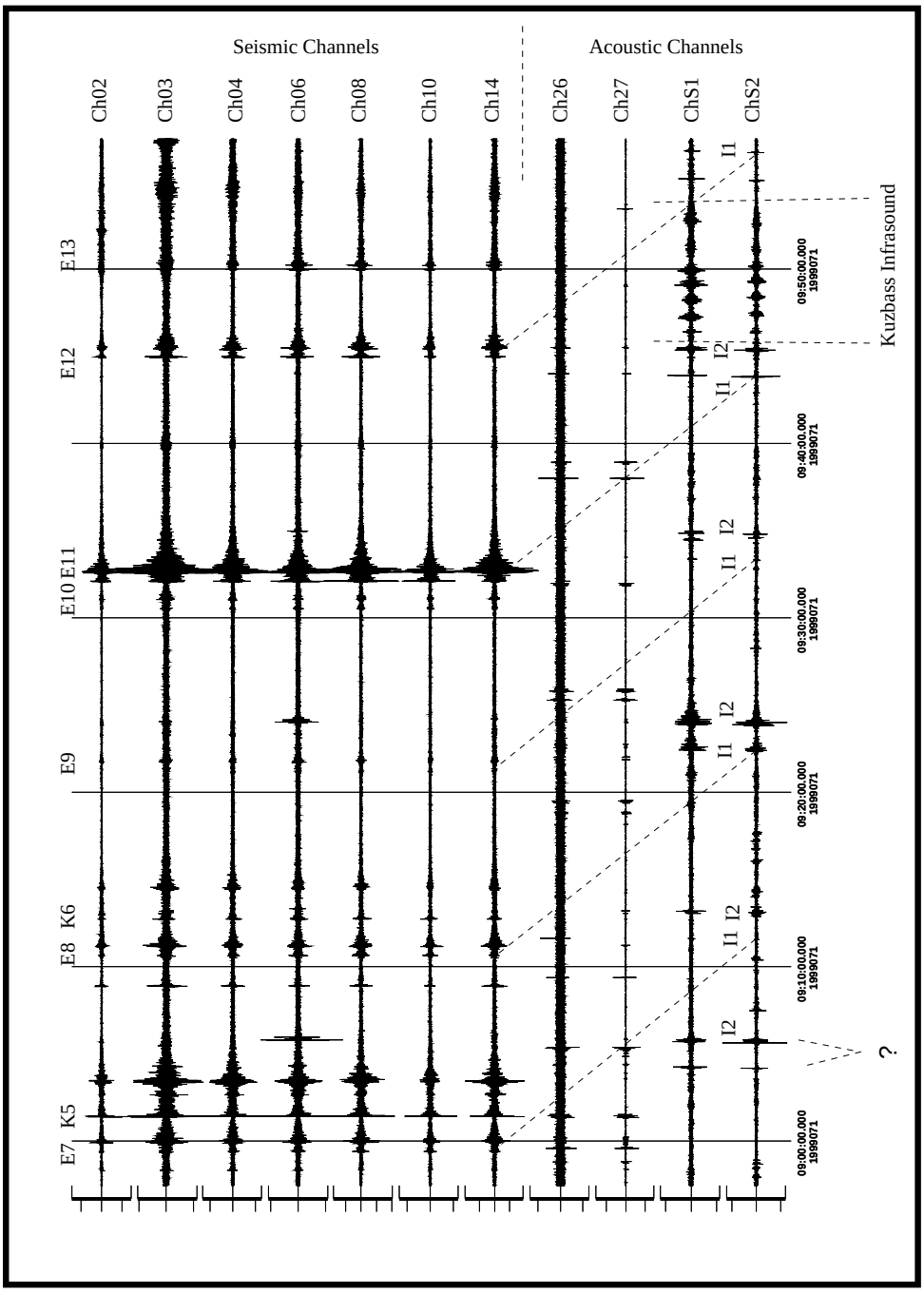

Figure 3. Example data from the Kurchatov seismic cross-array and acoustic triangle array for spring, 1999. During the one hour period shown are 7 Ekiabstuz events with associated infrasound arrivals, infrasound arrivals (?) believed to be produced by an Ekibastuz event that did not generate a seismic signal, and infrasound arrivals from a Kuzbass mine event, 700 km away.

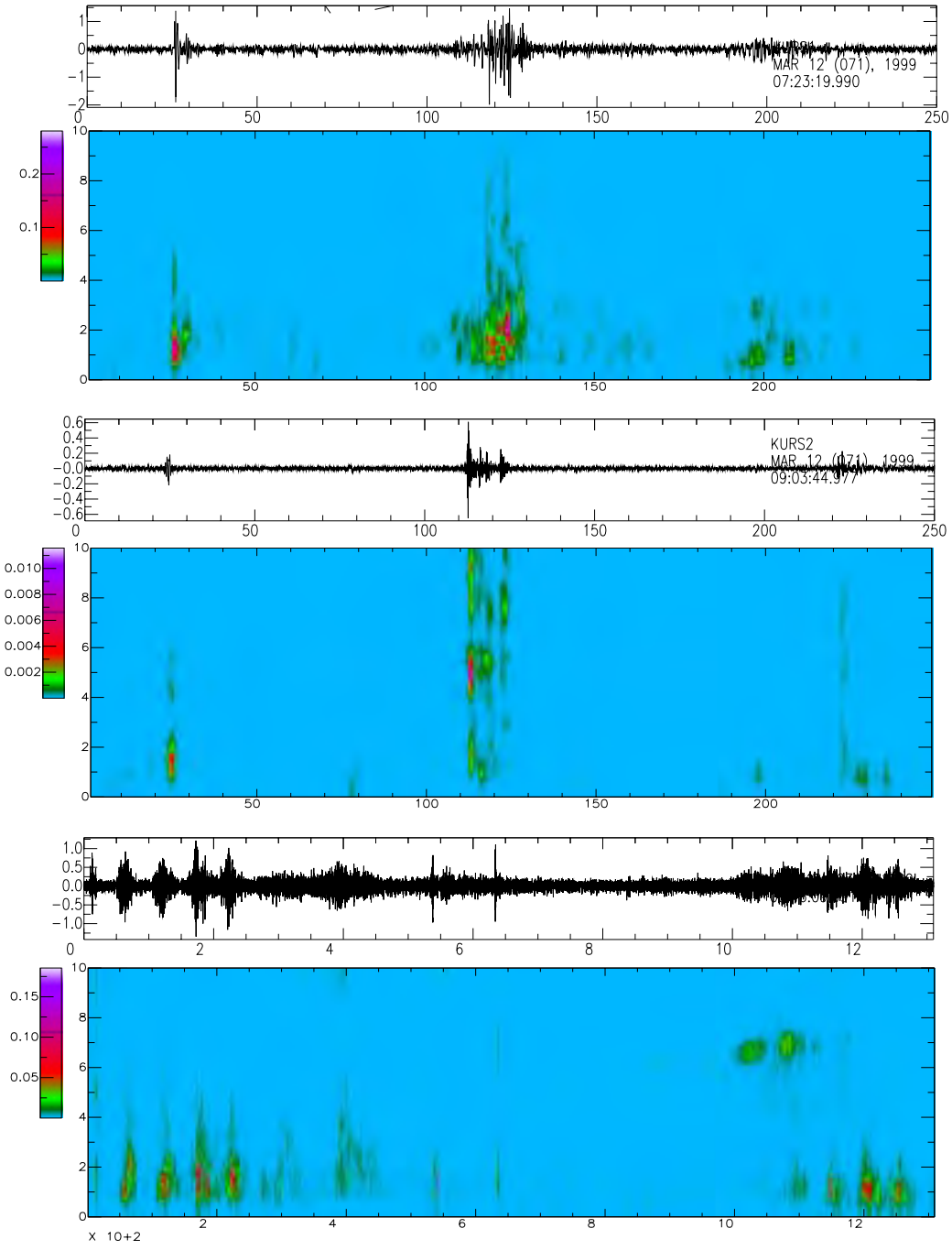

Figure 4. Example data from the large-aperture infrasound array for spring, 1999. Top panel: Infrasound record (band-passed) and corresponding spectrogram of an Ekibastuz explosion. Middle panel: Same for another Ekibastuz explosion. Bottom panel: Same for infrasound arrivals from a Kuzbass event. Note the larger time scale for the last event.

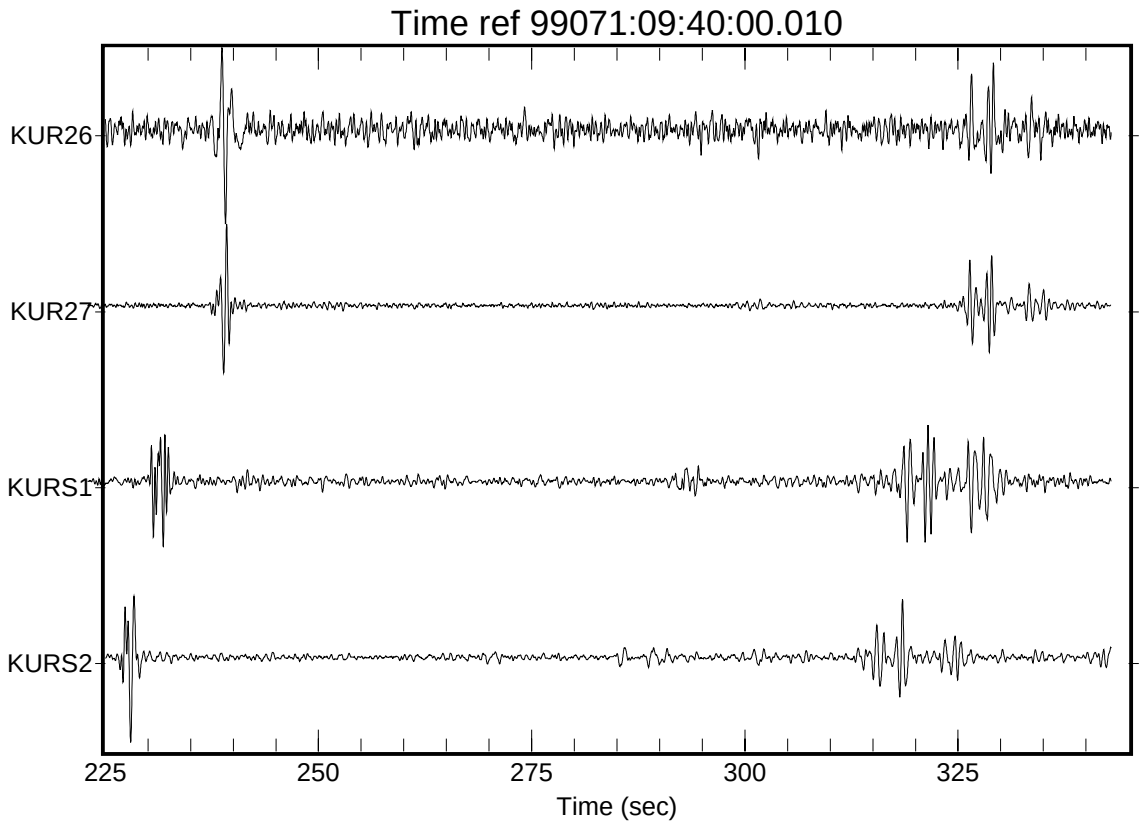

Figure 5. Infrasound signals from an Ekibastuz explosion on 03/12/1999 at 09:40. Notice the second arrivals about 85 s after the first arrivals.

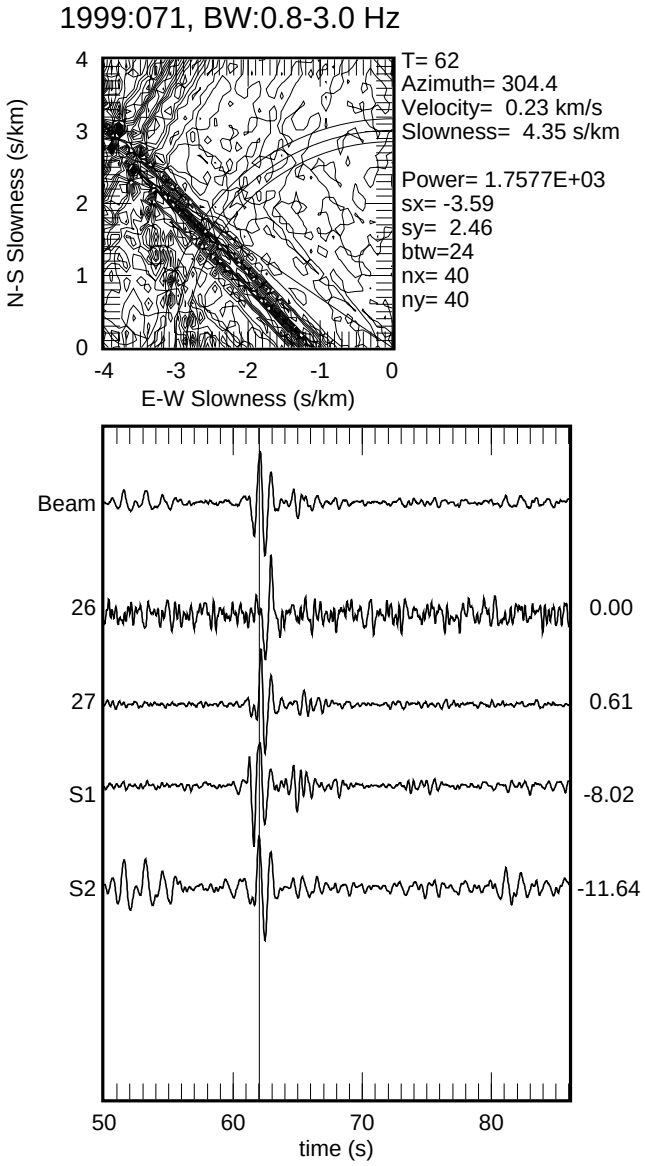

Figure 6. Beam forming of the infrasound signals from the Ekibastuz explosion on 03/12/1999 at 09:40 shown in Figure 5. Notice that the beam is calculated for the first arrivals.

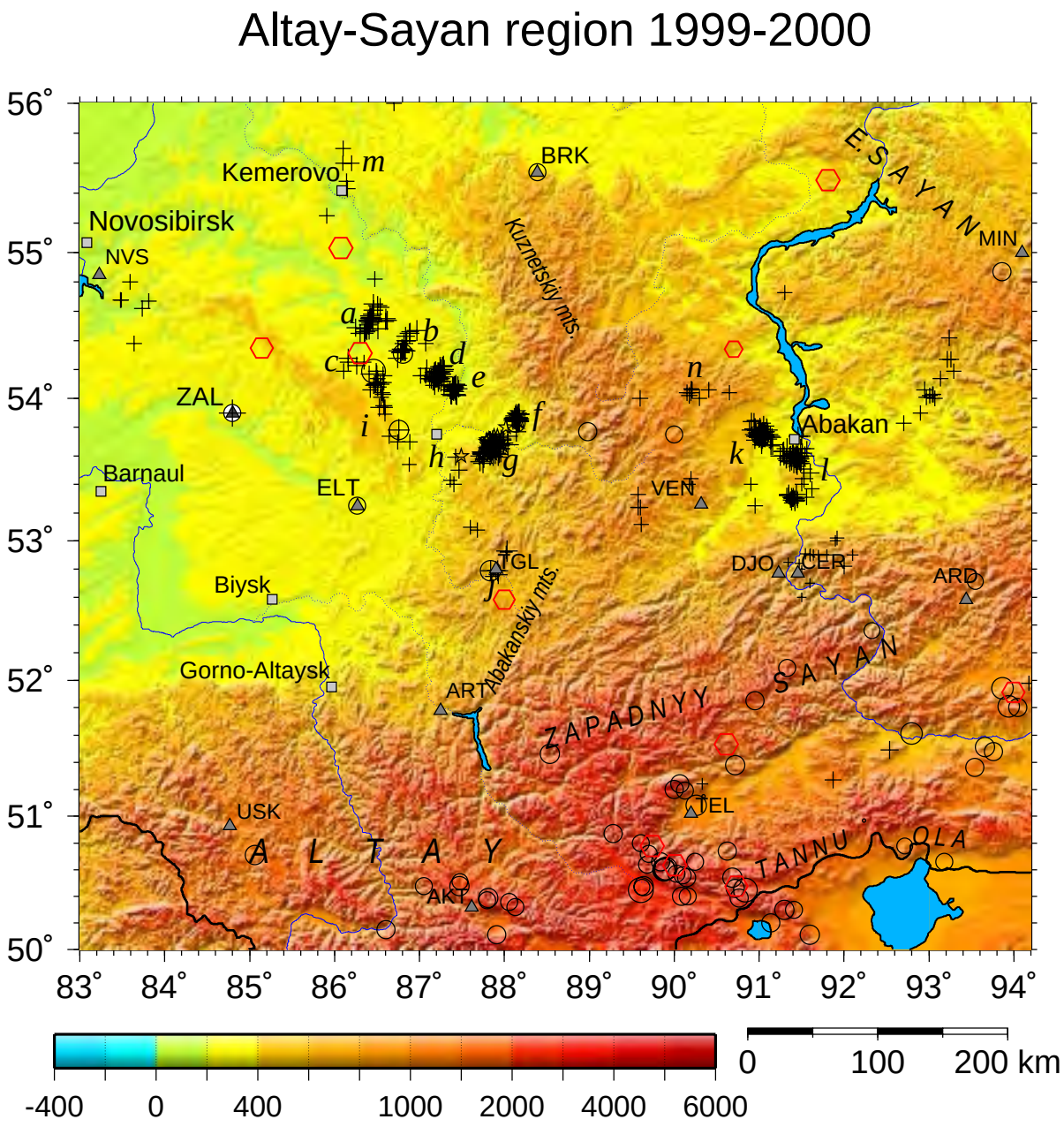

Figure 7. Locations of REB events in Southwestern Siberia during 1995–1997 and mining blasts in 1999–2000. Mining areas in Kuzbass-Abakan region are indicated by cluster of events. Primary IMS network station, ZAL and other local seismic stations in the region are indicated for reference.

INFRAMAP PROPAGATION MODELING ENHANCEMENTS AND THE STUDY OF RECENT BOLIDE EVENTS

David E. Norris and Robert G. Gibson

BBN Technologies

Sponsored by Defense Threat Reduction Agency

Contract No. DTRA01-00-C-0063

ABSTRACT

Enhancements to the propagation modeling capabilities of the InfraMAP analysis tool kit are being developed in several areas. InfraMAP (Infrasound Modeling of Atmospheric Propagation) consists of three infrasound propagation models (3-D ray trace, normal mode, and parabolic equation), two atmospheric characterizations (HWM and MSISE), a global topography database, and user interfaces for model execution and data visualization. InfraMAP has been delivered to the research and development test bed and is currently being utilized by Comprehensive Nuclear-Test-Ban Treaty researchers and analysts.

Three specific types of InfraMAP enhancements are addressed here. First, a low-frequency absorption model has been integrated for use by both ray- and parabolic-equation (PE) propagation analyses. The absorption model predicts both classical (translation, diffusion) and relaxation (rotation, vibration) losses. Absorption is calculated from temperature, pressure, and atmospheric gas densities, which are determined using the environmental model MSISE. Second, a waveform synthesis capability has been integrated into the ray model. Eigenray solutions for a specific source-receiver scenario are used to synthesize a time-based waveform. A user-defined source waveform is convolved with weighted impulse functions at the eigenray arrival times. The impulse weighting is based upon a calculated absorption loss along each ray path. Finally, improved environmental variability modeling capabilities are being pursued to model the propagation variability induced by the environment. A sample from the Naval Research Laboratory atmospheric statistics database has been investigated for use in improving predictions of propagation variability.

Propagation modeling studies have been performed for several recent bolide events, including the 1997 El Paso, Texas, bolide, the 2000 Acapulco bolide, the 2000 Yukon bolide and the 2001 Pacific bolide. Predicted absorption curves are compared to the spectra of observed waveforms. Nominal source localizations are computed from measured station azimuths. Enhanced localizations that correct for predicted azimuth deviation are also calculated for comparison. The dependence of eigenray arrival times on source height is shown to be a viable discriminator for source height estimation.

KEY WORDS: infrasound, long-range propagation, modeling, bolides, atmosphere

OBJECTIVE

The objective of this effort is to improve the utility of the InfraMAP software. InfraMAP is an integrated software tool kit designed to support nuclear explosion monitoring research and analysis. It is composed of geospatial, environmental, and propagation models integrated with a menu-driven interface. Figure 1 is a graphical representation of the main InfraMAP menus.

Enhancements to InfraMAP are being developed to increase the modeling capabilities of the tool, which, in turn, will lead to improved prediction accuracy for scenarios of interest to the nuclear explosion monitoring community. New functionality is being added to both the propagation and environmental models. In this paper, several InfraMAP enhancements are described and applied to the study of bolide events. Bolides provide an excellent source of infrasound, and comparisons between predictions and observations are used to help quantify the modeling performance.

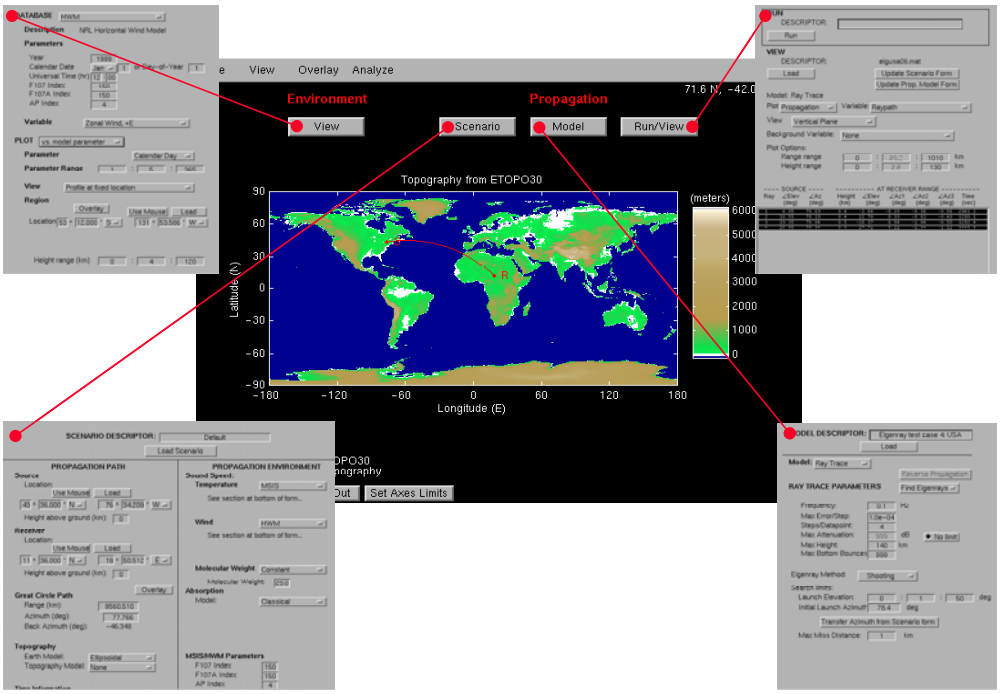

Figure 1. Screen graphic of main InfraMAP menus.

RESEARCH ACCOMPLISHED

Modeling improvements have been integrated into the InfraMAP software toolkit in several distinct areas. Here, the areas of propagation loss, synthetic waveforms, and environmental variability are addressed.

Propagation Loss

Predicting the loss of an infrasonic signal as it propagates from source to receiver is important in the study of network performance. It helps determine the receiver station coverage and detection threshold for a given event scenario. It also aids in determining the observability of acoustic paths that sample the thermosphere, a region of high acoustic absorption. Thermospheric paths are of particular interest because, when analyzed along with lower atmospheric paths, they can be used to estimate source position.

The two main sources of acoustic attenuation are spreading loss and environmental absorption. Spreading loss in acoustic pressure is inversely proportional to range for spherically expanding waves and the square root of range for cylindrically expanding waves. The PE propagation model is solved in cylindrical coordinates and includes the cylindrical spreading loss in its amplitude predictions. In the ray-tracing model, amplitudes associated with individual rays include losses from spherical spreading.

An acoustic absorption model has been integrated for use with the PE and ray codes to improve the accuracy of the amplitude predictions. The absorption model chosen was developed specifically for use with low frequencies and altitudes up to 160 km (Sutherland and Bass, 1996). It includes the contributions from both classical (translation and diffusion) and relaxation (rotation and vibration) losses. The model computes absorption from vertical profiles of temperature, pressure, and the concentration of gases that make up the air. All of these input variables are obtained from the MSISE model (Picone et al., 1997).

Figure 2 gives example profiles of predicted absorption coefficients at 0.2 and 0.5 Hz. Translation and diffusion losses are plotted together as classical loss, of which the diffusion loss makes up less than 1% of the sum. Below 60 km, vibrational loss dominates, but the total absorption is still relatively small. Propagation of

a 0.5-Hz signal over a 500-km path would only experience about 0.5 dB of attenuation in this region (neglecting spreading loss). The effects are much different within the thermosphere. At 120 km, the absorption coefficient increases dramatically with frequency; at 0.2 Hz, it is 0.1 dB/km, and at 0.5 Hz, it increases to 1 dB/km. Even acoustic signals that sample these regions for a small percentage of their propagation path can experience significant attenuation. As an example, a 0.5-Hz signal that spends 10% of its 500-km path at 120 km or above would have an absorption loss of at least 50 dB.

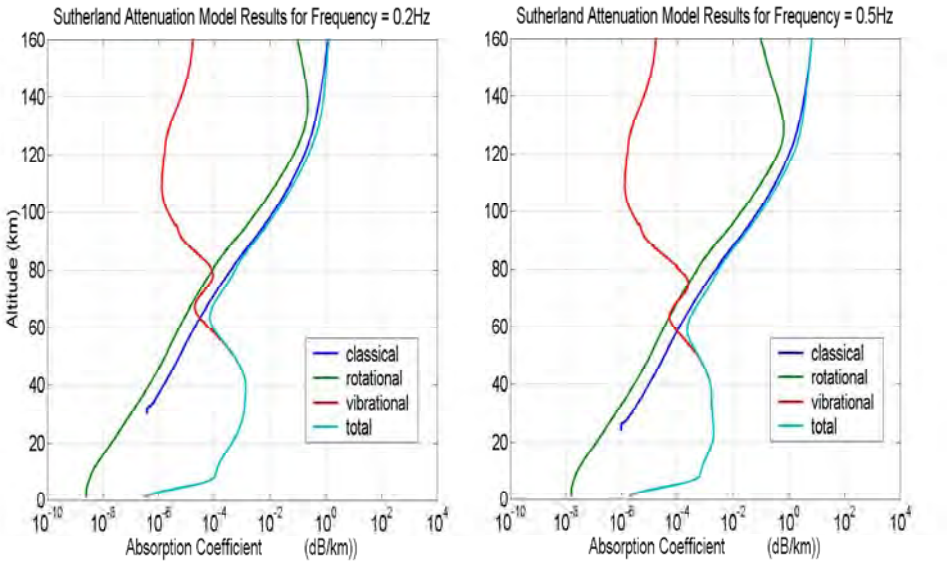

Figure 2. Absorption coefficients computed from a low-frequency, high-altitude model (Sutherland and Bass, 1996) at 0.2 and 0.5 Hz.

Comparisons were made of PE amplitudes with and without the atmospheric absorption effects. Results are shown in Figure 3 for a source at the ground. The amplitude predictions are made for upwind conditions, so a stratospheric return, with an upper turning height of 40-60 km, is not present. In the cases where absorption is not included, significant thermospheric energy reaches a receiver on the ground at 500-km range. With absorption included, a received signal at 500-km range would still contain a thermospheric return at 0.2 Hz, although the amplitude is reduced. However, at 0.5 Hz, the signal experiences strong absorption at altitudes between 110 and 120 km, and any thermospheric energy arriving at the receiver will be heavily attenuated.

Synthetic Waveforms

The integrated ray model within InfraMAP is useful for predictions of travel times and azimuth deviations. However, its output cannot be directly compared with time-series waveforms, either from normal mode predictions or direct measurements. A synthetic waveform capability has been integrated into the ray model to enable these types of comparisons.

The source waveform must first be selected. It can be defined as blast wave, Gaussian waveform, or user-defined waveform. The blast wave is computed from the formulation used in InfraMAP's normal mode code (Pierce and Posey, 1970). Figure 4 shows a blast wave for a 1-kT source on the ground. The synthetic waveform is computed by convolving the source waveform with weighted impulse functions at the arrival times of the selected rays. The impulse functions are weighted by the attenuation loss calculated over each ray. An application of the synthetic waveform functionality is presented in the Tagish Lake bolide study below.

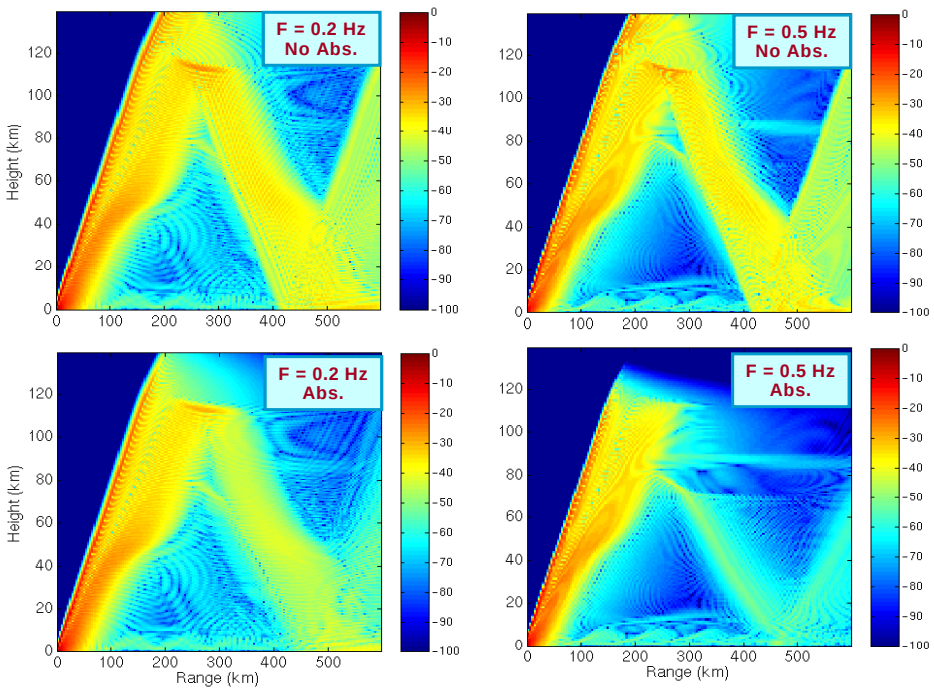

Figure 3. Comparison of PE amplitude predictions with and without absorption. Absorption effects at 0.5 Hz are apparent in the thermosphere, where energy propagating above 115 km is heavily attenuated.

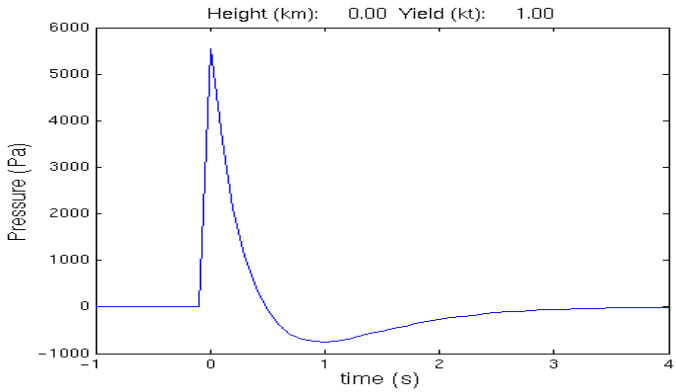

Figure 4. Blast waveform model for a 1-kT source on the ground (Pierce and Posey, 1970).

Environmental Variability

The main environmental models integrated in InfraMAP are HWM-93 for winds (Hedin, 1996) and MSISE-90 for temperature and gas densities (Picone et al., 1997). These are empirical models based on climatological data. They provide mean predictions from the ground up to several hundred kilometers and resolve both diurnal and seasonal trends in the variables.

In predicting infrasound propagation for a given scenario, it is important to predict not only the mean parameters, but also the uncertainty about the mean. The propagation uncertainties are needed to quantify the area of uncertainty in the source localization predictions. In the baseline version of InfraMAP, a variance model was integrated to compute this uncertainty. It was based upon a Monte Carlo analysis of ray propagation

through multiple environmental perturbation realizations. These realizations were based upon a user-selected power-law spectrum that defines the relevant length scales.

Recently, a new variability dataset has been generated at the Naval Research Laboratory (NRL) (Drob and Picone, 2000). It quantifies the variance of the mean HWM and MSISE predictions over a global grid. Below 50 km, this dataset was derived from daily numerical weather prediction (NWP) analysis fields. Above 50 km, it was derived from UARS-HRDI satellite data.

An example of the variance database is given in Figure 5. The plot image shows the 15-day average standard deviation of the meridional winds at 0 degrees longitude. As identified by Dr. Doug Drob at NRL, the prominent areas of variability are the mid-latitude troposphere jet streams at 5 - 15 km, and the high- to mid-latitude winter stratospheric vortex at 40 - 60 km. We are currently investigating the NRL variance database for use in improving the modeling of the environmental variability. These improvements will then be used in quantifying the propagation variability and localization uncertainty.

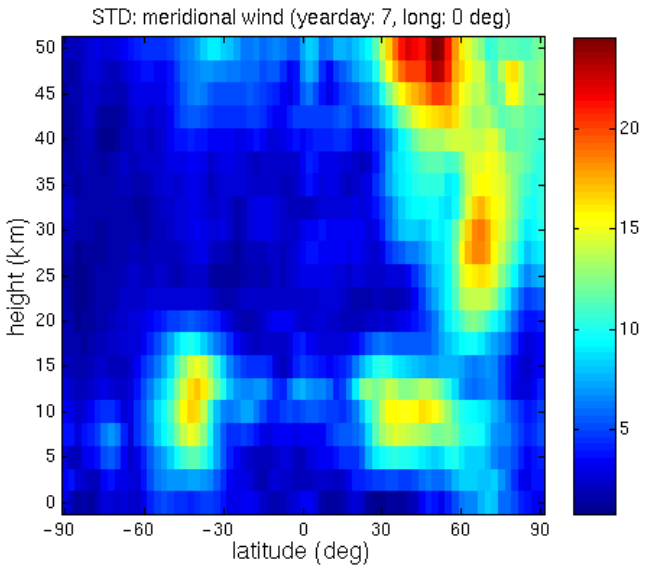

Figure 5. Example of the variance database from the NRL atmospheric statistics database (DOE-AT04-99AL66330). A sample data set was informally provided to BBN by Dr. Doug Drob (NRL-7643) for DTRA/DOE - CTBT R&D scientific investigation and product development.

Comparison Studies

Bolides are excellent impulsive sources of opportunity for acoustic frequencies below a few Hertz. When combined with ground truth data, they can support research and development for nuclear explosion monitoring. Infrasonic modeling of recent bolide events has been used to evaluate the enhanced modeling capabilities of InfraMAP and to quantify their accuracy with respect to observations. In this paper, we present results from three bolide events: the El Paso bolide of 9 Oct 1997, the Tagish Lake bolide of 18 Jan 2000, and the Pacific bolide of 23 Apr 2001. General information concerning these and other bolides can be found at the URL: http://phobos.astro.uwo.ca/~pbrown/usaf.html .

El Paso Bolide

On 9 Oct 1997, a large bolide traveled above Texas near El Paso. The height of the bolide, as determined from satellite observations, was 29 km. This bolide was detected at both the Los Alamos DLIAR array (range 445 km) and the Southern Methodist University TXIAR array (range 359 km). The received data at TXIAR has been studied to evaluate the ability to verify or refine the source height estimate.

To model the bolide signal, eigenrays were computed over a range of source height from 0 to 50 km. Figure 6 shows the eigenray solutions at 30-km source height. Over the range of heights, there are 1-3 stratospheric eigenrays and 2-3 thermospheric eigenrays.

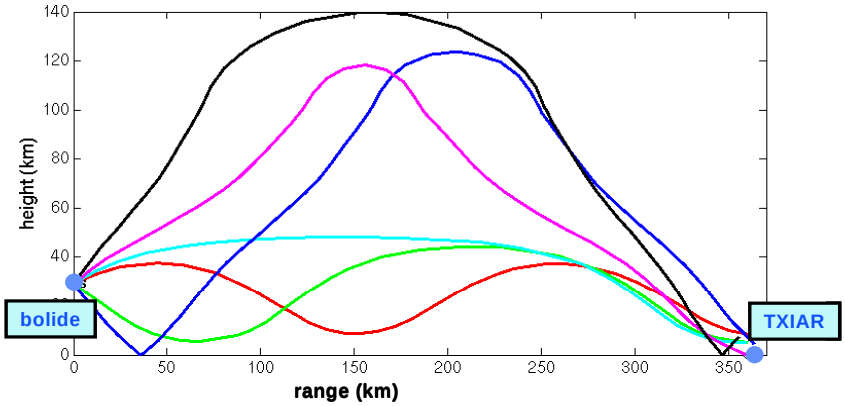

Figure 6. Eigenray solution between El Paso bolide at source height of 30 km and receiver at TXIAR.

Synthetic waveforms were next computed for each source height and mapped into an image as a function of arrival time and source height (bottom of Figure 7). A Gaussian waveform of standard deviation 10 sec was used as the source function. For sources near the ground, single eigenrays can be observed, which then split into multiple eigenrays as the height increases. The split rays for a given v-shaped branch correspond to two similar paths, one propagating up at the source, the other propagating down, reflecting off the ground, and then propagating up. The eigenray image can be compared to the measured waveform (top of Figure 7), and a source height estimate can be made by correlating the measured arrival times with the predicted amplitudes. The three measured arrivals match the predictions at source heights of 33, 26, and 23 km, respectively. Although there is a spread in these heights, they are in general agreement with the satellite-determined source height of 29 km.

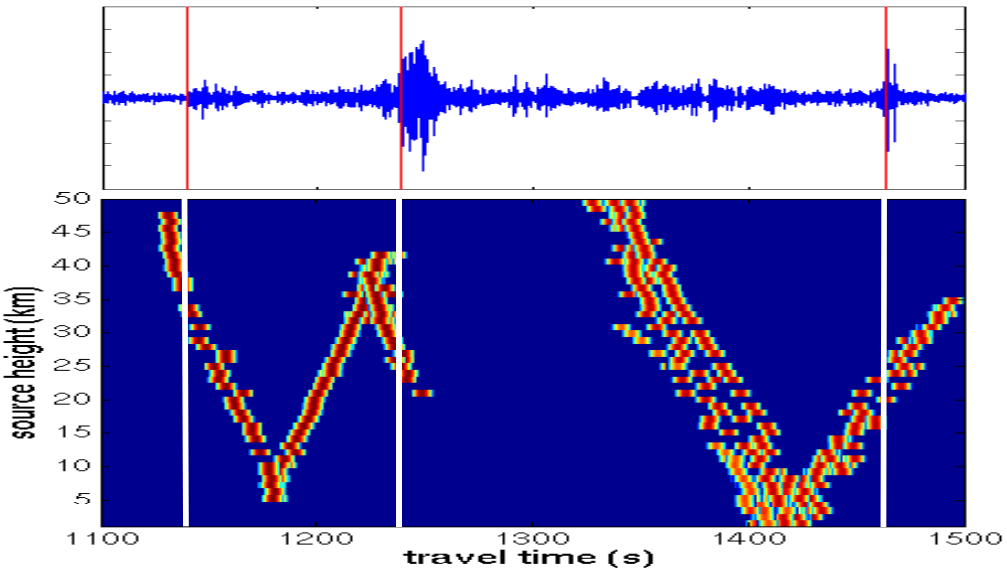

Figure 7. Comparison of measured arrival times (above) with synthetic waveform prediction from eigenrays solved over 0 to 50 km (below).

Tagish Lake Bolide

On 18 January 2000, sensors aboard Department of Defense (DoD) satellites detected the impact of a meteoroid at 16:43:43 UTC near Whitehorse in the Yukon Territory, Canada. The object detonated at an altitude of 25 km at 60.25 degrees North latitude, 134.65 degrees West longitude.

An infrasonic signal was detected at the International Monitoring System (IMS) station in Lac du Bonnet, Canada, a range of 2641 km from the bolide. A received waveform is shown in Figure 8. This waveform is filtered over the frequency band of 1.0 - 1.5 Hz. The main arrival appears at an arrival time of approximately 8200 sec with a possible secondary arrival at 11,300 sec.

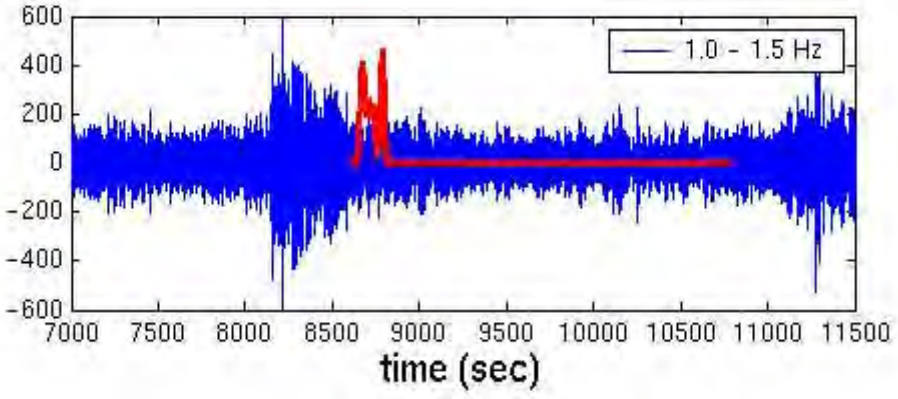

Figure 8. Filtered waveform measured at Lau de Bonnet IMS station (blue), and synthetic waveform generated from eigenrays (red). Amplitude units are arbitrary.

Measurements across the three elements of the array were beamformed using an F-K processing algorithm. The results were inconsistent across the observed waveform, possibly due to low signal-to-noise ratios or loss in coherence of the signals across the array, resulting from turbulence. The strongest coherent cluster in the F-K slowness plane was found using a time window from 8400 - 8500 sec and a frequency band of 0.2 - 1.0 Hz. The back azimuth for this cluster was 306.5 deg.

Eigenrays were computed for this path and are shown in Figure 9. Both stratospheric and thermospheric rays are present. The stratospheric rays have back azimuths at approximately 310 deg, and the thermospheric at approximately 311 deg. These predictions differ by several degrees from the measured value of 306.5 deg.

Synthetic waveforms were generated from the eigenrays for comparison with the measurements. The source function was a Gaussian waveform with a standard deviation of 10 sec. The predictions are overlaid on the waveforms in Figure 8. A bias of approximately 500 sec is apparent in the arrival times. This difference may be due to discrepancy between the predictions of temperature and wind from the HWM and MSISE models and the actual environmental conditions during the propagation. It may also result from inadequate modeling of the source function.

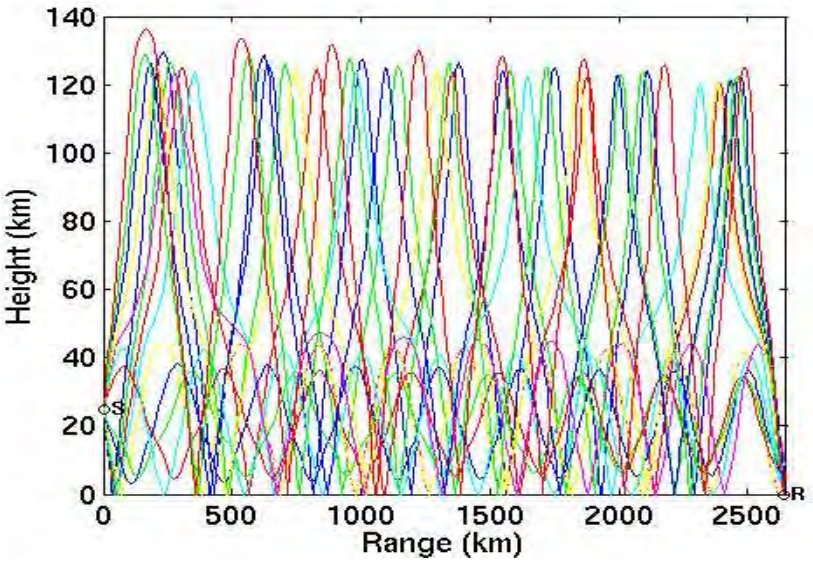

Figure 9. Eigenrays from Tagish Lake bolide to Lac du Bonnet IMS station.

Pacific Bolide

On 23 April 2001, a large bolide was observed over the Pacific Ocean in the area between California and Hawaii. This bolide was observed at several infrasonic stations. We used data from five stations in a study to determine the bolide location (Figure 10). The IMS arrays used were IS59 (Hawaii), IS10 (Lac du Bonnet, Canada), IS57 (Pinon Flats, California). Two additional IMS prototype arrays were also used: SGAR (St. George, Utah) and DLIAR (Los Alamos, New Mexico).

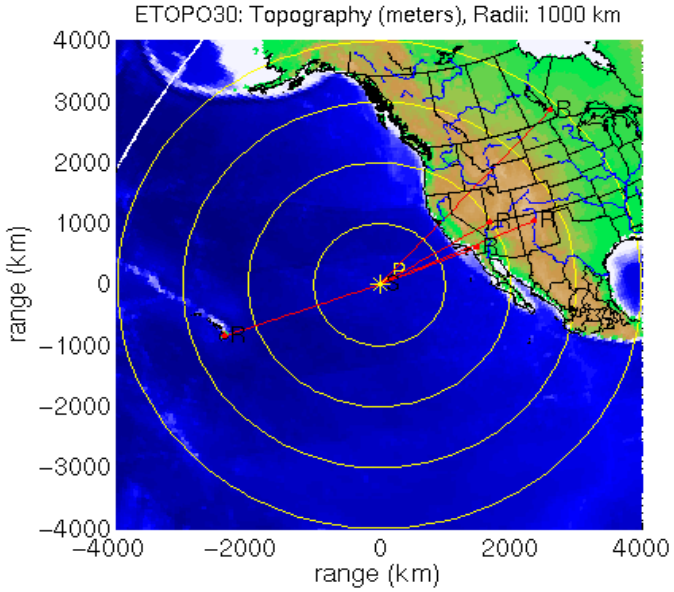

Figure 10. Nominal location of Pacific bolide and great circle paths to infrasonic stations. Yellow circles are contours of constant distance from source with 1000-km interspacing.

An iterative technique was used to estimate source location from azimuths and travel times at the five stations, incorporating environmental effects. Signal onset times, peak of signal correlation, and signal duration were estimated from the measured waveforms. Back azimuths were calculated by beamforming, using an F-K analysis technique. An initial location estimate was determined from the intersections of fans of rays propagated back from the five stations, using the mean observed azimuth at the station to launch each ray. Modeled signal velocities (range/travel time for each ray) were used to estimate the event time, and the initial location was perturbed to improve consistency in the event time estimates. A nominal event height was selected, and eigenrays were then calculated between the estimated location and each station. Consistency in event time was again used to perturb the location estimate, and eigenrays were recalculated.

The estimated location for the Pacific bolide, determined using the iterative ray-tracing technique, is shown in Figure 11. Also shown is the location determined from DoD satellite observations, as reported in a press release from 22 May 2001 (http://phobos.astro.uwo.ca/~pbrown/usaf.html). The colored line segments represent the projections of the initial fan of rays from each of the five stations used in the study.

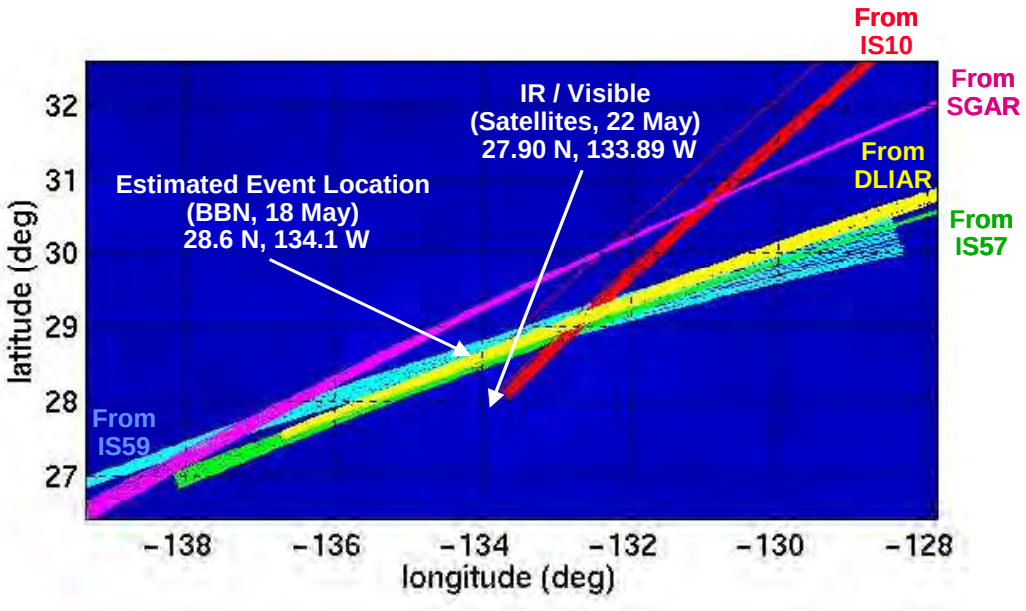

Figure 11. Estimated source location of the Pacific bolide from infrasonic modeling and from satellite observations. The colored line segments represent the projections of the initial fan of rays from each of the five stations used in the localization.

CONCLUSIONS AND RECOMMENDATIONS

Several enhancements have been made to the modeling capabilities of the InfraMAP tool kit. An absorption model developed for low frequencies and high altitudes has been integrated into the package. Absorption is particularly significant within the thermosphere. PE modeling for upwind propagation over a 500-km path indicates that thermospheric energy becomes heavily attenuated at the frequency increases from 0.2 to 0.5 Hz.

A synthetic waveform capability has been added to the ray model. The source waveform can be specified as a blast waveform, Gaussian waveform, or user-defined waveform. The source waveform is convolved with ray arrival times and weighted by ray attenuation factors to synthesize a received waveform.

Environmental variability is necessary to determine variability in the propagation predictions and ultimately the uncertainty of source localizations. The baseline environmental variability model is based on a power-law perturbation spectrum. The task of implementing an improved model has begun with the evaluation of a

HWM/MSISE gridded database of wind and temperature variances. A sample of this database has been provided by Doug Drob of the Naval Research Laboratory.

Large bolides provide a strong source for infrasound and, in conjunction with ground truth data from satellites, were used to evaluate the performance of the models. Source height estimates of the El Paso bolide were made using data at the TXIAR station. The propagation range in this case is under 400 km. Synthetic waveforms were computed from eigenray solutions over a range of hypothesized heights. They were then compared with the detected arrivals in the measured waveform. The predicted heights all fell within 6 km of the ground truth height. This result is significant in that it suggests that information important to source location can be predicted from single-station data.

Arrival times and back azimuths were predicted at the IMS Lac du Bonnet station for the Tagish Lake bolide. This propagation path is over 2500 km. Both stratospheric and thermospheric eigenrays were found along the path. A measured back azimuth was computed from the data using an F-K analysis, but the azimuth was not consistent over the entire signal. The measured azimuth differed from the predictions by several degrees. Comparison of arrival times indicates a 500-sec lag in the predictions. The bias may result from discrepancies in the environmental models or from inadequate modeling of the source.

The Pacific bolide was detected at multiple stations and provided the opportunity to perform multi-station source localization. Using three IMS stations and two prototype stations, a source localization was computed that was in reasonable agreement with the satellite-derived position.

Research topics that would support improved modeling of infrasonic events are listed below.

1. There are two types of infrasound from bolides: a linear blast wave associated with supersonic flight, and an impulsive point source associated with fragmentation. The relative strength of these two sources and modeling them for use in linear infrasound propagation models are areas that need further study.
2. The Tagish Lake bolide predictions suggest the possibility that a bias exists in the environmental models for the day and time of this event. Further improvements to the environmental models in InfraMAP should be investigated. In addition, data assimilation of empirical models with *in situ* measurements should be pursued to increase the accuracy of the propagation predictions.
3. The largest errors contributing to source localization uncertainty are generally in the back azimuth estimates. Improvements in either the array geometries or beam-forming algorithms would be desirable to help reduce this error term.

REFERENCES

Drob, D. and J. Picone (2000), Statistical Performance Measures of the HWM-93 and MSISE-90 Empirical Atmospheric Models and the Relation to Infrasonic CTBT Monitoring, *Proceedings of the 22nd Annual Seismic Research Symposium*, New Orleans, Sept. 12-15.

Hedin, A. E, E. L. Fleming, A. H. Manson, F. J. Schmidlin, S. K. Avery, R. R. Clark, S. J. Franke, G. J. Fraser, T. Tsuda, F. Vial, and R. A. Vincent (1996), Empirical wind model for the upper, middle, and lower atmosphere, *J. Atmos. Terr. Phys.*, **58**, 1421-1447.

Picone, J. M., A. E. Hedin, S. L. Coffey, J. Lean, D. P. Drob, H. Neal, D. J. Melendez-Alvira, R. R. Meier, and J. T. Mariska (1997), The Naval Research Laboratory program on empirical models of the neutral upper atmosphere, in *Astrodynamics: Advances in the Astronautical Sciences*, Vol. 97, edited by F. R. Hoots, B. Kaufman, P. J. Cefola, and D. B. Spencer, American Astronautical Society, San Diego, Ca.

Pierce, A. D. and J. W. Posey (1970), *Theoretical Prediction of Acoustic-Gravity Pressure Waveforms Generated by Large Explosions in the Atmosphere*, Technical Report AFCRL-70-0134, Air Force Cambridge Research Laboratories, Bedford, Mass.

Sutherland, L., and H. Bass (1996), Atmospheric Absorption in the Atmosphere at High Altitude, *7th Long Range Sound Propagation Symposium*, Lyon, France.

DETECTION AND LOCATION CAPABILITIES OF MULTIPLE INFRASOUND ARRAYS

Robert H. Shumway

University of California, Davis

Sponsored by The Defense Threat Reduction Agency

Contract No. DTRA01-00-C0082

ABSTRACT

In the first phase of this contract, we have developed an integrated approach to using wavenumber parameters and their covariance properties from a collection of local arrays for estimating location, along with an uncertainty ellipse. Hypothetical wavenumber estimators and their uncertainties are used as input to a Bayesian nonlinear regression that produces fusion ellipses for event locations using probable configurations of detecting stations in the proposed global infrasound array. The network capability is characterized as a function of separate local-array characteristics, including signal-to-noise ratios, bandwidth, array geometry, local correlation and coherent interfering signals. A summary map displays the average areas of the 90% posterior probability ellipses for each hypothetical location, assuming a random configuration of detecting stations.

In the second phase of the project, we are developing local-array parameters that will be used as input for estimating the capabilities of the global International Monitoring System (IMS). A small-array theory has been given in previous work that characterizes the detection probabilities and large sample variances of the local-array optimal maximum likelihood detectors. We are working on assessing the local-array performance of the multiple signal F-statistic as well as those of alternative high resolution detectors produced by Capon (1969) and the multiple signal classification (MUSIC) algorithm proposed by Schmidt (1979). For pure and mixed infrasound signals from two explosions, we find that all statistics have comparable resolution. The F-statistic retains a number of theoretical advantages, namely (1) a known large sample distribution that yields detection and false alarm probabilities (2) direction of arrival (DOA) estimators with means and covariance matrix determined by the Cramer-Rao lower bound and (3) easily estimated signal-to-noise ratios. Hence, the maximum likelihood procedure produces the input necessary for evaluating the global location performance of the IMS.

With the above in mind, current efforts are focused on analyzing events in the infrasound database located at the Center for Monitoring Research. We are planning to develop from the CMR R&D Test Bed Infrasound Waveform Library information on detection probabilities and estimated variances for real IMS type arrays as a function of bandwidth, signal-to-noise and geometry. These characteristics are needed for input into the multiple station global location simulation.

KEY WORDS: maximum likelihood, Bayes, multiple signal estimation and detection, nonlinear regression, F-Statistics, high resolution, MUSIC

OBJECTIVE

Monitoring explosive events using a collection of small infrasound arrays can lead to improved detection performance and to predictive uncertainty regions for the location of an explosive event. This project seeks to determine the detection performance of small infrasound arrays and to estimate the variances associated with the estimated wavenumber parameters that are directly related to velocity and azimuth. These characteristics are then used as input to a nonlinear regression program for location and will determine the overall uncertainty ellipse for locating a given event. In the early phase of this project, we have developed a methodology for integrating wavenumber estimators from detecting local arrays into an overall estimator for location and its associated posterior probability region. Global capability is expressed as a contour map showing areas of 90% posterior probability ellipses as a function of the expected configuration of detecting stations (see, for example, Shumway, 2000).The expected configuration is based on the signal detection capabilities of the given collection of sub-arrays and the variance properties of the maximum likelihood estimators of velocity and azimuth for each sub-array. The contour map is based on simulations involving 500 hypothetical events originating from each point on a 5-degree grid covering the surface of the earth. Each event is detected at a random configuration of International Monitoring Stations (IMS).

In our current research efforts, we are focusing on the problems involved in evaluating the local sub-array input parameters that determine location uncertainty and the average areas mentioned above. The characteristics of interest are sub-array detection probabilities and estimators for the variance of the wavenumber estimates corresponding to the velocity and azimuth of the propagating signal. In previous reports and papers (Shumway et al, 199, Shumway1999 and Shumway, 2000), we have characterized small array performance for the optimum single signal detector in terms of bandwidth, signal-to-noise ratio, array configuration, and signal decorrelation. We are currently applying this technique to a number of events contained in the infrasound database located at the Center for Monitoring Research, referred to in the sequel as the CMR R&D Test Bed Infrasound Waveform Library The database contains earthquakes, explosions, bolides and missile launches. There is a meteorite recorded at six IMS type stations that could provide useful input parameters for evaluating global location capabilities.

A second objective of this next phase is investigate the effects of interfering signals and (or) correlated noise on the conventional F detector, which is based on the assumptions that signals are perfectly correlated and that noise is spatially white. We also consider the performance of alternative estimators that are advertised to be effective in a multiple signal context. Among these are the single and multiple signal F detectors of Shumway (1983), the estimator of Capon (1969) and the MUSIC estimator proposed by Schmidt (1979). We evaluate these alternative estimators here on a mixture of two signals constructed by adding the Small Fry nuclear explosion, contrived to arrive at 225 degrees to an interfering signal arriving at 135 degrees. Figure 1 shows the primary event in the left hand column and the interfering invent in the center, with the sum (SF+.5GS) shown in the last column. The event is assumed to be observed at the three component triangular array with approximately 1 km sides, as described by Shumway et al (1998).It can be seen that the mixture obscures the primary signal quite effectively.

RESEARCH ACCOMPLISHED

In order to investigate possible approaches to evaluating the effect of contaminating signals such as the one in Figure 1, we consider frequency domain version of single and multiple station signal detectors with velocity and azimuth parameterized by a probe vector at wavenumber $\boldsymbol{\theta} = (\theta_1, \theta_2)'$, i.e.,

$$\boldsymbol{x}(\boldsymbol{\theta}) = \left(e^{2\pi \boldsymbol{r}_1' \boldsymbol{\theta}}, \ldots, e^{2\pi \boldsymbol{r}_N' \boldsymbol{\theta}}\right)', \tag{1}$$

where the array coordinates in km, relative to a center sensor at the origin, are denoted by $\boldsymbol{r}_j = (rj1, rj2, j = 1, \ldots, N$; in Figure 1, there are $N = 3$ sensors.

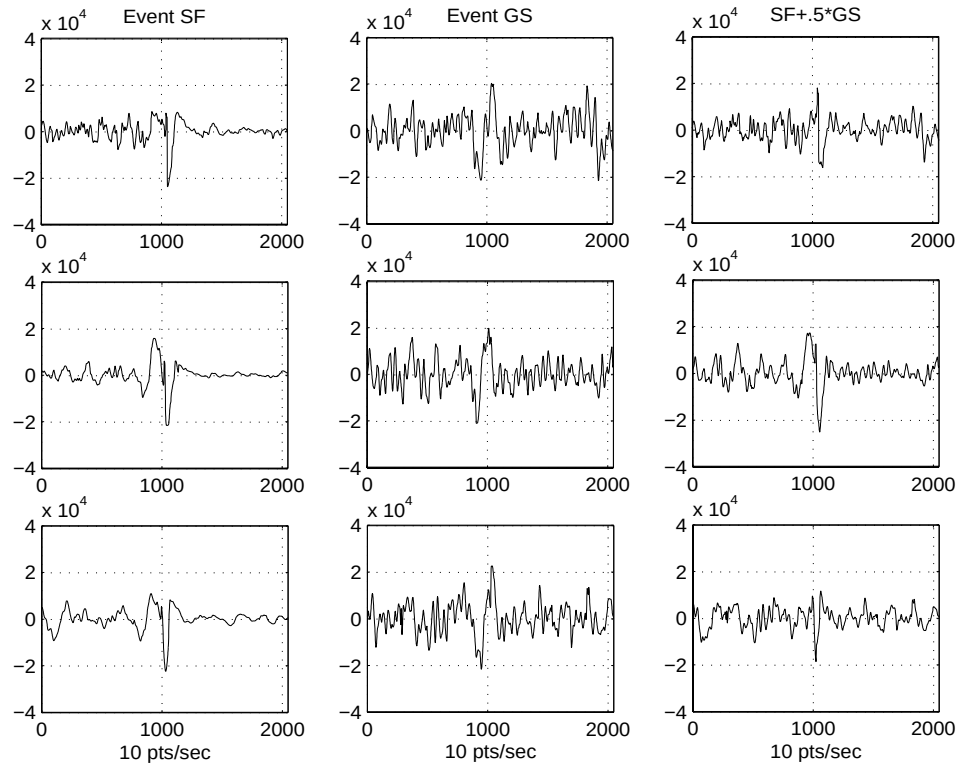

Figure 1. Infrasound explosive signals from 225° and 135° and a mixture sampled at 5 Hz at a triangular array with 1 km sides .

For the classical maximum likelihood solution in either the fixed or random signal case, the estimated wavenumber vector is the one maximizing the beam power, say

$$B(\boldsymbol{\theta}) = \boldsymbol{x}^*(\boldsymbol{\theta}) S\, \boldsymbol{x}(\boldsymbol{\theta}), \tag{2}$$

where

$$S = \sum_{k=1}^{K} \mathbf{Y}_k \mathbf{Y}_k^* \tag{3}$$

is the spectral matrix evaluated at K frequencies in the neighborhood of some assumed signal frequency f_0, and $\mathbf{Y}_k$ denotes the $N \times 1$ vector of discrete transforms of the observed waveform. It should be noted that (2) is realized simply online by filtering the signal in the neighborhood of the center frequency and delaying and summing at the velocity and azimuth matching the wavenumber vector. A power detector is then applied to the resulting beam to get an approximation to (2). All detectors here are expressed in terms of the spectral matrix S to provide a rough comparison to other detectors introduced below. Shumway et al (1999) have also derived the large-sample covariance matrix of the maximum likelihood estimator $\hat{\boldsymbol{\theta}}$, which can then be directly incorporated into the nonlinear least squares program for location (See Shumway, 2000).

The maximum likelihood detector, derived from a likelihood ratio test of no-signal in either the random or fixed signal case is the F-Statistic

$$F_1(\boldsymbol{\theta}) = \frac{\boldsymbol{x}^*(\boldsymbol{\theta}) S\, \boldsymbol{x}(\boldsymbol{\theta})/N}{\mathrm{tr}(S) - \boldsymbol{x}^*(\boldsymbol{\theta}) S\, \boldsymbol{x}(\boldsymbol{\theta})/N}(N-1), \tag{4}$$

which has an F distribution with $2K$ and $2K(N-1)$ numerator and denominator degrees of freedom respectively when the wavenumber is correct (tr denotes trace). For online applications,

one can filter the channels into the frequency band of interest and then use the ordinary time domain F-Statistic with $2BT$ and $2BT(N-1)$ degrees of freedom. The numerator is proportional to the output of a power detector and the denominator can be computed as the difference between the stacked power and the beam power in the numerator, when the data have been filtered into a frequency band of width B Hz and the sample length is T seconds. Among the advantages of this detector are (a) optimality under perfect signal correlation and spatially white noise,)(b) known statistical distribution that does not depend on signal and noise parameters and (c) existence of an easily applied online time version for monitoring applications. Potential disadvantages of the simple F detector are lack of robustness to signal correlation, investigated theoretically in Shumway et al (1999) and interfering signals. These latter two aspects are assessed here. We also study three alternative estimators that may have some potential for improved estimation in the mixed signal case.

The first is due to Capon (1969) and involves maximizing the quadratic form

$$C(\boldsymbol{\theta}) = \left[\boldsymbol{x}^*(\boldsymbol{\theta})S^{-1}\boldsymbol{x}(\boldsymbol{\theta})\right]^{-1}. \tag{5}$$

over possible wavenumber vectors $\boldsymbol{\theta}$. Under the assumption that the theoretical spectral matrix of the vector $\boldsymbol{Y}_k$ is Σ, coupled with the Gaussian assumption, this statistic has a distribution proportional to chi-squared, where the proportionality constant is $\boldsymbol{x}^*(\boldsymbol{\theta})\Sigma^{-1}\boldsymbol{x}(\boldsymbol{\theta})$ (see Capon and Goodman, 1970, for the exact result). Hence, the distribution is known but depends on nuisance parameters in the spectral matrix Σ. Furthermore, asymptotic results for the estimator $\hat{\boldsymbol{\theta}}$ maximizing (5) are not available so there the inputs required for assessing global location uncertainty are not available. the statistic is sometimes referred to as a maximum likelihood estimator but the connection to maximum likelihood is tenuous at best. If S were the maximum likelihood estimator of the noise covariance matrix Σ (it is not) under the fixed signal model, $C(\boldsymbol{\theta})$ would be the maximum likelihood estimator of the variance of the best linear unbiased estimator.

An estimator based on the eigen vectors of S is the centerpiece of the Multiple Signal Characteristic (MUSIC) statistics suggested by Schmidt (1979). A good summary of the statistical properties of this estimator is Stoica and Nehorai (1989). If we let $\boldsymbol{w}_1, \ldots, \boldsymbol{v}_N$ be the eigen vectors of S, then the MUSIC estimator is the value of $\boldsymbol{\theta}$ maximizing

$$M(\boldsymbol{\theta}) = \left[x^*(\boldsymbol{\theta})\left(\sum_{j=M+1}^{N} \boldsymbol{v}_j \boldsymbol{w}_j^*\right)\boldsymbol{x}(\boldsymbol{\theta})\right]^{-1}, \tag{6}$$

where $M < N$ is the assumed number of signals and $\boldsymbol{w}_{M+1}, \ldots, \boldsymbol{v}_N$ are the $N - M$ smallest eigen values. The estimator follows from the fact that for the spatially white noise model with correlated signals, the wavenumber vectors are orthogonal to the matrix containing the last $N - M$ eigen vectors as columns. Pre-multiplying by $\boldsymbol{x}^*(\boldsymbol{\theta})$ and taking the inverse leads to (6). Stoica and Nehorai (1989) have derived the large sample covariance matrix for a linear array.

A third possibility is a multiple fixed signal approach via likelihood ratio tests as proposed by Shumway (1983).This proceeds by minimizing the squared error

$$SSE2(\boldsymbol{\theta}) = \sum_{k=1}^{K} ||\boldsymbol{Y}_k - \boldsymbol{x}(\boldsymbol{\theta}_1)S_{1k} - \boldsymbol{x}(\boldsymbol{\theta}_2)S_{2k}||^2$$

over $\boldsymbol{\theta} = (\boldsymbol{\theta}_1', \boldsymbol{\theta}_2')', S_{1k}, S2k, k = 1, \ldots, K$ corresponding to two signals at wave-numbers $\boldsymbol{\theta}_1$ and $\boldsymbol{\theta}_2$. Denote the maximized value of the above by $SSE2(\hat{\boldsymbol{\theta}})$ and the maximized value with no second signal as $SSE1(\hat{\boldsymbol{\theta}}_1)$. Then, the multiple signal F-statistics for test the no-second-signal hypothesis is

$$F_2(\boldsymbol{\theta}) = \frac{N-2}{2}\frac{[SSE1(\hat{\boldsymbol{\theta}}_1) - SSE2(\hat{\boldsymbol{\theta}})]}{SSE2(\hat{\boldsymbol{\theta}}_2)}, \tag{7}$$

which converges to an F distribution with $2K$ and $2K(N-2)$ degrees of freedom.

We have tested the methods on the pure signal in the left-hand column of Figure 1 and on the mixture in the right-hand column. The result are shown in Figure 2, 3 and 4 and summarized in Table 1. All plots are constructed using a center frequency of .05 Hz, corresponding to the spectral peak of the observed data and $K = 13$ in the spectral matrix, which implies a bandwidth of $(13/1024)5 = .06$ Hz so that the frequency spans the interval $.03 - .09$ Hz.

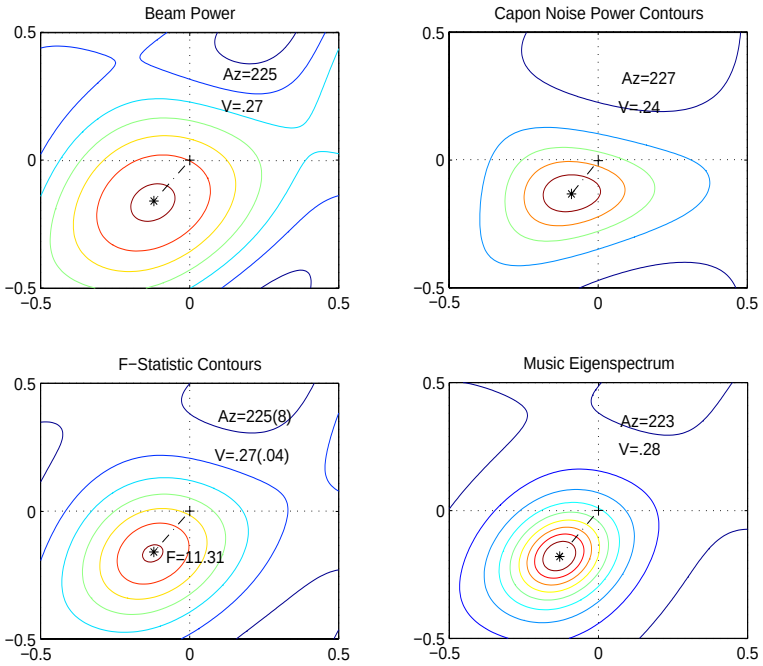

Figure 2. Detectors applied to pure infrasound explosive signal from 225°. Standard errors of the maximum likelihood estimators are in parentheses on the F-Statistic contour.

Figure 2 shows the wavenumber plots of the beam detector (2), F-Statistic (4), Capon detector (5) and the MUSIC detector (6) for the pure signal case. All statistics give azimuths within ±2° of the known azimuth. The standard deviation of the maximum likelihood azimuth estimator was 8°. F value of 11.31 exceeds the .001 significance point of the F-Statistic with $2(13) = 26$ and $2(13)(3-1) = 52$ degrees of freedom. The peaks in the beam power and Capon statistics are approximately the same width; the Capon contours are slightly distorted due to the non-diagonal spectral matrix S. The F-Statistic and MUSIC plots promise more resolution, due to narrower peaks.

We see in Figure 3 that narrow peaks do not necessarily translate into an improved ability to separate mixed signals. The detectors applied to the mixture still focus on the stronger signal. Estimators for the azimuth are biased, ranging from 215 to 217°, indicating that the contaminating signal has pulled these values toward its azimuth of 135°. Hence, there is no appreciable difference between the bias terms for the three methods. The standard deviations of the azimuth estimators are approximately doubled to 17° and the F value is reduced to 3.55, which still exceeds the .001 significance value. It is clear that the presence of the contaminating signal in this case increases the estimated variance, implying that this particular array will have less influence on the overall location.

wavenumber plots for the two multiple signal possibilities, MUSIC in (6) and the multiple signal F detector (7) are shown in Figure 4. The MUSIC estimator (6) in the bottom panel uses values of

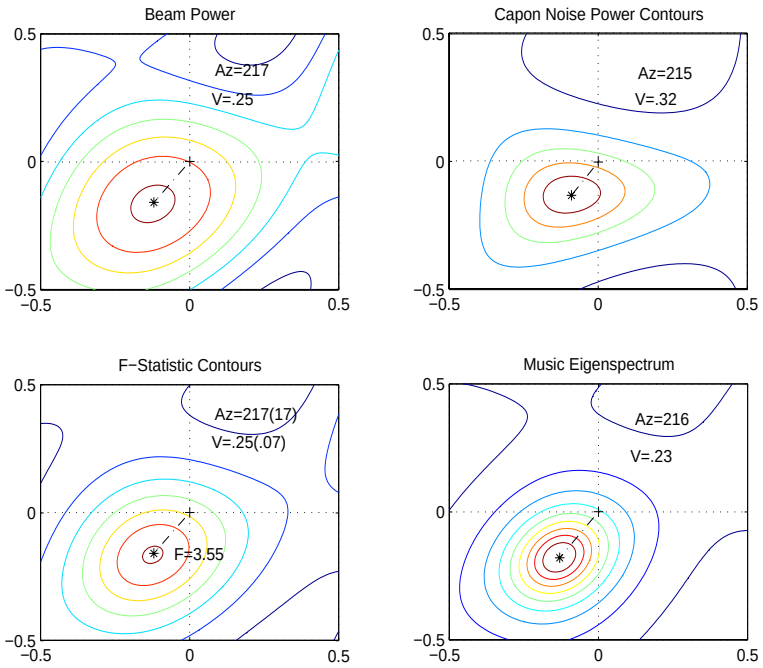

Figure 3. Single signal detectors applied to mixture of tw o pure infrasound explosive signals.

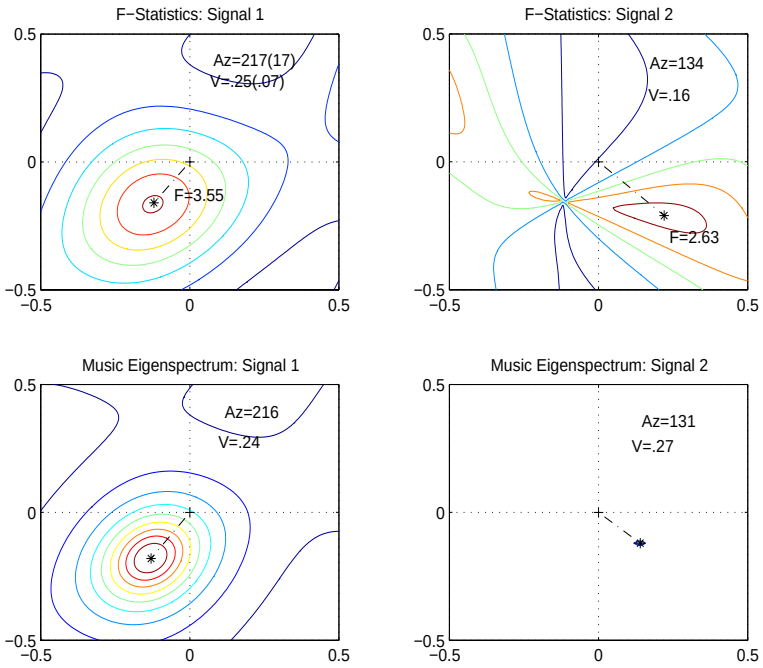

Figure 4. Multiple signal detectors applied to mixture of tw o infrasound explosive signals.

$M = 1$ for the single signal model and $M = 2$ for the tw o-signal version. Curiously, the t w o signal model focuses only on the imbedded signal velocit y and azimuth, whereas the single signal model peaks for the stronger signal. The F-Statistics are taken as $F_1(\hat{\boldsymbol{\theta}}_1)$ in the left hand column and

$F_2(\hat{\theta}_1, \hat{\theta}_2)$ in the second column, where we assume the biased value for $\hat{\theta}_1$ in the computation of the statistic (7). The F-Statistic for the second signal, given the first signal at 217° is 2.63, which still exceeds the .01 false alarm level of 2.55 with $2(13) = 26$ and $2(13)(3-1) = 26$ degrees of freedom in the numerator and denominator.

A convenient summary of the results is given in Table 1 and we note the relative robustness of the single station F detector. Not also that despite a bias of about 8° in the maximum likelihood estimator, the increase in standard deviation still puts the estimated value within half a standard deviation of the ground truth azimuth of 225°.

Table1: Estimation by Different Methods for Single and Mixed Events Using Single and Multiple Signal Detectors

Event	SF225 Only	Mix	
Detectors	SF225	SF225	GS135
Single F	225(8)	217(17)	-
F-Values	11.31	3.55	-
Capon	227	215	-
Multiple F	225	217	134
F-Values	11.31	3.55	2.63
MUSIC	223	216	131

CONCLUSIONS AND RECOMMENDATIONS

We conclude that the performance of the likelihood based statistics under the assumptions of spatially white noise and possible signal decorrelation are relative robust to departures from these assumptions. We have also examined the Capon and MUSIC detectors as possible competitors to the F-Statistic and have note that they do not improve performance in the mixed signal case and do have convenient expressions for the variances of the estimated wavenumber parameters. We note that the likelihood based approaches produce large sample variances for the estimated wavenumber parameters (velocity and azimuth) that are needed for input into the nonlinear location simulations.

A reasonable number of calibration events are needed to give realistic inputs for the previously developed software that produce area uncertainty contours for the location of events detected by random configurations of detecting stations in the IMS network.for these inputs, we are currently downloading a number of events contained in the CMR R&D Test Bed Infrasound Waveform Library. Events available are a California earthquake, several gas pipe explosions, a Titan IV B launch and some bolides.

REFERENCES

Capon, J. (1969). High-resolution frequency-wavenumber spectrum analysis. *Proc.IEEE*, 57, 1408-1418.

Capon, J. and N.R. Goodman (1970). Probability distribution for estimators of the frequency wavenumber spectrum. *Proc.IEEE* (letters), 58, 1785-1786.

Schmidt, R.O.(1979). Multiple emitter location and signal parameter estimation. *Proc.RADC Spectral Estimation Workshop*, 243-258. Rome, Italy. dan Road, MS-62301, Fort Belvoir, Virginia.

Shumway, R.H. (1983). Replicated time series regression: An approach to signal estimation and detection. *Handbook of Statistics Vol. 3*, Chapt. 18, 383-408, Time Series in the Frequency Domain. D.R. Brillinger and P.R. Krishnaiah ed., North Holland.

Shumway, R.H., S.E. Kim and R.R. Blandford (1999). Nonlinear estimation for time series observed on arrays. Chapter 7, Ghosh ed. *Asymptotics, Nonparametrics and Time Series*, 227-258. New York: Marcel Dekker.

Shumway, R.H. (1999). Signal detection and estimation of directional parameters for multiple arrays. Technical Report DTRA-TR-99-50, Defense Threat Reduction Agency, 8725 John. J. Kingman Road, MS-62301, Fort Belvoir, VA 22060-6201

Shumway, R.H. (2000). Detection and location capabilities of multiple infrasound arrays. *Proceedings of 22nd Annual Seismic Research Symposium on Monitoring a Comprehensive Nuclear-Test Ban Treaty (CTBT), Sept 12-15, 2000, New Orleans.*

Stoica, P. and A. Nehorai (1989). MUSIC, maximum likelihood, and Cramer-Rao lower bound. *IEEE Trans. Acoustics, Speech and Signal Processing*, 37, 720-741.

BOLIDES AND OTHER INFRASOUND EVENTS

Rodney W. Whitaker, Peter G. Brown, Douglas O. ReVelle, Thomas D. Sandoval,
J. Paul Mutschlecner, and Nicole M. Bueck

Los Alamos National Laboratory

Sponsored by National Nuclear Security Administration
Office of Nonproliferation Research and Engineering
Office of Defense Nuclear Nonproliferation

Contract No. W-7405-ENG-36

ABSTRACT

During the past year, we have processed infrasound data from at least 13 bolide events, including the important recent events of 23 April 2001 and 25 August 2000. Bolides represent a source of significant natural impulsive signals that can be detected by infrasound arrays and networks and may not have detections by other technologies. As more International Monitoring System (IMS) infrasound stations come online, detections of these events will increase. Analysis of these multiple-station event detections will allow tuning of detection and location algorithms. Work by various groups on the April 2001 event already has shown this. We will present data from all 13 events, detected by one to eight stations (not all of which are IMS); however, more detailed results will be made for the 4/23/01 and 8/25/00 events for which some space-based data have been released. Some results on the bolide events will illustrate the features of Infra_tool, an infrasound analysis tool for use within MATSEIS.

We will also review some recent work and analysis of infrasound from earthquakes observed with Los Alamos National Laboratory (LANL) arrays. This data set illustrates the value of using wind-corrected amplitudes in the analysis. These natural impulsive events have many of the characteristics of interest to the IMS. Such data will be essential for exercising and refining detection and location algorithms and thus calibrating the infrasound network.

KEY WORDS: infrasound, bolide, location, earthquake, wind correction

OBJECTIVE

We discuss data from recent bolide events detected infrasonically on various infrasound arrays, including newly established ones as part of the International Monitoring System (IMS). Recent results on infrasonic signals from earthquakes are also presented.

Observations of large bolides and their associated effects on Earth's atmosphere are now available from several instrumental techniques. Satellite instruments [Tagliaferri et al, 1994], photographs [Ceplecha et al. 1993], video observations [Brown et al. 1994], seismic data [Qamar, 1994], and infrasound recordings [ReVelle, 1998] all contribute to our observational understanding of these rare events. The latter technique, in particular, can be used when a meteoroid penetrates deeply enough (50- to 90-km altitude) into the atmosphere and creates a blast wave of sufficiently low frequency to propagate to the Earth's surface [eg. ReVelle, 1976]. For large bolide events, the blast wave created by the hypersonic passage of the meteoroid may propagate to very large distances at infrasonic frequencies and be detectable by differential low-frequency microphones on the ground, if meteorological conditions are favorable. The global flux of larger bodies with energies ~ 1kT TNT (1 kT TNT = 4.185×10^{12} J) is more than 10 per year [ReVelle, 1997].

RESEARCH ACCOMPLISHED

Bolides

Table 1 gives recent bolide events detected by various infrasound arrays. Included in this table, by each event, are the stations detecting the event. Of particular interest are the events of 8/25/00 and 4/23/01 in the eastern and east-central Pacific for which more detailed data are given.

Table 1: Recent bolides detected on various infrasound arrays.

Date	Time (UT)	Source lat	Source long	Energy (kt)	Stations
February 18, 2000	9:29	0.864N	109.151E	15	WRAI
August 25, 2000	1:12	14.45N	106.1W	8	DLIAR, PDIAR, ISM, IS59
January 18, 2000	16:43	60N	225.29E	5	PDIAR
July 19, 2000	17:40	17.7S	94E	0.5	WRAI
August 16, 1999	5:18	35.02N	107.17W	0.1	DLIAR, LA
August 14, 1999	7:16				DLIAR
November 21, 1995	9:18	38.2N	103.9W	0.05?	LA
October 4, 1996	0:00	36.1N	117.6W	0.05?	SGAR, NTS, PDIAR, LA
June 13, 1998	13:30	34.2N	103.3W	0.1	SGAR
October 9, 1997	18:47	31.8N	106.1W	0.25	DLIAR, LA
August 11, 1998	9:30	20S	128E	9.3	WRAI, ALICE SPRINGS
August 11, 2000	18:45	35.1N	106.4W	?	DLIAR
April 23, 2001	6:12	28.38N	132.90W	11	SGAR, DLIAR, NVIAR, IS10, NTS,IS57, IS59, IS26

where: Alice Springs was a temporary array near Alice Springs, Australia.
DLIAR is the Los Alamos, NM, prototype array.
ISM or IS10 is the Canadian array near Lac du Bonnet, Manitoba.
IS26 is the array in Freyung, Germany.
IS57 is the Pinon Flat, CA, array.
IS59 is the Hawaii array.
LA is the small scale Los Alamos array.
NTS is a small-scale Los Alamos array at the Nevada Test Site.
NVIAR is the array near Mina, NV.
PDIAR is a small scale Los Alamos array at the Pinedale Seismic Research Facility near Pinedale, WY.
SGAR is a Los Alamos array near St. George ,UT.
WRAI is the array at Warramunga, Australia.

Correlation analysis summary plots are shown in Figure 1 for three of the events. These were done with the Infra_tool.m tool within Matseis. (See notes on Figure.)

Tables 2 and 3 provide analysis details for the August and April events. Analysis was done in part with the Matseis software package from Sandia National Laboratories. We did not have calibration data for some arrays and not all stations have physical pressure units. Most headings are self-explanatory. Durations were based on the time during which the cross-correlation coefficient was two sigma above the pre-event background noise values.

To estimate source energy, the observed period at maximum amplitude of the signal may be related (with numerous assumptions) to an empirical formulation derived from Air Force recorded infrasound data of near surface nuclear tests in the 1960's [cf. ReVelle, 1997]. This is a validated approach, in the sense that observed wave periods could be directly compared to known yields, but suffers from the drawback that it is only appropriate for low-altitude spherical nuclear detonations. It must thus be considered an approximation only for higher altitude bolide line-source explosions and short (<400 km) ranges, particularly since a number of effects

may change the period at maximum amplitude during propagation [ReVelle, 1974]. However, it has been found to be in reasonable agreement with energy estimates for several bolide events observed infrasonically and with other methods [eg. ReVelle et al. 1998]. This empirical energy relation is given as :

$$Log(E/2) = 3.34 - \log(P) - 2.58 \qquad (1)$$

where E is the total energy of the event (in kT), and P is the period at maximum amplitude in seconds of the stratospheric arrival, also known as the main acoustic arrival.

Table 2. Observed signal characteristics associated with the April 23, 2001, bolide. The table gives the period at maximum amplitude (T_{maxamp}), peak-to-peak pressure (in millipascals) and trace velocity (in km/s). The duration of the signal is referenced to the levels at which the signal correlation returns to within 2σ of the noise background.

Station	**Location**	**Azimuth of Arrival**	**Range (km)**	**Time of Max Amplitude**	**Duration (seconds)**
IS59	19.6N, 155.9W	62.5	2526	08:27:56	740
DLIAR	35.9N, 106.3W	259.3	2626	08:44:43	780
SGAR	37.0N, 113.6W	252.0	2039	08:12:30	1050
IS26	48.9N, 13.7E	327.3	9526	16:26:00	480
NTS	36.7N, 116.0W	240.3	1833	08:00:58	1440
IS57	33.6N, 116.5W	247.1	1666	07:51:46	520
IS10	50.2N, 96.0W	244.2	3931	09:58:47	440
NVIAR	38.4N, 118.3W	236.1	1753	07:56:21	420
FLRS	48.8N, 0.48E	314.6	10315	15:45:00	-
UAF	64.8N,147.7W	151.0	4183	10:16:00	540

Station	**T_{maxamp} (seconds)**	**Peak Pres. (mPa)**	**Trace Velocity**	**Yield (Eq (1))**
IS59	4.14 ± 0.54	470	0.340 ± 0.015	0.61± 0.27
DLIAR	4.05 ± 0.33	400	0.337 ± 0.018	0.56±0.16
SGAR	4.47 ± 0.68	449	0.358 ± 0.069	0.78±0.40
IS26	-	25	0.346 ± 0.05	-
NTS	3.07±0.45	552	0.305±0.015	0.22±0.11
IS57	3.90±0.40	-	0.302±0.016	0.50±0.17
IS10	5.14±1.01	-	-	1.25±0.83
NVIAR	4.59±0.47	-	0.341±0.002	0.85±0.30
FLRS	-		0.291	
UAF	-	-	0.317	

Table 3. Observed signal characteristics associated with the August 25, 2000, bolide. The table values are the same as given in Table 1. Note that as many stations had not been calibrated at this time, few peak pressure measurements are available. PDIAR was experiencing complex instrumental noise problems and thus the period and amplitude measurements are suspect and array processing was not possible. Microphone alignment problems with IS10 prevented reliable array processing.

Station	Location	Azimuth of Arrival	Range (km)	Time of Max Amplitude (UT)	Duration (seconds)	T_{maxamp} (seconds)
IS59	19.6N, 155.9W	90.2	5304	06:05:25	830	6.04 ± 0.28
DLIAR	35.9N, 106.3W	185.1	2381	03:28:00	620	7.20 ± 1.67
IS10	50.2N, 96.0W	-	4079	05:11:00	600	6.68±0.83
IS25	5.21N, 52.73W	282.6	5925	06:21:55	-	-
PDIAR	42.8N, 109.8W	-	3171	07:56:21	420	4.59±0.47
UAF	64.8N,147.7W	139	6415	07:09:00	-	-

Station	Yield (Eq(1))	Peak Pressure	Trace Velocity
IS59	2.1±0.3	-	0.339 ± 0.015
DLIAR	3.7±2.9	125	0.361 ± 0.055
IS10	2.9±1.2	-	-
IS25	-	-	0.338±0.003
PDIAR	1.1±0.3	200	-
UAF	-	-	0.359

To determine the likely location for the April event, we used the best infrasound bearings (determined at maximum amplitude of the signal) and found their individual intersections (see Figure 2). To determine the most probable location, all bearing intersections were weighted by the sine of the angle of intersection, following [Greene and Howard, 1975], and then a weighted average position for the most probable location for the event determined. The bearings from NTS and UAF are most uncertain and these are excluded for our location determination. The best fit location using these weighting procedure places the event at 28° 23N and 132° 54'W. For comparison, the satellite data indicate a location near 27° 54'N and 133° 53'W. This represents a linear difference of 110 km in ground location. Given the poor azimuthal distribution in station coverage for the event and the fact that we have applied no wind corrections to these bearings, this is remarkably good agreement over baselines of the order of several thousand kilometers. Using an observed time for the event from satellite records of 06:12 UT, we derive mean signal speeds from 0.26-0.31 km/s with most signals between 0.28-0.29 km/s. These are typical stratospherically ducted returns.

It is clear that as more infrasound stations come on line, data on bolides will begin to accumulate. These natural impulsive events have many of the characteristics of interest to the IMS. These data will be quite valuable for exercising and refining detection and location algorithms.

Earthquakes

Recently we have re-examined our data on infrasound from earthquakes, obtained mostly during the time of the Los Alamos infrasound program for detecting underground nuclear tests at the Nevada Test Site. The data and results are being reviewed for consistency, etc. We present results in Figure 3, where infrasound amplitudes are plotted against the body wave magnitude, Mb. Two normalizations are used. In the upper plot we normalize raw amplitudes to a distance of 250 km by assuming amplitude is proportional to $R^{-1.2}$, where R is the range in km. The lower plot retains this but uses wind-corrected amplitude, Mutschlecner and Whitaker (1999). In the upper right corner of each plot, the regression equation is given along with the correlation coefficient of the fit. The improvement in correlation is obvious.

SUMMARY AND CONCLUSIONS

The two bolide events discussed in detail here show how well such events can be detected by arrays of infrasound sensors. Given the azimuthal coverage and number of stations, the location of the 4/23/01 event, using only infrasound data, is really quite good. These events clearly demonstrate the ability of these arrays to detect and locate impulsive atmospheric events. Bolide detections will increase as more IMS infrasound station become operational and will provide excellent test beds for refining detection and location software, as well as exercising the ways in which systematic wind effects can be incorporated to improve analysis results.

Some care needs to be used in comparisons of processing results from different researchers and organizations. If processing parameters are not the same, or nearly the same, then differences in results can be expected. For example, source bearings from slowness planes or FK planes with different number of points in the search space cannot be expected to yield the same results or to agree. Results with different band pass filters can also yield different results. Perhaps it is time to begin discussion, within the community of infrasound researchers, of what a standard set of such parameters should be. This would help to ensure that results for different organizations can be compared on an equal footing and add confidence to the results.

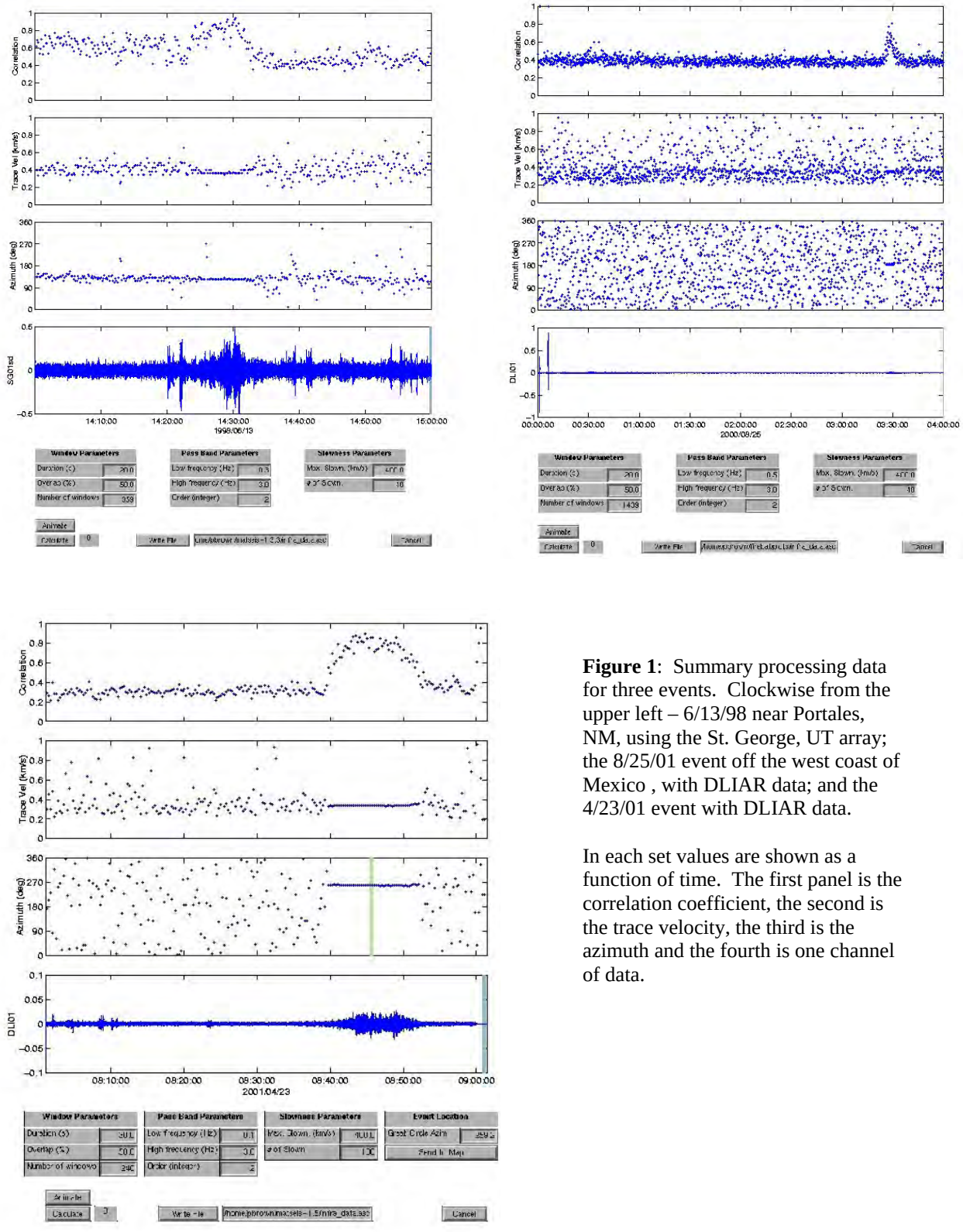

Figure 1: Summary processing data for three events. Clockwise from the upper left – 6/13/98 near Portales, NM, using the St. George, UT array; the 8/25/01 event off the west coast of Mexico , with DLIAR data; and the 4/23/01 event with DLIAR data.

In each set values are shown as a function of time. The first panel is the correlation coefficient, the second is the trace velocity, the third is the azimuth and the fourth is one channel of data.

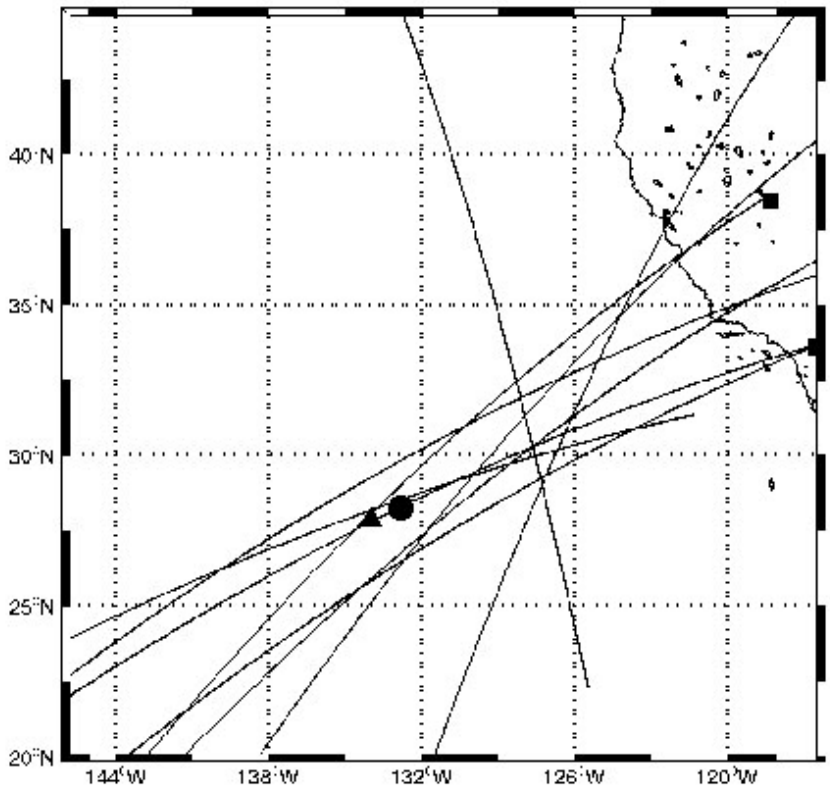

Figure 2: A plot of the various azimuths for the arrays detecting the 4/23/01 event. The circle is the location determined from the weighting of the individual intersections. The triangle is the announced location from satellite data.

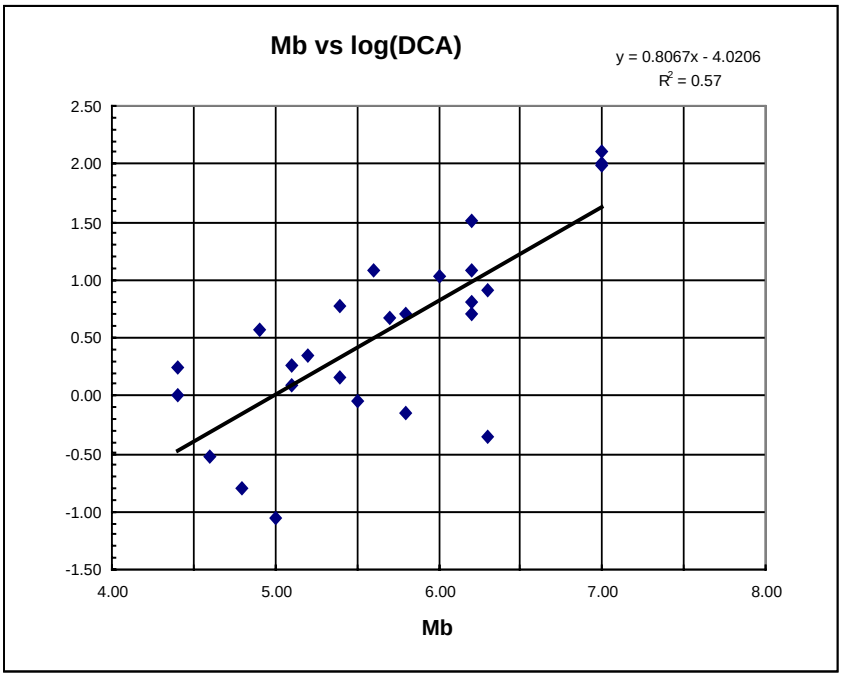

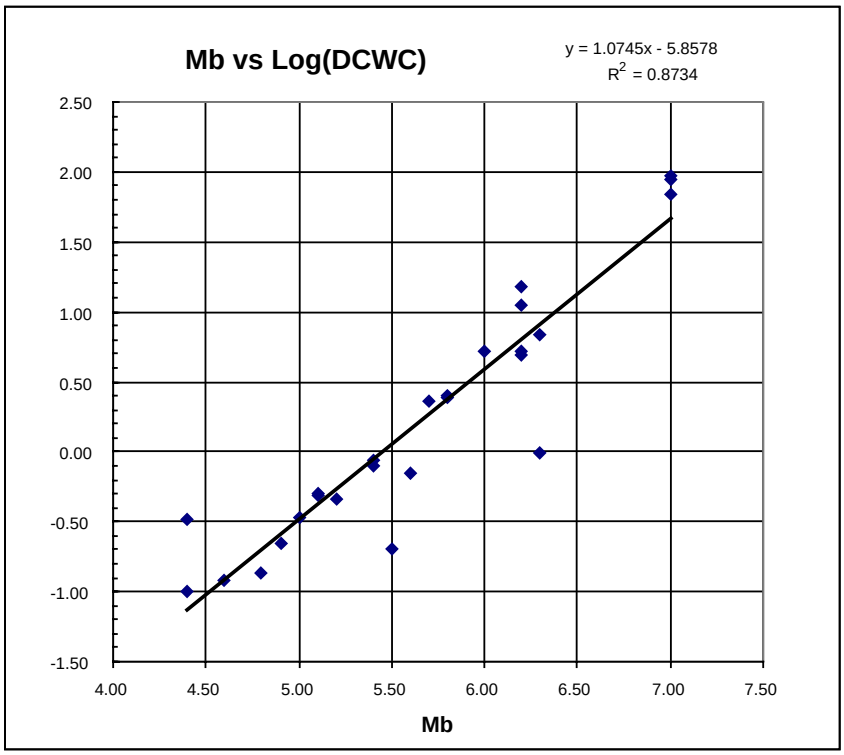

Figure 3: Infrasonic earthquake amplitude data as a function of Mb.

REFERENCES

Brown, P., Z. Ceplecha, R.L. Hawkes, G.W. Wetherill, M. Beech, and K. Mossman (1994), The Orbit and Atmospheric Trajectory of the Peekskill meteorite from video records, *Nature, 3*67, 624-626.

Ceplecha, Z., J. Borovica, W.G. Elford, D.O. ReVelle, R.L. Hawkes, V. Porubcan, and M. Simek (1998), Meteor Phenomena and Bodies, *Sp. Sci. Rev., 84*, 327-471.

Greene, G.E. and J. Howard (1975), Natural Infrasoun : A one Year Global Study, *NOAA Tech. Report ERL 317-WPL 37*, Boulder CO.

Mutschlecnet, J.P., R.W. Whitaker and L.H. Auer (1999), An Empirical Study of Infrasonic Propagation, LA-13620-MS, Los Alamos National Laboratory.

Qamar A. (1995), Space shuttle and meteroid (sic) - tracking supersonic objects in the atmosphere with seismographs. *Seismological Research Letters 66*, 6 – 12.

ReVelle, D.O. (1974), Acoustics of Meteors, PhD Dissertation, University of Michigan.

ReVelle D.O. (1976), On Meteor-Generated Infrasound. *J. Geophys. Res. 8*1, 1217-1240.

ReVelle, D.O. (1997), Historical detection of atmospheric impacts of large super-bolides using acoustic-gravity waves, *Ann. N.Y. Acad. Swci., 822*, 284-302.

ReVelle, D.O., R.W. Whitaker and W.T. Armstrong (1998), Infrasound from the El Paso Superbolide of October 9, 1997, in *Proceeding of SPIE*, edited by C.B. Johnson, T.D. Maclay and F.A. Allahdadi, pp. 66-78, The international society for optical engineering v.3434, Washington.

Tagliaferri, E., R. Spalding, C. Jacobs, S.P. Worden, and A. Erlich (1994), Detection of meteoroid impacts by optical sensors in Earth orbit, in *Hazards due to Comets and Asteroids*, edited by T. Gehrels, pp. 199-220, Univ. of Arizona Press, Tucson, Arizona.

THE OPTIC FIBER INFRASOUND SENSOR

Mark Zumberge and Jonathan Berger

Scripps Institution of Oceanography

Sponsored by Defense Threat Reduction Agency

Contract No. DTRA01-99-C-0056

ABSTRACT

A goal of current infrasound research is to devise systems to maximize the detection capability for signals of interest in the presence of ambient noise in the frequency range of a few millihertz to a few hertz. It has been well demonstrated that the principal source of noise in the requisite frequency band is turbulence in the wind field. To reduce the effects of this noise, we have designed a new type of infrasonic sensor using optical fibers as distributed sensing elements. The design addresses the limitations of the standard pipe filters currently used to average wind-generated, turbulent pressure fluctuations. In addition to maximizing the signal-to-noise ratio, the system has the capability to help estimate signal azimuth and phase velocity.

The principal advantages of the OFIS (optical fiber infrasound sensor) over the standard pipe filter/microbaragraph combination are:

> The OFIS measures the integrated pressure variations along its length, *not* an acoustical sum of the pressure at many points, as is the case for the pipe filter.
>
> The speed of light rather than the speed of sound governs the OFIS response. The OFIS response is thus flat across the entire infrasound frequency band. The standard pipe filter response is certainly not flat and is extremely difficult to determine in practice.
>
> The OFIS can be made arbitrarily long and deployed in an arbitrary geometry. As its output is the integral of the pressure field along its length, the OFIS is inherently sensitive to signal directivity and can be deployed as a directional array element.

We have assembled a prototype optical fiber infrasound sensor, have performed laboratory evaluations, and have run comparisons of the new sensor with more traditional sensors in the field. Field experiments are conducted at the Infrasound test facility, part of the Cecil and Ida Green Pinon Flat Observatory. This facility includes a variety of infrasound spatial filters and recording systems, including an 8-element infrasound array composed of four 18-m and four 70-m spatial filters. This test bed has proved to be ideal for this kind of research as wind speeds vary from near zero to > 10 m/s.

The development of a new interferometric fringe data acquisition system has been a key component of this effort. We can now construct arbitrarily long lengths of the sensor. The remaining task is to investigate the best deployment geometry for optimizing the sensor as a component in an array.

Key Words: Infrasound
Optical fibers
Spatial filter

(This Page Intentionally Blank)

Data Processing and Analysis

A COMPARISON OF TIME- AND FREQUENCY-DOMAIN AMPLITUDE MEASUREMENTS

Hans E. Hartse

Los Alamos National Laboratory

Sponsored by National Nuclear Security Administration
Office of Nonproliferation Research and Engineering
Office of Defense Nuclear Nonproliferation

Contract No. W-7405-ENG-36

ABSTRACT

We have been investigating regional body wave detection thresholds and seismic event identification methods. The basis of this research requires accurate phase and noise amplitude measurements, generally involving frequencies of about 1 Hz and higher [for example, P_n/(0.75-1.5 Hz)]. Here, we examine the differences between amplitude measurements made in the time domain and measurements made in the frequency domain and how those differences might affect regional seismic discrimination and detection threshold estimates.

We have worked with WMQ data for several years. We have retrieved and measured seismograms recorded at WMQ from about 1800 events from throughout central Asia for the years ranging from 1986 to 2000. Event-station distances range out to about 2500 km and event magnitudes range from about m_b 2.5 to over 6.0. We measured WMQ BHZ seismograms over the P_n, P_g, S_n, and L_g phases using time domain root mean square (RMS) and frequency domain Fast Fourier Transform (FFT) methods.

For RMS amplitude measurements, we use the instrument response to correct the entire seismogram into displacement. We then bandpass filter, cut the time-window based on velocity and event-station distance, and measure amplitude as a Log_{10} RMS value. For the spectral method, we cut the phase time-window from a seismogram that has been instrument-corrected into acceleration. We then taper, FFT, and divide by angular frequency twice to convert into displacement. We initially instrument-correct the seismogram into acceleration in an effort to reduce the large amplitudes of the longer period microseism relative to the shorter-periods that are of interest to us for discriminant tests. We smooth and resample the spectra at a rate of 0.05 Log_{10} frequency. To compare RMS and spectral amplitudes for a given event, phase, and band we average the displacement spectra over the same band used during the RMS procedure. When comparing the two methods, we convert the RMS amplitudes to pseudo-spectral amplitudes following Parseval's Theorem.

In general, RMS amplitudes of all phases are slightly larger than the corresponding spectral amplitudes. This is because Log_{10} averaging of the spectral amplitudes emphasizes the higher frequencies within a band. These higher frequencies are lower in amplitude because of the "roll-off" in frequency of the seismic source and the greater attenuation at higher frequencies along the seismic path. The actual ratios obtained using the two methods tend to be nearly the same. This is because the small offsets in the RMS amplitudes relative to the spectral amplitudes are about the same for both phases, and the offsets therefore cancel when the RMS ratio is formed.

We found that spectral measurements of short P_n windows (out to event-station distances of about 700 km) are sometimes unusually large compared to the RMS measurements. This occurrence is most pronounced for low-magnitude events when the measurement window is short. Initially we assumed the problem was with our frequency-domain measurements, but we traced this occurrence to a delay introduced by applying a one-pass filter during the time-domain measurement procedure. The delay was moving the P_n energy down the trace and outside of the measurement window. After changing to a two-pass filter, the RMS amplitudes closely matched the spectral amplitudes.

KEY WORDS: phase amplitude, detection, identification

OBJECTIVE

Any phase detection, magnitude estimation, amplitude tomography, or discrimination analysis applied to treaty monitoring situations requires careful, consistent amplitude measurements. To confirm that we are obtaining good estimates of signal and noise, we measured phase and noise amplitudes of regional seismic data using both time-domain and frequency-main methods. As Parseval's Theorem states that frequency-

domain and RMS time-domain measurements are equivalent, our objective is to compare the two methods to confirm that each approach is robust and consistent. Below, we describe our data, processing, and a comparison of our results.

RESEARCH ACCOMPLISHED

At we have worked with station WMQ data for several years. We have retrieved and measured seismograms recorded at WMQ from throughout central Asia for the years ranging from 1986 to 2000. Event-station distances range out to about 2500 km and event magnitudes range from about mb 2.5 to over 6.0. We measured WMQ BHZ seismograms (about 1800 in all) over the P_n, P_g, S_n, and L_g phases using both the time domain and frequency domain methods.

For time-domain processing we pick phase arrivals and then instrument-correct each waveform into units of displacement in meters. The entire seismogram is de-meaned, tapered, and bandpass filtered. Typically, we measure several one-octave (or slightly narrower) bands between 0.5 and 8 Hz. The entire instrument-corrected and bandpass-filtered waveform is saved for data windowing and measurement processes. Phase measurement windows are defined by the velocities in Table 1, and the phase pick time. The phase window length is defined by the "fast" and "slow" velocities and the event-station distance, but the data window is centered over the picked arrival time. If any segment of the waveform record is not available for the time window of interest, then no amplitude measurements are attempted. Hence, for triggered data we will sometimes measure P_n and P_g, but will not be able to measure S_n and L_g. After determining time windows, the filtered seismogram is cut and an RMS amplitude is measured and stored as a Log_{10} value.

Our frequency domain processing is patterned after the Rodgers et al. (1997) processing model. A data window is cut from an instrument-corrected seismogram, an FFT is run, and the spectra are smoothed and evenly sampled over 0.05 log frequency intervals. We cut data and noise windows exactly as described under our time domain processing. Prior to FFT we taper the data (or noise) window, checking and adjusting taper length to ensure the taper does not extend into the phase arrival pick, or the theoretical phase arrival time (if no pick was made). Following FFT, we then write an amplitude spectra file, being careful to save those portions of the spectra that fall within the passband we used during the instrument correction. Further, when working with short time windows, we only save the low-frequency portions of the spectra that are represented by at least 2 cycles within the time window of interest. For instance, for a 4-second-long P_n window, we would only save spectra of 0.5 Hz and greater.

After converting each frequency point along the spectra into a Log_{10} value, we interpolate along the saved spectra at an interval of 0.01 in Log_{10} frequency, We then smooth with a half-width of 5 and then decimate to every fifth log-frequency sample. Hence, we save the smoothed spectra as Log_{10} amplitude values sampled every 0.05 Hz in log frequency. The final spectral range is controlled by the instrument type and the data window length. When working with a particular passband for discrimination, magnitude, or path calibration research, we average over the appropriate spectral samples to obtain a single amplitude value. With the 0.05 Hz in log frequency sampling interval, a one-octave band will be composed of 6 spectral samples that can be averaged to obtain a single amplitude value.

For comparison purposes we convert the RMS amplitudes to pseudo-spectral amplitudes following Parseval's Theorem, and obtain an average spectral value for a given band as described above. We look at the trend and scatter found between the RMS and spectral amplitude populations by plotting each event's RMS amplitude versus its spectral amplitude (such as in Figure 1A), and by plotting the difference between the two methods for each event versus distance (such as Figure 1D).

Figures 1, 2, and 4 compare P_n and S_n RMS amplitudes to spectral amplitudes. The band is 0.75-1.5 Hz. For Figure 1 we applied a four-pole, one-pass Butterworth filter to measure RMS amplitudes, and we estimated spectra from displacement records (following Rodgers et al. (1997). For the P_n results, the spectral amplitudes (Figure 1A) are often much larger than the RMS amplitudes. This same trend is seen in the S_n results (Figure 1B), but the scatter is more limited.

Assuming the scatter of Figure 1 is related to problems with the FFT on short data windows (only 2 to 9 seconds for P_n) in the presence of strong microseism emphasized on the displacement records, we changed our approach to the FFT. We instrument-corrected into acceleration to de-emphasize the longer periods, ran the FFT, and then divided the spectra by angular frequency twice to obtain displacement spectra. Figure 2 shows amplitude results using this modified approach. Scatter is eliminated on the S_n comparison (Figure 2B), and scatter is nearly eliminated on the P_n comparison (Figure 2A). We still find a few P_n spectral amplitudes that are large relative to the RMS amplitudes. This happens when the data window is short [only 2.5 to 5 seconds and event station distances are between about 300 and 500 km (Figure 2C)].

We assumed the remaining P_n scatter was still related to the FFT in the presence of strong microseism despite running the FFT on acceleration records. However, high-pass filtering at 0.5 Hz in an effort to eliminate the microseism prior to FFT did not reduce scatter. Hence, we re-examined our time-domain procedure and found that the four-pole, one-pass Butterworth filter we were applying was introducing a delay that was moving a significant portion of the P_n signal out of the measurement window. The delay is greatest when a narrow filter (relative to the total bandwidth) is applied. Further, the short time window at distances of between 300 and 500 km, combined with an emergent P_n arrival creates a situation where the delay can significantly change the RMS amplitude estimate (Figure 3). We made new RMS measurements using a two-pole, two-pass filter, and nearly eliminated the problem with the P_n scatter (Figure 4). We did not encounter signal-generated noise problems when applying the two-pass filter.

In Figures 1, 2, and 4 the spectral amplitudes were obtained by averaging the Log_{10} values of the spectra. Rodgers et al. (1997) argue that this approach emphasizes the higher frequencies in a given band. To test this idea, we compare the RMS amplitudes to linearly averaged spectra as shown in Figure 5. The Log_{10} averaging reveals a slight trend between the spectral and RMS amplitude differences as distance increases (Figures 4C and 4D). With linear spectra averaging, this trend is only very slightly present (Figures 5C and 5D). Further, scatter is reduced slightly when comparing Figures 5A to 4A and 5B to 4B.

For discrimination, how these measurement methods affect ratios is especially important. Figure 6 compares P_n/S_n ratios for the 0.75-1.5 Hz and the 4-8 Hz bands. The RMS results are obtained using two-pass filters and the spectra have been linearly averaged. The ratios of both bands show good one-to-one trends (Figures 6A and 6B), and the differences between the ratios show almost no trend with distance or measurement window length (Figures 6C and 6D). Log_{10} averaging of the spectra produces nearly the same result.

CONCLUSIONS AND RECOMMENDATIONS

Overall, Figures 4 and 5 show that RMS and spectral measurements are essentially equivalent, and the differences between linear and Log_{10} spectral averaging appear slight. Further, ratios obtained with time-domain measurements are essentially equivalent to ratios obtained with frequency-domain measurements as we expect from Parseval's Theorem. We have now been able to confirm that we have two consistent techniques for measuring regional waveform amplitudes. This investigation did reveal a few signal-processing pitfalls. The FFTs on the short segments of displacement waveforms were apparently contaminated by strong, longer-period microseism. The FFT in acceleration (to enhance the short periods of interest) followed with two divisions by angular frequency corrected the problem. We also uncovered a delay problem with a one-pass filter applied to time-domain data. We corrected this problem by applying a two-pass filter. We did not encounter significant signal-generated noise problems by applying the two-pass filter. When applied with care, we recommend either the time-domain RMS method or the frequency-domain method for regional-phase amplitude measurements.

REFERENCES

Rodgers, A.J., T. Lay, W.R. Walter, and K.M. Mayeda, (1997), A Comparison of Regional-Phase Amplitude Ratio Measurement Techniques, Bull. Seismol. Soc. Am., 87, 1613-1621.

Table 1. Velocities Used For Defining Phase Windows

Phase	V_{ph} $(km\ s^{-1})$	V_{fast} $(km\ s^{-1})$	V_{slow} $(km\ s^{-1})$
P_n	8.10	8.2	7.6
P_g	6.15	6.2	5.2
S_n	4.60	4.7	4.0
L_g	3.50	3.6	3.0

P_n Amplitude Comparisons for 0.75-1.5 Hz Band with FFT in Displacement

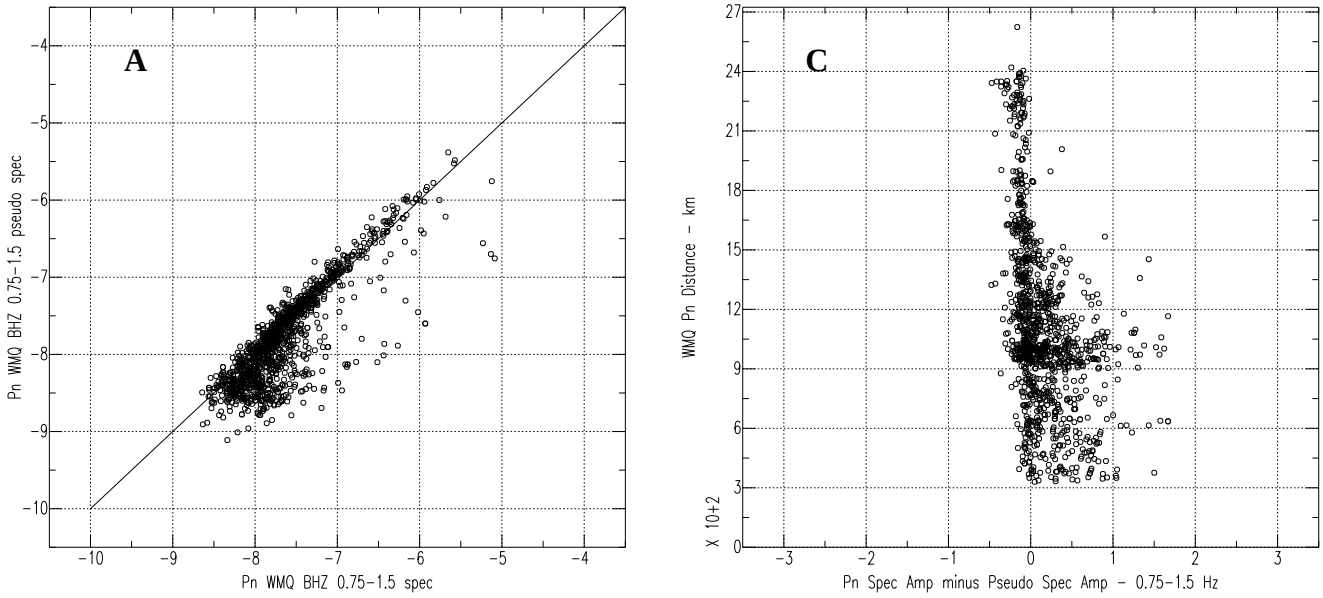

S_n Amplitude Comparisons for 0.75-1.5 Hz Band with FFT in Displacement

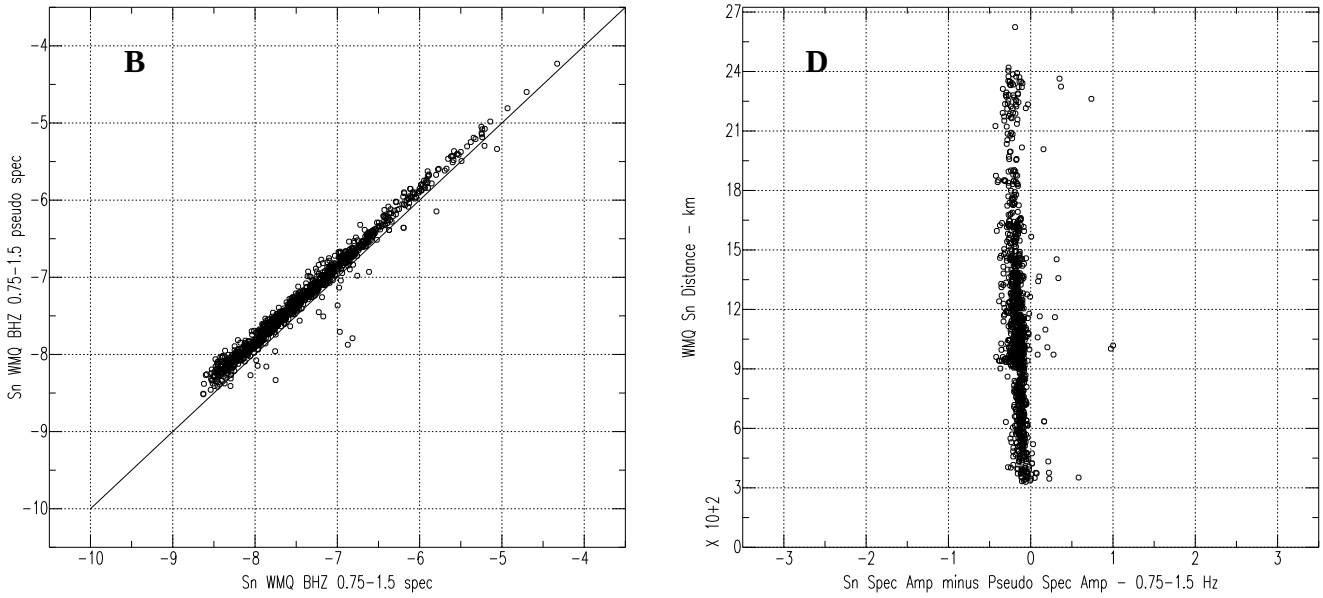

Figure 1. P_n and S_n comparisons between pseudo-spectral amplitudes derived from RMS measurements and spectral amplitudes derived from FFT measurements of displacement seismograms. **A** shows P_n pseudo-spectra (vertical axis) versus P_n spectra estimated directly from displacement waveforms, and **B** shows S_n pseudo-spectra versus S_n spectra estimated directly from displacement waveforms. **C** and **D** show event-station distance on vertical axes versus the difference between spectral and pseudo-spectral amplitudes. Measurement scatter is significant, with many spectral amplitudes much larger than the RMS-derived amplitudes. All measurements are presented in the Log_{10} domain.

P_n Amplitude Comparisons for 0.75-1.5 Hz Band with FFT in Acceleration

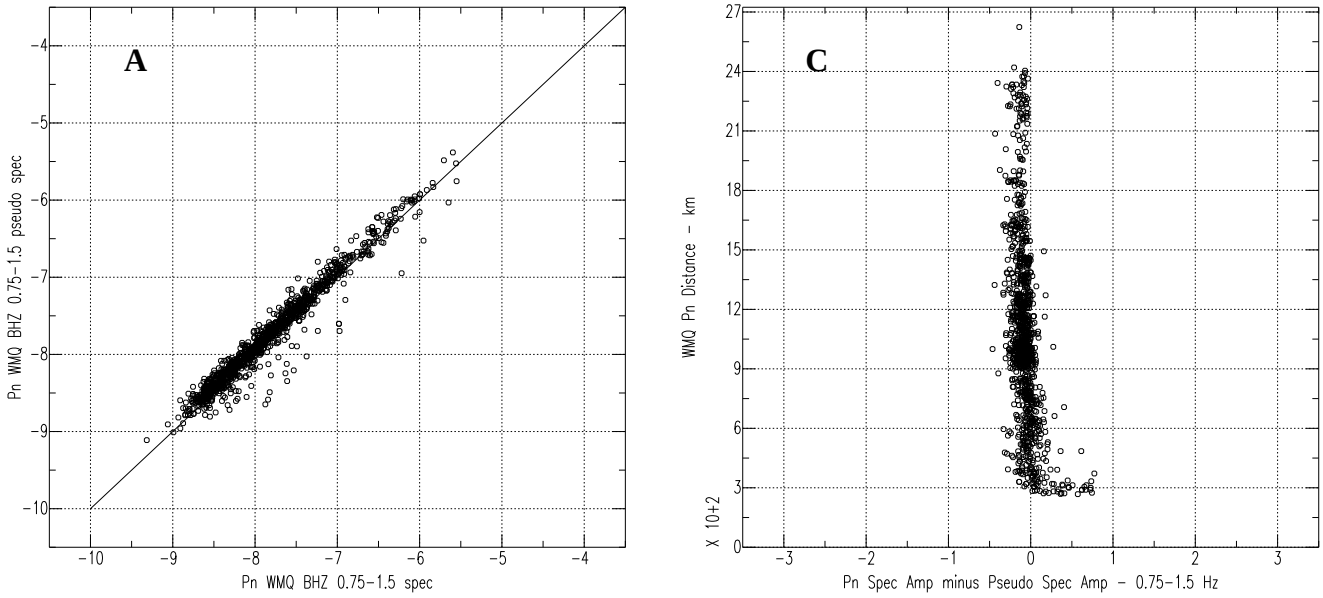

S_n Amplitude Comparisons for 0.75-1.5 Hz Band with FFT in Acceleration

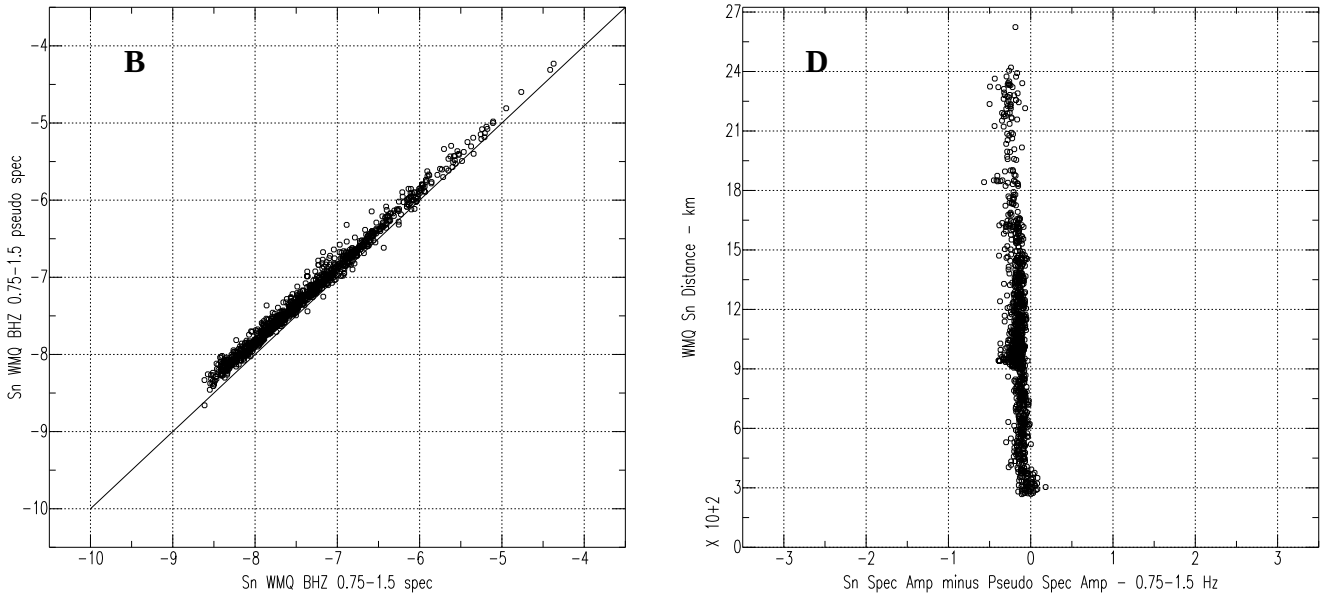

Figure 2. P_n and S_n comparisons between pseudo-spectral amplitudes derived from RMS measurements and spectral amplitudes derived from FFT measurements of acceration seismograms. **A** shows P_n pseudo-spectra (vertical axis) versus P_n spectra estimated from acceleration waveforms division by angular frequency twice to obtain displacement spectra. **B** shows S_n pseudo-spectra versus S_n spectra estimated from acceleration waveforms and division by angular frequency twice. **C** and **D** show event-station distance on vertical axes versus the difference between spectral and pseudo-spectral amplitudes. Measurement scatter is significantly reduced compared to Figure 1 (the case of FFT on displacement waveforms). Some scatter for P_n still remains at short event-station distances between about 300 and 500 km (**A** and **C**).

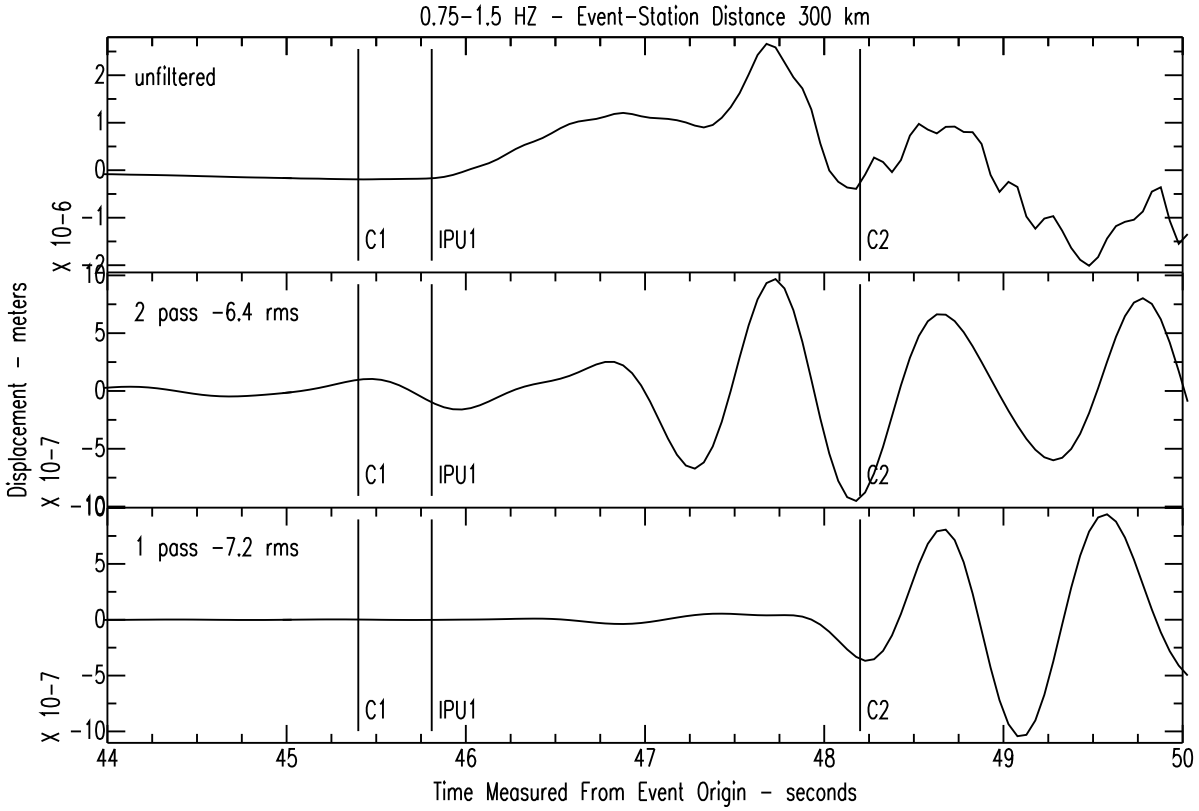

Figure 3. Example where a one-pass 0.75-1.5 Hz Butterworth filter has introduced a delay that pushes the largest P_n amplitudes out of the measurement window, producing an erroneously small RMS amplitude estimate. The top trace is unfiltered, the middle trace has a two-pass 0.75-1.5 Hz filter applied, and the bottom trace has the one-pass filter applied. The C1 and C2 markers indicate the measurement window. Note how the amplitude peak just to the left of C2 on the top and middle traces has been pushed to the right of the C2 marker on the bottom trace. The event-station distance is 300 km, and the event magnitude is 4.7.

P_n Amplitude Comparisons for 0.75-1.5 Hz Band with FFT in Acceleration

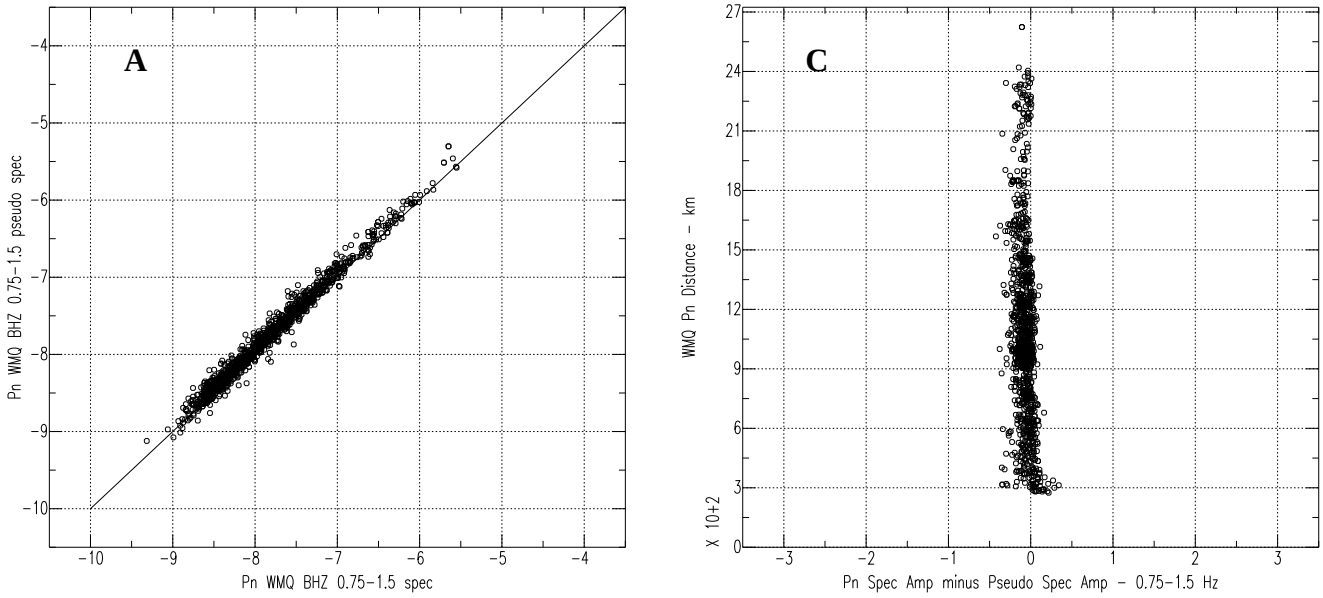

S_n Amplitude Comparisons for 0.75-1.5 Hz Band with FFT in Acceleration

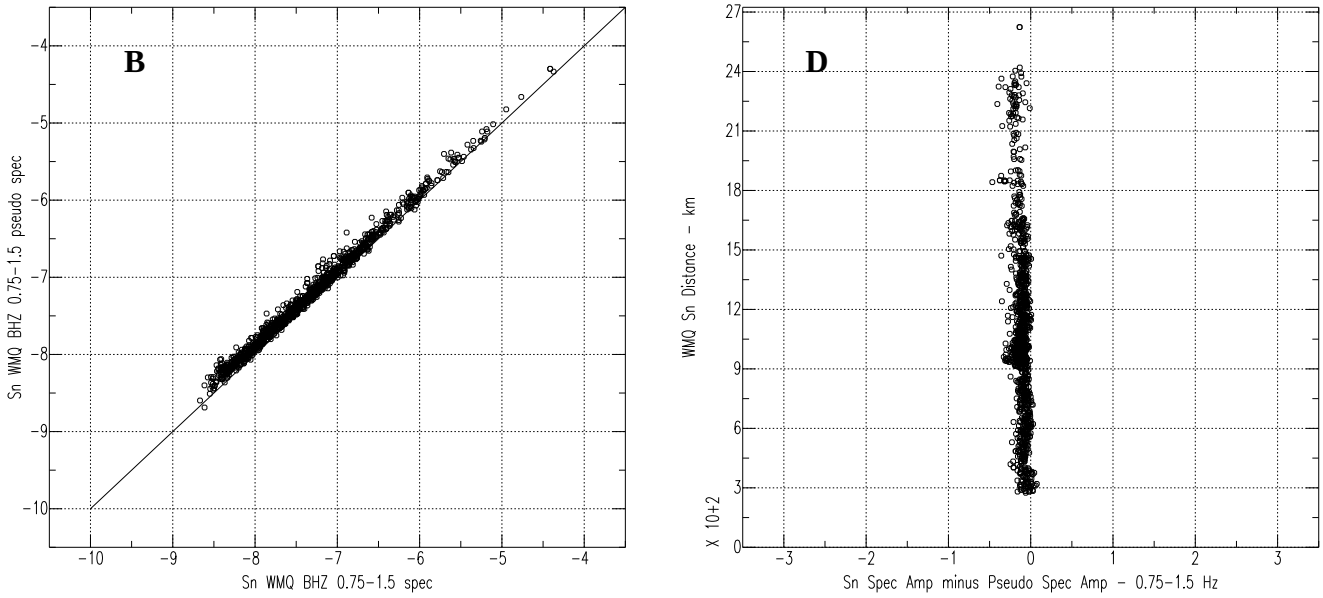

Figure 4. Same as Figure 2, but the time domain measurements have been made with a two-pass filter, rather than a one-pass filter. The delay produced with the one-pass filter had pushed some P_n energy out of the RMS measurement window for the case of event-station distances near 300 km (see Figure 3). Hence, in Figure 2A, the scatter was caused by underestimation of signal strength in the time domain. Here, a two-pass filter has been applied, the delay does not occur, and the P_n scatter has been eliminated. With the longer windows measured for S_n, the scatter is not present (compare Figure 2B with Figure 4B.

P_n Amplitude Comparisons for 0.75-1.5 Hz Band with FFT in Acceleration

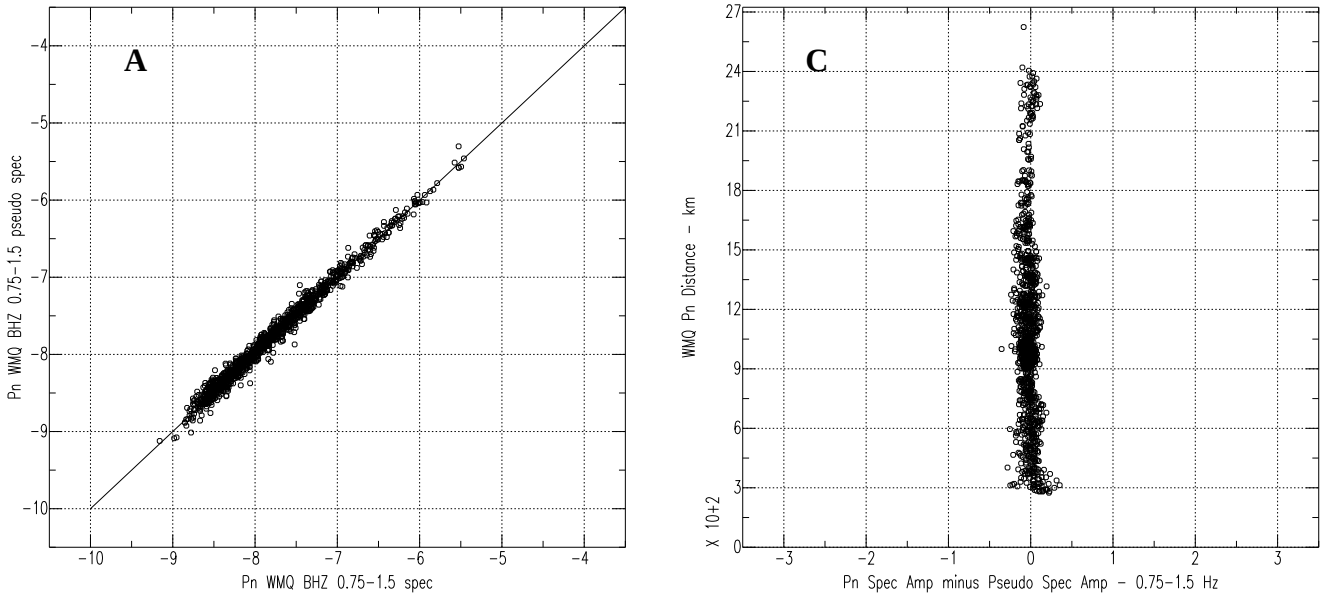

S_n Amplitude Comparisons for 0.75-1.5 Hz Band with FFT in Acceleration

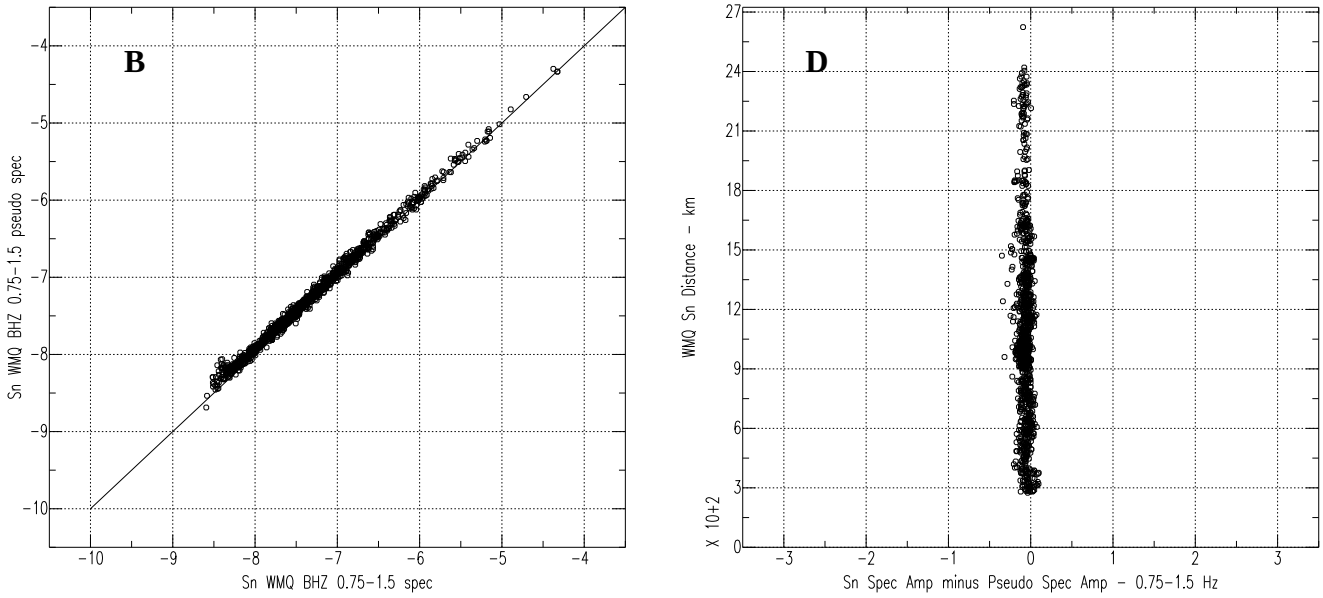

Figure 5. Same as Figure 4, but spectral averaging has been done on linear amplitudes rather than Log_{10} amplitude values. The pseudo-spectra are obtained using a two-pass filter. This is the closest agreement we obtain between spectral and time-domain amplitude measurements.

P_n/S_n Amplitude Ratio Comparisons for 0.75-1.5 Hz Band with FFT in Acceleration

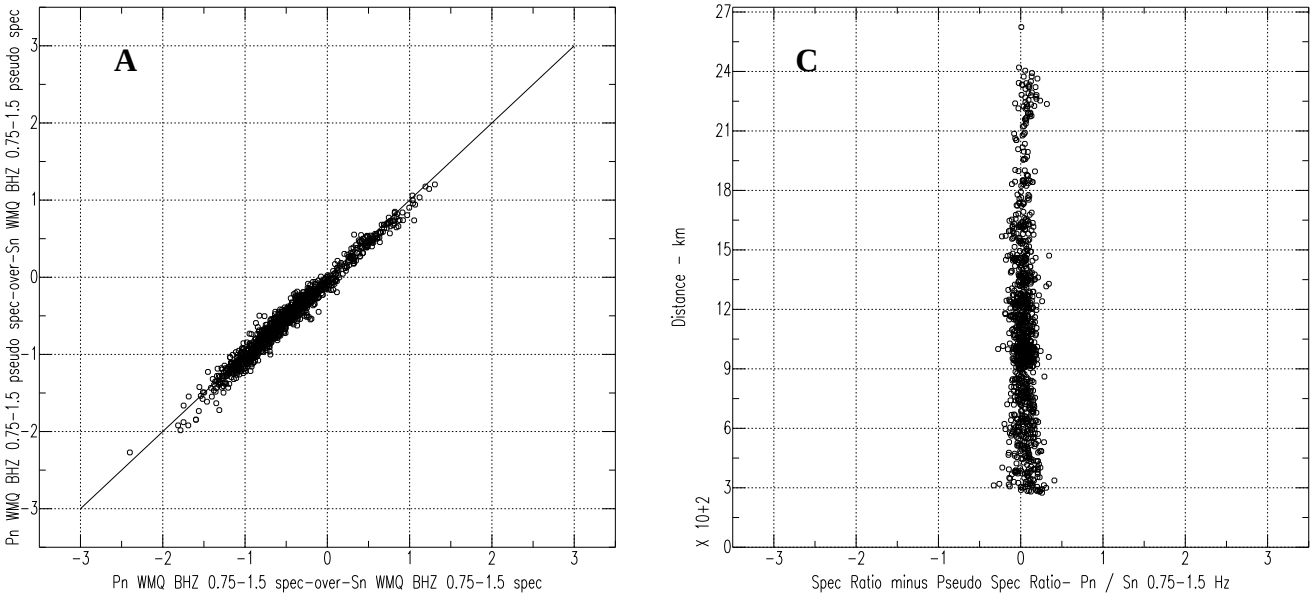

P_n/S_n Amplitude Ratio Comparisons for 4-8 Hz Band with FFT in Acceleration

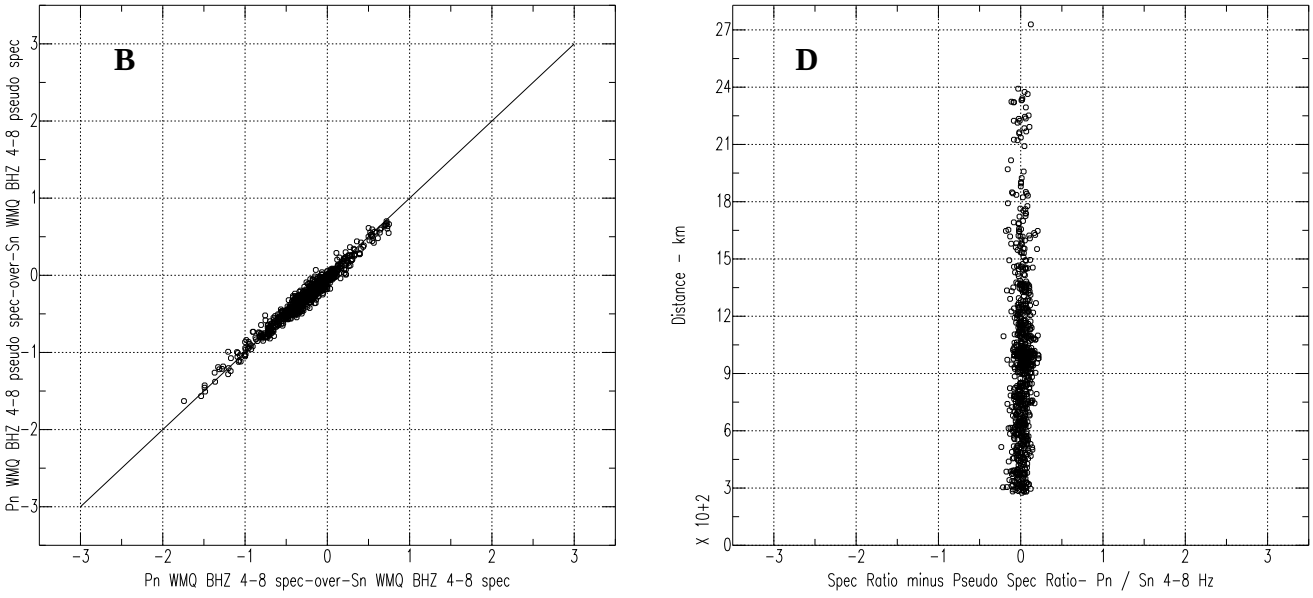

Figure 6. Comparisons of P_n/S_n ratios formed with amplitudes obtained by time-domain and frequency-domain measurements. Linear spectral amplitudes are averaged and pseudo-spectra are obtained using a two-pass filter. For both the 0.75-1.5 Hz and the 4-8 Hz bands the two measurement methods provide very similar results, and only a slight trend with event-station distance can be seen (**C** and **D**). Although not shown here, results obtained through averaging of logrithmic spectral amplitudes are nearly the same.

THE NNSA GROUND-BASED NUCLEAR EXPLOSION MONITORING MULTI-REGION KRIGING MODEL

James R. Hipp

Sandia National Laboratories

Sponsored by National Nuclear Security Administration
Office of Nonproliferation Research and Engineering
Office of Defense Nuclear Nonproliferation

Contract No. DE-AC04-94AL85000

ABSTRACT

The National Nuclear Security Administration (NNSA) Ground-Based Nuclear Explosion Monitoring (GNEM) multi-region kriging model provides a convenient mechanism for merging seismic statistical models developed specifically for bounded regions, over a much broader area in a smooth and continuous fashion. The method involves defining a set of kriging and travel-time model parameters within specific seismic provinces whose boundaries are defined by an enclosing polygon. Each polygon's boundary edges are further characterized using a set of transition blending functions that describe the reduction in influence of the polygon's statistical and model parameters as a point of interest moves from within the polygon boundary to outside the boundary. Spatial domains that are not covered by specific region-dependent polygons inherit a default set of kriging parameters and travel-time models. The entire collection of seismic provinces and the default region determine the extent of the multi-region model.

Region-based statistical and model parameters are averaged at points of interest using an assigned weight based on the amount of influence exerted by each of the regions that are near the point of interest. The weights are normalized to the total influence exerted by all regions influencing the point of interest. Transitions at the vertices of the polygons are smoothed using a patching circle to ensure that the entire bounding influence transition is continuous and differentiable everywhere. With this approach, not only statistical model parameters such as kriging, correlation, shape, and range can be regionally integrated over a broad area, but so can region-dependent model parameters such as total travel time, ellipticity corrections, model variance, and bulk static corrections. In fact, any regional based parameter can be successfully deployed over the entire multi-region domain.

Using this approach, a set of statistically distinct spatial regions can be combined into a single continuous interpolated surface for use by client applications that communicate with the NNSA Parametric Grid Library (PGL). Elements of the multi-region model are currently used by the NNSA Calibration Integration Tool (CIT) and the Client GNEM Interface (CGI) Library.

KEY WORDS: seismic kriging, polygon, multi-region

OBJECTIVE

To improve the U.S. National Data Center (USNDC) capability to perform nuclear explosion monitoring, researchers at the U.S. Department of Energy (DOE) national laboratories are collaborating to develop a collection of data and associated access tools collectively known as the Knowledge Base (KBase). The KBase will consist of many types of information, which will improve the performance of all major monitoring technologies. The number of different data sets in the KBase is expected to be huge, but viewed from an information representation perspective, there are only four basic types of data: reference event information, parametric grid information, contextual information, and supporting information. In this report parametric grid information is the primary focus, and in particular, the new Multi-Region Kriging (MRK) model.

The MRK is an extension to the Modified Bayesian Kriging (MBK) model developed by the national laboratories and described below. The MRK extends the MBK by allowing the development of a set of kriging statistical parameters for a collection of adjacent regions and providing a framework that treats the collection as an unique entity that can provide smooth residual and associated error results across the entire multi-region area. This paper will provide a brief overview of the MBK method and then give a synopsis of the MRK method before describing some of the mechanical details involved in the formulation of an MRK representation.

RESEARCH ACCOMPLISHED

The sections below give an overview of the new Multi-Region Kriging (MRK) capability developed by the national laboratories. The first section describes the Modified Bayesian Kriging (MBK) method which remains the workhorse in both mono- and multi-region kriging problems. The MBK is the primary tool for evaluating seismic path correction residuals and associated errors. References relating to the MBK are provided so that the interested reader can learn more about the method if desired. The next section describes the MRK methodology and defines its basic construction and terminology. The remaining section illustrates in greater detail the process of converting MBK parameters for use in the MRK framework.

Bayesian Kriging Overview

Researchers at the national laboratories associated with the GNEM project use kriging primarily to develop seismic travel-time residual path corrections and associated errors. Other data development efforts, however, are also beginning to employ the method to generate results and associated errors (e.g. magnitude, azimuth and slowness corrections, etc.). The kriging method provides a means of linearly interpolating values from a data set based on the spatial correlation characteristics of the data itself. The term kriging actually refers to a family of interpolation techniques, most of which are Best Linear Unbiased Estimator (BLUE) processes (e.g. Wackernagel, 1995). As with other linear interpolation methods, the kriged estimate of the actual value *Zp* at a given point *Xp* is a weighted combination of the values at the *n* known observations,

$$Z_P = \sum_{i=1}^{n} w_i (X_P) Z_i ,$$

where Z_i and w_i are the value and weight of the i*th* observation, respectively. Kriging has two important features that distinguish it from other linear interpolation methods, however. First, in kriging the weights are determined such that the variance of the predicted error is minimized. Second, kriging produces an estimate of the error associated with the interpolated value.

The kriging method employed by the GNEM project employs a modified version of simple kriging (zero mean kriging). We call the method Modified Bayesian Kriging, or MBK (Schultz et al., 1998). MBK is based on simple kriging where we assume that the mean has been removed from the data before employing the kriging process. The modifications concern the behavior of the observation measurement error and the influence of the observations relative to the distance to an interpolation location.

Generally, kriging imposes an observation dependent modeling error that is the same for all points. However, for most of the physical seismological data sets considered for GNEM analysis the measurement error varies from one observation to the next. For this reason, our MBK model utilizes observation dependent measurement error when performing kriging calculations.

The second modification in MBK allows for use of *a priori* range of influence information for each point. For many typical GNEM data sets the spatial sampling is poor but the analyst may have some additional information that cannot be derived from the data due to the limited sampling (e.g. the scale length of a tectonic province). In the MBK model the influence of the observations on the kriging result at a distance can be controlled through the use of smooth neighborhood kriging. This method can reduce or eliminate the influence of points based solely on the distance between the point and the interpolation point of interest. This behavior makes MBK behave much better as an extrapolator when interpolating in regions that lack good spatial characteristics (point coverage and density).

These two modifications are the primary changes employed over simple kriging in the MBK model. Other subtle changes do exist but are not relevant to the current discussion. The interested reader who desires more detailed information concerning the MBK method and its development should consult Schultz et al.

Multi-Region Approach

As discussed in the MBK approach above, sometimes the complexity of geophysical regions can force the modification of standard analytical models so that the inherent complexity is more correctly represented. In the case of the MBK, the simple kriging models were extended to incorporate observation dependent measurement errors and distance dependent influence on the kriged results. These modifications tend to yield very good results within the confines of geographical regions where the same set of kriging statistics apply. However, as the spatial extent (range) of the data increases the properties of the statistical parameters used in performing the kriging analysis, such as background model error and the correlation range and shape, can also change. These changes, for example, can be caused by perturbations in geophysical properties, such as amorphous inhomogeneities, or by sharp discontinuities, such as a tectonic province boundaries. Generally, one simply reformulates the statistical properties of distant regions and uses those in place of the original formulation. A modeling problem, however, can occur at or near the boundaries or regions of overlap between two or more models. In those regions different results can be produced at the same location depending on which set of statistical properties are used. This causes discontinuities in the spatial solution from one model to the next. This, in turn, presents difficulties for certain analytical processes (e.g. seismic location) where smoothness guarantees solution stability. What is needed is an approach that captures the complexity sufficiently so that statistical properties can change with position but does so in a smooth and continuous fashion so that there are no solution discontinuities.

To accomplish this we have defined separate statistical regions that are modeled with discrete polygonal boundaries. We refer to these regions interchangeably as kriging or statistical regions, when describing statistical attributes, or polygon regions, when discussing geometric qualities. Regions that are not contained by a specific kriging polygon are said to reside in the default kriging polygon. Figure 1 below shows an example of a set of polygons that define specific statistical regions of influence. Notice that the polygon boundaries may or may not lie adjacent to other separate and independent statistical regions. The polygon outlined in red[1] will be used in the remainder of this discussion to illustrate the particular properties of these statistical or kriging polygons, and their impact relative to providing a global solution over all polygons in the region collection.

Aside from the specific polygon boundaries, we must define a transition region about the fixed polygon boundary of each unique statistical region that controls the amount of influence that the regions statistics confers on any arbitrary location. Further, we require that the change in influence as the position changes be a smooth and continuous process. The transition region serves to shift the influence of the polygon's statistical properties from all influencing, for points that are contained completely within the fixed polygon's inner transition boundary, to no influence, for regions that lie completely outside of the polygon's exterior, or outer, transition boundary. Figure 2a illustrates the concept of a transition region. The extent of the transition region is determined by defining vertices for both the inner and outer transition boundaries. Each inner and outer transition vertex is associated with a specific vertex of the polygon boundary. These vertices have no placement restrictions other than they must form polygons that do not have any self-crossings (edges that intersect) nor do they cross the defining kriging polygon. In other words, the inner transition boundary is completely contained within its associated polygon boundary and does not self-intersect, and the outer transition boundary lies completely exterior to its associated polygon boundary and does not self-intersect.

[1] Because this information is impossible to convey without the use of color, and the printed Proceedings are in black and white as a cost-saving measure, we refer the reader to one of the electronic versions of this Proceedings for interpreting the figures in this paper. The electronic versions can be found at http://www.nemre.nn.doe.gov/review2001 or on the CD ROM version of the Proceedings. Or, readers should feel free to contact the authors.

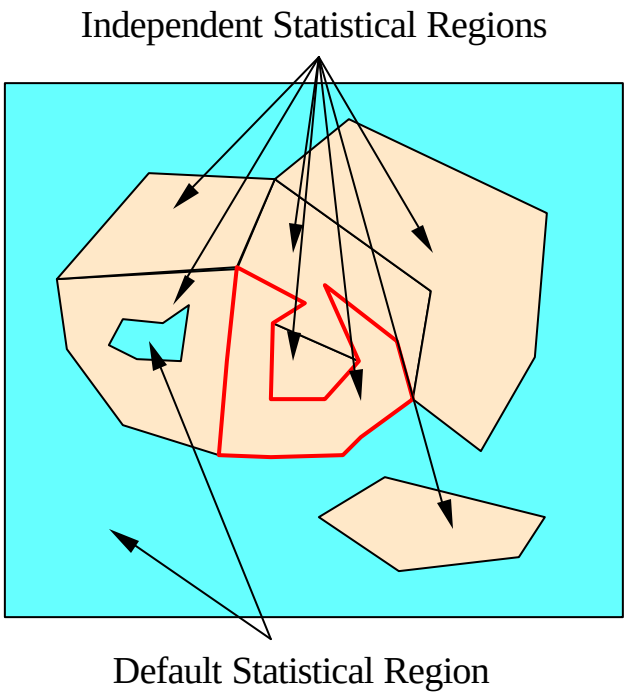

Figure 1. This depiction illustrates an example collection of polygons that represent a set of discrete areas, each with roughly constant statistical properties. The default region is considered to be any and all regions in the model that are not contained within one of the independent statistical regions. The statistical region outlined in **red** is used throughout the remainder of the paper as an example statistical region for purposes of clarifying the details of the model.

Next we map a smooth shape function between the transition boundaries that has a value of one with a slope of zero at the inner transition boundary, and a value of zero with a slope of zero at the outer transition boundary. The shape of the function is not important but it should be monotonically smooth. With this model we can assign a weight for the amount of influence provided by a statistical region relative to an arbitrary point. Points that are on or completely within the inner transition boundary have a weight of one (i.e. complete influence), while points that lie on or completely exterior to the outer boundary have a weight of zero (i.e. no influence). Points that lie between the inner and outer boundaries have an intermediate value between one and zero depending on the shape of the function and the mapping projection at those locations.

Lastly, we ensure differentiability in the transition region around the boundary vertices by specifying a patch circle that connects the edges of a vertex at an equal but arbitrary distance away from the vertex. This distance, referred as the Tangent-Point-Distance, or TPD, can be adjusted to control the amount of curvature around the vertex and must be specified for both the inner and outer transitions at each vertex. The TPD position along each edge that connects with an inner or outer boundary vertex is arbitrary but must be chosen so that the circle formed between two tangent points on either side of a boundary vertex contains the kriging polygon boundary vertex within the confines of the transition region. Figure2b depicts the transition region with the TPD patch circles connected to the inner and outer transition boundaries. Figure 2c shows the same diagram with the completed circle patch at each vertex of the inner and outer transition. Finally, Figure 2d shows the plane view of the transition surface after mapping a hermite shape function into the transition region. The dark red area has a value of one while the blue area has a value of zero. Figure 3 shows a corresponding three-dimensional view of the surface.

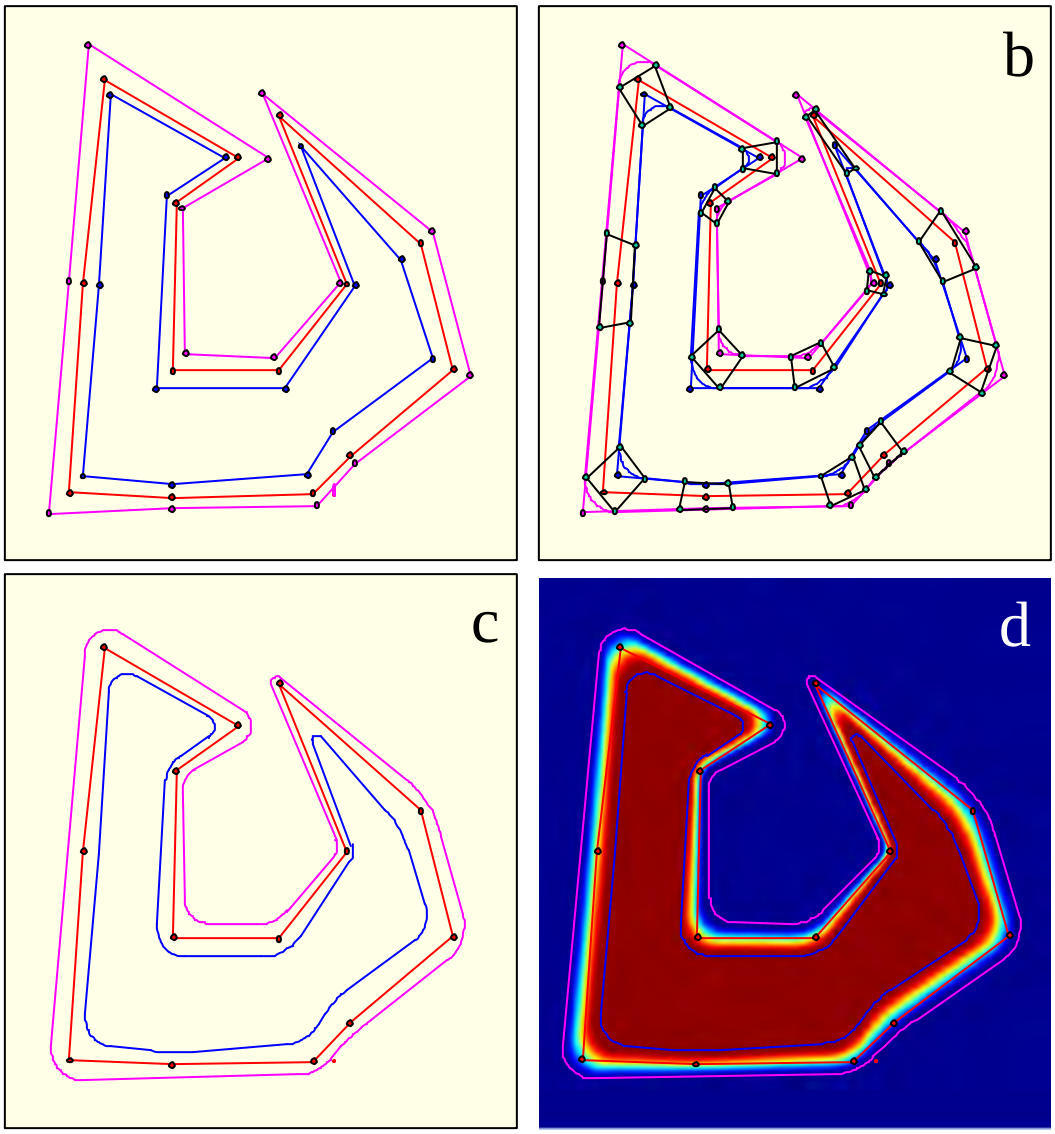

Figure 2. **a)** This panel illustrates an example polygon boundary (**red** edges and vertices) enclosed by an outer transition boundary (**magenta** edges and vertices), and containing an inner transition boundary (**blue** edges and vertices). **b)** This panel shows the construction of the TPD patch points (**green** vertices) with the existing inner and outer transition boundary edges. **c)** This panel depicts the completed smooth inner and outer transition boundaries. **d)** This panel shows a plane view of the final surface with the mapped hermite transition function that moves from a value of one (**dark red**), inside the inner transition boundary, to a value of zero (**dark blue**) outside the outer transition boundary.

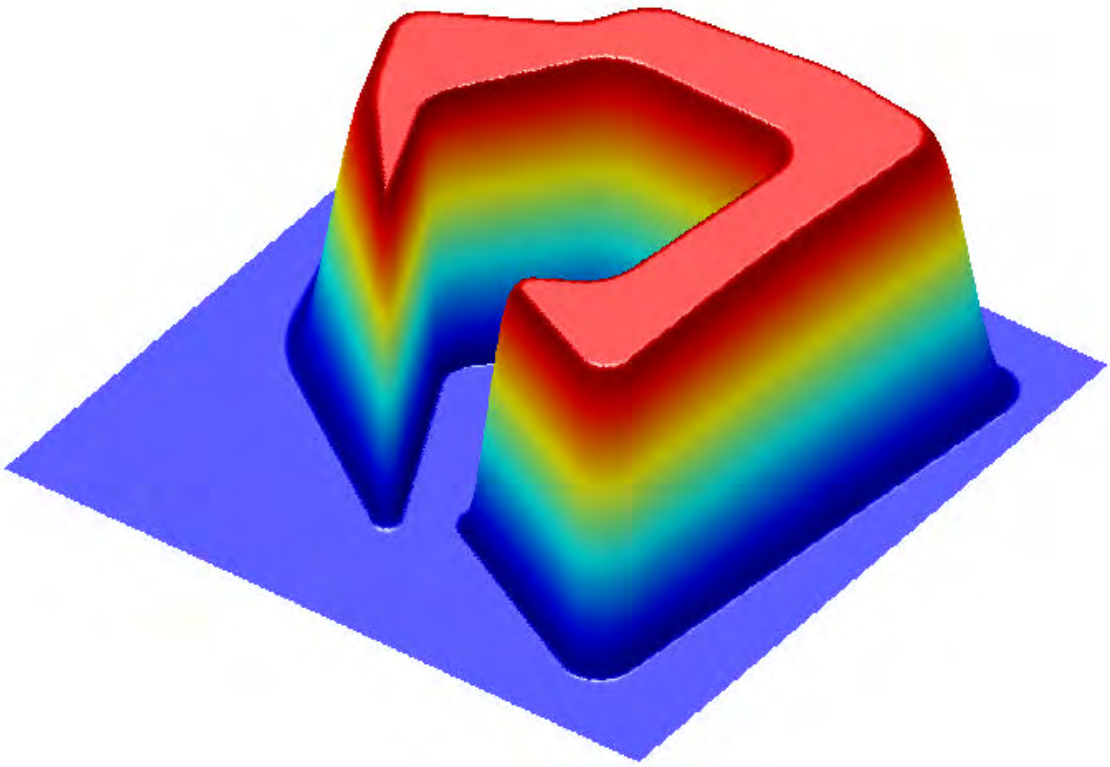

Figure 3. This Figure illustrates a three-dimensional view of the patched and mapped transition weight surface for the example polygon shown in Figure 1 and 2. Notice the smooth curvature everywhere. The shape of the monotonic hermite polynomial function is evident as we move from a region that is completely contained by the inner transition (a weight of one and colored **red**), to a region that is completely outside of the outer transition (a weight of zero and colored **blue**).

Region Based Weights

We now have a means for defining the amount of influence that a particular statistical region can have at an arbitrary point. The researcher is free to design the shape of a statistical region transition zone to be almost anything. Rapid changes in statistical influence caused by crossing over tectonic boundaries are easily modeled by making the distance between the inner and outer transition small. Gradual changes in statistical influence due to large-scale amorphous heterogeneity in the Earth are modeled by making the distance between the inner and outer transition boundaries large. Given this flexible influence weight strategy, we can consider methods for weighting the intrinsic statistical properties of each unique kriging region.

Given the design of the MRK model above, we define the amount of influence that each statistical property should receive based on position. If a position lies completely within the inner transition region of a polygon we allow that statistical property to be totally weighted ($T = 1$ where T is the transition weight of some statistical region). On the other hand, if a position lies completely outside of a polygon's outer transition boundary, we allow no influence for the statistical properties from that region ($T = 0$). Points that lie between the inner and the outer transition boundaries will have some intermediate value ($0 ? T ? 1$).

Given any position-dependent property of a statistical region we can define an average value accommodating all influencing regions by summing the weighted value of the parameter from each region with its associated transition weight. The transition weights are evaluated at some interpolation position X_P. The expression for this averaging technique can be written as

$$\overline{A}_P = \sum_R T^R(X_P) A^R(X_P),$$

where $A^R(X_P)$ is a regional property to be averaged in the *Rth* region evaluated at a point X_P, and $T^R(X_P)$ is the weight of the *Rth* region evaluated at X_P. The weights T^R are normalized across all regions R that influence a specific point X_P. Typical point-dependent parameters that may use this weighting scheme in the MRK model include the background model variance and the correlation range. We also use this scheme to average the base model travel time if the kriging regions defined within the MRK model utilize different base model representations.

We can perform the same weighting for properties that depend on the distance between two points such as correlation. For these cases, however, we need to make some assumptions about how points correlate across different statistical regions. First, if two points lie completely contained within a region's inner transition boundary, and further, they are not contained by any other polygon's outer transition boundary, then the two points are assumed to be correlated completely using the containing region's statistics. Second, if two points are completely contained by different regions such that both points lie completely within their respective regions inner transition boundaries, and further, neither point is contained by any other polygon's outer transition boundary, then the two points are considered to be completely uncorrelated. Figure 4 illustrates these kinds of relationships and depicts other cases that are intermediate to the two described above.

If we assume that each point for which we are trying to determine correlation contributes some weight to the process then in the first case (above) both weights are one, while in the second case at least one weight is zero. This kind of a relationship implies bilinear weighting of the correlation parameter with respect to a region. This relationship can be defined as

$$\overline{r}_{ij}^R = T^R(X_i) T^R(X_j) r_{ij}^R(h_{ij}).$$

In this expression the correlation between the two points, relative to region R's statistics, are scaled by the product of the weights in region R evaluated at both points positions (X_i, and X_j). The parameter h_{ij} is the distance between the two points. Notice that if both points lie completely within region R's inner transition boundary then both weights are 1, and the average value is simply the region R correlation using the distance between the two points. Also notice that if either point lies completely outside of region R's outer transition boundary then at least one weight is zero so that average correlation is zero between the two points. We can normalize these weights to the average value of both weights and sum the effect of other influencing regions to yield an average correlation at any point regardless of how many statistical regions influence the solution. This expression can be written as

$$\overline{r}_{ij} = \frac{\sum_R T^R(X_i) T^R(X_j) r_{ij}^R(h_{ij})}{\sum_R \left(T^R(X_i) + T^R(X_j)\right)/2}.$$

This expression utilizes all influencing statistical correlation definitions to find the average correlation between any two points in a collection of discrete statistical regions. For readers interested in how correlation, correlation range, background model variance, and other parameters are used in the MBK model please see Schultz et al. (1998).

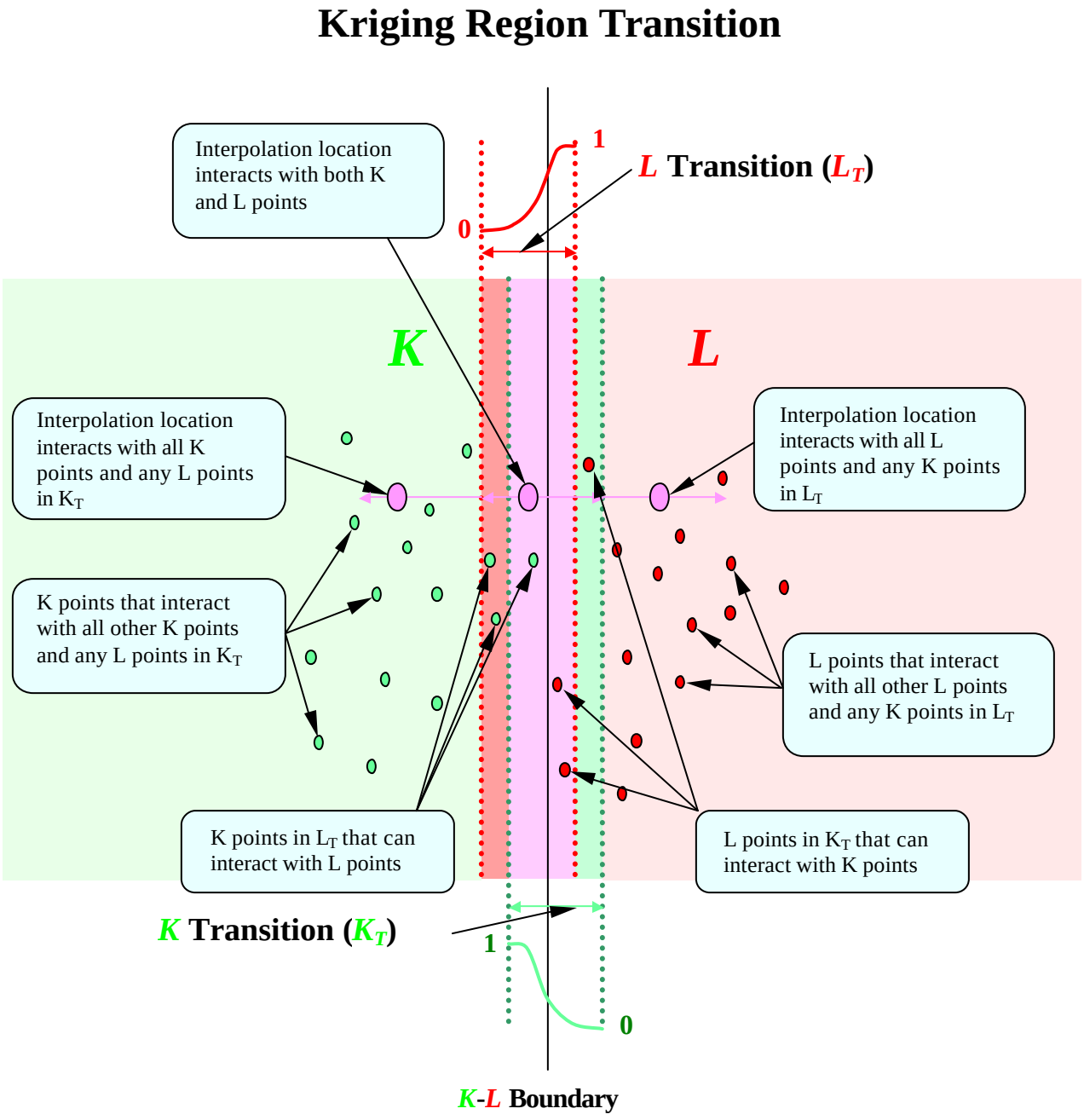

Figure 4. This Figure illustrates the possibilities for data observation correlation interaction between two adjacent kriging regions that share a common boundary. The two regions (***K*** and ***L*****)** both have defined transition intervals (***K*****$_T$** and ***L*****$_T$**) that overlap with one another.

CONCLUSIONS AND RECOMMENDATIONS

In this paper we have presented the new Multi-Region Kriging (MRK) model used by DOE researchers to expand the Modified Bayesian Kriging (MBK) model across regional boundaries where statistical properties differ from one region to the next.

First we summarized the MBK model which uses the basic simple kriging method which attains a solution by minimizing the predicted error, and provides an associated error term at the requested interpolation location. We also defined the major modifications in the MBK model that introduce observation-dependent error and the use of a priori neighborhood range of influence information to aid the MBK model's extrapolation capability.

Next we turned our attention to the MRK model and developed the basic construction methodology and terminology necessary to describe the MRK. This discussion included the definition of a collection of statistically dissimilar spatial regions that may be disjoint from, or adjacent to, other statistical regions in the collection. Then we described the necessary requirements to define a monotonic transition region that provides for a smooth transition in a regions influence weight as a function of spatial position. We also illustrated the process to use circle patching at the vertices of the defining polygons to smoothly change direction from one polygon edge to the next.

Finally, we defined how the statistical properties in a kriging region can be spatially averaged accounting for the regions that influence any arbitrary point. In particular, we considered point-dependent properties such as background modeling variance and correlation range, and point-to-point distance-dependent properties such as correlation.

REFERENCES

Schultz, C., S. Myers, J. Hipp, and C. Young (1998), Nonstationary Bayesian Kriging: Application of Spatial Corrections to Improve Seismic Detection, Location and Identification, *Bull. Seism. Soc. Am*., 1275-1288.

Wackernagel, H. (1995), Multivariate Geostatistics, Springer, Berlin.

REGIONAL SEISMIC THRESHOLD MONITORING

Tormod Kværna, Svein Mykkeltveit, Erik Hicks, Frode Ringdal, and Johannes Schweitzer

NORSAR

Sponsored by Defense Threat Reduction Agency

Contract No. DTRA01-00-C-0107

ABSTRACT

Beginning in September 2000, a large number of small seismic events has been detected in the area near the accident of the submarine Kursk. According to an official Russian announcement, these were underwater explosions carried out by the Russian Navy. This explosion sequence, with numerous explosions ranging in magnitude from very small (about 1.0 on the Richter scale) to fairly large (about magnitude 2.5), provides a unique opportunity to investigate the performance of the threshold monitoring technique. We have thus implemented an experimental site-specific threshold monitoring procedure to monitor the Kursk accident area in the Barents Sea, which has proved to be an efficient tool for revealing small events in this region.

As an integral part of our work to develop an optimized, automatic capability to monitor the seismicity of Novaya Zemlya and adjacent waters of the Kara and Barents Seas, a database of records from seismic events in the area has been compiled, based on information contained in bulletins published by various agencies. The database comprises records from 43 events, carefully selected so as to cover the area with ray paths in the best possible way. Since the major part of the area under study is basically aseismic, the majority of the events in this database is confined to Svalbard, the western Barents Sea, northern Norway, the Kola Peninsula and Novaya Zemlya. The events are earthquakes, mining blasts, other chemical and nuclear explosions, and some are of unknown nature. Magnitudes range from 2 to 4.5, except for two nuclear explosions with magnitudes exceeding 5. Records have been compiled from the ARCES, FINES, NORES, Apatity and Spitsbergen arrays and from the Amderma 3-component station, and have been supplemented by waveforms for KBS, KEV and LVZ requested from Incorporated Research Institutions for Seismology (IRIS). All events have been reanalyzed, and revised event origins as well as consolidated phase identifications have been obtained. The database is being used to determine travel times and frequency-dependent attenuation relations for the various regional phases. This effort will also provide information on the efficiency of Sn and Lg propagation in this area and its correlation with regional geological structures. The information derived from this study will be quantified in terms of parameters that will be needed in the regional seismic threshold monitoring of Novaya Zemlya and adjacent areas.

An important input parameter to regional seismic threshold monitoring is the uncertainty associated with the regional phase attenuation models. From pair-wise comparisons of P-amplitudes from the explosions detonated in the area near the Kursk accident, we find for the arrays on mainland Fennoscandia (ARCES, Apatity, FINES, NORES, and HFS) an inherent single-array magnitude scatter (standard deviation) of about 0.10-0.13 magnitude units. The locations of these explosions show a distribution over a 30-50 km wide area, which is significantly smaller than the resolution of a regional threshold monitoring scheme for Novaya Zemlya and adjacent waters of the Kara and Barents Seas. This suggests that we would be unable to operate any regional threshold monitoring application with an uncertainty better than 0.1 magnitude units for P-phases. Preliminary data analysis indicates that an existing regional P-based attenuation model for Fennoscandia and adjacent areas exhibits a scatter of about 0.25 magnitude units when considering events in the entire Barents Sea region.

KEY WORDS: seismic regionalization, threshold monitoring, Barents Sea, data processing and analysis

OBJECTIVE

The main objective of this research is to develop and test a new, advanced method for applying regional seismic array technology to the field of nuclear test ban monitoring. To that end, we address the development and testing of a method for optimized seismic monitoring of an extended geographical region, using a sparse network of regional arrays and three-component stations. Our earlier work on optimized site-specific threshold monitoring serves as a basis for the development of this new method. Emphasis of the research is on algorithms that can be efficiently applied in a real-time monitoring environment, which are using primarily automated processing, and which can be readily implemented in an operational CTBT monitoring system.

RESEARCH ACCOMPLISHED

One of the main research tasks to be addressed in this contract is the development of an optimized, automatic capability to monitor the seismicity of Novaya Zemlya and adjacent waters of the Kara and Barents Seas. In order to accomplish this, we need to derive the data processing parameters applicable to this region. These include a mapping of the occurrence of the different regional phases, travel-time and amplitude-distance curves for the different seismic phases, and the uncertainties associated with the regional attenuation models.

However, we will first report on an experimental implementation of a site-specific threshold monitoring procedure for the submarine Kursk accident area in the Barents Sea, which has proved to be an efficient tool for revealing small events in this region.

Monitoring of the submarine Kursk accident area

On 12 August 2000, signals from two presumed underwater events in the Barents Sea were recorded by Norwegian seismic stations. The first of these events, at 07.28.27 GMT, was relatively small, measuring 1.5 on the Richter scale. The second event, 2 minutes and 15 seconds later, was much more powerful, with a Richter magnitude of 3.5. These events were associated with the accident of the submarine Kursk, although the exact sequence of events leading to this disaster is still unknown.

The area in the Barents Sea where the Kursk accident occurred has no known history of significant earthquake activity. Beginning in September 2000, a number of small seismic events were detected in this area (Ringdal et al. 2000). According to an official Russian announcement in November, these signals were generated by underwater explosions near the Kursk accident area, carried out by the Russian Navy.

This explosion sequence, with numerous explosions ranging in magnitude from very small (about 1.0 on the Richter scale) to fairly large (about magnitude 3.0) provides a unique opportunity to investigate the performance of the threshold monitoring technique. We have implemented an experimental site-specific threshold monitoring procedure to monitor the Kursk accident area in the Barents Sea, and present in the following some of the results from this investigation.

We first note that the timing patterns of the explosions show some single explosions and some compressed sequences with explosion intervals of 1-2 minutes. The waveforms have similar characteristics, although they are not identical. These explosions were well recorded by the ARCES array (distance 500 km), but the FINES, SPITS and NORES array also detected several of the events. In addition, the Apatity array station on the Kola Peninsula (not an IMS station) provided useful recordings. These stations were thus included in the monitoring scheme.

Figure 1 shows the summary plot with threshold traces for 20 November 2000, where the upper panel shows the network threshold trace and the subsequent panels show the 5 individual station thresholds (P-phases). Following the calculation of the magnitude thresholds the automated analysis contains the following steps:

- Detection of significant threshold peaks on the network trace, using the long-term median as the basis. The detection limits are shown by the line (blue) plotted above each threshold trace. Note that several peaks are identified on the network threshold trace which have to be investigated in more detail.

- Associating seismic phases detected at each station to the time intervals with high network magnitude thresholds.
- Comparing the azimuth and slowness of the associated phases to the expected values for phases originating at or near the Kursk accident area. The number of stations and phases having a close match are used to form a metric indicating the likelihood of the event occurring in the target region. This metric is shown above the upper network threshold trace, where numbers 2 or higher indicate a high likelihood that the event occurred at or near the Kursk accident area.

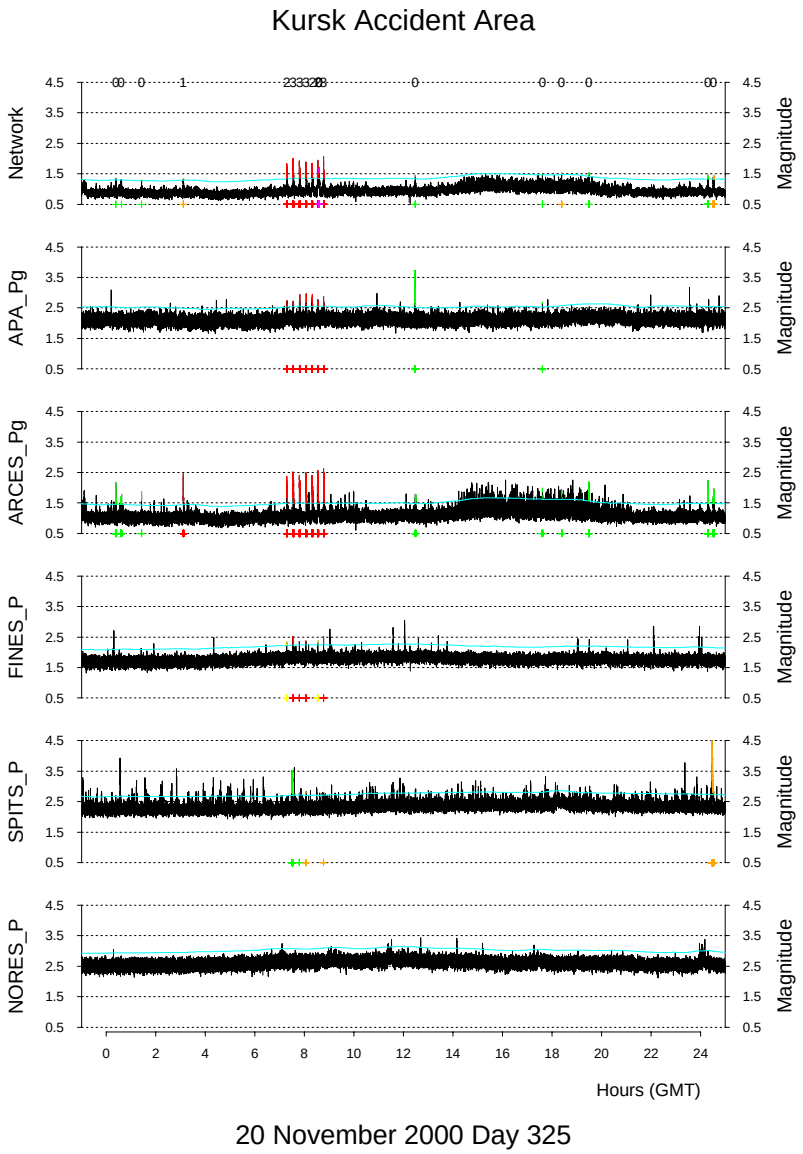

Figure 1. Site-specific threshold monitoring of the Kursk accident area for 20 November 2000 (day 325). The plot shows the 5 individual station thresholds (P-phases), with the combined threshold trace on top. Peaks which are likely to be caused by events in or near the Kursk accident area are indicated by the numbers 2 or 3 (red peaks) on top of the figure, above the network threshold trace.

The plot in Figure 1 shows seven consecutive (red) peaks on the top network trace which are indicated by metric number 2 or 3. These peaks all correspond to real explosions from the Kursk accident area, as has

been verified by interactive waveform analysis. The explosions occur between 7 and 9 GMT, and are almost equidistant in time (15 minute intervals).

The site-specific threshold monitoring of the Kursk accident area has been implemented and tested for several months in NORSAR's experimental pipeline. The associated automatic explanation facility has provided us with a very convenient tool for detecting events in this region and for purposes of continuous monitoring.

Pn station magnitudes

Access to applicable amplitude attenuation curves for the different regional phases is key to this project. The study by Jenkins et al. (1998) provides useful results on this subject for regional phases in Fennoscandia as well as in other stable tectonic regions. In order to utilize their results, we have to validate our time-domain measurements used for threshold monitoring, and we would also like to evaluate the applicability of their attenuation models for distances below 200 km and for events located in the Novaya Zemlya and Barents Sea regions. Using the phase readings of NORSAR's analyst reviewed regional seismic bulletin as a starting point, we have carried out time-domain measurements of the regional phases and compared these to the predictions of the regional phase attenuation models of Jenkins et al. (1998).

The NORSAR analyst produces a bulletin of regional seismic events. Using data from the regional arrays NORES, ARCES, HFS, FINES, Apatity, and SPITS, an average of about 90 events are analyzed every month. However, due to numerous explosions in the Kursk accident area, a total number of 167 events were analyzed during November 2000. The starting point for the analyst review are the locations and magnitudes provided by NORSAR's fully automatic bulletin generated by the Generalized Beamforming method (Kværna et al., 1999). The analyst is focusing on regional events with magnitude greater that 1.5, but also other events of interest in the European Arctic are included in the reviewed bulletin.

For the time period 10 November 2000 to 28 February 2001 NORSARs regional bulletin contains a total of 376 events. Since 10 November 2000 all incoming waveform data from all arrays have been stored permanently on disk and can thereby be directly accessed by any analysis program. This has facilitated our development of an application which analyzes the phase amplitudes reported in the regional bulletin. So far we have focused our attention on the Pn phase, but we also plan to include analysis of the other regional phases (Pg, Sn, Lg).

The Pn amplitude was measured on a beam steered with the azimuth and apparent velocity estimated from f-k analysis. The amplitude was measured in four different frequency bands using the short-term average (STA) within a 5 second window starting at the onset of the arriving phase. The frequency bands used were 2-4 Hz, 3-6 Hz, 4-8 Hz, and 8-16 Hz.

The time-domain STA amplitudes of each filter band were made comparable with the spectral amplitudes used by Jenkins et al. (1998), using the relation

$$\bar{A} \approx \frac{STA \cdot resp_{f_c}}{f_c},$$

where f_c is the center frequency of the passband and $resp_{f_c}$ is the displacement response at this center frequency. The amplitudes were then corrected for frequency dependent attenuation using the distance dependent term

$$acorr = \left(\frac{\Delta}{200}\right)^{-(a f_c + b)}$$

where Δ is the distance in km, f_c is the center frequency and *a* and *b* are the Pn attenuation coefficients derived by Jenkins et al (1998) for stable continental regions (*a = 0.08, b = 1.44*).

Station magnitudes were then calculated using the relation

$$stamag = log_{10}(\bar{A} \cdot acorr)$$

Note that the absolute scale of these station magnitudes is arbitrary and that these magnitudes are internally consistent for measurements within each separate frequency band. The problem of addressing the absolute scale of the station magnitudes will be discussed at a later stage.

Scatter of Pn station magnitudes

For each of the four frequency bands both the Pn amplitude of the beam and the corresponding signal-to-noise ratio (SNR) were measured. The frequency band 3 to 6 Hz provides the overall best SNR for the Pn phases analyzed in this study, and we will in the following present statistics on the station magnitudes for this frequency band for phases with SNR > 3.

Out of the total number of 376 events, 75 were associated with explosions detonated in the vicinity of the site of the submarine Kursk accident. Figure 2 shows pair-wise comparisons of Pn station magnitudes, using ARCES as the reference station. We have split the events into two groups.

- Events not in the Kursk accident area
- Events in the Kursk accident area, believed to have a location scatter of a few tens of kilometers

ARCES - Apatity array

The two upper panels of Figure 2 show the magnitude comparison between ARCES and the Apatity array. The 36 events not in the Kursk accident area are quite randomly distributed on mainland Fennoscandia and in the western part of the Barents Sea. The Pn magnitudes at the Apatity array have a negative bias of -0.135 as compared to ARCES, and the magnitude difference has a scatter of 0.263.

For the 57 events in the Kursk accident area satisfying the SNR criterion, the Apatity array has a comparable negative bias (-0.137) seen in relation to ARCES, and the magnitude difference has a slightly smaller scatter of 0.198.

ARCES - SPITS

The two middle panels of Figure 2 show the magnitude comparison between ARCES and SPITS. The 50 events not in the Kursk accident area are almost all located in the western part of the Barents Sea and on the mid-Atlantic ridge. The Pn magnitudes at SPITS have a consistent positive bias of 0.228 as compared to ARCES, and the magnitude difference has a scatter of 0.328.

For the 23 events in the Kursk accident area the positive bias is only 0.09 with a scatter of 0.143.

Six events in the Khibiny Massif area on the Kola Peninsula are the only events from mainland Fennoscandia providing Pn observations at SPITS. For these six events SPITS has a negative bias of 0.333 as compared to ARCES, and the magnitude difference has a scatter of 0.122.

ARCES - FINES

The two lower panels of Figure 2 show the magnitude comparison between ARCES and FINES. The 121 events not in the Kursk accident area are quite randomly distributed on mainland Fennoscandia and a few events are located on the mid-Atlantic ridge. The Pn magnitudes at FINES have a negative bias of -0.119 as compared to ARCES, and the magnitude difference has a scatter of 0.264.
For the 48 events in the Kursk accident area, FINES has a very large positive bias as compared to ARCES (0.473), and the scatter is only 0.168. For the five common events located in the Khibiny Massif, the pattern is quite reversed. FINES has a negative bias of -0.638 as compared to ARCES, and the scatter is 0.132.

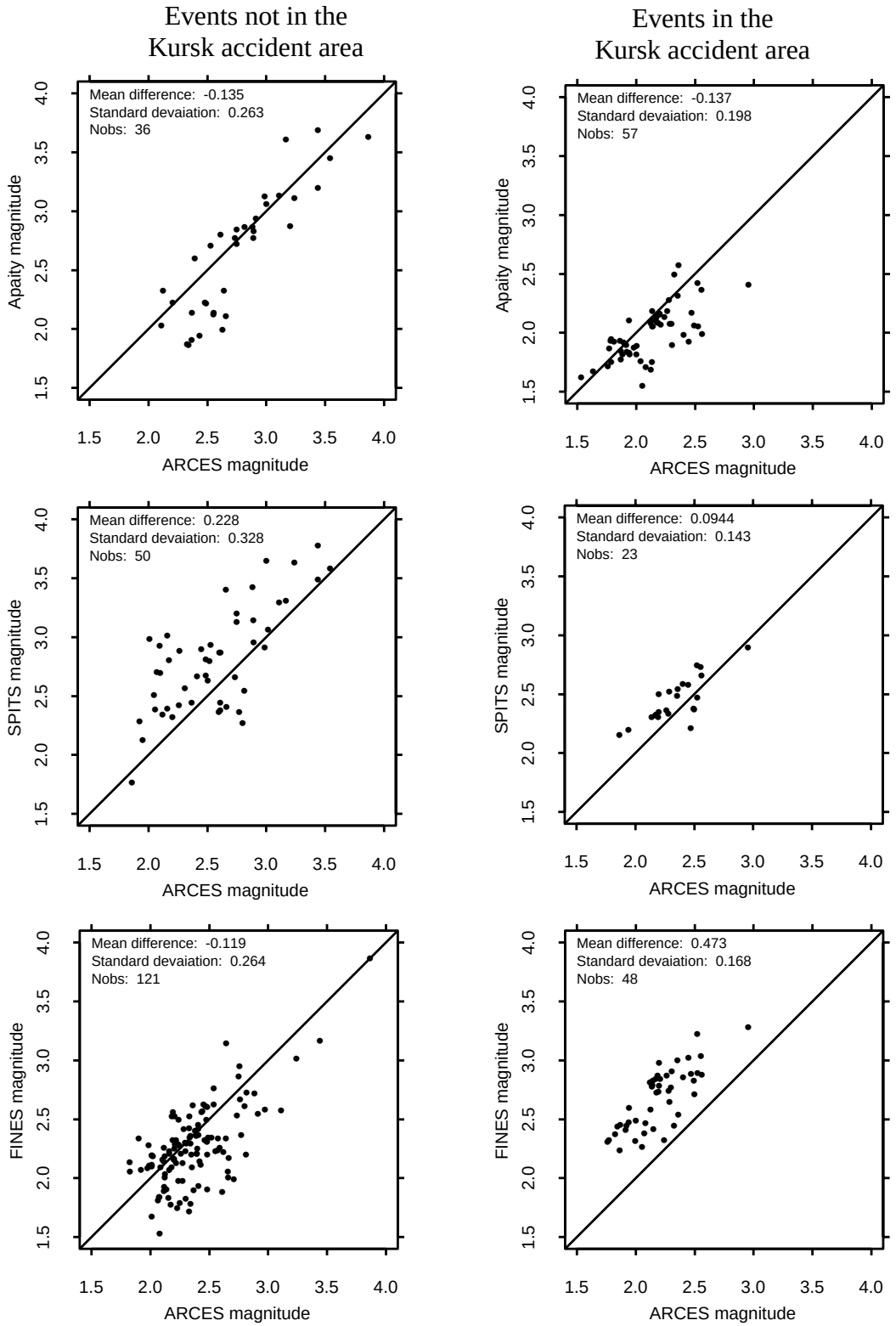

Figure 2: Pair-wise comparisons of STA-based Pn station magnitudes in the frequency band 3.0-6.0 Hz. Notice that the absolute level of the magnitude scale is arbitrary, such that the plots only give information on the internal consistency.

Pair-wise comparisons of ARCES-NORES and ARCES-HFS Pn station magnitudes showed a scatter of the same order as was found for ARCES-FINES (see Figure 2). However, there appeared to be a systematic bias in the station magnitudes between NORES and HFS. For 98 events outside the Kursk accident area HFS has a consistent positive bias of 0.221, with a standard deviation of 0.211 as compared to NORES. This is in accordance with our experience that HFS consistently provides larger ML estimates than NORES, based on Lg amplitudes. With these observations at hand we would like to further investigate this, e.g., by comparing the background noise levels and by independent measurements of the system response at HFS. The NORES system response has been verified through several independent measurements.

An event database for Novaya Zemlya and adjacent waters of the Kara and Barents Seas

As an integral part of our work to develop an optimized, automatic capability to monitor the seismicity of Novaya Zemlya and adjacent waters of the Kara and Barents Seas, a database of records from seismic events in the area has been compiled, based on information contained in bulletins published by various agencies.

The database comprises currently records from 43 events (see Figure 3), selected so as to cover the area with ray paths in the best possible way. Since the major and in particular the central part of the area under study is basically aseismic, the majority of the events in this database is confined to the mid-Atlantic ridge system, Svalbard, the western Barents Sea, northern Norway, the Kola Peninsula and Novaya Zemlya. The events are earthquakes, mining blasts, other chemical and nuclear explosions, and some are of unknown nature. Magnitudes range from 2 to 4.5, except for two nuclear explosions with magnitudes exceeding 5. Records have been compiled from the ARCES, FINES, NORES, Apatity and Spitsbergen arrays and from the Amderma 3-component station, and have been supplemented by waveforms for KBS, KEV and LVZ requested from Incorporated Research Institutions for Seismology (IRIS). Figures 4 and 5 show the ray-paths to the stations ARCES and SPITS.

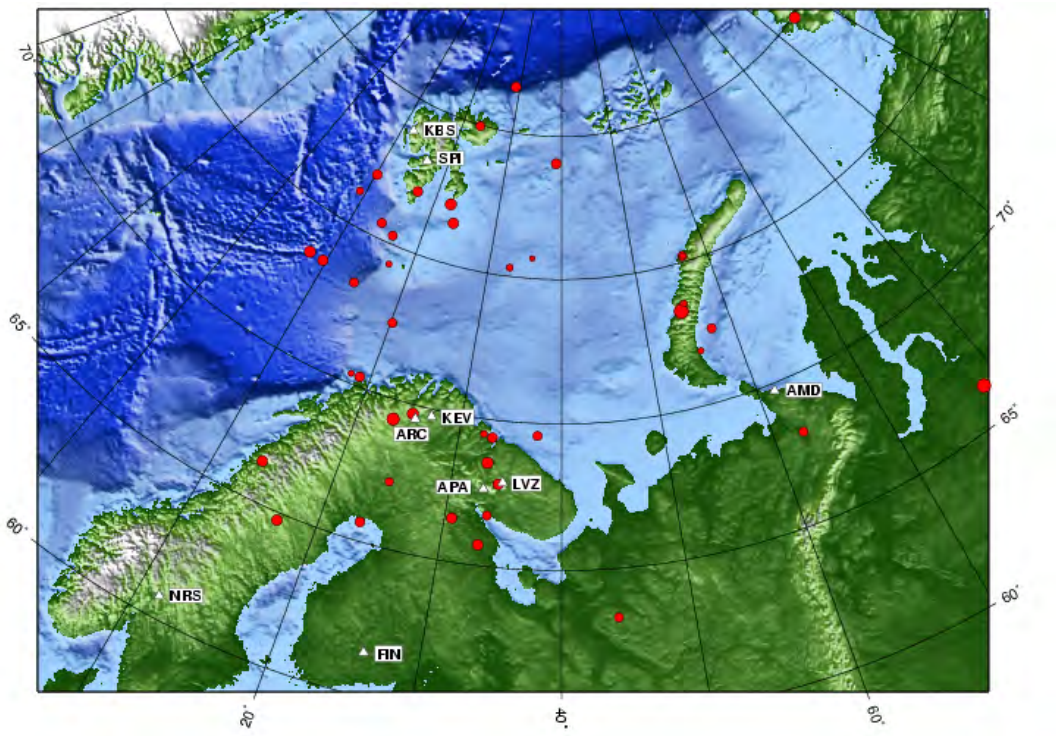

Figure 3. Map with events and stations used for deriving wave propagation characteristics of the Barents Sea and adjacent areas. The event symbol sizes are proportional to the event magnitudes.

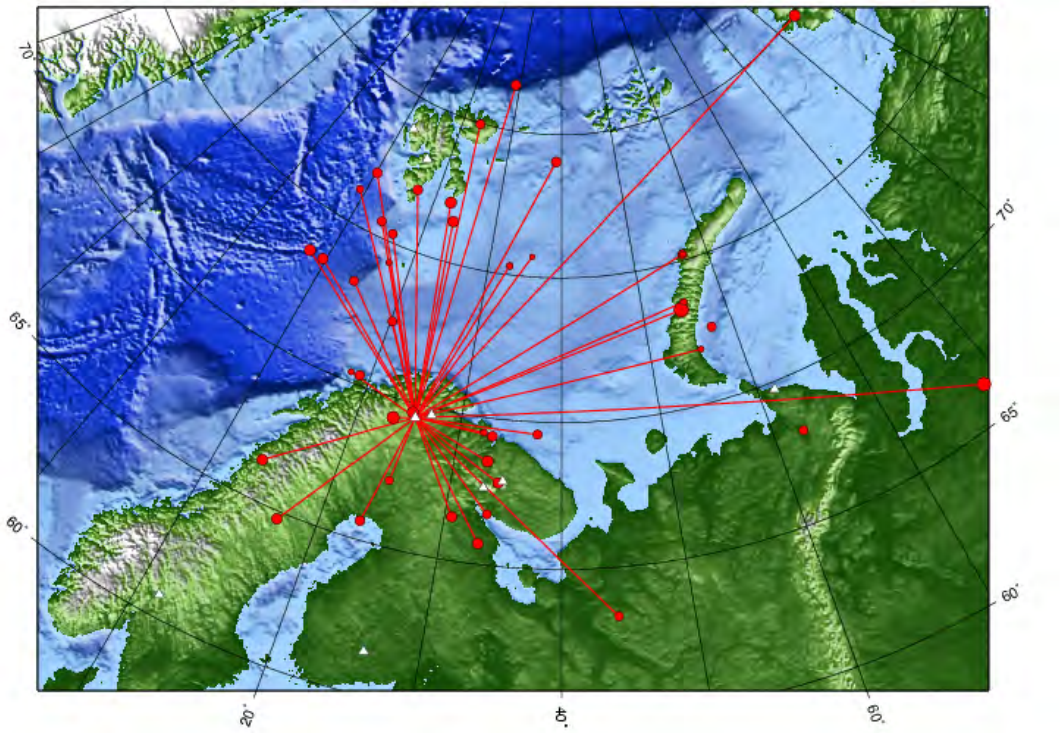

Figure 4. Map showing the ray-paths of the database events recorded at the ARCES array.

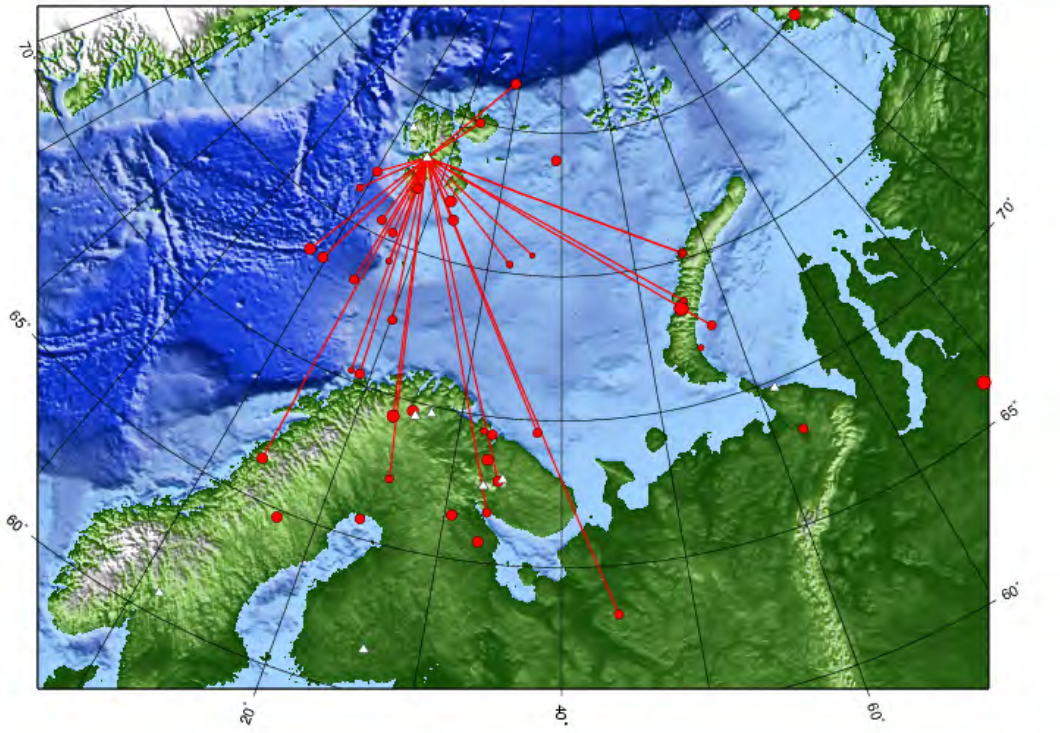

Figure 5. Map showing the ray-paths of the database events recorded at the SPITS array.

All events have been reanalyzed, and revised event origins as well as consolidated phase identifications have been obtained. Figure 6 shows analyzed waveforms and phases identified for one event in the database.

Figure 6. Panels showing the results after analyst review of the 21 January 1996 event located in Finnmark, northern Norway. Note the absence of Lg for paths crossing the Barents Sea. The panels show vertical component recordings at the following seven stations (from top to bottom): ARCES, KEV, Apatity, LVZ, SPITS, KBS, and AMD.

The database is being used to determine travel times and frequency-dependent attenuation relations for the various regional phases. This effort will also provide information on the efficiency of Sn and Lg propagation in this area and its correlation with regional geological structures. The information derived from this study will be quantified in terms of parameters that will be needed in the regional seismic threshold monitoring of Novaya Zemlya and adjacent areas.

CONCLUSIONS AND RECOMMENDATIONS

We have established an experimental application of the site-specific threshold monitoring technique for the submarine Kursk accident area in the eastern Barents Sea, using data from the arrays Apatity, ARCES, SPITS, FINES, NORES and HFS. The daily results are being made available on NORSAR's internal web pages, which has provided us with a practical tool for monitoring the activity in this area. Along with this work, we are now in the process of implementing the software to be used for site-specific threshold monitoring at the Center for Monitoring Research (CMR). This will enable the CMR to run this processing method for any given target area. The only requirements are that each target area must be tuned, preferably based on recordings of previous events in the region, and that access is provided to continuous seismic data, preferably from those stations that are the most sensitive to events in the target area.

Pair-wise comparisons of station magnitudes confirm that the Pn regional phase attenuation model of Jenkins et al. (1998) is a valid approximation for Fennoscandia and adjacent areas. Excluding events in the Kursk accident area, the pair-wise magnitude scatter when comparing with ARCES is almost similar (0.26-0.28) for all arrays on mainland Fennoscandia (Apatity, FINES, NORES, and HFS). If we assign equal variance to the individual array estimates (which would seem to be a reasonable assumption), the inherent single array magnitude scatter would be 0.2 magnitude units (dividing by $\sqrt{2}$).

For SPITS the scatter is somewhat larger (0.328), but the majority of events detected at SPITS are located in the western part of the Barents Sea and on the mid-Atlantic ridge, which have a more tectonic style of Pn attenuation characteristics.

For P-amplitudes from the explosions detonated in the area near the Kursk accident, we find for the arrays on mainland Fennoscandia (ARCES, Apatity, FINES, NORES, and HFS) an inherent single-array magnitude scatter (standard deviation) of about 0.10-0.13 magnitude units. The locations of these explosions show a distribution over a 30-50 km wide area, which is significantly smaller than the resolution of a regional threshold monitoring scheme for Novaya Zemlya and adjacent waters of the Kara and Barents Seas. This suggests that we would be unable to operate any regional threshold monitoring application with a uncertainty better than 0.1 magnitude units for P-phases.

A database of records from 43 seismic events in the Novaya Zemlya area and adjacent waters of the Kara and Barents Seas has been compiled and manually analyzed. The events have been carefully selected so as to cover the area with ray paths in the best possible way. Using the analyst reviewed phase readings as the starting point, we will in our further work investigate various parameters related to seismic wave propagation, i.e., travel-times, phase amplitudes, attenuation relations and the efficiency of Sn and Lg propagation. This information will be applied in the parameterization of a regional threshold monitoring processing scheme for Novaya Zemlya and adjacent waters of the Kara and Barents Seas.

ACKNOWLEDGEMENTS

We would like to thank Berit Paulsen for reanalyzing the events of the Novaya Zemlya/Barents Sea database in a an accurate and consistent manner.

REFERENCES

Jenkins, R.D., T.J. Sereno, and D.A. Brumbaugh (1998), Regional attenuation at PIDC stations and the transportability of the S/P discriminant. AFRL-VS-HA-TR-98-0046, Science Applications International Corporation, San Diego, CA, USA.

Kværna, T., J. Schweitzer, L. Taylor, and F. Ringdal (1999), Monitoring of the European Arctic using Regional Generalized Beamforming, Semiannual Technical Summary 1 October 1998 - 31 March 1999, NORSAR Sci. Rep. 2-98/99, Kjeller, Norway.

Ringdal, F., T. Kværna, and B. Paulsen (2000), Seismic events in the Barents Sea at and near the site of the Kursk submarine accident in 12 August 2000, Semiannual Technical Summary 1 April - 30 September 2000, NORSAR Sci. Rep. 1-2000/2001, Kjeller, Norway.

LLNL MIDDLE EAST, NORTH AFRICA AND WESTERN EURASIA SEISMIC RESEARCH DATABASE

Jennifer L. O'Boyle, Stanley D. Ruppert, Teresa F. Hauk, Douglas A. Dodge,
Flori Ryall, and Michael A. Firpo and LLNL GNEM R&E Staff

Lawrence Livermore National Laboratory

Sponsored by National Nuclear Security Administration
Office of Nonproliferation Research and Engineering
Office of Defense Nuclear Nonproliferation

Contract No. W-7405-ENG-48

ABSTRACT

The Lawrence Livermore National Laboratory (LLNL) component of the National Nuclear Security Administration (NNSA) Ground-Based Nuclear Explosion Monitoring Research and Engineering (GNEM R&E) program has made significant progress populating a comprehensive Seismic Research Database (SRDB) to be used for deriving calibration parameters for the Middle East, North Africa and Western Eurasia (ME/NA/WE) regions. The LLNL SRDB provides not only a coherent framework in which to store and organize very large volumes of collected seismic waveforms, associated event parameter information, and spatial contextual data, but also provides an efficient data processing/research environment for deriving location and discrimination correction surfaces. The SRDB is a flexible and extensible framework consisting of a relational database (RDB), Geographical Information System (GIS), and associated product/data visualization and data management tools. This SRDB framework is designed to accommodate large volumes of data (almost 3 million waveforms from 57,000 events) in diverse formats from many sources (both LLNL-derived research and integrated contractor products), in addition to maintaining detailed quality control and metadata. We have developed expanded look-up tables for critical station parameter information (including location and response) and an integrated and reconciled event catalog data set (including specification of preferred origin solutions and associated phase arrivals) for the PDE, CMT, ISC, REB and selected regional catalogs. Using the SRDB framework, we are combining travel-time observations, event characterization studies, and regional tectonic models to assemble a library of ground-truth information and phenomenology (e.g. travel-time and amplitude) correction surfaces required for support of the ME/NA/WE regionalization program. We also use the SRDB to integrate data and research products from a variety of sources, such as contractors and universities, to merge and maintain quality control of the data sets. Corrections and parameters distilled from the LLNL SRDB provide essential contributions to the National Nuclear Security Administration Knowledge Base (NNSA KB) for the ME/NA/WE region and will improve capabilities for underground nuclear explosion monitoring. The LLNL information products will facilitate calibration of International Monitoring System (IMS) stations (primary and auxiliary), their surrogates (if not yet installed) and selected gamma stations necessary to complete the ME/NA/WE regionalization efforts. In addition to an overview of selected individual information products, we present an overview of our visualization, integration, validation, and organizational processes. Development of these processes and the LLNL SRDB was necessitated by both the very large amount of data and information involved, over 2 terabytes, and the varied data and research result formats utilized. Products assembled, integrated and validated using the LLNL SRDB are grouped into 5 major categories:

1. Reference and Contextual Information
2. Detection Data
3. Calibration and Ground Truth Data
4. Event Location Products
5. Event Identification Products

KEY WORDS: seismic, database, knowledge base, GIS, visualization, integration

OBJECTIVE

The primary objective of the Lawrence Livermore National Laboratory (LLNL) Seismic Research Database (SRDB) is to facilitate development of information products for the LLNL Ground-Based Nuclear Explosion Monitoring Research and Engineering (GNEM R&E) Middle East, North Africa and Western Eurasia (ME/NA/WE) regionalization program. The LLNL SRDB provides efficient access to, and organization of, thousands of seismic events and associated waveforms, while also providing the framework to store, organize, integrate and disseminate information products for delivery into the National Nuclear Security Administration Knowledge Base (NNSA KB).

The SRDB provides a unified framework for all seismic data and information products as outlined in Figure 1. This requires the reconciliation and merging of data derived from different sources and methods and of varying quality, along with the ranking of the data sets based on relative quality. Integration occurs on many levels in order to generate data, data sets, databases or knowledge bases. The SRDB also allows for the integration of LLNL research with contractor research products and other available data sets. In order to efficiently organize information within the SRDB, it was necessary to automate procedures needed to create and update database tables, but a large effort is still required by technicians and scientists to load special data sets, review results of automated processing and resolve quality issues. Sufficient metadata (including measurement procedures, codes, comments and measurement errors) are stored at each step in the data creation and analysis process to allow re-creation or verification of results at any stage in the processing flow.

LLNL information products created using the SRDB may be grouped under two major categories: primary data products and derived products. The primary products are those developed in the process of collecting the raw materials for calibration: ground truth data, waveform data, event catalogs, phase pick information, regional station information and instrument responses. The derived products (distilled from the organized raw seismological data) are models and corrections that improve detection, location and identification functions. To calibrate International Monitoring System (IMS) seismic stations (primary and auxiliary), as well as a variety of other stations that experience has shown to be useful, the LLNL SRDB must incorporate and organize the following categories of primary and derived measurements, data and metadata:

Contextual and Raw Data
1. Station Parameters and Instrument Responses
2. Global and Regional Earthquake Catalogs
3. Selected Calibration Events
4. Event Waveform Data
5. Geologic/Geophysical Data sets
6. Geophysical Background Model

Measurements and Research Results
1. Phase Picks
2. Travel-time and Velocity Models
3. Rayleigh and Love Surface Wave Group Velocity Measurements
4. Phase Amplitude Measurements and Magnitude Calibrations
5. Detection and Discrimination Parameters

Corrections and parameters distilled from the LLNL SRDB provide needed contributions to the NNSA KB for the ME/NA/WE region and will improve capabilities for nuclear explosions monitoring. The LLNL contributions support critical functions in detection, location, feature extraction, discrimination, and analyst review. Figure 2 outlines the processes of data collection, research and integration that result in contributions to the NNSA KB.

RESEARCH ACCOMPLISHED

The LLNL SRDB is a framework consisting of an ORACLE relational database (RDB), Geographical Information System (GIS), and associated product/data visualization and data management tools. The SRDB is necessary for the storage and organization of very large volumes of collected seismic waveforms, associated event parameter information, and spatial contextual data, but also provides an efficient data processing/research environment for deriving location and discrimination correction surfaces. Figure 3 outlines the interaction between all components of the SRDB. The relational database is organized in CSS3.0 (Center for Seismic Studies Version 3.0) format with custom extensions. This format provides parameter defined tables for

different elements of seismic data, such as event and station information, as well as allowing for customized tables to be developed for specific research needs or results and the compatibility with other organizations provides for easy delivery and integration of products.

Contextual and Raw Data

Station Parameters

Seismic station information is a metadata requirement needed to support all stages of seismic waveform analysis. These metadata include such parameters as station operation dates, location and elevation, type of channels and instruments, sampling rates, and instrument responses. Our main source of this information is Incorporated Research Institutes for Seismology (IRIS) "dataless" SEED files, which are provided by each of the networks affiliated with IRIS. Other station information has been obtained through Internet station books and AutoDRM systems. CSS3.0 **site** and **sitechan** table entries (listing station location, available channels, sensor orientations, operation dates, etc.) were created for almost all IRIS affiliated networks as well as many other stations with waveforms in the SRDB. All station parameters are reviewed among existing information sources, and conflicts must be resolved between sources and in reference to waveforms available before database tables are updated.

Network codes are appended to station codes, and location codes are appended to channel names when multiple stations and/or instruments are concurrently operating with the same name. Over 1800 station and array element table entries have been updated, but reliable parameter data do not exist for some stations if only minimal or inconsistent information is available. **Instrument** and **sensor** tables are used to document instrument type and response for each station and channel. The Seismic Analysis Code (SAC) has been modified to interpret response information in RESP or FAP format for use in performing instrument response corrections on waveform data by using the EVALRESP software library available from IRIS.

Event Bulletins

Reference event locations and origin time information are necessary in most stages of our seismic processing and research. Bulletin information from many global, local, and regional earthquake catalogs has been incorporated into the LLNL SRDB and provides a much larger source for event selection. This combined and reconciled source facilitates comparison of event parameters provided by multiple networks with different degrees of location accuracy and provides a wider range of magnitudes and event types. The global catalogs include: United States Geological Survey (USGS) Monthly (Final) Preliminary Determination of Epicenters (PDE) catalog, Bulletin of the International Seismological Centre (ISC), Harvard Centroid Moment Tensor (CMT) catalog, and the International Data Centre Reviewed Event Bulletin (REB). We have also compiled numerous regional and local catalogs for the ME/NA/WE region, including Jordan, Israel, Scandinavia and the Kola Peninsula. A special catalog was compiled for events in the European Arctic and Novaya Zemlya in collaboration with NORSAR. Figure 5 shows a map of the event location coverage provided by several of the bulletins in the ME/NA/WE region. We have established a number of collaborative agreements with countries and institutes in our study region to obtain both local seismic catalogs and ground truth information as well as seismic waveform data.

Waveforms

We are collecting seismic data from IMS primary and auxiliary stations, as well as surrogate stations (for IMS stations not yet installed) and other stations needed to support calibration in the region of study. We have obtained up to 10 years of continuous data for important ME/NA/WE stations from IRIS, Institut de Physique du Globe de Paris GEOSCOPE program, the GEO-Forschungs Zentrum/Potsdam, Germany GEOFON program and other data centers. Current data are being supplied by an LLNL joint project with the Jordan Natural Resources Authority from two seismometers deployed in Jordan. Data for particular events has been obtained from the prototype International Data Center (PIDC) and the United States National Data Center (US NDC). The Center for Monitoring Research (CMR) and NORSAR have provided waveforms for special regions/events, such as the Novaya Zemlya test site. Stations in the ME/NA/WE region with event waveforms stored in the SRDB are shown in Figure 4.

Most of the archived waveforms in the LLNL SRDB are from events located within the ME/NA/WE region and occurring between 1976 and 2001. Our current data collection emphasis is on events recorded between 1990 and the present, except for IMS surrogate stations no longer in operation or for special events such as nuclear tests. Although the continuous data remain archived on tapes, data segments for seismic events are extracted

from the continuous waveforms. The number of waveforms in the SRDB is now almost 3 million, which represents 57,000 seismic events. In addition to individual event waveform segments and continuous data traces managed by the SRDB, we also maintain an archive of active and passive seismic data from various field deployments, which include IRIS/PASSCAL experiments in Tanzania, Pakistan, Caspian Sea, and Turkmenistan. We are also archiving the very long Former Soviet Union Peaceful Nuclear Explosion (PNE) refraction profiles collected by the USGS under contract to the Department of Energy.

Other Reference and Ground Truth Data sets

Projects to develop reference data sets include waveform correlation and subspace detectors to provide statistics on mining activity (see the LLNL Detection Program abstract (Harris *et al*., this Proceedings)) and a regionalization model based on *a priori* geophysical knowledge used as a reference model for model-based correction surfaces. Collaborations with Cornell University, USGS and other organizations allow us to obtain reference data sets useful as background and supporting information for research. Most of these data sets are provided as Geographic Information System (GIS) products, which allow us to integrate them with LLNL data sets. The data sets include geographic, geopolitical, mining industry, geologic and tectonic information for the ME/NA/WE region. We also collect photographs and satellite imagery to support ground truth determination.

Measurements and Research

Phase Information

LLNL researchers and analysts have made phase picks for over 1600 events to yield over 20,000 travel-time observations available to the LLNL research team for location and discrimination projects. Phase information is recorded in the **arrival** and **assoc** tables, along with pick and waveform quality and other comments that are recorded in a **remark** table. Augmenting the LLNL picks, we added 30 million ISC phase arrival measurements from 1964-1998 and almost 2 million REB arrivals to be used for travel-time correction studies. Phase picks have also been entered into the SRDB from a reviewed subset of the ISC bulletin (Engdahl *et al*., 1998) and a few Scandinavian bulletins.

Seismic Location Research

Seismic location researchers utilize event catalogs (especially ground truth), waveforms and phase picks to develop travel-time corrections. Improvement in seismic location is accomplished by combining model-based and empirical travel-time corrections. After a calibration model is applied, empirical corrections are calculated using Modified Bayesian Kriging algorithm with travel-time residuals for suitably well located calibration events. The travel-time and velocity models developed through this research are an important part of the SRDB. See the LLNL Calibration Program (Myers *et al*., this Proceedings) and LLNL Seismic Location (Schultz *et al*., this Proceedings) papers for more details about these aspects of the LLNL GNEM R&E research.

Event Identification and Magnitude Research

The event identification researchers also use event catalogs, waveforms and phase picks to develop products that provide seismological information to improve the ability to identify underground nuclear explosions, by discriminating them from the background of earthquakes. The magnitude research results in calibration products and magnitudes for 1-Hz regional phases, broadband coda waves, and long-period surface waves. This provides the necessary calibration information for regional data in order to calculate seismic magnitudes for use by nuclear monitoring functions (detection, location, identification, and characterization). Custom tables in the SRDB database store measurements and related parameters for surface wave group velocities, body wave amplitudes and magnitudes. See the LLNL Identification Program (Walter *et al*., this Proceedings) and LLNL Calibration Program (Myers *et al*., this Proceedings) papers for more details about these aspects of the LLNL GNEM R&E research.

Validation and Testing

The SRDB provides the framework to perform end-to-end process validation and testing of research results. Validation and assessment tasks include the definition and evaluation of specific metrics, analysis and use of metrics to define the stopping criteria for particular location and identification tasks, and ranking and performance evaluation of calibration activities. Success and efficient implementation of validation and assessment tasks require a framework that ties research results to data and measurements used to create each calibration product and that also supports statistical and visualization tools for performing the validation tasks. The metadata inherent in the SRDB allow multiple realizations of calibration products, created with different

processes and assumptions, to be created, stored, and compared with one another. Thus the SRDB facilitates the distillation, documentation, and delivery of information products.

Data Utilities

Data Input

We have written a set of 130 C++ classes designed primarily as components of computer programs for use by LLNL GNEM R&E. A class is a software abstraction of an entity from the problem domain, which combines all of the attributes and actions of a single entity into one data type. This allows programmers to work at a higher level of abstraction, thus improving productivity and software maintainability. Of the classes we designed, about 10 are service classes with no specific seismological capability, *e.g.* time class, architecture class, etc. All the remaining classes are specialized to some degree for use in seismological applications. All of the collection classes have database-aware specializations as well, since most of the programs developed with the classes interact extensively with the SRDB database. The class library has built-in support for the CSS3.0, SAC, GSE2.0, and PC-SUDS data formats. Using the classes has proven to be an effective means of building the utility programs required to support the SRDB as described in the following paragraphs.

To manage and update the large number of response files for stations maintained in the LLNL SRDB, we have automated the required processing and quality control steps. As we load information into the **instrument** and **sensor** tables, the automated system separates the RESP file into individual epochs, removes overlapping epochs and verifies that the epochs correspond to those in the station parameter tables. New RESP files are created from these results with the station and channel names modified if necessary.

We have developed an automated method to load various bulletins of different formats into native-format database tables, which retain many of the fields provided in the original bulletin, as well as assign a unique origin identifier (*orid*) to each event. Individual bulletins are then merged into a single CSS3.0 **origin** table retaining the author of the original bulletin. A space-time correlation algorithm is used to reconcile events between individual catalogs. Events common to multiple bulletins will be assigned common event identifiers (*evid*) while retaining unique *orid*s. The **event** table stores the preferred origin for each event based on a ranked list of catalog preferences. Phase arrivals provided with native catalogs are loaded into the **assoc** and **arrival** tables.

To generate the event waveforms for the SRDB, we have developed an automated way of extracting waveforms based on events selected from an **origin** table and adding entries for these waveforms into the appropriate database tables. Waveforms are extracted from continuous data in the native format and then converted to CSS3.0 format. Currently, we can perform waveform extraction on data in SAC, SEED, CSS, SEGY and GSE formats. Information already in the database is used to determine station parameters and event origins, which are then used in determining the appropriate time window of data to extract. The program checks waveforms for poor or missing signals, which are then recorded in a metadata table. If waveforms for a specific event are segmented, the segments will be merged together; if a gap exists between segments, the space will be filled with zero-value data points. If two segments overlap, a correlation test is done before the two segments are joined.

Data Access

Different researcher needs for data and metadata require that subsets of data be provided in a format easily accessible to many diverse types of software and analysis tools. Therefore, the SRDB access tools have been designed to utilize the power of the relational database to facilitate efficient queries and data retrieval. The Seismic Analysis Code (SAC) software used by LLNL researchers provides direct access to database table information and waveforms and uses the response files to perform instrument response corrections. PL/SQL language can be used to make database queries on contents of any of the available database tables.

For spatial queries and organization, we have adopted a Geographic Information System (GIS), which provides a framework to store and manipulate spatially defined data. The GIS is linked with the ORACLE database to provide joint spatial and relational queries. We have integrated a large number of our research and contextual data sets into the GIS. A customized framework provides an organized menu system for accessing the data sets and also includes additional functionality developed in collaboration with Sandia National Laboratories. Researchers can use the GIS to browse many of their research data sets and also to perform basic comparisons, queries, and analyses. It also provides a way to use LLNL products in conjunction with other data sets, including integrated contractor products.

Given the large quantity of data now managed by the SRDB, the need arose to create the efficient "production" level seismic data selection, processing and visualization tools necessary to meet programmatic and NNSA KB needs. These tools, along with data browsers to allow visualization and quick access to both data and delivered information products, were developed in collaboration with Sandia National Laboratories. The tools provide such functionality as deriving location corrections, making amplitude and magnitude measurements, and developing discriminants.

CONCLUSIONS AND RECOMMENDATIONS

The data sets and information products contained and organized within the LLNL SRDB may be grouped under 5 major categories:

1. Reference and Contextual Information
2. Detection Data
3. Calibration and Ground Truth Data
4. Event Location Products
5. Event Identification Products

The SRDB allows for the collection of raw and contextual seismic data to be used in research, provides an interface for the researchers to access data, provides a framework to store research results and integrate contractor data sets, and supports assembly and dissemination of data sets to the NNSA KB. A wide range of information products required to support the ME/NA/WE regionalization program are being derived from waveforms, station parameters, and event origin information contained in the LLNL SRDB. Corrections and parameters derived, assembled, integrated and validated using the LLNL SRDB provide essential contributions to the NNSA Knowledge Base for the ME/NA/WE region and will improve capabilities for underground nuclear explosion monitoring. The LLNL portion of the NNSA KB supports critical functions in detection, location, feature extraction, identification, and analyst review in the Middle East, North Africa and Western Eurasia.

We have made a major effort to provide a product development environment that encourages the natural synergies among each of the separate research efforts of the LLNL GNEM R&E researchers. The derivation of reference and ground truth data sets and location and identification products takes place in an integrated environment with changes and improvements in one area being used to facilitate development of the remaining areas. We utilize the LLNL SRDB as an integrating framework to provide the basis for synergistic development of all LLNL GNEM R&E. By combining travel-time observations, event characterization studies, and regional wave-propagation studies for ground truth and regional events, we have assembled a substantial library of ground truth information (origin times, locations, depths, magnitudes), mine explosion statistics, tomographic models and travel-time and body-wave correction surfaces.

REFERENCES

Engdahl, R., R. van der Hilst, and R. Buland (1998), Global teleseismic earthquake relocation with improved travel-times and procedures for depth determination, *Bull. Seismol. Soc. Am.*, **88**, 722-743.

Harris, D., W. Walter, A. Rodgers, A. Sicherman, S. Myers, and C. Schultz (2001), LLNL Detection Program: Broad Area Characterization of Phase Detectability and Empirical Detectors for Specific Sources, 23rd Annual DTRA/NNSA Seismic Research Review Proceedings.

Myers, S., K. Mayeda, W. Walter, C. Schultz, A. Rodgers, A. Hofstetter, J. O'Boyle, and S. Ruppert (2001), LLNL Calibration Program: Data Collection, Ground Truth Validation, and Regional Coda Magnitude, 23rd Annual DTRA/NNSA Seismic Research Review Proceedings.

Schultz, C., M. Flanagan, F. Ryall, S. Myers, W. Hanley, J. Swenson, D. Dodge and M. Pasyanos (2001), LLNL Seismic Location: Validating Improvement Through Integration of Regionalized Models and Empirical Corrections, 23rd Annual DTRA/NNSA Seismic Research Review Proceedings.

Walter, W., A. Rodgers, M. Pasyanos, K. Mayeda, A. Sicherman, and D. Harris (2001), LLNL Identification Program: Regional Body-Wave Correction Surfaces and Surface-Wave Tomography Models to Improve Discrimination, 23rd Annual DTRA/NNSA Seismic Research Review Proceedings.

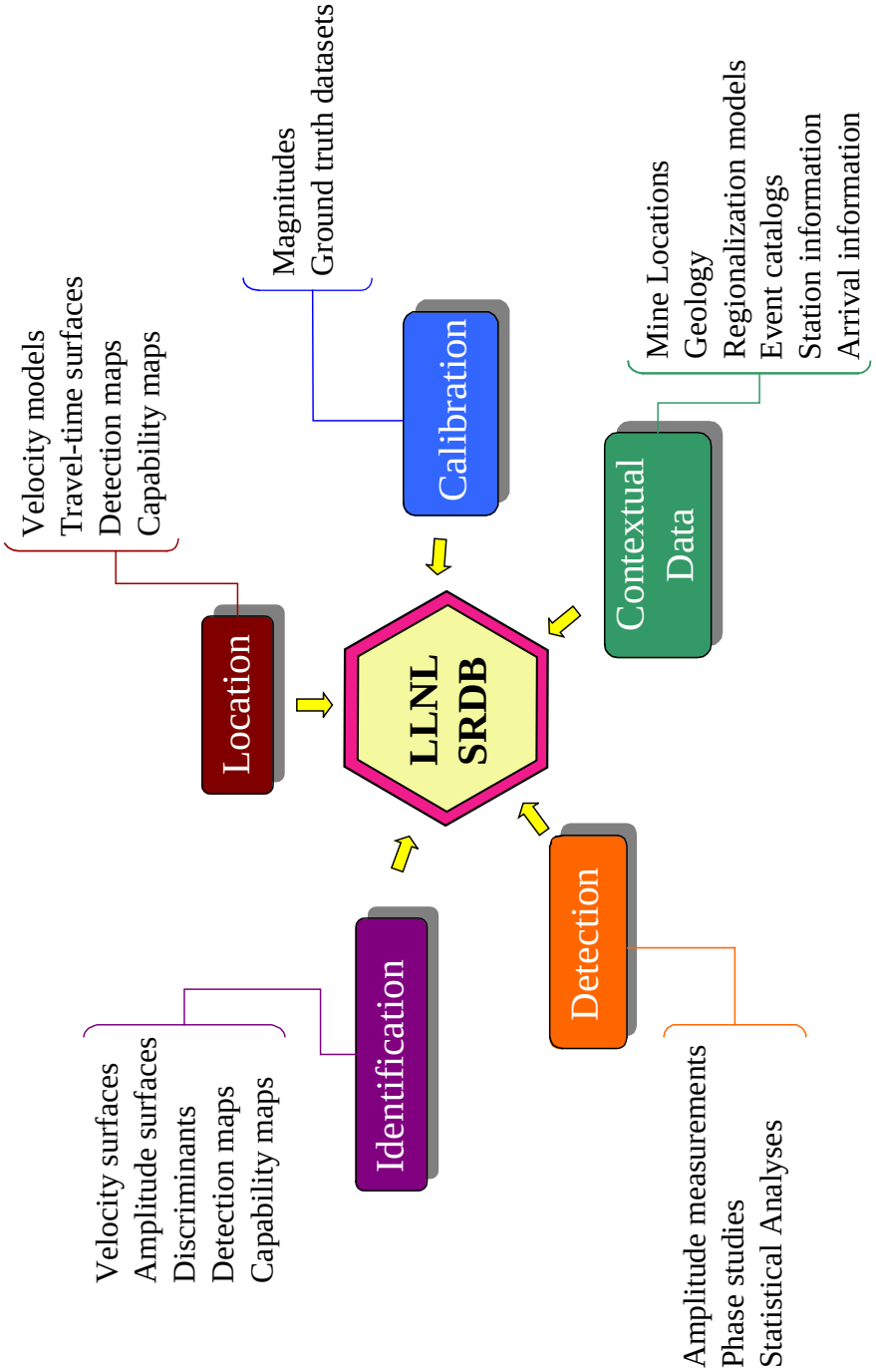

Figure 1. The LLNL SRDB provides a unified framework for contextual/reference data and information products. The SRDB provides efficient access to, and organization of, thousands of seismic events and associated waveforms, while also providing the framework to store, organize, integrate and disseminate information products for delivery into the National Nuclear Security Administration Knowledge Base (NNSA KB).

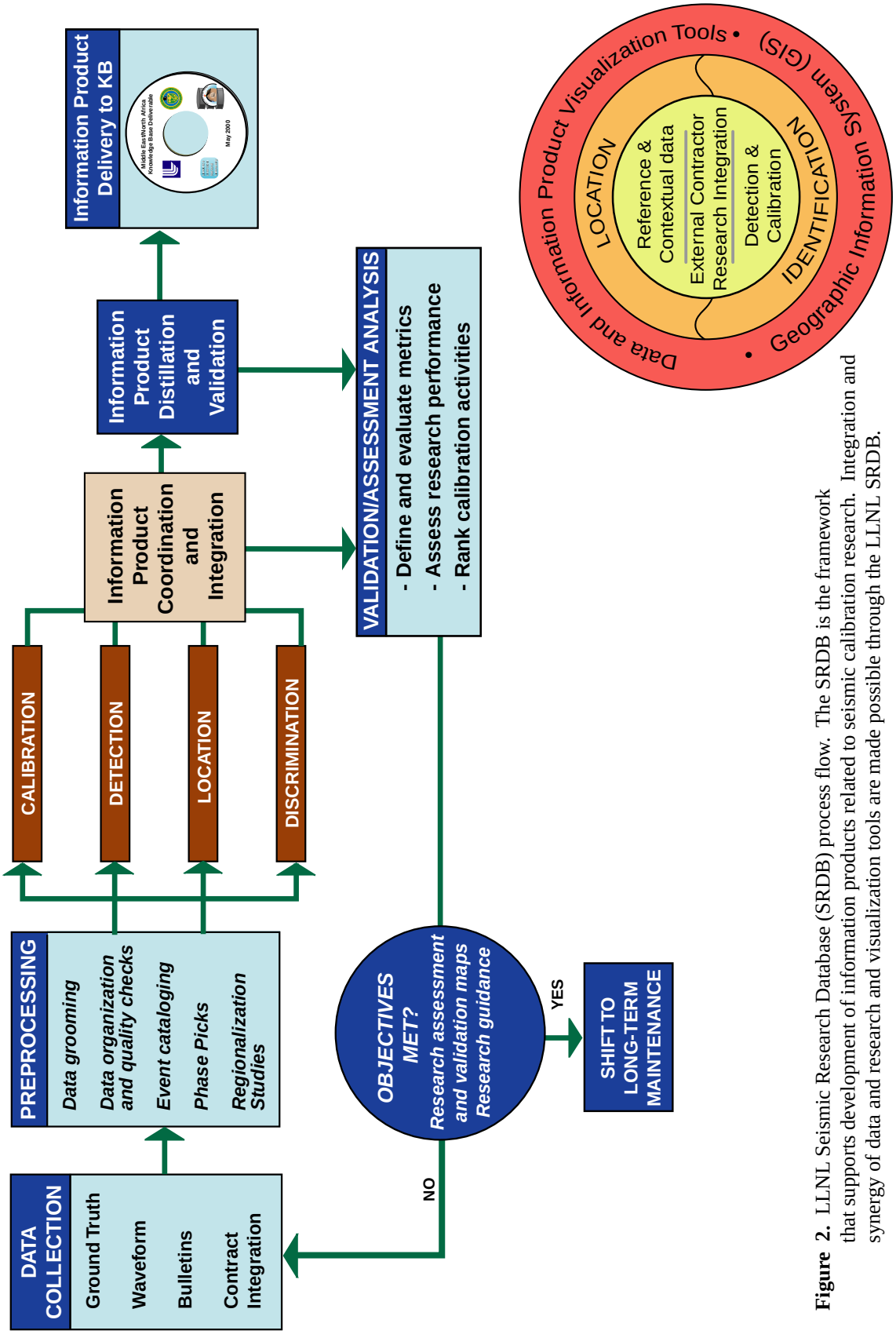

Figure 2. LLNL Seismic Research Database (SRDB) process flow. The SRDB is the framework that supports development of information products related to seismic calibration research. Integration and synergy of data and research and visualization tools are made possible through the LLNL SRDB.

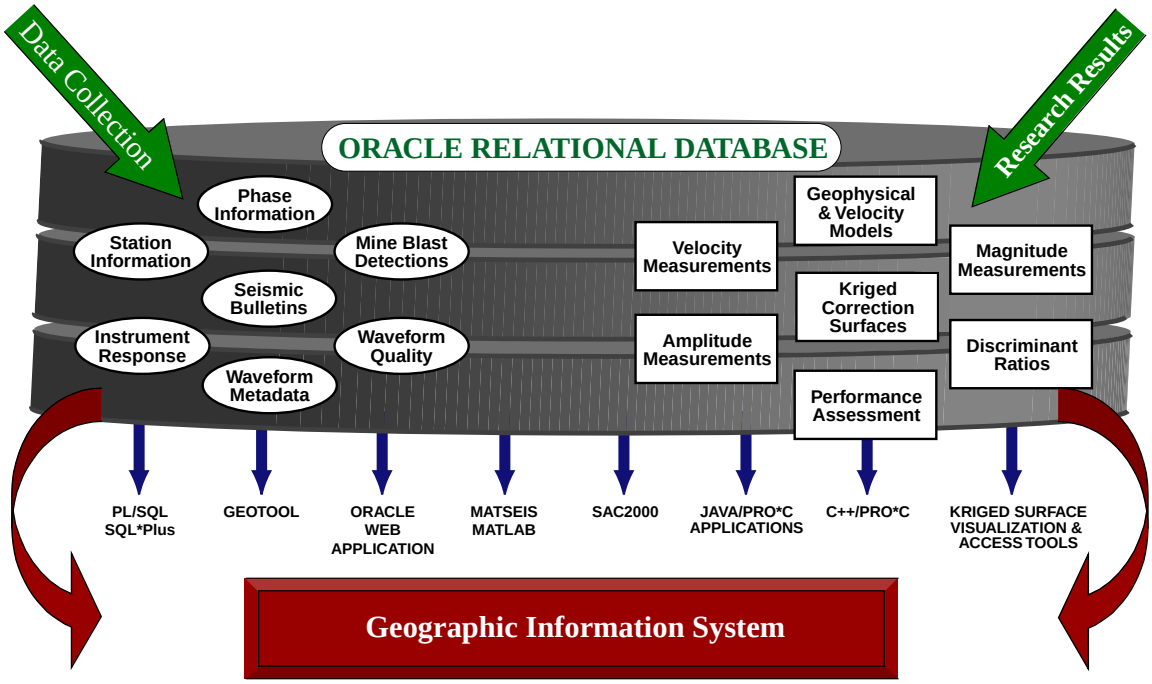

Figure 3. The LLNL SRDB integrates a relational database, a Geographic Information System (GIS) and visualization/data management processes. Many aspects of LLNL GNEM R&E are contained within the database and can be accessed using a wide variety of tools.

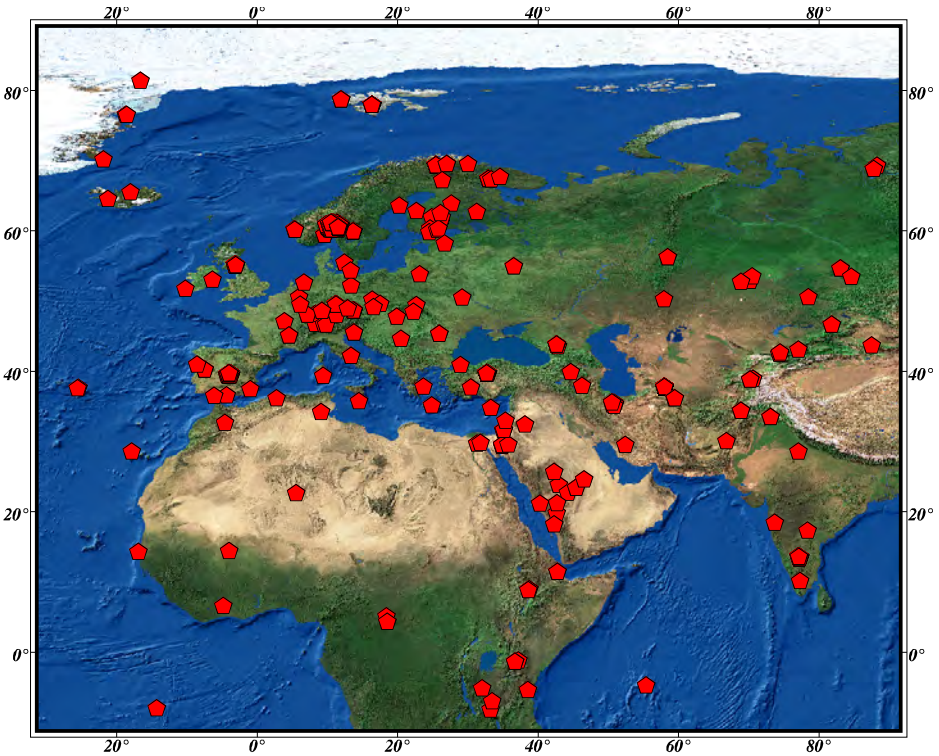

Figure 4. Seismic stations in the ME/NA/WE region with event waveforms stored in the LLNL SRDB.

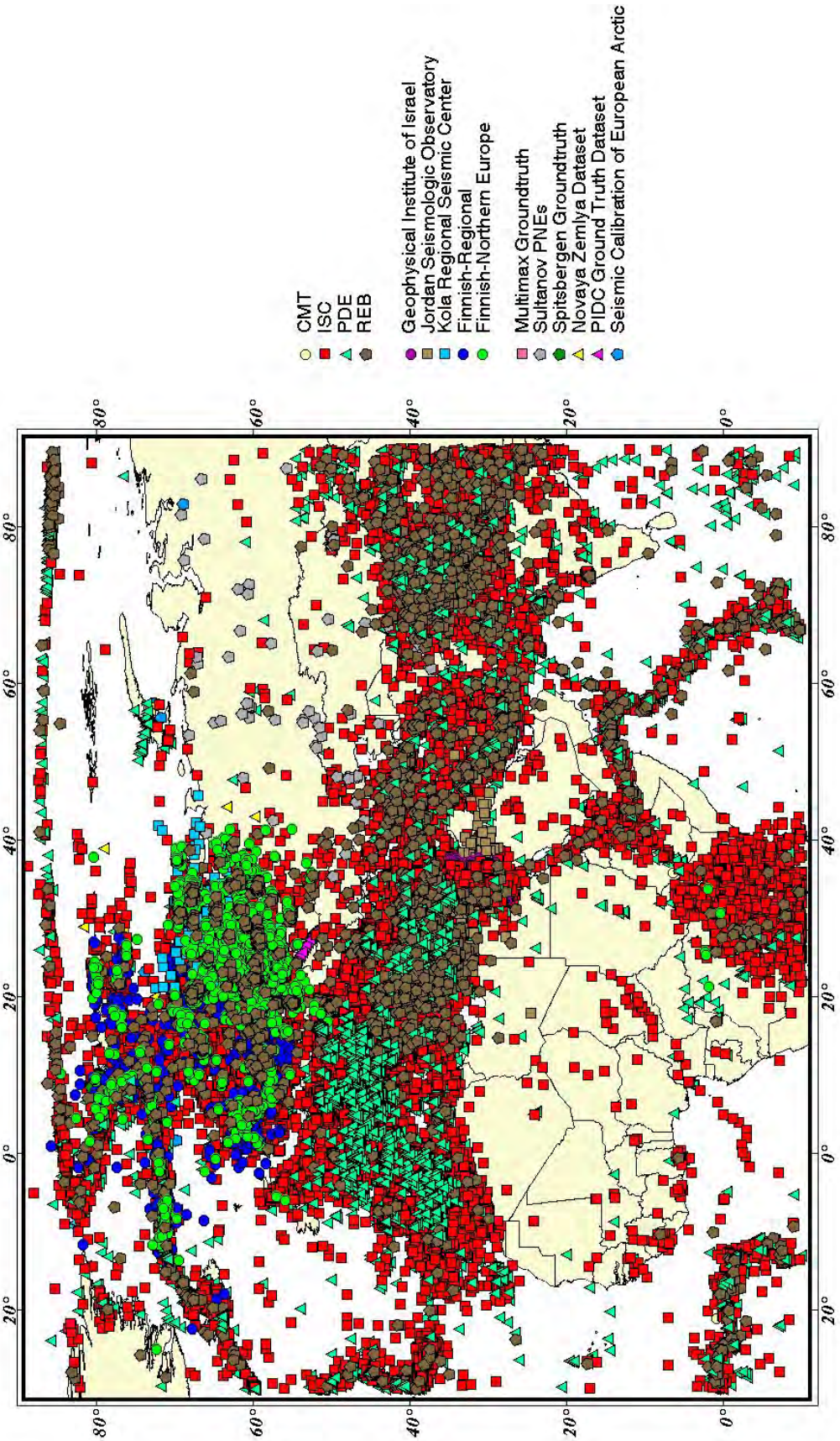

Figure 5. Plot of seismic events in the ME/NA/WE region. The SRDB contains multiple seismic event catalogs that have been reconciled into one database table. These catalogs range in scope from global to regional to special ground truth datasets and provide a much broader range of event magnitudes and event types than any single catalog.

SUPPORT SYSTEM FOR NUCLEAR EXPLOSION MONITORING RESEARCH AND DEVELOPMENT

Robert L. Woodward, Benjamin C. Kohl, and Robert G. North

Center for Monitoring Research
Science Applications International Corporation

Sponsored by Defense Threat Reduction Agency

Contract No. DTRA01-99-C-0025

ABSTRACT

The Research and Development Support System (RDSS) at the Defense Threat Reduction Agency's (DTRA) Center for Monitoring Research (CMR) provides a broad range of support to the nuclear explosion monitoring research and development (R&D) community. This support covers all aspects of R&D, from support for basic research to integration and testing of R&D results.

The RDSS provides researchers with an interface to the wide range of data resources available at CMR, such as: near-real-time waveform data from International Monitoring System (IMS) and other stations; multi-terabyte seismic, hydroacoustic and infrasonic waveform archives; radionuclide databases; and past and present products of both the Prototype International Data Center (PIDC) and the International Data Centre (IDC).

Databases and products available through the RDSS are continually updated and improved. For example, the locations of historical nuclear explosions can, in some cases, be refined to levels suitable for designation as Ground Truth 1 (GT1) or GT2 through the use of high-resolution (1-meter) panchromatic and multi-spectral satellite imagery available from commercial vendors. The process involves the analysis and interpretation of the imagery to identify features that provide constraints on the location. Features are characterized as either providing direct location information (e.g. subsidence craters) or constraining information (e.g. adits, tailings) and are correlated to seismic solutions resulting in the establishment of ground truth locations. One-meter-resolution commercial satellite imagery was also obtained and analyzed for the test sites at Novaya Zemlya, Lop Nor, India, and Pakistan. The ground truth locations obtained for the May 28 and May 30, 1998, underground nuclear tests in Pakistan were used to evaluate the locations produced at CMR using Joint Hypocenter Determination. Imagery data products, including detailed annotated maps derived from the imagery, are being made available through the RDSS web site.

The RDSS receives deliveries from DTRA-sponsored researchers, redistributes these research results, and adds delivered results, when appropriate, to existing databases to create value-added products. Recent deliveries include such items as a unique set of infrasound recordings from atmospheric nuclear explosions in the Former Soviet Union and hydroacoustic recordings of underwater explosions.

The RDSS uses the facilities and capabilities of CMR to evaluate R&D results to assess their potential impact on monitoring system capability. Testing can range from the full data load of the IMS stations and the full processing environment of the IDC, to highly specific tests confined to special data sets. For example, Source Specific Station Corrections (SSSC's) being delivered to the RDSS will be tested under the full IMS data load in both automatic and interactive processing environments.

The RDSS web site (http://www.cmr.gov/rdss) provides a central location for information about the RDSS. The web site provides access to all items delivered to the RDSS, as well as RDSS data and products such as the satellite imagery described above.

KEY WORDS: nuclear explosion monitoring, evaluation, testing, monitoring capability, research and development, satellite imagery, ground truth

OBJECTIVE

The purpose of the Research and Development Support System (RDSS) at the Defense Threat Reduction Agency's (DTRA) Center for Monitoring Research (CMR) is to improve nuclear explosion monitoring capability by supporting the R&D community with a broad range of resources.

The Center for Monitoring Research provides an environment for testing and evaluating promising research results at a wide range of scales. Further, research results delivered to the RDSS are permanently organized and archived in a manner that facilitates their accessibility by the research community. The results of nearly 100 DTRA Program Research and Development Announcement (PRDA) R&D contract projects covering seismic, hydroacoustic, and infrasonic topics are to be archived at CMR over the next three years.

This paper discusses some of the resources available to the R&D research community at CMR and highlights a few recent reports and data sets received from PRDA contractors. We also give a brief description of evaluations of upcoming SSSC's and moment tensor software deliveries. Finally, we conclude with a general overview of resources available for those who will become contributors of products to CMR in the next few years.

RESEARCH ACCOMPLISHED

The Center for Monitoring Research (CMR) houses many unique resources that facilitate research work. Researchers may take advantage of the large volume of seismic, hydroacoustic, infrasound, and radionuclide data, as well as special tools and functionality built to maximize information available for each data technology. In addition, a wide variety of special data products (both databases and data sets) have been assembled to support monitoring research. These data sets are routinely maintained and are augmented with new data as they become available. Commercial satellite imagery is the most recent addition to the suite of special data products maintained at CMR.

Researchers may also take advantage of the results of the DTRA PRDA research program that are delivered to the RDSS. These results are reviewed, archived and redistributed by the RDSS. The PRDA results are distributed in their raw (as delivered) form, and if appropriate, in value-added form (e.g. added to related data to create a new product).

Finally, researchers may take advantage of the facilities and test capabilities provided by the RDSS. Testing environments can be arranged at any scale, from the full data-load of the IMS network and the full-processing environment of the IDC monitoring system, to highly specific arrangements with historical data sets. Supporting facilities include a large UNIX-based computing environment, databases, data archives, and so forth.

In the remainder of this paper we highlight, and provide some details, on the various data, data products, and capabilities that are available to the R&D community via the RDSS located at CMR.

Data Resources Available

Under the Prototype International Data Center (PIDC) project, the CMR has been continuously acquiring and archiving time-series and radionuclide data since 1992. The IMS network is a global network of sensors and, when completed, will comprise 170 seismic stations, 11 hydroacoustic stations, and 60 infrasonic stations. CMR has been processing and archiving these data on a continual 24/7 basis since 1992 for seismic stations, 1995 for hydroacoustic stations, and 1998 for infrasound stations. The processing performed at CMR utilizes data fusion, allowing signals from all three technologies to contribute to analysis of an event, thereby maximizing event information.

Much interest has been expressed in CMR's hydroacoustic and infrasound data archives, as these technologies are a relatively new and rapidly developing part of the IMS network. The hydroacoustic component of the IMS network comprises six hydrophone stations and five T-phase stations (land-based seismic stations configured to detect hydroacoustic signals), providing global coverage of the world's oceans. The hydrophone stations are actually groups of sensors in close proximity. CMR has developed tools to help analyze the source azimuth of

hydroacoustic signals, their spectral characteristics, and the means to extract specific measurements from each signal that is identified by the automatic system. CMR is presently receiving data from the IMS hydrophone station at Diego Garcia, in the Indian Ocean. This station has two triangular groups of sensors, with the sensor groups separated by roughly 200 km.

Infrasound stations of the IMS network are already globally distributed, and include locations in Canada, Hawaii, Antarctica, Germany, Bolivia, and Mongolia. These large baseline stations, with separations of one to three km between sensors, as shown in Figure 1, are designed to detect low-frequency sound waves in the atmosphere, and have been successful at detecting events at long distances.

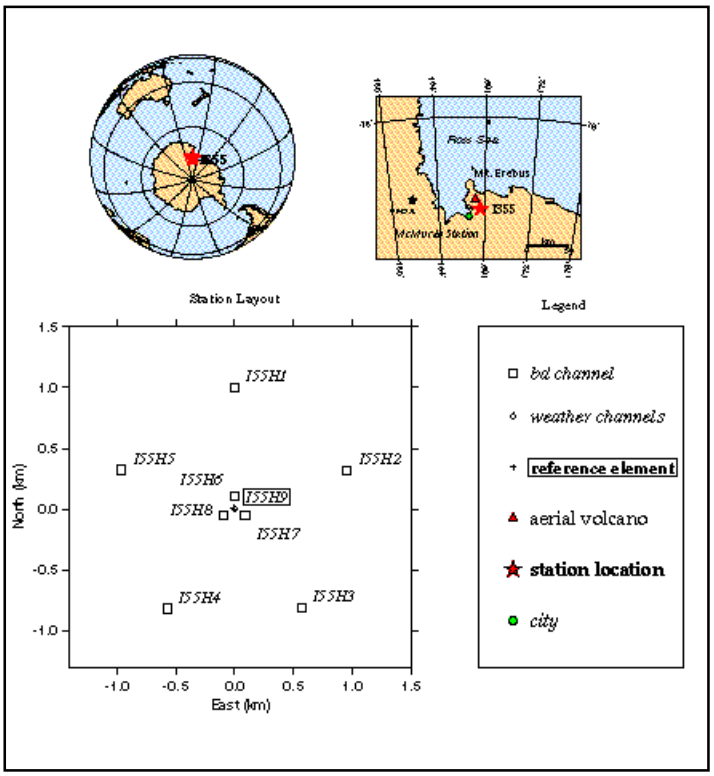

Figure 1. IS55 Infrasonic array, located at Windless Bight, Antarctica, installed on 2001032 (oldest detection date at CMR: 2001149).

Researchers can request and take advantage of all CMR data, from raw waveforms, to individual signal characteristics, to whole event characterization. The data are easily accessed from remote sites by using the AutoDRM (Automatic Data Request Manager) interface, an e-mail-based request mechanism. RDSS users are also provided access to bulletins and data obtained from the IDC in Vienna, Austria.

Special Databases Available

The RDSS produces a variety of special databases and data products that are useful to monitoring research and development, and these are summarized in Table 1. These data products provide data and metadata assembled in a manner to maximize their utility for research purposes. Where appropriate, data being delivered to the RDSS by PRDA contractors are added to these databases, such that the value of both the delivered data, and the database, are increased.

Table 1. Special data sets available to R&D community via the RDSS.

Radionuclide	• High-resolution gamma-ray spectroscopy • Beta-gamma coincidence spectroscopy
Ground Truth	• Nuclear and chemical explosions, industrial events, earthquakes, mixed data sets
Reference Event	• Small- to medium-sized, well located, uniformly globally distributed events
Nuclear Explosion	• Nuclear explosions (1945 – 1993), announced nuclear explosions since 1984, and Australian Geological Survey Organization database (1945 – 1996)

Commercial Satellite Imagery Available

As part of an ongoing effort to update and improve the data sets available through the RDSS, high resolution, 1-meter panchromatic and 4-meter multi-spectral satellite images were obtained from commercial vendors. The objective of the effort was to utilize imagery in conjunction with re-analysis of seismic data to obtain definitive locations of historical nuclear explosions with an accuracy suitable for designations as Ground Truth 1 (GT1) or GT2 events. To achieve this objective, the following approach was used:

1. Acquire and process high-resolution commercial satellite imagery for each of the test sites at Novaya Zemlya, Lop Nor, India, and Pakistan.

2. Analyze the imagery to identify features in one of three categories:

   A. direct evidence of disturbances resulting from nuclear detonations, typically collapse features. These provide an unambiguous constraint on the location. The accuracy of the location depends solely on the accuracy of the registration of the imagery with respect to established location benchmarks. In principle, direct evidence of the disturbance would allow an interpretation resulting in a GT0 location; however, limitations in the accuracy of the imagery's registration result in designations as GT1.

   B. direct evidence of test site artifacts highly correlated with locations of nuclear tests. Typically, these are the surface manifestations of shaft emplacements. The features include roads, buildings, fences and organized patterns of all of these. The features allow for interpretations resulting in GT1 designations.

   C. direct evidence of test site artifacts constrained to the vicinity of nuclear detonations. These are typically features associated with the tunnel emplacements of nuclear tests. The features include roads, adits and tailing piles, all adjacent to mountainous terrain suitable for providing the necessary overburden to contain the event. An analysis of the features evidenced in the imagery, in conjunction with analysis of the terrain data in the vicinity, result in GT1 or GT2 designations.

3. Estimate the uncertainties of the locations of the features. To determine uncertainties, highly visible and distinct but spatially constrained features, such as the intersections of major roadways, are identified on a number of different sources. Older imagery from lower resolution sensors (SPOT, LANDSAT, KVR), digital terrain elevation data, and high-resolution maps available through the National Imagery and Mapping Agency were registered with respect to one another, demonstrating variations of no more than several hundred meters.

The results of the imagery analysis are assembled in a series of imagery products that are available through the RDSS web site. The imagery products are provided in Portable Document Format (PDF) to insure maximum portability and all include progressive levels of zoom so that researchers can make independent assessments as to the nature of the features annotated in the imagery products (Figure 2).

As review of the imagery by CMR analysts progresses, the imagery products will be updated with the latest interpretations and periodically uploaded to the RDSS web site. Table 2 presents a list of the imagery products available through the RDSS web site as of August, 2001.

Table 2. List of imagery products available through the RDSS web site.

Site	Acquisition Dates	Imagery Type	Summary of Features	# of Nuclear Tests Within Area of Imagery
Novaya Zemlya	June 26, 2000 July 20, 2000 August 3, 2000	1-meter panchromatic, mosaic of 3 images	Roads, adits, tailings, collapse features	31 events
Lop Nor	February 26, 2000	1-meter pan + 4-meter multi-spectral	Roads, adits	6 events
	July 1, 2000	1-meter pan + 4-meter multi-spectral	surface features related to shaft emplacements	13 events
India	August 10, 2000	1-meter pan + 4-meter multi-spectral	surface features related to shaft emplacements	2 events
Pakistan	July 9, 2000	1-meter pan + 4-meter multi-spectral	Roads, adit	1 event
	July 9, 2000	1-meter panchromatic	surface features related to shaft emplacements	1 event

The imagery products for Novaya Zemlya and Lop Nor include within their bounds the locations of numerous historical nuclear explosions. Currently there remain ambiguities as to which particular features correlate with specific nuclear explosions recorded seismically. At the Indian and Pakistani sites this is not the case and an unambiguous identification of the ground truth locations is possible.

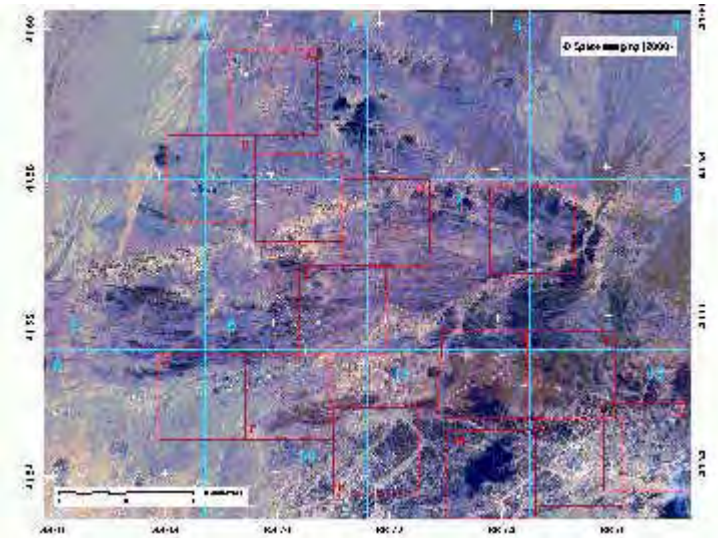

Figure 2. Overview image (July 1, 2000) of the eastern portion Lop Nor test site. The area depicted in this image covers the part of the test site where more than a dozen nuclear tests were conducted, all with shaft emplacements. The imagery product available via the RDSS includes two levels of zoom, the first at a scale of 1:15000 and the second at a scale of 1:7500 and containing areas with features possibly correlating to test artifacts.

The GT locations for the May 28 and May 30, 1998, Pakistani nuclear tests are listed in Table 3, along with the locations obtained by CMR's nuclear monitoring detection system in 1998, based on the IMS stations operating at the time and without the benefit of ground truth information. The absolute locations for the two events,

obtained utilizing the IMS data, were systematically biased to the northwest. Table 3 also lists a JHD solution obtained for the May 30, 1998, test based on holding the May 28, 1998, test fixed at the ground truth location.

Table 3. Location estimates for the 1998 Pakistan nuclear tests. The ground truth estimates presented below are direct interpretations from 1-meter resolution commercial satellite imagery.

Date	Solution	Latitude	Longitude	Uncertainty	Distance from Ground Truth
May 28, 1998	GT estimate from imagery	28.7924 N	64.9456 E	500 meters	-
	REB	28.90	64.90	Semi-major = 10.4 km Semi-minor = 8.4 km Strike = 178	13 km
	JHD	28.7924 N	64.9456 E	-	fixed
May 30, 1998	GT estimate from imagery	28.3589	63.8584	500 meters	-
	REB	28.49	63.78	Semi-major = 11.4 km Semi-minor = 9.4 km Strike = 4	17 km
	JHD	28.411	63.864	Semi-major = 6.6 km Semi-major = 5.2 km Strike = 8	6 km

PRDA Contract Results Available

A key component for success of the RDSS is the receipt, test, and acceptance of results from the R&D community. In general, the RDSS expects three types of deliveries: technical reports, data to receive and store, and software components or parametric results to evaluate and possibly integrate into a monitoring system. A number of deliveries from PRDA contractors has already been received and these are summarized in Table 4.

Table 4. Summary of products received by the RDSS.

	Contract/Task Title	Performing Org.	P.I.	Products Received
1	Development of a Dynamic Infrasound Knowledge Database	BBN Tech.	Farrell	Software and User's Guide
2	Enhanced Depth Determination Using Cepstral Techniques	Weston Geophysical	Reiter	Software for cepstral F-stat analysis; Scientific Rpt. "Application of a Cepstral F-Statistic for Improved Depth Estimation"
3	Characterization of Reflected Arrivals for Hydroacoustic Test Ban Monitoring	BBN Tech.	Gibson	Final Report (Draft); database 15 events between 1965 and 1970
4	Feasibility of the Use of 3D Models to Improve Regional Locations in W. China, Central Asia, and Parts of the Middle East	Univ. of Colorado at Boulder	Ritzwoller	Final Report, "Use of the Kyrgyz Seismic Network to Assess the Performance of the Int'l. Monitoring System in and Around Kyrgyzia"; database KNET and CAB
5	Long-Period Surface Wave Dispersion and NDC Global Association Database	Boston College	Harkrider	Final Technical Report; FORTRAN versions travel time codes

	Contract/Task Title	**Performing Org.**	**P.I.**	**Products Received**
6	Infrasound Excitation and Propagation Research	Maxwell Tech.	Stevens	Technical Report (Draft); database SAC format files; IDG, Final Report
7	Statistical Calibration & Regionalization of China & Surrounding Region	New Mexico State Univ.	Hearn, Ni	bulletins of Chinese earthquakes 1985, 1986, and 1991-1995
8	Collection and Analysis of Regional Seismic Data for Underground Explosions	Mission Research Corp.	Fisk	Final Technical Report (Draft), "Regional Seismic Event Characterization Using Bayesian Calibration"; waveform database
9	Development of Ultrahigh Sensitivity Xenon Detectors for Enhancement of Ability to Monitor Nuclear Testing	Univ. of Cincinnati	Valentine	Final Report
10	Discr., Det., Dep., Loc., and Wave Propagation Studies Using Intermed. Period Surface Waves in the Mid-East, C. Asia, and the Far East	Univ. of Colorado at Boulder	Levshin	Final Report (Draft)
11	Advanced Regional Array Studies	NORSAR	Kvaerna	Final Report (Draft)
12	Source Char. and Reg. Discr. of N. Idaho Rockbursts and Earthquakes	Univ. of Idaho	Sprenke	Final Scientific/Technical Report (Draft), "Rockburst Model Validation"
13	Signal Det. and Estimation Directional Parameters for Multiple Arrays	Univ. of CA, Davis	Shumway	Final Scientific Report (Draft)
14	Joint Inversion of Receiver Function and Surface Wave Dispersion for Local Crustal Structure in the Mideast	St. Louis Univ.	Herrmann, Ammon	Final Report , "Lithospheric structure of the Arabian shield from the joint inversion of receiver function and surface-wave dispersion observations"
15	Various contracts	Columbia Univ., LDEO	Kim, Richards	Report "Borovoye Digital Seismogram Archive for Underground Nuclear Tests during 1966-1996"; waveform data files
16	Development of Event Screening Procedures	Australian Geol. Survey Org.	Jepsen	Summary; database nuclear and chemical events, CSS3.0 format
17	A Ground Truth Database for Regional Seismic Research	Multimax	Henson	313 CEB events China, FSU, and N. Am
18	A Damage Mechanics Model for Underground Nuclear Explosions	Univ. Southern CA	Sammis	Final Technical Report
19	Basic Research on Seismic Monitoring Problems	Univ. of CA, Berkeley	Johnson	Final Report

In the following discussion we highlight two examples of recent deliveries that are likely to prove very useful to the nuclear explosion monitoring R&D community.

PRDA Results -- Example 1

CMR received a preliminary report from Maxwell Technologies, associated with research conducted under the DTRA contract titled "Infrasound Excitation and Propagation Research" (Stevens, 2000; Stevens et al, 2000). The report covers topics in the areas of modeling of infrasound signals from atmospheric explosions, evaluation of IMS network performance for infrasound signals, and analysis of infrasound instrumentation. The delivery consisted of a draft final report, provided primarily to describe the accompanying data set. The report contains tables describing event locations, time, and yield, station locations, calculated infrasound magnitudes, and two appendices describing how instrument responses are defined and which instruments were used at which stations.

The Maxwell infrasound data set is comprised of a total of 220 data files in SAC format and consists of signals recorded at 17 locations in the former Soviet Union (e.g. Figure 3), from 22 atmospheric nuclear explosions

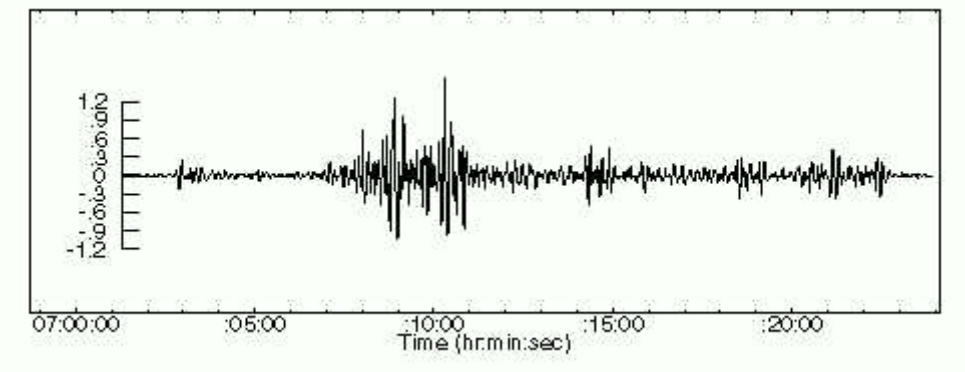

Figure 3. A 13-kT shot at Semipalatinsk recorded at Yeniseysk on 1961/10/04.

ranging in size from 0.8 kT to 58 MT. A total of 138 of the waveforms have measurable, unclipped signals, known instrument responses, yields and calibrations. This is a unique data set that will be useful for source scaling studies, testing signal detection and characterization, and other aspects of infrasonic modeling and processing.

PRDA Results -- Example 2

BBN Technologies recently submitted the report "Characterization of Reflected Arrivals and Implications for Hydroacoustic Test-Ban-Treaty Monitoring" (Pulli, et al, 2000a, 2000b). The study included a review of historical and contemporary data sets and a CD-ROM of these edited data sets along with source and receiver information.

The BBN contract assessed the potential use of long-range hydroacoustic reflections for the location of hydroacoustic events. A data set of source information and hydroacoustic waveform data for 15 events - 12 "Chase" and one other underwater explosion, and two Aleutian underground nuclear explosions (Longshot and Milrow) - was assembled in CSS3.0 format with source information provided in tabular form for each event. In most cases, the absolute location of the source is known, but some event locations had to be inferred from the recorded signals. The waveform data are from the Wake and Ascension MILS arrays and from single hydrophones at three other Pacific locations.

The waveforms collected in the BBN study are valuable for a number of research purposes, such as validating travel times and algorithms for estimating arrival azimuth, and testing source characterization of underwater explosions. The BBN analysis of these data for reflections demonstrated that these were usually easy to identify, and included a recommendation that location algorithms should use the reflected as well as the direct arrival.

The deliverable items submitted by both Maxwell Technologies and BBN Technologies are examples of research reports with accompanying data sets that are extremely valuable to the R&D community. All deliveries received by the RDSS (Table 4) are being made available to the R&D community in the form in which they

were delivered (see URL below). In addition, the data sets submitted by Maxwell will be added to the CMR Nuclear Explosion and Infrasound databases. The data sets contributed by BBN Technologies will be added to both the CMR Nuclear Explosion (Longshot and Milrow recordings) and Hydroacoustic databases.

Evaluation and Testing Capabilities Available

Many of the deliveries to the CMR R&D Support System comprise software components, parametric results, or other components that are to be evaluated. To perform such evaluations, a test plan, with evaluation criteria, is generated by the researcher in collaboration with RDSS staff.

Deliveries that require testing at the full scale of the NTDS require special planning. For example, the DTRA IMS Location Calibration Program is funding three consortia to provide SSSC's for stations of the IMS. In this endeavor, integration, testing, and evaluation are required at CMR to ensure that the results produced by the three consortia are compatible with the nuclear explosion monitoring system software. Demonstration of location improvements will require extended full-scale operational test and evaluation and this will be crucial to producing a consistent and tested product.

In another testing effort at the RDSS, investigators at the University of California, Berkeley (UCB), and RDSS staff are working on a plan for integrating UCB's automated moment tensor software (Dreger, et al, 2000) into the explosion monitoring system. One component of enhanced monitoring involves augmented source characterization capabilities, some examples of which may include robust depth estimation or consistency with tectonic release. The purpose of the UCB effort is to develop software to automatically determine moment tensors for seismic events recorded at the IMS network stations. To achieve this goal, the software must be capable of functioning automatically, and must be tightly integrated into the monitoring system environment.

Computing Facilities Available

A comprehensive infrastructure environment exists at CMR to support the RDSS user community and the R&D Support System itself. A substantial Commercial Off the Shelf (COTS) software and hardware environment is maintained and documented on the RDSS web site, and includes over 60 servers, over 90 work stations, mass storage systems, multiple Oracle instances, multiple web sites (open and secure) multiple networks, and firewall security. A number of these resources can be utilized directly by the R&D community (e.g. accounts are available for direct use of the Oracle database), while others are used to provide community support (e.g. the mass storage system is used to archive and serve data).

CONCLUSIONS AND RECOMMENDATIONS

The RDSS makes use of all the facilities, resources, and expertise of CMR for the purpose of improving nuclear monitoring and verification capabilities. This role can be summarized in terms of the following broadly stated goals:

- • The RDSS supports the R&D community, from the inception of research through to testing and archiving of results. Such support can take the form of providing access to current IMS data, production results, IDC results, data archives, and more.

- • The RDSS archives research results to ensure important work is not lost and results can be shared readily amongst the R&D community.

- • The RDSS provides a mechanism for the test, evaluation, and integration of R&D results. Testing can be conducted at various scales, ensuring proper test environments. Such test and evaluation provides the US government with quantitative measures of current monitoring capability, identifying obstacles and establishing expectations for achieving improved capability.

Most importantly, we note that the RDSS is a collaboration between DTRA, the R&D community, and CMR. A wide range of CMR staff, including scientific, software development, testing, and infrastructure support teams are available to support all phases of R&D activity. Please watch for news and developments (or contact us) at:

http://www.cmr.gov/rdss . The web site contains a wide range of information, such as listings of current DTRA contracts, contract deliverables received, documents describing the access and use of the RDSS, and information on RDSS resources available.

REFERENCES

Dreger, D., B. Romanowicz, and J. Stevens, (2000), Development of Automated Moment Tensor Software at the Prototype International Data Center, Proceedings of the 22nd Annual Seismic Research Symposium, Vol. 3, 365-373.

Pulli, J., Z. Upton, R. Gibson, J. Angell, T. Farrell, and R. Nadel, (2000a), Characterization of Reflected Arrivals and implications for Hydroacoustic Test-Ban-Treaty Monitoring, BBN Technical Memorandum W1380, contract DSWA01-97-C-0164.

Pulli, J., Z. Upton, R. Gibson, and T. Farrell, (2000b), Modeling Long-Range Hydroacoustic Reflections in the Atlantic and Pacific Oceans, Proceedings of the 22nd Annual Seismic Research Symposium, Vol. 3, 75-84.

Salzberg, D., R. Woodward, and R. North, (2000), Delivering Research Results to the DTRA CMR R&D Testbed, Proceedings of the 22nd Annual Seismic Research Symposium, Vol. 3, 419-427.

Stevens, J., (2000), Infrasound Excitation and Propagation Research, Maxwell Technologies, draft final report, contract DSWA01-97-C-0129.

Stevens, J., D. Adams, G. Baker, H. Xu, J. Murphy, I. Divinov, and V. Bourchik, (2000), Infrasound Modeling Using Soviet Explosion Data and Instrument Design Criteria from Experiments and Simulations, Proceedings of the 22nd Annual Seismic Research Symposium, Vol. 3, 259-269.

Woodward, R., D. Salzberg, and R. North, (2000), A Testbed for Nuclear Explosion Monitoring Research and Development, Proceedings of the 22nd Annual Seismic Research Symposium, Vol. 3, 441-445.

COMPARISON OF CLUSTER ANALYSIS METHODS FOR IDENTIFYING REGIONAL SEISMIC EVENTS

Christopher J. Young[1], Bion J. Merchant[1], Richard C. Aster[2]
Sandia National Laboratories[1]
New Mexico Institute of Mining and Technology[2]

Sponsored by National Nuclear Security Administration
Office of Nonproliferation Research and Engineering
Office of Defense Nuclear Nonproliferation

Contract No. DE-AC04-94AL85000

ABSTRACT

In recent years, nuclear explosion and non-proliferation monitoring have focused on smaller yield events, creating two major issues. First, smaller events are typically more difficult to detect and locate. Second, as characterized by the Richter/Gutenberg frequency of occurrence relation, there are many more small events than large events so the monitoring workload is exponentially increased. These issues represent a new challenge for the nuclear explosion monitoring community, but for regional network operators they are commonplace and, to a large extent, solved. These operators routinely locate and identify large numbers of events at least as small as those of interest to the monitoring community, often on the basis of as little as one waveform. The operators accomplish this seemingly impossible task by simply viewing and recognizing the similar waveforms from repeating seismic sources such as mines. Such an analyst-intensive, subjective process is not generally appropriate for nuclear explosion monitoring, but the effectiveness of this technique suggests that automated pattern recognition techniques could have a significant impact on monitoring. In this paper we will show how cluster analysis (CA) techniques can be used to automate the waveform recognition problem and compare the performance of different CA methods.

Cluster analysis is the term for a family of techniques for aggregating similar entities into groups or clusters. In this study we compare three different CA techniques: agglomerative hierarchical clustering (represented by dendrograms), Q-mode factor analysis, and ordination. Our data set consists of 651 regional distance events recorded by the New Mexico Institute of Technology network from July 1997 through February 1998. The events are predominantly mining explosions from operations in western New Mexico, as well as southeast Arizona. Because we have full-network recordings for these events, we are able to locate events from within each cluster to tie the clusters to known mining regions. All of the cluster techniques are based on a similarity matrix formed by comparing each entity with every other entity. For this study, we base our measure of similarity on normalized waveform correlations for a single station. The resulting clusters depend strongly on the processing parameters applied to the waveforms (phase windowing, filtering, Hilbert enveloping). Our results suggest that dendrograms of the Hilbert enveloped waveforms produce the most useful results, while factor analysis may prove useful as an auxiliary technique. Ordination produced marginally useful results only after non-linear rescaling of the similarity data, and we do not think it shows promise with this type of data.

None of the CA techniques automatically determine how many clusters are represented in the data. This decision is often made subjectively, but it can be based on the application of clustering criteria. We compared several proposed clustering criteria methods to determine which work the best for our data set, but none performed well in general.

KEY WORDS: cluster analysis, dendrograms, factor analysis, ordination

OBJECTIVE

The objective of this study is to investigate the use of cluster analysis techniques to identify similar seismic events based on waveform correlation. Because of the strong dependence of seismic Green's functions on source mechanism and source location at frequencies typically observed in regional studies (> 1 Hz), a high correlation value indicates both a similar location and a similar source type, and both types of information are of great importance to the nuclear explosion and non-proliferation monitoring community.

Currently, location and identification are accomplished by minimizing the misfit between a set of low-order parameters derived from the waveforms from a network (i.e. arrivals and various measurements associated with them) and the corresponding parameters predicted by Earth models. Because this parametric misfit minimization approach is model-based, it can be used to evaluate events anywhere on the Earth, which is one of the main reasons why it is used so widely. However, the model-based approach does not work well for smaller events which are typically recorded at fewer stations. In these cases, there are often too few observations to locate and identify the events. This is a significant concern if we seek to lower the monitoring magnitude threshold.

For small events, waveform correlation can provide much better results than the model-based approach if an archived set of similar events is available. Experienced seismic network analysts often can identify an event as coming from a given region based on a single waveform. The analysts do this by matching the present waveform with memories of others which were known to have come from that region. This technique works because the seismogram resulting from a given source-to-receiver path is as unique as a fingerprint. Paradoxically, this is exactly the same reason why synthetic waveforms produced from models are not typically used in operational monitoring systems: the resolution of most models is not sufficient to match the source-receiver path and reproduce the fine details of the observed waveforms.

Our study follows the lead of Riviere-Barbier and Grant (1993), who showed how waveform correlation-based dendrograms could be used to identify regional mine blasts recorded by the FINESA array. In that study, the authors carefully determined the optimal signal processing parameters to yield the best clusters and painstakingly ground-truthed their events to tie the clusters to mines. They did not, however, focus much on cluster analysis itself. They chose one of the simplest and most reliable methods, the formation of dendrograms by complete linkage hierarchical clustering, and applied it to their data set. In this study, we provide a more thorough investigation of various cluster analysis techniques and assess their applicability to the event location and identification problem.

We simulate the small event monitoring problem using a set of regional events recorded by the New Mexico Tech Seismic Network (NMTSN). The events were generated by an automatic, grid-based system (Withers et al., 1999) running between July 2, 1997, and February 27, 1998. In all, 651 events were detected and located, but clearly there are problems with the automatically generated catalog (Figure 1, left). First, the grid itself is coarse (10-km spacing) for events outside central New Mexico, so the locations have an inherent limitation. Second, even allowing for the coarseness of the grid, the events do not exhibit the linear features (faults) and point features (mines, volcanoes, etc.) that one would expect. In fact, it is known that the bulk of the events recorded by the NMTSN come from 5 areas: 4 mining regions in western New Mexico and southeastern Arizona, and the region of the magma body near Socorro (Figure 1, right -- see Balch et al., 1997 for information about the Socorro magma body). Thus, much of the scatter in the locations of the events probably reflects gross event mis-location

We tried to classify these events using only the waveforms from a single station of the NMTSN, station CAR. However, because we have full network data for the events, we can ground truth any of them by re-timing the arrivals for the various phases, and re-locating using an appropriate regional travel time model.

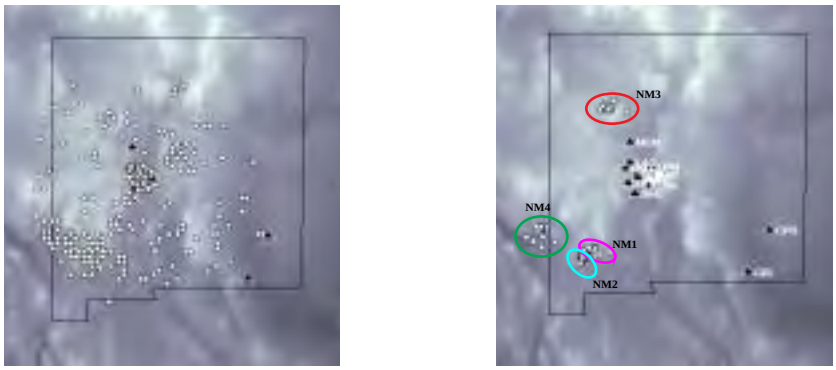

Figure 1. (left) The full 651 events detected and located by a grid-based automatic system running on data from the NMTSN for the period of July 2, 1997, through February 27, 1998. **(right)** The 60-event training subset, the 4 identified mining regions, and the NMTSN (15 stations). In both cases the background image is topography and the outline shows the New Mexico border. Because some of the information is impossible to convey without the use of color, and the printed Proceedings are in black and white as a cost-saving measure, we refer the reader to one of the electronic versions of the Proceedings for interpreting the figures in this paper. The electronic versions can be found at http://www.nemre.nn.doe.gov/review2001 or on the CD ROM version of the Proceedings. Or, readers should feel free to contact the authors.

Many of the global monitoring stations are located in areas at least as seismically active as New Mexico, so it is likely that these stations will detect a large number of regional events that will not be recorded at the other stations (given the typical global monitoring network station spacing). Typically, these events cannot be located and thus they determine the magnitude threshold for the network in the vicinity of the stations. The only way to lower the threshold for the network (other than adding more stations) is to better utilize the information in the waveform from a single station. One way to do this is by cluster analysis using full waveforms.

CLUSTER ANALYSIS

Cluster analysis (CA) is the term for a family of techniques for aggregating similar entities into groups or clusters. Much of the CA methodology comes from the field of numerical taxonomy, which involves trying to group similar organisms to establish evolutionary relationships (e.g. Ludwig and Reynolds, 1988). We compare three different CA techniques: agglomerative hierarchical clustering (represented by dendrograms), Q-mode factor analysis, and ordination. All of the cluster techniques are based on a similarity matrix formed by comparing each entity with every other entity. For this study, we use as our measure of similarity the absolute value of the normalized waveform correlation (i.e. best lagged cross-correlation divided by the autocorrelations).

Hierarchical Clustering (Dendrograms)

Hierarchical clustering is an iterative process in which similar entities are repeatedly joined to form a tree (e.g. Davis, 1986). One begins by selecting the most similar pair of entities, in our case waveforms, from the similarity matrix and joining these together on the dendrogram. All of the similarities between each of these entities and all of the other entities in the similarity matrix must now be replaced by a similarity between the newly formed group and all of the other entities (e.g. one can average the individual similarities). Doing this will shrink the dimension of the matrix by 1. Once this has been accomplished, the process is repeated until the matrix is reduced to a dimension 1, and an entire dendrogram has been built. The only trick in hierarchical clustering is in the method chosen for calculating similarities between a newly formed group and the remaining entities. There are many methods to calculate the similarity between an entity k and a group, ij, formed by the fusion of entities i and j, but all of the ones we are tested can be represented with the formula (Lance and Williams, 1967):

$$\mathbf{d_{k(i,j)}} = \alpha_i \mathbf{d_{ki}} + \alpha_j \mathbf{d_{kj}} + \beta \mathbf{d_{ij}} + \gamma \left| \mathbf{d_{ki}} - \mathbf{d_{kj}} \right|$$

Where d_{ij} is the distance (i.e. 1 - similarity) between groups *i* and *j*. By choosing different values for the weights α, β, γ this formula can represent any of the standard hierarchical formulas. For example, for single linkage $\alpha_i = \alpha_j = \frac{1}{2}, \beta = 0$ and $\gamma = -\frac{1}{2}$. For complete linkage, the only difference is that $\gamma = \frac{1}{2}$.

Q-mode Factor Analysis

Q-mode factor analysis is essentially a principal components technique. Again, one begins with the similarity matrix. In this case, however, we simply calculate the eigenvectors of this matrix and then plot these against each other, scaled by the eigenvalues, to identify the groups. As would be expected, the eigenvectors corresponding to the highest eigenvalues will be the most significant, but it turns out that the first eigenvector contains the centroid position and thus should be ignored (Davis, 1986), so we plot the second and the third eigenvectors.

The Q-mode refers to the fact that we solve for the eigenvectors of the Q matrix, which is defined to be the matrix of data vectors dotted with each other. The alternative is R-mode in which we would decompose the R matrix, which is defined to be the matrix of variable vectors dotted with each other. R-mode factor analysis is used to establish correlations between variables (as opposed to between entities). This is not the goal of our study, so we do not investigate R-mode factor analysis.

Ordination

The final CA process we investigate is ordination. This technique has proved very successful in mining text-based data sets (e.g. newspaper and magazine articles) and has had only a limited number of applications to other types of data. However, ordination is ultimately based on the same sort of similarity matrix, so it can readily be applied to our data set. To ordinate a set of entities, the entities are placed in a plane such that their relative positions agree as closely as possible with the similarity information in the similarity matrix. This is done through a computationally intensive, iterative Monte Carlo process in which the entities are assigned initial positions and then moved randomly to see if their new positions agree better with the similarity matrix information. Interested readers should refer to Wylie et al. (2000) for more information.

RESEARCH ACCOMPLISHED

Preliminary Data Analysis

As stated above, the NMTSN events are expected to be dominated by 5 sources: 4 mining regions and the local events associated with the magma body near Socorro. The mining events are typically much more common than the magma body events. To create a training set to test our cluster analysis techniques, we had an experienced NMTSN analyst scan three months of our data (from August through October) to identify representative events known to come from the mining regions (60 events in all). These events were then hand-picked and re-located using the one-dimensional regional travel-time model that New Mexico Tech has developed for the area. The locations of these events are shown in Figure 1 (left). Hereafter we will refer to this as the training set. Though there is still some scatter in the locations of these events, the 4 mining regions are clear. Because these events lie outside the NMTSN, significant further improvement of these locations is unlikely without adding data from other stations in the region.

Representative waveforms for NMTSN station CAR for each mining region are shown in Figure 2. The distance to NM1 is ~190 km, to NM2 is ~ 220 km, to NM3 is ~190 km, and to NM4 is ~260 km. The NMTSN analysts try to pick Pn, Pg, Sn, and Sg for these events. For the Socorro magma body events, they also try to pick magma body converted phases (PzP and SzP). See Withers et al. (1999) for examples of waveforms and discussions of the regional phases.

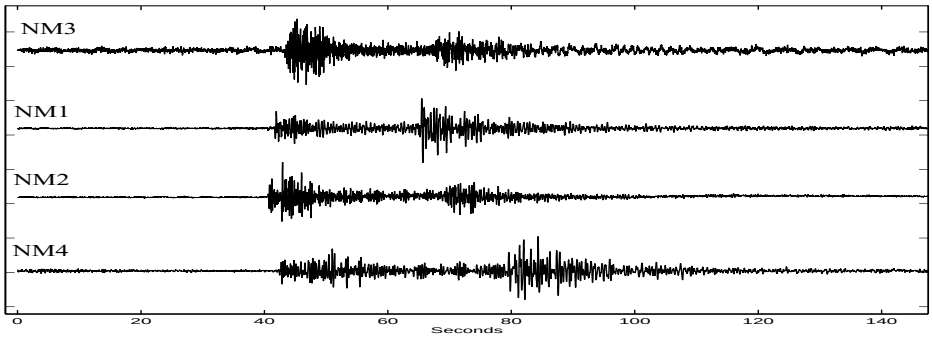

Figure 2. Typical waveforms for station CAR for each of the 4 mining regions.

The data are sampled at 100 sps, but we find that the usable frequency content is generally below 15 Hz. Lowering the sample rate improves the speed of the waveform correlations, so we down-sampled the data to 25 sps (an anti-alias filter was applied). All of our clustering was done using the waveforms for station CAR, which was chosen simply because it is a typical station near the center of the network.

Clustering of the Training Set

To assess the effectiveness of the CA techniques, we began by clustering the training set, with the expectation that we should identify the 4 mining regions. Based on trial and error, we determined that a 55-second-duration waveform window, with a 5-second lead time relative to the theoretical Pn arrival time were effective parameters for this data. We clustered this data three times: first, with no signal processing; second, with a 2- to 10-Hz, bandpass filter; and finally using a Hilbert envelope on the waveforms.

Dendrograms

We began with unfiltered waveforms, and tried building dendrograms using several of the cluster methods (flexible, median, group mean, centroid, single linkage, complete linkage) which are described by the Lance and Williams equation. To summarize the results, we found that most of the methods were equally effective in clustering the waveforms from the 4 mining regions. However, the flexible method consistently produced the clearest dendrograms. This result contradicts Jardine and Sibson (1971), who showed that the single linkage method is the only method that satisfies a set of necessary simple conditions (continuity, minimum distortion, etc.). However, we are in good company; many other researchers have found that while single linkage may be mathematically superior, it does not necessarily produce the best solutions (e.g. Williams et al, 1971; Gower, 1988). Our experience is nicely summed up by Davis (1986):

> *Most researchers who use clustering methods experiment with a variety of similarity measures and clustering techniques, and they choose the combination that yields the most satisfactory results with their data.*

The flexible method produced the best results for us, so we use it as our default choice for producing dendrograms. The flexible method properly refers to any choice of weights such that $\alpha_i = \alpha_j$ and $\alpha_i + \alpha_j + \beta = 1$, but we mean the particular set of weights suggested by Ludwig and Reynolds (1988), i.e. $\alpha_i = \alpha_j = 0.625$ and $\beta = -0.25$. This method can join groups at similarity values less than 0, as can be seen in some of our dendrograms. Such similarity values are artifacts of the method and are not physically meaningful, but they do not compromise the usefulness of the flexible method for identifying groups, which is our goal.

Deciding where to cut the stems of a dendrogram is a subjective process. In general, one should seek to set the level at the highest possible similarity value which still yields distinct groups. For the unfiltered data, 4 obvious groups were apparent and an appropriate threshold was easy to set. Conveniently, the 4 groups turn out to represent the 4 mining regions very well: the NM1 group has 3 mis-identified (2 NM4, 1 NM2), 1 in NM3; the NM2 group has 0 mis-identified, 1 in NM1; the NM3 group has 1 mis-identified (NM1), 0 in other

groups; and the NM4 has 0 mis-identified, 2 in NM1. In all, we have only 4 errors out of 60 events identified, or a 7% error rate.

If the misidentifications are due to poor signal-to-noise ratios (SNR s), then an obvious way to improve the result is to apply a filter to improve the SNR. Based on an examination of spectrograms of the waveforms, we determined that the best SNR is in the 2- to 10-Hz band. Thus we applied a 2- to 10-Hz band pass filter to all of the waveforms and re-clustered. With the band pass filtering, the two NM4 events which were in the NM1 group move to the NM4 group, improving our identification results to 58 out of 60, or a 3% error rate.

We next tried applying a Hilbert envelope to the waveforms, the method recommended by Riviere-Barbier and Grant (1993). This is a form of non-linear low-pass filtering, so the waveforms are in effect smoothed. This leads to better correlation within the mining region clusters. The dendrogram and corresponding enveloped waveforms are shown in Figure 3. Each waveform is lagged for maximum correlation with the one directly above it. The results are the same as for the bandpass case (58 out of 60 identified correctly), but the tightness of the clusters and the separation between the clusters are better. Further, because the enveloping smooths the high frequencies, we can down-sample further before applying the enveloping (we down-sampled to 10 sps), which can dramatically speed up the processing time for large data sets.

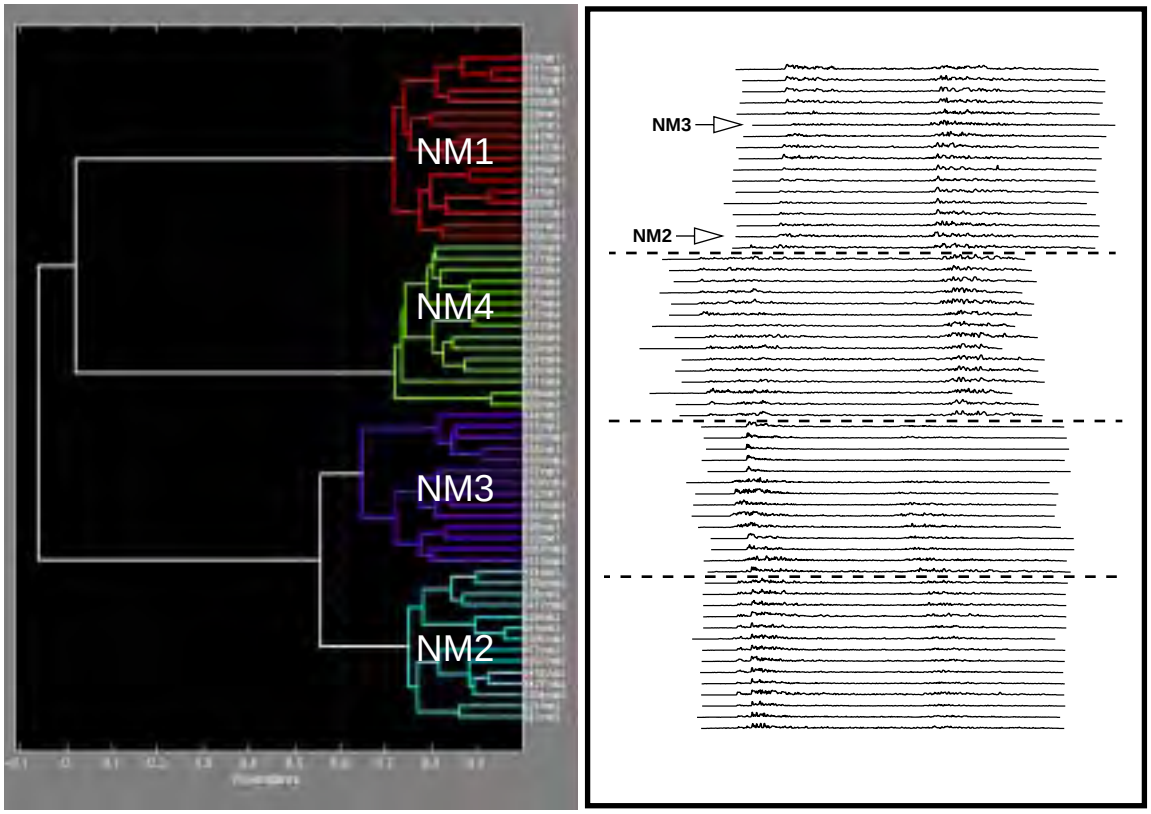

Figure 3. Dendrogram and corresponding waveforms for Hilbert enveloped training set. NM1 group has 2 mis-identified (1 NM2, 1 NM3), 0 in other groups; NM2 has 0 mis-identified, 1 in NM1; NM3 has 0 mis-identified, 1 in NM1; NM4 has 0 mis-identified, 0 in other groups.

Factor Analysis

Next, we applied factor analysis to the training set. For brevity, we show only the results for the Hilbert enveloped training set (Figure 4, left). We color the entities to identify the corresponding clusters in the dendrogram, but it is important to note that this information is not derived from the factor analysis. With the colors, it is apparent that the locations of the different mining region events are segregated on the factor analysis plot, but only the NM4 cluster (green) is well-isolated. This result is typical of many applications of factor analysis that we tried, and it illustrates two key problems with the method. First, as the clusters are not

necessarily simple geometric shapes, one would have to use some sort of generalized shape to lasso the entities within them. Secondly, unless the clusters are well-separated, and they generally are not, assigning entities in overlapping regions may be difficult. Note that these problems do not occur with the dendrogram. Admittedly, choosing the threshold at which to cut the tree can be difficult, but once it is done, grouping the entities is trivial.

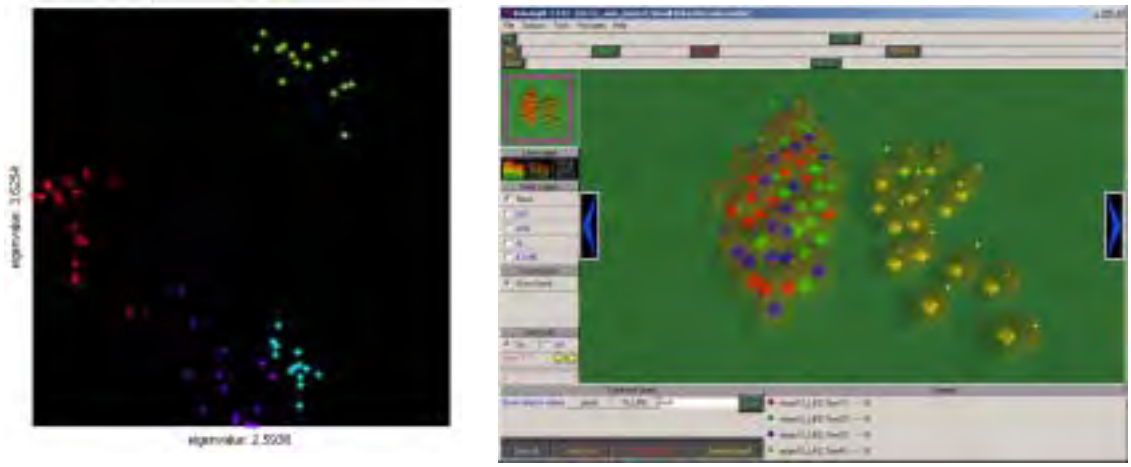

Figure 4. (left) Factor analysis for the Hilbert enveloped training set. Color coding corresponds to the dendrogram in Figure 4, i.e. NM1 = red, NM2 = cyan, NM3 = purple, NM4 = green. **(right)** VxInsight ordination plot for the Hilbert enveloped training set. NM1 = red, NM2 = green, NM3 = blue, NM4 = gold.

Based on this result and others from our analysis of the training set, we conclude that factor analysis may be useful as an auxiliary tool to verify the clustering derived from a dendrogram, but that for identifying similar waveforms it is not by itself a sufficient method.

Ordination

Again, we show only the results for the Hilbert enveloped case for brevity. In this case, we use the Sandia National Laboratories-developed VxInsight software to make a landscape of the ordination results. This is in essence a 2-D histogram. Ordination of the similarity matrix of the 60-event training set led to a plot with no separation of the mining regions at all. Given the high quality of this training set, and the impressive results provided by the dendrograms, this result was surprising. By investigating the software using some synthetic similarity matrices, we were able to establish that the range of similarities for the Hilbert enveloped test set was too small. To improve the ordination performance, we then tried to rescale the similarities in the matrix. A simple linear scaling (i.e. min gets 0, max gets 1) did not improve the results at all. Application of a non-linear scaling using a simple S curve shape did, however, lead to an improved result (Figure 4, right). The topology is similar to that for factor analysis, though the groups are even less distinct. The NM4 group is well separated, while the other groups are not.

Overall, we did not find that ordination worked well for identifying the mining regions in the training set. At best it seems to yield results that are similar to those derived from factor analysis, but this is only with some additional data processing. Without the additional processing, ordination did not separate the mining regions at all.

Clustering of the Full Set

The full set of 651 events includes the 60-event training set analyzed in the previous section. This is advantageous in that we can track where these events end up in the clusters produced for the full event clustering and use this information to make inferences about the clusters. It is also representative of a real monitoring scenario where an analyst would have a set of identified reference events which would be used to identify new events.

The dendrogram and corresponding color coded map for the 651-event set with Hilbert envelope method applied are shown in Figure 5.

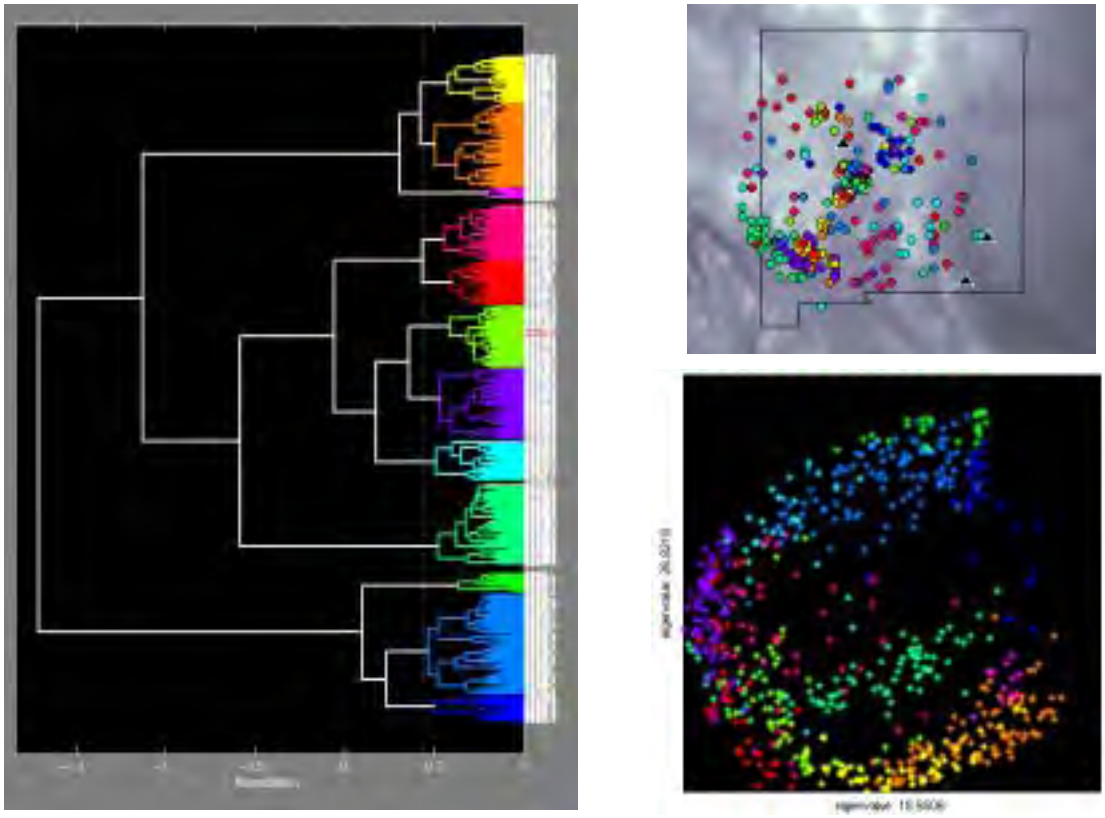

Figure 5. Dendrogram, color coded event map, and factor analysis plot for Hilbert enveloped full data set (651 events).

For the discussion which follows, we will refer to the colors of the dendrogram groupings as (from top to bottom): yellow, orange, pink, rose, red, spring green1, purple, cyan, sea green, spring green2, light blue, dark blue.

In this case, the decision of where to set the threshold to define the groups was less clear than for the training set, so we investigated several numerical methods. Cophenetic correlation refers to the correlation between the actual entity correlations in the similarity matrix and the predicted values from the dendrogram. Ideally, these would correlate perfectly, but with real data sets, they seldom do and the cophenetic correlation tends to decrease as the dendrogram is built. Sneath and Sokal (1973) suggested that a large drop in cophenetic correlation as a new group is formed might indicate a good place to set the threshold, but we seldom found this to be true. Other methods involve tracking the within-group and between-group variances as the dendrogram is built (Everitt, 1993). In the CA lingo, the W matrix contains all of the within-group variance information, and the trace of W gives the overall sum of the within-group variances. Theoretically, the minimum of trace(W) should occur at the proper threshold. Similarly, the B matrix contains all of the between-group variances and the trace of B gives the overall between-group variance. Thus, the maximum of trace(B) should occur at the proper threshold. We made plots of trace(W), trace(B), and trace(B)/trace(W) for many of the dendrograms formed for this study (training and full sets), but did not find the results useful. Ultimately, the threshold used for Figure 5 was determined by eye, with the goal of placing the training set events in separate groups. We were able to accomplish this by setting the threshold at 0.44. All NM4 test events are in the sea green group, all NM2 test events are in the purple group, all NM3 events are in the spring green1 group, and the NM1 events spread through the yellow (3), orange (7), and pink (3) subgroups of a higher order group. The scatter of the corresponding colored points on the map as compared to those in Figure 1 give some idea of the mislocations for each of the mining regions.

Even when the locations of the events are poorly known, sometimes the timing of the events can still offer important information which can be used to identify the events, particularly when combined with the groups identified by CA. As an example of this, we show histograms by day of week and hour of data for the clustering shown in Figure 6.

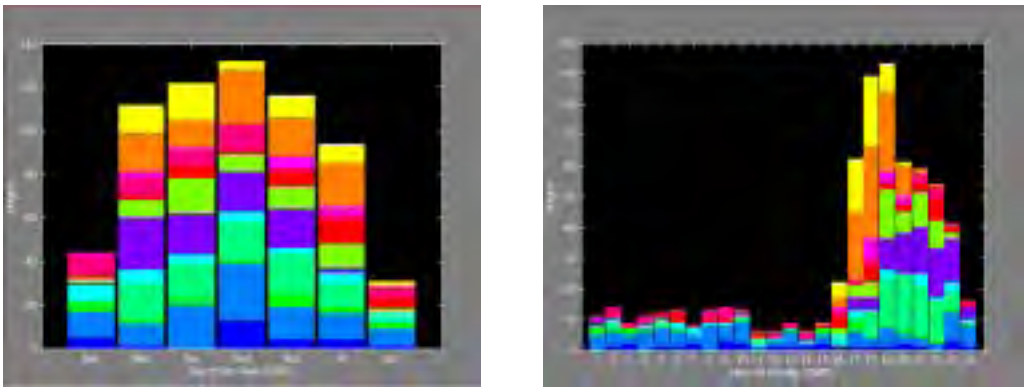

Figure 6. Histograms for Hilbert enveloped full data set. **(left)** By day of the week. **(right)** By hour of the day in GMT (subtract 6 hours to get local time). The colors correspond to the groups identified in Figure 5.

We have found these types of diagrams to be useful in separating man-made and naturally occurring events. A careful examination of Figure 6 shows that the NM mining region groups occur during the work-week and the local work-day time only, indicative of man-made events. If it is known that the data set under analysis contains groups of mining events, these types of histograms could be used to set the thresholds to cut the dendrogram.

Examining the colored bars for the remaining groups, we first note that all show no work-week or work-day dependence, suggesting that they are dominated by earthquakes. The spring green2 group are all are from within the network, and may be Socorro magma body events. The rose, red, cyan, and blue groups all plot diffusely throughout the state and each group contains a variety of waveforms, so it is likely that each group does contain events from all over the state.

We also applied factor analysis to the full event set (Figure 5), and found the results to be consistent with those for the training set. Again, the factor analysis plot of the eigenvectors corresponding to the second and third greatest eigenvalues does tend to put each of the groups in different areas, but the clusters are not well-separated, and there are many areas of overlap between the groups. Using this plot, it would be difficult to identify the entities within each cluster, though the plot might be useful for establishing how distinct the dendrogram clusters are (e.g. calculating distances between the centroids).

We might be able to improve this result by using the information in some of the other eigenvectors, and we are currently pursuing this idea. There are as many eigenvectors as there are events in the set being clustered (651 for our full event set). We found that other eigenvector combinations are more effective for identifying certain clusters, but that no single pair works best for all clusters. One can easily add another dimension and make a 3-D plot to evaluate eigenvector triplets, but we found these plots to be difficult to interpret.

CONCLUSIONS AND RECOMMENDATIONS

In this study, we have extended the waveform correlation-based cluster analysis (CA) work of Riviere-Barbier and Grant (1993), which used only complete linkage dendrograms, by evaluating several additional CA techniques to identify clusters of similar waveforms. We examined several alternative agglomerative hierarchical clustering methods (i.e. dendrogram producing methods), as well as factor analysis and ordination. We used a data set of 651 regional events recorded by the New Mexico Tech Seismic Network (NMTSN), from which we extracted a training set of 60 well-located, ground-truthed events coming from the 4 known mining regions in western New Mexico and southeastern Arizona.

Our results suggest that dendrograms seem to be the most effective cluster analysis technique, but that the complete linkage method used by Riviere-Barbier and Grant is not the best choice. We found the flexible method of Ludwig and Reynolds (1988) produces dendrograms which are at least as effective in grouping like waveforms and which make the groupings more apparent. Choosing the threshold level to identify the groups for the dendrograms remains problematic. We investigated a variety of numerical techniques and found none of them to be generally effective. Thus, we ultimately were forced to subjectively choose thresholds which looked reasonable on the dendrograms and isolated the mining regions.

The other CA techniques we tried were less effective. Ordination failed outright at first, but we were able to make it produce marginally useful results by a non-linear scaling of the correlation information. Factor analysis provided better results than ordination without any need for the rescaling, but still does not work well for assigning the individual events to clusters. We do think, however, that factor analysis might prove useful as an auxiliary tool to assess the quality of the groupings identified with the dendrograms, and intend to further investigate this possible use.

ACKNOWLEDGEMENTS

We thank Helen Koller for her assistance in using the VxInsight software to produce the ordination plots and Jeff Hampton and Neill Symons for their thorough reviews of the manuscript.

REFERENCES

Balch, B., Hartse, H., Sanford, A., and K. Lin (1997). A new map of the geographic extent of the Socorro midcrustal magma body, *Bull. Seismol. Soc. Amer.*, 87, 174-182.

Davis, J. C. (1986). Statistics and data analysis in geology, J. Wiley & Sons, New York.

Everitt, B. S. (1993). Cluster analysis, Edward Arnold, London.

Gower, J. C. (1988). Classification, geometry and data analysis, In Classification and Related Methods of Data Analysis (H. H. Bock, ed), Elsevier, North-Holland.

Lance, G. N. and W. T. Williams (1967). A general theory of classificatory sorting strategies: 1. Hierarchical systems, *Comp. J.*, 9, 373-380.

Ludwig, J. A. and J. F. Reynolds (1988). Statistical ecology: a primer on methods and computing, J. Wiley & Sons, New York.

Riviere-Barbier, F. and L. T. Grant (1993). Identification and location of closely spaced mining events, *Bull. Seismol. Soc. Amer.*, 83, 1527-1546.

Sneath, P. H. A. and R. R. Sokal (1973). Numerical taxonomy, Freeman, San Francisco.

Williams, W. T., Lance, G. N., Dale, M. B., and H. T. Clifford (1971). Controversy concerning the criteria for taxomonometric strategies, *J. Comp.*, 14, 162-165.

Withers, M., R. Aster, and C. Young (1999). An automated local and regional seismic event detection and location system using waveform correlation, *Bull. Seismol. Soc. Amer.*, 89, 657-669.

Wylie, B. N., Boyack, K. W., Davidson, G. S., and D. K. Johnson (2000). Visualization of information spaces with VxInsight, Sandia Labs Report #SAND2000-3100.

Other Topics

DISCUSSION OF RELIABLE MULTICAST DEPLOYMENT PROGRESS FOR THE CONTINUOUS DATA PROTOCOL

Deborah A. Agarwal

Ernest Orlando Lawrence Berkeley National Laboratory

Sponsored by National Nuclear Security Administration
Office of Nonproliferation Research and Engineering
Office of Defense Nuclear Nonproliferation

Contract No. DE-M9AL-66156.501

ABSTRACT

The International Monitoring System (IMS) seismic sensor data are currently collected using point-to-point networking protocols. Multicast communication allows a single transmission of the data from a sensor to be received by multiple sites (point-to-multipoint). This capability has the potential to improve fault tolerance and possibly efficiency of the sensor data collection and dissemination process. An experiment was conducted to demonstrate the collection and dissemination of seismic sensor data using reliable multicast communications. Telcordia and SAIC created a prototype multicast-capable version of the Continuous Data (CD-1) protocol as an experiment. This prototype version used the RMTP reliable multicast protocol available from Talarian Corporation to transport the sensor data. The experiment demonstrated that reliable multicast is a viable technology for use in transmitting the seismic data.

The CD-1.1 protocol has since been developed and released. The CD-1.1 protocol incorporates many enhancements that make it better suited than the CD-1 protocol to the use of reliable multicast. Initial studies into the feasibility of implementing a reliable multicast version of the CD-1.1 protocol have begun. This paper provides an overview of the current progress in the study of the possible use of reliable multicast in the transmission of continuous data from IMS stations and the current state of reliable multicast development.

KEY WORDS: communications, multicast, reliable

OBJECTIVE

Reliable multicast is a communication capability that can be used in the network to allow a message to be sent from a single sender to multiple receivers. It uses IP multicast for the transmission of messages on the network. IP multicast is a simple communication mechanism that allows a single message to be sent to a group of receivers at the network level. With reliable multicast the receivers in a group can be reached by sending a single message. Using unicast the messages would need to be sent to each receiver individually by the sender or a site acting as a forwarder.

IP multicast is an unreliable messaging service implemented in the hosts and routers of the network. Multicast packets are sent addressed to an address in the multicast address range. Applications that wish to receive the multicast packets open a connection to the multicast address. The multicast capability provides an efficient means of transmitting a packet through the network to reach all the receivers. The IP multicast communication mechanisms are now a standard part of the internet protocol suite, and they co-exist with the unicast Transmission Control Protocol (TCP). and User Datagram Protocol (UDP) mechanisms. The IP multicast mechanisms do not replace the unicast mechanisms; they instead provide an additional service.

Reliable multicast is effectively the multicast equivalent of the TCP protocol. Reliable multicast provides reliable delivery of messages to multiple receivers. It uses IP multicast to provide the message dissemination capability and adds reliable delivery mechanisms. Reliable multicast is not yet a standard communication protocol that is part of the operating systems of hosts. Reliable multicast is instead run as an application-level

protocol. An instance of the reliable multicast software is run at each of the senders and receivers participating in a reliable multicast session. The software then uses IP multicast for its underlying communication mechanism. There are several commercial and freeware reliable multicast protocols available today. Two of the existing reliable multicast protocols are the Multicast Dissemination Protocol (MDP)0 and the Reliable Multicast Transport Protocol (RMTP)0.

The CD-1 protocol is the protocol currently in use for sending continuous data from the IMS seismic sensors. The CD-1 protocol runs at the sender of the data and at the receiver and is responsible for transmission of the data to the receiver. The CD-1 protocol is designed to provide transmission of continuous data between a sender and receiver pair. The CD-1 protocol retrieves the data from a Last In First Out (LIFO) Heap at the sending side and stores it in a Disk Loop at the receiving site. The protocol uses a TCP connection to transmit the data from the LIFO Heap to the receiver. TCP provides unicast, reliable, source-ordered delivery of messages between the sender and receiver. CD-1 delivers data only while there is a TCP connection between the sender and the receiver. When the connection is down, the sender buffers data locally in the LIFO heap waiting until a connection can be re-established to the receiver. Some amount of data may be lost by the CD-1 protocol when a TCP connection is closed due to a failure.

The objective of the work reported in this paper is to study the potential use of reliable multicast as a communication mechanism for the CD-x protocol. The expected benefits of this change are improved fault-tolerance and efficiency.

RESEARCH ACCOMPLISHED

Early work on the study focused on the IP multicast capabilities of the network and some suggestions for appropriate reliable multicast protocols. The CD-1 protocol, the IMS data rates, and data delivery criteria were also studied. The findings from these early studies are reported in (Agarwal, 1999; Multicasting, 1999). At the completion of these preliminary studies, an experiment was conducted. In the experiment a prototype multicast-capable version of the continuous data protocol (CD-1) was created[1]. The purpose of the experiment was to provide a small-scale technical feasibility trial of the use of reliable multicast as a transport mechanism for the continuous data. A detailed discussion of the experiment is contained in Agarwal et al, 2000.

A Multicast Experiment Using the CD-1 Protocol

At the beginning of the experiment, the CD-1 protocol was the only implemented version of the continuous data protocol. The CD-1 protocol contains no end-to-end reliability mechanisms, so it was not an ideal candidate for long-term use with reliable multicast. However, the use of CD-1 for a technical feasibility prototype allowed rapid development for testing. To reduce development cost and time, a goal of the prototype multicast-enabled implementation of CD-1 was to use as much of the existing code as possible. Another goal of the experiment was to have a comparable frame loss rate to that exhibited by the existing CD-1 protocol implementation.

At the beginning of the experiment, the MDP and RMTP-II reliable multicast protocols were evaluated. These are the two protocols identified by the earlier study to be the best candidates for use with the CD-x protocol. The principle deciding factors were the application-programming interface (API) and the availability of commercial support. The RMTP-II protocol provided both these features and was thus chosen for use in the experiment. The experiment also provided an opportunity to test the robustness of the RMTP-II from Talarian Corporation.

The CD-1 protocol's original design was based on an assumption that the underlying data transmission was unicast. The LIFO heap at the CD-1 sender is used to buffer up data waiting for transmission to the receiver. The multicast-enabled version of CD-1 replicates the sender's LIFO Heap at the receiver. Reliable multicast is

[1] The design, implementation, and testing of the multicast-enabled version of the CD-1 protocol were carried out by Telcordia Technologies and SAIC, sponsored by U.S. Department of Defense, Defense Threat Reduction Agency, Contract No. DTRA01-99-C-0025.

then inserted between the LIFO heaps and is used to transfer the data between the sender's and receivers' LIFO Heaps. This process allowed the changes to the existing CD-1 protocol implementation to be minimized.

During failures, there is more needed to provide behavior equivalent to the original behavior of the CD-1 system. If the sender crashes and recovers, the sending of data in the unicast CD-1 was discontinued during the crash and resumed after the recovery. The behavior of the multicast-enabled CD-1 is the same in this case. The crash of a receiver in the unicast CD-1causes the sender to buffer up data until the receiver recovers and re-establishes a connection. But, if the multicast-enabled version of the CD-1 software were to stop transmitting when any one receiver was down, then the perceived reliability of the CD-1 software from the other receiver(s) would be less than the original unicast CD-1 software. In the multicast version, if a receiver crashes, the frame sending continues, and the operational receivers continue to receive frames. When the receiver recovers, it rejoins the multicast group and resumes receiving frames. The missed frames were stored in a "catch-up" LIFO Heap at the sender, and the frames are sent to the recovered receiver using a unicast TCP connection in parallel with the ongoing multicast connection. "Catch-up" frames and new frames are merged at the receiver.

The prototype multicast-based CD-1 implementation was tested in several configurations to evaluate its performance. The initial tests of the system were performed at Telcordia using two receivers. These tests only sent data through to the LIFO Heap at the receiver. The next series of tests were between Telcordia and the Prototype International Data Center (PIDC). In these tests, the sender was at Telcordia and the receivers were at Telcordia and the PIDC. This configuration allowed testing with a moderate latency link over the internet. They also allowed the software to be tested all the way through to the Disk Loop Manager (DLMan).

The tests between Telcordia and the PIDC were run continuously for eight days. Six times during the eight days, the receiver at the PIDC became unreachable from the sender at Telcordia. In each of these cases, the catch-up channel was activated when the receiver rejoined the multicast channel. The correct transfer of the merged catch-up and multicast data to the DLMan at the receiver was also tested.

The final tests used a version of the RMTP-II protocol that allowed the network loss and latency characteristics to be emulated. In these tests characteristics representative of the satellite network were emulated. All the test configurations used one sender and two receivers. In these emulations, the network delay between the sender and the receivers used an exponential distribution with a mean of 1.2 seconds, a standard deviation of 0.2 seconds and cut-offs at 1.0 and 1.7 seconds. The loss probability was set to 0.5%. The CD-1 prototype performed well in this test. Successful tests of all combinations of system start-up and recovery/catch-up were also performed. The tests between Telcordia and the PIDC were left running for four weeks. The data transfer ran without a problem during that time and showed results comparable to the original unicast CD-1.

The CD-1.1 Protocol

At the beginning of the multicast study, the CD-1.1 version of the protocol existed only in specification form. The CD-1.1 protocol has since been implemented and the implementation of the CD-1.1 protocol is currently undergoing testing at the PIDC using TCP communication[2]. The CD-1.1 protocol includes several features that should make it easier to use other protocols besides TCP for data transmission. These features include retransmission request mechanisms, self-describing data frames, and a more flexible connection set-up method. These features are expected to make the integration of reliable multicast with CD-1.1 more straightforward than was the case with CD-1. In particular, the connection set-up frame contains a field that can be used for specifying a multicast address for use in data transmission. The retransmission request mechanisms provide a means of retrieving lost data. These are directly of benefit to both a unicast and multicast-based version of CD-1.1 since they will allow any missing frames to be retrieved directly through CD-1.1. In CD-1 missing frames could only be retrieved through bulk data request mechanisms.

Multicast Standards Activities

Reliable multicast and IP multicast development efforts have made significant advances since the beginning of the CD-1 multicast experiment. There are many groups within the Internet Engineering Task Force (IETF)

[2] A beta version of the software is available from http://www.pidc.org/

working on multicast-related standards for the internet. The two groups of primary interest to this study are the Source Specific Multicast (SSM) working group[3] and the Reliable Multicast Transport (RMT) working group[4].

Source-specific multicast is an IP multicast capability that allows members of a multicast group to subscribe to a specific source (Bhattacharyya Draft). This allows the receiver to restrict the multicast to delivery of messages generated by that specific source only. This capability is being added to the internet to improve handling of well-known multicast sources, access control, and scalability of the multicast address space. The first two of these are directly applicable to the IMS network since the IMS sites are normally well-known sources. This capability will allow the receivers to subscribe specifically to the data sources of interest and not receive traffic from the other members of the multicast group. The SSM working group is likely to finish its work quickly since many of the router vendors already have working versions of source-specific multicast.

The RMT working group is tackling the problem of providing internet standards for reliable multicast protocols. Since reliable multicast protocols are generally built with application-specific goals in mind, the protocols have different message delivery properties and different methods of achieving reliability (Handley, 2000). For example, some reliable multicast protocols use retransmission requests to retrieve missed messages and others use forward error-correcting codes (FEC) to eliminate the need for retransmissions. With FEC, redundant data are placed in each message and the net effect is that the receiver will be able to reconstruct the entire data stream despite missing some of the packets. Some reliable multicast protocols provide bulk-data transfer capabilities and some are intended for support of real-time applications. This difference is generally seen in the timeliness of retransmissions. Some bulk-data transfer protocols wait to send retransmissions until all the data has been sent once. Some reliable multicast protocols acknowledge messages that have been received. whereas others send negative acknowledgements indicating what messages are missing.

Despite the differences between reliable multicast protocols, there are many common tasks that are shared by these protocols. The RMT working group is defining standardized building blocks for reliable multicast protocols (Whetten, 1998). The intent of these building blocks is to identify the common components and standardize these components. At present, several building blocks are under development. These building blocks address congestion control, message reliability mechanisms, and mechanisms for router assistance. The idea is for each protocol to be composed of a subset of the building blocks along with any specialized components it requires. The benefit of this approach is that the building blocks are many of the underlying core components of a reliable multicast protocol and standardizing these improves the robustness of all the protocols that use them. The Talarian Corporation personnel involved in RMTP-II are also heavily involved in these standards activities and will likely be quick to adopt the standards.

CONCLUSIONS AND RECOMMENDATIONS

The use of reliable multicast as a method of sending continuous data from the IMS stations continues to be studied. Initial work studied the network, IMS data rates, and the continuous data protocols. An experiment was conducted using a version of the CD-1 protocol that was modified to use reliable multicast communication as the underlying data transport mechanism instead of TCP. The experiment demonstrated the feasibility of using reliable multicast for transmission of continuous data. The fault-tolerance introduced by this approach was also demonstrated in the experiment. The CD-1.1 protocol is now available as a beta release. The CD-1.1 protocol provides many new features that are likely to ease the integration of multicast data transmission capabilities. A possible future activity will be to develop a reliable multicast-based version of the CD-1.1protocol.

Over the past several years there have also been several developments in reliable multicast and IP multicast capabilities for the Internet. There are several important multicast related standards activities within the IETF. The building blocks being designed to standardize reliable multicast are likely to provide robust versions of components critical to reliable multicast protocols. Source-specific multicast is another IETF activity that promises to provide improved access control and multicast routing.

[3] The SSM working group charter can be viewed at http://www.ietf.org/html.charters/ssm-charter.html. The group's working documents are available at http://sith.maoz.com/SSM/.
[4] The RMT working group charter can be viewed at http://www.ietf.org/html.charters/rmt-charter.html.

REFERENCES

Agarwal, D., P. Melliar-Smith, L. Moser, and R. Budhia (1998), "Reliable Ordered Delivery Across Interconnected Local-Area Networks," Transactions on Computer Systems, vol. 16, no. 2, May.

Agarwal, D. (1999), "Using Multicast in the Global Communications Infrastructure for Group Communication," in the Proceedings of the 22nd Annual Seismic Symposium, Las Vegas, Nevada, September.

Agarwal, D., R. Stead, J. E. Burns, N. Shah, and N. Kyriakopoulos (2000), "Initial Results Of The CD-1 Reliable Multicast Experiment," published at the Global Communications Infrastructure Workshop, Vienna, Austria, October.

Berket, K., D. A. Agarwal, P. M. Melliar-Smith, and L. E. Moser (2001), "Overview of the InterGroup Protocols," Proceedings of the 2001 International Conference on Computational Science. LNCS 2073. Springer-Verlag. pp. 316-25.

Bhattacharyya, S., C. Diot, L. Giuliano, R. Rockell, J. Meylor, D. Meyer, G. Shepherd, B. Haberman (2001), "An Overview of Source-Specific Multicast(SSM) Deployment," Internet Draft <draft-ietf-ssm-overview-00.txt>. Working Group URL - http://sith.maoz.com/SSM/.

Handley, M., S. Floyd, B. Whetten, R. Kermode, L. Vicisano, and M. Luby (2000), "The Reliable Multicast Design Space for Bulk Data Transfer," Internet Draft, Internet Engineering Task Force, RFC 2887, August.

Macker, J. and W. Dang, "The Multicast Dissemination Protocol version 1 (mdpv1) Framework," Technical white paper, US Naval Research Laboratory, available from http://tonnant.itd.nrl.navy.mil/docs/mdpv1.ps .

Whetten, B., M. Basavaiah, S. Paul, T. Montgomery, N. Rastogi, J. Conlan, T. Yeh (1998), "The RMTP-II Protocol," Internet Draft, draft-whetten-rmtp-ii-00.txt and draft-whetten-rmtp-ii-app-00.txt, April.

Whetten, B., L. Vicisano, R. Kermode, M. Handley, S.Floyd, and M. Luby (2001), "Reliable Multicast Transport Building Blocks for One-to-Many Bulk-Data Transfer," Internet Draft, Internet Engineering Task Force, RFC 3048, January.

"Formats and Protocols for Continuous Data CD-1.1," (2000), Published by Scientific Applications International Corporation as part of the International Data Centre Documentation, July. Available from http://www.pidc.org/librarybox/idcdocs/downloads/343.pdf .

"Multicasting in the GCI - A Report of Study Results," (1999), available on the CTBT Expert's Communication System as CTBT/WGB/TL-3/9/Rev.1/Amend.1, 2 September.

NNSA KNOWLEDGE BASE INTEGRATION, VALIDATION, AND DELIVERY OF OPERATIONALLY USEFUL INFORMATION PRODUCTS

Dorthe B. Carr[1], David P. Gallegos[1], Preston B. Herrington[1], D. Craig Pearson[2], Steven R.Taylor[2], Aaron A. Velasco[2], John J. Zucca[3], David B.Harris[3], Stanley D. Ruppert, [3] and Leslie A. Casey[4]

Sandia National Laboratories[1]
Los Alamos National Laboratory[2]
Lawrence Livermore National Laboratory[3]
National Nuclear Security Administration[4]

Sponsored by National Nuclear Security Administration
Office of Nonproliferation Research and Engineering
Office of Defense Nuclear Nonproliferation

Contract No. DE-AC04-94AL85000

ABSTRACT

The National Nuclear Security Administration (NNSA) Ground-Based Nuclear Explosion Monitoring Research & Engineering (GNEM R&E) program provides research and development in support of U.S. nuclear explosion monitoring. Specifically, the GNEM R&E program provides products that will be utilized by the Air Force Technical Applications Center (AFTAC) in their nuclear explosion monitoring and treaty monitoring missions. To serve this role, NNSA must develop, track, and integrate products as they move from the research level to operations and must ensure that these products are reliable and technically correct.

NNSA's responsibilities include:

1. Development of operationally useful products (scientific data and the tools to manipulate them) that support the U.S. nuclear explosion monitoring mission at AFTAC,
2. Integration of technical products developed by NNSA and others into a comprehensive and cohesive package (Knowledge Base) that can be readily utilized by AFTAC,
3. Technical assessment, validation, and verification of all products prior to delivery to AFTAC, and
4. Delivery and integration support of the operational Knowledge Base to AFTAC.

The practical implementation of the development, integration, assessment and delivery of operational products occurs through the process of creating periodic Knowledge Base releases. Specifically, the Knowledge Base is comprised of a set of Information Products, which generally include pertinent datasets and analytical tools. In addition, each Information Product also includes critical supporting information (metadata) about the datasets and tools.

This paper describes implementation of the Knowledge Base development and integration process, including the utilization of technical working groups to coordinate and evaluate Information Products.

KEY WORDS: Knowledge Base, integration, validation, information products

OBJECTIVE

The National Nuclear Security Administration (NNSA) Ground-Based Nuclear Explosion Monitoring Research & Engineering (GNEM R&E) Program is continuing the process of compiling Information Products (IP) into a cohesive and comprehensive Knowledge Base (KB) for use by the Air Force Technical Applications Center (AFTAC) in fulfilling their nuclear explosion and treaty monitoring missions. A technically sound and traceable process has been defined to ensure the integrity and utility of research results as they migrate into information products that will be used in the Knowledge Base. A process for validating, verifying, and

logically integrating the information products is required to ensure technically reliable and useful Knowledge Base deliveries. This paper provides a general overview of the Knowledge Base evaluation and integration process to facilitate effective participation in the process by all contributors of research products. In doing so, it is intended that this paper also provide transparency into the overall process.

IMPROVEMENTS TO THE INTEGRATION PROCESS

A process for migrating research results into information products for use in the NNSA Knowledge Base has been developed to ensure that the delivery of a NNSA Knowledge Base contains technically accurate and relevant information products that are in a form that is useful for operational monitoring. This process has been implemented through one Knowledge Base release.

If any process is to retain its effectiveness, it must be continuously assessed and improved wherever possible. During the initial implementation of the Knowledge Base Integration Process, a rigorous evaluation was conducted. Two improvements were identified and have been added:

1. The use of Knowledge Base working groups (WGs) to better address validation of data sets and information products and
2. More explicit descriptions of how the integration process works for software products and algorithms.

This paper describes the integration process (Moore *et al.*, 2000), with the refinements included.

The organizational structure of the Knowledge Base is shown in Figure 1. The fundamental building blocks of the Knowledge Base are referred to as *data sets*. A data set is a collection of data usually all of the same kind (e.g., event data, contextual data, parametric grid data). *Metadata* accompany each data set and describe the content, source, quality and condition of the data set. At the next level up, a combined grouping of data sets makes up an *Information Product*, which is organized around a defined logical theme. An information product comprises:

- One or more conceptually related data sets and/or tools
- Metadata corresponding to each data set
- An information product release document, which provides a detailed description of the information product

Finally, the Knowledge Base is composed of several Information Products.

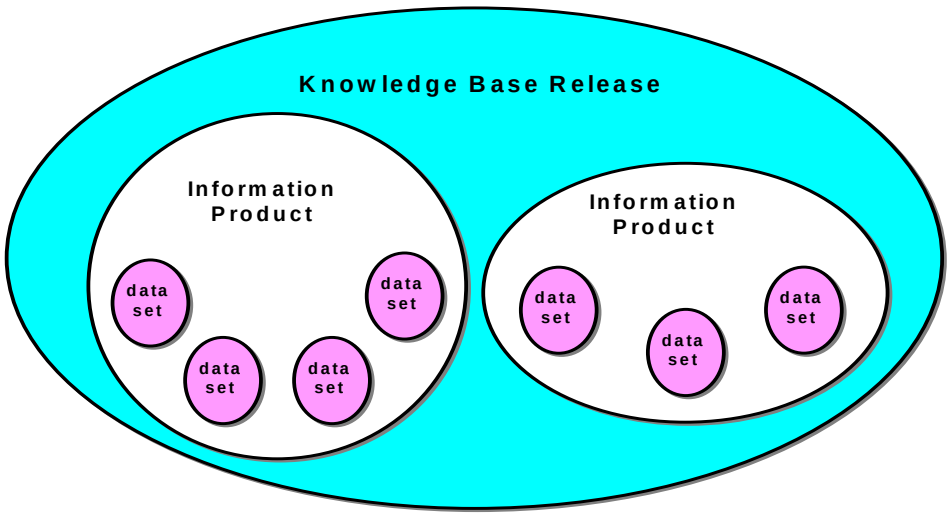

Figure 1 - Knowledge Base Components

In addition to data sets, the Knowledge Base also contains a number of viewing, analysis, manipulation, and population tools, to facilitate AFTAC's evaluation and use of the Knowledge Base contents. The tools would go through a similar evaluation process as the datasets. In fact, the evaluation of some of the tools (e.g., Knowledge Base population tools) is closely linked to the evaluation and acceptance of many of the datasets.

The participants in the Knowledge Base integration process are shown in Figure 2. The flow of information from Contributors to Scientific Integrators to Knowledge Base (KB) Integrator corresponds to integration of products shown in Figure 1. That is, principal investigators develop products at the level of the data sets depicted in Figure 1. Several principal investigators may contribute data sets to a Product Integrator, who in turn compiles or integrates these into an information product. The theme or concept of a given Information Product is defined beforehand, based on requirements, to ensure that the appropriate data sets go to the correct Product Integrator. The Product Integrator delivers the Information Product to a Knowledge Base Coordinator, who is responsible for verifying that the Information Product is complete and that it has been technically validated prior to integration into the Knowledge Base. The Knowledge Base Coordinators work with the Knowledge Base Integrator to combine several Information Products into a single Knowledge Base. The integrated Knowledge Base is then evaluated and validated by the Integration Board (IB) / Vetting Panel prior to being delivered to the Operational Users.

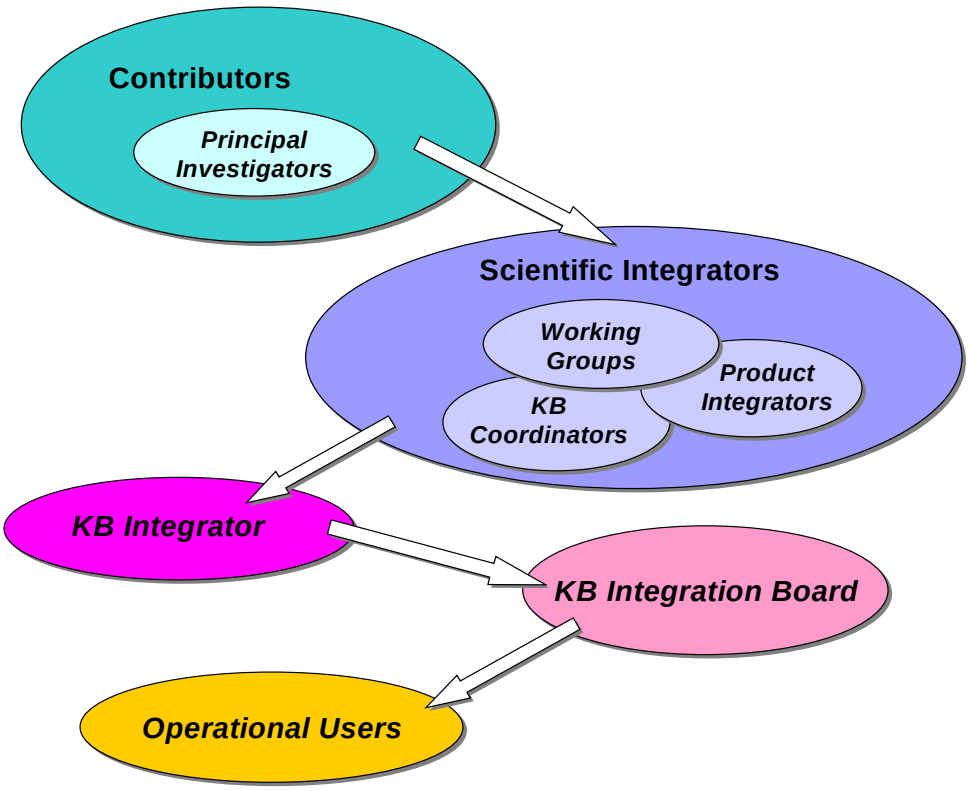

Figure 2 - Knowledge Base Integration Process Participants

The integration and evaluation process is shown in greater detail in Figure 3 and is derived from Moore *et al.* (2000). The single most significant change to the integration process since the initial implementation has been the addition of technical working groups.

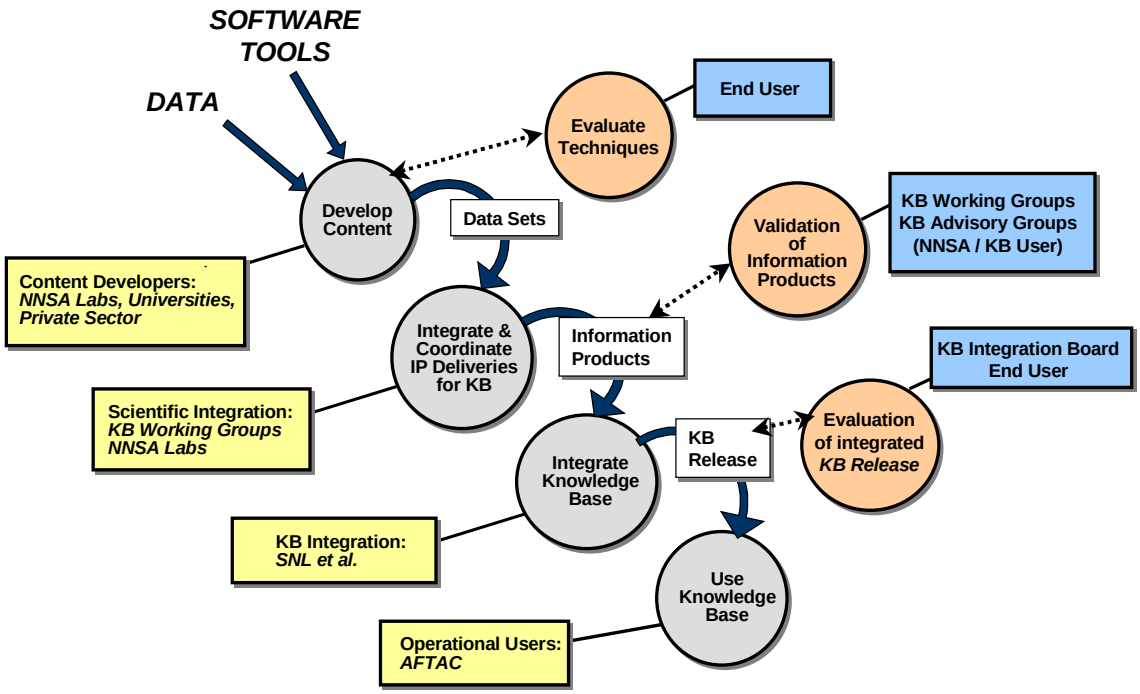

Figure 3 - Knowledge Base Evaluation and Integration Process

In Figure 3, the center series of elements, beginning with “DATA” and "SOFTWARE TOOLS," depicts how data and algorithms are integrated into data sets, then into Information Products, and finally, into a complete Knowledge Base Release. The boxes to the left of this integration series are the specific players who conduct each of the steps. The circular elements to the right of the integration series represent the technical evaluation and subsequent validation that occurs at each step in the process. The boxes to the far right are the specific players that conduct these evaluations. A key characteristic of this process is that the end user (AFTAC) is involved throughout the integration and evaluation process, from the validation of techniques for content development through the evaluation of the integrated Knowledge Base release. This is important because the end user is critical in the early-on determination of relevancy and usefulness of any given data set or Information Product, as well as evaluation of technical accuracy. Another key characteristic of this process is that products (i.e., data sets, Information Products, Knowledge Base) are verified and validated at each step in the process.

The addition of technical working groups has provided not only coordination early on and throughout the process, but has provided an additional component of technical assessment throughout the process. The working groups comprise NNSA technical personnel and representatives from AFTAC. For a given Knowledge Base Release, these working groups will serve the primary functions of verification, validation, and coordination associated with a specific Information Product, which may become part of a Knowledge Base Release. Generally, the working groups would interact with researchers to provide technical guidance and feedback for the research products that form the basis for Information Products. To satisfy this function, the working groups specifically have the following tasks:

- Identify outstanding technical issues, assign some level of priority to those issues, and develop strategies and technically sound methodologies for addressing these issues
- Validate the use of a specific methodology for developing a given Information Product
- Coordinate schedule, formats, and Information Product structure (including metadata)
- Develop and follow a schedule of critical meetings
- Validate site-specific models and the data created through implementation of those models
- Assess and report on the quality of any empirical data to be delivered or used
- Assess and report on the operational usefulness of tools and datasets
- Identify support for researchers, and
- Assist with metadata preparation.

The validation and coordination support, which is provided by the working groups, positions each resulting Information Product for review by the appropriate Knowledge Base Advisory Group. The Knowledge Base Advisory Groups can then verify that the Information Products are technically accurate, cohesive and complete.

Following review of the individual Information Products by the Knowledge Base Advisory Groups, the aggregate set of Information Products is integrated into a proposed Knowledge Base Release and submitted to Knowledge Base Integration Board for review and approval. Once approved, the Knowledge Base is delivered to the end user (AFTAC).

CONCLUSIONS AND RECOMMENDATIONS

The process of validating, verifying, and managing the information products is critical to the successful integration of scientific research to support operational monitoring systems at AFTAC. This process has been modified to provide coordination, integration and validation of products from the onset through the employment of working groups to identify technical issues and to develop methodologies for addressing these issues. The two significant improvements this year are

1. The addition of Knowledge Base Working Groups to better address validation of data sets and information products and
2. More explicit descriptions of how the integration process works for software products and algorithms.

This integration process results in coordinated products from researchers at different organizations. It also involves the researchers at NNSA and the customer at AFTAC in the integration process as the working groups take an active role in defining, creating and validating information products.

Continued success of the integration process relies on the following:

- All contributors, whether DOE-funded or not, are knowledgeable about the process.
- The process continues to be evaluated and refined as new requirements emerge and as various types of research evolve.
- Feedback is received from the end-users concerning the usefulness of the format and functionality.
- Feedback is received from the end-users regarding the validity of the content and functionality.

REFERENCES

Moore, S., H. Armstrong, D. Carr, R. Keyser, E. Shepherd, L. Wilkening, C. Young, M. McCornack, J. Aguilar-Chang, A. Velasco, S. Ruppert, T. Hauk, and C. Schultz (2000), The Integration Process Design for Incorporating *Information Products* into the Department of Energy *Knowledge Base*, Sandia National Laboratories, Report No. SAND2000-0597, Albuquerque, NM (also available from http://www.nemre.nn.doe.gov/shared/papers/KnowledgeBase/sand.pdf).

NUCLEAR SOURCES AND ASSETS DATABASE (NUSAD) DEVELOPMENT

Joel C. Rynes and Daniel Leussing

Veridian Systems

Sponsored by Defense Threat Reduction Agency

Contract No. DTRA01-99-C-0031

ABSTRACT

The Nuclear Sources and Assets Database (NUSAD) has been developed and is being maintained by the Atmospheric Radionuclide Monitoring Program at the Center for Monitoring Research (CMR). NUSAD is an Oracle-based database that contains information regarding nuclear sources and assets throughout the world. A source is any facility that could potentially release radionuclides and an asset is any device that can detect radionuclides. The database can be accessed through the NUSAD Geographical Display Tool (GDT). The GDT is a graphical user interface that provides users not only the capability to view, enter, and modify NUSAD data but also to geographically visualize the data on configurable maps. The NUSAD GDT consists of the ArcIMS geographical information system (GIS) coupled with NUSAD and specialized Java-based software. The database and the GDT will be used to assist in identifying the source of radionuclides found in data from the International Data Centre (IDC) and other institutions. This paper describes the data contained in NUSAD and demonstrates the capabilities of the NUSAD GDT.

KEY WORDS: radionuclide monitoring, geographical information system, CMR, IDC, ArcIMS

OBJECTIVE

The objective of this work was to create and make available to authorized users a database of worldwide devices that could potentially release or potentially measure airborne radionuclides. These data could then be used to help determine the source of radionuclides found in data from the IDC or other institutions and to identify additional assets to either confirm or contradict IDC data. Anticipated users of the database are the United States (US) National Data Center (NDC) and other authorized institutions investigating the cause of a potential nuclear event. Due to the critical nature of its use, it is essential that this database maintains the utmost accuracy and integrity. In addition, it is essential that an interface be provided with the database so that users can easily and quickly interact with its data.

RESEARCH ACCOMPLISHED

NUSAD has continuously grown and evolved since its conception in 1998. It originally consisted of a few Microsoft Excel spreadsheets that contained nuclear reactors and nuclear facilities within the US and worldwide nuclear assets. In 1999, the database was converted to Oracle and worldwide nuclear reactors and facilities were added to the database. In 2000, the NUSAD Data Entering Tool (DET) was created. The DET is a Java-based graphical user interface (GUI) that allows users to easily view, edit, and insert NUSAD data. Previously NUSAD users had to use the Structured Query Language (SQL) to access NUSAD data.

Substantial development occurred in 2001. The entire database underwent a Quality Assurance and Quality Control (QA/QC) program to ensure database accuracy and integrity. The NUSAD Geographical Display Tool (GDT) was created. The GDT is a web-based ArcIMS[1] with Java-applets GUI that allows users to

[1] Commercially available geographical information system produced by Environmental Science Research Incorporation (ESRI)

interact with NUSAD data on a geographical background (maps). Finally, a list of US radioactive material (RAM) license holders was added to the database.

This section begins with a description of current content of the database and a description of the QA/QC program. Next, the NUSAD DET is discussed. The section concludes with a description of the NUSAD GDT.

NUSAD Description

The content of NUSAD has evolved continuously since 1998 and it is anticipated that the database content will continue to evolve over the next several years. The current state of NUSAD will be described here. NUSAD contains three broad classes of data: assets, sources, and geographical. Table 1 summarizes the types of data currently contained in NUSAD. Table 1 also shows the reference in which the majority of the data for each type came from. However, in most cases the data were also cross-referenced and/or supplemented with other data sources. Information on each reference is included in the database, such as the title, publication details, author's name, and how its data were used in NUSAD.

Table 1: Data Contained in NUSAD

Class	Type	Area	Major Reference
Asset	International Monitoring System (IMS) stations	World	CTBT Treaty and Working Group B publications
	Collateral monitoring stations	World	Appendix F and Prototype International Data Centre (PIDC) database
	Direct radiation stations	World	Miscellaneous
Source	Nuclear power reactors	World	International Atomic Energy Agency's (IAEA) Power Reactor Information System (PRIS)
	Research reactors and government facilities	US	US Department of Energy
	Radioactive Material (RAM) License holders	US	US Nuclear Regulatory Commission and individual states governing nuclear organizations
	Research reactors and other radiation handling facilities	World	IAEA
	Past nuclear explosions	World	PIDC database
Geographical	Countries, regions, and states	World	Central Intelligence Agency's (CIA) World Factbook 2000
	Cities	World	United Nation's (UN) Demographic Yearbook 1995
	Country borders and geographical features (*e.g.*, rivers, lakes)	World	Libraries included with ArcIMS

An asset is any device that can detect radionuclides. The three types of assets are International Monitoring System (IMS) stations, collateral stations, and direct radiation stations. The IMS stations consist of the 79 particulate and 40 xenon radionuclide stations as defined in the Comprehensive Nuclear-Test-Ban Treaty (CTBT). The status of each station (planned or operational) is updated as needed. Collateral monitoring stations consist of atmospheric monitoring stations not included in the IMS network in which data could be obtained to supplement the IMS station data. An example of a collateral station is a station in the Center of Slovak Radiation Monitoring Network. Direct radiation stations record the absolute magnitude of radiation

present at a site. They do not differentiate between the type of radiation, and, more importantly, the type of radionuclides present. An example of a direct radiation station is a station in the Neighborhood Environmental Watch Network (NEWNET) operated by Los Alamos National Laboratory. Pertinent information regarding each asset is recorded in the database including the station's name, location (address, latitude, longitude, and elevation), sensor type and design, point of contact information, data format, and how to obtain data from the station.

A source is any facility that could potentially release radionuclides. Table 2 lists the types of sources currently included in NUSAD. Data for nuclear power plants predominantly came from the Power Reactor Information System (PRIS) maintained by the International Atomic Energy Agency (IAEA). Data for other nuclear facilities come from a variety of references summarized in Table 1. NUSAD also contains a list of RAM license holders within the US. These data come from each state's governing nuclear organization and the US Nuclear Regulatory Commission (NRC). Pertinent information regarding each source is recorded in the database including the source's name, location, point of contact information, organization(s) responsible for maintaining the source, and the types of nuclides potentially emitted from the source. Additional information is recorded for nuclear reactors including design type, power capacity, and information pertaining to the reactor history (*e.g.*, criticality date).

Table 2: NUSAD Source Types

Code	Source Type
NPP	Nuclear power plant
NRF	Nuclear research facility
KTS	Known nuclear test site
PTS	Potential nuclear test site
FRP	Fuel reprocessing facility
UEF	Uranium enrichment facility
WFP	Weapon fabrication plant
FFP	Fuel fabrication plant
NWL	Nuclear weapons lab
RPF	Radioisotope production facility
NMF	Nuclear medical facility
FSF	Fuel storage facility
RAM	Other radioactive material license

Because the NUSAD data is to be displayed on maps, the database must also contain geographical data. The majority of geographical features (*e.g.*, rivers) and country borders came from the geographic data provided with ArcIMS. These data are provided in shapefile[2] format and are not technically part of the Oracle component of NUSAD but are displayed with the NUSAD data in the GDT. Additional data were required to fill gaps in the ArcIMS libraries. These data are regions, countries, states, and cities. The city data contains location and population. The references for the geographical data are given in Table 1.

The data contained in NUSAD must be accurate and beyond reproach in order for it to be considered a reliable source of information. Hence, a QA/QC program was established to determine the reliability of a source of information (*i.e.*, a reference) and the accuracy of material entered into NUSAD. The execution of the QA/QC program follows the step process depicted in Figure 1. The material contained in NUSAD is drawn from various official and unofficial references. A reliability rating numbered five through one is assigned to each reference where a rating of five represents a very dependable reference and rating of one

[2] A shapefile is the format used by ESRI products to represent spatial data and is the de facto standard file format often used in geographical information systems.

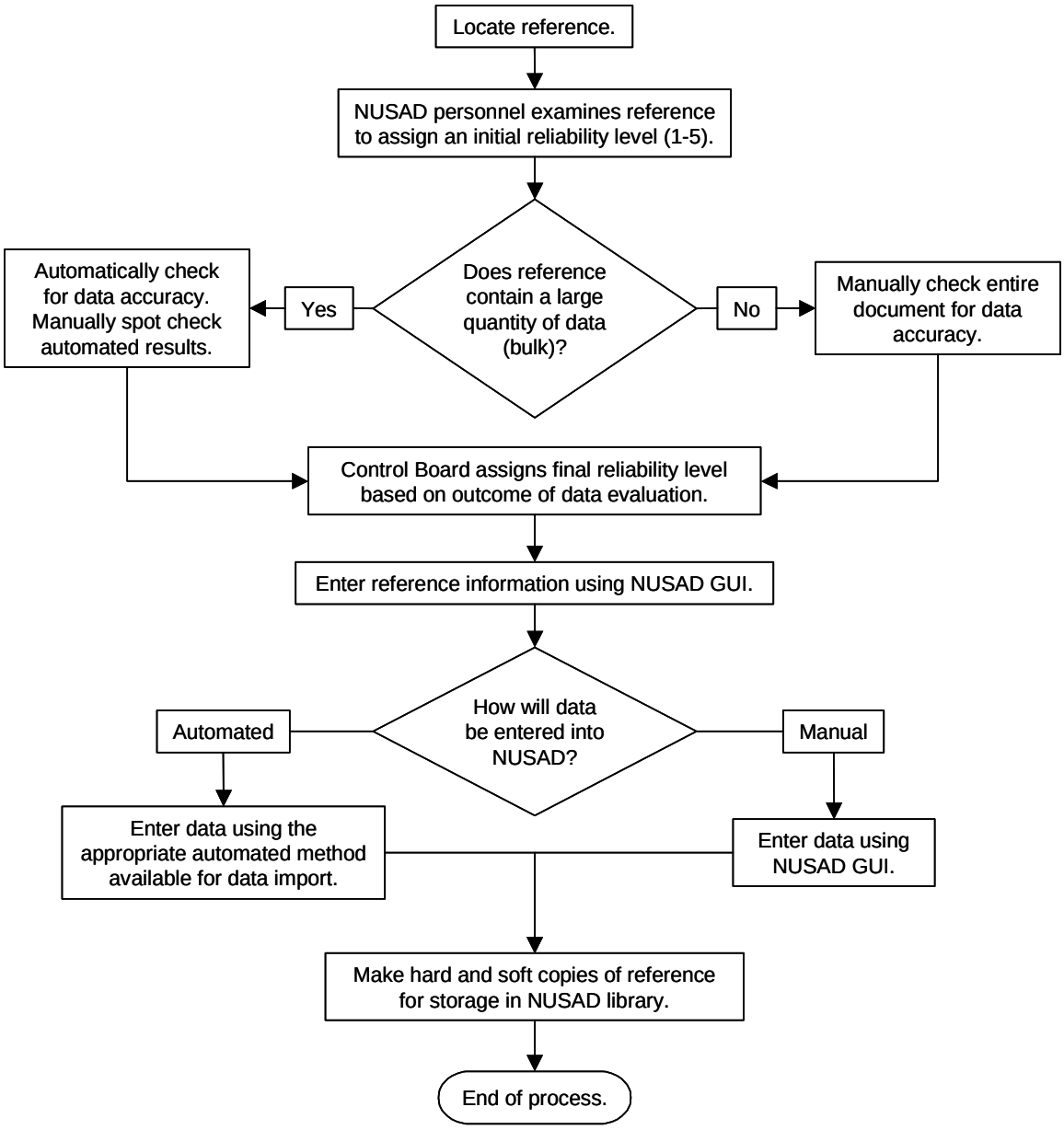

Figure 1: Flowchart of QA/QC Procedure

denotes an unreliable reference. Factors that affect the reliability rating include the consistency of their content with other works received, the date of publication, the publisher, the author, and the author's position on the topic discussed in the document. The ratings are stored in NUSAD and the NUSAD reference library.

The position (longitude and latitude) of most assets, sources, and cities are stored in NUSAD. Each position is also assigned a reliability rating that is based on reliability of its reference, the precision of the data, and how the position was obtained. Many of the source and asset references did not contain position data. In these cases the position had to be estimated from its address or nearest city. The position reliability rating informs a NUSAD user on the precision and accuracy of each position datum.

Data Entering Tool

The NUSAD data are stored in an Oracle database. When properly connected to the database all data can be viewed using SQL. However, this method requires substantial knowledge of SQL and the database schema. The DET was created to provide easier access to the data. It provides an interface to the database that allows users to easily enter, delete, modify, and view data. The DET is implemented as a Java application and thus may be run on any platform that supports the Java runtime environment. Supported platforms include Windows 2000/NT and most UNIX workstations. The NUSAD DET application may connect to the database via any workstation that has a connection to the Internet provided the user has proper authorization.

The NUSAD DET provides two main methods for viewing and editing data in the database: the browser window and the editor window. The browser window displays multiple data elements in a tabular format that provides an overview of specific database tables or table combinations. The data displayed in a browser window was determined to be the most pertinent representing that data type. The editor window is required to access all data related to a particular data element. A list of the possible browser windows is shown in Figure 2. Figure 3 shows the Source Browser Window. The editor windows can be accessed through the browser windows.

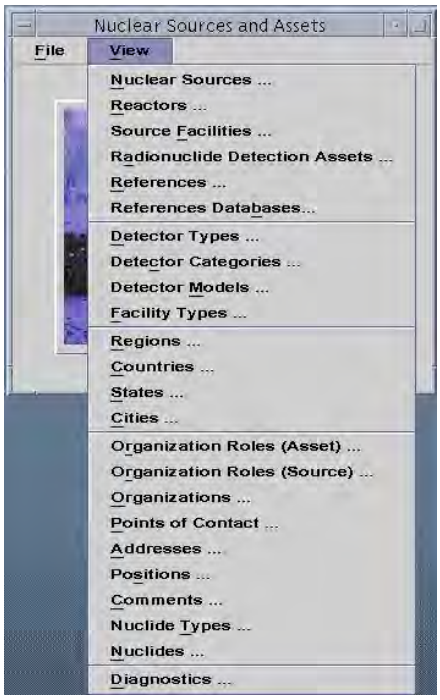

Figure 2: List of Browser Windows

The editor windows provide a more detailed view of the data for an individual entry in the database. The editor window uses a data entry format that allows users to edit all individual fields associated with a data

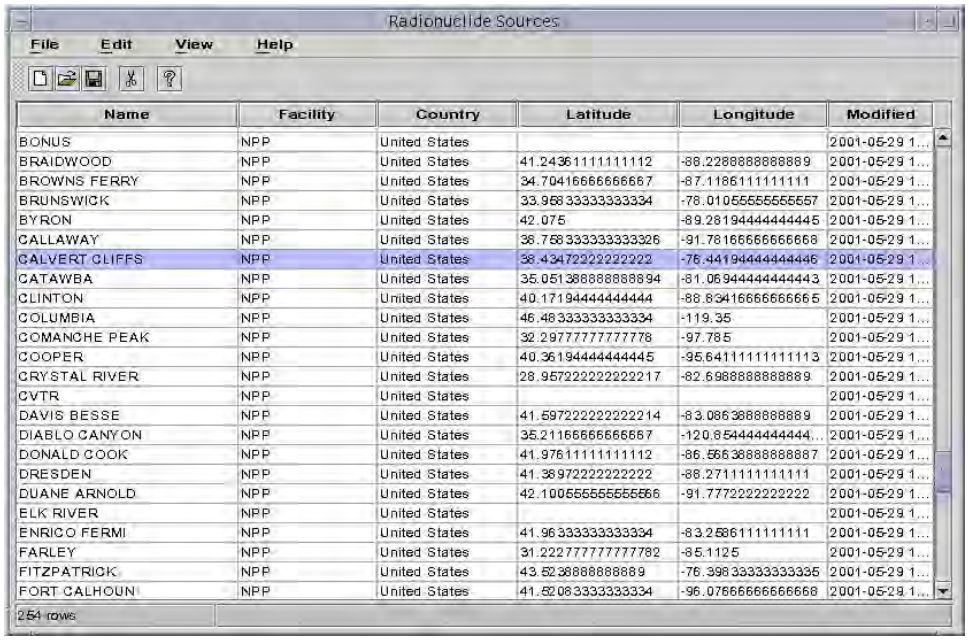

Name	Facility	Country	Latitude	Longitude	Modified
BONUS	NPP	United States			2001-05-29 1...
BRAIDWOOD	NPP	United States	41.24361111111112	-88.2288888888889	2001-05-29 1...
BROWNS FERRY	NPP	United States	34.70416666666667	-87.1186111111111	2001-05-29 1...
BRUNSWICK	NPP	United States	33.95833333333334	-78.01055555555557	2001-05-29 1...
BYRON	NPP	United States	42.075	-89.28194444444445	2001-05-29 1...
CALLAWAY	NPP	United States	38.758333333333326	-91.78166666666668	2001-05-29 1...
CALVERT CLIFFS	NPP	United States	38.43472222222222	-76.44194444444446	2001-05-29 1...
CATAWBA	NPP	United States	35.051388888888894	-81.05944444444443	2001-05-29 1...
CLINTON	NPP	United States	40.17194444444444	-88.83416666666665	2001-05-29 1...
COLUMBIA	NPP	United States	46.48333333333334	-119.35	2001-05-29 1...
COMANCHE PEAK	NPP	United States	32.29777777777778	-97.785	2001-05-29 1...
COOPER	NPP	United States	40.36194444444445	-95.64111111111113	2001-05-29 1...
CRYSTAL RIVER	NPP	United States	28.95722222222217	-82.6988888888889	2001-05-29 1...
CVTR	NPP	United States			2001-05-29 1...
DAVIS BESSE	NPP	United States	41.597222222222214	-83.08638888888889	2001-05-29 1...
DIABLO CANYON	NPP	United States	35.21166666666667	-120.854444444444...	2001-05-29 1...
DONALD COOK	NPP	United States	41.97611111111112	-86.56638888888887	2001-05-29 1...
DRESDEN	NPP	United States	41.38972222222222	-88.2711111111111	2001-05-29 1...
DUANE ARNOLD	NPP	United States	42.100555555555556	-91.7772222222222	2001-05-29 1...
ELK RIVER	NPP	United States			2001-05-29 1...
ENRICO FERMI	NPP	United States	41.96333333333334	-83.2586111111111	2001-05-29 1...
FARLEY	NPP	United States	31.222777777777782	-85.1125	2001-05-29 1...
FITZPATRICK	NPP	United States	43.52388888888889	-76.39833333333335	2001-05-29 1...
FORT CALHOUN	NPP	United States	41.52083333333334	-96.07666666666668	2001-05-29 1...

Figure 3: Source Browser Window

element. Using this window a user can also add new entries or delete existing entries from the database. An example of the Source Editor Window and the Reactor Editor Window is shown in Figures 4 and 5, respectively. Many of the sources, assets, and references contained in NUSAD have web pages associated with them not maintained as part of NUSAD. However, links to these web pages are stored in NUSAD. A user can open these web pages in their default browser from some editor windows.

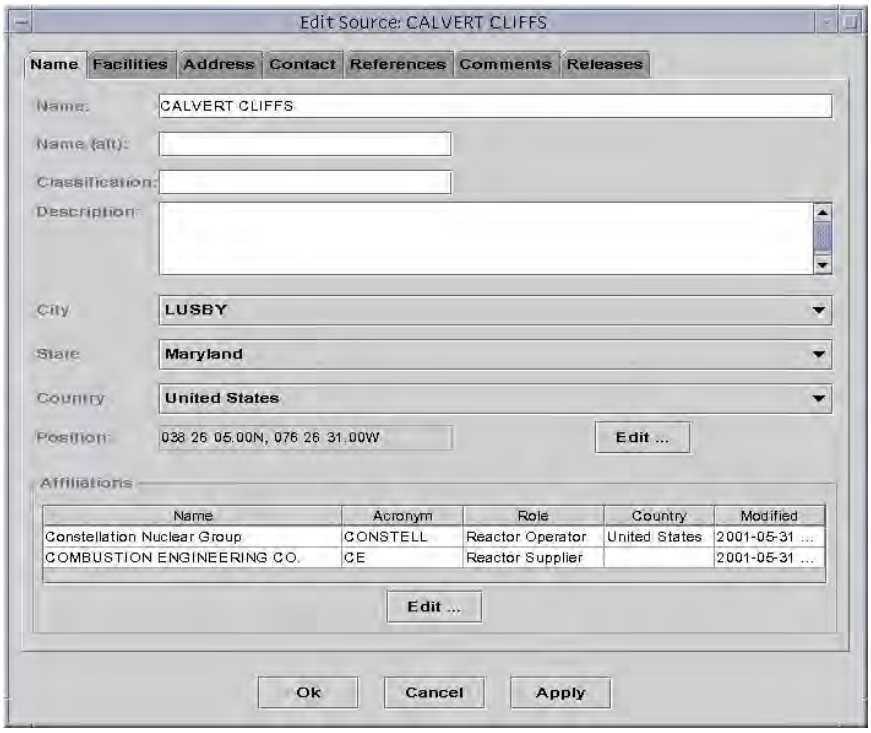

Figure 4: Source Editor Window

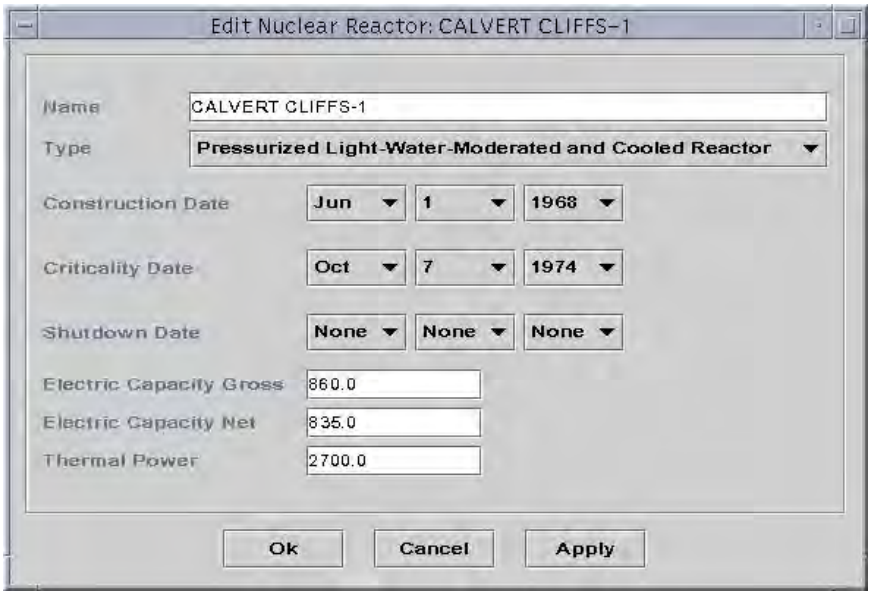

Figure 5: Reactor Editor Window

Geographical Display Tool

The GDT allows users to geographically visualize NUSAD data on configurable maps. The GDT consists of the ArcIMS geographical information system (GIS) coupled with NUSAD and specialized Java-based software. Users with Internet access and proper authorization can log onto the GDT server and download the GDT client. Using the GDT client running through Microsoft's Internet Explore (Netscape is not currently supported), the user can select the map configuration and the NUSAD data to be displayed. The user submits a request to the GDT server. The GDT server then processes this request and returns a shapefile containing the requested information. The GDT client displays the shapefile as a map. Figure 6 shows a world map with IMS stations and nuclear power plants displayed. All maps are downloaded in worldview. However, the user can manipulate the worldview by zooming in or by changing the baseline projection. Figure 7 shows map of northern Europe with IMS stations, collateral stations, nuclear power plants, and known nuclear test sites displayed.

All of the data types listed in Table 2 along with IMS stations, collateral stations, direct radiation stations, and certain geographical features can be display through the GDT. Each data type is displayed as a discrete symbol on the map. Combinations of certain data types can also be displayed as discrete symbols. Once a

Figure 6: NUSAD GDT – World View

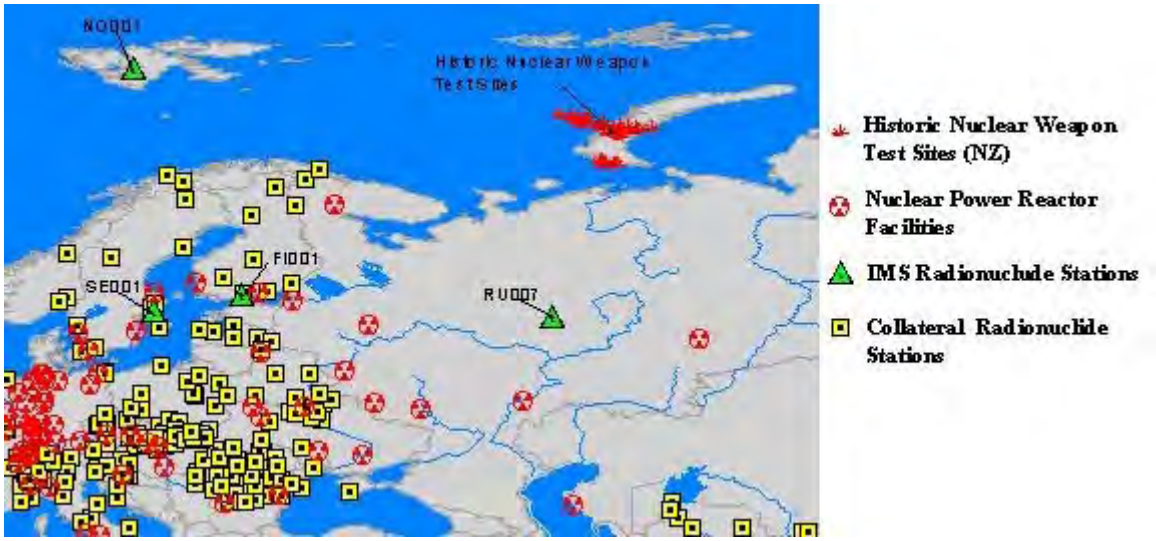

Figure 7: NUSAD GDT – Northern Europe View

data type is downloaded it can be turned on or off without downloading a new map. However, additional data will have to be downloaded if new data types are to be displayed.

The symbols used on the map contain hot-links so that a user can easily obtain additional information concerning the data. A mouse over a particular symbol displays the name of the data element. A click on the symbol provides the user with a selection of auxiliary windows that can be opened with an additional click. The auxiliary windows are a table viewer displaying pertinent information about the data element and the NUSAD DET[3] preloaded to the selected item.

CONCLUSIONS AND RECOMMENDATIONS

The Nuclear Sources and Assets Database (NUSAD) has been developed and is being maintained at the CMR. NUSAD is an Oracle-based database that contains information regarding nuclear sources and assets throughout the world. All data has undergone a QA/QC program to ensure accuracy and integrity. The NUSAD data can be accessed using the DET and the GDT. The DET is a Java-based GUI that provides an interface to the database allowing users to easily enter, delete, modify, and view all data in the database. The GDT is an ArcIMS-based GIS that allows users to geographically visualize NUSAD data on configurable maps. The DET and the GDT can be used to interact with NUSAD data from within CMR or via the Internet with proper authorization. NUSAD with the DET and the GDT can be used to assist in identifying the source of radionuclides found in data from the IDC and other institutions. It can also be used to identify additional assets to either confirm or contradict IMS station data.

Three recommendations will be made to enhance NUSAD. First, in order for the NUSAD to obtain maximum usefulness, its data must remain current. Certain data must periodically be investigated to ensure its accuracy. For example, several of the nuclear assets originally identified in 1998 have recently ceased operations; a static database would not reflect this change. Maintaining a quality database is an ongoing effort. Second, the quantity and quality of nuclear source data, excluding nuclear reactors, within the US is superior compared to data for the rest of the world. Additional work needs to be performed to identify and quantify worldwide nuclear sources other than nuclear reactors. Finally, as described in Seber (2000), databases also exist that are similar to NUSAD but orientated towards seismic events instead of radionuclide releases. It would be useful to merge these data sets (and data viewers) so that individuals or organizations researching the cause of a potential nuclear event can obtain all pertinent auxiliary information from one location and in one format.

REFERENCES

Seber, D., E. Sandvol, C. Sandvol, C. Brindisi, and M. Barazangi (2000), Global and Regional GIS Database Development in Support of CTBT Monitoring, Proceedings of 22nd Annual DOD/DOE Seismic Research Symposium, 12-15 September, 2000.

[3] Assuming the DET is installed locally on the user's computer.

REGIONAL GIS DATABASES IN SUPPORT OF CTBT MONITORING

Eric Sandvol, Dogan Seber, Christine Sandvol, Carrie Brindisi,
and Muawia Barazangi

Cornell University

Sponsored by Defense Threat Reduction Agency

Contract No. DTRA01-00-C-0209

ABSTRACT

To fully exploit the effectiveness of different monitoring technologies, a large knowledge base is being built. A database encompassing basic geologic information such as bedrock geology, faults, and geophysical information needs to be collected and combined for many different regions. The specific regions that our study focuses on are the United States and the Middle East and North Africa. The interest in the United States is to develop a database that can be used in the CTBT to guide on-site inspections. For the Middle East and North Africa, improvement in monitoring to advance CTBT compliance and verification is desired. The objective is to collect, evaluate, and analyze geological, geophysical, and seismic data in a Geographic Information System database; and deliver files containing such data to DTRA.

Currently, we have developed complete digital depth-to-Moho and depth-to-basement maps for the Middle East and North Africa region and evaluated them using 3-D gravity modeling. We have also made our first version of gridded depth-to-Moho and depth-to-basement maps of the United States. These data sets are now being evaluated and checked for accuracy and completeness. We have compiled an initial Lg attenuation map for the U.S. A first-order seismic velocity database consisting of Pn and Pg velocities in the U.S. is also being compiled along with geology and fault maps. Different types of databases are already collected and evaluated for the Middle East, North Africa, and the USA.

An important component of our research is to develop complete metadata for all collected data sets. As we develop and finalize a data set, we are also developing a complete FGDC standard metadata files to accompany the digital data sets. These metadata files will be delivered along with the data sets to the R & D testbed at the Center for Monitoring Research. Most of the Cornell databases can be accessed via our web site: http://atlas.geo.cornell.edu/

KEY WORDS: GIS, databases, Middle East, North Africa, USA

OBJECTIVE

Our main objective is to facilitate and enhance the capability of the U.S. National Data Center and the International Monitoring System to accurately locate, calibrate, and evaluate seismic events in the Middle East, North Africa, and the United States, by developing an interactive, diversified geophysical, geological, and geographical digital databases to assist in compliance with and verification of the Comprehensive Nuclear-Test-Ban Treaty (CTBT). We are also developing and improving the design of menu-driven, easy to use, custom-made tools as well as metadata for all developed data sets. The metadata will provide the necessary information about the quality, resolution, accuracy, and techniques that were used in collecting the original data. Another objective is to deliver results of the original research on crustal and upper mantle structures of the Middle East and North Africa, and the character of regional seismic wave propagation for the purpose of obtaining a better understanding of high-frequency wave propagation in this region.

RESEARCH ACCOMPLISHED

Our efforts in global and regional GIS database development in support of CTBT monitoring have been going on successfully. We have added new data sets to our digital library and revised our data access tools in the past year. We have updated a number of databases.

We have finalized the depth-to-basement map for the U.S. and nearby regions (Figure 1). This basement map is a compilation of 13 different depth-to-basement data sets. The maps that comprise these data set were collected and digitized at Cornell University and were later compiled by the ArcInfo command topogrid into one 5-km-resolution grid. A sediment depth map of the United States was clipped and used to 'fill in' this hole. The University of California at San Diego data were correlated for ocean depth using the Smith and Sandwell (1997) values. A polygon coverage was created of the area missing data and was used to clip the depth-to-sediment grid (10-km resolution). The clipped grid was then converted to a point coverage. The depth-to-sediment data were used in the absence of any other useful depth-to-basement data for these regions and was used in the gridding process to help constrain the data in these regions. When using this grid in these regions, users should be aware that these data are not depth-to-metamorphic basement and use it accordingly.

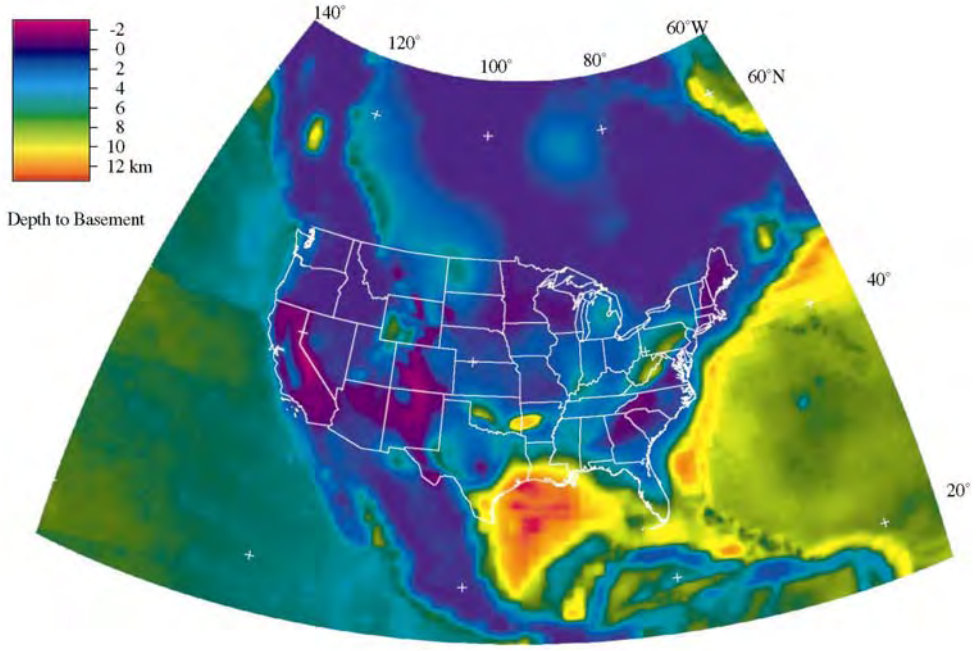

Figure 1. Depth to metamorphic basement for North America.

We have finalized a detailed Moho map for all of North America (Figure 2). An extensive literature search for estimates of Moho depth in the continental United States revealed 58 published papers. The authors had employed different methods to determine depth: seismic reflection and refraction, receiver functions, ray tracing, amplitude modulation, gravity, travel-time residuals, surface waves, refraction tomography, and PmP arrival times. Several methods were used to put the data into digital form. From papers that listed depths at point locations, the data were built as an ArcInfo point coverage. From papers that contained a depth profile, a point coverage was made of data from several locations. From papers that contained a contour map of Moho depth, the contours were scanned, digitized (using R2V software), built as an ArcInfo line coverage, and then converted to a point coverage using the ARCPOINT command in ArcInfo. In one case, we received from the authors (Das and Nolet, 1998) an ASCII file of the published grid and put it into ArcInfo grid format. To correct for elevation, we first created a long-wavelength topography grid by traversing a 3X3 low-pass filter

800 times over the United States Geological Survey gtopo30 grid. This smoothed topography grid was then subtracted from the Das and Nolet (1998) grid. We resampled it to 500 m cell size and converted it to a point coverage with the ArcInfo command, GRIDPOINT.

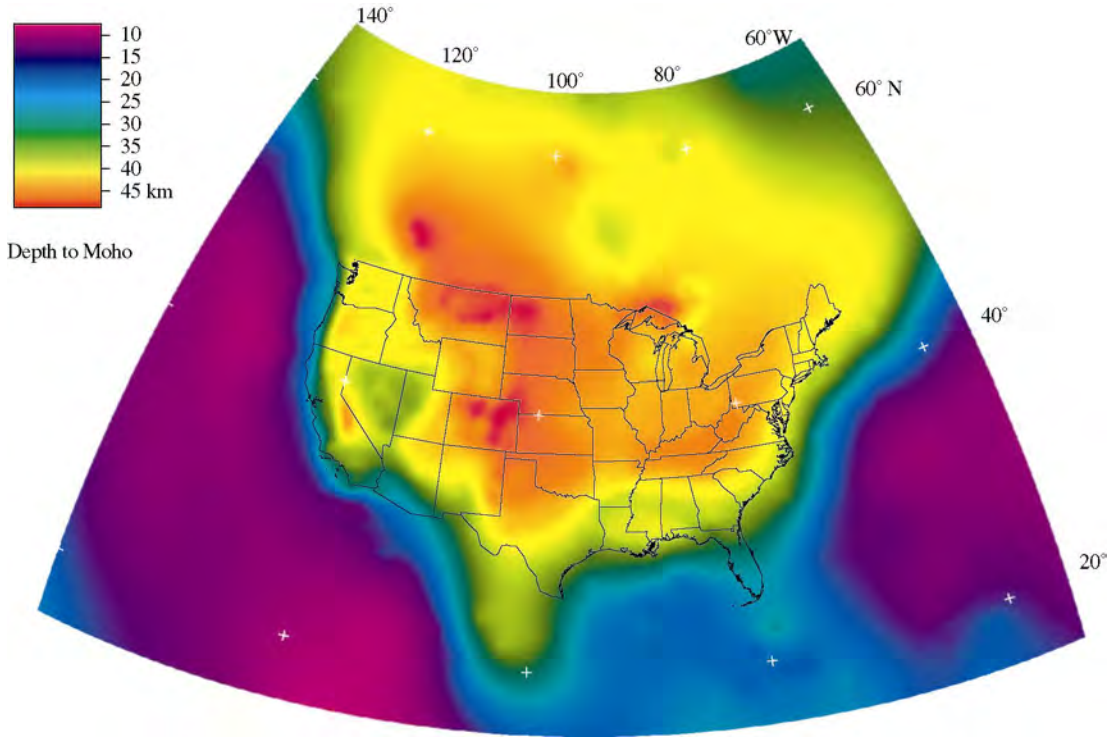

Figure 2. A depth to Moho map for North America. This map was created using a wide variety of techniques to image crustal thickness.

In the published papers, Moho depth was variously stated as depth from the surface and depth from sea level; we have chosen to use sea level as our datum. Where the published values were defined as depth from sea level, or where values were depth from surface but the surface elevation was within our error limits, no modification was necessary. Where correction was necessary, one of four different methods was employed: in coverages with few points, the elevation at each location was subtracted. In contour coverages for a region with a narrow range of elevations, the mean elevation was subtracted from all values. Where the contours covered a broad range of elevation, we gridded the contours, subtracted the smoothed USGS topography grid, and then re-contoured the resulting grid. The offshore coverage had many points; these were corrected outside of ArcInfo using global bathymetry data. Data from Soller et al. (1982) were used only where there were no other data. To do this, a polygon was drawn by eye around all the non-Soller data, and then Soller points (already depth-corrected) inside the polygon were erased. The data were smoothed to prevent high-frequency vertical relief due to mutually inconsistent datasets; we smoothed differences of less than 3 km.

In our efforts to compile a comprehensive Moho depth data set, we not only record the point and the corresponding depth value, but also record all other relevant information such as the author names, publication source, the method used in obtaining the Moho point. This is extremely useful for researchers as they will always want to know about the details, resolution, and accuracy of the final gridded Moho map. These original point/contour information will be critical in judging the accuracy of the Moho map of the U.S. Results of this work will be essential to improve event locations and IMS calibration for the USA.

In the Middle East and North Africa region we have improved our data coverage extent of the Moho and basement maps by collecting more data sets. We have now a complete crustal model for the entire Middle East and North Africa. This model is now being evaluated with independent data sources such as Bouguer gravity

data and three-dimensional gravity modeling to determine which regions have reliable depth-to-Moho values, and which regions might need additional revisions.

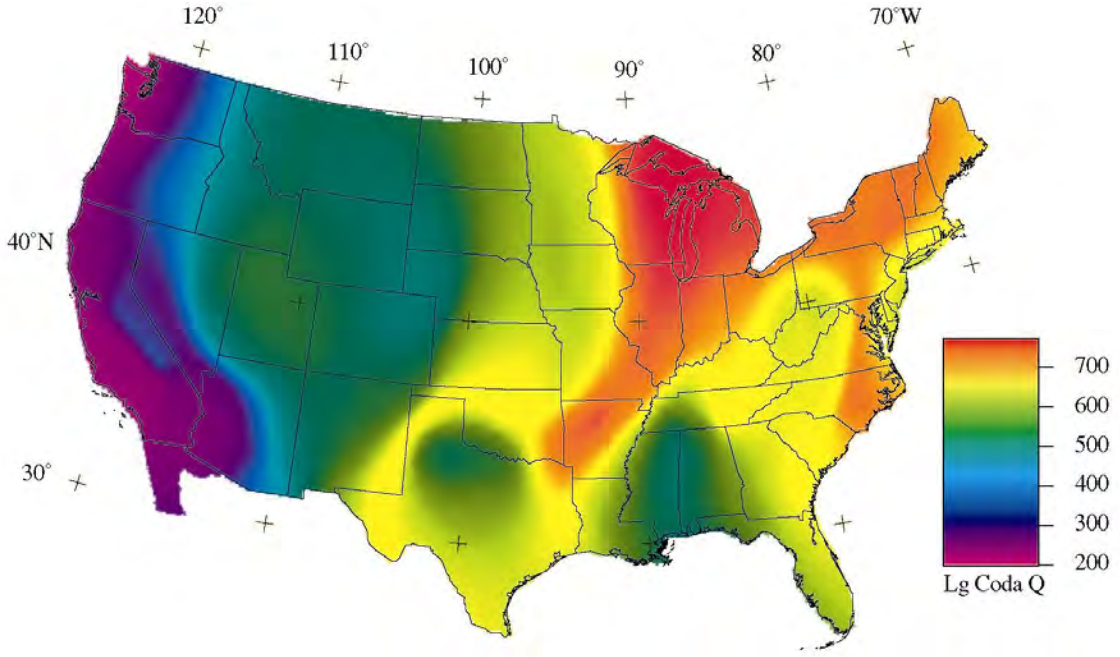

Figure 3. Lg coda Q map for the conterminous United States which were created using measurements taken from Baqer and Mitchell (1998).

In order to create a Lg coda Q map for the entire United States (Figure 3) we used 218 Lg coda Q measurements of Baqer and Mitchell (1998). For each pair, an arc connecting the event and station was created and given the 1 Hz Q value. Points were drawn along each arc and assigned the same Q value. Then a contour coverage was created, based on the point values. Finally, the contours were used to create a grid in Arc Info. The resulting map is an estimate of the spatial variation in Lg coda Q for the conterminous United States.

We are continuing to improve upon the Pn tomographic models for the Middle East. Our current model using approximately 3.5 years of phase data from Syria National Network, we have identified a very prominent low velocity zone that extends along most of the Dead Sea Fault System (DSFS) (Figure 4) that was suggested in early work (Hearn and Ni, 1994). The origin of this low-velocity zone is unclear as the most recent studies of the DSFS have concluded that it is not a simple rift. We are significantly expanding the available phase data in the region by picking phases from a number of temporary networks in the region including data from the Eastern Turkey Seismic Experiment.

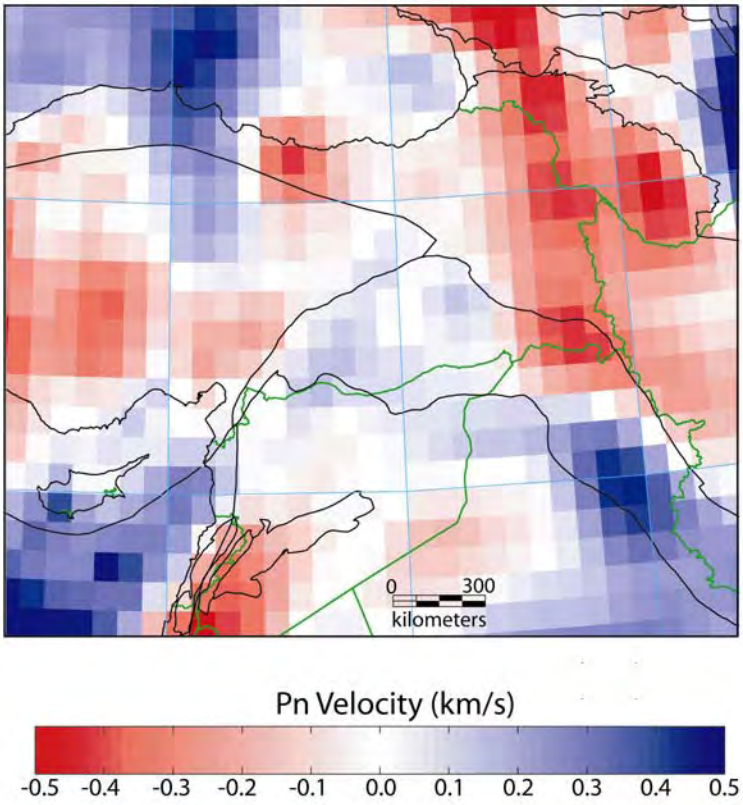

Figure 4. Pn tomographic model for the Northern Middle East.

CONCLUSIONS AND RECOMMENDATIONS

We have been collecting and organizing available seismological, geophysical, and geological data sets for the Middle East, North Africa and the United States into a comprehensive Geographic Information System (GIS). In addition to the GIS databases and tools, we have been developing a special World Wide Web (WWW) site for our databases. All the data sets in our GIS system are documented with a standard metadata format in order to explain the source and nature of the data, their resolution, and their accuracy. The developed system and its efficiency in using and analyzing information will help CTBT researchers and decision makers to fuse and integrate the results of the four established monitoring technologies (seismic, hydroacoustic, infrasound, and radionuclide) to reach a conclusion in a very short time. The system also significantly contributes to the better location and calibration of suspect events for any given region. This system will also help in On Site Inspection efforts.

We recommend that ongoing efforts to develop databases be expanded to include higher resolution data sets not only for the regions of the Middle East, North Africa, and the U.S., but also to most regions on Earth. Such developed information system and data sets will help to achieve better event locations with the required accuracy as stated in the CTBT.

REFERENCES

Baqer, S., and B. Mitchell (1998), Regional Variation of the LG Coda Q in the Continental Unites States and its Relation to Crustal Structure and Evolution, *Pure and appl. geophys.*, 153, 613-638.

Das, T., and G. Nolet (1998), Crustal Thickness Map of the Western United States by Partitioned Waveform Inversion, *Journ Geophys. Res*., 103, 30021-30038.

Hearn, T., and J. Ni (1994), Pn Velocities Beneath Continental Collision Zones: the Turkish-Iranian Plateau, *Geophys. J. Int.*, 117, 273-283.

Smith, W. H. F., and D. T. Sandwell (1997), Global Seafloor Application of Spatial Topography from Satellite Altimetry and Ship Depth Soundings, *Science*, 277 (5334), 1956-1962. (available at ftp://topex.ucsd.edu/pub/global_topo_2min/).

Soller, D. R., R. D. Ray, and R. D. Brown (1982), A New Global Crustal Thickness Map, *Tectonics*, 1, 125-149.

Acknowledgements

The National Nuclear Security Administration and the Defense Threat Reduction Agency gratefully acknowledge the important contributions of the following people for their work on the "Proceedings for the 23rd Seismic Research Review on Worldwide Monitoring of Nuclear Explosions."

Authors of papers for excellent research, good technical content and willing cooperation in electronic submission.

Ms. Leslie A. Casey (NNSA) for review and clearance of abstracts and papers related to NNSA contracts, and for providing NNSA financial support for the Proceedings.

Ms. Francesca C. Chavez (LANL) for administrative support.

Dr. Anton M. Dainty (DTRA) for review and clearance of abstracts and papers related to DTRA contracts.

Mr. Marvin D. Denny (NNSA/DICHROMA) for overall review of the abstracts and papers.

Ms. Mary L. Girven (SNL) for making everyone's job easier with web-based technology for abstract and paper submission, on-line review and approval tools, and creation of the master files for the hardcopy and CD versions of the Proceedings.

Mr. Michael Pankratz (LANL) for classification review of the compiled Proceedings.

Ms. Ruth N. Robichaud (LANL) for artwork for the CD label.

Dr. Stanley D. Ruppert (LLNL) for making and jacketing the CD copies.

Dr. Frederick R. Schult (AFTAC) for review and clearance of abstracts and papers related to AFTAC contracts.

Dr. N. Jill Warren (LANL) for technical editing of the papers and abstracts.

Dr. John (Jay) Zucca (LLNL), Dr. David B. Harris (LLNL), Mr. Preston B. Herrington (SNL), Mr. David P. Gallegos (SNL), Mr. J. Mark Harris (SNL), Dr. D. Craig Pearson (LANL), Dr. Steven R. Taylor (LANL), Dr. Ned A. Wogman (PNNL), Mr. Dale N. Anderson (PNNL) for a myriad of internal management reviews of DOE laboratory abstracts and papers.